Methods in Molecular Biology 2393

Springer Protocols

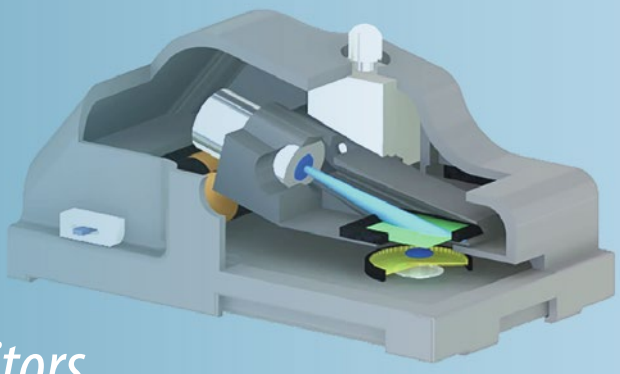

Miguel R. Ossandon
Houston Baker
Avraham Rasooly *Editors*

# Biomedical Engineering Technologies

## Volume 1

MOREMEDIA

Humana Press

# METHODS IN MOLECULAR BIOLOGY

*Series Editor*
**John M. Walker**
**School of Life and Medical Sciences**
**University of Hertfordshire**
**Hatfield, Hertfordshire, UK**

For further volumes:
http://www.springer.com/series/7651

For over 35 years, biological scientists have come to rely on the research protocols and methodologies in the critically acclaimed *Methods in Molecular Biology* series. The series was the first to introduce the step-by-step protocols approach that has become the standard in all biomedical protocol publishing. Each protocol is provided in readily-reproducible step-by-step fashion, opening with an introductory overview, a list of the materials and reagents needed to complete the experiment, and followed by a detailed procedure that is supported with a helpful notes section offering tips and tricks of the trade as well as troubleshooting advice. These hallmark features were introduced by series editor Dr. John Walker and constitute the key ingredient in each and every volume of the *Methods in Molecular Biology* series. Tested and trusted, comprehensive and reliable, all protocols from the series are indexed in PubMed.

# Biomedical Engineering Technologies

## Volume 1

Edited by

**Miguel R. Ossandon**

*Division of Cancer Treatment and Diagnosis, National Cancer Institute, NIH, Bethesda, Maryland, USA*

**Houston Baker and Avraham Rasooly**

*Division of Cancer Treatment and Diagnosis, National Cancer Institute, Rockville, Maryland, USA*

Humana Press

*Editors*
Miguel R. Ossandon
Division of Cancer Treatment and Diagnosis
National Cancer Institute, NIH
Bethesda, Maryland, USA

Houston Baker
Division of Cancer Treatment and Diagnosis
National Cancer Institute
Rockville, Maryland, USA

Avraham Rasooly
Division of Cancer Treatment and Diagnosis
National Cancer Institute
Rockville, Maryland, USA

ISSN 1064-3745 ISSN 1940-6029 (electronic)
Methods in Molecular Biology
ISBN 978-1-0716-1802-8 ISBN 978-1-0716-1803-5 (eBook)
https://doi.org/10.1007/978-1-0716-1803-5



This Humana imprint is published by the registered company Springer Science+Business Media, LLC, part of Springer Nature.
The registered company address is: 1 New York Plaza, New York, NY 10004, U.S.A.

# Dedication

This book is dedicated to my wife, Melanie Celeste Ossandon, and in the memory of my mother, Rosa Eliana Carrizo, and my brother, Ruben Alfredo Ossandon.

# Preface

This is the Third Edition of *Biosensors and Biodetection: Methods and Protocols* published in the Springer Protocols Methods in Molecular Biology series. Biosensing, bioengineering, and biomedical technologies are discussed from an experimental point of view alongside detailed protocols useful in developing similar devices. While the first (volumes 503–504) and second (volumes 1571–1572) editions of the Methods in Molecular Biology series focused on biosensor technologies, in this edition we expanded the scope of subjects to include non-sensor biomedical technologies.

This edition complements and broadens the previous editions by presenting new technologies not included in previous editions which are still relevant today. For example, the Kretschmann configuration for surface plasmon resonance (SPR) or the fabrication of various electrochemical electrodes is well described in the previous editions, and we refer the reader to the previous editions.

The third edition includes two volumes:

Volume 1 *Biosensors and Imaging Technologies* provides experimental protocols on biosensors and medical imaging technologies such as tomography, MRI, and NMR.

Volume 2 *Biomedical Technologies* is focused on biomedical technologies including molecular and cellular analytical methods, experimental new drug delivery approaches, guided surgery, implants, and tissue engineering.

## Biosensor and Biodetection Technologies

A biosensor is defined by the International Union of Pure and Applied Chemistry (IUPAC) as "*A device that uses specific biochemical reactions mediated by isolated enzymes, immunosystems, tissues, organelles or whole cells to detect chemical compounds usually by electrical, thermal or optical signals*" [1]. All biosensors are based on a two-component system:

1. Biological recognition element(s) (ligands) such as an enzyme, antibody, DNA, or cell that facilitates a specific binding or biochemical reaction with the target analyte. The ligand determines the specificity of the biosensor.
2. Signal conversion unit (transducer) which converts ligand binding into a measurable signal (e.g., electrical, optical, piezoelectric).

Dr. Leland C. Clark pioneered research on biosensors in the early 1960s and developed the "enzyme electrode" concept for glucose concentration measurement using the enzyme Glucose Oxidase (GOD) [2], thereby incorporating both ligand and transducer. Glucose monitoring is essential for diabetes patients. Even today the most common clinical biosensor technology for glucose analysis is the electrochemical detection method envisioned by Clark more than sixty years ago. Current glucose monitoring is performed using rapid point of care biosensors made possible through advances in electronics that have enabled sensor miniaturization and simple, rapid, and accurate analysis.

## Biosensing Modalities

1. *Direct (label-free) recognition sensors* in which the biological interaction is directly measured by the transducer (e.g., change of refraction index) without any enzymatic or biochemical assay.
2. *Indirect detection sensors* which rely on labeling utilizing secondary elements. The most commonly used secondary elements are enzymes (usually catalytic) and fluorescent tags.

## Ligands for Biosensors

Ligands are molecules that bind specifically with the target molecule to be detected. The most important properties of ligands are affinity and specificity. Of the various types of ligands used in biosensors, immunosensors—particularly antibodies—are the most common biosensor recognition element. Antibodies (Abs) are highly specific and versatile and bind strongly and stably to specific antigens. However, Ab ligands have limited long-term stability and are difficult to produce in large quantities for multi-target biosensor applications where many ligands are needed.

Other types of ligands such as aptamers and peptides are more suited to high-throughput screening and chemical synthesis. Aptamers are protein-binding nucleic acids (DNA or RNA) selected from random pools based on their ability to bind other molecules with high affinity. Peptides are another potentially important class of ligand suitable for high-throughput screening due to their ease of selection. However, the affinity of peptides is often lower than that of antibodies or aptamers, and peptides vary widely in structural stability and thermal sensitivity.

Volume 1 focused mainly on biosensor or imaging device transducers and applications. It includes four technologies (1) Optical Sensors, (2) Electrochemical Sensors, (3) Quartz Crystal Microbalance Sensors, and (4) Monitoring and Imaging Technologies. While the chapters address biological questions, the focus of this volume is the detection and analytical technologies used to answer the question.

1. *Optical-based detection* is very versatile and encompasses a broad array of technologies including direct, label-free, and indirect methods as discussed above. The most notable label-free modality is probably surface plasmon resonance (SPR), which enables real-time, label-free, and noninvasive detection. While in the previous edition we described SPR devices based on the Kretschmann prism configuration or Grating-coupled SPR sensors, in this edition we present localized surface plasmon resonance (LSPR) associated with metal nanostructures. Other optical label-free technologies described in Volume 1 include photonic crystals and waveguide interferometers. Fluorescence is the most widely used modality for indirect optical detection, especially for detection of multiple analytes using a wide array of fluorophores. These fluorophores could be coupled with numerous detection modalities including smart phones which enable point of care analysis. This edition provides protocols for several optical analytical modalities not addressed in the previous edition including spectrometry and spectroscopy.
2. *Electrochemical biosensors* are probably the most widely used biosensors for clinical applications due to their use for glucose monitoring by diabetes patients. Commercial

electrochemical biosensor devices are relatively low cost and widely available. The devices can be adapted for other applications by using assays generating glucose, such as the DNA-invertase assay, which catalyze the hydrolysis of sucrose into glucose which then can be measured by electrochemical glucose monitors. The chapters in this part provide protocols on diverse electrochemical biosensors including DNA generated electric current biosensor, on-chip impedimetric monitoring of bacterial viability and electrochemical aptamer-based sensors for molecular monitoring in situ in the living body, and other technologies.

3. *Quartz crystal microbalance (QCM)* encompasses a piezoelectric class of direct detection biosensors which are not widely used, probably because of their relative complexity. However, the technology has become more accessible in recent years. QCMs are very sensitive and work by measuring changes in frequency of a quartz crystal resonator produced by mass variations of bound analytes. The chapters in this part describe analysis of cancer cell detection and in vitro metabolic flux in living cells.
4. *Monitoring and imaging technologies* provides experimental protocols for several imaging modalities including MRI, NMR, tomography, and ultrasound imaging. These protocols address various aspects of imaging including imaging agents, computation (machine learning; and mixed models), and several tomography modalities including electrical impedance and bioluminescence tomography and protocols on magnetic resonance fingerprinting. Also discussed is an important imaging technology based on ultrasonic devices; this includes a wearable ultrasound sensor for monitoring respiratory behavior, a minimally invasive ultrasonic transducer for studying neuromodulation, and an acoustic angiography device which provides high-resolution, three-dimensional maps of microvasculature.

While recognizing the impossibility of describing the fast-moving field of biosensing in a single publication, this book presents descriptions of experimental methods for the basic types of biodetection technologies, including optical and electrochemical biosensors and imaging technologies. We hope to provide the reader a sense of the enormous importance and potential for these devices.

This book describes the basic types, designs, and applications of biosensors and imaging technologies from an experimental point of view. We have assembled manuscripts representing the major technologies in the field and have included enough technical information so that the reader can both understand the technology and carry out the experiments described.

The target audience for this book includes medical, engineering, and biomedical researchers who are developing biomedical technologies. Other target groups are biologists and clinicians who ultimately benefit from development and application of the technologies.

In addition to research scientists, the book may also be useful as a teaching tool for bioengineering, biomedical engineering, and biology faculty and students. To better represent the field, most topics are described in more than one chapter. The purpose of this redundancy is to bring several experimental approaches to each topic, to enable the reader to choose an appropriate design, to combine elements from different designs in order to better standardize methodologies, and to provide readers more detailed protocols.

***Bethesda, MD, USA*** ***Miguel R. Ossandon***
***Rockville, MD, USA*** ***Houston Baker***
***Rockville, MD, USA*** ***Avraham Rasooly***

## References

1. International Union of Pure and Applied Chemistry (1992) IUPAC compendium of chemical terminology, 2nd edn (1997). International Union of Pure and Applied Chemistry, Research Triangle Park, NC
2. Clark LC Jr, Lyons C (1962) Electrode systems for continuous monitoring in cardiovascular surgery. Ann N Y Acad Sci 102:29–45

# Contents

# Contributors


Khalil Abnous • *Pharmaceutical Research Center, Pharmaceutical Technology Institute, Mashhad University of Medical Sciences, Mashhad, Iran; Department of Medicinal Chemistry, School of Pharmacy, Mashhad University of Medical Sciences, Mashhad, Iran*

Semra Akgönüllü • *Department of Chemistry, Hacettepe University, Ankara, Turkey*

Mona Alibolandi • *Pharmaceutical Research Center, Pharmaceutical Technology Institute, Mashhad University of Medical Sciences, Mashhad, Iran; Department of Pharmaceutical Biotechnology, School of Pharmacy, Mashhad University of Medical Sciences, Mashhad, Iran*

Matthew Allen • *Center for Systems Biology, Massachusetts General Hospital, Boston, MA, USA*

Cortney N. Armitano-Lago • *Department of Exercise and Sport Science, University of North Carolina at Chapel Hill, Chapel Hill, NC, USA*

Netzahualcóyotl Arroyo-Currás • *Department of Pharmacology and Molecular Sciences, Johns Hopkins University School of Medicine, Baltimore, MD, USA*

Miquel Avella-Oliver • *Instituto Interuniversitario de Investigación de Reconocimiento Molecular y Desarrollo Tecnológico (IDM), Universitat Politècnica de València, Universitat de València, Valencia, Spain; Departamento de Química, Universitat Politècnica de València, Valencia, Spain*

Ambika G. Bajpayee • *Department of Bioengineering, Northeastern University, Boston, MA, USA; Department of Mechanical Engineering, Northeastern University, Boston, MA, USA*

Monireh Bakhshpour • *Department of Chemistry, Hacettepe University, Ankara, Turkey*

Jayden Charles Booth • *School of Electrical, Computer and Energy Engineering, Arizona State University, Tempe, AZ, USA*

Nick Bottenus • *Department of Biomedical Engineering, Duke University, Durham, NC, USA; Department of Mechanical Engineering, University of Colorado Boulder, Boulder, CO, USA*

Mathilde Bouché • *Department of Radiology, University of Pennsylvania, Philadelphia, PA, USA*

Xiangli Bu • *College of Electrical and Information Engineering, Nanjing University of Aeronautics and Astronautics, Nanjing, China*

Derrick Butler • *Department of Electrical Engineering, The Pennsylvania State University, University Park, PA, USA; Materials Research Institute, The Pennsylvania State University, University Park, PA, USA*

Cesar M. Castro • *Center for Systems Biology, Massachusetts General Hospital, Boston, MA, USA; Cancer Center, Massachusetts General Hospital, Boston, MA, USA*

Junseok Chae • *School of Electrical, Computer and Energy Engineering, Arizona State University, Tempe, AZ, USA*

Su-youne Chang • *Department of Neurologic Surgery, Mayo Clinic, Rochester, MN, USA; Department of Physiology and Biomedical Engineering, Mayo Clinic, Rochester, MN, USA*

Ang Chen • *School of Electrical, Computer and Energy Engineering, Arizona State University, Tempe, AZ, USA*

Cassidy Chen • *IBIS Lab, Department of Chemical and Biomedical Engineering, University of South Florida, Tampa, FL, USA*

Monica Cheng • *Department of Radiology and Imaging Sciences, Indiana University School of Medicine, Indianapolis, IN, USA*
Zetao Chen • *Biosensor National Special Laboratory, Key Laboratory for Biomedical Engineering of Education Ministry, Department of Biomedical Engineering, Zhejiang University, Hangzhou, People's Republic of China*
Ashutosh Chilkoti • *Department of Biomedical Engineering, Pratt School of Engineering, Duke University, Durham, NC, USA*
Daniel T. Chiu • *Department of Chemistry, University of Washington, Seattle, WA, USA*
Gihoon Choi • *Department of Electrical Engineering, Pennsylvania State University, University Park, PA, USA*
Paolo Cifani • *Memorial Sloan Kettering Cancer Center, New York, NY, USA*
Kelly Cohen • *Department of Aerospace Engineering, University of Cincinnati, Cincinnati, OH, USA*
Marshall Colville • *Graduate Field of Biophysics, Cornell University, Ithaca, NY, USA*
Kirstin Cook • *Department of Neurosurgery, University of California, Los Angeles, Los Angeles, CA, USA*
David P. Cormode • *Department of Radiology, University of Pennsylvania, Philadelphia, PA, USA; Department of Bioengineering, School of Engineering and Applied Sciences, University of Pennsylvania, Philadelphia, PA, USA*
Philippe Dauphin-Ducharme • *Département de chimie, Université de Sherbrooke, Sherbrooke, QC, Canada*
Paul A. Dayton • *Joint Department of Biomedical Engineering, University of North Carolina at Chapel Hill and North Carolina State University, Chapel Hill, NC, USA*
Hamid Dehghani • *School of Computer Science, University of Birmingham, Birmingham, UK*
Zijian Deng • *Department of Radiation Oncology and Molecular Radiation Sciences, Johns Hopkins University, Baltimore, MD, USA; Department of Radiation Oncology, University of Texas Southwestern Medical Center, Dallas, TX, USA*
Adil Denizli • *Department of Chemistry, Hacettepe University, Ankara, Turkey*
Paula Do • *Western Regional Research Center, Foodborne Toxin Detection and Prevention Research Unit, Agricultural Research Service, United States Department of Agriculture, Albany, CA, USA*
Aida Ebrahimi • *Department of Electrical Engineering, The Pennsylvania State University, University Park, PA, USA; Materials Research Institute, The Pennsylvania State University, University Park, PA, USA; Department of Materials Science and Engineering, The Pennsylvania State University, University Park, PA, USA; Department of Biomedical Engineering, The Pennsylvania State University, University Park, PA, USA*
Arzum Erdem • *Faculty of Pharmacy, Ege University, Izmir, Turkey*
Michael J. Evans • *Department of Radiology and Biomedical Imaging, University of California San Francisco, San Francisco, CA, USA; Helen Diller Family Comprehensive Cancer Center, University of California San Francisco, San Francisco, CA, USA; Department of Pharmaceutical Chemistry, University of California San Francisco, San Francisco, CA, USA*
Cassio M. Fontes • *Department of Biomedical Engineering, Pratt School of Engineering, Duke University, Durham, NC, USA*
Qiaoqiang Gan • *Department of Electrical Engineering, University at Buffalo, The State University of New York, Buffalo, NY, USA*

Bilwaj Gaonkar • *Department of Neurosurgery, University of California, Los Angeles, Los Angeles, USA*
Rex E. Gerald II • *Department of Electrical and Computer Engineering, Missouri University of Science and Technology, Rolla, MO, USA*
Mark A. Green • *Department of Radiology and Imaging Sciences, Indiana University School of Medicine, Indianapolis, IN, USA*
Weihua Guan • *Department of Biomedical Engineering, Pennsylvania State University, University Park, PA, USA*
Andrew Joshua Halton • *School of Electrical, Computer and Energy Engineering, Arizona State University, Tempe, AZ, USA*
Jacob T. Heggestad • *Department of Biomedical Engineering, Pratt School of Engineering, Duke University, Durham, NC, USA*
Bradley Hernlem • *Western Regional Research Center, Foodborne Toxin Detection and Prevention Research Unit, Agricultural Research Service, United States Department of Agriculture, Albany, CA, USA*
Todd Hollon • *NYU Langone Neurosurgery Associates, New York, NY, USA*
Jie Huang • *Department of Electrical and Computer Engineering, Missouri University of Science and Technology, Rolla, MO, USA*
Angus M. Hucknall • *Department of Biomedical Engineering, Pratt School of Engineering, Duke University, Durham, NC, USA*
Cesar S. Huertas • *Integrated Photonics and Applications Centre, School of Engineering, RMIT University, Melbourne, VIC, Australia*
Gary D. Hutchins • *Department of Radiology and Imaging Sciences, Indiana University School of Medicine, Indianapolis, IN, USA*
Hyungsoon Im • *Center for Systems Biology, Massachusetts General Hospital, Boston, MA, USA; Department of Radiology, Massachusetts General Hospital, Boston, MA, USA*
Iulian Iordachita • *Laboratory for Computational Sensing and Robotics, Johns Hopkins University, Baltimore, MD, USA*
Seyed Hamid Jalalian • *Students Research Committee, Department of Pharmaceutical Nanotechnology, School of Pharmacy, Mashhad University of Medical Sciences, Mashhad, Iran; Academic Center for Education, Culture and Research (ACECR)-Mashhad Branch, Mashhad, Iran*
Sangmoo Jeong • *Memorial Sloan Kettering Cancer Center, New York, NY, USA*
Daizong Ji • *Biosensor National Special Laboratory, Key Laboratory for Biomedical Engineering of Education Ministry, Department of Biomedical Engineering, Zhejiang University, Hangzhou, People's Republic of China*
Daniel Y. Joh • *Department of Biomedical Engineering, Pratt School of Engineering, Duke University, Durham, NC, USA*
Konstantinos Kalpakis • *Department of Computer Science and Electrical Engineering, University of Maryland Baltimore County, Baltimore, MD, USA*
Wenjie Kang • *Joint International Research Laboratory of Animal Health and Food Safety and Single Molecule Nanometry Laboratory (Sinmolab), Nanjing Agricultural University, Nanjing, China*
Alex Kentsis • *Memorial Sloan Kettering Cancer Center, New York, NY, USA*
Kayvan R. Keshari • *Memorial Sloan Kettering Cancer Center, New York, NY, USA*
Adam W. Kiefer • *Department of Exercise and Sport Science, University of North Carolina at Chapel Hill, Chapel Hill, NC, USA*

Eun Sok Kim • *Department of Electrical and Computer Engineering, University of Southern California, Los Angeles, CA, USA*
Kihwan Kim • *Department of Biomedical Engineering, Case Western Reserve University, Cleveland, OH, USA*
Min Ku Kim • *Weldon School of Biomedical Engineering, Purdue University, West Lafayette, IN, USA*
David S. Kinnamon • *Department of Biomedical Engineering, Pratt School of Engineering, Duke University, Durham, NC, USA*
Tod E. Kippin • *Neuroscience Research Institute, UC Santa Barbara, Santa Barbara, CA, USA*
Tomasz Kobiela • *Laboratory of Biomolecular Interactions Studies, Chair of Drug and Cosmetics Biotechnology, Faculty of Chemistry, Warsaw University of Technology, Warsaw, Poland*
Seda Koyun • *Department of Chemistry, Hacettepe University, Ankara, Turkey*
Jason E. Kreutz • *Department of Chemistry, University of Washington, Seattle, WA, USA*
Laura M. Lechuga • *Nanobiosensors and Bioanalytical Applications Group, Catalan Institute of Nanoscience and Nanotechnology (ICN2), CSIC, BIST and CIBER-BBN, Bellaterra, Barcelona, Spain*
Chi Hwan Lee • *Weldon School of Biomedical Engineering, Purdue University, West Lafayette, IN, USA; Department of Speech, Language, and Hearing Sciences, Purdue University, West Lafayette, IN, USA; School of Mechanical Engineering, Purdue University, West Lafayette, IN, USA*
Hakho Lee • *Center for Systems Biology, Massachusetts General Hospital, Boston, MA, USA; Department of Radiology, Massachusetts General Hospital, Boston, MA, USA*
Jiahao Li • *Joint International Research Laboratory of Animal Health and Food Safety and Single Molecule Nanometry Laboratory (Sinmolab), Nanjing Agricultural University, Nanjing, China*
Shuang Li • *Biosensor National Special Laboratory, Key Laboratory for Biomedical Engineering of Education Ministry, Department of Biomedical Engineering, Zhejiang University, Hangzhou, People's Republic of China*
Xiaoqing Li • *College of Chemistry and Chemical Engineering, Central South University, Changsha, Hunan, People's Republic of China*
Runli Liang • *Biodesign Center for Bioelectronics and Biosensors, Arizona State University, Tempe, AZ, USA; School of Electrical, Computer and Energy Engineering, Arizona State University, Tempe, AZ, USA*
Michael Lim • *Department of Neurosurgery, Johns Hopkins University, Baltimore, MD, USA; Department of Neurosurgery, Stanford University, Stanford, CA, USA*
Fei Liu • *Joint International Research Laboratory of Animal Health and Food Safety and Single Molecule Nanometry Laboratory (Sinmolab), Nanjing Agricultural University, Nanjing, China*
Jason Liu • *Department of Biomedical Engineering, Pratt School of Engineering, Duke University, Durham, NC, USA*
Jing Liu • *Joint International Research Laboratory of Animal Health and Food Safety and Single Molecule Nanometry Laboratory (Sinmolab), Nanjing Agricultural University, Nanjing, China*
Lei Liu • *Biosensor National Special Laboratory, Key Laboratory for Biomedical Engineering of Education Ministry, Department of Biomedical Engineering, Zhejiang University, Hangzhou, People's Republic of China*

Qingjun Liu • *Biosensor National Special Laboratory, Key Laboratory for Biomedical Engineering of Education Ministry, Department of Biomedical Engineering, Zhejiang University, Hangzhou, People's Republic of China*
Shiyi Liu • *School of Electrical, Computer and Energy Engineering, Arizona State University, Tempe, AZ, USA*
Sze Shin Low • *Biosensor National Special Laboratory, Key Laboratory for Biomedical Engineering of Education Ministry, Department of Biomedical Engineering, Zhejiang University, Hangzhou, People's Republic of China*
Yanli Lu • *Biosensor National Special Laboratory, Key Laboratory for Biomedical Engineering of Education Ministry, Department of Biomedical Engineering, Zhejiang University, Hangzhou, People's Republic of China*
Guangzhong Ma • *Biodesign Center for Bioelectronics and Biosensors, Arizona State University, Tempe, AZ, USA*
Ryan MacPherson • *Department of Exercise and Sport Science, University of North Carolina at Chapel Hill, Chapel Hill, NC, USA*
Luke Macyszyn • *Department of Neurosurgery, University of California, Los Angeles, Los Angeles, CA, USA*
Georgia A. Malandraki • *Weldon School of Biomedical Engineering, Purdue University, West Lafayette, IN, USA; Department of Speech, Language, and Hearing Sciences, Purdue University, West Lafayette, IN, USA*
Ángel Maquieira • *Instituto Interuniversitario de Investigación de Reconocimiento Molecular y Desarrollo Tecnológico (IDM), Universitat Politècnica de València, Universitat de València, Valencia, Spain; Departamento de Química, Universitat Politècnica de València, Valencia, Spain*
Carla J. Mathias • *Department of Radiology and Imaging Sciences, Indiana University School of Medicine, Indianapolis, IN, USA*
Xueling Meng • *School of Electrical, Computer and Energy Engineering, Arizona State University, Tempe, AZ, USA*
R. Michael van Dam • *Crump Institute for Molecular Imaging, University of California Los Angeles, Los Angeles, CA, USA; Department of Molecular and Medical Pharmacology, University of California Los Angeles, Los Angeles, CA, USA; Bioengineering Department, University of California Los Angeles, Los Angeles, CA, USA*
Chase Miller • *IBIS Lab, Department of Chemical and Biomedical Engineering, University of South Florida, Tampa, FL, USA*
Jouha Min • *Center for Systems Biology, Massachusetts General Hospital, Boston, MA, USA*
John H. Molinski • *Thayer School of Engineering Investigator, Dartmouth-Hitchcock Medical Center, Lebanon, NH, USA*
Jennifer L. Mueller • *Department of Mathematics and School of Biomedical Engineering, Colorado State University, Fort Collins, CO, USA*
Isabel G. Newsome • *Joint Department of Biomedical Engineering, University of North Carolina at Chapel Hill and North Carolina State University, Chapel Hill, NC, USA*
David Y. Oh • *Division of Hematology/Oncology, Department of Medicine, University of California San Francisco, San Francisco, CA, USA; Helen Diller Family Comprehensive Cancer Center, University of California San Francisco, San Francisco, CA, USA*
Cordelia Orillac • *NYU Langone Neurosurgery Associates, New York, NY, USA*
Daniel A. Orringer • *NYU Langone Neurosurgery Associates, New York, NY, USA*
Miguel R. Ossandon • *National Cancer Institute, Rockville, MD, USA*

Aydogan Ozcan • *Electrical and Computer Engineering and Bioengineering Departments, Henry Samueli School of Engineering and Applied Science, University of California, Los Angeles, Los Angeles, CA, USA*

Timothy J. Palinski • *Thayer School of Engineering Investigator, Dartmouth-Hitchcock Medical Center, Lebanon, NH, USA*

Heun Park • *Weldon School of Biomedical Engineering, Purdue University, West Lafayette, IN, USA*

Sangwoo Park • *Graduate Field of Biophysics, Cornell University, Ithaca, NY, USA*

Matthew Paszek • *Graduate Field of Biophysics, Cornell University, Ithaca, NY, USA; Robert Frederick Smith School of Chemical and Biomolecular Engineering, Cornell University, Ithaca, NY, USA; Field of Biomedical Engineering, Cornell University, Ithaca, NY, USA; Kavli Institute for Nanoscale Science, Cornell University, Ithaca, NY, USA*

Dhananjay S. Phatak • *Department of Computer Science and Electrical Engineering, University of Maryland Baltimore County, Baltimore, MD, USA*

Ayse Kevser Piskin • *Medical Biochemistry Department, Hacettepe University, Ankara, Turkey*

Kevin W. Plaxco • *Center for Bioengineering, UC Santa Barbara, Santa Barbara, CA, USA; Department of Chemistry and Biochemistry, UC Santa Barbara, Santa Barbara, CA, USA*

Kyle L. Ploense • *Center for Bioengineering, UC Santa Barbara, Santa Barbara, CA, USA*

Rosa Puchades • *Instituto Interuniversitario de Investigación de Reconocimiento Molecular y Desarrollo Tecnológico (IDM), Universitat Politècnica de València, Universitat de València, Valencia, Spain; Departamento de Química, Universitat Politècnica de València, Valencia, Spain*

Anna Pyayt • *IBIS Lab, Department of Chemical and Biomedical Engineering, University of South Florida, Tampa, FL, USA*

Mohammad Ramezani • *Pharmaceutical Research Center, Pharmaceutical Technology Institute, Mashhad University of Medical Sciences, Mashhad, Iran; Department of Pharmaceutical Biotechnology, School of Pharmacy, Mashhad University of Medical Sciences, Mashhad, Iran*

Avraham Rasooly • *National Cancer Institute, National Institutes of Health, Rockville, MD, USA*

Reuven Rasooly • *Western Regional Research Center, Foodborne Toxin Detection and Prevention Research Unit, Agricultural Research Service, United States Department of Agriculture, Albany, CA, USA*

Rachel Diane Rhoades • *School of Electrical, Computer and Energy Engineering, Arizona State University, Tempe, AZ, USA*

Banafsheh Salehi • *Department of Radiological Sciences, University of California, Los Angeles, Los Angeles, CA, USA*

Gabriel Sancho-Fornes • *Instituto Interuniversitario de Investigación de Reconocimiento Molecular y Desarrollo Tecnológico (IDM), Universitat Politècnica de València, Universitat de València, Valencia, Spain*

Anoop Sathyan • *Department of Aerospace Engineering, University of Cincinnati, Cincinnati, OH, USA*

Crystal Schmitt • *IBIS Lab, Department of Chemical and Biomedical Engineering, University of South Florida, Tampa, FL, USA*

Daniel M. Sforza • *Department of Radiation Oncology and Molecular Radiation Sciences, Johns Hopkins University, Baltimore, MD, USA*
Yanke Shan • *Joint International Research Laboratory of Animal Health and Food Safety and Single Molecule Nanometry Laboratory (Sinmolab), Nanjing Agricultural University, Nanjing, China*
Congcong Shen • *College of Chemistry and Chemical Engineering, Central South University, Changsha, Hunan, People's Republic of China*
Xinhao Shi • *College of Electrical and Information Engineering, Nanjing University of Aeronautics and Astronautics, Nanjing, China*
Paula L. Silva • *Department of Psychology, University of Cincinnati, Cincinnati, OH, USA*
Rebecca N. Silva • *Department of Chemistry, University of Cincinnati, Cincinnati, OH, USA*
Sean L. Simpson • *Department of Biostatistics and Data Science, Wake Forest School of Medicine, Winston-Salem, NC, USA*
Avtar Singh • *Applied and Engineering Physics, Cornell University, Ithaca, NY, USA; Broad Institute, Cambridge, MA, USA*
Nathaniel J. Smith • *Department of Radiology and Imaging Sciences, Indiana University School of Medicine, Indianapolis, IN, USA*
Anna Sobiepanek • *Laboratory of Biomolecular Interactions Studies, Chair of Drug and Cosmetics Biotechnology, Faculty of Chemistry, Warsaw University of Technology, Warsaw, Poland*
Brian S. Sorg • *National Cancer Institute, Rockville, MD, USA*
Amogha Tadimety • *Thayer School of Engineering Investigator, Dartmouth-Hitchcock Medical Center, Lebanon, NH, USA*
Seyed Mohammad Taghdisi • *Targeted Drug Delivery Research Center, Pharmaceutical Technology Institute, Mashhad University of Medical Sciences, Mashhad, Iran*
Nongjian Tao • *Biodesign Center for Bioelectronics and Biosensors, Arizona State University, Tempe, AZ, USA; School of Electrical, Computer and Energy Engineering, Arizona State University, Tempe, AZ, USA*
Luis Antonio Tortajada-Genaro • *Instituto Interuniversitario de Investigación de Reconocimiento Molecular y Desarrollo Tecnológico (IDM), Universitat Politècnica de València, Universitat de València, Valencia, Spain; Chemistry Department, Universitat Politècnica de València, Valencia, Spain*
Tyler Tripp • *IBIS Lab, Department of Chemical and Biomedical Engineering, University of South Florida, Tampa, FL, USA*
Gregory J. Tsongalis • *Thayer School of Engineering Investigator, Dartmouth-Hitchcock Medical Center, Lebanon, NH, USA*
Bin Wang • *Joint International Research Laboratory of Animal Health and Food Safety and Single Molecule Nanometry Laboratory (Sinmolab), Nanjing Agricultural University, Nanjing, China*
Charlie Wang • *Department of Biomedical Engineering, Case Western Reserve University, Cleveland, OH, USA*
Jia Wang • *Crump Institute for Molecular Imaging, University of California Los Angeles, Los Angeles, CA, USA; Department of Molecular and Medical Pharmacology, University of California Los Angeles, Los Angeles, CA, USA; Bioengineering Department, University of California Los Angeles, Los Angeles, CA, USA*
Jiasi Wang • *Department of Chemistry, University of Washington, Seattle, WA, USA*

Ken Kang-Hsin Wang • *Department of Radiation Oncology and Molecular Radiation Sciences, Johns Hopkins University, Baltimore, MD, USA; Department of Radiation Oncology, University of Texas Southwestern Medical Center, Dallas, TX, USA*
Shaopeng Wang • *Biodesign Center for Bioelectronics and Biosensors, Arizona State University, Tempe, AZ, USA*
Xin Wang • *Joint International Research Laboratory of Animal Health and Food Safety and Single Molecule Nanometry Laboratory (Sinmolab), Nanjing Agricultural University, Nanjing, China*
Junnian Wei • *Department of Radiology and Biomedical Imaging, University of California San Francisco, San Francisco, CA, USA*
Qingshan Wei • *Department of Chemical and Biomolecular Engineering, College of Engineering, NC State University, Raleigh, NC, USA*
Ralph Weissleder • *Center for Systems Biology, Massachusetts General Hospital, Boston, MA, USA; Department of Radiology, Massachusetts General Hospital, Boston, MA, USA; Department of Systems Biology, Harvard Medical School, Boston, MA, USA*
John W. Wong • *Department of Radiation Oncology and Molecular Radiation Sciences, Johns Hopkins University, Baltimore, MD, USA*
Ning Wu • *College of Electrical and Information Engineering, Nanjing University of Aeronautics and Astronautics, Nanjing, China*
Yun Wu • *Department of Biomedical Engineering, University at Buffalo, The State University of New York, Buffalo, NY, USA*
Xiangkun Xu • *Department of Radiation Oncology and Molecular Radiation Sciences, Johns Hopkins University, Baltimore, MD, USA; Department of Radiation Oncology, University of Texas Southwestern Medical Center, Dallas, TX, USA*
Minghui Yang • *College of Chemistry and Chemical Engineering, Central South University, Changsha, Hunan, People's Republic of China*
Handan Yavuz • *Department of Chemistry, Hacettepe University, Ankara, Turkey*
Bryan Yoo • *Department of Radiological Sciences, University of California, Los Angeles, Los Angeles, CA, USA*
Xin Yu • *Department of Biomedical Engineering, Case Western Reserve University, Cleveland, OH, USA*
Xie Zeng • *Department of Electrical Engineering, University at Buffalo, The State University of New York, Buffalo, NY, USA*
Chenzhen Zhang • *Department of Bioengineering, Northeastern University, Boston, MA, USA*
Diming Zhang • *Biosensor National Special Laboratory, Key Laboratory for Biomedical Engineering of Education Ministry, Department of Biomedical Engineering, Zhejiang University, Hangzhou, People's Republic of China*
Jianwei Zhang • *School of Electrical, Computer and Energy Engineering, Arizona State University, Tempe, AZ, USA*
John X. J. Zhang • *Thayer School of Engineering Investigator, Dartmouth-Hitchcock Medical Center, Lebanon, NH, USA*
Peng Zhang • *Department of Chemistry, University of Cincinnati, Cincinnati, OH, USA*
Qingqing Zhang • *Biosensor National Special Laboratory, Key Laboratory for Biomedical Engineering of Education Ministry, Department of Biomedical Engineering, Zhejiang University, Hangzhou, People's Republic of China*
Yichen Zhang • *Thayer School of Engineering Investigator, Dartmouth-Hitchcock Medical Center, Lebanon, NH, USA*

Arsenii Zhdanov • *IBIS Lab, Department of Chemical and Biomedical Engineering, University of South Florida, Tampa, FL, USA*

Chen Zhu • *Department of Electrical and Computer Engineering, Missouri University of Science and Technology, Rolla, MO, USA*

Warren R. Zipfel • *Graduate Field of Biophysics, Cornell University, Ithaca, NY, USA; Applied and Engineering Physics, Cornell University, Ithaca, NY, USA; Broad Institute, Cambridge, MA, USA; Nancy E. and Peter C. Meinig School of Biomedical Engineering, Cornell University, Ithaca, NY, USA; Kavli Institute for Nanoscale Science, Cornell University, Ithaca, NY, USA*

# Part I

## Optical

# Chapter 1

# A Compact Surface Plasmon Resonance Biosensor for Sensitive Detection of Exosomal Proteins for Cancer Diagnosis

**Yun Wu, Xie Zeng, and Qiaoqiang Gan**

## Abstract

Exosomes are nanosized (50–150 nm) extracellular vesicles released by all types of cells in the body. They transport various biological molecules, such as DNAs, RNAs, proteins, and lipids from parent cells to recipient cells for intercellular communication. Exosomes, especially those from tumor cells, are actively involved in caner development, metastasis, and drug resistance. Recently, many studies have shown that exosomal proteins are promising biomarkers for cancer screening, early detection and prognosis. Among many detection techniques, surface plasmon resonance (SPR) is a highly sensitive, label-free, and real-time optical detection method. Commercial prism-based wavelength/angular-modulated SPR sensors afford high sensitivity and resolution, but their large footprint and high cost limit their adaptability for clinical settings. We have developed an intensity-modulated, compact SPR biosensor (25 cm × 10 cm × 25 cm) for the detection of exosomal proteins. We have demonstrated the potential application of the compact SPR biosensor in lung cancer diagnosis using exosomal epidermal growth factor receptor (EGFR) and programmed death-ligand 1 (PD-L1) as biomarkers. The compact SPR biosensor offers sensitive, simple, fast, user-friendly, and cost-effective detection of exosomal proteins, which may serve as an in vitro diagnostic test for cancer.

**Key words** Surface plasmon resonance, Biosensor, Exosome, EGFR, PD-L1, In vitro diagnostics, Cancer diagnosis

## 1 Introduction

Exosomes are cell secreted small (30–150 nm) extracellular vesicles [1–3]. They transport various cargos, such as DNAs, RNAs, proteins, and lipids, from parent cells to recipient cells for cell–cell communication [1–3]. Exosomes play important roles in cancer initiation, progression, metastasis and drug resistance, and thus have become promising cancer biomarkers [4, 5]. Recent studies have shown that exosomal proteins are promising biomarkers for cancer screening, early detection, and prognosis. For example, exosomal glypican-1 expression distinguished early- and late-stage

Miguel R. Ossandon et al. (eds.), *Biomedical Engineering Technologies: Volume 1*, Methods in Molecular Biology, vol. 2393, https://doi.org/10.1007/978-1-0716-1803-5_1, 

pancreatic cancer patients from healthy controls and patients with benign pancreatic diseases with very high sensitivity and specificity [6]. The levels of exosomal PD-L1 differentiated responders from nonresponders to anti-PD-1 immunotherapy [7].

The expression of exosomal proteins can be measured by many methods, such as western blot, enzyme-linked immunosorbent assay (ELISA), flow cytometry, surface plasmon resonance (SPR), and liquid chromatography–mass spectrometry (LC-MS). Among them, SPR is a highly sensitive, label-free, and real-time optical detection method based on an attenuated total reflection (ATR) geometry. As shown in Fig. 1, a thin layer of metal film (e.g., a 50-nm-thick Au film) is deposited on top of the prism surface. A laser beam is employed to illuminate the glass/metal surface. At a specific incident angle, that is, resonance angle, nearly all light tunnels through the thin metal film and is coupled to surface plasmon (SP) modes propagating along the upper metal surface, leading to a sharp resonance dip in the reflectivity curve (Fig. 1b). This dip is extremely sensitive to the surface refractive index change induced by the absorption of biomolecules, which underlies the principle to use SPR technique to monitor biomolecular interactions on the metal surface [8, 9]. As shown in Fig. 1b, the most

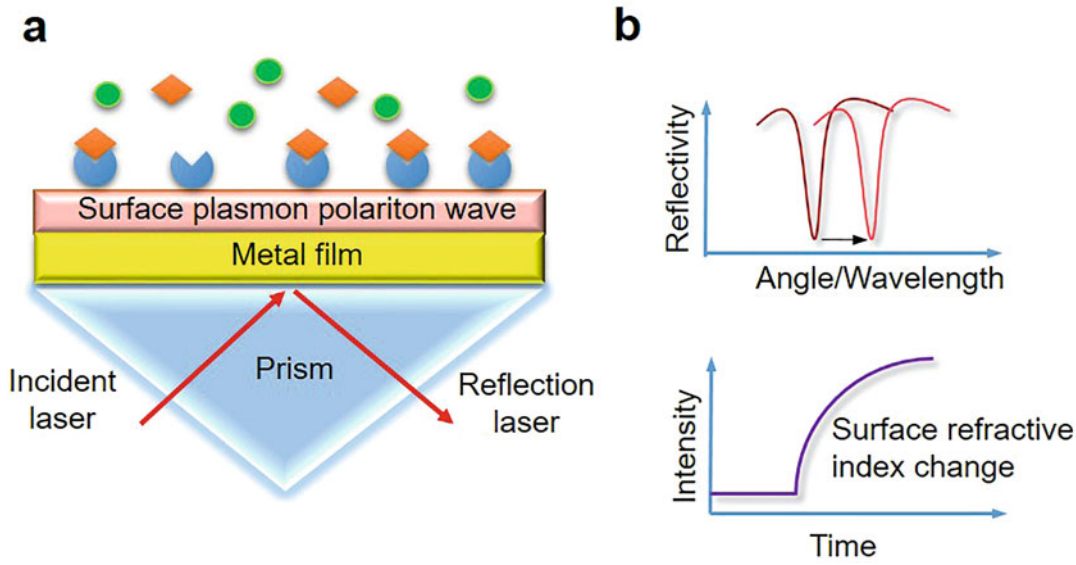


**Fig. 1** Sensing mechanism of SPR. A thin layer of metal film is deposited on the prism surface. When a laser beam is shed on the glass/metal surface at a specific incident angle, that is, resonance angle, nearly all light tunnels through the thin metal film and is coupled to surface plasmon (SP) modes propagating along the upper metal surface, leading to a sharp resonance dip in the reflectivity curve. The absorption of biomolecules on the surface changes local refractive index, affects the optical properties of SP modes and results in the change of coupling wavelength, resonance angle, or intensity of reflected light, which are the three widely used sensor outputs for the detection of biomolecules

frequently used SPR sensor outputs are resonance angle, coupling wavelength and intensity of reflected light.

Commercial SPR instruments, such as Biacore 2000 SPR instrument and Biacore 3000 SPR instrument (GE healthcare), have been used to measure the levels of several exosomal proteins, including CD63 and CD9, CD24, CD44, EpCAM, and HER2 for cancer diagnosis [10, 11]. These prism-based SPR instruments typically use wavelength and angular modulation and provide high detection sensitivity (~0.3 pg/mm$^2$), however, their large footprint, the need of a bulky coupling prism and high cost limit their applications in clinical settings [12]. To overcome these challenges, miniaturized versions of prism-based SPR sensors have been developed as compact and low-cost devices to enable sensitive, simple and fast measurements of various biomolecules [13, 14]. For example, the first portable SPR system, Spreeta™ 2000, was developed by Texas Instrument in 1999–2000 [15, 16]. Recently, several portable, prism-based SPR biosensors have been developed to detect antibodies [17, 18], pathogens [19], and bacteria [20]; however, their applications in the detection of exosomal proteins for cancer diagnosis have not yet been explored.

We have developed an intensity-modulated, compact SPR biosensor with dimensions as small as 25 cm × 10 cm × 25 cm [21]. As shown in Fig. 2, the compact SPR biosensor consists of a continuous wave solid state laser at 785 nm, an optical splitter, a prism, a small rotation stage, a mirror, and two photodetectors. The input laser beam is split into two beams by an optical splitter, that is, a sensing beam (50% laser energy) and a reference beam (50% laser energy). The sensing beam goes through the prism and reaches the gold-coated biochip sitting on the small rotation stage. By adjusting the angle of the stage, the SP mode is launched at the gold surface, which interacts with biomolecules bound on the surface. The binding of exosomal proteins to antibodies changes local refractive index, affects the optical properties of the SP modes, changes the intensity of the reflected laser beam, and thus permits optical detection of exosomal proteins (Fig. 2c). The intensity of reference beam is used to normalize the reflection intensity signals. The normalized intensity (i.e., reflection intensity/reference intensity × 100%) is reported as SPR signals.

To measure the expression of exosomal proteins by compact SPR biosensor, deionized (DI) water is first applied to the biochip to set the SPR angle and collect the baseline intensity signals ($I_{water}$). Then DI water is replaced with PBS, and the intensity signals of PBS ($I_{PBS}$) are recorded. Exosomes are then added after removing PBS, and incubated on the biochip at room temperature to allow the capture of exosomes by antibodies. Finally, the biochip is washed with PBS three times to remove unbounded exosomes, and the intensity signals of captured exosomes ($I_{exosome}$) are

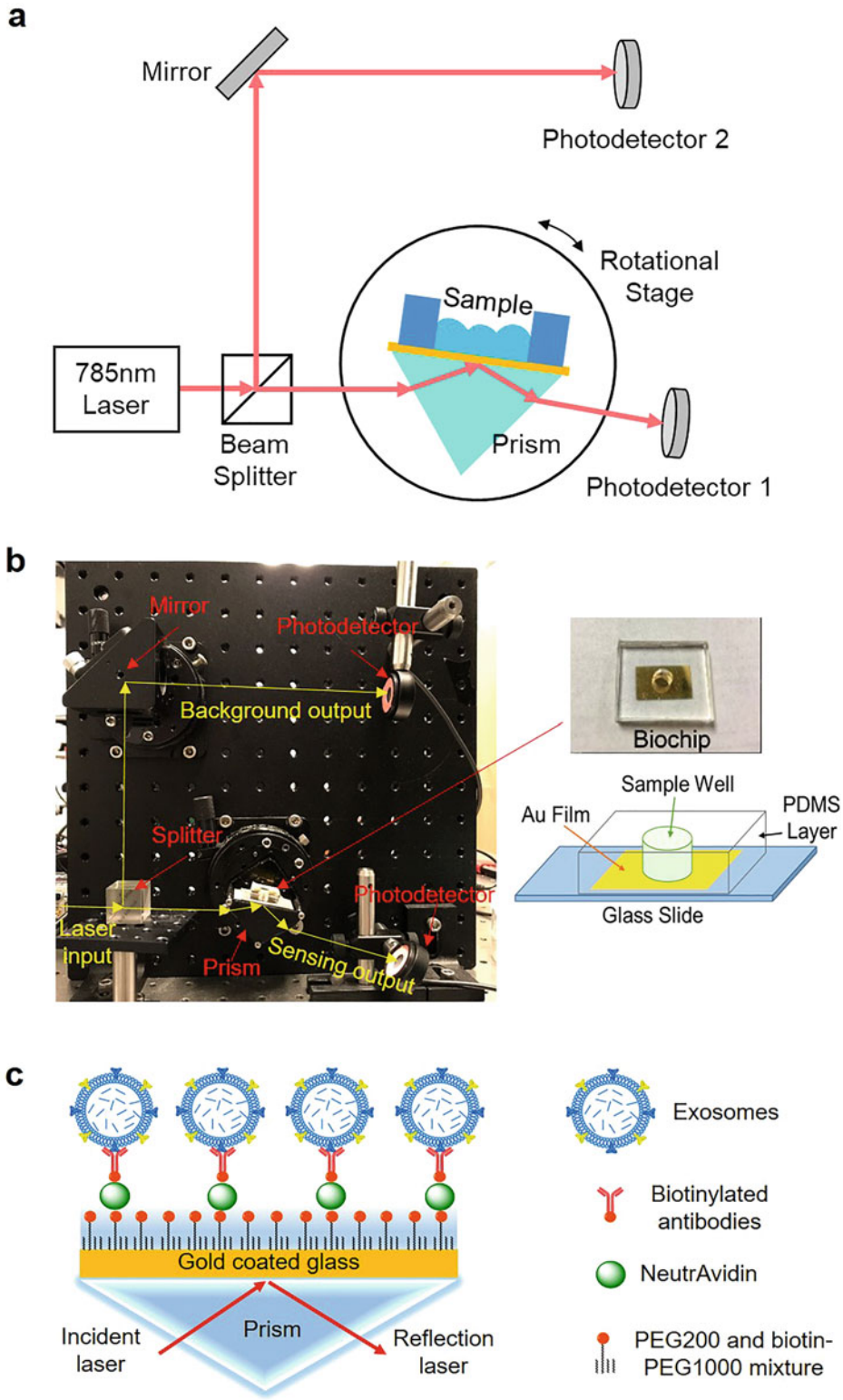


**Fig. 2** Overview of compact SPR biosensor. (**a**) Schematic diagram and (**b**) photos of compact SPR biosensor and the biochip. (**c**) Schematic diagram of exosomal protein detection via compact SPR biosensor. (Reproduced from Liu et al. [21] with permission from ACS Publications)

recorded. The expression of exosomal protein ($E$) is calculated using the following equation:

$$E = \frac{I_{\text{exosome}} - I_{\text{PBS}}}{I_{\text{PBS}} - I_{\text{water}}} \quad (1)$$

In this chapter, we introduce the procedure of setting up the compact SPR biosensor and the protocol of using the compact SPR biosensor to measure the expression exosomal proteins in human serum samples for cancer diagnosis. Lung cancer is selected as the disease model. Epidermal growth factor receptor (EGFR) and programmed death-ligand 1 (PD-L1) are selected as the biomarkers.

## 2 Materials

### 2.1 Optical Components of the Compact SPR Biosensor

1. A solid state laser at 785 nm (Coherent, Cat #: OBIS 785 LX, 100 mW).
2. A 50:50 beam splitter cube (Thorlabs, Cat #: BS017).
3. A right-angle prism dielectric mirror, 750–1100 nm, L = 25.0 mm (Thorlabs, Cat #: MRA25-E03).
4. A rotational stage (Newport, Cat #: 481-A).
5. A prism (Thorlabs, Cat #: PS 911).
6. A cage cube (Thorlabs, Cat #: CCM1-4ER).
7. Two photodetectors (Thorlabs, Cat #: S121C).
8. Analog handheld laser power meter console (Thorlabs, Cat #: PM100A).
9. Index-matching fluid (Thorlabs, Cat #: MOIL-30).

### 2.2 Materials and Supplies

1. Glass slides (Fisher Scientific, Waltham, MA) are cut into smaller square pieces with length of 25 mm.
2. Centrifuge tubes and microcentrifuge tubes (Fisher Scientific).
3. Deionized water.
4. Acetone (VWR, Radnor, PA).
5. Isopropyl alcohol (Fisher Scientific).
6. Nitrogen gas (Airgas Inc., Buffalo, NY).
7. SYLGARD® 184 silicone elastomer kit (Dow Corning Corporation, Midland, MI) is used to prepare the polydimethylsiloxane (PDMS) sheet following the manufacturer's protocol. Briefly, the two components are mixed at 10:1 mass ratio. The mixture is poured into a P150 petri dish to form a liquid layer with thickness of 5 mm. The mixture is then degassed to remove air bubbles, and cured at room temperature to form the PDMS sheet.

8. P150 petri dishes (Fisher Scientific).
9. Biopunch tissue punches (Ted Pella Inc., Redding, CA).
10. Phosphate buffered saline (PBS, 1×, pH = 7.4) is prepared by mixing 10× PBS buffer (Fisher Scientific, Cat #: BP3994) with DI water at volume ratio of 1:9 and stored at room temperature.
11. Methyl-polyethylene glycol-thiol (PEG200, MW = 200 g/mol, Thermo Fisher Scientific, Waltham, MA, Cat #: 26132) is dissolved in 1× PBS at the concentration of 10 mM and stored in aliquots at −20 °C.
12. Biotinylated-polyethylene glycol-thiol (biotin-PEG1000, MW = 1000 g/mol, Nanocs, New York, NY, Cat #: PG2-BNTH-1K) is dissolved in 1× PBS at the concentration of 10 mM and stored in aliquots at −20 °C.
13. The mixture of PEG200 and biotin-PEG1000 (molar ratio of 3:1, 10 mM) is prepared by mixing 3 parts of 10 mM PEG200 with 1 part of 10 mM biotin-PEG1000. The mixture is stored in aliquots at −20 °C.
14. NeutrAvidin (Thermo Fisher Scientific, Cat #: 31000) is dissolved in DI water at the concentration of 50μg/mL and stored in aliquots at −20 °C.
15. Biotinylated anti-EGFR antibodies (Abcam, Cambridge, MA, clone number EGFR1, 0.1 mg/mL) is diluted in 1× PBS to working concentration of 50μg/mL before use.
16. Biotinylated anti-PD-L1 antibodies (Thermo Fisher Scientific, clone number MIH1, 0.5 mg/mL) is diluted in 1× PBS to working concentration of 50μg/mL before use.
17. De-identified human serum samples are obtained from Roswell Park Comprehensive Cancer Center (Buffalo, NY).
18. Total exosome isolation reagent (from serum, Thermo Fisher Scientific, Cat #: 4478360).

### 2.3 Equipment

1. Ultrasonic cleaner (Branson 2800, Branson Ultrasonics, Penfield, NY).
2. AXXIS electron-beam evaporator (Kurt J. Lesker Company, Jefferson Hills, PA).
3. Eppendorf centrifuges (5804R and 5424R, Hauppauge, NY).
4. PE-50 XL benchtop low pressure plasma system (Plasma Etch, Inc., Carson City, Nevada).

## 3 Methods

### 3.1 Setup of the Compact SPR Biosensor (See Fig. 2a, b)

1. Install the laser and the heat sink on the optical table, and then place the beam splitter cube at the laser output to split the light into one sensing beam (yellow line in Fig. 2a, b) and one reference beam (blue line in Fig. 2a, b).
2. Install the rotational stage, reflection mirror, and photodetector 2 in Fig. 2a, b on an optical breadboard, and then fix the breadboard vertically on the optical table so that the reference beam can be reflected into the photodetector 2 by the mirror.
3. Mount the prism into an empty cage cube which is fixed on the rotational stage so that the prism can rotate together with the stage.
4. Rotate the prism roughly to tune the incident angle of the laser beam close to the SPR angle. Install photodetector 1 in Fig. 2a, b on the optical table, and adjust its location and angle to collect the reflected light from the prism.
5. Apply a drop of refractive-index matching fluid at the incoming light spot on the prism, and place the biochip atop so that an even thin layer of refractive-index matching fluid is sandwiched between the prism and the biochip (*see* **Note 1**).
6. Use the micrometer of rotational stage to finely scan the incident angle while monitoring the reflected light intensity to approach the minimum intensity position (i.e., the SPR resonance condition).
7. The setup is ready to monitor biomolecular interactions on the biochip surface by recording the intensity change of the reflected light in real time.

### 3.2 Preparation of the SPR Biochip (See Fig. 2c)

To prepare the SPR biochip shown in Fig. 2c, a glass slide is thoroughly cleaned and then coated with a 49 nm Au thin film. A PDMS sheet with a 6 mm hole is bound on the glass slide to serve as the sample well.

1. The glass slide is immersed in 40 mL acetone in a 50 mL centrifuge tube and cleaned with an ultrasonic cleaner for 10 min at room temperature. Then the glass slide is dried with a nitrogen gas stream.
2. The glass slide is immersed in 40 mL isopropyl alcohol in a 50 mL centrifuge tube and cleaned with an ultrasonic cleaner for 10 min at room temperature. Then the glass slide is dried with a nitrogen gas stream.
3. The glass slide is immersed in 40 mL DI water in a 50 mL centrifuge tube and cleaned with an ultrasonic cleaner for

10 min at room temperature. Then the glass slide is dried with a nitrogen gas stream.

4. A 2-nm Ti adhesion layer followed by a 49-nm Au thin film are deposited on the sensing area of the glass slide by electron-beam evaporation at the deposition rate of 1 Å/s (*see* **Note 2**).
5. A square PDMS sheet with length of 20 mm and thickness of 5 mm is prepared. A hole of 6 mm is punched using a tissue punch in the middle of the PDMS sheet to be used as the sample well.
6. The PDMS sheet with the 6-mm hole and the gold-coated glass slide are treated with oxygen plasma for 5 min. Then the PDMS sheet is bound onto the glass surface by firm press. The biochip is ready for use (*see* **Note 3**).

### 3.3 Surface Modification of the SPR Biochip

Antibodies against exosomal protein targets are conjugated on the surface of the biochip through biotin–avidin interaction. The compact SPR biosensor can be used to monitor the surface modification process (Fig. 3).

1. The sample well of the biochip is cleaned by three times of washing with DI water, 50μL DI water each time (*see* **Note 4**).
2. The mixture of PEG200 and biotin-PEG1000 (molar ratio of 3:1, 10 mM in 1× PBS, 50μL) is added to the sample well. The biochip is incubated at room temperature for 1 h.
3. Unbound mixture of PEG200 and biotin-PEG1000 is removed from the sample well by three times of 1× PBS washing, 50μL 1× PBS each time.
4. NeutrAvidin (50μg/mL, 50μL) is added to the sample well. The biochip is incubated at room temperature for 1 h.

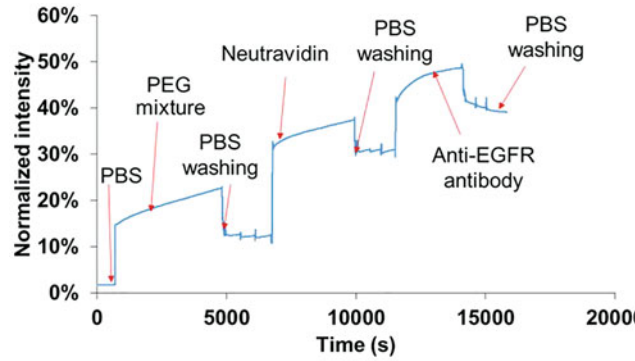


**Fig. 3** Compact SPR biosensor monitors the biochip surface modification process. A representative real-time SPR response upon the addition of PBS, PEG mixture, NeutrAvidin, and anti-EGFR antibodies during the biochip surface modification. (Reproduced from Liu et al. [21] with permission from ACS Publications)

5. Unbound NeutrAvidin is removed from the sample well by three times of 1× PBS washing, 50μL 1× PBS each time.
6. Biotinylated antibodies, such as biotinylated anti-EGFR antibodies or biotinylated anti-PD-L1 antibodies (50μg/mL, 50μL) are added to the sample well. The biochip is incubated at room temperature for 1 h to conjugate antibodies on the surface of the biochip through biotin–avidin interaction.
7. Unbound antibodies are removed from the sample well by three times of PBS washing, 50μL 1× PBS each time. The surface modification of the biochip is completed (*see* **Note 5**).

### 3.4 Isolation of Exosomes from Human Serum Samples

1. Human serum samples are centrifuged at 10,000 × *g* for 30 min to remove debris. The supernatant is collected and transferred to a new tube.
2. To isolate exosomes from serum samples, 10μL total exosome isolation reagent (from serum) is added to 50μL serum. The mixture is incubated at 4 °C for 30 min and centrifuged at 10,000 × *g* for 1 h at 4 °C to pellet exosomes. The supernatant is removed and the exosome pellet is resuspended in 50μL 1× PBS (*see* **Note 6**).
3. The exosome solution is sonicated in the ultrasonic bath for 10 min at room temperature to better disperse exosomes in PBS (*see* **Note 7**).

### 3.5 Detection of Exosomal Proteins Via the Compact SPR Biosensor

1. The sample well of the biochip is rinsed with DI water for total three times, 50μL DI water each time. Then 50μL fresh DI water is added to the sample well.
2. The laser is turned on and aligned to the center of the sample well.
3. The angle of the rotation stage is adjusted so that the intensity of the reflected light reaches the lowest value. The intensity of the reflected light ($I_{water}$) is recorded at room temperature for 15 min or till signal is stabilized.
4. The DI water is removed. 50μL 1× PBS is added to the sample well. The intensity of the reflected light ($I_{PBS}$) is recorded at room temperature for 15 min or till signal is stabilized.
5. The 1× PBS is removed. 50μL exosomes are added to the sample well. The intensity of the reflected light at room temperature for 100 min or till signal is stabilized.
6. The exosomes are removed by three times of 1× PBS washing, 50μL 1× PBS each time (*see* **Note 8**).

7. 50μL 1× PBS is added to the sample well. The intensity of the reflected light ($I_{exosome}$) at room temperature for 15 min or till signal is stabilized.
8. Representative real time SPR curves for the detection of exosomal EGFR and exosomal PD-L1 are shown in Fig. 4. The expression of exosomal protein ($E$) is calculated using Eq. (1).

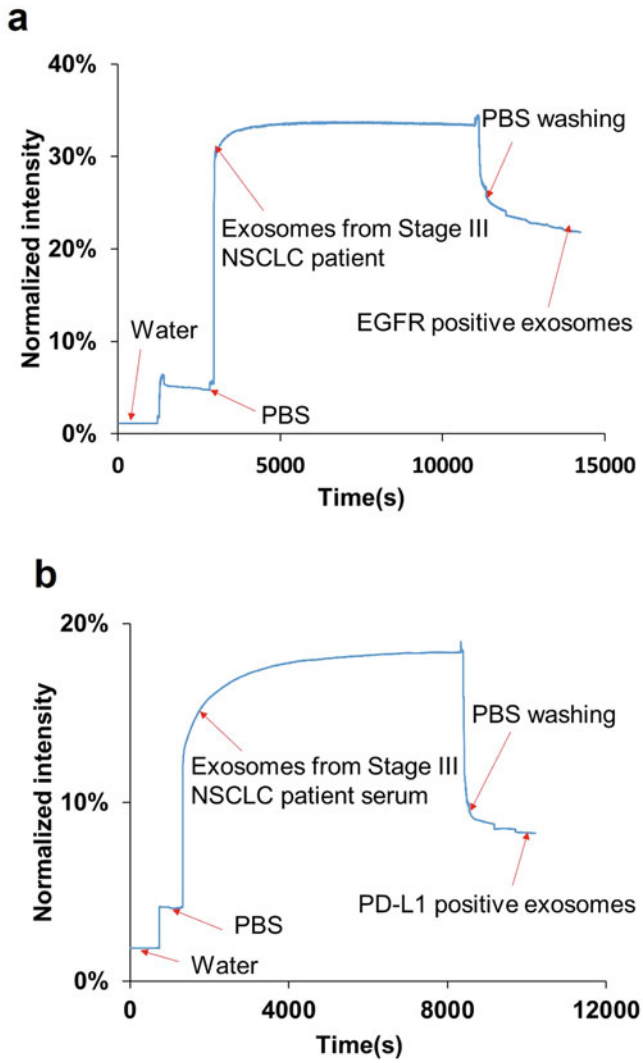


**Fig. 4** Compact SPR biosensor detects exosomal proteins in serum samples from non–small cell lung cancer (NSCLC) patients. (**a**) A representative real-time response curve of compact SPR biosensor detecting exosomal EGFR in the serum sample from a stage III lung cancer patient. (**b**) A representative real-time response curve of compact SPR biosensor detecting exosomal PD-L1 in the serum sample from a stage III lung cancer patient. (Reproduced from Liu et al. [21] with permission from ACS Publications)

## 4 Notes

1. Carefully put the biochip on top of the prism and avoid any bubble formation. A tape can then be used to secure the biochip on the prism.
2. To ensure the tight binding of PDMS sheet on the glass slide to prevent leakage in the following experiments, only selected area of the glass slide is coated with gold for sensing. Other area used for PDMS binding is better not to be coated with gold.
3. A 50 g weight can be put on top of the PDMS sheet overnight to help tightly bind the PDMS sheet on glass surface.
4. Carefully remove liquid from the sample well. Do not scratch the surface of the biochip.
5. The biochip can be stored at 4 °C for up to 7 days.
6. The exosome pellet may not be visible. Remove supernatant carefully from the opposite side of the microcentrifuge tube to avoid disturbing the exosome pellet.
7. To better disperse exosomes in PBS, exosomes can be passed through a 27G needle several times. The dispersion, size, and number concentration of exosomes can be characterized by nanoparticle tracking analysis (NanoSight, Malvern Panalytical Inc., Westborough, MA).
8. The SPR signals after each PBS wash can be recorded to monitor the washing process as shown in Figs. 3 and 4.

### References


1. Kowal J, Tkach M, Thery C (2014) Biogenesis and secretion of exosomes. Curr Opin Cell Biol 29:116–125
2. Yanez-Mo M, Siljander PR, Andreu Z et al (2015) Biological properties of extracellular vesicles and their physiological functions. J Extracell Vesicles 4:27066
3. Tkach M, Thery C (2016) Communication by extracellular vesicles: where we are and where we need to go. Cell 164(6):1226–1232
4. Azmi AS, Bao B, Sarkar FH (2013) Exosomes in cancer development, metastasis, and drug resistance: a comprehensive review. Cancer Metastasis Rev 32(3–4):623–642
5. Li W, Li C, Zhou T et al (2017) Role of exosomal proteins in cancer diagnosis. Mol Cancer 16(1):145
6. Melo SA, Luecke LB, Kahlert C et al (2015) Glypican-1 identifies cancer exosomes and detects early pancreatic cancer. Nature 523 (7559):177–182
7. Chen G, Huang AC, Zhang W et al (2018) Exosomal PD-L1 contributes to immunosuppression and is associated with anti-PD-1 response. Nature 560:382–386
8. Homola J, Yee SS, Gauglitz G (1999) Surface plasmon resonance sensors: review. Sensors Actuators B Chem 54(1–2):3–15
9. Homola J, Piliarik M (2006) Surface plasmon resonance (SPR) sensors. In: Homola J (ed) Surface plasmon resonance based sensors. Springer Series on Chemical Sensors and Biosensors, vol 4. Springer, Berlin Heidelberg, pp 45–67
10. Grasso L, Wyss R, Weidenauer L et al (2015) The emerging role of extracellular vesicles as biomarkers for urogenital cancers. Anal Bioanal Chem 407(18):5425–5432
11. Rupert DL, Lasser C, Eldh M et al (2014) Determination of exosome concentration in solution using surface plasmon resonance spectroscopy. Anal Chem 86(12):5929–5936

12. Raether H (1988) Surface plasmons on smooth and rough surfaces and on gratings. Springer, Berlin
13. Schasfoort RB (2017) Handbook of surface plasmon resonance. Royal Society of Chemistry, London
14. Melendez J, Carr R, Bartholomew DU et al (1996) A commercial solution for surface plasmon sensing. Sens. Actuators. B. Chem. 35 (1–3):212–216
15. Elkind J, Stimpson D, Strong AA et al (1999) Integrated analytical sensors: the use of the TISPR-1 as a biosensor. Sens Actuators B Chem 54(1):182–190
16. Soelberg SD, Chinowsky T, Geiss G et al (2005) A portable surface plasmon resonance sensor system for real-time monitoring of small to large analytes. J Ind Microbiol Biotechnol 32(11–12):669–674
17. Liu Y, Liu Q, Chen S et al (2015) Surface plasmon resonance biosensor based on smart phone platforms. Sci Rep 5:12864
18. Zhang XL, Liu Y, Fan T et al (2017) Design and performance of a portable and multichannel SPR device. Sensors 17(6):1435
19. Tokel O, Yildiz UH, Inci F et al (2015) Portable microfluidic integrated plasmonic platform for pathogen detection. Sci Rep 5:9152
20. Wang S, Xie J, Jiang M et al (2016) The development of a portable SPR bioanalyzer for sensitive detection of *Escherichia coli* O157:H7. Sensors 16(11):1856
21. Liu C, Zeng X, An Z et al (2018) Sensitive detection of Exosomal proteins via a compact surface Plasmon resonance biosensor for cancer diagnosis. ACS Sensor 3(8):1471–1479

# Chapter 2

# Electrochemistry Coupling Localized Surface Plasmon Resonance for Biochemical Detection

**Zetao Chen, Yanli Lu, Qingqing Zhang, Diming Zhang, Shuang Li, and Qingjun Liu**

## Abstract

Localized surface plasmon resonance (LSPR) associated with metal nanostructures has developed into highly useful sensor techniques. LSPR spectroscopy often shows absorption peaks which could be used for biomedical detection. Here we report nanoplasmonic sensors using LSPR on nanostructures such as nanoparticles, nanocups, and nanocones to recognize biomolecular. These sensors can be modified for quantitative detection of explosives and evaluation of enzymatic activity. Electrochemical LSPR sensors can also be designed by coupling electrochemistry and LSPR spectroscopy measurements for biochemical detection. Multiple sensing information can be obtained and electrochemical LSPR property can be investigated for biosensors. In some applications, the electrochemical LSPR biosensor can be used to quantify heavy metal ions, neurotransmitters, and sialic acid. The biosensors exhibit better performance than those of conventional optical LSPR measurements. With multitransducers, the nanoplasmonic biosensor can provide a promising approach for biochemical detection in environmental monitoring, healthcare diagnostics, and food quality control.

**Key words** Localized surface plasmon resonance (LSPR), Nanostructure, Two-dimensional material, Electrochemistry, Biochemical detection

## 1 Introduction

Optical detection is particularly a promising method because it allows for remote transduction without any physical connection between excitation sources and detecting elements. In recent years, several nanostructured sensors such as photonic crystal, whispering gallery mode (WGM), and surface plasmon resonance (SPR) are increasingly being employed by optical spectroscopy for bio-molecular detection [1–3]. These sensors can respond to target molecules at low concentrations by observing shifts in resonance wavelength before and after conjugation of biomolecules to the sensor surfaces. A common drawback, however, is that optical biosensors, such as SPR and WGM, often required a complex

Miguel R. Ossandon et al. (eds.), *Biomedical Engineering Technologies: Volume 1*, Methods in Molecular Biology, vol. 2393, https://doi.org/10.1007/978-1-0716-1803-5_2, 

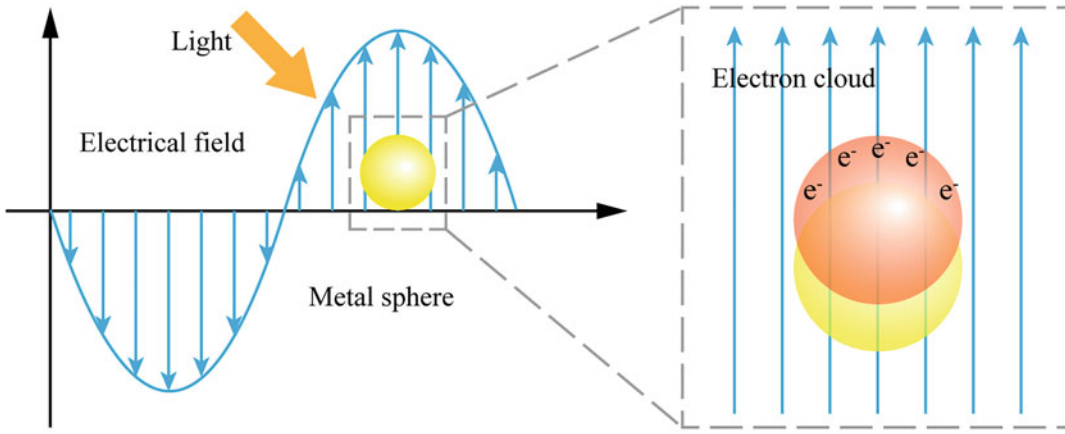


**Fig. 1** Schematic of localized surface plasmon resonance (LSPR), where the free conduction electrons in the metal sphere are driven into oscillation due to coupling with incident light

system. There is a need to fabricate devices that ensure precise alignment of light coupling to biodetection volume and generate the desired optical phenomena.

Metal nanostructures have recently been reported to modulate localized surface plasmon resonance (LSPR) spectroscopy for probing biomolecular interactions [4–6]. LSPR is often induced by incident light when it interacts with noble metal nanostructures, such as gold nanoparticles (AuNPs), that have smaller sizes than the wavelength of the incident light (Fig. 1). The light can be coupled in direct perpendicular transmission between incident light and spectrometer to obtain LSPR wavelength shifts without complex optical coupling [7–9]. Thus, it can be measured by a robust optical sensing platform minimizing the alignment requirement. For the enhancement of optoelectronic properties of metal nanoparticle, two-dimensional (2D) materials such as graphene oxide (GO) and molybdenum disulfide ($MoS_2$) are ideal building blocks because of their large specific surface area and rich binding sites [10, 11]. Besides, GO functionalized nanoparticles can exhibit unique physical and chemical properties such as ultrasensitive features and excellent catalytic properties [12, 13]. When combining the AuNPs with $MoS_2$ sheets, the plasmonic-electrical effect, including the plasmon-induced "hot electrons," could play a significant role in enhancing optical properties of optic devices [14]. Therefore, the nanocomposites of noble metal particles and 2D materials could take advantages of each nanomaterial to present outstanding optical properties for biochemical detection.

Other detection techniques such as electrochemistry can also be combined with LSPR spectroscopy while providing unique advantages in sensitivity and selectivity. To generate stable LSPR spectroscopy with the coupling of electrochemical, nanochips such as nanocups and nanocones were fabricated by scanning beam

lithographies, such as electron beam lithography (EBL) and focused ion beam (FIB) lithography [15, 16]. Multiple sensing information can be obtained and electrochemical LSPR property can be investigated for the electrochemical LSPR biosensors which was designed by coupling electrochemistry and LSPR spectroscopy measurements. In some applications, the electrochemical LSPR biosensor can be used to quantify heavy metal ion, neurotransmitters and sialic acid. The biosensors exhibit better performance than those of conventional optical LSPR measurements. For instance, voltammetry can be used to modulate electrochemical reactions on nanostructures and provide additional selectivity to LSPR monitoring of small molecule interactions [17].

Nanoimprint lithography is a method of fabricating nanometer scale patterns, and offers advantages including low cost, high throughput, and high resolution. It often creates nanostructure patterns by molding and curing of monomer or polymer resist on nanostructured template, while adhesion between the resist and the template is controlled to allow proper release. Nanoimprint lithography is currently used to fabricate devices for electrical, optical, photonic and biological applications [18, 19]. In our work, nanocomposites of 2D materials and AuNPs were synthesized and nanostructures such as nanocup and nanocone were fabricated for biosensor applications [20–24]. The nanocomposites of AuNPs and 2D materials such as graphene oxide (GO) and $MoS_2$ can be synthesized for the detection of explosives and evaluation of enzymatic activity. Nanoplasmonic biosensors coupling with electrochemical technique using nanocups or nanocones can be employed to quantify heavy metal ions, neurotransmitters, and sialic acid.

## 2 Materials

### 2.1 Optical and Electrochemical Measurement System

1. Halogen cold light source (DT-MINI-2, Ocean Optics Inc., Dunedin, Florida, USA).
2. Spectrophotometer (USB2000+, Ocean Optics Inc., Dunedin, Florida, USA).
3. Three fiber bundles (QP230-0.25-XSR, Ocean Optics Inc., Dunedin, Florida, USA).
4. Optical fiber attenuator (FVA-ADP-UV, Ocean Optics Inc., Dunedin, Florida, USA).
5. Collimating lens (F230APC-633, Thorlabs Inc., Newton, New Jersey, USA).
6. Absorb sample pool (SPL-CUV-ABS, Pulei Inc., Hangzhou, China).

7. Multimode microplate reader (SpectraMax Paradigm, Molecular Devices Co., USA).
8. Electrochemical workstation (CHI 660E, CH Instruments, Texas, USA).
9. Ag/AgCl reference electrode (CHI 111, CH Instruments, Texas, USA).
10. Pt counter electrode (CHI 102, CH Instruments, Texas, USA).

### 2.2 Acquisition and Immobilization of Sensitive Materials

1. Phosphate buffer saline (PBS) (*see* **Note 1**).
2. Mercaptophenyl boronic acid (MPBA).
3. Octapeptides (Cys-Leu-Val-Pro-Arg-Gly-Ser-Cys, CLVPRGSC) (*see* **Note 2**).
4. Tetrapeptides (Cys-Arg-Gly-Cys, CRGC) (*see* **Note 2**).
5. TNT-specific peptides (WHWQRPLMPVSIC) (*see* **Note 1**).

### 2.3 Fabrication of Nanocup and Nanocone Devices

1. UV light-curing flood lamp system (EC-Series, Dymax, USA).
2. E-beam evaporation system (FC/BJD2000, Temescal, USA).
3. Scanning electron microscope (SEM, XL30-ESEM, Philips, Netherland).
4. Centrifuge (TGL-16, Cence, China).
5. Nanocone quartz template fabricated by e-beam lithography.
6. UV curable polymer (NIL-UV-Si, GuangDuo Nano Ltd., Suzhou, China).
7. Dimethyl dichlorosilane (CP, Aladdin, Shanghai, China).
8. Titanium (>99.99%, Sigma-Aldrich, USA).
9. Gold (99.99%, Sigma-Aldrich, USA).
10. (Poly)ethylene terephthalate (PET) substrate.
11. Teflon roller.
12. Transparent epoxy resin adhesive.
13. Graphite (>99.95%, Aladdin, Shanghai, China).
14. Chloroauric acid ($HAuCl_4$, >99.9%, Aladdin, Shanghai, China).
15. Trisodium citrate ($Na_3C_6H_5O_7$, >98%, Aladdin, Shanghai, China).
16. Molybdenum disulfide ($MoS_2$, diameter 0.1–4 μm, Aladdin, Shanghai, China).
17. Sodium hydroxide (NaOH, >96%, Aladdin, Shanghai, China).
18. $K_4[Fe(CN)_6]/K_3[Fe(CN)_6]$ (AR, Aladdin, Shanghai, China).

### 2.4 Reagents for Biochemical Detection

1. Thrombin (human, Sigma-Aldrich, USA).
2. Human serum albumin (HAS, Sigma-Aldrich, USA).
3. Insulin (porcine, Sigma-Aldrich, USA).
4. 2,4,6-trinitrotoluene (TNT).
5. Dopamine hydrochloride solution (Sigma-Aldrich, USA).
6. Serotonin (AR, Aladdin, Shanghai, China).
7. Sialic acid (Sigma-Aldrich, USA).

## 3 Methods

### 3.1 Preparation of Biosensors

#### 3.1.1 Construction of Nanocomposites with Specific Peptides

AuNPs can be synthesized by sodium citrate reduction method and used for the optical LSPR detection [25]. Nanocomposites of AuNPs and 2D materials can be prepared for use in LSPR spectroscopy for monitoring the binding events occurring on the surface of composites. The synthesis process of graphene oxide (GO) and AuNPs is showed in Fig. 2a.

1. Through the chemical oxidation and exfoliation of the graphite powder, the graphene oxide (GO) flakes are obtained.

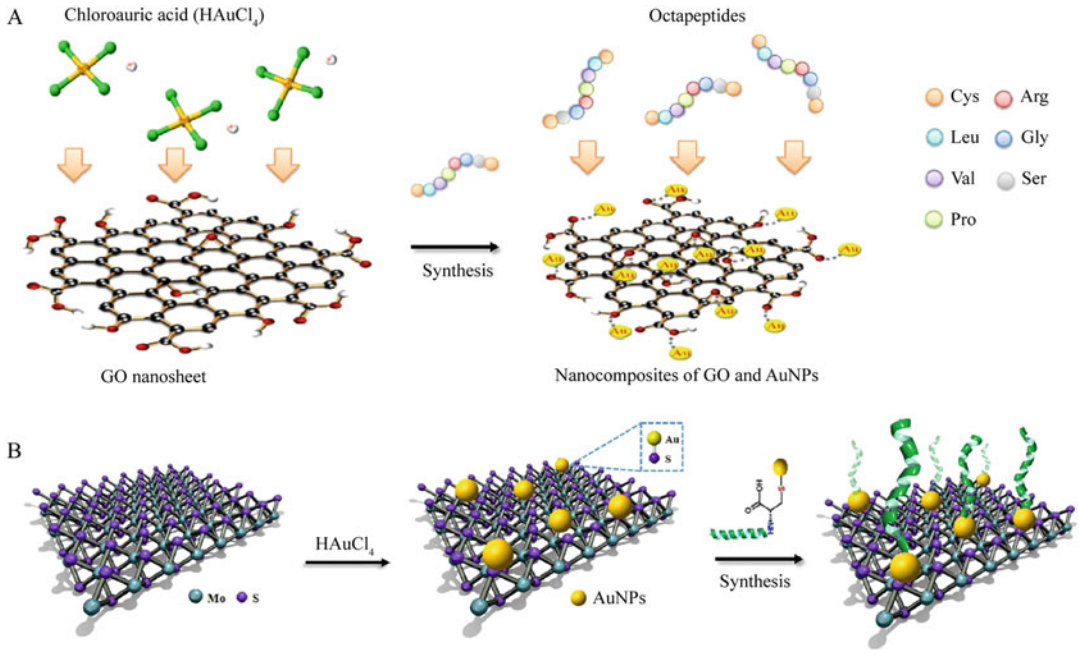


**Fig. 2** The synthesis of nanocomposites and the immobilization of sensitive peptides. (**a**) Synthesis process of AuNPs@GO and the self-assembly immobilization process of octapeptides on the nanocomposites. (**b**) The synthesis process of AuNPs@$MoS_2$ and the immobilization process of TNT-specific peptides on AuNPs@$MoS_2$ through Au-S covalent bonds

2. 1.225 mL of 1% chloroauric acid ($HAuCl_4$) is mixed with 3 mL well-dispersed GO solution (~0.5 mg/mL) and 150 mL deionized water.
3. After standing in the dark for 30 min, the mixture is heated to 80 °C with continuously stirring, and then 2.1 mL of 1% trisodium citrate ($Na_3C_6H_5O_7$) is added for the reduction of $HAuCl_4$ to AuNPs (~37.8 nm in diameter).
4. The heating is kept at 80 °C for 1 h, while the stir is lasted for 75 min. With further centrifugation at 350 × *g* for 10 min, the nanocomposites (AuNPs@GO) are finally obtained.
5. Specifically designed octapeptides (Cys-Leu-Val-Pro-Arg-Gly-Ser-Cys, CLVPRGSC) and tetrapeptides (Cys-Arg-Gly-Cys, CRGC) are synthesized by solid-phase peptide synthesis (SPPS) [26, 27], which the octapeptides are synthesized as the optimal cleavage site and the tetrapeptides are synthesized as the easiest design of the compared peptide sequence. These two kinds of peptides are immobilized on the nanocomposites through Au-S bond.

To chemically combine $MoS_2$ and AuNPs, the synthesis is carried out by one-step conjugation in aqueous solvents without any reducing reagent, as showed in Fig. 2b.

1. 60 mL aqueous dispersion of $MoS_2$ (0.1 mg/mL, synthesized by intercalation-exfoliation) is sonicated for 2 h, then is added into a 100 mL Erlenmeyer flask. While the $MoS_2$ aqueous dispersion is under vigorous stirring, $HAuCl_4$ is added to it until the concentration of $HAuCl_4$ became 0.01%.
2. After stirring for 10 min at room temperature (~22 °C), the reaction mixture is heated to 60 °C for 5 min. Finally, the nanocomposites of $MoS_2$ with AuNPs (AuNPs@$MoS_2$) are purified by centrifugation (1600 × *g* for 30 min at 4 °C) and stored at 4 °C in an opaque glass container for the sensing studies.
3. The TNT-specific peptide chain ( WHWQRPLMPVSIC ) is synthesized with solid-phase peptide synthesis (SPPS) by stepwise addition of protected amino acids to growing peptide chains, which could be synthesized commercially. Then the peptides are dissolved in PBS (0.1 M, pH 7.2) at 1 mg/mL for composites biofunctionalization.
4. For assembling the nanocomposites with peptides, 10 mL freshly prepared AuNPs@$MoS_2$ solution is adjusted to pH 8.0 with sodium hydroxide (NaOH), then 100 μL TNT-specific peptides (1 mg/mL) is added. The mixture is preserved at 4 °C in the dark for 12 h for assembling the peptides with AuNPs through Au-S covalent bonds.

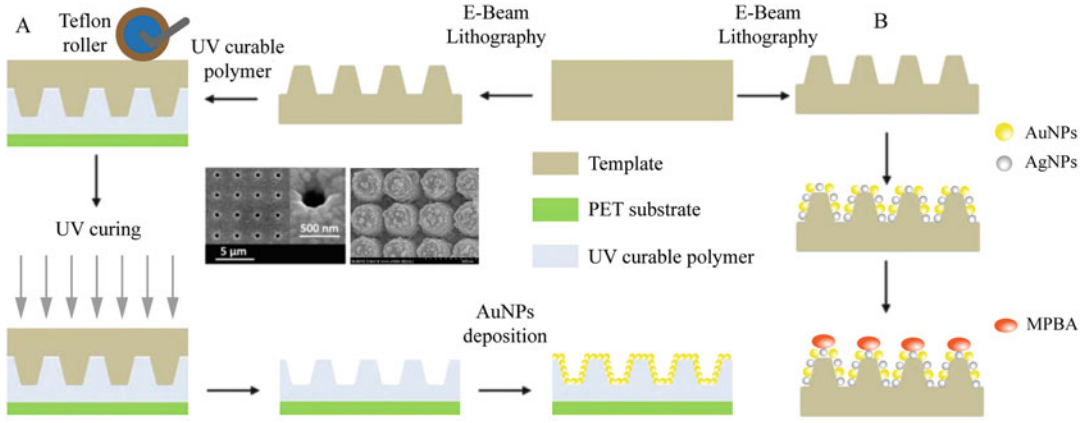


**Fig. 3** The fabrication process of nanochips. (**a**) Flowchart for nanocup-based nanochip fabrication by nanoimprint lithography. (**b**) Fabrication and functionalization process of the nanocone-based nanochip

*3.1.2 Fabrication of LSPR Nanochips*

The nanochips consist of nanocup or nanocone devices and sensitive material such as MPBA. The nanocups and nanocones can be fabricated for use in LSPR spectroscopy for biochemical detection [28, 29]. The nanostructures are imprinted by nanocone template made on quartz substrate and deposited with AuNPs by following steps, as showed in Fig. 3a.

1. A master nanocone array (nanocone height is 500 nm, and pitch 350 nm, periodicity 350 nm) is fabricated on glass substrates using the laser interference lithography patterning and reaction ion etching technique. It is passivated with dimethyl dichlorosilane solution for 30 min and then rinsed three times with ethanol and deionized water. This promotes the formation of a hydrophobic silane layer on the template, which in turn promotes removal of cured polymer replica with nanocup structures.
2. The two-dimensional square lattice is transferred to a flexible and optically transparent polydimethylsiloxane (PDMS) film using nanoreplica molding process. 5 μL of UV-curable polymer (NOA-61) is evenly spread on the top of the nanocone master through a Teflon roller and a PET sheet of 250 mm thick is carefully put on top of the polymer, to avoid the bubble formation and to act as a substrate.
3. To obtain the nanocup array structure, a UV light-curing flood lamp system is used at average power density of 105 mW $cm^{-2}$ to solidify the UV polymer on the template and PET interface. The polymer is cured by UV light for 60 s at room temperature.
4. To deposit AuNPs, 5 nm thick Titanium is deposited first and used as adhesive layer. Then, AuNPs are deposited on sidewalls and bottom of nanocups. The depositions are both performed

with a six pocket e-beam evaporation system. The diameter of nanoparticles is about 20 nm.

Finally, the structure of the nanocup arrays with nanoparticles on sidewalls is successfully fabricated. The left inset of Fig. 3a shows a scanning electron microscope image of the nanocup arrays.

The nanocone arrays are fabricated by nanoreplica molding technique and modified with nanoparticles where the top and side of the walls are closely packed with AuNPs and silver nanoparticles (AgNPs), as showed in Fig. 3b.

1. The original nanocone array on the flexible (poly)ethylene terephthalate (PET) substrate is fabricated by laser interference lithography and reaction ion etching techniques. A 4-in. silicon oxide with the thickness of 100 nm is sputtered on the nanocone array using K-J-Lesker-PVD-75 system to make the surface hydrophilic.
2. AuNPs are deposited onto the nanocone array by electron beam evaporation with a sixpocket system (FC/BJD-2000, Temescal Inc., USA). AgNPs are deposited by electrochemical reduction. The mercaptophenyl boronic acid (MPBA) is immobilized firmly on the nanochip by the metal-S bond for sensitive sialic acid sensing. The right inset of Fig. 3a shows a scanning electron microscope image of the nanocone arrays.

### 3.2 Nanocomposites for LSPR Spectroscopy Detection

#### 3.2.1 AuNPs@GO as Substrates for Thrombin Detection

As the resonant absorption of nanocomposites is adjustable via the surface refractive index, the change of the particle surface could reflect in the shifts of absorption peaks. Due to the thrombin could cleave Arg-Gly sites on peptides, it could divide the octapeptides into two sections and lead to the redispersion of nanocomposite molecules from aggregation status induced by the octapeptides (Fig. 4a). The detection of thrombin demonstrated the evaluation of enzymatic activity. Based on this, the thrombin could be detected through the following steps [21].

1. In the presence of sodium citrate, AuNPs (~37.8 nm in diameter) could be reduced from chloroauric acid, and nucleate grow on the GO nanosheets due to electrostatic interactions between particles and oxygen groups (Fig. 4b).
2. 3 mL AuNPs@GO is mixed with 150 μL octapeptides at 1.2 mM and oscillated at 300 × *g* for 1 min. Then, 150 μL thrombin solutions at different concentrations (1 fM to 10 pM) are added respectively into the mixed solutions and oscillated at 300 × *g* for another 1 min and incubated for 10 min before dose-dependence measurements, with PBS applied as control.
3. Mixtures are immediately placed into the quartz cuvette for absorption spectroscopic measurement (Fig. 4c). It could be

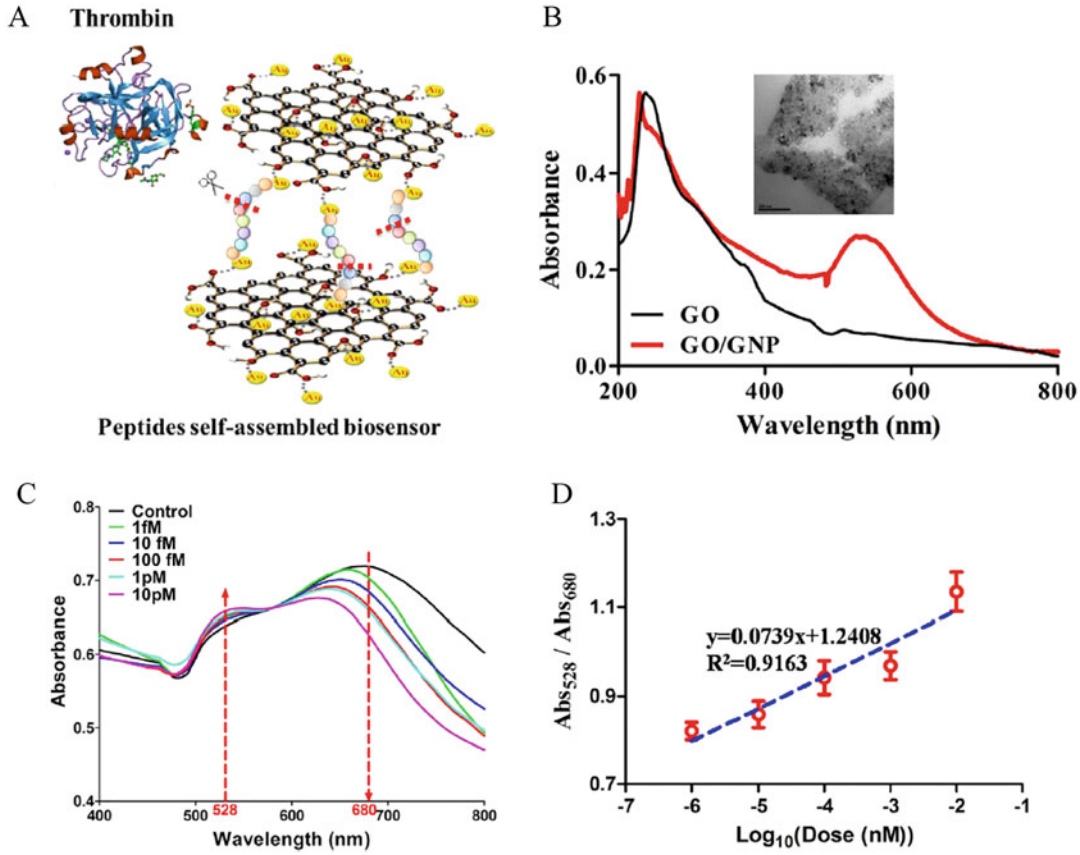


**Fig. 4** The LSPR spectroscopy detection of thrombin. (**a**) Detection mechanism of the biosensor. (**b**) Optical characterization of the nanocomposites compared with graphene oxide. The TEM image of the composites was shown as inset. (**c**) Absorption spectra for detection of thrombin at different concentrations (1 fM to 10 pM). (**d**) Statistical results of the 528–680 nm absorbance ratios ($Abs_{528}/Abs_{680}$) compared with the control trail ($n = 3$)

seen that with thrombin dose increasing, the responding spectra demonstrated an increase of the absorption peak at ~528 nm, while a decreasing absorbance could also be seen at wavelength larger than 600 nm.

4. This absorbance ratio could be employed for quantitative analysis. As shown in Fig. 4d, the absorption ratio values ($Abs_{528}/Abs_{680}$) exhibited a good linear relationship with the logarithm of thrombin doses.
5. To evaluate the specificity of the biosensor, human serum albumin (HSA) and insulin (porcine) are chosen for the comparison with thrombin detection. HSA is a serum albumin protein composed of several hundreds of amino acids like thrombin, which is the major component of blood. The insulin is an important protein hormone with only 51 amino acids, which regulates the sugar level in the blood. All of them are essential proteins in the blood.

### 3.2.2 AuNPs@$MoS_2$ as Substrates for Explosive Detection

Based on the nanocomposites of 2D $MoS_2$ and AuNPs which are synthesized by a one-step green process, a biosensor is constructed for explosive detection [20]. The AuNPs@$MoS_2$ is used as sensor substrate and TNT-specific peptides are employed as biosensitive components for the detection of explosives. When exposed to 2,4,6-trinitrotoluene (TNT), the biosensor showed significant absorption peak changes in visible spectra with a concentration-dependent behavior. The charge-transfer interactions happened between the peptides and explosive molecules, which could invoke optical absorption changes (Fig. 5a). Based on this, the TNT could be detected by the following steps.

1. Firstly, TNT is diluted into nine different concentrations ($2 \times 10^{-7}$, $4 \times 10^{-7}$, $1 \times 10^{-6}$, $2 \times 10^{-6}$, $4 \times 10^{-6}$, $1 \times 10^{-5}$, $2 \times 10^{-5}$, $4 \times 10^{-5}$, $1 \times 10^{-4}$ M) with anhydrous methanol (Fig. 5b). Then 20 μL different concentrations of TNT are added to the peptide-functionalized AuNPs@$MoS_2$ (200 μL) respectively. Anhydrous methanol (20 μL) is also added to the peptide-functionalized AuNPs@$MoS_2$ as the control trial.
2. To confirm the function of TNT-specific peptides, AuNPs@$MoS_2$ without being functionalized are used to detect TNT solutions ($4 \times 10^{-7}$, $2 \times 10^{-6}$, $4 \times 10^{-6}$, $2 \times 10^{-5}$, $4 \times 10^{-5}$ M) by repeating the same procedures.
3. To compare the performance of AuNPs@$MoS_2$, pure AuNPs, and pristine $MoS_2$ for TNT detection, the same steps are performed to detect TNT using functionalized AuNPs and $MoS_2$.
4. To evaluate the specificity of the biosensor, 4-NT and DNT are chosen to be detected with the biosensor, because they are also nitroaromatic explosives which are the analogues of TNT (Fig. 5c). 4-NT and DNT are dissolved in anhydrous methanol at five concentrations ($4 \times 10^{-7}$, $2 \times 10^{-6}$, $4 \times 10^{-6}$, $2 \times 10^{-5}$, $4 \times 10^{-5}$ M). The same operation steps are repeated for the detection of 4-NT and DNT.
5. The stability of the biosensor is also tested with the same procedures. 48 mL AuNPs@$MoS_2$ is functionalized with peptides on the first day, then in the following days, 3 mL AuNPs@$MoS_2$ solution is daily removed and centrifuged at $1600 \times g$ for 30 min at 4 °C to remove unbound peptides. The sediment is then redispersed in deionized water and the centrifugation process is repeated several times to guarantee a relatively pure aqueous solution of peptide-functionalized AuNPs@$MoS_2$. These functionalized nanocomposites then are used to detect $4 \times 10^{-6}$ M TNT, which lasted for 16 days so as to test the stability of the biosensor (Fig. 5d).

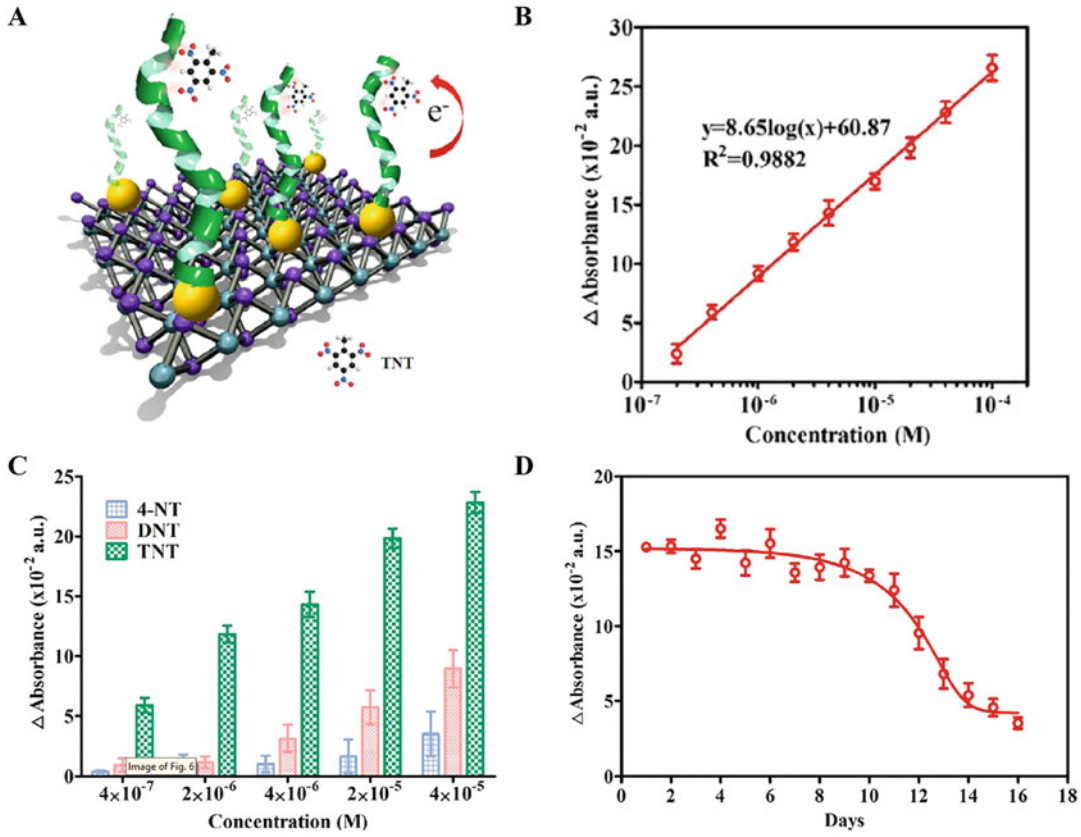


**Fig. 5** The LSPR spectroscopy detection of explosive detection. (**a**) The sensing mechanism with which the biosensor could capture TNT molecules and induce absorption peak changes. (**b**) Concentration-dependent curves of peak-value changes read from absorption spectra. (**c**) Selectivity analysis of the biosensor responses to 4-NT, DNT, and TNT (mean ± SD, $n = 5$). (**d**) The biosensor based on AuNPs@$MoS_2$ detected $4 \times 10^{-6}$ M TNT for 16 days to test the stability of the sensor (mean ± SD, $n = 3$)

### *3.3 Electrochemical LSPR Biosensor for Small Molecule Detection*

LSPR is not only influenced by refractive index change on the nanostructure surface, but also by potential and current density on the surface of a metal film [28]. Thus, LSPR sensors can be combined with electrochemistry to implement synchronized electrical and optical responses. The combination of electrochemistry and optical LSPR measurement can provide a multitude of information from different signal transductions and provide novel approaches to elucidate detailed processes for electrochemical reactions.

#### *3.3.1 Electrochemical LSPR Measurement*

The apparatus for electrochemical LSPR measurement is depicted in Fig. 6a. Optical measurement is performed in transmission mode. The light is emitted from the source below the nanostructure such as nanocup array device, delivered through the device and finally received by a spectrophotometer. The LSPR signal is measured and analyzed by transmission spectroscopy.

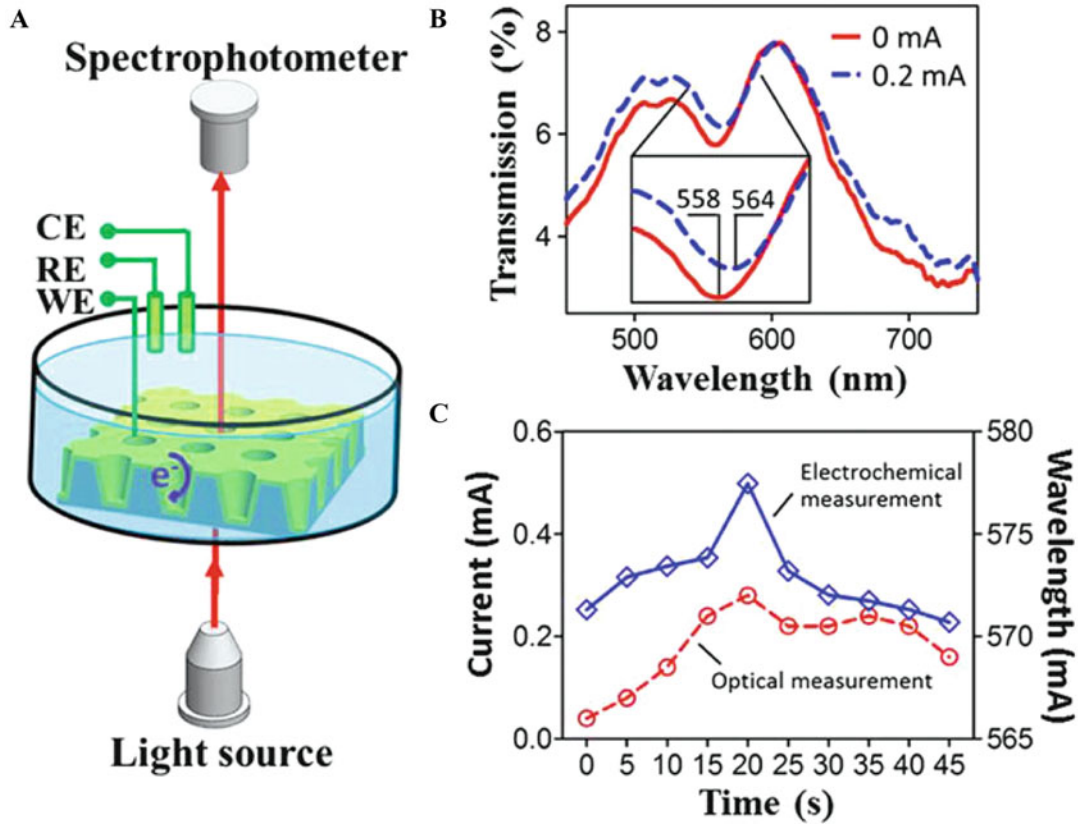


**Fig. 6** Electrochemical coupling LSPR spectroscopy measurement. (**a**) Schematic of experimental apparatus for synchronous electrochemical and optical measurement. (**b**) Transmission LSPR spectroscopy of nanocup with different surface currents. (**c**) Synchronous measurement of LSPR and electrochemistry in CV scanning

1. For electrochemical measurements the potential-dynamic electrochemical measurement of cyclic voltammetry (CV) is used to investigate the electrochemistry properties of nanocup device and the electrochemical modulation to LSPR. The nanocup device is used as working electrode, while platinum electrode is used as counter and the Ag/AgCl electrode is used as reference electrode. The 3-electrode system is utilized for the applying of potentials and the detection of electrochemical signals.
2. In the synchronous measurement, the range of the transmission spectrum is from 300 to 1000 nm with step of 0.5 nm. The transmission spectrum can be recorded when the surface of nanocup had RI change and electrochemical current (Fig. 6b). The electrochemical reactions are measured using an electrochemical workstation in a standard three-electrode system. 5 mM $K_4[Fe(CN)_6]/K_3[Fe(CN)_6]$ (1:1) is employed as redox couple in aqueous solution for electrochemical characterization. The scanning rate of CV is fixed at 0.02 V/s and the

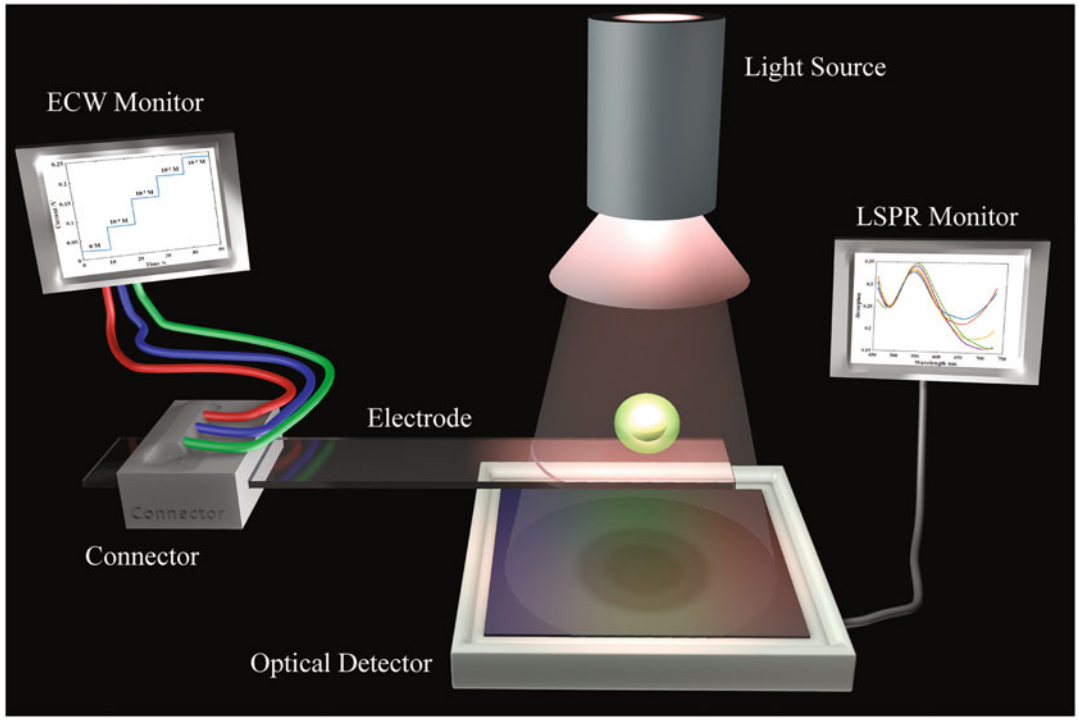


**Fig. 7** The schematic diagram of the electrochemical coupling LSPR measurement

transmission spectrum is simultaneously recorded and saved every 5 s. Thus, the transmission spectrum is obtained to represent optical LSPR, in 0.1 V steps during voltage scanning with different electrochemical current (Fig. 6c).

3. Figure 7 shows a schematic diagram of the electrochemical LSPR measurement apparatus. For optical detection, there are three fiber bundles, two collimating lenses, an optical fiber attenuator, a light source, and a spectrophotometer. Fiber bundles are used to provide optical linkage between the lens, the attenuator, the light source and, the spectrophotometer. The spectrophotometer is also directly connected to the light source by data cable. Thus, the spectrophotometer can synchronously capture light emitted by the light source and delivered through nanocup devices.
4. For electrochemical detection, the nanocup device is used as working electrode, while platinum and Ag/AgCl electrodes are used as counter electrode and reference electrodes, respectively. These three electrodes are all linked to an electrochemical workstation and inserted into a spectrometer measuring cell filled with redox solution. Careful arrangement of these three electrodes should maintain successful delivery through the cell.

5. The electrochemical LSPR measurements for nanocup are further carried out and analyzed with transmission spectrum and synchronous CV scanning. As seen in Fig. 6b, a significant LSPR dip shift is recorded in the transmission spectrum when electrochemical current on the nanocup surface is changed from 0 to 0.2 mA. The resonance wavelength is shifted from 558 to 564 nm but there is no significant shift observed for LSPR peaks.
6. Optical measurements within CV scanning are carried out and the wavelength shifts of LSPR dips are shown in Fig. 6c. During scanning, the wavelength of dip is shifted from 566 nm to 573 nm with an increase of current from 0.25 to 0.5 mA. When the current returned to 0.25 mA, the wavelength also decreased with declining current. These results indicate that the current change on the nanocup surface can modulate LSPR of nanocup and produce a wavelength shift in LSPR. The LSPR in transmission dip around 550 nm can be enhanced by electrochemical current and can be analyzed as an indicator in electrochemical LSPR detecting.

#### *3.3.2 Electrochemical LSPR Spectroscopy for Heavy Metal Ion Detection*

Utilizing electrochemical for the enhancement of LSPR on nanocup, electrochemical LSPR biosensors can be fabricated with higher sensitivity in the synchronous measurement mode. Combining the electrochemical method with LSPR measurement, the dual detection system demonstrated a detection limit of part-per-billion level for aqueous heavy metal ions, such as lead, copper, and zinc [24]. The detection process involves the following steps.

1. The measuring system for heavy metal detection is included a standard three-electrode system and a perfusion system (Fig. 8a). The nanocup device is utilized as working electrode while platinum and Ag/AgCl are used as counter-electrode (CE) and reference electrode (RE), respectively. A halogen cold light source and a CCD camera serve as LSPR measurement system. The nanocup is placed against the chamber wall and perpendicular to the light pathway. In addition, a perfusion system is introduced to enable sample solution loading and internal circulation, which is generally required in stripping voltammetry to promote thorough heavy metal ions electroplating onto the nanocup meanwhile remove the gas bubbles generated during the electrochemical reaction.
2. Standard divalent lead, zinc, and copper solutions (Sigma-Aldrich co., LLC) are diluted with sodium acetate buffer solution (pH 5) to desired concentrations (ranging from 10 to 100 μg/L). For analysts of divalent lead, zinc, and copper, the deposition potential is typically set to be −1.47 V. Since every heavy metal has its own oxidization potential, therefore

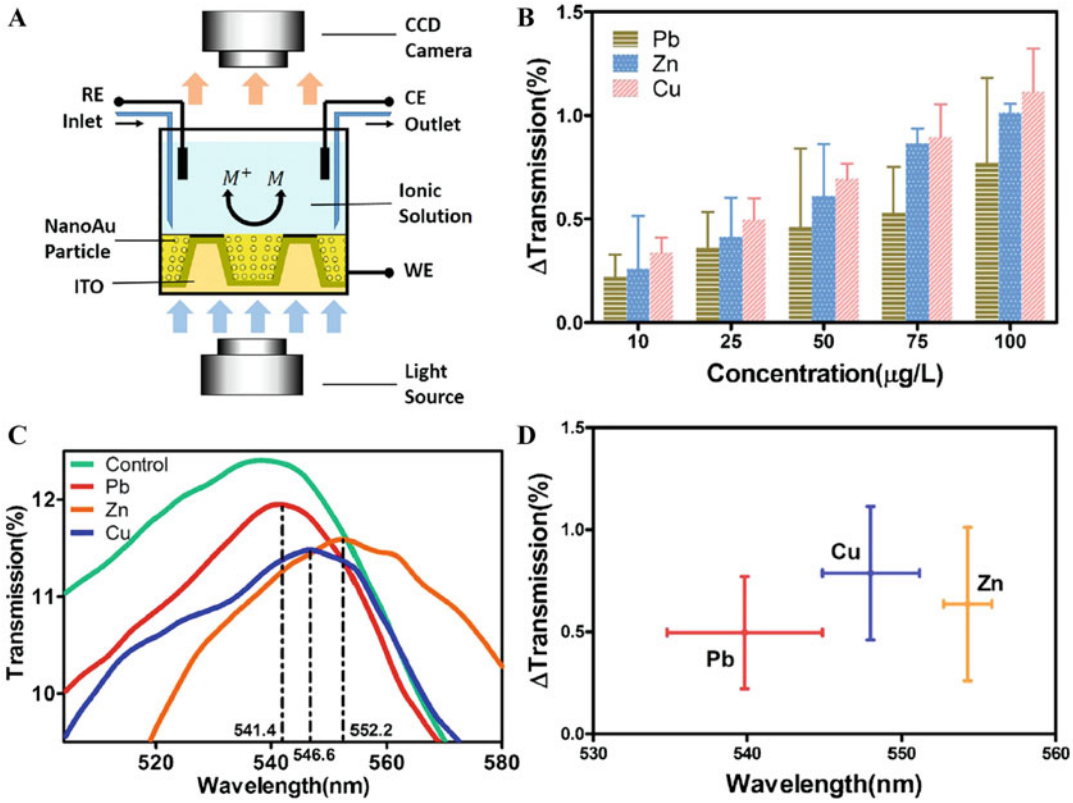


**Fig. 8** Electrochemical LSPR sensor based on nanocup array for heavy metal ion detection. (**a**) Schematic illustration of experimental apparatus for the detection system. (**b**) Statistic for transmission changes of LSPR characteristic peak of lead, copper, and zinc. (**c**) LSPR spectra observed at nanocup surface as different heavy metal galvanized onto the sensing region (blank buffer solution was used as control). (**d**) Plot for variations of transmission bank peak wavelength and transmission intensity changes

during the positive sweep, different metal electroplated on the working electrode is oxidized to the ionic form at different potential. The spectrometer is set to monitor the entire electrochemical process and thereof recorded the corresponding LSPR signal (Fig. 8b).

3. When electroplated with heavy metal layer, the transmission decreases while the characteristic peak demonstrates a bathochromic shift, as shown in Fig. 8c. The coverage of heavy metal layers alters the refractive index condition on the interaction surface, and therefore changes the electron density distribution, which in turn changes the plasmonic absorbance band and eventually causes a bathochromic shift in transmission spectrum.
4. For lead-galvanized nanocup, the transmission peak appears at 539.8 ± 5.1 nm, while 548.0 ± 3.1 nm and 554.2 ± 1.5 nm for copper- and zinc-galvanized nanocup respectively.

Figure 8d plots the variance of transmission changes and wavelength shifts of characteristic peaks under a series of concentration. There is no significant overlapping of transmission peak wavelength between different heavy metal ions, which validated the feasibility to the differentiate metal ions by their transmission peak wavelength when galvanized onto nanocup surface.

#### 3.3.3 Electrochemical LSPR Spectroscopy for Neurotransmitters Detection

The electrochemical LSPR spectroscopy measurement system can also be used in neurotransmitters detection [22]. The detection can be performed by the following steps.

1. The coupled measuring system is comprised of two components, that is, the LSPR monitoring system and the electrochemical measuring system. For the LSPR monitoring system, a halogen cold light source (DT-MINI-2, Ocean Optics Inc., Dunedin, USA) is utilized as light source, while a spectrophotometer receptor (USB2000p, Ocean Optics Inc., Dunedin, USA) is used to record the transmission spectrum of the nanostructured electrode.
2. Electrochemical LSPR detection for neurotransmitters. Using the coupled measuring system, the optical and electrochemical detection for neurotransmitters could be implemented simultaneously (Fig. 9a, b). The stock solution of dopamine and serotonin are diluted by PBS solution to desired concentrations (5 μmol/L, 25 μmol/L, 50 μmol/L, 75 μmol/L and 100 μmol/L), and then loaded into the electrochemical reaction chamber before conducting the LSPR-CV detection process.
3. The mixed solution is detected by CV and transmission spectroscopy simultaneously. In Fig. 9c, the CV of mixed solution of dopamine and serotonin at 25 μmol/L, 50 μmol/L, and 75 μmol/L, respectively is shown. As seen from the inset, two anodic currents for dopamine and serotonin appeared respectively on the potential of 0.14 V and 0.30 V, as reported in relevant publications.
4. LSPR responses curve is obtained alone with the CV current, as shown in Fig. 9d, where the concentration of each neurotransmitter (dopamine, serotonin) is 25 μmol/L (obtained by combining the standard solution of 50 μmol/L), while the concentration of ascorbic acid is made as 100 μmol/L.

#### 3.3.4 Electrochemical LSPR Spectroscopy for Sialic Acid Detection

The nanocone-based LSPR nanochip is decorated by AuNPs and AgNPs for dynamic electro-optical spectroscopy. Mercaptophenyl boronic acid (MPBA) is immobilized firmly on the nanochip by the metal-S bond for sensitive sialic acid sensing. Then the biosensor is

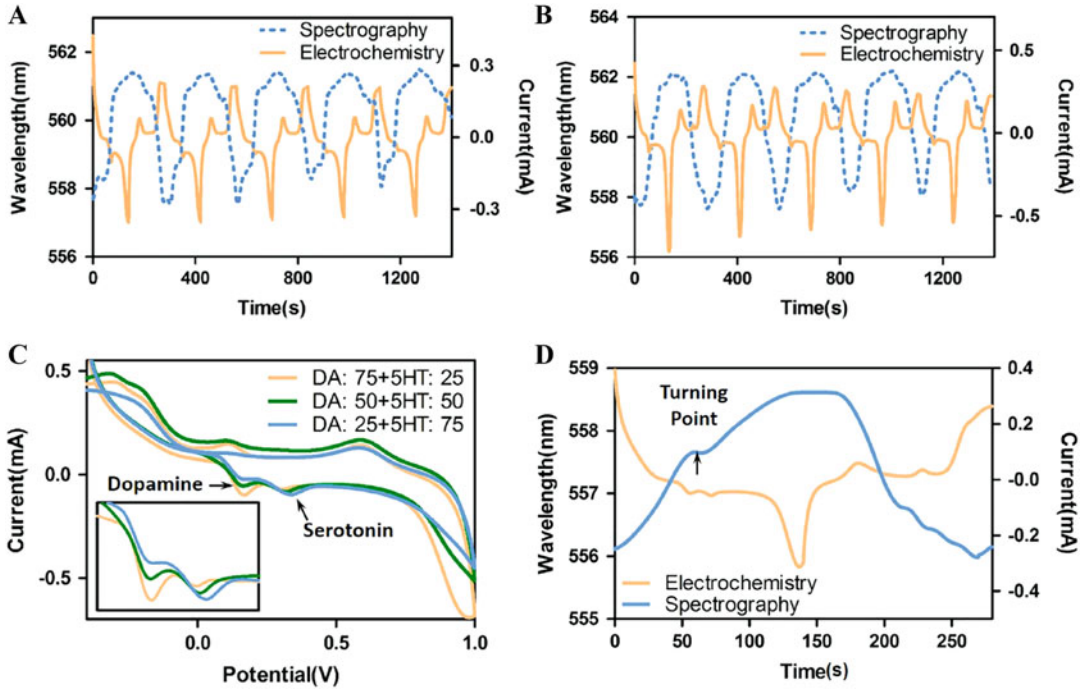


**Fig. 9** Electrochemical LSPR sensor based on nanocup array for neurotransmitter detection. LSPR and electrochemical responses of dopamine (**a**) and serotonin (**b**) during CV. (**c**) Cyclic voltammogram (CV) of the mixed solution at 25 μmol/L, 50 μmol/L and 75 μmol/L (inset is the CV at the range of 0.1–0.5 V), anodic currents for dopamine and serotonin could be clearly seen as marked in the figure. (**d**) Spectroelectrochemical responses of the mixed solution. Corresponding to the two anodic currents, bathochromic shift of the second transmission peak was divided into two stages, separated by the turning point, and each corresponded to different neurotransmitters

constructed and the detection for sialic acid can be performed by the following steps [23].

1. LSPR detection is carried out on a reflection spectrum system (Fig. 10a). The spectroscopy system includes a halogen cold laser (DH-mini UV-Vis-NIR, Ocean Optics Inc., Dunedin, USA) and a spectrophotometer (USB2000 +, Ocean Optics Inc., Dunedin, USA). The emitting probe with six fiber bundles delivers incident light to the nanochip. The receptor probe with one fiber bundle delivers reflected light to the spectrophotometer. The range of the reflection spectra used is from 400 to 650 nm with 0.36 nm intervals. Electrochemistry detection is carried out on a PARSTAT 4000 electrochemical workstation (AMETEK Inc., USA) with the nanochip as working electrode (WE), platinum as counter electrode (CE), and Ag/AgCl as reference electrode (RE). The electrochemical responses are monitored by linear sweep voltammetry (LSV). The range of the potential is from 0 to 0.3 V with a scan rate of 0.05 V/s.

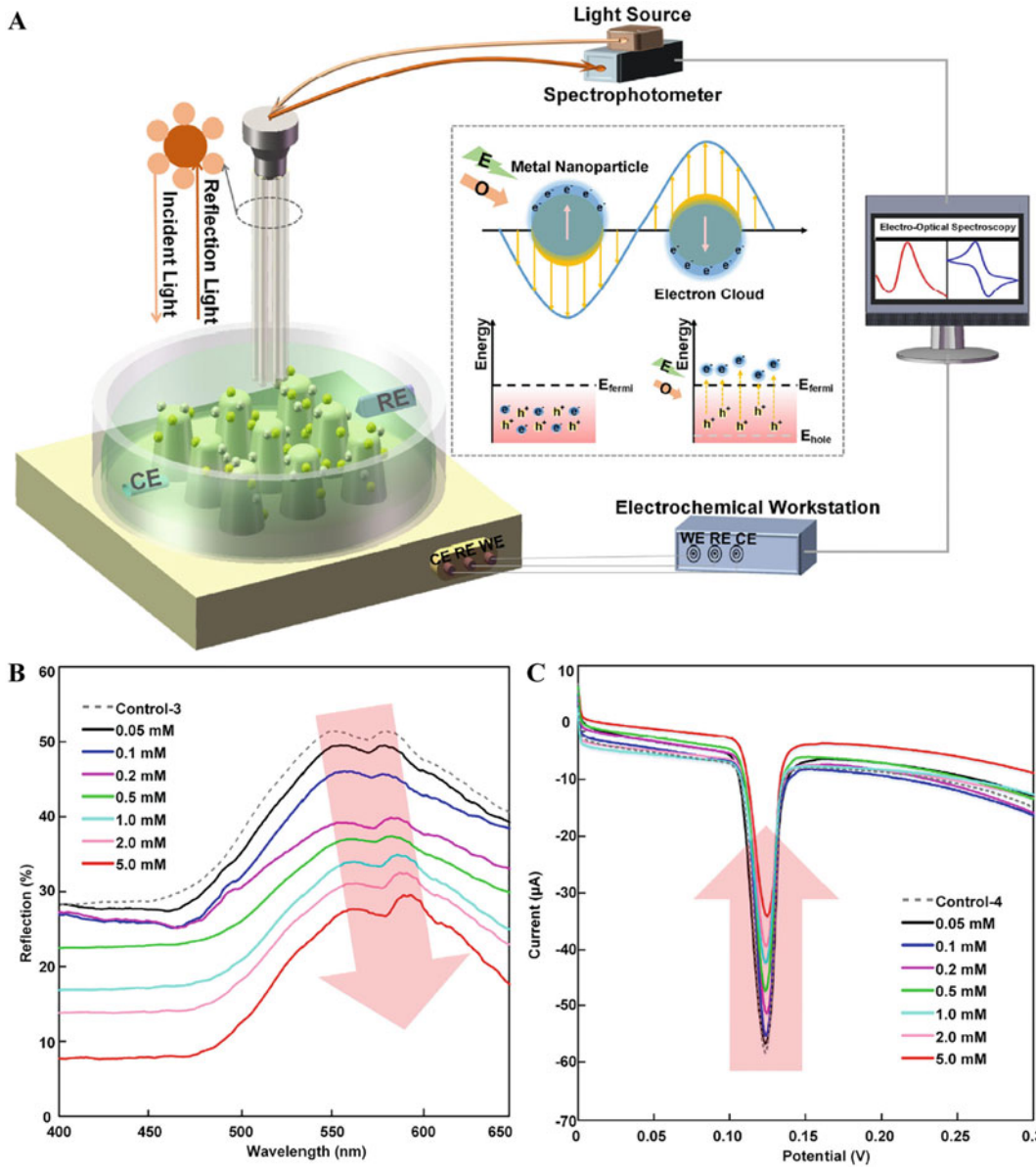


**Fig. 10** Electrochemical LSPR sensor based on nanocone array for sialic acid detection. (**a**) The apparatus of the system and the schematic diagram of electrochemical LSPR (*WE* working electrode, *CE* counter electrode, *RE* reference electrode, *E* electrochemical signal, *O* optical signal, $e^-$ hot electrons, $h^+$ hot holes, the dashed black line depicted the conduction band with a Fermi energy ($E_{fermi}$) and the dashed blue line indicated the energy level of the hot holes ($E_{hole}$)). (**b**) The reflection spectra with different concentrations of sialic acid under linear sweep voltammetry (LSV). (**c**) The linear sweep voltammograms with different concentrations of sialic acid under LSPR

2. In order to detect sialic acid, MPBA thiol-containing boronic acid, is modified on the nanochip through stable metal-S covalent bonds. PBS with pH of 7.4 is taken as the solvent for sialic

acid as the MPBA has special binding affinity with sialic acid in physiological environment with pH value of 7.4. The sialic acid is prepared with different desired concentrations, 0.05 mM, 0.1 mM, 0.2 mM, 0.5 mM, 1 mM, 2 mM and 5 mM, respectively. The relationship between sialic acid and the characteristic peaks and valley of LSPR with the impact of LSV is showed in Fig. 10b, and the relationship between sialic acid and currents of LSV with the impact of LSPR is showed in Fig. 10c.

3. For specificity detection, sodium chloride, potassium chloride, L-glutamic acid, human serum albumin, uric acid, lactic acid, and ascorbic acid are applied as control groups. The concentrations of these substances are all 1 mM with PBS as solvent. In addition, the same batch of the functionalized nanochip are tested with 1 mM sialic acid for 1 day, 2 days, 3 days, 4 days, 5 days, 6 days, 7 days, 15 days, 30 days, and 50 days for stability verification.

## 4 Notes

1. Phosphate buffer saline (PBS) is used as the solvent for proteins. The solution is prepared by dissolving 137 mM NaCl, 2.68 mM KCl, 1.47 mM $KH_2PO_4$, and 8.10 mM $Na_2HPO_4$ in pure water and pH is fixed at 7.4.
2. Peptides used in our study are synthesized by the standard solid phase method. Synthesized peptides are tested by high-performance liquid chromatography (HPLC) and mass spectrometry (MS) to verify amino acid sequence and purity. The peptides are stored in the form of freeze-dried powders before experiments and dissolved in PBS at 500 μg/mL.

## Acknowledgments

This work was supported by National Key Research and Development Program (Grant No. 2018YFC1707701), the National Natural Science Foundation of China (Grant No. 81801793, 31671007), the China Postdoctoral Science Foundation (Grant No. 2018M630677, 2019T120518).

### References

1. Homola J (2008) Surface plasmon resonance sensors for detection of chemical and biological species. Chem Rev 108(2):462–493. https://doi.org/10.1021/cr068107d
2. Vollmer F, Arnold S (2008) Whispering-gallery-mode biosensing: label-free detection down to single molecules. Nat Methods 5 (7):591–596. https://doi.org/10.1038/Nmeth.1221
3. Nair RV, Vijaya R (2010) Photonic crystal sensors: an overview. Prog Quant Electron 34

(3):89–134. https://doi.org/10.1016/j.pquantelec.2010.01.001
4. Saha K, Agasti SS, Kim C, Li X, Rotello VM (2012) Gold nanoparticles in chemical and biological sensing. Chem Rev 112 (5):2739–2779
5. Willets KA, Van Duyne RP (2007) Localized surface plasmon resonance spectroscopy and sensing. Annu Rev Phys Chem 58:267–297
6. Mayer KM, Hafner JH (2011) Localized surface plasmon resonance sensors. Chem Rev 111(6):3828–3857
7. Gao HW, Henzie J, Odom TW (2006) Direct evidence for surface plasmon-mediated enhanced light transmission through metallic nanohole arrays. Nano Lett 6(9):2104–2108. https://doi.org/10.1021/Nl061670r
8. Anker JN, Hall WP, Lyandres O, Shah NC, Zhao J, Van Duyne RP (2008) Biosensing with plasmonic nanosensors. Nat Mater 7 (6):442–453. https://doi.org/10.1038/Nmat2162
9. Stewart ME, Anderton CR, Thompson LB, Maria J, Gray SK, Rogers JA, Nuzzo RG (2008) Nanostructured plasmonic sensors. Chem Rev 108(2):494–521. https://doi.org/10.1021/Cr068126n
10. Dreyer DR, Park S, Bielawski CW, Ruoff RS (2010) The chemistry of graphene oxide. Chem Soc Rev 39(1):228–240. https://doi.org/10.1039/B917103G
11. Wang T, Du K, Liu W, Zhang J, Li M (2015) Electrochemical sensors based on molybdenum disulfide nanomaterials. Electroanalysis 27 (9):2091–2097. https://doi.org/10.1002/elan.201500117
12. Xiao H, Freddy B, Hua Z (2010) A brief review on graphene-nanoparticle composites. COSMOS 6(2):159–166. https://doi.org/10.1142/s0219607710000607
13. Tang Y, Hu H, Zhang MG, Song J, Nie L, Wang S, Niu G, Huang P, Lu G, Chen X (2015) An aptamer-targeting photoresponsive drug delivery system using "off–on" graphene oxide wrapped mesoporous silica nanoparticles. Nanoscale 7(14):6304–6310. https://doi.org/10.1039/C4NR07493A
14. Clavero C (2014) Plasmon-induced hot-electron generation at nanoparticle/metal-oxide interfaces for photovoltaic and photocatalytic devices. Nat Photonics 8(2):95–103. https://doi.org/10.1038/nphoton.2013.238
15. Vieu C, Carcenac F, Pépin A, Chen Y, Mejias M, Lebib A, Manin-Ferlazzo L, Couraud L, Launois H (2000) Electron beam lithography: resolution limits and applications. Appl Surf Sci 164(1):111–117. https://doi.org/10.1016/S0169-4332(00)00352-4
16. Volkert CA, Minor AM (2011) Focused ion beam microscopy and micromachining. MRS Bull 32(5):389–399. https://doi.org/10.1557/mrs2007.62
17. Cheng XR, Wallace GQ, Lagugné-Labarthet F, Kerman K (2015) Au nanostructured surfaces for electrochemical and localized surface plasmon resonance-based monitoring of α-synuclein–small molecule interactions. ACS Appl Mater Interfaces 7(7):4081–4088
18. Boltasseva A (2009) Plasmonic components fabrication via nanoimprint. J Opt A Pure Appl Opt 11(11):114001
19. Pimpin A, Srituravanich W (2011) Review on micro-and nanolithography techniques and their applications. Eng J 16(1):37–56
20. Wu J, Lu Y, Wu Z, Li S, Zhang Q, Chen Z, Jiang J, Lin S, Zhu L, Li C, Liu Q (2018) Two-dimensional molybdenum disulfide (MoS2) with gold nanoparticles for biosensing of explosives by optical spectroscopy. Sensors Actuators B Chem 261:279–287. https://doi.org/10.1016/j.snb.2018.01.166
21. Zhang Q, Zhang D, Xu G, Xu Y, Lu Y, Li S, Liu Q (2017) Spectroscopic detection of thrombin with peptides self-assembled on gold nanoparticles hybridized graphene oxide. Sensors Actuators B Chem 242:443–449. https://doi.org/10.1016/j.snb.2016.11.073
22. Li N, Lu Y, Li S, Zhang Q, Wu J, Jiang J, Liu GL, Liu Q (2017) Monitoring the electrochemical responses of neurotransmitters through localized surface plasmon resonance using nanohole array. Biosens Bioelectron 93:241–249. https://doi.org/10.1016/j.bios.2016.08.105
23. Li S, Liu J, Lu Y, Zhu L, Li C, Hu L, Li J, Jiang J, Low S, Liu Q (2018) Mutual promotion of electrochemical-localized surface plasmon resonance on nanochip for sensitive sialic acid detection. Biosens Bioelectron 117:32–39. https://doi.org/10.1016/j.bios.2018.05.062
24. Li N, Zhang D, Zhang Q, Lu Y, Jiang J, Liu GL, Liu Q (2016) Combining localized surface plasmon resonance with anodic stripping voltammetry for heavy metal ion detection. Sensors Actuators B Chem 231:349–356. https://doi.org/10.1016/j.snb.2016.03.042
25. Frens G (1973) Controlled nucleation for the regulation of the particle size in monodisperse gold suspensions. Nat Phys Sci 241:20. https://doi.org/10.1038/physci241020a0
26. Kongsuphol P, Arya SK, Chung Wong C, Polla LJ, Park MK (2014) Coiled-coil peptide based

sensor for ultra-sensitive thrombin detection. Biosens Bioelectron 55:26–31. https://doi.org/10.1016/j.bios.2013.11.070

27. Guillier F, Orain D, Bradley M (2000) Linkers and cleavage strategies in solid-phase organic synthesis and combinatorial chemistry. Chem Rev 100(6):2091–2158. https://doi.org/10.1021/cr980040+
28. Zhang D, Lu Y, Jiang J, Zhang Q, Yao Y, Wang P, Chen B, Cheng Q, Liu GL, Liu Q (2015) Nanoplasmonic biosensor: coupling electrochemistry to localized surface plasmon resonance spectroscopy on nanocup arrays. Biosens Bioelectron 67:237–242. https://doi.org/10.1016/j.bios.2014.08.022
29. Gartia MR, Hsiao A, Pokhriyal A, Seo S, Kulsharova G, Cunningham BT, Bond TC, Liu GL (2013) Colorimetric plasmon resonance imaging using nano lycurgus cup arrays. Adv Opt Mater 1(1):68–76

# Chapter 3

# Preparation of Surface Plasmon Resonance Aptasensor for Human Activated Protein C Sensing

**Semra Akgönüllü, Seda Koyun, Handan Yavuz, Arzum Erdem, and Adil Denizli**

## Abstract

Nucleic acid aptamers are an emerging class of artificial ligands and have recently gained attention in several areas. Here we report the design of a surface plasmon resonance (SPR) aptasensor for highly sensitive and selective sensing of human activated protein C (APC). First, DNA aptamer (DNA-Apt) specific for APC is complexed with N-methacryloyl-L-cysteine (MAC) monomer. Then, 2-hydroxyethyl methacrylate (HEMA) and cyanamide are mixed with the DNA-Apt/MAC complex. The SPR aptasensor is characterized by atomic force microscopy, ellipsometry, and contact angle measurements. Selectivity of SPR aptasensor is carried out in the presence of myoglobin (Myb), hemoglobin (Hb), and bovine serum albumin (BSA). Limit of detection (LOD) and limit of quantification (LOQ) values are 1.5 ng $mL^{-1}$ and 5.2 ng $mL^{-1}$, respectively. DNA-Apt SPR aptasensor performance for APC detection is also examined in artificial plasma.

**Key words** Activated protein C, Surface plasmon resonance, DNA aptamer, Aptasensors

## 1 Introduction

Biomolecular recognition plays the main role in nature. There are various biomolecular couples in biological systems, including hormones and hormone receptors, antibodies and antigens, enzymes and substrates, and DNA promoters and transcription factors. Most of these biomolecules have high binding force and specificity, and their interactions are well known. These natural biomolecular couples are of huge interest in diverse biological and biomedical applications, one of which is biosensing. However, many biomolecules (e.g., antibodies and enzymes) have fragile functional structures. They can be easily denatured and lose initial functions in an environment different from its ideal conditions. For this reason, these molecular couples have limited analytic applications in many cases. As a result, it is of great interest and significance to discover synthetic ligands that recognize target molecules and are stable in hard

Miguel R. Ossandon et al. (eds.), *Biomedical Engineering Technologies: Volume 1*, Methods in Molecular Biology, vol. 2393, https://doi.org/10.1007/978-1-0716-1803-5_3, 

biological and chemical conditions. Nucleic acid–based aptamers are a kind of artificial ligands that have great potential for a variety of biosensor applications. Additionally, aptamers have unique characteristics not found in natural biomolecules. Aptamers can be chemically synthesized in a simple and reproducible style. They can be chosen in physiological or nonphysiological conditions against various target analytes [1].

Aptamers are short single-stranded 15–40 bases long DNA or RNA molecules, which can be chosen from combinatorial libraries of artificial oligonucleotides [2, 3]. Aptamers can recognize inorganic or organic target molecules such as amino acids, proteins, toxins, drugs, and even living cells [4–6]. They are also named "chemical antibodies" owing to being isolated from a synthetic operation by Systematic Evolution of Ligands by EXponential (SELEX) enrichment. Figure 1 shows the general SELEX process. This process starts with the production of the random DNA/RNA library that contains up to $10^{14}$ to $10^{15}$ single-stranded oligonucleotides. The DNA or RNA aptamers are fabricated by combinatorial chemical synthesis methods. The target molecules and oligonucleotides are incubated to enable molecular recognition during the selection of the aptamers. In theory, the aptamers will bind to the targets and the unbound oligonucleotides will be removed because of different physical properties. After washing, the oligonucleotide sequences bound to the targets will be

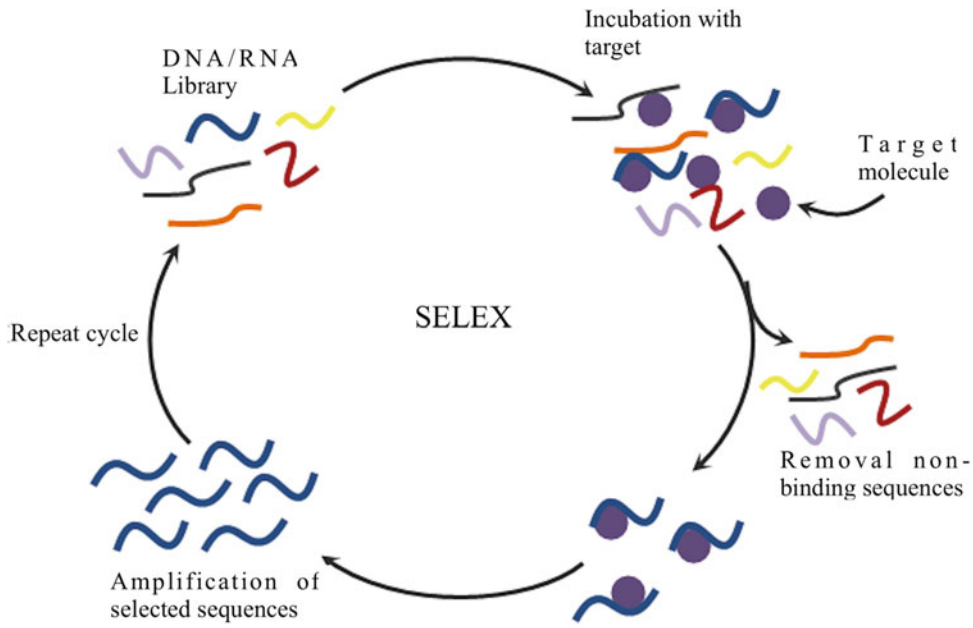


**Fig. 1** The diagram of SELEX procedure

amplified to produce the new library for further selection. The process is generally repeated [1].

Additionally, aptamers have unique characteristics not found in natural biomolecules. Recently, interest in the use of aptamers in the biorecognition area has increased [4]. Their unique features to attach to specific targets have made them a reliable recognition element. Compared to other recognition elements, aptamers generated from in vitro selection have many advantages, including high affinity and perfect specificity [7]. Aptamers can be easily fabricated, conducive to surface modifications, have low immunogenicity, and offer stability and good affinity to targets [8]. Therefore, they have been used for the detection of biomarkers, in order to enable the early detection of diseases [2]. Also, aptamers have gained prominence because of their capability to bind target proteins [9].

Aptamers as recognition elements in biosensors have created a new type of sensors called aptasensors [2] in combination with diverse analytical techniques such as fluorescent [10], optic [11], piezoelectric [12], and electrochemical [13] aptasensors for fast and sensitive detection of targets. These methods have excellent advantages in terms of sensitive recognition, rapid response, simple portability, a modest requirement of sample volumes, and easy signal amplification [7].

Optic sensors for sensing biological and chemical analytes are a rapidly growing area with potential applications in many important fields such as medical diagnostics, food analysis, environmental monitoring, agriculture, security, genomics, and proteomics. The optic biosensors offer a unique technology that enables label-free and direct observation of biomolecular interaction in real time. In optic biosensors, refractive index change is induced by biomolecular interactions and they are typically based on interferometric transducers. These transducers are based on spectroscopy of guided modes of dielectric waveguides or metal-dielectric waveguides. In the last two decades, surface plasmon resonance (SPR) based biosensors have been increasingly utilized for label-free detection, real-time analyses of various biological and chemical molecules [14].

As shown in Fig. 2, when polarized light is passed through the prism in the sensor chip coated with a thin metal film (e.g. gold) on its surface, the light is reflected by the metal film, which acts as a mirror. Upon changing the angle of incidence and monitoring the intensity of the reflected light, it is observed that the intensity of the reflected light exceeds at least (Fig. 2, line A). At this angle of incidence, the reflected light induces surface plasmon resonance, inducing surface plasmons, resulting in a decrease in the intensity of reflected light. The free electrons of the metal film can interact with the photons of p-polarized light; it reduces the intensity of reflected light by inducing a wave-like oscillation of free electrons [15].

Surface plasmon resonance is a perfect method for monitoring changes in the refractive index in the immediate surroundings of

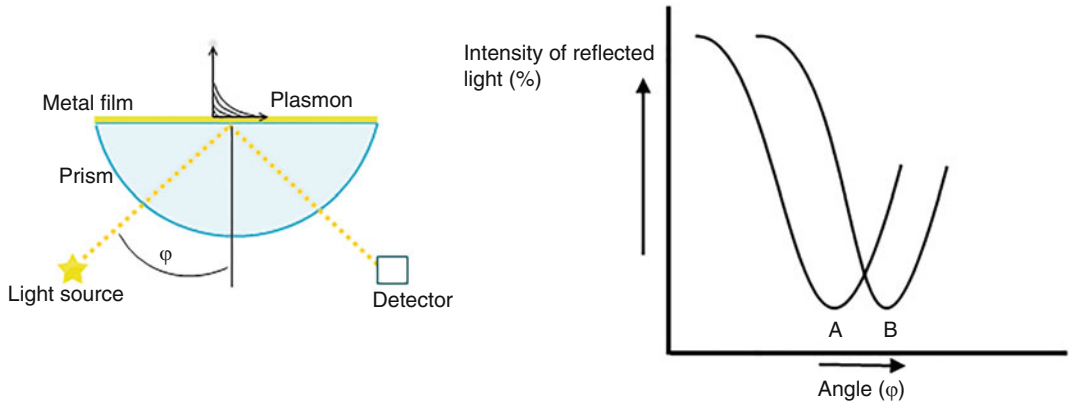


**Fig. 2** Schematic diagram of surface plasmon resonance excitation

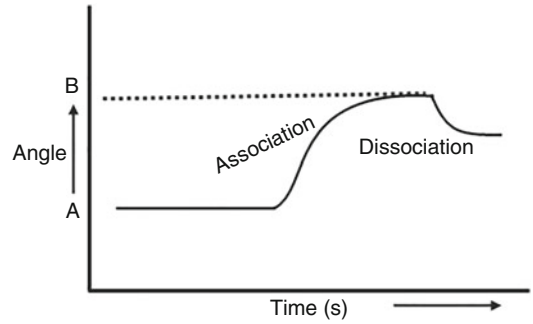


**Fig. 3** A sensorgram: principle of detection of analyte–ligand (e.g., target–aptamer) interactions by an SPR sensor

the metal surface. When the refractive index changes, the minimum intensity observed angle will change as shown in Fig. 2, where line A shows the graph of the reflected light intensity versus the incoming angle and B is plot after the change in the refractive index. SPR can not only measure the difference between these two conditions but also the change in time if the angle of resonance observed at the bottom changes. Figure 3 shows the shift of the so-called sensorgram of time. If this change is due to a biomolecular interaction, the kinetics of interaction can be examined in real time [16].

Surface plasmon resonance (SPR) sensors have been well utilized as a highly sensitive biosensor that can detect association and dissociation of biomolecules on a gold-coated chip without labeling and in real time [17–20]. SPR biosensors are effective tools for real-time detection of interactions of diverse chemical and biological targets [21–23]. SPR biosensors have been also applied for the detection of analytes of interest in medical diagnostics (cancer markers, antibodies, proteins, hormones, drugs, toxis, and allergy markers) and environmental protection (phenols, aromatic hydrocarbons, polychlorinated biphenyls, and pesticides) [14, 24].

Protein C (PC) is a clotting inhibitor and the most important anticoagulant and antithrombotic agent of the human coagulation mechanism. In human blood it is found at a concentration of 4.0 μg/mL. In plasma, human protein C circulates as a zymogen. Protein C is activated on endothelial cells by thrombin bound to thrombomodulin. Activated Protein C (APC) is the key enzyme of the protein C pathway [19]. APC is the blood protease with anticoagulant properties. Also, APC is a cell-signaling activity mediated by protease-activated receptor 1. A real-time, fast, low detection limit, cost-effective, and reliable approach approach for the development of highly sensitive and selective detection methods has been presented for APC monitoring [19]. Here, we report an SPR-based aptasensor for selective detection of human activated protein C.

## 2 Materials

### *2.1 Optical System for Surface Plasmon Resonance*

1. The SPR analysis is carried for APC kinetic analysis using SPR imager II (GWC Technologies, WI, USA) (Fig. 4a) (*see* **Note 1**).
2. The SPRchipTM sensor chip is designed for the SPRimager®II.
3. Quartz Halogen Lamps (6 V 10 W 2000 Hz), (4 mm base) (Catalog No. L6402, International Light Technologies, Peabody, MA, USA).
4. SPR gold chips (SPRchipTM); 1 mm × 18 mm × 18 mm with gold surface thickness ~ 50 nm (Fig. 4b) are obtained from the GWC Technologies.

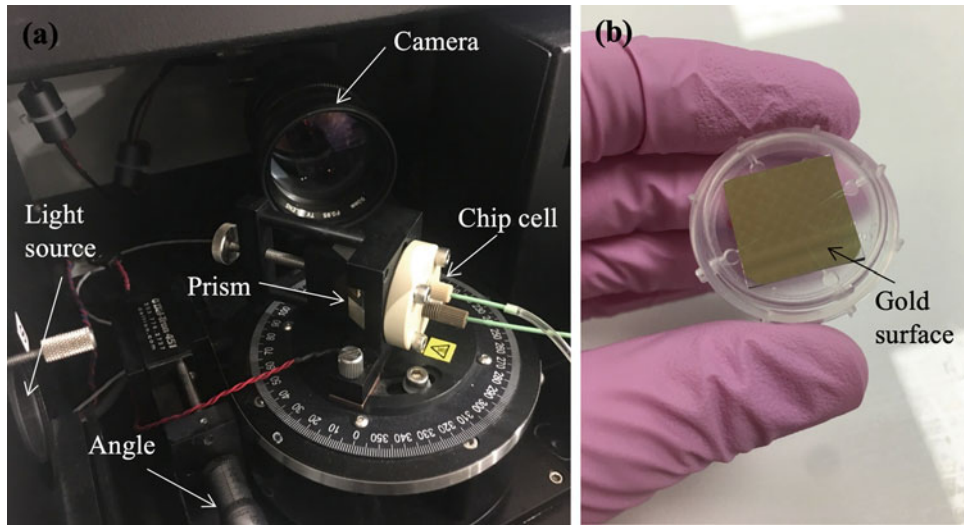


**Fig. 4** (**a**) A surface plasmon resonance (SPR) apparatus; and (**b**) SPR chip

5. Refractive index of glass: 1.72.
6. SF10 equilateral prism is obtained from GWC Technologies.
7. Refractive index matching oil is utilized between the disposable SPR sensor chip and the prism.
8. Fisherbrand lens paper 4″ × 6″ (Catalog No: 11-996, Fisher Scientific, USA) is used for prism cleaning.
9. CCD camera: it captures data on the entire SPR sensor chip surface simultaneously with a camera.

### 2.2 UV Light

The UV lamp is utilized to initiate polymerization.

1. The UV light is supplied from UVP (Cambridge, UK).
2. Black-Ray B-100AP High Intensity UV lamp is 100 W and provides 360 nm UV.
3. At 18 in. (457 mm), it produces a highly intense center of UV irradiance approximately 5 in. (127 mm) in diameter.
4. Lamp head rotates 360° when attached to a base (Fig. 5).

### 2.3 Contact Angle (CA) Analysis

The chip surface hydrophilicity is analyzed by contact angle analysis (CA): The CA analysis of the unmodified, DNA-Apt SPR aptasensor is performed with KRUSS DSA 100 (Hamburg, Germany) (Fig. 6a).

**Fig. 5** UV light apparatus

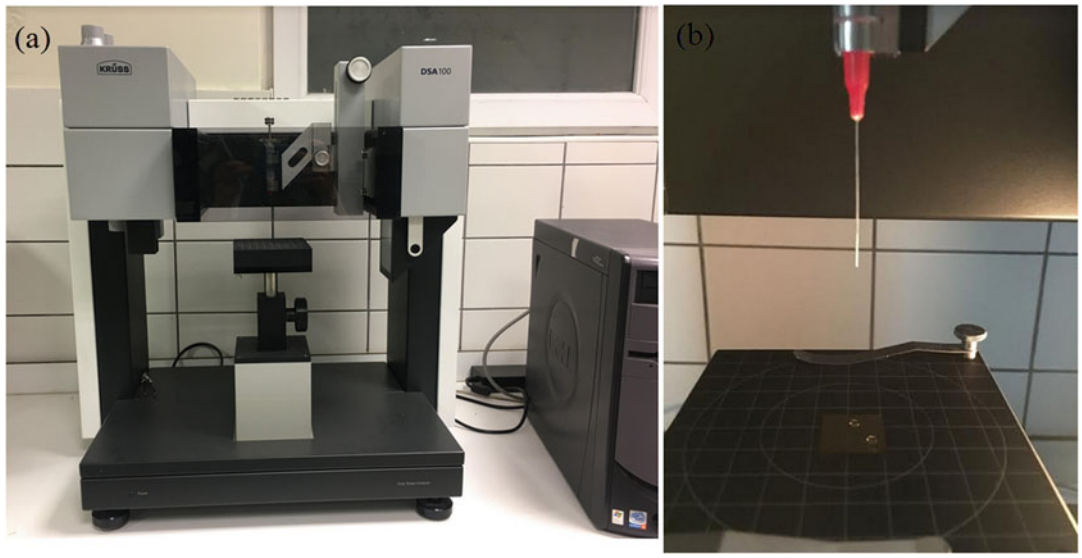


**Fig. 6** (**a**) Contact angle apparatus; and (**b**) needle

1. The instrument configuration includes microscope optics, high-resolution and high-speed camera, lens, syringes, and focusing and control elements in a closed housing.
2. A disposable syringe (volume, 1 mL) with stainless steel needle (Ø, 0.5 mm) with a PP Luer-lock connector is used (Fig. 6b).
3. The surface tension and liquid–liquid interfacial tension are measured using the pendant drop method. The sessile drop method is applied for the measurements and average CA values are calculated for the SPR aptasensors.

### *2.4 Atomic Force Microscope*

The SPR chip surface roughness is characterized by an atomic force microscope (AFM) (Park System, XE-100E, Korea).

### *2.5 Ellipsometry*

Nanofilm-EP3 Nulling Ellipsometer, Accurion GmbH, Germany is used to analyze the SPR chip surface thickness.

### *2.6 Working Solution*

1. 0.1 M phosphate buffered saline (PBS) of pH 7.4 is used as an adsorption buffer for the SPR aptasensor system (*see* **Note 2**).
2. Deionized water is obtained from the nanopore water purification system (Barnstead D3804 NANOpure®). Pure water has a resistance of 18.0 MΩ/cm. It is used as a cleaning solution.
3. $H_2SO_4$–$H_2O_2$ mix (hot or acidic piranha solution) is used as a cleaning and activating agent for SPR chip surface; $H_2SO_4$ and $H_2O_2$ 3:1 (Catalog No: 64271, Merck, Darmstadt, Germany).
4. Ethyl alcohol (EtOH) is used as a washing solution for the SPR chip surface (*see* **Note 3**).

5. L-Cysteine methyl ester (Sigma-Aldrich, St. Louis, MO) is used for the synthesis of MAC monomers.
6. Methacryloyl chloride (Sigma-Aldrich, St. Louis, MO) is used for the synthesis of MAC monomers.
7. 2-Hydroxyethyl methacrylate (HEMA) is used as a monomer (Sigma-Aldrich, St. Louis, MO).
8. 0.1 mmol cyanamide (Sigma-Aldrich, St. Louis, MO) is utilized in the design of aptasensors.
9. NaCl is used as a desorption agent.
10. α,α′-Azoisobutyronitrile (AIBN) (Sigma-Aldrich, St. Louis, MO) is used as initiator for polymerization starts.
11. Allyl mercaptan ($CH_2CHCH_2SH$) of 3 mM (Sigma-Aldrich, St. Louis, MO) is used for the thiol group.
12. Human activated protein C (APC) is obtained from Haemtech (VT, USA).
13. Artificial human plasma is supplied by Tokra Medical (Ankara, Turkey).
14. Single-stranded activated protein C (APC) specific DNA aptamer is obtained by Ella Biotech (Berlin, Germany).
15. The 5′-amino-linked single-stranded DNA Aptamer (DNA-Apt), which is specific for APC [25] and also the short synthetic oligonucleotide (random DNA) are supplied from T IBMOLBIOL (Berlin, Germany). The DNA-Apt and random DNA stock solutions (500 μg $mL^{-1}$) are prepared in ultrapure water and kept frozen.
16. *DNA Aptamer*
    5′-$NH_2$-C6-GCC TCC TAA CTG AGC TGT ACT CGA CTT ATC CCGGAT GGG GCT CTT AGG AGG C-3′.
17. *Random-DNA*
    5′-$NH_2$-C6-CAAA GAA GTG GCA GGA AGA GTC GAA GGT CTT GTTGTC ATT GCT GCA CAC CTT-3′.

### 2.7 Synthesis of N-Methacryloyl-L-Cysteine (MAC) Monomer

Polymerizable MAC monomer includes a thiol group, a linker group, connected to the aptamer.

1. 5.0 g of L-cysteine methyl ester and 0.2 g of $NaNO_2$ are dissolved in 30 mL of aqueous $K_2CO_3$ solution (5%, v/v).
2. This solution is chilled down to 0 °C.
3. 4.0 mL of methacryloyl chloride is poured slowly into this solution, under a nitrogen atmosphere and is stirred magnetically at room temperature for 2 h.
4. The reaction mixture is adjusted at pH 7.0.

5. The unreacted methacryloyl chloride is extracted with ethyl acetate.
6. The aqueous phase is evaporated in a rotary evaporator.
7. The residue (i.e., MAC) is crystallized in a 1:1 (v/v) ethanol–ethyl acetate system.

## 3 Methods

### 3.1 Prepared of DNA-Apt SPR Aptasensor

DNA-Apt for SPR aptasensor is immobilized onto the gold surface of an SPR chip by the following procedure: (1) Thiol modification of SPR chip (2) Apt-Aptamer is complexed with MAC monomer (3) Apt-Aptamer-MAC is mixed HEMA and cyanamide (4) monomer mixture is poured onto the SPR chip gold surface for the preparation of DNA-Apt nanofilm based SPR chip surface.

#### 3.1.1 Thiol Modification of SPR Chip

Surface modification of SPR aptasensors is performed for the attachment of thiol groups.

1. The SPR gold surface is cleaned in an acidic piranha solution and then dried.
2. Allyl mercaptan ($CH_2CHCH_2SH$) of 3 mM is dropped onto the gold surface of the SPR chip (Fig. 7a).
3. SPR chip is incubated overnight in a fume hood to introduce thiol groups to the gold surface.
4. SPR chip surface is cleaned with ethyl alcohol for removal of unbound allyl mercaptan molecules and dried.

#### 3.1.2 Design of DNA-Apt SPR Aptasensor

1. 0.1 mmol MAC-APC specific DNA aptamer (100 μg/mL) complex is prepared using MAC as the monomer (*see* **Note 4**).
2. 0.25 mmol HEMA, 0.1 mmol cyanamide, and MAC-DNA-Aptamer complex are mixed together (Fig. 7b).
3. 2.0 mg AIBN is added to the last solution.
4. The last solution (10 μL) is dropped on the SPR surface (*see* **Note 5**).
5. The polymerization is initiated under the UV light (100 W 360 nm UV) for 30 min (Fig. 5).
6. The DNA-Apt SPR aptasensor is cleaned with ethyl alcohol–water solution (50%, v/v).

### 3.2 Characterization of SPR Chip

DNA-Apt SPR aptasensor chip surface is characterized by the contact angle, atomic force microscope, and ellipsometry analysis.

Atomic force microscope (AFM) enables high-resolution scanning of the surface. AFM is used to image the topography of solid

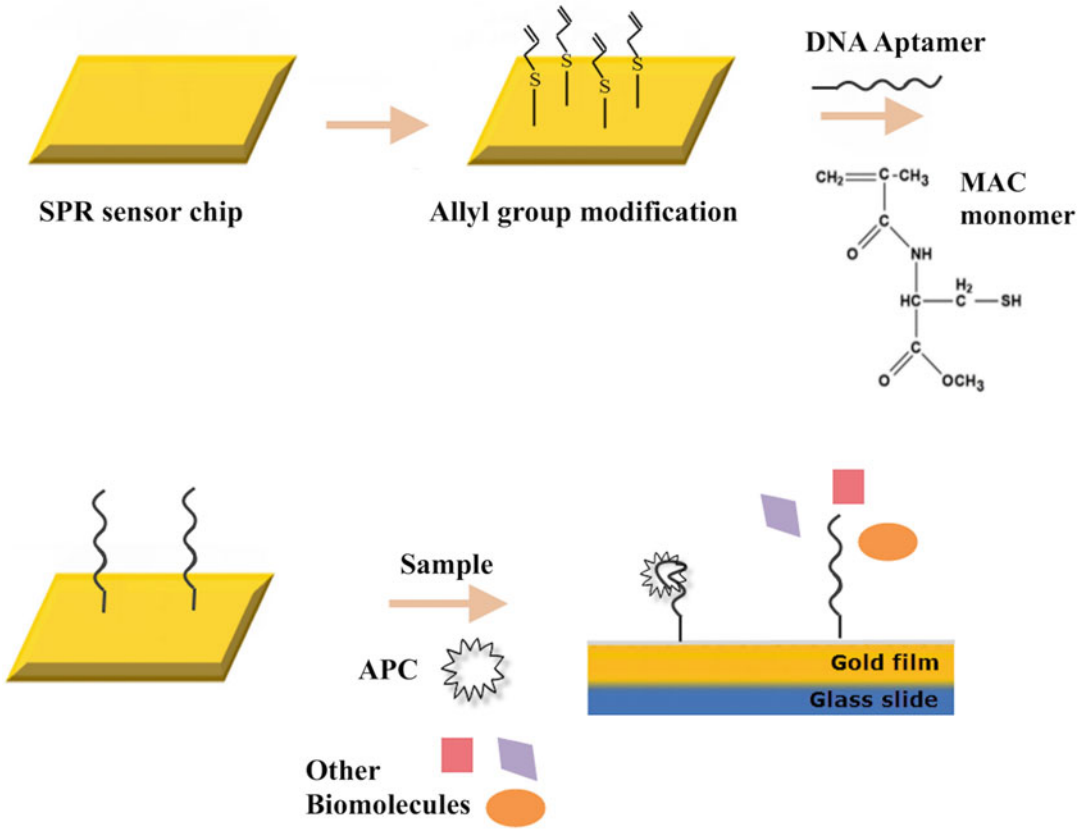


**Fig. 7** Schematic diagram of design of SPR aptasensor chip; (**a**) thiol modification; (**b**) preparation of aptamer-based SPR chip

surfaces at high resolution. It can also be utilized to measure force–distance curves [26].

1. SPR chip was placed on the device.
2. AFM analysis is performed in noncontact mode.
3. XY Scanner: 45 μm × 45 μm—XY scanning resolution: 0.02 nm.
4. Z-scanner: 12 μm—Optical microscope: 800×-ADC/DAC full 16 bit resolution.
5. The lever is usually silicon or silicon nitride.
6. Desired chip zone is shown using a Pt/Ir alloy wire with a diameter of 0.25 mm.
7. The chip surface topographic image resolution is about 0.5 μm (about 50 nm).
8. Surface images and 3D images are taken at different scales.

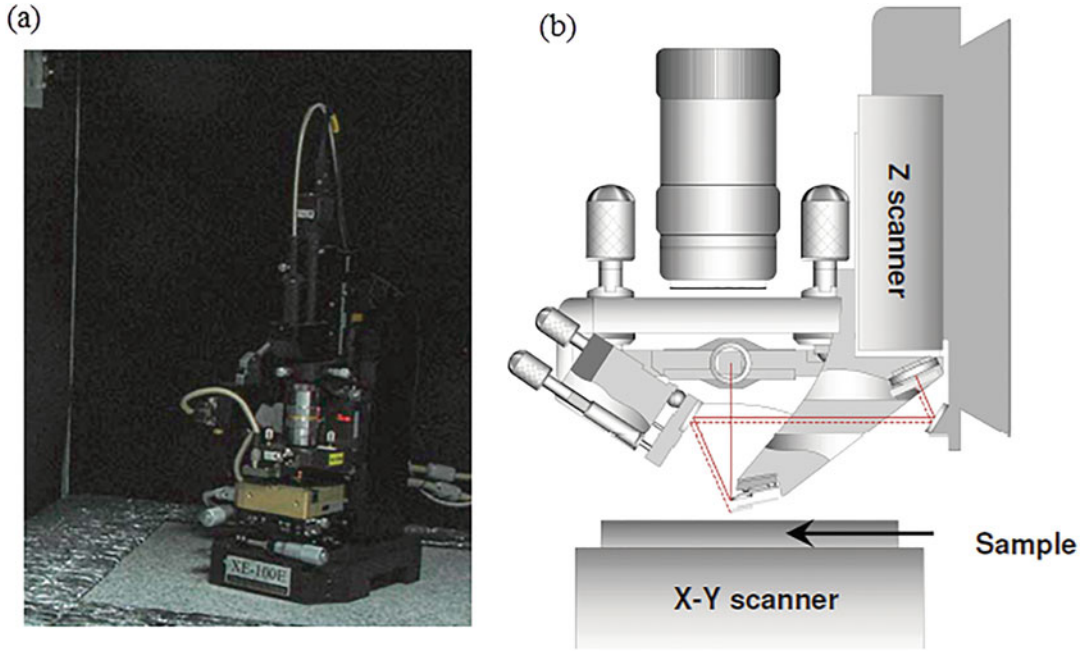


**Fig. 8** (**a**) AFM apparatus and (**b**) working principle

9. The sample field of $10 \times 10\ \mu m^2$ is displayed with a resolution of $256 \times 256$ pixels and the $2\ \mu m\ s^{-1}$ scanning rate.
10. In Fig. 11b an AFM image of the DNA-Apt chip is displayed; the roughness value of the DNA-Apt chip is calculated as 5.24 (Fig. 8).

Contact angle analysis is performed for surface hydrophilicity of modified SPR chip surface.

Contact angle (CA) between a liquid and a solid surface (e.g. chip surface) is analyzed with a contact angle device. A tangent ($\theta$, angle) is formed between the solid surface and the liquid. The probability of determining solid surface tensions from contact-based has been defined by Young in 1805. The contact angle of a liquid drop on a solid surface is identified by the mechanical equilibrium of the drop under the action of three interfacial tensions (Figs. 6 and 9).

These interfacial tensions are solid–liquid, $\gamma_{sl}$; solid–vapor, $\gamma_{sv}$; and liquid–vapor, $\gamma_{lv}$. This mechanical equilibrium correlation is represented by Young's equation:

$$\gamma_{lv} \cos\theta = \gamma_{sv} - \gamma_{sl} \tag{1}$$

where $\theta\Upsilon$ is a contact angle which can be entered into Young's equation [27]. A contact angle less than 90° shows that the wetting of the solid surface is suitable and a fluid spread over a large field on the solid surface. A contact angle greater than 90° usually shows

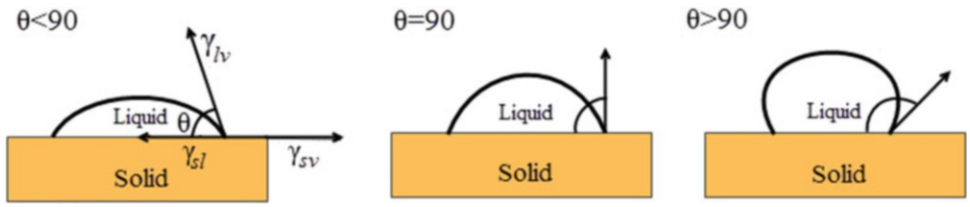


**Fig. 9** Schematic diagram of a sessile-drop contact angle method

that wetting of the solid surface is unfavorable and a fluid reduces its contact with the surface and forms a compact liquid droplet [28].

1. The contact angle value of DNA-Apt SPR chip is determined as 58.2° (Fig. 11a). The sessile drop method is applied to the chip surface and average contact angle values are calculated for the SPR aptasensor chip.
2. The contact angle value of bare chip is calculated as 65.2°.

DNA-Apt SPR aptasensor average surface thickness is characterized using a Nanofilm-EP3 Imaging Nulling Ellipsometer. The imaging ellipsometer uses classical null ellipsometry and real-time ellipsometric contrast imaging (Fig. 10).

1. The laser beam is elliptically polarized after it passes through a linear polarizer (P) and a quarter-wave plate (C). The elliptically polarized light is then reflected off the sample (S) onto an analyzer (A) and imaged onto a CCD camera through a long working distance objective.
2. Light source: Laser (L) is a broadband laser for the highest image quality with a wavelength of 532 nm and an incidence angle of 62°.
3. CCD camera: High quality, monochrome GigE CCD camera. Wavelength: 360–1000 nm 1392 × 1040 pixel, 12 bits, max. 25 frames per second (fps).
4. An objective for focus scanner is used (10× objective); lateral ellipsometric resolution: 2 μm, FOV: 400 μm × 400 μm, depends on AOI.
5. In the chip surface layer thickness analysis, a four-zone auto nulling method integrating the sample field of almost 50 μm × 50 μm is followed by a fitting algorithm.
6. In Fig. 11c the ellipsometry image of the DNA-Apt chip is shown. The polymer film thicknesses value is calculated as 94.0 ± 2.10 nm.

1. The DNA-Apt SPR aptasensor is used for kinetic analysis with SPR imager II.

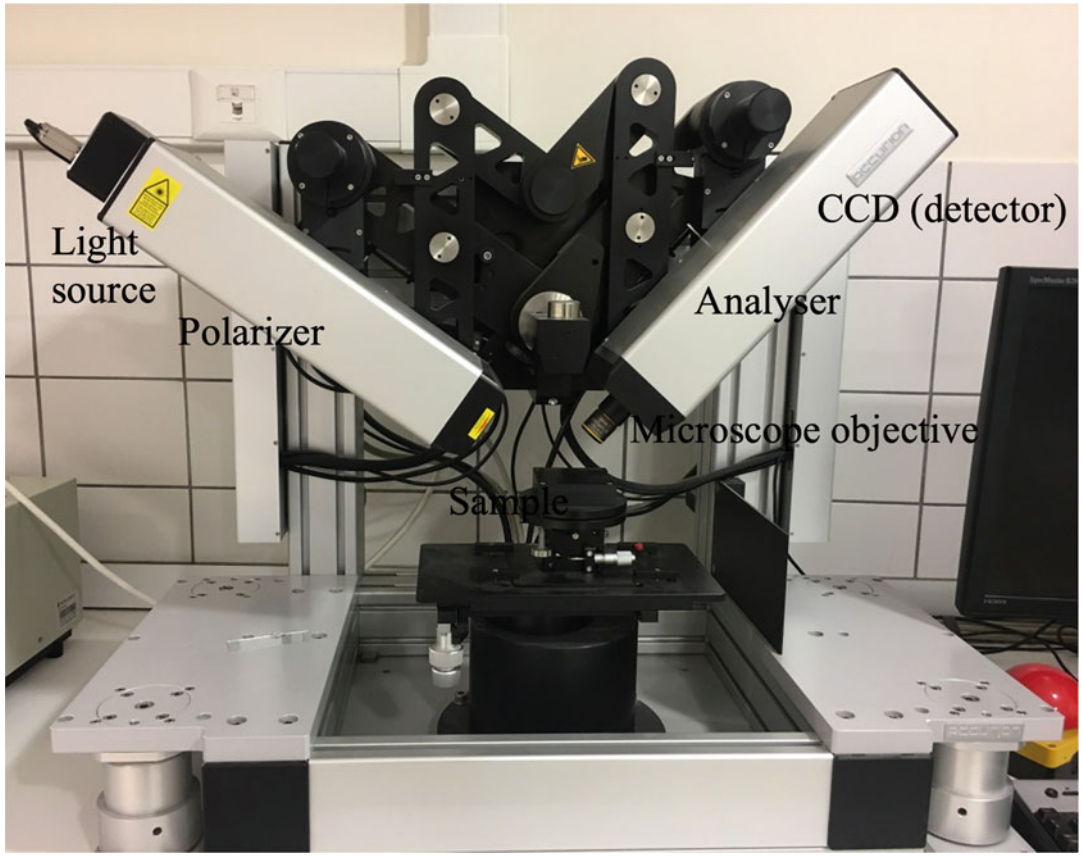


**Fig. 10** Ellipsometry apparatus

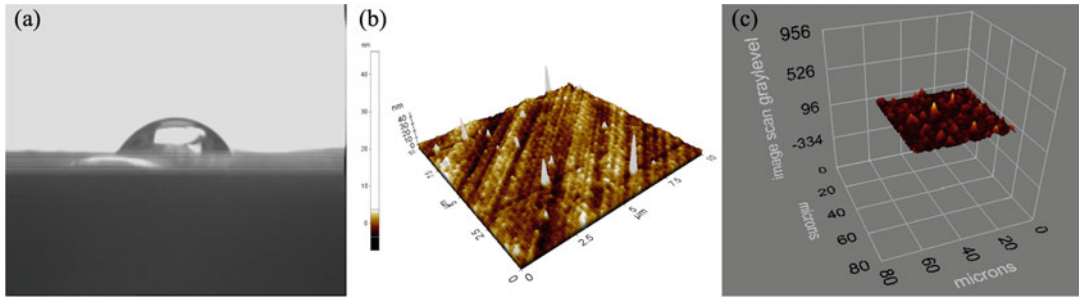


**Fig. 11** (**a**) Contact angle image; (**b**) AFM image; (**c**) ellipsometry image of DNA-Apt aptasensors chip

### *3.3 Kinetic Analysis with DNA-Apt SPR Aptasensor*

2. A stable angle is set manually at the left angle flank of the SPR-dip.
3. A peristaltic pump (IDEX/Ismatec REGLO-CPF Digital Peristaltic Pump) delivers the liquid sample to the chip cell at a rate of 0.5 mL/min.

4. DNA-Apt SPR aptasensors interact with APC solutions in the concentration linear range from 0.005 to 4.0 μg/mL.
5. The SPR aptasensors are cleaned with ethanol solution and pure water.
6. The system is equilibrated pH 7.4 PBS buffer solutions for 3 min, then protein adsorption APC solution for 10 min.
7. After 10 min, the system attained rebalance.
8. 0.025 M NaCl is utilized in the desorption step of the DNA-Apt SPR aptasensor.
9. SPR aptasensor system is washed with deionized water for 5 min.
10. In this SPR sensor system, the primary SPR response is in PIU (Pixel Intensity Unit). The SPR signal change obtained in PIU is converted to the real change in reflectivity, $\Delta R\%$.
11. The SPR sensor signal response is a linear function of the surface coverage supplied $\Delta\%\ R \leq 10\%$.
12. As seen in Fig. 12a, as the APC concentration rises, the $\Delta R$ value increases. The $\Delta R_{max}$ value reached equilibrium at around 4.0 μg $mL^{-1}$ and the equilibrium value is set at 5.82.
13. DNA-Apt SPR aptasensor is performed for the determination of APC in artificial plasma.
14. DNA-Apt SPR aptasensor performance has been also examined for the detection of APC in artificial plasma samples. APC concentrations ranging from 0.005 μg $mL^{-1}$ to 0.5 μg $mL^{-1}$ were spiked to artificial plasma samples.
15. As shown in Fig. 12b, changes in the DNA-Apt SPR aptasensor response from APC spiked artificial plasma samples are directly proportional to the increase in spiked APC concentration.

### 3.4 Selectivity

Selective recognition is important for sensing analysis. Aptamers have perfect characteristics and attach to specific targets.

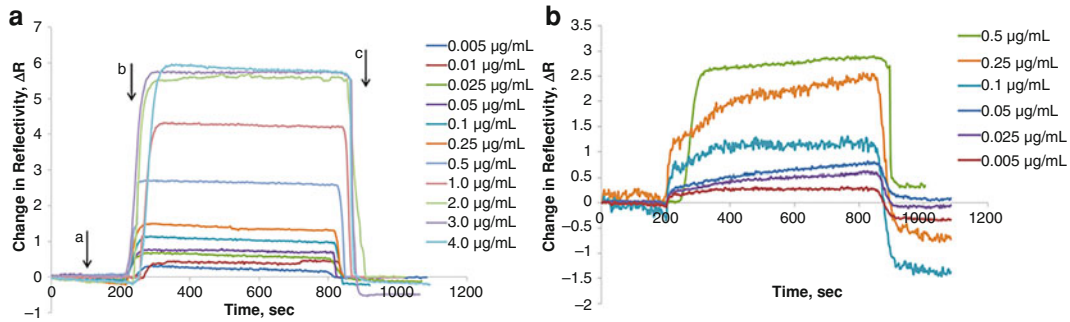


**Fig. 12** (**a**) The real-time APC detection at different concentrations; (**a**) equilibration; (**b**) adsorption; (**c**) regeneration; and (**b**) real-time APC detection from spiked biological sample

1. Human activated protein C (APC), 1.0 μg $mL^{-1}$.
2. Bovine serum albumin (BSA) (Catalog No. 3059, Sigma-Aldrich, St. Louis, MO).
3. Myoglobin (Myb) (Catalog No. M1882, Sigma-Aldrich, St. Louis, MO).
4. Hemoglobin (Hb) (Catalog No. H2500, Sigma-Aldrich, St. Louis, MO).
5. The protein interaction is performed in the presence of 1.0 μg/mL APC and other proteins (BSA, Myb, and Hb) with DNA-Apt aptasensors (*see* **Note 6**).
6. The $\Delta R_{max}$ value results show that there is decreased binding between the DNA-Apt and other proteins (Fig. 13 and Table 1). In Table 1, we compared isoelectric points (pI) and molecular weight (MW) values of human plasma proteins.

### 3.5 Reusability

Reusability is the most important advantage of SPR based aptasensors. The reusability of the sensor is also one of the main aspects of aptasensor applications. In the desorption step, NaCl solution is used to remove the APC attached to the chip surface. Reusability of aptasensor is repeated APC adsorption–desorption cycles.

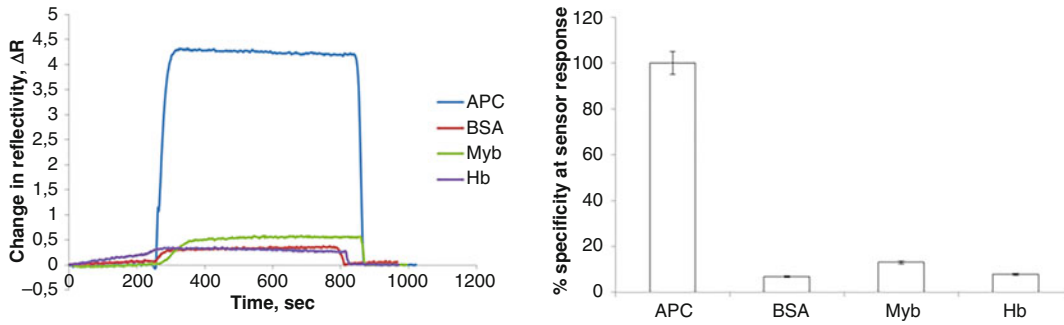


**Fig. 13** Selectivity of DNA-Apt SPR aptasensors; comparison of DNA-Apt SPR aptasensor with BSA, Hb, and Myb

**Table 1**
**Isoelectric points (pI) and molecular weight ($M_W$) values of human plasma proteins**

| Protein | pI | $M_W$ (kDa) |
|---|---|---|
| APC | 4.4–4.8 | 62 |
| BSA | 4.9 | 67 |
| Hb | 6.8–7.0 | 64.5 |
| Myb | 6.8–7.2 | 17 |

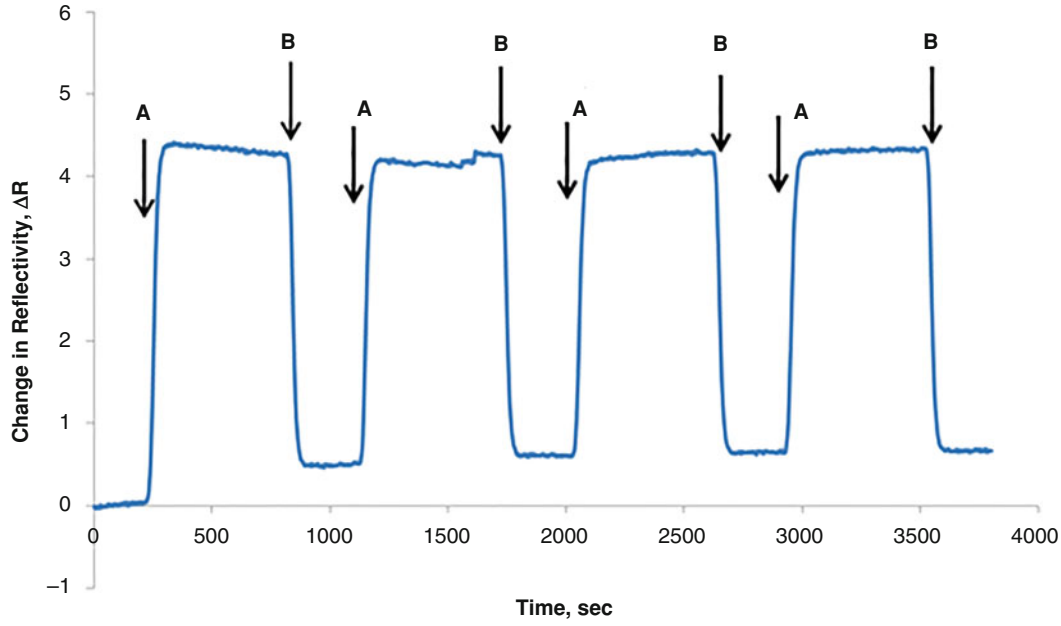


**Fig. 14** Reusability of DNA-Apt SPR aptasensor; (**a**) adsorption (**b**) desorption

1. Reusability of the DNA-Apt SPR aptasensor is displayed by four equilibration–adsorption–desorption cycles that are repeated using aqueous APC protein solutions.
2. 1.0 μg/mL of APC sample sequentially interacts with the SPR aptasensors (*see* **Note 7**).
3. The SPR aptasensor reusability results for APC detection is displayed in Fig. 14.
4. Fig. 14 shows (a) adsorption (b) desorption steps.
5. Results displayed that the SPR signal response reduced by 0.68% after four cycles.

### 3.6 Isotherm Models

APC analyte–DNA-Apt SPR aptasensor interactions are determined by carrying out kinetic analysis, equilibrium binding parameter (Scatchard), and Langmuir, Freundlich, and Langmuir–Freundlich adsorption isotherm models. The isotherm model can be assessed using the following equations.

Equilibrium kinetic analysis:

$$\mathrm{d}\Delta R/\mathrm{d}t = k_{\mathrm{a}} C \Delta R_{\max} - (k_{\mathrm{a}} C + k_{\mathrm{d}})\Delta R \tag{2}$$

Scatchard:

$$\Delta R_{\mathrm{ex}}/[C] = K_{\mathrm{A}}\left(\Delta R_{\max} - \Delta R_{\mathrm{eq}}\right) \tag{3}$$

Langmuir:

$$\Delta R = \{\Delta R_{\max}[C]/K_{\mathrm{D}} + [C]\} \tag{4}$$

Freundlich:

$$\Delta R = \Delta R_{\max}[C]^{1/n} \tag{5}$$

Langmuir–Freundlich:

$$\Delta R = \left\{\Delta R_{\max}[C]^{1/n}/K_{\mathrm{D}} + [C]^{1/n}\right\} \tag{6}$$

1. $\Delta R$ is the response measured by binding.
2. $C$ is APC protein concentration (μg $\mathrm{mL}^{-1}$).
3. $1/n$ refers to Freundlich exponent; $k_{\mathrm{d}}$ ($\mathrm{s}^{-1}$) and $k_{\mathrm{a}}$ (μg $\mathrm{mLs}^{-1}$) values refer to the forward and reverse kinetic rate constants (*see* **Note 8**).
4. $K_{\mathrm{D}}$ (μg $\mathrm{mL}^{-1}$) and $K_{\mathrm{A}}$ $(\mu\mathrm{g/mL})^{-1}$ are forward and reverse equilibrium constants.
5. Max, eq, and ex indicate maximum, equilibrium, and experimental, respectively.

The calculated parameters for all models are shown in Table 2. For APC molecule, the linearity of the Langmuir equation is better than Freundlich and Langmuir–Freundlich isotherm models. The best-fitted model to describe the interaction between the DNA-Apt SPR aptasensor and APC molecule is the Langmuir model. According to these results, the binding of APC onto DNA-Apt SPR aptasensor is monolayer. The $\Delta R_{\max}$ value calculated by the Langmuir model is close to the experimental $\Delta R_{\max}$ value [29, 30] (Figs. 15 and 16).

**Table 2**
**Kinetic and isotherm parameters**

| Equilibrium analysis (Scatchard) | | Association kinetic analysis | | Langmuir | | Freundlich | | Langmuir–Freundlich | |
|---|---|---|---|---|---|---|---|---|---|
| $\Delta R_{\max}$ | 7.942 | $\Delta R_{\max}$ | 0.003 | $\Delta R_{\max}$ | 8.312 | $\Delta R_{\max}$ | 3.478 | $\Delta R_{\max}$ | 17.331 |
| $K_{\mathrm{A}}$ (μg/mL)$^{-1}$ | 0.975 | $K_{\mathrm{D}}$ (μg/mL) | 0.002 | $K_{\mathrm{D}}$ (μg/mL) | 1.120 | $1/n$ | 0.465 | $1/n$ | 0.465 |
| $K_{\mathrm{D}}$ (μg/mL) | 1.025 | $K_{\mathrm{A}}$ (μg/mL)$^{-1}$ | 1.428 | $K_{\mathrm{A}}$ (μg/mL)$^{-1}$ | 0.892 | $R^2$ | 0.9882 | $K_{\mathrm{D}}$ (μg/mL) | 0.015 |
| $R^2$ | 0.929 | $R^2$ | 0.700 | $R^2$ | 0.994 | | | $K_{\mathrm{A}}$ (μg/mL)$^{-1}$ | 64.716 |
| | | | | | | | | $R^2$ | 0.993 |

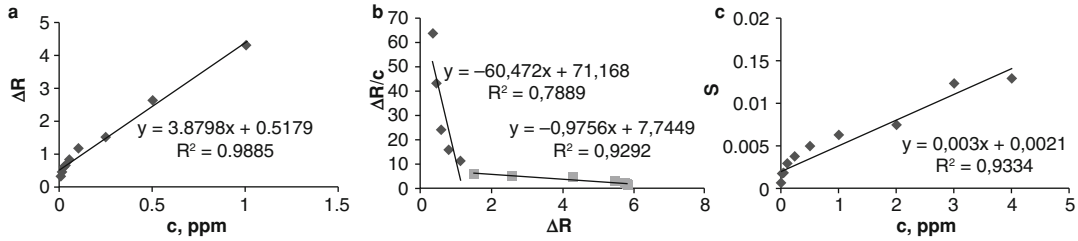


**Fig. 15** Mathematical approaches for determination of kinetic parameters. (**a**) Concentration dependency of APC-Apt SPR aptasensor. (**b**) Equilibrium analysis (Scatchard). (**c**) Association kinetics analysis

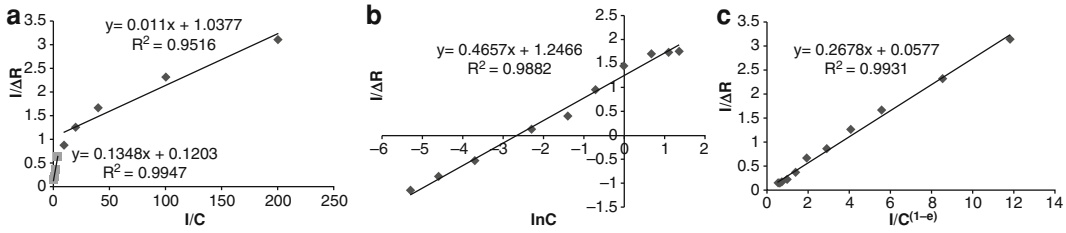


**Fig. 16** Mathematical approaches for determination of isotherm parameters. (**a**) Langmuir; (**b**) Freundlich; (**c**) Langmuir–Freundlich

## 4 Notes

1. SPRimagerII of GWC Technologies (Madison, WI, USA) was originally designed by Robert M. Corn's group of the University of California–Irvine.
2. PBS buffer is prepared by dissolving 0.01 M disodium hydrogen phosphate ($Na_2HPO_4$) (Catalog No. 106586, Merck, Darmstadt, Germany), 0.002 M potassium dihydrogen phosphate ($KH_2PO_4$) (Catalog No. 104873, Merck, Darmstadt, Germany), 0.0027 M potassium chloride (KCl) (Catalog No. 104936, Merck, Darmstadt, Germany), and 0.137 M sodium chloride (NaCl) (Catalog No. 746398, Sigma-Aldrich, St. Louis, MO) in 500 mL of pure water.
3. The SPR aptasensors are washed with ethyl alcohol–water solution (50%, v/v).
4. Complex formation is performed in the rotator for 1 h.
5. A volume of 10 μL dropped onto the chip surface is dispersed homogeneously by spin coating.
6. PBS solution (pH 7.4) is used as an adsorption buffer.
7. In reusability study, % change in reflectivity values is obtained for four cycles.

8. When applying the equilibrium kinetic analysis, the slope of curves and plotted concentration vs. slope curve to determine $k_a$ and $k_d$ are calculated.

## References


1. Zhou J, Battig MR, Wang Y (2010) Aptamer-based molecular recognition for biosensor development. Anal Bioanal Chem 398:2471–2480
2. Eivazzadeh-Keihan R, Pashazadeh-Panahi P, Baradaran B, Maleki A, Hejazi M, Mokhtarzadeh A, de la Guardia M (2018) Recent advances on nanomaterial based electrochemical and optical aptasensors for detection of cancer biomarkers. Trends Anal Chem 100:103–115
3. Ghorbani F, Abbaszadeh H, Dolatabadi JEN, Aghebati-Maleki L, Yousefi M (2019) Application of various optical and electrochemical aptasensors for detection of human prostate specific antigen: a review. Biosens Bioelectron 142:111484
4. Erdem A, Congur G (2014) Voltammetric aptasensor combined with magnetic beads assay developed for detection of human activated protein C. Talanta 128:428–433
5. Tombelli S, Minunni M, Mascini M (2005) Analytical applications of aptamers. Biosens Bioelectron 20:2424–2434
6. Willner I, Zayats M (2007) Electronic aptamer-based sensors. Angew Chem Int Ed 46:6408–6418
7. Zhang L, Wan S, Cansiz S, Cui C, Liu Y, Cai R, Hong C, Teng I-T, Shi M, Wu Y, Dong Y, Tan W (2017) Aptasensor with expanded nucleotide using DNA nanotetrahedra for electrochemical detection of cancerous exosomes sai wang. ACS Nano 11:3943–3949
8. Mokhtarzadeh A, Tabarzad M, Ranjbari J, de la Guardia M, Hejazi M, Ramezani M (2016) Aptamers as smart ligands for nano-carriers targeting. TrAC Trend Anal Chem 82:316–327
9. Kawde AN, Rodriguez MC, Lee TMH, Wang J (2005) Label-free bioelectronic detection of aptamer–protein interactions. Electrochem Commun 7:537–540
10. Sadeghi AS, Mohsenzadeh M, Abnous K, Taghdisi SM, Ramezani M (2018) Development and characterization of DNA aptamers against florfenicol: fabrication of a sensitive fluorescent aptasensor for specific detection of florfenicol in milk. Talanta 182:193–201
11. Wang S, Dong Y, Liang X (2018) Development of a SPR aptasensor containing oriented aptamer for direct capture and detection of tetracycline in multiple honey samples. Biosens Bioelectron 109:1–7
12. Wang L, Wang R, Chen F, Jiang T, Wang H, Slavik M, Wei H, Li Y (2017) QCM-based aptamer selection and detection of salmonella typhimurium. Food Chem 221:776–782
13. Erdem A, Congur G, Mese F (2014) Electrochemical detection of activated protein c using an aptasensor based on pamam dendrimer modified pencil graphite electrodes. Electroanalysis 26:1–12
14. Homola J, Hegnerová K, Vala M (2009) Surface plasmon resonance biosensors for detection of foodborne pathogens and toxins. Proc SPIE 7167:716705–716701
15. Schasfoort RBM (2017) Introduction to surface Plasmon resonance. In: Richard B, Schasfoort M (eds) Handbook of surface Plasmon resonance, 2nd edn. The Royal Society of Chemistry, London, UK, pp 1–24
16. Yanase Y, Hiragun T, Yanase T, Kawaguchi T, Ishii K, Hide M (2013) Application of SPR imaging sensor for detection of individual living cell reactions and clinical diagnosis of type I allergy. Allergol Int 62:163–169
17. Yanase Y, Suzuki H, Tsutsui T, Uechi I, Hiragun T, Mihara S, Hide M (2007) Living cell positioning on the surface of gold film for SPR analysis. Biosens Bioelectron 23:562–567
18. Horii M, Shinohara H, Iribe Y, Suzuki M (2011) Living cell-based allergen sensing using a high resolution two-dimensional surface plasmon resonance imager. Analyst 136:2706–2711
19. Koyun S, Akgönüllü S, Yavuz H, Erdem A, Denizli A (2019) Surface plasmon resonance aptasensor for detection of human activated protein C. Talanta 194:528–533
20. Zeng S, Baillargeat D, Ho H-P, Yong K-T (2014) Nanomaterials enhanced surface plasmon resonance for biological and chemical sensing applications. Chem Soc Rev 43:3426–3452
21. Koca Esentürk M, Akgönüllü S, Yılmaz F, Denizli A (2019) Molecularly imprinted based surface plasmon resonance nanosensors for microalbumin detection. J Biomater Sci Polym Ed 30(8):646–661

22. Saylan Y, Akgönüllü S, Yavuz H, Ünal S, Denizli A (2019) Molecularly imprinted polymer based sensors for medical applications. Sensors 19:1279
23. Saylan Y, Yılmaz F, Derazshamshir A, Yılmaz E, Denizli A (2017) Synthesis of hydrophobic nanoparticles for real-time lysozyme detection using surface plasmon resonance sensor. J Mol Recognit 30(9):e2631
24. Akgönüllü S, Yavuz H, Denizli A (2020) SPR nanosensor based on molecularly imprinted polymer film with gold nanoparticles for sensitive detection of aflatoxin B1. Talanta 219:121219
25. Erdem A, Congur G (2014) Dendrimer modified 8-channel screen printed electrochemical array system for impedimetric detection of activated protein C. Sens Actuators B Chem 196:168–174
26. Butt H-J, Cappella B, Kappl M (2005) Force measurements with the atomic force microscope: technique, interpretation and applications. Surf Sci Rep 59(1–6):1–152
27. Kwok DY, Neumann AW (1999) Contact ref contact angle measurement and contact angle interpretation. Adv Colloid Interf Sci 81 (3):167–249
28. Yuan Y, Lee TR (2013) Contact angle and wetting properties. In: Bracco G, Holst B (eds) Surface science techniques. Springer series in surface sciences, vol 51. Springer, Berlin, Heidelberg
29. Battal D, Akgönüllü S, Yalcin M, Yavuz H, Denizli A (2018) Molecularly imprinted polymer based quartz crystal microbalance sensor system for sensitive and label-free detection of synthetic cannabinoids in urine. Biosens Bioelectron 111:10–17
30. Bakhshpour M, Özgür E, Bereli N, Denizli A (2017) Microcontact imprinted quartz crystal microbalance nanosensor for protein C recognition. Colloids Surf B Biointerfaces 151:264–270

# Chapter 4

# Large-Scale Nanogrooved Photonic Crystals for Label-Free Biosensing by Guided-Mode Resonance

**Miquel Avella-Oliver, Gabriel Sancho-Fornes, Rosa Puchades, and Ángel Maquieira**

## Abstract

We have developed large-scale one-dimensional photonic crystals from standard recordable Blu-ray disks, tailored to sense unlabeled biorecognition events on their surface. These materials rely on coating, with layers of 80 nm of titanium oxide, nanogrooved polycarbonate plates obtained from regular disks. As a result, they present guided-mode resonances that we have demonstrated that can be exploited to quantify biorecognition events by means of the bandgap positions in the transmission spectra. These photonic crystals have displayed well-correlated dose–response curves in immunoassays to quantify IgGs, C-reactive protein, and lactate dehydrogenase. The detection limit reached is 16 ng/mL, 2μg/mL, and 18 ng/mL, respectively. Herein we describe the experimental procedures and methods to fabricate and functionalize these photonic crystals, perform immunoassays on them, set up an optical system to measure their response, and process the resulting data to perform bioanalytical determinations in label-free format.

**Key words** Photonic crystal, Guided-mode resonance, Groove, Grating, Titanium oxide, Blu-ray disk, Immunoassay, CRP, LDH

## 1 Introduction

A key aspect in the field of biosensing is the development of simple, affordable, and user-friendly biosensors that overcome the limitations of standard benchtop analytical systems and support the use of these bioanalytical devices out of specialized labs [1–3]. Along these lines, the progress in nanoscience and nanotechnology in the recent years has given rise to a growing control in the development of nanostructured materials and an increasing understanding of light–matter interaction events at the nano and micro scale [4, 5]. These advances have materialized in a great scientific activity on transduction phenomena and nanomaterials to sense biorecognition events, for example by means of surface plasmon resonance [6, 7], interferometry [8], or surface-enhanced Raman scattering [9], among others. Another group of important advances within

Miguel R. Ossandon et al. (eds.), *Biomedical Engineering Technologies: Volume 1*, Methods in Molecular Biology, vol. 2393, https://doi.org/10.1007/978-1-0716-1803-5_4, 

this context are the ones based on photonic crystals tailored to transduce biorecognition events [10]. Rather than a particular optical principle, the term photonic crystal refers to optically active materials constituted by periodic (one-, two-, or three-dimensional) lattices at the nanoscale that may present different light-matter interaction phenomena.

All these bioanalytical approaches involve important solutions for the development of biosensors. For instance, they enable direct detection of unlabeled macromolecules and real-time measurement of biorecognition processes [11, 12]. However, these systems also involve expensive materials together with costly, complex, and nonscalable fabrication methods, which limits the scope of the resulting biosensors and their potential impact in daily applications. Herein we describe a simple method to create inexpensive and large-scale one-dimensional photonic crystals from standard Blu-ray disks and to use them for label-free immunosensing.

Compact disk systems are consumer electronics that has demonstrated a huge potential to develop point-of-care biosensors [13–16]. The disks are circular platforms (12 cm diameter, 1.2 mm thickness) constituted by an assembly of superposed layers. One of them is made of polycarbonate and contains a groove, embedded on one side, that extents as a spiral along the disk. The structural features of the grooved pattern as well as the multilayered configuration depends on the type of compact disk system (CD, DVD, Blu-ray, etc.) as well as on the data recording specifications of the disks (read-only memory, recordable, or rewritable) (Table 1). The multilayered structure of rewritable Blu-ray disks (BD-R is

**Table 1**
**Characteristic features of recordable CD, DVD and Blu-ray disks**

| | CD-R | DVD-R | BD-R |
|---|---|---|---|
| Layers[a] | Label<br>Reflective metal<br>Recording dye<br>(grooved structure)<br>PC (1.2 mm) | Label<br>PC (0.6 mm)<br>Reflective metal<br>Recording dye<br>(grooved structure)<br>PC (1.2 mm) | Label<br>PC (1.1 mm)<br>Reflective metal<br>Recording dye<br>(grooved structure)<br>Protective polymer (0.1 mm) |
| Period[b] | 1600 nm | 740 nm | 320 nm |
| Height[b] | 200 nm | 175 nm | 20 nm |
| Width[b] | 600 nm | 320 nm | 130 nm |
| Price[c] | ~0.2 € | ~0.25 € | ~0.55 € |

[a]Layered structure of the disks (laser incidence from the bottom). The term "label" refers to the printed or printable coating typically included onto the disks, and "PC" means polycarbonate. The position of the "grooved structure" within the layered assembly is indicated in parentheses. Omitted layer thickness values are neglectable at the millimetric scale
[b]Topographical features of the grooved polycarbonate structures. Groove dimensions may slightly change from brands and manufacturers (*see* **Note 2**)
[c]Approximate price per disk

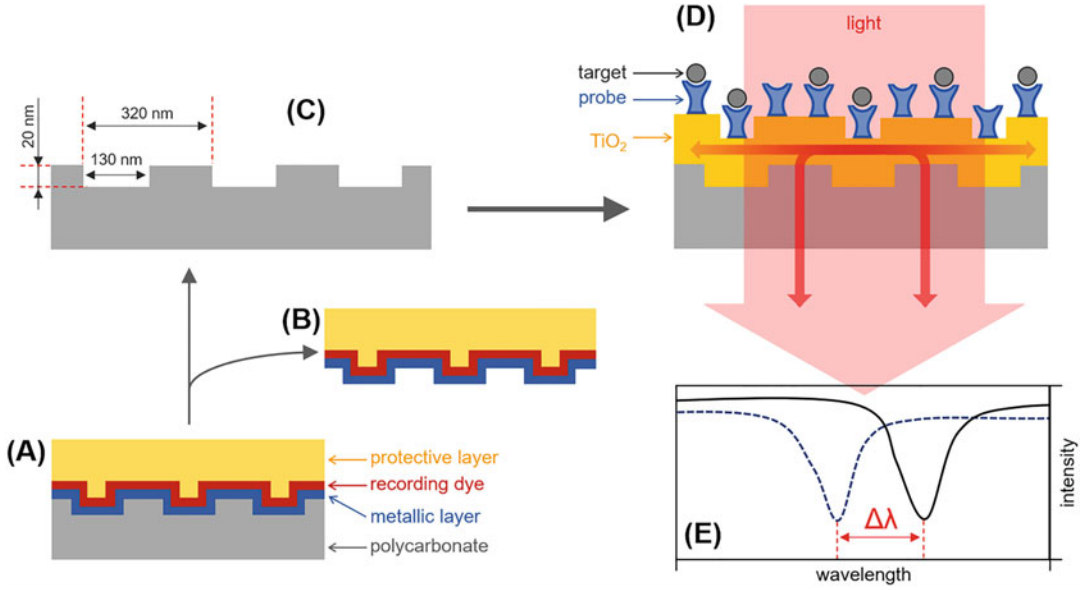


**Fig. 1** General scheme of the method to develop and apply these photonic crystals for label-free biosensing, including (**a**) original multilayered structure of BD-R disks, (**b**) part of the BD-R removed, (**c**) polycarbonate plate with the nanogrooved grating, (**d**) scheme of the photonic crystal measuring an assay, and (**e**) example of the bandgaps in the polychromatic transmission spectra and the resulting wavelength shift ($\Delta\lambda$) generated by the biorecognition event

constituted by a 1.1 mm thick polycarbonate layer, whose nanogrooved structure is coated with a thin film of a reflective metal, followed by a film of a recording dye, and a 100μm thick protective polymeric layer on top (*see* **Note 1**), as schematized in the Fig. 1a. For the BD-R disks used in this approach, the periodicity of the grooved nanostructure along the radial direction of the disk is 320 nm, the depth of the grooves is about 20 nm, and their width is about 130 nm (*see* **Note 2**) (Fig. 1c).

The main idea behind this development is to use the nanogrooved structure of the disks as an optically active material from which creating functional nanomaterials for biosensing. This is a homogeneous, extremely inexpensive (~0.55 €/disk) and large-scale (more than 85 $cm^2$/disk) structure that is massively fabricated in the industry. Therefore, exploiting these materials for bioanalysis introduces attractive possibilities toward simple, affordable, and deliverable to end users label-free biosensors. Other state-of-the-art developments have used this concept to transduce biointeractions by means of surface-enhanced Raman scattering [17], diffraction-based sensing [18], and Fano resonance [19]. Herein we describe one-dimensional photonic crystals based nanogrooved polycarbonate chips from standard BD-R disks, coated with a film of 80 nm of titanium oxide, and tailored to transduce

biorecognition events on their surface by means of guided-mode resonances (Fig. 1d).

The guided-mode resonance phenomenon of these materials relies on the waveguide behavior of the titanium oxide on polycarbonate (*see* **Note 3**). The nanogrooved structure of the BD-R disks acts as a diffractive grating that couples, in the titanium oxide film, a given range of wavelengths of an incident white light (*see* **Note 4**). Then, the guided light leaks out of the waveguide and interferes with the incident beam, which creates bandgaps in the transmission spectrum. The wavelengths that meet these coupling conditions depend on the thickness of a biological layer on the material. Consequently, binding events of unlabeled biorecognition assays performed on these photonic crystals can be monitored by means of the wavelength shifts in the resulting transmission bandgaps (Fig. 1e).

The original study on the experimental and theoretical aspects, as well as the optical and structural characterizations to conceive and apply these materials was presented in a previous publication [20]. Herein we focus on a detailed description of the practical procedures to fabricate and use the optimized material resulting from the original study. In particular, this chapter reports a comprehensive description of the materials and protocols to obtain the nanogrooved polycarbonate plates from standard BD-R disks, coat them with titanium oxide, covalently attach biological probes on them, arrange the optical measurement setup, perform unlabeled biorecognition assays, and process the resulting data to quantify the concentration of different targets in samples.

## 2 Materials

### 2.1 Chemicals

1. Phosphate-buffered saline (PBS) was prepared to yield 8 mM $Na_2HPO_4$, 2 mM $KH_2PO_4$, 137 mM NaCl, and 2.7 KCl mM at pH = 7.4 in purified water (MilliQ, Millipore Iberica), and filtered through 0.2μm pore size syringe filters (Fisher Scientific).
2. PBS-T was prepared as PBS, but including polysorbate 20 (Tween 20, Sigma-Aldrich) 0.05% v/v in its composition.
3. Ethanol (96% v/v extrapure, Scharlau).
4. Glutaraldehyde solution (25% wt in $H_2O$), (3-aminopropyl) triethoxysilane (99%) (*see* **Note 5**), bovine serum albumin (BSA), lactate dehydrogenase from rabbit muscle (LDH), C-reactive protein (CRP), rabbit anti-BSA IgGs, and mouse anti-CRP IgGs from Sigma-Aldrich. Rabbit anti-LDH IgGs were obtained by rabbit immunization (*see* **Notes 6** and **7**).

### 2.2 Photonic Crystal Preparation

1. Ultra-high-vacuum magnetron sputtering system (ATC series, AJA International Inc.).
2. Computer numerical control drilling machine (Bungard CCD).
3. UV lamp (UVOH 150 LAB, FHR, 254 nm, 50 mW/cm$^2$).
4. Oven (J.P. Selecta, mod 210).
5. Hydrophobic ink pen (Mini PAP Pen, Thermo Scientific).

### 2.3 Optical Setup

1. Breadboard, optical post assemblies (posts, holders, mounts, etc.), and other standard optomechanical components from Thorlabs.
2. White light source (Schott-Fostec ACE DDL, tungsten halogen lamp, 380–780 nm, max. 150 W) coupled to a lightline split into four lines (Fostec 02/00).
3. Planoconvex spherical lens (Linos px f150, focal length 150 mm).
4. Diaphragm (Thorlabs D36S).
5. Silver rectangular plane mirror in an adjustable cube mount from Linos.
6. Fiber adapter (Linos 25/FSMA).
7. Fiber optic probe (Avantes FC-UV200-2-SR).
8. Spectrophotometer (Avantes AvaSpec-2048TEC-USB2) (*see* **Note 8**).

## 3 Methods

All the stages involved in the fabrication and use of these photonic crystals for label-free biosensing are described in this section and schematized in Fig. 2.

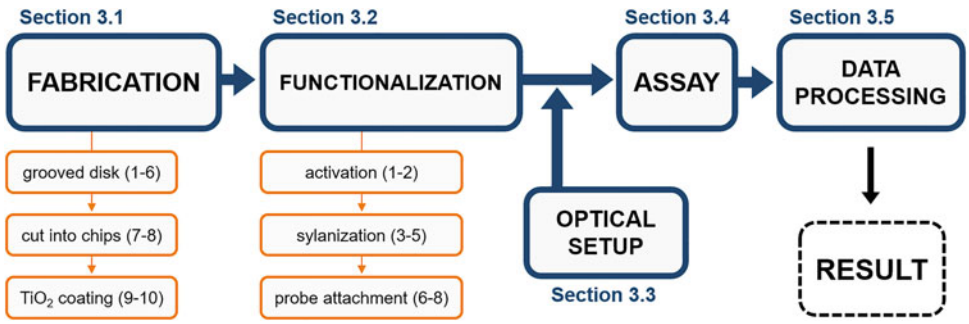


**Fig. 2** Flow chart of the methods involved in the fabrication and use of these photonic crystals to perform bioanalytical determinations in label-free format. The numbers in parentheses indicate the protocol steps described within the corresponding section

### 3.1 Fabrication

The fabrication of the photonic crystals relies on obtaining the internal grooved structure of standard recordable Blu-ray disks (BD-R, MediaRange 4x speed 25 GB) (*see* **Note 2**), cutting the disks into chips, and coat them with $TiO_2$. The corresponding procedure is disclosed in the following steps:

1. Make a circular cut on the protective layer of the disks in an external diameter (about 11.6 cm) using a utility knife (Fig. 3a) (*see* **Note 9**).
2. Lift up a small part of the protective layer by inserting the tip of the utility knife into the groove of the previous circular cut (*see* **Note 10**). Then, take the lifted part with the fingers (using lab gloves) and peel off the whole protective layer by pulling it toward the opposite edge of the disk (Fig. 3b) (*see* **Notes 11** and **12**).

   An alternative strategy in this step is to firmly attach a piece of adhesive tape (about 4 cm long) on the circular cut, and pull from it to lift up and peel off protective layer.

   Another option in this step is to peel off the protective layer by blowing a high stream of compressed air in the circular cut. It may be especially useful in small parts that may remain attached to the disk.

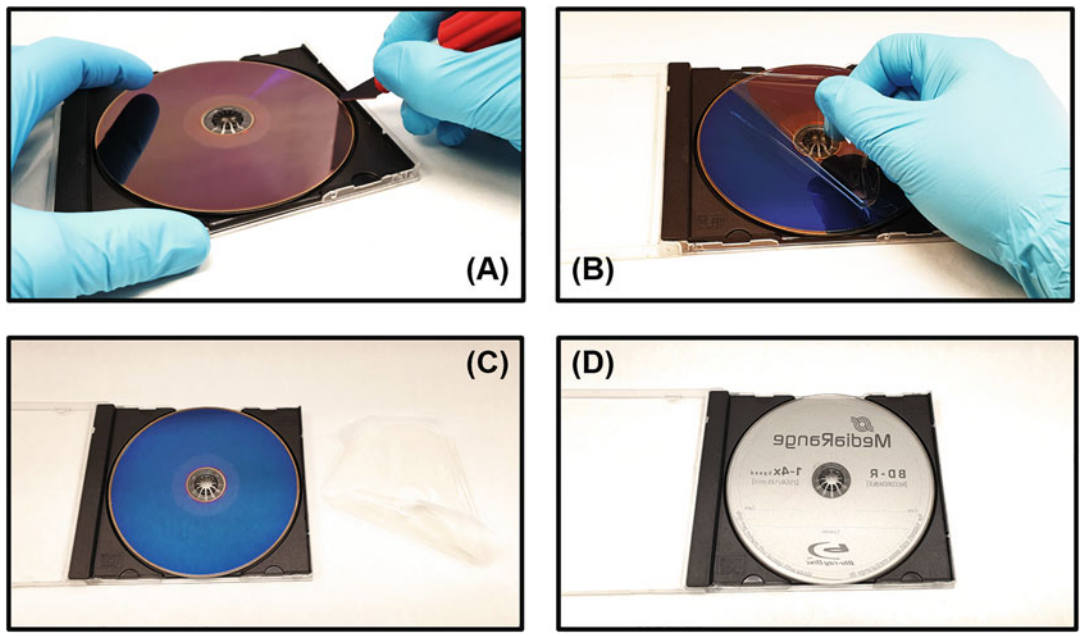


**Fig. 3** Photographs of the procedure to obtain the raw nanogrooved polycarbonate plates from standard recordable Blu-ray disks: (**a**) making the external circular groove on the disk, (**b**) peeling off the protective layer, (**c**) the disk without the protective layer (left) and the removed protective layer (right), and (**d**) the resulting nanogrooved polycarbonate disk after dissolving the metallic and the recording dye layers (*see* **Note 16**)

3. Immerse the disks (grating side up) in a solution of hydrochloric acid (1 M) for 60 min at room temperature in the fume cupboard to remove the metallic layer on the grooved pattern (*see* **Notes 13** and **14**).
4. Rinse the disks by immersing them (grating side up) into three successive baths of purified water (Milli-Q, Millipore Iberica).
5. Rinse the disks by immersing them (grating side up) into three successive baths of ethanol, to remove potential residues of the recording dye.
6. Rinse again the disks by immersing them (grating side up) into a bath of purified water. Dry the disks using a stream of compressed air (Fig. 3c) (*see* **Note 15**).
7. Design the cutting pattern (Fig. 4a) and cut the disks into rectangular chips (1.5 × 1.2 cm) using a computer numerical control drilling machine (drill diameter = 1 mm, rotational speed = 50,000 rpm, translational speed = 750 mm/min) (*see* **Note 17**).
8. Repeat **steps 4** and **5**.
9. Coat the nanogrooved side of the disks with 80 nm of $TiO_2$ by ultra-high-vacuum magnetron sputter deposition (Fig. 4b).
10. To separate the chips, cut the joints of the cut disk (Fig. 4a) using the utility knife. Once isolated, manipulate the chips from the edges, with tweezers, in order to avoid scratches on the grating side.

A practical strategy to store and handle the disks after the fabrication (as well as along intermediate steps) is fixing them face down (grooved grating down) in standard compact disks cases.

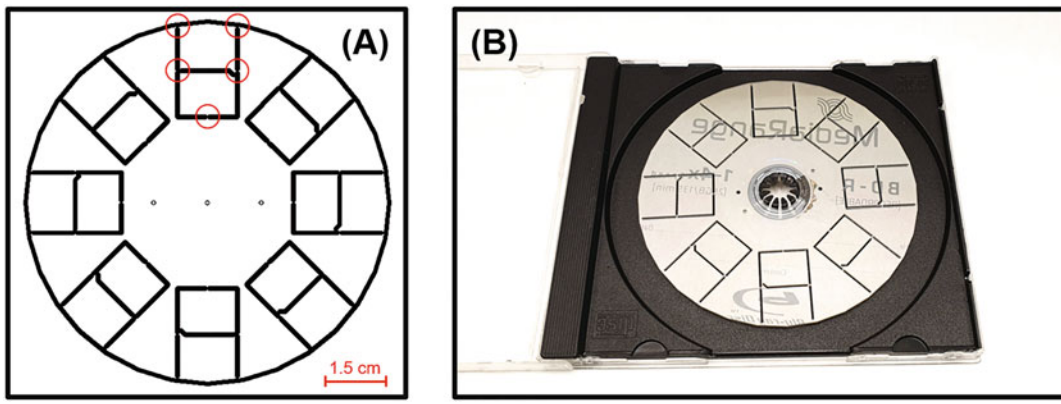


**Fig. 4** (**a**) Image of the cutting pattern used to cut the disks in the computer numerical control drilling machine. The red circles in the top-center chip indicate the joints (about 0.5 mm long) created in all the chips to keep them attached to the disk. (**b**) Photograph of the resulting disks after the whole fabrication process

### 3.2 Functionalization

Once fabricated the chips, the surface of the photonic crystals is functionalized to covalently attach the probes (BSA, anti-CRP IgG, and anti-LDH IgG for the assays herein addressed) on the titanium oxide film, according to the following procedure:

1. Wash the chips by immersion in EtOH for 5 min in an orbital stirrer (~40 rpm) and dry them using a stream of compressed air (*see* **Note 18**).
2. Put the chips (grating face up) under a UV lamp (254 nm, 50 mW/cm$^2$) for 10 min. Meanwhile, prepare a solution of (3-aminopropyl)triethoxysilane (2% in ethanol) to be ready by the end of the irradiation.
3. Immediately after the irradiation, immerse the chips in the (3-aminopropyl)triethoxysilane solution for 30 min (*see* **Note 19**) and stir (orbital stirring, ~40 rpm) at room temperature.
4. Rinse the chips by immersion in ethanol and dry them with compressed air.
5. Bake the chips in an oven at 95 °C for 30 min. Next, wash them by immersion in PBS and dry the chips with compressed air.
6. Immediately afterward, immerse the chip in a solution of glutaraldehyde (2.5 v/v in PBS) for 30 min (orbital stirring at ~40 rpm) at room temperature (*see* **Note 20**). Rinse the chips by immersion in purified water and dry them using a stream of compressed air.
7. Immerse the chips in solutions of probe (BSA, anti-CRP IgG or anti-LDH IgG, 100μg/mL in PBS) for 30 min (orbital stirring, ~40 rpm) at room temperature.
8. Rinse the chips by immersion in PBS-T and dry them using a compressed air stream.

### 3.3 Measurement System

A custom optomechanical setup is used to measure the optical response (the polychromatic transmission spectra) of the photonic crystals. This setup basically relies on a collimated beam of white light that hits the chips (with the assays on them) and a spectrophotometer that collects the spectra of the light transmitted through the material. A photograph of the measurement system is shown in Fig. 5, and the steps to arrange it are described below:

1. Clamp one of the lightlines in the optomechanical setup, set the intensity control knob of the light source to its nine o'clock position (*see* **Note 21**).
2. To collimate the beam, fix the planoconvex spherical lens at 150 mm from the output of the lightline (*see* **Note 22**) and align it for the light beam to hit perpendicularly the center of the lens.

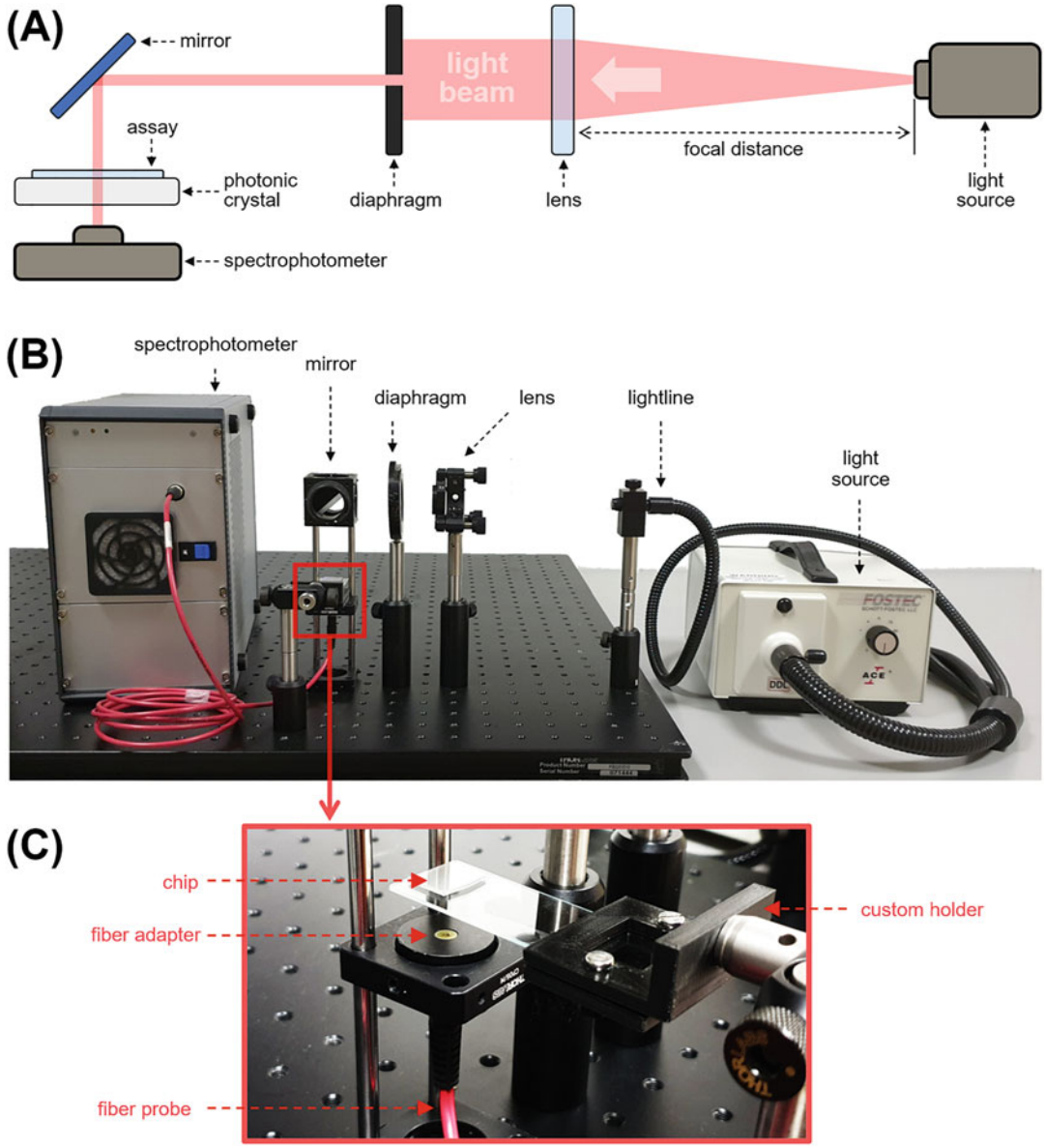


**Fig. 5** Optomechanical setup employed to experimentally measure the polychromatic transmission spectra of the photonic crystals: (**a**) schematic diagram, (**b**) real image, and (**c**) zoomed view of the photonic crystal within the system

3. Fix a diaphragm after the collimation lens and parallel to it. Align the diaphragm with the center of the light beam and set its aperture to 3 mm of diameter.
4. Set a mirror after the diaphragm to reflect the beam perpendicularly toward the breadboard.

5. Attach the chip (grating side up) on a glass slide by using small strips of adhesive tape in two sides of the chip, fix the glass slide in the optomechanical setup (*see* **Note 23**), and align it for the center of the chip to be hit by the light beam.
6. Fix the tip of the fiber optic probe (using a fiber adapter) below the chip and align it for the light beam to hit perpendicularly the center of the probe.
7. Connect the other tip of the fiber optic probe to the spectrophotometer.
8. Connect the spectrophotometer to a personal computer (transmission spectra acquired with the software AvaSoft 7.8 for USB2).

The photonic response of these materials involves two bandgaps in the transmission spectra upon irradiation of unpolarized light, one from the coupling of the transverse magnetic (TM) polarization and the other from the transverse electric (TE) polarization. In raw chips of the photonic crystals, the TM bandgaps appear centered at around 525 nm and the TE ones at around 590 nm (Fig. 6a). The bandgaps generated by the TE are the ones selected to sense biointeractions on the materials by means of wavelengths shifts [20].

Besides, if the irradiation angle tilts along the perpendicular direction of the grooves, both bandgaps split symmetrically into two and the separation between them increases together with the incident angle, whereas the averaged wavelength remains constant (Fig. 6b) [20]. An effective strategy to enable robust measurements and to minimize potential imprecision and artifacts coming from

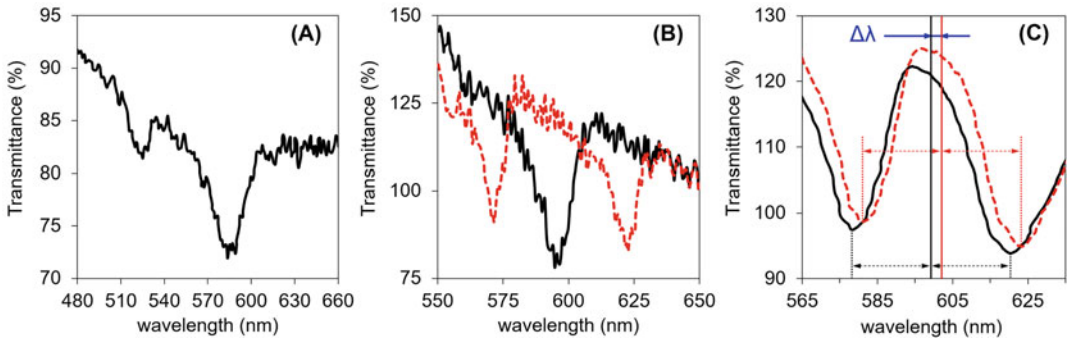


**Fig. 6** Photonic response. (**a**) Transmission spectra of the raw material with the TM (left) and TE (right) bandgaps. (**b**) TE bandgap at perpendicular irradiation (black continuous line) and split TE bandgaps upon an irradiation angle of 6° (red dashed line). (**c**) Processed transmission spectra of a functionalized photonic crystal before (black continuous line) and after (red dashed line) the incubation of target IgGs (100μg $mL^{-1}$). Dotted vertical lines correspond to the bandgaps position, continuous vertical lines represent the averaged wavelength of the split bandgaps of each spectrum, and the difference between them corresponds to the wavelength shift ($\Delta\lambda$) generated by the assay and used as analytical signal

the incidence angle and the curvature of the grooved structure, is to use a chip holder with a fixed tilt (along the perpendicular direction of the nanogrooves), and then use the averaged wavelength of the two split bandgaps as analytical signal. The custom holder used in this development (**step 5** above) tilts the chip 5° (*see* **Note 24**), which separates the split TE bandgaps about 42 nm (*see* **Note 25**).

### 3.4 Assays

To perform and measure biorecognition assays on the photonic crystals, the transmission polychromatic spectra of the chips were assessed after incubating target solutions on the chip, according to the following procedure:

1. Delimit the assay area on the chip by drawing a circle (4 mm diameter) with a hydrophobic ink pen on the grating side (*see* **Note 26**).
2. Acquire the initial (before the sample incubation) transmission spectra of the assay area.
3. Dispense solutions (40μL per assay area) containing different concentrations of the targets (anti-BSA IgGs, CRP and LDH in this work) in PBS-T on the photonic crystal, and incubate them for 30 min at room temperature.
4. Rinse the chips with PBS-T, then with purified water, and finally dry them in an air stream.
5. Acquire the transmission polychromatic spectra (535–752 nm) by averaging 50 scans (integrating time = 1 s) of each spot of the grid (Fig. 6c).

The number of assays per chip can be increased by performing successive target incubations on the same assay area. For that, repeat several times the **steps 3–5** above. This strategy enables to minimize the consumption of chips in characterization assays, but it must be noted that to obtain a neglectable accuracy deviation, the incubated solutions must contain an increasing concentration of target and the concentration difference between two successive incubations should be at least one order of magnitude (*see* **Note 27**). As observed in Fig. 7, the target concentration in different immunoassays correlates well with the resulting signal in the experimental dose-response curves. From these results, the detection (SNR = 3) and quantification (SNR = 10) limits obtained are 16 ng/mL (100 pM) and 465 ng/mL (3.1 nM) of anti-BSA IgGs, 2μg/mL (87 nM) and 7μg mL (304 nM) of CRP, and 18 ng/mL (13 nM) and 50 ng/mL (36 nM) of LDH, respectively.

### 3.5 Data Processing

Once the assay is performed on the functionalized chips and analyzed in the measurement system, the resulting spectra are processed with a Savitzky–Golay filter using Origin Pro 8 software (OriginLab Corporation) to smooth them. For each acquisition,

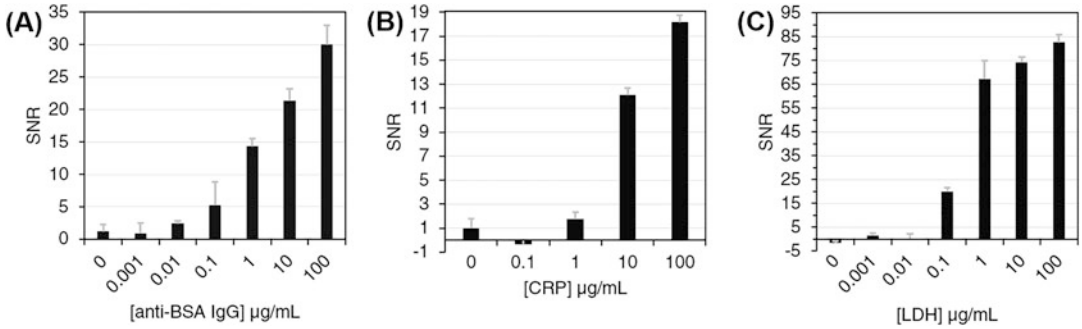


**Fig. 7** Dose-response curves of different label-free immunoassays obtained with the method herein described: (**a**) BSA probes and anti-BSA IgG targets, (**b**) anti-LDH IgG probes and LDH targets, and (**c**) anti-CRP IgG probes and CRP targets

the position of the two longer wavelengths valleys (split TE band-gaps) is averaged. The wavelength sifts ($\Delta\lambda$) generated by the assay (used as analytical signal) are determined by subtracting the averaged wavelength before the target incubation (**step 2** in Subheading 3.4) to the one after it (**step 5** in Subheading 3.4) (Fig. 6c). Experimental noise values are calculated as the standard deviation of the $\Delta\lambda$ obtained from the measurement of ten blank samples (0µg/mL of target). Signal-to-noise ratios are determined by dividing each $\Delta\lambda$ by the calculated noise value (Fig. 7).

## 4 Notes

1. The metal used is typically aluminum, and the recording dye in BD-R disks is made of an organic compound not specified by the manufacturers. Regarding the protective layer, various compositions are employed by the different manufacturers. For example, TDK corporation employs the one named durabis®.
2. We have experimentally observed that the dimensions of the nanogrooved structure can slightly differ from BD-R disks fabricated by different manufacturers. Note that slight structural differences in the starting nanogrooved pattern may modify the optical response of the resulting materials.
3. The refractive indexes of titanium oxide and polycarbonate (at 632.8 nm) are 2.8736 and 1.58132, respectively. This significant difference supports the waveguide behavior of the titanium oxide layer.
4. It is important to note that, despite the spiral shape of the nanogrooved structure along the disks, the period of the grooves is about eight orders of magnitude shorter than the diameter of the disk. Therefore, the curvature of the grating

becomes neglectable, especially in outer radius of the disk and incident beam diameters of a few millimeters.

5. Store this silane in a desiccator and manipulate it under inert (nitrogen) atmosphere.
6. We used a custom anti-LDH antiserum produced in our lab by rabbit immunization, but there are many commercially available options for anti-LDH IgGs.
7. All the bioreagents were stored in frozen (−20 °C) aliquots and diluted before use.
8. For sensitive bioanalytical measurements in this system, the resolution of the spectrophotometer used in the measurement setup should be at least 0.1 nm.
9. A practical trick to easily create this circular cut at constant diameter is to place the disk in an individual compact disk case, hold firmly the tip of the knife on the selected diameter with one hand, and rotate the disk with the other along the whole perimeter of the cut.
10. This step may create slight scratches on the disk surface, close to the circular cut, caused by the knife tip. However, note that the outer diameter of the disks (above 10 cm) will be subsequently removed in order to fit the disk into the sputtering chamber.
11. Pull it carefully and slowly in order to try to peel it off in one piece. If the protective layer breaks during the pulling process, peel off the remaining parts on the disk as before. After removing the protective layer, both the metallic and the recording dye layers normally remain attached on the polycarbonate side, but they can be peeled off together with the protective layer in some instances. In any case, do not omit the **steps 3–5** of this procedure.
12. Beyond this point, the nanogrooved structure is not protected, so the disks and the subsequent chips must be manipulated from the sides in order to avoid scratches and damaging of the structure.
13. Suitable containers to carry out immersions of the whole disks are crystalizing dishes and the lids of 25-pack disk cases.
14. Along the immersion in hydrochloric acid, it must be observed that the original blueish color of the remaining metallic parts on the disk becomes colorless.
15. Another practical way to dry the disks is by centrifugation, for example by using a custom centrifuge adapted to spin compact disks.
16. Most BD-R disks are labeled on the unstructured side of the polycarbonate layer, and some of these labels are resistant to

the hydrochloric acid solution of the **step 3** in Subheading 3.1. These labels can be solved with harsher chemical conditions, and it may be necessary in some instances depending on the configuration (color, thickness, homogeneity, etc.) of this layer. However, with the BD-R disks used in this development, we have experimentally observed that this label does not interfere with the measurements. In Fig. 3c, it can be observed the back side of the remaining label on the bottom of the polycarbonate plate.

17. Polycarbonate can melt and solidify on the drill during the process. To obtain a clean cut, this must be often checked, and the drill must be cleaned when necessary.

    Besides CNC drilling machines, other methods can also be used to cut the disks into chips. A simple alternative is a sharp utility knife, although the thickness of this polycarbonate plate (1.1 mm) needs for multiple iterations to be completely cut. Another simple option are scissors, while in this case special care must be took to avoid plane deformations by shearing in the resulting chips. A laser cutter can also be used for this purpose, and in this case special effort must be put into protecting the disk and optimizing the cutting conditions in order to avoid the grooved surface to become damaged by the fumes generated during the cutting process.

18. All the immersions of the chip along the functionalization protocol are performed in glass vials.

19. Shorter times may lead to an inefficient functionalization, and we have experimentally observed that the titanium oxide layers may generate small cracks under longer reaction times.

20. The titanium oxide surface becomes hydrophobic after the **step 3** of the protocol in the Subheading 3.2, which makes the chip float in aqueous solutions. Therefore, this immersion is performed on the surface of the glutaraldehyde solution, with the grating side of the chip down.

21. This position of the knob corresponds to a 10% of the lamp intensity, which leads an intensity of about 3.75 W per lightline (according to the specifications of the light source). We have experimentally observed that high light intensities must be avoided in order to obtain well-defined bandgaps in the transmission spectra.

22. The distance between the output of the light source and the collimation lens is critical and it must be set according to the focal distance of the employed lens (150 mm in this case). Beyond this point the beam is collimated, the distance between the rest of the elements of the optical setup is not critical and it can be qualitatively determined from Fig. 5b, c.

23. A custom 3D printed piece was fabricated and used to fix this glass slide and mount it in the setup. Alternatively, commercially available optomechanical accessories can be used for this purpose.
24. To tilt the chip in the right direction, it is important to take into account the orientation of the grating in the **step 5** of the protocol for the measurement system.
25. Alternative setup configurations with incident light angles (along the perpendicular direction of the groove) above 8–9° would overlap the split bandgaps coming from both polarizations, thus hindering the determination of their spectral position. In this case, a linear polarizer could be included somewhere in the beam path between the lens and the photonic crystal, and set it to polarize the light along the nanogroove direction, thus filtering out the TM polarization and its corresponding bandgaps in the transmission spectrum.
26. This is useful to keep aqueous solutions on the chip during the incubations, and can also be used to avoid different solutions to merge along their incubation on multiple assay areas in a single chip. Besides, a simple alternative for this purpose is to use custom incubation masks with circular chambers in an adhesive film.
27. Other potential strategies (not studied in this work) to increase the number of assays performed per chip are either regenerating the chip by applying harsh chemical conditions (and then carry out a new functionalization) or removing the bound targets by incubating chaotropic agents (and then performing a new assay).

## Acknowledgments

This work was supported by the Spanish Ministry of Economy and Competitiveness (CTQ2013-45875-R and CTQ2016-75749-R), FEDER, and Generalitat Valenciana (APOSTD/2019/120).

### References

1. Zarei M (2017) Portable biosensing devices for point-of-care diagnostics: recent developments and applications. TrAC Trends Anal Chem 91:26–41. https://doi.org/10.1016/J.TRAC.2017.04.001
2. Nayak S, Blumenfeld NR, Laksanasopin T, Sia SK (2017) Point-of-care diagnostics: recent developments in a connected age. Anal Chem 89:102–123. https://doi.org/10.1021/acs.analchem.6b04630
3. Mahato K, Srivastava A, Chandra P (2017) Paper based diagnostics for personalized health care: emerging technologies and commercial aspects. Biosens Bioelectron 96:246–259. https://doi.org/10.1016/J.BIOS.2017.05.001
4. Su S, Sun Q, Gu X et al (2019) Two-dimensional nanomaterials for biosensing applications. TrAC Trends Anal Chem

119:115610. https://doi.org/10.1016/J.TRAC.2019.07.021

5. Song S, Qin Y, He Y et al (2010) Functional nanoprobes for ultrasensitive detection of biomolecules. Chem Soc Rev 39:4234–4243. https://doi.org/10.1039/c000682n
6. Mahmoudpour M, Ezzati Nazhad Dolatabadi J, Torbati M, Homayouni-Rad A (2019) Nanomaterials based surface plasmon resonance signal enhancement for detection of environmental pollutions. Biosens Bioelectron 127:72–84. https://doi.org/10.1016/J.BIOS.2018.12.023
7. Zeng Y, Hu R, Wang L et al (2017) Recent advances in surface plasmon resonance imaging: detection speed, sensitivity, and portability. Nano 6:1017–1030. https://doi.org/10.1515/nanoph-2017-0022
8. Makarona E, Petrou P, Kakabakos S et al (2016) Point-of-need bioanalytics based on planar optical interferometry. Biotechnol Adv 34:209–233. https://doi.org/10.1016/J.BIOTECHADV.2016.02.005
9. Liu Y, Zhou H, Hu Z et al (2017) Label and label-free based surface-enhanced Raman scattering for pathogen bacteria detection: a review. Biosens Bioelectron 94:131–140. https://doi.org/10.1016/J.BIOS.2017.02.032
10. Inan H, Poyraz M, Inci F et al (2017) Photonic crystals: emerging biosensors and their promise for point-of-care applications. Chem Soc Rev 46:366–388. https://doi.org/10.1039/c6cs00206d
11. Carrascosa LG, Huertas CS, Lechuga LM (2016) Prospects of optical biosensors for emerging label-free RNA analysis. TrAC Trends Anal Chem 80:177–189. https://doi.org/10.1016/J.TRAC.2016.02.018
12. Fathi F, Rahbarghazi R, Rashidi M-R (2018) Label-free biosensors in the field of stem cell biology. Biosens Bioelectron 101:188–198. https://doi.org/10.1016/J.BIOS.2017.10.028
13. Morais S, Puchades R, Maquieira Á (2016) Disc-based microarrays: principles and analytical applications. Anal Bioanal Chem 408:4523–4534. https://doi.org/10.1007/s00216-016-9423-1
14. Avella-Oliver M, Morais S, Carrascosa J et al (2014) Total analysis systems with thermochromic etching discs technology. Anal Chem 86:12037–12046. https://doi.org/10.1021/ac502640j
15. Avella-Oliver M, Morais S, Puchades R, Maquieira Á (2016) Towards photochromic and thermochromic biosensing. TrAC Trends Anal Chem 79:37–45
16. Sancho-Fornes G, Avella-Oliver M, Carrascosa J et al (2019) Enhancing the sensitivity in optical biosensing by striped arrays and frequency-domain analysis. Sensors Actuators B Chem 281:432–438. https://doi.org/10.1016/j.snb.2018.10.130
17. Avella-Oliver M, Puchades R, Wachsmann-Hogiu S, Maquieira A (2017) Label-free SERS analysis of proteins and exosomes with large-scale substrates from recordable compact disks. Sensors Actuators B Chem 252:657–662. https://doi.org/10.1016/j.snb.2017.06.058
18. Avella-Oliver M, Carrascosa J, Puchades R, Maquieira Á (2017) Diffractive protein gratings as optically active transducers for high-throughput label-free Immunosensing. Anal Chem 89:9002–9008. https://doi.org/10.1021/acs.analchem.7b01649
19. López-Muñoz GA, Estevez M-C, Peláez-Gutierrez EC et al (2017) A label-free nanostructured plasmonic biosensor based on Blu-ray discs with integrated microfluidics for sensitive biodetection. Biosens Bioelectron 96:260–267. https://doi.org/10.1016/J.BIOS.2017.05.020
20. Sancho-Fornes G, Avella-Oliver M, Carrascosa J et al (2019) Disk-based one-dimensional photonic crystal slabs for label-free immunosensing. Biosens Bioelectron 126:315–323. https://doi.org/10.1016/j.bios.2018.11.005

# Chapter 5

# Plasmonic Nanoparticle Conjugation for Nucleic Acid Biosensing

**Amogha Tadimety, Yichen Zhang, John H. Molinski, Timothy J. Palinski, Gregory J. Tsongalis, and John X. J. Zhang**

## Abstract

This chapter details the use of gold nanorods conjugated with peptide nucleic acid probes for sequence-specific detection of circulating tumor DNA (ctDNA). ctDNA is gaining increased attention as a biomarker for liquid biopsy, the process of detecting molecules in the peripheral blood rather than a tissue sample. It has wide ranging applications as a diagnostic and prognostic biomarker with a similar mutational profile as the tumor. Plasmonic nanoparticles offer a relatively rapid, amplification-free method for detection of ctDNA through the use of sequence-specific peptide nucleic acid (PNA) probes. In this chapter, we discuss methods for probe design, conjugation to plasmonic particles, and ctDNA quantitation with the resulting sensor. This chapter is a resource for those looking to use plasmonic gold particles for sensing in a solution format for a range of applications.

**Key words** Biosensor, Liquid biopsy, Nanosensor, Plasmonic, Localized surface plasmon resonance, Gold nanorod, Circulating tumor DNA, Peptide nucleic acid

## 1 Introduction

### *1.1 Liquid Biopsy and Circulating Tumor DNA*

Earlier detection of cancer is widely considered to be one of the largest unmet needs in the cancer space. Currently, the most common diagnostic methods include imaging and tissue biopsy, which can be burdensome for the patient because of cost and invasiveness. There are also some recent blood protein biomarker tests that are slowly becoming more widely used. As the field rapidly trends toward personalized care, molecular diagnostics are becoming more promising for individualized monitoring of patient tumor burden, as well as genetic and phenotypic characteristics [1]. Such tests could inform patient diagnosis and prognosis, as well as provide information for targeted therapy [2, 3]. Specifically, genomic analysis of cancers has become the standard of care for precision medicine [4].

Miguel R. Ossandon et al. (eds.), *Biomedical Engineering Technologies: Volume 1*, Methods in Molecular Biology, vol. 2393, https://doi.org/10.1007/978-1-0716-1803-5_5, 

Liquid biopsy is growing in popularity because of the promise of minimally invasive cancer detection. The most common liquid biopsy biomarkers currently being studied include circulating tumor cells (CTCs), circulating tumor DNA (ctDNA), and exosomes [5, 6]. ctDNA is a particularly promising biomarker because it can capture both the genetic and epigenetic changes within a tumor. Moreover, its short half-life allows for a representative snapshot of the tumor's current genetic profile [7, 8]. Enrichment and quantitation of ctDNA, however, is a challenge because of its low concentration and the presence of non–tumor-specific cell-free DNA in the blood.

### 1.2 Plasmonic Biosensing

One challenge with the capture of ctDNA is that it exists in extremely low concentration in the blood, and unlike cells, DNA fragments are small enough that they cannot be detected using conventional imaging [9, 10]. Thus, local enhancement is necessary for the spectroscopic detection of ctDNA in a patient fluid sample.

Surface plasmon resonance (SPR)—the collective electron-electromagnetic wave oscillation at a metal-dielectric interface—has been used extensively to monitor biochemical interactions which locally change the refractive index near the sensor surface [11]. This resonance results in highly enhanced electric fields which are sensitive to changes in the local environment and can transduce minute changes in the local refractive index (down to ppm concentrations) without the need for fluorescent labeling for signal amplification [12] . Such label-free operation not only simplifies the measurement setup, but also avoids contamination/interference of the fluorophores with the target analytes [13]. Furthermore, owing to their high sensitivity, SPR sensors enable fast, real-time monitoring of target analytes, including real-time binding dynamics (e.g., protein–peptide interactions) [14]. The combination of high sensitivity, real-time operation, and compatibility with biological samples has established SPR sensing as an important tool for biochemical investigations.

Metallic nanoparticles which support localized surface plasmon resonance (LSPR) have also been investigated for sensing applications. The LSPR modes depend on the nanoparticle material, geometry, and surrounding dielectric environment. Importantly, the LSPR modes—including resonance wavelength, bandwidth, and electric field decay profiles—may be tailored to the specific application through careful design of the nanoparticle geometry and arrangement (i.e., ordered arrays). The electric field decay length, in particular, plays in important role in the sensitivity of the device [13]. For optimal sensitivity, It is desirable for the field decay length to spatially overlap with the target analytes of interest [13, 15]. In general, the field decay profiles in LSPR sensors are better matched to the dimensions of biochemical target analytes

(10s of nm, compared to 100s of nm in SPR systems); however, the main benefit is that the LSPR field profiles may be tailored almost arbitrarily by appropriate design of the nanoparticle, opening a wide range of possibilities in highly sensitive, target-specific biosensing. LSPR-based biosensors typically use a simpler experimental setup and are less sensitive to thermal and vibrational variation. Given the freedom of design and the desirable sensing characteristics, LSPR-based nanoparticles are used as the sensing platform for this work.

In the context of biosensing, LSPR-based sensors show spectral resonance shifts that increase in wavelength as monolayers on surface of the nanoparticle increase in thickness and/or refractive index [9, 13]. Thus, we can functionalize nanoparticles with a selective probe for ctDNA capture and confirm the successful conjugation through a spectral red-shift [10, 16, 17]. Then, with increased concentrations of ctDNA in solution, we will expect the spectra to lead to further successive red shifts [9].

### 1.3 Gold Nanorods Biosensing Platform

This chapter outlines the use of gold nanorods for sequence-specific capture and detection of ctDNA [9, 18]. The principle of operation for the sensor is that the gold nanorods are conjugated with peptide nucleic acid (PNA) capture probes complementary to the ctDNA sequence of interest (Fig. 1). The resonance spectrum of these starting nanorods in solution is measured before putting in contact with the analyte. The conjugated rods are suspended in the sample of interest, and if ctDNA is present it will bind to the PNA probes. Due to the LSPR modes on the nanoparticle, this binding will cause a red shift in the optical response that can be measured by a shift in the peak location of the optical absorbance spectrum. The two

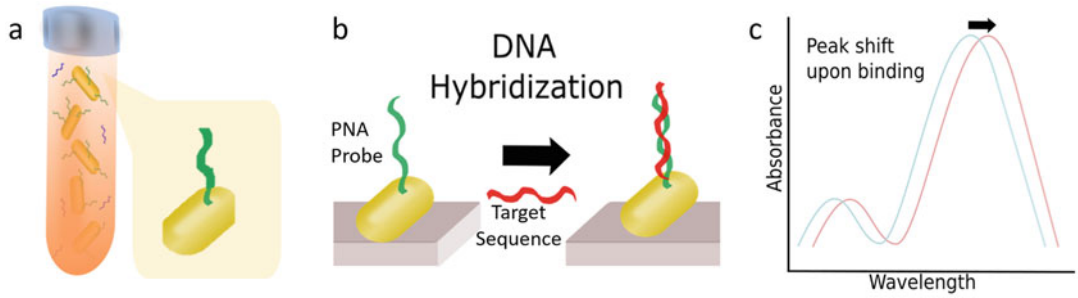


**Fig. 1** Sensor Principle of Operation. (**a**) Functionalized gold nanorods are introduced to the sample that may contain ctDNA. (**b**) ctDNA will bind in a sequence-specific manner to PNA probes on gold nanorods. (**c**) Change in local refractive index will induce an LSPR-based resonance shift and peak wavelength can be measured. (Reprinted from *Biosensors and Bioelectronics*, 130, Amogha Tadimety, Yichen Zhang, Kasia M. Kready, Timothy J. Palinski, Gregory J. Tsongalis, John X.J. Zhang, "Design of peptide nucleic acid probes on plasmonic gold nanorods for detection of circulating tumor DNA point mutations", 236–244, (2019), with permission from Elsevier)

spectra can be processed and peak shift, corresponding to concentration of ctDNA in solution, can be quantified.

### 1.4 Peptide Nucleic Acids

Peptide nucleic acids (PNAs) are a class of synthetic bioprobes that have a hybrid peptide-nucleic acid structure [19]. They consist of the same type of nucleobases found in nucleic acids bound to a peptide backbone [20, 21]. PNAs can selectively bind double-stranded and single-stranded DNA sequences with high sequence-specific affinity [22]. In this study, PNA probes complementary to ctDNA sequences of interest are conjugated to plasmonic nanoparticles for sequence-specific capture and detection.

### 1.5 Applications

The techniques proposed in this chapter put forth a platform that can be used for one-step capture and quantitation of ctDNA. The same methodology could be used for detection of cell-free DNA for noncancer applications. Some of the example applications for this platform are detailed below.

#### 1.5.1 Cancer Diagnosis and Targeted Therapy

ctDNA is generally understood to harbor somatic mutations representative of the host tumor [8]. It has been detected in more than 75% of patients with advanced cancers, and about half of patients with localized tumors using digital droplet PCR [23]. One of the greatest promises of liquid biopsies is the potential to detect cancer before the presentation of clinical signs or a lesion on standard imaging scans. If this is the case, the detection of ctDNA could lead to earlier diagnosis of cancer and determination of the appropriate personalized therapy.

#### 1.5.2 Companion Diagnostics

Companion diagnostics are diagnostic tests that are approved to determine if a patient is an eligible candidate for a particular therapy. They have exploded in the research and clinical fields upon the growth of precision and personalized medicine, and are relied on to determine potential safety and efficacy of personalized treatments. The techniques outlined in this chapter could be applied to companion diagnostics because they allow for the detection of patient-specific somatic mutations that may indicate eligibility for personalized molecular therapies. As the field begins to further understand the underlying genetic mechanisms of disease, the application space for rapid DNA detection will grow.

#### 1.5.3 Noncancer Applications

A number of noncancer conditions have been known to release cell-free DNA into the bloodstream that could be captured using a similar methodology. Cell-free DNA has been associated with conditions including pregnancy, organ transplantation, stroke, autoimmune disorders, and myocardial infarction [24]. For the development of diagnostics for some of these other conditions, the techniques outlined in this chapter could be applied.

### 1.6 Trends in Molecular Pathology

Extensive work has been done using massively parallel DNA sequencing for the detection of somatic variants in human tumors which help oncologists select the best and most appropriate therapy for the patient. However, obtaining tumor tissue may not always be feasible in patients with advanced disease due to the intolerability of the invasive nature of the procedure. In addition, monitoring of disease progression and resistance to therapy would require multiple biopsies at various time points, making this a less desirable practice. Identification of biomarkers in the "liquid biopsy" is very appealing because it only requires a simple blood draw and can be performed at multiple time points during the course of the patient's disease. The simplicity of acquiring this type of specimen makes use of the liquid biopsy very feasible for monitoring disease progression, response to therapy and development of resistance [25]. In addition, there is a significant amount of work being done to see if detection of ctDNA can be used for early detection of disease in asymptomatic patients and to detect relapse or metastases. Because the use of plasmonic nanosensors does not require any DNA/RNA extraction or PCR amplification steps, this technology could provide a rapid assessment of ctDNA in a cost effective manner with a throughput suitable for the clinical laboratory.

## 2 Materials

### 2.1 Required Reagents/Supplies [9]

1. Carboxylated Gold Nanorods (Nanopartz, C12-40-780-TC-DIH-50, Conjugated Gold Nanorods 40 × 124 nm, SPR = 780 nm, 2.5 mg/mL, OD = 50, 1 mL, Carboxyl Polymer, DIH).
2. PNA Probes (PNABio, 15 base pair sequence, 50 nmol concentration, HPLC purified; multiple sequences ordered but the primary G12V mutation probe had a sequence of TAC GCC AAC AGC TCC (Melting temperature 42.5 °C WT and 47.2 °C Mutant). The lyophilized PNAs are dissolved to 100μM in TE Buffer and stored in the freezer until use.
3. After thermodynamic simulation is complete, additional PNA probes are ordered. (PNABio, 15 base pair sequence, 50 nmol concentration, HPLC purified; modified PNA probes had a sequence of TAC GCA AAC AGC TCC (melting temperature 24 °C WT and 36.5 °C Mutant) and TACGCG AAC AGC TCC (melting temperature 24 °C WT and 37.8 °C Mutant)). The lyophilized PNAs are dissolved to 100μM in TE Buffer and stored in the freezer until use.
4. Synthetic Duplex and Oligo DNA (IDTDNA, 100 nmol, mutant and wild type double stranded oligo sequences are 5′-ACT TGT GGT AGT TGG AGC TGG TGG CGT AGG CAA GAG TGC CT-3′ and 5′-ACT TGT GGT AGT TGG

AGC TGT TGG CGT AGG CAA GAG TGC CT-3′). The lyophilized sequences are dissolved to 100μM in TE Buffer and stored in the freezer until use.

5. 96-well plates (Falcon, Multiwell flat bottom plates with lids, sterile, 353072).
6. Low Retention Eppendorf tubes (Fisherbrand microcentrifuge tubes, 0.6 mL graduated, flat cap tubes, low retention, 02-681-311).

### 2.2 Working Solutions [9]

1. Activation Buffer is prepared from 0.1 M MES (MEX monohydrate, Sigma, 69892-100G) and 0.5 M NaCl (sodium chloride, Sigma, S7653-250G) and buffered to pH 6.0 in molecular grade water. This buffer is stored under refrigeration.
2. 10 mM CTAB (Hexadecyltrimethylammonium bromide or Cetrimonium bromide, Sigma, H9151-25G) is prepared in molecular grade water. The solution is stored under refrigeration.
3. 375 mM EDC (*N*-(3-dimethylaminopropyl)-*N*′-ethylcarbodiimide hydrochloride, Sigma-Aldrich, E7750-5G) is prepared in Activation Buffer. The solution must be prepared fresh for each conjugation procedure.
4. 937.5 mM NHS (*N*-hydroxysuccinimide, Sigma-Aldrich, 130672-5G) is prepared in Activation Buffer. The solution must be prepared fresh for each conjugation procedure.
5. Tris-EDTA (TE) Buffer is prepared from 10 mM Tris HCl (Tris Hydrochloride, 1 M Solution (pH 8.0/Mol. Biol.), Fisher BioReagents, BP1758-100) and 0.1 mM EDTA (Ethylenediaminetetraacetic acid disodium salt dihydrate, Millipore Sigma, E5134-50G) in molecular grade water. The solution may be stored at room temperature until use.

### 2.3 Instrumentation for Conjugation and Readout

1. Centrifuge (Eppendorf Centrifuge 5810 R with microcentrifuge attachment).
2. Vortexer (Fisher Vortex Genie 2, Cat. No. 12-812).
3. pH Meter (Hanna Instruments Edge).
4. Weighing Scale (Ohaus Adventurer Pro Balance).
5. Microplate Reader (Tecan Spark 10 M with NanoQuant plate).
6. Sonicator, Ultrasonic Cleaner (Elma E 60 H Elmasonic).
7. Qubit 3 Fluorometer (Invitrogen by ThermoFisher Scientific).

### 2.4 Computational

1. MATLAB

## 3 Methods

### 3.1 PEG Carboxylation of Bare Gold Nanorods

The described protocols can be performed on either bare gold nanorods (in CTAB surfactant) or on carboxylic acid functionalized gold nanorods. Most of the results reported in this chapter are based on carboxylated gold nanorods, but there is a simple protocol for the carboxyl functionalization of bare gold nanoparticles if necessary [26].

1. The CTAB layer on the surface of the gold nanoparticles can be replaced with thiol-PEG-carboxylate.
2. 100μL of 0.5 mM thiol-PEG-carboxylate is mixed with 1 mL of concentrated CTAB coated gold nanorods.
3. The mixture is incubated for 30 min with sonication [26].
4. The free CTAB and thiol molecules can be removed through centrifugation.
5. These carboxylated nanoparticles can be directly used for PNA conjugation after this step.

### 3.2 Spectral Measurement

1. 2μL of the sample is carefully pipetted onto the sensing spot on the NanoQuant plate from Tecan (Fig. 2a). This reduces the amount of sample used to take a spectral measurement.
2. Then an absorbance scan is performed using the Spark 10 M microplate reader from 400 to 1000 nm wavelengths with a step size of 1 nm.

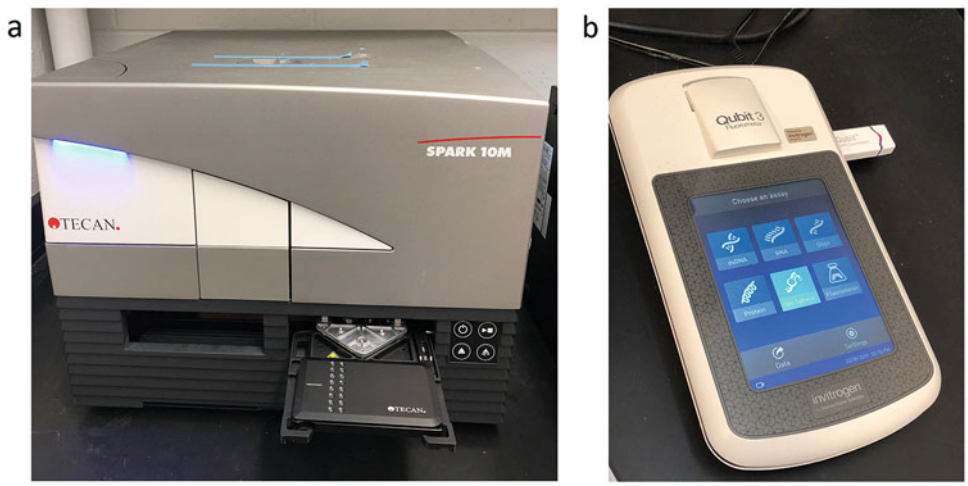


**Fig. 2** Instrumentation. (**a**) Tecan Spark 10 M Microplate Reader used for Absorbance Spectrum Measurement. NanoQuant Plate also pictured. (**b**) Qubit Fluorometer used for synthetic ctDNA quantitation

3. This process takes a few seconds and the resulting Excel data is exported and saved for further analysis of resonant peak location.

### 3.3 PNA Conjugation of Carboxylated Nanorods

This section details the methodology for conjugation of PNA probes to carboxylated gold nanorods [9, 18, 27]. For all data presented in this section 40 × 124 nm carboxyl functionalized gold nanorods (Nanopartz) are used (*see* **Note 1**).

1. First, 20μL of concentrated Au-COOH nanorods is pipetted into a low retention Eppendorf tube.
2. The sample is centrifuged down at 3750–4250 × *g* for 8 min to pellet the nanorods.
3. Then, the supernatant is removed carefully without disturbing the rods.
4. The rods are resuspended into 100μL of 10 mM CTAB solution in DI $H_2O$.
5. The resulting mixture (at a concentration of OD 1) is sonicated briefly in ice cold water until the rods are properly resuspended before the absorbance spectrum is measured using the methodology detailed in Subheading 3.2.
6. Then the rods are spun down once more at the same conditions before the supernatant is removed, leaving only the nanorod pellet.
7. 1μL each of 375 mM EDC and 937.5 mM NHS stocks are added to the tube along with 98μL of Activation Buffer.
8. The solution is mixed well using sonication in ice cold water and allowed to incubate for 15 min at room temperature while mixing.
9. After this activation step, the rods are centrifuged once more and supernatant pipetted away to remove excess NHS.
10. Finally, 2.4μL of 100μM PNA probe in Activation Buffer is added to the pelleted nanorods along with 97.6μL of Activation Buffer raised to a pH of 7.0 (using carbonate-bicarbonate buffer) (*see* **Note 2**).
11. The mixture is once again sonicated in ice cold water to redisperse and allowed to incubate for 2 h under mixing at room temperature.
12. The absorbance spectrum is measured once again to ensure successful conjugation of PNA probes to the nanorods, as evidenced by a significant red shift and flattening of the absorbance peak (Fig. 3a) (*see* **Note 3**).

One of the most critical characteristics of a ctDNA sensor is the ability to be both highly sensitive and highly specific. The specificity

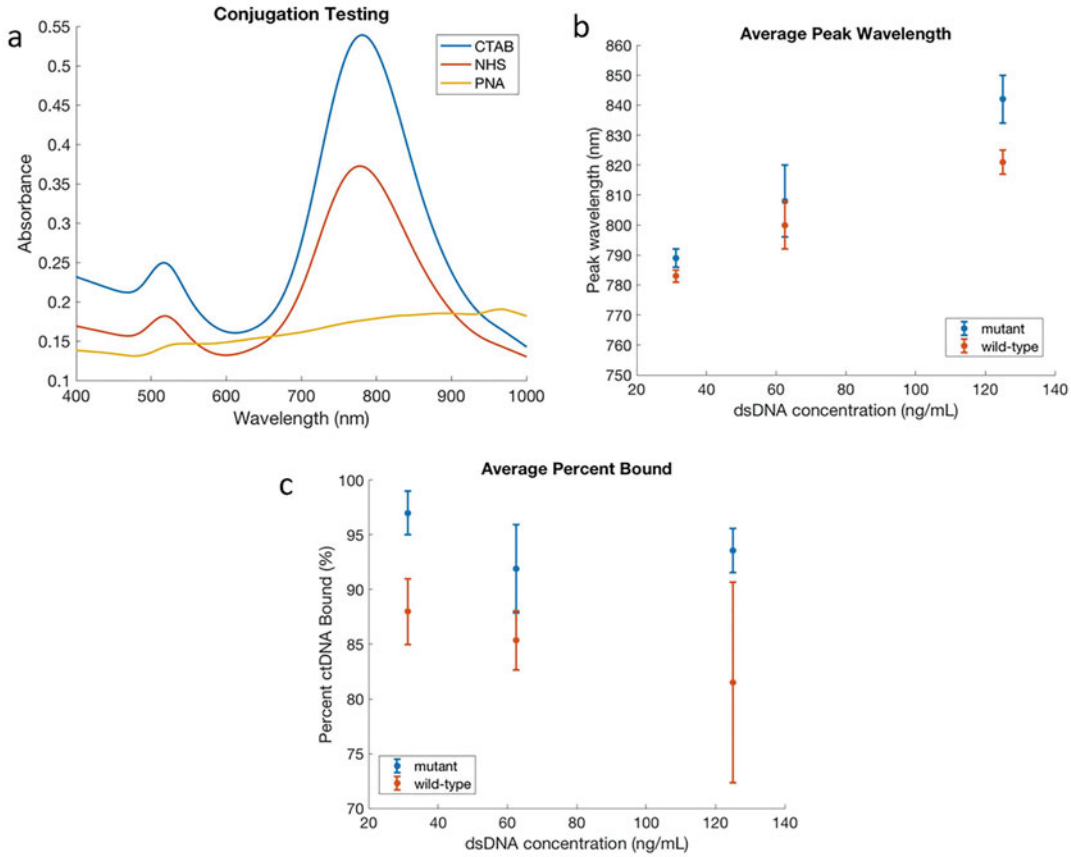


**Fig. 3** Conjugation Benchmarking and Sensing Results. (**a**) Absorbance spectra during and after conjugation, demonstrating red shift and flattening after conjugation. (**b**) Peak location at increasing synthetic ctDNA concentrations showing linear sensor range. (**c**) Percent of synthetic ctDNA in solution bound to sensor. (Adapted from *Biosensors and Bioelectronics*, 130, Amogha Tadimety, Yichen Zhang, Kasia M. Kready, Timothy J. Palinski, Gregory J. Tsongalis, John X.J. Zhang, "Design of peptide nucleic acid probes on plasmonic gold nanorods for detection of circulating tumor DNA point mutations", 236–244, (2019), with permission from Elsevier)

### *3.4 Design of PNA Probe for Enhanced Specificity*

is an important factor to be able to distinguish single point mutations from the tumor from a wild-type background. In order to improve the selectivity for the specified mutation compared to the wild-type sequence, a series of thermodynamic simulations are conducted using a two state hybridization simulation from DINAMelt, a resource from the Rensselaer Polytechnic Institute [9].

1. The artificial addition of a secondary mutation to the PNA probe is a promising method for improving specificity because it will produce a probe with two mismatches to the wild-type and only one to the mutant.
2. The starting point for the simulations is a 15 bp PNA sequence with the G12V mutation centered.

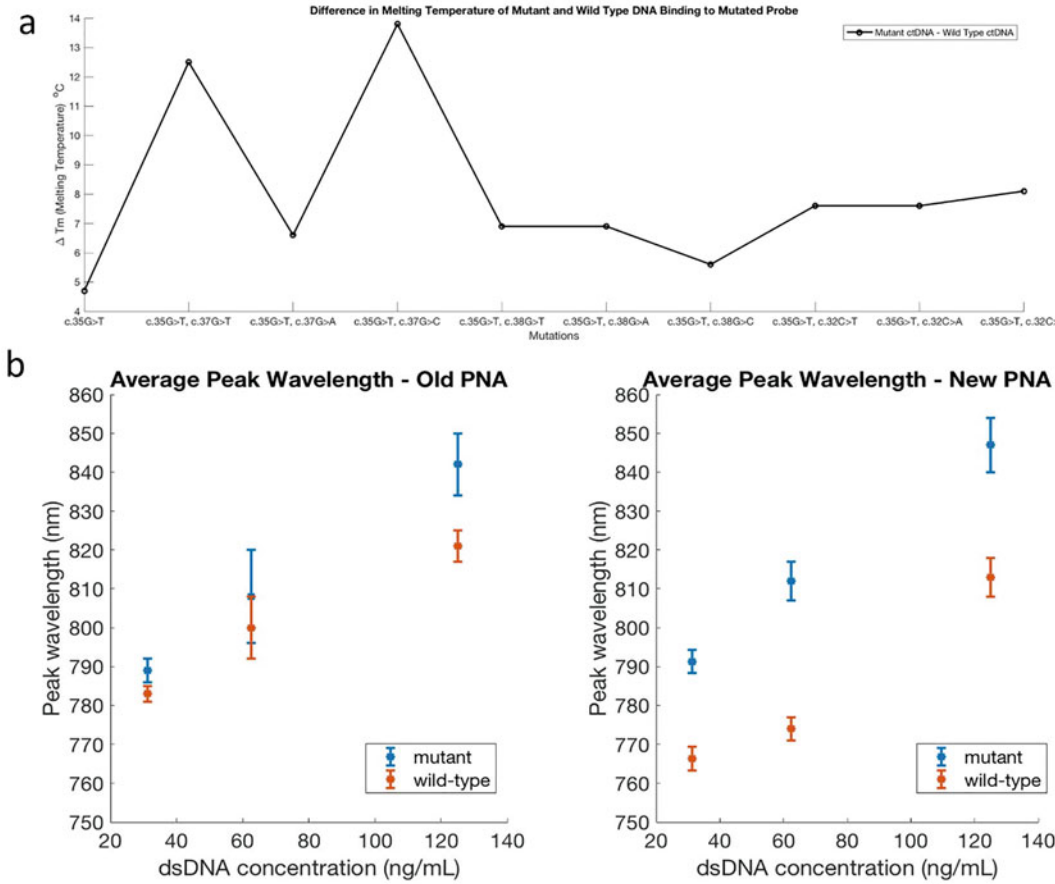


**Fig. 4** PNA Simulation and Specificity Improvement. (**a**) Results of DINAMelt simulation demonstrating two candidate PNA probes with improved specificity for mutant sequence over wild type. (**b**) Improvement in specificity shown by larger gap between mutant and wild type sensor calibration lines. (Adapted from *Biosensors and Bioelectronics*, 130, Amogha Tadimety, Yichen Zhang, Kasia M. Kready, Timothy J. Palinski, Gregory J. Tsongalis, John X.J. Zhang, "Design of peptide nucleic acid probes on plasmonic gold nanorods for detection of circulating tumor DNA point mutations", 236–244, (2019), with permission from Elsevier)

3. The sequences with the addition of a second mutation are modeled, and two candidate redesigned probes showed significant improvements in specificity for the mutant over the wild type (Fig. 4).
4. These two are studied and indeed demonstrated a significant improvement in specificity for the mutant synthetic ctDNA sequence over the wild type (Fig. 4).

### *3.5 Conjugated Rod Storage*

1. The gold nanorods can be stored at the resulting concentration after conjugation in the refrigerator stably for up to a week.
2. Before using them, the UV-Vis spectrum can be measured to ensure that the PNA probe is still attached.

3. If the spectrum is same as immediately after conjugation, the rods are still conjugated and can be used for testing (*see* **Note 4**).

### 3.6 ctDNA Detection Using Absorbance Measurement

1. After conjugation, gold nanorods are centrifuged at 3750–4250 × *g* for 8 min and the supernatant removed.
2. A range of synthetic ctDNA solutions are prepared from 0 ng/mL to 125 ng/mL in TE Buffer and spiked into patient serum.
3. Then the solution to be measured is added to the nanorods and mixed to a final nanorod concentration in the measured solution of OD 0.25 (corresponding to 7.75 pM nanorods).
4. In this study all tests are run with a total reaction volume ranging from 20 to 200μL. All ctDNA detection studies are conducted at room temperature. Throughout this process, care is taken to avoid sonicated the conjugated nanorods for a long time period (*see* **Note 5**).
5. The nanorods are incubated in the solution with synthetic ctDNA for 10 min before the absorbance spectrum is measured.
6. From the resulting spectra the location of the resonance peak at each synthetic ctDNA concentration is calculated according to the methodology detailed in Subheading 3.8. These data can be seen in Fig. 3b.

### 3.7 ctDNA Binding Benchmarking Using Qubit

A Qubit assay kit is used to quantify the amount of synthetic ctDNA remaining in the solution after gold nanorod capture.

1. After the nanorod binding to ctDNA in the test solutions, the rods are spun down at 3750–4250 × *g* for 8 min and the supernatant is used for Qubit analysis.
2. The Qubit assay is performed according to package instructions to determine the concentration of synthetic ctDNA remaining in the supernatant and is compared to the starting concentration.
3. The results quantifying the percentage of synthetic ctDNA captured and detected by the gold nanorod sensors can be seen in Fig. 3c.

### 3.8 Analysis of Resulting Spectra

The location of the resonance peak from the optical absorbance is calculated using a MATLAB script [9].

1. The raw data file from the UV-Vis spectrometer is inputted to the script, and the user is prompted to provide the range of wavelengths containing the resonant peak. (Input = Excel file from UV-Vis plate reader, wavelength boundaries of the peak).
2. The curve is smoothed using Lowess smoothing (1% smoothing) to remove noise from measurement data.

3. From this smoothed curve, the center of mass within the peak bounds is calculated to determine the wavelength corresponding to the resonant peak. This involved numerical integration under the curve, followed by dividing by the wavelength range to get the center of mass.
4. The script returned the location of the peak wavelength for each absorbance measurement. (Output = Peak wavelength in nm).

This script is used for the calculation of all peak locations reported in this chapter.

Through generation of multiple probes and patterning, multiplexing or the ability to analyze multiple ctDNA strands simultaneously can be incorporated with this approach. Such analysis provides overhead in data output and thus diagnostic potential, so can be beneficial within clinical settings. With this excess in obtainable data, advanced data analysis methodologies are also increasingly important to reduce data complexity and provide actionable results. For spectral based analysis, techniques such as machine learning have recently been investigated, allowing for automated data processing and analysis. Integration of diagnostic and data analysis within this platform thus provides an intriguing route for automated diagnostic platform development.

### 3.9 Potential for On-Chip Implementation

On-chip implementation of nanoparticles for plasmonic sensing provides a means toward highly multiplexed and microfluidic-enabled analysis. Through microfluidic manipulation, on-chip interactions can be highly controlled to allow for on-chip detection and high levels of multiplexing. On-chip implementation of nanoparticles typically requires patterning through microfabrication techniques such as lithography or microprinting techniques. Order and arrangement can be controlled with lithography techniques, yet expensive equipment is required. Conversely, microprinting techniques provide little control over orientation but are widely accessible. For microfluidic integration, patterning is often performed on glass slides to allow for device bonding. Following this patterning and conjugation, microfluidic devices can be coupled to facilitate on-chip interactions and analysis (*see* **Note 6**).

## 4 Notes

1. *Note on Optimization of Testing Conditions*: A number of experiments are run to determine the optimal testing conditions and concentrations for this LSPR-based gold nanorod sensing process [9]. We study the optimal incubation time of the conjugated rods with the synthetic ctDNA, the optimal concentration of nanorods to use, and the stability of the

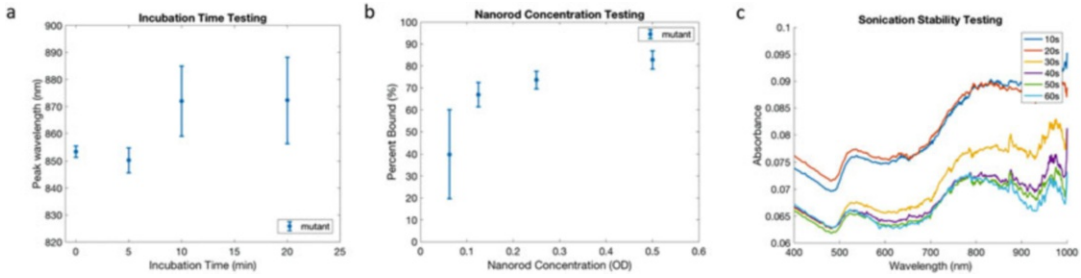


**Fig. 5** Testing Condition Optimization. (**a**) Testing to determine optimal synthetic ctDNA and conjugated nanorod incubation time. (**b**) Testing to determine optimal nanorod concentration for sensing. (**c**) Testing to demonstrate effects of sonication on conjugation. (Adapted from *Biosensors and Bioelectronics*, 130, Amogha Tadimety, Yichen Zhang, Kasia M. Kready, Timothy J. Palinski, Gregory J. Tsongalis, John X.J. Zhang, "Design of peptide nucleic acid probes on plasmonic gold nanorods for detection of circulating tumor DNA point mutations", 236–244, (2019), with permission from Elsevier)

conjugated rods to sonication. The results of these experiments can be seen in Fig. 5. These results demonstrate that 10 min is an appropriate incubation time, that OD 0.25 nanorod concentration is ideal for sensing, and that the rods are stable under sonication for about 30 s.

2. *Note about pH*: The protocols are written so that the initial EDC/NHS coupling occurs at the optimal pH of 6.0, but the coupling of the PNA molecule occurs closer to the physiological pH of 7.0. When testing be careful to maintain pH in the region of 7.0.
3. *Note about coagulation*: Our protocol verifies successful conjugation when the resulting absorbance spectrum is significantly flattened in amplitude and exhibited a large red-shift. We have determined that this is due to the coagulation of gold nanoparticles into large clumps, rather than even dispersion, after the conjugation protocol. Upon the introduction of synthetic ctDNA the particles redisperse and the curve blue-shifts back [9].
4. *Note on Bulk Refractive Index Testing*: One proxy for investigation of plasmonic nanoparticle behavior is bulk refractive index sensitivity testing. The plasmonic nanoparticles can be dispersed in solutions of a range of refractive indices and optical spectra obtained [28].
5. *Note on Sonication*: At many stages of the conjugation and testing protocols the nanoparticles are pelleted and redispersed. In general, both a vortex mixer and ultrasonic bath can be used for particle dispersion. We have found that sonication in ice-cold water for less than 30 s bursts is ideal for maintaining the conjugated probe to the gold nanorod. The cold-water bath also helps to ensure the stability of the PNA probe.

6. *Note on Nanoparticle Geometry*: While the described experiments are conducted on gold nanorods, the techniques should translate directly for gold nanoparticles of other geometries. The optical absorbance spectra will change depending on the nanoparticle shape and this can be modeled using simulation software.

## Acknowledgments

The authors declare no conflict of interest. We would like to acknowledge financial support from the National Institutes of Health (NIH) Director's Transformative Research Award (R01HL137157), Norris Cotton Cancer Center Developmental Funds Pilot Projects, and the Thayer School of Engineering PhD Innovation Program. We would like to acknowledge Dr. Nanjing Hao and Dartmouth undergraduates Kasia Kready '17, Cathy Li '19 and George C. Cheng '19 for their assistance with this project.

### References

1. Song Y, Huang YY, Liu X et al (2014) Point-of-care technologies for molecular diagnostics using a drop of blood. Trends Biotechnol 32:132–139
2. Netto G, Saad R, Dysert P (2003) Diagnostic molecular pathology: current techniques and clinical applications, part I. BUMC Proc 75246:379–383
3. Dietel M (2016) Molecular pathology: a requirement for precision medicine in cancer. Oncol Res Treat 39:804–810
4. Tsongalis GJ, Coleman WB (2017) Somatic mutation analysis of human cancers : challenges in clinical practice. J Clin Pharmacol 57:60–66
5. Tadimety A, Closson A, Li C et al (2018) Advances in liquid biopsy on-chip for cancer management: technologies, biomarkers, and clinical analysis. Crit Rev Clin Lab Sci 55:1–23
6. Tadimety A, Syed A, Nie Y et al (2017) Liquid biopsy on chip: a paradigm shift towards the understanding of cancer metastasis 9:22–49
7. Anker P, Mulcahy H, Chen XQ et al (1999) Detection of circulating tumour DNA in the blood (plasma/serum) of cancer patients. Cancer Metastasis Rev 18:65–73
8. Anker P, Mulcahy H, Stroun M (2003) Circulating nucleic acids in plasma and serum as a noninvasive investigation for cancer: time for large-scale clinical studies? Int J Cancer 103:149–152
9. Tadimety A, Zhang Y, Kready KM et al (2019) Design of peptide nucleic acid probes on plasmonic gold nanorods for detection of circulating tumor DNA point mutations. Biosens Bioelectron 130:236–244
10. Nguyen AH, Sim SJ (2015) Nanoplasmonic biosensor: detection and amplification of dual bio-signatures of circulating tumor DNA. Biosens Bioelectron 67:443–449
11. Homola J, Yee SS, Gauglitz G (1999) Surface plasmon resonance sensors: review. Sens Actuators B Chem 54:3–15
12. Sakai G, Ogata K, Uda T et al (1998) A surface plasmon resonance-based immunosensor for highly sensitive detection of morphine. Sens Actuators B Chem 49:5–12
13. Mayer KM, Hafner JH (2011) Localized surface Plasmon resonance sensors. ACS Chem Rev 111:3828–3857
14. Wegner GJ, Wark AW, Lee HJ et al (2004) Real-time surface plasmon resonance imaging measurements for the multiplexed determination of protein adsorption/desorption kinetics and surface enzymatic reactions on peptide microarrays interactions were examined using an array composed of five differ. Anal Chem 76:8735–8742
15. Kedem O, Vaskevich A, Rubinstein I (2011) Improved sensitivity of localized surface plasmon resonance transducers using reflection measurements. J Phys Chem Lett 2:1223–1226

16. Joshi GK, Deitz-mcelyea S, Liyanage T et al (2015) Short noncoding RNA sensing at Attomolar concentrations allows for quantitative and highly Speci fi c assay of MicroRNA-10b in biological fluids and circulating exosomes. ACS Nano 9(11):11075–11089
17. Ma X, Truong PL, Anh NH et al (2015) Single gold nanoplasmonic sensor for clinical cancer diagnosis based on specific interaction between nucleic acids and protein. Biosens Bioelectron 67:59–65
18. Tadimety A, Zhang Y, Tsongalis GJ et al (2017) Screening circulating nucleic acids of pancreatic ductal adenocarcinoma using a Plasmonic Nanosensor. J Mol Diagnostics 915:1050
19. Endo T, Kerman K, Nagatani N et al (2005) Label-free detection of peptide nucleic acid—DNA hybridization using localized surface plasmon resonance based optical biosensor related to tumor necrosis factor. The nanoparticle layer. Anal Chem 77:6976–6984
20. Lohse J, Dahl O, Nielsen PE (1999) Double duplex invasion by peptide nucleic acid: a general principle for sequence-specific targeting of double-stranded DNA. Proc Natl Acad Sci U S A 96:11804–11808
21. Siddiquee S, Rovin K, Azriah A (2015) A review of peptide nucleic acid. Adv Tech Biol Med 3:1–10
22. Zhang N, Appella DH (2010) Advantages of peptide nucleic acids as diagnostic platforms for detection of nucleic acids in resource-limited settings. J Infect Dis 201:S42–S45
23. Perakis S, Speicher MR (2017) Emerging concepts in liquid biopsies. BMC Med 15:75
24. Jiang P, Lo YMD (2016) The long and short of circulating cell-free DNA and the ins and outs of molecular diagnostics. Trends Genet 32 (6):360–371
25. Conway A, Mitchell C, Kilgour E et al (2019) Molecular characterisation and liquid biomarkers in Carcinoma of Unknown Primary ( CUP ): taking the ‘ U ’ out of ‘ CUP’. Br J Cancer 120(2):141–153
26. Joshi PP, Yoon SJ, Hardin WG et al (2013) Conjugation of antibodies to gold nanorods through fc portion: synthesis and molecular specific imaging. Bioconjug Chem 24 (6):878–888
27. Tadimety A, Zhang Y, Palinski TJ et al (2018) Plasmonic gold nanorods with sequence specific conjugation for circulating tumor DNA screening. In: Int Conf Opt MEMS Nanophotonics 2018-July:1–5. IEEE, Lausanne, Switzerland
28. Stewart ME, Anderton CR, Thompson LB et al (2008) Nanostructured plasmonic sensors. Chem Rev 108:494–521

# Chapter 6

# Ultrasensitive Label-Free Nucleic-Acid Biosensors Based on Bimodal Waveguide Interferometers

**Cesar S. Huertas and Laura M. Lechuga**

## Abstract

The bimodal waveguide (BiMW) biosensor is an innovative common path interferometric sensor based on the evanescent field detection principle. This biosensor allows for the direct detection of virtually any biomolecular interaction in a label-free scheme by using specific biorecognition elements. Due to its inherent ultrasensitivity, it has been employed for the monitoring of relevant nucleic-acid sequences such as mRNA transcripts or microRNAs present at the attomolar–femtomolar concentration level in human samples. The application of the BiMW biosensor to detect these nucleic acids can be a powerful analytical tool for diagnosis and prognosis of complex illnesses, such as cancer, where these biomarkers play a major role. The BiMW sensor is fabricated using standard silicon-based microelectronics technology, which allows its miniaturization and cost-effective production, meeting the requirements of portability and disposability for the development of point-of-care (PoC) sensing platforms.

In this chapter, we describe the working principle of the BiMW biosensor as well as its application for the analysis of nucleic acids. Concretely, we show a detailed description of DNA functionalization procedures and the complete analysis of two different RNA biomarkers for cancer diagnosis: (1) the analysis of mRNA transcripts generated by alternative splicing of *Fas* gene, and (2) the detection of miRNA 181a from urine liquid biopsies, for the early diagnosis of bladder cancer. The biosensing detection is performed by a direct assay in real time, by monitoring the changes in the intensity pattern of the light propagating through the BiMW biosensor, due to the hybridization of the target with the specific DNA probe previously functionalized on the BiMW sensor surface.

**Key words** Nanophotonic biosensor, Waveguide interferometer, Silicon photonics, Nucleic acid detection, Biofunctionalization, Biorecognition, Optical biosensor, NA biosensor, miRNA, RNA

## 1 Introduction

In the last decade, nucleic acids have been pointed out as key players in vital cellular mechanisms, such as cell division, differentiation, and metabolism [1–3]. Their function is possible due to a highly structured gene regulation machinery that acts at different expression levels, from the DNA sequence and its transcription to mRNA, to protein translation. Different types of biomarkers, including DNA epigenetic marks, transcriptional regulation processes, and

Miguel R. Ossandon et al. (eds.), *Biomedical Engineering Technologies: Volume 1*, Methods in Molecular Biology, vol. 2393, https://doi.org/10.1007/978-1-0716-1803-5_6, 

noncoding RNA regulators such as miRNAs, have already been proven to be more accurate and predictive biomarkers than the protein levels tested at the clinic [4], constituting a very promising diagnostic tool that can foster personalized therapeutics. These mechanisms are gaining more and more importance in complex illnesses such as cancer, where this intricate regulation is modified to favor the expression of oncogenes and to enhance the cancer metabolism that will promote the tumor outgrowth and spreading. The study of this complex network is one of the main focuses in current research with the objective to promote the development of new therapies based on each individual molecular profile, signifying a step toward to precision medicine.

The conventional analytical methodologies used for nucleic acid analyses are based on polymerase chain reaction (PCR) amplification and sequencing methods. While they are very efficient and widely applied in nucleic acid research, their application in the clinical context remains a challenge due to some intrinsic limitations, such as the time to perform the analysis or the large quantity of sample necessary for the detection [5]. In addition, the lack of standardized protocols and the need for specialized equipment and skilled technicians, complicate their translation, specially to not-so-well equipped laboratories. The dynamism and heterogeneity of illnesses such as cancer requires the development of more cost-efficient and faster tests able to cover the space-temporal changes during the disease development and treatment. Therefore, it is mandatory to achieve reliable diagnostic tools that ensure a sensitive, rapid, and simple analysis, which can complement or even substitute the classical analytical techniques and will definitely transform the diagnostic field.

In this context, biosensors present some singularities that put them at the front line for the development of fast, user-friendly and low-cost technology for the detection of nucleic acids in different clinical contexts, overcoming some of the main drawbacks of classical analytical techniques [5]. Modern biosensors are portable, easy-to-use, and highly sensitive and can operate in real-time and in situ. Among biosensors, silicon photonics based biosensors are one of the most interesting options due to their high sensitivity and their great potential for integration in PoC devices [6] (for fundamental information about silicon photonics biosensors, readers are referred to references (6, 7)). Within silicon photonics based biosensors, interferometric biosensors are highly suitable for nucleic-acid analysis due to their ultrahigh sensitivity, selectivity and their great potential to be miniaturized and integrated with microfluidics for complete PoC devices [5].

### 1.1 Silicon Photonic Interferometers

Interferometric biosensors rely on the confinement of light within structures of conductive or dielectric material called waveguides. Light propagates through these structures in the form of guided

modes, which have unique field distribution and propagation velocities that depend on the waveguide geometry (core thickness and refractive index) and on the working wavelength. Guided modes are characterized by their effective refractive index ($N_{\text{eff}}$), which is related to the propagation constant $\beta$ through:

$$\beta \equiv k_0 N_{\text{eff}} \tag{1}$$

where $k_0$ is the wavevector. The wavevector is given by $k_0 \equiv \frac{2\pi}{\lambda_0} = \frac{\omega}{c}$, where $\lambda_0$ is the wavelength of the light in the free space, related to the angular frequency by $\omega = 2\pi c/\lambda_0$.

The condition for the propagation constant for a guided mode is given by

$$k_0 n_2 < \beta < k_0 n_1. \tag{2}$$

which can be rewritten as a function of the effective refractive index as

$$n_2 < N_{\text{eff}} < n_1. \tag{3}$$

Therefore, each mode is defined by their propagation constant, $\beta_{\text{m}}$. Waveguides admitting only one solution for the propagation constants $\beta_{\text{m}}$ are called single-mode, while structures supporting more than one mode are referred to as multimode waveguides.

These guided modes generate an evanescent field that extends beyond the waveguide surface (sensing area), with a penetration depth normally between 100 and 500 nm and with an exponential decay profile from the waveguide surface. This evanescent field is extremely sensitive to variations in the refractive index changes of the external medium and will produce a change in the propagation of the guided modes, creating an interference pattern at the output of the waveguide. The most common interferometric device is the Mach–Zehnder Interferometer (MZI), where the incoming light splits in two beams of equal intensity that travel through two single-mode waveguides and are recombined before arriving at a detector, which collects the interferometric signal. For biosensing applications, one of the arms is used as a reference while the other acts as a sensing one. This configuration is very susceptible to fabrication errors which must allow a symmetric splitting/recombination of the light and have balanced losses between the two arms. To solve this issue, the BiMW interferometer has been proposed, achieving interferometric signals by harnessing waveguide structures that allow the propagation of different light modes [8].

### 1.2 The BiMW Interferometric Biosensor

The BiMW biosensor is a novel common path interferometer, designed to avoid beam splitting and recombination of light as happens in the classical MZI device. In the BiMW interferometer, monochromatic and polarized laser light is coupled in a straight single mode rib waveguide (4 μm width × 1.5 nm height) which supports a single mode (150 nm thickness). This propagating

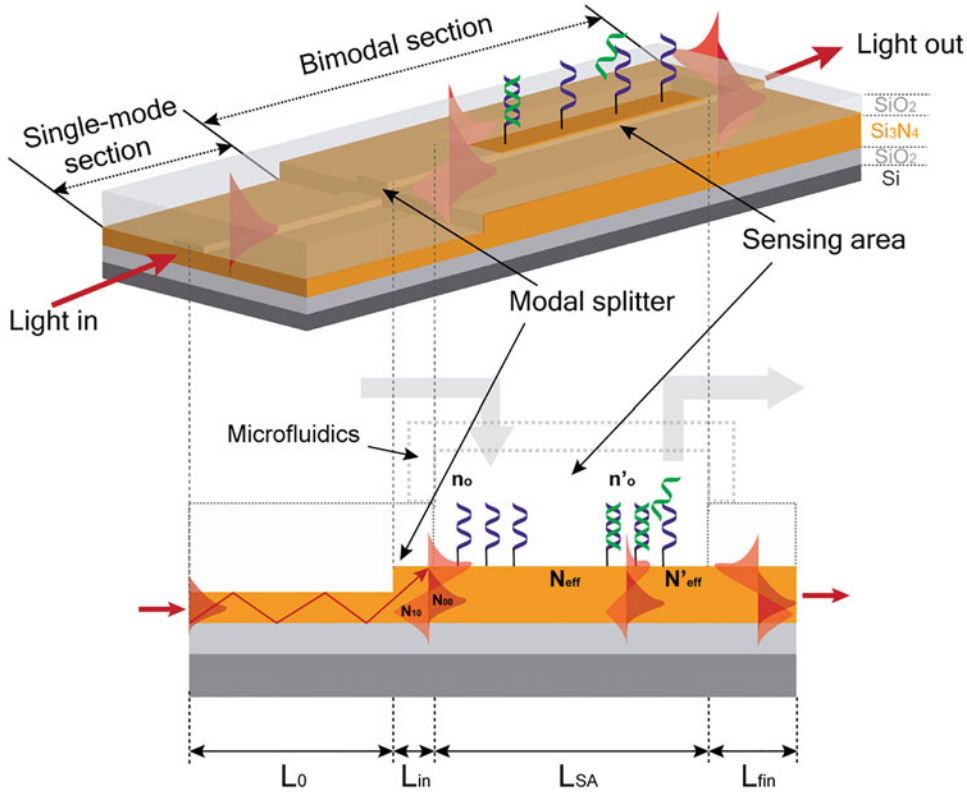


**Fig. 1** The BiMW interferometer biosensor working principle. Monochromatic and polarized laser light is coupled in the single-mode input waveguide and after the modal splitter, two modes are excited which propagate until the device output. The longitudinal view of the BiMW interferometer is shown, indicating the dimensions of each section and the change of the effective refractive index after a hybridization event occurs

single guided mode is coupled into a bimodal rib waveguide (300–350 nm thickness) by passing through a step-junction (modal splitter), and it splits into two transversal modes with the same polarization (*see* Fig. 1). A sensing area is opened along the bimodal section of the waveguide, so that the evanescent field generated by each mode is in contact with the external medium and it is sensitive to variations of the refractive index of the environment. Due to the presence of two propagating modes in a common path with different evanescent field profiles, any change in the refractive index will affect them differently, generating an interference pattern at the device output.

On the sensor surface, when a hybridization event occurs between a DNA probe layer of refractive index $n_0$ and its complementary target sequence, the refractive index of the biosurface changes ($n'_0$), as shown in Fig. 1. This variation of the external refractive index affects the effective refractive index of the propagating modes ($N_{00}$ for fundamental mode and $N_{10}$ for first order mode), producing a phase change ($\Delta\varphi$):

$$\Delta\varphi = 2\pi \frac{L_{SA}}{\lambda}(\Delta N_{10} - \Delta N_{00}) \tag{4}$$

where $L_{SA}$ is the length of the sensor area and $\lambda$ is the working wavelength. As can be appreciated, $L_{SA}$ is a parameter that is linearly dependent to the phase change and strongly affects to the final sensitivity of the biosensor. Therefore, a value of 15 mm has been adopted to ensure a high sensitivity while keeping a reasonable homogeneous length of the BiMW device ($L_0 = 3$ mm, $L_{in} = 4.5$ mm and $L_{fin} = 8.5$ mm; $L_{total} = 31$ mm).

The phase difference is recorded by a two-section photodetector and is directly related to the concentration of the target sequence in the sample analyzed. The phase shift induced by the biomolecular interaction taking place on the sensor surface is quantified from the variation of the output intensity distribution, by monitoring the signal $S_R$:

$$S_R = \frac{I_{up} - I_{down}}{I_{up} + I_{down}} \tag{5}$$

where $I_{up}$ and $I_{down}$ are the intensities collected by the upper and lower sections of the detector, respectively, and $S_R$ is usually expressed as a percentage. The signal $S_R$ is related to the refractive index change occurring in the sensing area of the device by

$$S_R \propto V \cos(\Delta\Phi(t)). \tag{6}$$

where $V$ is the fringe amplitude (visibility factor). This factor corresponds to the amplitude of the $S_R$ oscillation (interference fringes) and is defined as

$$V = \frac{S_{R,max} - S_{R,min}}{2}. \tag{7}$$

Equation 6 is the fundamental equation used for the quantification of the experimental data when the device is operated in standard conditions, that is, with monochromatic light excitation. The phase difference is determined by the variation between the initial value, $\Delta\varphi_1$, and the final value, $\Delta\varphi_2$, given by the number of fringes, where a complete fringe represents a phase difference of $2\pi$ (*see* Fig. 2a).

The BiMW signal is limited by the periodicity of the output signal with the phase variations, which impedes a direct and non-ambiguous readout. To solve these limitations, a simple, reliable and cost-effective phase modulation system has been incorporated to provide directly a linear output signal. It is based on the modulation of the incident wavelength and Fourier transform deconvolution, transforming such interferometric readout into a real-time linear signal [9], as shown in Fig. 2b. Therefore, by measuring the output light intensity the sensor response can be determined in a quantitative way [8].

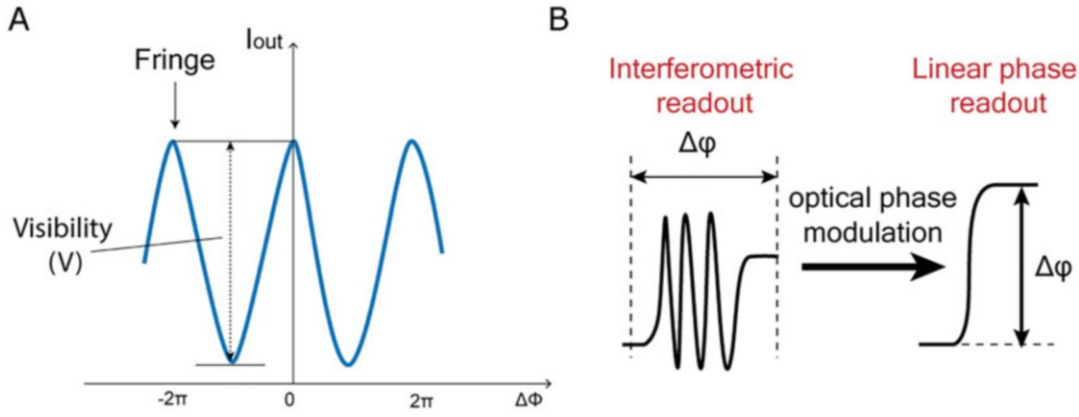


**Fig. 2** The BiMW interferometer biosensor signal. (**a**) Interferometric signal originated after the recombination of the two waveguides. If there is a hybridization event, each traveling light mode will experience a phase change, generating an interference pattern at the output of the waveguide. The interferometric signal consists of a sequence of fringes. The difference between the peak and the null of each fringe is called visibility. The number of fringes is correlated quantitatively with the concentration of the hybridized target sequence. (**b**) Optical phase modulation of the interferometric interferences. (Reprinted from [11] Copyright © 2016, American Chemical Society)

The BiMW biosensor can be fabricated with standard microelectronic technology, including photolithography and etching processes. This kind of fabrication allows for wafer-level packaging, producing numerous sensors in the same process with accurate precision and reproducibility, reducing the time and the manufacturing costs. The single path configuration of the BiMW interferometer enhances the tolerance to fabrication errors and makes possible to incorporate a higher number of biosensors in a reduced space. In our standard production process at Clean Room facilities, 20 interferometers of 31 mm total length are fabricated over a silicon substrate (*see* Fig. 3).

The BiMW interferometer has demonstrated to be one of the most sensitive devices for label-free analysis, reaching sensitivity to bulk refractive index changes of $10^{-7}$ to $10^{-8}$ RIU, meaning that it has the potential ability to detect biomolecular interactions at attomolar–femtomolar (aM–fM) concentration range [5]. However, this limit of detection (LOD) does not only depend on the sensor itself but also on a combination of three important parameters: (1) the proper design of nucleic acid–based probes, (2) their covalent attachment to the sensor surface (biofunctionalization process), and (3) the detection conditions employed for nucleic acid hybridization.

Here, we report the application of the BiMW sensor for the development of ultrasensitive nucleic acid-based biosensors. We describe the methodology to design specific probes, to generate antifouling and accessible bioreceptor monolayers, and how to

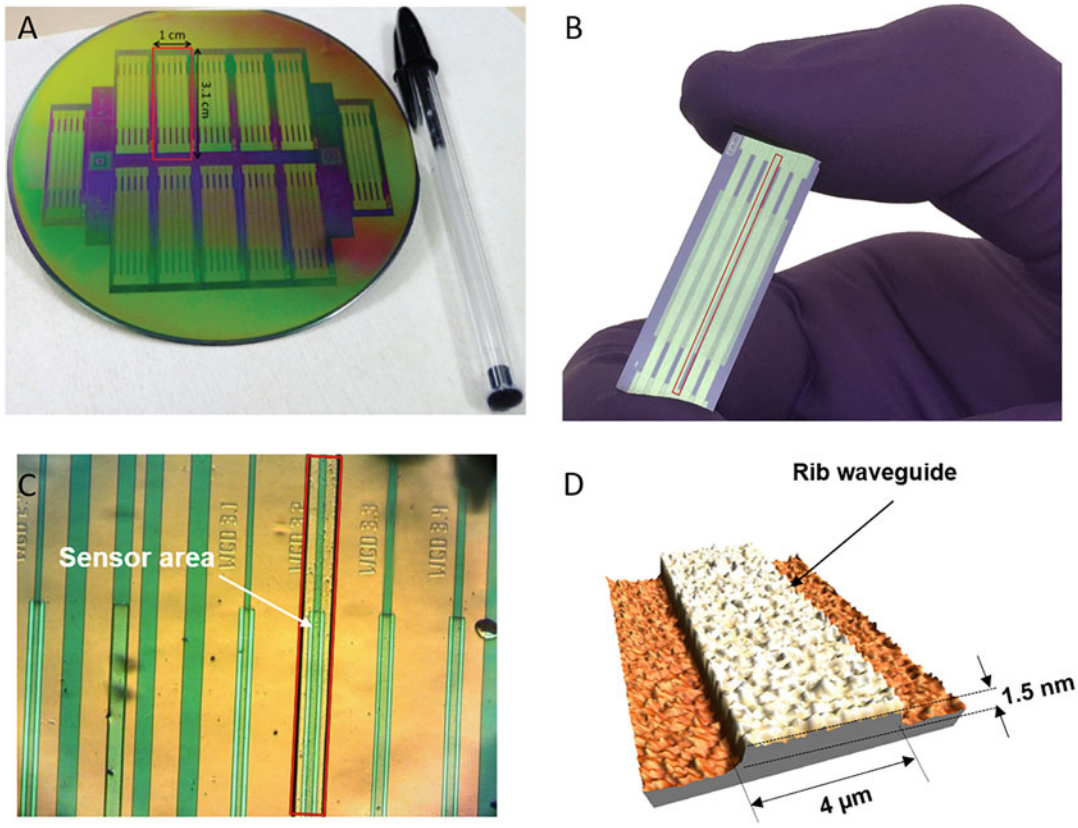


**Fig. 3** The BiMW sensor chip. (**a**) Photograph of a wafer with 12 BiMW chips, resulting in a total of 240 sensors. (**b**) BiMW chip containing 20 independent sensors. (**c**) Microscope photograph of individual bimodal waveguides. (**d**) 3D AFM image of the BiMW rib waveguide

specifically detect the nucleic acid target. In particular, two applications of interest in cancer diagnosis are described: *Fas* gene alternative splicing [10] and miRNA 181a regulation in bladder cancer [11]. The methodologies described here fully demonstrate the powerful potential of the BiMW biosensor for NA analysis. This biosensor could be potentially applied for the identification of other NA biomarkers, such as DNA methylation marks [12] or aptamer based biosensors [13].

## 2 Materials

### 2.1 Equipment

1. UV Ozone Cleaner—ProCleaner™ Plus (BioForce Nanosciences, USA) (*see* **Note 1**).
2. Ultrasonic bath FB 15054, from Fisher Scientific (Madrid, Spain).
3. ABBE refractometer (Optic Ivymen System, Spain).

4. Clean Room facilities: the BiMWs are fabricated from a standard 4-in (p-type) Si wafer with a thickness of 500 μm purchased from Siltronic Company. The fabrication of the BiMW is done at Clean Room facilities (class 100) using standard microelectronics optical photolithography, reactive ion etching, wet etching, and various deposition methods. Over the Si substrate a 2 μm thick layer of thermal oxide ($n_{\text{bottom, clad}} = 1.46$) is grown. Then, a 340 nm thick core layer of $Si_3N_4$ ($n_{\text{core}} = 2.00$) is deposited by Low Pressure Chemical Vapor Deposition (LPCVD). An absorbent layer of polycrystalline Si ($n_{\text{poly}} = 4.06$) of 100 nm is deposited by LPCVD over a silicon dioxide ($SiO_2$) layer of 200 nm previously deposited. Finally, a $SiO_2$ ($n_{\text{top,clad}} = 1.46$) layer 1.5 μm thick is deposited by Plasma Enhanced Chemical Vapor Deposition (PECVD).

### 2.2 Setup Components

1. Polymeric flow channels are fabricated by soft-lithography using the SYLGARD™ silicone elastomer kit that consists of a polydimethylsiloxane (PDMS) silicon elastomer and curing agent.
2. Syringe pump (NE300, New Era) for maintaining a constant flow during the biochemical detection process.
3. An injection valve (V-451, Idex) allows the injection of different solutions without changing the flow rate.
4. Linearly polarized laser diode (ML101J27, Mitsubishi diode laser nominal wavelength $\lambda_0 = 660$ nm) is used as light source. A Temperature controller (TED 200C, Thorlabs) and current controller (LDC220C, Thorlabs) are employed to stabilize the laser diode.
5. To couple the light into the waveguide a lens system is used, composed by collimated lens (C240TME-D, Thorlabs), polarization-dependent isolator (IO-3D-660-VLP, Thorlabs), and coupling objective 40× (Achro, Leica).
6. A two-sectional photodetector (S4349, Hamamatsu) is employed for collecting the light at the end of the device. The signals are amplified through standard benchtop instrumentation (PDA200C, Thorlabs).
7. A digital acquisition card (6251, National instruments) for reading the photodetector signal in real time. The signal acquisition is controlled by a LabVIEW-based application.
8. Three-axis precision microposition stage (Nanomax-TS, Thorlabs) is used for laser-BiMW alignment.
9. A temperature sensor (AD590, Thorlabs) is used to achieve a temperature feedback circuit together with a thermoelectric cooler (TEC3-1.5, Thorlabs), operated through a benchtop temperature controller (TED200C, Thorlabs) allowing a temperature resolution of 0.01 °C.

### 2.3 Reagents

1. Sodium Dodecyl Sulfate (SDS, L3771-500G), anhydrous Toluene 99.8% (244511-1 L), sodium phosphate monobasic ≥99% ($NaH_2PO_4$, 71505-1 kg), sodium phosphate dibasic ≥99% ($Na_2HPO_4$, S0876-500 g), sodium chloride ≥99.5% (NaCl, S9625-1 kg-D), Sodium Citrate dihydrate ≥99% (SSC, W302600-1 kg-K), potassium chloride ≥99.5% (KCl, 60128-250 g-F), sodium carbonate ≥99% ($Na_2CO_3$, S7795-500 g), *N*,*N*-dimethylformamide anhydrous ≥99.8%, (DMF, 227056-100 mL), triethylamine ≥99% ($NEt_3$, T0886-100 mL), pyridine anhydrous 99.8% (270970-100 mL), cross-linking molecule *p*-phenylene diisothiocyanate 98% (PDITC, 258555-5 g), 3-aminopropyltriethoxy silane ≥98%, (APTES, A3648-100 mL), *N*,*N*-Diisopropylethylamine 99.5% (DIPEA, 387649-100 mL), tetramethylammonium Chloride ≥99% (TMAC), and formamide ≥99.5% (FA, F9037-100 mL) can be purchased from Sigma-Aldrich.
2. Amine- and carboxyl-SH-PEGs (SH-PEG-$NH_2$, MW 3400 g/mol, $NH_2$-PEG-SH-3400-1 g; SH-PEG-$CO_2H$, MW 2000 g/mol, CM-PEG-SH-2000-1 g) can be purchased from Laysan Bio.
3. Acetone (161007.1211), ethanol absolute (161086.1211), methanol (161091.1211), nitric acid (65%, 473255.1611) and hydrochloric acid (HCl 37%, 471020.1611) can be purchased from Panreac.
4. Deionized water from a Milli-DI® Water Purification System, Merck Millipore, USA.
5. mRNA isoforms and microRNA sequences can be obtained from Ensembl gene browser (http://www.ensembl.org/index.html) and miRNA database miRbase (http://www.mirbase.org), respectively. DNA probes and DNA/RNA synthetic targets can be purchased from IBA GmbH (Göttingen, Germany). Table 1 summarizes the sequences employed in this work. Each probe should include three main elements: (1) The functional group: DNA probe sequences incorporate a SH-functional group at the 5′-end to enable coupling with PDITC-activated monolayer in $Si_3N_4$ surfaces (*see* **Note 2**); (2) the vertical spacer: a spacing sequence of 15 thymines (poly$T_{15}$) is included between the functional group and the matching region for enhancement of target accessibility (*see* **Note 3**); and the sequence itself: each probe sequence must be carefully designed to maximize the specificity of the interaction (*see* **Note 4**). Finally, to fully enhance the hybridization efficiency of the probes, they need to be assessed in terms of formation of secondary structures and self-annealing conformations (*see* **Note 5**).

**Table 1**
**List of the sequences employed in the experiments. Used for optimization of the methodology, real sample analysis, and optimization of Fas gene alternative splicing analysis**

| Name | Sequence |
|---|---|
| *Fas gene alternative splicing detection* | |
| *Fas57* probe | 5′-(SH)-Poly$T_{15}$-CTTTCTCTTCACTTCCTCTTTG-3′ |
| *Fas56* probe | 5′-(SH)-Poly$T_{15}$-AGATCTGGATCCTTCCTCTTTG-3′ |
| *Fas57* isoform | 5′-ATGTGAACATGGAATCATCAAGGAATGCACACTCACCAGCAACACC AAGTGCAAAGAGGAAGTGAAGAGAAAGGAAGTACAGAAAACATGCAGA AAGCACAGAAAGGAAAACCAAGGTTCTCATGAATCTCCAACTTTAAATCCT-3′ |
| *Fas567* isoform | 5′-ATGTGAACATGGAATCATCAAGGAATGCACACTCACCAGCAACACCAAGT GCAAAGAGGAAGGATCCAGATCTAACTTGGGGTGGCTTTGTCTTCTTCTTT TGCCAATTCCACTAATTGTTTGGGTGAAGAGAAAGGAAGTACAGAAAACATGCAG AAAGCACAGAAAGGAAAACCAAGGTTCTCATGAATCTCCAACTTTAAATCCT-3′ |
| *miRNA 181a detection* | |
| miR-181a probe | 5′-Poly$T_{15}$-ACTCACCGACAGCGT-3′ |
| Pre-miR-181a | 5′-GUGGUUGCUUCAGUGAACAUUCAACGCUGUCGGUGAGUUUGGGAUUAA AGUGAAAACCAUCGACCGUUGAUUGUACCCUCCAGCUAACCAUCC-3′ |
| miR-181a | 5′-AACAUUCAACGCUGUCGGUGAGU-3′ |
| miR-181b | 5′-AACAUUCAUUGCUGUCGGUGGGU-3′ |
| miR-181c | 5′-AACAUUCAACCUGUCGGUGAGU-3′ |
| miR-181d | 5′-AACAUUCAUUGUUGUCGGUGGGU-3′ |

### 2.4 Buffer Composition

1. Saline sodium citrate (SSC) 20× buffer: 3 M NaCl, and 0.3 M sodium citrate, pH adjusted to 7.4. Store at 4 °C. Different dilutions of this buffer are employed depending on each application. For AS isoforms detection, we employ hybridization solution 1: 3× SSC (0.45 M in NaCl, 0.045 M) in combination with 45% Formamide (FA). For miRNA-181a detection, we employ hybridization solution 2: 5×SSC (0.75 M in NaCl, 0.075 M) in combination with 40% FA and 3 M Tetramethylammonium Chloride (TMAC) (*see* **Note 6**).
2. Immobilization solution: Carbonate buffer (CB) ($NaHCO_3$ 0.1 M, $Na_2CO_3$ 0.1 M, EDTA 1 mM, pH 9.2). The reaction between the thiol group in the DNA probes and the Isothiocyanate (R-NCS) group in the PDITC is amine catalyzed by addition of 1 equivalent of triethylamine ($NEt_3$).
3. Alkaline hydrolysis buffer for random RNA fragmentation: carbonate–bicarbonate 50 mM, EDTA 1 mM, pH 9.2. *Stop solution*: 3 M sodium acetate, pH 5.2.
4. Site specific RNA cleavage buffer (RNase H enzyme buffer): 50 mM Tris–HCl, 75 mM KCl, 3 mM $MgCl_2$, 10 mM DTT, pH 8.3.
5. Buffer solutions were prepared by using $H_2O$ milliQ incubated O/N with 2% DEPC and autoclaved at 121 °C for 1 h. All solid materials were autoclaved at 121 °C/20 min for plastic and 134 °C/10 min for glass.

## 3 Methods

To design the BiMW biosensor, core and cladding thicknesses for the single-mode and bimodal sections must be previously defined (*see* **Note 7**). In addition, since the sensitivity of the BiMW transducer is directly related to the dimension of the interacting surface (i.e., longer sensing areas will render higher sensitivities, *see* Eq. 4), a compromise between the total length of the BiMW chip and the number of devices per wafer needs to be reached to achieve a cost-effective fabrication process.

Once defined the optimum BiMW dimensions, lithographic masks are designed to pattern the design on a thin silicon substrate called wafer. This process is performed using standard microelectronic technology at Clean Room facilities and should be reproducible and guarantee the same reliable performance for all the BiMW transducers.

Once fabricated, the BiMW should be mounted in a custom-designed optical setup. The light from a polarized laser diode is confined into a rib waveguide (4 μm width × 1.5 nm height) single-mode section (end-fire coupled) using a lens system (*see* Fig. 4).

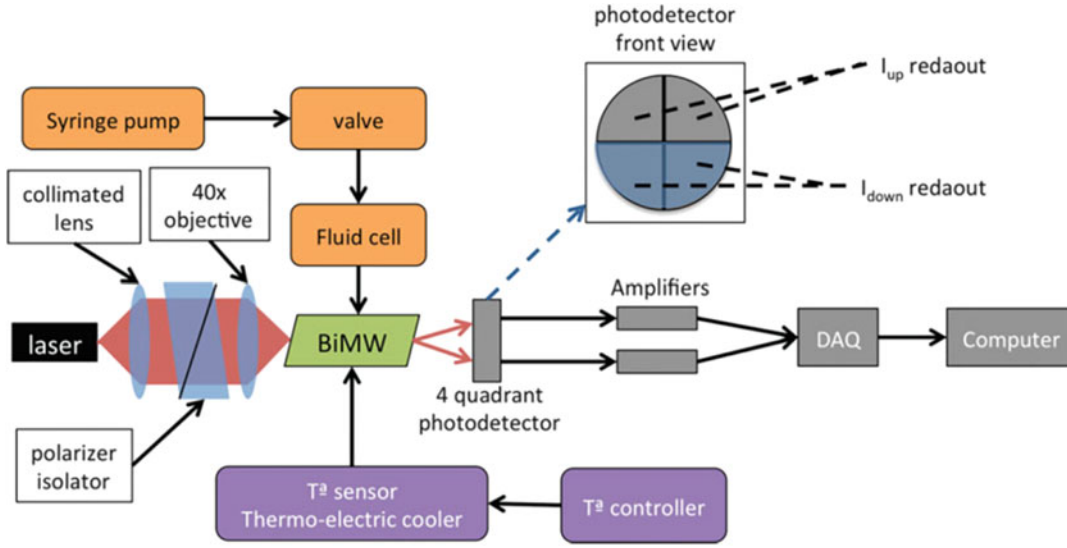


**Fig. 4** Scheme of the BiMW biosensor experimental setup. (Reprinted from [24])

The interferometric signal of the BiMW biosensor generates a variation of the output intensity distribution. Therefore, for light readout, a two-section photodetector is employed. The photodetector must be placed directly at the BiMW output, and the total intensity must be divided in the up and down section of the photodetector. The interferometric signal is processed by a phase modulation system based on Fourier transform deconvolution in order to avoid signal ambiguity and improve the performance of the BiMW [9].

### 3.1 BiMW Simulation

1. To design a BiMW, we need to choose optimal materials, which ensure a cost-effective fabrication, a further integration onto a complete LOC platform, and a highly sensitive device. As the transducers are designed for biosensors applications, $SiO_2$/$Si_3N_4$/$SiO_2$ waveguides are selected [7]. Table 2 summarizes the parameters employed in the calculation, relative to the materials, refractive indices and their thicknesses.
2. Once the material is defined, core dimensions are analyzed to ensure the best sensitivity of the device. For that, different considerations have to be taken into account [8]:
   (a) Single-mode behavior (mode $TE_{00}$ or $TM_{00}$) in *single-mode section* in Fig. 1.
   (b) Bimodal behavior (mode $TE_{00}$ and $TE_{10}$ or $TM_{00}$ and $TM_{10}$) in *bimodal section* in Fig. 1.
   (c) Performances achievable in the clean room facilities.

   Table 3 summarizes the optimal parameters for core dimensions in a BiMW for a $\lambda = 660$ nm and TE polarization.

**Table 2**
**Layer parameters employed for the evaluation of the single-mode and bimodal condition**

| Layer | Material | Thickness (nm) | Refractive index |
|---|---|---|---|
| Top cladding | Water/$SiO_2$ | 1500 | 1.33/1.46 |
| Core | $Si_3N_4$ | 150–340 | 2.00 |
| Bottom cladding | $SiO_2$ | 2000 | 1.46 |

**Table 3**
**Optimal parameters for core dimensions in a high sensitivity BiMW**

| Section | $t_{core}$ (nm) | $h_{rib}$ (nm) | $w_{rib}$ (nm) |
|---|---|---|---|
| Single-mode | 150 | 1.5 | 3000 |
| Bimodal | 340 | 1.5 | 3000 |

3. Once the core dimensions are defined, the sensor design is completed by choosing the length of the different sections. It is required to take into account the following considerations:
   (a) The need to adapt a microfluidic system to the BiMW for biosensing applications.
   (b) To ensure high sensitivity while keeping a reasonable total length.
   (c) Distribution of the BiMWs in 4-inch silicon wafer to optimize cost-effective fabrication.

   The following values were chosen: $L_0 = 3$ mm, $L_{in} = 4.5$ mm, $L_{sa} = 15$ mm, and $L_{fin} = 8.5$ mm (*see* Fig. 1).
4. In a 4-inch silicon wafer, 240 BiMW are distributed in 12 different chips (1 cm wide × 3.1 cm long) with 20 sensors per chip (*see* Fig. 3).

### 3.2 BiMW Fabrication

Figure 5 summarizes the fabrication process explained below.

1. The fabrication processing starts with a 4-in. (p-type) Si wafer with a thickness of 500 μm, over which a 2 μm thick layer of thermal oxide is grown. Then a 340 nm thick core layer of $Si_3N_4$ is deposited by LPCVD.
2. The thickness of the $Si_3N_4$ is reduced 190 nm to obtain a 150 nm single-mode section using a wet etching process with 75% phosphoric acid at 160 °C. A hard mask constituted by a layer of $SiO_2$ deposited by PECVD and defined by photolithography is employed in this step to protect unexposed regions.

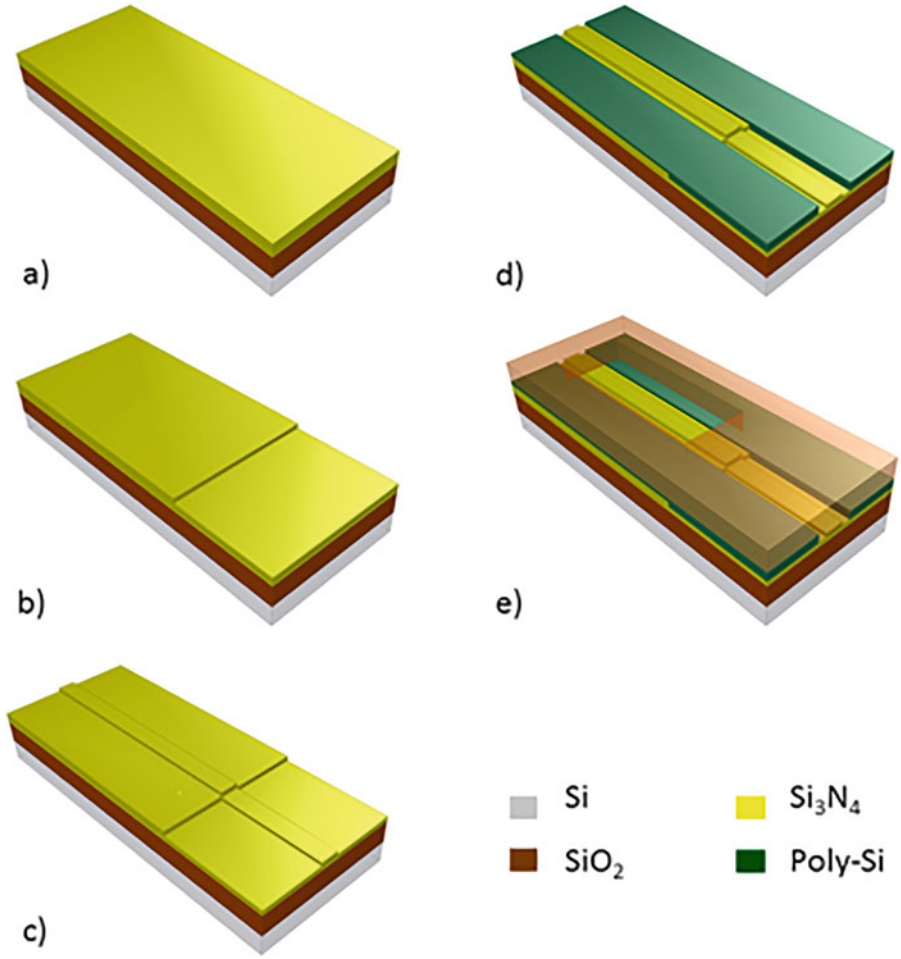


**Fig. 5** Scheme of the fabrication process of the integrated BiMW sensor. (**a**) A layer of $SiO_2$ and $Si_3N_4$ is deposited on a Si wafer. (**b**) Step-junction etched in $Si_3N_4$ layer for single-mode section definition. (**c**) Rib structure is defined. (**d**) Polycrystalline deposition over the $Si_3N_4$ and etching process to open desired window on this layer. (**e**) $SiO_2$ deposition and sensing area opening. (Reprinted from [24])

3. Using a wet etching process with BHF and a standard photolithography process, the rib structure of the waveguide (3 μm in width and 1.5 nm in height) is defined. The low etching rate of the BHF for $Si_3N_4$ allows a deep control of the process.
4. A 100 nm layer of polycrystalline Si is grown by LPCVD over 200 nm of $SiO_2$deposited by PECVD, which is introduced to improve the adhesion to the underlying $Si_3N_4$ surface. A standard lithography process is used to define the structure. Dry etching (RIE) is employed to remove the polycrystalline Si layer and 150 nm of silicon dioxide, to ensure vertical sidewalls. Then, a wet etching process is used to eliminate the remaining

50 nm of $SiO_2$. Polycrystalline Si layer is employed as absorbing material to define lateral bands along the waveguide path.

5. A $SiO_2$ layer 1.5 μm thick is deposited by PECVD as top cladding layer. In order to open the sensing area a standard lithography process is done, employing a wet etching process with BFH to remove the desired $SiO_2$.

### 3.3 BiMW Microfluidic Cell Fabrication

1. Mix thoroughly elastomer and curing agent at 10:1 ratio.
2. Remove air bubbles originating from the mixing process by a vacuum degassing process.
3. Pour degassed mix into a master fluidic mold (*see* **Note 8**).
4. Cure the mixture for 1 h at 75 °C to ensure cross-linking of the polymer.
5. Release the solid PDMS fluidic cell from the mold.
6. Expose the fluidic cell to $UV/O_3$ with the fluidic channels facing up for 2 min.
7. Cover fluidic channels with and 10% polyethylene glycol coating (PEG200, Sigma-Aldrich) aqueous solution (*see* **Note 9**).
8. Incubate in a hot plate at 100 °C for 25 min.
9. Rinse sequentially with EtOH and water.
10. Dry with $N_2$ flux.
11. Punch each channel edges with a biopsy punch to create an inlet and an outlet for liquid flow and insert polytetrafluoroethylene (PTFE) tubes (*see* **Note 10**).

### 3.4 BiMW Setup Configuration

1. BiMW sensor chip is placed in an aluminum custom-made holder as Fig. 6 shows. Into the holder a temperature stabilization is included, and all the system is mounted on a 3-axis stage. In this way, it is possible to optimally in-coupling the laser light into the waveguide of micro/nano dimensions of the selected BiMW biosensor.
2. The output light of the laser diode (ML101J27, Mitsubishi diode laser nominal wavelength $\lambda_0 = 660$ nm) is focused at the input of a BiMW biosensor. The light intensity is periodically modulated with a sinusoidal profile by a voltage input supplied through an acquisition card, controlled by a dedicated LabVIEW software. Laser optical cavity temperature is kept constant by a temperature controller (ITC510, Thorlabs), whereas precision microposition stages allow the alignment of the optical components (Nanomax-TS, Thorlabs).
3. To guarantee an optimal in coupling of the laser beam, a lenses system is employed. Two lenses focus the laser light in the desired BiMW sensor. Between these two lenses, a

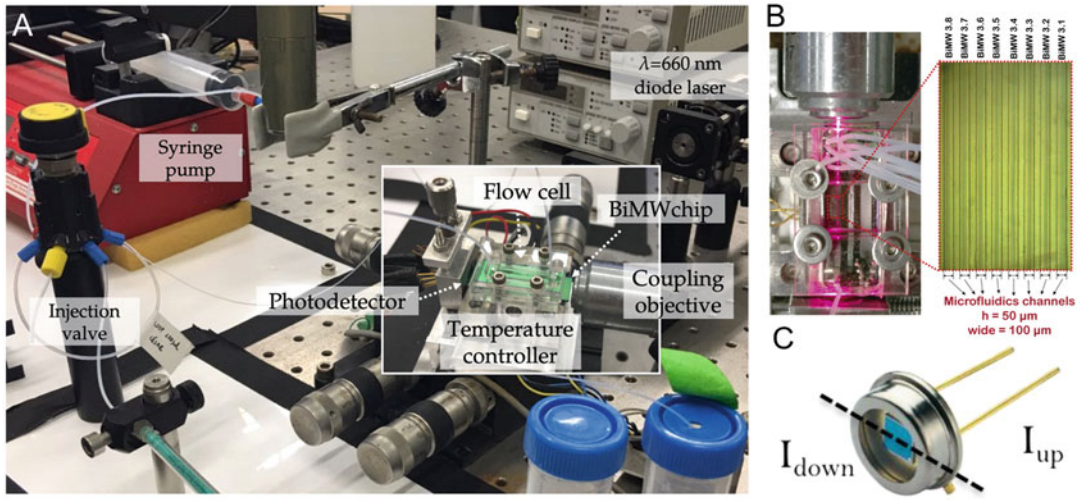


**Fig. 6** Experimental setup employed for the BiMW biosensor. (**a**) Photograph of the setup, including the objective, the XYZ-translation stage, the chip holder with embedded TEC element, the fluidic housing and fluidic tubes, the temperature controller, and the photodetector. (Reprinted from [25] Copyright © 2018, Elsevier B.V). (**b**) Top view of a light-coupled BiMW biosensor and zoom-in of independent microfluidic channels. (**c**) Photograph of the photodetector

polarization-dependent isolator is placed to avoid optical back reflections and to guarantee the required polarization.

4. The photodetector is joined in a two-axis stage assembly to the aluminum chip holder, to ensure the right and close position of the photodetector at the BiMW biosensor output. This position is essential if a modulated signal is employed [8].
5. A digital acquisition card connected to a computer is employed to process the photodetector signal. A custom-made LabVIEW software acquires a continuous photodetector signal in real time and is configured to adjust the signal to the quadrature point and to apply the Fourier transform deconvolution, transforming the interferometric readout into a real-time linear signal, as shown in Fig. 7 (*see* **Note 11**).
6. All the biological interactions must be performed in a liquid medium. For that reason, the PDMS fluid cell must be placed on top of the sensor chip. To seal the chip and avoid liquid leaks between the PDMS channels and the BiMW chip, four screws and a methacrylate sheet are employed, as Fig. 8 shows.
7. The flow delivery system is mounted by connecting a syringe pump with an injection valve and this one to the cell flow inlet through the Teflon tubes. The length of the tubes should be reduced as much as possible to minimize diffusion effects. The loop of the injection valve has a variable length, depending on the desired volume. Here, a 250 µL loop has been used for nucleic acid analyses. An extra tube is used from the cell outlet to the waste (*see* **Note 12**).

**Fig. 7** Screenshot of the BiMW biosensor software implemented in LabVIEW

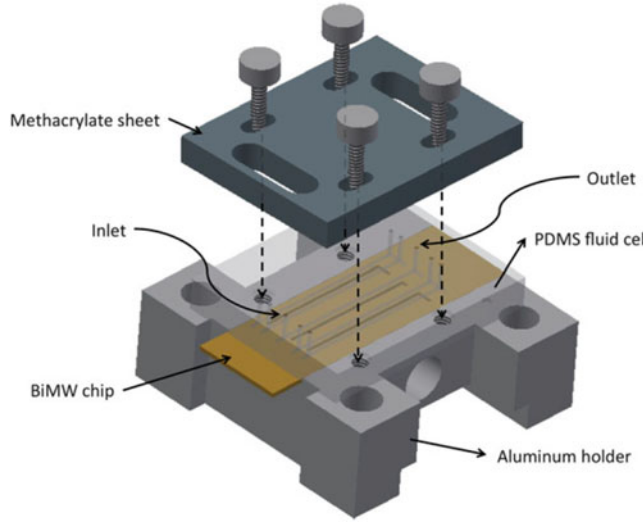


**Fig. 8** Scheme of the BiMW biosensor fluidic cell. (Reprinted from [24])

8. Place a syringe loaded with the desired running buffer in the syringe pump and introduce the flow rate parameters necessaries for the bioassay (*see* **Note 13**).

### 3.5 BiMW Biofunctionalization for NA Analyses

For the application of the BiMW interferometer for nucleic acid analyses, the sensor surface must be functionalized with a DNA probe complementary to the target sequence, which will provide the sensor selectivity. The DNA probe must be carefully designed and include a proper proportion of CG nucleotides to maximize the hybridization efficiency. Also, the hybridization conditions should be carefully optimized to avoid cross-hybridization from noncomplementary sequences that may be present in the same sample. Finally, the generated bioreceptor layer should equip the sensor with fouling resistance to avoid the random interaction of other molecules on the sensor surface that can perturb the hybridization.

The most widely approach applied to chemical modification of $Si_3N_4$ surfaces are based on the molecular grafting of the native oxide layer present onto this material by forming self-assembled monolayer (SAM) of alkyl-silanes. Among the wide variety of commercially available silanes, APTES ((3-Aminopropyl) triethoxysilane) is one of the most employed for chemical modification of silicon based photonic devices. Surfaces modified with APTES present 3-aminopropyl moieties allow the further covalent immobilization of bioreceptors presenting carboxyl groups in their structure. Moreover, by using different cross-linker molecules, the variety of bioreceptors that can be covalently attached is multiplied.

We describe the use of APTES to chemically modify the BiMW sensor chips. APTES-activated sensor chips are modified with a cross-linker molecule: *p*-phenylene diisothiocyanate (PDITC). PDITC displays two isothiocyanate groups, which can couple the free amine groups of a bioreceptor. Additionally, PDITC has the potential to form well-organized assemblies driven by π–π stacking, rendering to the sensor surfaces with improved antifouling properties [14]. Thiol-modified probes are then covalently attached to the free isothiocyanate group, yielding thiocarbamate bonds in a fast reaction [15]. Depending on the application, each probe will incorporate a specific sequence complementary to the nucleic acid of interest.

In order to avoid contamination of the sensor surface and to enhance silanization efficiency and reproducibility, the BiMW sensor chips are thoroughly cleaned and oxidized forming a freshly prepared oxide layer with a high density of silanol groups (reactive hydroxyl groups). This procedure is carried out immediately prior to the surface biofunctionalization. Cleaned and oxidized sensor chips are very susceptible to contamination and must not be stored in air. Figure 9 shows a scheme of the different steps of the functionalization protocol.

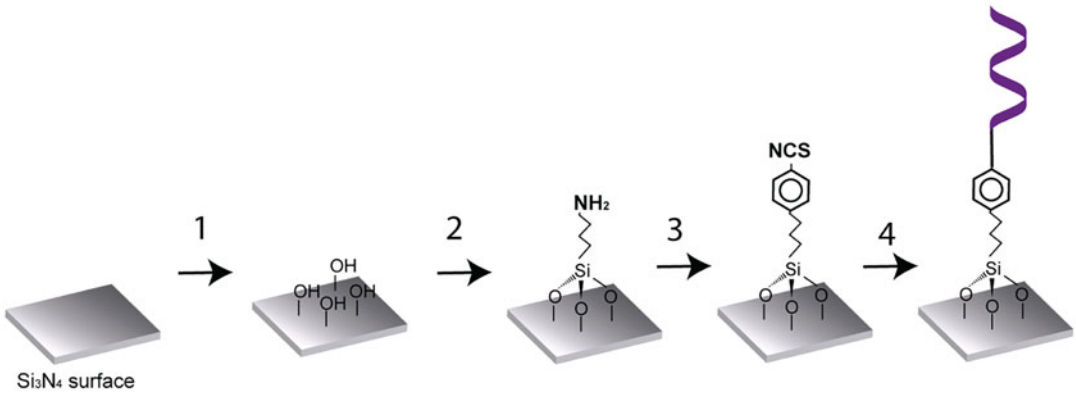


**Fig. 9** Functionalization scheme/protocol of the BiMW biosensor: (1) cleaning and oxidation; (2) APTES silanization; (3) surface activation of APTES-modified surface with PDITC, and (5) covalent attachment of DNA probe

*3.5.1 Cleaning Procedure*

1. Sonicate sequentially the BiMW sensor chip in acetone, ethanol and water for 5 min and dry under nitrogen ($N_2$) stream.
2. Immerse the sensor chip in a mixture of methanol and hydrochloric acid 37% (1:1, v/v) and sonicate for 10 min.
3. Finally, rinse the sensor chip thoroughly with deionized water and dry under $N_2$ stream.

*3.5.2 Oxidation Procedure*

1. Activate the BiMW sensor surface by exposition to UV/$O_3$ for 1 h (*see* **Note 1**).
2. Immerse the sensor chip in 15% $HNO_3$ at 75 °C for 25 min.
3. Rinse generously the sensor chip with deionized water, dry carefully under nitrogen flow and immediately immerse it in the silanization solution.

*3.5.3 BiMW Interferometer Silanization Procedure Using APTES*

1. Clean and oxidize the BiMW sensor chip according to the previous sections.
2. Immediately immerse the BiMW sensor chip in a water-free toluene solution containing 1% APTES, and 0. 0.3% v/v of *N*, *N*-diisopropylethylamine (DIPEA) under an argon atmosphere at RT for 1 h. DIPEA catalyzes the hydrolysis reaction in the absence of water molecules.
3. Rinse thoroughly the sensor chip with toluene solution and dry under $N_2$ stream.
4. Perform a dry curing by incubation of the silanized sensor chip at 110 °C for 1 h.

*3.5.4 Covalent Immobilization of DNA Probes*

1. APTES-modified BiMW surfaces are reacted with 20 mM PDITC in a solution of 10% anhydrous pyridine in *N*-dimethylformamide (DMF) for 1 h in darkness. PDITC is very sensitive to light.

2. Rinse thoroughly with DMF solution and water, sequentially and dry under $N_2$ stream.
3. At this point, the functionalized BiMW sensor chip is positioned on the experimental setup, and the PDMS flow-chamber mounted on top.
4. Initiate a continuous flow of $Na_2CO_3$ buffer at pH 9.5 and wait until a baseline is obtained.
5. Inject 250 μL of the immobilization solution into the flow cell at a constant flow rate of 5 μL/min. Probe concentration must be optimized depending on each application and different lateral spacers can be considered, depending on the specific application (*see* **Note 14**).
6. BiMW sensor chip is now functionalized and ready to be employed for sample evaluation. Once functionalized, sensor chips must be stored at 4 °C if they are not used immediately.
7. Different characterization techniques can be employed after each functionalization step to assess that the proper surface chemistry is in place over the $Si_3N_4$ BiMW biosensor surface [10]: (1) Water Contact Angle (WCA) measurement can be used as an indication of the surface wettability and obtained using Easy drop standard apparatus (Krüss GmbH, Hamburg – Germany-); (2) X-ray photoelectron spectroscopy (XPS) can be performed using a PHOIBOS 150 analyzer (SPECS GmbH, Berlin, [Germany]) in ultrahigh vacuum conditions (base pressure 1 × 10–10 mbar) and a monochromatic K-alpha X-ray source (81486.7 eV at a take-off angle of 0 and 54°) to assess the elemental composition of the surface; and (3) immobilized fluorescent probes can be employed and observed using a Zeiss Axio Observer Z1m optical microscope, to ensure the proper covalent bonding of the DNA probe to the silane monolayer (*see* **Note 15**).

### 3.6 mRNA Alternative Splicing Analysis Using BiMW

For the analysis of *Fas* gene AS, we aim to identify two different messenger RNA (mRNA) isoforms, *Fas*567 and *Fas*57, which are transcribed from the same *Fas* gene mRNA precursor. This precursor contains a series of coding sequences, called exons, are reorganized differently by the AS regulatory mechanism to produce different versions of mature mRNAs (isoforms). This process leads to proteins with different/opposite functions: *Fas*567 isoform is translated into an apoptotic cell membrane receptor that participates in the activation of the programmed cell death (apoptosis) while *Fas*57 encodes a protein that is soluble with an anti-apoptotic function since it competes with the receptor by the interaction with the same ligand (*see* Fig. 10). Misbalanced isoform ratio expression can favor the onset of cancer. Therefore, analyses of alternative splicing isoforms can help in cancer diagnosis. Each

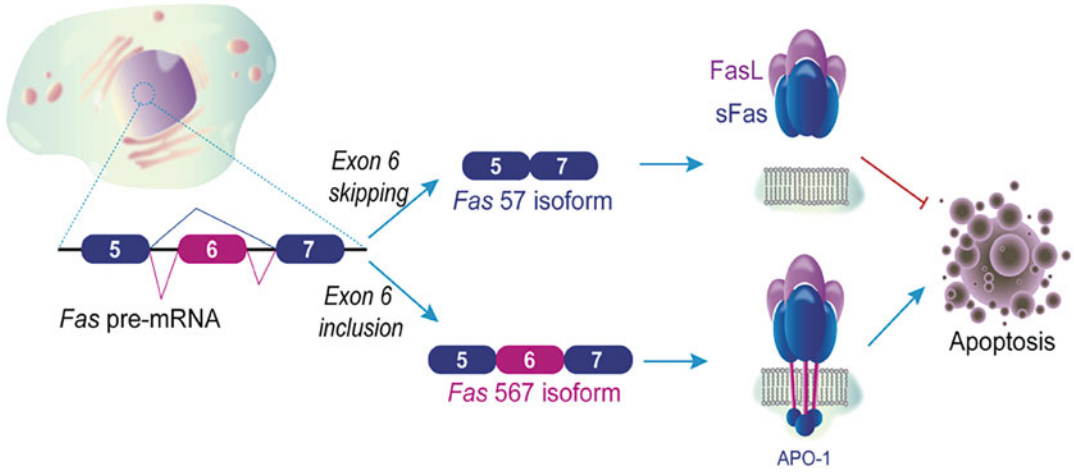


**Fig. 10** Schematic representation of the different RNA and protein isoforms generated by alternative splicing of *Fas* gene/CD95. (Reprinted from [16] Copyright © 2015 Elsevier B.V)

mRNA isoform consists of long RNA sequences of up to 1000 nucleotides (nt). This makes the detection difficult because of the generation of secondary structures that may hinder the DNA sequence of interest. Here we present two different fragmentation protocols: a random mRNA fragmentation [16] and a site-specific cleavage [17], that should be performed prior isoform detection (*see* Fig. 11). Independent BiMW biosensors are functionalized with specific probes for each isoform, targeting the 5–7 and 5–6 splice junctions for *Fas*57 and *Fas*567 respectively (*see* Fig. 12). These splice junctions are key features for the specific recognition of each isoform. However, they imply the inclusion of a shared sequence from exon 5 in both probes, and then a highly stringent buffer is employed during detection in order to avoid cross-hybridization from the off-target sequences.

The length of mRNA isoforms presents some challenges for their direct and label-free hybridization detection with the BiMW biosensor. mRNA sequences are long single-stranded RNA sequences of thousands of nucleotides. The intrinsic flexibility of RNA moieties increases the likelihood of base-pairing and backbone interactions, generating secondary and tertiary structures in the mRNA sequences. The formation of these complex structures conceals the target sequence of interest (i.e., the splice junctions 5–6 and 5–7 of *Fas567* and *Fas57,* respectively), hindering their accessibility to the DNA probe immobilized at the BiMW sensor surface. For that reason, a fragmentation step is introduced in the protocol in order to generate the fragment of interest. This fragmentation allows for the direct detection of native mRNA sequences without the need for previous PCR amplification. This will greatly reduce the time of the analysis while minimizing the

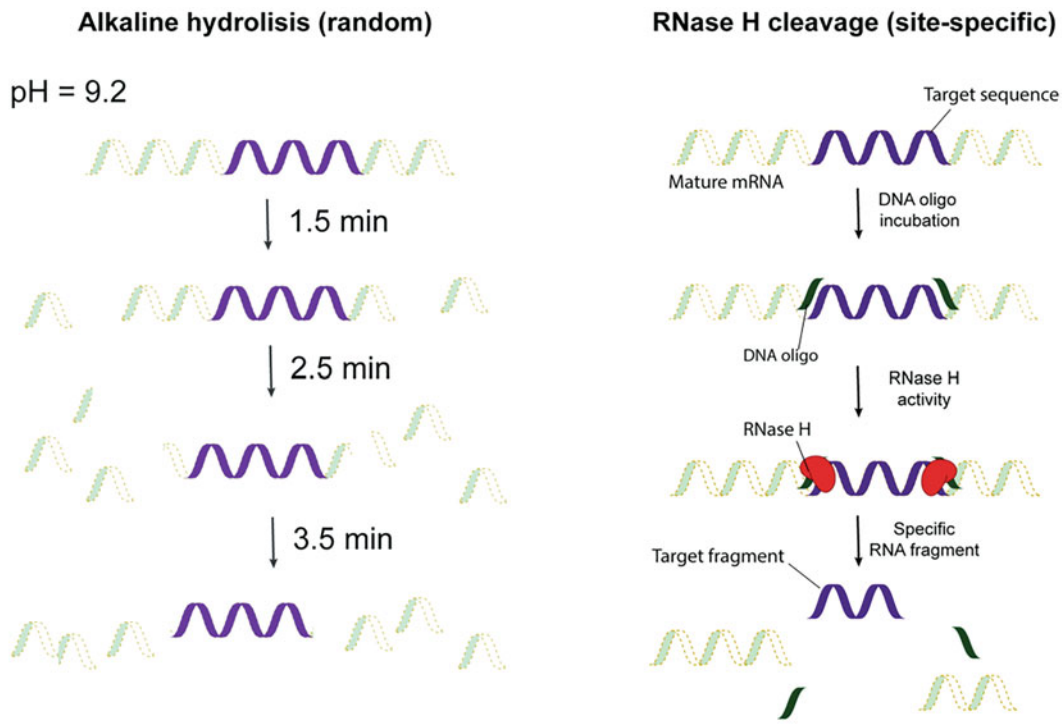


**Fig. 11** RNA fragmentation strategies employed for the detection of alternative splicing events in HeLa cells with the BiMW biosensor: (*left*) Alkaline hydrolysis, which relies on the random fragmentation of RNA moieties in an alkaline medium (pH = 9.2); (*right*) site-specific RNA cleavage, which relies on the specific activity of RNase H enzyme. Both strategies are optimized to generate RNA fragments showed in Table 2. (Adapted from [17] Copyright © 2019, American Chemical Society)

error produced by the amplification process. Two fragmentation approaches are described: alkaline hydrolysis [16] and RNase H cleavage [17] (*see* Fig. 11). Alkaline hydrolysis relies on the base-catalyzed hydrolyzation of the phosphodiester bond in the ribose sugar-phosphate backbone of RNA sequences. While this fragmentation approach offers a fast performance, it also involves a random cleavage, and put at risk the integrity of the RNA sample by disruption of the sequence of interest. For that, depending on the RNA integrity, different incubation times should be applied.

On the other hand, RNase H cleavage is a site-specific, enzyme-dependent reaction, offering a more controlled fragment generation. RNase H degrades RNA sequences that are hybridized to a DNA sequence. Therefore, this methodology employs DNA oligonucleotides that are complementary to upstream and downstream RNA segments flanking the specific RNA sequence of interest in each *Fas* isoform (Table 4). Once hybridized, these fragments will initiate the degradation of the RNA sequence that are forming the duplex in the presence of RNase H enzyme, liberating the fragment of interest. Both fragmentation protocols are performed off-sensor

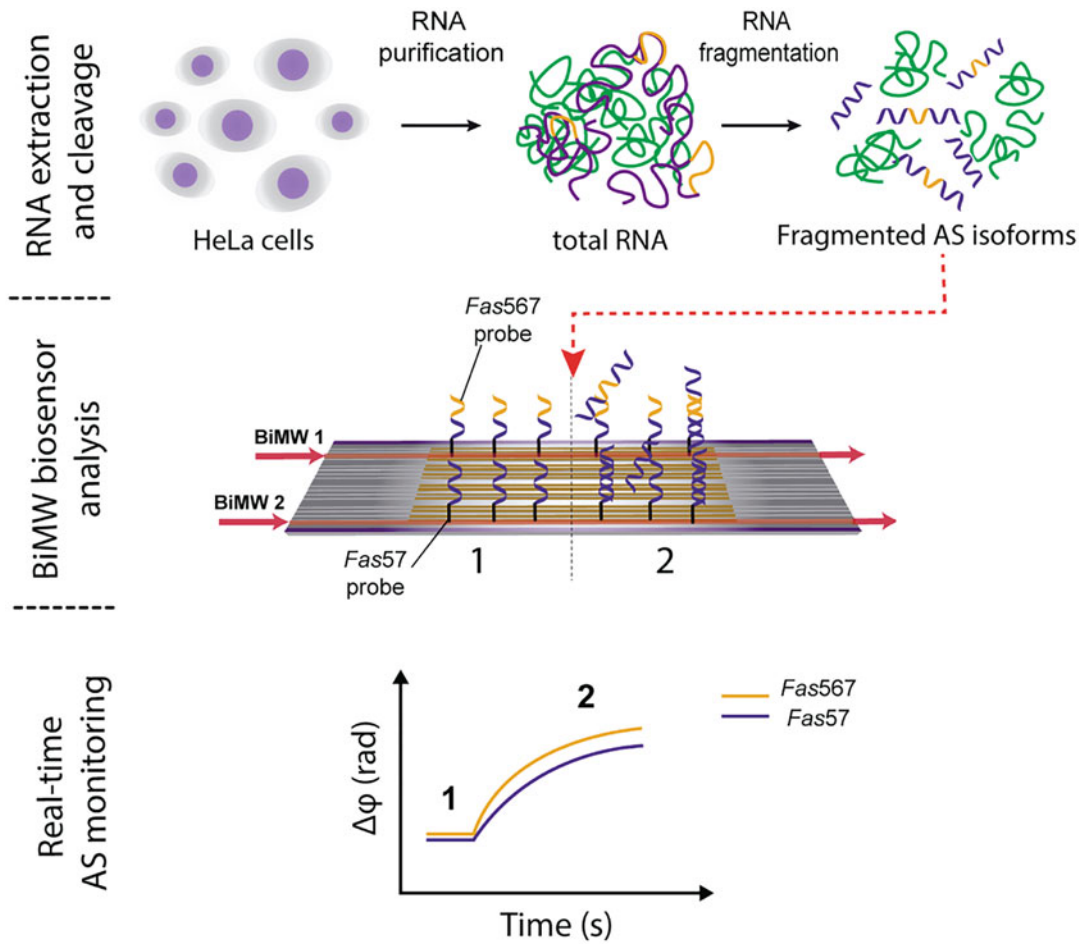


**Fig. 12** BiMW biosensor for specific detection of *Fas* AS isoforms in HeLa cells. (Adapted from [17] Copyright © 2019, American Chemical Society)

prior to the analysis of *Fas* isoforms. We have employed total RNA purified from different HeLa cell lineages presenting different expression profiles.

*3.6.1 Alkaline Hydrolysis*

1. Preheat total RNA sample at 95 °C for 15 s.
2. Mix the sample with preheated 1× alkaline hydrolysis buffer to initiate the hydrolysis reaction.
3. Incubate at 95 °C for 3 min (*see* **Note 16**).
4. Add 1 μL RNA random fragmentation stop solution.
5. Place the sample on ice until use.
6. The total RNA sample is fragmented and ready for its analysis with the BiMW biosensor.

*3.6.2 RNase H Cleavage*

1. For DNA fragmentation probe annealing with RNA isoforms, incubate isolated total RNA with 10 μM of each DNA probe at 95 °C for 2 min.
2. Place the sample on ice for 5 min to cool it down.
3. Incubate annealed RNA samples with 100 U/mL RNase H in 1×RNase H buffer at room temperature for 60 min.
4. Incubate the sample at 65 °C for 15 min to inactivate the enzyme.
5. Place the sample on ice until use.
6. The total RNA sample is fragmented and ready for its analysis with the BiMW biosensor. The generated fragments are listed in Table 4.

*3.6.3 Biofunctionalization of the AS BiMW Biosensor*

1. Initiate a continuous flow of $Na_2CO_3$ buffer at pH 9.5 and wait until a baseline is obtained.
2. Inject 250 μL of the immobilization solution into the flow cell at a constant flow rate of 5 μL/min. For *Fas* gene AS isoform detection, prepare the immobilization solution consisting of mix solution containing either SH-*Fas57* or SH-*Fas56* probe and 6-mercapto-1-hexanol (MCH) lateral spacer at a 20:1 molar ratio in 1 μM total concentration in 0.1 M $Na_2CO_3$ buffer at pH 9.5 (*see* **Note 17**). Then, flow each solution in independent BiMW sensors for the parallel detection of each isoform.
3. Wash with a continuous flow of $Na_2CO_3$ buffer at pH 9.5 and wait until a baseline is obtained. At this point, the thiolated probe should have reacted with the activated PDITC surface and there should be a positive sensor phase change, displacing the new baseline a few radians over the initial one according to the number of DNA probes attached to the surface (*see* Fig. 13a, b). This phase change in the baseline indicates that the DNA probe coupling through thiocarbamate bonds has taken place at the sensor surface.

*3.6.4 Biosensor Calibration*

1. Initiate a continuous flow of the AS hybridization buffer: 3× SSC/FA45% and wait until stabilization of the interferometric signal. This buffer will be used to perform *Fas* isoforms direct detection assay (*see* **Note 18**).
2. Prepare a series of standard solution at different concentrations of synthetic *Fas567* and *Fas57* isoforms employing the hybridization buffer. For each isoform, concentrations from 50 to 1 pM were employed. A control signal should be employed to demonstrate the specificity of the hybridization event. In the case of AS, the noncomplementary isoform can be employed as the off-target control. The synthetic sequences are listed in Table 1.

**Table 4**
**List of the sequences employed for the site-specific cleavage of *Fas* gene RNA isoform using RNase H enzyme**

| Name | Length (nt) | Sequence |
|---|---|---|
| *Fas* 567 isoform fragment after RNase H | 214 | 5′-CCAAAUGUGAACAUGGAAUCAUCAAGGAAUGCACACUCACCAGCAACACCAAG UGCAAAGAGGAAGGAUCCAGAUCUAACUUGGGGUGGCUUUGUCUUCUUCUUU UGCCAAUUCCACUAAUUGUUUGGGUGAAGAGAAAGGAAGUACAGAAAACAUGCAG AAAGCACAGAAAGGAAAACCAAGGUUCUCAUGAAUCUCCAACUUUAAAUCCU-3′ |
| *Fas* 57 isoform fragment after RNase H | 149 | 5′-CCAAATGTGAACATGGAATCATCAAGGAATGCACACTCACCAGCAACACCAAGTGCA AAGAGGAAGTGAAGAGAAAGGAAGTACAGAAAACATGCAGAAAGCACAGAAAGGAAAA CCAAGGTTCTCATGAATCTCCAACTTTAAATCCT-3′ |
| *Fas* exon 4 probe | 25 | 5′-TGCAAGGGTCACAGTGTTCACATAC-3′ |
| *Fas* exon 8 probe | 25 | 5′-CAGATAAATTTATTGCCACTGTTTC-3′ |

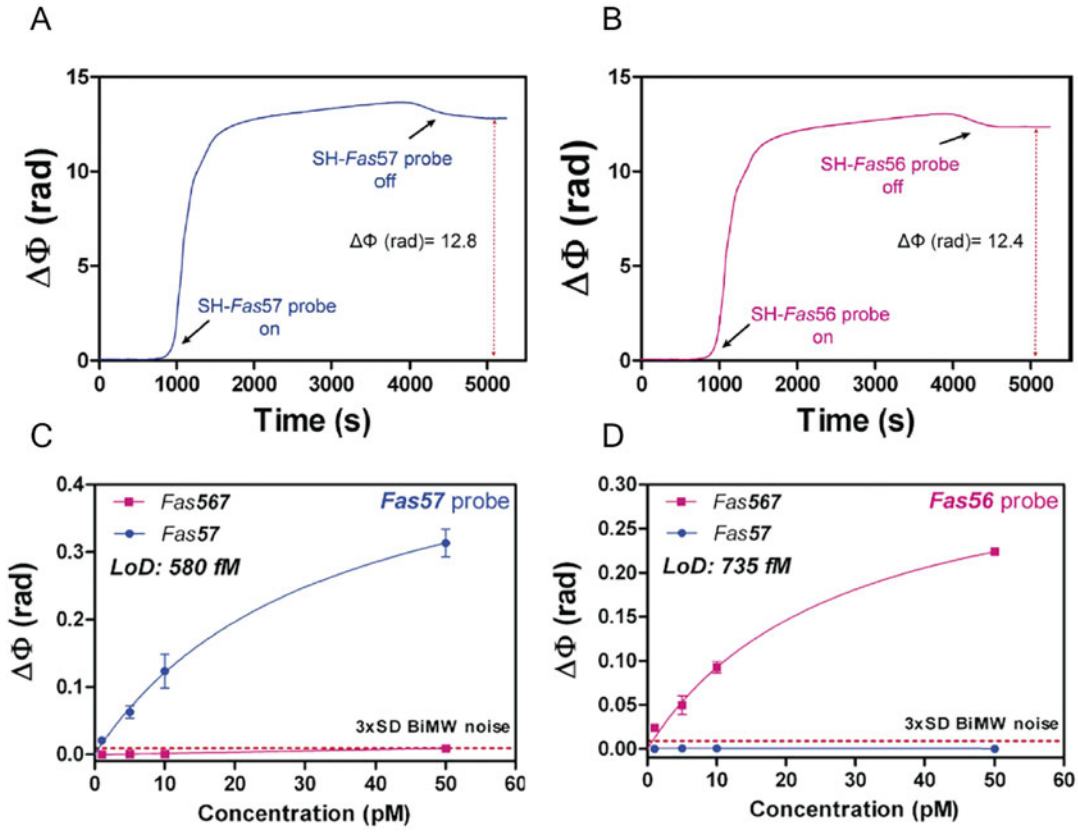


**Fig. 13** *Fas* gene AS isoform assessment with the BiMW biosensor. Real-time immobilization signals of SH-*Fas*57 (**a**) probe and SH-*Fas*56 probe (**b**). Black arrows indicate the entrance ("on") and exit ("off") of the DNA probes in the sensor area during the interaction with the sensor surface. BiMW calibration curves for *Fas*57 probe (**c**) and *Fas*56 probe (**d**). Solid lines (blue and pink) correspond to the nonlinear fit of the calibration curves. Red dashed line corresponds to 3×SD SPR noise, which is the limit for the minimum signal detectable. All data show mean ± SD of triplicate measurements. (Reprinted from [10] Copyright © 2017, Springer Nature)

3. Inject into the flow cell the different solutions with a regeneration step in between and monitor the phase shift (sensor response) of the two different sensors, that is, *Fas567* and *Fas57* biosensors. The regeneration solution must be empirically optimized (*see* **Note 19**). For *Fas* isoform detection, an aqueous solution containing 50% FA was employed.
4. Construct a plot of sensor response vs. *Fas* gene isoform concentration for each DNA probe and fit the data to an appropriate curve-fitting model to obtain a calibration curve (*see* Fig. 13c, d). Increasing concentrations of the target sequence should produce higher sensor responses. A signal saturation can be reached with the highest concentrations of the target sequences. Note that off-targets should generate negligible

phase shifts, which indicates that the sensor response is selective and free from cross-hybridization. Limit of detection (LOD) should be in the desired range for the application. If not, try to optimize immobilization and hybridization conditions. mRNA isoforms level in normal and cancer tissues can be found at the low pM concentration [18]. The biosensor is ready for HeLa cell samples evaluation.

#### 3.6.5 HeLa Cell Sample Analysis

1. Initiate a continuous flow of the AS hybridization buffer: 3× SSC/FA45% and wait until stabilization of the interferometric signal. This buffer will be used to perform *Fas* isoforms direct detection assay (*see* **Note 18**).
2. Dilute fragmented HeLa samples (Subheading 3.5) in the hybridization buffer.
3. Inject the HeLa cell sample with unknown concentration of *Fas* isoforms into the flow cell at a 15 μL/min rate. *Fas567* and *Fas57* generated fragments will hybridize with their complementary DNA probes immobilized in independent sensor surfaces. The BiMW signal intensity will depend on the concentration of each isoform on each sample.
4. Allow to wash off the unbound target by the continuous flow of the buffer for a few minutes to obtain a stable baseline. This step will produce a shift phase of the baseline level if there is a specific hybridization from the free isoform fragments present in the sample.
5. Regenerate the surface by injecting an aqueous solution with 50% FA at 15 μL/min for 20 min and wait until stabilization of the signal (surface conditioning). At this point, the biosensor surface is ready for the evaluation of a second sample.
6. The concentration of each isoform in the analyzed samples can be calculated by interpolating the sensor response in the previously obtained calibration curve.

### 3.7 MiRNA 181 Detection

miRNAs are short sequences containing around 19–23 nt that do not participate actively in the protein production, but rather work as RNA regulators of different processes by interacting with DNA promoters or interrupting RNA translation [19] (*see* Fig. 14). In order to quantify miRNA-181a in urine samples of bladder cancer patients, a highly antifouling sensor surface must be generated to avoid nonspecific adsorptions from undesired molecules found in this biofluid, as shown in Fig. 15. We present a protocol for the generation of an antifouling surface based on the combination of different PEG molecules that generate a zwitterionic monolayer that presents a strong antifouling effect in urine samples at 1:10 dilution. Although in this case there is no need for the sequence fragmentation due to the short sequence of the miRNA, great care

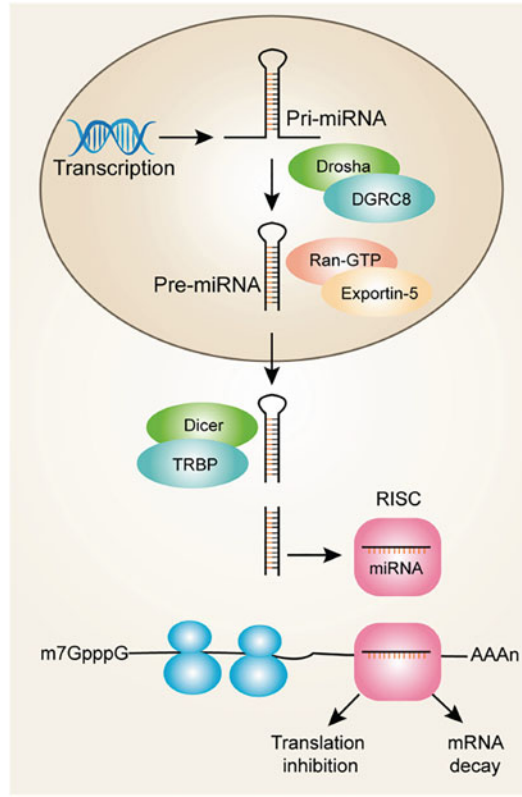


**Fig. 14** Schematic representation of miRNA biogenesis

must be taken to avoid cross-hybridization with miRNA family members which, in some cases, only differ in one nucleotide.

*3.7.1 Biofunctionalization of the Sensor Surface*

1. Initiate a continuous flow of $Na_2CO_3$ buffer at pH 9.5 and wait until a baseline is obtained.
2. Inject 250 μL of the immobilization solution into the flow cell at a constant flow rate of 5 μL/min. For miRNA-181a detection, prepare a solution containing a mix of SH-miR181a probe and SH-PEGs $CO_2H/NH_2$ at a molar ratio of 1:1 in 2 μM total concentration (*see* **Note 20**).
3. Wash with a continuous flow of $Na_2CO_3$ buffer at pH 9.5 and wait until a baseline is obtained. At this point, the thiolated probe should have reacted with the activated PDITC surface and there should be a positive sensor phase change, displacing the new baseline a few radians over the initial one (*see* Fig. 16a). This phase change in the baseline indicates that the DNA probe coupling through thiocarbamate bonds has taken place at the sensor surface.

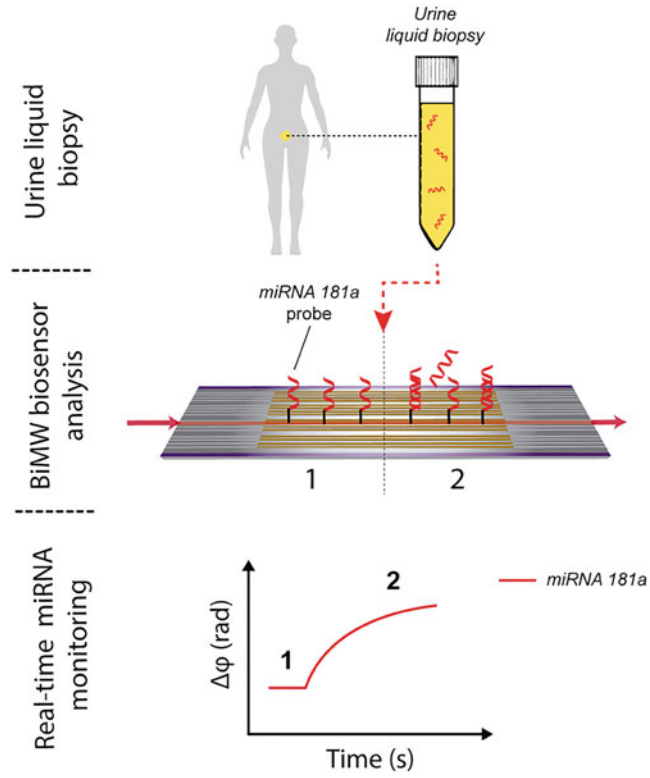


**Fig. 15** BiMW biosensor for specific detection of miRNA 181a in urine liquid biopsies from bladder cancer patients

*3.7.2 Biosensor Calibration*

1. Initiate a continuous flow of the miRNA-181a hybridization buffer: 5× SSC/FA40%/TMAC and wait until stabilization of the interferometric signal. This buffer will be used to perform miRNA-181a direct detection assay (*see* **Note 18**).
2. Prepare a series of standard solution at different concentrations of miRNA-181a employing the hybridization buffer. MiRNAs physiological concentrations are found in a wide range of concentrations, from aM to nM concentration [20]. We covered concentrations from 10 aM to 10 nM. A control signal should be employed to demonstrate the specificity of the hybridization event. In the case of miRNA 181a, the different homologous sequences can be employed as the off-target controls.
3. Inject into the flow cell the different miRNA-181a solutions with a regeneration step in between and monitor the phase shift (sensor response). The regeneration solution must be empirically optimized (*see* **Note 19**). For miRNA-181a detection, an aqueous solution containing 35% FA was employed.
4. Corroborate the selectivity of the biosensor by injecting into the flow cell different solutions containing miRNA-181a family

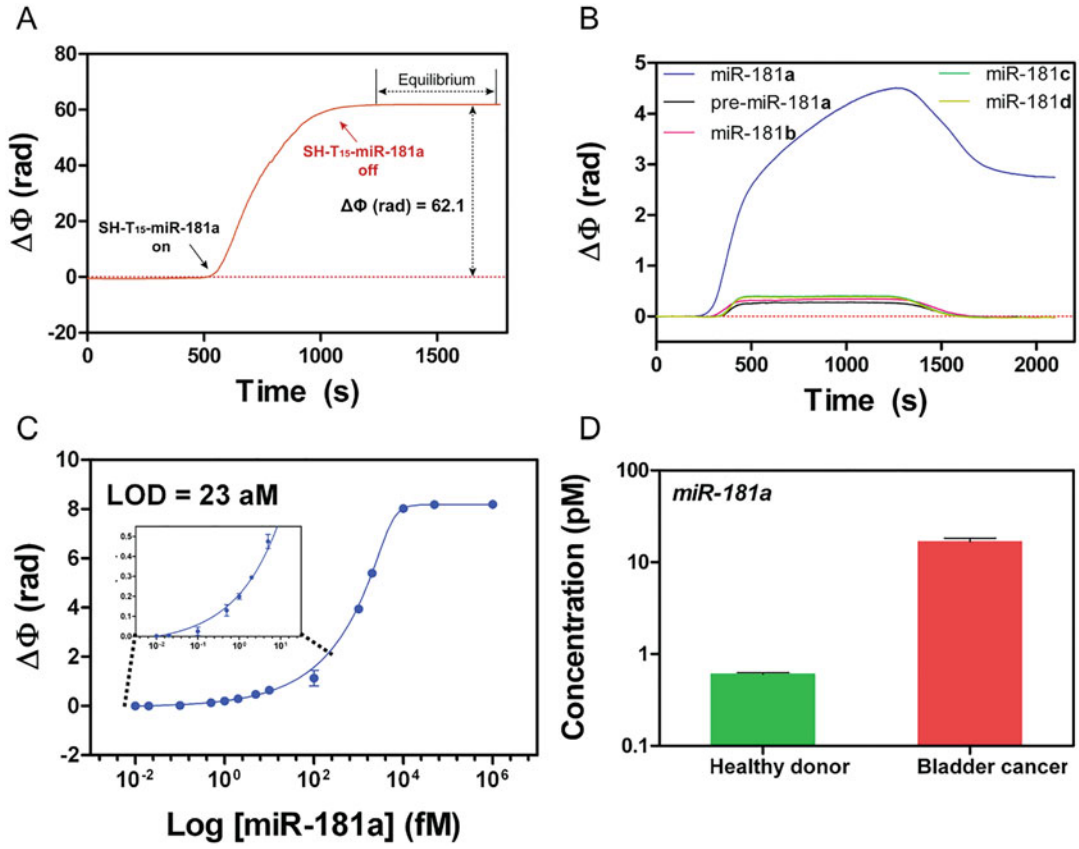


**Fig. 16** MiRNA 181a assessment with the BiMW biosensor. (**a**) Real-time BiMW response to the immobilization of the SH-T15-miR181a probe and SH-PEG $CO_2H/NH_2$ mix over a PDITC-activated APTES monolayer (step 4). The sensogram shows the interaction of the injected solution with the PDITC-activated APTES monolayer (SH-$T_{15}$-miR-181a on) reaching the equilibrium (SH-$T_{15}$-miR-181a off) and giving rise to a notable increment of the phase-modulated signal. (**b**) BiMW sensogram showing the specific detection of miR-181a (blue line) and discrimination of pre-miR-181a (black) and its homologous miRNAs 181b (purple), 181c (green), and 181d (yellow) at 100 pM concentration. (**c**) Calibration curve obtained for different concentrations of miR-181a standard solutions (10 aM to 10 nM) in semilog scale. Solid blue line corresponds to the exponential fit of the calibration curve ($R^2 = 0.99$). All data show mean ± standard deviation (SD) of triplicate measurements. (**d**) Concentrations of miR-181a in urine samples from healthy donors (0.6 pM) and bladder cancer patients (16.7 pM) obtained by interpolation of the BiMW biosensor signal in the calibration curve. (Reprinted from [11] Copyright © 2016, American Chemical Society)

members at an intermediate concentration (Table 3 shows the different homologous sequences). Homologous sequences should not generate any phase shifts (*see* Fig. 16b).

5. Construct a plot of sensor response vs. miRNA-181a concentration and fit the data to an appropriate curve-fitting model to obtain a calibration curve. Increasing concentrations of the target sequence should produce higher sensor responses (*see* Fig. 16c). A signal saturation can be reached with the highest

concentrations of the target sequences. Note that off-targets should generate negligible phase shifts, which indicates that the sensor response is selective and free from cross-hybridization. Limit of detection (LOD) should be in the desired range for the application. If not, try to optimize immobilization and hybridization conditions. The biosensor is ready for the evaluation of bladder cancer patient urine samples.

#### *3.7.3 Urine Sample Analysis from Bladder Cancer Patients*

1. Initiate a continuous flow of the miRNA-181a hybridization buffer: 5× SSC/FA40%/TMAC and wait until stabilization of the interferometric signal. This buffer will be used to perform miRNA-181a direct detection assay (*see* **Note 18**).
2. Dilute urine samples 1:10 in the highly stringent hybridization buffer.
3. Inject the samples with unknown concentration of miRNA-181a into the flow cell at a 15 μL/min rate. miRNA-181a will hybridize with the complementary DNA probe immobilized in the sensor surface. The BiMW biosensor signal intensity will depend on the concentration of the miRNA on each sample.
4. Allow to wash off the unbound target by the continuous flow of the buffer for a few minutes to obtain a stable baseline. This step will produce a shift phase of the baseline level if there is a specific hybridization from the free miRNA-181a present in the sample.
5. Regenerate the surface by injecting an aqueous solution with 50% FA at 15 μL/min for 20 min and wait until stabilization of the signal (surface conditioning). At this point, the sensor surface is ready for the measurement of a second sample.
6. The concentration of miRNA-181a in the analyzed samples can be calculated by interpolating the sensor response in the previously obtained calibration curve (*see* Fig. 16d) (*see* **Note 21**).

### *3.8 Data Analysis*

For the evaluation of each application, relevant analytical *figure of merits* should be obtained from the biosensor analysis.

1. First, the calibration curve should be obtained. It will allow determining the concentration of our target nucleic acid in an unknown sample by the comparison of the biosensor response to a set of standard samples of known concentration. For that, the phase variation ($\Delta\varphi$) produced by the standards is plotted versus analyte known concentrations (*see* Fig. 13c, d, and 16c). The standard curve can be fit using different fitting methods, that is, nonlinear regression (curve fitting) or linear regression, among others (*see* **Note 22**).

2. The experimental detection limit (LOD) will provide the sensitivity of your biosensor and can be obtain by interpolating to the regression curve the value corresponding to the target concentration giving a $\Delta\varphi$ (rad) in the hybridization signal at least three times higher than that of the standard deviation of the DNA/RNA control signal ($3\times\Delta\sigma$). For example, in a linear regression curve,

$$y = mx + a. \tag{8}$$

where $y$ is the $\Delta\varphi$, $m$ is the slope, $x$ is the concentration, and $a$ is the intercept. Therefore, the LOD will be given by

$$\mathrm{LOD} = \frac{3 \times \Delta\sigma - \mathrm{a}}{m}. \tag{9}$$

3. Limit of quantification (LOQ) is defined as the target concentration giving $\Delta\varphi$ (rad) in the hybridization signal at least ten times higher than that of the standard deviation of the DNA control or the RNA control signal and must agree with the smaller concentration measured experimentally. In a linear regression curve, the LOQ will be given by

$$\mathrm{LOQ} = \frac{10\Delta\sigma - \mathrm{a}}{m}. \tag{10}$$

4. The coefficients of variation determine the robustness and repeatability of the BiMW biosensor and can be obtained from multiple measurements of a concrete nucleic acid concentration by calculating the ratio of the standard deviation ($\Delta\sigma_{\mathrm{mean}}$) to the mean, expressed in percentages (% CV):

$$\mathrm{CV}\ (\%) = \frac{\Delta\sigma_{\mathrm{mean}}}{\mathrm{Mean}} \times 100 \tag{11}$$

   Individual assay variation can be calculated after analysis of three replicates of the target at different concentrations. Inter-assays variations can be calculated gathering together all three replicates from the individual assays obtained from two different operators.

5. Percentages of off-target cross-hybridization will demonstrate the selectivity of your biosensor and should be calculated by dividing the average signal intensity of the off-targets into the average signal intensity of the complementary RNA sequence.

6. Agreement of the biosensor with the corresponding gold-standard technique should be calculated in order to validate clinically the biosensor performance by applying the Bland–Altman model for replicate measurements (*see* **Note 23**).

## 4 Notes

1. UV/Ozone plasma treatment can be replaced by Plasma cleaner reactor: Standard plasma system Femto version A (40 kHz, 0–100 W) from Diener Electronic GmbH (Ebhausen, Germany). Treatment times must be carefully optimized. Both oxidative pretreatments render highly hydrophilic surfaces (water contact angle lower than 5°).
2. Other functional groups can be included depending on the surface chemistry approach. For surface chemistry approaches, please refer to [5].
3. Vertical spacers improve the accessibility of the target sequence to the monolayer by enhancing the mobility of the attached DNA probes and reducing steric hindrance. Other vertical spacers different to poly T can be employed, such as chains of carbons (being C6 and C12 widely employed) [5].
4. For alternative splicing isoforms, probes sequences should be complementary to the splice-junction sequences (i.e., the sequences flanking the exon junction after intron removal). The different isoforms share most of their sequence since they are generated from the same mRNA precursor. However, the splice-junction is a unique feature that differentiate between isoform and will, therefore, promote the specific detection of each isoform [16]. For miRNA detection, the probe design is constrained because of the miRNA short sequence. However, since miRNA sequences normally have homologous counterparts, one must avoid the seed sequence or seed region, normally situated at positions 2–7, which is share among all the miRNAs that belong to the same family. Also, one should try to include the region that contains the most mismatched nucleotides possible with respect to their homologous [21].
5. There are several software available that can be employed for secondary structure and self-annealing prediction of different probes and targets. In this work we have employed Oligo Analyzer software and RNA fold webserver.
6. Cross-hybridization from mRNA isoforms or homologous miRNAs should be prevented in the BiMW biosensor to avoid false positives. Buffer composition, such as buffer ionic strength, or some additives, such as FA and TMAC, can help to reduce nonspecific interactions and to enhance detection selectivity. Cross-hybridization can also be prevented by the introduction of locked nucleic acids (LNAs) in the probe sequence, which increase the specificity and foster the discrimination of nucleotide mismatches. Different combinations should be optimized depending on the target sequence [5].

7. Fabrication tolerances at the clean room facilities where the fabrication is done must be taking into account when designing a device of micro/nanodimensions.
8. The fluidic mold can be obtained by using a milling machine or by 3D printing, for low-resolution rapid prototyping. On the other hand, standard photolithography microfabrication techniques can be employed to create wafer-based molds for high-resolution applications [22].
9. Incubation with PEG200 will help the blockade of the microfluidic channels to reduce PDMS hydrophilicity, reducing nonspecific adsorption of molecules present in the samples.
10. The size of the biopsy punch will depend on the diameter of the Teflon tubes employed and should be slightly smaller, to prevent leakages.
11. A main limitation of interferometric sensors is the nature and complexity of the interferometric signal. In the BiMW sensor, the interferometric response is due to the phase difference between the sensing mode (first order mode) and the reference mode (fundamental mode). For maximum sensor response, the interferometric signal must be positioned at the quadrature point. However, factors as temperature fluctuations or large refractive index variations can shift the interferometric response toward a peak or a null of the sinusoid signal, which is translated in sensitivity decays. In order to avoid this ambiguity, signal processing methods have been proposed for interferometers [9, 23].
12. RNA is easily degradable in the presence of RNases. To prevent from RNase activity during the evaluations, the microfluidic must be cleaned by sequentially flowing SDS 0.5%, HCl 0.1 M, EtOH 100%, 0.5 M NaOH, and sterile $H_2O$.
13. Flow rate should be carefully optimized in each application to maximize the biosensor performance.
14. Prevention of nonspecific adsorptions of sample matrix components is particularly important when working with label-free optical sensors, in which an overvalued sensor response due to nonspecific adsorption of matrix components is difficult to discriminate and leads to false positive results. Different lateral spacers can be employed, including MCH and PEG molecules [5] to avoid this effect.
15. Contact angle values should be compared with their corresponding values in the literature. In this work, the values for Untreated, APTES-modified, PDITC-modified and DNA functionalized $Si_3N_4$ surface were $35.1 \pm 1.19$, $67.1 \pm 0.11$, $59.6 \pm 0.12$, and $51.7 \pm 0.82$ [10].

16. Incubations time for alkaline fragmentation will vary depending on three parameters: (1) sample integrity, (2) sample concentration, and (3) desired fragment size. Therefore, it must be optimized for each sample.
17. MCH is a small molecule commonly used in DNA monolayers to promote the orientation of the DNA probes, control the probe density and enhance the resistance to nonspecific adsorptions of nucleic acids or other molecules present in the sample to the sensor surface.
18. Saline solutions containing an adequate percentage of FA reduce the presence of secondary structures in DNA/RNA sequences and increase specificity of the hybridization by lowering the melting temperature of oligonucleotides. **WARNING** : Formamide is a known carcinogen. Carry out all steps involving pure formamide manipulation in a fume hood.
19. The regeneration procedure depends on the hybridized sequence. The ideal regeneration buffer should effectively disrupt the DNA–DNA or DNA–RNA interaction preserving the receptor activity. In practice, all regeneration buffers cause some damage on the biolayer immobilized onto the sensor surface, limiting the number of cycles that the same receptor surface can be reused. Usually, FA concentrations between 35% and 50% in aqueous solution are employed for efficient bioreceptor regeneration [5].
20. Mixed SAMs containing PEG-$CO_2H$ and PEG-$NH_2$SAM form a zwitterionic surface, providing monolayers with high resistance to fouling effects from complex biological fluids.
21. To further increase the sensitivity of the biosensor, a second step can be added, involving a signal enhancement via an anti-DNA–RNA antibody interaction with the hybridized miRNA [21].
22. For the data analysis we have employed two analytical software: Origin 8.0 software (OriginLab, Northampton, MA) and GraphPad Prism (GraphPad Software, San Diego, CA).
23. Clinical validation of nucleic acid analysis can be performed by comparing the BiMW biosensor results with conventional quantitative technologies such as RT-qPCR.

## Acknowledgments

ICN2 is supported by the "Severo Ochoa Centers of Excellence" Program from the Spanish Ministry of Science (MINECO) (Grant No. SEV-2017-0706).
Dr. Cesar S. Huertas is a recipient of an RMIT Vice Chancellor's Postdoctoral Fellowship.

A substantial part of the content of this chapter has been adapted from a previous version of this chapter [24] the doctoral thesis Nanophotonics biosensors for deciphering cell regulation pathways [21].

## References


1. Mens MMJ, Ghanbari M (2018) Cell cycle regulation of stem cells by MicroRNAs. Stem Cell Rev Rep 14:309–322
2. Fatica A, Bozzoni I (2014) Long non-coding RNAs: new players in cell differentiation and development. Nat Rev Genet 15:7–21
3. Mori MA (2018) Editorial: non-coding RNAs: entwining metabolism and aging. Front Endocrinol (Lausanne) 9:111
4. Girotti MR, Gremel G, Lee R et al (2016) Application of sequencing, liquid biopsies, and patient-derived xenografts for personalized medicine in melanoma. Cancer Discov 6:286–299
5. Huertas CS, Calvo-Lozano O, Mitchell A et al (2019) Advanced evanescent-wave optical biosensors for the detection of nucleic acids: an analytic perspective. Front Chem 7:724
6. Hunsperger RG (2009) Integrated optics: theory and technology, 6th edn. Springer, New York
7. Haruna M, Nishihara H (1989) Optical integrated circuits. 56:469–472
8. Zinoviev KE, González-Guerrero AB, Domínguez C et al (2011) Integrated bimodal waveguide interferometric biosensor for label-free analysis. J Light Technol 29:1926–1930
9. Dante S, Duval D, Sepúlveda B et al (2012) All-optical phase modulation for integrated interferometric biosensors. Opt Express 20:7195
10. Huertas CS, Domínguez-Zotes S, Lechuga LM (2017) Analysis of alternative splicing events for cancer diagnosis using a multiplexing nanophotonic biosensor. Sci Rep 7:41368
11. Huertas CS, Fariña D, Lechuga LM (2016) Direct and label-free quantification of microRNA-181a at Attomolar level in complex media using a Nanophotonic biosensor. ACS Sensors 1:748–756
12. Huertas CS, Aviñó A, Kurachi C et al (2018) Label-free DNA-methylation detection by direct ds-DNA fragment screening using polypurine hairpins. Biosens Bioelectron 120:47–54
13. Aviñó A, Jorge AF, Huertas CS et al (2019) Aptamer-peptide conjugates as a new strategy to modulate human α-thrombin binding affinity. Biochim Biophys Acta Gen Subj 1863:1619–1630
14. Gandhiraman RP, Gubala V, Nam LCH et al (2010) Deposition of chemically reactive and repellent sites on biosensor chips for reduced non-specific binding. Colloids Surfaces B Biointerfaces 79(1):270–275
15. Gokmen MT, Brassinne J, Prasath RA et al (2011) Revealing the nature of thio-click reactions on the solid phase. Chem Commun (Camb) 47:4652–4654
16. Huertas CS, Carrascosa LG, Bonnal S et al (2016) Quantitative evaluation of alternatively spliced mRNA isoforms by label-free real-time plasmonic sensing. Biosens Bioelectron 78:118–125
17. Huertas CS, Bonnal S, Soler M et al (2019) Site-specific mRNA cleavage for selective and quantitative profiling of alternative splicing with label-free optical biosensors. Anal Chem 91:15138–15146
18. Ragan C, Zuker M, Ragan MA (2011) Quantitative prediction of miRNA-mRNA interaction based on equilibrium concentrations. PLoS Comput Biol 7(2):e1001090
19. O'Brien J, Hayder H, Zayed Y et al (2018) Overview of microRNA biogenesis, mechanisms of actions, and circulation. Front Endocrinol (Lausanne) 9:402
20. Qu A, Sun M, Xu L et al (2019) Quantitative zeptomolar imaging of miRNA cancer markers with nanoparticle assemblies. Proc Natl Acad Sci U S A 116(9):3391
21. Huertas CS, Villaverde A, Lechuga LM (2016), Nanophotonic biosensors for deciphering cell regulation pathways. https://ddd.uab.cat/pub/tesis/2016/hdl_10803_368562/csh1de1.pdf
22. Szydzik C, Niego B, Dalzell G et al (2016) Fabrication of complex PDMS microfluidic structures and embedded functional substrates by one-step injection moulding. RSC Adv 6:87988–87994
23. Knoerzer M, Szydzik C, Ren G et al (2019) Optical frequency comb based system for photonic refractive index sensor interrogation. Opt Express 27:21532

24. Herranz S, Gavela AF, Lechuga LM (2017) Label-free biosensors based on bimodal waveguide (BiMW) interferometers. Methods Mol Biol 1571:161–185

25. Chocarro-Ruiz B, Herranz S, Fernández Gavela A et al (2018) Interferometric nanoimmunosensor for label-free and real-time monitoring of Irgarol 1051 in seawater. Biosens Bioelectron 117:47–52

# Chapter 7

# Azimuthal Beam Scanning Microscope Design and Implementation for Axial Localization with Scanning Angle Interference Microscopy

**Marshall Colville, Sangwoo Park, Avtar Singh, Matthew Paszek, and Warren R. Zipfel**

## Abstract

Azimuthal beam scanning, also referred to as circle scanning, is an effective way of eliminating coherence artifacts with laser illumination in widefield microscopy. With a static excitation spot, dirt on the optics and internal reflections can produce an uneven excitation field due to interference fringes. These artifacts become more pronounced in TIRF microscopy, where the excitation is confined to an evanescent field that extends a few hundred nanometers above the coverslip. Unwanted intensity patterns that arise from these imperfections vary with path of the excitation beam through the microscope optical train, so by rapidly rotating the beam through its azimuth the uneven illumination is eliminated by averaging over the camera exposure time. In addition to being useful from TIRF microscopy, it is also critical for scanning angle interference microscopy (SAIM), an axial localization technique with nanometer-scale precision that requires similar instrumentation to TIRF microscopy. For robust SAIM localization, laser excitation with a homogeneous profile over a range of polar angles is required. We have applied the circle scanning principle to SAIM, constructing an optimized instrument configuration and open-source hardware, enabling high-precision localization and significantly higher temporal resolution than previous implementations. In this chapter, we detail the design and construction of the SAIM instrument, including the optical configuration, required peripheral devices, and system calibration.

**Key words** Azimuthal beam scanning TIRFM, Circle-scanned TIRFM, Interference microscopy, Scanning-angle interference microscopy, Live-cell imaging, Fluorescence microscopy, Localization microscopy

## 1 Introduction

Fluorescence microscopy is a critical tool for structural and functional studies of biological specimens. The characteristic excitation and emission spectra of different fluorescent probes can be easily separated by microscope optics, allowing for visualization of multiple, independent spectra components within a sample. The ability to perform multiplexed spatial investigations has yielded significant

Miguel R. Ossandon et al. (eds.), *Biomedical Engineering Technologies: Volume 1*, Methods in Molecular Biology, vol. 2393, https://doi.org/10.1007/978-1-0716-1803-5_7, 

insight into subcellular structural organization. However, widefield fluorescence microscopy lacks axial resolution—the entire sample volume within the field-of-view is excited in a conventional widefield microscope and an image pixel contains fluorescence signal from regions outside the focal plane. Several types of microscopy have been developed to reduce or eliminate out-of-focus fluorescence. Widefield microscopies such as total internal reflection fluorescence microscopy (TIRFM) use the nanoscale-limited extent of an evanescent field to excite fluorophores only in the region near the interface between two media of differing refractive indices. Confocal and multiphoton microscopies eliminate out-of-focus fluorescence by raster scanning a focused beam and collecting signal just from the focal volume of the objective lens either through an optically conjugate pinhole (confocal) or by the intrinsic localization of the excitation by a nonlinear optical process (multiphoton).

Scanning angle interference microscopy (SAIM), utilizes a patterned excitation field to impart axial information on the sample [1]. Placing a reflective surface behind the sample generates standing waves of excitation by interference of the incoming excitation light with the back-reflected wave. The spatial frequency of the interference fringes is well defined and can be controlled by altering the angle of incidence of the excitation light on the reflective surface (Fig. 1a). As the incidence angle is changed, the relative

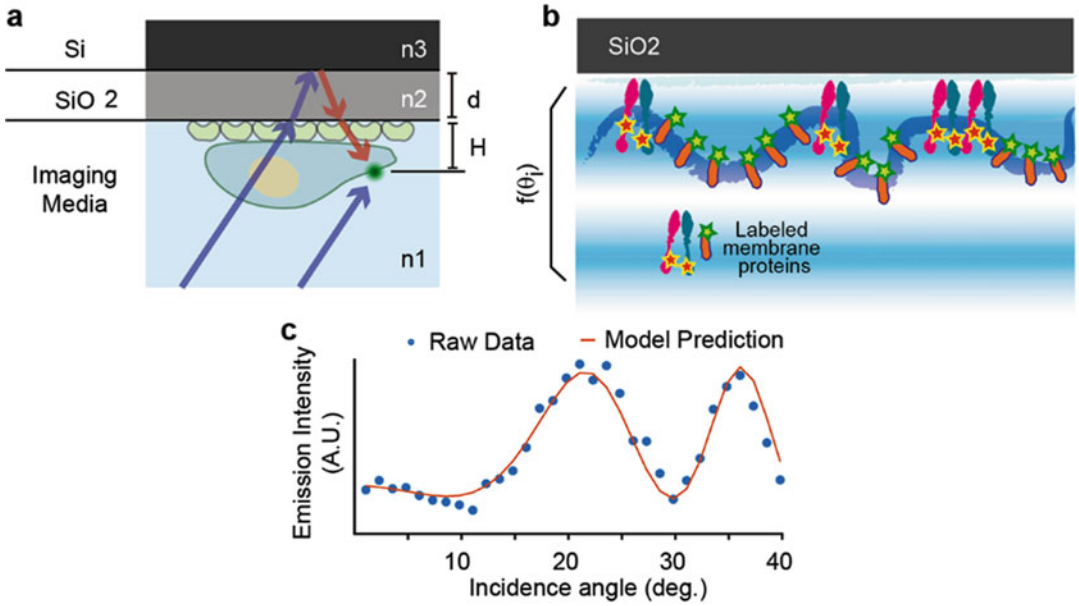


**Fig. 1** Surface-generated interference and axial localization in SAIM. (**a**) Samples are prepared on a silicon substrate with a defined layer of thermal oxide. (**b**) Standing wave excitation pattern that changes as a function of the angle of incidence (anti-nodes are spaced on the order of $\lambda/2$; illustration not scale). (**c**) Example raw data from a single pixel in a SAIM experiment with Fibronectin-Cy3 (blue dots) and fitted intensity profile with the optical model (red line). For imaging Fibronectin-Cy3 on silicon substrate with 1.917 μm of silicon oxide, raw data was obtained from 1.25° to 40° in 1.25° increments

intensity of fluorescently labeled structures within the sample varies as the standing wave excitation pattern changes. These periodic fluctuations are described by a mathematical model and depend on the fluorophore to reflective surface distance and the thickness of the $SiO_2$ layer (Fig. 1b) [2]. In a SAIM experiment, images are collected over a series of excitation incidence angles. Intensity data from individual pixels over the image series is then computationally fit to the model to determine the height of the sample. From this data, topographical maps of the features of interest are reconstructed.

A key requirement for artifact-free, high axial precision SAIM is an even excitation profile over the full range of incidence angles. Lasers are commonly used in modern fluorescence microscopes to provide a high-intensity source of collimated excitation. Although the SAIM method could be configured using a conventional fluorescence excitation source (e.g. arc lamp) and a series of annular masks, the short coherence length of the light source and relatively slow switching time of the masks are make this mode impractical [3]. The use of laser illumination provides a longer coherence length and produces a high quality standing wave interference pattern. However, the higher coherence also gives rise to unwanted interference effects such as speckles, fringes, and rings caused by imperfections and internal reflections in the optical train [4]. Total Internal Reflection Fluorescence (TIRF) microscopes also suffer from these artifacts which reduce the uniformity of the illumination field. A variety of techniques have been developed to eliminate laser-induced excitation artifacts [5–7]. One commonly applied approach in localization-based super-resolution TIRF imaging is to use a circularly scanned beam. The laser is focused on the peripheral edge of the objective back aperture and rotated continuously while maintaining a constant angle with respect to the optical axis [8, 9]. In a circle-scanning microscope the excitation light is focused on the rear focal plane of the objective by a scan lens so that the beam exiting the front pupil is collimated (Fig. 2a, left). The beam direction is controlled with a pair of close-coupled galvanometer-mounted scanning mirrors, one each for the $X$- and $Y$-axis (Fig. 2a). The scanning mirrors are positioned in the optical train to form an image of the apparent center of rotation (typically the midpoint between the mirrors) on the sample, preventing translation of the beam and providing a constant excitation profile throughout the scanning mirror's range of motion. In the sample plane, the beam can be described by its angular deflection in each axis, $\theta_x$ *and* $\theta_y$, which are proportional to the scanning mirror positions. The deflections can be easily transformed to a spherical coordinate system to obtain a polar angle, $\theta$, and azimuthal angle, $\psi$, of deflection. The polar angle corresponds to the excitation angle on incidence. When $\theta$ is kept constant and $\psi$ is continuously varied, the beam forms a cone above the objective (Fig. 2b).

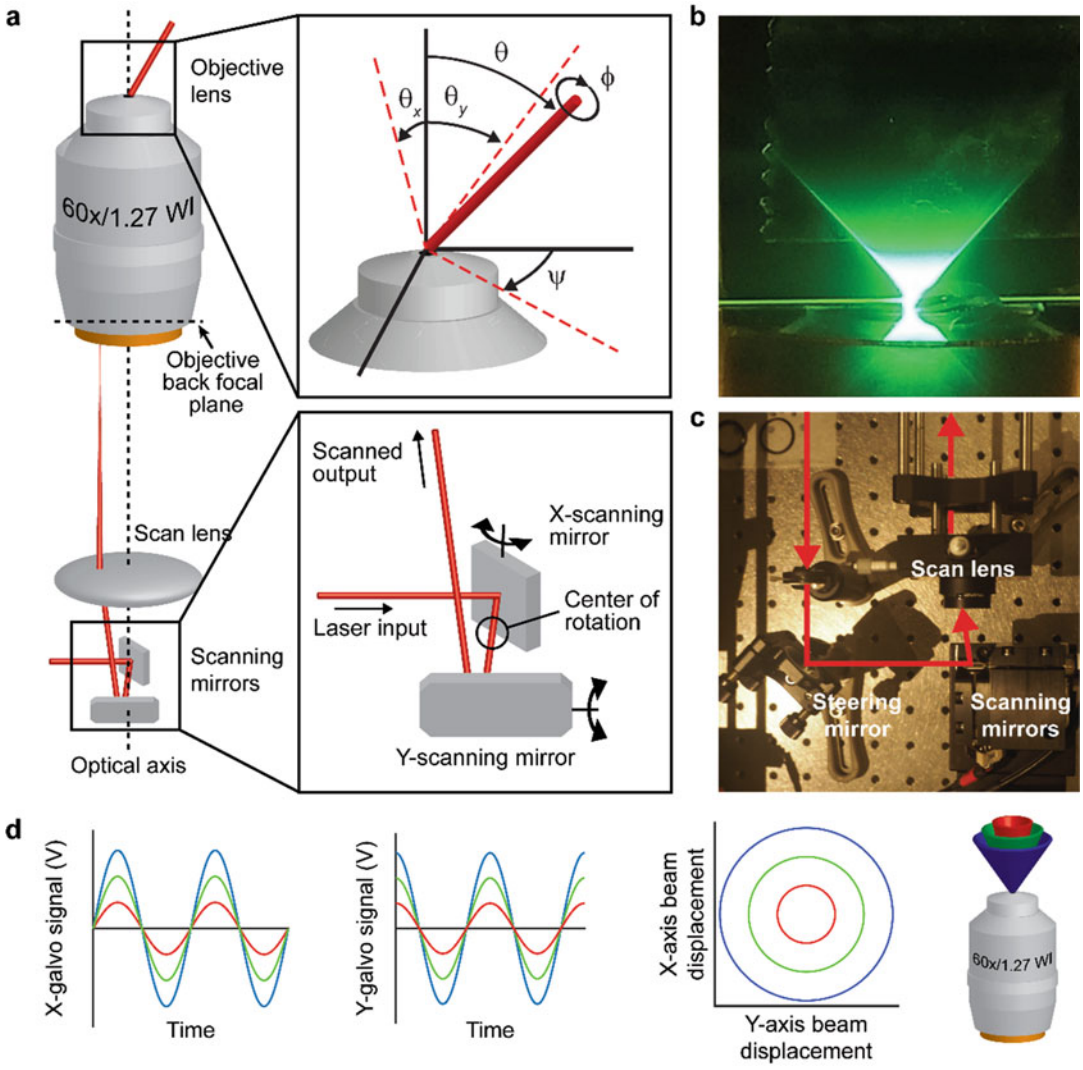


**Fig. 2** Principles of circle-scanning excitation. (**a**) Top: The excitation beam in the sample plane is described by three coordinates, the angles $\theta_x$ and $\theta_y$, and polarization, $\varphi$. $\theta_x$ and $\theta_y$ coordinates can be mapped to a polar angle, $\theta$, and azimuthal angle $\psi$. Bottom: A pair of galvanometer-mounted scanning mirrors are used to set the polar and azimuthal angles of the scanned excitation beam. (**b**) A circle-scanned beam projected onto a sheet of fluorescent plastic. (**c**) Image of the optical configuration of the scanning mirror and scan lens system. (**d**) Left: Per-axis command signals used to generate a series of polar scan angles with constant azimuthal velocity. Right: Beam position in the objective back aperture for a series of polar scan angles and 3D schematic of the excitation outputs

Implementation of a circle-scanning system is straightforward, requiring only a few optical components (Fig. 2c). In order to maintain a constant velocity in $\psi$, the scanning mirrors are driven with sine waves (Fig. 2d). The frequency of the waveforms is matched with one axis offset by 90° in time, creating a circular scan pattern on the objective back focal plane.

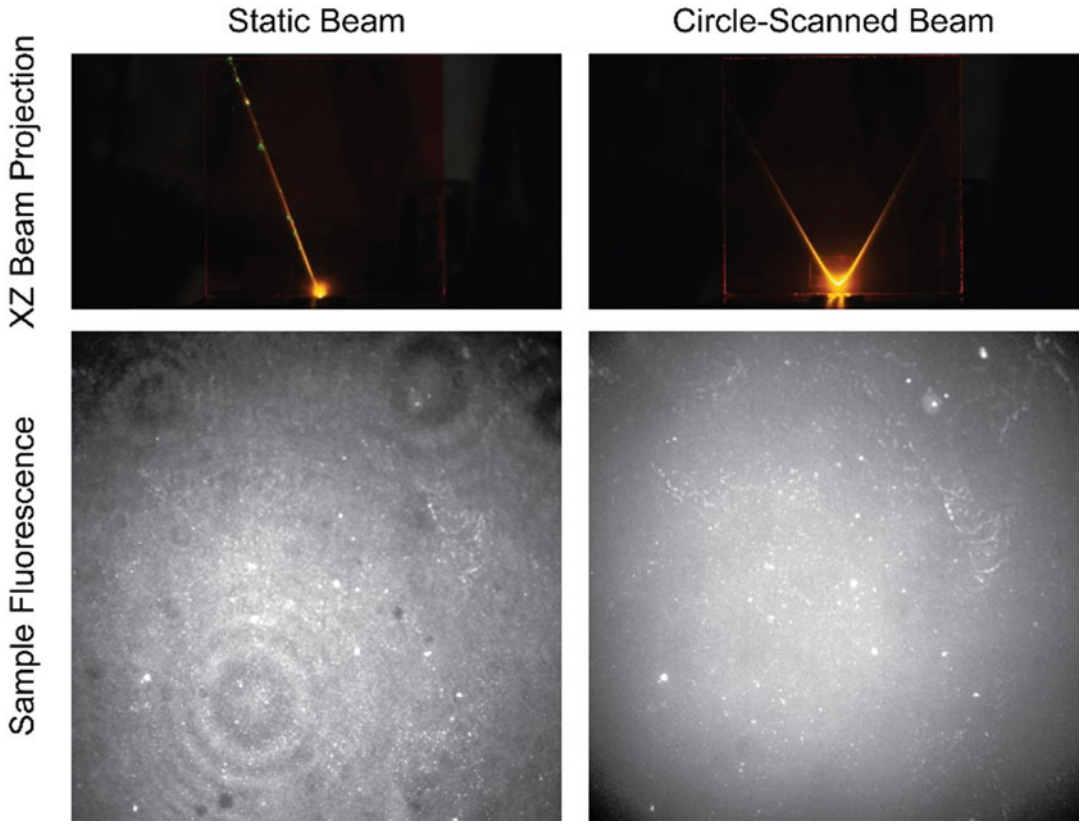


**Fig. 3** Comparison of static and circle-scanned image quality in TIRFM and SAIM. Top: Projection of the excitation laser from the objective lens onto a vertical screen. Bottom: Images of a fluorescent monolayer on a silicon wafer chip

Use of a scanning mode in SAIM significantly improves the quality of the excitation field, and in turn the reconstruction accuracy [10]. Figure 3 illustrates these effects on a fluorescent test sample. The sample was prepared by binding a homogeneous dye layer to a silicon waver chip, typically used in SAIM. On the left a static beam, where the laser deflection was held at constant $\theta$ and $\psi$, was used to excite the sample. Diffraction rings and dark spots caused by imperfections in the excitation optics are clearly visible. When the beam is scanned in $\psi$ at a constant $\theta$, as in the image on the right, the rings disappear and the illumination is even over the field of view.

In biological specimens the interference artifacts are less apparent, but negatively affect the quality of SAIM reconstructions. Figure 4 illustrates the benefits of circle-scanning SAIM. Human epithelial cells expressing a fluorescent derivative of the bulky, membrane-anchored mucin Muc1 were fixed and imaged with both static and circle-scanning laser excitation. In the top row, a single frame from a SAIM dataset is shown. The image on the left

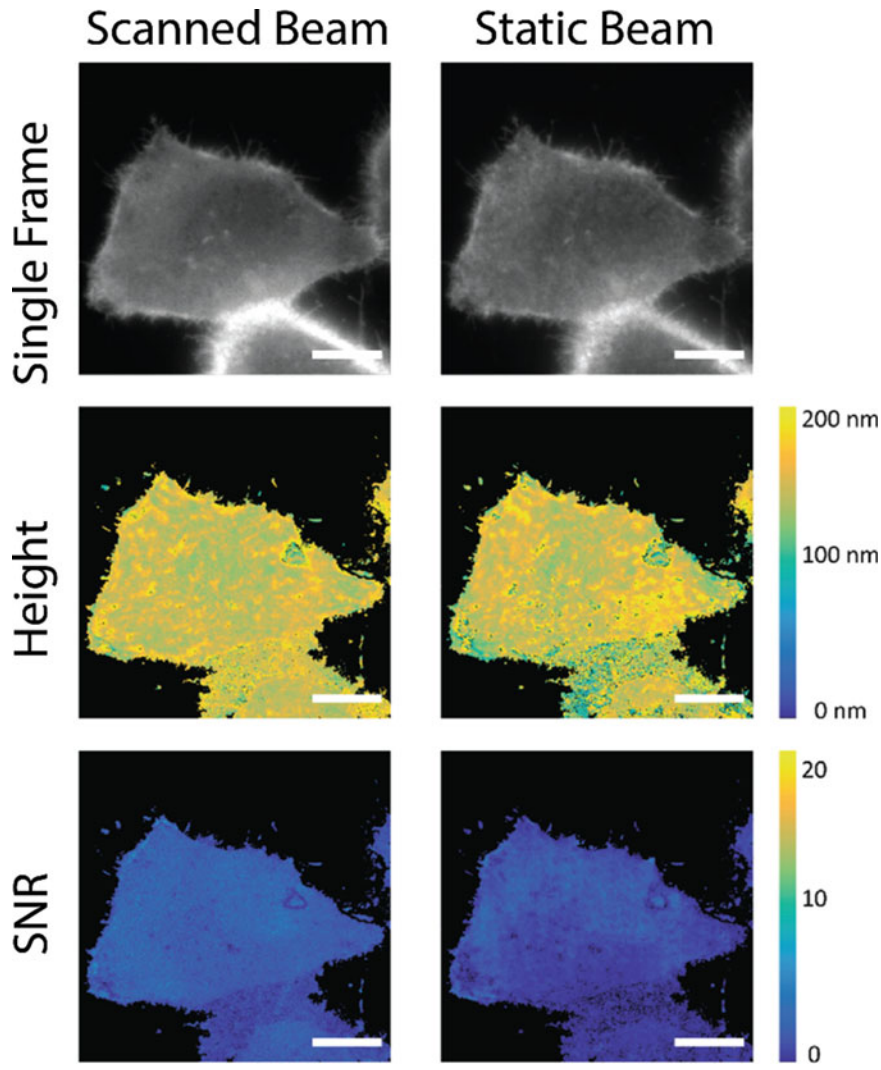


**Fig. 4** Circle-scanning reduces reconstruction artifacts in cellular imaging with SAIM. Top: A single exposure at a polar incidence angle of 28.75° illustrating the speckled appearance of the fluorescent glycoprotein Muc1 on the ventral membrane of an epithelial cell without circle-scanning (right) versus the more even fluorescence observed with circle-scanning (left). Middle: Height reconstructions from the cell shown above. Bottom: colormaps of the signal-to-noise ratio (SNR) with (left) and without (right) circle-scanning excitation

was acquired with circle scanning, and the image on the right without. Coherence artifacts manifest as a speckled appearance in the cellular membrane that is absent in the circle-scanned image. The reconstructed height maps are shown in the center row. The benefits of circle scanning in SAIM are most clearly depicted by the increased signal-to-noise ratio, depicted in the bottom row of images.

With circle-scanning we have been able to reliably reconstruct height maps of features previously difficult to resolve such as the

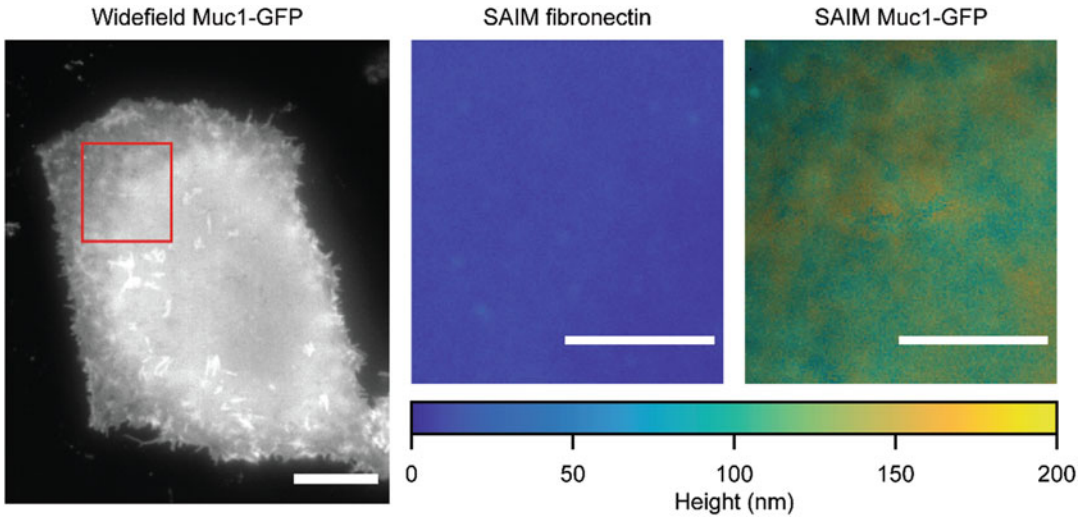


**Fig. 5** Mapping the plasma membrane topography of adherent cells with SAIM. Left: Widefield view of a human epithelial cell ectopically expressing the fluorescent glycoprotein Muc1-GFP. Scale bar: 10 μm. Center: Height reconstruction of the substrate bound matrix protein fibronectin. Right: Height reconstruction of GFP in the same region. Center and right images correspond to the boxed region in the widefield image. Scale bars: 5 μm

membrane-bound glycoprotein Muc1 (Fig. 5) [11]. We have recently demonstrated the benefits of both circle-scanning and hardware-based synchronization of peripheral devices in SAIM [10]. When working with live biological samples it is important to obtain the entire set of images in as short a time as possible. Accurate reconstruction of the sample topography assumes that features do not move between the acquisition of the first and last images. Furthermore, the high-intensity excitation light can be toxic to live samples and cause unwanted photobleaching. In this chapter we detail the preparation of live-cell SAIM samples, the construction of a high-speed, circle-scanning microscope optimized for SAIM, and a basic procedure for performing SAIM experiments.

## 2 Materials

### *2.1 Silicon Substrates*

1. 4″ silicon wafers with 19,000 Å thermal oxide (Addison Engineering Inc., San Jose, CA).
2. Blue dicing tape (Blue Tape—18074; Semiconductor Equipment Crop, Moorpark, CA).
3. Silicon wafer dicing saw (DAD3240; DISCO, Tokyo, Japan).
4. Film thickness measurement system (F50-EXR; Filmetrics, San Diego, CA).

5. Piranha solution: 25% (v/v) hydrogen peroxide solution (30% w/w) in concentrated sulfuric acid (*see* **Note 1**).
6. Wafer cleaning solution: 50% (v/v) concentrated hydrochloric acid in methanol.
7. HPLC-grade acetone.
8. Sodium hydroxide solution: 1 M in deionized water.
9. Plasma cleaner (PDC-32G, Harrick Plasma, Ithaca, NY).
10. MPTS solution: 4% (v/v) (3-mercaptopropyl)trimethoxysilane in absolute ethanol.
11. GMBS solution: 4 mM 4-maleimidobutyric acid *N*-hydroxysuccinimide ester in absolute ethanol.
12. Fibronectin solution: 50 mg/mL human plasma fibronectin dissolved in PBS (*see* **Note 2**).

### 2.2 Cell Culture

1. MCF 10A human epithelial cells (ATCC# CRL-10317; American Type Culture Collection, Manassas, VA).
2. Cell culture medium: 5% (v/v) donor horse serum, 1% (v/v) penicillin-streptomycin solution, 10 μg/mL insulin, 500 ng/mL hydrocortisone, 100 ng/mL cholera toxin, and 10 ng/mL epidermal growth factor dissolved in 1:1 DMEM:F12.
3. Imaging media: 119 mM NaCl, 5 mM KCL, 25 mM HEPES buffer, 2 mM $CaCl_2$, 2 mM $MgCl_2$, 6 g/L glucose, 1 g/L bovine serum albumin dissolved in deionized water at pH 7.4.
4. Glass bottom imaging dishes (coverslip thickness: No. 1.5, well diameter: 14 mm).

### 2.3 Circle-Scanning Optical Components (See Note 3)

1. Vibration isolation optical table.
2. Single-band laser cleanup filters (diameter: 1″, mounted; ZET405/20×, ZET488/10×, ZET561/10×, ZET635/20×; Chroma Tech. Corp., Bellows Falls, VT).
3. Long-pass laser dichroic mirrors (diameter: 1″, mounted; ZT405rdc, ZT488rdc, and ZT561rdc; Chroma).
4. Broadband beam steering mirrors (diameter: 1″, quantity: 7; BB1-E02; Thorlabs Inc., Newton, NJ).
5. Kinematic mirror mounts (quantity: 10; KS1; Thorlabs).
6. Iris diaphragms (quantity: 2; ID15; Thorlabs).
7. Air-spaced achromatic doublet scan lens (*f*: 30 mm, diameter: 1″; ACA254–030-A, Thorlabs).
8. Mounting tube for scan lens (length: 0.45″; SM1L03; Thorlabs).
9. M = 1 zero-order vortex half-wave retarder (WPV10L-532; Thorlabs).

10. XY translation mount (ST1XY-S; Thorlabs).
11. Broadband elliptical mirrors (diameter: 2″, quantity: 2; BBE2-E02; Thorlabs).
12. Right-angle kinematic mirror mounts for 2″ elliptical mirrors (KCB2EC; Thorlabs).
13. Achromatic doublet relay lenses (*f*: 300 mm, diameter: 2″, quantity: 2; AC508–300-A; Thorlabs).
14. Quick release cage system lens mounts (LCP90F; Thorlabs).
15. Optical cage system components for periscope construction (Thorlabs).
16. Optical posts and bases for mirrors (Thorlabs).
17. Optical power meter (PM100D and S122C; Thorlabs).
18. Neutral density filters for laser attenuation during alignment.
19. Laser collimation test device (shearing interferometer SI035; Thorlabs).
20. Beam alignment aids (1″ optic alignment plate LMR1AP, iris diaphragm SM2D25D in removable 60 mm cage plate QRC2A, and 60 mm cage alignment plate LCPA1; Thorlabs).

### 2.4 Electronics and Peripheral Devices

1. 405 nm laser diode module (IQ1C100(LD2070); Power Tech. Inc., Little Rock, AR).
2. 488 nm diode-pumped solid-state laser module (Sapphire 488 LP; Coherent Inc., Santa Clara, CA).
3. 560 nm fiber laser module (VFL-560; MPB Communications Inc., Montreal, Quebec).
4. 642 nm fiber laser module (VFL-642; MPB).
5. Mechanical beam shutter (SHB1T, Thorlabs).
6. Visible spectrum acousto-optic tunable filter (AOTF) and multichannel RF driver ($\lambda = 400$–650 nm; AOTFnC-400.650-TN and MPDS8CD6; AA Opto-Electronic, Orsay, France).
7. Mounted XY galvanometer scanning mirror set with driver (6215H galvanometers and 673 series dual servo driver; Cambridge Technology, Bedford, MA).
8. Scanning mirror driver heatsink (3.5 × 4 in., HeatsinkUSA, Greenville, MI).
9. Thermal paste (Corning© 340, Dow, Midland, MI or GC Electronics Type Z9 Silicone heat sink compound, Rockford, IL).
10. DC power supplies (output: 28 Vdc, 5.4 A, quantity: 2).
11. Power supply protection diodes (Axial can, $I_o$: 10 A min).
12. Enclosure for scanning mirror driver and power supplies.

13. Electrical hook-up wire, connectors, power switch, indicator light, and ventilation fan.
14. Coaxial SMA cables for controller/servo driver connection.
15. Coaxial BNC cable for controller/shutter connection.
16. DB25 male to female cable for controller/AOTF driver connection.
17. USB 2.0 type A-male to B-male cable for controller/computer connection.
18. Instrument controller (details and complete list of materials available from https://github.com/mjc449/SAIMscannerV3).
19. PICkit 4 in-circuit debugger (PG164140; Microchip Technology Inc., Chandler, AZ).
20. USB webcam for scanning system calibration.

### 2.5 Imaging System

1. Inverted fluorescence microscope (e.g. Eclipse Ti2; Nikon Instruments Inc., Melville, NY).
2. Objective lens (CFI Plan Apo IR 60× WI, N.A. = 1.27; Nikon).
3. Quad bandpass fluorescence filter set with single-band emission filters (TRF89902-EM, mounted; Chroma).
4. Motorized emission filter wheel (LB10-B and LB10-NWE; Sutter Instrument, Novato, CA).
5. Scientific camera (Zyla 4.2 sCMOS; Andor, Concord, MA).
6. Computer workstation for data acquisition and instrument control (*see* **Note 4**).

### 2.6 Software

1. Instrument controller graphical interface (SSv3 Control Panel; available from https://github.com/mjc449/SAIMscannerV3).
2. MPLAB Integrated Programming Environment (available from https://microchip.com/mplab/mplab-integrated-programming-environment; Microchip).
3. Micro-Manager [12] (available from https://micro-manager.org).
4. FIJI [13] (available from https://fiji.sc).
5. SAIM analysis plugin for ImageJ [14] (available from https://imagej.net/Saim).

## 3 Methods

### 3.1 SAIM Sample Preparation

The surface-generated interference pattern required for axial localization is created by preparing samples on a highly reflective substrate. Polished silicon wafers are an inexpensive, easy-to-work-with material for preparing SAIM samples. Wafers are commercially available with a range of thermal oxide thickness, and previous work has shown oxide layers of ~2 μm to be an ideal thickness for SAIM imaging [1]. The silicon dioxide surface of the wafers is functionalized with an appropriate matrix protein, such as fibronectin or collagen, to enhance cellular attachment.

The following protocol is generally applicable to all adherent cell lines. The choice of matrix protein will depend on the cell line under study. For poorly adherent cell lines, the silanization and protein binding steps can be replaced with a 30-min incubation in poly-L-lysine solution; however, morphology and motility may be altered.

1. Affix dicing tape Blue Tape—18074; Semiconductor Equipment Crop) to the reflective surface of the wafer.
2. Using a wafer dicing saw, cut the wafer into 5 mm × 5 mm chips (*see* **Note 5**).
3. Remove the chips from the dicing tape with tweezers. Put the chips on a thin film measurement system (F50-EXR; Filmetrics). Edit film recipes to "SiO2 on Si" with 19,000 Å as a nominal value. Measure the oxide layer thickness of the chips (*see* **Note 6**).
4. Thoroughly clean the chips by incubation for 30 min in hot piranha solution. If piranha solution is not available, clean the chips by successive 30-min incubations in wafer cleaning solution, acetone, and 1 M sodium hydroxide solution in an ultrasonic bath. Rinse the chips thoroughly with deionized water after each cleaning step. Store the chips submerged in deionized water until use.
5. Dry the chips thoroughly under a stream of pure nitrogen. Place the chips in a clean dry dish with the reflective side facing up and plasma clean for 60 s.
6. Remove from the plasma cleaner and add enough MPTS solution to completely cover the chips in the dish. Cover the dish and incubate for 30 min at room temperature.
7. Rinse the chips three times with absolute ethanol then add enough GMBS solution to completely cover the chips. Cover the dish and incubate for 30 min at room temperature.
8. Rinse the chips once with absolute ethanol then three times with PBS. Rinses should be performed in rapid succession to preserve GMBS reactivity. Immediately cover the surface of the

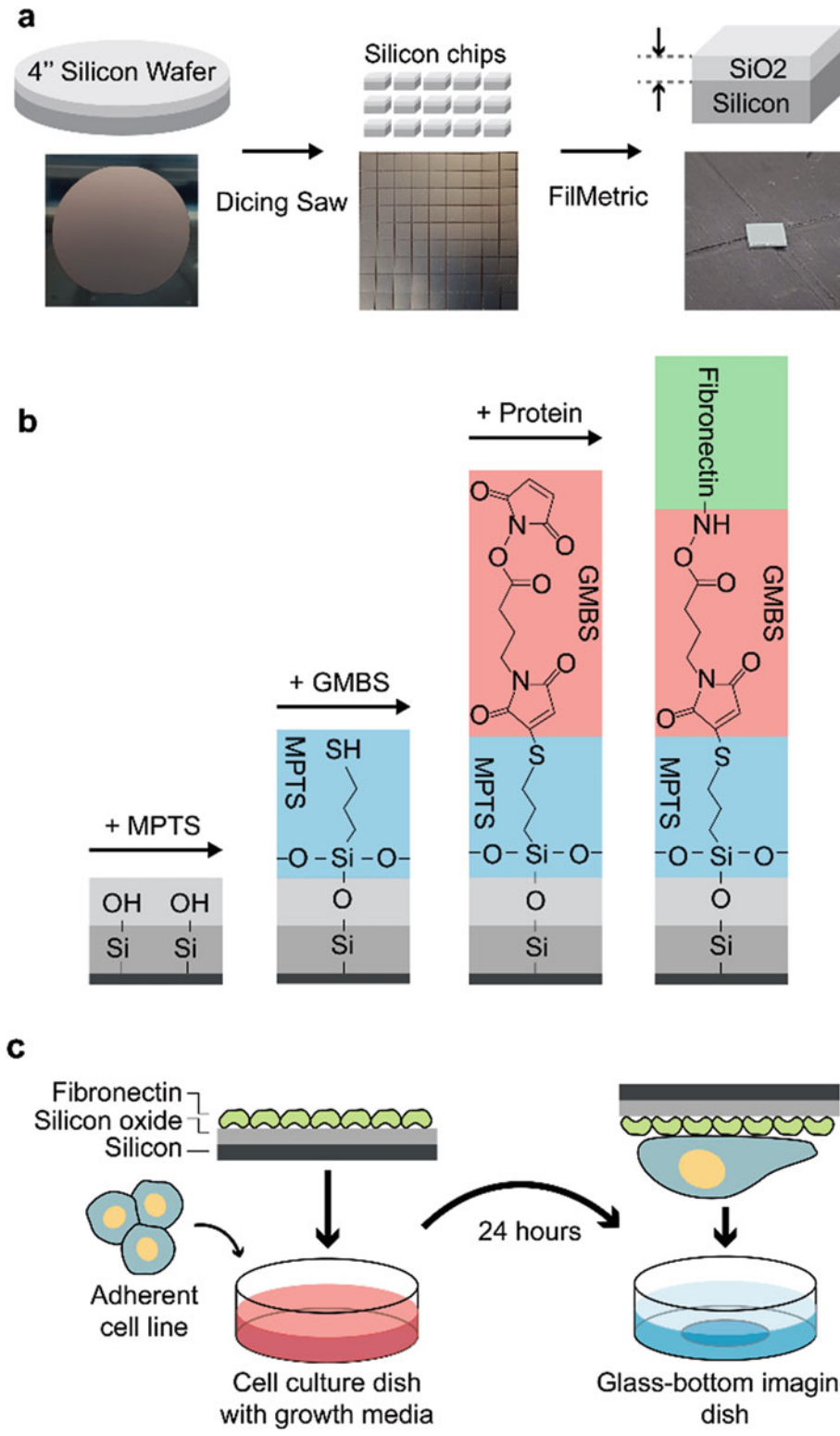


**Fig. 6** Sample preparation for SAIM imaging. (**a**) Silicon wafers with a layer of thermal oxide are diced into 5 mm chips using a dicing saw. The thickness of the silicon dioxide layer is measured for each chip. (**b**) Chips are chemically functionalized to promote cellular adhesion with the extracellular matrix protein fibronectin. (**c**) Functionalized chips are placed in a culture dish and adherent cells are culture on the reflective surface of the chips. After 24 h the chips are inverted into a glass-bottom imaging dish for SAIM data collection

chips with fibronectin solution. Incubate at room temperature for 2 h or 4 °C overnight.

9. Rinse the functionalized chips thoroughly with PBS. If the chips will not be used immediately, they should be stored in sterile PBS containing 0.05% (w/v) sodium azide.
10. Rinse the chips with sterile PBS to remove storage buffer and transfer, reflective side up, to a clean cell culture dish. Seed cells onto the chips at a density of 10,000 $cm^{-2}$. Cover with cell culture media and incubate at 37 °C and 5% $CO_2$ for 24 h (*see* **Note 7**).
11. Prepare glass bottom imaging dishes by adding 1.5 mL of imaging media and placing in the cell culture incubator for 1 h to equilibrate.
12. Using tweezers, remove a single chip from the cell culture dish, invert, and place in the imaging dish with the reflective side facing downward. Position the chip in the center of the glass-bottom well (*see* **Note 8**).

### *3.2 Microscope and Imaging System Setup (See Note 9)*

The location of the microscope body on the optical table will dictate the placement of the scanning optics, laser launch, and other peripheral devices. Therefore, it is important to leave sufficient space behind and around the microscope for the other components. As the largest and heaviest component of the system, the microscope body forms the base from which to build the scanning optics and laser launch (*see* **Note 10**).

1. Prepare the microscope body by removing the epi-fluorescence illuminator and optics if equipped. Bolt the microscope body securely to the table in its final position. Mount the objective lens and insert the quad-bandpass filter cube into the microscope body.
2. Load the emission filters into the filter wheel. Attach the filter wheel and camera to the microscope per the manufacturer's instructions.
3. Connect the camera, filter wheel, and instrument controller to the computer. In the Micro-Manager software add the camera and filter wheel to a new hardware profile (*see* **Note 11**).
4. Connect the camera's TTL auxiliary output to the instrument controller's trigger input. Configure the camera output to "fire all" in Micro-Manager.

### *3.3 Laser Launch Construction*

The laser launch combines the four monochromatic laser beams into a single polychromatic beam using dichroic mirrors (Fig. 7a). The polychromatic beam is directed through the AOTF, which is responsible for wavelength selection, intensity control, and high-speed shuttering on the order of 10 μs [10]. A mechanical shutter is

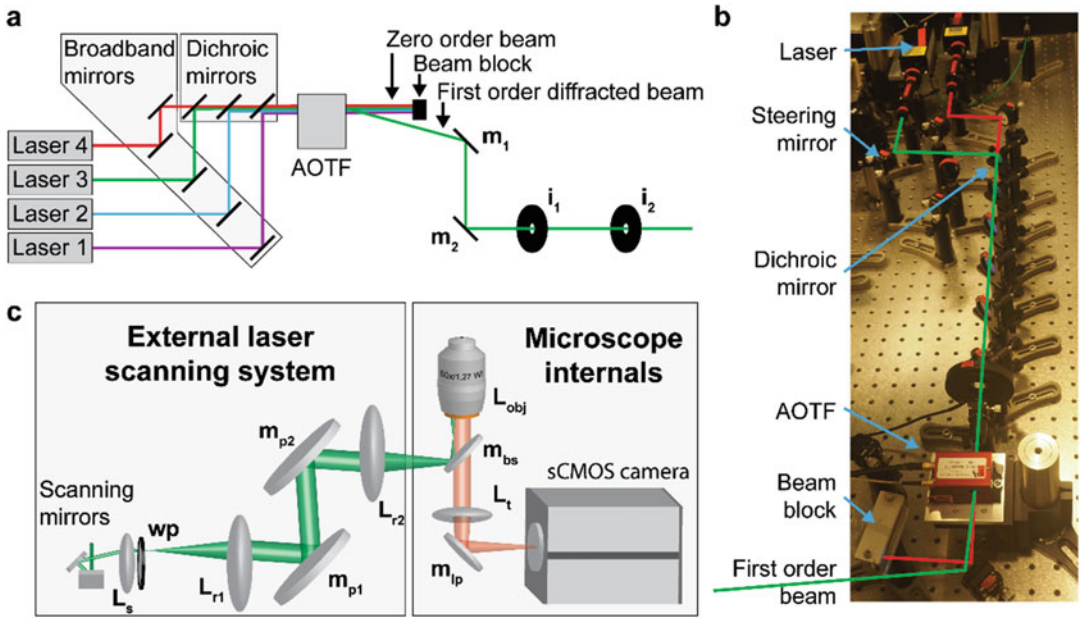


**Fig. 7** Circle-scanning system construction. (**a**) Four individual free-space lasers are combined to form a single, colinear beam in the laser launch. The AOTF selects the excitation wavelength by modulating the intensity of the first-order diffracted beam. The individual lasers are made colinear by alignment on irises $i_1$ and $i_2$. Steering mirrors $m_1$ and $m_2$ are used to align the excitation beam on the scanning system entrance pupil. (**b**) Image of the laser launch with individual components labeled. Note that both transmitted beams from the AOTF are reflected by mirror $m_1$ before the zero-order beam is intercepted by the beam block, unlike in (**a**). (**c**) Schematic diagram of the laser scanning and imaging systems with key components in their relative positions. $L_s$ scan lens, *wp* vortex retarder, $L_{r1}$, $L_{r2}$ relay lenses, $m_{p1}$, $m_{p2}$ elliptical periscope mirrors, $L_{obj}$ objective lens, $m_{bs}$ fluorescence beam splitting mirror, $L_t$ tube lens, $m_{lp}$ light path selection mirror

included as a low-speed safety interlock (close time of approximately 9 ms), and iris diaphragms are used to align the lasers, ensuring a colinear beam and proper alignment on the scanning optics entrance pupil. It is important that the alignment irises are placed between the AOTF and scanning mirrors to account for the small but present wavelength-dependent variation in the first-order diffracted beam direction.

1. Attach the laser modules to the optical table securely using optical posts. The 405 and 488 nm laser heads are cooled by forced air to ambient temperature through integral systems in the laser head and can be mounted with standard mechanical components. The 560 and 642 nm fiber laser modules can be located on a convenient equipment shelf, with their second harmonic generators (laser heads) are bolted to aluminum heat sinks with thermal conductive paste and mounted to the optical table via posts. The emission windows of all laser heads should lie in a single plane at the same height as the AOTF and scanning mirrors. The laser heads are mounted such that the

output beams are parallel to one another. Further details on laser alignment are provided in Subheading 3.5.

2. Mount the dichroic long-pass mirrors in kinematic mirror mounts and attach to the optical table with optical posts. Position the mirrors in a straight line and orient at 45° to the AOTF (Fig. 7a, b). The 642 nm laser does not require a dichroic mirror, a broadband mirror should be used in its place.
3. Mount the broadband mirrors in kinematic mirror mounts. Position the mirrors such that the beam path forms a 90° angle between the laser emission window, broadband mirror and dichroic mirror (Fig. 7a, b). Secure the mirrors to the table.
4. Position the mechanical shutter immediately after the final dichroic mirror and directly in the beam path.
5. Attach the AOTF to an optical post using an appropriate heat sink and mount in the beam path (*see* **Note 12**). Position the beam block to intercept the zero-order transmitted beam from the AOTF and secure both the AOTF and beam block to the optical table.
6. Mount the broadband beam steering mirrors $m_1$ and $m_2$ in Fig. 7a to the optical table. Mirror $m_1$ reflects the first-order diffracted beam from the AOTF onto $m_2$, which reflects the beam into the entrance pupil of the scanning optics.
7. Connect the AOTF to the multichannel RF driver with the supplied cables. Connect the RF driver to the instrument controller with a DB25 cable. Connect the mechanical shutter TTL input to the instrument controller output with a BNC cable and configure the shutter controller for external triggering.

### 3.4 Circle-Scanning Optics Construction

The circle scanning subsystem controls the beam deflection (polar and azimuthal angles) in the sample plane by relaying an image of the scanning mirrors to the sample plane of the microscope (Fig. 7c). It is critical that the image of the excitation beam center of rotation is relayed onto the sample. Misalignment of the optical elements can lead to distortion of the excitation profile in the sample plane, compromising data quality.

1. Assemble the laser scanning optics in the cage system according to Fig. 6c. The scan lens $L_s$ is glued into its mounting tube and attached to the fixed side of the XY translation mount. The vortex retarder is mounted in the translation mount and oriented to produce s-polarized excitation in the sample plane.
2. Starting with the second relay lens, $L_{r2}$, adjust the position of each lens in the cage system according to Fig. 8 (*see* **Note 13**).
3. Mount the scanning mirrors on an appropriate optical post. Position the scanning mirrors such that their exit pupil is

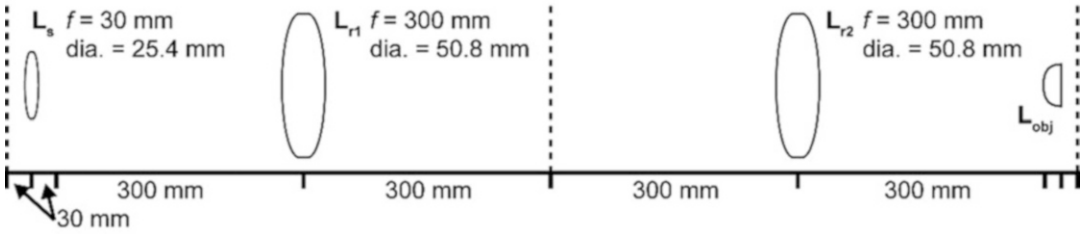


**Fig. 8** Arrangement of lenses within the laser scanning subsystem. Each lens pair forms a 4*f* system. $L_s$ scan lens, $L_{r1}$ *and* $L_{r2}$ relay lenses, $L_{obj}$ objective lens

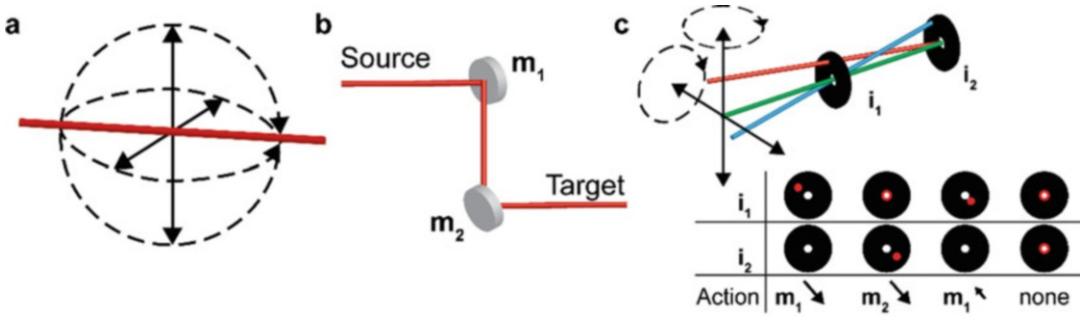


**Fig. 9** Definition of laser orientation and alignment within the optical system. (**a**) A beam is described by its position (solid lines) and angular direction (dashed arcs). (**b**) Beam alignment is set with two mirrors. (**c**) Top: Schematic diagram of two-point beam alignment using a pair of iris diaphragms, $i_1$ and $i_2$. Bottom: Beam position and corrective actions to align a laser to a pair of irises. The beam position on each of the irises is denoted by the red spot

aligned with the optical axis of the cage system. At this point the $\Upsilon$-axis scanning mirror should be centered in the scan lens with its rotational axis orthogonal to the optical axis of the cage system.

4. Ensure that the final beam steering mirror from the laser launch, $m_2$ in Fig. 6a, is centered in the scanning mirror entrance pupil.

### *3.5 Laser Alignment*

The laser beam within the optical system can be described by its offset and direction with respect to the optical axis of the system, giving four coordinates (Fig. 9a). Two mirrors are employed, giving 4 degrees of freedom in orienting the beam (Fig. 9b). Similarly, two reference points, formed by a pair of irises, are used to check beam alignment (Fig. 9c). Proper beam alignment with respect to the optical axis is critical in maintaining high-quality circle-scanned excitation. Small errors in beam position within the optical train can degrade the surface-generated interference pattern in SAIM experiments. Alignment of the lasers can be affected by multiple sources including changes in ambient temperature and mechanical

perturbations. The beam alignment of each laser within the laser launch is verified against the permanently mounted irises, shown in Fig. 7a, at the beginning of each imaging session. Individual lasers are adjusted with the first broadband mirror and dichroic mirror that the laser encounters without altering mirrors in the polychromatic beam path ($m_1$ and $m_2$ in Fig. 7a). The same procedure can be employed to align the beam in the scanning mirror entrance pupil and entrance to the microscope. For the scanning mirrors an additional set of post-mounted irises are temporarily inserted immediately after the polychromatic beam steering mirrors $m_1$ and $m_2$ in Fig. 7a. To align the beam on microscope excitation port the removeable cage system iris and alignment plate should be placed between the second periscope mirror and the microscope excitation port. Alignment begins with the laser launch, followed by the scanning mirrors' entrance pupil and finally the microscope excitation port. The following procedure depicted schematically in Fig. 9c applies in all cases.

1. Close both iris diaphragms until the opening is approximately the diameter of the beam.
2. Adjust the position of the beam on iris 1 using mirror 2,until the beam is centered in the iris.
3. Using mirror 1 while observing the beam position on iris 2, move the beam in a straight line directly away from the center of the iris.
4. Re-center the beam in iris 1 with mirror 2 and check its position on iris 2.
5. Repeat **steps 3** and **4** until the beam is centered in both irises.
6. Scanning Mirror Electronics.

The scanning mirror driver requires a high-quality bipolar power supply for proper operation. A circuit diagram for the series connection of two 28 V DC supplies is given in Fig. 10a. The diodes protect the power supplies during startup and shutdown

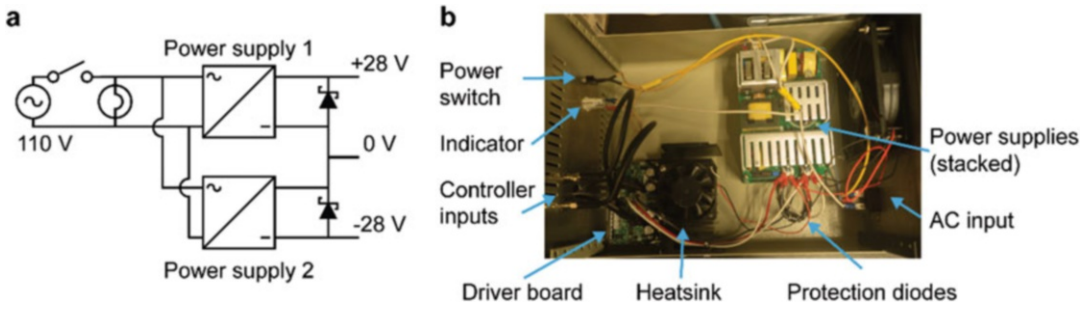


**Fig. 10** Scanning mirror power supplies and driver layout. (**a**) Power supply circuit diagram. (**b**) Image of the power supply and driver layout within the enclosure

from harmful current inversions but are reverse-biased in normal operation. Diodes with a small forward voltage drop and fast switching are selected. The scanning mirrors' driver must be securely mounted to an external, extruded aluminum heatsink within the power supply enclosure as shown in Fig. 10b. This will allow for adequate passive heat dissipation during operation. When arranging the components within the enclosure ensure that the driver heatsink is between the driver board and power supplies (Fig. 10b). A thin layer of thermal conductive paste (GC Electronics Type Z9 Silicone heat sink compound) is applied to the driver mating surface before mounting. Once all components are mounted in the enclosure make the electrical connections according to the circuit diagram and the manufacturer's instructions. Ensure that all components have a low-resistance ground connection to the enclosure and AC input ground conductor.

### 3.6 Circle-Scanning Calibration

Before collecting data, the circle scanning system must be properly configured through the controller software. It is essential that the scanned beam is centered on and aligned to the optical axis. The waveform generators within the controller are fully programmable through the controller software for easy tuning of the scanned beam profile to correct ellipticity and alignment.

The scanned beam polar angle is proportional to the output waveform amplitude of the instrument controller, however, the relationship between output amplitude and scan angle must be determined empirically. The waveform output is described in digital to analog converter (DAC) units and the conversion factor (calibration constant) to scan angle is determined by linear regression. A user friendly, image-based calibration tool is included to simplify the calibration procedure (Fig. 11). The following alignment, tuning and calibration procedure should be performed at the beginning of each imaging session.

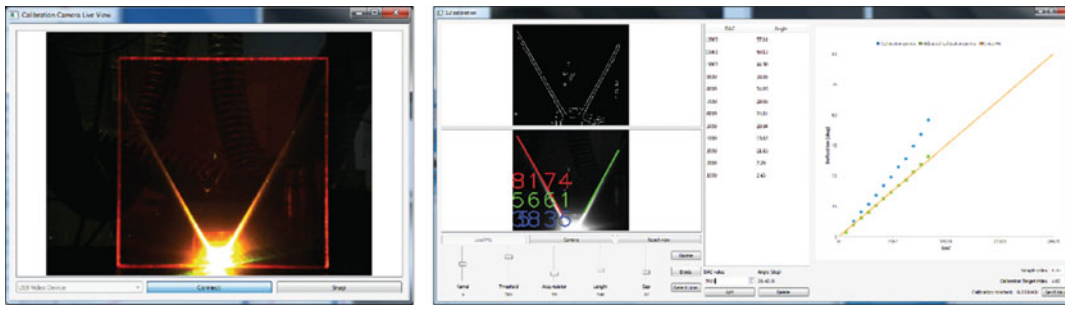

**Fig. 11** Circle-scanning system calibration. Left: An inexpensive webcam attached to the instrument computer is used to capture images of the scanned excitation beam on a fluorescent target. Right: The calibration image is run through an edge detection algorithm to find the edges of beam. A series of images at different scan angles is used to determine the calibration value

1. Prepare a dilute solution of carboxyfluorescein (405 and 488 nm lasers) or rhodamine B (560 nm laser) in water and add approximately 2 mL to a glass bottom imaging dish. The solution should be dilute enough to visualize the entire beam within the sample (~100 μM is usually sufficient, although the exact concentration does not matter). Mount the dish on the microscope stage.
2. Start the controller software and connect to the device. Enable the excitation laser by clicking "On" under "Laser Controls". Increase the power manually until the beam is clearly visible.
3. Under "Scanning Controls" click "Scan" and gradually increase the radius until a clearly visible cone is formed by the excitation laser in the dish. Check the box next to "Advanced" to enable the scan center, phase and Y-scale controls. Using these controls, center the excitation cone on the optical axis. The phase and Y-scale controls can be used to correct ellipticity in the scan profile.
4. Once the scanning system has been properly tuned in the software click the "Calibrate" button to open the calibration tool. Remove the alignment sample from the microscope and place the calibration target onto the stage (*see* **Note 14**). In the lower right of the calibration window enter the refractive indices of the calibration medium and sample medium (*see* **Note 15**). Connect a USB webcam to the computer.
5. In the calibration window click the "Camera" button. Select the USB webcam from the drop-down menu and click "Connect". A live feed from the camera is displayed (Fig. 11, left). Set the scan radius to 1000 DAC units in the main window. Position the webcam to obtain a clear view of the beam on the calibration target. Click "Snap" in the camera window to send a still image to the calibration window.
6. In the calibration window, click and drag on the greyscale image to zoom in on the portion of the image containing the scanned beam. Below the image adjust the kernel size, accumulator, minimum length and maximum gap values until a clear view of the beam outline appears in the upper image. Click "Detect Lines." The red and green lines overlaid on the lower window should align with the edges of the beam pattern. If the beam edges are not properly highlighted adjust the detection parameters and repeat the detection until they are. Enter the current DAC value in the field below the data table and click "Add" to add the calibration point to the list. The new point will be added to the graph on the right side of the window. The graph displays the raw data (blue dots), refractive index corrected data (green squares) and best fit line for the current list of points.

7. Repeat **steps 5** and **6** in increments of 1000 DAC units until the beam is no longer clearly visible on the calibration target. Once enough points have been collected click "Send Value" in the lower right of the calibration window to update the calibration value in the main software.

### 3.7 Performing Circle-Scanning SAIM Experiments

Circle scanning SAIM experiments are designed in the controller software as combination of excitation profiles and scan angle sequences. Excitation profiles are laser intensity settings, controlled by the AOTF, describing the relative power of each channel. The experiments are built in steps, with each step containing a laser profile and angle sequence (Fig. 12). For each step the AOTF channel settings are updated before the first exposure of the camera and the scan angle is set to the first value in the sequence (*see* **Note 16**). After each exposure the scan angle is set to the next sequence value while the AOTF channel settings remain unchanged. When exposure of the last angle in the sequence is finished the experiment proceeds at the next step in the list, updating the AOTF channels are setting the scan angle to the first value in the new sequence. Profiles and sequences can be reused indefinitely within an experiment, and the experiment can be set to continue from any step when the end is reached.

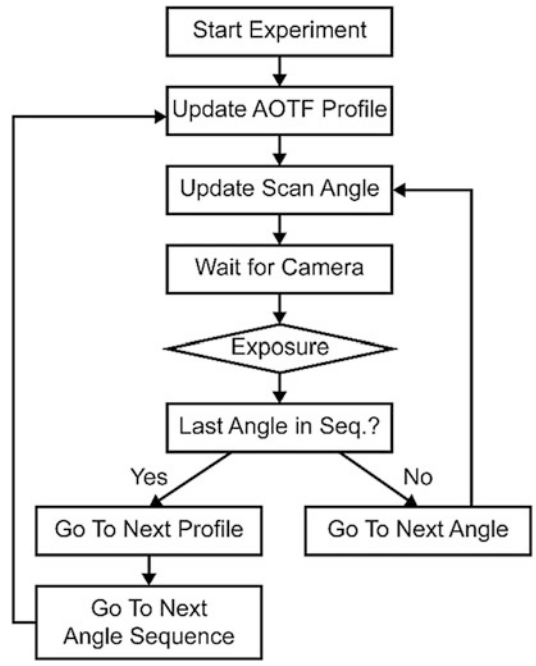


**Fig. 12** Control flow diagram of a generalized experimental sequence. Sequences of scan angles and excitation profiles are stored in the instrument controller memory. The sequences and profiles are connected in a linked list of experimental steps

1. In the controller software main window click "Fire On" to enable the AOTF shutter. Start the live view in Micro-Manager. Adjust the laser intensities in the controller software to the desired level. Click "Add" under "Laser Profiles" in the controller software to add the current AOTF setting as a new profile. To update a profile, select the profile, adjust the power and click "Update". The old levels will be overwritten with the current settings.
2. To set the scan angles click "New" under "Scan Angle Sequences" in the controller software. A dialog box will open. Set the first and last angles and total number of angles for the sequence (*see* **Note 17**). Click "OK" to close the window and save the sequence.
3. In the "Experiment Design" section of the controller software click "Add" and a dialog window will open. Select the step, sequence, and profile number then click "Add" to close the window and add the step to the experiment.
4. Steps can be reordered in the experiment list using the "Up" and "Down" buttons. The "Delete" button will remove the currently selected step. Selecting a step in the list and clicking the "Loop" button will cause the experiment to continue from the selected step when the end of the list is reached.
5. Once the experiment has been defined click "Start". At this point the controller is placed in autonomous operation. At the end of each of the camera's exposures the controller will go to the next scan angle and, if applicable, update the AOTF profile.
6. For data collection in simple experiments with a single excitation profile the multi-dimensional acquisition feature in Micro-Manager provides an easy and convenient interface. For more complex experiments including multiple color channels, multiple stage positions, or delays between exposure sequences the scripting interface in Micro-Manager should be used.
7. For processing, images are organized in stacks by excitation wavelength. Each stack contains a single sequence of excitation angles. For details on SAIM data processing in Fiji *see* [14]. Alternatively, a highly optimized command line analysis program is supplied as C/C++ source code in the instrument controller project repository. Compiling the analysis program requires additional open-source and proprietary libraries and should be done on the analysis workstation. For more details *see* [10].

## 4 Notes

1. Piranha solution should be prepared fresh before use. Use extreme caution when mixing and handling. Always keep piranha solution in a chemical fume hood and wear proper personal protective equipment. Check local regulations concerning the preparation, use and disposal of piranha solution. If proper equipment for preparation and disposal of piranha solution is not available wafer cleaning solution can be used as a less-effective substitute.
2. To create a fluorescent surface on the SAIM substrate the matrix protein can be dye labeled. We routinely label fibronectin using the following procedure:
   (a) Dissolve Cy3-*N*-hydroxysuccinimide ester in anhydrous DMOS, make 25 ng aliquots and lyophilize.
   (b) Add 1 mL of a 1 mg/mL fibronectin solution in PBS to a lyophilized aliquot of the dye.
   (c) Incubate at room temperature for 1 h with mixing.
   (d) Remove the free dye by dialysis against 1 L of PBS overnight at 4 °C.
3. Specific parts for mechanical components (e.g. optical posts, post bases, and optical cage components) should be selected based on materials on hand and the mechanical dimensions of the microscope, lasers, and other components.
4. When selecting an instrument control and acquisition computer it is important to match the storage capacity and speed with the camera's data generation rate. Scientific cameras often produce data fast then the storage speed of a single hard disk or solid-state drive over a SATA connection. With a sufficiently large free memory pool (RAM), the incoming images can be spooled in a buffer, allowing the camera to run at full speed until the system memory is full. Alternatively, a properly configured redundant array of inexpensive disks (RAID) can achieve write speeds that exceed the camera's data generation rate. However, hardware RAID controllers are expensive and can be difficult to configure and maintain. PCIe-connected solid-state drives are relatively inexpensive, readily available, and fast enough to handle the full-framerate of scientific cameras, making them our preferred storage method.
5. If a dicing saw is not available, the wafer can be sectioned into chips with a diamond-tipped scribe. In this case the wafer should be placed reflective side down on a clean tissue. Draw the scribe across the back of the wafer several times using a straight-edge. Press down on the scribed line to snap the wafer.

Clean silicon particles from the chip with a blast of clean compressed air before proceeding.

6. The silicon oxide film thickness can vary significantly over the surface of the wafer. It is important to measure the thickness on each chip before proceeding with functionalization and imaging.
7. For fluorescent protein fusions, the culture should be transfected 24 h prior to seeding on the silicon chips. Follow the transfection protocol provided by the reagent supplier.
8. If vibrations or buoyancy are an issue the silicon chips can be held with a small, nonreactive metal weight. We have found that a stainless steel ¼″-20 nut works well for this purpose. The weight should be sterilized with 70% ethanol and equilibrated to the sample temperature.
9. Many of the peripheral devices have external power supplies and driver modules. These should be placed on a convenient equipment shelf that is detached from the optical table to prevent the transmission of vibrations to the optical system. Vibration producing equipment should be isolated from the optical system wherever possible.
10. It is advisable to build a "mock-up" of the completed system using the major components (lasers, AOTF, scanning mirrors, periscope mechanical components and microscope) on the optical table before assembly. Use a tape measure or ruler and masking tape on the table top to indicate the approximate placement of the lenses and mirrors. This will ensure that there is adequate space for placement of all the components and serve as a guide during construction.
11. Instructions for configuring and running Micro-Manager are available at https://micro-manager.org or the Micro-Manager mailing list.
12. The AOTF orientation relative to the beam path is important for proper operation. During initial system construction it is useful to align the lasers using 2 iris diaphragms temporarily mounted long the path of the polychromatic beam. Once aligned, the AOTF should be positioned and tuned according to the manufacturer's instructions using an optical power meter. After this the irises can be relocated and used as $i_1$ and $i_2$ in Fig. 7a.
13. Coarse positioning of the lenses within the scanning system can be done with a ruler; however, final adjustment should be made with respect to the excitation laser collimation. This is particularly true of the distance between the second relay lens and the objective lens. The objective lens is constructed of many individual optical elements and its rear focal plane must be

determined empirically. We recommend the following procedure for fine-tuning the lens' positions within the system after coarse assembly (use proper precautions to prevent dangerous eye exposure to the laser beams). Before starting, ensure that the scanning mirrors are in a neutral, centered position and the lasers are aligned to the optical axis of the cage system.

(a) Remove the scan lens and first relay lens. Place a drop of water and glass coverslip on the microscope sample holder. Enable one of the excitation lasers so that a spot is visible on the ceiling above the microscope. Adjust the second relay lens ($L_{r2}$ in Fig. 8) to minimize the projected spot size. Secure the relay lens in the cage system.

(b) Remove the objective lens from the microscope and insert the first relay lens ($L_{r1}$ in Fig. 8) into the cage system. Place the shearing interferometer into the beam path on top of the microscope stage. Adjust the position of $L_{r1}$ until a collimated beam is achieved.

(c) Attach the scan lens to the XY translator and place the shearing interferometer immediately after $L_{r1}$. Adjust the position of the XY translator/scan lens assembly until a collimated beam is achieved.

(d) Mount the objective lens to the microscope body and prepare a dilute fluorescent solution in a glass-bottom dish. We typically use carboxyfluorescein dissolved in deionized water with the 488 nm laser for this step. The solution should completely fill the dish to give the best view of the beam. Adjust $L_{r2}$ to form a collimated beam in the solution.

(e) Repeat steps ii and iii to finalize the axial positioning of the scanning system lens stack.

14. A simple calibration target can be constructed from a rectangular piece of fluorescent plastic, such as that in Fig. 11. The plastic is attached to a 90° mounting bracket. The plastic is positioned vertically in the sample holder and the beam projected along its surface. Alternatively, a piece of plain white paper can be suspended directly above the objective, however positioning the paper is more difficult than the rigid plastic sheet.

15. Entering accurate values for the target and sample refractive indices is critical to accurate calibration of the system. The "Sample index" value should be that of the actual sample to be imaged during experiments. The "Calibration Target Index" should be set to that of air if the beam is being projected onto the surface of the fluorescent plastic sheet. If the beam is propagating inside the plastic then the refractive index of the material should be entered in this field. The refractive

index values can be changed at any time during calibration and the new values will be applied to all existing data points.

16. The emission filter wheel is the slowest peripheral device in the system. For this reason, the experimental sequence prioritizes scan angle changes over excitation profile changes. In some cases it may be necessary to change excitation profiles with each exposure. In this case sequences should be limited to a single angle and a step should be added to the experiment profile for each exposure in the acquisition.
17. The range of angles to scan should encompass at least 1 full cycle in the intensity oscillation profile for accurate reconstruction of the sample topography. The number of angles should balance acquisition speed, photodamage to the sample, and data size. For samples prepared on substrates with 19,000 Å thermal oxide we typically use minimum and maximum scan angles of 1.25° and 40°, respectively. If the data will be processed using the Fiji plugin [14] the specific number of angles is less important. The analysis software included in the instrument controller project repository has been optimized for sequence lengths that are multiples of 16 (e.g. 16, 32, 64), with 32 being the preferred number. While sequences of any length can be analyzed, deviation from this pattern will increase analysis time.

## Acknowledgements

This work was funded by NIH-NCI R33-CA193043 (WRZ and MJP).

### References

1. Paszek MJ, DuFort CC, Rubashkin MG, Davidson MW, Thorn KS, Liphardt JT, Weaver VM (2012) Scanning angle interference microscopy reveals cell dynamics at the nanoscale. Nat Methods 9:825–827
2. Lambacher A, Fromherz P (1996) Fluorescence interference-contrast microscopy on oxidized silicon using a monomolecular dye layer. Appl Phys A Mater Sci Process 63:207–217
3. Ajo-Franklin CM, Ganesan PV, Boxer SG (2005) Variable incidence angle fluorescence interference contrast microscopy for Z-imaging single objects. Biophys J 89:2759–2769
4. Goodman JW (2007) Speckle phenomena in optics: theory and applications. Roberts and Company Publishers, Greenwood Village, CO
5. Dingel B, Kawata S (1993) Speckle-free image in a laser-diode microscope by using the optical feedback effect. Opt Lett 18:549–551
6. Mattheyses AL, Shaw K, Axelrod D (2006) Effective elimination of laser interference fringing in fluorescence microscopy by spinning azimuthal incidence angle. Microsc Res Tech 69:642–647
7. Fiolka R, Belyaev Y, Ewers H, Stemmer A (2008) Even illumination in total internal reflection fluorescence microscopy using laser light. Microsc Res Tech 71:45–50
8. Fu Y et al (2016) Axial superresolution via multiangle TIRF microscopy with sequential imaging and photobleaching. Proc Natl Acad Sci U S A 113:4368–4373

9. Chen Y et al (2018) Multi-color live-cell super-resolution volume imaging with multi-angle interference microscopy. Nat Commun 9:4818
10. Colville MJ, Park S, Zipfel WR, Paszek MJ (2019) High-speed device synchronization in optical microscopy with an open-source hardware control platform. Sci Rep 9:1–13
11. Shurer CR et al (2017) Genetically encoded toolbox for glycocalyx engineering: tunable control of cell adhesion, survival, and cancer cell behaviors. ACS Biomater Sci Eng 4 (2):388–399. https://doi.org/10.1021/acsbiomaterials.7b00037
12. Edelstein A, Amodaj N, Hoover K, Vale R, Stuurman N (2010) Computer control of microscopes using μmanager. In: Ausubel FM et al (eds) Current protocols in molecular biology. John Wiley & Sons, Inc., Hoboken, New Jersey
13. Schindelin J et al (2012) Fiji: an open-source platform for biological-image analysis. Nat Methods 9:676–682
14. Carbone CB, Vale RD, Stuurman N (2016) An acquisition and analysis pipeline for scanning angle interference microscopy. Nat Methods 13:897–898

# Chapter 8

# Computational Optics for Point-of-Care Breast Cancer Profiling

**Jouha Min, Matthew Allen, Cesar M. Castro, Hakho Lee, Ralph Weissleder, and Hyungsoon Im**

## Abstract

With the global burden of cancer on the rise, it is critical to developing new modalities that could detect cancer and guide targeted treatments in fast and inexpensive ways. The need for such technologies is vital, especially in underserved regions where severe diagnostic bottlenecks exist. Recently, we developed a low-cost digital diagnostic system for breast cancer using fine-needle aspirates (FNAs). Named, AIDA (artificial intelligence diffraction analysis), the system combines lens-free digital diffraction imaging with deep-learning algorithms to achieve automated, rapid, and high-throughput cellular analyses for breast cancer diagnosis of FNA and subtype classification for better-guided treatments (Min et al. ACS Nano 12:9081–9090, 2018). Although primarily validated for breast cancer and lymphoma (Min et al. ACS Nano 12:9081–9090, 2018; Im et al. Nat Biomed Eng 2:666–674, 2018), the system could be easily adapted to diagnosing other prevalent cancers and thus find widespread use for global health.

**Key words** Point-of-care diagnostics, Breast cancer, Cellular analysis, Global health, Artificial intelligence, Deep-learning algorithms

## 1 Introduction

Advances in digital image sensors and computation algorithms have introduced new capabilities in microscopy. Computational optics, where digital images are analyzed by numerical algorithms, can overcome the physical limitations of conventional optics. A particular example is lens-free digital diffraction microscopy [1, 2] that records light diffraction patterns of microscopic objects and then numerically reconstructs object images (Fig. 1). Even without any lens in the optical system, a computational algorithm can retrieve object images at submicron resolution [3, 4]. The field-of-view of lensfree diffraction system is defined by the size of an image sensor, which typically ranges from $mm^2$ to even over $cm^2$. Therefore, the system can achieve both high-resolution and large field-of-view in a simple and portable optical configuration. The digital diffraction

Miguel R. Ossandon et al. (eds.), *Biomedical Engineering Technologies: Volume 1*, Methods in Molecular Biology, vol. 2393, https://doi.org/10.1007/978-1-0716-1803-5_8, 

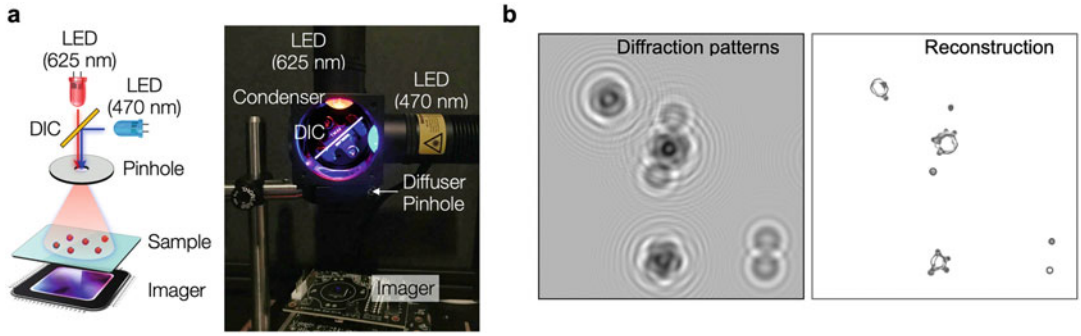


**Fig. 1** Digital diffraction imaging for wide field-of-view (FOV) microscopy. (**a**) Schematic and photograph of the imaging system consisting of light-emitting diodes (LEDs, $\lambda = 470$ and 625 nm), a dichromatic mirror (DIC), a pinhole (with a diffuser), and an imager. A sample is placed directly above the imager. (Reproduced from ref. 1 with permission from ACS Publishing Center). (**b**) Cells are immunolabeled with microbeads, and their diffraction patterns are recorded (left). The diffraction images are then digitally reconstructed into object images (right). (Reproduced from ref. 4 with permission from Nature Publishing Group)

imaging approach has been used to image various biological objects such as *C. elegans* [5], tissue sections [6], cells [7], *S. aureus* [8], and even nanometer-scale objects (nanospheres, viruses) [9–11].

Besides morphological imaging, we have been particularly interested in applying the system for molecular and cellular diagnostics. The first-generation system, termed D3 (*d*igital *d*iffraction *d*iagnostics), was developed as an add-on module to a smartphone to detect target cancer cells labeled with immunomicrobeads [7]. With its large field-of-view imaging capability, the system enabled molecular analyses on thousands of individual cells in a single still image. We subsequently applied the D3 assay to screen for high-risk pre–cervical cancer changes and showed excellent agreement with gold-standard pathology. The D3 assay was further extended to other disease targets, including human papillomavirus (HPV) DNA and lymphoma cells [7, 12, 13].

AIDA (artificial intelligence diffraction analysis) is a new technology with novel features to further improve the detection capability, accuracy, and feasibility of operation in resource-limited settings [1]. First, we used chemically orthogonal immunochromogens to detect multiple tumor markers of interest simultaneously. In this approach, we also develop deep-learning algorithms for automated and rapid image analysis. Deep neural networks extracted hidden features from diffraction patterns, enabling instant analyses of individual cells. The deep-learning analysis was 400-times faster than the previous image reconstruction method, and the cell detection and classification accuracy was over 90%.

We were particularly interested in implementing this technology for FNAs of breast lesions. It is not uncommon that the time from self-discovery of a palpable breast lesion to surgical treatment often takes 6–12 months in low- and middle-income countries.

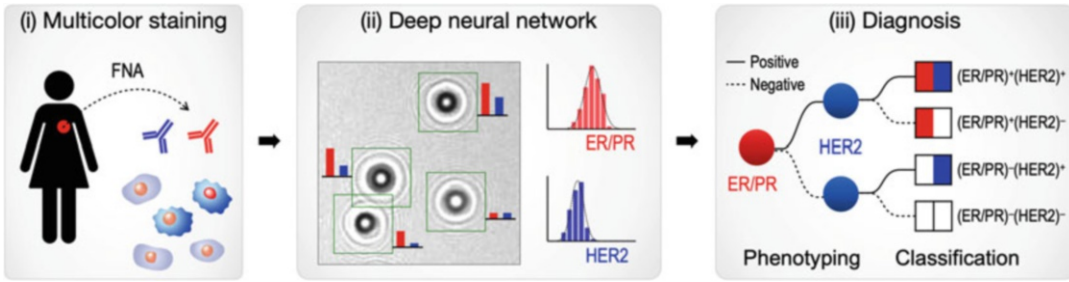


**Fig. 2** Schematic of the workflow. (i) Cellular samples obtained from breast cancer patients via fine-needle aspiration are immunostained for triple markers: ER/PR in red and HER2 in blue. (ii) Diffraction patterns of stained and unstained cells are imaged by the AIDA device. (iii) Deep learning algorithms based on convolutional neural networks are applied to identify cancer cells and extract their color information directly from raw images. The ER/PR and HER2 expression levels are analyzed to classify breast cancer subtypes. (Reproduced from ref. 1 with permission from ACS Publishing Center)

This long delay is mostly due to inefficient systems, scant cellularity of specimens, and lack of expert pathology services [14, 15]. Compared to conventional microscopy, AIDA has much lower assay cost, does not require specialists to determine a diagnosis (aided by deep-learning algorithms), and interrogates a much larger number of cells with single image acquisition. Figure 2 shows the AIDA workflow for breast cancer analysis. Once cells were obtained by FNAs, they were immunostained for ER/PR in red and HER2 in blue. Deep learning algorithms were then used to identify breast cancer cells and their subtypes based on ER/PR and HER2 expression directly from raw diffraction images within a few seconds. Such capacity surpasses even flow cytometers or skilled cytopathologists scanning across slides. In essence, combined with trained neural networks, AIDA can automatically extract clinically relevant information with minimal human curation in short periods.

Here, we introduce the AIDA methods, including collection/storage of FNA clinical specimen, immunoassay procedures, and deep learning algorithms for analysis.

## 2 Materials

The following materials are necessary to collect and store FNA samples and process them using the AIDA system. All reagents are stored as recommended by suppliers. Notably, proper antibody storage temperature is important to minimize degradation.

### *2.1 FNA Sample Collection/Storage*

1. CytoRich Red (ThermoFisher B9990801).
2. 2% bovine serum albumin (BSA).
3. PBS (Thermo Scientific 28372 or 28348).
4. Cell strainers, 70μm (Fisher 08-771-2).

5. Microcentrifuge tubes.
6. Centrifuge (Eppendorf 5810R).

### 2.2 Reagents for AIDA Assays

1. Antibodies in Table 1.
2. HRP anti-rabbit secondary antibody (Vector Labs PI-1000).
3. AP anti-rat IgG secondary antibody (Vector Labs).
4. Immpact NovaRed Peroxidase (HRP) (Vector Labs SK-4805).
5. Vector Blue Alkaline Phosphatase (AP) (Vector Labs SK-5300).
6. BD Perm/Wash buffer (BD biosciences 554723).
7. 2% bovine serum albumin (Fisher, BP1605-100).
8. Normal goat serum (CST 5425S).
9. Cell-Tak (Corning 354240).
10. PBS (Thermo Scientific 28372 or 28348).
11. Microcentrifuge tubes.

### 2.3 AIDA Imaging System

1. High power green LED ($\lambda = 470$ nm, Thorlabs M470D2).
2. High power red LED ($\lambda = 625$ nm, Thorlabs M625D2).
3. Condenser lens ($f = 16$ mm, NA = 0.68, Thorlabs ACL25416U).
4. Dichromatic mirror (550 nm cutoff, Thorlabs DMLP550R).
5. 220-grit optical diffuser (Thorlabs DGUV10).
6. 50-μm aperture (Thorlabs P50C).

**Table 1**
**List of antibodies**

| Antibody | Clone | Cat No. | Vendor |
|---|---|---|---|
| Anti-human ER-a antibody (rabbit monoclonal) | D6R2W | 13258S | Cell signaling technologies |
| Anti-human PR A/B antibody (rabbit monoclonal) | D8Q2J | 8757S | Cell signaling technologies |
| Anti-human HER-2 antibody (rat monoclonal) | ICR55 | ICR55 | Bio-rad |
| Rabbit IgG, monoclonal isotype control | DA1E | 3900 | Cell signaling technologies |
| Purified rat IgG2a, κ isotype control antibody | | 400,501 | BioLegend |
| ImmPRESS™ HRP anti-rabbit IgG (peroxidase) polymer | | MP-7451 | Vector labs |
| ImmPRESS™ AP anti-rat IgG (alkaline phosphatase) polymer | | MP-5404 | Vector labs |

7. CMOS imager (On-Semiconductor MT9P031).
8. Index-matching fluid (70% glycerol, $n \sim 1.47$).
9. Glass coverslips (#1, 22 × 22 mm, Fisher 12-518-105).
10. Custom-designed, 3D printed case.
11. Three-dimensional printer (Formlabs Form 2).
12. Flocking papers (Edmund Optics 54-585).
13. Disc magnets (diameter, 3.2 mm, K&J Magnetics D201).

## 3 Methods

All procedures are performed at room temperature unless otherwise specified.

### 3.1 AIDA Imaging System

The light source had two LEDs—with emission wavelengths of 470 nm and 625 nm, respectively, and a dichromatic mirror with 550 nm cutoff A 220-grit optical diffuser was used to improve the uniformity of light illumination. A 50-μm aperture was placed after the diffuser to produce a partially coherent light source for diffraction imaging. Optical components are aligned inside a custom-made holder. Diffraction images are recorded by a monochromatic 10-megapixel CMOS imager mounted on a USB 3.0 interface board (Imaging Source). The pixel size is 2.2μm, and the field of view is $5.7 \times 4.3$ mm$^2$. We make a device body using a 3D printer and lightproofed the inside with flocking papers. The entry door to the sample loading was snap-fastened to the body via four pairs of disc magnets. The overall size of the device is 11.8 ($L$) × 12.3 ($W$) × 15.6 ($H$) cm$^3$.

### 3.2 FNA Sample Collection/Storage

1. FNA samples are obtained as part of a standard-of-care, clinically indicated image-guided biopsy.
2. Ultrasound or computed tomography guidance is used to confirm the correct 18G needle position within a given mass lesion.
3. Two coaxial 20G FNA passes are made to yield material for cytopathology and AIDA analysis.
4. Additional core biopsies are obtained for conventional pathology workup which served as the gold standard.
5. FNA samples are fixed in CytoRich Red (ThermoFisher) for 15–30 min (no longer than 2 h).
6. The cells are washed with 2% BSA-PBS buffer and centrifuged at 400 × $g$ for 5 min (*see* **Notes 1** and **2**).
7. The cells are resuspended with 2% BSA-PBS buffer and filtered through a cell strainer (70μm) to obtain a single-cell suspension (*see* **Note 3**).
8. The samples can then be processed as described below (*see* **Note 4** for long-term storage).

### 3.3 AIDA Assay

1. The cells in the FNA samples are permeabilized with BD Perm/Wash buffer (or BD fix/perm if using cultured cell lines) for 15 min.
2. The cells are washed two times with BD Perm/Wash buffer and centrifuged at 400 × *g* for 5 min between each wash.
3. The cells are then blocked with BD Perm/Wash buffer supplemented with 2% bovine serum albumin (BSA) and 5% normal goat serum for 15 min.
4. The cells are labeled with a cocktail of primary antibodies—anti-human ER antibody (rabbit monoclonal, 2.36μg/mL), anti-human PR antibody (rabbit monoclonal, 0.62μg/mL), and anti-human HER2 antibody (rat monoclonal, 0.625μg/mL)—for 30 min (*see* **Note 5**).
5. The cells are washed two times with BD Perm/Wash buffer and centrifuged at 400 × *g* for 5 min between each wash.
6. Subsequently, the cells are labeled with a 1:1 (v/v) mix of HRP anti-rabbit and AP anti-rat IgG secondary antibody for 30 min.
7. The cells are washed two times with BD Perm/Wash buffer and centrifuged at 400 × *g* for 5 min between each wash. After the final spin, cells are resuspended in 100μL PBS.
8. The labeled cells are then captured on the surface of an imaging chamber using a cocktail of antibodies against EpCAM, EGFR, HER2, and MUC1, and unbound cells are removed by washing with fresh PBS.
9. The captured cells are incubated with the 3,4-dihydroxyphenylalanine (DOPA)-based bioadhesive (Cell-Tak, Corning) to tightly bind to the surface (*see* **Note 6**).
10. The cells are finally stained with ImmPACT NovaRED Peroxidase (HRP) for 5 min and Vector Blue Alkaline Phosphatase (AP) substrates for 10 min (*see* **Note 7**).
11. Right before imaging, the captured and stained cells are placed in a glycerol-based mounting solution (70% glycerol, 5–10μL) to optically match the refractive index of cells (*see* **Note 8**).
12. Two images per sample (pre- and poststaining) are taken using the AIDA at 470 and 625 nm wavelengths (*see* **Note 9**).

### 3.4 Deep Learning Algorithm

Recorded diffraction images are analyzed by two convolution neuron networks (CNNs); one for cell detection and another for color classification. All codes are written using Python 3.6.1 and run on a computer with an Intel i7-7700HQ CPU at 2.80 GHz. Keras with Tensorflow is used to build and train the models (*see* **Note 10**).

#### 3.4.1 For Cell Detection

1. First apply a maximally stable extremal regions (MSER) blob detection algorithm to find regions containing cell-like objects.

2. Once regions have been proposed by the MSER algorithm (*see* **Note 11**), analyze the subarea images with a CNN trained to identify regions containing cells. To train the network, we generate a set of images of about 10,000 diffraction patterns from cells and the same number of additional patterns from noncells (e.g., debris, air bubble, dust) (*see* **Note 12**). 70% of the images are used for training, and 30% of the images are used for validating the trained network.

*3.4.2 For Cell Classification*

1. Analyze the detected cells using the color classification model (*see* **Note 13**) that detects the positivity of HER2 and ER/PR expressions based on a pair of cell diffraction patterns measured at 470 nm and 625 nm illumination (Fig. 3).

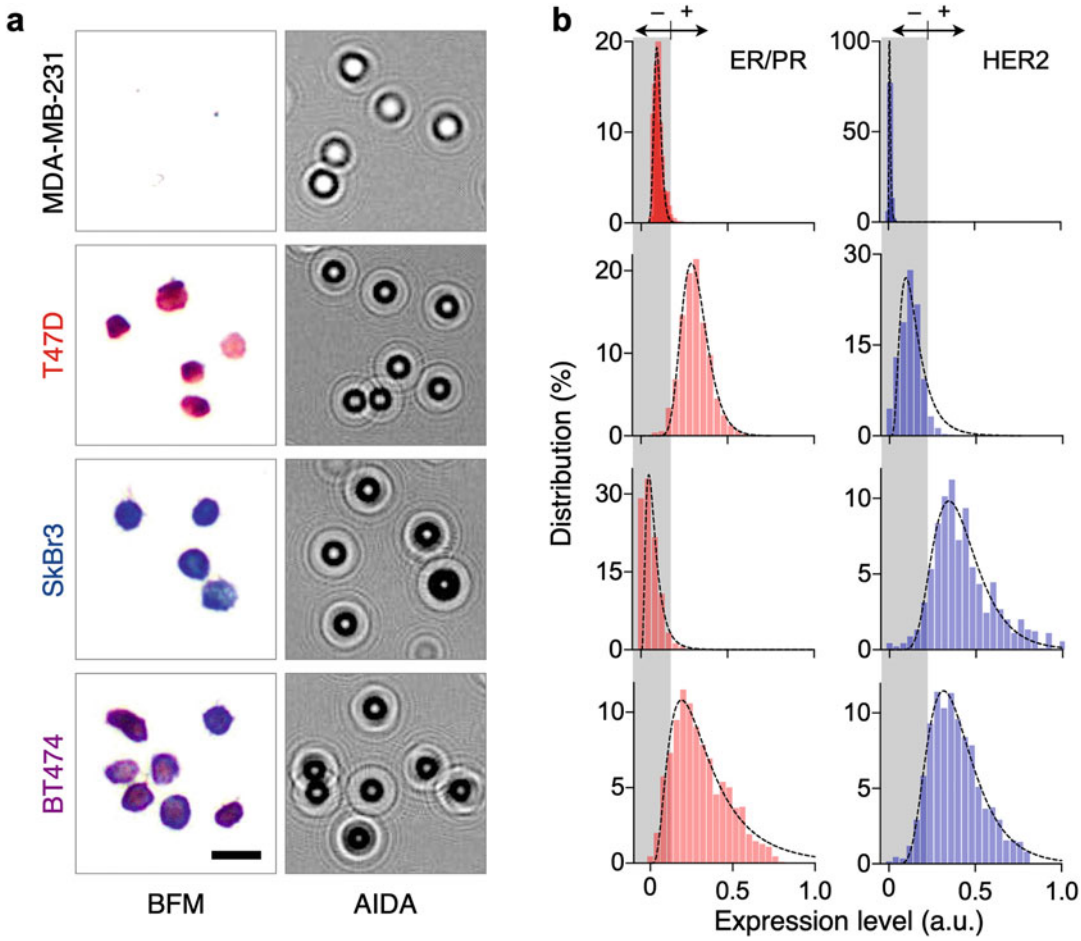


**Fig. 3** Quantitative molecular profiling with AIDA. (**a**) Breast cancer cell lines representing four subtypes (MDA-MB-231, TNBC; T47D, Lum-A; SkBr3, HER2+; and BT474, Lum-B) were stained for ER/PR (red) and HER2 (blue), and imaged via bright field microscopy (BFM) and AIDA. (**b**) ER/PR and HER2 expression profiles were obtained from diffraction images. (Reproduced from ref. 1 with permission from ACS Publishing Center)

2. Classify each cell into one of the four categories: LUM-B $(ER/PR)^{+}(HER2)^{+}$, LUM-A $(ER/PR)^{+}(HER2)^{-}$, HER2 positive $(ER/PR)^{-}(HER2)^{+}$, triple-negative $(ER/PR)^{-}(HER2)^{-}$.
3. Apply the Adam optimization algorithm (*see* **Note 14**) to iteratively tune the weights in each layer by minimizing the cross-entropy loss function.
4. Similar to the cell detection network, images are split into two sets (a 7:3 ratio) for training and validation, respectively (*see* **Note 15**).

## 4 Notes

1. A pellet of cells may be visible, depending on the volume of the sample.
2. It may be useful to resuspend the sample in a consistent volume so that all processed samples are in an equal final volume (50μL).
3. Multiple cell strainers may be necessary to process one sample, as the strainers may clog.
4. FNA samples after fixation with Cytorich Red may be stored at −80 °C for later use.
5. Using the index-matching solution (70% glycerol) reduces background signals of prestained cells.
6. Cell-Tak bioadhesive is applied as follows. First, Cell-Tak solution is prepared by using 10μL Cell-Tak, 285μL sodium bicarbonate, pH 8.0 and 5μL 1 N NaOH (added immediately before coating) to make 300μL solution. 100μL of the Cell-Tak solution is added to the captured cells and allowed a minimum of 20 min for adsorption. The Cell-Tak solution is then aspirated and rinsed twice with sterile water.
7. The ImmPACT NovaRED Peroxidase (HRP) for ER/PR stains cells in red and the Vector Blue Alkaline Phosphatase (AP) substrates for HER2 stains cells in blue. If both markers are positive, the cells turn in purple (Fig. 3)
8. We combine ER and PR together to assess the hormone receptor status.
9. A total of four images are taken; two images before staining (after **step 6**) and another two images after staining (after **step 8**) at 470 and 625 nm, respectively. Then, the differences in individual cells are calculated.
10. Basic source codes are available through the website of the Center for Systems Biology (https://csb.mgh.harvard.edu).

11. The Maximally Stable Extremal Regions (MSER) algorithm is a blob detection algorithm. To detect blobs, the algorithm thresholds an image with a sequence of decreasing threshold values. At each threshold value, the algorithm detects regions of connected pixels which are above the threshold. A region is defined to be stable if it appears for several threshold values. The number of threshold values to use, how much to vary them at each step, and how many thresholds a region must appear before it is considered stable are all hyperparameters.
12. More than 5000 concatenated diffraction images are recommended for the network training. When constructing the training set, data augmentation techniques (random rotations, horizontal mirroring, vertical mirroring of images) can be applied to ensure the translation invariance of the network output.
13. The color classification model had eight convolutional layers with the final layer flattened to a vector of size 768. This vector is the input to three fully connected layers, which produce the final output of four classes based on the positivities of HER2 and ER/PR. Each convolutional layer used a parametrized rectified linear unit activation function. Batch normalization is applied after each convolutional layer, and a single dropout layer is used after the sixth convolutional layer to reduce overfitting.
14. The Adaptive moment estimation (ADAM) algorithm is a gradient descent method [16]. It maintains an exponentially moving average of the first and second moments of the gradient. ADAM dynamically adjusts the step-size of each update for every parameter by scaling the mean estimation inversely with the estimated standard deviation of the gradient.
15. The ground truth for each input image (i.e., color intensities) should be obtained by performing mathematical reconstruction of diffraction patterns; the mean pixel intensity inside each reconstructed cell image is calculated and converted to a molecular expression value. Once the network is trained, the mathematical reconstruction is not necessary, and expression levels can be obtained directly from diffraction images.

## Acknowledgments

This work was supported in part by UH3-CA202637 (R.W.), R33CA202064 (R.W.), R21CA236561 (R.W.), T32CA079443 (J.M., R.W.), V-Foundation for Cancer Research (R.W., C.M.C.), Massachusetts General Hospital Center for Innovation in Early Cancer Detection (C.M.C., H.I.), R00CA201248 (H.I.),

R21CA217662 (H.I,), Fundamental Research Program of the Korean Institute of Materials Science (PNK 6070; H.I.), R01CA229777 (H.L.), U01CA233360 (H.L., C.M.C), MGH Scholar Fund (H.L.), DoD-W81XWH1910199 (H.L.), and DoD-W81XWH1910194 (H.L.).

## References

1. Min J, Im H, Allen M et al (2018) Computational optics enables breast cancer profiling in point-of-care settings. ACS Nano 12:9081–9090
2. Im H, Pathania D, McFarland PJ et al (2018) Design and clinical validation of a point-of-care device for the diagnosis of lymphoma via contrast-enhanced microholography and machine learning. Nat Biomed Eng 2:666–674
3. Bishara W, Sikora U, Mudanyali O et al (2011) Holographic pixel super-resolution in portable lensless on-chip microscopy using a fiber-optic array. Lab Chip 11:1276–1279
4. Song J, Leon Swisher C, Im H et al (2016) Sparsity-based pixel super resolution for lens-free digital in-line holography. Sci Rep 6:24681
5. Cui X, Lee LM, Heng X et al (2008) Lensless high-resolution on-chip optofluidic microscopes for Caenorhabditis elegans and cell imaging. Proc Natl Acad Sci U S A 105:10670–10675
6. Greenbaum A, Zhang Y, Feizi A et al (2014) Wide-field computational imaging of pathology slides using lens-free on-chip microscopy. Sci Transl Med 6:267ra175
7. Im H, Castro CM, Shao H et al (2015) Digital diffraction analysis enables low-cost molecular diagnostics on a smartphone. Proc Natl Acad Sci U S A 112:5613–5618
8. Veli M, Ozcan A (2018) Computational sensing of Staphylococcus aureus on contact lenses using 3D imaging of curved surfaces and machine learning. ACS Nano 12:2554–2559
9. Arlett JL, Myers EB, Roukes ML (2011) Comparative advantages of mechanical biosensors. Nat Nanotechnol 6:203–215
10. Mudanyali O, McLeod E, Luo W et al (2013) Wide-field optical detection of nanoparticles using on-chip microscopy and self-assembled nanolenses. Nat Photonics 7:247–254
11. Su J (2015) Label-free single molecule detection using microtoroid optical resonators. J Vis Exp 106:e53180
12. Im H, Park YI, Pathania D, Castro CM, Weissleder R, Lee H (2016) Digital diffraction detection of protein markers for avian influenza. Lab Chip 16:1340–1345
13. Pathania D, Im H, Kilcoyne A et al (2016) Holographic assessment of lymphoma tissue (HALT) for global oncology field applications. Theranostics 6:1603–1610
14. Anderson BO, Ilbawi AM, El Saghir NS (2015) Breast cancer in low and middle income countries (LMICs): a shifting tide in global health. Breast J 21:111–118
15. Chandika AB, Gakwaya AM, Kiguli-Malwadde E, Chalya PL (2012) Ultrasound guided needle aspiration versus surgical drainage in the management of breast abscesses: a Ugandan experience. BMC Res Notes 5:12
16. Kingma DP, Ba J (2014) Adam: a method for stochastic optimization. arXiv:1412.6980

# Chapter 9

# DNA Genotyping Based on Isothermal Amplification and Colorimetric Detection by Consumer Electronics Devices

**Luis Antonio Tortajada-Genaro**

## Abstract

The point-of-care testing of DNA biomarkers requires compact biosensing systems and consumer electronic technologies provide fascinating opportunities. Their portability, mass-produced components, and high-performance readout capabilities are the main advantages for the development of novel bioanalytical methods.

This chapter describes the detection of single nucleotide polymorphisms (SNP) through methods based on user-friendly optical devices (e.g., USB digital microscope, flatbed scanner, smartphone, and DVD drive). Loop mediated isothermal amplification (LAMP) enables the required discrimination of each specific variant prior to the optical reading. In the first method, products are directly hybridized to the allele-specific probes attached to plastic chips in an array format. The second method, allele-specific primers are used, enabling the direct end-point detection based a colorimetric dyer and a microfluidic chamber chip. In both approaches, devices are employed for chip scanning.

A representative application to the genotyping of a clinically relevant SNP from human samples is provided, showing the excellent features achieved. Consumer electronic devices are able to register sensitive precise measurements in terms of signal-to-noise ratios, image resolution, and scan-to-scan reproducibility. The integrated DNA-based method lead a low detection limit (100 genomic DNA copies), reproducible (variation <15%), high specificity (genotypes validated by reference method), and cheap assays (<10 €/test). The underlying challenge is the reliable implementation into minimal-specialized clinical laboratories, incorporating additional advantages, such as user-friendly interface, low cost, and connectivity for telemedicine needs.

**Key words** DNA sensing, Isothermal amplification, Single-nucleotide polymorphism, Smartphone, Compact disc

## 1 Introduction

Advances in nucleic acid biomarkers and molecular techniques are offering new opportunities in a wide range of fields such as personalized medicine, food safety, biotechnology, biochemical research or drug screening [1, 2]. For instance, pharmacogenetic studies can predict a patient's response to certain therapies, based on the

Miguel R. Ossandon et al. (eds.), *Biomedical Engineering Technologies: Volume 1*, Methods in Molecular Biology, vol. 2393, https://doi.org/10.1007/978-1-0716-1803-5_9, 

genetic variants associated with the drug absorption, metabolism, and effect [3, 4]. The most common variants in human DNA are point mutations or single nucleotide polymorphisms (SNPs), which can provide variable protein expression, modifying cell functionalities and reaction mechanisms [5]. However, the current genotyping systems require highly expensive or complex methods, compromising their adoption close to the point-of-need [6]. Therefore, the development of novel methods is essential to diffuse this kind of genetic testing in less specialized facilities [7, 8]. In recent years, several studies have examined the capabilities of point-of-care (POC) genetic testing [9, 10]. The scientific challenge is to obtain highly efficient testing methods, which have to be accurate and sensitive enough to detect even minority variants, but also practical and economically feasible.

In DNA-based diagnostic methods, amplification reaction is important because an effective increment in the copy number for the target region is needed for reaching good assay sensitivity and selectivity [11, 12]. Polymerase chain reaction (PCR) is the most widely used method, but there are significant limitations for POC applications or for the integration in miniaturized devices [13]. The main drawbacks are specific instrument for strict temperature control, high-influence of inhibitors in complex samples, susceptibility to amplification yield variations related to reaction conditions or the formation of air bubbles. Also, the exposition to heat can potentially cause DNA damage such as C to T deamination. In the last years, isothermal reactions have opened new approaches for the development of innovative analytical methods [14]. Rapid and efficient amplification is achieved at a constant temperature under simple conditions (e.g., water bath). Also, they allows the use of minimally processed samples and makes it the method of choice for a fast screening of individual DNA samples. Most of the reported methods possess impressive sensitivity for the detection of nucleic acids, and some have achieved commercial success, including loop mediated isothermal amplification (LAMP), strand displacement amplification (SDA), rolling circle amplification (RCA) and recombinase polymerase amplification (RPA). Thus, isothermal reactions greatly simplify the implementation of DNA-based methods in miniaturized platforms combined to devices used in resource-limited settings [15, 16].

Several researchers have demonstrated the capability of assays based on isothermal amplification methods to discriminate single-nucleotide variations. Most relevant methods involves an allele-specific hybridization [17, 18] or amplification using allele-specific primers [19]. However, the detection allele-selective products is usually achieved by expensive and bulky laboratory equipment (e.g., fluorescence qPCR thermocycler, electrochemical stations, real-time turbidimeter or fluorescence scanner).

In this chapter, we provide methods to exploit consumer electronic devices as user-friendly optical read-out applied to DNA-based diagnosis. They are ordinarily employed for entertainment, communications and home-office activities, such as smartphones, scanners, and compact disc drives. But, in the last years, these optoelectronic devices have been demonstrated the capabilities to make biosensing more accessible to society [20–23]. Herein, several details for their conversion into a DNA detection platform are provided in two assay formats. The first method is LAMP combined to allele-specific hybridization in array format on a planar chip (LAMP-array). The second method is a direct allele-specific LAMP in a microfluidic reaction chamber (on chip-LAMP). Also, a relevant example is included, describing the recommended measurement conditions and the potential of the unmodified commercial technologies. The selected application is a POC system able to genotype SNPs for supporting psychiatric pharmacogenetics. A rapid and specific increment of target DNA regions at constant temperature (62 °C), avoiding the requirement of thermal cyclers. The proposed conditions yields a high amplification factor ($10^8$ to $10^9$) in 60 min incubation, enabling the optical detection. These performances endorsed their potential as a competitive alternative to the current equipment and methods.

## 2 Materials

### 2.1 LAMP Reaction

1. The amplification buffer (20 mM Tris–HCl, 10 mM $(NH_4)_2SO_4$, 50 mM KCl, 2 mM MgSO4, 0.1% Tween 20, pH 8.8) from New England Biolabs (USA).
2. Bst polymerase 2.0 from New England Biolabs (USA).
3. Desoxinucleotides (dNTPs) from Jena Biosciences (Germany).
4. Betaine from Sigma (USA).
5. For LAMP incubation, several heating devices can be used such thermal blocks (example, digital heat block from VWR), ovens, etc. Also, thermal cyclers can be employed.

### 2.2 LAMP-Array Method

1. Planar chip with oligo probes immobilized on chip surface. The chip can be purchased or tailored fabricated in laboratory (e.g., array spotter).
2. LAMP labeling reagent, for example, digoxigenin-11-deoxyuridine triphosphate (DIG-dUTP) from Jena Biosciences (Germany).
3. Sodium citrate from Panreac (Spain).
4. Sodium chloride from Panreac (Spain).
5. Formamide from Acros Organics (Belgium).

6. Denhardt's reagent from Thermo Fisher Scientific (USA).
7. Reagents for colorimetric staining of chip, for example, immunoreactions based on peroxidase-conjugated antibodies from Abcam (UK) and substrate from SDT (Germany).

### 2.3 On-Chip LAMP Method

1. One-chamber chip, for example, rhombic chamber chip (reaction volume 10μL, Zeonor material) from microfluidic ChipShop (Germany). Alternatively, a three-layer chip can be used.
2. Inlet/outlet connectors from ChipShop (Germany).
3. Hydroxynaphthol blue from Sigma (USA)

### 2.4 Reading by Consumer Electronic Devices

1. USB digital microscope is a portable microscope (Dino-Lite AM4013MZT, AnMo Electronics Co., Taiwan) based on a color CMOS system (resolution 1.3 Megapixel, maximum frame rate: 30 fps).
2. Smartphone. Images are captured by a smartphone (MotoG first generation, Motorola, EEUU) using a homemade chamber ($8 \times 6.7 \times 4.4$ cm).
3. Flatbed scanner. An office scanner (Perfection 1640SU Office, Epson, Japan), which incorporated a CCD image sensor, is also employed in the reflectance mode.
4. Compact disc drive. The assays performed on digital versatile disc (DVD) are directly read by a DVD drive (LG DVD GSA-H42N, LG Electronics Inc., USA), which incorporated a data acquisition board model (DT9832A-02-OEM; Data Translation, Marlboro, MA, USA).
5. ImageJ free-access software from National Institutes of Health (USA).

### 2.5 Application to Patient Diagnosis

1. DNA design software, for example, PrimerExplorer (http://primerexplorer.jp/e). Alternatively, manual design algorithm for LAMP primers following restriction indicated in Ref. 24.
2. DNA extraction kit, for example, Purelink Genomic DNA mini kit from Thermo Fisher Scientific (USA).
3. Instrument for the quantification of genomic DNA content, for example, NanoDrop 2000 spectrophotometer from Thermo Fisher Scientific (USA).
4. Kit for reference method, for example, Big Dye Terminator Cycle Sequencing from Thermo Fisher Scientific (USA).
5. Instrument for reference method, for example, fluorescence-capillary sequencer (ABI 3130xl Genetic Analyzer) from Applied Biosystems (USA).

## 3 Methods

### 3.1 Design of Oligonucleotides

1. In isothermal amplification techniques, a correct selection of oligonucleotides is important. LAMP primers are designed for the target SNP, following the restrictions such as melting temperature, length, and distances between primers [24]. A detailed description of design restriction is summarized in **Note 1**.
2. In the LAMP-array method, an additional restriction is that the stem-loop product is designed to have the SNP in its loop region. Then, array probes are designed to directly hybridize the stem-loop product by its loop structure. The hybridization must produce a high variation of Gibbs free energy. The polymorphism is positioned at a central position to increase selectivity. To improve hybridization yields and to reduce the surface effect, a polythymine tail is incorporated into the 5′-end of the allele-specific probes.
3. In the on chip-LAMP method, the specific restriction is that the polymorphism is located at the 5′-end of both FIP and BIP.

### 3.2 Assay: LAMP-Array

1. Figure 1 summarizes the biorecognition processes in LAMP-array method. It is based on an isothermal amplification of the specific region combined to an allele-specific solid-phase hybridization in array format (wild-type or mutant variant).
2. The LAMP reaction is carried out in 200μL propylene vials, containing 12.5μL of amplification mixture. In vial format, the

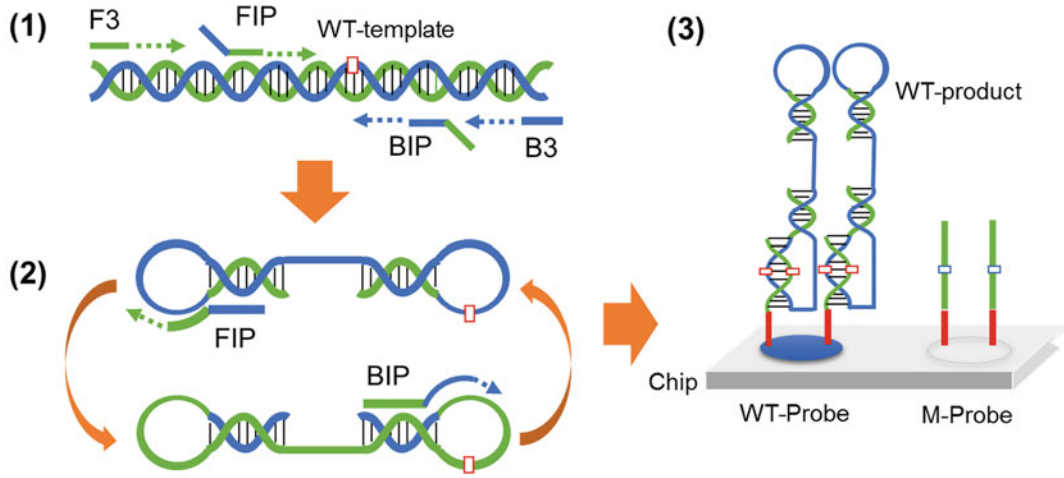


**Fig. 1** Scheme of the LAMP-array method. (1) The forward and backward outer primers (F3 and B3) are used to displace the inner-extended sequences (FIP and BIP primers). (2) The generated stem-loop structures are further duplicated by additional reaction cycles. (3) The LAMP product (wild-type variant) hybridizes to the allele-specific probe immobilized on the chip surface

amplification mixture is composed of amplification buffer (1×), 1.5 M betaine, 6 mM $MgSO_4$, 1.2 mM dNTPs, 10μM DIG-dUTP, 0.2μM of outer primers, 1.2μM of inner primers and 0.32 U/μL Bst polymerase 2.0. The studied DNA template is added at 0.32 ng/μL (approximately 100 copies per μL). Solutions are incubated at 62 °C for 60 min.

3. The array-based identification is compatible with several chip materials and immobilization techniques. A successful approach is a planar chip tailored-fabricated from polycarbonate slides [25] (*see* **Note 2**). In this surface, the probes are anchored to the chip surface via streptavidin/biotin chemistry, although other techniques are also feasible (*see* **Note 3**).
4. Amplification products in hybridization buffer are dispensed on the chip with the immobilized probes and incubated at 37 °C for 60 min. A recommended hybridization solution is composed by formamide (30%) and Denhardt's reagent (2.5×, Thermo Fisher Scientific, USA) in a sodium saline citrate buffer (SSC 1×: NaCl 150 mM, sodium citrate 15 mM at pH 7).
5. The chip is flushed by washing buffer. The washing solutions can be diluted SSC buffers (0.1× and 0.01×). Later, the chip is stained incubating labeled reagents, generating a colored product (*see* **Note 4**).
6. The chip is then washed with distilled water, dried, and stored until reading by consumer electronic devices.

### 3.3 Assay: In-Chip LAMP

1. Figure 2 summarizes the biorecognition processes in in-chip LAMP method. It is based on an allele-specific isothermal amplification (wild-type or mutant variant) in a chamber chip.
2. The platform is a rhombic chamber chip. Inlets and outlets are connected directly to Tygon tubing. The material is cyclic-olefin polymer, which is a transparent thermopolymeric substrate suitable for mass production. The chamber-shape allows for the handling of reagents in a reduced scale, reproducible and safety.
3. Two reaction mixtures are prepared, composed by reagents, DNA extract and the correspondent primer (wild-type or mutant). The amplification mixture is composed described previously, except the betaine concentration (0.75 M) and the presence of 300μM of hydroxynaphthol blue [25].
4. Each LAMP mixture is loaded to the microfluidic chip (10μL) and incubated at 62 °C for 60 min. A blue product is formed in case of presence of target template due to the decomposition of magnesium–hydroxynaphthol blue complex for the formation of magnesium pyrophosphate.
5. The chip is stored until reading by consumer electronic devices.

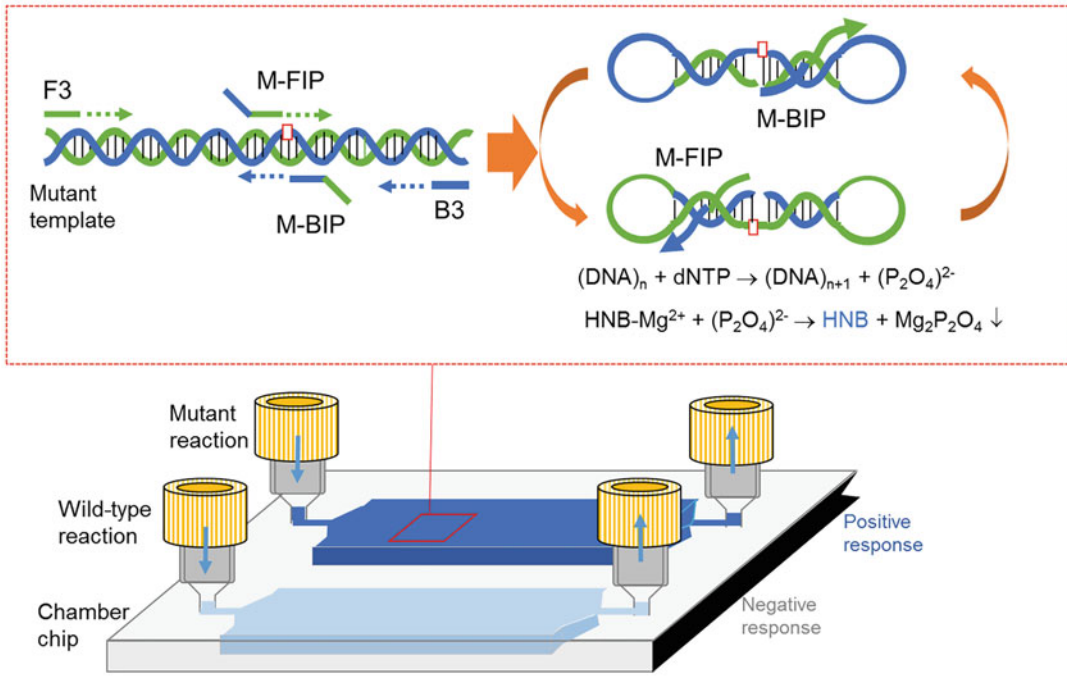


**Fig. 2** Scheme of the on chip AS-LAMP method. The insert indicates the reaction for mutant variant, showing the duplication of target region and the consequent formation of blue product

### *3.4 Chip Imagining*

1. Several consumer electronic devices can be used for the imagining of DNA-assays performed in plastic chips (planar chips or chamber-chips) (Fig. 3).
2. USB digital microscope. Images are captured by vertically positioning the equipment over the chip at a 5 cm distance and employing the microscope internal LED as the light source (maximum illumination 18,500 lx). The DinoCapture 2.0 software is employed to record the image at the 1.3-megapixel resolution.
3. Smartphone. The chip is introduced in the reading chamber. The system had a frontal rectangular aperture for the smartphone camera, a lateral hole used to illuminate the chip by an external optical fiber light source (cold light, 90°, power 20 W, LE.5209 model, Euromex, Holland), and an aperture for inserting the assay chip. After adjusting the focus and exposure (75% level), images are captured (rear camera 5-megapixel CMOS).
4. Flatbed scanner. The support is positioned over the equipment bed and scanning is carried out at a 1600 dpi (dots per inch) resolution using the own scanner software (disabled autocorrection functions).

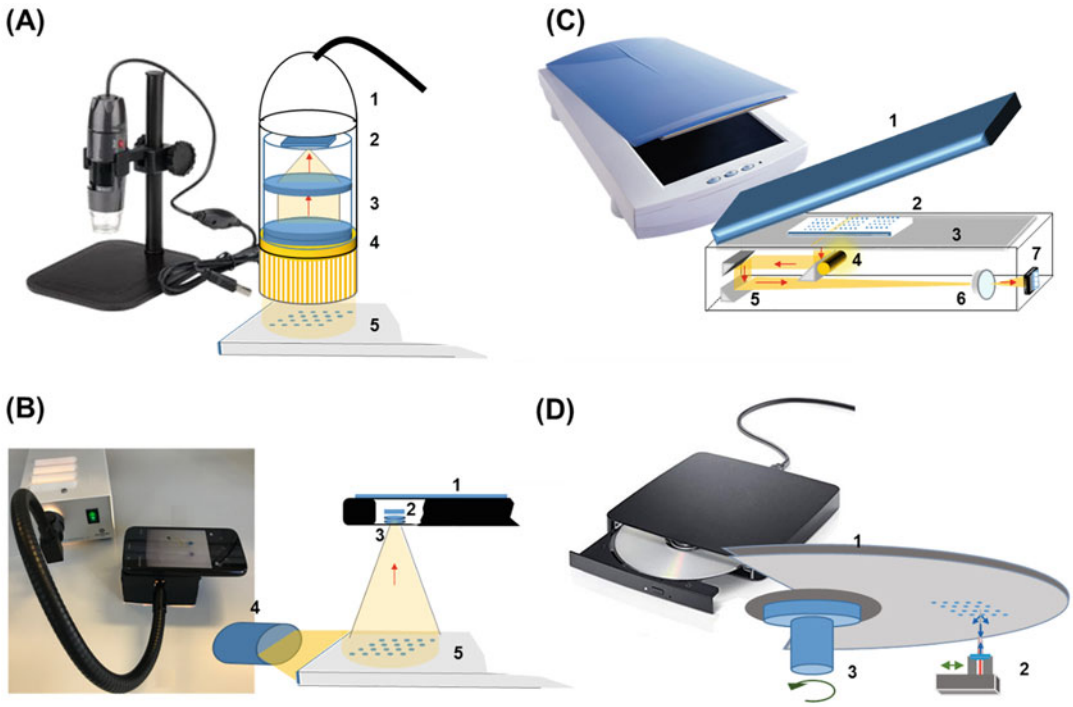


**Fig. 3** Reading schemes by sensing devices (not on scale): (**a**) Portable microscope: (1) USB connection; (2) CMOs chip; (3) internal lens; (4) illumination ring; (5) assay chip. (**b**) Smartphone: (1) smartphone screen; (2) CMOs chip; (3) internal lens; (4) external illumination; (5) assay chip. (**c**) Documental flatbed scanner: (1) cover lid; (2) assay chip; (3) glass screen; (4) lamp; (5) mirrors; (6) lens; (7) CCD chip. (**d**) DVD drive: (1) disc with array on bottom layer; (2) DVD pickup; (3) rotor

5. Compact disc drive. The reading conditions are adjusted by a custom software: rotation speed of 4 × (13.46 m/s) and 21 dB gain at a detection rate of 1700 mega-samples/s.
6. For camera-based systems, a reference color palette is placed in the detection assembly close to the chips.
7. The ImageJ free-access software is used to process the images. The software provided signal-to-noise ratios are calculated as the net spot signal, divided by the background standard deviation.

### *3.5 Selection of Reading Device*

1. Under the described working conditions, the four low-cost devices are capable of quantifying the intensities of microarray spots (LAMP-array) or the colorimetric signal of reaction chambers (in-chip LAMP) resulting from a DNA recognition process. Robust high signal-to-noise ratio are registered (Fig. 4).
2. The specifications of each device are summarized in Table 1. All devices provide a low-cost, robust, sensitive, specific, and easily readable analysis.

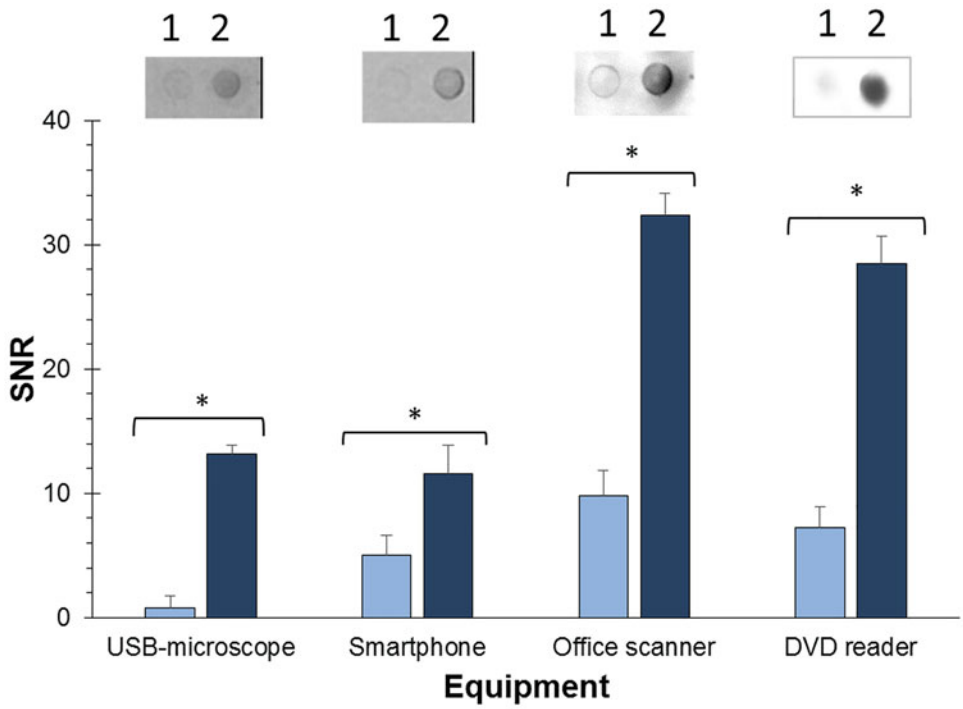


**Fig. 4** Signal-to-noise ratio recorded for genotyping images using the studied consumer electronic devices: Wild-type test (1) and mutant test (2). Sample: mutant homozygous individual. All the data are shown as mean ± standard deviation (3 replicates). *$p$-value $<0.05$. (Adapted from Talanta 2019 with permission from Elsevier)

3. To address the needs of a specific nucleic acid testing at a point-of-care level, several recommendations should be considered (*see* **Notes 5–8**) [26].

### *3.6 Application to Patient Diagnostics*

1. As proof of concept, the genotyping of the rs1954787 polymorphism, located in the *GRIK4* gene, is described. The discrimination between genotypes supports the determination the genetic predisposition against an antidepressant treatment [27–29].
2. LAMP primers and probes are specifically designed for each target SNP. The oligonucleotides used for the chosen application are listed in Table 2.
3. The method is valid for a wide range of clinical samples, such as epithelial tissue, blood, hair. In the tested assay, the samples are epithelial tissues obtained by buccal smear. DNA extracts showing a 260/280 nm absorbance ratio lower than 1.8 are rejected (low-purity criteria). Extracts are diluted to 4 ng/μL and stored at −20 °C until further use.
4. Human DNA extracts are analysed by LAMP-array and in-chip LAMP methods (*see* **Note 9**). A no-template control and

**Table 1**
**Comparison of the studied consumer electronic devices used as DNA array readers. (Adapted from Talanta 2019 with permission from Elsevier)**

| Device | Microscope | Smartphone | Office Scanner | DVD reader |
|---|---|---|---|---|
| Dimensions | 16 × 6 × 6 cm | 13 × 6.6 × 1.2 cm | 44 × 29 × 10 cm | 27.0 × 11.7 × 5.6 cm |
| Weight | 100 g | 143 g | 4500 g | 2700 g |
| Acquisition software | DinoCapture2.0 | Android 4.3 | Epson | Home-made |
| Connectivity | Laptop—USB port | Direct | Laptop—USB port | Laptop—USB port |
| Energy requirements | USB supply (2 W) | Phone battery (2070 mAh, ~8 W) | External power supply (200 W) | External power supply (48 W) |
| Reading process | Manual, 10 min | Manual, 0.5 min | Automatic, 7 min | Automatic, 13 min |
| Reading area | 6 mm × 6 mm (0.36 $cm^2$) | 25 mm × 75 mm (19 $cm^2$) | 216 mm × 296 mm (640 $cm^2$) | ∅120 mm-disc (83 $cm^2$) |
| Samples per chip | 10 | 10 | 10 | 36 |
| Measurements per chip[a] | 10 | 1 | 1 | 1 |
| Resolution (pixel width) | 10μm | 17μm | 10μm | 10μm |
| Scan-to-scan variation[b] | 0.1% | 3.2%/0.4% | 0.1% | 0.8% |
| Spot location variation[b] | 3.6% | 5.2%/0.6% | 0.5% | 2.5% |
| Interspot variation[c] | 4.6% | 9.8% | 2.9% | 8.0% |
| Background variation | 3.2% | 4.0% | 1.1% | 3.2% |
| DNA sensitivity[d] | 100 copies | 100 copies | 100 copies | 100 copies |
| Detector prize | €150 | €100 | €100 | €350 (prototype) |

[a]Required measurements to read the entire chip
[b]Replicates = 3, smartphone values with/without a colour palette
[c]Replicates = 5
[d]Minimal copy number of the template needed to generate a signal-to-noise ratio above 3

nontarget DNA template (e.g., *Salmonella typhimurium*) can be used to check for false-positive assays.

5. Examples of chip images are shown in Fig. 5a, b, respectively. Both methods provided a specific response profile depending on the genetic variant.
6. The assay sensitivity is 50 copies for LAMP-array method and 100 copies for in-chip LAMP method. The analysis time is 140 and 70 min, respectively.
7. A discrimination index is constructed based on the signal-to-noise ratio associated with the wild-type (WT) and mutant (M) responses, according to the following equation:

**Table 2**
**List of the oligonucleotides for the wild-type (WT) and mutant (M) discriminations**

| Method | Function | Sequence (5′–3′) |
|---|---|---|
| LAMP | FIP | CATCGTGCCTTCACCCAAT-AGGAAGTACAACCAAAAGCA |
| Array | BIP | GTAGCTGGTGCTGCTATTAAC-ACCCACCTCTTCCCTCCTA |
| | F3 | AAGAAGTGGACTGGTTTGAGAA |
| | B3 | GCAGAGCATCTCAAATTTAGG |
| | WT-probe | [BtnTg]-T10-AGACTGGTTAT-**T**-GGAAGGTGCGG |
| | M-probe | [BtnTg]-T10-AGACTGGTTAT-**C**-GGAAGGTGCGG |
| | C+ | [BtnTg]-T10-TTGTCATGGGCCTCGTGTCGGAAAACC-Dig |
| | C- | [BtnTg]-T10-CAACCGCGAGAAGATGACCCAGATCA |
| On chip | WT-FIP2 | AATAACCAGTCTCCAATTG-ATTTTGAGGAAGTACAACC |
| LAMP | M-FIP2 | GATAACCAGTCTCCAATTG-ATTTTGAGGAAGTACAACC |
| | WT-BIP | TAGAAGGTGCGGAATTGGG-AGTTAATAGCAGCACCAGCT |
| | M-BIP | CAGAAGGTGCGGAATTGGG-AGTTAATAGCAGCACCAGCT |
| | F3 | AAGAAGTGGACTGGTTTGAGAA |
| | B3 | GCAGAGCATCTCAAATTTAGG |
| Sequencing | FP | AAGAAGTGGACTGGTTTGAGAA |
| | RP | GCAGAGCATCTCAAATTTAGG |
| | Marker | GCAGAGCATCTCAAATTTAGG |

*FIP* forward inner primer, *BIP* backward inner primer, *[Btn-Tg]* biotin with a triethylene glycol spacer, *T10* thymine tail (10 nucleotides), *[Dig]* digoxigenin, *C+* positive control, *C−* negative control, *FP* forward primer, *RP* reverse primer

(WT − MUT)/(WT + MUT). A discrimination graph makes easier the genotype decision rule (Fig. 5c).

8. Reference results (Sanger sequencing) revealed a perfect correlation with the genotypes determined by the LAMP-based assays.
9. Mutant homozygous (CC) have a better chance of positive responses to depression treatment. In heterozygous patients (CT) is expected to give a normal response for drugs like citalopram. Homozygous wild-type genotype (TT) indicates a higher risk of a nonresponse.
10. The achieved LAMP discrimination process and their combination to a low-cost detector show excellent performances. These methods can be extrapolated other target genetic biomarkers, including SNPs, mutations and other specific regions. This offers researchers the chance to develop integrated systems, which enable quicker monitoring of genetic

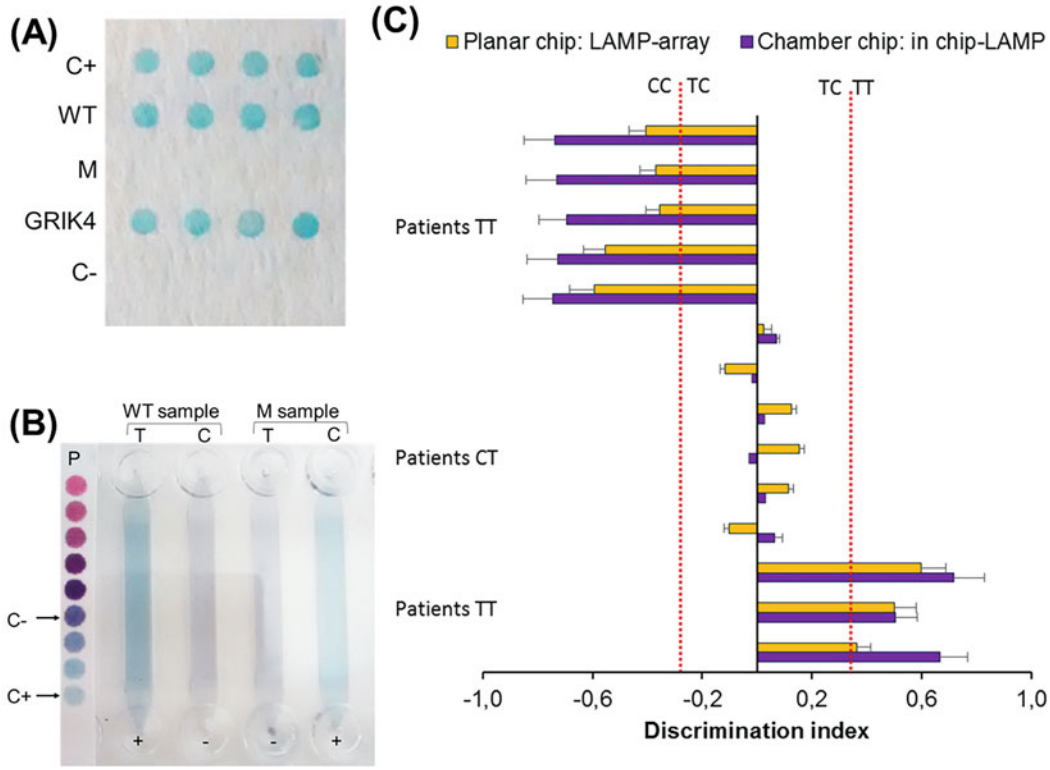


**Fig. 5** Genotype analysis of rs1954787 polymorphism using the proposed LAMP-based methods combined with smartphone detection. (**a**) LAMP-array method: wild-type human DNA extract. (**b**) On chip-LAMP method: wild-type and mutant human DNA extracts. The image includes the colour pattern (P) used for smartphone detection. (**c**) Genotyping analysis of human samples. *C+* positive control, *C−* negative control, *WT* wild-type, *M* mutant. (Adapted from Biosensors and Bioelectronics 2018 with permission from Elsevier)

predispositions to develop certain diseases or to predict genomic-related responses to drug therapies.

## 4 Notes

1. Specific design restrictions are incorporated by considering the general conditions of LAMP reaction [25] and the specific restrictions aimed to the genotyping of single-nucleotide variations [30]. Limited size of target sequences (18–22 nt), limited distance between target sequences (e.g., distance F3-FIP up to 12 nt, distance B3-BIP up to 12 nt), similar %GC (35–65%), similar melting temperatures of primers ($T_m$ 55–65 °C), and low self-annealing (up to 8 nt) are the main restrictions. Also, the absence of significant hybridization to the erroneous template or between primers (low $\Delta G$ associated to duplex structure) is critical. A recommend restriction for genotyping

purposes is similar length and melting temperature between wild-type and mutant variants. The objective is to effectively amplify all the targets by minimizing the risk of unbalanced amplification or cross-reactivity. Although the LAMP primers can be designed manually, and software programs are strongly recommended. Therefore, the in silico design workflow eliminated the sets that did not fulfil restrictions. Nevertheless, our recommendation is to check several sets because the experimental performances can vary respect to the expected amplification yield or selectivity.

2. Recommended substrates are thermopolymeric materials because they show excellent features for optical detection and are suitable for mass production. This approach also works on a low scale in terms of the amount of reagents, cost and waste. In this study, a planar polycarbonate slide (Makrolon) is employed (chip dimensions 7.5 × 2.5 cm).
3. A useful immobilization technique is a noncovalent direct attachment of biotin-functionalized probes to streptavidin-adsorbed surface [31–32]. In our study, each mixture of streptavidin (10 mg/L) and 5′-biotinylated-probe (100 nM) in printing buffer (50 mM carbonate buffer, pH 9.6 and 1% glycerol (v/v)) is transferred to the surface in array format. The spotter is a noncontact printer (AD 1500 BioDot Inc., CA, USA), and the working volume, temperature, and relative humidity are controlled at 40 nL, 25 °C, and 90%, respectively. A recommended array format is a spot diameter of 450μm, a center-to-center distance of 1 mm, and four replicates per probe.
4. Using digoxigenin-dUTP a labeling reagent, an effective staining is achieved by immunoreactions [32]. An option is anti-digoxigenin primary antibody and peroxidase-conjugated secondary antibody prepared in phosphate buffered saline (phosphate 10 mM, NaCl 150 mM, 0.05% Tween 20, pH 7.4). Then, the incubation is performed at room temperature for 30 min, followed by rinsing with washing solution (e.g., phosphate buffered saline). An effective peroxidase substrate is 3,3′,5,5′-tetramethylbenzidine, forming a blue precipitate over the positive spots in 2 min.
5. Two categories can be defined depending on the employed sensing principle. The first is composed of digital imaging devices, which consists of an array of pixel sensors that converts light intensity into electrical current (charge coupled device or a complementary metal–oxide–semiconductor). The optical sensors installed in USB microscopy, smartphones, and documental scanners provide images of the assay platform. The second category is based on compact disc technology, where

assays are performed on the optical disc surface and a disc drive acts as the optical scanner. The image is formed from the data captured in each radius.

6. Several authors have coupled optical elements to exploit consumer electronics as instruments for more sophisticated detection principles, such as bright-field microscopy, or as electrochemical, fluorescence or cytometric analyses. According to our experience, unmodified commercial technology has its advantages, such as robustness, continuous updating, is affordable, and offers high-working tolerance, familiarity, and minimal maintenance.
7. All system fulfil WHO requirements, and corresponds to the acronym "ASSURED": affordable, sensitive, specific, user-friendly, rapid and robust, equipment-free, and delivered to those who need it. However, there are differences in terms of measured area per reading, resolution and reproducibility.
8. Regarding the operational characteristics for POC applications in remote scenarios, the smartphone presented the best features: lightweight, small size, internal data processing, direct connectivity, and low-energy. Despite its excellent optical performance, the USB microscope offers limited applications in low-resource environments. On the other hand, compact disc drives and scanners also have an important potential, with commercially available portable external slim units (USB power supply) and handheld scanners, respectively.
9. Human subjects are recruited according to ethics with informed consents.

## Acknowledgments

Financial support from FEDER, BIOHOLOG (MINECO CTQ2016-75749-R).

### References

1. Davey JW, Hohenlohe PA, Etter PD, Boone JQ, Catchen JM, Blaxter ML (2011) Genome-wide genetic marker discovery and genotyping using next-generation sequencing. Nat Rev Genet 12(7):499
2. Rabbani B, Nakaoka H, Akhondzadeh S, Tekin M, Mahdieh N (2016) Next generation sequencing: implications in personalized medicine and pharmacogenomics. Mol BioSyst 12 (6):1818–1830
3. Caudle KE, Klein TE, Hoffman JM, Muller DJ, Whirl-Carrillo M et al (2014) Incorporation of pharmacogenomics into routine clinical practice: the clinical pharmacogenetics implementation consortium (CPIC) guideline development process. Curr Drug Metab 15 (2):209–217
4. Whirl-Carrillo M, McDonagh EM, Hebert JM, Gong L, Sangkuhl K et al (2012) Pharmacogenomics knowledge for personalized medicine. Clin Pharmacol Ther 92(4):414–417
5. Karki R, Pandya D, Elston RC, Ferlini C (2015) Defining "mutation" and "polymorphism" in the era of personal genomics. BMC Med Genomics 8(1):37
6. Shen W, Tian Y, Ran T, Gao Z (2015) Genotyping and quantification techniques for single-

nucleotide polymorphisms. Trends Anal Chem 69:1–13

7. Woolley CF, Hayes MA (2014) Emerging technologies for biomedical analysis. Analyst 139(10):2277–2288
8. Vashist SK, Luppa PB, Yeo LY, Ozcan A, Luong JH (2015) Emerging technologies for next-generation point-of-care testing. Trends Biotechnol 33(11):692–705
9. Dobson MG, Galvin P, Barton DE (2007) Emerging technologies for point-of-care genetic testing. Expert Rev Mol Diagn 7 (4):359–370
10. Nayak S, Blumenfeld NR, Laksanasopin T, Sia SK (2016) Point-of-care diagnostics: recent developments in a connected age. Anal Chem 89(1):102–123
11. Zarei M (2017) Portable biosensing devices for point-of-care diagnostics: recent developments and applications. Trends Anal Chem 91:26–41
12. Jayanthi VSA, Das AB, Saxena U (2017) Recent advances in biosensor development for the detection of cancer biomarkers. Biosens Bioelectron 91:15–23
13. Deng H, Gao Z (2015) Bioanalytical applications of isothermal nucleic acid amplification techniques. Anal Chim Acta 853:30–45
14. Zhao Y, Chen F, Li Q, Wang L, Fan C (2015) Isothermal amplification of nucleic acids. Chem Rev 115(22):12491–12545
15. Craw P, Balachandran W (2012) Isothermal nucleic acid amplification technologies for point-of-care diagnostics: a critical review. Lab Chip 12(14):2469–2486
16. Giuffrida MC, Spoto G (2017) Integration of isothermal amplification methods in microfluidic devices: recent advances. Biosens Bioelectron 90:174–186
17. Nakamura N, Ito K, Takahashi M, Hashimoto K, Kawamoto M, Yamanaka M, Atsuo Taniguchi A, Kamatani N, Gemma N (2007) Detection of six single-nucleotide polymorphisms associated with rheumatoid arthritis by a loop-mediated isothermal amplification method and an electrochemical DNA chip. Anal Chem 79(24):9484–9493
18. Jiang YS, Bhadra S, Li B, Wu YR, Milligan JN, Ellington AD (2015) Robust strand exchange reactions for the sequence-specific, real-time detection of nucleic acid amplicons. Anal Chem 87(6):3314–3320
19. Zhang L, Zhang Y, Wang C, Feng Q, Fan F, Zhang G, Kang X, Qin X, Sun J, Li Y, Jiang X (2014) Integrated microcapillary for sample-to-answer nucleic acid pretreatment, amplification, and detection. Anal Chem 86 (20):10461–10466
20. Morais S, Tortajada-Genaro L, Maquieira Á (2014) Array-on-a-disk? How Blu-ray technology can be applied to molecular diagnostics. Expert Rev Mol Diagn 14(7):773–775
21. Grudpan K, Kolev SD, Lapanantnopakhun S, McKelvie ID, Wongwilai W (2015) Applications of everyday IT and communications devices in modern analytical chemistry: a review. Talanta 136:84–94
22. Zhang D, Liu Q (2016) Biosensors and bioelectronics on smartphone for portable biochemical detection. Biosens Bioelectron 75:273–284
23. Tortajada-Genaro LA, Niñoles R, Mena S, Maquieira Á (2019) Digital versatile discs as platforms for multiplexed genotyping based on selective ligation and universal microarray detection. Analyst 144(2):707–715
24. Notomi T, Mori Y, Tomita N, Kanda H (2015) Loop-mediated isothermal amplification (LAMP): principle, features, and future prospects. J Microbiol 53(1):1–5
25. Yamanaka ES, Tortajada-Genaro LA, Pastor N, Maquieira Á (2018) Polymorphism genotyping based on loop-mediated isothermal amplification and smartphone detection. Biosens Bioelectron 109:177–183
26. Tortajada-Genaro LA, Yamanaka ES, Maquieira Á (2019) Consumer electronics devices for DNA genotyping based on loop-mediated isothermal amplification and array hybridisation. Talanta 198:424–431
27. Horstmann S, Lucae S, Menke A, Hennings JM, Ising M, Roeske D, Müller-Myhsok B, Holsboer F, Binder EB (2010) Polymorphisms in GRIK4, HTR2A, and FKBP5 show interactive effects in predicting remission to antidepressant treatment. Neuropsychopharmacology 35(3):727
28. Milanesi E, Bonvicini C, Congiu C, Bortolomasi M, Gainelli G, Gennarelli M, Minelli A (2015) The role of GRIK4 gene in treatment-resistant depression. Gen Res 97: e14
29. Amare AT, Schubert KO, Baune BT (2017) Pharmacogenomics in the treatment of mood disorders: strategies and opportunities for personalized psychiatry. EPMA J 8(3):211–227
30. Tortajada-Genaro LA, Puchades R, Maquieira Á (2017) Primer design for SNP genotyping based on allele-specific amplification—application to organ transplantation pharmacogenomics. J Pharm Biomed Anal 136:14–21
31. Tortajada-Genaro LA, Mena S, Niñoles R, Puigmule M, Viladevall L, Maquieira Á (2016) Genotyping of single nucleotide polymorphisms related to attention-deficit

hyperactivity disorder. Anal Bioanal Chem 408 (9):2339–2345

32. Yamanaka ES, Tortajada-Genaro LA, Maquieira Á (2017) Low-cost genotyping method based on allele-specific recombinase polymerase amplification and colorimetric microarray detection. Microchim Acta 184 (5):1453–1462

# Chapter 10

# Evaluation of Tumor Development Using Hemoglobin Saturation Profile on Rodent Dorsal Window Chamber

**Miguel R. Ossandon, Brian S. Sorg, Dhananjay S. Phatak, and Konstantinos Kalpakis**

## Abstract

Tumor development can be indirectly evaluated using features of the tumor microenvironment (TME), such as hemoglobin saturation (HbSat), blood vessel dilation, and formation of new vessels. High values of HbSat and other features of the TME could indicate high metabolic activity and could precede the formation of angiogenic tumors; therefore, changes in HbSat profile can be used as a biomarker for tumor progression. One methodology to evaluate HbSat profile over time, and correlate it with tumor development in vivo in a preclinical model, is through a dorsal skin-fold window chamber. In this chapter, we provide a detailed description of this methodology to evaluate hemoglobin saturation profile and to predict tumor development. We will cover the surgical preparation of the mouse, the installation/maintenance of the dorsal window chamber, and the imaging processing and evaluation to the HbSat profile to predict new development of new tumor areas over time. We included, in this chapter, step by step examples of the imaging processing method to obtain pixel level HbSat values from raw pixels data, the computational method to determine the HbSat profile, and the steps for the classification of the areas into tumor and no-tumor.

**Key words** Tumor angiogenesis, Image analysis, Tumor microenvironment, Hemoglobin saturation, Animal models, Window chamber

## 1 Introduction

Hemoglobin saturation analysis has multiple potential applications such as study of brain metabolism [1], neural activation [2] or to evaluate risk of neural damage in children with sickle cell disease. In cancer development, oxygenation and hemoglobin saturation (HbSat) along with development of new vessels, dilatation, deformation, or destruction of existing vessels can provide valuable information of tumor progression and how tumor development can alter local metabolism, producing physiological changes in the tumor microenvironment (TME) [3, 4]. For example, high metabolism, which is the characteristic of many cancers, produces early

Miguel R. Ossandon et al. (eds.), *Biomedical Engineering Technologies: Volume 1*, Methods in Molecular Biology, vol. 2393, https://doi.org/10.1007/978-1-0716-1803-5_10, 

changes in levels of oxygenation around the tumor resulting in local changes of HbSat in tumor microvessels followed by a decrease in oxygenation in the central part of the tumor [5]. Several studies have shown that the HbSat is useful in distinguishing tumor areas from both normal fibroglandular and adipose tissues [6, 7]. Other studies have shown that in spite of the intense angiogenesis, tumors can still be underserved with oxygen due to hyper metabolism of the cancer [6–8]. As the tumor progresses, the central low-oxygenated internal part of the tumor grows and microvessels around the margin of the tumor have a significant increase in HbSat [5]. This spatial distribution of HbSat is iterated because the tumor grows creating an HbSat profile from tumor proliferation to necrosis (areas with low HbSat).

In summary, the changes in oxygenation and spatiotemporal distribution of the HbSat can provide insight in overall tumor progression [4, 9] and can be helpful in early tumor detection or the evaluation of response to treatment. Therefore, in clinical cancer research, hemoglobin saturation can be used to evaluate tumor aggressivity [10] or to study the correlation of optical signatures with morphological features [11]. Hemoglobin saturation can also be used to evaluate effects of therapy on blood flow [12], or as a biomarker for tissue perfusion in the development of skin sores [13], and so on.

One of most effective methodologies to study tumor development in vivo with microvessel resolution is the dorsal skin-fold window chamber. For example, Fig. 1 shows a picture of a tumor developed from 4T1 mouse mammary carcinoma cells injected in a dorsal skin-fold window chamber in an athymic nude mouse. The picture was taken 4 days after the implantation of 5000 tumor cells. The tumor cells were transfected with reporter genes of red

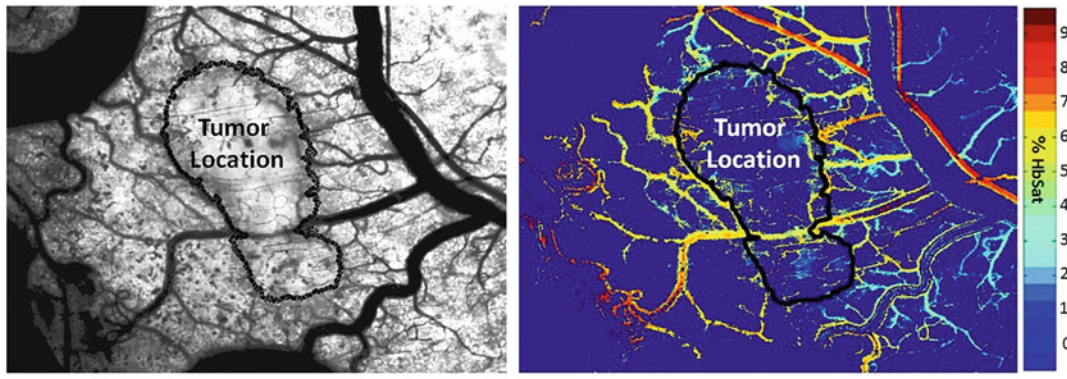


**Fig. 1** (**a**) Tumor grown in dorsal skin-fold window chamber 4 days after tumor cell implantation. (**b**) The margin of the tumor is represented in black. The pixel values were replaced by HbSat values and displayed as a color map. Note the high hemoglobin saturation values (orange-red) in areas surrounding the tumor margin

fluorescent protein (RFP) for identification of the tumor location (Fig. 1a, b). The RFP vector was engineered by splicing the RFP coding sequence cloned from pDsRed2-N1 into pLPCX (BD Biosciences, San Jose, California) by EcoRI-NotI digestions as described in [14]. The picture shows details of the vascularity as the tumor progresses and the hemoglobin saturation pattern. The central part of the tumor (Fig. 1b) shows low levels of saturation corresponding to the necrotic center of the tumor. Outside the tumor limits, the picture shows higher levels of hemoglobin saturation, these areas of high HbSat outside the margin of the tumor indicate increased metabolism consistent with future tumor growth and show that the HbSat preceded the formation of the tumor.

The dorsal skin-fold window chamber technology coupled with a computational analysis of the hemoglobin saturation can provide a powerful tool for basic research to study tumor development, and for clinical researchers to predict tumor aggressivity and early stages that can lead to early cancer detection.

In this chapter, we will provide a methodology for analysis of hemoglobin saturation in tumor areas to evaluate tumor progression on consecutive days in a mouse model. We will cover the installation and configuration of the window chamber; the implantation of the 4T1 tumor cells (or any cancer cells of interest); Image acquisition, and the computational analysis and evaluation of the tumor areas using hemoglobin saturation values [15].

## 2 Materials

### 2.1 Imaging System for Hemoglobin Saturation Mapping

1. Zeiss Axio Scope microscope (Carl Zeiss, Incorporated, Thornwood, New York) or similar upright microscope with long working-distance objectives.
2. Tabletop centrifuge and 10 mL conical centrifuge tubes. The centrifuge should be refrigerated, or it can be a conventional centrifuge placed in a cold room at 4 °C.
3. Environmental chamber (various vendors).
4. Anesthesia Induction Chamber (for gas anesthesia).
5. Filtered deionized water.
6. A 100-W tungsten halogen lamp or similar broadband source used for transillumination (for hemoglobin saturation mapping).
7. A 100-W mercury lamp or other appropriate continuous visible spectrum excitation source used for epi-illumination for fluoresce images.
8. For RFP fluorescence imaging: A 545-nm bandpass excitation filter with 30-nm bandwidth and a 570-nm longpass dichroic beamsplitter (Chroma Technology Corporation, Rockingham,

Vermont). A similar packaged filter set can be used for RFP fluorescence imaging.

9. For GFP fluorescence imaging: A 480-nm bandpass excitation filter with a 40-nm bandwidth and a 505-nm longpass dichroic beamsplitter (Chroma Technology Corporation, Rockingham, Vermont). A similar packaged filter set can be used for GFP fluorescence imaging.
10. A scientific-grade digital camera (CCD or sCMOS) preferably cooled to at least −20 °C.
11. For image magnification: A 2.5×, 5×, or 10× Fluar objective (Carl Zeiss, Incorporated, Thornwood, New York) or similar high-quality long working-distance objective that fits with the microscope employed.
12. Bandlimited optical filtering for hyperspectral imaging: A liquid crystal tunable filter (LCTF) with a 400-to 700-nm (visible light) transmission range positioned in front of the camera to be used for imaging or similar spectral imaging tunable filter element when used with a separate scientific-grade digital camera. An all-in-one commercial camera system specifically designed for spectral imaging can also be used provided that the image data obtained from the system can be imported into a computing environment as raw pixel data.
13. 4T1 mouse mammary carcinoma cells transfected with the gene for DsRed and the gene for enhanced GFP. These cells were created in the laboratory of Mark W. Dewhirst, DVM, PhD (Duke University, Durham, NC).
14. Fischer 344 rats (Charles River Laboratories, Wilmington, MA) (to obtain fresh hemoglobin for hemoglobin saturation calibration).
15. 5% (w/v) sodium dithionite (Millipore Sigma, Burlington, MA).
16. Square profile glass capillary tubes with 100- and 200-μm pathlength (VitroCom, Mountain Lakes, New Jersey).
17. Index-matching immersion oil (Cargille type A, Ted Pella, Incorporated, Redding, California).
18. Standard commercial UV/Vis spectrophotometer capable of measuring high-resolution (1 nm or better) visible light absorption spectra..
19. Dulbecco's Modified Eagle Medium with 10% serum (various vendors).
20. Rhodamine 6G (Millipore Sigma, Burlington, MA).
21. Phosphate-buffered saline (PBS).
22. Saline solution (0.9% sodium chloride).
23. 1-mL gas-tight glass syringe (Bioanalytical Systems, Incorporated, West Lafayette, Indiana).

24. Polyethylene tubing (Clay Adams PE50, Becton Dickinson, Franklin Lakes, New Jersey).
25. A syringe pump (Bioanalytical Systems, Incorporated, West Lafayette, Indiana).
26. A 1-nM solution of Methyl green and a 1-nM solution of Methyl blue (Millipore Sigma, Burlington, MA).
27. Anesthetic cocktail, ketamine 100-mg/kg and xylazine 10-mg/kg.
28. Buprenorphine (analgesic, various vendors).
29. 70% isopropanol and a cotton swab.
30. Optics cleaning solution (equal parts of methanol, ether, and acetone).
31. Ophthalmic solution (various vendors).
32. Any white light lamp suitable for small animal surgery and transillumination of mouse skin (one with a "gooseneck" or similar flexible delivery system is ideal).
33. Forceps, surgical scissors, curved sharp tipped scissors.
34. Athymic nude mice or appropriate mouse model from a commercial vendor (The Jackson Laboratory, Charles River Laboratories, etc.). Mouse models other than nude mice will need to have the hair removed on the window chamber skin to help improve light transmission through the window chamber.
35. 12-mm-diam round glass coverslips and glass slides (various vendors, e.g., Fisher Scientific).
36. 2× Titanium window chamber and C-clamps (APJ Trading Co Inc. Ventura, California).
37. Small animal electric hair clippers.
38. Skin markers.
39. Depilatory cream (Nair™).
40. 1 mL Hamilton gastight glass syringes (Hamilton Company, Reno, NV).
41. 30G ½ in. needle with a slight bend applied to it in the direction of the beveled tip.
42. 16–18-gauge sterile needle.
43. Heparin and heparin needle (25–26 gauge).
44. Nonabsorbable 4-0 surgical suture.
45. MATLAB software (The Mathworks, Inc., Natick, Massachusetts) or other computing environment that can handle custom with the ability to import and process digital images using mathematical operations, both on matrix level or on a pixelwise basis.

## 3 Method

### 3.1 System Calibration

Reference spectra of the pure components of interest: oxyhemoglobin ($HbO_2$), deoxyhemoglobin (Hb-R), RFP and GFP, were acquired on the imaging system to account for effects due to the emission spectra of the illumination sources, the wavelength dependent transmission bandwidth of the LCTF, the transmission of the optics on the microscope, and the detection sensitivity of the camera.

#### 3.1.1 Preparation of Solutions of Oxy- and Deoxyhemoglobin [16]

1. Blood is collected from anesthetized (45-mg/kg pentobarbital, IP) Fischer 344 rats via cardiac puncture with a heparinized needle such that the rat is exsanguinated (typically several milliliters can be obtained).
2. The total collected blood is centrifuged at 1000 × *g* for 10 min and the plasma supernatant is discarded.
3. The remaining pelleted blood cells are gently washed by mixing them with 3–4 mL cold PBS and centrifuge them at 1000 × *g* for 10 min and the supernatant is discarded. This step is repeated three times.
4. The cells are hemolyzed by adding 4 parts of filtered deionized water to 1 part of red cells and incubated for 10 min.
5. To remove the cells stroma and lysate debris, centrifuge for 30 min at 1200 × *g*. Retain the hemoglobin rich cell lysate supernatant and discard the pellet.
6. A 1/10th volume of 10× concentrated PBS is added to the cell-free hemolysate. The hemolysate should be used immediately for calibration.
7. Oxyhemoglobin solutions are obtained by repeatedly inverting the hemolysate solution in room air for several seconds.
8. Deoxyhemoglobin solutions are created by adding powdered sodium dithionite at 5% (w/v) to the hemolysate solution.

#### 3.1.2 Calibration

1. Square profile glass capillary tubes with a 200-μm pathlength submerged in index-matching immersion oil on a glass slide are used for calibrating the solutions of hemoglobin on the microscope system (*see* Subheading 3.1.1, **steps 7** and **8**). An image of a blank field on the slide is used for flat-field correction. There will be some minor dimensional variations, but these are generally negligible.
2. Separately, absorption spectra measurements are collected in a spectrometer with a spectral-slit width of 1 nm in order to determine the concentration of hemoglobin in the freshly prepared hemolysate solutions used for obtaining calibration spectra on the imaging system (Fig. 2 [9]).

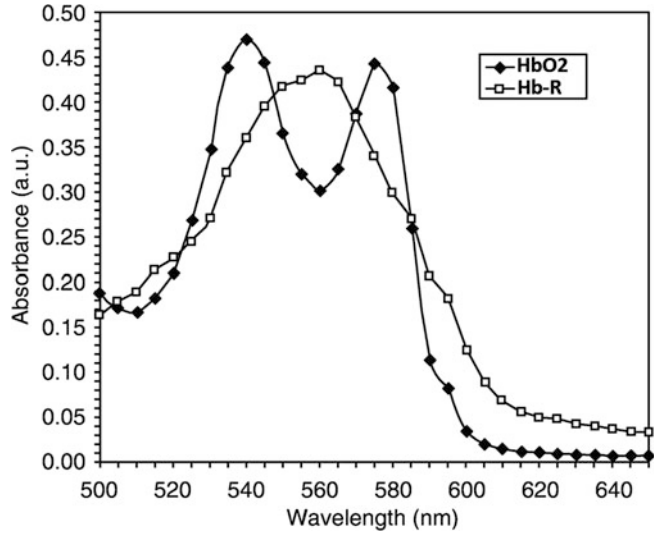


**Fig. 2** Typical absorbance spectra of oxy- and deoxyhemoglobin solutions in 200-μm pathlength measured from 500 to 650 nm in 5 nm intervals on the microscope imaging system

3. Measure the extinction coefficient of oxy- and deoxyhemoglobin at the wavelength that will be used for image acquisition in the optical system chosen for the experiments (e.g., 500–575 nm in 5 nm intervals for this experiment) [5] using the glass capillary tubes (*see* **Note 1**).
4. The concentration of hemoglobin in the calibration solution is estimated from the oxyhemoglobin solution (previous step) using the Kahn method using spectra values collected on a commercial spectrometer [16, 17]. The concentration of hemoglobin is calculated by multiplying the fractional absorption of oxyhemoglobin by a calibration factor of 155. The fractional absorption of oxyhemoglobin is calculated subtracting the tangential baseline at 578 nm ($\Upsilon$) from the total absorption of oxyhemoglobin at 578 nm [17] as follows:

$$\text{Plasma hemoglobin in}\frac{\text{mg}}{\text{dl}} = (A_{578} - \Upsilon) \times 155$$

where $(A_{578} - \Upsilon)$ is the fractional absorption of oxyhemoglobin and Y is the calculated tangential baseline at 578 nm.

The tangential Absorption baseline $\Upsilon$ is calculated subtracting from absorbance at 562 nm as follows:

$$\Upsilon = A_{562} - X$$

where $X$ is the drop in absorption from 562 nm calculated as follows:

$$X = \frac{A_{562} - A_{598}}{2.25}$$

Combining the formulas together we have

$$\text{Plasma hemoglobin in } \frac{\text{mg}}{\text{dl}} = (A_{578} - A_{562} - X) * 155$$

$$= (A_{578} - A_{562} - \frac{A_{562} - A_{598}}{2.25}) * 155$$

$$= (A_{578} - \frac{1.25A_{562}}{2.25} - \frac{A_{598}}{2.25}) * 155$$

$$= 155 * A_{578} - 86.1 * A_{562} - 68.9 * A_{598}.$$

**The calibration factor of 155 (mg per dl) and the correction factor of 2.25 are constants determined by Kahn* et al.

The hemoglobin concentration in mol/L (M) can be obtained from this calculation using the molecular weight (g/mol) of hemoglobin. In previous experiments, 64,500 g/mol is used as the molecular weight. The window chamber imaging system effective extinction coefficients ($M^{-1}$ $cm^{-1}$) for oxy- and deoxyhemoglobin can be calculated by first converting the absorption spectra obtained on the imaging system to absorbance values and then dividing by the concentration of hemoglobin (M) and the pathlength of the capillary tube (cm). The effective extinction coefficients are used in Subheading 3.4.5.

#### 3.1.3 GFP and RFP Fluorescence

GFP and RFP fluorescence spectra are acquired on the window chamber spectral imaging system as follows:

1. 4T1 cells excusing expressing GFP or RFP are cultured in Dulbecco's Modified Eagle Medium with 10% serum on coverslips until a confluent layer is achieved.
2. The coverslips are rinsed in PBS to remove growth media (to remove the pH indicator phenol red which may contaminate the GFP and RFP fluorescence emission spectra).
3. A small drop of PBS is placed on a glass slide.
4. A coverslip with cells is placed cell-side down on the drop of PBS on the top of the slide.
5. Fluorescence images of GFP are acquired from 520–570 nm in 5-nm intervals.
6. Fluorescence images of RFP are acquired from 580–630 nm in 5-nm intervals.
7. A fluorescence image of an alcohol solution containing Rhodamine 6G is used for flat-field correction.

### 3.2 Mouse Preparation

All implanted materials for and surgical instruments must be sterilized prior to surgery. Autoclaving can be used for heat tolerant

materials while gas sterilization should be used for heat sensitive materials.

### 3.2.1 Window Chamber Installation

A titanium window chamber is surgically implanted under anesthesia (intraperitoneal anesthetic cocktail) to athymic nude mice (mice of 25 g or greater weight is recommended). Once the mouse is anesthetized, its eyes need to be kept lubricated with sterile ophthalmic solution [5] since the window chamber installation procedure can take up to 30 min per mouse. The procedure to implant the window chamber by described by Moy et al. [5] as follows:

1. If the mouse has fur, then gently remove dorsal hair from the dorsum from the back legs to the ears using the electric clippers followed by application of depilatory cream.
2. Gently stretch the dorsal skin of the mouse using your fingers and hold in place.
3. Secure the skin using the C-clamps (Fig. 3a).
4. Transilluminate the skin with white light to visualize the blood vessels and chose the area for placement of the window chamber.
5. Place a window chamber support frame in the desired location (as a template) to mark the location of the holes for screw placement.
6. With a large gauge sterile needle (16–18 gauge), open the holes for the screws, a scissors can be used to expand the holes (The holes must accommodate the spacers, but careful not to make the holes too large since the saline solution used later can leak out).
7. Place the screws in one frame along with the spacers and align the frame with the skin and push the screws with the spacers

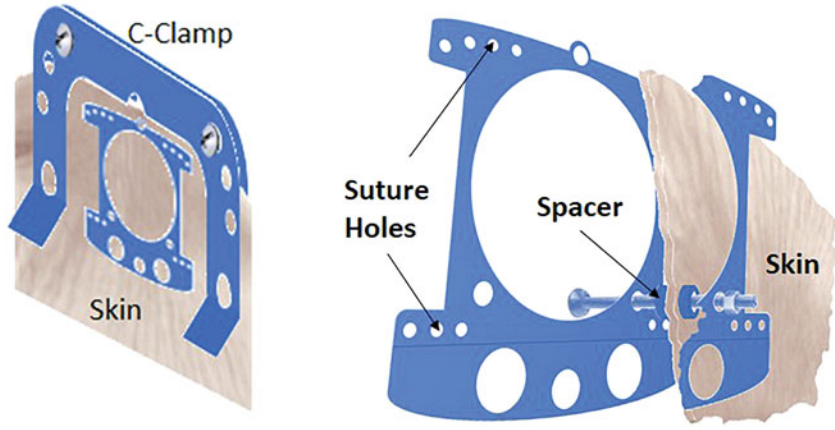


**Fig. 3** (**a**) C-Clamp and widow chamber positions. (**b**) Window chamber assembly details

through the skin. The spacer should lie directly in the screw holes to minimize potential for infection as shown in Fig. 3b.

8. Using forceps clean the screw of any connective tissue.
9. Place the second frame aligned with the screw and secure the window chamber frame with the provided nuts.
10. Suture the frames with nonabsorbable 4-0 surgical suture in each corner of the chamber frame.
11. Remove the C-Clamp.

*3.2.2 Window Chamber Incision and Implantation of Tumor Cells*

1. With forceps carefully lift the skin (on the side of the chamber where the experiments will be performed) and make a small incision with a surgical scissors.
2. Make a circular cut to remove the skin to create the window. The cut must be of smaller diameter than the actual window as the skin will stretch creating a larger opening. After the skin is removed the exposed area must be moistened with drops of warm sterile saline solution.
3. Using sharp-tipped forceps gently lift the facia off the underside of the apposed skin surface and remove it using a curved sharp tipped scissors.
4. Using a 1 mL syringe fitted with the 30G ½ in. needle with the slight bend applied to it, inject 10 μL of a 4T1 mouse mammary carcinoma cell suspension ($5 \times 10^3$ cells) into the dorsal skin flap. The needle should be inserted as superficial as possible in the dermis (the needle can be bent to 30° angle to aid in the position of the needle in the window chamber).
5. Fill the chamber with saline solution and place a round glass coverslip (make sure that there are no trapped air bubbles under the coverslip).
6. Insert the retaining ring to secure the coverslip (the retaining ring is provided with the widow chamber kit).
7. Give the animal a subdermal injection of buprenorphine at a volume equal to 0.16% of the body mass (analgesic).

   Animals are housed in an environmental chamber at 33 °C and 50% humidity with free access to food and water and standard 12-h light–dark cycles. These environmental conditions help with keeping the window chamber hydrated and the raised skin flap of the window chamber close to body temperature.

*3.2.3 Window Chamber Maintenance*

Window chamber maintenance can be done while the animal is anesthetized for the experimental procedure (e.g., in vivo imaging).

1. While the mouse is anesthetized, inspect the sutures and replace any that are missing or chewed completely through.

Prior to placing the sutures, swab the area with 70% isopropanol and a cotton swab. Antibiotic ointment can also be applied to the suture sites and any other areas that require wound treatment.

2. Inspect the nuts on the back of the window chamber and tighten any that need tightening (do not overtighten).
3. Mark the tail of the mouse in any place where the marker identifying the mouse number has faded.
4. Gently clean the window chamber glass using a cotton swab and the optics cleaning solution to remove debris from the window.

### 3.3 In Vivo Imaging Acquisition

#### 3.3.1 Gas Anesthesia (Recommended)

1. Open the valve on the main gas cylinder. The gas on the outflow size of the regulator should be at about 6 psig.
2. Place the mouse in the induction chamber and turn the flow rate to about 5 L/min. Turn the isoflurane to 4.5%.
3. When the mouse has stopped moving in the induction chamber and the breathing has slowed slightly, immediately remove the mouse from the induction chamber.
4. Reduce the isoflurane concentration to about 1–1.25% and reduce the flow rate to about 1 L/min. Place the mouse's nose in the nosecone of the gas anesthesia tube, and observe the respiration rate. The mouse should be lightly anesthetized for imaging and minor window chamber maintenance.
5. **NOTE**: For longer imaging sessions (>20 min), gas anesthesia is mandatory.

#### 3.3.2 Ketamine/Xylazine Anesthesia (Optional Substitute for Gas Anesthesia—Not Recommended)

1. Prepare the standard ketamine/xylazine mixture (10 mg/mL ketamine, 1 mg/mL xylazine in 0.9% saline).
2. Wipe the abdomen with 70% isopropanol prior to administering the anesthesia.
3. Inject the mix intraperitoneal with a 30G needle (give a slightly lower dose than would be used for surgery).
4. **NOTE**: For longer imaging sessions (>20 min), ketamine/xylazine should not be used. Gas anesthesia is mandatory.

#### 3.3.3 Mouse Positioning and Image Acquisition

Image acquisition can be done using the camera controllers provided by the vendor or customizing a LabView application or other software controlling hardware for this purpose (Fig. 4).

1. Carefully place the screws of the window chamber into the appropriate holes on the window chamber positioning holder on the microscope stage. Make sure that the window chamber sits as flat as possible. This will securely hold the window in

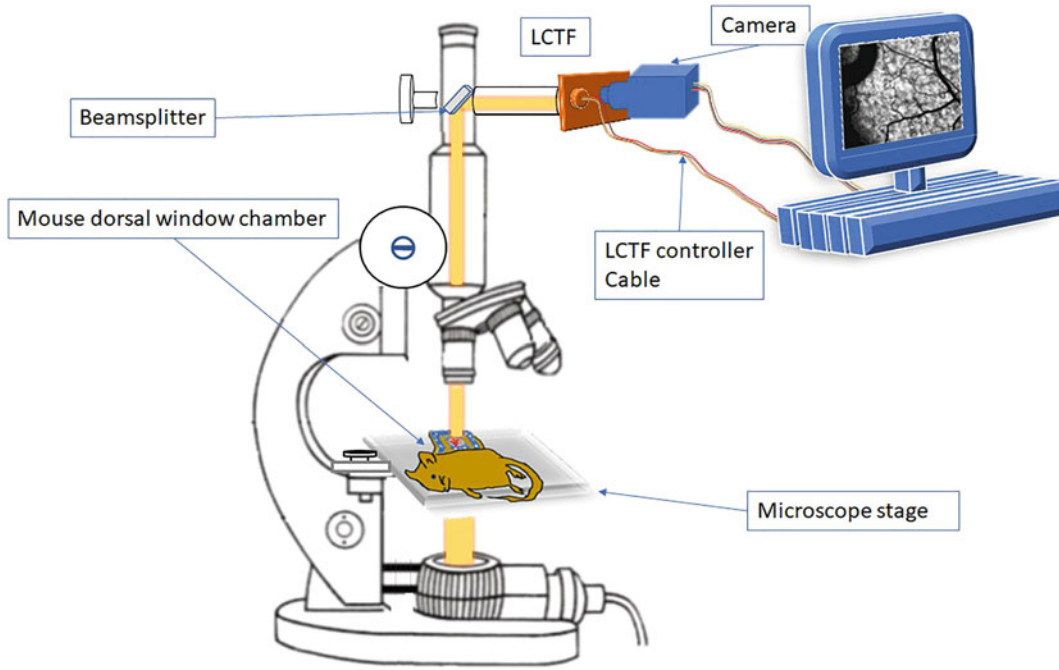


**Fig. 4** Schematic of the image system showing the basic components necessary for image acquisition, processing and analysis

place and allow for positioning by use of the manual stage positioning controls.

2. Look through the eyepieces at the window chamber using the 2.5× objective to position the window at the appropriate imaging area, inspect the field of view and the condition of the window chamber, and to look for movement artifacts caused by breathing and a loose fit of the window chamber in the positioning holder. If necessary, tape the window chamber securely in place to prevent movement artifacts.
3. Change the beamsplitter so all light is directed toward the camera, and close the shield for the eyepieces to prevent room light from reaching the window though the eyepieces.
4. Use the images generated by the camera system (video if possible) for precise focusing of the image just prior to data acquisition. This will ensure the optimal focus in the event that the focal planes of the camera and eyepieces are not coincident.
5. Adjust the light level so that there is a small amount of saturation of the image in avascular background areas that are not part of the region of interest. This will ensure that sufficient light is transmitted through the window.
6. Acquire the spectral imaging data sets as needed for the particular experiment.

7. **NOTE** : For hemoglobin saturation mapping, images are acquired from 500 to 575 nm in 5 nm intervals. Fluorescence images of GFP and RFP are acquired from 520 to 570 nm and 580 to 630 nm respectively at 5 nm intervals. Depending on spectral variations in light output levels of the transillumination light source, wavelength-dependent camera sensitivity, and so on, it may be necessary to have longer exposure times at some wavelengths to achieve an acceptable signal to noise ratio if the imaging system configuration allows for this capability.

### 3.4 Imaging Processing

Imaging processing is done using MATLAB software. A similar computing software suite can be used as well. All images are converted into double-precision arrays for mathematical processing. Images are processed to create pseudo color hemoglobin saturation maps from the hyperspectral imaging (*see* **Note 2**).

#### 3.4.1 Flatfield and Raw Image Data Set

1. Create a flatfield image ($I_{flat}(x, y, \lambda)$) by taking a slightly defocused image of a blank field (there should be no debris or other sharply focused objects in the view [18]. The flatfield image is used to account for inhomogeneities of light intensity across the image field. Only one flatfield image should be necessary for all the experiments.
2. Load $I_{flat}(x, y, \lambda)$ and the raw hyperspectral image data set ($I_{raw}(x, y, \lambda)$) into computer memory. The $I_{raw}(x, y, \lambda)$ should be at minimum recognized as arrays of integer data. The raw unprocessed pixel values of the images should be in the range of $0$ *to* $2^n - 1$ where $n$ is the bit depth of the image. If the images are read as integer arrays, then after importing the images, convert all images from integer value arrays into floating point number arrays for mathematical calculations.

#### 3.4.2 Normalized Flatfield Image and Flatfield Correction

1. Find the average of the pixel values in the flatfield image. If there is more than one flatfield image, do this individually for each image (*see* **Note 3**).
2. Divide the pixel values in the flatfield image by its corresponding average to normalize the flatfield image.
3. On a pixelwise basis, divide each spectral image by the flatfield image. If there is a flatfield image for each wavelength of acquisition, divide each spectral image by its corresponding flatfield image. Calculate the flatfield corrected image ($I_{flat\_corr}(x, y, \lambda)$) as follows:

$$I_{flat\_corr}(x, y, \lambda) = \frac{I_{raw}(x, y, \lambda)}{I_{flat}(x, y, \lambda)}$$

*3.4.3 Convert Flatfield Corrected Pixel Values to Absorbance Values*

1. Identify regions of interest (ROIs) to be used as reference values for unattenuated light $I_0(\lambda)$. Unattenuated light is light transmitted with zero or insignificant absorption. The $I_0(\lambda)$ values are wavelength-specific; therefore, each image should have its own value.
2. To obtain the $I_0(\lambda)$, manually select a few small avascular regions in the images (ROIs) in a given $I_{flat\_corr}(x, y, \lambda)$ and take the average of the values of the ROIs. That average is used as the $I_0(\lambda)$ for the image. Note: The ROIs in each $I_{flat\_corr}(x, y, \lambda)$ image, in terms of their $(x,y)$ locations, must be the same for all wavelengths and correspond exactly to matching ROIs across all images at all wavelengths. Ideally, ROIs selected in one image will be mapped to the same locations across all images to ensure consistency of $(x,y)$ locations at all wavelengths.

*3.4.4 Convert Raw Pixels Values to Absorbance Values*

1. To avoid the potential of performing an undefined mathematical operation, prior to the calculation, the pixels values on the $I_{flat_{corr}}(x, y, \lambda)$ image, that are less than or equal to zero, must be set to the lowest nonzero values (e.g., 1) to avoid taking $\log_{10}(0)$ which is mathematically undefined.
2. Using the values for $I_0(\lambda)$, perform the following operation on each image in the spectral image data set: Divide each pixel by $I_0(\lambda)$ and calculate the negative $\log_{10}$. The result is the absorbance value for that pixel at that wavelength.

$$I_{\mathrm{Abs}}(x, y, \lambda) = -\log_{10}\left(\frac{I_{\mathrm{flat\_corr}}(x, y, \lambda)}{I_0(\lambda)}\right)$$

3. To suppress background "noise" that is not a blood vessel, pixels on the $I_{Abs}(x, y, \lambda)$ image with values greater than the $I_0(\lambda)$ value can be set to one (1), so the absorbance calculation does not result in negative absorbances and these pixels can be suppressed as background pixels when calculating hemoglobin saturation from the absorbance values.

*3.4.5 Calculate Pixel Hemoglobin Saturation from Absorbance Values*

Using calibration data of extinction coefficients for oxyhemoglobin ($\varepsilon_\lambda^{HbO_2}$) and deoxyhemoglobin ($\varepsilon_\lambda^{Hb_R}$) (from system calibration **step 2**), solve for hemoglobin saturation using linear regression according to Shonat [19] (*see* **Note 4**) as shown below:

$$A_\lambda = \log\left(\frac{I_0}{I}\right) = \left[\varepsilon_\lambda^{HbO_2}\right][HbO_2]\,L + \left[\varepsilon_\lambda^{Hb_R}\right][Hb_R]\,L + SL$$

This equation can be solved using a matrix-based method [19] through a rearrangement of the Shonat model equation considering that hemoglobin saturation ($Hb_{Sat}$) is the quotient of oxyhemoglobin ($HbO_2$) divided by total Hemoglobin, and total

hemoglobin ($Hb_{Total}$) is the sum of oxyhemoglobin plus deoxyhemoglobin ($Hb_R$) as follows:

$$Hb_{sat} = \frac{HbO_2}{Hb_{Total}} \quad \text{Therefore, } HbO_2 = Hb_{sat} * Hb_{Total}$$

$$Hb_{Total} = HbO_2 + Hb_R \text{ Therefore, } Hb_R = Hb_{Total} - HbO_2$$

Replacing in $Hb_R$ in the formula:

$$A_{(x,y,\lambda)} = [\varepsilon_\lambda^{HbO_2}] * [HbO_2] * L + [\varepsilon_\lambda^{Hb_R}] * [Hb_{Total} - HbO_2] * L + SL$$

$$= ([\varepsilon_\lambda^{HbO_2}] * [HbO_2] + [\varepsilon_\lambda^{Hb_R}] * [Hb_{Total} - HbO_2]) * L + SL$$

$$= ([\varepsilon_\lambda^{HbO_2} * HbO_2] + [\varepsilon_\lambda^{Hb_R} * Hb_{Total} - \varepsilon_\lambda^{Hb_R} * HbO_2]) * L + SL$$

$$= (\varepsilon_\lambda^{HbO_2} * HbO_2 - \varepsilon_\lambda^{Hb_R} * HbO_2 + \varepsilon_\lambda^{Hb_R} * Hb_{Total}) * L + SL$$

$$= ([\varepsilon_\lambda^{HbO_2} - \varepsilon_\lambda^{Hb_R}] * HbO_2 + \varepsilon_\lambda^{Hb_R} * Hb_{Total}) * L + SL$$

Replacing in $HbO_2$ in the formula:

$$= ([\varepsilon_\lambda^{HbO_2} - \varepsilon_\lambda^{Hb_R}] * Hb_{Sat} * Hb_{Total} + \varepsilon_\lambda^{Hb_R} * Hb_{Total}) * L + SL$$

$$= ([\varepsilon_\lambda^{HbO_2} - \varepsilon_\lambda^{Hb_R}] Hb_{Sat} + \varepsilon_\lambda^{Hb_R}) * L * Hb_{Total} + SL$$

$$= [\varepsilon_\lambda^{HbO_2} - \varepsilon_\lambda^{Hb_R}] Hb_{Sat} * L * Hb_{Total} + \varepsilon_\lambda^{Hb_R} * L * Hb_{Total} + SL$$

To simplify the equation, we can use auxiliary variables:

$$a = Hb_{Sat} * L * Hb_{Total}$$

$$b = L * Hb_{Total}$$

$$c = SL$$

$$\varepsilon_{\Delta\lambda} = \varepsilon_\lambda^{HbO_2} - \varepsilon_\lambda^{Hb_R}$$

Substituting these variables in the equation results in the following:

$$A_{(x,y,\lambda)} = \varepsilon_{\Delta\lambda} * a + \varepsilon_\lambda^{Hb_R} * b + c$$

The coefficients $a$, $b$, and c can be found using linear squares regression. Then Hemoglobin saturation can be found by dividing $a$ by $b$:

$$\frac{a}{b} = \frac{Hb_{Sat} * L * Hb_{Total}}{L * Hb_{Total}} = Hb_{Sat}$$

Multiply $Hb_{Sat}$ by 100 to obtain the percentage of hemoglobin saturation (*see* **Notes 5** and **6**).

### 3.5 Example

The following high-level overview example can be used as guidance for one method of solving the linear regression equation using matrices with Matlab or other similar computing environment (in the Matlab computing environment, matrix operations are performed faster than conditional loop operations).

Create the following vectors and matrices:

$$pixel\_abs = \begin{bmatrix} A(x,y,\lambda_1) \\ \vdots \\ A(x,y,\lambda_n) \end{bmatrix}$$

*pixel _ abs* is a *nx1* vector of absorbance values over the wavelength range for a specific pixel (*x*,*y*) under consideration, where $n =$ the number of wavelengths in the spectral image data set.

$$C = \begin{bmatrix} \varepsilon_{\Delta}(\lambda_1) & \varepsilon_{\mathrm{HbR}}(\lambda_1) & 1 \\ \vdots & \vdots & \vdots \\ \varepsilon_{\Delta}(\lambda_n) & \varepsilon_{\mathrm{HbR}}(\lambda_n) & 1 \end{bmatrix}$$

*C* is a *nx3* matrix where the first column contains the $\varepsilon_{\Delta}(\lambda)$ coefficients, the second column contains the $\varepsilon_{\mathrm{HbR}}(\lambda)$ coefficients, the last column contains ones, and *n* is the number of wavelengths in the spectral image data set.

$A = C^T C$ is a $3 \times 3$ square matrix that results from the matrix multiplication *C* transpose times *C* where *T* is the matrix transpose operator.

$b_{pix} = C^T pixel\_abs$ is a $3 \times 1$ vector resulting from the matrix multiplication of *C* transpose times the *pixel_abs* vector, where *T* is the transpose operator.

$x = A^{-1} b_{pix}$ is the $3 \times 1$ vector resulting from the matrix multiplication of *A* inverse times $b_{\mathrm{pix}}$.

In Matlab, the preferred way to solve this linear system is to use $x = A \backslash b_{pix}$ which employs Gauss-Jordan elimination to solve for the matrix inverse of *A*.

The coefficients for the alternate form of the model equation can be found in the vector *x*, where $x_1 = a$, $x_2 = b$, and $x_3 = c$.

The $R^2$ fit of the regression model to the pixel absorbance data can be compared against a threshold value selected by the user to decide whether to accept the $Hb_{Sat}$ calculation or suppress it as background noise. A procedure to determine the $R^2$ value is as follows:

$$err = \begin{bmatrix} A(x,y,\lambda_1) \\ \vdots \\ A(x,y,\lambda_n) \end{bmatrix} - \left( a * \begin{bmatrix} \varepsilon_{\Delta}(\lambda_1) \\ \vdots \\ \varepsilon_{\Delta}(\lambda_n) \end{bmatrix} + b * \begin{bmatrix} \varepsilon_{\mathrm{HbR}}(\lambda_1) \\ \vdots \\ \varepsilon_{\mathrm{HbR}}(\lambda_n) \end{bmatrix} + c * \begin{bmatrix} 1 \\ \vdots \\ 1 \end{bmatrix} \right)$$

where *err* is a $n \times 1$ vector of the difference between the absorbance spectrum measured at the pixel versus that computed from the regression fit to the data and *a*, *b*, and *c* are the coefficients for the model equation found from the linear regression.

$SSe = sum(err. * err)$ is the error sum of squares; this is a scalar value obtained by elementwise multiplication of the *err* vector (i.e., square the elements of the *err* vector) and then summing the elements of the resulting vector.

$$tot = \begin{bmatrix} Abs(x,y,\lambda_1) \\ \vdots \\ Abs(x,y,\lambda_n) \end{bmatrix} - mean\left( \begin{bmatrix} Abs(x,y,\lambda_1) \\ \vdots \\ Abs(x,y,\lambda_n) \end{bmatrix} \right) \begin{bmatrix} 1 \\ \vdots \\ 1 \end{bmatrix}$$

where *tot* is a $n \times 1$ vector of the absorbance values of a pixel (*x*,*y*) minus the mean absorbance value of the pixel.

$SSt = sum(tot. * tot)$ is the total sum of squares; this this is a scalar value obtained by elementwise multiplication of the *tot* vector (i.e., square the elements of the *tot* vector) and then summing the elements of the resulting vector.

$R2 = 1 - \frac{SSe}{SSt}$ is the $R^2$ value of the fit of the regression model to the data (*see* **Note 7**).

### 3.6 Evaluation of Tumor Areas

To evaluate tumor development, the mouse is imaged (as previously described in Subheading 3.3) on consecutive days. For this example, two set of images (from day 1 to day 5) are obtained from the previous steps: (1) A Gray scale image (Fig. 5a) that corresponds to the transmitted light image, from which structural characteristics (e.g., vascularity) of tissue inside the window chamber can be evaluated. (2) a data image (Fig. 5b) that corresponds to pixelwise mapping of hemoglobin saturation values of blood vessels in the tissue (*see* Subheading 3.4).

#### 3.6.1 Registration

Since the structure of tissue and vascularity is not evident in the data images, the registration is performed in the gray-scale images and then projected to the data images for the purpose of hemoglobin saturation evaluation (*see* **Note 8**). The registration steps are

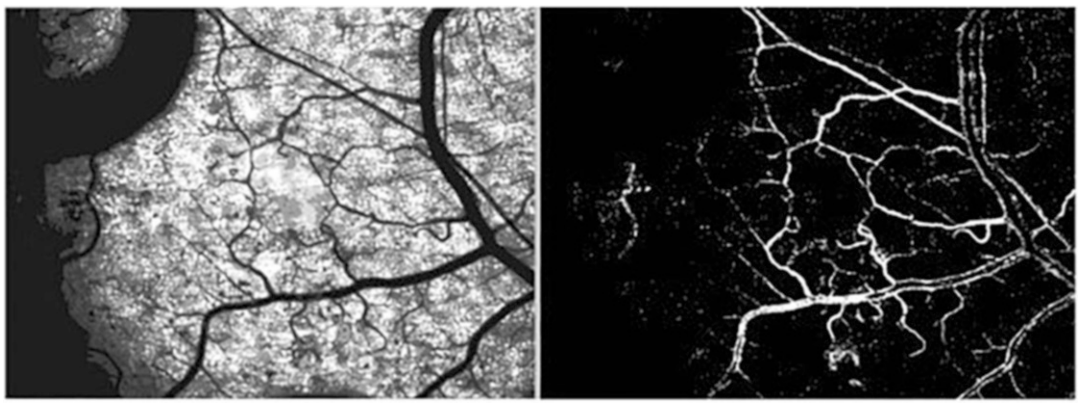

**Fig. 5** (**a**) Gray-scale image showing details of the vasculature of the tissue. (**b**) Data image. The data image contains the hemoglobin saturation values of blood vessels

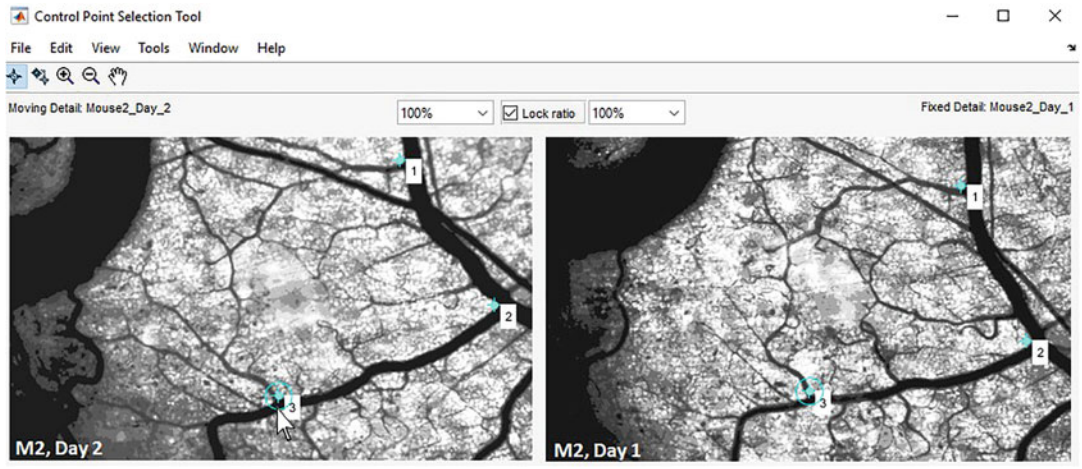


**Fig. 6** Control point selection tool. The image for day one is used as base to register the image for day two

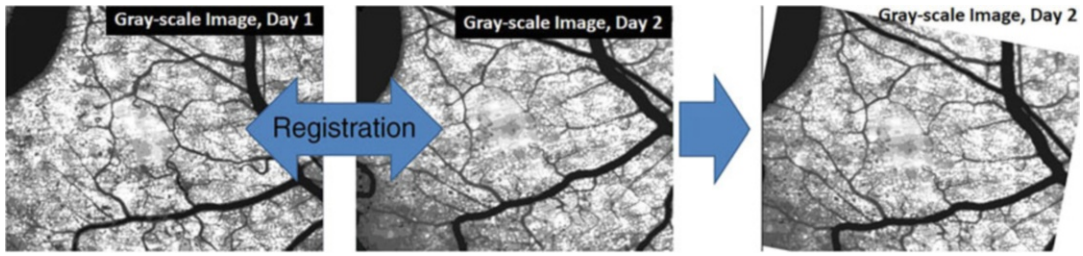


**Fig. 7** Visualization of the registration of image at day 2 with respect to the image at day 1

implemented using the MATLAB functions "fitgeotrans" and "imwarp," and visualized using "imshowpair."

1. Using the MATLAB control point selection tool *cpselect* or other similar application, proceed to select control points for the registration (*see* **Note 9**). In Fig. 6, the coordinates selected in day one will be considered fixed points and the corresponding coordinates for day two will be the moving points for the registration.
2. Using the MATLAB function *fitgeotrans o*r other appropriate application generate the appropriate geometrical transformation based in the control point from the previous step, in our case we used "nonreflective similarity" as transformation type (Fig. 7).

   *"fitgeotrans(fixedPoints, movingPoints,'NonreflectiveSimilarity')"*

   Where the moving points are the corresponding points selected on the image for day 2.
3. Using *imwarp* and *"imshowpair*, we can generate the transformed imaged and compare it with the original.

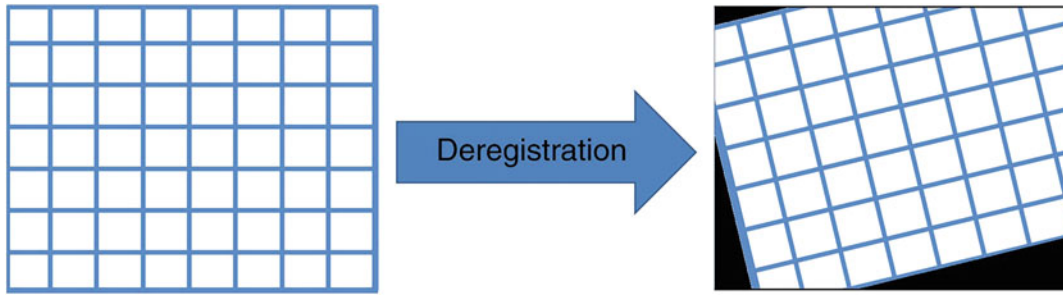


**Fig. 8** A copy of the mesh is deregistered using the spatial transformation provided by *fitgeotrans*

*3.6.2 Segmentation and Mapping*

The segmentation of the images is based on a mesh of 20 × 20 pixel windows with the same dimensions of the base image. Using the control points from the previous step we can reverse the registration process switching their position in *fitgeotrans* function. We call this process *deregistration*.

1. Create a mesh with the same dimensions as the base image with windows of 20 × 20 pixels. Make a copy of the mesh and using *fitgeotrans*, deregistered the copy of the mesh (Fig. 8). Noticed that the controls point are switched in the function *fitgeotrans*.
   *"fitgeotrans(movingPoints, fixedPoints,'NonreflectiveSimilarity')"*
2. The deregistered mesh is overlaid in the unregistered data image for day 2. The original mesh is overlaid in the image for day 1 (Fig. 9).
3. The resulting images from the previous steps are segmented/labeled using the MATLAB functions *bwconncomp* and *labelmatrix* (Fig. 10), (*see* **Note 10**).
4. The labeled image for day 2 is registered using the original control points (Fig. 11).
5. Since the registration is performed using the original control points, the windows of the mesh can be mapped in both images (day 1 and day 2) using the center of mas of each 20x20 widow (Fig. 12). This can be accomplished using the MATLAB function *regionprops*, using the centroid property.
6. The labels of the corresponding regions for each day are stored in a matrix (Regions X Days), for further data analysis. Table 1 shows an example of this matrix (in which the regions and days correspond to the rows and columns of the matrix respectively).

*3.6.3 Classification and Ground Truth*

The tumor location on each day is identified through the tumor cells transfected with reporter genes of red fluorescence protein (RFP).

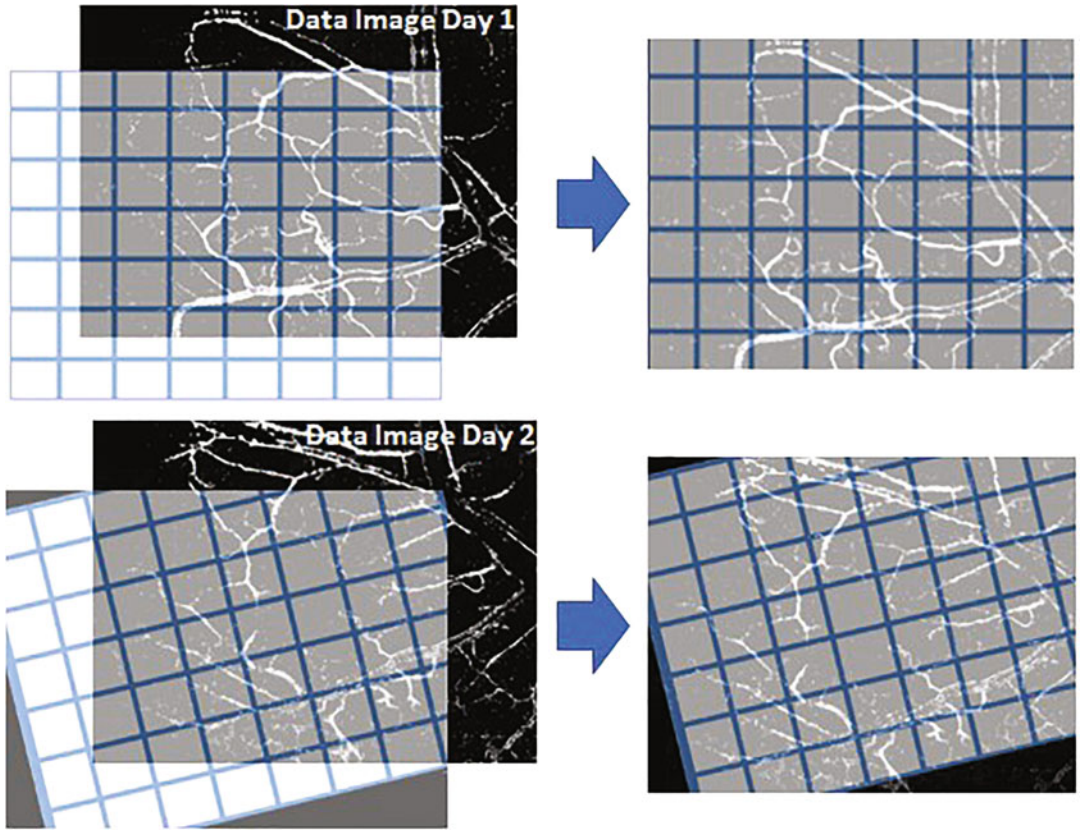


**Fig. 9** The deregistered mesh is overlaid on the unregistered data image for day 2 (lower half), the original mesh is overlaid over the data image for day 1 (upper half)

1. The areas of newly developed tumors every day are determined by subtracting the tumor areas of previous days as follows:

$$T_j^{new} = T_j^{all} - T_j^{new} - T_{(1:j-1)}^{new};\ \ for\ all\ \ \ j > 0$$

where:

$$T_j^{new} = New\ tumor\ areas\ developed\ at\ day\ j$$

$$T_j^{all} = All\ tumor\ areas\ present\ at\ day\ j$$

$$T_{1:j-1}^{all} = All\ tumor\ areas\ form\ day\ 1\ to\ the\ day\ before\ j$$

The vector $T$ represents a one-dimensional (1-D) vector containing the labels of the tumor areas at particular day, for example, the vector $T_5^{all}$ represent all tumor areas found at day five and vector $T_{1:4}^{all}$ represent all tumor areas developed form day 1 to day 4:

$$T_5^{all} = \langle 39\ \ 41\ \ 55\ \ 63\ \ 82\ \ 99\ \ 106\ \ 109\ \ 201 \rangle$$

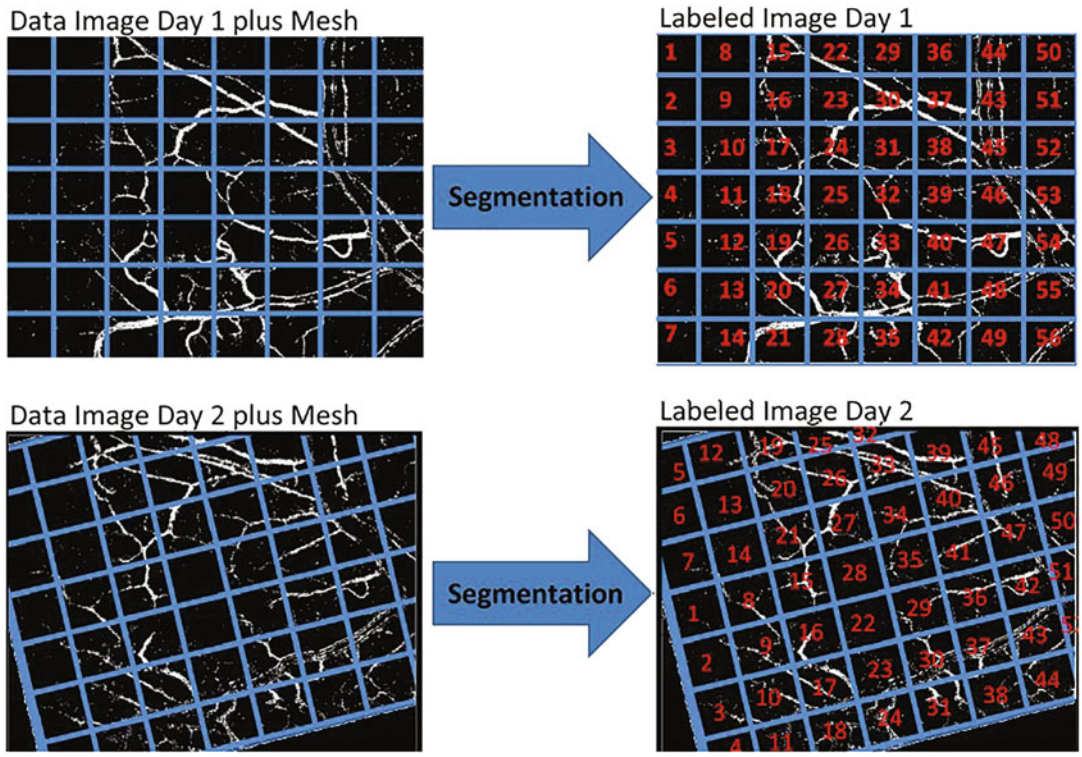


**Fig. 10** The data image for days 1 and 2, are segmented/labeled based upon the overlaid mesh, the numbers in red represent the indices of the connected components of the binary image

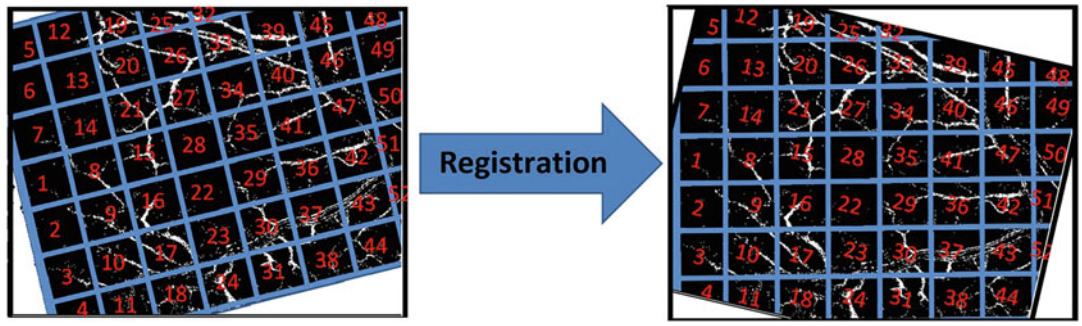


**Fig. 11** The labeled image day 2 is registered using the original control points

$$T_{1:4}^{all} = \langle 39 \quad 55 \quad 63 \quad 99 \quad 109 \quad 201 \rangle$$

$$T_{5}^{new} = T_{5}^{all} - T_{1:4}^{all} = \langle\, 41 \quad 82 \quad 106 \,\rangle$$

In this example, areas 41, 82, and 106 are new areas of tumor developed at day 5 (not present before day 5), and areas 39, 55, 63, 99, 109, and 201 are areas of tumor found at day 5 but developed before day 5.

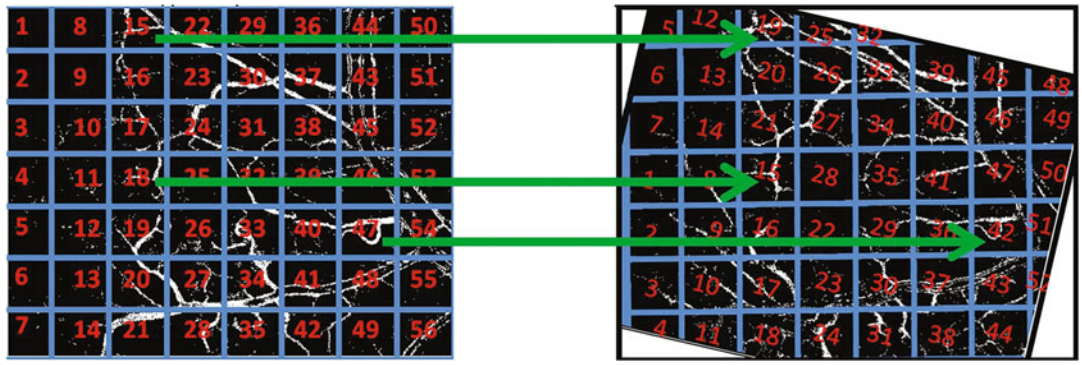

**Fig. 12** Using the center of mass, the windows in the labeled base data image for day 1 on the left and labeled image for day 2 on the right can be mapped. For example, window 47 in day 1 corresponds to window 42 in day 2

**Table 1**
**Sample of the mapped registered regions of the images. For example, region 1688 in day 1 is equivalent to region 1636 on day 2 and region 1442 on day 3, and so on**

| Day 1 | Day 2 | Day 3 | Day 4 | Day 5 |
|---|---|---|---|---|
| 1688 | 1636 | 1442 | 1306 | 1306 |
| 1689 | 1637 | 1443 | 1307 | 1307 |
| 1690 | 1638 | 1444 | 1308 | 1308 |
| 1691 | 1639 | 1445 | 1309 | 1309 |
| 1692 | 1640 | 1446 | 1310 | 1310 |
| 1693 | 1641 | 1447 | 1311 | 1311 |
| 1694 | 1642 | 1448 | 1312 | 1312 |
| 1695 | 1643 | 1449 | 1313 | 1313 |
| 1696 | 1644 | 1450 | 1314 | 1314 |
| 1697 | 1645 | 1451 | 1315 | 1315 |
| 1698 | 1646 | 1452 | 1316 | 1316 |
| 1699 | 1647 | 1453 | 1317 | 1317 |

2. Region classification and ground truth: (Fig. 13): The 20 × 20 pixel windows in the images are classified as *normal* (0), *tumor* (1), or *unknown* (3) for each day. All the windows completely inside the boundary of the area determined by RFP are classified as tumor (*see* **Note 11**). All the other regions are classified by default as unknown (3).
3. The classification of each region (e.g., normal, tumor, or unknown) is stored in a matrix similar to the mapped registered regions using day 1 as the reference for the region label (Table 2).

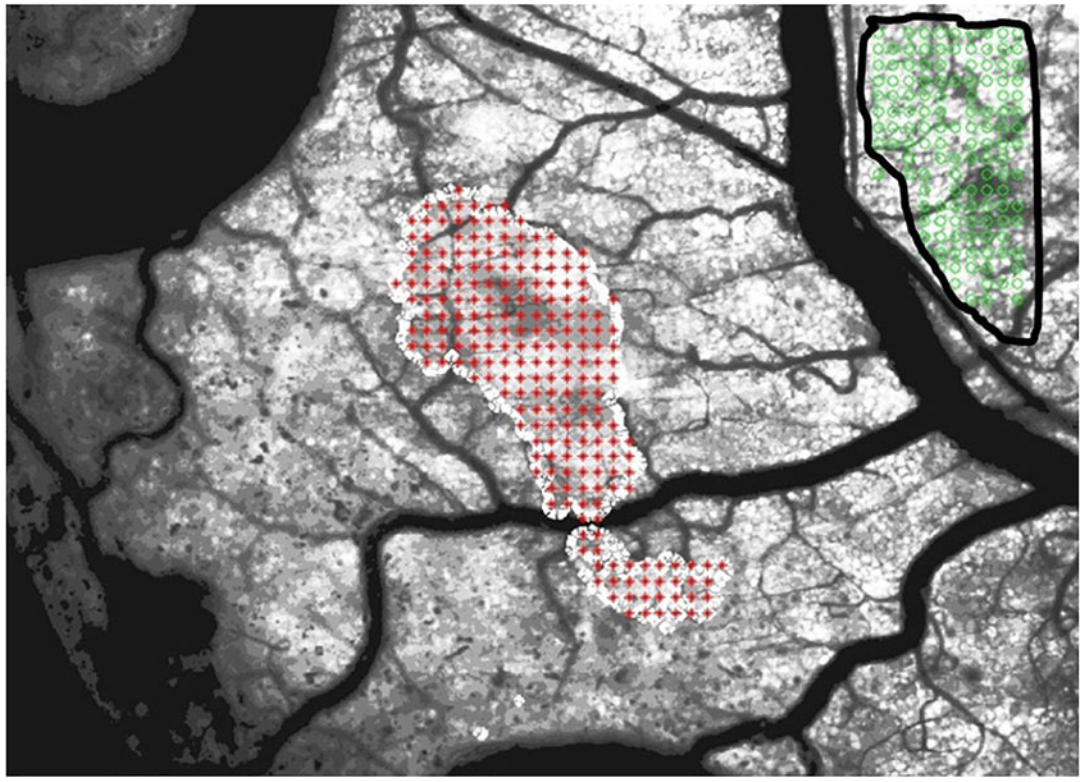

**Fig. 13** Selection of tumor (red) and normal (green) areas. Each area corresponds to 20 × 20 pixels window

**Table 2**
**Sample of classes assigned to the 20 × 20 pixels regions. For example, region reference 1692 is classified as unknown for days one and two, and classified as tumors for days three, four, and five (since reference region 1692 corresponds to regions 1692, 1640, 1446, 1310, and 1310 for days one, two, three, four, and five respectively in Table 1)**

| Region # | Day 1 | Day 2 | Day 3 | Day 4 | Day 5 |
|---|---|---|---|---|---|
| 1688 | 1 | 1 | 1 | 1 | 1 |
| 1689 | 3 | 1 | 1 | 1 | 1 |
| 1690 | 3 | 1 | 1 | 1 | 1 |
| 1691 | 3 | 1 | 1 | 1 | 1 |
| 1692 | 3 | 3 | 1 | 1 | 1 |
| 1693 | 3 | 3 | 3 | 1 | 1 |
| 1694 | 3 | 3 | 3 | 1 | 1 |
| 1695 | 3 | 3 | 3 | 1 | 1 |
| 1696 | 3 | 3 | 3 | 1 | 1 |
| 1697 | 3 | 3 | 3 | 3 | 1 |
| 1698 | 3 | 3 | 3 | 3 | 3 |
| 1699 | 3 | 3 | 3 | 3 | 3 |

**Table 3**
**Example parameter $\mu$ (derived from hemoglobin saturation values) for regions 1688 to 1699. Zero values represent regions with no valid reading of hemoglobin saturation. As in Table 2, the region label from day one is used as reference.**

| Region | Day 1 | Day 2 | Day 3 | Day 4 | Day 5 |
|---|---|---|---|---|---|
| 1688 | 13.8604 | 44.6940 | 0.0000 | 55.7158 | 31.2408 |
| 1689 | 17.2185 | 36.8673 | 43.7655 | 52.5014 | 0.0000 |
| 1690 | 11.6666 | 27.1354 | 43.0212 | 0.0000 | 0.0000 |
| 1691 | 12.1686 | 32.5329 | 40.7397 | 0.0000 | 7.2751 |
| 1692 | 20.1976 | 29.3611 | 41.2858 | 49.1509 | 0.0000 |
| 1693 | 25.8735 | 0.0000 | 41.2630 | 26.9634 | 30.1315 |
| 1694 | 15.6661 | 31.8931 | 42.3157 | 35.3762 | 0.0000 |
| 1695 | 25.8520 | 36.0995 | 51.7541 | 54.9333 | 49.4275 |
| 1696 | 28.1438 | 50.2987 | 73.0799 | 58.8295 | 58.4680 |
| 1697 | 34.0566 | 29.7618 | 39.2229 | 58.2234 | 56.6358 |
| 1698 | 34.4324 | 23.9875 | 42.2999 | 54.9324 | 63.9347 |
| 1699 | 27.7016 | 25.6562 | 17.2053 | 0.0000 | 72.1146 |

*3.6.4 Region Features*

For each region/window $r$ of $20 \times 20$ pixels in an image at day $t$, we fit, using maximum-likelihood estimation, a logistic distribution to the histogram of the hemoglobin saturation values of its pixels. Recall that the probability density function of the logistic distribution with location (mean) $\mu$ and scale $s$ parameters is given by the following equation:

$$p(x|\,\mu, s) = \frac{e^{-\frac{(x-\mu)}{s}}}{s\left[1 + e^{-\frac{(x-\mu)}{s}}\right]^2}$$

The estimated location parameter $\mu_t^{(r)}$ of this distribution is used as a feature of the region $r$ at day $t$ (*see* **Note 12**). The $\mu_t^{(r)}$ feature for each region $r$ for every day $t$ is stored in a matrix along with the corresponding matching region (Table 3).

This $\mu_t^{(r)}$ hemoglobin saturation map combination with the registered regions map can now be used to study hemoglobin saturation variations and tumor progression in different applications.

*3.6.5 Example*

As a proof of concept to demonstrate utility of this procedure [15], we use the hemoglobin saturation values represented as the $\mu_t^{(r)}$ feature to forecast new development of tumor areas in future days. For example, by Table 2 we know that regions 1696 and 1697 are unknown areas for day 1, 2, and 3. Can we forecast if the tumor will develop in these areas for the next day (day 4) using only the

hemoglobin saturation values of days 1, 2, and 3? To answer this question, notice that the hemoglobin saturation values in region 1696 constantly increases from 28.1 to 73.0 during days 1, 2, and 3, in contrast, the values for region 1697 are substantially less changed. Since as we stated before hemoglobin saturation increases often precede the formation of tumor, this steady increase of hemoglobin saturation may indicate that region 1696 will develop tumor in day 4. To test this hypothesis, we have developed a delta feature ($\delta$) that integrate accumulative values of hemoglobin saturation overtime to forecast tumor development in future days.

We define the delta feature $\delta^{(r)}_{t_2 \to t_f}$ (or simple $\delta$) feature of a region r for a time period [ $t_s$, $t_f$] as follows:

$$\delta^{(r)}_{t_s \to t_f} = \frac{\sum_{t=t_s}^{t_f - 1} [\mu^{(r)}_{t+1} - \mu^{(r)}_{t}]}{\mu^{(r)}_{t_f - 1}} = \frac{\mu^{(r)}_{t_f} - \mu^{(r)}_{t_s}}{\mu^{(r)}_{t_f - 1}}$$

where $t_s$ and $t_f$ is the starting and final day respectively, and where and where the day a prediction is to be made is no earlier than $t_f$. Any region with a missing a $\mu^{(r)}_t$ reading between $t_s$ and $t_f$ is omitted from further analysis.

The $\delta$ feature for each region is stored in a matrix using the region's day 1 label as a reference, as shown in Table 4.

**Table 4**
**Example of $\delta$ features for regions 1688 to 1699. Any area missing a $\mu^{(r)}_t$ reading between days one and three is marked as NaN in all calculations of $\delta$ (e.g., areas 1688 and 1693). Column 3 [$\delta$ (2, 3)] is used for forecasting the occurrence of tumor regions in day 5 in this example.**

| Region | $\delta$(1, 2) | $\delta$(2, 3) | $\delta$(3, 4) | $\delta$(4, 5) |
|---|---|---|---|---|
| 1688 | NaN | NaN | NaN | NaN |
| 1689 | 1.141138 | 0.720068 | 0.806182 | NaN |
| 1690 | 1.325901 | 1.155489 | NaN | NaN |
| 1691 | 1.673515 | 0.878224 | NaN | NaN |
| 1692 | 0.45369 | 0.718235 | 0.70129 | NaN |
| 1693 | NaN | NaN | NaN | NaN |
| 1694 | 1.035799 | 0.835592 | 0.465785 | NaN |
| 1695 | 0.396392 | 0.717522 | 0.561913 | 0.429166 |
| 1696 | 0.787204 | 0.893385 | 0.419892 | 0.515459 |
| 1697 | –0.12611 | 0.173589 | 0.616141 | 0.387803 |
| 1698 | –0.30334 | 0.327984 | 0.484636 | 0.537067 |
| 1699 | –0.07384 | –0.40911 | NaN | NaN |

We assessed the capability of the $\delta$ feature for forecasting the occurrence of tumor by conducting the following experiment. We evaluate 97 normal regions along with 176 tumor regions and 61 normal regions along 52 tumor regions from two different mice. These regions are within valid $\mu_t^{(r)}$ readings in days 1–3. The $\delta_{t_1 \to t_3}^{(r)}$ feature is used to classify regions as tumor/normal in day 5 by using a logistic regression model for each mouse:

$$logit(odds\ ratio\ of\ tumor\ in\ region\ r\ at\ day\ 5) \sim 1 + \delta_{t_1 \to t_3}^{(r)}$$

Using this methodology accumulating the hemoglobin saturation values from day 1 to day 3 in the delta feature $\delta_{t_1 \to t_3}^{(r)}$ are able to forecast tumor areas at day 5 with an AUC of 0.90 and 0.85 in those two different mice.

## 4 Notes

1. Extinction coefficient data ($\varepsilon_{\mathrm{HbO2}}$, $\varepsilon_{\mathrm{HbR}}$) should be obtained on the spectral imaging system that will be used in experiments. Data from the literature or data obtained on a spectrophotometer should not be used. This is because spectral imaging systems can have passbands that vary significantly with wavelength and this can alter the effective extinction coefficients measured on these systems from those in the literature and obtained on spectrophotometers with fixed passbands.
2. It is assumed that the image processing and analysis software can recognize and load images into the computing environment such that the image data can be treated as mathematical arrays for calculations, processing, and analysis.
3. It is possible that there is no significant wavelength-dependent variability in the flatfield images for the spectral range of image acquisition. In this event, it is possible that a single flatfield image at a selected wavelength (e.g., one in the middle of the wavelength range) can be used to satisfactorily correct all the images rather than having a distinct flatfield image for each wavelength.
4. Check that the hemoglobin saturation values are in an acceptable range (e.g., 0% to 100%). Due to noise, it may be desirable to extend the acceptable range to something like −5% to 105% and then assign values less than 0% the value of 0% and values greater than 100% assign the value of 100%.
5. Flag pixels with $Hb_{Sat}$ values that are out of the acceptable range or have an unacceptable regression fit so that they can be removed from consideration when making pseudocolor $Hb_{Sat}$ maps and when calculations of $Hb_{Sat}$ in ROIs are performed in other analyses.

6. The pixel $Hb_{Sat}$ values can be saved in a file that can be used to create pseudocolor image maps of blood vessel hemoglobin saturation and for subsequent ROI statistical analysis of distinct ROI locations.
7. Check that the $R^2$ value for the fit of the regression is acceptable (e.g., $R^2$ values $<0.9$ indicate an unacceptable fit).
8. The images are registered using the previous day image as a base. For example, image for day 2 is registered based in image taken at day 1; image day 3 is registered based in image day 2 and so on.
9. The control points are pixel coordinates of similar features in both images.
10. Bwconncomp is run on the whole image.
11. Since changes in hemoglobin saturation preceded the formation of the tumor, the normal regions are selected in an area far away from the original inception of the tumor cells.
12. We opted for the logistic distribution after a visual inspection of quality of fit of distributions to the histograms of the hemoglobin saturation values of tumor and normal regions.

## Acknowledgments

The data used in the examples is collected in the laboratory of Mark W. Dewhirst (Duke University, Durham, North Carolina). The authors are grateful for the permission to repurpose the data for use in this project.

### References

1. Lücker A et al (2018) The relation between capillary transit times and hemoglobin saturation heterogeneity. Part 2: capillary networks. Front Physiol 9:1296
2. Hadjistassou C, Moyle K, Ventikos Y (2016) Reproducing the hemoglobin saturation profile, a marker of the blood oxygenation level dependent (BOLD) fMRI effect, at the microscopic level. PLoS One 11(3):e0149935
3. Carpenter CM et al (2007) Image-guided optical spectroscopy provides molecular-specific information in vivo: MRI-guided spectroscopy of breast cancer hemoglobin, water, and scatterer size. Opt Lett 32(8):933–935
4. Cheng X et al (2003) Breast cancer detection by mapping hemoglobin concentration and oxygen saturation. Appl Opt 42 (31):6412–6421
5. Moy AJ et al (2011) Wide-field functional imaging of blood flow and hemoglobin oxygen saturation in the rodent dorsal window chamber. Microvasc Res 82(3):199–209
6. Brooksby B et al (2006) Imaging breast adipose and fibroglandular tissue molecular signatures by using hybrid MRI-guided near-infrared spectral tomography. Proc Natl Acad Sci U S A 103(23):8828–8833
7. Palmer GM et al (2006) Monte Carlo-based inverse model for calculating tissue optical properties. Part II: application to breast cancer diagnosis. Appl Opt 45(5):1072–1078
8. Chance B et al (2005) Breast cancer detection based on incremental biochemical and physiological properties of breast cancers: a six-year, two-site study. Acad Radiol 12(8):925–933
9. Sorg BS et al (2005) Hyperspectral imaging of hemoglobin saturation in tumor

microvasculature and tumor hypoxia development. J Biomed Opt 10(4):44004

10. Anderson PG et al (2016) Optical mammography: bilateral breast symmetry in hemoglobin saturation maps. J Biomed Opt 21 (10):101403
11. Anderson PG et al (2015) Broadband optical mammography: chromophore concentration and hemoglobin saturation contrast in breast cancer. PLoS One 10(3):e0117322
12. Heu F et al (2013) Effect of low-level laser therapy on blood flow and oxygen- hemoglobin saturation of the foot skin in healthy subjects: a pilot study. Laser Ther 22(1):21–30
13. Aliano KA, Stavrides S, Davenport T (2013) The use of hemoglobin saturation ratio as a means of measuring tissue perfusion in the development of heel pressure sores. Surg Technol Int 23:69–71
14. Moeller BJ et al (2004) Radiation activates HIF-1 to regulate vascular radiosensitivity in tumors: role of reoxygenation, free radicals, and stress granules. Cancer Cell 5(5):429–441
15. Ossandon MR et al (2014) Forecasting new development of tumor areas using spatial and temporal distribution profiles of hemoglobin saturation in a mouse model. J Med Imaging 1(1):014503
16. Malinauskas RA (1997) Plasma hemoglobin measurement techniques for the in vitro evaluation of blood damage caused by medical devices. Artif Organs 21(12):1255–1267
17. Kahn SE, Watkins BF, Bermes EW Jr (1981) An evaluation of a spectrophotometric scanning technique for measurement of plasma hemoglobin. Ann Clin Lab Sci 11(2):126–131
18. Shotton D (1993) An introduction to digital image processing and image display in electronic light microscopy. In: Shotton D (ed) Electronic light microscopy—techniques in modern biomedical microscopy. Wiley-Liss, New York, pp 39–70
19. Shonat RD et al (1997) Near-simultaneous hemoglobin saturation and oxygen tension maps in mouse brain using an AOTF microscope. Biophys J 73:1223–1231

# Chapter 11

# Automated Multidimensional Nanoscale Chromatography for Ultrasensitive Targeted Mass Spectrometry

**Paolo Cifani and Alex Kentsis**

## Abstract

Recent advances in nanoscale separations and high-resolution mass spectrometry permit highly sensitive and accurate analyses of complex protein mixtures. Here, we describe improved methods for nanoscale multidimensional chromatography coupled to targeted mass spectrometry (tMS) to achieve ultrasensitive quantification of peptides in complex proteomes. The presented chromatographic system consists of capillary strong-cation exchange (SCX) chromatography column, from which peptides are eluted directly onto high-resolution reversed-phase (RP) analytical columns and nanoelectrospray ion source. SCX pre-fractionation is used to separate phosphorylated peptides, permitting their ultrasensitive quantification. Resolution and robustness of this chromatographic system, together with the orthogonality of SCX and RP separations, permit scheduling of large panels of targeted MS assays. This design also enables seamless scaling to three-dimensional separations, thereby enabling large-scale, ultrasensitive quantitative proteomics.

**Key words** Mass spectrometry, Proteomics, Chromatography, Reversed phase, Strong cation exchange, Multidimensional chromatography, Accumulated ion monitoring, Nanoscale separation, Electrospray ionization

## 1 Introduction

Targeted mass spectrometry (tMS) allows sensitive, specific, and robust peptide quantification for proteomic studies [1, 2]. Instrumentation for tMS usually includes reversed phase chromatographic separation systems, hyphenated to mass spectrometers via electrospray ionization (ESI) sources [3]. This instrumentation permit to resolve peptides based on their hydrophobicity, ionize them to gas phase, isolate the corresponding ions, and measure their ion current. Sensitivity and comprehensiveness of tMS strongly depends on chromatographic resolution, as the number of coeluting targeted peptides determines the duty cycle of the method, and nearly isobaric contaminant molecules coeluting

Miguel R. Ossandon et al. (eds.), *Biomedical Engineering Technologies: Volume 1*, Methods in Molecular Biology, vol. 2393, https://doi.org/10.1007/978-1-0716-1803-5_11, 

with the targets of interest reduce the sensitivity of their detection [4]. High-resolution reversed phase separations have been achieved using ultralong and narrow bore column geometries, and low particle diameter or monolithic stationary phases [5, 6]. Proteome prefractionation using separation modes orthogonal to the on-line acidic reversed phase chromatography exponentially increases the overall resolution, and permits to improve exposure of specific classes of analytes, such as chemically modified peptides [7, 8]. However, most offline prefractionation methods require milligram scale sample amounts, and are thus not suitable for the analysis of rare cell populations or other minute specimens such as diagnostic biopsies. To overcome this limitation, we and others recently developed automated and nanoscale prefractionation achieved using multidimensional chromatographic platforms for ultradeep data dependent proteome discovery [9, 10].

Here we describe a chromatographic system that enables automated multidimensional separation of tryptic peptides combining high-resolution strong-cation exchange (SCX) chromatography to capillary reverse phase separation on-line with ESI emitter. While in principle this platform is compatible with any ESI-MS implementation, the high-resolution of peptide separation makes it ideal to be coupled with accumulated ion monitoring (AIM) analysis using ion trap instruments [4]. Nonetheless, the method is fully compatible with other tMS implementations such as selected and parallel reaction monitoring [1, 2], as the reproducibility of separation enables robust assay scheduling. The SCX chromatographic mode was chosen because of its efficiency in resolving phosphorylated peptides, and because the mobile phases used are volatile and compatible with subsequent reversed phase separation and ESI. The method here described is optimized to improve resolution and reproducibility of prefractionation using SCX stepwise elution and long linear reversed phase separations, and is therefore amenable for tMS applications [4]. SCX fractionation is performed in a capillary format, with elution obtained using an optimized step gradient of ammonium acetate or formate, delivered from autosampler vials and driven by an isocratic pump. While traditionally SCX elution used a gradient of potassium chloride in phosphate buffers, we found that this approach is less desirable for capillary chromatography because nonvolatile salts may precipitate, thus clogging capillary lines and electrospray ion sources. The risk of precipitation of SCX elution buffer was highly reduced by using volatile cations and by periodically flushing the injection system and relevant HPLC components with 0.1% formic acid. Moreover, organic solvent was omitted in the SCX buffers to improve peptide retention by the reversed phase trap column.

A second issue considered was column geometry, as this parameter is critical to achieve adequate resolution. While short and wide-bore (>150 μm inner diameter x <3 cm length) trap-like columns

are desirable because of their low resistance and robustness, we found this geometry to be not amenable for high-resolution SCX. Instead, well resolved and reproducible SCX separation were achieved using 25 cm × 100 μm inner diameter columns. Beside column geometry, elution volumes are critical to achieve efficient chromatographic separation using step gradients. When the volume of elution buffer used for step elution substantially exceeds the volume of the column, significant mass elution is often observed, resulting in decreased chromatographic resolution. It is important to note that the volumes of mobile phase necessary to drive samples and SCX buffers through the chromatographic lines may also contribute to gradient-independent mass elution. To alleviate this, the chromatographic method here described minimizes the volume of mobile phase driven through the SCX column. Finally, as variable volumes of SCX elution buffer reduce reproducibility of the separation, we implemented a metered injection of salt plugs obtained by first filling the injection loop entirely with an excess of elution buffer, then delivering the content of the loop using the isocratic pump to equilibrate the lines before and after the SCX column, and finally including the SCX column in the flow-path for the exact time required to deliver the volume element. Once the required volume of elution buffer has been delivered, the loop is excluded from the flow path to reduce mass elution.

Importantly, the chromatographic configuration here described enables to bypass the SCX column to load peptide directly on the reversed phase trap column, and thus to omit sample prefractionation without any remodeling of the capillaries. This feature permits to switch between single- and two-dimensional separation without physically reconfiguring the chromatographic components.

## 2 Materials

### 2.1 Reagents

1. Formic Acid 99+% (Thermo Scientific).
2. Acetonitrile Optima LC/MS grade (Fisher Scientific).
3. Water Optima LC/MS grade (Fisher Scientific).
4. Methanol LC/MS grade (Honeywell).
5. Formamide (Sigma Life Science).
6. Ammonium hydroxide (Sigma-Aldrich).
7. Ammonium formate (Sigma-Aldrich).
8. Ammonium bicarbonate (Sigma-Aldrich).
9. Dithiothreitol (Sigma Life Science).
10. Iodoacetamide (Sigma Life Science).
11. Guanidine Hydrochloride (Sigma Life Science).

12. LysC protease (Wako Pure Chemical Industries, part nr. 125–05061).
13. Porcine trypsin protease, sequencing grade (Promega, part nr. V5111).
14. Bovine Serum Albumin (Sigma Life Science).
15. Casein (Sigma Life Science).
16. KaSil potassium silicate solution (PQ Corporation, part nr. COS.301341).
17. SCX stationary phase: Polysulfoethyl A 5 μm, 200 Å particles (PolyLC, Part nr. 410.992.5400).
18. Trap column stationary phase: POROS10 R2 reversed phase 10 μm, 2000 Å particles (Applied Biosystems, part nr. 1-1118-02).
19. Analytical column stationary phase: ReproSil-Pur 120 C18-AQ, 1.9 μm particles (Dr. Maisch GmbH, part nr. r119.aq.).
20. Compressed High purity helium, with pressure regulator manifold.
21. PhoStop phosphatase inhibitor tablets (Roche Applied Science, part nr. 04906845001).

### 2.2 Consumables

1. 1.7 ml Maxymum Recovery tubes (Axygen, part nr. MCT-175-L-C).
2. 2 ml glass ampoules, flat bottom (Kimble Chase, part nr. 60940A 2).
3. Fused silica with 75 μm inner diameter (ID) and 360-μm outer diameter (OD) (Polymicro, cat. no. TSP075375).
4. Fused silica with 150-μm ID and 360-μm OD. (Polymicro, cat. no. TSP150375).
5. Fused silica with 100-μm ID and 360-μm OD. (Polymicro, cat. no. TSP100375).
6. Fused silica with 50-μm ID and 360-μm OD. (Polymicro, cat. no. TSP050375).
7. Fused silica with 20-μm ID and 360-μm OD. (Polymicro, cat. no. TSP020375).
8. Integrated ferrule/nut (Valco, part nr. C360NFPK).
9. 0 dead volume metal unions, 50-μm ID (Valco, part nr. C360UFS2).
10. Fitting ferrules 1/32OD (SCIEX, part nr. 910-00087).
11. Nuts 1/32 OD (SCIEX, part nr. 910-00085).
12. Sleeves, PEEK, 1/32OD, .015″ID, (SCIEX, part nr. 910-00088).

13. Quick mount tee, 0 dead-volume 50-μm ID (Valco, part nr. C360QTPK2).
14. Glass filters for solvent inlet, 2 μm (Agilent, part nr. 5041-2168).
15. Autosampler vials.
16. Autosampler caps.
17. Magnetic stirrer 3 mm (Sigma Aldrich).
18. ESI uncoated silica emitters, tip 10 μm ID (New Objective, part nr. FS360-20-10-D-20).
19. C18 solid phase extraction macro spin column (Nest Group, part nr. SMM SS18V).

### 2.3 Equipment

1. Silica capillary cutter.
2. Optional: silica capillary end polishing station.
3. Thermostated heating block.
4. Vortex mixer.
5. Pressure vessel for capillary packing, equipped with gas manifold.
6. Magnetic stirrer.
7. Bunsen gas burner.
8. Silica capillary laser puller P200 (Sutton instruments).
9. Nano HPLC system (Eksigent nanoLC400).
10. Thermo Fusion mass spectrometer (Thermo Scientific).
11. Picoview ESI ion source (New Objective).
12. Computer, with MaxQuant 1.5 and related software components.

## 3 Methods

The chromatographic setup (Fig. 1) was designed for a chromatographic system including two 10-port rotary valves and one 6-port valve, along with one autosampler, one binary nano pump (flow rate range 100–1000 nl/min), and one isocratic micropump (flow rate range 0.5–10 μl/min). In our setup, the final reverse phase column is in line with a nanoelectrospray ion source, and thus with a high-resolution mass spectrometer capable of analyzing both precursor and fragment ions.

In this system, solution in autosampler vials are initially aspirated in an element of peek tubing (10 μl volume), and then delivered by the isocratic pump either to the SCX column or directly to the RP trap column. The flow-through from the SCX column may be routed either to the trap column, thus loading for

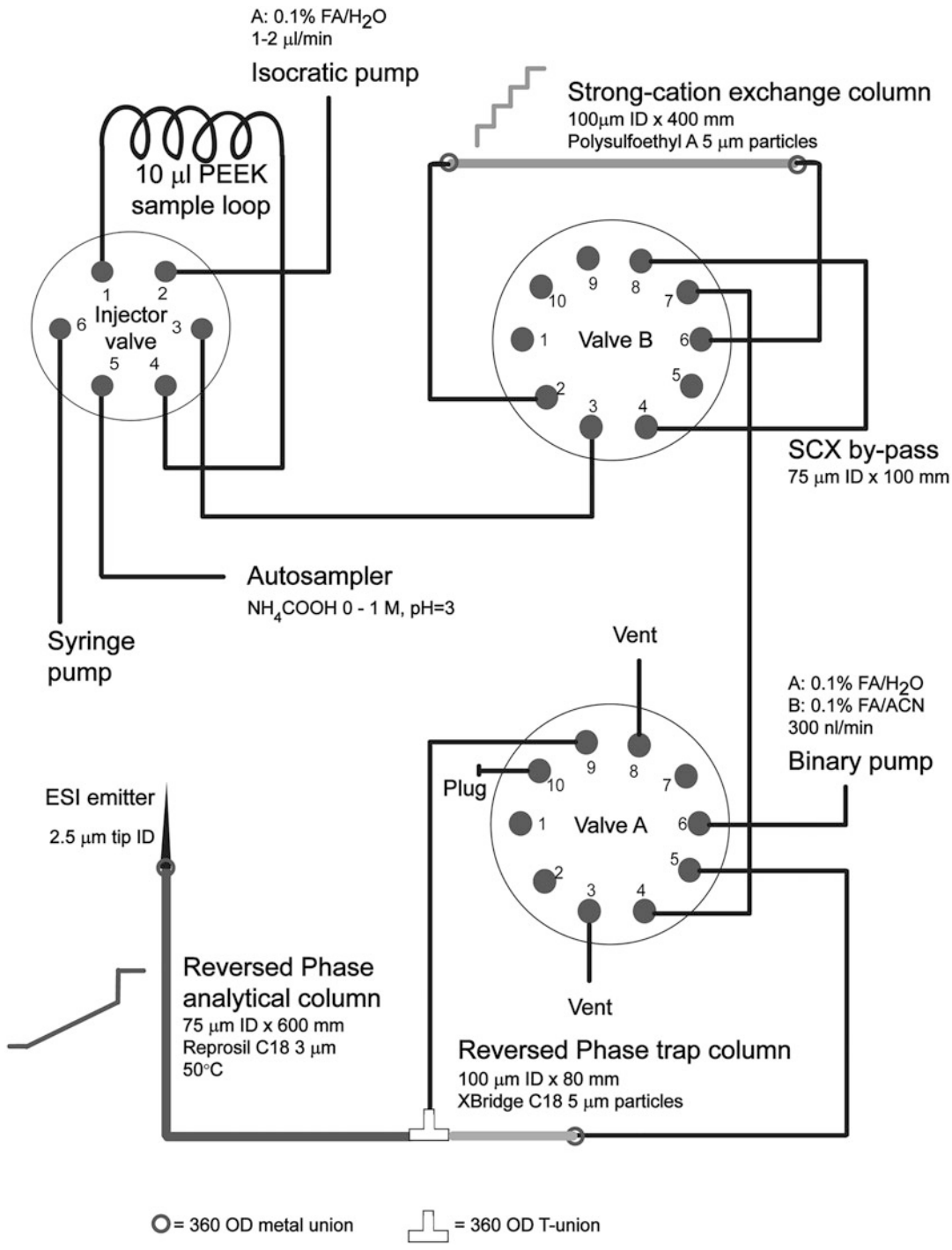


**Fig. 1** Overview of the chromatographic system. Schematic showing the configuration of the capillary lines and columns, and other key components, required for SCX-RP separation

the subsequent reverse phase, or to waste, as in the case of SCX column regeneration.

For final reverse phase chromatography, we adopted a vented setup in which peptides are loaded at a relatively high flow rate on a trap column and coincidentally purified, while the flow-through is directed to waste. Once the trap column is put online with the analytical column, peptide separation is obtained by a gradient of acetonitrile elution.

### 3.1 Columns Preparation

1. Preheat the block to 95 °C.
2. In a clean Axygen tube mix 180 µl K silicate with 20 µl formamide.
3. Vortex and incubate for 5 min at room temperature.
4. Use the silica cutting tool to cut.
   (a) A 1 m piece of 75 µm ID silica capillary.
   (b) A 30 cm piece of 100 µm ID capillary.
   (c) A 1 m piece of 100 µm ID capillary.
5. Keeping the capillary almost horizontal, dip one end into the silicate solution until the liquid flows into the lumen for 2–3 cm (15–30 s).
6. Position the liquid-filled end of the capillary under the heating block and incubate for 1 h at 95 °C to polymerize silicate [11].
7. Using the silica capillary cutter, cut the fritted end to obtain a 2 mm frit.
8. Optional: inspect the fritted end to verify optimal cut and/or polish the end using appropriate abrasive sandpaper.
9. Dissolve stationary phases in methanol, in clean glass ampoules.
10. Wash particles three times in methanol (let silica particles sediment to the bottom of the vial, carefully aspirate the remaining methanol before resuspending the particles in fresh methanol).
11. Fill fritted capillary using the pressure vessel. Regulate helium pressure to <1500 psi (140 bar) and <500 psi (35 bar) for 75 µm ID and 100 µm ID columns, respectively.
    (a) Analytical RP column: 75 µm ID.
    (b) SCX column and reversed phase trap column: 100 µm ID.
12. Pack reversed phase columns. Mount the columns onto the HPLC outlet and drive 10 column volumes (CV) of 0.1% formic acid (FA) in 5% acetonitrile (ACN) in water, followed by 10 CV 0.1% FA in 85% ACN in water. Repeat ten times and verify that pressure remains stable for at least 1 h under continuous operation at fixed composition and flow rate.

13. Pack SCX column. Mount the columns onto the HPLC outlet and drive 10 column volumes (CV) of 0.1% formic acid (FA) in water, progressively increasing the flow rate from 0.1 to 0.5 μl/min. Avoid using organic solvent. Verify that pressure remains stable for at least 1 h under continuous operation at fixed composition and flow rate.
14. Visually inspect the columns to ensure homogenous packing of the stationary phases.
15. Insert the open side of each column into an integrated ferrule, and cut the column to the final length, immediately before mounting them:
    (a) SCX column: 400 mm.
    (b) RP trap column: 80 mm.
    (c) RP analytical column: 600 mm.

### 3.2 Assembly of the Chromatographic Setup

1. Assemble the chromatographic setup as described in Fig. 1. All silica capillaries used for connections are 50 μm ID.
2. Prepare LC mobile phases:
    (a) Buffer A: 0.1% FA in water.
    (b) Buffer B: 0.1% FA in acetonitrile.
    (c) Needle wash: 50% methanol in water

    Mobile phases should be prepared in light-protected clean glass bottles, and mobile phase line should be provided with glass filters.
3. Set column heater to 50 °C and wait for temperature to stabilize. CAUTION: Prolonged exposure to temperatures >65 °C may accelerate degradation of silica-based stationary phases.
4. Monitoring the backpressure, verify correctness of flow-path and absence of leaks. Typical pressures are as follows (note that pack pressure may vary by up to 15% because of frit features and environmental temperature).

| Columns tested | Flow rate (buffer A) | Driving pump | Injector valve position | Valve A position | Valve B position | Expected pressure (psi) |
|---|---|---|---|---|---|---|
| SCX | 0.5 μl/min | Isocratic | 1–2 | 1–2 | 1–2 | 5000 |
| Trap RP | 2 μl/min | Isocratic | 1–2 | 1–10 | 1–10 | 500 |
| Analytical + trap RP | 300 nl/min | Binary | NA | 1–10 | 1–2 | 7000 (50 °C)<br>9000 (25 °C) |
| SCX + trap RP | 0.5 μl/min | Isocratic | 1–2 | 1–10 | 1–2 | 5500 |
| SCX + trap RP + loop | 0.5 μl/min | Isocratic | 1–6 | 1–10 | 1–2 | 5500 |

5. Prepare elution solutions, mixing 0.1% formic acid (pH = 2.8) and 1 M ammonium formate–0.1% formic acid (pH = 2.8). Prepare high-pH elution/reconditioning buffer, titrating 1 M ammonium formate solution with $NH_3OH$ to obtain pH = 9. Since ammonium formate is volatile, solutions in autosampler vials should be replaced weekly. Stock solution should be kept in clean glass bottles and refrigerated. Ammonium formate powder should be stored in a desiccator cabinet. Suggested elution solution concentrations are as follows.

| Fraction number | Ammonium formate (mM) | pH | Expected eluted peptides |
|---|---|---|---|
| 1 | 0 | 3 | $z = 1$ and phosphorylated |
| 2 | 80 | 3 | $z = 1$ and phosphorylated |
| 3 | 200 | 3 | $z = 2$ |
| 4 | 1000 | 3 | $z = 3$–4 |
| 5 | 1000 | 9 | $z > 4$ |

### 3.3 Programming the Liquid Chromatographer Methods

The following HPLC programs are optimized for an Eksigent nanoLC400 instrument, with the setup described.

1. Program 1: SCX sample load (low-resolution SCX elution).

| # | Command | Description |
|---|---|---|
| 1 | Initialize | Autosampler device |
| 2 | Valve | Switch injection valve to load (6-1) |
| 3 | Valve | Switch valve A to load (1–10) |
| 4 | Valve | Switch valve B to SCX (1–10) |
| 5 | Wash | Prewash needle using washing buffer |
| 6 | Wait | For binary pump ready to start |
| 7 | Wait | For isocratic pump ready to start |
| 8 | Get sample | 5 µl pick up, 13.6 µl: 2 mm from bottom* |
| 9 | Valve | Switch injection valve to inject (1, 2) |
| 10 | Start | Start isocratic pump (1 µl/min buffer A, 20 min) |
| 11 | Wait | For isocratic pump injection complete |
| 12 | Start | Start binary pump (see below) |
| 13 | Valve | Switch valve A to inject (1, 2) |
| 14 | Wash | Prewash needle using washing buffer |
| 15 | Wait | For binary injection complete |

*: sample volume may vary. The syringe pump draws first a volume of buffer A equal to 13.6 µl minus sample volume + 2 µl, then the sample, then 2 µl buffer A

Binary pump gradient.

| Time (min) | Flow rate (nl/min) | Buffer A (%) | Buffer B (%) |
|---|---|---|---|
| 0 | 300 | 95 | 5 |
| 5 | 300 | 95 | 5 |
| 65 | 300 | 62 | 38 |
| 70 | 300 | 20 | 80 |
| 100 | 300 | 20 | 80 |
| 102 | 300 | 95 | 5 |
| 120 | 300 | 95 | 5 |

2. Program 2: high-resolution SCX elution (this program minimizes mass elution from mobile phase used to drive elution volume elements through the SCX column).

| # | Command | Description |
|---|---|---|
| 1 | Initialize | Autosampler device |
| 2 | Valve | Switch injection valve to load (6-1) |
| 3 | Valve | Switch valve A to load (1–10) |
| 4 | Valve | Switch valve B to 1D (inject, 1–10) |
| 5 | Wash | Prewash needle using washing buffer |
| 6 | Wait | For binary pump ready to start |
| 7 | Wait | For isocratic pump ready to start |
| 8 | Get sample | Fill loop with sample/plug (35 μl): 2 mm from bottom* |
| 9 | Valve | Switch injection valve to inject (1, 2) |
| 10 | Start | Start isocratic pump (0.5 l/min buffer A, 40 min) |
| 11 | Valve | Switch injection valve to inject (1, 2) |
| 12 | Wait | 1:30 min |
| 13 | Valve | Switch valve B to SCX (load, 1–10) |
| 14 | Wait | 4 min |
| 15 | Valve | Switch injection valve to load (1, 2) |
| 16 | Wait | 4 min |
| 17 | Start | Start binary pump (see below) |
| 18 | Valve | Switch valve A to inject (1, 2) |
| 19 | Valve | Switch valve B to 1D (inject, 1-2) |
| 20 | Wait | 15 min |
| 21 | Wash | Prewash needle using washing buffer |
| 22 | Wait | For binary injection complete |

Binary pump gradient.

| Time (min) | Flow rate (nl/min) | Buffer A (%) | Buffer B (%) |
|---|---|---|---|
| 0 | 300 | 95 | 5 |
| 5 | 300 | 95 | 5 |
| 95 | 300 | 78 | 32 |
| 105 | 300 | 20 | 80 |
| 130 | 300 | 20 | 80 |
| 132 | 300 | 95 | 5 |
| 160 | 300 | 95 | 5 |

3. Program 3: Single dimension RP analysis

| # | Command | Description |
|---|---|---|
| 1 | Initialize | Autosampler device |
| 2 | Valve | Switch injection valve to load (6-1) |
| 3 | Valve | Switch valve A to load (1–10) |
| 4 | Valve | Switch valve B to 1DRP (1, 2) |
| 5 | Wash | Prewash needle using washing buffer |
| 6 | Wait | For binary pump ready to start |
| 7 | Wait | For isocratic pump ready to start |
| 8 | Get sample | 5 µl pick up, 13.6 µl: 2 mm from bottom* |
| 9 | Valve | Switch injection valve to inject (1, 2) |
| 10 | Start | Start isocratic pump (1 µl/min buffer A, 20 min) |
| 11 | Wait | For isocratic pump injection complete |
| 12 | Start | Start binary pump (see below) |
| 13 | Valve | Switch valve A to inject (1, 2) |
| 14 | Wash | Prewash needle using washing buffer |
| 15 | Wait | For binary injection complete |

*: sample volume may vary. The syringe pump draws first a volume of buffer A equal to 13.6 µl minus sample volume + 2 µl, then the sample, then 2 µl buffer A

Binary pump gradient.

| Time (min) | Flow rate (nl/min) | Buffer A (%) | Buffer B (%) |
|---|---|---|---|
| 0 | 300 | 95 | 5 |
| 5 | 300 | 95 | 5 |
| 95 | 300 | 78 | 32 |

(continued)

| Time (min) | Flow rate (nl/min) | Buffer A (%) | Buffer B (%) |
|---|---|---|---|
| 105 | 300 | 20 | 80 |
| 130 | 300 | 20 | 80 |
| 132 | 300 | 95 | 5 |
| 160 | 300 | 95 | 5 |

4. Program 4: reconditioning and equilibration. SCX column is reconditioned by injecting 10 µl SCX reconditioning buffer (1 M ammonium formate, pH = 9), with flow-through directed to waste. Reverse phase columns are reconditioned and equilibrated in parallel.

| # | Command | Description |
|---|---|---|
| 1 | Initialize | Autosampler device |
| 2 | Valve | Switch injection valve to load (6-1) |
| 3 | Valve | Switch valve A to inject (1, 2) |
| 4 | Valve | Switch valve B to SCX (1–10) |
| 5 | Wash | Prewash needle using washing buffer |
| 6 | Wait | For binary pump ready to start |
| 7 | Wait | For isocratic pump ready to start |
| 8 | Get sample | Fill loop with SCX recondition buffer (15 µl): 2 mm from bottom* |
| 9 | Valve | Switch injection valve to inject (1, 2) |
| 10 | Start | Start isocratic pump (0.5 µl/min buffer A, 65 min) |
| 14 | Start | Start binary pump (see below) |
| 17 | Wait | For binary injection complete |

Binary pump gradient.

| Time (min) | Flow rate (nl/min) | Buffer A (%) | Buffer B (%) |
|---|---|---|---|
| 0 | 300 | 80 | 20 |
| 10 | 300 | 20 | 80 |
| 40 | 300 | 20 | 80 |
| 45 | 300 | 95 | 5 |
| 70 | 300 | 95 | 5 |

### 3.4 Prepare and Install the Electrospray Emitter (see Notes 1 and 2 )

1. Use the silica cutting tool to cut a 50 cm piece of 20 µm ID silica capillary.
2. Using the gas burner, burn approximately 1 cm of the polyimide coating, 10 cm from the end of the capillary. Let the capillary cool to room temperature and carefully wipe-off burnt

polyimide debris using a Kimwipe soaked with methanol. **CAUTION**: stripped silica is extremely fragile. Hot silica may fracture if placed in contact with liquids before cooling down.

3. Mount the capillary on the laser puller, with the inner edge of the fritted section 2 cm from the laser target (center of the mirror cover).
4. Pull the silica capillary using the following program (*see* **Note 3**) [12]:

```
HEAT=250, FIL= , VEL=25, DEL=180, PULL=25
HEAT=250, FIL= , VEL=25, DEL=180, PULL=25
HEAT=250, FIL= , VEL=25, DEL=180, PULL=25
HEAT=250, FIL= , VEL=25, DEL=180, PULL=25
```

5. Using a microscope, check the tip geometry at 4× magnification and the diameter at 20× magnification (*see* **Notes 4** and **5**).

### 3.5 Preparation of SCX Peptide Standard

1. Prepare a 2 mg/ml solution of BSA and casein in 1 M guanidine hydrochloride/100 mM ABC pH 8.5. Mix equal volumes of the two solutions to obtain a 1:1 (v/v) BSA/casein standard solution and freeze in 500 µl aliquots.
2. To 500 µl standard, add 55 µl 100 mM DTT/100 mM ABC (freshly prepared). Incubate at 56 °C for 30 min.
3. Let the solution cool to room temperature (25 °C).
4. Add 60 µl 550 mM iodoacetamide/100 mM ABC (freshly prepared). Incubate at room temperature for 20 min, in the dark.
5. Add 65 µl 100 mM DTT/100 mM ABC (freshly prepared). Incubate at 56 °C for 20 min.
6. Add 335 µl 100 mM ABC.
7. Add 50 µl of 0.2 µg/ µl LysC protease in 100 mM ABC. Incubate 8 h at 37 °C.
8. Transfer half the LyC digest (525 µl), in a clean tube. Acidify with 1% (5 µl) formic acid, and freeze.
9. To the remaining 525 µl LysC digest, add 975 µl of 50 mM ABC.
10. Add 50 µl of 0.2 µg/µl Trypsin protease in 100 mM ABC. Incubate 16 h at 37 °C.
11. Acidify with 1% (15 µl) formic acid.
12. Mix 3 volumes tryptic digest with 1 volume LysC digest and mix by vortexing.
13. Desalt by solid phase extraction, using 4 macro spin columns.

| Step | Buffer | Volume (μl/column) | Centrifugation |
|---|---|---|---|
| Activation | 99.9% ACN/0.1% FA | 300 | 100 rcf/60 s |
| Equilibration | 99.9% water/0.1% FA | 2 × 300 | 100 rcf/60 s |
| Loading | Sample | 500 | 100 rcf/120 s |
| Wash#1 | 99.9% water/0.1% FA | 300 | 100 rcf/120 s |
| Wash#2 | 99.9% water/0.1% FA | 300 | 200 rcf/120 s |
| Elution | 60% ACN in water/0.1% FA | 400 | 200 rcf/120 s |

14. Divide the eluate in ten 100 μl aliquots (100 μg/aliquot) and vacuum centrifuge to dryness.
15. Just before injection, resuspend one aliquot in 200 μl 0.1% FA/3% ACN (0.5 μg/ μl).

### 3.6 SCX Standard Quality Control

1. Using LC Program 3 (Single dimension RP analysis), analyze 1 μg (2 μl) SCX standard.
2. Submit the MS raw file to MaxQuant for peptide spectral matching against a fasta file containing the protein sequences of BSA and casein. Set C-carbamidomethylation as fixed modification. Set M, oxidation, S/T/Y-phosphorylation and N/Q deamidation as variable modifications. Set proteolysis specificity to trypsin and allow for up to 5 missed cleavages.

### 3.7 Determination of Sample Recovery from the SCX Column

Recondition and equilibrate columns using LC Program 4 (columns reconditioning and equilibration).

1. Blank SCX load. Using LC Program 1 (SCX sample load) inject 5 μl 0.1% FA in water.
2. Blank SCX elute. Using LC Program 1 inject 10 μl SCX reconditioning buffer (1 M ammonium formate–25% ACN, pH = 9).
3. Search all MS raw files generated in **steps 1** and **2** as described in Subheading 3.6, **step 2**. Verify absence of contaminants.
4. Recondition and equilibrate columns using LC Program 4 (columns reconditioning and equilibration).
5. Standard SCX load. Using LC Program 1 (SCX sample load) inject 2 μl of SCX standard
6. Standard SCX bulk elution. Using LC Program 1 inject 4 μl SCX reconditioning buffer (1 M ammonium formate pH = 9). Repeat once.
7. Using LC Program 3 (Single dimension RP analysis), analyze 1 μg (2 μμl) SCX standard.

8. Search all MS raw files generated in **steps 6** and 7 as described in Subheading 3.6, **step 2**. Verify that >95% peptides elute in a single SCX fraction. Verify that extracted ion chromatograms (XIC) for peptides have similar intensity (±10%) in SCX and 1D RP experiments.

### 3.8 SCX Fractionation

1. Recondition and equilibrate columns using LC Program 4 (reconditioning and equilibration).
2. Standard SCX load. Using LC Program 1 (SCX sample load) inject 2 μl of SCX standard
3. Standard SCX fractionation. Using LC Program 2 inject 4 μl ammonium formate plugs at 80 and 200 mM (pH 2.8).
4. Using LC Program 1 inject 10 μl ammonium formate 1 M (pH 2.8).
5. Using LC Program 1 inject 10 μl SCX reconditioning buffer (1 M ammonium formate, pH = 9).
6. Search all MS raw files generated in **steps 2–5** as described in Subheading 3.6, **step 2**.

### 3.9 Troubleshooting

*3.9.1 Clogging of Unions and Capillary Lines. Possible Causes Include*

1. Column frits leaking stationary phase. Suggested solution: replace column. Kasil polymerization to produce frits should be optimized before attempting to pack columns.
2. Particulate accumulating in the outer part of capillary being inadvertently introduced in the lines when mounting into frits and sleeves. Suggested solution: cut the silica capillaries after they are inserted in the fittings and avoid touching the open ends. Avoid storing columns with open ends for extended time.
3. Particulate contamination of bulk stationary phase. Make sure spatulas, magnets, and glass ampoules are kept clean.
4. Degradation of silica stationary phase. Prolonged exposure to pH > 9 may induce hydrolysis of unprotected silica particles. Possible solutions: after SCX column reconditioning at high pH, ensure appropriate column washing with 0.1% formic acid in water.
5. Salt precipitation in the lines. Salt precipitation may occur if nonvolatile salts (such as KCl) are used for elution. Suggested solution: elute peptides using volatile salts such as ammonium formate or ammonium acetate.
6. Silica fragments from capillary end cutting. Cutting silica capillary may produce debris and particulate that enter the column or the downstream component producing clogs. Suggested solution: using a phase microscope, inspect all ends to ensure that a clean cut perpendicular to the silica wall is obtained. Small silica splinters may be removed using a silica polishing station. All lines and column should be flushed before being mounted.

*3.9.2 Insufficient Retention of Peptides on SCX Columns. Possible Causes Include*

1. Excessive salt concentration in loaded sample. Suggested solution: thoroughly desalt peptide sample by solid phase extraction. Avoid using phosphate buffers.
2. Incorrect pH of SCX loading buffer. For best retention all solution must have pH below the p$K_a$ of aspartate (3.86). Suggested solution: titrate the pH of all buffers with formic acid to obtain pH = 2.8.
3. Excessive peptide amount loaded on SCX column. Suggested solution: do not exceed SCX column loading capacity. We observed >90% peptide retention on 100 μm ID × 150 mm SCX column when loading up to 15 μg tryptic peptides in 0.1% formic acid in water.

*3.9.3 Insufficient Resolution of SCX Column. Possible Causes Include*

1. Sample or mobile phases contain TFA or other modifier that interfere with peak focusing by SCX. Suggested solution: use ammonium formate and formic acid as mobile phase modifiers, or ammonium acetate.
2. Isocratic (mass action) elution is the main mode of chromatographic separation. Suggested solution: avoid using more than 2 column volume to drive salt plugs. Verify accurate calibration of HPLC flow meters.

*3.9.4 Insufficient Retention of Peptides on the Trap Column. Possible Causes Include the Following*

1. The SCX mobile phase and/or the salt plugs contain organic solvents. Do not use more than 2% acetonitrile or methanol in the buffer resuspension buffer. Avoid adding any organic solvent to the isocratic pump mobile phase.
2. The fractions eluting from the SCX column exceed the loading capacity of the reverse phase trap column. This may be determined by excessive sample amount or incorrect salt concentration in the SCX plugs. Suggested solution: carefully determine sample concentration. Prepare fresh ammonium formate solutions.

## 4 Notes

1. To reduce surface and irregularities of the emitters produced as per Subheading 3.4, **steps 1–5**, the tips may be etched by dipping the terminus in hydrofluoric acid for 30–45 s. After etching, tips should be rinsed in clean water. Etching may reduce the irregularities in the cross section of the tip but results in slightly larger and less reproducible tip ID. Prolonged etching may damage the tip.
2. Alternatively to the procedure in Subheading 3.4, **step 1–5**, commercial 10 μm ID electrospray emitters may be used.

3. Because of variable optical, mechanical and environmental conditions of the laser puller, the program described in Subheading 3.4, **step 4** is may require optimization on the specific instrument being used.
4. Setting the ESI emitters to be washed in 50% water/methanol during sample loading and SCX fractionation highly reduces depositing of salt and organic matter on the tip and thus improves maintaining ionization efficiency constant over time.
5. Narrow bore emitters require careful voltage optimization for optimal performance. Progressively decreasing voltage as a function of water content in the buffer highly improves spray efficiency and stability. For the suggested elution profile and flow-path, the following voltage gradient may be used:

| Time (min) | Voltage (V) |
|---|---|
| 0 | 1750 |
| 30 | 1700 |
| 50 | 1650 |
| 70 | 1600 |
| 90 | 1550 |
| 110 | 1500 |
| 130 | 1450 |
| 155 | 0* |

*: emitter moved to washing station

## References


1. Picotti P, Bodenmiller B, Mueller LN, Domon B, Aebersold R (2009) Full dynamic range proteome analysis of S. cerevisiae by targeted proteomics. Cell 138(4):795–806
2. Gallien S, Duriez E, Crone C, Kellmann M, Moehring T, Domon B (2012) Targeted proteomic quantification on quadrupole-orbitrap mass spectrometer. Mol Cell Proteomics 11 (12):1709–1723
3. Aebersold R, Mann M (2003) Mass spectrometry-based proteomics. Nature 422 (6928):198–207
4. Cifani P, Kentsis A (2017) High sensitivity quantitative proteomics using automated multidimensional nano-flow chromatography and accumulated ion monitoring on quadrupole-Orbitrap-linear ion trap mass spectrometer. Mol Cell Proteomics 16(11):2006–2016
5. Urisman A, Levin RS, Gordan JD, Webber JT, Hernandez H, Ishihama Y et al (2017) An optimized chromatographic strategy for multiplexing in parallel reaction monitoring mass spectrometry: insights from quantitation of activated kinases. Mol Cell Proteomics 16 (2):265–277
6. Tolstikov VV, Lommen A, Nakanishi K, Tanaka N, Fiehn O (2003) Monolithic silica-based capillary reversed-phase liquid chromatography/electrospray mass spectrometry for plant metabolomics. Anal Chem 75 (23):6737–6740
7. Gilar M, Olivova P, Daly AE, Gebler JC (2005) Orthogonality of separation in two-dimensional liquid chromatography. Anal Chem 77(19):6426–6434
8. Antberg L, Cifani P, Sandin M, Levander F, James P (2012) Critical comparison of

multidimensional separation methods for increasing protein expression coverage. J Proteome Res 11(5):2644–2652

9. Ficarro SB, Zhang Y, Lu Y, Moghimi AR, Askenazi M, Hyatt E et al (2009) Improved electrospray ionization efficiency compensates for diminished chromatographic resolution and enables proteomics analysis of tyrosine signaling in embryonic stem cells. Anal Chem 81 (9):3440–3447
10. Le Bihan T, Duewel HS, Figeys D (2003) On-line strong cation exchange micro-HPLC-ESI-MS/MS for protein identification and process optimization. J Am Soc Mass Spectrom 14(7):719–727
11. Dhabaria A, Cifani P, Kentsis A (2015) Fabrication of capillary columns with integrated frits for mass spectrometry. Nature Publishing Group, Berlin. http://www.nature.com/protocolexchange/protocols/3925
12. Cifani P, Dhabaria A, Kentsis A (2015) Fabrication of nanoelectrospray emitters for LC-MS. Nature Publishing Group, Berlin. http://www.nature.com/protocolexchange/protocols/3981

# Chapter 12

# Clinical Translation of Stimulated Raman Histology

**Cordelia Orillac, Todd Hollon, and Daniel A. Orringer**

## Abstract

Stimulated Raman histology (SRH) images are created by the label-free, nondestructive imaging of tissue using stimulated Raman scattering (SRS) microscopy. In a matter of seconds, these images provide real-time histologic information on biopsied tissue in the operating room. SRS microscopy uses two lasers (pump beam and Stokes beam) to amplify the Raman signal of specific chemical bonds found in macromolecules (lipids, proteins, and nucleic acids) in these tissues. The concentrations of these macromolecules are used to produce image contrast. These images are acquired and displayed using an imaging system with five main components: (1) fiber coupled microscope, (2) dual-wavelength fiber-laser module, (3) laser control module, (4) microscope control module, and (5) a computer. This manuscript details how to assemble the dual-wavelength fiber-laser module and how to generate an SRH image.

**Key words** Stimulated Raman histology, Stimulated Raman scattering microscopy

## 1 Introduction

Stimulated Raman scattering (SRS) microscopy is a rapid, nondestructive, label-free imaging technique that provides histologic images with submicron spatial resolution. SRS microscopy uses the molecular vibrational properties of chemical bonds and the concentration of macromolecules (lipids, proteins, and nucleic acids) to produce image contrast [1–3]. Freudiger, Xie, and colleagues developed SRS microscopy in 2008, and it has since been applied to biomedical and brain tumor imaging [1, 4, 5]. Recent breakthroughs in fiber laser technology have led to the development of the first clinical SRS microscope (Invenio Imaging, Inc., Menlo Park, California) (Fig. 1) [6]. The clinical SRS microscope produces histologic images by mapping two Raman shifts within each specimen: 2845 $cm^{-1}$, which corresponds to $CH_2$ bonds that are abundant in lipids, and 2930 $cm^{-1}$, which corresponds to $CH_3$ bonds that predominate in proteins and DNA. The stimulated Raman signal generated from each channel produces image contrast similar in appearance to that found in standard brightfield

Miguel R. Ossandon et al. (eds.), *Biomedical Engineering Technologies: Volume 1*, Methods in Molecular Biology, vol. 2393, https://doi.org/10.1007/978-1-0716-1803-5_12, 

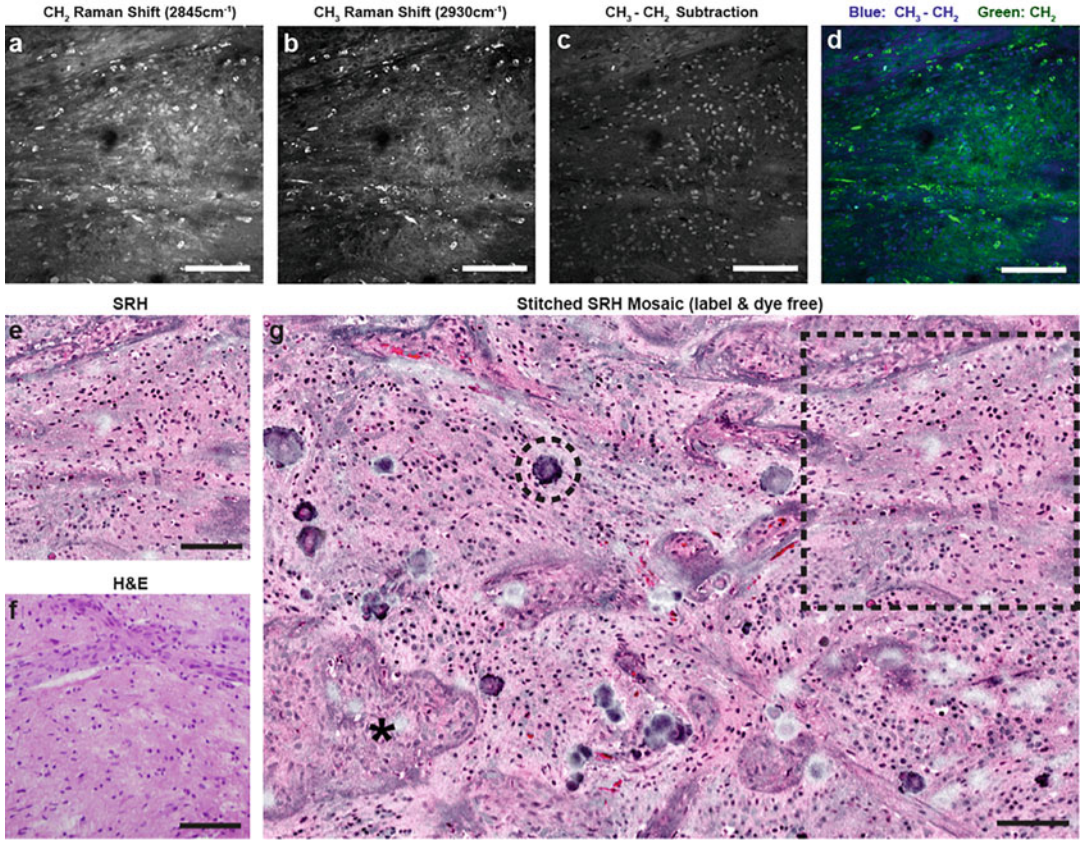


**Fig. 1** The creation of a virtual H&E slides with the clinical SRS microscopy. (**a**–**c**), $CH_2$ (**a**) and $CH_3$ (**b**) images are acquired and subtracted (**c**). (**d**) The $CH_2$ image is assigned to a green channel, while the $CH_3$–$CH_2$ image is assigned to the blue channel, creating a two-color blue–green image. (**e**, **f**) Applying an H&E lookup table, SRH images (**e**) adopt an appearance similar to conventional H&E staining (**f**). (**g**) Mosaic tiled image of several SRH FOVs to create a mosaic of imaged tissue. The asterisk (*) indicates a focus of microvascular proliferation, the dashed circle indicates calcification and the dashed box demonstrates how the FOV in **e** fits into the larger mosaic. Scale bars, 100 μm

microscopy with hematoxylin and eosin (H&E) staining. The application of H&E pseudocoloring of SRS microscopic images is referred to as stimulated Raman histology (SRH). SRH has been applied in the bedside imaging of fresh surgical specimens in over 1000 patients across the US.

While the research applications of SRS microscopy are broad and in a constant state of evolution, this chapter will focus on the methodological aspects of obtaining stimulated Raman histology for clinical fresh tissue imaging. The chapter will also touch on how we have employed an innovation in biomedical engineering to solve a critical problem in surgical pathology: the physical and temporal disconnection of the operating theatre and the pathology lab. The implications of creating a means for fresh tissue imaging at the bedside and the implications SRH may have on the fields of surgical pathology and surgical oncology as its use expands are explored.

### 1.1 Technical Execution of Stimulated Raman Scattering Microscopy

Coherent Raman scattering (CRS) microscopies including coherent anti-Stokes Raman scattering (CARS) microscopy and stimulated Raman scattering (SRS) microscopy, have enabled the rapid, label-free microscopic imaging of unprocessed tissue specimens. These techniques provide natural contrast using characteristic vibrational frequencies for different compounds such as lipids, proteins, and DNA to create images of biologic specimens. The nonlinearity of signal intensity in CRS techniques allows for 3D imaging, avoiding the need for thin-sectioning of specimens prior to imaging [1, 7]. CRS microscopies are more sensitive compared to spontaneous Raman scattering microscopy with faster imaging speed [1, 3, 8]. The use of SRS microscopy has some benefits compared to CARS as it provides a non-resonant background, has a linear relationship between chemical concentration and signal intensity, and has a nondistorted spectrum identical to that of spontaneous Raman scattering [1, 9, 10]. SRS has been used to image a number of biologic specimens including liver and brain pathologies both in vivo and ex vivo [4, 11, 12].

In SRS, two lasers are tuned to the pump ($\omega_P$) and Stokes frequencies ($\omega_S$) of a given bond and coincide on the sample at a specified depth. When the difference frequency between two lasers ($\Delta\omega = \omega_P - \omega_S$), or Raman shift, matches that of a particular molecular vibrational frequency $\Omega$, the Raman signal is amplified [1]. In SRS, no amplification is produced when $\Delta\omega \neq \Omega$ and therefore does not exhibit any nonresonant background. The lack of a nonresonant background has a profound effect on image clarity and enables the creation of images that approach the appearance of traditional phase contrast microscopy used in a clinical context.

The laser-system typically used for SRS is a synchronously pumped picosecond optical parametric oscillator (OPO) [13]. This free-space OPO system is very susceptible to environmental changes and requires continuous water-cooling. As such, this state-of-the-art setup is not suitable for use in a clinical environment. To make this technology available in the clinical setting, a fiber-laser module has been developed (Fig. 2) [6].

### 1.2 Processing of SRS Images and Stimulated Raman Histology (SRH)

Biologic tissues are imaged using SRS by mapping lipids and proteins at Raman shifts of 2845–2850 $cm^{-1}$($CH_3$bonds) and 2930-2940 $cm^{-1}$($CH_2$bonds) respectively [3, 11, 12, 14]. A subtracted $CH_3$–$CH_2$ image can be created that highlights the nucleus and makes the cytoplasm seemingly vanish [12]. Sufficient contrast for tissue histology can be created with an image overlay in which $CH_3$–$CH_2$ is assigned a blue channel and $CH_2$ image is assigned a green channel.

$CH_2$and $CH_3$ images produced are foreign to clinicians accustomed to traditional staining techniques such as H&E staining. The images obtained from SRS can be recolored in order to

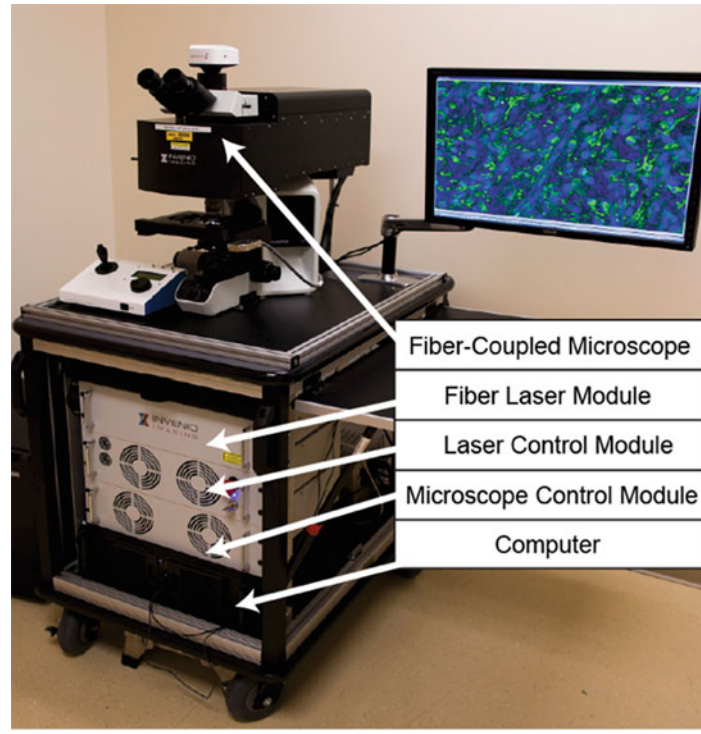


**Fig. 2** Fiber-laser based optical schematic for portable SRS microscopy. A prototype SRS microscope with labeled essential component modules

produce stimulated Raman histology (SRH) images that resemble a traditional H&E-stained slide familiar to them [14]. Roughly, the 2845 $cm^{-1}$ grayscale image is mapped to an eosin-like red/pink color while the 2930–2845 $cm^{-1}$ channel is mapped to a dark-blue/violet color resembling the hematoxylin stain. These two images are superimposed to produce an SRH image resembling a conventional H&E stained slide (Fig. 1).

### *1.3 Future Directions of SRH*

Other biomedical optical technologies are currently being used for fresh tissue imaging of brain tumor specimens. Optical coherence tomography [15], confocal microscopy [16, 17], and third-harmonic generation microscopy [18] have been used to image normal brain and brain tumor specimens. Raman spectroscopy has been used to detect brain tumor infiltration both ex vivo and in vivo [19–21]. Wide-field fluorescence imaging using exogenous 5-aminolevulinic acid (5-ALA) for tumor labeling is currently being used for fluorescence guided brain tumor surgery [22]. SRH is unique among these existing technologies in its submicron spatial resolution, label-free tumor detection, video-rate image acquisition, subcellular image contrast, and virtual H&E color scheme. In addition, SRH has been validated as a clinical imaging technique for producing histopathologic images with diagnostic accuracy

equal to standard light microscopy and is a Class I exempt, FDA-registered device.

Future applications of SRH microscopy include intraoperative guidance of tumor resection and accurate identification of brain-tumor margins. Serial imaging from within the tumor resection cavity can provide real-time data on tumor infiltration. Greater extent of resection improves progression-free and overall survival in infiltrative gliomas and brain metastasis [17, 23–25]. Having real-time knowledge about tumor infiltration could have an impact on intraoperative decision-making. Additionally, the combination of SRH data with available surgical navigation systems can be used synergistically to guide resection and potentially allow for targeted radiotherapy. Rapid, accurate pathologic diagnosis of the most common pediatric posterior fossa tumors effects intraoperative decision-making. While greater extent of resection improves clinical outcomes in pediatric ependymomas and pilocytic astrocytomas, the effect of greater extent of resection in medulloblastomas is less clear [26–28]. Unnecessarily aggressive brain tumor resection can increase perioperative morbidity and mortality without improved clinical outcome. SRH provides intraoperative histopathologic diagnosis of adult and pediatric brain tumor with the potential guide brain tumor resection. By integrating SRH microscopy into the surgical workflow, we aim to leverage a breakthrough in optics to create a new paradigm for intraoperative pathology and ultimately improve the safety and accuracy of brain tumor surgery.

## 2 Materials

To produce SRH images, an imaging system with five main components that were mounted on a portable, self-contained clinical cart (Fig. 2) [14]:

1. a fiber-coupled microscope (NIO Imaging System, Invenio Imaging) with a motorized stage;
2. a dual-wavelength fiber-laser module
3. a laser control module
4. a microscope control module
5. a computer for image acquisition, display, and processing.

### 2.1 Dual-Wavelength Fiber-Laser Module

In order to achieve the stimulated excitation of vibrational transitions for SRS imaging, synchronized narrow-band pulse trains are required. The pulse trains are generated by the filtering of a broadband supercontinuum from a fiber-oscillator with amplification in the respective gain media, Erbium (Er) and Ytterbium (Yb). The difference frequency between the two major gain media corresponds to the high wavenumber region of Raman spectra [29]. The module is constructed using the following items [6].

1. Er-doped fiber oscillator at 1560 nm, mode-locked with a carbon nanotube saturable absorber at a repetition rate of 59 MHz.
2. Normal dispersion Er-doped preamplifier.
3. Low nonlinearity Er-doped power amplifier.
4. Periodically pooled lithium niobate (PPLN) crystal (Covesion, MSHG1550-1.0-10).
5. Yb-doped preamplifier.
6. Narrowband filter.
7. Low-nonlinearity Yb-doped power amplifier.
8. Fiber-optic tunable filter (Agiltron, FOTF-01-6).

## 3 Methods

The clinical SRS microscope using a dual-wavelength fiber-laser module is set up as described previously [6, 14].

### *3.1 Setup of the Dual-Wavelength Fiber-Laser Module (Fig. 3)*

1. The pulse trains are generated by the filtering of a broadband supercontinuum from a Er-doped fiber-oscillator at 1560 nm, mode-locked with a carbon nanotube saturable absorber at a repetition rate of 59 MHz.
2. The output of the oscillator goes through an optical isolator and is split into two arms to generate the Stokes and pump beams for SRS.
3. The first arm (the Stokes beam)
   (a) It is frequency-shifted in a supercontinuum generator unit based on a highly nonlinear fiber (HNLF).
   (b) An Yb-doped preamplifier is used to increase the power of the spectral range around 1 mm to 40 mW.
   (c) A tunable filter is used to produce a picosecond pulse train that can be amplified in a low-nonlinearity Yb-doped power amplifier and then passed through an isolator and collimator.
   (d) The laser output is scaled to approximately 150 mW for the Stokes beam.
   (e) A transform-limited pulse duration of 2 ps is chosen.
4. The second arm (the pump beam):
   (a) It is amplified to 80 mW in a normal-dispersion Er-doped preamplifier
   (b) A narrowband filter is used to reduce the bandwidth for SRS.
   (c) The power (2.2 mW after filtering) is restored in a low-nonlinearity Er-doped power amplifier.

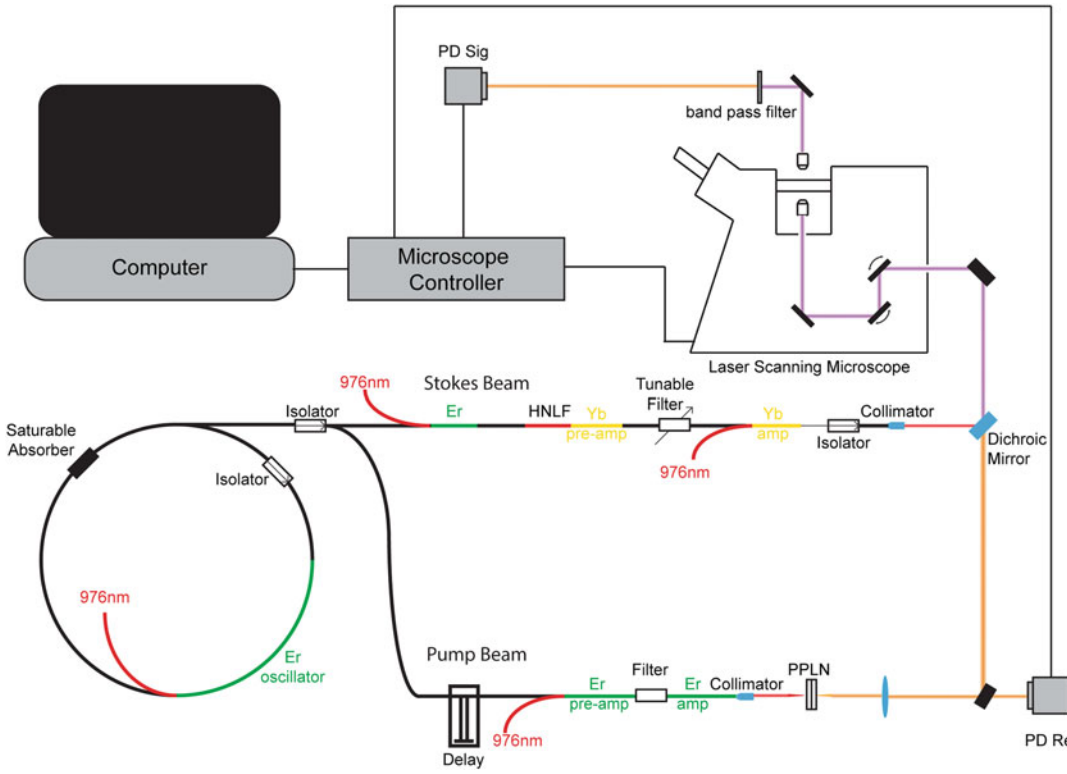


**Fig. 3** Optical and fiber laser diagram designed for SRS microscopy including essential components of the dual-wavelength fiber-laser-coupled microscope. The top arm of the laser diagram indicates the scheme for generating the Stokes beam (red) and the bottom arm generates the pump beam (orange). Both beams are combined (purple) and passed through the specimen. *Er amp* erbium amplifier, *Er pre-amp* erbium preamplifier, *HNLF* highly nonlinear fiber, *PD* photodiode, *PPLN* periodically poled lithium niobate, *Yb amp* ytterbium-doped amplifier, *Yb pre-amp* ytterbium-doped preamplifier

(d) The beam is passed through a collimator and output is frequency doubled in a periodically poled lithium niobate (PPLN) crystal.

(e) The laser output is scaled to 120 mW for the pump beam.

(f) A portion of the pump beam is passed through a photodiode reference to form the reference beam and passed to the microscope controller where autobalance detection is used for noise-cancellation.

5. Precise tuning of the difference frequency between pump and Stokes beams is achieved with motorized fiber optic tunable filters; the Stokes beam is tuned to between 1010 nm and 1040 nm and the pump beam is kept fixed at 790 nm (*see* **Note 1**).

6. The two beams are overlapped using a free space dichroic mirror and passed through the specimen.

7. The pump beam is detected by the autobalance detection after the Stokes beam is filtered out by a band pass filter and passed through a photodiode signal.

Fresh tissue (~3 mm thick) is placed on an uncoated glass slide and flattened to a thickness of 120 μm similar to a standard squash preparation. 50 μL of normal saline is added to the tissue and a coverslip is applied to the tissue and adhered to the slide. The slide is then placed on the motorized stage of the microscope (*see* **Note 1**).

### 3.2 Generating an SRH Image with the NIO Imaging System

1. Power on NIO.
2. Follow prompts to enter patient name, demographic information.
3. Use prefilled saline syringe to fill chamber with 40 cc of distilled water.
4. Await tissue.
5. Surgeon/proceduralist allocates biopsied tissue (*see* **Note 2**).
6. Prepare tissue of interest. Trim any coagulated or bloody regions. For tissues sample to detect or diagnose tumor, select most translucent sample possible. Ideal tissue size is dictated in part by the compressibility of the tissue. Tissue should not deform imaging chamber or prevent it from sealing easily.
7. Place tissue into NIO slide cassette and seal by running a figure over each of the edges of the coverslip.
8. Follow prompts to enable white light acquisition of tissue within chamber. Note- imager door must be open during acquisition of white light image.
9. Select acquisition position and size of desired SRH image. Try to avoid tissue edges when selecting imaging site.
10. Close imager door as prompted by graphical user interface.
11. Press acquire. Image acquisition time will be several minutes depending on function of system and desired image size *see* **Note 3**).
12. Review SRH image.

## 4 Notes

We provide our institution's protocol for imaging fresh brain tumor specimens with SRH. Critical steps in the protocol include specimen collection and handling, microscope preparation, and image acquisition. As with any imaging modality, there is a learning curve in the process of developing the technical skill to ensure excellent image quality with each specimen. There is an array of variables that

affect signal to noise ratio, and, therefore, image quality, including those intrinsic to the imaging modality and those intrinsic to the tissue sample itself.

1. From the standpoint of the tissue sample, it is important to be mindful of the fact that the clinical SRH imager works in transmission mode, meaning that light must traverse the tissue to create signal. Consequently, signal to noise ratio is best when transmission of light through the sample is highest. We have not quantitatively evaluated a degree of light transmission that is required to generate an acceptable SRH image because of the subjective nature of such a determination. That said, we have appreciated the highest image quality in specimens that tend to be more transparent. As a caveat, tissues that are extremely transparent may have that property because they are acellular or loosely organized. Such specimens are not likely to create excellent images- simply because there is not much to image. On the other hand of the spectrum, tissues that are highly fibrotic or opaque do not readily allow for light transmission and may also result in poor image quality.

   Another element related to light transmission that can degrade image quality is tissue compressibility. Cortex and white matter, as well as most tumors of the central nervous system are highly compressible, creating the opportunity to "pancake" a thin layer of tissue within an imaging chamber even when starting with a specimens that is several mm in size. With less compressible tissue such as breast, prostate or head and neck biopsies, the thickness of the specimen plays a crucial role in ensuring image quality. The imaging chamber is design with a 125 micron distance between the bottom of the chamber and the coverslip surface. Approximating this thickness with the tissue section ensures that tissue will be transparent and compressible enough to produce acceptable image quality.

   Careful tissue handling is essential in ensuring that tissue architecture will be preserved. The user will develop his/her own ability to judge the appropriate amount of tissue to load into a chamber. Best practice can preserve tissue architecture in with gentle compression leading to images that retain diagnostic histologic images. Along these lines, we also advise keeping tissue specimens moist from the time they are harvested to the time they are imaged.

2. As with conventional histology, SRH image quality is also driven by the integrity of the tissue that is being imaged. SRH has been widely deployed in human brain tumors, many of which contain necrotic areas given their rapid growth. Due to tissue degradation and cell death, imaging of necrotic tissue, which often comprises the largest volume of an aggressive malignancy will generally result in poor image quality. In

some cases, viable tumor, which is essential for diagnosis is only found at the margins of a lesion and may be difficult to isolate. We have found that collecting an array of tissue, including uninvolved tissue adjacent to a lesion can serve as a good comparison to the viable tumor and in some cases necrotic tumor.

3. From the standpoint of the imager, we recommend a protocol to ensure consistent laser power using a standard such as PDMS. The signal strength at CH2 and CH3 Raman shifts should be recorded at the beginning of each session, as well as the two photon absorbance measurement. The field flatness must be verified as well. We have noted that laser alignment may need to be tuned periodically to ensure precise beam overlap. Clinical SRH imagers are temperature sensitive and designed to be in a well air-conditioned operating room environment. Operation of the system in a poorly ventilated space with ambient room temperature of greater than 72° Fahrenheit may degrade image quality. In addition, some imagers appear to heat with prolonged imaging periods. In settings where ambient temperature approaches 72°, we have noted that continuous imaging for 6 h of more may cause the system to overheat resulting in a visible degradation in signal to noise ratio within the image.

In summary, clinical SRH imaging protocols can be adapted to a variety of scientific and clinical applications in medicine. A sound understand of the scientific basis of stimulated Raman scattering microscopy and its clinical implementation as stimulated Raman histology is essential for successful use of this exciting technology. Collaboration between imagers and skilled clinicians—both from surgical and pathology disciplines can be useful in ensuring the most appropriate specimens are secured and prepared for imaging. With sound technique, SRH can unlock histology independent of a traditional pathology lab.

## References

1. Freudiger CW, Min W, Saar BG, Lu S, Holtom GR, He C et al (2008) Label-free biomedical imaging with high sensitivity by stimulated raman scattering microscopy. Science 322 (5909):1857–1861
2. Lu F-K, Basu S, Igras V, Hoang MP, Ji M, Fu D et al (2015) Label-free DNA imaging in vivo with stimulated Raman scattering microscopy. Proc Natl Acad Sci U S A 112 (37):11624–11629
3. Saar BG, Freudiger CW, Reichman J, Stanley CM, Holtom GR, Xie XS (2010) Video-rate molecular imaging in vivo with stimulated Raman scattering. Science 330 (6009):1368–1370
4. Ji M, Orringer DA, Freudiger CW, Ramkissoon S, Liu X, Lau D et al (2013) Rapid, Label-Free Detection of Brain Tumors with Stimulated Raman Scattering Microscopy. Sci Transl Med 5(201):201ra119
5. Ji M, Lewis S, Camelo-Piragua S, Ramkissoon SH, Snuderl M, Venneti S et al (2015) Detection of human brain tumor infiltration with

quantitative stimulated Raman scattering microscopy. Sci Transl Med 7(309):309ra163

6. Freudiger CW, Yang W, Holtom GR, Peyghambarian N, Xie XS, Kieu KQ (2014) Stimulated Raman scattering microscopy with a robust fibre laser source. Nat Photonics 8 (2):153–159
7. Zumbusch A, Holtom GR, Xie XS (1999) Three-dimensional vibrational imaging by coherent anti-stokes Raman scattering. Phys Rev Lett 82(20):4142–4145
8. Evans CL, Xie XS (2008) Coherent anti-stokes Raman scattering microscopy: chemical imaging for biology and medicine. Annu Rev Anal Chem 1(1):883–909
9. Ozeki Y, Dake F, Kajiyama S, Fukui K, Itoh K (2009) Analysis and experimental assessment of the sensitivity of stimulated Raman scattering microscopy. Opt Express 17(5):3651
10. Saar BG, Zeng Y, Freudiger CW, Liu Y-S, Himmel ME, Xie XS et al (2010) Label-free, real-time monitoring of biomass processing with stimulated Raman scattering microscopy. Angew Chem Int Ed Engl 49(32):5476–5479
11. Ozeki Y, Umemura W, Otsuka Y, Satoh S, Hashimoto H, Sumimura K et al (2012) High-speed molecular spectral imaging of tissue with stimulated Raman scattering. Nat Photonics 6(12):845–851
12. Freudiger CW, Pfannl R, Orringer DA, Saar BG, Ji M, Zeng Q et al (2012) Multicolored stain-free histopathology with coherent Raman imaging. Lab Investig 92(10):1492–1502
13. Ganikhanov F, Carrasco S, Sunney Xie X, Katz M, Seitz W, Kopf D (2006) Broadly tunable dual-wavelength light source for coherent anti-stokes Raman scattering microscopy. Opt Lett 31(9):1292
14. Orringer DA, Pandian B, Niknafs YS, Hollon TC, Boyle J, Lewis S et al (2017) Rapid intraoperative histology of unprocessed surgical specimens via fibre-laser-based stimulated Raman scattering microscopy. Nat Biomed Eng 1 (2):0027
15. Kut C, Chaichana KL, Xi J, Raza SM, Ye X, McVeigh ER et al (2015) Detection of human brain cancer infiltration ex vivo and in vivo using quantitative optical coherence tomography. Sci Transl Med 7(292):292ra100
16. Foersch S, Heimann A, Ayyad A, Spoden GA, Florin L, Mpoukouvalas K et al (2012) Confocal laser endomicroscopy for diagnosis and histomorphologic imaging of brain tumors in vivo. PLoS One 7(7):e41760
17. Sanai N, Snyder LA, Honea NJ, Coons SW, Eschbacher JM, Smith KA et al (2011) Intraoperative confocal microscopy in the visualization of 5-aminolevulinic acid fluorescence in low-grade gliomas. J Neurosurg 115 (4):740–748
18. Witte S, Negrean A, Lodder JC, de Kock CPJ, Testa Silva G, Mansvelder HD et al (2011) Label-free live brain imaging and targeted patching with third-harmonic generation microscopy. Proc Natl Acad Sci U S A 108 (15):5970–5975
19. Hollon T, Lewis S, Freudiger CW, Sunney Xie X, Orringer DA (2016) Improving the accuracy of brain tumor surgery via Raman-based technology. Neurosurg Focus 40(3):E9
20. Jermyn M, Mok K, Mercier J, Desroches J, Pichette J, Saint-Arnaud K et al (2015) Intraoperative brain cancer detection with Raman spectroscopy in humans. Sci Transl Med 7 (274):274ra19
21. Kalkanis SN, Kast RE, Rosenblum ML, Mikkelsen T, Yurgelevic SM, Nelson KM et al (2014) Raman spectroscopy to distinguish grey matter, necrosis, and glioblastoma multiforme in frozen tissue sections. J Neuro-Oncol 116 (3):477–485
22. Stummer W, Pichlmeier U, Meinel T, Wiestler OD, Zanella F, Reulen H-J (2006) Fluorescence-guided surgery with 5-aminolevulinic acid for resection of malignant glioma: a randomised controlled multicentre phase III trial. Lancet Oncol 7 (5):392–401
23. Orringer D, Lau D, Khatri S, Zamora-Berridi GJ, Zhang K, Wu C et al (2012) Extent of resection in patients with glioblastoma: limiting factors, perception of resectability, and effect on survival. J Neurosurg 117 (5):851–859
24. Patchell RA, Tibbs PA, Walsh JW, Dempsey RJ, Maruyama Y, Kryscio RJ et al (1990) A randomized trial of surgery in the treatment of single metastases to the brain. N Engl J Med 322 (8):494–500
25. Sanai N, Polley M-Y, McDermott MW, Parsa AT, Berger MS (2011) An extent of resection threshold for newly diagnosed glioblastomas. J Neurosurg 115(1):3–8
26. Pollack IF, Claassen D, Al-Shboul Q, Janosky JE, Deutsch M (1995) Low-grade gliomas of the cerebral hemispheres in children: an analysis of 71 cases. J Neurosurg 82(4):536–547
27. Thompson EM, Hielscher T, Bouffet E, Remke M, Luu B, Gururangan S et al (2016) Prognostic value of medulloblastoma extent of resection after accounting for molecular subgroup: a retrospective integrated clinical and molecular analysis. Lancet Oncol 17 (4):484–495

28. Tihan T, Zhou T, Holmes E, Burger PC, Ozuysal S, Rushing EJ (2008) The prognostic value of histological grading of posterior fossa ependymomas in children: a Children's oncology group study and a review of prognostic factors. Mod Pathol 21(2):165–177

29. Bégin S, Burgoyne B, Mercier V, Villeneuve A, Vallée R, Côté D (2011) Coherent anti-stokes Raman scattering hyperspectral tissue imaging with a wavelength-swept system. Biomed Opt Express 2(5):1296

# Chapter 13

# Ex Vivo and In Vitro Methods for Detection of Bioactive Staphylococcal Enterotoxins

**Reuven Rasooly, Paula Do, and Bradley Hernlem**

## Abstract

*Staphylococcus aureus* is a major bacterial cause of clinical infections and foodborne illnesses.

Through the synthesis of a group of Staphylococcal enterotoxins (SEs), gastroenteritis occurs and the SEs function as superantigens to massively activate T cells. The ability to rapidly detect and quantify SEs is imperative in order to learn the causes of staphylococcal outbreaks and to stop similar outbreaks in the future. Also, the ability to discern active toxin is essential for development of food treatment and processing methods. Here, we discuss the various methodologies for detection and analysis of SEs.

**Key words** Staphylococcal enterotoxins, Food poisoning, Detection methods, Activity assay, T-cells

## 1 Introduction

Staphylococcal enterotoxins (SEs) are members of a family of some 23 different staphylococcal and streptococcal exotoxins which share structural motifs, have emetic activity and are causative agents of bacterial food poisoning that affects about a quarter million people every year in the USA [1]. These toxins act on the gastrointestinal tract, induce emesis, and activate the immune system. SEs bind to the major histocompatibility complex (MHC) class II molecules of antigen presenting cells (APC) and also bind to the variable region (Vβ) on the T-cell receptor forming a bridge between APC and T-cells, leading to cytokine secretion and $CD4^+$ T-cell proliferation. Previous work has shown that there is a relationship between the emetic activity of SEs and their superantigenic activity. This was demonstrated, for example, by site-directed mutagenesis of Staphylococcal enterotoxin type C2 resulting in both an inhibition of its emetic activity and elimination of its superantigenic activity [2].

Miguel R. Ossandon et al. (eds.), *Biomedical Engineering Technologies: Volume 1*, Methods in Molecular Biology, vol. 2393, https://doi.org/10.1007/978-1-0716-1803-5_13, 

### 1.1 Detection and Analysis of SEs

The ability to rapidly detect and quantify SEs is very important, epidemiologically to identify the causes of staphylococcal outbreaks and to stop similar outbreaks in the future. The most common techniques are immunological methods using antibodies specific to the target SE. These methods include latex agglutination, enzyme-linked immunosorbent assay (ELISA), ELISA Lab-on-a-Chip (ELISA-LOC), real-time surface plasmon resonance (SPR) to detect the binding of the SEs toxin(s) to antibodies immobilized on the surface of a sensor, and nanoparticle based immune assays. The detection and analysis of SEs in food and other complex samples may result in nonspecific responses caused by antibody cross-reactivity with unrelated antigens [3]. Western blotting has the potential to overcome some of the major problems associated with detection of toxins in food, because the size determination of the protein bound by an antibody increases the specificity of detection. Another approach to increase specificity is the use of mass spectrometry to verify the SEs bound on an SPR chip. However, while immunoassays can measure the presence of SEs they cannot differentiate between the active form of SEs, which is a threat to public health, and inactive SEs [4]. The ability to discern active toxin is also important for development of food treatment and processing methods. Cooking and pasteurization are forms of heat treatment that inactivate Staphylococcal Enterotoxin A (SEA) [5]. Pulsed ultraviolet (UV) light has also been applied to inactivate SEA [6].

### 1.2 In Vivo Measurement of SE Activity

The current accepted method to detect biologically active SEs is to administer SEs directly into the stomach of monkeys or kittens and then observe for any emetic response [7, 8]. This method of detection is expensive, difficult to reproduce, and has low sensitivity. The administration of 10 μg SEA produces vomiting in 50% of the animals [7–9]. These in vivo monkey or kitten bioassay are not very practical for many settings and raise ethical concerns regarding the use of experimental animals. Bavari et al. and Hufnagle et al. demonstrated a novel ex vivo technique utilizing human peripheral blood mononuclear cells (PBMC) in which they measured T-cell proliferation using 3H thymidine incorporation [10, 11]. However, using PBMCs from healthy human donors adds complexity and they are not always available. In addition, this method produces radioactive waste and is therefore not a desirable alternative method to the in vivo bioassays for detection of active SEs.

### 1.3 Ex Vivo Assays for Detection of Biologically Active SEs

To overcome the inherent limitations of such bioassays, our lab developed several mouse cell-based assays as an alternative method for measuring the activity of SEs. These methods based on the superantigen activity of SEs include an ex vivo splenocyte proliferation assay and a cytokine secretion assay (see diagram right arm).

#### 1.3.1 DNA Quantitation to Measure Splenocyte Proliferation

This method is based on DNA labeling. After incubation of splenocytes with SEs, cell proliferation is measured by labeling the proliferating cells' DNA with bromodeoxyuridine (5-bromo-2-deoxyuridine, BrdU) and then quantifying the incorporated BrdU by immunohistochemistry. BrdU labeling is shown to be highly correlated with SEA concentration ($R^2 = 0.99$) and can detect as little as 20 pg/mL of SEA, which is far more sensitive than most enzyme-linked immunosorbent assays. Our assay can also distinguish between active toxin and inactive forms of the toxin [12]. By applying immunomagnetic beads that capture and concentrate the toxin, our assay is able to overcome matrix interference.

#### 1.3.2 Ex Vivo Cytokine Secretion Assay for Detection of Biologically Active SEs

An alternative to BrdU labeling of DNA, we used several ex vivo approaches to detect cell activation of splenocytes or primary naïve $CD4^+$ T-cells exposed to biologically active SEs. These methods utilize the induction by SEs of differential expression of cytokines including IL-2 [13, 14], IFN-γ [15], TNF [16], or the cell surface CD154 [17]. Cytokines can be measured by flow cytometry [14, 16], qRT-PCR [15]. These assays can be used for food testing [12–14]. The ex vivo method has advantages over the in vivo monkey and kitten bioassay because one mouse spleen can provide enough cells for roughly 500 assays. However, ex vivo splenocyte based assays still require the use of animals which raises ethical concerns.

### 1.4 In Vitro Assays for Detection of Biologically Active SEs

The Lautenberg Chemical Safety Act encourages the development and adoption of alternatives to testing on animals for chemical toxicity methodologies. To entirely avoid the need to use animals, we took a step further to eliminate this concern by replacing the mouse splenocytes with human cell lines to avoid all animal testing. The activity assay is based on using two cell lines: a $CD4^+$ T-cell line in combination with a B-cell line which presents the SE-MHC class II complex to the $CD4^+$ T-cell line. We use several alternative methods for measuring the activity of SEs (see diagram left arm).

#### 1.4.1 Cytokine Quantitation to Measure Biologically Active SEA

The assay utilizes CCRF-CEM, a human $CD4^+$ T-cell line, and Raji B- cells. This T-cell line is specifically activated by SEA resulting in measurable secretion of IL-2. Application of this in vitro assay showed that increasing concentrations of SEA induced a dose dependent IL-2 secretion in the range of 0.001 ng/mL to 10 ng/mL SEA [14]. The assay is highly specific to biologically active SEA, compared with the related SEs toxin subtypes B, D, and E or heat inactivated SEA, which produce no secretion of IL-2.

#### 1.4.2 Bioluminescence Based Assay for Detection of Biologically Active SEE

To measure SEE, we utilize a genetically engineered human T-lymphocyte Jurkat cell-line expressing the luciferase reporter gene under the regulation of nuclear factor of activated T-cells response element (NFAT-RE) combined with a Raji B-cell line

that presents the SEE-MHC class II to the engineered T cell line. NFAT-RE regulates CD154, a surface marker that we previously found to indicate activation by SEs [17]. Exposure of the above mixed culture to SEE induces differential expression of the luciferase gene and bioluminescence can be measured by fluorimeter or CCD camera over a 6-log range. The limit of detection of biologically active SEE is 1 fg/mL which is $10^9$ times more sensitive than the monkey and kitten bioassay [18].

#### 1.4.3 T-Cell Receptor Vβ Based Assay for Detection of Biologically Active SEE

SEE induces internalization of TCR Vβ8 protein in a dose-dependent manner. This phenomenon can be utilized and it was demonstrated that increasing concentrations of SEE reduced TCR Vβ8 protein levels in a dose-dependent manner as measured by flow cytometry [19]. Similarly, SEA induces reduction in TCR Vβ9 protein in a dose-dependent manner [20]. Both of these specific assays can discriminate between biologically active and inactive SE. After stimulation, cells are stained with fluorescently conjugated anti-Vβ (Vβ8 or Vβ9) mAb and fluorescence is measured by flow cytometry.

This chapter describe ex vivo and in vitro methods for detection of bioactive staphylococcal enterotoxins.

## 2 Materials

### 2.1 Chemical and Reagents

#### 2.1.1 Toxin Isolation from Matrix

1. Dynabeads M-280 tosylactivated (Invitrogen, Carlsbad, CA).
2. DynaMag (Invitrogen, Carlsbad, CA).
3. Dynabeads Mouse CD4 L3T4 Isolation Kit, (Invitrogen/Life Technologies, Carlsbad, CA, USA).
4. Isolation buffer: PBS supplemented with 0.1% BSA and 2 mM EDTA.
5. DETACHaBEAD® mouse CD4 (Invitrogen/Life Technologies, Carlsbad, CA, USA).
6. 100 mM Glycine-HCl, pH 2.5.
7. 0.1 M Sodium borate buffer, pH 9.5.
8. 0.2 M Tris–HCl, pH 8.5.

### 2.2 Chemical and Reagents for the Ex Vivo Assay

1. C57BL/6 female mice (The Jackson Laboratory Sacramento, CA).
2. Centrifuge.
3. $CO_2$ incubator.
4. 70% alcohol.
5. 6 $cm^3$ syringe and 18 ½ gauge needle.
6. Phosphate buffered saline (PBS), pH 7.4.

7. Bovine serum albumin (BSA) (Hyclone, Logan, UT).
8. 200 mM glutamine (Gibco).
9. Antibiotic–antimycotic (Gibco; containing penicillin, streptomycin, and amphotericin B).
10. Nonessential amino acid mix (Gibco).
11. 100 mM sodium pyruvate (Gibco).
12. β-mercaptoethanol (Sigma).
13. Trypan blue (Fisher Scientific).
14. 1 M $H_2SO_4$.
15. Hemocytometer (Fisher Scientific).
16. 5-bromo-2-deoxyuridine (BrdU) Cell Proliferation Assay (Calbiochem, San Diego, CA).
17. BrdU Cell Proliferation Assay Kit (Millipore Sigma, Cat no. 2750).
18. BD Cytometric Bead Array (CBA).
19. Mouse Th1/Th2/Th17 Cytokine Kit (BD Catalog No. 560485) or BD CBA Human Th1/Th2/Th17 Cytokine Kit (560484).
20. CD154 Enrichment and Detection Kit (PE), mouse (Miltenyi, Catalog No. 130-093-129).
21. Lysis buffer (0.15 M $NH_4Cl$, 10 mM $KHCO_3$, 0.1 mM $Na_2EDTA$).
22. Russ-10 cell culture medium.
    450 mL of RPMI 1640 medium without glutamine.
    50 mL fetal bovine serum.
    5 mL 200 mM glutamine.
    5 mL antibiotic–antimycotic (10,000 U/mL penicillin, 10,000 μg/mL streptomycin, and 25 μg/mL of amphotericin B).
    5 mL nonessential amino acid mix.
    5 mL 100 mM sodium pyruvate.
    0.25 mL of 100 mM β-mercaptoethanol.

### 2.3 Media and Buffers for the In Vitro Assay

1. Dead cell stain eFluor 780 (eBioscience, catalog no. 65-0865-18).
2. BD OptEIA™ Human IL-2 ELISA Set (BD, Catalog No. 555190).
3. BD OptEIA™ Human IL-10 ELISA Set (BD, Catalog No. 555157).
4. BioGlo luciferase assay system (Promega, Catalog no. G7940).

5. CCRF-CEM human lymphoblastoid T-cell line (ATCC® CCL-119).
6. Raji human Burkitt's lymphoma B cell line (ATCC® CCL-86).
7. Genetically engineered Jurkat T cell-line (Promega, Catalog No. J1621) which expresses the luciferase reporter gene under control of NFAT-RE response elements.
8. Anti-SEA antibody (Toxin Technology, Sarasota, FL).
9. APC conjugated anti-mouse CD4 antibody (e.g., eBiosciences, Catalog No. 17-0041-82).
10. PacBlue-labeled mouse anti-human CD19 antibody (eBioscience, catalog no. MHCD1928).
11. PE-labeled mouse anti-human Vβ9 antibody (eBioscience, catalog no. 12-4899-42.
12. FITC-labeled mouse anti-human Vβ8 antibody (BD, Catalog no. 555606).
13. PE-labeled mouse anti-human CD19 antibody (BD, Catalog no. 555413).
14. Modified RPMI 1640 cell culture medium.
    450 mL of RPMI 1640 medium (ATCC modification*), Gibco, catalog No. A1049101.

    50 mL fetal bovine serum.

    5 mL nonessential amino acid mix.

    5 mL antibiotic–antimycotic (10,000 U/mL penicillin, 10,000 μg/mL streptomycin, and 25 μg/mL of amphotericin B).
15. Selective cell culture medium.
    450 mL of RPMI 1640 medium (ATCC modification*), Gibco, catalog No. A1049101.

    50 mL fetal bovine serum.

    5 mL nonessential amino acid mix.

    200 μg/mL hygromycin B.

    * RPMI is modified with 2 mM L-glutamine, 10 mM HEPES, 1 mM sodium pyruvate, 25 mM glucose, and 18 mM sodium bicarbonate.
16. A flow cytometer with one 488-nm or 532-nm laser and one 633-nm or 635-nm laser and fluorescence detection channels capable of distinguishing 576-nm, 660-nm, and >680-nm fluorescence. FACSAria Fusion cytometer (BD Biosciences, San Jose, CA).
17. A BioTek microplate reader or equivalent.

## 3 Methods

### 3.1 Staphylococcus Enterotoxins Isolation Methods

Toxin isolation from food matrix and reduction of *food matrix interference* can be achieved by applying immunomagnetic beads that separate toxin and concentrate SEs from food.

#### 3.1.1 Conjugation of Magnetic Beads with Anti-SE Antibody

1. Wash 100 μL Dynabeads M-280 tosylactivated twice with 600 μL of 0.1 M sodium borate buffer, pH 9.5, and diluted in the same buffer to $2 \times 10^9$ beads/μL.
2. Add 30 μg of purified antibody against the SE subtype of interest to $1 \times 10^8$ beads (50 μL).
3. Incubate the antibody and bead mixture for 24 h at 37 °C on a slow shaker to facilitate covalent binding.
4. Wash the coated beads twice for 5 min at 4 °C with 1 mL phosphate buffered saline (PBS), pH 7.4, containing 0.1% bovine serum albumin (BSA), wash once for 4 h at 37 °C with 0.2 M Tris–HCl, pH 8.5, containing 0.1% BSA, and wash once more for 5 min at 4 °C with PBS, pH 7.4, containing 0.1% BSA.
5. Resuspend the beads in 50 μL of Tris-BSA buffer.

#### 3.1.2 Toxin Binding and Disassociation of SEA from Beads

1. Add 15 μL anti-SE conjugated immunomagnetic beads prepared in Subheading 2.11 to a 4 mL food or analytical sample and incubate 24 h at 4 °C with a tilting motion.
2. Place sample on a DynaMag magnet for 2 min to collect the beads.
3. Wash beads twice with PBS, pH 7.4, containing 0.1% BSA. Elute toxin from beads with 7.5 μL of 100 mM glycine–HCl (pH 2.5) and then neutralize with 7.5 μL of 2× Tris-buffered saline (TBS) (pH 8.3).
4. Use toxin eluent in assay procedure of choice.

### 3.2 Mouse Cell Isolation and Analysis Methods

In order to ex vivo study the effect of enterotoxins on lymphocytes, suspensions from lymph nodes are needed.

#### 3.2.1 Murine Splenocyte Isolation

1. Sacrifice C57BL/6 female mice by cervical dislocation and rinse with 70% alcohol.
2. Aseptically remove spleen (which is located at the left side of the abdomen) and disrupt using a syringe and needle in Russ-10 cell culture medium.
3. Centrifuge cells at 200 × *g* and 4 °C for 10 min.
4. Lyse red blood cells by adding red cell lysis buffer (0.15 M $NH_4Cl$, 10 mM $KHCO_3$, 0.1 mM $Na_2EDTA$) and incubate

for 5 min at room temperature. Spin the cells (200 × *g*, 10 min) and remove the lysis buffer.

5. Resuspend cells in Russ-10 medium, and count viable cells using trypan blue and a hemocytometer.

#### 3.2.2 Positive Isolation of Murine CD4⁺ T-Cells

1. Resuspend freshly isolated splenocytes (from Subheading 3.2.1) in isolation buffer (PBS supplemented with 0.1% BSA and 2 mM EDTA) at a concentration of $1 \times 10^7$/mL.
2. Incubate cells with washed Dynabeads (25 μL of Dynabeads per $10^7$ cells) for 20 min on ice with gentle rotation.
3. Following incubation, place the cells and Dynabeads on a magnet for 2 min and remove the supernatant from the cell-bead pellet.
4. Wash the bead-bound cells three times with isolation buffer.
5. Resuspend the bead-bound cells in Russ-10 media ($10^7$ cells per 100 μL of media).
6. Add DETACHaBEAD® mouse CD4 (10 μL per $10^7$ cells).
7. Incubate cells for 45 min with gentle rotation at room temperature. Wash the detached cells three times with isolation buffer and resuspend in media.

### 3.3 Murine Cell-Based Methods for Measuring the Activity of Staphylococcal Enterotoxins

To overcome the inherent limitations of in vivo monkey or kitten bioassays we describe an in vitro T cell proliferation assay based on SEs superantigen activity as an alternative method for measuring the activity of staphylococcal enterotoxins.

#### 3.3.1 T Cell Proliferation Assay for Measuring the Activity of Staphylococcal Enterotoxins (for this Step Use the BrdU Cell Proliferation Assay Kit)

1. Using murine splenocyte cells (from Subheading 3.2.1) or $CD4^+$ T cells (from Subheading 3.2.2) place cells in 96-well plates ($1 \times 10^6$ cells/mL in a total volume of 0.2 mL) in Russ-10 medium.
2. Add analyte sample and concentrations of SEA (ranging from 400 ng/mL to 4 pg/mL) to a final volume of 0.2 mL.
3. Incubate plates at 37 °C in a 5% $CO_2$ incubator.
4. After 48 h incubation, quantify cell proliferation by adding (5-bromo-2-deoxyuridine) BrdU to cells 20 μL/well. Incubate the cells for 4 h at 37 °C.
5. Remove the labeling medium by spinning the plate at 200 × *g* for 10 min. Pour off medium.
6. Add 200 μL/well of the fix denature reagent to the cells. Incubate for 30 min at RT.
7. Remove the fix denature reagent by pouring off.
8. Air dry the cells by incubating at room temperature until dry (*see* **Note 2**).

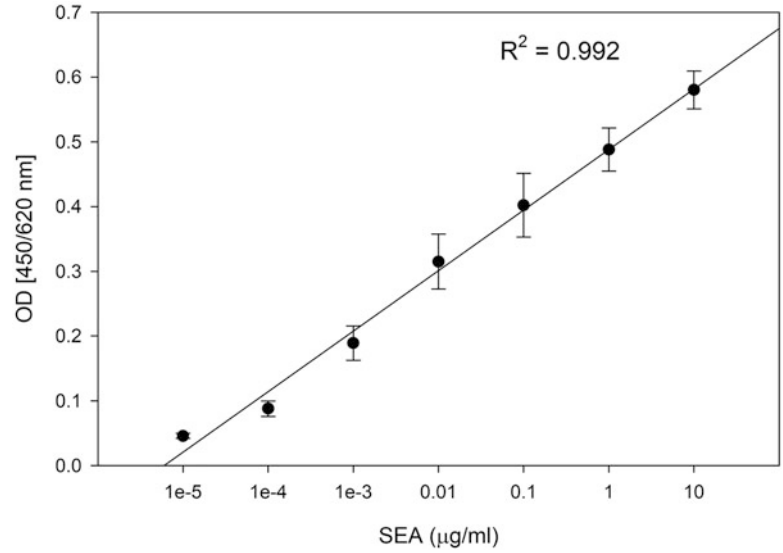


**Fig. 1** Detection of SEA in cell culture medium. Cells were spiked with increasing concentrations of SEA. After incubation for 2 days newly synthesized DNA was measured BrdU labeling. The incorporation of BrdU into the DNA was measured by the ratio OD [450/620 nm]. Error bars represent standard errors

9. Add Anti-BrdU solution 100 µL/well. Incubate at RT for 90 min.
10. Wash plate three times with wash solution.
11. Add 100 µL/well of substrate solution and incubate at RT until development is sufficient for reading (5–30 min).
12. To stop reaction, add 25 µL/well of 1 M $H_2SO_4$.
13. Record spectroscopic measurements of $OD_{620nm}$ and $OD_{450nm}$.
14. The incorporation of BrdU into the DNA is measured by the ratio OD [450/620 nm] as shown in Fig. 1.

### 3.4 Measuring T-Cell Cytokines Resulting from Enterotoxins Activation

In ex vivo and in vitro assay enterotoxins stimulate *cytokine* production in *dose* and time *dependent manner*.

#### 3.4.1 Cytometric Bead Array for Detection of SE Activity (for this Step Use the BD CBA Mouse Kit)

Cytometric Bead Arrays are useful when surveying a range of possible cytokine effects resulting from enterotoxins activation of splenocytes or $CD4^+$ T cells. Multiple cytokines can be analyzed at once in a single sample of 50 µL. The cytometric bead array is useful in the beginning to determine which cytokine is released and then subsequently a cytokine ELISA kit can be used (Subheading 2.3).

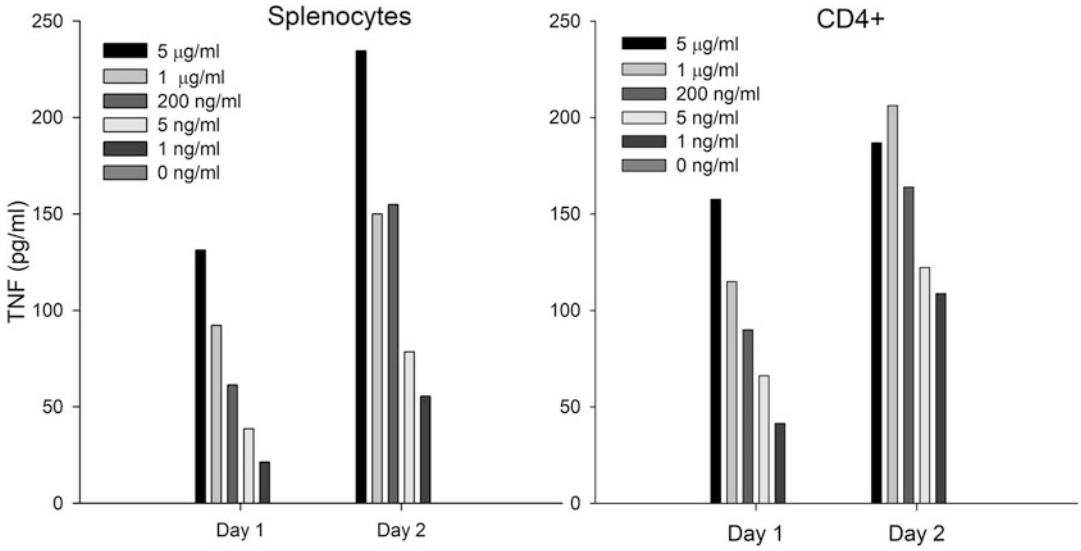


**Fig. 2** Flow cytometric analysis for quantification of biologically active SEA. Primary naïve $CD4^+$ T-cells or splenocytes were spiked with increasing concentrations of SEA. After 24 h or 48 h of stimulation with SEA, TNF protein secretion was measured by flow cytometry

1. Using murine splenocyte cells (from Subheading 3.2.1) or $CD4^+$ T cells (from Subheading 3.2.2) place cells in 96-well plates ($1 \times 10^6$ cells/mL in a total volume of 0.2 mL) in Russ-10 medium.
2. Into each filled well add 100 μL toxin test sample or SE control covering the range 400 ng/mL to 4 pg/mL diluted in media.
3. Incubate plates at 37 °C in a 5% $CO_2$ incubator for 24 and/or 48 h.
4. Remove supernatant from wells.
5. Analyze cytokines secreted into the well supernatant following the respective manufacturer's procedures for the BD CBA Mouse.

*3.4.2 ELISA (Enzyme Linked Immunosorbent Assay) for Detection of SE Activity (for this Step Use Cytokine ELISA Kits)*

Enterotoxins type A stimulate proliferation of $CD4^+$ T cells resulting in release of cytokines such TNF-α, IL-2, and IFN-γ in a *dose-dependent manner*. As shown in flow cytometry analysis (Fig. 2), with increasing levels of SEA, levels of TNF-α increased as well in both splenocytes and naïve $CD4^+$ T-cells.

More practical and inexpensive quantitative ELISA assay (Subheading 2.3) can be used for detection of one of those cytokines. Due to the fact that this kit is specific to one cytokine it is useful after using the Cytometric Bead Array (Subheading 2.2, **item 16**).

1. Using murine splenocyte cells (from Subheading 3.2.1) or $CD4^+$ T cells (from Subheading 3.2.2) place cells in 96-well

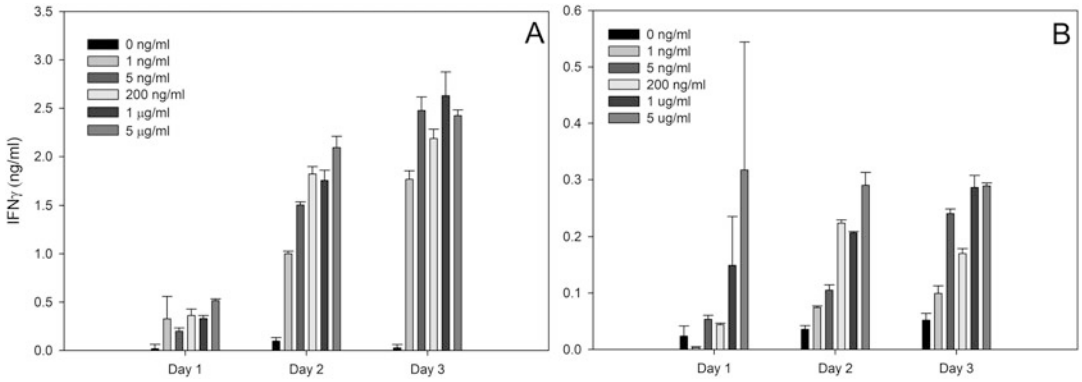


**Fig. 3** Quantification of biologically active SEA using IFNγ ELISA assay. Increasing concentrations of SEA was incubated with splenocytes. (**a**) or $CD4^+$ T-cells (**b**). After 24 h, 48 h, or 72 h of stimulation with SEA, IFNγ protein secretion was measured by ELISA assay. Error bars represent standard error

plates ($1 \times 10^6$ cells/mL in a total volume of 0.2 mL) in Russ-10 medium.

2. Into each filled well add 100 µL toxin test sample or SE control covering the range 400 ng/mL to 4 pg/mL diluted in media.
3. Incubate plates at 37 °C in a 5% $CO_2$ incubator for 48 h.
4. Remove supernatant from wells.
5. Analyze selected cytokines secreted into the supernatant following the respective manufacturer's procedures for Cytokine ELISA Kit, such as BD OptEIA Human IL-2 ELISA kit (Cat 555190) for the target cytokine and type of cells used.

As shown in Fig. 3, increasing concentrations of SEA were incubated with splenocytes (Fig. 3a) or $CD4^+$ T-cells (Fig. 3b). After a 24 h, 48 h, or 72 h stimulation with SEA, IFNγ protein secretion was measured by ELISA assay.

As shown in Fig. 4, the quantitative *detection* of biologically active *SEA* in various complex food products such as beef, chicken, milk and green bean can be measured by IL-2 secretion.

### *3.4.3 Measuring Murine Cell Surface Receptors for Rapid Detection of Active SEA*

The flow cytometry data presented in Fig. 5 show that short-term (2–6 h) ex vivo exposure of primary naïve $CD4^+$ T-cells to SEA induces differential expression of the T cell surface receptor CD154 levels in a time and dose-dependent manner.

1. Follow Subheadings 3.2.1 and 3.2.2 to obtain $CD4^+$ T-Cells.
2. Place cells in 96-well plates ($1 \times 10^6$ cells/mL in a total volume of 0.2 mL) in Russ-10 medium.
3. Add analyte sample and a range of concentrations of SEA (ranging from 400 ng/mL to 4 pg/mL) to a final volume of 0.2 mL.

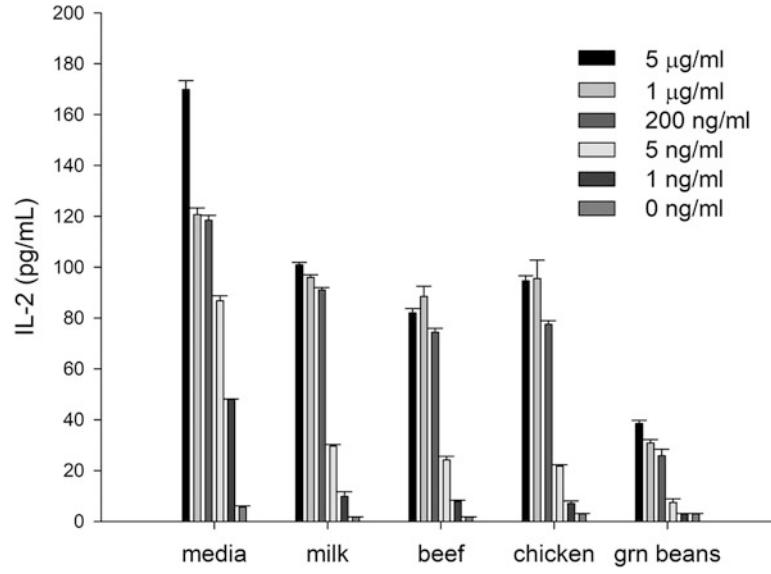


**Fig. 4** Utilizing IL-2 secretion measurement for detecting biologically active SEA in various food matrices. Different food matrices were spiked with various concentrations of SEA and incubated for 24 h. Immunomagnetic beads were used to isolate SEA. The isolated toxin was incubated with splenocytes. IL-2 secretion was measured by ELISA

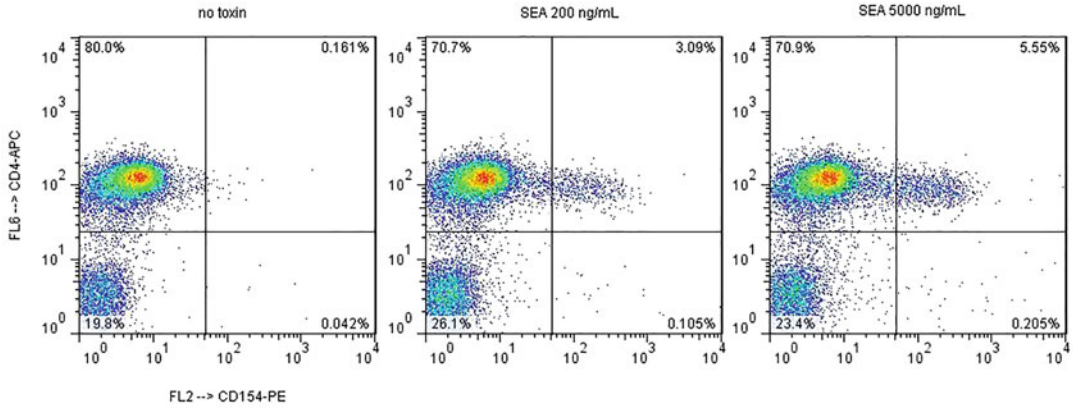


**Fig. 5** Analysis of the expression of the T cell surface receptor CD154 after incubation with SEA in milk. Fifteen microliters of milk spiked with increasing concentrations of SEA was added to 185 μL of 1 × 10 cells mL-1. After incubation for 6 h, expression of CD154 was measured by flow cytometry

4. Incubate samples at 37 °C in a 5% $CO_2$ incubator for 6 h.
5. Prepare the cells for flow cytometry by removing the media and washing the cells two times with PBS by spinning at 200 × g for 10 min each.
6. Following manufacturer's instructions, add 4 μL of CD154 detection cocktail to each sample. Also add 0.125 μg per

$1 \times 10^6$ APC conjugated anti-mouse CD4 antibody (eBioscience, Catalog No. 17-0041-82).

7. Incubate samples at 4 °C for 30 min.
8. Wash samples twice in 200 μL PBS (200 × *g*, 10 min) and then resuspend in 0.5 mL PBS.
9. Transfer samples through a cell strainer to remove any clumps, into a suitable flow cytometer sample tube, for example, BD Catalog No. 352235, 5-mL polystyrene tube with cell strainer snap cap.
10. Analyze samples by flow cytometry, recording forward and side light scattering, and fluorescence in the PE and APC channels. Create a gate around the cell population in the SSC v FSC plot to exclude debris. Plot the data from that gate in an APC v PE dot plot and identify the percent of population that is CD4 and CD154 positive.

## 3.5 Methods for Measuring SEs Utilizing Human T-Cell Line

The use of human T-cell lines is an alternate method that would not require the harvesting of any tissues from living animals.

### 3.5.1 Biochemiluminescent Jurkat Cells for Measuring Active Staphylococcal Enterotoxin Type E (SEE)

We apply a genetically engineered T cell-line expressing the luciferase reporter gene under the regulation of nuclear factor of activated T-cells response element (NFAT-RE), combined with a Raji B-cell line that presents the SEE-MHC (major histocompatibility complex) class II to the engineered T cell line. The exposure of the above mixed culture to SEE induces differential expression of the luciferase gene which is measured as bioluminescence.

1. Maintain Jurkat cells in selective media (Subheading 2.3, **item 15**) in a humidified 5% $CO_2$ atmosphere in an incubator kept at 37 °C. Maintain Raji cells in modified RPMI 1640 media (Subheading 2.3, **item 14**) in a humidified 5% $CO_2$ atmosphere in an incubator kept at 37 °C (*see* **Note 1**).
2. Prepare suspension of Jurkat cells in selective RPMI 1640 media (Subheading 2.3, **item 15**) to a concentration of $2 \times 10^6$ cells/mL. Prepare suspension of Raji cells in cell culture medium to a concentration of $2 \times 10^6$ cells/mL.
3. In wells of a white 96-well clear bottom plate combine 50 μL aliquots of Jurkat suspension with 25 μL aliquots of Raji suspension and 25 μL aliquots of test sample or toxin standards.
4. Incubate plate for 5 h at 37 °C and then equilibrate to room temperature for 10–15 min.
5. Follow the manufacturer's instructions for the luciferase assay system and quantify the luciferase expression in each well with a microplate reader.

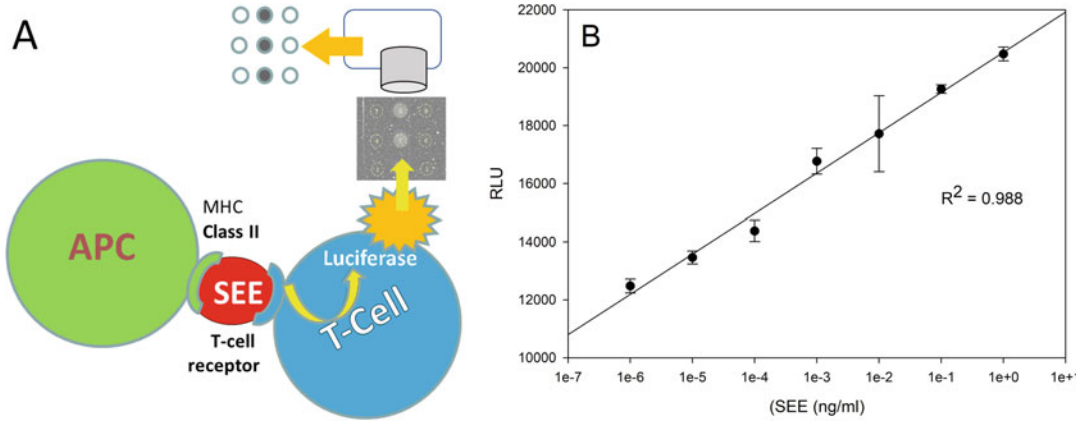


**Fig. 6** (**a**) Model of the bioluminescence assay for measuring biologically active SEE. Jurkat reporter cells were plated with Raji cells in a 96-well plate. The mixed cultures were coincubated with various concentrations of SEE for 5 h. The emission result was detected by luminometer (**b**). Error bars represent standard errors

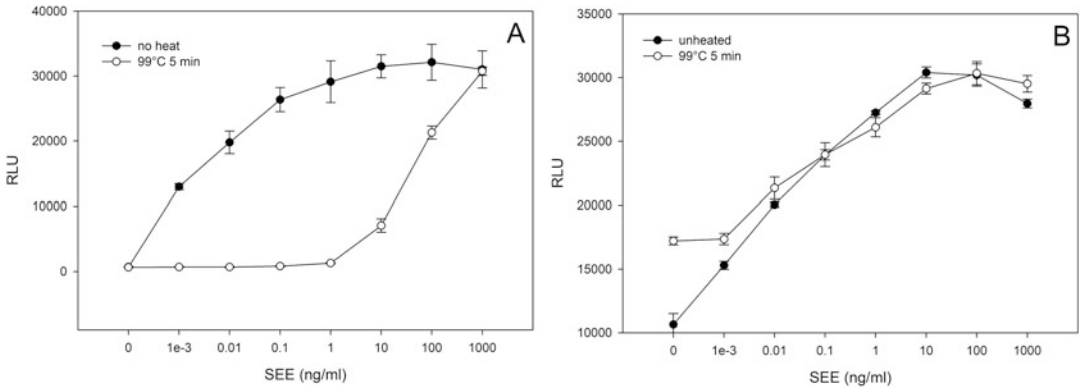


**Fig. 7** Bioluminescence assay for measuring biologically active SEE in PBS and milk Thermal treatment at 99 °C for 5 min reduces the biological activity of SEE in PBS. However, milk has a protective effect on SEE retained from its initial activity. PBS (**a**) and milk (**b**) spiked with increasing concentrations of SEE were treated at 99 °C for 5 min. Thermal treated spiked PBS or milk (15 μL) was added to the Jurkat reporter cells. After incubation for 5 h, the luciferase enzyme activity was determined. Photon emission was detected by luminometer. Error bars represent standard errors

The exposure of the genetically engineered T cell-line expressing the luciferase reporter gene under the regulation of nuclear factor of activated T-cells response element (NFAT-RE), combined with a Raji B-cell line that presents the SEE-MHC to SEE induces expression of the luciferase gene resulted in bioluminescence is read out in a dose dependent manner over a 6-log range (Fig. 6). The limit of detection of biologically active SEE is 1 fg/mL which is $10^9$ times more sensitive than the monkey and kitten bioassay.

The method can be used for food analysis. As shown in Fig. 7, SEE can be detected in complex food samples including milk. The control for these experiments was heat treated SEE in PBS which

reduced biological activities. Such experiment demonstrates that heat inactivation of SEE was less effective in milk than in buffer.

### 3.5.2 T-Cell Receptor Vβ8 Expression on Jurkat Human T-Cells for Quantifying Biologically Active Enterotoxin Type E (SEE)

In addition to the luciferase-based detection described above which requires the luciferase genetic construct, SEE can be detected when it is presented by Raji B-cell line in combination with a Jurkat T cell-line which manifests reduced TCR Vβ8 protein levels in a dose dependent manner (*see* **Note 3**). This assay can be used as faster alternative to a genetically engineered T cell-line expressing the luciferase reporter gene (Subheading 3.5.1).

1. Maintain Jurkat cells in selective media (Subheading 2.3, **item 15**) in a humidified 5% $CO_2$ atmosphere in an incubator kept at 37 °C (*see* **Note 1**). Maintain Raji cells in modified RPMI 1640 media (Subheading 2.3, **item 14**).
2. Prepare suspension of Jurkat and Raji cells in modified RPMI 1640 media (Subheading 2.3, **item 14**) to a concentration of $2 \times 10^6$ cells/mL.
3. In wells of a 96-well plate combine aliquots of 50 μL Jurkat suspension with aliquots of 25 μL Raji suspension and 25 μL aliquots of test sample or toxin standards.
4. Incubate plate for 2 h at 37 °C.
5. Remove the media and wash the cells twice with PBS by spinning at 200 × *g* for 10 min each.
6. Label cells with FITC anti-Vβ8 (6 μg per $1 \times 10^6$ cells), PE anti-CD19 (6 μg per $1 \times 10^6$ cells), and eFluor 780 (1 μL per $1 \times 10^6$ cells) and incubate in the dark at 4 °C for 30 min.
7. Wash cells twice with PBS as above and transfer samples through a cell strainer to remove any clumps, into a suitable flow cytometer sample tube, for example, BD Catalog No. 352235 5-mL polystyrene tube with cell strainer snap cap.
8. Analyze samples by flow cytometry, using compensation and recording forward and side light scattering and fluorescence in the FITC (520-nm), PE (576-nm), and eFluor 780 (780-nm) channels. Create a gate around the cell population in the SSC v FSC plot to exclude debris. From the gated population exclude the CD19 positive (B cell) and eFluor 780 positive (dead) cells. From the remaining population record the FITC anti-Vβ8 fluorescence and calculate the mean.

The assay for quantifying biologically active SEE utilizing T-Cell receptor Vβ8 expression on Jurkat Human T-Cells is shown in Fig. 8. As the level of SEE increases, the level of T-Cell receptor Vβ8 Expression on Jurkat Human T-Cells decreases.

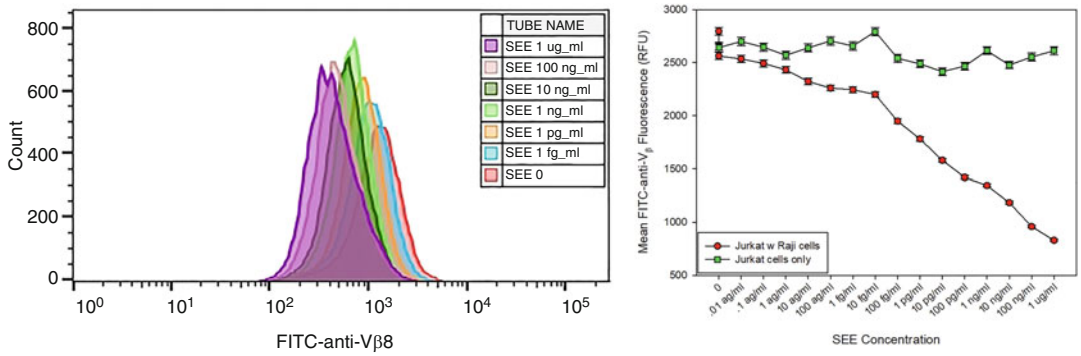


**Fig. 8** T-Cell Receptor Vβ8 8 expression on Jurkat Human T-Cells for quantifying biologically active enterotoxin type E. SEE induced specific reduction in TCR Vβ8 protein in a dose dependent manner. The mixed Jurkat T cell and Raji B cell were coincubated with increasing concentrations of SEE for 2 h. Cells were stained with FITC conjugated anti-Vß8 mAb after stimulation. Fluorescence intensity was measured by flow cytometry. (**a**) Shows histograms and mean florescence for live T-cell population (**b**) shows the plot of the results of the Vβ8 expression of Jurkat Human T-Cells with and without Raji B-cell line exposed to different level of the toxin

*3.5.3 Measuring Active SEA Based on T-Cell Receptor Vβ9 Expression on CCRF-CEM Human T-Cells*

Various toxins have different specificity for the Vβ receptor. SEA exhibits specificity to Vβ9. Such toxin specificity can be used for the toxin biological typing. A cell-based assay for SEA quantification in which biologically active SEA is presented by Raji B-cell line to CCRF-CEM T-cell line resulting in internalization of Vβ9 within 2 h with dose dependency over a 6-log range of SEA concentrations (Fig. 9). The method for SEA analysis is as follows.

1. Maintain cell lines in modified RPMI 1640 media (Subheading 2.3, **item 14**) in a humidified 5% $CO_2$ atmosphere in an incubator kept at 37 °C (*see* **Note 1**).
2. Prepare suspensions of CCRF-CEM and Raji cells in cell culture medium (Subheading 2.3, **item 14**) to a concentration of $2 \times 10^6$ cells/mL.
3. In wells of a 96-well plate combine aliquots of 50 μL CCRF-CEM suspension with aliquots of 25 μL Raji suspension and 25 μL aliquots of test sample or toxin standards.
4. Incubate plate for 2 h at 37 °C.
5. Remove the media and wash the cells twice with PBS by spinning at 200 × *g* for 10 min each.
6. Label cells with PE anti-Vβ9 (0.125 μg per $1 \times 10^6$), PacBlue anti-CD19 (0.125 μg per $1 \times 10^6$), and eFluor 780 (1 μL per $1 \times 10^6$ cells) and incubate in the dark at 4 °C for 30 min.
7. Wash cells twice with PBS as above and transfer samples through a cell strainer to remove any clumps, into a suitable flow cytometer sample tube, for example, BD Catalog No. 352235 5-mL polystyrene tube with cell strainer snap cap.
8. Analyze samples by flow cytometry, recording forward and side light scattering and fluorescence in the PacBlue (455-nm), PE

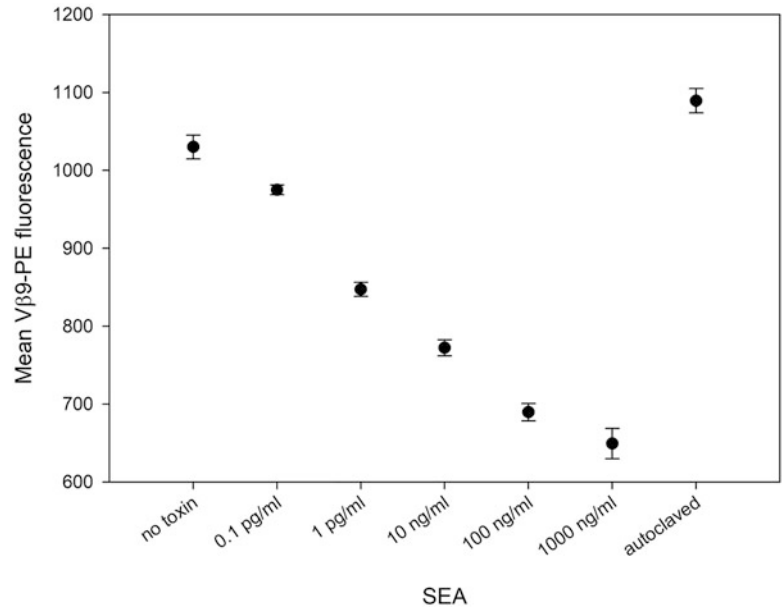


**Fig. 9** SEA induced reduction in TCR Vβ9 protein in a dose dependent manner. The mixed CCRF-CEM T-cells and Raji B cells were coincubated with increasing concentrations of SEA for 2 h. After stimulation the cells were stained with FITC conjugated anti-Vβ9 mAb. Mean florescence intensity for Vβ9 in live T-cell population was measured by flow cytometry

(576-nm), and eFluor 780 (780-nm) channels. Create a gate around the cell population in the SSC v FSC plot to exclude debris. From the gated population exclude the CD19 positive (B cell) and eFluor 780 positive (dead) cells. From the remaining population record the PE anti-Vβ9 fluorescence and calculate the mean.

The results in Fig. 9 show the SEA induced reduction in TCR Vβ9 protein.

### *3.5.4 SEA Activity Analysis Utilizing CCRF-CEM Human T-Cell Cytokine Secretion*

Another approach for cell-based SEA activity analysis is analysis of cytokine secretion. similar to the other SEA assays described above, the biologically active SEA is presented by Raji B-cell line to CCRF-CEM T-cell line. However, in this assay IL-2 and IL-10 secretion was measured by cytometric bead array to identify the most secreted cytokines. An alternative more practical and inexpensive approach is quantitative ELISA assay which was used for detection of one of those cytokines (Subheading 2.3).

1. Maintain cell lines in modified RPMI 1640 media (Subheading 2.3, **item 14**) in a humidified 5% $CO_2$ atmosphere in an incubator kept at 37 °C.
2. Prepare suspensions of CCRF-CEM and Raji cells in cell culture medium (Subheading 2.3, **item 14**) to a concentration of $2 \times 10^6$ cells/mL.

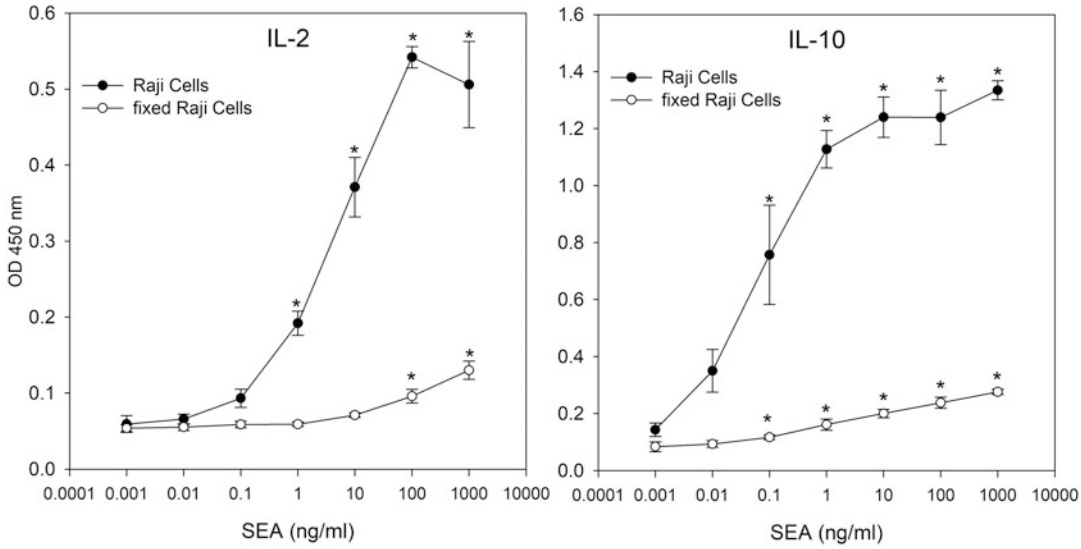


**Fig. 10** Activation of T-cells SEA superantigen leads to substantially higher cytokine production. CCRF-CEM T-cells and metabolic function Raji B-cells or fixed dead Raji B-cells were mixed in a coculture and were incubated for 24 h with increasing concentrations of SEA. Induction of IL-2 or IL-10 secretion was measured by ELISA. Error bars represent standard errors

3. In wells of a 96-well plate combine aliquots of 50 μL CCRF-CEM suspension with aliquots of 25 μL Raji suspension and 25 μL aliquots of test sample or toxin standards.
4. Incubate plate for 24 h at 37 °C.
5. Follow manufacturer's instructions for the respective ELISA sets to analyze IL-2 and IL-10 secreted into the supernatant.

The results of the assay to analyze IL-2 and IL-10 secreted into the supernatant are shown in Fig. 10.

## 4 Notes

1. For human cell-lines maintain cells in culture between $3 \times 10^5$ and $2 \times 10^6$/mL. Do not allow cells to grow to a density greater than $3 \times 10^6$/mL.
2. When measuring T-cell proliferation in mouse cells, the plate can be kept in +4 °C for 1 week after removal of fix denature reagent.
3. The limit of detection using the in vitro bioluminescence assay for the detection of biologically active SEE is 1 fg/mL which is $10^9$ times more sensitive than the monkey and kitten bioassay.

## References


1. Scallan E, Hoekstra RM, Angulo FJ, Tauxe RV, Widdowson MA, Roy SL, Jones JL, Griffin PM (2011) Foodborne illness acquired in the United States--major pathogens. Emerg Infect Dis 17:7–15. https://doi.org/10.3201/eid1701.P11101
2. Hui J, Cao Y, Xiao F, Zhang J, Li H, Hu F (2008) *Staphylococcus aureus* enterotoxin C2 mutants: biological activity assay in vitro. J Ind Microbiol Biotechnol 35:975–980. https://doi.org/10.1007/s10295-008-0372-3
3. Park CE, Akhtar M, Rayman MK (1992) Non-specific reactions of a commercial enzyme-linked immunosorbent assay kit (TECRA) for detection of staphylococcal enterotoxins in foods. Appl Environ Microbiol 58:2509–2512
4. Fujikawa H, Igarashi H (1988) Rapid latex agglutination test for detection of staphylococcal enterotoxins A to E that uses high-density latex particles. Appl Environ Microbiol 54:2345–2348
5. Hu J, Lin L, Chen M, Yan W (2018) Modeling for predicting the time to detection of staphylococcal enterotoxin a in cooked chicken product. Front Microbiol 9:1536. https://doi.org/10.3389/fmicb.2018.01536
6. Rajkovic A, Tomasevic I, De Meulenaer B, Devlieghere F (2017) The effect of pulsed UV light on *Escherichia coli* O157:H7, *Listeria monocytogenes*, salmonella typhimurium, Staphylococcus aureus and staphylococcal enterotoxin a on sliced fermented salami and its chemical quality. Food Control 73:829–837
7. Bergdoll MS (1988) Monkey feeding test for staphylococcal enterotoxin. Methods Enzymol 165:324–333. https://doi.org/10.1016/s0076-6879(88)65048-8
8. Bennett RW (2005) Staphylococcal enterotoxin and its rapid identification in foods by enzyme-linked immunosorbent assay-based methodology. J Food Prot 68:1264–1270. https://doi.org/10.4315/0362-028x-68.6.1264
9. Bergdoll MS, Borja CR, Robbins RN, Weiss KF (1971) Identification of enterotoxin E. Infect Immun 4:593–595
10. Bavari S, Hunt RE, Ulrich RG (1995) Divergence of human and nonhuman primate lymphocyte responses to bacterial superantigens. Clin Immunol Immunopathol 76:248–254. https://doi.org/10.1006/clin.1995.1123
11. Hufnagle WO, Tremaine MT, Betley MJ (1991) The carboxyl-terminal region of staphylococcal enterotoxin type A is required for a fully active molecule. Infect Immun 59:2126–2134
12. Rasooly R, Do PM (2009) In vitro cell-based assay for activity analysis of staphylococcal enterotoxin A in food. FEMS Immunol Med Microbiol 56:172–178. https://doi.org/10.1111/j.1574-695X.2009.00561.x
13. Rasooly R, Do P, Hernlem BJ (2017) Interleukin 2 secretion by T cells for detection of biologically active staphylococcal enterotoxin type E. J Food Prot:1857–1862. https://doi.org/10.4315/0362-028X.JFP-17-196
14. Rasooly R, Do P, He X, Hernlem B (2018) Alternative to animal use for detecting biologically active Staphylococcal enterotoxin type A. Toxins (Basel) 10:540. https://doi.org/10.3390/toxins10120540
15. Rasooly R, Hernlem BJ (2014) Quantitative analysis of staphylococcus enterotoxin A by differential expression of IFN-gamma in splenocyte and CD4(+) T-cells. Sensors (Basel) 14:8869–8876. https://doi.org/10.3390/s140508869
16. Rasooly R, Hernlem B (2012) TNF as biomarker for rapid quantification of active Staphylococcus enterotoxin A in food. Sensors (Basel) 12:5978–5985. https://doi.org/10.3390/s120505978
17. Rasooly R, Hernlem BJ (2012) CD154 as a potential early molecular biomarker for rapid quantification analysis of active Staphylococcus enterotoxin A. FEMS Immunol Med Microbiol 64:169–174. https://doi.org/10.1111/j.1574-695X.2011.00874.x
18. Rasooly R, Do P, Hernlem B (2016) Sensitive, rapid, quantitative and in vitro method for the detection of biologically active Staphylococcal enterotoxin type E. Toxins (Basel) 8:150. https://doi.org/10.3390/toxins8050150
19. Rasooly R, Do P, He X, Hernlem B (2017) TCR-Vβ8 as alternative to animal testing for quantifying active SEE. J Environ Anal Toxicol 7:1–6. https://doi.org/10.4172/2161-0525.1000527
20. Rasooly R, Do P, He X, Hernlem B (2019) T cell receptor Vbeta9 in method for rapidly quantifying active Staphylococcal enterotoxin type-A without live animals. Toxins (Basel) 11:399. https://doi.org/10.3390/toxins11070399

# Chapter 14

# An Ultracompact Real-Time Fluorescence Loop-Mediated Isothermal Amplification (LAMP) Analyzer

**Gihoon Choi and Weihua Guan**

## Abstract

Low-cost access to the highly sensitive and specific detection of the pathogen in the field is a crucial attribute for the next generation point-of-care (POC) platforms. In this work, we developed a real-time fluorescence nucleic acid testing device with automated and scalable sample preparation capability for field malaria diagnosis. The palm-sized battery-powered analyzer equipped with a disposable microfluidic reagent compact disc described in the companion Chap. 16 which facilitates four isothermal nucleic acid tests in parallel from raw blood samples to answer. The platform has a user-friendly interface such as touchscreen LCD and smartphone data connectivity for on-site and remote healthcare delivery, respectively. The chapter mainly focuses on describing integration procedures of the real-time fluorescence LAMP analyzer and the validation of its subsystems. The device cost is significantly reduced compared to the commercial benchtop real-time machine and other existing POC platforms. As a platform technology, self-sustainable, portable, low-cost, and easy-to-use analyzer design should create a new paradigm of molecular diagnosis toward a variety of infectious diseases at the point of need.

**Key words** Point-of-care, Nucleic acid testing, Real-time, Fluorescence, Analyzer, Malaria

## 1 Introduction

In the current healthcare landscape, the ability to diagnose, monitor, and manage diseases near the site of patient care is increasingly essential for rapid clinical decision-making [1, 2]. Over the past decade, point-of-care (POC) technologies have been offered accessible diagnosis, low-cost, reduced sample/reagent volumes, and rapid analysis time. Current POC devices for pathogen screening in the field almost exclusively focus on immunoassay-based rapid diagnostic tests (RDTs), which can detect various biological analytes (e.g., cholesterol, lipids, HbA1c, cardiac markers, CD4+, HIV proteins, histidine-rich protein II, influenza, cardiac marker, and cancer markers) [2]. The integrated colorimetric and fluorometric lateral flow assay in paper strips [3] and microfluidic reagent cartridge [4] were analyzed by electrochemical and optical readout

Miguel R. Ossandon et al. (eds.), *Biomedical Engineering Technologies: Volume 1*, Methods in Molecular Biology, vol. 2393, https://doi.org/10.1007/978-1-0716-1803-5_14, 

using smartphone methods, allowing excellent portability, simplicity, low-cost, and fast turnaround time. However, most RDTs have an insufficient limit of detection to identify samples with low analyte concentration [5]. The insufficient detection limit is often problematic for the identification of asymptomatic carriers in the case of infectious diseases (e.g., malaria parasite, HIV, HPV, Zika, Ebola, and dengue) where early diagnosis and timely treatment is essential to prevent the transmission of diseases [6].

Nucleic acid testing (NAT) methods enable much-enhanced sensitivity [7, 8], which is highly desired for identifying asymptomatic infections [7, 9–12]. Among various molecular amplification assays, loop-mediated isothermal DNA amplification (LAMP) has emerged as a promising technology for field use due to its simplicity, rapidness, sensitivity, and specificity [8, 9, 11, 13–15]. In particular, LAMP has been used in POC application due to its robustness against the crude samples (blood, saliva, nasal swab, etc.), which contains amplification inhibitors [16–18]. Unfortunately, most LAMP-based test still requires bulky peripheral equipment and skilled technicians for the sample process [8–22]. Besides, necessary infrastructures such as electricity for powering equipment are often limited in remote clinical settings [23–25]. Therefore, there is a strong desire to develop a molecular diagnostic system that can be easily deployed to clinical sites.

Various POC LAMP platforms were reported to enable highly sensitive field diagnosis. For example, electric-free noninstrumented nucleic acid amplification (NINA) platform uses exothermic chemical reaction as a heating element to facilitate colorimetric RT-LAMP assay for a qualitative HIV-1 and malaria test in a tube [26, 27]. Microfluidic Biomolecular Amplification Reader (μBAR) system was developed by converging microfluidics, optics, and electronic technologies to perform NATs on microfluidic reagent cartridge for quantitative HIV-1 testing [20]. A battery-powered compact genetic testing instrument (Gene-Z) were integrated with multi-channel fluorescence sensors and aluminum heater for multiplexed detection for foodborne pathogens such as *E. coli* and *S. aureus* [28]. Many CD-like centrifugal platforms [29] for the LAMP test were also reported to achieve high-throughput and multiplexed detection of foodborne pathogens [30].

Despite significant effort and progress toward field deployment of NATs assays, highly integrated DNA sample preparation from raw peripheral blood for molecular assays remains a bottleneck [31, 32]. Current sample preparation usually involves lengthy or error-prone manual processes such as gravity-driven filtration [33], centrifugation [34]. Although a few emerging POC NAT devices (e.g., Alere q system [35, 36], Cobas Liat system [37], and Cepheid Xpert Omni platform [38]) have successfully integrated the sample preparation step, a low-cost LAMP-based NAT is not readily available for the screening test. For the promising LAMP technologies

to be used as malaria screening tests in the field, the DNA extraction method should be simple, rapid, scalable, fully automated, free of cross-contamination, and seamlessly integrated with the amplification for immediate analysis.

POC technologies play an important role in modern healthcare industries since they can expedite the flow of patient care, reduce the wait times and cost, and increase the access to sensitive and specific diagnostics. The ASSURED (Affordable, Sensitive, Specific, User-friendly) criteria are the key considerations for POC device development. Recent POC technologies focus on mobile and automated platforms that open up the diagnostic opportunities in a resource-limited setting where the well-established healthcare infrastructures and quality medical care are not available. Besides, simplicity and ease of use are attributes of most POC devices, allowing patients to perform self-testing (e.g., glucose, HIV, STD, and malaria) at the primary care before seeing healthcare professionals.

A microcontroller is a miniaturized computer on a single integrated circuit. A typical MCU includes a processor, memory, and input/output peripherals. MCU also supports analog-to-digital converter (ADC), and digital-to-analog converter (DAC) allows the microprocessor to interface with external analog sensor devices without additional computing components. Due to its small size, low-power consumption, and cost, it has been widely used in portable electronic devices such as cellphones, cameras, and medical devices. Those attributes can be applied to the POC LAMP devices, which often requires an automatic process for controlling peripheral electronics such as digital image sensor, thermal module, display, and data interfacing module.

Here, we present a real-time fluorescence LAMP device suitable for field detection of malaria with automated and scalable sample preparation capability (Table 1). The palm-sized platform unprecedentedly integrated with thermal, optical, electromechanical, data/interfacing subsystems for streamlined nucleic acid sample process from raw blood samples to isothermal amplification preformed in a disposable microfluidic reagent compact disc described in the companion Chap. 16. More specifically, a restive heating source was feed-back controlled to maintain the isothermal nucleic acid amplification temperature at 65 °C. The optical module consists of an optical excitation source and color sensors, enabling the detection of green fluorescence light during the nucleic acid amplification process. The servo motor was used to rotate the microfluidic reagent compact disc against the stationary permanent magnet to actuate the magnetic beads to the designated reagent chambers on the disc for performing magnetic interaction–based nucleic acid sample extraction/purification assay. Touchscreen display provides a user-friendly interface for ease of use. During the amplification process, the optical signal was real-time

**Table 1**
**Comparison of NAT POC devices for malaria diagnosis. (Reproduced from Biosensors and Bioelectronics 2018 with permission from Elsevier [48])**

| Assay | Detection method | Real-time ability | Automation | Sample processing | LOD (p/μl) | "Sample-to-Answer" Turnaround Time | References |
|---|---|---|---|---|---|---|---|
| LAMP | Fluorescence | Yes | Automated | Magnetic bead-based extraction | 0.6 | <40 min | This work |
| LAMP | Turbidity | No | Manual | Gravity-driven filtration | 2 | <1 h | [33] |
| LAMP | Turbidity | No | Manual | Thermal lysis centrifugation | 5 | 60–80 min | [34] |
| LAMP | Fluorescence | Yes | Manual | Gravity-driven filtration | 5 | 45 min | [42] |
| LAMP | Hydroxynaphthol blue (HNB) | No | Manual | Saponin–Chelex lysis | 1–5 | Not reported | [43] |
| PCR | Fluorescence | Yes | Manual | Off-chip | 5 | <1 h | [44] |
| PCR | Fluorescence | Yes | Manual | Off-Chip | 2 | Not reported | [45] |
| RPA | Interferometer | Yes | Manual | Dimethyl adipimidate/ thin film extraction | 1 | ~1.2 h | [46, 47] |
| HDA | Lateral flow strip | No | None | None | 200 | ~2.5 h | [48] |

plotted on the embedded screen or smartphone via an integrated Bluetooth module. The user can perform post-analysis since raw data were stored in the memory card through a micro SD card module. The detailed automated sample process on microfluidic reagent compact disc will be discussed in the Chap. 16. The platform is capable of processing four samples simultaneously in parallel. The device dramatically minimizes the manual workload needed for performing the NATs and offers low-cost and accurate diagnosis performance quickly and automatically at point of need.

## 2 Materials

### 2.1 Instrumentation

1. Materials and supplies: Table 2

   *Thermal Subsystem:* Aluminum plate (CP-0.91-0.91, custom Thermoelectric), power resistor (PWR263S-20-2R00J, Digi-Key), N-channel power MOSFET (63J7707, Digi-Key), thermistor (95C0606, Digi-Key), epoxy (DP100-clear, 3M), thermal paste (AATA-5G, Artic Alumina).

**Table 2**
**Bill of materials for the analyzer. (Reproduced from Biosensors and Bioelectronics 2018 with permission from Elsevier [48])**

| System | Description | Part# | Function | Unit cost ($) | Unit Qty. | Ext. cost ($) |
|---|---|---|---|---|---|---|
| Electronics | Arduino Mega 2560 R3 | DEV-1106 | Microcontroller | 45.95 | 1 | 45.95 |
| Electronics | 36-pin stripe male header | 392 | Headpins | 4.95 | 0.083 | 0.41 |
| Electronics | DC barrel power Jack/ connector | PRT-00119 | Power connector | 1.25 | 1 | 1.25 |
| Electronics | Shield stacking headers for Arduino | 85 | Wire sockets | 1.95 | 0.33 | 0.64 |
| Electronics | Premium male/male jumper wires | 758 | Wires | 3.95 | 0.75 | 2.96 |
| Electronics | Trimmer potentiometer, 500 Ω | 62J1468 | LED adjustment | 1.98 | 4 | 7.92 |
| Electronics | Through hole resistor, 10 kΩ | 38K0328 | Temperature control | 0.09 | 5 | 0.45 |
| Electronics | Through hole resistor, 47 Ω | 38K0326 | Resistors for LED | 0.09 | 2 | 0.18 |
| Electronics | Capacitor 470 μF | 65R3137 | Power stabilizing | 0.11 | 1 | 0.11 |
| Electronics | Capacitor 0.33 μF | 46P6304 | Voltage regulating | 0.27 | 1 | 0.27 |
| Electronics | Capacitor 0.1 μF | 46P6667 | Voltage regulating | 0.354 | 1 | 0.354 |
| Electronics | Diode, standard, 1 A, 50 V | 78K2043 | Diode | 0.07 | 1 | 0.07 |
| Electronics | 26 pin wire connector | 1171 | Wiring | 4.95 | 1 | 4.95 |
| Electronics | 26 pin GPIO ribbon cable | 862 | Wiring | 2.95 | 1 | 2.95 |
| Servo | Micro size - high torque servo | 2307 | Actuation of disc | 11.95 | 1 | 11.95 |
| Magnets | Neodymium disc magnet nickel | 58605K33 | Holding magnetic beads | 2.69 | 4 | 10.76 |
| Thermal | Cold plate | CP-0.91-0.91 | Heating stage | 5.75 | 0.25 | 1.44 |
| Thermal | Power resistor | PWR263S-20-2R00J | Heater | 4.12 | 4 | 16.48 |
| Thermal | N Channel power MOSFET | 63J7707 | Switch for Peltier heater | 1.66 | 1 | 1.66 |
| Thermal | Thermistor | 95C0606 | Temperature sensing | 7.34 | 1 | 7.34 |
| Optics | Color sensor | 1334 | Detection | 7.16 | 4 | 28.64 |

(continued)

**Table 2**
**(continued)**

| System | Description | Part# | Function | Unit cost ($) | Unit Qty. | Ext. cost ($) |
|---|---|---|---|---|---|---|
| Optics | Optical plastic light guide | #02-538 | Guiding light | 2.55 | 0.24 | 0.61 |
| Optics | CREE LED, blue, T-1 3/4 (5 mm) | 04R6674 | Fluorescence excitation | 0.21 | 1 | 0.21 |
| Bluetooth | Bluetooth low energy (BLE 4.0) | 1697 | Bluetooth connectivity | 19.95 | 1 | 19.95 |
| LCD | 3.5″ TFT 320 × 480 | 85 | Touchscreen LCD | 39.95 | 1 | 39.95 |
| SD | MicroSD card breakout board | 254 | SD module | 7.5 | 1 | 7.50 |
| Enclosure | Adjustable-friction hinge | 1791A44 | Hinge | 6.72 | 2 | 13.44 |
| Enclosure | ABS filament | 90003001 | 3D platform material | 18.5 | 0.4 | 7.40 |
| Enclosure | Acrylic sheet, 1/8″ thick, 12″ × 24″ | 8505K12 | Holding plates | 13.46 | 0.7 | 9.42 |
| Enclosure | Screws (M4 cap screw) | W8S038 | Hinge holding | 3.25 | 0.04 | 0.13 |
| Enclosure | Screws (M3 set screw) | SS3M6 | For holding color sensor | 9.25 | 0.0006 | 0.01 |
| | | | **Total cost** | | | **$245.35** |

*Optical subsystem*: Color sensor module (1334, Adafruit), Optical grade plastic light guide (dia. 2.8 mm, #02-538, Edmund Optics), Optical grade plastic light guide (dia. 1 mm, #02-536, Edmund Optics), Blue LED (04R6674, Digi-Key).

*Electromechanical subsystems*: Capacitor 470 μF (65R3137, Digi-key), High torque servo motor (2307, Adafruit), Neodymium disc magnet (58605K33, McMaster), 5 V voltage regulator (L7805CV, Digi-Key), Acrylic solvent (IPS4-4OZ, ePlastics), and 1/8″ acrylic sheet (8505K12, ePlastics).

*Data/Interfacing subsystem*: microSD card breakout board (254, Adafruit), 3.5″ TFT Touchscreen breakout (2050, Adafruit), BLE 4.0 breakout (1697, Adafruit).

2. 3D printer (MakerBot Replicator+, USA).
3. $CO_2$ laser cutting machine (Epilog Helix 24 Laser System, USA).
4. Custom printed circuit boards (PCB) were manufactured by the commercial vendors (OSH Park, USA).

5. CAD software: Eagle PCB design tool (Autodesk, USA), AutoCAD (Autodesk, USA), and SolidWorks 2015 (DS SolidWorks Corp., USA).
6. MCU programming: Arduino software (IDE).

## 3 Methods

The real-time LAMP Analyzer presented here designed to amplify DNA in a disposable microfluidic compact disc described in the companion Chap. 16.

### 3.1 Analyzer Overview

1. The assembled and exploded views of the analyzer are shown in Fig. 1.
2. The analyzer has four parallel testing units and has a small footprint of $10 \times 12 \times 12$ cm$^3$.
3. The fully integrated analyzer consists of thermal, optical, electromechanical, and data/interfacing subsystems. The functional subsystems inside the analyzer are illustrated in the block diagram (Fig. 2).
4. A customized printed circuit board (PCB) with an embedded microcontroller unit (MCU) operates the whole device from sample preparation to result (Fig. 2).
5. A rechargeable 9 V portable Lithium-ion battery powers the entire system and could last for >15 h before recharging (Fig. 2).

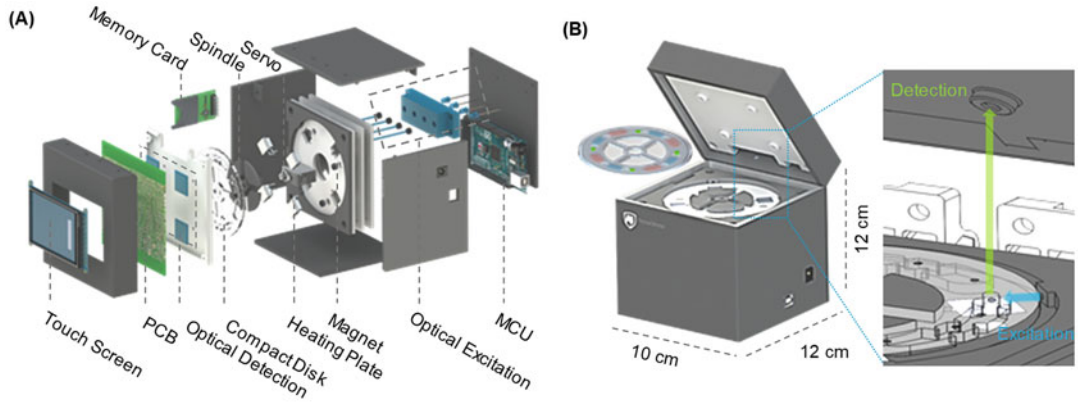


**Fig. 1** Overview of the device. (**a**) Exploded view of the device, showing the assembly of various components. (**b**) Schematic of the assembled device and the quadplex microfluidic reagent compact disc. The form factor of the analyzer is palm-sized. The reagent compact disc is secured to the spindle platter. A real-time fluorescence sensing scheme is integrated on the analyzer. (Reproduced from Biosensors and Bioelectronics 2018 with permission from Elsevier [40])

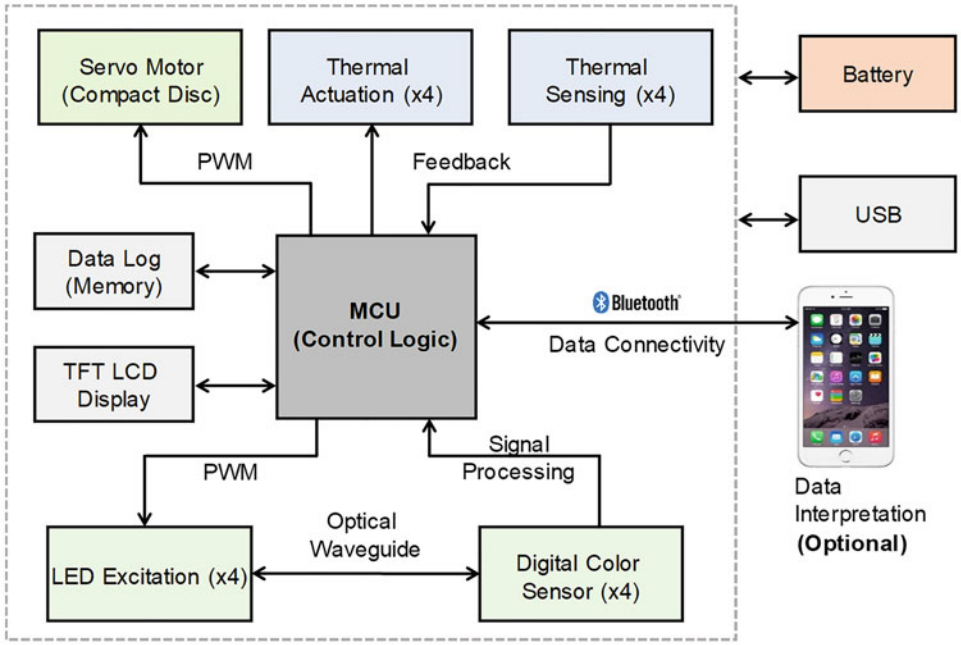


**Fig. 2** System block diagram with interconnected subsystems. The platform consists of four main functional subsystems: mechanical subsystem (servo motor/spindle platter/compact disc), an optical subsystem (LED/optical sensor), a thermal subsystem (heater/thermal sensor), and data subsystem (Bluetooth). Each module was controlled by a microprocessor on a customized PCB board. The diagnostic results can be optionally reported to a smartphone user interface. (Reproduced from Lab on a Chip 2016 with permission from the Royal Society of Chemistry [41])

### *3.2 Thermal Subsystem*

1. The thermal module consists of four resistive-heating elements (2 Ω power resistor for each), N-channel power MOSFET, and microthermistor. Figure 3a shows one unit of the thermal module. The 9 V rechargeable battery (max output current: 2 A) was used to power the heating elements via control PCB, which contains control circuits for all subsystems (Fig. 4a).
2. *Fabrication steps:* Four resistive-heating elements were connected in series with wires to maintain the uniform temperature among each testing unit (Fig. 3b, c). The aluminum heating plate was drilled from the side to make space for micro-thermistor, which were embedded in the center of the heating plate for real-time temperature monitoring (Fig. 3b). After inserting the thermistor, we introduced a drop of epoxy to fix it. Each power resistor was bonded to the backside of an aluminum heating plate by thermal paste.
3. To simplify the wiring, most electronic circuits for the thermal module were integrated into the control PCB (Fig. 4a). Only active components such as heating elements and thermistors were wired using jump wire to place them close to the reaction

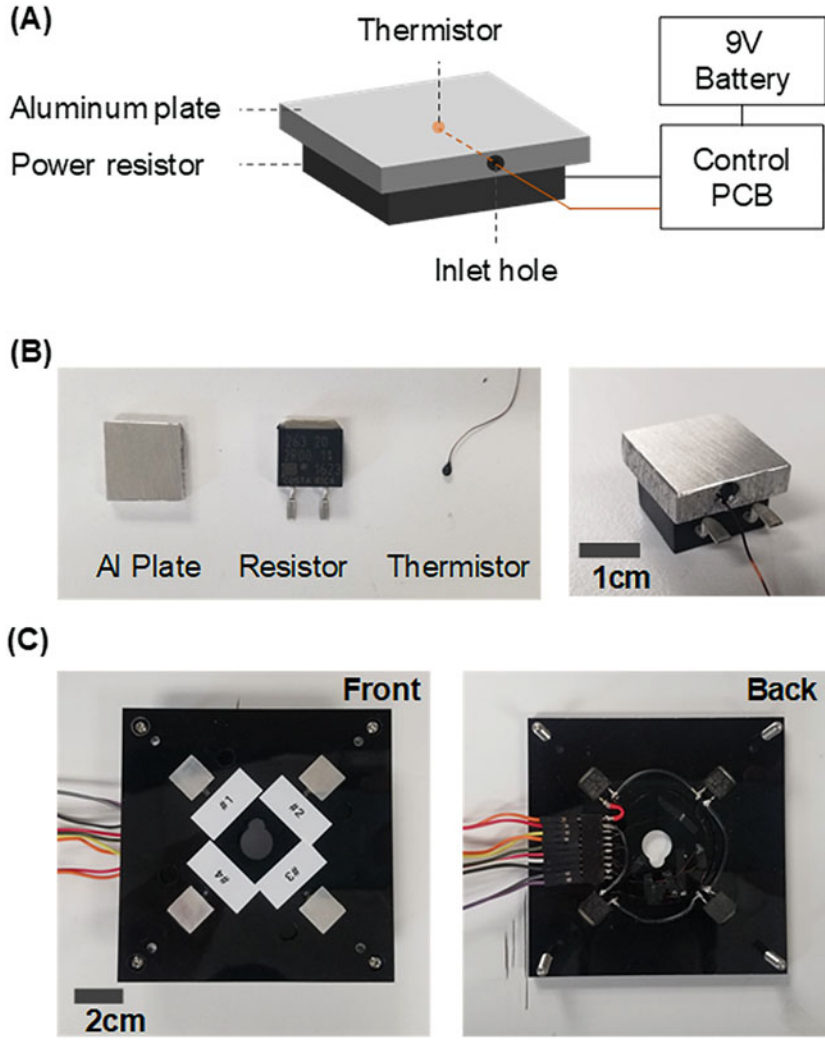


**Fig. 3** Integrated thermal subsystem. (**a**) Schematic of the thermal subsystem. The thermistor is embedded in the Aluminum plate. Control PCB interfaces with a thermistor to monitor temperature and supply the power to the resistive heating element. (**b**) Photo image of each component and assembled thermal unit. (**c**) 4-plex thermal module integrated into the analyzer part. Four heating elements were connected in series using wires

chamber on a reagent compact disc. Figure 4b showed a detailed thermal control circuit diagram.

4. Negative feedback control was used to maintain the desired constant temperature (65 °C) during the DNA amplification (Fig. 5). The N-channel power MOSFET was controlled using digital output from MCU. For example, MOSFET shuts off when temperature reading overshot the set temperature. Whereas, the MOSFET was turned on when the temperature reading was lower than the set temperature.

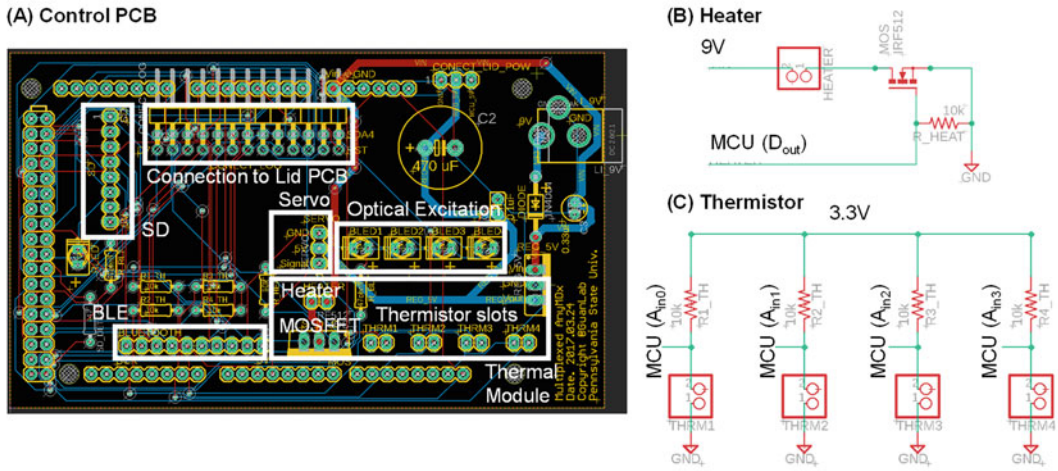


**Fig. 4** Electronics for the thermal subsystem. (**a**) Control PCB design. The thermal module is integrated into the control PCB. The actual heating element and thermistors were connected to the pin connector on the PCB board using wires. (**b**) Circuit diagram for heating element control. A 9 V external battery powers the heating sources. The digital output from MCU gates the MOSFET. (**c**) Circuit diagram for the thermistor circuit to measure the temperature. 3.3 V was used as a reference voltage to obtain the resistance of the thermistor based on its temperature

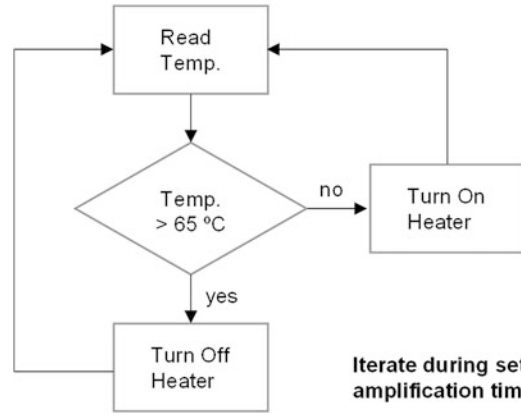


**Fig. 5** Feedback thermal control sequence. The most recent temperature from the thermistor is compared with the set temperature (65 °C). If the current temperature is higher than the set temperature, the heater is electronically shut down by the MOSFET switch. If the current temperature reading is lower than the set temperature, the heater is turned on. This process repeats until the amplification process ends

5. A custom-built thermal control code was uploaded into the MCU board through the computer using open-source Arduino Software (IDE). The program reads and updates the most recent temperature values every 3 s during the DNA amplification process. The temperature reading was recorded on a micro

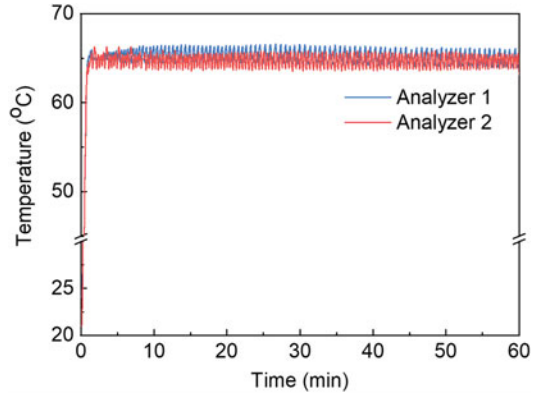


**Fig. 6** The feedback-controlled reaction temperature profiles as a function of time (blue curve: Analyzer 1, red curve: Analyzer 2). (Reproduced from Lab on a Chip 2016 with permission from the Royal Society of Chemistry [41])

SD card for validation purposes. Once the code is uploaded, MCU can operate the thermal control sequence by itself without a computer connection.

6. To evaluate the temperature fluctuation, the temperature was monitored for 60 min by an external independent thermocouple module (NI-9211, National Instruments).
7. Figure 6 shows the temperature on the aluminum heating plate can reach the set temperature (65 °C) within 40 s and continuously maintain a temperature between 64.5 and 66.5 °C.

### 3.3 Optical Subsystem

The microfluidics assay presented in this chapter is performed with an automated device described in the companion Chap. 16.

The automated device described in the companion Chap. 16.

1. For real-time tracking of fluorescence signal during the DNA amplification, we used a blue LED ($\lambda = 488$ nm) as an optical excitation light source and color sensor as an optical detector (Fig. 7). Four blue LEDs were embedded in custom-built fiber coupler and directed toward individual reaction chambers through polymer optical fibers (*see* **Note 1** for fiber preparation). The incidence of the excitation light was perpendicular to the optical sensor to minimize the excitation interference (Fig. 7). The green cellophane film was used only to allow the green light to the color sensor.
2. Customized fiber coupler was 3D printed to facilitate the tight coupling of an incoherent LED light source to the optical fiber (Fig. 8a). On the bottom side of the fiber coupler, there are four spatially isolated LED holes to mechanically secure the LED blubs and vertically align with the optical fiber. Similarly, front of the optical fiber was inserted from the top side of the coupler and mechanically secured by the epoxy. Optical fiber

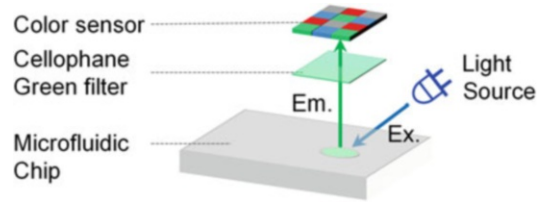


**Fig. 7** Schematics for fluorescence sensing module. The blue LED ($\lambda = 488$ nm) excites fluorescence dye from the side of the microfluidic chip. The color sensor is vertically aligned with the reaction chamber and monitors the green emission light ($\lambda = 515$ nm) from the microfluidic chip (*see* also Fig. 1b). The green cellophane film was placed below the color sensor to minimize the background by filtering red and blue light

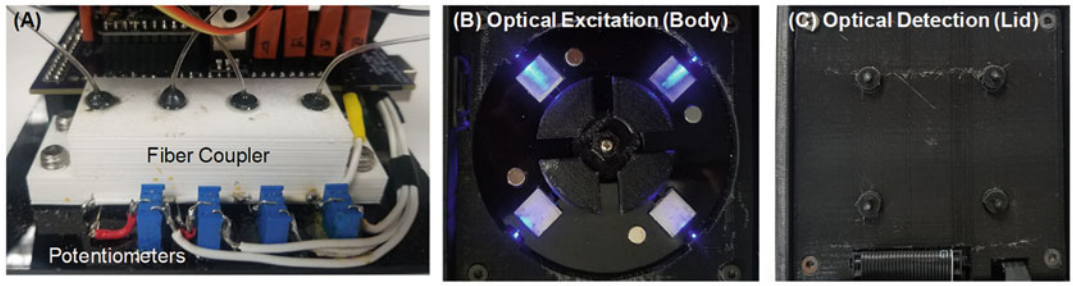


**Fig. 8** Photo image of the integrated optical subsystem. (**a**) Custom-built fiber coupler. The blue LED light sources were inside of the fiber coupler. The plastic optical fiber socket was aligned with the center of the blue LED bulb top. Potentiometers were connected with each blue LED to calibrate the intensity manually. (**b**) Optical excitation. The output of blue LED lights shines from the 3D printed sidewalls. (**c**) Optical detection. The image showed the lid side of the analyzer. The color sensors were embedded inside the analyzer lid. The locations of the four optical fibers were where the four-color sensors were placed

end was inserted into the 3D printed fiber holder and fixed by epoxy (*see* Fig. 8b). The optical detection side fibers were secured on the 3D printed lid cover (*see* Fig. 8c). When the lid was closed, the optical fibers aligned with the reaction chamber in the microfluidic chip. Black enclosure covers entire optical subsystem components (e.g., fibers, LEDs, and color sensors) to prevent interference from unwanted background light.

3. The color sensor (TCS3472, TAOS) includes a $3 \times 4$ photodiode array, four Analog-to-Digital Converters (ADC), data registers, and $I^2C$ interface. The photodiode array comprises red-filtered, blue-filtered, and green-filtered photodiodes; thus, it is capable of RGB sensing (Fig. 7). The four ADCs convert the amplified photodiode current to 16-bit digital output in parallel. The digital outputs were sent to the MCU through the $I^2C$ communication port at 400 kHz. Internal integration time and gain can be adjusted by accessing the

register setting. The TCS 3472 has a timing register that can control the internal integration time of ADC channels (2.4, 24, 50, 101, 154, 700 ms). Similarly, internally generated gain (1×, 4×, 16×, and 60×) can be selected for conversion by accessing the control register. The longer integration time and higher gain increase sensitivity at the low light level. For the optimal green fluorescence detection, we set the gain at 60 and integration time at 700 ms. Note that gain and integration time should be carefully determined based on the experimental and environmental conditions due to the dynamic range of the color sensor (*see* **Note 2**). Dark ADC count has a range of 0 to 5, which is differ by two to three orders of magnitude with green fluorescence light count (Fig. 10a). The color sensor was designed to operate in the temperature range of −30 to 70 °C. We operated the sensor at uniform room temperature (25 °C), and no temperature-dependent noise, such as thermionic emission, was observed.

4. Figure 9 shows the circuit diagram of the optical module. Each LED was connected in parallel to ensure the uniformity of the excitation light (Fig. 9a). Potentiometers were used to calibrate the optical uniformity further (*see* **Note 3**). Figure 9b shows schematics for the optical detection sensor wiring. The sensor was powered by Arduino (3.3 V). The $I^2C$ bus (SCL and SDA) was connected to the MCU for data transfer. The received optical data was recorded in a micro SD card via the integrated SD card breakout.

5. *Uniformity.* For the quadruplex parallel NAT device, the fluorescence sensing consistency among different channels is essential for quantitative analysis. We tested fluorescent Calcein dye at various known concentrations. At each concentration, identical Calcein aliquots were loaded into the four reaction chambers for fluorescence intensity measurement. Figure 10a shows the relative fluorescence unit (RFU) distribution from each optical channel at different concentrations. The quantitative uniformity among the four channels is excellent, as seen by the small standard deviation for the RFU values. Moreover, as expected, the mean fluorescence intensity was proportional to the Calcein concentration, and a twofold Calcein concentration difference could be discriminated (inset in Fig. 10a). To further validate the fluorescence sensing uniformity during the real-time LAMP process, four identical 1 μl of *Pf* genomic DNA was directly loaded into each reaction chamber, and the real-time amplification curve was monitored (Fig. 10b). We repeated each test three times. The variation of threshold time ($T_t$) among different fluorescence sensing channels was ~1.5 min (inset of Fig. 10b). These results validate the fluorescence sensing uniformity among different optical channels.

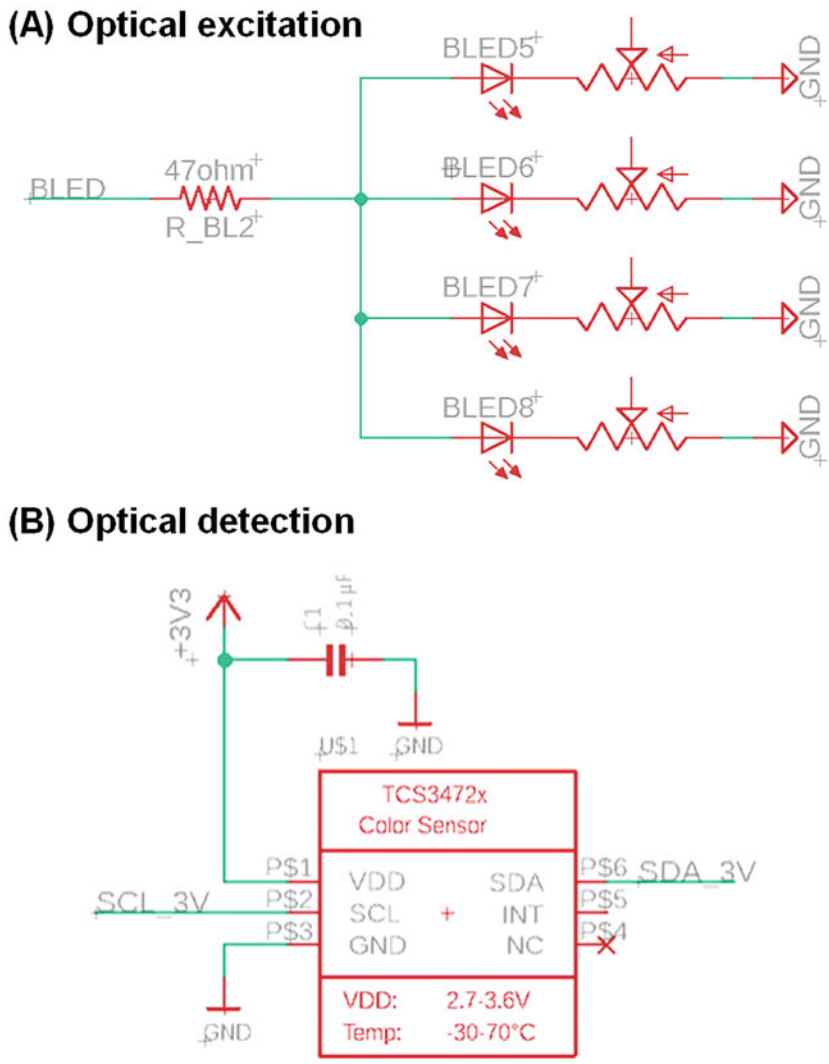


**Fig. 9** Circuit diagram for the optical module. (**a**) Optical excitation circuit. (**b**) Optical detection circuit. 3.3 V was derived from the MCU to power the color sensors. SCL and SDA pins were wired to the MCU for $I^2C$ communication

6. *Quantitative*. A series of tenfold dilutions of *Pf* genomic DNA in Tris-EDTA buffer was used to validate the quantitative ability of the device. For each concentration, a set of three identical *Pf* genomic DNA samples and one internal negative control were loaded into each of the four reaction chambers on the disc. The DNA sample volume is 1 µl, and the LAMP master mix is 24 µl. Figure 10c shows real-time amplification results from various concentrations of *Pf* genomic DNA. The mean and standard deviation of the amplification threshold time ($T_t$) was obtained from the triplicates for each concentration. As shown in the bottom subplot of Fig. 10c, a clear linear

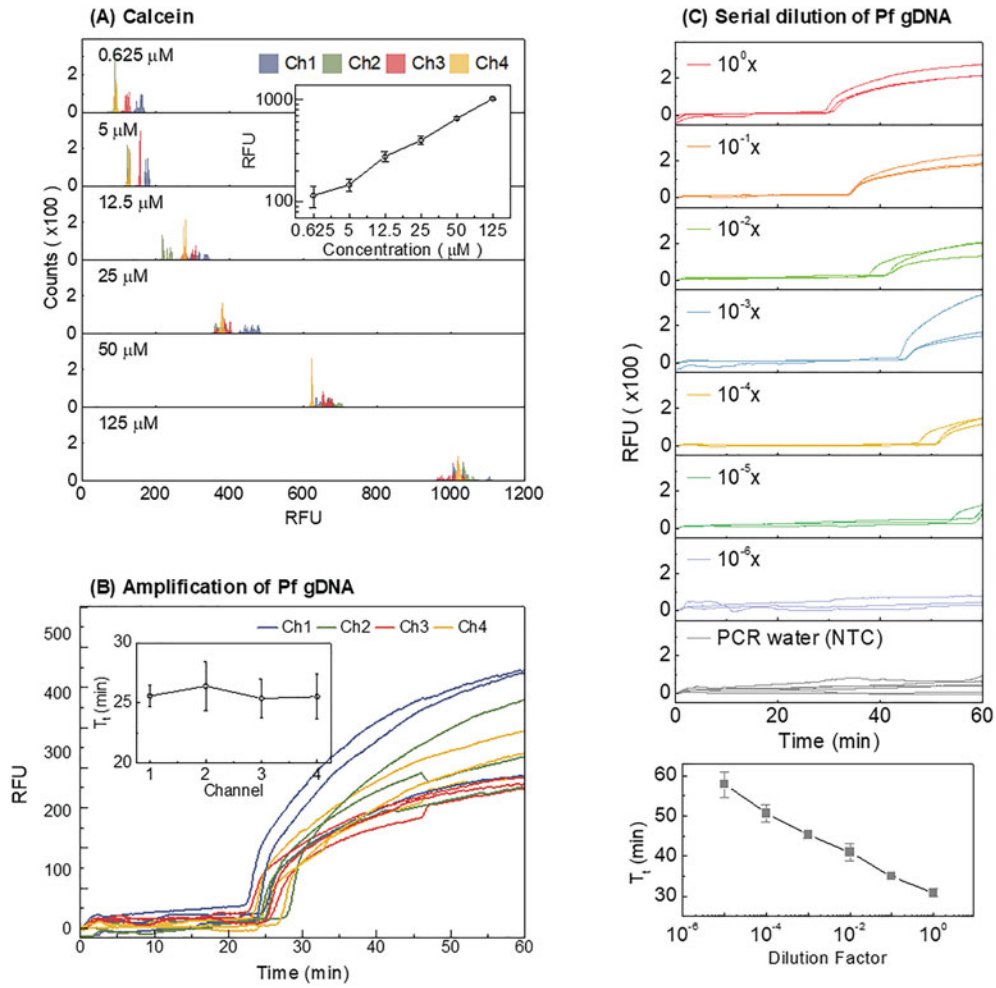


**Fig. 10** Validation of the optical sensing uniformity. (**a**) With fluorescent Calcein dye, the RFU distribution for the four optical channels was evaluated at a series of Calcein concentration. A linear dependence of the RFU on the Calcein concentration was observed in the range of 0.625–125 μM. The RFU variation from the four channels is small. (**b**) With *Pf* genomic DNA at constant concertation, the variations of the amplification threshold time ($T_t$) obtained from the real-time curve is ~1.5 min. (**c**) Amplification curves for tenfold serially diluted *Pf* genomic DNA samples. The bottom plot shows the calibration curve for the *Pf* genomic DNA. Standard deviation values are from triplicates. (Reproduced from Biosensors and Bioelectronics 2018 with permission from Elsevier [40])

relationship was observed between $T_t$ and the dilution factor, which could be used as a reference curve for quantification. The quantitative ability is important for assessing parasite load in the blood, a useful indicator for determining the proper anti-malarial drug dosage [39].

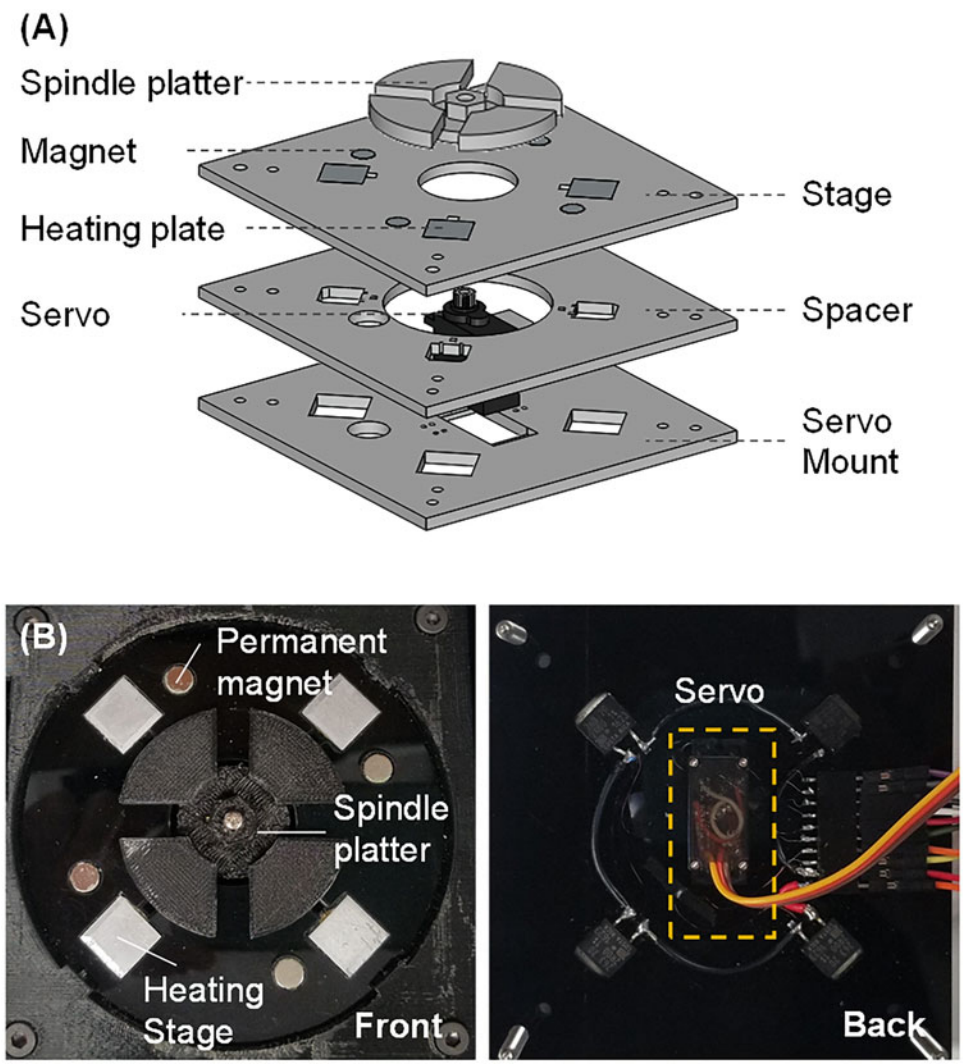


**Fig. 11** Photo image and schematics of the integrated electromechanical subsystems. (**a**) Exploded view of the amounting layers. Permanent magnets and aluminum heating plates were placed on the stage layer. The level of stage layer was adjusted by a spacer to make the servo shaft exposed to the outside. (**b**) Assembled view. Spindle platter was screw-tightened on the servo motor shaft

### *3.4 Electro-mechanical Subsystem*

1. Figure 11 shows the integrated electromechanical subsystem and components. The three laser-machined PMMA layers held the four permanent magnets, thermal modules, and servo motor for a streamlined sample process (Fig. 11a, *see* **Note 1**). Each layer was aligned with M4 screws and permanently fixed with an acrylic solvent. The servo was fixed on the servo mount layer using screws. Magnets and heating plates were tightly fit to the patterned stage layer and supported by the spacer (Fig. 11a). The permanent magnet was used to facilitate

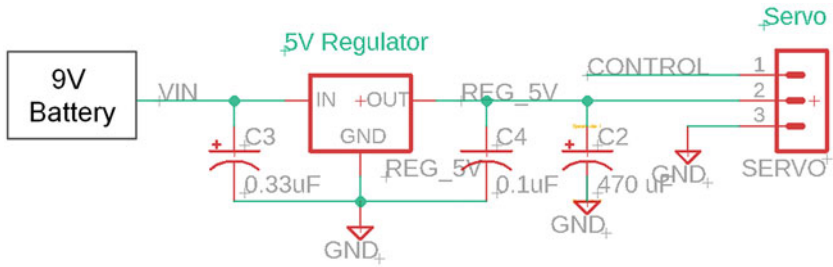


**Fig. 12** Circuit diagram for an electromechanical subsystem. 9 V is regulated to 5 V using a voltage regulator. Regulated 5 V powers the servo. The control wire is connected to the PWM terminal in MCU

charge-switchable magnetic bead-based assay for the nucleic acid sample preparation (Detailed Magnetic bead-based assay is discussed in the companion Chap. 16).

2. After assembling the PMMA layers, 3D printed spindle platter was installed at the high-torque servo motor shaft to rotate the microfluidic reagent compact disc (Fig. 1b). Spindle platter was designed to avoid optical interference from the other blue LED light sources for uniform excitation among four channels (Fig. 1b).
3. Figure 12 shows the circuit diagram of the integrated electromechanical subsystem. To power the servo, we derived 5 V from 9 V battery using a voltage regulator. To prevent the power fluctuation during servo actuation, we connected a capacitor (470 μF) to the power line. The servo was controlled by the pulse width modulation (PWM) signal. For example, 1 ms, 1.5 ms, and 2 ms pulse width corresponds to the −90°, 0°, and +90° turns, respectively. Therefore, specific servo shaft position and direction of the rotation can be programmed via the PWM command in Arduino IDE.
4. The spindle platter structure holds the microfluidic reagent compact disc (Fig. 1b); thus, the disc rotates along with the servo. The magnet underneath of the disc interacts with magnetic beads inside of the reagent disc. By the disc rotating against the stationary magnet, magnetic beads can be actuated into a different location in the reagent disc (Please, refer to the companion Chap. 16).

### *3.5 Data/Interfacing Subsystems*

1. The fluorescence signal was transferred to the internal MCU memory through $I^2C$ communication at a constant interval (~5 s). The optical data was displayed on the LCD touchscreen or smartphone (via Bluetooth) in real-time. The LCD touchscreen breakout supports the $X$–$Y$ coordinate system. Therefore, each data point can be plotted at the specified position on the screen. We assign time progression for $X$-coordinate and optical data for $Y$-coordinate.

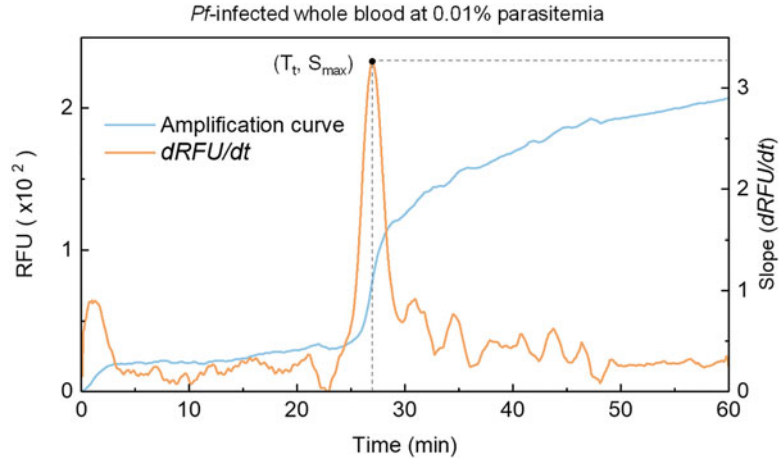


**Fig. 13** Determination of the threshold time ($T_t$). A real-time amplification curve (blue) and the corresponding differential profile (d*RFU*/d*t*, orange). The threshold time ($T_t$) was determined at the maximum slope of RFU ($T_t$ threshold time, *t* time, $S_{max}$ maximum value of the slope). (Reproduced from Biosensors and Bioelectronics 2018 with permission from Elsevier [40])

2. A built-in moving average algorithm smoothed the optical signal with background noise removed. More specifically, the arithmetic mean of a given set of data (data span = 10) was taken every moving window. Open-source moving average library for Arduino IDE is available online (http://arduino.cc/playground/Main/RunningAverage).
3. The threshold time ($T_t$) was obtained when the slope of RFU (d*RFU*/d*t*) reached the peak (Fig. 13).
4. Collected data is saved in the micro SD card in .txt format for export.

### *3.6 Arduino Microcontroller Unit (MCU) Interface*

1. The microcontroller board includes a microprocessor (ATmega2560), flash memory (256 kB), 16 analog inputs, 54 digital inputs/outputs, 4 serial ports, and USB connection. Arduino board can be powered by an external power source (9 V battery) using the Vin pin. 9 V input voltage is regulated down to 5 V and 3.3 V by the internal voltage regulator. ATmega2560 support two-wire serial interface ($I^2C$) and serial peripheral interface (SPI) for communicating with peripheral devices such as color sensor, LCD touchscreen, Bluetooth, and SD card module.
2. We stacked the customized PCB board (Fig. 4a) on top of the commercial Arduino board to reduce the wiring.
3. The control sequence for all integrated electronic devices was combined into a single program using Arduino IDE and uploaded to the MCU. Therefore, no computer connection is required to operate the analyzer.

### 3.7 Enclosures and System Integration

1. All enclosures (body and lid) were 3D printed using ABS material.
2. The lid enclosure was patterned to hold the LCD touch screen and four optical sensors (Fig. 1a). The bottom cover of the lid enclosure has holes to couple optical fibers for collecting green emission light.
3. Multiple laser-patterned PMMA layers were stacked together to hold aluminum heating plates, magnets, and servo (Fig. 11b). On top of the PMMA layers, we placed a 3D printed optical fiber holder to align the excitation light facing the reaction chamber (Fig. 8b).
4. Afterward, all overlaid layers were secured into the body enclosure using M4 screws.
5. Control PCB and 3D printed fiber coupler with four blue LEDs were secured on the bottom cover of the enclosure (Fig. 14).
6. All necessary electronic wires and optical fibers were connected (Fig. 14), then the bottom cover was assembled to the body enclosure.
7. The 3D printed spindle platter was assembled at the servo shaft (*see* **Note 1**).
8. Finally, body and lid enclosures were joined by the hinges.

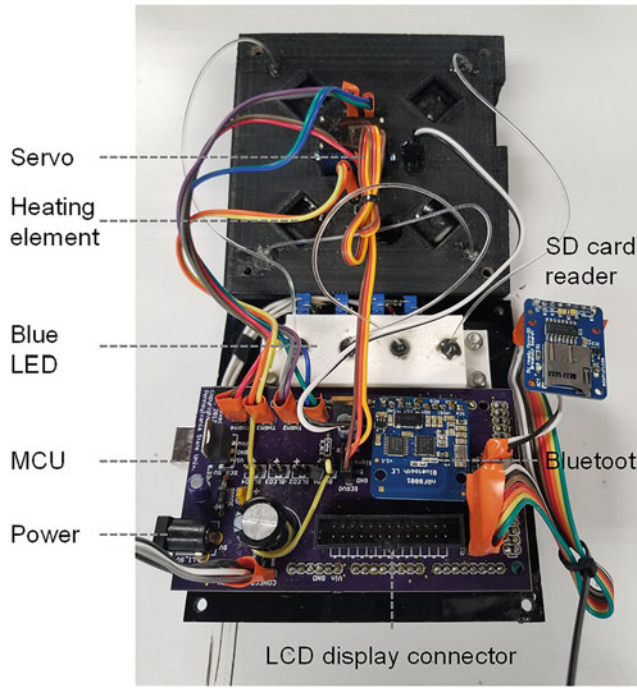


**Fig. 14** Assembled analyzer without enclosure. The LCD touchscreen is connected through ribbon cables (LCD is located in the lid)

### 3.8 Cost Analysis

1. The prototype analyzer presented in this work could be built for a total amount of ~$245.35 (Table 2 for cost breakdown).

## 4 Notes

1. To minimize the optical power loss (e.g., insertion and return loss), the end surface of the fiber was first polished with 2000 grit polishing paper, then further smoothed with a 3 μm polishing film.
2. Gain and analog-to-digital converter (ADC) integration time are important photodiode parameters for the optimal fluorescence readings. While higher gain and longer integration time can amplify the optical signal and increase the sensitivity of the photodiode, the reading can exceed the dynamic range and be saturated. On the other hand, the photodiode is not enough to distinguish weak green emission light from background noise with lower gain and shorter ADC integration time. For example, the dynamic range of photocounts at 700 ms integration time is 0 to 65,535. The light intensity beyond this range will not be resolved. We experimentally confirmed that photocounts from maximum fluorescence dye concentration did not exceed the dynamic range with the selected gain (60×) and integration time (700 ms) setting (*see* a subset of Fig. 10a).
3. We used a potentiometer, which can physically adjust the resistor values by turning the knob. However, the programable approach using a Pulse Width Modulation (PWM) method can be an alternative for simply excitation LED light intensity adjustment.
4. Magnetic beads were actuated by rotating the reagent compact disc against a stationary permanent magnet. Since the magnetic force is inversely proportional to the distance squared, a small gap between the disc bottom and the magnet top can cause the failure of magnetic bead actuation. For the reliable magnetic actuation, a flat permanent magnet holding layer is desired.
5. A 90-degree rotational turn of a servo is sufficient to cover the entire testing unit on microfluidic reagent disc. We set the servo angle (90°) as a reference position to maximize the range of rotational motion. During the spindle platter assembly, we placed the reaction chamber in the microfluidic disc to vertically align with the permanent magnet position.

## Acknowledgments

This work was supported by grants National Science Foundation under Grant No. 1710831, 1912410, and 1902503. We express

our gratitude to Dr. Liwang Cui, Dr. Jun Miao, and Xiaolian Li for providing cultured malaria samples. W.G. acknowledges the support from Penn State Startup Fund.

## References


1. Vashist SK (2017) Point-of-care diagnostics: recent advances and trends. Biosensors (Basel) 7(4):62
2. Vashist SK, Luppa PB, Yeo LY et al (2015) Emerging Technologies for Next-Generation Point-of-Care Testing. Trends Biotechnol 33 (11):692–705
3. Mauk M, Song J, Bau HH et al (2017) Miniaturized devices for point of care molecular detection of HIV. Lab Chip 17(3):382–394
4. Laksanasopin T, Guo TW, Nayak S et al (2015) A smartphone dongle for diagnosis of infectious diseases at the point of care. Sci Transl Med 7(273):1–11
5. Chiu DT, deMello AJ, Di Carlo D et al (2017) Small but perfectly formed? Successes, challenges, and opportunities for microfluidics in the chemical and biological sciences. Chem 2 (2):201–223
6. Chen H, Liu K, Li Z et al (2019) Point of care testing for infectious diseases. Clin Chim Acta 493:138–147
7. Wu L, van den Hoogen LL, Slater H et al (2015) Comparison of diagnostics for the detection of asymptomatic *Plasmodium falciparum* infections to inform control and elimination strategies. Nature 528(7580):S86–S93
8. Hopkins H, Gonzalez IJ, Polley SD et al (2013) Highly sensitive detection of malaria Parasitemia in a malaria-endemic setting: performance of a new loop-mediated isothermal amplification kit in a remote Clinic in Uganda. J Infect Dis 208(4):645–652
9. Vallejo AF, Martinez NL, Gonzalez IJ et al (2015) Evaluation of the loop mediated isothermal DNA amplification (LAMP) kit for malaria diagnosis in *P. vivax* endemic settings of Colombia. PLoS Negl Trop Dis 9(1):e3453
10. Modak SS, Barber CA, Geva E et al (2016) Rapid point-of-care isothermal amplification assay for the detection of malaria without nucleic acid purification. Infect Dis 9:1–9
11. Aydin-Schmidt B, Xu WP, Gonzalez IJ et al (2014) Loop mediated isothermal amplification (LAMP) accurately detects malaria DNA from filter paper blood samples of low density Parasitaemias. PLoS One 9(8):e103905
12. Morris U, Khamis M, Aydin-Schmidt B et al (2015) Field deployment of loop-mediated isothermal amplification for centralized mass-screening of asymptomatic malaria in Zanzibar: a pre-elimination setting. Malar J 14:1–6
13. Han ET, Watanabe R, Sattabongkot J et al (2007) Detection of four plasmodium species by genus- and species-specific loop-mediated isothermal amplification for clinical diagnosis. J Clin Microbiol 45(8):2521–2528
14. Polley SD, Mori Y, Watson J et al (2010) Mitochondrial DNA targets increase sensitivity of malaria detection using loop-mediated isothermal amplification. J Clin Microbiol 48 (8):2866–2871
15. Safavieh M, Kanakasabapathy MK, Tarlan F et al (2016) Emerging loop-mediated isothermal amplification-based microchip and microdevice Technologies for Nucleic Acid Detection. ACS Biomater Sci Eng 2 (3):278–294
16. Tomita N, Mori Y, Kanda H et al (2008) Loop-mediated isothermal amplification (LAMP) of gene sequences and simple visual detection of products. Nat Protoc 3(5):877–882
17. Goto M, Honda E, Ogura A et al (2009) Colorimetric detection of loop-mediated isothermal amplification reaction by using hydroxy naphthol blue. BioTechniques 46(3):167–172
18. Notomi T, Mori Y, Tomita N et al (2015) Loop-mediated isothermal amplification (LAMP): principle, features, and future prospects. J Microbiol 53(1):1–5
19. Kim J, Johnson M, Hill P et al (2009) Microfluidic sample preparation: cell lysis and nucleic acid purification. Integr Biol 1(10):574–586
20. Myers FB, Henrikson RH, Bone J et al (2013) A handheld point-of-care genomic diagnostic system. PLoS One 8(8):e70266
21. Liao SC, Peng J, Mauk MG et al (2016) Smart cup: a minimally-instrumented, smartphone-based point-of-care molecular diagnostic device. Sensor Actuat B Chem 229:232–238
22. Liu CC, Mauk MG, Hart R et al (2012) A low-cost microfluidic Chip for rapid genotyping of malaria-transmitting mosquitoes. PLoS One 7(8):e42222
23. Choi S (2016) Powering point-of-care diagnostic devices. Biotechnol Adv 34(3):321–330
24. Abel G (2015) Current status and future prospects of point-of-care testing around the globe. Expert Rev Mol Diagn 15(7):853–855

25. Jung WE, Han J, Choi JW et al (2015) Point-of-care testing (POCT) diagnostic systems using microfluidic lab-on-a-chip technologies. Microelectron Eng 132:46–57
26. Singleton J, Osborn JL, Lillis L et al (2014) Electricity-free amplification and detection for molecular point-of-care diagnosis of HIV-1. PLoS One 9(11):e113693
27. Curtis KA, Rudolph DL, Morrison D et al (2016) Single-use, electricity-free amplification device for detection of HIV-1. J Virol Methods 237:132–137
28. Stedtfeld RD, Tourlousse DM, Seyrig G et al (2012) Gene-Z: a device for point of care genetic testing using a smartphone. Lab Chip 12(8):1454–1462
29. Gorkin R, Park J, Siegrist J et al (2010) Centrifugal microfluidics for biomedical applications. Lab Chip 10(14):1758–1773
30. Kim TH, Park J, Kim CJ et al (2014) Fully integrated lab-on-a-disc for nucleic acid analysis of foodborne pathogens. Anal Chem 86 (8):3841–3848
31. Dineva MA, MahiLum-Tapay L, Lee H (2007) Sample preparation: a challenge in the development of point-of-care nucleic acid-based assays for resource-limited settings. Analyst 132 (12):1193–1199
32. Kolluri N, Klapperich CM, Cabodi M (2018) Towards lab-on-a-chip diagnostics for malaria elimination. Lab Chip 18:75–94
33. Lucchi NW, Gaye M, Diallo MA et al (2016) Evaluation of the Illumigene malaria LAMP: a robust molecular diagnostic tool for malaria parasites. Sci Rep 6:36808. https://doi.org/10.1038/srep36808
34. Sema M, Alemu A, Bayih AG et al (2015) Evaluation of non-instrumented nucleic acid amplification by loop-mediated isothermal amplification (NINA-LAMP) for the diagnosis of malaria in Northwest Ethiopia. Malar J 14. https://doi.org/10.1186/s12936-12015-10559-12939
35. Jani IV, Meggi B, Vubil A et al (2016) Evaluation of the whole-blood Alere Q NAT point-of-care RNA assay for HIV-1 viral load monitoring in a primary health care setting in Mozambique. J Clin Microbiol 54 (8):2104–2108
36. Hsiao NY, Dunning L, Kroon M et al (2016) Laboratory evaluation of the Alere q point-of-care system for early infant HIV diagnosis. PLoS One 11(3):e0152672
37. Nolte FS, Gauld L, Barrett SB (2016) Direct comparison of Alere i and cobas Liat influenza a and B tests for rapid detection of influenza virus infection. J Clin Microbiol 54 (11):2763–2766
38. Gous N, Scott L, Berrie L et al (2016) Options to expand HIV viral load testing in South Africa: evaluation of the GeneXpert (R) HIV-1 viral load assay. PLoS One 11(12): e0168244
39. Dormond L, Jaton K, de Valliere S et al (2015) Malaria real-time PCR: correlation with clinical presentation. New Microbes New Infect 5:10–12
40. Choi G, Prince T, Miao J et al (2018) Sample-to-answer palm-sized nucleic acid testing device towards low-cost malaria mass screening. Biosens Bioelectron 115:83–90
41. Choi G, Song D, Shrestha S et al (2016) A field-deployable mobile molecular diagnostic system for malaria at the point of need. Lab Chip 16(22):4341–4349
42. Xu G, Nolder D, Reboud J et al (2016) Paper-origami-based multiplexed malaria diagnostics from whole blood. Angew Chem 55 (49):15250–15253
43. Britton S, Cheng Q, Sutherland CJ et al (2015) A simple, high-throughput, colourimetric, field applicable loop-mediated isothermal amplification (HtLAMP) assay for malaria elimination. Malar J 14:335
44. Nair CB, Manjula J, Subramani PA et al (2016) Differential diagnosis of malaria on Truelab Uno(R), a portable, real-time, MicroPCR device for point-of-care applications. PLoS One 11(1):e0146961
45. Taylor BJ, Howell A, Martin KA et al (2014) A lab-on-chip for malaria diagnosis and surveillance. Malar J 13:179. https://doi.org/10.1186/1475-2875-1113-1179
46. Liu Q, Nam J, Kim S et al (2016) Two-stage sample-to-answer system based on nucleic acid amplification approach for detection of malaria parasites. Biosens Bioelectron 82:1–8
47. Shin Y, Lim SY, Lee TY et al (2015) Dimethyl adipimidate/thin film sample processing (DTS); a simple, low-cost, and versatile nucleic acid extraction assay for downstream analysis. Sci Rep 5:14127. https://doi.org/10.1038/Srep14127
48. Li Y, Kumar N, Gopalakrishnan A et al (2013) Detection and species identification of malaria parasites by isothermal, tHDA amplification directly from human blood without sample preparation. J Mol Diagn 15(5):634–641

# Chapter 15

# Digital Quantification of Human Viral RNA and DNA Using a Self-Digitization Chip

**Jiasi Wang, Jason E. Kreutz, and Daniel T. Chiu**

## Abstract

Digital nucleic acid quantitation methods show excellent sensitivity and specificity for pathogen detection. Droplet digital PCR (ddPCR) is the most advanced digital nucleic acid quantitation method and has been commercialized, but is not suitable for many point-of-care applications due to its complex instrumentation. Here we describe a simple microfluidics-based self-digitization (SD) chip for quantifying nucleic acids at the point of care with minimal instrumentation. We demonstrate the clinical diagnostic capability of this platform by applying it to quantifying human viral DNA and RNA. SD chips with a range of well numbers and volumes are tested, and isothermal methods are used to amplify the DNA and RNA to a detectable level. Sample concentration is determined based on the measured volume in the wells and the number of wells with fluorescence greater than a threshold based on a Poisson distribution. Concentration measurements over the low concentration range of 0–100 molecules/μL showed a strong correlation ($R^2 = 0.99$) with measurements using a real-time PCR assay, demonstrating the sensitivity and specificity of the SD chip platform.

**Key word** Digital nucleic acid quantification, Self-digitization (SD) chip, Isothermal amplification, Point-of-care (POC) tests, Viral RNA and DNA

## 1 Introduction

PCR is the most widely used DNA amplification method for gene detection and pathogen diagnosis [1]. Conventional quantitative PCR (qPCR) relies on the time-to-positivity (TTP, the time for fluorescence intensity to pass a defined threshold), which is susceptible to variability in amplification efficiency. In addition, qPCR is a relative quantitation method which requires an independent measurement of a standard curve to estimate target DNA concentrations. Digital PCR is an increasingly popular method which allows for absolute quantification of DNA or RNA without a standard curve [2, 3]. The strategy of digital PCR is to separate a sample into many small volume (pL–nL) partitions. Each partition may or may not contain a target nucleic acid molecule. After amplification, the

Miguel R. Ossandon et al. (eds.), *Biomedical Engineering Technologies: Volume 1*, Methods in Molecular Biology, vol. 2393, https://doi.org/10.1007/978-1-0716-1803-5_15, 

absolute concentration of the sample is determined based on Poisson statistics by comparing the number of positive (sample-containing) partitions to the total number of partitions. The advantages of digital PCR relative to qPCR include (a) absolute quantification—no standard curve using an independent method; (b) high tolerance of variation in amplification efficiency; and (c) high sensitivity and accuracy even at low nucleic acid concentrations.

Droplet digital PCR (ddPCR) is the most advanced digital nucleic acid quantitation method and has been commercialized [4]. ddPCR involves partitioning an aqueous sample into many small volume (pL-nL) water-in-oil droplets. Bio-Rad's QX200 is a representative ddPCR platform and is becoming widely used in fundamental research and clinical diagnosis. However, this platform requires sophisticated instrumentation—including separate instruments for droplet generation and detection, involves a time-consuming program (>5 h), and is expensive (~$200k), making it unsuitable for low-resource settings.

Point-of-care (POC) tests are needed for diagnoses in field settings and low-resource settings. Microfluidic technique is promising in POC applications because it facilitates miniaturization and automation. Soft lithography represents a flexible and inexpensive strategy to produce microstructures or nanostructures from elastomeric polymer such as polydimethylsiloxane (PDMS). Here we introduce a microfluidic device, called self-digitization (SD) chip (Fig. 1), which automatically partitions a sample into isolated wells to allow digital nucleic acid quantification, and can be combined with isothermal nucleic acid amplification and simple fluorescence detection methods to allow for minimal instrumentation [5, 6]. Loop-mediated isothermal amplification (LAMP) is an isothermal (63 °C) amplification method developed by Notomi et al. in 2000. It became popular because it is sensitive, fast, and convenient. LAMP can amplify target DNA in a short time, but cannot detect RNA. In contrast, the nucleic acid sequence-based amplification (NASBA) is an isothermal (41 °C) amplification method that amplifies single-stranded RNA.

Here, we demonstrate the capability of the SD chip platform by quantifying human papillomavirus (HPV) DNA and human immunodeficiency virus (HIV) RNA using an SD chip with these two isothermal amplification methods [7, 8]. The SD chip achieves accurate quantitation even at low concentrations (1–100 copies/μL), demonstrating its sensitivity and specificity, and motivating further development of this platform for POC diagnostic applications.

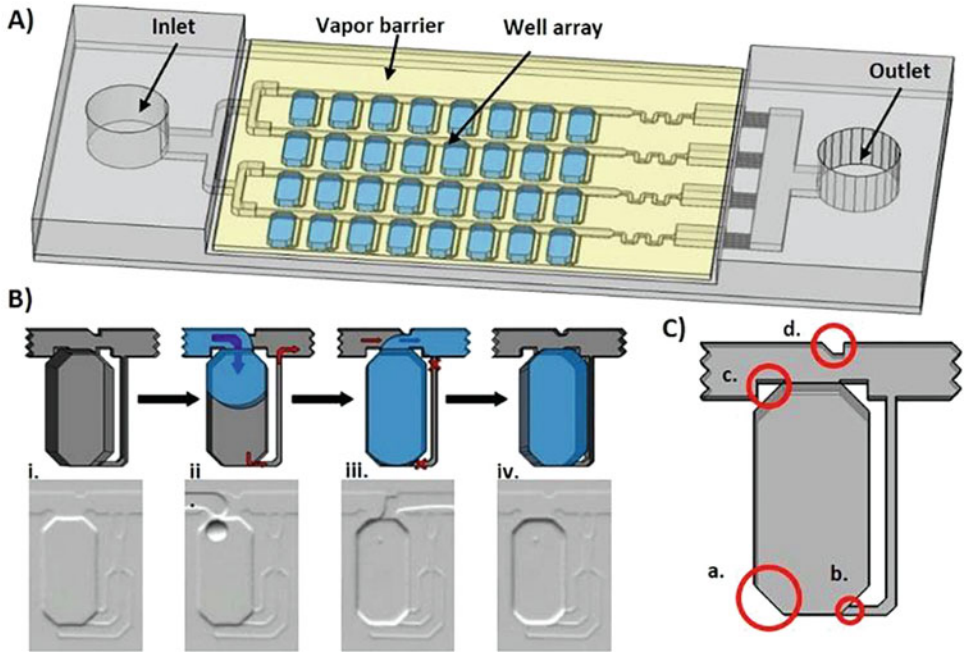


**Fig. 1** Self-digitization (SD) chip design. (**a**) The SD chip is composed of PDMS with microchannels and wells (blue). (**b**) Sample filling is illustrated for a single well in schematics (top row) and photographs (bottom row). In the schematics, oil is dark gray and aqueous sample is blue. Stages of sample filling: (i) The chip is primed with oil. (ii) Aqueous sample is added and fills the channels and wells. (iii) Additional oil is added, displacing the aqueous solution from the channels but not from the wells. (iv) The aqueous sample is partitioned into individual wells. (**c**) SD chip design: To improve sample filling efficiency, beveled corners (**a**) and drainage channels (**b**) were added to the design. Notches in the channel (**c**, **d**) were added to facilitate flow breakoff during filling

## 2 Materials

### *2.1 Chip Fabrication*

1. Poly(dimethylsiloxane) (PDMS, Sylgard 184; Dow Corning, Midland, MI), stored at room temperature.
2. High-resolution photomasks with channel and well patterns are printed using a photoplotter (Fineline Imaging, Colorado Springs, CO).
3. SU-8-2050 photoresist (Microchem, Newton, MA), stored at 4 °C.
4. (Tridecafluoro-1,1,2,2-tectrhydrooctyl)trichlorosilane (Gelest Inc., Morrisville, PA).
5. Glass coverslips (Electron Microscopy Sciences, Hatfield, PA).
6. Mask aligner (Newport Corporation, Irvine, CA).
7. Polychlorotrifluoroethylene (PCTFE) plastic film (Ted Pella Inc., Redding, CA, USA).
8. 15-gauge punch sharpened by sandpaper.

9. Double Sided Kapton® Tape, 19 mm × 32.9 m (3/4″ × 36 yards) (Ted Pella Inc., Redding, CA, USA).
10. ImageJ software are from https://imagej.nih.gov/ij/download.html.

### 2.2 Digital Quantification

1. The oil phase is composed of 91% TEGOSOFT DEC (Evonik Industries, Essen, Germany), 9% light mineral oil (Sigma-Aldrich, St. Louis, MO), and 0.04% Abil WE 09 (Evonik Industries), except as indicated.
2. Vacuum pump (DOA-P104-AA, Gast Manufacturing, Benton Harbor, MI).
3. Eppendorf Mastercycler (Eppendorf, Hamburg, Germany), fitted with a flat adapter.
4. Typhoon FLA9000 imaging system (GE Healthcare, Pittsburgh, PA).
5. All DNA is purchased from Integrated DNA Technologies, Inc. (IDT, Coralville, IA) and is dissolved in Tris-EDTA buffer (pH 7.5). Primer sequences for loop-mediated isothermal amplification (LAMP) are the following: F3: 5′-CGC GTC CTT TAT CAC AGG-3′; FIP: 5′-GGC ACC ATA TCC AGT ATC TAC CAT AAT TGC CCC CCT TTA GAA CT-3′; LF: 5′-TCA CCA TCT TCC AAA ACT G-3′; B3: 5′-TGG AAT CCC CAT AAG GAT-3′; BIP: 5′-TGC AAG ATA CTA AAT GTG AGG TAC CGC AGA CAT TTG TAA ATA ATC A-3′; LB: 5′-ATT GGA TAT TTG TCA GTC T-3′. Primer sequences for nucleic acid sequence-based amplification (NASBA) are the following: sense primer: 5′-CTCAATAAAGCTTGCCTTGA-3′; T7 antisense primer: 5′-AATTCTAATACGACTCACTA TAGGGAGAGGGGCGCCACTGCTAGAGA -3′; molecular beacon: 5′-FAM-CGCTTCCA GTAGTGTGTGCCCGTCTG TGGAAGCG -3IABkFQ-3′ (self-hybridizing regions are underlined).
6. HIV-1 RNA (group M, subtype B) (SeraCare Life Sciences Inc., Milford, MA).
7. NASBA Kit (Life Sciences Advance Technologies, St. Petersburg, FL), including 3× NASBA reaction buffer (NECB-1-24), NASBA enzyme cocktail (NEC-1-24), and 6× nucleotide mix (NECN-1-24). NASBA reaction buffer is composed of 40 mM Tris–HCl (pH 8.5), 70 mM KCl, 12 mM $MgCl_2$, 1 mM each of the dNTPs, 2 mM each of the ribonucleoside 5′ triphosphates, 10 mM dithiothreitol, and 15% dimethyl sulfoxide.
8. Bovine serum albumin (BSA), RNase inhibitor, Tris–borate–EDTA (TBE) buffer, Calcein (high purity), and dNTPs (Thermo Fisher Scientific, Waltham, MA).

9. Bst 2.0 WarmStart® DNA Polymerase and Isothermal Amplification Buffer (New England Biolabs, Ipswich, MA). Isothermal Amplification Buffer is composed of 20 mM Tris buffer (pH 8.8), 10 mM KCl, 6 mM $MgSO_4$, 10 mM $(NH_4)_2SO_4$, 0.1% Tween 20, 2.8 mM each dNTPs, and 0.8 M Betaine.
10. HPV-18 plasmid (full genome length, 45152D) is purchased from American Type Culture Collection (Manassas, VA). HPV-16, 31, and 45 plasmids are obtained from Seattle Children's Research Institute.
11. HIV-negative human plasma (SeraCare, Milford, MA).
12. HIV-1 LAI (group M, subtype B) strain and HIV-2 ROD9 (group A) strain are obtained from the Center for Emerging and Re-emerging Infectious Diseases, Division of Allergy and Infectious Diseases, Department of Medicine, University of Washington, Seattle, USA.
13. Bio-Rad CFX96 Real-Time PCR instrument (Bio-Rad Laboratories, Hercules, CA).
14. Mupid-exU submarine electrophoresis system (Eurogentec, Seraing, Belgium).
15. Ssofast Evagreen Supermix and Bio-Rad QX100 ddPCR oil (Bio-Rad Laboratories).

## 3 Methods

### 3.1 SD Chip

#### 3.1.1 SD Chip Design

To partition the aqueous sample into small individual volumes, conventional microfluidic based methods require valves and pumps, and complex fluidic control. To address this challenge, we designed a microfluidic system containing a main channel with adjacent side cavities, which enabled the sample to self-digitize into individual cavities from the main channel without the requirement of complex fluidic manipulations. To further increase the speed by which self-digitization occurs, we added drainage channels that connect the cavities back to the main channel. The purpose of the drainage channels are to facilitate displacement of the oil present in the cavities during entrance of the aqueous phase into the cavities. The exact geometries of the drainage channels can be varied as long as they are sufficiently narrow to prevent entrance of the aqueous phase.

Several designs are tried in our previous work, including serpentine channel, bifurcated channel, and different shapes of cavities (wells). We have found that aspect ratio between the cross-sectional area of the well opening and the cross-sectional area of the main channel should be higher than 2 to give a good digitization efficiency. The height of well should be higher than that of the main channel, thus requiring two-layer fabrication to prepare the chip.

The pattern of the first layer is for the main channel with height of ~25 μm, and the pattern of the second layer is for well with height of ~100 μm.

The SD chip used in this study had parallel channels that connect inlet and outlet reservoirs, with a series of wells connected to and adjacent to the channels (Fig. 1a. The height of the bifurcating channels remained the same as the main channel, and the width of the bifurcating channels could be varied without affecting much the function of the chip. The SD chip is primed with an immiscible oil phase to wet the inner walls of the channel and wells and is then filled with aqueous sample. The flow rate is about 0.1 μL/s. The aqueous sample fills the wells to reduce their interfacial energy, displacing the oil, until all channels and wells are filled. The displaced oil is pushed to the outlet through the channel. Additional oil is then added to displace the aqueous sample from the channels but not from the wells, because the interface tension of oil phase is lower than aqueous phase. The aqueous sample is partitioned into individual isolated wells (in Fig. 1a, the partitioned aqueous sample is blue). Figure 1b depicts these sample filling steps for a single well.

Several SD chip design features are added to improve the sample filling efficiency (Fig. 1c). Beveled corners are added to the wells to reduce high energy distortions of aqueous sample in the wells; a drainage channel connecting each well with a channel is added to improve the efficiency of oil drainage; and notches on both sides of each channel adjacent to a well are added to facilitate flow breakoff during sample filling.

#### *3.1.2 SD Chip Master Fabrication*

There is only one master, because it is made by two-step lithography and thus one replication is sufficient to replicate the two-layer features on the master. Therefore, there is only one chip produced with each master. SU-8-2050 photoresist is spin-coated onto a clean silicon wafer at 2500 rpm for 90 s and baked at 95 °C for 5 min. The SU-8-coated wafer is covered by a photomask with the desired pattern (Fig. 2) and exposed to UV light to cross-link the photoresist (*see* **Note 1**), then baked again at 95 °C for 5 min. The wafer is washed using PGMEA and isopropyl alcohol to dissolve and remove nonexposed SU-8. The wafer is then baked at 155 °C for 10 min, producing the main channel features with a thickness of 25 ± 1 μm. The second layer, corresponding to the well features, is fabricated using the same procedure as above except using a slower spin (1100 rpm) so that the photoresist thickness is 100 ± 3 μm (height of the well) rather than 25 ± 1 μm (height of the channel) (*see* **Note 2**). After washing and baking as above, the two-layer master Explain is coated with (tridecafluoro-1,1,2,2 tetrahydrooctyl)trichlorosilane using gas-phase deposition to prevent the master from sticking to the PDMS SD chip.

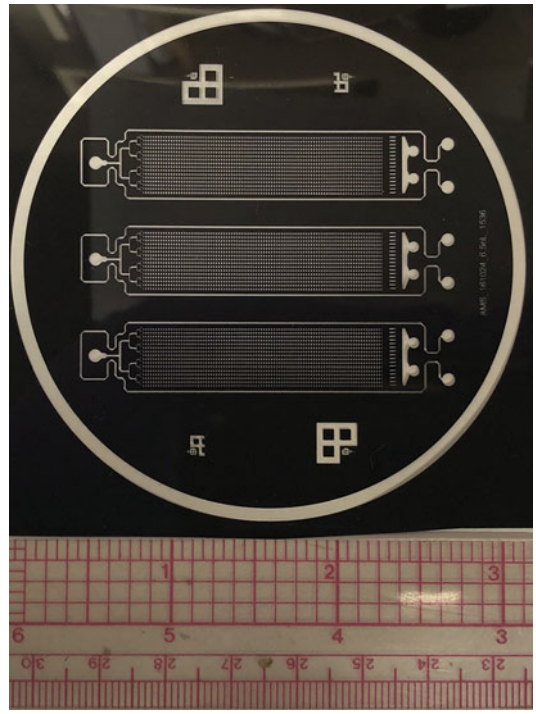

**Fig. 2** Representative images of photomasks of SD chip corresponding to the well pattern

*3.1.3 SD Chip Fabrication*

PDMS monomer is mixed with catalyst at a 5:1 weight ratio. Degassed PDMS is spin-coated onto the fabricated master and a glass slide to prevent sticking (*see* **Note 3**). This coated master and glass slide are cured at 70 °C for 3 h. The molded PDMS replica is peeled from the master and holes are punched to create the inlet and outlet. The molded PDMS layer and PDMS-coated glass slide are exposed to oxygen plasma and the PDMS layer is permanently sealed to the glass slide. PDMS slabs with a thickness of ~8 mm are cut into 8x8 mm squares for each inlet and outlet and punched with holes to create sample reservoirs. The reservoir pieces are bonded to the chip so that the reservoir sits on holes in the PDMS layer (Fig. 3). The PDMS-glass chip is then baked at 115 °C for at least 1 day. A PCTFE plastic film is treated with oxygen plasma and bond to the top of the chip (*see* **Note 4**), to prevent evaporation during the LAMP reaction.

*3.1.4 Digitization Experiments*

To prime the SD chip with oil, the chip is placed under vacuum (−10 bar). Oil is added, and the vacuum is removed causing the oil to fill the chip. The PDMS is strong enough to prevent well collapse. Double-sided Kapton tape is applied to the outlet reservoir to attach a PDMS adaptor which is connected to vacuum for sample loading (Fig. 4). Aqueous sample is added to the inlet reservoir and a vacuum is applied to the outlet. After the chip is filled with aqueous sample, additional oil is added to the inlet and

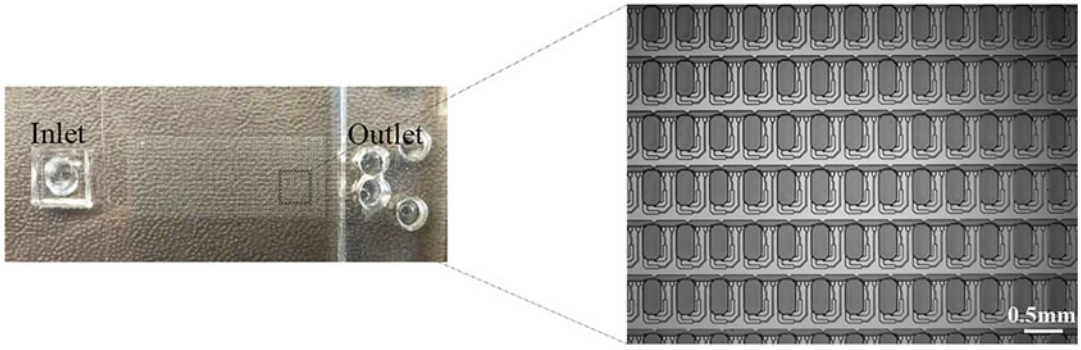


**Fig. 3** Left: Photograph of an SD chip sealed onto a glass slide. Right: Enlarged view of the SD chip wells

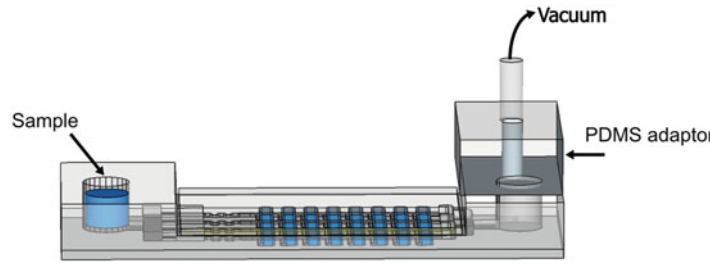


**Fig. 4** Schematic of sample loading into an SD chip. Aqueous sample was added to the inlet and a vacuum pump was connected to the outlet reservoir via a PDMS adapter

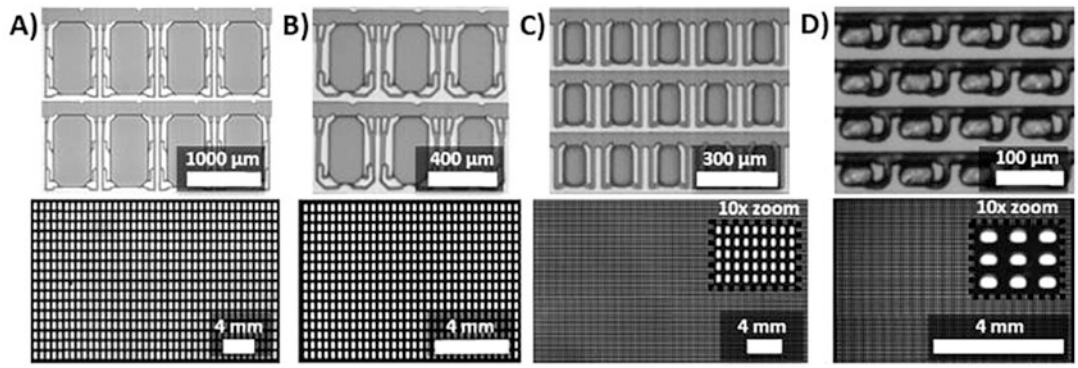


**Fig. 5** The SD chip can be scaled to different well numbers and volumes. Brightfield (top) and fluorescent (bottom) images depict SD chips with (**a**) 640,100-nL wells, (**b**) 1024 7.5-nL wells, (**c**) 25,600 1-nL wells, and (**d**) 10,240 50-pL wells

flowed through the channels. The surface tension of oil phase is lower than aqueous phase, so the oil just displaced the aqueous sample from the channels but not from the wells. Partitioning the aqueous sample into individual wells. Brightfield and fluorescence photographs are obtained using an Olympus MVX10 stereoscope (Fig. 5). To demonstrate the compatibility of the SD chip with various assay formats, we designed four SD chips with four different

well properties: 640 wells (1000 × 520 × 200 μm) with a well volume of 100 nL and a total volume of 60 μL (Fig. 4a); 1024 wells (400 × 200 × 100 μm) with a well volume of 7.5 nL and a total volume of 8 μL (Fig. 4b); 10,240 wells (200 × 100 × 80 μm) with a well volume of 1.5 nL and a total volume of 15 μL (Fig. 4c); 10,240 wells (30 × 50 × 35 μm) with a well volume of 50 pL and a total volume of 0.5 μL (Fig. 4d). The aqueous sample is digitized effectively in all four SD chips. To demonstrate that this sample digitization method is compatible with different oil phases, we tested two oil mixtures: [1] 68.3% mineral oil, 31.3% hexadecane, 0.4% TEGOSOFT DEC, and 0.018% Abil WE 09 (Fig. 5a–c), and [2] a 2:1 ratio of Bio-Rad QX100 ddPCR oil and FC-40 (Fig. 5d), and both oil mixtures worked well (*see* **Note 5**).

### 3.2 Digital LAMP (dLAMP) for Quantification of HPV DNA

#### 3.2.1 Loop-Mediated Isothermal Amplification (LAMP)

Loop-mediated isothermal amplification (LAMP) is a rapid (<1 h) and robust isothermal DNA amplification method [9]. Figure 6 shows the LAMP reaction mechanism. LAMP employs four primers (F3, FIP, BIP, and B3), which recognize six distinct sites flanking the amplified DNA sequence, resulting in high specificity. LAMP is dependent on the displacement activity of *Bst* DNA polymerase. Two additional primers (LF and LB) are used to increase the efficiency of the reaction [10]. LAMP allows for amplification of only a few copies of DNA to detectable levels in less than 60 min at a constant temperature of 60–70 °C, making it suitable for POC diagnostic applications.

In our experiments, Calcein is used as a fluorescent indicator. The fluorescence of Calcein is quenched by manganese ions ($Mn^{2+}$). During the LAMP reaction, a large amount of pyrophosphate ion byproduct is formed; this pyrophosphate ion binds strongly with $Mn^{2+}$ to generate an insoluble salt, reducing the quenching of Calcein and resulting in greater fluorescence [11].

#### 3.2.2 Detection of HPV DNA Using dLAMP

We combined sample digitization using an SD chip with amplification using LAMP (dLAMP). An SD chip is primed with oil as described above. The LAMP reaction mixture (25 μL) is composed of the following: 1× Isothermal Amplification Buffer, 8 units of Bst 2.0 WarmStart® DNA Polymerase, 4 mM $MgSO_4$, 1.4 mM of each dNTP, 0.8 M betaine, 1.2 mg $mL^{-1}$ BSA, 50 μM Calcein, 1 mM $MnCl_2$, HPV-18 plasmid DNA, and HPV-18 LAMP primers (0.2 μM F3, 0.2 μM B3, 1.6 μM FIP, 1.6 μM BIP, 0.8 μM LF, 0.8 μM LB). Calcein is premixed with $MnCl_2$ solution at a 1:20 molar ratio before adding it to the reaction mixture. The LAMP sample is loaded into the inlet reservoir and into the SD chip by applying vacuum to the outlet, followed by adding excess oil to displace the aqueous sample from the channels (*see* **Note 6**). The chip is then imaged before the start of the LAMP reaction to calculate the volume in each well, and then the chip is placed on an Eppendorf Mastercycler with an in situ adapter at 63 °C for

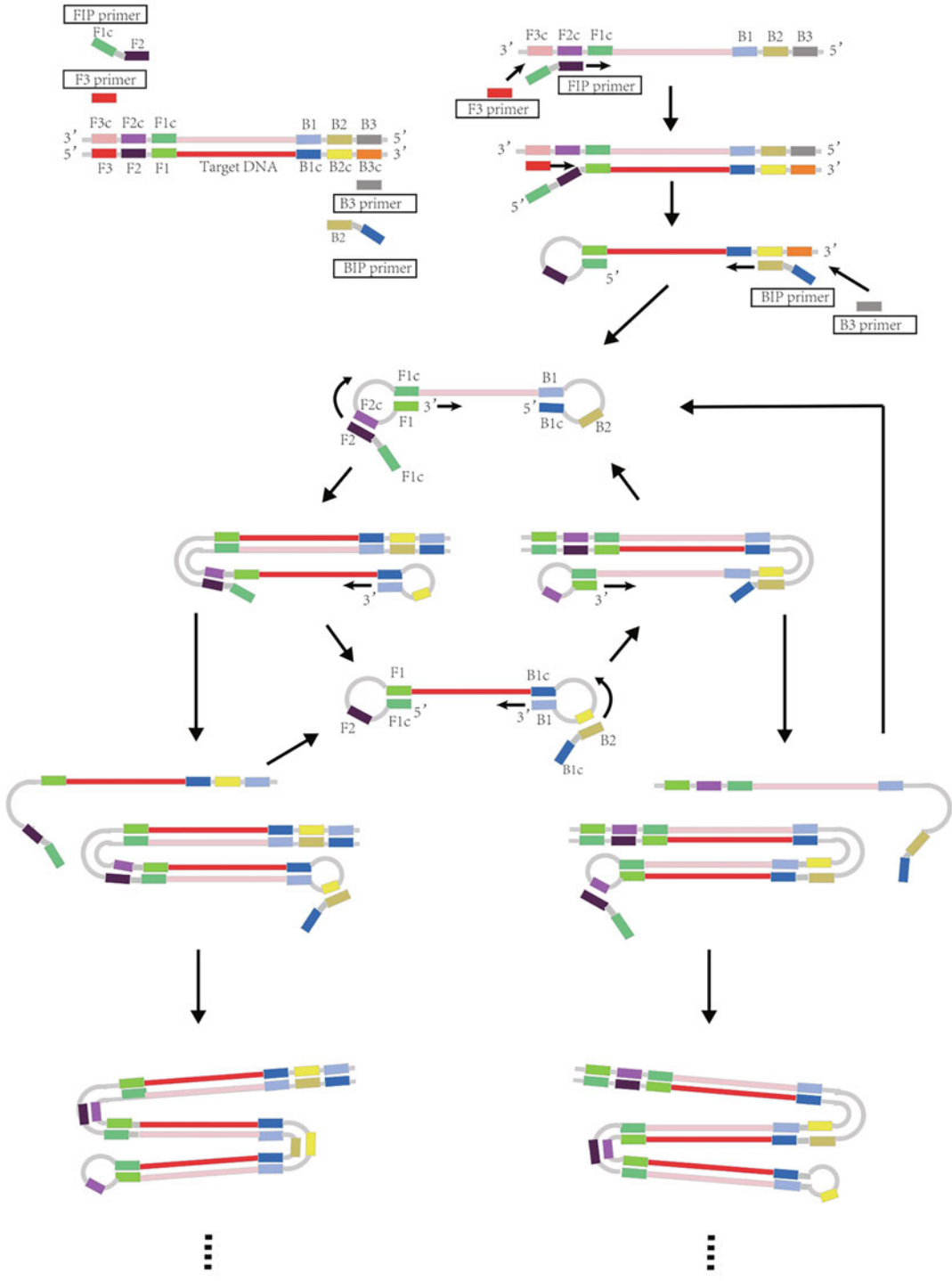


**Fig. 6** DNA amplification using LAMP


**Fig. 7** The Eppendorf Mastercycler with an in situ adapter with a flat surface

90 min. The adapter has a flat surface thus the chip could be put on it. Mineral oil is added between chip and adapter to confirm chip is heated evenly (Fig. 7).

*3.2.3 SD Chip Imaging*

Once the reaction is complete, the SD chip is imaged using a Typhoon FLA9000 imaging system with excitation at 473 nm, at an image resolution of 10 μm. For detection of the HPV-18 gene at a concentration of $3.1 \times 10^4$ molecules/mL, an SD chip consisting of 1520 well with a well volume of 3.3 nL is used (Fig. 8a).

*3.2.4 Sample Volume in each Well*

Well heights are measured using a home-built interferometer [12]. Sample volumes in each well are determined using images taken before amplification, analyzed using ImageJ software (http://rsbweb.nih.gov). We analyzed the relative pixel intensity in each well, which correlates with the height of the fluorescent solution. If a well is completely filled, a plateau in a line scan at the maximum pixel intensity is observed (Fig. 9). The average value of the pixels in this plateau is multiplied by the pixel area to obtain the integrated intensity expected for a full well. The filling ratio for each well is calculated by dividing the actual integrated intensity of the well by the integrated intensity expected for a full well. The actual

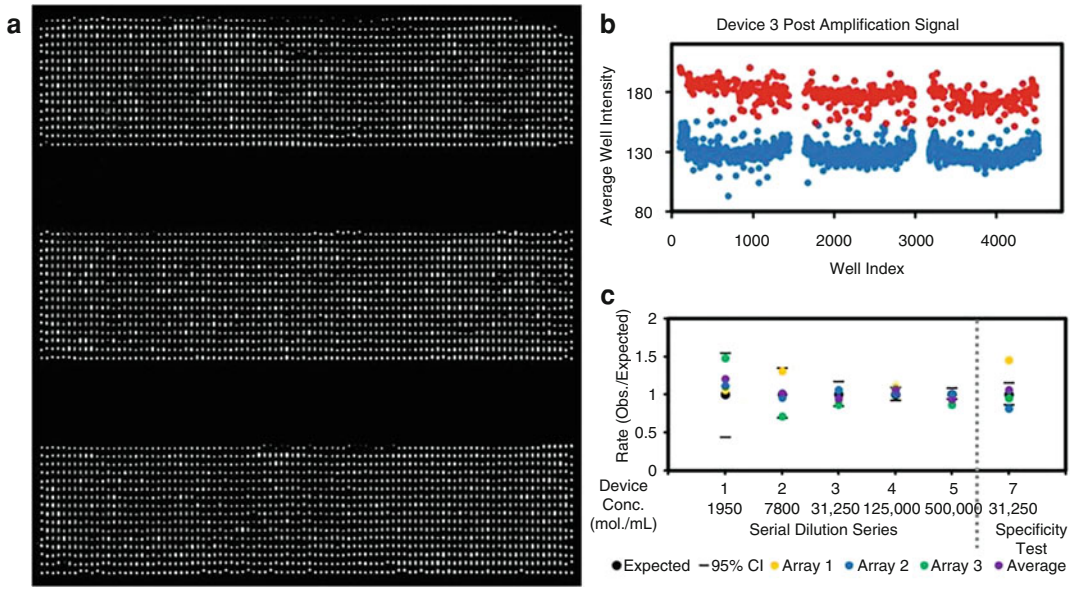


**Fig. 8** (**a**) Images of the dLAMP HPV-18 gene assay. The HPV-18 plasmid concentration was ~3.1 × $10^4$ molecules/mL. (**b**) Plot of well pixel intensities from images in panel **a**. Red dots represent wells defined as positive (in which HPV-18 was detected); blue dots represent wells defined as negative (no HPV-18 detected). (**c**) dLAMP HPV-18 quantification results shown as the ratio of measured and expected HPV-18 concentrations in six chips. Dashes represent 95% confidence intervals based on the expected concentrations

total volume of sample in the chip is calculated using the filling ratio for each well. The average actual filled volume is about 95.0%, and about 10% of wells are excluded in analysis.

### 3.2.5 *Data Analysis*

Wells with a filling ratio less than 50% or that lost >20% of their volume during amplification are excluded from analysis (*see* **Note 7**). To distinguish positive and negative wells after amplification, the average well pixel intensity is used to generate a bimodal histogram of well intensities, and the minimum value between the two modes is used as the initial threshold to define positive and negative wells. Using this threshold, the average intensity of positive and negative wells is calculated. The midpoint of the two average intensities is used to set a new threshold, and this process is repeated until the number of positive and negative wells converged.

The number of target DNA molecules followed a standard Poisson distribution, and is calculated using the equation, $\lambda = -\ln(1 - k/n)$, where $\lambda$ is the mean number of target DNA molecules per well, $n$ is the total number of wells analyzed, and $k$ is the number of positive wells. The concentration is calculated using the equation, $c = n\lambda/v$, where $n$ is the number of wells analyzed and $v$ is the total volume in the chip. As shown in Fig. 8c, chips 1–5 show dLAMP results with different HPV-18 concentrations. The ratio of measured-to-expected concentration is used to show the

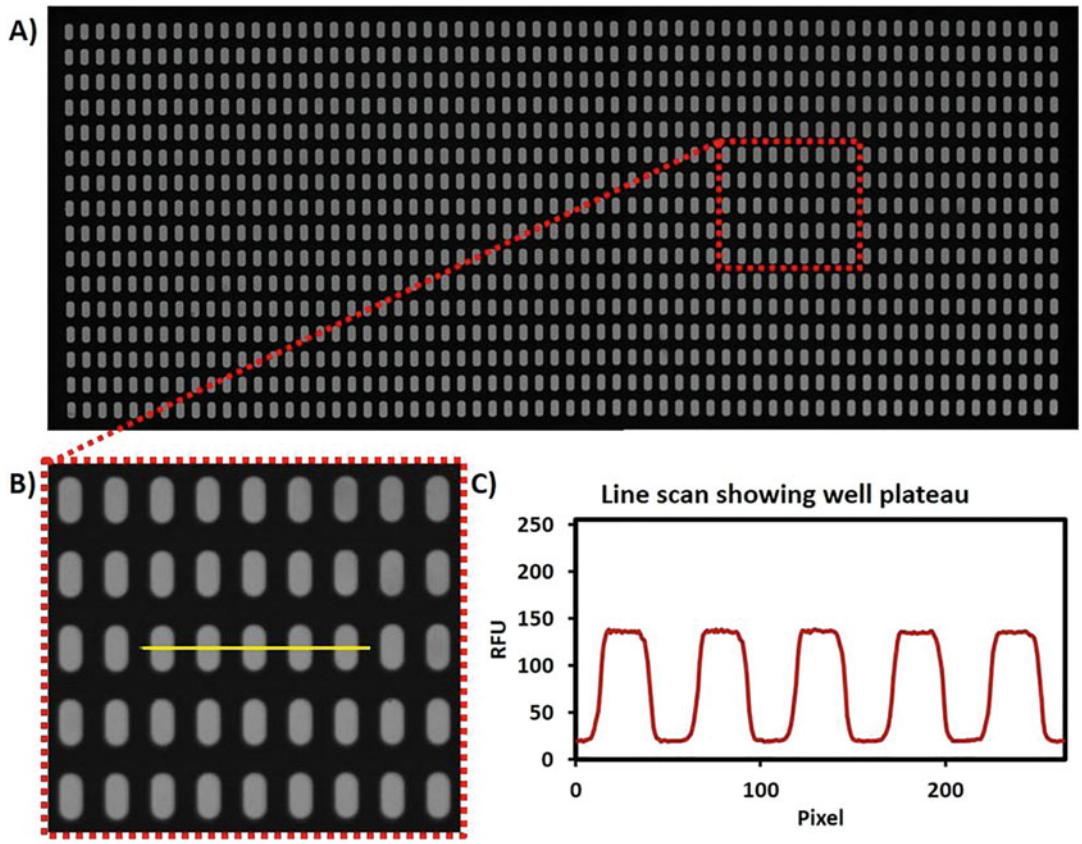


**Fig. 9** (**a**) Fluorescent image of SD chip with 1024 7.5-nL wells. (**b**) Enlarged view showing wells and line scan (yellow). (**c**) Plot of the line scan fluorescence, showing plateaus where the well is full

results. The ratio fell within the 95% confidence intervals except for one sample in chip 5. Chip 7 tests the specificity of the assay, which contains HPV 16, 18, 31, and 45 plasmids at $3.1 \times 10^4$ molecules/mL each. The average values fall within the 95% confidence interval in each case (*see* **Note 8**).

### *3.3 Digital NASBA (dNASBA) for Quantitation of HIV RNA*

#### *3.3.1 NASBA Mechanism*

Nucleic acid sequence-based amplification (NASBA) is an isothermal (41 °C) RNA amplification method which amplifies single-stranded RNA $10^9$-fold in 1–2 h [13]. The NASBA reaction uses three enzymes (reverse transcriptase, RNase H, and T7 RNA polymerase) and two primers (sense primer and T7 antisense primer which contains a T7 promoter region) to mimic the in vivo retroviral replication of RNA (Fig. 10). The NASBA reaction is monitored using a fluorescent beacon whose emission increases when the probe is hybridized with RNA [14]. Like LAMP, NASBA is a simple isothermal nucleic acid amplification method suitable for use in POC diagnostic applications.

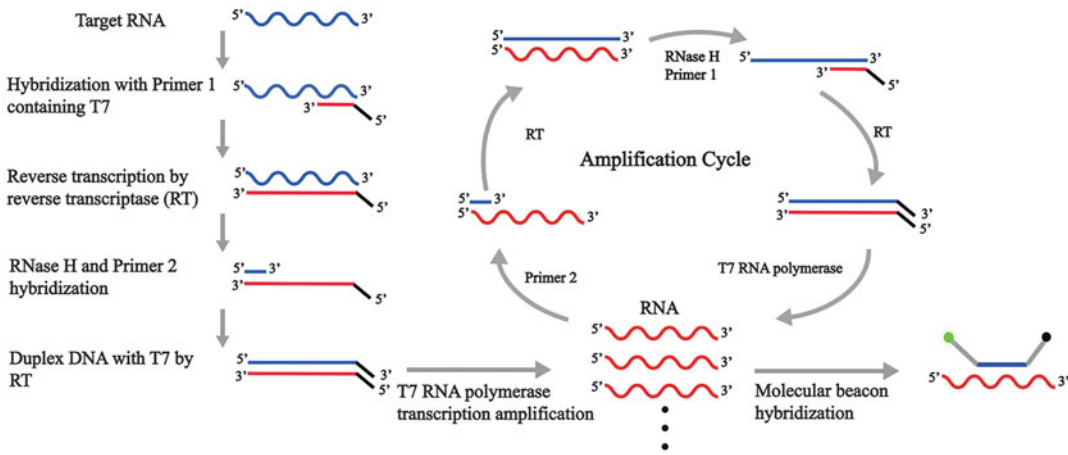


**Fig. 10** RNA amplification using NASBA

*3.3.2 Quantitative Detection of HIV RNA Using dNASBA*

To increase the amplification efficiency, the template RNA is pre-heated at 70 °C before the NASBA reaction. T7 antisense primer is mixed with HIV RNA in 3× NASBA reaction buffer and heated at 70 °C for 1 min followed by cooling to 41 °C. The NASBA reaction mixture (20 μL) is composed of the following: 1× enzyme cocktail, 1× nucleotide mix, 250 nM sense and T7 antisense primers, 80 nM molecular beacon, various concentrations of HIV RNA, 5 units of RNase Inhibitor, 0.5% BSA, 0.05% Tween 20, and DNase- and RNase-free $H_2O$. SD chip sample filling is performed as described above. The SD chip is place into the Eppendorf Mastercycler with an in situ adapter and maintained at 41 °C for 110 min.

Following dNASBA, the SD chip is imaged using the same protocol as for dLAMP. Figure 11a shows representative results for the dNASBA assay using 0–100 copies/μL of HIV-1 RNA. More and more positive chambers are observed with increasing HIV-1 RNA concentration, while the negative control (no HIV-1 RNA) showed no signal. The measured concentration of HIV-1 RNA based on Poisson statistics showed a good correlation with the input concentration ($R^2 = 0.99$, Fig. 11b), indicating that the dNASBA assay is a reliable method for quantifying HIV-1 RNA over this low concentration range.

*3.3.3 Quantitative Detection of HIV RNA in Plasma Using dNASBA*

dNASBA is used to quantify HIV-1 RNA in human plasma. HIV-1 LAI (group M, subtype B) is used as the positive strain and HIV-2 ROD9 (group A) is used as a negative (control) strain to test the specificity of the assay. Viral cultures are diluted with HIV-free human plasma, are inactivated by heating at 65 °C for 15 min, and are stored at −80 °C until use. To lyse the virus and release RNA, inactivated sample is mixed with 5% Triton X-100 at a 1:1 ratio and is incubated at room temperature for 2 min. The samples are then serially diluted into dNASBA reaction mixtures. The

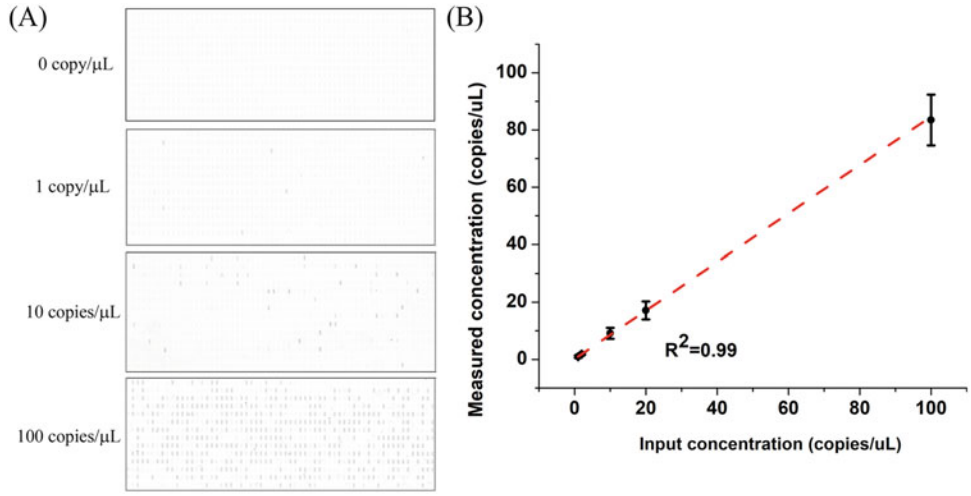


**Fig. 11** Quantitative results for dNASBA using an SD chip with different HIV-1 RNA concentrations (0–-100 copies/μL). (**a**) Images of dNASBA results using a 10× serial dilution of HIV-1 RNA. (**b**) Least-squares regression curve. Measured HIV-1 RNA concentrations are plotted against input concentrations. Error bars represent standard deviation

concentrations of HIV-1 RNA as measured using dNASBA are 1559 ± 158, 152 ± 19, and 13 ± 4 copies/μL, while the concentrations of the same samples as measured using an Abbott RealTime PCR assay are 1692 ± 138, 163 ± 8.5 and 15 ± 0.6 copies/μL ($n = 3$), showing a strong correlation ($R^2 = 0.99$) (Fig. 12). A negative control sample with HIV-2 virus (>1000 copies/μL in the Abbott RealTime PCR assay) is also tested to verify the specificity of the dNASBA reaction, and the false-positive rate is <0.03%. These results demonstrate the sensitivity and specificity of dNASBA for quantifying human viral RNA in plasma samples.

These studies demonstrate that the SD chip, combined with isothermal nucleic acid amplification, can be used for accurate quantification of human viral DNA or RNA at low concentrations with minimal instrumentation, making this platform well-suited for use in POC diagnostics in resource-limited settings.

## 4 Notes

1. The UV light passed through the transparent regions of the photomask.
2. The second photomask is aligned with the first layer on the wafer using the mask aligner.
3. PDMS is spin-coated on master with 300 rpm for 60 s, and on glass slide with 2000 rpm for 60 s.
4. The SD chip bonded with PCTFE plastic film is heated for more than 2 h at 70 °C to secure the film.

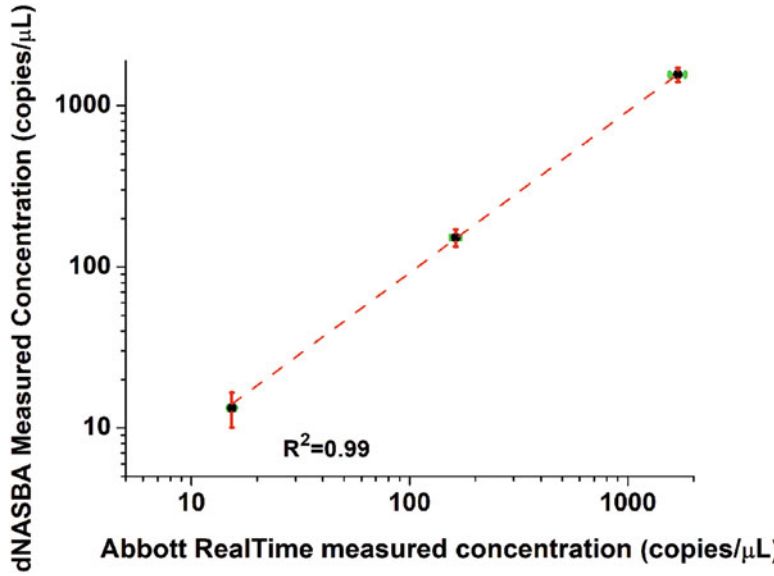


**Fig. 12** Quantitative detection of HIV-1 RNA in human plasma. HIV-1 RNA concentrations measured using dNASBA are plotted against those measured using an Abbot RealTime PCR assay. Vertical error bars (red) represent the standard deviation of the dNASBA assay; horizontal error bars (green) represent the standard deviation of the Abbott RealTime assay ($n = 3$)

5. The aqueous sample here is 1× Ssofast Evagreen Supermix with 2 mg/mL BSA, 500 nM generic primer, and fluorescein in 0.3× PBS.
6. The filling process takes 2–5 min.
7. About 23% of wells are excluded during data analysis after amplification.
8. Control experiment using HPV 16, 31, and 45 plasmids with same concentration is also performed and the false-positive rate is about 0.1%.

## Acknowledgments

This research is supported by National Institutes of Health (R01EB021150, UG3CA211139) and the Bill & Melinda Gates Foundation. We gratefully acknowledge the Royal Society of Chemistry for the permission of use of the Figs. 1, 2, 3, 4, 6, 7, 8, 9, 10.

*Conflicts of interest*: The authors declare the following competing financial interests: DTC and JEK have financial interest in Lamprogen Inc., which has licensed the SD chip technology from the University of Washington.

## References


1. Saiki R, Scharf S, Faloona F, Mullis K, Horn G, Erlich H, Arnheim N (1985) Enzymatic amplification of beta-globin genomic sequences and restriction site analysis for diagnosis of sickle cell anemia. Science 230:1350–1354
2. Vogelstein B, Kinzler KW (1999) Digital PCR. Proc Natl Acad Sci U S A 96:9236–9241
3. Quan P-L, Sauzade M, Brouzes E (2018) dPCR: a technology review. Sensors 18:1271
4. Perkins G, Lu H, Garlan F, Taly V (2017) Chapter three—droplet-based digital PCR: application in cancer research. In: Makowski GS (ed) Advances in clinical chemistry. Elsevier, Amsterdam, pp 43–91
5. Cohen DE, Schneider T, Wang M, Chiu DT (2010) Self-digitization of sample volumes. Anal Chem 82:5707–5717
6. Gansen A, Herrick AM, Dimov IK, Lee LP, Chiu DT (2012) Digital LAMP in a sample self-digitization (SD) chip. Lab Chip 12:2247–2254
7. Wang J, Kreutz JE, Thompson AM, Qin Y, Sheen AM, Wang J, Wu L, Xu S, Chang M, Raugi DN et al (2018) SD-chip enabled quantitative detection of HIV RNA using digital nucleic acid sequence-based amplification (dNASBA). Lab Chip 18:3501–3506
8. Kreutz JE, Wang J, Sheen AM, Thompson AM, Staheli JP, Dyen MR, Feng Q, Chiu DT (2019) Self-digitization chip for quantitative detection of human papillomavirus gene using digital LAMP. Lab Chip 19:1035–1040
9. Notomi T, Okayama H, Masubuchi H, Yonekawa T, Watanabe K, Amino N, Hase T (2000) Loop-mediated isothermal amplification of DNA. Nucleic Acids Res 28:e63–e63
10. Nagamine K, Hase T, Notomi T (2002) Accelerated reaction by loop-mediated isothermal amplification using loop primers. Mol Cell Probes 16:223–229
11. Tomita N, Mori Y, Kanda H, Notomi T (2008) Loop-mediated isothermal amplification (LAMP) of gene sequences and simple visual detection of products. Nat Protoc 3:877–882
12. Yen GS, Fujimoto BS, Schneider T, Huynh DTK, Jeffries GDM, Chiu DT (2011) A rapid and economical method for profiling feature heights during microfabrication. Lab Chip 11:974–977
13. Compton J (1991) Nucleic acid sequence based amplification. Nature 350:91–92
14. Leone G, van Schijndel H, van Gemen B, Kramer FR, Schoen CD (1998) Molecular beacon probes combined with amplification by NASBA enable homogeneous, real-time detection of RNA. Nucleic Acids Res 26:2150–2155

# Chapter 16

# Sample-to-Answer Microfluidic Nucleic Acid Testing (NAT) on Lab-on-a-Disc for Malaria Detection at Point of Need

**Gihoon Choi and Weihua Guan**

## Abstract

One of the grand challenges for field-deployable NATs is related to the front end of the assays—nucleic acid extraction from raw samples. The ideal nucleic acid sample preparation should be simple, scalable, and easy-to-operate. In this chapter, we present a lab-on-a-disc NAT device for sample-to-answer malaria diagnosis. The parasite DNA sample preparation and subsequent real-time LAMP detection are seamlessly integrated on a disposable single microfluidic compact disc, driven by energy-efficient, non–centrifuge-based magnetic field interactions. Each disc contains four parallel testing units, which could be configured either as four identical tests or as four species-specific tests. When configured as species-specific tests, it could identify two of the most life-threatening malaria species (*P. falciparum* and *P. vivax*). The reagent disc with a 4-plex analyzer (discussed in Chapter 1) is capable of processing four samples simultaneously with 40 min turnaround time. It achieves a detection limit of ~0.5 parasites/μl for whole blood, sufficient for detecting asymptomatic parasite carriers. The assay is performed with an automated device described in Chapter 14. The combination of sensitivity, specificity, cost, and scalable sample preparation suggests the real-time fluorescence LAMP device could be particularly useful for malaria screening in field settings.

**Key words** Point-of-care, Microfluidic, Nucleic acid testing, Malaria

## 1 Introduction

Malaria is a mosquito-borne disease caused by *Plasmodium* parasites, predominately in resource-limiting areas of low- and middle-income countries. Among five parasite species, *P. falciparum (Pf)* and *P. vivax (Pv)* pose the greatest threat to the human. *Pf* is the most prevalent malaria parasite on the African continent. *Pv* is the dominant malaria parasite in most countries outside of sub-Saharan Africa. Increased malaria control efforts have resulted in a dramatic reduction in global malaria incidence over the past decade. The World Health Organization (WHO) thus endorsed the ambitious goal of achieving worldwide malaria elimination and eradication. A change in focus from malaria control to elimination requires the identification and treatment of both symptomatic and

Miguel R. Ossandon et al. (eds.), *Biomedical Engineering Technologies: Volume 1*, Methods in Molecular Biology, vol. 2393, https://doi.org/10.1007/978-1-0716-1803-5_16, 

asymptomatic carriers to reduce the parasite reservoir and interrupt malaria transmission. As a result, the effectiveness of elimination strategies highly depends on low-cost access to sensitive and specific malaria screening tests [1]. Current screening test methods rely almost exclusively on microscopy (thin and thick blood smears) and immunological rapid diagnostic tests (RDTs, detecting antigens in human blood). While they perform sufficiently well in high transmission regions for diagnosing people with symptomatic malaria, both methods could miss a significant portion of asymptomatic parasite carriers in low-transmission areas due to the detection limit of ~100 parasites/μl [2, 3]. During the course of malaria elimination, the proportion of low-density and asymptomatic infections increases, thus rapid and highly sensitive point-of-care field test is increasingly needed to identify all infected individuals for treatment.

Lower parasite density can be identified by nucleic acid tests (NATs), often by PCR, which has an excellent detection limit of <1 parasite/μl depending on the assay type [4–6]. However, PCR-based assays are poorly suited to perform in field settings as they require specialized equipment for sample preparation and skilled personnel [7]. Alternative NATs, such as loop-mediated isothermal amplification (LAMP) assays [8–17], recombinase polymerase amplification (RPA) assays [18, 19], as well as helicase dependent amplification (HAD) assays [20], have shown high analytical sensitivity and great potential for field deployment by integrating with microfluidic [21] and paper-based devices [22]. Among isothermal methods, LAMP is the most studied assay for malaria detection and holds great promise for commercialization. For instance, the illumigene malaria LAMP assays could reliably and sensitively detect *Plasmodium* by combining a manual blood sample preparation step with an incubator reader [23]. Despite great effort and progress toward field deployment of malaria NATs assays, highly integrated DNA sample preparation from raw peripheral blood for molecular assays remains a bottleneck [24, 25]. For example, current nucleic acid sample preparation is often limited at point-of-care settings due to lengthy or error-prone manual processes such as gravity-driven filtration [23] and centrifugation [26]. The ideal sample preparation should be simple, scalable, and easy-to-operate.

To bring the NATs to the field, the test assay with a streamlined sample process has been incorporated with various microfluidic-based lab-on-chip (LOC) technologies. The existing microfluidic LOC devices for NATs can be categorized based on the fluid driving mechanisms (e.g., pump-based [27], paper-based [27, 28], and centrifugal devices [29, 30]). While the pump-based approach is intuitive for precise fluid control, the benchtop syringe pump, multiple tubings, and complex valving make the system bulky and difficult to be integrated for POC application

[31]. The low-cost paper-based approach uses capillary action to move the liquid on a paper substrate; thus, reagents can be delivered sequentially without the pump and complex tubings. For example, Phillips et al. developed a microfluidic rapid and autonomous analytical device (MicroRAAD) for the RT-LAMP HIV-1 test. The device used paper membranes' wicking ability and porous structure for sequential sample process from viral particle isolation to amplification in automated fashion [28]. However, lacking adequate sensitivity and quantitative ability are challenges to be addressed [32]. Prior works on lab-on-a-disc platforms for NATs exclusively utilized centrifugal forces to drive liquid to the desired location in the microfluidic disc [29, 30]. While it works great for various diagnostic applications, the centrifugal forces are energy-hungry.

The demand for microfluidic chip fabrication technique has been increased due to the growing need for lab-on-a-chip devices in medicine and healthcare. Poly(methyl methacrylate) (PMMA) is a polymer, which is widely used for microfluidic chip fabrication due to its rigid mechanical property, optical transparency, low-cost, and rapid prototyping. Precise micromachining of PMMA is available using laser drilling or micromilling techniques. Among various lamination methodologies (e.g., thermal bonding and adhesive film), the solvent-based lamination technique showed excellent PMMA–PMMA bonding strength without requiring thermal pressing, which often causes deformation in microfluidic channel dimensions. Besides, the surface property of PMMA can be engineering by laser irradiation [33]. More specifically, PMMA becomes more hydrophilic when it is exposed to the high-power laser during the laser cutting process. Such property allows various liquid manipulation techniques such as structural-pinning effect-based passive valving. Enhanced wettability of the PMMA surface can be used to securely hold the stationary liquid droplet under mechanical shock.

In this chapter, we present a "sample-to-answer" microfluidic reagent compact disc for field detection of *Pf* and *Pv*. The device uses a noncentrifugal method for solid-phase DNA extraction by actuating the DNA-carrying magnetic beads against the stationary reagent droplets. All reagents for streamlined sample process are preloaded and separated on the microfluidic reagent disc by teeth-shaped passive valves. The preloaded and ready-to-use microfluidic reagent disc contains four parallel testing units. It could be configured either as four identical tests to increase the testing throughput or as four species-specific tests to distinguish *Plasmodium* genus, *Pf and Pv* species. Each test unit automatically performs the parasite DNA binding, washing, elution, and immediate real-time isothermal amplification and fluorescence detection described in Chapter 14. This seamless integration from the sample to result on a single microfluidic reagent compact disc simplifies the complex

NATs process. The assay is performed with an automated device described in Chap. 14. The device could deliver sensitive (~0.5 parasites/μl) NAT results directly from a small volume of raw blood samples within 40 min for a material cost around $1/test.

## 2 Materials

### 2.1 Microfluidic Reagent Disc

1. Materials and supplies: Table 1.
2. $CO_2$ laser cutting machine (Epilog Helix 24 Laser System, USA).
3. Ultrasonic cleaning bath (CPX-952-218R, USA).
4. Cleaning reagents: Detergent, 2% (w/v) Sodium hypochlorite (NaOCl), and $H_2O$.
5. 0.030“ clear plexiglass acrylic sheet (ACRYCLR0.030PM26.5X43, ePlastics), 0.060” clear plexiglass acrylic sheet (ACRYCLR0.060FM24X48, ePlastics), acrylic adhesive Weld-On 4(IPS4-4OZ, ePlastics), PCR Plate Sealing Adhesive Film (MSB1001, Bio-Rad), water-oil repellent (UNIDYNE™ TG-5601, Daikin, Japan).
6. ChargeSwitch® Forensic DNA Purification Kits (CS11200, Invitrogen).

### 2.2 Loop-Mediated Isothermal Amplification Assay

1. LAMP master mix (25 μl): isothermal buffer (20 mM Tris–HCl, 10 mM $(NH_4)_2SO_4$, 50 mM KCl, 2 mM $MgSO_4$, 0.1% Tween 20, pH 8.8), PCR grade $H_2O$, $MgSO_4$ (7 mM), Betaine (0.4 M) $MnCl_2$ (0.75 mM), calcein (25 μM), deoxyribonucleotide triphosphates (dNTPs, 1.4 mM), *Bst* 2.0 DNA polymerase, DNA template, and primer sets (0.2 mM F3 and B3c, 1.6 mM FIP and BIP, and 0.8 mM LF and LB) (*see* Table 2).
2. Primer sets for the genus-, *Pf*-, and *Pv*-specific LAMP amplification are listed in Table 3.

## 3 Methods

The microfluidics assay presented in this chapter is performed with an automated device described in Chap. 14.

### 3.1 Microfluidic Reagent Compact Disc Fabrication

1. The microfluidic reagent compact disc has a diameter of 9.6 cm and a thickness of 3.2 mm. The top, spacer, and bottom polymethyl methacrylate (PMMA), known as acrylic, layers are designed using AutoCAD and patterned by a $CO_2$ laser cutting machine (Laser power: 75 W).
2. Figure 1a shows the separate image of each laser-patterned layer before assembly. All reagent loading inlets are patterned

**Table 1**
**Microfluidic reagent disc cost. Bill of materials for the analyzer. (Reproduced from Biosensors and Bioelectronics 2018 with permission from Elsevier [50])**

| Reagents | Vendor | Function | Stock vol. (ml) | Unit cost ($) | Vol. (μl)/test | Ext. cost ($)/ test |
|---|---|---|---|---|---|---|
| Ultrapure PCR water | VWR | LAMP master mix | 20 | 91.88 | 7.25 | 0.033 |
| F3 | IDT | LAMP master mix | 1.4 | 9.22 | 0.25 | 0.002 |
| B3 | IDT | LAMP master mix | 1.5 | 10.22 | 0.25 | 0.002 |
| FIP | IDT | LAMP master mix | 1.0 | 7.14 | 2.00 | 0.013 |
| BIP | IDT | LAMP master mix | 1.4 | 9.18 | 2.00 | 0.013 |
| LF | IDT | LAMP master mix | 1.7 | 11.86 | 1.00 | 0.007 |
| LB | IDT | LAMP master mix | 1.3 | 8.61 | 1.00 | 0.007 |
| Calcein | Sigma-Aldrich | LAMP master mix | 8000 | 133.00 | 0.63 | 0.000 |
| $MnCl_2$ | Sigma-Aldrich | LAMP master mix | 100 | 62.60 | 1.88 | 0.001 |
| Betaine | Sigma-Aldrich | LAMP master mix | 1.5 | 24.25 | 2.00 | 0.032 |
| dNTP mix | Thermo fisher | LAMP master mix | 3.2 | 107.00 | 3.50 | 0.117 |
| *Bst* polymerase | NEB | LAMP master mix | 1 | 264.00 | 1.00 | 0.264 |
| NEB isothermal buffer | NEB | LAMP master mix | 6 | 24.00 | 2.5 | 0.010 |
| $MgSO_4$ | NEB | LAMP master mix | 6 | 20.00 | 1.75 | 0.006 |
| Lysis buffer | Invitrogen | Sample Prep. | 800 | 142.00 | 1000.00 | 0.178 |
| Binding buffer | Invitrogen | Sample Prep. | 20 | 28.97 | 30.00 | 0.043 |
| Wash buffer | Invitrogen | Sample Prep. | 100 | 144.84 | 150.00 | 0.217 |
| Proteinase K | Invitrogen | Sample Prep. | 1 | 1.45 | 10.00 | 0.014 |
| Magnetic beads | Invitrogen | Sample Prep. | 2 | 2.90 | 10.00 | 0.014 |
| Acrylic adhesive | ePlastics | Compact disc | 118 | 9.69 | 1.5 | 0.041 |
| 1/32″ acrylic sheet | ePlastics | Compact disc | – | 14.98 | – | 0.025 |
| 1/16″ acrylic sheet | ePlastics | Compact disc | – | 17.72 | – | 0.030 |
| | | | | | **Total costTotal cost** | **$ 1.07** |

**Table 2**
**Reagent setup of the LAMP master mix. (Reproduced from Lab on a Chip 2016 with permission from the Royal Society of Chemistry [50])**

| Component | Concentration | Volume (μl) |
|---|---|---|
| PCR grade water | 1× | 4.25 |
| Primer sets | – | 6.50 |
| Isothermal buffer | 1× | 2.50 |
| Betaine | 0.4 M | 2.00 |
| $MgSO_4$ | 7.00 mM | 1.75 |
| Calcein | 25.00 μM | 0.63 |
| $MnCl_2$ | 0.75 mM | 1.88 |
| dNTP mix | 1.40 mM | 3.50 |
| *Bst* DNA polymerase | 0.32 Unit/μl | 1.00 |

on 0.03″ thick top layer. 0.06″ thick spacer with 0.03″ thick bottom layer provides chambers to hold all reagents such as binding, washing, and LAMP master mix (Figs. 1 and 2).

3. The patterned top, spacer, and bottom PMMA layers are initially washed with detergent to remove residues from laser cutting.
4. All three layers are aligned using the alignment hole and permanently laminated with adhesive solvent. Before applying the adhesive, we stack patterned layers and align them using alignment holes (Fig. 1b). The liquid adhesive solvent is applied by a syringe from the side of the disc. The small gap between PMMA layers induces capillary action and aids the adhesive solvent in flowing naturally over the area. Pressing the PMMA layers disturbs the capillary action; thus, it is not recommended. Although adhesive showed a good amount of bonding strength after 5 min, we normally cure more than 1 h at room temperature for better bonding.
5. The assembled disc is cleaned with 2% sodium hypochlorite (NaOCl) and distilled water in order to eliminate inhibitory substances, which could cause chemical interference (*see* **Note 1**).
6. The assembled disc has four testing units, and each unit contains three working chambers (Fig. 2): binding (220 μl), washing (150 μl), and reaction chambers (25 μl).
7. Each reagent chamber is isolated by a valve chamber (80 μl) to prevent the reagent mixing. The valving chambers are filled with FC-40 oil or air (Figs. 1 and 3). The FC-40 oil, which seals the LAMP reaction chamber, helped prevent master mix

**Table 3**
**Primer sets for the genus-, *Pf*-, and *Pv*-specific LAMP amplification. (Reproduced from Biosensors and Bioelectronics 2018 with permission from Elsevier [50])**

| Species | Primer | Sequence (5′ → 3′) |
|---|---|---|
| *Plasmodium* genus | F3 | TCGCTTCTAACGGTGAACT |
| | B3c | AATTGATAGTATCAGCTATCCATAG |
| | FIP (F1c–F2) | GGTGGAACACATTGTTTCATTTGATCTCATTCCAATGGAACC TTG |
| | BIP (B1–B2c) | GTTTGCTTCTAACATTCCACTTGCCCGTTTTGACCGGTCATT |
| | LF | CACTATACCTTACCAATCTATTTGAACTTG |
| | LB | TGGACGTAACCTCCAGGC |
| *P. falciparum* | F3 | CTCCATGTCGTCTCATCGC |
| | B3c | AACATTTTTTAGTCCCATGCTAA |
| | FIP (F1c–F2) | ACCCAGTATATTGATATTGCGTGACAGCCTTGCAATAAATAA TATCTAGC |
| | BIP (B1–B2c) | AACTCCAGGCGTTAACCTGTAATGATCTTTACGTTAAGGGC |
| | LF | CGGTGTGTACAAGGCAACAA |
| | LB | GTTGAGATGGAAACAGCCGG |
| *P. vivax* | F3 | GGTACTGGATGGACTTTATAT |
| | B3c | GGTAATGTTAATAATAGCATTACAG |
| | FIP (F1c–F2) | CCAGATACTAAAAGACCAACCCACCATTAAGTACATCACT |
| | BIP (B1–B2c) | GCTAGTATTATGTCTTCTTTCACTTAATATACCAAGTG TTAAACC |
| | LF | GATAACATCTACTGCAACAGG |
| | LB | CTACTGTAATGCATCTAAGATC |

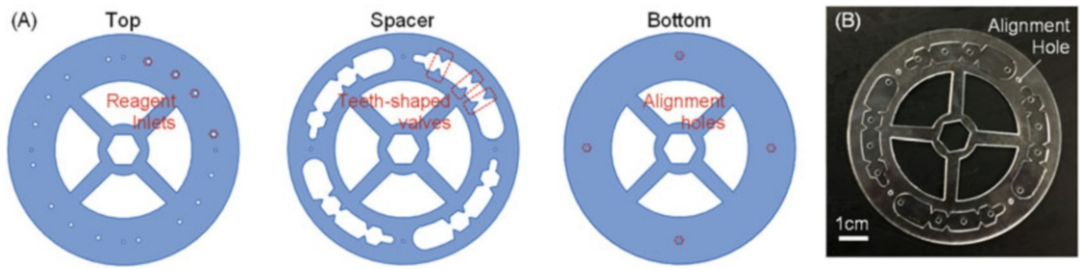


**Fig. 1** (**a**) Schematics of the laser-patterned PMMA layers for microfluidic reagent disc fabrication. The top layer has inlets for reagent loading. The spacer layer has reagent chambers and valves (*see* Fig. 2b for the functionality of each chamber). (**b**) Photo image of the assembled disc

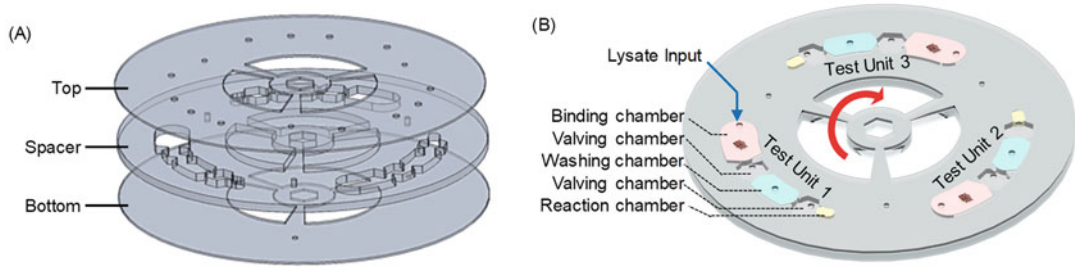


**Fig. 2** Illustration of reagent compact disc and integrated sample preparation on the compact disc. (**a**) Exploded view of the reagent compact disc showing three-patterned PMMA layers. (**b**) Assembled view of the reagent compact disc showing three independent testing units. Each test unit consists of five chambers: a DNA binding chamber (binding buffer pH 5.0), a washing chamber (washing buffer pH 7.0), a LAMP reaction chamber (master mix, pH 8.8), and two valving chambers. All reagents are preloaded on the compact disc in a ready-to-use format. The lysate was prepared by collecting 20 μl malaria-infected blood into 1 ml of lysis buffer in a microcentrifuge tube. (Reproduced from Lab on a Chip 2016 with permission from the Royal Society of Chemistry [50])

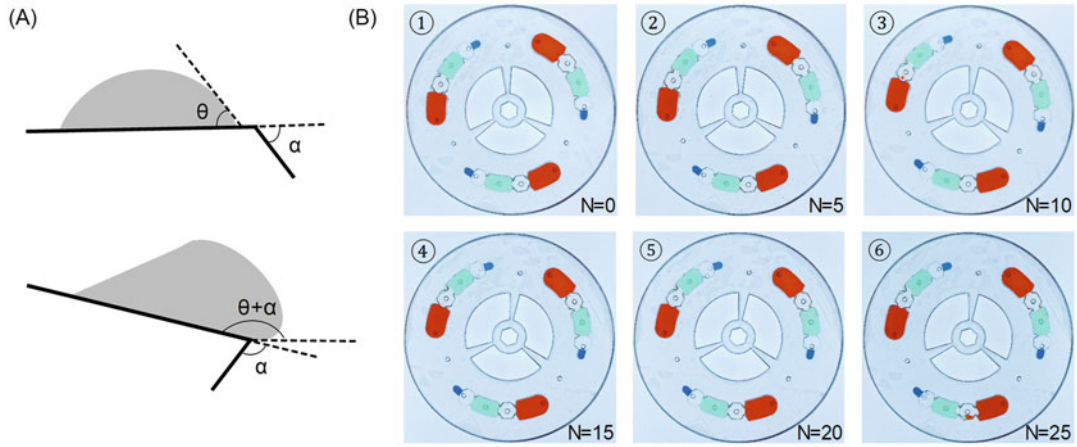


**Fig. 3** Illustration of the pinning effect and photo images of the drop test results. (**a**) A droplet on a solid surface with a contact angle of $\theta$, which will be increased up to $\theta + \alpha$ when moving toward a three-phase edge, where $\alpha$ is a bending angle [34]. This implies that larger α allows a higher activation barrier for the passive valve. (**b**) The drop test to evaluate the robustness of the teeth-shaped passive valves on the reagent compact disc under the harsh mechanical vibration (*N* denotes the number of drops). (Reproduced from Lab on a Chip 2016 with permission from the Royal Society of Chemistry [50])

evaporation during the thermal process. The air-filled valve is surface treated with water-oil repellent to create a barrier for the amphiphilic lysis buffer (*see* **Note 2** for surface treatment technique). Unlike other lab-on-a-chip devices, there is no liquid movement in the reagent compact disc. Instead, magnetic beads are moved from chamber to chamber by magnetic interaction and disc rotation. Therefore, active valving is not

necessary for the system. (The detailed description for the tooth-shaped active valve is available in Subheading 3.2).

8. All liquid phase reagents (beads, washing buffer, and LAMP master mix) and FC-40 oil are loaded into the designated chamber in the disc immediately before use (Fig. 2 and **Note 3**). The loading order is the master mix (25 μl, reaction chamber), FC-40 oil (80 μl, valving chamber), washing buffer (150 μl, washing chamber), binding buffer (30 μl, binding chamber), and magnetic beads (10 μl, binding chamber) (Fig. 2b). The reagents could also be preloaded into the disc and would last for at least 1 week if stored at 4 °C.
9. After the sample loading, the whole disc is sealed with pressure-sensitive adhesive (PSA) to avoid potential cross-contamination from the environment.

### 3.2 Robustness Under Mechanical Shock

1. Structural pinning effect [34, 35] and modified surface tension are the underlying principles that enable the teeth-shaped valves to hold the liquid in each chamber securely. The pinning effect refers to the fact that a sharp bending angle ($\alpha$) of the teeth structure radically increases the liquid/vapor interface area and raises the activation energy, which prevents fluid from overcoming the barrier (Fig. 1—spacer layer and Fig. 3) [34]. The enhanced surface tension is another important aspect of our passive valve structure. The valve surface is treated with water-oil repellent to increase the activation barrier by introducing a higher surface tension [34], which also helps circumvent cross-contamination during sample preparation.
2. To demonstrate the robustness of the passive valve for preventing the reagents from mixing under the harsh mechanical vibration, we perform a drop test on the microfluidic compact disc. Three different colors of food dyes are preloaded into each reagent chamber for visualization of any liquid movement. Each reagent-loading hole is sealed with pressure-sensitive adhesive (PSA) to prevent leakage. The disc is dropped from a height of 20 cm along a guiding rod toward a rigid surface for 25 times. The disc is inspected every five drops with naked eyes to confirm the functionality of the valve. The result showed that the teeth-shaped valve endured 25 consecutive drops without reagents mixing (Fig. 3).

### 3.3 The Workflow of Malaria Blood Testing

The reagent compact disc is equipped with a real-time fluorescence detector (discussed in Chapter 1) to perform a streamlined process. The workflow of the device consists of four steps (Fig. 4).

1. The 20 μl of finger-prick blood is collected using a capillary tube and lysed in the collection tube filled with 1000 μl of lysis buffer.

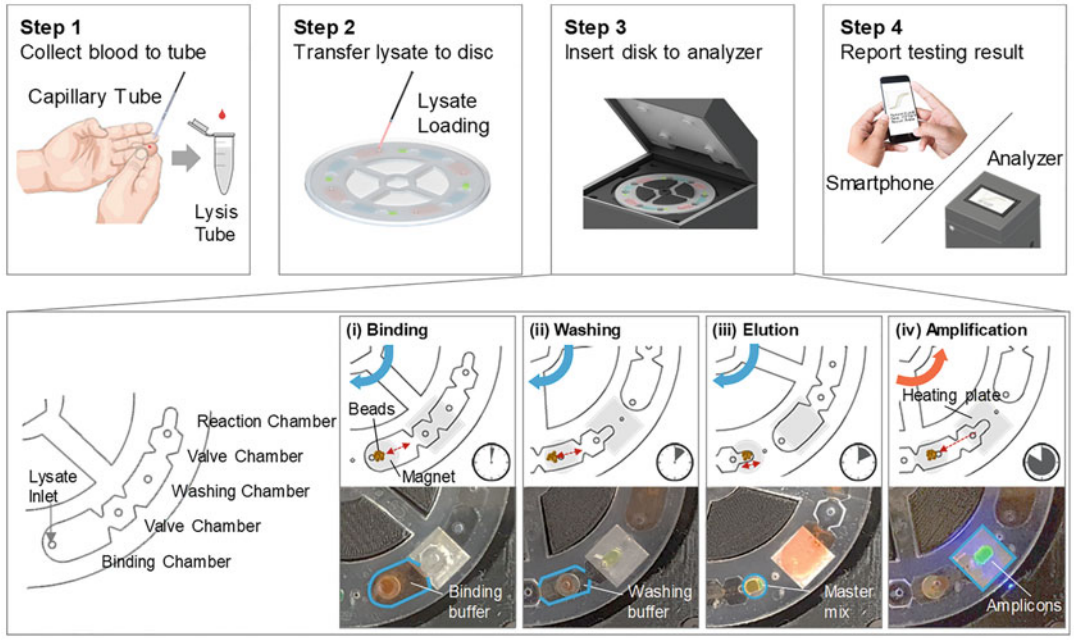


**Fig. 4** The workflow of the device. In step 1, whole blood is collected into the lysis buffer by the capillary tube. In step 2, the lysate is loaded into the binding chamber of the four testing units. In step 3, the disc is sealed and inserted into the analyzer, which then performs automated sample preparation and amplification. This automated process consists of four steps: binding (3 min), washing (4 min), elution (3 min), and amplification (40 min). During the amplification process, the real-time fluorescence signal from each testing unit was recorded and analyzed. Finally, in step 4, the testing results are reported. (Reproduced from Biosensors and Bioelectronics 2018 with permission from Elsevier [51])

2. 180 μl of blood lysate is transferred into each binding chamber of the testing units on the reagent compact disc.
3. After loading the sample, the disc is sealed with PSA tape and inserted into the mobile analyzer for a streamlined nucleic acid sample preparation and amplification process (enlarged view of **step 3** in Fig. 4).
4. During the amplification, the fluorescence intensity data are recorded on a nonvolatile memory card and displayed on the LCD screen in real time. Users also have an option to receive the results using a smartphone.

### *3.4 Streamlined Sample Preparation*

In contrast to the conventional lab-on-a-disc devices that rely on energy-hungry centrifugal forces [36–39], a noncentrifugal and energy-efficient magnetic interaction method is used. More specifically, the pH charge switchable magnetic beads are directed from chamber to chamber by rotating the disc against a stationary magnet underneath of the disc. The process for each sample consists of the following three steps: binding, washing, and elution (**step 3** of Fig. 4).

1. The negatively charged parasite DNAs first bind to the pH-sensitive charge-switchable magnetic beads at pH 5.0. During the binding process (~3 min), the reagent compact disc is rotated back and forth slowly to ensure thorough mixing of the beads and the lysate. More specifically, the initial disc position is where the binding chamber inlet is aligned with the permanent magnet underneath the disc (*see* **step 3** of Fig. 4). The disc rotates by the servo control until the magnet locates underneath the entrance of the air-filled valve chamber. Due to the magnetic interaction, the magnetic beads are actuated toward the valve entrance, where the magnet is positioned. Then, we rotate back the disc to the initial position and repeat the process to capture the maximum number of DNA-binding magnetic beads. Once this process is completed, the DNA-binding magnetic beads are transferred to the washing chamber by magnetic actuation.
2. The DNA washing process lasts for about 4 min, and the magnetic beads with purified DNAs are further transferred to the reaction chamber (LAMP master mix).
3. The LAMP master mix has a pH of 8.8, which switches the surface charge of the magnetic beads toward negative. The negatively charged DNAs are therefore repelled off from the magnetic beads and eluted into the master mix.
4. The residual magnetic beads are removed from the reaction chamber before initiating the LAMP reaction. The entire sample preparation is multiplexed for four samples and could be finished in less than 10 min with minimal user intervention.

### 3.5 Primer Validation

1. To validate the LAMP primer sets for specifically detecting *Pf*, *Pv*, and pan-Plasmodium, we perform a cross-reactivity test using extracted *Pf* and *Pv* genomic DNA on a benchtop real-time PCR instrument (Bio-Rad CFX96). Each analysis is performed in triplicate.
2. As shown in Fig. 5a, *Pf*- and *Pv*- specific assays can pick up the corresponding genomic sample specifically without cross-reactivity. In contrast, the pan-Plasmodium assays can pick up any *Plasmodium* species (*Pf* and *Pv*). No amplification is observed with the negative control (PCR grade water).
3. We perform gel electrophoresis in 2% agarose gel to further evaluate each amplicon (Fig. 5b). A clear ladder-like pattern with multiple bands of different molecular sizes is observed due to the stem-loop DNA structures with several inverted repeats within LAMP amplicons [40]. The length of the bands show confirmative agreement with the length of the target sequence (213-, 127-, and 220-bp bands are expected from *Pf*, *Pv*, and pan-Plasmodium products, respectively) [41, 42].

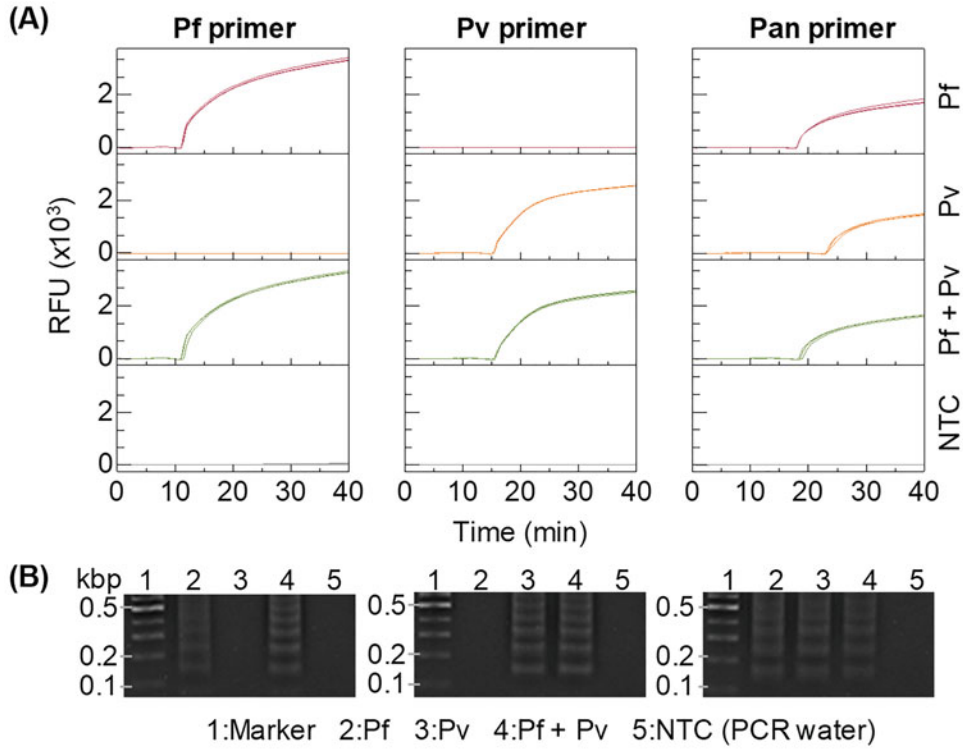


**Fig. 5** Validation of the species- and genus-specific LAMP assays using laboratory purified *Pf* and *Pv* genomic DNA. (**a**) Amplification curves obtained from real-time PCR. PCR grade water was used as a no template control (NTC). (**b**) Gel electrophoresis image (2% agarose gel). Ladder-like bands in the gel image confirm the amplicons from species- and genus-specific LAMP reactions. (Reproduced from Biosensors and Bioelectronics 2018 with permission from Elsevier [51])

### *3.6 Sensitivity Test*

1. To evaluate the analytical sensitivity of our device in the real-world settings, we ten-fold diluted the *Pf*-infected whole blood with healthy blood to create mock samples with 10-6% to 1% parasitemia. The parasite DNA samples are automatically prepared on the compact disc. Each parasitemia sample is performed in triplicate, together with negative control on a single disc (four reactions per run).
2. As shown in Fig. 6a, a whole blood sample with parasitemia higher than $10^{-5}$% could be identified. Since parasitemia is the ratio of the parasitized RBCs to the total RBCs, $10^{-5}$% parasitemia would correspond to 0.5 parasites/μl (normal RBC count is ~$5 \times 10^6$ cells/μl [3]). Although a rigorous report of the limit of detection (i.e., analytical sensitivity) requires a statistical comparison with the analytical blank and should be expressed as a probability with confidence intervals [43], a quick eyeball of the data shown in Fig. 6a suggests the whole blood sensitivity is around 0.5 parasites/μl. The WHO estimates that analytical sensitivity needs to be lower than

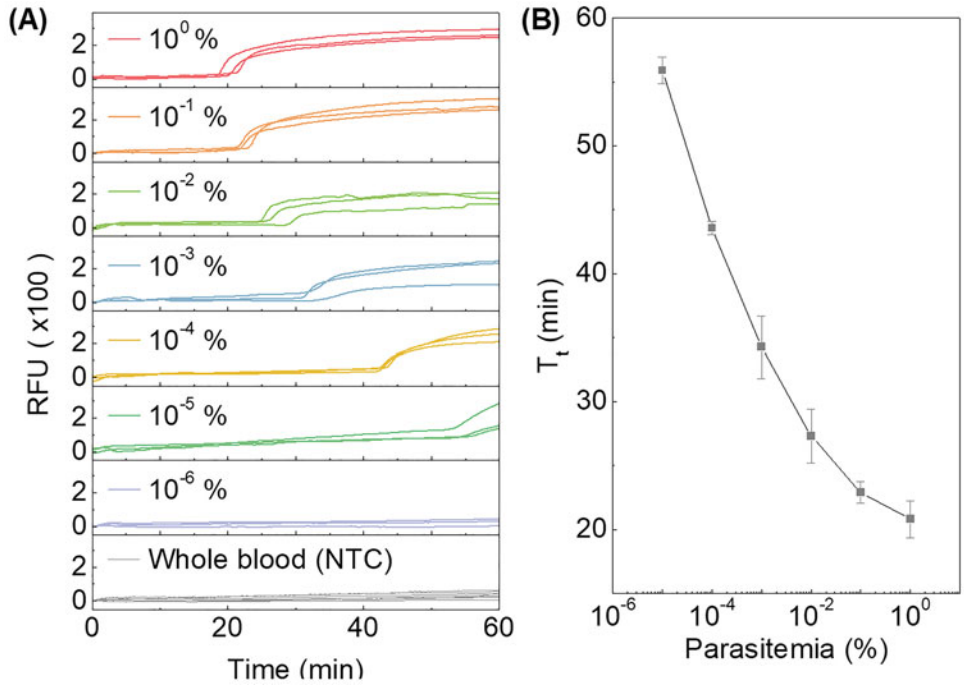


**Fig. 6** Sensitivity test with *Pf*-infected whole blood sample (**a**) Amplification curves for tenfold serially diluted *Pf*-infected whole blood samples. Healthy human blood was used as an NTC. (**b**) The resulting calibration curve for the whole blood sample. Standard deviation values are from triplicates. (Reproduced from Biosensors and Bioelectronics 2018 with permission from Elsevier [51])

2 parasites/μl for identifying low-level infection in a preelimination setting [44]. This sensitivity achieved in our device is comparable to other NAT methods (1–5 parasites/μl) [25] and suitable for detecting low-level asymptomatic carriers [2, 45–47]. No amplification is observed for the healthy whole blood sample, which suggests the background human genomic DNA has negligible interferences.

3. The amplification threshold time ($T_t$) is extracted for each parasitemia, and the results are shown in Fig. 6b. The inversely proportional relationship between $T_t$ and parasitemia confirmed that the quantitative ability is still valid with whole blood samples. It is interesting to note that the calibration curve shown in Fig. 6b is not exactly linear, which is likely because the DNA extraction efficiency is nonlinear for different cell numbers [48].

### 3.7 Specificity Test

1. To evaluate the specificity of the device, we prepare whole blood samples spiked randomly with *Pf* and *Pv*. Those sample's species information is recorded but blinded to the tester. The reagent compact disc is configured as species-specific tests, as shown in Fig. 7a. Each test disc incorporates an internal

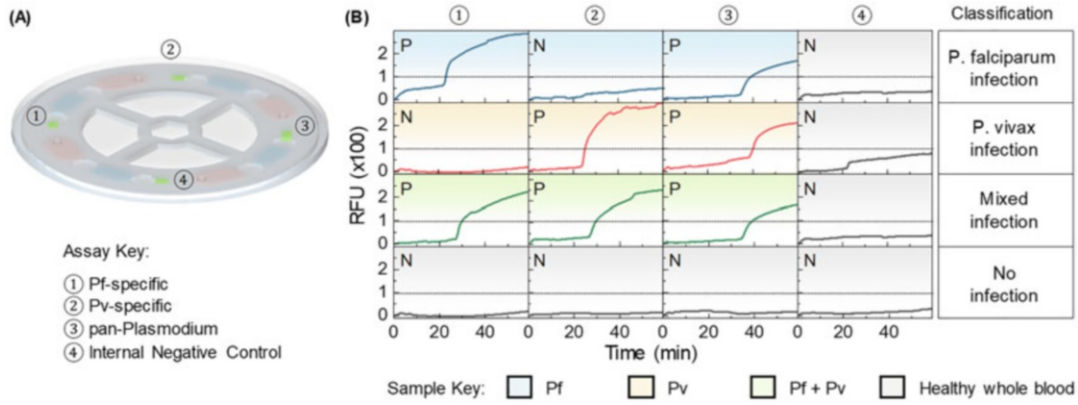


**Fig. 7** Species- and genus-specific tests using spiked whole blood samples. (**a**) The reagent compact disc was configured as species-specific tests. The testing unit 1 and 2 contains *Pf*- and *Pv*- specific primer sets, respectively. The testing unit 3 has a genus-specific primer set. Testing unit 4 is for internal negative control. (**b**) The result from a representative set of samples (i.e., *Pf*, *Pv*, mixed, and healthy). A threshold of 100 RFU (dashed line) is experimentally determined for positive and negative differentiation. The species information for a particular infected whole blood sample can be derived from four qualitative results on the single microfluidic disc (each row). (Reproduced from Biosensors and Bioelectronics 2018 with permission from Elsevier [51])

negative control unit to monitor the test quality. A threshold of 100 RFU is experimentally determined to differentiate positive and negative results.

2. Figure 7b shows the result from a representative set of samples (i.e., *Pf*, *Pv*, mixed, and healthy). The species information for a particular infected whole blood sample can be derived from four qualitative results on the single microfluidic disc. For example, the *Pf*-infected sample (first row of Fig. 7b) can be identified by the *Pf*-specific assay as well as the genus-specific assay. In contrast, the mixed infection sample can be detected when *Pf*-, *Pv*-, and genus-specific assays all show positive. Since *Pf* and *Pv* are the two most prevalent species that pose the greatest threat to the human, identification of these major malaria parasite species in the field could provide the malaria transmission profile to the healthcare workers and enable the effective malaria eradication strategy [25].

### 3.8 Test Cost Analysis

1. The disposable reagent compact disc (including the sample preparation and the amplification reagents) costs ~$1.07 per each test (Table 1). Note that this cost analysis is only to provide a ballpark figure to the interested researchers to replicate the system.

## 4 Notes

1. Detergent and distilled water are not sufficient to eliminate the amplification inhibitors in microfluidic reagent compact disc, often cause false-negative results. Sodium hypochlorite (NaOCl) is a strong oxidizing agent, an effective decontaminating reagent for various contaminants such as organic/inorganic chemicals, proteins, enzymes, and nucleic acids [49]. To remove the potential contaminants, all functional chambers are filled with a 2% NaOCl solution for 30 min, then thoroughly washed with distilled water. The washed chambers are blow-dried with compressed air.
2. To treat the PMMA surface, the valving chamber is first filled with liquid phase water–oil repellent for 2 min, then removed using a pipette. The repellent wetted PMMA surface is dried at 150 °C for 2 min. The treated surface has a lower interaction with liquids than the internal interaction within the liquid, thus repels the water-based amphiphilic lysis buffer.
3. While loading the liquid phase reagent, air bubbles can be easily trapped in the chamber. Air bubbles possibly disrupt the magnetic bead movements in the reagent chamber. If air bubbles are trapped in the reaction chamber, they interfere with the optical signal since the bubbles move during the thermal process. Slightly lifting the binding chamber side of the testing unit during the loading process is helpful in avoiding trapping of air bubbles.

## Acknowledgments

This work was supported by grants National Science Foundation under Grant No. 1710831, 1912410, and 1902503. We express our gratitude to Dr. Liwang Cui, Dr. Jun Miao, and Xiaolian Li for providing malaria samples. The following reagent is obtained through BEI Resources Repository, NIAID, NIH: *Plasmodium vivax*, Strain Chesson, MRA-383, and strain Achiote, MRA-369, contributed by W. E. Collins. W.G. acknowledges the support from Penn State Startup Fund.

### References

1. Slater HC, Ross A, Ouedraogo AL et al (2015) Assessing the impact of next-generation rapid diagnostic tests on *Plasmodium falciparum* malaria elimination strategies. Nature 528 (7580):S94–S101
2. Wongsrichanalai C, Barcus MJ, Muth S et al (2007) A review of malaria diagnostic tools: microscopy and rapid diagnostic test (RDT). Am J Trop Med Hyg 77(6):119–127

3. Moody A (2002) Rapid diagnostic tests for malaria parasites. Clin Microbiol Rev 15 (1):66–78
4. Snounou G, Viriyakosol S, Zhu XP et al (1993) High-sensitivity of detection of human malaria parasites by the use of nested polymerase chain-reaction. Mol Biochem Parasit 61(2):315–320
5. Han ET, Watanabe R, Sattabongkot J et al (2007) Detection of four plasmodium species by genus- and species-specific loop-mediated isothermal amplification for clinical diagnosis. J Clin Microbiol 45(8):2521–2528
6. Reddy V, Ravi V, Desai A et al (2012) Utility of IgM ELISA, TaqMan real-time PCR, reverse transcription PCR, and RT-LAMP assay for the diagnosis of chikungunya fever. J Med Virol 84 (11):1771–1778
7. Britton S, Cheng Q, McCarthy JS (2016) Novel molecular diagnostic tools for malaria elimination: a review of options from the point of view of high-throughput and applicability in resource limited settings. Malar J 15 (1):88
8. Oriero EC, van Geertruyden JP, Nwakanma DC et al (2015) Novel techniques and future directions in molecular diagnosis of malaria in resource-limited settings. Expert Rev Mol Diagn 15(11):1419–1426
9. Goyal K, Kaur H, Sehgal A et al (2015) RealAmp loop-mediated isothermal amplification as a point-of-care test for diagnosis of malaria: neither too close nor too far. J Infect Dis 211 (10):1686
10. Morris U, Khamis M, Aydin-Schmidt B et al (2015) Field deployment of loop-mediated isothermal amplification for centralized mass-screening of asymptomatic malaria in Zanzibar: a pre-elimination setting. Malar J 14:205
11. Hsiang MS, Greenhouse B, Rosenthal PJ (2014) Point of care testing for malaria using LAMP, loop mediated isothermal amplification. J Infect Dis 210(8):1167–1169
12. Patel JC, Lucchi NW, Srivastava P et al (2014) Field evaluation of a real-time fluorescence loop-mediated isothermal amplification assay, RealAmp, for the diagnosis of malaria in Thailand and India. J Infect Dis 210 (8):1180–1187
13. Han ET (2013) Loop-mediated isothermal amplification test for the molecular diagnosis of malaria. Expert Rev Mol Diagn 13 (2):205–218
14. Singh R, Savargaonkar D, Bhatt R et al (2013) Rapid detection of Plasmodium vivax in saliva and blood using loop mediated isothermal amplification (LAMP) assay. J Infect 67 (3):245–247
15. Surabattula R, Vejandla MP, Mallepaddi PC et al (2013) Simple, rapid, inexpensive platform for the diagnosis of malaria by loop mediated isothermal amplification (LAMP). Exp Parasitol 134(3):333–340
16. Sirichaisinthop J, Buates S, Watanabe R et al (2011) Evaluation of loop-mediated isothermal amplification (LAMP) for malaria diagnosis in a field setting. Am J Trop Med Hyg 85 (4):594–596
17. Sattabongkot J, Tsuboi T, Han ET et al (2014) Loop-mediated isothermal amplification assay for rapid diagnosis of malaria infections in an area of endemicity in Thailand. J Clin Microbiol 52(5):1471–1477
18. Kersting S, Rausch V, Bier FF et al (2014) Rapid detection of Plasmodium falciparum with isothermal recombinase polymerase amplification and lateral flow analysis. Malar J 13:99
19. Cordray MS, Richards-Kortum RR (2015) A paper and plastic device for the combined isothermal amplification and lateral flow detection of plasmodium DNA. Malar J 14:472
20. Li Y, Kumar N, Gopalakrishnan A et al (2013) Detection and species identification of malaria parasites by isothermal, tHDA amplification directly from human blood without sample preparation. J Mol Diagn 15(5):634–641
21. Liu Q, Nam J, Kim S et al (2016) Two-stage sample-to-answer system based on nucleic acid amplification approach for detection of malaria parasites. Biosens Bioelectron 82:1–8
22. Xu G, Nolder D, Reboud J et al (2016) Paper-origami-based multiplexed malaria diagnostics from whole blood. Angew Chem 55 (49):15250–15253
23. Lucchi NW, Gaye M, Diallo MA et al (2016) Evaluation of the Illumigene malaria LAMP: a robust molecular diagnostic tool for malaria parasites. Sci Rep 6:36808. https://doi.org/10.1038/srep36808
24. Dineva MA, MahiLum-Tapay L, Lee H (2007) Sample preparation: a challenge in the development of point-of-care nucleic acid-based assays for resource-limited settings. Analyst 132 (12):1193–1199
25. Kolluri N, Klapperich CM, Cabodi M (2018) Towards lab-on-a-chip diagnostics for malaria elimination. Lab Chip 18:75–94
26. Sema M, Alemu A, Bayih AG et al (2015) Evaluation of non-instrumented nucleic acid amplification by loop-mediated isothermal amplification (NINA-LAMP) for the diagnosis of malaria in Northwest Ethiopia. Malar J 14:44. https://doi.org/10.1186/s12936-12015-10559-12939

27. Reboud J, Xu G, Garrett A et al (2019) Paper-based microfluidics for DNA diagnostics of malaria in low resource underserved rural communities. Proc Natl Acad Sci U S A 116 (11):4834–4842
28. Phillips EA, Moehling TJ, Ejendal KFK et al (2019) Microfluidic rapid and autonomous analytical device (microRAAD) to detect HIV from whole blood samples. Lab Chip 19 (20):3375–3386
29. Stumpf F, Schwemmer F, Hutzenlaub T et al (2016) LabDisk with complete reagent prestorage for sample-to-answer nucleic acid based detection of respiratory pathogens verified with influenza a H3N2 virus. Lab Chip 16 (1):199–207
30. Gorkin R, Park J, Siegrist J et al (2010) Centrifugal microfluidics for biomedical applications. Lab Chip 10(14):1758–1773
31. Sun Y, Quyen TL, Hung TQ et al (2015) A lab-on-a-chip system with integrated sample preparation and loop-mediated isothermal amplification for rapid and quantitative detection of salmonella spp. in food samples. Lab Chip 15(8):1898–1904
32. Chiu DT, deMello AJ, Di Carlo D et al (2017) Small but perfectly formed? Successes, challenges, and opportunities for microfluidics in the chemical and biological sciences. Chem 2 (2):201–223
33. Wang Z, Zheng H, Lim C et al (2009) Polymer hydrophilicity and hydrophobicity induced by femtosecond laser direct irradiation. Appl Phys Lett 95(11):111110
34. Gao LC, McCarthy TJ (2006) Contact angle hysteresis explained. Langmuir 22 (14):6234–6237
35. Oner D, McCarthy TJ (2000) Ultrahydrophobic surfaces. Effects of topography length scales on wettability. Langmuir 16(20):7777–7782
36. Madou M, Zoval J, Jia GY et al (2006) Lab on a CD. Annu Rev Biomed Eng 8:601–628
37. Kim TH, Park J, Kim CJ et al (2014) Fully integrated lab-on-a-disc for nucleic acid analysis of food-borne pathogens. Anal Chem 86 (8):3841–3848
38. Nolte DD (2009) Invited review article: review of centrifugal microfluidic and bio-optical disks. Rev Sci Instrum 80(10):101101
39. Kong LX, Perebikovsky A, Moebius J et al (2016) Lab-on-a-CD: a fully integrated molecular diagnostic system. J Lab Autom 21 (3):323–355
40. Notomi T, Okayama H, Masubuchi H et al (2000) Loop-mediated isothermal amplification of DNA. Nucleic Acids Res 28(12):E63
41. Polley SD, Mori Y, Watson J et al (2010) Mitochondrial DNA targets increase sensitivity of malaria detection using loop-mediated isothermal amplification. J Clin Microbiol 48 (8):2866–2871
42. Britton S, Cheng Q, Grigg MJ et al (2016) Sensitive detection of Plasmodium vivax using a high-throughput, Colourimetric loop mediated isothermal amplification (HtLAMP) platform: a potential novel tool for malaria elimination. PLoS Negl Trop Dis 10(2): e0004443
43. Long GL, Winefordner JD (1983) Limit of detection. A closer look at the IUPAC definition. Anal Chem 55(7):712A–724A
44. WHO (2017) World Malaria Report 2017. 1-196
45. Vallejo AF, Martinez NL, Gonzalez IJ et al (2015) Evaluation of the loop mediated isothermal DNA amplification (LAMP) kit for malaria diagnosis in P. vivax endemic settings of Colombia. PLoS Negl Trop Dis 9(1):e3453
46. Modak SS, Barber CA, Geva E et al (2016) Rapid point-of-care isothermal amplification assay for the detection of malaria without nucleic acid purification. Infect Dis 9:1–9
47. Hopkins H, Gonzalez IJ, Polley SD et al (2013) Highly sensitive detection of malaria parasitemia in a malaria-endemic setting: performance of a new loop-mediated isothermal amplification kit in a remote clinic in Uganda. J Infect Dis 208(4):645–652
48. Katevatis C, Fan A, Klapperich CM (2017) Low concentration DNA extraction and recovery using a silica solid phase. PLoS One 12(5): e0176848
49. Wilson IG (1997) Inhibition and facilitation of nucleic acid amplification. Appl Environ Microb 63(10):3741–3751
50. Choi G, Song D, Shrestha S et al (2016) A field-deployable mobile molecular diagnostic system for malaria at the point of need. Lab Chip 16(22):4341–4349
51. Choi G, Prince T, Miao J et al (2018) Sample-to-answer palm-sized nucleic acid testing device towards low-cost malaria mass screening. Biosens Bioelectron 115:83–90

# Chapter 17

# Charge Sensitive Optical Detection for Measurement of Small-Molecule Binding Kinetics

**Shaopeng Wang, Guangzhong Ma, Runli Liang, and Nongjian Tao**

## Abstract

Charge sensitive optical detection (CSOD) technique is a label-free method for real-time measurement of molecular interactions. Traditional label-free optical detection techniques mostly measure the mass of a molecule, and they are less sensitive to small molecules. In contrast, CSOD detects the charge of a molecule, where the signal does not diminish with the size of the molecule, thus capable for studying small molecules. In addition, CSOD is compatible with the standard microplate platform, making it suitable for high-throughput screening of drug candidates. In CSOD, an optical fiber functionalized with the probe molecule is dipped into a well of a microplate where an alternate perpendicular electrical field is applied to the fiber, which drives the fiber into oscillation because of the presence of surface charge on the fiber. The binding of the target molecules changes the charge of the fiber, and thus the amplitude and phase of the oscillating fiber, which are precisely measured through tracking of the optical images of the fiber tip.

**Key words** Charge sensitive optical detection, CSOD, Small molecule, Optical fiber, Binding kinetics, Optical imaging, Label free detection

## 1 Introduction

Charge sensitive optical detection (CSOD) is a recently developed label-free technique for measuring molecular interactions. The technique has been demonstrated for quantifying the kinetics of proteins, peptides and small molecule ligands binding to protein receptors [1], including membrane proteins stabilized in nanodiscs [2]. Most molecules relevant to biomedical research and applications are charged or have charged chemical groups. Even for neutral molecules, the charge distribution on a sensor surface is likely be altered upon binding. CSOD converts the charge changes induced by molecular bindings into an optical signal that does not decrease with the size (mass) of the molecule, making it particularly attractive for studying small molecules, and biochemical interactions that

Nongjian Tao was deceased at the time of publication.

Miguel R. Ossandon et al. (eds.), *Biomedical Engineering Technologies: Volume 1*, Methods in Molecular Biology, vol. 2393, https://doi.org/10.1007/978-1-0716-1803-5_17, 

involve small mass changes, which are often beyond the detection limit of traditional mass sensitive label-free detection methods. In addition, CSOD uses standard microplate for sample handling, which is suitable for high-throughput screening and analysis.

### 1.1 Principle of CSOD

An optical fiber is dipped in a well of a standard microplate with buffer solution, and an alternating electric field is applied in the direction perpendicular to the fiber using a pair of parallel electrodes in the well (Fig. 1a). Charge is typically present on the fiber surface so that the fiber is driven into oscillation by the applied field. The oscillation amplitude is detected by tracking the tip position of the fiber using a differential optical detection method. To study molecular interactions, the fiber tip is functionalized with molecular receptors, and the ligand molecules are introduced into the solutions in the well (or relocate the fiber to a well containing the ligand molecule solution). Upon binding of the ligand molecules onto the molecular receptors, the surface charge of the fiber

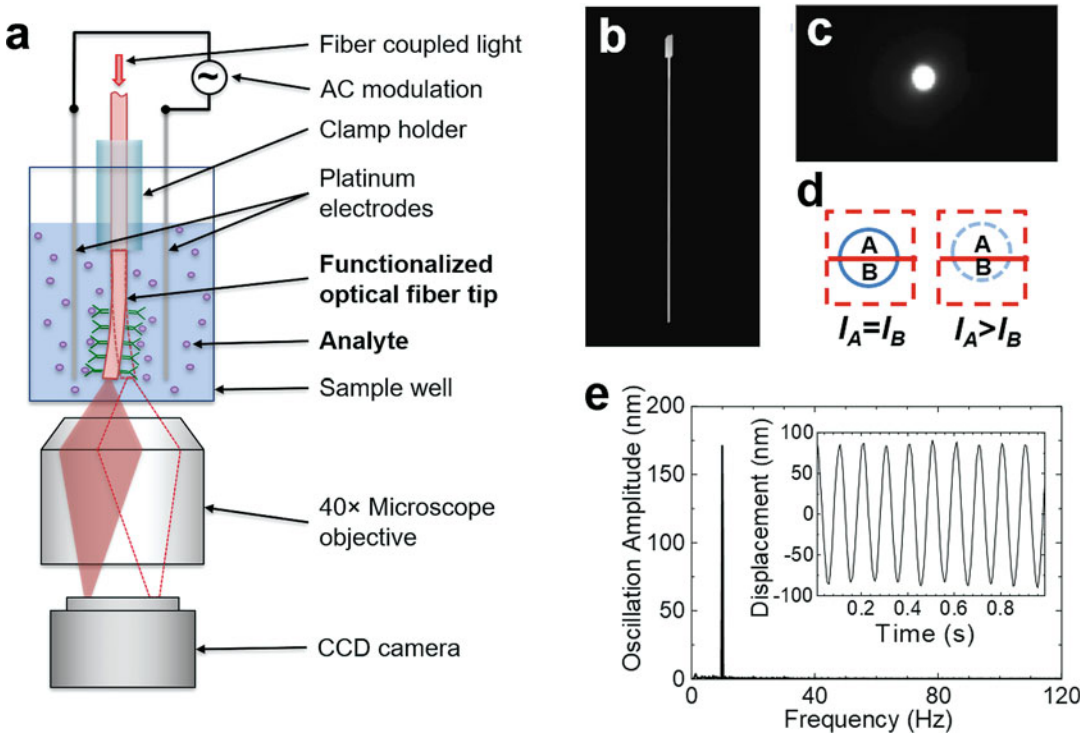


**Fig. 1** Principle of the CSOD technique. (**a**) Schematic illustration of the CSOD setup. (**b**) A typical optical fiber with etched tip viewed from side. (**c**) Image of the fiber tip viewed from the bottom of the microplate well. (**d**) Differential optical detection for accurate determination of the fiber oscillation amplitude. (**e**) Fast Fourier transform (FFT) of the fiber oscillation. Inset: Oscillation displacement signal in time domain before FFT. The amplitude and frequency of the applied voltage are 2 V and 10 Hz, respectively. The length and diameter of the fiber are 8.5 mm, and 11μm, respectively. The buffer is 40 times diluted 1× PBS. (Adapted with permission from [1])

changes, which is quantified precisely by monitoring the oscillation amplitude.

The key measurable signal of CSOD is the oscillation amplitude of the fiber tip, $x_s$, which is proportional to the effective fiber surface charge density, $\sigma$, given by

$$x_s = \frac{2\pi\left|\overrightarrow{E(\omega)}\right|\sigma r l}{\sqrt{\left(k_{\text{eff}} - m_{\text{eff}}\omega^2\right)^2 + (c\omega)^2}} \quad (1)$$

where $\omega$ is the oscillation angular frequency; $|\overrightarrow{E(\omega)}|$ is the electric field; $k_{\text{eff}}$, $m_{\text{eff}}$, $r$, and $l$ are the effective spring constant, mass, radius, and length of the optical fiber (Fig. 1b), respectively; and $c$ is the damping coefficient. $\overrightarrow{E(\omega)}$ is generated by applying a voltage between two electrodes inserted in the solution of the well, which is frequency dependent (*see* **Note 1**). $k_{\text{eff}}$ and $m_{\text{eff}}$ can be calculated from the diameter and length of the fiber, and $c$ can be obtained from the frequency dependent amplitude. From the measured oscillation amplitude, $x_s$, the surface charge density of the fiber is determined according to Eq. (1), which allows for monitoring the binding of molecules onto the fiber surface.

### 1.2 Differential Detection of Fiber Oscillation Amplitude

Accurate measurement of the fiber oscillation amplitude is realized by a differential optical detection method, which tracks the position of the optical fiber tip via optical imaging. The fiber tip is imaged as a bright spot (Fig. 1c) from the bottom of the well. The differential optical detection method determines the oscillation amplitude by dividing the bright spot into two regions with similar total intensity, $A$ and $B$, perpendicular to the oscillation direction (Fig. 1d). $(I_A - I_B)/(I_A + I_B)$ is monitored continuously, where $I_A$ and $I_B$ are the intensities of regions $A$ and $B$, respectively. $(I_A - I_B)/(I_A + I_B)$ is proportional to the oscillation amplitude of the fiber with a calibration factor determined with the following steps (Fig. 2). $A$ and $B$ regions are selected (marked by blue and red boxes, respectively), and then shifted vertically by different numbers of pixels to mimic the fiber movement (Fig. 2a). One pixel is determined to be 0.74 μm from the optical system and physical size of CCD camera. The differential intensity vs. pixel shift is determined from the image to produce a calibration curve (Fig. 2b).

The differential detection method rejects common noises in $A$ and $B$, allowing sensitive tracking of the fiber oscillation. The inset of Fig. 1e shows the oscillation of a fiber driven by a sinusoidal potential with frequency 10 Hz and amplitude 2 V. In addition, fast fourier transform (FFT) filter is used to further remove noises at frequencies different from the applied electric field. The FFT of the time domain data shows a sharp peak (Fig. 1e). From the peak height in the FFT spectrum, we determine the oscillation amplitude of the fiber. Using the combined differential detection method and

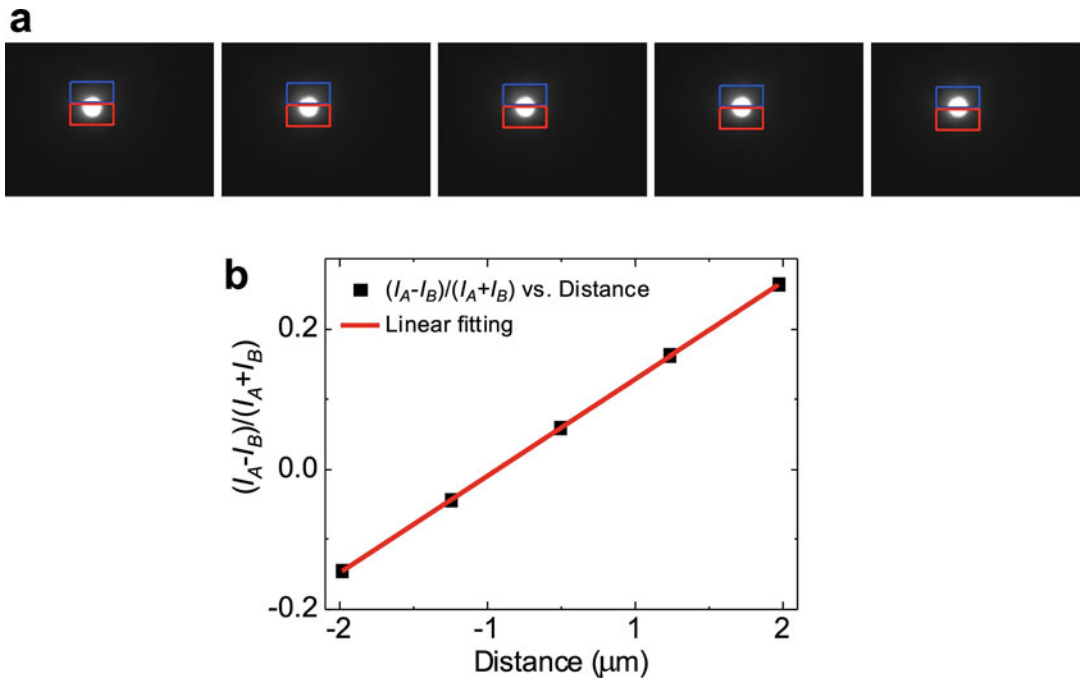


**Fig. 2** Calibration of oscillation amplitude. (**a**) Shifting region of interest (ROI) (red and blue boxes) to mimic fiber movement. From left to right, the ROI is shifted by −2, −1, 0, +1, +2 pixels, where "−" and "+" indicates moving the ROI upward and downward, respectively. (**b**) Relationship between differential intensity $(I_A - I_B)/(I_A + I_B)$ and fiber movement (shifting of ROI), where the red line is a linear fit to the experimental data (black square)

FFT filter, we achieved a detection limit of 0.25 nm for the oscillation amplitude, corresponding to an effective charge detection limit of ~0.25 electron charge/μm$^2$. Note that peak quality in the FFT spectrum increases with time duration, and we used a typical time duration of 1 s, which is fast enough for most molecular binding processes.

## 2 Materials

### *2.1 Equipment and Part for CSOD Setup*

1. An inverted microscope (e.g., Olympus IX70) with a motorized XY sample stage (e.g., Ludl Electronic Products, Ltd. BioPrecision 2) that can hold a standard 96-well microplate.
2. Objective with proper zoom and working distance (e.g., LUCPLFLN, 40× Olympus phase-contrast objective, numerical aperture 0.6, working distance 2.7–4.0 mm). The working distance need to be long enough to image the fiber tip inside a microplate well from the bottom. 20–40× objective is recommended.

3. LED light: A visible LED light (e.g., M505L3 mounted LED, Thorlabs, wavelength: 505 nm, max power 440 mW).cs
4. A pair of positive lenses (e.g., AC254-040-A-ML, from Thorlabs) for collimating and focusing the LED light into fiber probe. Mounting hardware for lenses and fiber probe, including adjustable 1 in. lens tube, ½ in. post and base, and XYZ translation stage, can be purchased from Thorlabs. Alternatively, a fiber launch system could be used here.
5. CCD or CMOS camera for recording the fiber probe image (e.g., AVT Pike F-032, with 640 × 480 pixels, pixel size 7.4 μm).
6. Motorized Z translation stage for moving fiber probe in and out of wells (e.g., A-LSQ075B, ZABER).
7. Platinum sheet for fabrication of in-well electrodes.
8. Function generator (e.g., 33120A Agilent Arbitrary Waveform Generator).
9. Potentiostat (e.g., Pine Instrument AFCBP1 Bipotentiostat).
10. Uncoated, clear and flat bottom 96-well microplates (e.g., #655101, Greiner Bio-One).
11. A humidifier for generation of water vapor and a home-made plastic chamber.

### 2.2 Tools and Chemicals for Fiber Probe Fabrication

1. 105 μm core multimode visible optical fiber (e.g., Thorlabs FG105UCA), other type of fiber could be used.
2. Optical fiber stripper, (e.g., Thorlabs T06S13).
3. Hydrofluoric acid (47%) (e.g., from Avantor Performance Materials).
4. Sulfo-(*N*-hydroxysuccinimide (NHS))-biotin and streptavidin (e.g., from Thermo Scientific).
5. KcsA-Kv1.3 nanodisc, empty nanodisc, and compound **1** are obtained from Amgen Inc.
6. 1× phosphate buffered saline (1× PBS, e.g., from Fisher Scientific).
7. Nanodisc buffer (20 mM tris(hydroxymethyl)aminomethane (Tris), 100 mM NaCl, and 0.5 mM ethylenediaminetetraacetic acid (EDTA), pH 7.4).
8. Horse serum is purchased from ATCC.
9. Other chemicals are from Sigma-Aldrich.
10. 3-(aminopropyl)triethoxysilane (APTES) (for fiber surface functionalization).
11. *Casein* (for blocking non-specific binding).

12. DI water with a resistivity of 18.2 MΩ·cm, filtrated with 0.45 μm filter, is used in all experiments.
13. Desiccator.
14. Argon gas.
15. Magic tape.
16. Ventilated chemical hood for fiber etching and cleaning.
17. Optional for batch fiber processing: Microcapillaries for holding the fiber probe (VWR #53440-023).
18. Optional for batch fiber processing: Microcapillary puller (e.g., P-97 Flaming/Brown Micropipette Puller, Shutter Instrument Co.).

## 3 Methods

Figure 3 shows an overview of the major steps of CSOD sensor fabrication and measurement process.

### 3.1 CSOD Instrumentation

Figure 4 shows the major component of our CSOD setup.

1. An inverted microscope with a CCD camera is used for recording fiber oscillation.
2. A 96-well microplate with a pair of platinum electrodes (*see* **Note 2**) (8 mm × 4 mm × 0.2 mm, and 8 mm distance) inside the wells is mounted on a motorized x/y microscope stage.

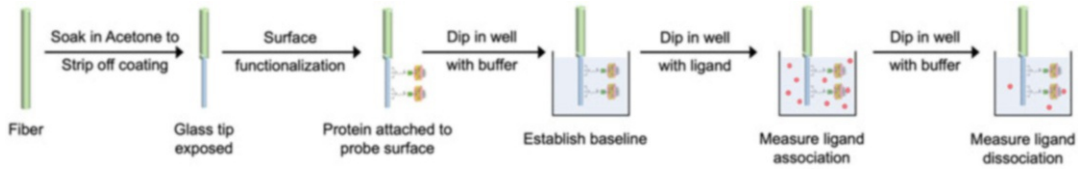


**Fig. 3** Overview schematic of a typical CSOD measurement process

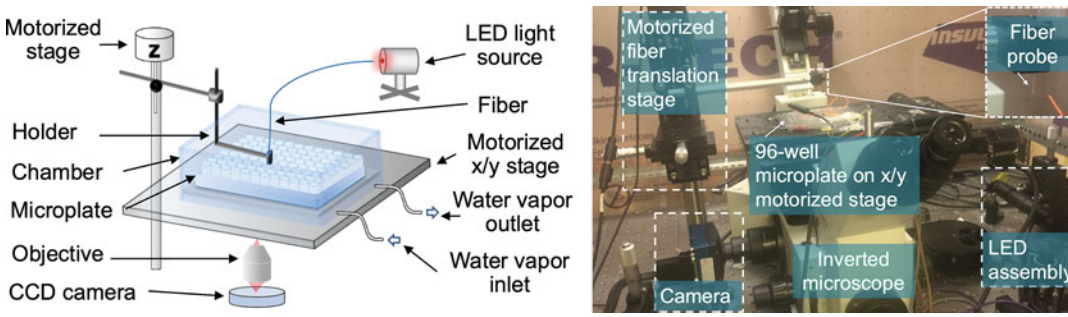


**Fig. 4** Schematic (left) and photo (right) of a microscope based CSOD setup with major component labeled. The plastic chamber is removed in the photo to reveal the microplate. (The schematic is adapted with permission from [2], Copyright 2016 American Chemical Society)

3. The electric field is created with a two-electrode setup. A sinusoidal voltage wave generated by a function generator is applied between the two electrodes via a potentiostat. The applied voltage is controlled with a MATLAB program. The amplitude and frequency of the applied voltage are 4 V and 40 Hz, respectively.
4. An LED light source is mounted on a XYZ translation stage and is focused onto the end of the fiber via a pair of lenses.
5. A CCD or CMOS camera is used to record the image of the optical fiber tip.
6. The software also controls the movement of stages for switching the fiber among wells.
7. When switching the fiber tip from one well to another, the fiber is pulled out of the first well vertically by a motorized translation stage, and then the plate is moved horizontally with the motorized microscope stage so that the second well is under the fiber tip, followed by moving the fiber tip downward into the second well.
8. Optionally, to minimize water evaporation from the fiber tip during the transfer, a plastic chamber, covering the microplate and the optical fiber, with a continuous supply of water vapor can be used (*see* **Note 3**).

### *3.2 Fabrication of CSOD Sensor Probe*

#### *3.2.1 Preparation of Optical Fiber Probes*

1. Optical fibers are cut to about 20–50 cm in length (depends on the distance between the light source and plate) using a fiber cutter.
2. The polymer coating layer on the fiber tip (length ~18 mm) is softened by soaking the fiber tip in acetone for 1 min. Then the tip is rinsed with DI water and dried with $N_2$.
3. The coating on the tip is stripped off using an optical fiber stripper.
4. For batch fiber processing and avoid fiber stacking to each other, glass microcapillaries (with 1.0 mm inner diameter) are pulled in a capillary puller to make a sharp tip with an inner diameter about 200 μm (between 125 μm to 250 μm) so that it can hold the tip stripped fiber in position and leave space between the tips for processing (Fig. 5) (*see* **Note 4** for pulling parameter for Shutter P-97 Puller). If only make a few fibers a time, the capillary can be skipped.
5. The bare fibers are inserted into glass microcapillaries to form a bundle (Fig. 5b).
6. The fibers are etched by soaking in 47% hydrofluoric acid for 30 min and 15 s to reach a diameter of ~10 μm. (Fig. 5d, *see* **Note 5**). **Warning**: hydrofluoric acid is corrosive, and this step need to be proceed in a ventilated chemical hood.

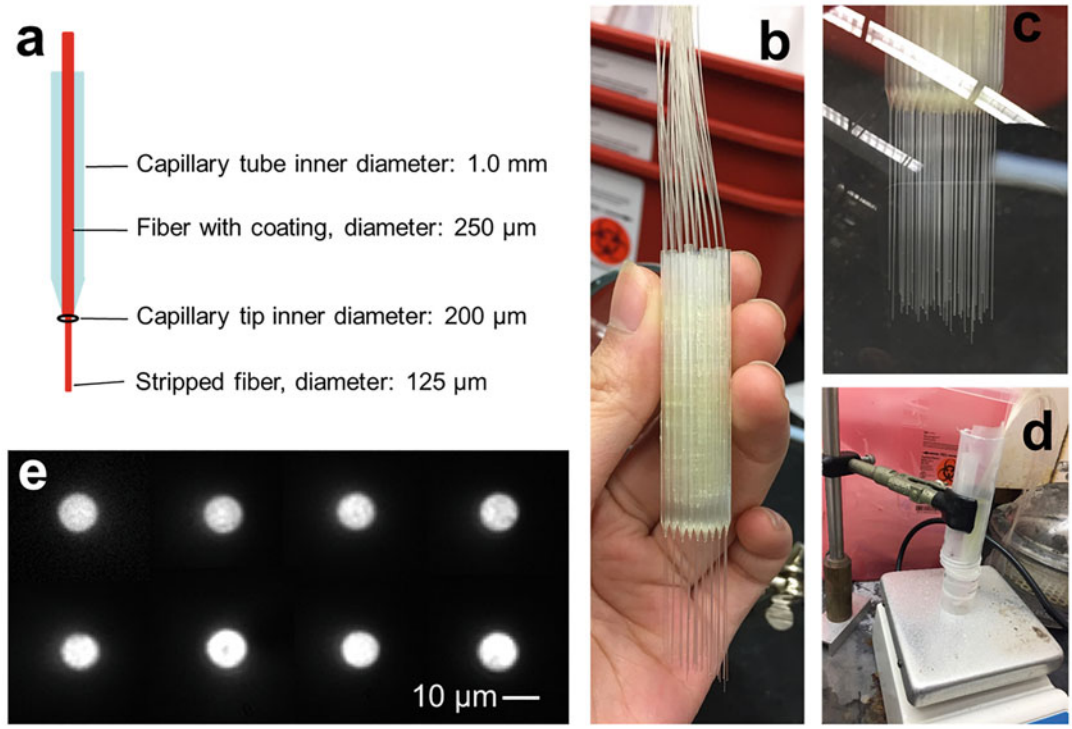


**Fig. 5** Batch fiber etching process. (**a**) A schematic illustrates the structure of a pulled capillary holding a stripped fiber. (**b**) Picture of 110 stripped fibers holding in bundled capillaries. (**c**) The stripped tips of the bundled fibers. (**d**) Bundled fibers in etching step. (**e**) Optical image of the tips of 8 fiber probes etched in a batch

7. The etched fibers are gently rinsed with DI water and dried with $N_2$ flow.
8. The tips are carefully cut to ~8 mm in length using sharp scissors (*see* **Note 6**).
9. The tips are cleaned with oxygen plasma for 3 min to remove surface contaminants.
10. For storage purpose, the fibers are placed in a desiccator filled with $N_2$ to minimize contamination.

*3.2.2 Surface Functionalization of Optical Fiber (Fig. 6)*

The procedure below using biotinylated KcsA-Kv1.3 nanodisc as an example to describe how to functionalize the optical fiber probe with protein targets. Any glass surface chemistry can be used for functionalize various biomolecules of interest.

1. The etched fiber tips are firstly functionalized with amine groups by coating the tips with APTES in gas phase, which took place in a desiccator.

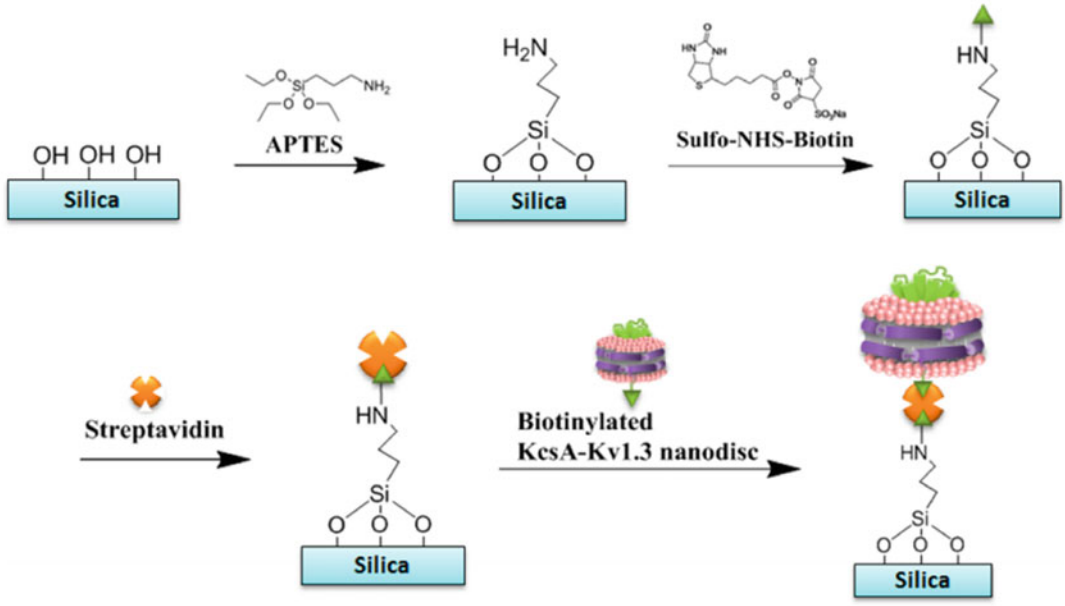


**Fig. 6** Surface chemistry for immobilizing nanodisc encapsulated membrane protein (the chimeric $K^+$ channel KcsA-Kv1.3) to the fiber probe (Reprinted with permission from [2], Copyright 2016 American Chemical Society)

2. A 100 mm petri dish is used to place the fibers. The fiber tips are stick to the wall of the dish. The fibers are coiled up in the dish and are fixed with magic tape.
3. The petri dish with fibers are placed at the bottom of the desiccator.
4. 500 µl APTES is added into a 35 mm petri dish, which is then placed in the 100 mm dish.
5. The desiccator is evacuated and sealed. The fibers are kept in this near vacuum environment for 18 h.
6. After the reaction, the fibers are taken out of the desiccator, rinsed with toluene and ethanol three times to remove any unbound APTES.
7. The fibers are then taped to a 100 mm glass petri dish and baked in an oven at 110 °C for 1 h to condense bound APTES.
8. The amine-coated tips are incubated in fresh NHS-Biotin solution (1.5 mg/ml in water) for 2 h to allow linking of biotin via NHS-amine reaction.
9. The biotin-coated tips are rinsed with DI water and dried with $N_2$ flow.
10. Then the tips are soaked in 50 µg/mL streptavidin solution (in 1× PBS) for 1 h to allow conjugation of streptavidin via biotin-streptavidin interactions.

11. After modification of streptavidin, the fibers are rinsed with 1× PBS and immediately applied to molecular receptors functionalization, or temporarily stored in 1× PBS.
12. The streptavidin coated fiber tips are immersed in 30 nM biotinylated KcsA-Kv1.3 nanodisc (in nanodisc buffer) for 1 h, to allow immobilization of nanodisc via biotin-streptavidin interaction (*see* **Note 7**).
13. The tips are then dipped in 40 times diluted nanodisc buffer containing 0.01% casein as blocker for at least 1 h (*see* **Note 8**).
14. The functionalized optical fibers are stored in this blocking buffer before use. Exposure of the fiber tips to air should be avoided.

### 3.3 Measurement of Molecular Interactions

To show the measurement of small molecule binding to nanodisc encapsulated membrane proteins with CSOD, a small molecule, compound **1** (4-(2-ethylpiperidin-1-yl)-2-methyl-6-phenyl-5*H*-pyrrolo[3,2-*d*]pyrimidine, MW = 320 Da), is measured with KcsA-Kv1.3 nanodisc coated optical fiber probes. KcsA-Kv1.3 is a chimeric potassium ion channel protein [3]. Compound **1** is not only a drug candidate for treating obesity through binding to Y5 receptor [4, 5], but also a blocker of the pore region of Kv1.3 channel [3]. Studying compound **1** and Kv1.3 interaction provides evidence for its potential side effects and demonstrates the capability of CSOD for small molecule drug screening. The steps of the binding kinetic measurement are:

1. The KcsA-Kv1.3 modified fiber tip is clamped on the fiber holder, which is then mounted on the Z translation stage.
2. The tip is immediately dipped in a well of a 96-well microplate containing only buffer (*see* **Note 9**). The fiber tip is driven into oscillation and the oscillation amplitude is recorded over time to establish a baseline.
3. The fiber tip is subsequently switched from the buffer well to a sample well containing compound **1** in the same buffer to start binding or association of compound **1** to KcsA-Kv1.3 in the nanodisc (*see* **Note 10**).
4. About 5 min after the start of association measurement, the tip is switched back to the original buffer well to start the dissociation of compound **1** from KcsA-Kv1.3.
5. Four different concentrations of compound **1** are measured by repeating **steps 1–4**.
6. Control experiments are performed by using empty nanodisc (no protein is encapsulated) functionalized fiber tip as the sensor probe (prepared by using empty nanodisc instead of KcsA-Kv1.3 nanodisc following **steps 1–14** in Sect. 3.2.2).

### 3.4 Data Processing

1. The oscillation images of the fiber are recorded by CCD camera at 247 frames per second, and the oscillation amplitude is extracted using the differential optical detection method mentioned above.
2. FFT is performed on the oscillation amplitude with 1 s time duration to further remove noises at frequencies other than that of the applied electric field.
3. The oscillation amplitude change of the fiber is plotted with time to generate the binding kinetics curve, which is then fitted to the first order kinetics model with Scrubber (*see* **Note 11**). The association rate constant ($k_a$), dissociation rate constant ($k_d$), and dissociation constant ($K_D$) are determined from the fittings.

Figure 7a shows the kinetic curves at four concentrations of compounds **1**, as well as global fitting of the data with the first order

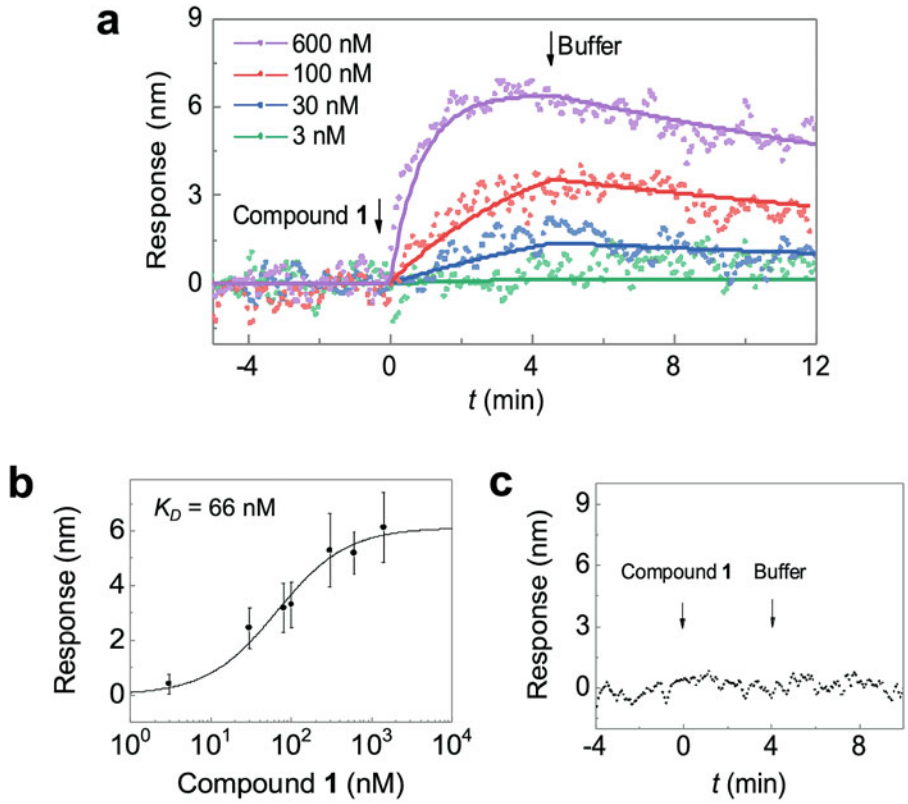


**Fig. 7** CSOD measurement of KcsA-Kv1.3 nanodisc to compound **1** binding kinetics and equilibrium analysis. (**a**) CSOD response to compound **1**. The data points are fitted with first-order kinetics (solid curves). The arrows mark the starting point of association phase and dissociation phase, respectively. (**b**) Equilibrium analysis. Each concentration is repeated three times to create the error bar. (**c**) Negative control experiment with empty nanodisc fiber probe dipped into 2.8μM compound **1** solution. The buffer is 40 times diluted nanodisc buffer with 0.01% casein and pH 7.4. (Adapted with permission from [2], Copyright 2016 American Chemical Society)

kinetic model (solid curves). The kinetic constants determined from the global fitting are $k_a = 1.8 \times 10^6$ $M^{-1}s^{-1}$, $k_d = 4.1 \times 10^{-2}$ $s^{-1}$, and $K_D = 22$ nM. Note that $K_D$ from the equilibrium analysis shown in Fig. 7b is 66 nM ($R^2 = 0.97$). The results are comparable with the values in literature (30 nM) [3]. Figure 7c shows no measurable binding signal in a negative control experiment using empty nanodisc coated fiber dipped in 2.8 μM compound **1**.

## 4 Notes

1. Frequency response of the oscillation amplitude.

   The effective spring constant, $k_{eff}$, of the cylindrical optical fiber probe is given by [6].

$$k_{eff} = \frac{3\pi E r^4}{4l^3}, \tag{2}$$

   where $E$, $r$, and $l$ are the Young's modulus, radius, and length of the optical fiber, respectively. The electric field strength applied on fiber probe is frequency dependent and given by

$$\left|\overrightarrow{E(\omega)}\right| = \left|\overrightarrow{E_0}\right| \frac{R_S}{\sqrt{R_S^2 + \frac{1}{(\omega C_{eff})^2}}}, \tag{3}$$

   where $R_S$ and $C_{eff}$ are the solution resistance and effective interfacial capacitance respectively. In order to determine the resistance and effective capacitance, we measured the impedance ($|Z(\omega)|$) at different frequencies. $|Z(\omega)|^2$ is given by

$$|Z(\omega)|^2 = R_S^2 + \frac{1}{(\omega C_{eff})^2}. \tag{4}$$

   By fitting $|Z(\omega)|^2$ and frequency ($\omega$), $R_S$ and $C_{eff}$ can be extracted. Fig. 8a shows the fitting of $|Z(\omega)|^2$ and frequency ($\omega$), from which we obtain $R_S = 1.68$ kΩ, and $C_{eff} = 22.11$ μF.

   From Eqs. (1) and (3), the frequency at which the oscillation amplitude reaches maximum is at

$$\omega_p = \sqrt[4]{\frac{k_{eff}^2}{\left(C_{eff}{}^2 c^2 - 2k_{eff} m_{eff} C_{eff}{}^2\right) R_S^2 + m_{eff}^2}}. \tag{5}$$

   We measured the oscillation amplitude of fiber at different frequencies, from which we determined $\omega_p$. Using Eqs. (1) and (3), we fit the oscillation amplitude vs. frequency shown in Fig. 8b.

2. Steel electrodes with the same dimension can be used as an alternative.

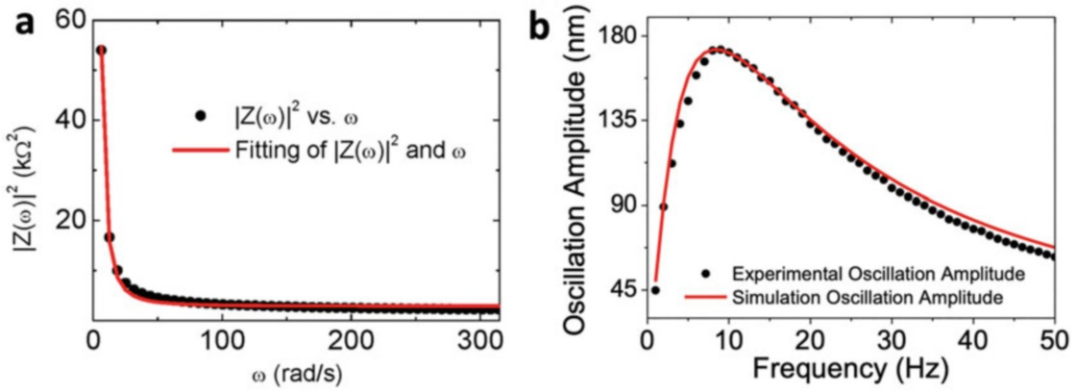


**Fig. 8** (**a**) $|Z(\omega)|^2$ vs. frequency, where the black dots are experimental data, and red line is a fit to Eq. (4). (**b**) Fiber oscillation amplitude vs. frequency, where the black dots are experimental data and the red line is the prediction of Eq. (1). Fiber diameter: 11μm, length: 8.5 mm. Buffer: 40 times diluted 1× PBS buffer [1]

3. It is extremely important to keep the fiber tip wet during the transfer. Drying out the fiber tip could lead to denaturation of the biomolecules modified on the tip, and introduce unexpected noises to the following measurements.
4. For Shutter P-97 puller, the pulling parameters are set as the following: 66 → clear → 0 → 2 → Air pressure: 500 → clear → 0 → 3 → DEL=1 → clear → 0 → 4 → 5 → clear → 0 → 5 → 5 → Heat 554 → Pull: 0 → VEL: 20 → DEL:1
5. Batch production can be performed if needed. We etch 110 fibers in a batch and the average diameter is 9.89 μm with a variation 0.45 μm. We also note that the etching time is sensitive to HF concentration and HF from different manufactures, which may lead to up to 5 μm variation in diameter.
6. Cut the fiber tip with sharp scissors, otherwise the tip may not be flat.
7. The streptavidin coated fiber tip serves as a good substrate for further functionalization with any biotinylated biomolecules, not limited to nanodisc.
8. The type and concentration of blocking reagent should be carefully tested and optimized for different biomolecules immobilized on the fiber tip. A good blocking protocol should minimize nonspecific interactions without affecting specific binding signal.
9. The buffer used here is 40 times diluted nanodisc buffer (ionic strength ~3 mM). Low ionic strength buffer (typically <10 mM) is preferred for CSOD measurement to reduce ionic screening of the charge on the fiber and hence enhance the oscillation.

10. Water vapor is continuously pumped into the chamber to avoid drying of the fiber tip and minimize the evaporation of the solution in the wells. Additionally, well-switching should be fast (~2 s) enough to minimize the time that the fiber is exposed to air.
11. Scrubber is a commercial software for fitting of the binding curves.

## Acknowledgments

We acknowledge financial support from National Institutes of Health under Award Number R33CA202834 and R44GM139535.

### References

1. Guan Y, Shan XN, Wang SP, Zhang PM, Tao NJ (2014) Detection of molecular binding via charge-induced mechanical response of optical fibers. Chem Sci 5(11):4375–4381. https://doi.org/10.1039/C4sc01188k. PubMed PMID: WOS:000343004300033
2. Ma G, Guan Y, Wang S, Xu H, Tao N (2016) Study of small-molecule-membrane protein binding kinetics with Nanodisc and charge-sensitive optical detection. Anal Chem 88 (4):2375–2379. https://doi.org/10.1021/acs.analchem.5b04366. Epub 2016/01/12. PubMed PMID: 26752355; PMCID: PMC5181645
3. Xu H, Hill JJ, Michelsen K, Yamane H, Kurzeja RJM, Tam T, Isaacs RJ, Shen F, Tagari P (2015) Characterization of the direct interaction between KcsA-Kv1.3 and its inhibitors. Biochim Biophys Acta Biomembr 1848(10, Part A):1974–1980. https://doi.org/10.1016/j.bbamem.2015.06.011
4. Norman MH, Chen N, Chen Z, Fotsch C, Hale C, Han N, Hurt R, Jenkins T, Kincaid J, Liu L, Lu Y, Moreno O, Santora VJ, Sonnenberg JD, Karbon W (2000) Structure−activity relationships of a series of Pyrrolo[3,2-d] pyrimidine derivatives and related compounds as neuropeptide Y5 receptor antagonists. J Med Chem 43(22):4288–4312. https://doi.org/10.1021/jm000269t
5. Holzer P, Reichmann F, Farzi A (2012) Neuropeptide Y, peptide YY and pancreatic polypeptide in the gut–brain axis. Neuropeptides 46(6):261–274. https://doi.org/10.1016/j.npep.2012.08.005
6. Chen S-H, Lin H-N, Ong P-M (2000) Spring constant measurement of a bent near-field optical fiber probe. Rev Sci Instrum 71(10):3788. https://doi.org/10.1063/1.1290503

# Chapter 18

# Mobile ELISA with a Transparent Incubator

**Arsenii Zhdanov, Cassidy Chen, Crystal Schmitt, Tyler Tripp, Chase Miller, and Anna Pyayt**

## Abstract

Enzyme-linked immunosorbent assay (ELISA) is one of the most important technologies for biochemical testing critical for diagnosis and monitoring of many diseases. Traditional systems for ELISA incubation and reading are expensive and bulky, thus cannot be used at point-of-care or in the field. Here, we designed and demonstrated a new miniature mobile phone-based system for ELISA. This mHealth system can be used to complete all steps of the assay, including incubation and reading. It can be fabricated at low cost, it is portable, and can transfer test results via mobile phone. We have designed incubation chamber, imaging enclosure, and data processing algorithm. We demonstrate how mobile ELISA can be calibrated for accurate measurements of cortisol and show successful measurements with the calibrated system. We show that the results acquired with our prototype match well the results obtained with the gold standard.

**Key words** Biomedical testing, mHealth, ELISA, Cortisol

## 1 Introduction

ELISA is one of the most popular platforms for biomedical testing, and currently thousands of reagent ELISA kits are commercially available for a great variety of proteins, biomarkers, hormones, and other molecules of interest. The instruments required for all steps of ELISA are a sample incubator, and a plate reader. Incubation is required to bind targeted protein with precoated antibodies in the test microwell. It has to be performed at constant temperature for a specific period of time. Incubation time and temperature conditions required for ELISA are different for different proteins. The plate reading can be done using a camera on a mobile phone [1]. Previous studies have already demonstrated benefits of using mobile phone cameras for optical readout of biological assays [2–5]. Phone cameras are convenient to use, widely available, and accurate enough for reliable measurements. However, systems that rely on mobile phone imaging require controlled light environment [6]. Any fluctuations in light conditions throughout the

Miguel R. Ossandon et al. (eds.), *Biomedical Engineering Technologies: Volume 1*, Methods in Molecular Biology, vol. 2393, https://doi.org/10.1007/978-1-0716-1803-5_18, 

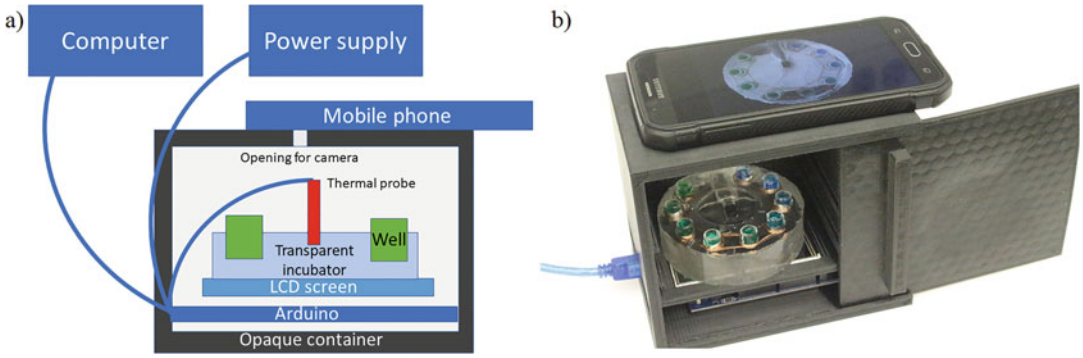


**Fig. 1** All components of a portable ELISA system including an enclosed compartment with the backlight source at the bottom, the transparent incubator, and the mobile phone camera on the top. (**a**) The schematics of the complete system. (**b**) The prototype

measurement lead to inevitable readout errors. To create the controlled light environment, the samples must be enclosed in an opaque container (Fig. 1). The mobile phone is situated on top of the container with the camera facing the samples through an opening. To prevent possible reflections, glares and other noise, the samples is illuminated by a backlight, such as an LED array or LCD screen emitting white light (Fig. 1). While previous mobile ELISA required incubation in water bath-based heater followed by transfer to an imaging tray [1], it would be much more convenient to have a transparent incubator that can be used for imaging without need to transfer incubated samples. We created a 10-well incubator out of polydimethylsiloxane (PDMS) with embedded copper wire for heating and thermal probe for real-time temperature monitoring (Fig. 2a). PDMS is an optically clear, nonflammable organic composite with a thermal conductivity (0.17 W/(m K)) [7]. PDMS can be processed in different shapes with the holders for the microwells by creating special molds. Controllable heating of each individual well can be done using resistive heating by a wire. Therefore, we made the heating element out of a copper wire looped around the microwells and embedded within the PDMS. Electrical current running through the wire generates heat that warms the samples to the required incubation temperature. The advantage of using copper wires for individual well heating in excellent heating uniformity of this approach in comparison to heating the whole chamber. The methods section describes the design and operation of the incubator as well as the readout testing.

## 2 Materials

1. Arduino Mega 2560 microcontroller from Digi-Key electronics.

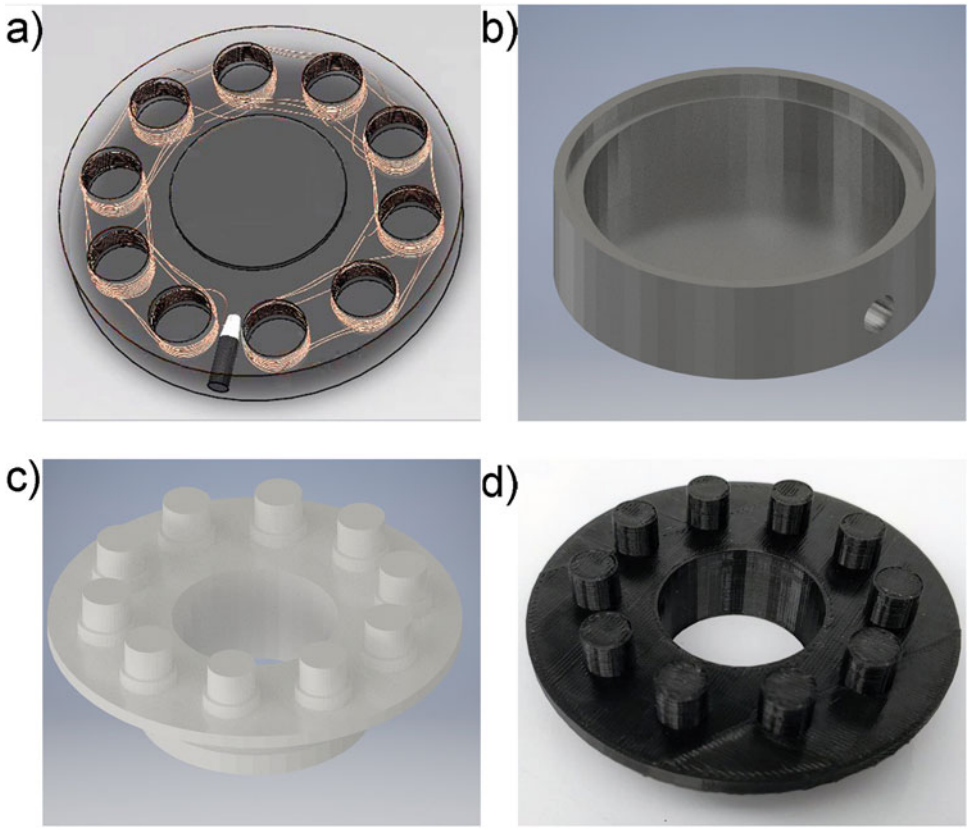


**Fig. 2** Transparent PDMS heater design. (**a**) 3D rendering of the incubator design demonstrating resistive heater surrounding each of the well holders (**b**) CAD design of the bottom mold (**c**) CAD design of the top mold with cylindrical protrusions for the microwells 7 mm in diameter and 7 mm in depth, (**d**) 3D printed mold

2. SYLGARD™ 184 Silicone Elastomer Kit from Digi-Key electronics.
3. Fisher Scientific™ AccuSkan™ FC Filter-Based Microplate Photometer (plate reader) from Fisher Scientific.
4. 3D printer—FDM 3D printer MakerBot Replicator from MakerBot.
5. PLA filament from MakerBot.
6. Camera equipped smartphone Galaxy Note 5 from Samsung.
7. Equipment for degassing—vacuum oven #3608 from Thermo Scientific.
8. Solid-state relay—5 V 2-Channel Low Level Trigger Solid State Relay SSR Module for Arduino DSP Z5Y9.
9. Temperature probe-Waterproof DS18B20 Digital Temp Sensor from Adafruit.
10. Thermal camera—FLIR T420 from FLIR.

11. Software for data analysis—Microsoft Excel.
12. Software for color components extraction and analysis—Adobe Photoshop 20.x.
13. GSC AC/DC Variable Power Supply from Fisher Scientific.
14. Lead Free Solder Wire Sn99.3 Cu0.7 with Rosin Core for Electronic 3.5 oz. 1.0 mm from Digi-Key electronics.
15. Cortisol Saliva ELISA Assay Kit SKU: CRT32-K01 from Eagle Biosciences.
16. Small LCD screen DT024CTFT from Digi-Key electronics.
17. Copper wire with a resistivity of 0.0171 × mm/m.

## 3 Methods

### 3.1 PDMS Incubator Design

To create a PDMS incubator in a desired shape, it needs to be molded. The mold for the incubator is designed in SolidWorks and 3D printed (MakerBot Replicator) (Fig. 2d). In order to create a heating element, joule heating is used where current runs through a wire. This heating is proportional to the resistance and amount of current ran through the wire. Copper wire has a resistivity of 0.0171 Ω mm/m. Resistivity is directly correlated to that value increases with length and decreases with gauge. We use copper wire that is covered with a polymer insulating layer. This insulation provides safety including protection from leakage of current and exposed wires. The top part of the designed mold has protrusions for the sample wells that are then looped with the copper wire (Fig. 2c). Electrical current running through the wire generates heat that warms the samples to the incubation temperature.

### 3.2 Prototyping

1. Design the mold in a CAD software (SolidWorks) with the top part having cylindrical protrusions for the microwells and an opening to pour uncured PDMS. The bottom part must be designed to seal tight around the top part to avoid spills and leaks. It should also have an opening for the wires to be connected to an external power source (Fig. 2b).
2. FDM 3D printer MakerBot Replicator is used to print the mold with 60% infill using PLA plastic.
3. The bottom layer of the mold is covered with tape to make the surface smoother, disassembly easier and to prevent the PDMS from leaking through the pores in plastic.
4. The 31 AWG copper wire is wrapped around the upper mold pegs with 6 loops (Fig. 3a).
5. The loose ends are stripped of coating and soldered to a standard 3.5 mm connector. The connector is then attached to the opening of the bottom mold.

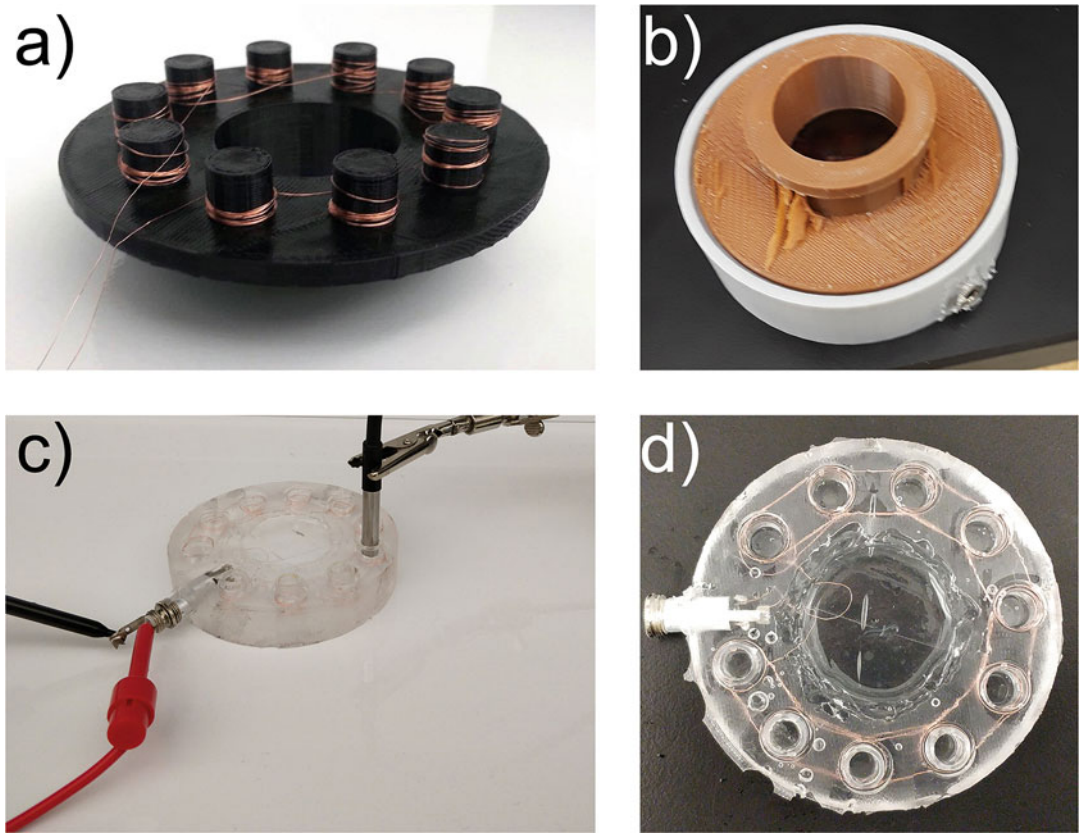


**Fig. 3** Heater fabrication: (**a**) 3D-printed mold with copper wire wrapped around the protrusions for individual well heating, (**b**) assembled 2-part mold, (**c**) PDMS heater testing (side view), (**d**) PDMS heater (top view)

6. The top and the bottom parts of the mold connect leaving an opening to pour PDMS (Fig. 3b).
7. The SYLGARD™ 184 Silicone Elastomer Kit is mixed by adding curing agent to the monomer at 1:10 ratio. Stir the mixture to achieve uniform composition.
8. In its prebaked phase, PDMS is degassed for 30 min in a vacuum chamber to remove oxygen bubbles.
9. After degassing, the PDMS mixture is gently poured into the mold embedding the copper wire.
10. The mold is placed in the oven for curing for 90 min at 75 °C.
11. Cut open and break the mold gently pulling out the top part protrusions leaving the wire embedded in the polymer (Fig. 3d).

### *3.3 Operation and Characterization*

Reliable incubation is one of the critical steps of ELISA. Fluctuations in temperature can result in a slow binding reaction or in protein denaturation. To test the consistency of the sample heating

in our incubator, we conducted a set of experiments monitoring temperature distribution in microwells (Fig. 3a).

1. Microwells are filled with 200μl of water and inserted into the copper wire surrounded openings in PDMS
2. A thermal probe is inserted in one of the sample wells for continuous temperature monitoring.
3. The copper wire heating element is connected to a variable power supply through a solid state relay.
4. The relay control ports are connected to the Arduino microcontroller to adjust the temperature after reading the data from the probe.
5. An Arduino Mega 2560 microcontroller is connected to the thermal probe and programmed to acquire temperature readings every 1 s. It also controlled the heaters through solid state relays. When the temperature probe connected to Arduino is reading less than 37 °C, the relays are enabled, and the heating element is powered. When the temperature is greater than 37 °C, the relays are closed, switching the heaters off. The resistive heating is operating by running current through the thin wire that is looped multiple times around each well. The device is powered using an external variable power supply. Arduino microcontroller received commands from a PC through a USB port. The smartphone is used for capturing the sample image. The images are then transferred to the PC and processed with computer software.
6. The heating process is also monitored with a FLIR thermal camera that allowed tracking temperature in all wells simultaneously, while using the temperature probe in one of the wells for reference (Fig. 4d).

We tested the heater with different currents to determine the optimal heating conditions. The initial current for the heater is set at 0.75 A, but after 10 min the temperature readings in the well saturated at 25 °C. Increasing the current to 1.2 A for the next 15 min raised the temperature to 35 °C, however it still reached saturation and was not high enough for the optimal ELISA incubation that had to be conducted at 37 °C. Then the current is raised to 2 A, and the desired temperature is obtained. Figure 4a shows the complete tuning curve and demonstrates that the relay successfully keeps the temperature at 37 °C. The heater is then tested at 1.7 A. It took 6 min to reach operating temperature and the temperature is kept at set point within 0.5 °C (Fig. 4c). This current is sufficient for the ELISA sample incubation.

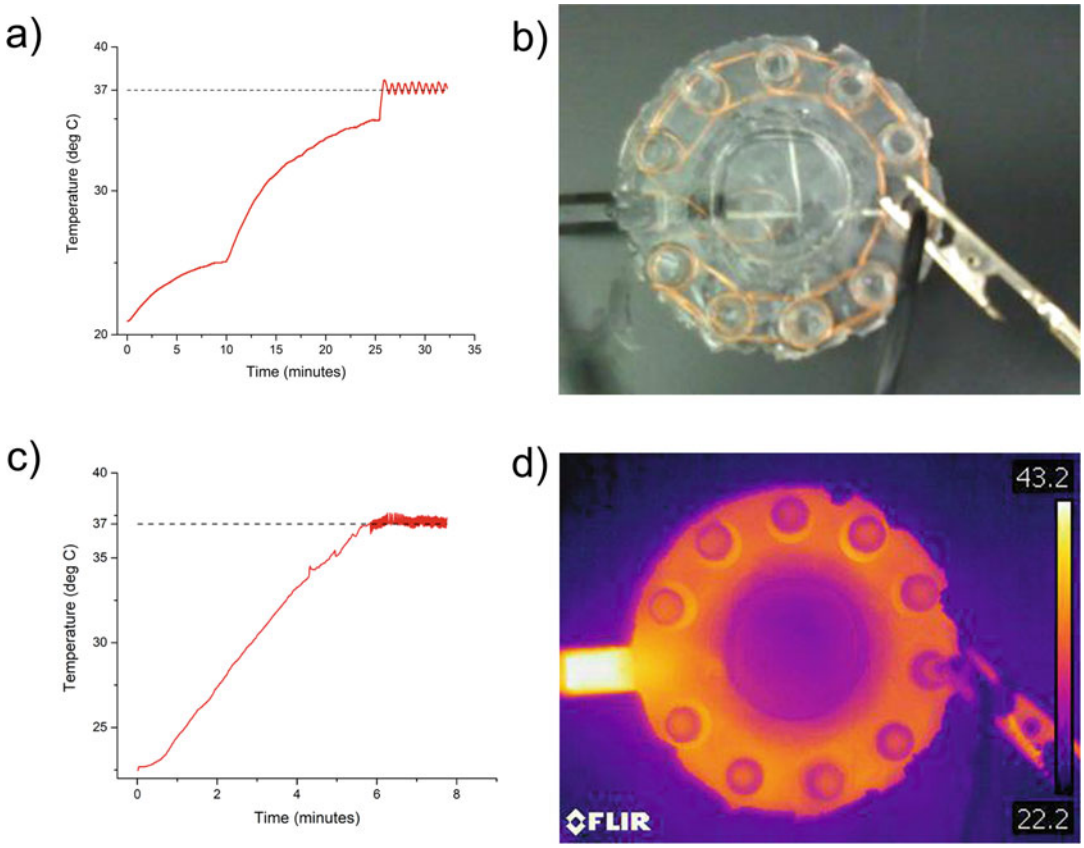


**Fig. 4** PDMS incubator testing. (**a**) PDMS incubator temperature tuning curve (three current regimes are demonstrated—0.75 A, 1.2 A, and 2 A respectively), (**b**) experimental setup (top view), (**c**) tuning curve at 1.7 A, (**d**) infrared thermal image of the working incubator

### *3.4 Calibration and Testing*

We have chosen cortisol ELISA kit to demonstrate that our point-of-care system performs in way similar to the traditional ELISA. Cortisol is a steroid hormone that is produced by the adrenal glands as a response to stress or low blood glucose concentration to promote gluconeogenesis. It helps regulating sleep cycle, reduces inflammation, and controls blood pressure [8–10]. Cortisol deficiency causes fatigue, loss of appetite, nausea, and abdominal pain. Cortisol supplements are often prescribed to control metabolism and reduce blood pressure [11]. The PDMS incubator performance is compared against a standard ELISA incubator, and the incubated samples are analyzed by the mobile phone as well as the plate reader.

1. Five calibration samples of known concentrations are used to create a calibration curve for the measurement (Table 1).
2. A second set of samples with same concentrations is prepared to test in the PDMS incubator against the standard one.

**Table 1**
**Cortisol calibration sample concentrations**

| Sample # | 1 | 2 | 3 | 4 | 5 |
|---|---|---|---|---|---|
| ng/ml | 0 | 10 | 50 | 150 | 500 |

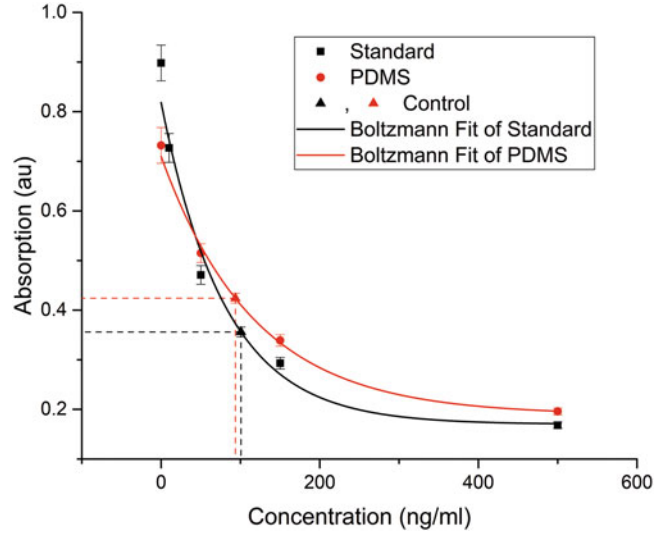


**Fig. 5** Two calibration curves based on the data obtained using a standard incubator and our PDMS incubator. Absorption data for the cortisol values and for the control samples are measured by the plate reader

3. The experiment followed the standard protocol developed for cortisol ELISA kit [12]. The PDF with all the details can be downloaded from this link [12].
4. 20μl samples are added to the precoated microwells and incubated at 37 °C for 1 h. Additional control samples are used for readout error calculation.
5. After incubation in the heaters, two sample sets are analyzed by both, the plate reader and the mobile phone camera.
6. Plate reader absorption values are shown on Fig. 5. The calibration is fitted with a Boltzmann Sigmoid equation (5.1) that is used to measure the control sample concentration [1]. The samples are illuminated from the back using a small LCD screen shining uniform white light.
7. Samples from both heaters are then photographed with the mobile phone, and red, green and blue (RGB) color components are extracted for each sample. Out of R, G and B channels the most sensitive channel to the concentration change is B. The values from the B channel are used to plot a calibration curve (Fig. 6). The RGB components are extracted using

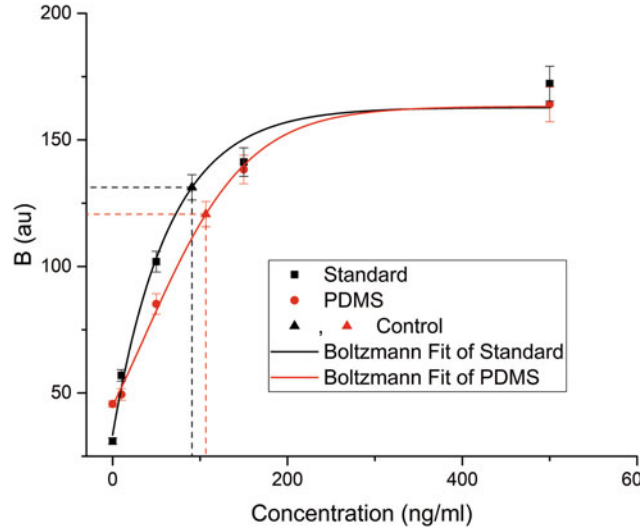


**Fig. 6** Two calibration curves based on the data obtained using a standard incubator and our PDMS incubator. Absorption data for the cortisol values and for the control samples are measured by the mobile phone camera Plate

**Table 2**
**Control sample readout error (%)**

| | Standard incubator | PDMS incubator |
|---|---|---|
| Plate reader | 2.68 | 1.55 |
| Optical readout | 1.71 | 1.67 |

Photoshop Histogram tool that allows measurements of each individual color component in a small area in the middle of each well. In the centers the of the wells images are free of artifacts and are most uniformly colored. While information about values in all channels is collected, only the most sensitive channel is chosen for the measurements.

8. Concentration values for control sample are calculated from the Boltzmann curves for both heaters and both type of readout to determine an error and check how consistent the PDMS heater is comparing to the standard one. The readings demonstrate that the control sample value error does not exceed 3% for both heaters and readout methods (Table 2). This proves that PDMS heater can be used for consistent and reliable measurements.
9. To test the consistency of the PDMS heater and accuracy of the optical readout, we prepare three samples with unknown concentrations. These samples are incubated alongside the known calibration samples in the PDMS heater.

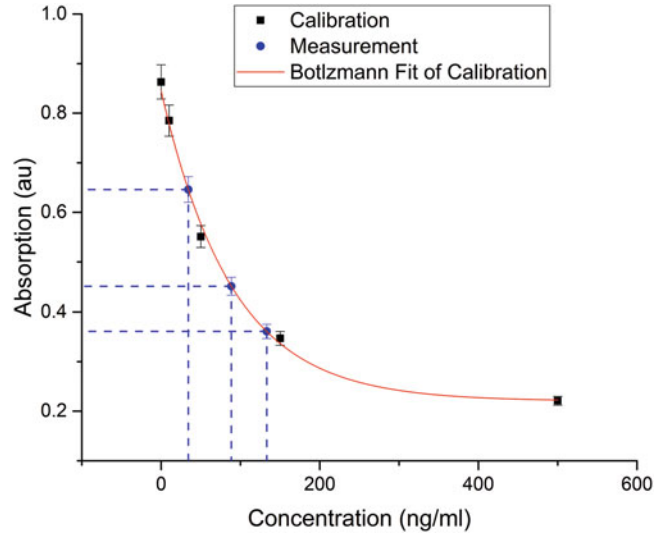


**Fig. 7** Measurement of unknown concentrations of cortisol using plate reader

**Table 3**
**Calculated values for unknown cortisol samples**

| Sample # | Plate reader measured concentration (ng/ml) | Prototype measured concentration (ng/ml) |
|---|---|---|
| 7 | 33.24 | 31.78 |
| 8 | 87.4 | 81.63 |
| 9 | 131.87 | 134.71 |

10. After incubation, conjugation with the antibody, adding substrate and other steps of ELISA, the samples are read by the plate reader and the mobile phone-based optical readout. The plate reader data is shown in Fig. 7.
11. Absorption values of unknown samples are projected on the calibration curve to determine concentrations (Table 3). Similarly, concentration values are acquired from the B channels of the optical readout (Fig. 8).
12. As seen in Table 3, concentration data measure by both systems matches within 7% accuracy, which is within measurement error of ELISA. That proves that PDMS heater and optical readout can be used in the portable mHealth ELISA system developed in this project.

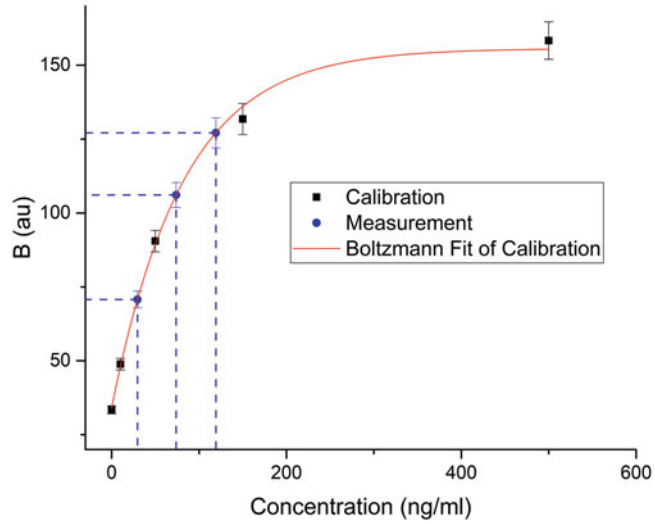


**Fig. 8** Measurement of unknown concentrations of cortisol using mobile phone

## 4 Notes

We have faced a number of challenges designing the operational prototype. The main challenge was optimizing the design so that we get consistent and reproducible results across multiple prototypes.

1. First, PDMS curing time depends on incubation temperature. According to the manufacturer, it takes approximately 2 h to completely cross-link material at 60 °C, whether at 150 °C the time is only 10 min. However, at temperatures higher than 90 °C, the plastic mold starts to deform (Fig. 9a). The shape of the resulted incubator is uneven (Fig. 9b) and it cannot have a uniform heating profile. To prevent the mold from damage, the PDMS mixture is cured at 75 °C for 90 min.
2. Additionally, the initial design of the upper mold pegs could not prevent thinner gauge wire from slipping off during mold disassembly. When the mold is pulled from the cured incubator, it is taking some of the wiring with it (Fig. 9c, d). Not only it compromises heating of the well with the loose wiring, but the whole heating system could not provide consistent heating. That is solved by adding notches on the protrusions to hold the wire and using thicker wire gauge.
3. Achievement of reliable and reproducible optical transparency of the heater is also important. An opaque or inconsistent incubator could make the color readings unreliable which would lead to readout errors. This is challenging, since the molds are created using 3D printers that move a heated plastic

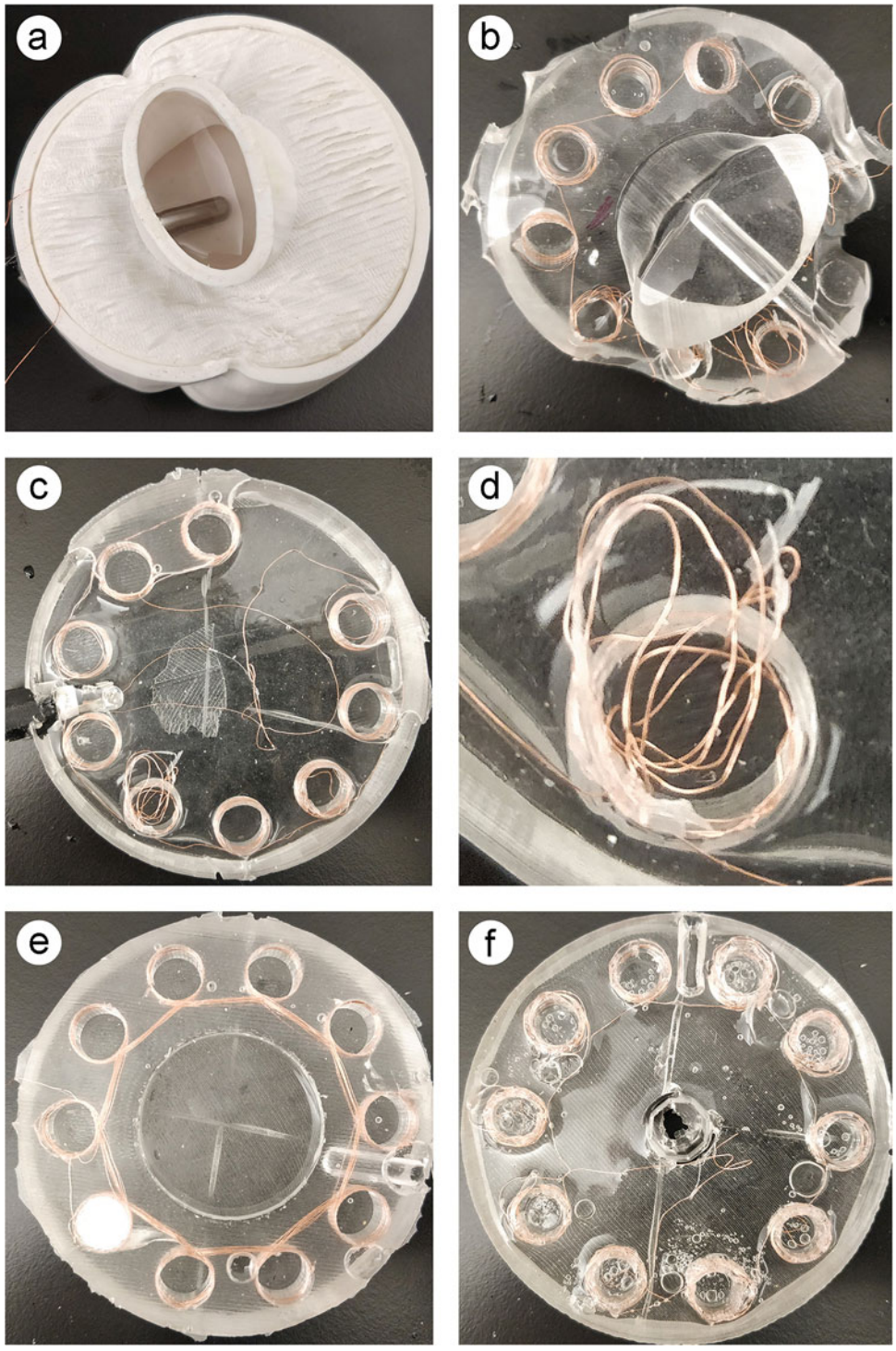


**Fig. 9** Challenges and failures that can be prevented: (**a**) 3D-printed mold damaged from excessive heat during PDMS curing (**Note 1**), (**b**) misshapen incubator, (**c**) dislodged wire caused by a thin gauge (**Note 2**), (**d**) unusable well with compromised wiring, (**e**) PDMS mix leaks into the mold and entraps one of the pegs (**Note 3**), (**f**) incubator compromised by air bubbles (**Note 4**)

extruder in a specific pattern to match the shape of a printed object. The motion of the extruder head creates uneven ridges that imprint into the incubator during molding (Fig. 9e). Moreover, during printing, the mold infill can be preprogrammed. Lesser fill uses smaller amounts of plastic and makes the mold easier to break off. However, PDMS can seep through the mold making it very difficult to separate the incubator from the mold. It may even cause breaking-off the pegs and trapping them in the incubator (Fig. 9e). Putting tape on the bottom surface of the mold makes it smoother and prevents the PDMS from leaking.

4. Finally, during mixing with curing agent, the mixture entraps a lot of air bubbles. During curing, they cause inconsistencies that are detrimental to colorimetric analysis (Fig. 9f). Proper degassing in a vacuum chamber is required to remove the air bubbles and to achieve proper optical clarity.

## References


1. Zhdanov A, Keefe J, Franco-Waite L, Konnaiyan KR, Pyayt A (2018) Mobile phone-based ELISA (MELISA). Biosens Bioelectron 103:138–142
2. McGeough CM, O'Driscoll S (2013) Camera phone-based quantitative analysis of C-reactive protein ELISA. IEEE Trans Biomed Circuits Syst 7(5):655–659
3. Vashist SK, van Oordt T, Schneider EM, Zengerle R, von Stetten F, Luong JH (2015) A smartphone-based colorimetric reader for bioanalytical applications using the screen-based bottom illumination provided by gadgets. Biosens Bioelectron 67:248–255
4. Raj KK et al (2017) mHealth dipstick analyzer for monitoring of pregnancy complications. IEEE Sens J 17:7311–7316
5. Archibong E, Konnaiyan KR, Kaplan H, Pyayt A (2017) A mobile phone-based approach to detection of hemolysis. Biosens Bioelectron 88:204–209
6. Konnaiyan KR (2015) Smartphone Based 3D Printed Colorimeter for Biomedical Applications, MS disseration, University of South Florida
7. Shik SY et al (2003) PDMS-based micro PCR chip with parylene coating. J Micromech Microeng 13:768
8. Dahlgren A, Kecklund G, Åkerstedt T (2005) Different levels of work-related stress and the effects on sleep, fatigue and cortisol. Scand J Work Environ Health 31(4):277–285
9. Dahlgren A, Kecklund G, Åkerstedt T (2006) Overtime work and its effects on sleep, sleepiness, cortisol and blood pressure in an experimental field study. Scand J Work Environ Health 32(4):318–327
10. Nijm J, Jonasson L (2009) Inflammation and cortisol response in coronary artery disease. Ann Med 41(3):224–233
11. Luo L et al (2015) Cortisol supplement combined with psychotherapy and citalopram improvesdepression outcomes in patients with hypocortisolism after traumatic brain injury. Aging Dis 6:418
12. Cortisol Saliva ELISA Assay Kit SKU: CRT32-K01 from Eagle Biosciences. https://eaglebio.com/wp-content/uploads/data-pdf/crt32-K01-cortisol-saliva-elisa-assay-kit-packageinsert.pdf

# Chapter 19

# Smartphone Enabled Point-of-Care Detection of Serum Biomarkers

**Jacob T. Heggestad, David S. Kinnamon, Jason Liu, Daniel Y. Joh, Cassio M. Fontes, Qingshan Wei, Aydogan Ozcan, Angus M. Hucknall, and Ashutosh Chilkoti**

## Abstract

Sandwich immunoassays are the gold standard for detection of protein analytes. Here, we describe an ultrasensitive point-of-care sandwich immunoassay platform for the detection of biomarkers directly from blood or serum using a custom-built smartphone detector. Testing undiluted blood or serum is challenging due to the complexity of the matrix. Proteins nonspecifically adsorb to and cells often adhere to the assay surface, which can drastically impact the analytical sensitivity of the assay. To address this problem, our assay is built upon a "nonfouling" polymer brush "grafted from" a glass slide, which eliminates nearly all nonspecific binding and therefore increases the signal-to-noise ratio and greatly improves the analytical performance of the test. The two components required to perform a sandwich immunoassay are inkjet-printed directly onto the surface: (1) "stable" capture antibodies that remain entrapped in the brush even after exposure to a liquid sample and (2) fluorescently labeled "soluble" detection antibodies that dissolve upon exposure to a liquid sample. The polymer brush provides hydration to the antibodies, allowing them to remain stable and active over prolonged periods of time. When a liquid sample containing a biomarker of interest is dispensed onto the chip, the detection antibodies dissolve and diffuse to the stable capture spots forming a complex that sandwiches the analyte and that has a fluorescence intensity proportional to the concentration of the biomarker in solution, which can be measured using a custom-built smartphone detector. As multiple capture antibodies can be printed as discrete capture spots, the assay can be easily multiplexed without the need for multiple fluorophores. This chip and detector platform can be utilized for the point-of-care detection of low-abundance biomarkers directly from blood or serum in low-resource settings.

**Key words** Point-of-care, Biomarker, Diagnostics, Polymer brush, Nonfouling, Smartphone, Fluorescence, Sandwich immunoassay

Jacob T. Heggestad, David S. Kinnamon and Jason Liu contributed equally with all other contributors.

Miguel R. Ossandon et al. (eds.), *Biomedical Engineering Technologies: Volume 1*, Methods in Molecular Biology, vol. 2393, https://doi.org/10.1007/978-1-0716-1803-5_19, 

## 1 Introduction

Multiplexed testing of multiple protein biomarkers from a small volume of a clinical specimen, such as a drop of blood or serum, has been recognized as a highly desirable attribute for point-of-care diagnostics [1]. Further, as biomarkers often circulate at subpicomolar concentrations in blood or other matrices such as saliva or urine, ultrasensitive detection schemes are required to match the performance of tests commonly performed in clinical laboratories, such as enzyme-linked immunosorbent assays (ELISA) [2]. Herein, we describe in detail our group's fabrication methodology for an ultrasensitive, multiplexable, self-contained, and portable immunoassay point-of-care test (POCT)—the D4 POCT—that addresses these needs. The D4 POCT contains all the necessary reagents needed to perform multiple sandwich immunoassays on-chip [3]. Antibody (Ab) reagents are inkjet-printed directly onto a nonfouling poly(oligo(ethylene glycol) methacrylate) (POEGMA) brush—also called poly(ethylene glycol)methyl ether methacrylate (PEGMEM)—"grafted from" a glass slide through surface-initiated atom-transfer radical polymerization (SI-ATRP), as summarized in Fig. 1a.

The POEGMA brush, which functions as the microarray substrate, is the core technology of the D4 POCT. Previous studies have demonstrated that POEGMA brushes with sufficient density and thickness greatly reduce protein adsorption and cellular adhesion at the substrate surface [4–6]. This reduction in nonspecific protein adsorption greatly improves the analytical performance of the assay by decreasing the background signal and thereby increasing the signal-to-noise ratio, enabling detection of protein analytes directly from complex biological milieu such as blood or serum without a reduction in analytical performance [7–9]. In addition, POEGMA brushes can be easily functionalized with an Ab or other proteins without the need for covalent conjugation. In the dry state, the brush acts like a reservoir enabling noncovalent attachment of Ab reagents for sensing. Upon hydration, the Abs remain stably entangled within the brush and therefore discrete spatial addresses on the chip can be printed with different capture antibodies (cAbs) targeting different biomarkers [8]. Further, fluorescently labeled detection Abs (dAb) are printed onto the chip in close proximity to the cAbs. However, in contrast to the cAbs that are directly printed on to the brush, the dAbs are printed on top of a trehalose excipient pad on the POEGMA brush allowing them to solubilize—because of dissolution of the underlying trehalose pad—after a liquid sample has been added to the surface. Because each cAb has a discrete spatial address, the assay can be multiplexed using only one fluorophore for all dAbs, which simplifies assay readout.

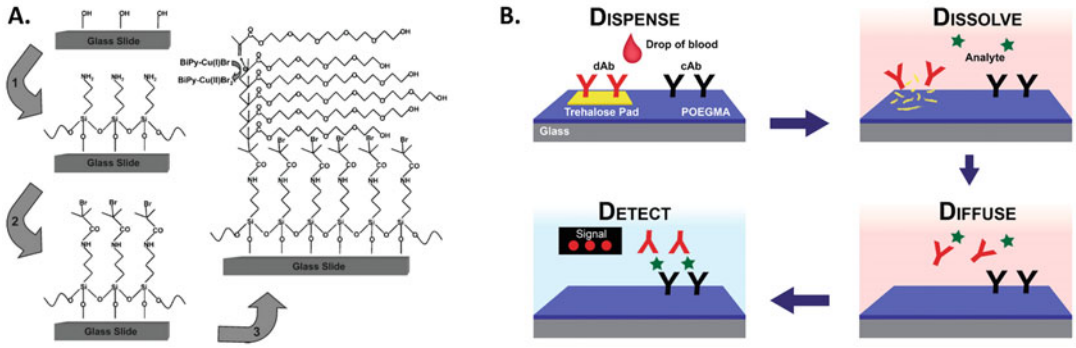


**Fig. 1** (**a**) Detailed overview of SI-ATRP of POEGMA brushes "grafted from" a glass slide. Reproduced from "Simple Fabrication of Antibody Microarrays on Nonfouling Polymer Brushes with Femtomolar Sensitivity for Protein Analytes in Serum and Blood" 2009 from Wiley. (**b**) Visual representation of the series of events that occur during the D4 assay after a sample is added

The D4 POCT is named for the series of events that occur during the assay procedure (Fig. 1b). First, the sample containing the biomarker(s) of interest is *D*ispensed onto the array. This triggers the "soluble" dAbs to *D*issolve into the sample and *D*iffuse toward the immobilized cAbs, forming a sandwich complex with the biomarker of interest. The resulting fluorescence intensity at the capture spots is proportional to the concentration of the analyte in the sample, which is *D*etected using a smartphone detector. As the smartphone-based detector was specifically designed for D4 fluorescent readout, it can be built at a fraction of the size and cost of traditional detectors, while maintaining clinical-grade performance independent of clinical infrastructure.

The D4 POCT platform is broadly applicable to diagnostics for many disease indications, as tests can be developed for any biomarker for which there is an Ab pair available. Herein, we provide detailed step-by-step instructions on how to fabricate the D4 POCT chips, operate the smartphone detector, generate dose–response curves from the data, and analyze results.

## 2 Materials

### *2.1 Growth of POEGMA Brushes*

1. Hydroquinone (HQ) and Monomethyl ether hydroquinone (MEHQ) Removal Column (DHR-4; Scientific Polymer Products Inc.).
2. Poly(ethylene glycol)methyl ether methacrylate (PEGMEM) average $M_n$ 300, contains 100 ppm MEHQ as inhibitor, 300 ppm BHT as inhibitor (Millipore Sigma).
3. 500 mL Dispensing burette with PTFE stopcock (DWK Life Sciences).

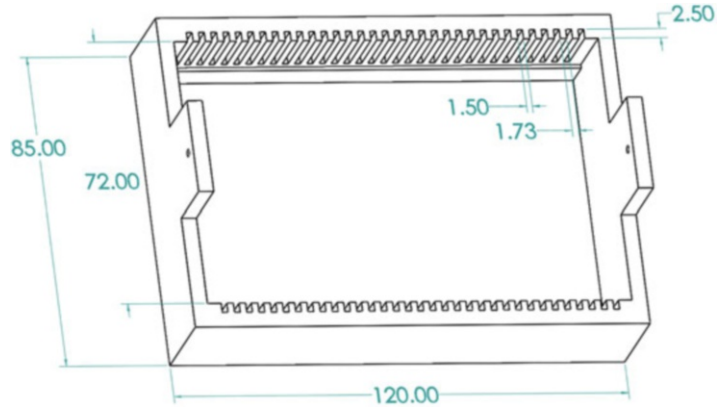


**Fig. 2** Dimensions for the custom PTFE holder used during SI-ATRP. Dimensions in mm

4. Lab stand with 2 vertically separated clamps (VWR International).
5. Two small disposable funnels, 40 mL (VWR International).
6. Two custom-made PTFE slide holders (Fig. 2) (emachineshop.com).
7. Nexterion glass slides B (Schott Inc.).
8. Fume hood.
9. ~20,100 × 130 mm rectangular glass staining dishes with lids (VWR International).
10. $SiO_2$ silicon wafer pieces (University wafers).
11. 25 g of 3-Aminopropyltriethoxysilane (APTES) (Gelest Inc.).
12. ~2 L of 200 proof (99.5% ethyl alcohol) ethanol (VWR International).
13. Centrifuge compatible with Beckman Coulter microplate carrier GH3.8 (362394) or similar assembly. (Beckman Coulter Inc.).
14. Two GH3.8 Beckman Coulter microplate carriers (Beckman Coulter Inc.).
15. Rubber stopper (VWR International).
16. Stainless steel laboratory cannula (VWR International).
17. 1,1,4,7,10,10-Hexamethyltriethylenetetramine (HMTETA) (Sigma-Aldrich).
18. Copper (II) bromide (Sigma-Aldrich).
19. Helium tank (Airgas Inc.).
20. Dichloromethane (DCM) (Sigma-Aldrich).
21. α-bromoisobutyrylbromide (BIB) (Sigma-Aldrich).

22. Triethylamine (TEA) (Sigma-Aldrich).
23. L(+) Sodium ascorbate (Sigma-Aldrich).
24. Argon tank (Airgas Inc.).
25. Glovebox (mBraun) Working gas: Argon.
26. Hydrogen peroxide (30%) (Sigma-Aldrich).
27. Sulfuric acid (Sigma-Aldrich).

### 2.2 Inkjet Printing of Abs

1. Monoclonal Interleukin 6 (IL-6) antibody (capture antibody), polyclonal IL-6 antibody (detection antibody), recombinant IL-6, monoclonal tumor necrosis factor alpha (TNF-α) antibody (capture antibody), polyclonal TNF-α antibody (detection antibody), TNF-α, monoclonal leptin antibody (capture antibody), polyclonal leptin antibody (detection antibody), recombinant human leptin. All proteins are available from R&D Systems (*see* **Note 1**).
2. Amicon Ultra 0.5 mL 100 kDa molecular weight cut-off (MWCO) filters (Sigma-Aldrich).
3. 1× PBS, without calcium and magnesium (Sigma-Aldrich).
4. Trehalose dihydrate (Sigma-Aldrich).
5. Alexa Fluor 647 antibody labeling kit (Invitrogen).
6. Scienion S11 sciFlexarrayer Inkjet Printer (Scienion).
7. PDC 70 type 3 tip (Scienion).
8. 384-well plate and 96-well plate (VWR International).
9. BioDot AD1520 BioJet Elite (Biodot).
10. TRUBlock (Meridian Life Science).
11. Nalgene Dessicator, 250 mm, with stopcock (VWR International).

### 2.3 D4 POCT Assembly and Generating a D4 Calibration Dose–Response Curve

1. Gravograph LS900 Laser Engraver (Gravotech Inc.).
2. 300LSE Double-sided adhesive, 0.17 mm (3 M).
3. 19.5″ × 19.5″ Clarex clear Acrylic, 1 mm (Astra Products Inc.).
4. 96-well deep well plate (VWR International).
5. Test media (Fetal Bovine Serum (FBS), Human Serum (HS), Human Whole Blood (HWB)) (Sigma-Aldrich).

### 2.4 D4 Fluorescence Imaging

1. Genepix 4400 (Molecular Devices).
2. Nokia Lumia 1020.
3. 638 nm 700 mW laser diode (Oclaro).
4. 1.1 Amp buck-boost laser diode driver.
5. 690/50 nm optical Filter (Semrock).
6. Collector Lens ($f_1 = 2.6$ mm, UCTronics).

7. uPrint SE Plus, Stratasys 3D printer.
8. 3D printed enclosure (acrylonitrile butadiene styrene plastic).
9. Dovetail linear translation stage with focusing knob (DT12, Thorlabs).
10. AAA battery holder.
11. Circuit switch and 22 AWG wire.
12. Red fluorescent beads (Cy5 ex/em, Polysciences).

### 2.5 Software

1. AutoCAD (Autodesk).
2. Gravostyle 8.0 software (Gravotech Inc.).
3. ImageJ (open source).
4. Excel (Microsoft).
5. GraphPad Prism (GraphPad Software).
6. Solidworks (Dassault Systemes).
7. Cura (open source).

## 3 Methods

The steps required for fabrication, assembly, testing, and analysis of the D4 POCT are outlined as a flow chart in Fig. 3. Various characterization techniques can be used to validate outcomes of certain steps. This Methods section will briefly discuss how to: prepare monomer solution for polymerization; fabricate nonfouling POEGMA brushes on glass slides; prepare, optimize, and print assay reagents onto the POEGMA brush; assemble and test the D4 POCT; and how to image and analyze the results of the test.

### 3.1 Removing Inhibitor from Monomer Solution

The PEGMEM monomer has inhibitors to prevent premature initiation of polymerization. These inhibitors must be removed prior to the polymerization process. This can be done by passing the PEGMEM solution through a hydroquinone (HQ) and monomethyl ether hydroquinone (MEHQ) Removal Column. This section details the steps to obtain inhibitor-free PEGMEM monomer for use in SI-ATRP.

1. Affix the 500 mL burette to the higher of the two clamps on the lab stand, then affix the SP2 column (DHR-4) to the lower clamp. Remove the two black caps of the inhibitor removal column. Place a disposable funnel at the top of the inhibitor removal column and align the burette outlet over the funnel. Place another small funnel at the top of the burette. Place a 50 mL beaker at the outlet of the inhibitor removal column.
2. With the stopcock of the burette closed, fill the column with PEGMEM. Slowly open the stopcock until the monomer starts to drip into the SP2 column. Carefully watch as the PEGMEM

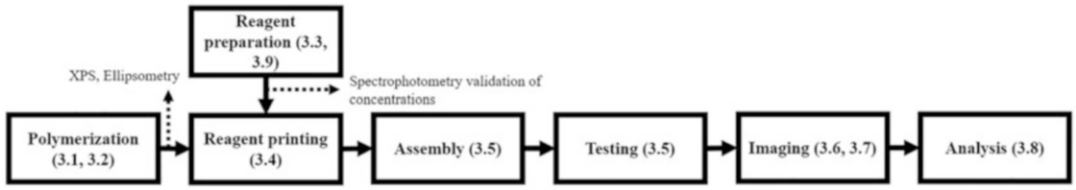


**Fig. 3** Flow chart detailing the steps of fabricating, assembling, testing, and analyzing the D4 POCT. Dotted lines indicate characterization techniques used to validate individual steps. The parentheses contain the associated Methods section number for each step

flows through the column to its outlet. Once saturated, the inhibitor-free PEGMEM will drip into the beaker. Collect the first 50 mL to pass through the removal column and discard.

3. Place a larger 500 mL beaker under the removal column to collect the rest of the PEGMEM solution. Adjust the stopcock such that the rate of flow into the column is roughly equal to the flow out. You want approximately 2–3 cm of PEGMEM sitting at the top of the SP2 column waiting to flow through with a visible amount of air above. Keep adjusting flow until these conditions are stable. Overflowing the column will cause PEGMEM to leak down the sides of the column into the beaker adding inhibitor-containing PEGMEM to your final solution (*see* **Note 2**). Each column can process 500 mL of PEGMEM.
4. After collecting the inhibitor-free PEGMEM, aliquot into 50 mL tubes and store at −20 °C until use. Do not leave at room temperature for an extended period.

### *3.2 Fabrication of POEGMA Brushes*

The core feature of the D4 POCT is the nonfouling polymer brush, grown using SI-ATRP. This section describes how to grow a POEGMA brush on previously untreated glass slides. First, glass slides are silanized with APTES. Second, BIB initiator is attached to the silanized surface. Finally, the POEGMA brush is "grafted from" the surface using the inhibitor-free monomer prepared in the previous section (Subheading 3.1). Polymerized slides are stable long term and can be fabricated in bulk. The following protocol can be scaled up or down as needed.

1. Open a fresh package of Nexterion glass slides and carefully place them into the custom PTFE holder making sure to only touch the edges of the slides and not the faces. A schematic of the PTFE holder with relevant dimensions is shown in Fig. 2. Rest a small silicon piece on top of the glass slides. Ensure the silicon piece undergoes every step of the following protocol, including wash steps (*see* **Notes 3** and **4**).

2. Inside the fume hood, add 250 mL of ethanol into a glass rectangular bowl and place on a magnetic stir plate. Add a stir bar and start stirring at 130–150 RPM. Do not apply heat.
3. Add 25 g of APTES into the bowl and allow to mix for 30 s.
4. Place the loaded PTFE holder into the glass rectangular bowl. Cover immediately and parafilm the lid to create an airtight seal.
5. Allow reaction to occur for 12–24 h (*see* **Note 5**).
6. Once the APTES reaction is complete, preheat an oven to (200 °C).
7. Arrange four clean rectangular dishes for sequential washing. Fill the first one with 250 mL of fresh ethanol, and the next three with 250 mL of DI water. Remove slides from the APTES solution, allowing excess liquid to drip, and then submerge completely into the prepared ethanol wash dish (*see* **Note 6**). Gently move the slide holder up and down to promote washing before moving the slide holder to the first of three DI water dishes. Repeat this process for the remaining two DI water dishes. Let the slide holder sit in the last DI water dish until they are loaded into the centrifuge.
8. Place two cleanroom wipes at the bottom of the centrifuge assemblies and load the deck of slides into the assembly. Load centrifuge, balance, and spin at 150 × *g* for 6 min (*see* **Note 7**).
9. Remove the slides from the centrifuge and place them into a clean bowl with a lid to prevent dust from contaminating the slides, leaving a small opening for moisture to evaporate. Load into the preheated oven and bake for 2 h. After loading, turn off the oven to allow gradient cooling.
10. (Do this step while APTES is curing). Combine 350 mL of DI water, 75 mL of inhibitor-removed PEGMEM, 50 μL of HMTETA, and 23–30 mg of Cu(II)Br into a 500 mL glass bottle equipped with a rubber stopper. Swirl the bottle to mix the reagents. Stick two to three needles into the rubber stopper to allow air to be displaced from inside the bottle. Stick a clean cannula through the rubber stopper and push to the bottom of the glass. Connect the cannula to the helium gas cylinder. Increase the gas pressure until a light bubbling of the mixture can be seen. Degas for at least 3 h. The mixture will turn from cloudy to clear when done degassing, and do not stop degassing until the solution is optically completely clear to the eye.
11. After curing, retrieve the APTES coated slides from the oven and set them aside to cool to room temperature. Inside the fume hood, place a clean rectangular dish onto a magnetic stir plate, and add a new clean stir bar. Fill the dish with 250 mL of DCM. Set the stir plate to 130–150 RPM. Add 5 mL of TEA

followed by 5 mL of BIB, and stir the solution for ~30 s before adding the slide holder. Cover with a glass lid. Allow the reaction to run for 30–45 min. The mixture will turn from clear to a slight yellow to orange color (*see* **Note 8**).

12. Repeat the sequential washing procedure from **step 7** but add an additional wash using DCM to start. Do this first DCM wash and subsequent transfer to ethanol solution inside of the fume hood.
13. Place two cleanroom wipes at the bottom of the centrifuge assemblies and load the slide holders. Load centrifuge with the assemblies ensuring it is properly balanced and spin at 150 × *g* for 6 min.
14. Measure 600–700 mg of sodium ascorbate and place in a loosely screwed 15 mL disposable conical.
15. Move the ATRP initiator functionalized glass slides into a new and clean PTFE holder (*see* **Note 9**).
16. Place slide holder into a new clean rectangular dish and cover with a glass lid. Transfer degassed monomer solution, ATRP initiator functionalized glass, and sodium ascorbate into a glovebox (Argon, with <30 ppm $O_2$ levels). Once inside, add the sodium ascorbate to the degassed monomer solution swirling vigorously until completely dissolved. The solution will turn from a light blue to a light purple color. Add the contents into the glass bowl containing the ATRP initiator functionalized glass. Cover with the glass lid. Polymerize for 3–5 h at room temperature.
17. Retrieve the dish from the glovebox. Conduct 4–5 DI water washes using the same sequential wash protocol as above. Do not wash with ethanol or DCM.
18. Place two cleanroom wipes at the bottom of the centrifuge assemblies and load the slide holders. Load centrifuge with the assemblies ensuring it is properly balanced and spin at 150 × *g* for 6 min.
19. Allow POEGMA-coated glass slides to air dry. Store POEGMA-functionalized glass slides in the original container to prevent the slide surfaces from rubbing against each other. Label appropriately. Store under vacuum desiccation with the Nalgene desiccator connected to house vacuum or vacuum pump until use (at least 24 h). Confirm the thickness of the POEGMA brush by running ellipsometry on the silicon wafer piece. Brush thicknesses >10 nm will be nonfouling; however, a 3–5 h polymerization should yield a thickness of approximately 30–60 nm [4, 6]. X-ray photoelectron spectroscopy (XPS) should be performed on the final polymerization

product to validate the elemental composition of the polymer brush on the surface.

### 3.3 Preparing Reagents for Inkjet Printing and Running Assays

The D4 POCT has unique requirements for how Ab reagents are prepared before inkjet printing. The cAb, dAb, and antigens for the immunoassays are either purchased commercially or recombinantly expressed in-house. The cAb and dAb must be buffer exchanged to remove preservatives prior to being printed. This section details the step-by-step process and requirements for the preparation of the cAb and dAb to be used for printing, and antigens for conducting an assay (Subheading 3.4).

We recommend that new adopters of this technology first fabricate a single analyte assay for IL-6 because the IL-6 Ab pair has a high affinity, so any deficiencies in assay fabrication or in carrying out the assay will be revealed by a LOD that is significantly higher than the low picomolar LOD that is expected, if all the fabrication and assay steps are carried out correctly. Next, we recommend fabricating and testing a multiplexed assay for two analytes on the same chip. The recommended analytes of the two-plex assay are: IL-6 and TNF-α or leptin.

1. Buffer exchange each cAb into 0.2 μm filtered 1× PBS with 0.05–0.1% (w/v) trehalose using an Amicon Ultra 0.5 mL 100 kDa MWCO filter. Concentrations for printing must be determined empirically, as discussed in Subheading 3.11. Generally, the cAb concentration will be in the range of 0.25–2.0 mg/mL. If the cAb concentration in the printing solution is <1 mg/mL, we recommend supplementing the printing solution with bovine serum albumin (BSA) to adjust the total protein concentration to be at least 1 mg/mL. This will help ensure a homogenous capture spot, by minimizing the chance of patchy or "coffee ring" morphologies.
2. Conjugate fluorescent dye to the dAbs using the AlexaFluor 647 Antibody Labeling Kit (or other fluorophore) according to manufacturer's instructions. After conjugation, use a UV-vis spectrophotometer to measure the protein concentration and degree of labeling (DoL), a measure of moles of dye per mole of protein. We use a NanoDrop for as it enables us to work with a small—2 μL—volume. Ensure that the DoL is acceptable for the given dye (i.e., for AF647, DoL = 2–7). Prior to printing, dAbs should be buffer exchanged into 0.2 μm filtered 1× PBS supplemented with 5–10% (w/v) trehalose (*see* **Note 10**).

$$\text{Protein concentration (M)} = \frac{\left[A_{280} - \left(A_{\text{dye}} * \text{CF}_{280}\right)\right] * \text{dilution factor}}{203,000}$$

$$\text{DoL} = \frac{A_{\text{dye}} * \text{dilution factor}}{\varepsilon_{\text{dye}} * \text{Protein concentration (M)}}$$

Concentrations for printing must be determined empirically for each individual dAb first, and then for the entire dAb "cocktail" (mixture of all dAbs) if developing a multiplexed test. The procedure for identifying dAb concentration is described in Subheading 3.11.

3. The antigens should be aliquoted into convenient sizes for running individual dose–response curves and stored according to manufacturer's instructions—typically −20 °C or −80 °C to minimize freeze–thaw cycles. For convenience, 10 μL aliquots are often stored at 100 μg/mL in 1× PBS.

### 3.4 Printing of Antibodies

Several companies (e.g., Arrayjet, Scienion, Perkin Elmer, M2 automation, MicroFab, and BioDot) sell noncontact inkjet printers specifically for biomedical applications (i.e., DNA/protein microarrays, biosensors) [10]. For D4 chip fabrication, any of these commercially available inkjet printers can be used that can achieve consistent spot morphologies and spot volumes; we use the Scienion S11 sciFlexarrayer for depositing cAb and the BioDot AD1520 Biojet Elite for depositing, trehalose pads, TRUblock, and dAb. The sciFlexarrayer provides picoliter precision for ultralow volume spots needed for the cAb. The BioDot is used for printing dAb spots because larger volume spots can be printed more quickly. Here, we describe the protocol for developing a two-plex test (against IL-6 and TNF-α) and a single analyte test (against leptin), as outlined in Joh et al. [3]. The fabrication process can be easily modified to include additional assays on the D4 chip. The outcome of this section will be D4 POCT chips that with a minor assembly step are ready for use.

1. Initialize and prime the Scienion S11 sciFlexarrayer liquid handling system with PDC-70, type-3 piezo dispense capillary tip.
2. Load the POEGMA-coated glass slides onto the Scienion vacuum platform leaving no gaps between the slides. Activate the vacuum.
3. Load a 384-well plate in the refrigerated sample holder. Add 10–20 μL of previously prepared cAbs into individual wells.
4. Starting with the initial voltage and pulse width identified for the Piezo Dispense Capillary, adjust the voltage and pulse width appropriately such that a consistent ~360 ± 5 pL droplet is obtained.
5. Design a print field. The IL-6 and TNF-α multiplexed test will consist of five spots for each biomarker for assay development. For assays to be imaged with the smartphone detector, only two spots should be printed to ensure they can be evenly excited. Leave a 250 μm pitch between spots within the same row, and 500 μm pitch between rows of spots. Repeat the print

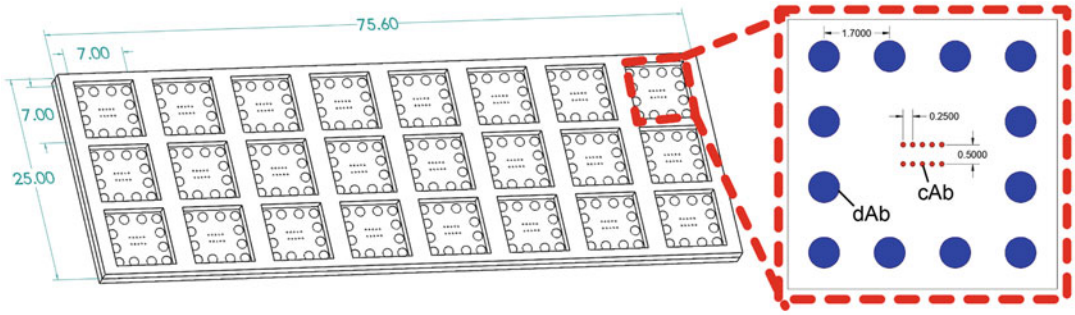


**Fig. 4** (Left) Schematic of the D4 after Ab printing and assembly with important dimensions. (*Right*) Close up of one D4 assay with Ab spacing for dAb (blue) and cAb (red). Dimensions in mm

field to make a 3 × 8 grid with 9.178 mm center-to-center spacing in the X direction, and 8.000 mm center-to-center spacing in the Y direction. Adjust the X and Y offsets of the full slide 3 × 8 grid such that the pattern is centered on the glass. The final printed array will resemble the design shown in Fig. 4. The same pattern can be used for the single analyte leptin test for additional redundancy (10 spots over 5) or printed as a single row of five spots (*see* **Note 11**).

6. Run the print procedure for the number of slides loaded, ensuring that the tip is flushed and cleaned between printing each cAb to prevent cross-contamination. The Scienion s11 sciFlexarrayer can print up to 40 slides per batch. After completion, the POEGMA substrate will be successfully functionalized with cAbs for biosensing.
7. When printing is complete, turn off the vacuum and carefully unload the slides from the deck and store in their original boxes with appropriate labelling.
8. Vacuum desiccate the slides for >2 h before any further processing.
9. Initialize the BioDot AD1520 liquid handling system. Flush the system with ethanol, followed by DI water, and then DI water supplemented with 10% (w/v) trehalose (all solutions should be 0.2 μm sterile filtered).
10. Load a 96-well plate into the BioDot and add the dAb cocktail with at least 80 μL excess of the desired print volume to the well plate. The amount of dAb per assay may change depending on what is determined in Subheading 3.11. Load ~400 μL of TRUBlock into an additional well. Set dispenser for 100 nL drop volumes (*see* **Note 12**).
11. The printing pattern consists of a 4 × 4 frame of 12 printed spots with 1.7 mm center-to-center spacing for all spots. There is a 9.178 mm center-to-center spacing in the *X*-direction and

8.000 mm center-to-center spacing in the $Y$-direction between the individual arrays. This pattern is centered on the glass slide and can be visualized in Fig. 4.

12. Print three passes of the spot pattern with the 10% (w/v) trehalose solution that is already primed from the initialization process. Then print the calculated amount of dAb as determined in Subheading 3.11. Then print two passes of TRU-Block (*see* **Note 13**).
13. Allow slides to dry in place for at least 15 min to ensure that the spots maintain their shape when they are unloaded.
14. Unload slides and store them in the original slide boxes and vacuum desiccate for >2 h and leave under desiccation until use (*see* **Note 14**).

### 3.5 Assembly of D4 POCT

The described iteration of the D4 POCT contains 24-tests on a single POEGMA-coated glass slide. To run all 24 tests in parallel without cross contamination, acrylic wells are adhered to POEGMA substrate to compartmentalize the individual tests. Here we describe the process of designing and fabricating these acrylic wells and how to attach them to the reagent-printed D4 slides.

1. Using an eCAD software such as AutoCAD create a 3 × 8 array of 7 $mm^2$ centered in a 25 × 75.6 mm rectangle.
2. Peel one side of the protective sheet, passivating the double-sided adhesive; peel one side of the protective cover on the acrylic sheet. Stick the exposed adhesive to the acrylic ensuring no bubbles are formed. Place the entire sheet, adhesive side up into the laser cuter.
3. Using the Gravograph laser cutter (with Gravostyle software) import the design and duplicate to a number that fits onto the acrylic sheet. Vector mode cut (Speed 20%, Power 75%, Repetitions 1, DPI 3600, Auto-focus selected).
4. Collect the cut patterns. Peel the backing on the adhesive side and carefully align and stick to the Ab printed polymerized glass slides. Press firmly to promote adhesion. Remove the remaining protective coating on the acrylic. The final assembly will resemble the design in Fig. 4 (*Left*).

### 3.6 Generating a D4 Calibration Dose–Response Curve

This section details the steps for creating a D4 calibration dose–response curve from a D4 assay, including the preparation of biomarker dilutions, and how to run, clean, and store the assay. The outcome of this section will be ready-to-image D4 chips. This section is designed for generating a calibration dose–response curve. If testing patient samples, skip **steps 1** and **2**.

1. Determine the highest test concentration desired for each biomarker. Calculate the amount of each antigen and any additional volume of media such that when mixed together the antigen cocktail consists of all tested antigens at their respective high concentrations (*see* **Note 15**).
2. Using a 96-well deep well plate perform 21 half-dilutions starting at the highest desired test concentration. Ensure the starting volume is double the needed volume as half will be lost to the subsequent dilution plus 50 μL excess to ensure homogenous sample volumes and compositions. Use the remaining three tests to run triplicate blanks (*see* **Note 16**).
3. Once prepared, add 50 μL of sample to each of the 24 wells of a single D4 chip. Incubate the samples for 1 h. This is best done in a dark place to prevent any premature photobleaching of the fluorophore.
4. After incubation, promptly dunk the slides into a 50 mL conical tube of wash buffer (0.1% Tween in 1× PBS). Secure the cap and gently shake up and down to promote the removal of sample media.
5. Remove the slide from the conical wash tube and place into a 50 mL conical tube of DI water and repeat the shaking process. Repeat the DI water wash two more times.
6. Load the slides into a 2000 RCF mini benchtop centrifuge equipped for spinning standard microscope glass slides. Spin for 15 s. Allow slides to air dry.
7. Store the slides under vacuum desiccation until imaging.

### 3.7 Smartphone Detector Fabrication

The portable smartphone detector is designed as an accessory to an existing commercial smartphone. The initial prototype was developed for a Nokia 1020 Smartphone camera due to its 41-megapixel rear-facing camera, but the same workflow described in this section can be adopted for any modern smartphone. The design utilizes a 75° oblique-angle excitation from the backside of the sample, which avoids the need for expensive dichroic optical elements and allows for an inexpensive and compact design. Figure 5 shows a cross-sectional view of the device prototype. The laser excites the dAb of the final sandwich complex with a fluorescence emission peak centered at ~670 nm. This light is filtered by the 690/50 nm bandpass optical filter, magnified by the external lens, and then collected by the Nokia smartphone lens and camera. Here we describe the design and manufacturing of the portable smartphone detector with a focus on key specifications such as the selection and location of optical components. A person with intermediate knowledge of a 3D-modeling software (Solidworks) and basic knowledge of 3D-printing software (Cura) will be able to develop a similar prototype with the same functionality.

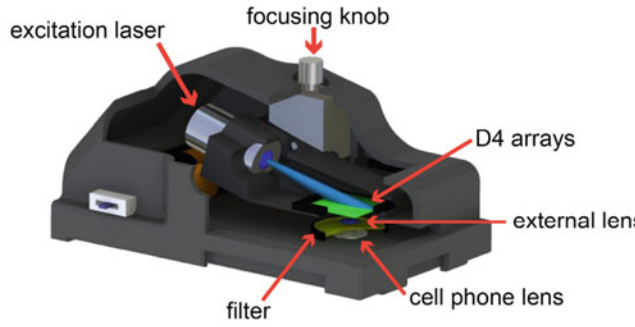


**Fig. 5** Cross section of the detector attachment that interfaces with a smartphone. Critical elements are labeled. Reproduced from "Inkjet-printed point-of-care immunoassay on a nanoscale polymer brush enables sub-picomolar detection of analytes in blood" 2017 from PNAS

1. For orientation, when the device is lying flat, the smartphone's rear-facing camera should be facing up vertically, with the phone touchscreen facing down vertically.
2. Affix the 690/50 nm optical filter as close to the camera's integrated lens as possible (<1 mm).
3. Affix the Collector Lens ($f_1 = 2.6$ mm) ~1 cm above the filter.
4. The sample slide should be situated as close as possible (>1 mm) to the external lens (~15 mm from the integrated camera lens).
5. The sample glass slide should be on a removable slide-holder for easier sample loading while also allowing horizontal translation of the sample to image multiple regions on the same slide. Ensure that the holder does not support the slide by its edges to not impede the passage of laser light through the substrate.
6. Collimate the excitation laser assembly by rotating the threaded lens attachment included in the laser assembly.
7. Affix the excitation laser at an incidence of ~75° from the back side and ~1.5 cm from the area of excitation on the backside of the sample slide.
8. Mount the laser and slide stage assembly together onto the dovetail translational stage. The translational stage's adjustment knob should be accessible to allow manual focus of the sample with respect to the camera's lens without shifting the region of laser excitation.
9. This configuration will yield a 0.8 $mm^2$ region for analysis. As a conservative approach only two spots of the D4 assay are imaged at a time (0.4 $mm^2$) with the results for larger arrays easily being stitched in post-processing.

10. A user-accessible integrated binary toggle switch can be integrated into the laser power supply wiring to allow the laser to be powered by either a AAA battery pack or a 5 V 1A barrel plug power supply.
11. Design and 3D print an enclosure for the optical components to avoid all possible external light from interfering with imaging. The enclosure should be printed with black acrylonitrile butadiene styrene (ABS) filament.
12. A combination of M3 socket cap screws and quick drying epoxy can be used to affix the necessary components to the enclosure.

### 3.8 Imaging

The assays are imaged on the Axon Genepix 4400 Microarray scanning system for initial assay development and optimization (Subheading 3.11). The standard operating procedure for the Genepix is followed for loading and imaging chips (Typical settings: 750 Gain, 100 Power, 5 μm resolution, Cy5 ex/em filter). Image analysis for the Genepix and the smartphone detector are the same and is described in Subheading 3.9. Once the assay printing conditions are optimized, assays should be imaged using the smartphone detector to determine the assay performance metrics (*see* Subheading 3.10).

1. Turn on the Nokia Lumia 1020 cellphone and navigate to the camera application.
2. Load three new AAA batteries into the battery holder or plug in the 5 V barrel jack to power the laser circuit.
3. Pipette 20 μL of low-density polystyrene fluorescent beads on an unpolymerized standard microscope slide and let it dry. Load the fluorescent sample into the imaging chamber and turn on the laser. Then using the dovetail focusing knob, adjust the focus so the sample is clearly defined and not blurry. The focusing knob will translate the slide closer or farther from the external lens. To help with focusing, change camera settings to maximum gain (high ISO) and low exposure time (high frame rate) (*see* **Note 17**).
4. Once focused, set the camera settings to lower gain and higher exposure for higher quality and lower noise images. This setting is dependent on your sample, laser beam intensity, and camera sensitivity; therefore, these parameters need to be optimized on a case-by-case basis.
5. Once the settings are properly set, remove the focusing sample and insert the D4 chip. Be sure to turn the laser off before loading. Then, turn on the laser and take a picture with the cell phone camera. After exposure is complete, turn off the laser (*see* **Note 18**).

6. Save all images with proper identification for later analysis. The initial images are recorded in raw DNG format and need to be converted to .tiff file formats by ImageJ for analysis.

### 3.9 Image Analysis

The fluorescence intensity of the cAb spots in a D4 chip is proportional to the concentration of the analyte of interest. As the POEGMA substrate is nonfouling, the intensity of the background is low. The average pixel intensity within the cAb spots is quantified using the open-source ImageJ software package. Figure 6 shows examples of the fluorescent spots as imaged by on a Genepix scanner (left) and on the mobile phone platform (right). The outcome of this section will be spot and background intensities for each tested data point.

1. Launch ImageJ and then open the .tiff image file of the D4 array you wish to analyze.
2. For each capture spot, draw a circle to establish a region of interest (ROI) that contains the entire spot while minimizing the inclusion of background. With Analyze, measure the ROI and record the average of the five spots (or two spots if using smartphone detector) for each biomarker of interest (*see* **Note 19**).
3. To measure the background, draw a rectangle in close proximity to the capture spots without overlapping any fluorescent spots (cAb or dAb), and use Analyze to determine the average fluorescence intensity. Dose-response data can then be generated with the average fluorescence intensity of the capture spots or with the background fluorescence intensity subtracted from the average fluorescence intensity of the capture spots of each analyte (*see* **Note 20**).

### 3.10 D4 Analysis

Prior to testing clinical samples, calibration dose–response curve (CDRC) for each biomarker in the D4 POCT should be generated. These CDRCs are then used to determine unknown concentrations of analyte in clinical samples. The CDRC's can also be used to characterize the figures-of-merit (FOM) for each assay, such as dynamic range (DR), limit-of-detection (LOD), and limit-of-blank (LOB). Figure 6 shows CDRC's for leptin on the benchtop Genepix scanner and the mobile phone scanner and Fig. 7 shows CDRC's for the 2-plex IL-6 and TNF-α test, demonstrating the specificity and sensitivity of the test [11]. This section details how to take the raw fluorescence intensities obtained in Subheading 3.9 to generate CDRC's. One of the outputs of this section is the five-parameter logistic curve (5-PL). This is a variation of a four-parameter logistic curve, which is the standard for a dose response that plateaus at the top and bottom of the curve and is symmetrical at the midpoint. The 5-parameter variation does not require the curve to be symmetrical making it more versatile for responses

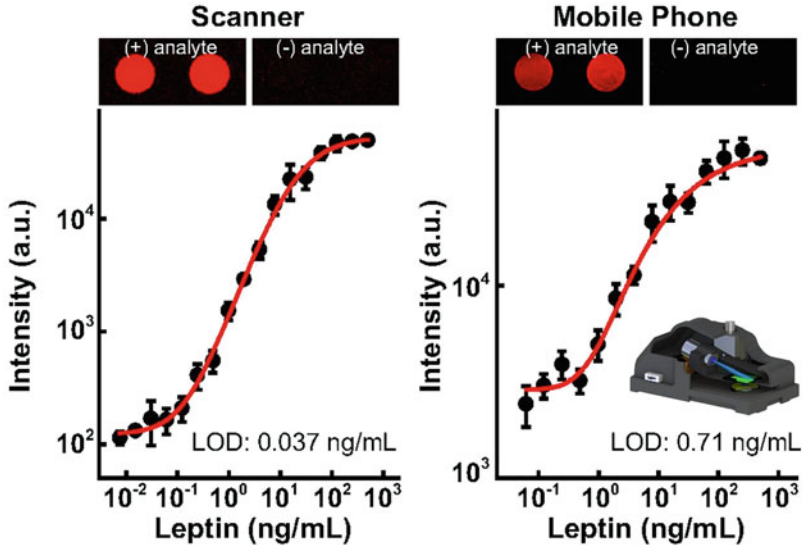


**Fig. 6** Dose response comparison between benchtop scanner (left) and mobile phone detector (right) for leptin. Representative spot morphologies are shown at the top. Reproduced from "Inkjet-printed point-of-care immunoassay on a nanoscale polymer brush enables sub-picomolar detection of analytes in blood" 2017 from PNAS

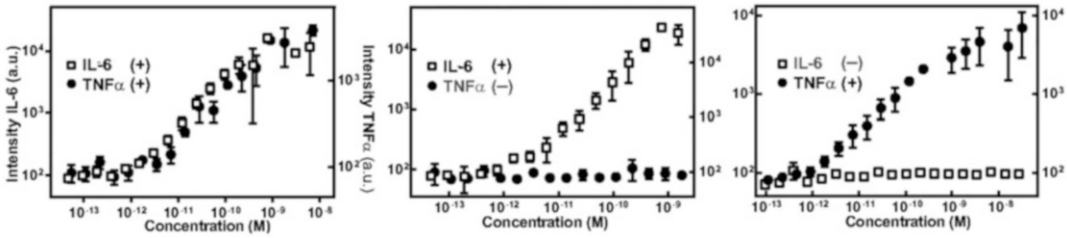


**Fig. 7** TNF-α and IL-6 multiplexed dose response with both analytes present (left), only IL-6 (middle), and only TNF-α (right) to demonstrate specificity. Reproduced from "Inkjet-printed point-of-care immunoassay on a nanoscale polymer brush enables sub-picomolar detection of analytes in blood" 2017 from PNAS

generated by the D4 that may not be symmetrical. The outcome of this section will be a CDRC which can be used to calculate the LOD and LOB using GraphPad Prism and Excel software or for testing unknown samples.

1. To create CDRCs, plot the biomarker concentrations on the *x*-axis and D4 fluorescence intensity on the *y*-axis in a graphing software (i.e., Excel or GraphPad Prism). For visualization, plot using a log-log scale.
2. For analysis of FOM, the data should be fit to a 5-parameter logistic curve (5-PL) [12].
3. Calculate the LOB and LOD, where LOB refers to "the highest apparent analyte concentration expected to be found when

replicates of a blank sample containing no analyte are tested" and LOD refers to "the lowest analyte concentration likely to be reliably distinguished from the LOB and at which detection is feasible." [11].

4. These can be calculated from the raw data, however to determine the LOB and LOD in units of concentration, the resulting 5-PL fit must be used.

$$\text{LoB} = \text{Mean}_{\text{blank}} + 1.645 * \text{SD}_{\text{blank}}$$

$$\text{LoD} = \text{LoB} + 1.645 * \text{SD}_{\text{low concentration}}$$

5. Log-transform all $x$ and $y$ values. Fit the log-transformed data to the 5-PL curve. In GraphPad, the following values will be fit (LogEC50, Hill slope, $S$, Top, Bottom, EC50).
6. Using these fit parameters and the equations below a curve will be generated that is fit to the data set. It will need to be inverse log transformed to be represented with the original data set:

$$\text{Log}X_b = \text{LogEC50} + \frac{\text{Log}\left(2^{1/S} - 1\right)}{\text{Hill slope}}$$

$$\text{Numerator} = \text{Top} - \text{Bottom}$$

$$\text{Denominator} = \left(1 + 10^{(\text{Log}X_b - X) * \text{Hill slope}}\right)^S$$

$$Y = \text{Bottom} + \frac{\text{Numerator}}{\text{Denominator}}$$

7. Substitute the log-transformed fluorescence intensity value for LOD and LOB (calculated above) for $Y$. Then, $X$ can be solved for to determine the concentrations of the LOD and LOB for each biomarker in terms of concentration in Excel.

### 3.11 Procedure for Empirically Determining Optimal cAb and dAb Concentrations for Printing

A D4 POCT can be developed against any biomarker for which an Ab pair exists. However, printing conditions for each Ab pair need to be optimized empirically for each individual assay. This section details the steps to empirically determine the optimal cAb and dAb concentrations for printing.

1. Using the same printing protocol as described above, print cAb at a variety of concentrations in a single array (for example: 0.5 mg/mL, 1 mg/mL, and 2 mg/mL). Print the trehalose, dAb, and TRUBlock stack systematically varying the concentrations of dAb on each of the chip's 8 rows such that subsequent rows of arrays contain an increased amount of dAb as seen in Fig. 8 (*see* **Note 21**).
2. Incubate 50 μL of blank (antigen-free) FBS on each array for 1 h. Wash, scan, and analyze the cAbs as above.

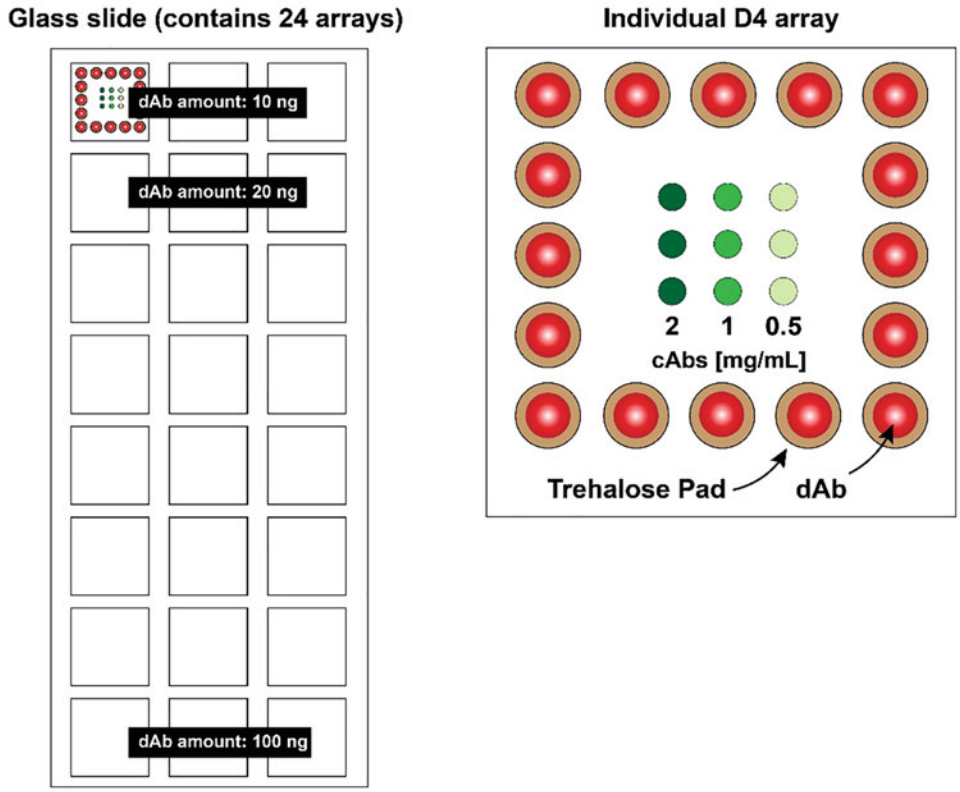


**Fig. 8** Visual explanation of how to systematically vary Ab concentrations for identification of optimal printing conditions

3. Systematically evaluate the fluorescence intensities of all the capture spots. Look for the dAb concentration condition where the intensity at the capture spots becomes elevated compared to the previous row. This will mark the onset of cross-reactivity. Once this threshold concentration has been identified, reduce dAb print concentration by 20%. Choose the cAb concentration that yields the best spot morphology. Repeat **steps 1–3** for each dAb.
4. Once the optimal dAb concentration is determined, combine all dAbs into a cocktail and perform the cross-reactivity screen (**step 3**) again with all the cAbs at their optimal concentrations. The total Ab concentration in the dAb cocktail may need to be adjusted (*see* **Note 22**).

## 4 Notes

1. These are specific examples. Any identified Ab pair can be used depending on the biomarker of interest in this system following the same protocols.
2. When removing inhibitor from the monomer, add cleanroom cloth at the top of the SP2 column so that if the monomer overflows, it will get absorbed in the cloth and not fall into your processed solution.
3. Including a small piece of $SiO_2$ silicon wafer during the entire polymerization process allows for ellipsometry measurements to be taken to evaluate the surface thickness at different steps of the protocol to confirm POEGMA growth and to troubleshoot if something goes wrong.
4. In addition to standard washing of the slide holders, they can be piranha cleaned to ensure the removal of previous reagent or growth. In a piranha safe Pyrex bowl that is large enough for the slide holders, make Piranha solution, which is a 3:1 Sulfuric acid:30% hydrogen peroxide solution and submerge slide holders in this solution. Incubate overnight. Follow proper safety precautions and protocols when working with piranha solution. Addition of hydrogen peroxide to sulfuric acid is a highly exothermic process and the piranha solution can react violently with organic compounds and has the ability to explode [13].
5. Typically, performing polymerization over two days is recommended. Start the APTES the night before the rest of the steps and start as early as possible the following day.
6. If the slides look cloudy or have precipitates on the surface after APTES functionalization, discard them.
7. If polymerizing an odd number of slide holders quickly measure the mass of one centrifuge assembly with the lid and wipes. Use that calculated mass to properly balance (within 10 g) the other side of the centrifuge. To circumvent this issue, use an even numbers of slide decks.
8. If the BIB is orange/red when pipetting from the stock it may have decomposed, and a new stock should be used.
9. Switch slide holders after the attachment of the ATRP initiator to avoid polymer growth on slide holders. It is best to keep half of the PTFE holders for prepolymerization steps, and the other half for the final polymerization step.
10. ThermoFisher provides a detailed troubleshooting guide on their website should the DoL be too low.

11. If multiplexing more than 2 biomarkers, use the same spacing convention (250 μm within rows, 500 μm between rows). Each row should correspond to a target analyte. Do not exceed a 3.3 × 3.3 mm square area or the capture spots will be too close to the subsequently printed detection spots.
12. The 80 μL excess during BioDot printing accounts for an estimated 50 μL "dead volume" that the tip cannot pick up without aspirating air +6 μL that is dispensed during priming steps +10 μL buffer as to ensure that the last drops are not diluted before printing. The BioDot can only aspirate a maximum of 250 μL at once, and the wells can typically only hold 400 μL. Depending on the number of slides printed, multiple aspirations of dAb may be needed.
13. If printing 1–7 slides, introduce a 2-min delay between printing steps to allow the spots to dry before the next printing pass.
14. Instead of a vacuum desiccator, storing POEGMA coated slides in a vacuum sealed pouch with silica desiccant is acceptable.
15. Typically, 21 half-dilutions are used to create a dose response that spans 6-logs. The physiologically relevant range of the antigen should be well within the tested range of concentration.
16. Described volumes are assuming $n = 3$ per dose concentration (3 chips in parallel) at 50 μL per test. This leaves a 50 μL excess to better ensure pipetting errors do not occur. These volumes can be adjusted depending on experimental conditions.
17. For camera focusing, around 10 fps is adequate; lower frame rates make focusing difficult.
18. Turn off the laser when not imaging or focusing to avoid photodamaging the samples or overheating the laser.
19. Even though the smartphone detector can only measure two spots at a time, arrays with more than two spots can be quantified by taking multiple images. The individual resulting intensity values are easily aggregated when analyzing the results in Excel or GraphPad.
20. Calibration dose–response curves can be generated with or without the subtraction of the average background intensity from the average intensity of the spot, as long as the choice is consistent through all analysis.
21. As a starting point, consider adjusting the lowest amount of dAb printed to be 10 ng and the highest to be 100 ng as demonstrated in Fig. 8.
22. The total dAb concentration will likely need to be titrated to avoid an elevation in background signal from the presence of

excess dAb in solution for multiplexed tests. To account for this, lower the initial concentration of dAbs tested during multiplexed optimization compared to the optimal concentrations determined previously for single dAb concentrations.

## References


1. Dincer C, Bruch R, Kling A, Dittrich PS, Urban GA (2017) Multiplexed point-of-care testing—xPOCT. Trends Biotechnol 35 (8):728–742
2. van Weemen BK (2005) The rise of EIA/E-LISA. Clin Chem 51(12):2226–2226
3. Joh DY, Hucknall AM, Wei Q, Mason KA, Lund ML, Fontes CM, Hill RT, Blair R, Zimmers Z, Achar RK, Tseng D, Gordan R, Freemark M, Ozcan A, Chilkoti A (2017) Inkjet-printed point-of-care immunoassay on a nanoscale polymer brush enables subpicomolar detection of analytes in blood. Proc Natl Acad Sci U S A 114(34):E7054–E7062
4. Ma H, Li D, Sheng X, Zhao B, Chilkoti A (2006) Protein-resistant polymer coatings on silicon oxide by surface-initiated atom transfer radical polymerization. Langmuir 22 (8):3751–3756
5. Hucknall A, Simnick AJ, Hill RT, Chilkoti A, Garcia A, Johannes MS, Clark RL, Zauscher S, Ratner BD (2009) Versatile synthesis and micropatterning of nonfouling polymer brushes on the wafer scale. Biointerphases 4 (2):FA50–FA57
6. Ma H, Wells M, Beebe TP, Chilkoti A (2006) Surface-initiated atom transfer radical polymerization of oligo(ethylene glycol) methyl methacrylate from a mixed self-assembled monolayer on gold. Adv Funct Mater 16 (5):640–648
7. Hucknall A, Rangarajan S, Chilkoti A (2009) In pursuit of zero: polymer brushes that resist the adsorption of proteins. Adv Mater 21 (23):2441–2446
8. Hucknall A, Kim DH, Rangarajan S, Hill RT, Reichert WM, Chilkoti A (2009) Simple fabrication of antibody microarrays on nonfouling polymer brushes with femtomolar sensitivity for protein analytes in serum and blood. Adv Mater 21(19):1968–1971
9. Heggestad JT, Fontes CM, Joh DY, Hucknall AM, Chilkoti A (2019) In pursuit of zero 2.0: recent developments in nonfouling polymer brushes for immunoassays. Adv Mater 32 (2):1903285
10. McWilliam I, Chong Kwan M, Hall D (2011) Inkjet printing for the production of protein microarrays. Methods Mol Biol 785:345–361
11. Armbruster DA, Pry T (2008) Limit of blank, limit of detection and limit of quantitation. Clin Biochem Rev 29(Suppl 1):S49–S52
12. Gottschalk PG, Dunn JR (2005) The five-parameter logistic: a characterization and comparison with the four-parameter logistic. Anal Biochem 343(1):54–65
13. Duke University: Occupational & Environmental Safety Office (2017) Duke OESO guidelines for safe use of piranha. https://www.safety.duke.edu/sites/default/files/GuidelinesPiranha.pdf

# Chapter 20

# Micromachined Optical Fiber Sensors for Biomedical Applications

**Chen Zhu, Rex E. Gerald II, and Jie Huang**

## Abstract

Optical fibers revolutionized the rate of information reception and transmission in telecommunications. The revolution has now extended to the field of physicochemical sensing. Optical fiber sensors (OFSs) have found a multitude of applications, spanning from structural health monitoring to biomedical and clinical measurements due to their unique physical and functional advantages, such as small dimensions, light weight, immunity to electromagnetic interference, high sensitivity and resolution, multiplexing, and remote operation. OFSs generally rely on the detection of measurand-induced changes in the optical properties of the light propagating in the fiber, where the OFS essentially functions as the conduit and physical link between the probing light waves and the physicochemical parameters under investigation. Several advanced micromachining techniques have been developed to optimize the structure of OFSs, thus improving their sensing performance. These techniques include fusion splicing, tapering, polishing, and more complicated femtosecond laser micromachining methods. This chapter discusses and reviews the most recent developments in micromachined OFSs specifically for biomedical applications. Step-by-step procedures for several optical fiber micromachining techniques are detailed.

**Key words** Optical fiber sensors, Micromachining, Biomedical, Biomechanical, Healthcare, Biosensors

## 1 Introduction

The fiber optic field has attracted extensive interest and undergone tremendous growth and advancement since the first realization of optical fibers as a telecommunication medium by C. Kao in 1960 [1]. The rapid development of optical fibers has led to the emergence of various high-quality, miniaturized, and affordable optoelectronic components and devices, resulting in numerous ideas for practical implementations using optical fibers, ranging from high-speed, long-haul, and large-capacity telecommunications, optical imaging to high-power light delivery. Optical fibers have also found applications in the sensing field because of their unique properties, such as small dimensions, light weight, immunity to electromagnetic interference (EMI), and low-transmission loss [2].

Miguel R. Ossandon et al. (eds.), *Biomedical Engineering Technologies: Volume 1*, Methods in Molecular Biology, vol. 2393, https://doi.org/10.1007/978-1-0716-1803-5_20, 

Optical fiber sensors (OFSs) have been widely and successfully used in an expansive range of sensing applications, such as structural health monitoring, down-hole monitoring, chemical and biological sensing, medical imaging, and environmental monitoring for the past four decades [3]. OFSs provide a convenient way of implementing optical sensing using integrated optics, simply by the direction of light to and collection of light from the regions under investigation via optical fibers. The OFS for biomedical applications was initially introduced in the field of endoscopy in the 1960s; to date, the endoscope has been the most successful biomedical application of OFSs [4]. In an optical fiber endoscope device, a fiber bundle is used for observing and imaging internal organs, where a portion of the fibers is used as the illumination fiber and the others are used to collect the images. The use of optical fibers enables the fabrication of an extremely compact endoscopic device with excellent flexibility and robustness, making it possible to observe and image internal orifices of the human body that are otherwise inaccessible. Due to the advancement of optical fiber sensing technology, the scope of OFSs for biomedical applications has expanded greatly to include measurements of a broad variety of physiological, chemical, and biological parameters [5]. Compared to conventional sensors employed in biomedical applications, which are based on solid-state sensing technologies (e.g., piezoresistive effect), biomedical OFSs offer outstanding advantages, including miniaturization, low cost, insensitivity to magnetic fields, chemical and corrosive inertness, biocompatibility, non-conductive, and the ability for remote operation. An obvious example is the applications of OFSs in magnetic resonance imaging (MRI) environments or in RF radiation treatment, where high magnetic/electric interferences exist, making it challenging for conventional transducers due to the metallic wires used for power and communications [6]. Additionally, the unique features of optical fibers for carrying information provide the possibility of integrating multiples sensors with diverse measurement capabilities into a single fiber, a task not possible using traditional electrical devices.

Generally, an OFS functions as the light transducer between physicochemical parameters of the investigated environment and light conduction in the OFS. The choice of a proper OFS for a specific biomedical application is dictated by both technological and practical issues, such as desired sampling volume, detection accuracy and limit, (non)invasiveness, environmental interference, which impose unique biomedical engineering challenges on fiber optic researchers [7]. Therefore, substantial caution should be used in the design and fabrication of OFSs with optimized structures and performance metrics for biomedical applications. Special requirements of the optical fiber components are diverse for the construction of different OFSs for specific applications. Taking advantage of the micromachining techniques, OFSs with various structures and

measuring performances are possible. The most commonly used micromachining process used in OFS fabrication is fusion splicing, where two pieces of optical fiber having identical or dissimilar properties are spliced together (e.g., single-mode fiber fused to a hollow-core fiber) [8]. The angle of cleavage of an optical fiber is also an important choice in the process of preparation for fusion splicing. Tapering and polishing of optical fibers are widely used for fabricating OFSs. Tapering is usually employed in developing microfibers or nanofibers which are used for ultra-sensitive chemical sensing [9]. Polishing is a versatile technique to remove a certain portion of an optical fiber to form special structures, for example, D-shaped/side-polished optical fibers [10]. On the other hand, by polishing a fiber endface to a selected angle, the light output from the optical fiber can be guided in a specific direction, which is desirable in biomedical applications, e.g., endoscope-internal imaging. In very recent years, with the advancement of laser techniques, femtosecond laser micromachining has been widely used for processing of transparent materials (e.g., glass) [11]. Different functional photonic micro/nano-structures have been successfully fabricated by micromachining methods applied to different substrates for a variety of applications, including sensing. Combining the one-step fabrication techniques enabled by femtosecond laser micromachining and the unique advantages of OFSs opens new avenues for developing a new generation of assembly-free OFSs with enhanced robustness, flexibility, and functionality.

In this chapter, we introduce micromachined optical fiber sensors for biomedical applications, including traditional methods of micromachining and more advanced ultrafast laser micromachining. The most recent developments in this field are reviewed.

Our review criteria were established to cover most of the recent advancements in micromachined OFSs for biomedical applications. Due to the rapid growth and development of micromachining methodologies and optical fiber sensing technologies, the majority of recently reported OFSs utilized one or more micromachining techniques during fabrication processes. However, most of these advanced sensors have not been demonstrated for in vivo clinical measurements, but they offer unparalleled advantages compared to conventional OFSs and they have huge potential to be further explored for real-world biomedical applications. Therefore, our review focuses on a basic introduction to the most recent developments in micromachining-assisted OFSs and their potential applications in biomedicine. Various optical fiber sensing techniques are discussed in detail for each specific measurand (e.g., temperature, pressure, biomarker) in clinical settings. Moreover, a few typical examples of sensing technique configurations are included for the reader's edification. The protocols for the optical fiber micromachining methods described in this chapter are based on the authors' years of experience in the optical fiber sensor arena and might vary

due to the rapid development and advancement of micromachining technologies.

The past two decades have witnessed the rapid growth of OFSs in biomedical applications. The light propagating capabilities and high flexibility of optical fibers attracted the first application of optical fibers in clinical settings for endoscopy in the 1960s. The emergence of the optical fiber imaging endoscope has enabled internal body observation and imaging, making possible the rapid determination of the presence of tumors, damaged or diseased tissue, and internal bleeding in organs. Since the 1960s, optical fibers and OFS have attracted significant attention from the healthcare industry. Besides the traditional endoscope probes, more advanced imaging techniques based on optical fibers have been developed, such as optical coherence tomography (OCT) and photoacoustic imaging, where under-skin and internal scanning can be made noninvasive. Another advanced area of optical fiber used in biomedical applications is optical fiber-based biosensors, including physical and biochemical OFSs. For instance, measurements of a broad variety of different physiological parameters such as blood flow, heart rate, respiration, temperature, pressure are enabled by physical OFSs; biochemical OFSs are employed to identify and quantify particular chemical compounds and metabolic variables, such as pH, blood oxygen, glucose or to measure specific biological species (e.g., biomarkers) for diagnostic purposes. This section will introduce the most recent developments in optical fiber biosensors for biomedical applications. Particularly, optical fiber biosensors fabricated by one or more micromachining processes discussed in Subheading 3 will be mainly focused on.

### 1.1 Temperature Sensors

Temperature is an essential and routinely monitored physiological parameter in biomedical environments, such as in operating rooms, therapeutic rooms, and intensive care units. For instance, in recent years, minimally invasive thermal treatments, such as high-intensity focused ultrasound ablation, radiofrequency/microwave ablation, laser ablation, and cryo-ablation, have become an effective and efficient way of localized tumor removal [12]. Accurate and real-time measurements of tissue temperatures can provide a clear end-point for completing tumor ablation. Among a variety of thermometric techniques used in biomedicine (e.g., thermocouples, thermistors), optical fiber thermometers are particularly suitable due to their unique features. Optical fiber thermometers are especially attractive in temperature measurements where immunity to electromagnetic interferences are required (e.g., in MRI).

Optical fiber temperature sensors rely on a variety of transduction principles, such as temperature-dependent fluorescence, the thermal-optic effect, and thermal expansion. Taking advantage of micromachining techniques, a variety of OFS thermometers have been proposed and demonstrated. One of the most widely investigated types of OFS thermometers is based on optical interference,

and embodiments include the Fabry–Perot interferometer (FPI), the Mach–Zehnder/Michelson interferometer (MZI/MI), the Sagnac interferometer, and the multimodal interferometer [13]. These interference-based OFSs are generally modified using a micromachining process that results in excitation of multi-path light beams. The optical path difference (OPD) of the light beams varies under the influence of temperature changes due to thermal expansion and/or the thermal-optic effect. Fusion splicing and femtosecond laser micromachining are versatile techniques used to fabricate these OFSs. A section of a special optical fiber (e.g., PCF or multimode fiber) was fusion spliced between two SMFs to form an FPI device or multimodal interferometer for temperature measurements [14, 15]. A refractive-index-modified dot fabricated in an SMF by a femtosecond laser together with the fiber-optic endface was demonstrated as an FPI for temperature sensing [16]. A miniaturized concave-shaped FPI (<100 μm) was reported for high-temperature applications fabricated by an advanced fusion splicing process [17]. Fiber-in-line MZIs fabricated by femtosecond laser micromachining were also demonstrated for measuring temperature, where a pair of microstructure were typically fabricated as the cladding mode exciter and combiner [18–21]. The thermal sensitivity of fiber Bragg grating (FBG) has also been exploited for medical applications [22]. An FBG is fabricated by introducing a periodic change in the index of refraction (i.e., Bragg grating) along a fiber core length by using a phase mask and a UV laser irradiation technique or by a femtosecond laser point-by-point (or plane-by-plane) micromachining. By tracking the shift of the Bragg wavelength of the FBG, the temperature variations can be determined [23]. Typically, these all-silica-fiber temperature sensors can function in a wide range of temperature environments, e.g., from −200 to 1000 °C due to the thermal stability of fused silica with satisfactory measurement resolution (e.g., ±0.5 °C). However, the temperature sensitivities of these sensors are not high enough due to the small coefficient of thermal expansion (CTE, ~$5 \times 10^{-7}$/°C) and low thermal-optical coefficient (TOE, ~$8.3 \times 10^{-6}$/°C) of silica. A promising solution to this issue is infiltrating liquid (e.g., liquid polymer, alcohol) with large TOE (>$10^{-4}$/°C) into holey fibers through the microholes which can be fabricated by femtosecond laser micromachining, and using the liquid-filled fibers as the building blocks for developing temperature sensors [24–27]. Typically, the sensitivity could be enhanced by approximate three orders of magnitude, although the dynamic range is limited to tens of degrees (e.g., 20–80 °C), which is good enough for most biomedical applications. Besides direct thermal measurements of bodies, a temperature OFS was also designed as a respiration sensor in an MRI system by measuring the temperature variations of airflow in exhaled air [28].

Microfibers enabled by tapering micromachining technique was also explored for developing temperature sensors, where microfibers with a reduced diameter (e.g., 1–50 μm) were used as the platform for the construction of the sensors [9]. Various interferometers were micromachined in microfibers, such as an MZI and an FPI [29, 30]. Microfiber-based Bragg gratings (MFBGs) have also been demonstrated for temperature sensing [31]. The EW in a tapered fiber is greatly enhanced due to the reduced diameter in the taper waist and is sensitive to the refractive index of the surroundings around the tapered region. Therefore, coating the microfiber sensors with materials having large TOC in the tapered region can dramatically enhance the temperature sensitivity of the microfiber [32, 33]. Compared with telecommunication optical fiber-based OFSs (i.e., fibers with a diameter of 125 μm), microfiber-based OFSs provide extreme compactness and faster response time. However, microfiber-based OFSs are generally fragile and require careful packaging for practical applications.

In addition to these point temperature sensors, OFSs also offer a prospect for multiplexed or fully distributed temperature sensing based on FBGs, scattering (Raman scattering, Rayleigh scattering, and Brillouin scattering), or cascaded fiber-in-line reflectors [34–39], allowing for mapping of temperature in the area of interest during medical treatment with high spatial resolution [40–42]. For example, the temperature distribution inside a liver tissue during an RF ablation procedure was successfully measured using a device predicated on Rayleigh scattering based optical frequency domain reflectometry (OFDR, Luna OBR4600) [40]. In real-time thermal mapping, the OFDR setup was configured with a spatial resolution of 200 μm for the entire optical fiber (<20 m), an update rate of 1 Hz, and an accuracy of 0.5 °C. The evolution of the spatial and temporal temperature changes in the liver tissue during RF ablation measured by the OFDR system was smooth and consistent with the anticipated physical effects. In turn, the distributed thermal mapping capability could be employed for the investigation of the fundamental physics of RF ablation and the corroboration of theoretical models.

### 1.2 Pressure Sensors

Pressure measurements in biomedical applications can be generally divided into two categories: monitoring isotropic pressure, such as intracranial and cardiovascular blood/fluid pressure monitoring, and sensing contact pressure, such as intervertebral pressure, force, and tactile sensing [43].

Fluid pressure measurements rely on monitoring the movement or deflection of a membrane under the influence of pressure. Intensity-modulated OFSs were originally demonstrated for measuring pressures in biomedical settings in the 1960s, where a movable reflectance membrane is interfaced with an optical fiber tip such that the intensity of light reflected and coupled into the

receiving fiber is modulated by pressure [44]. The applications of these intensity-modulated sensors are inevitably limited due to the drawback that the output signal can be modulated by a wide range of perturbations, such as the light source fluctuation and changes in reflectivity of the membrane due to oxidation. FPI is an excellent candidate for pressure measurements which offers the highest sensitivity and can be designed and implemented with great flexibility. Initially, a Fabry–Perot cavity is bonded to an optical fiber tip in an extrinsic configuration, where the pressure-sensitive diagram is larger in diameter than that of an optical fiber (125 μm) (which might raise a concern regarding further miniaturization) [45]. More recently, with the implementation of micromachining techniques, a new generation of miniaturized fiber-in-line FPI pressure sensors have been proposed, where the pressure-sensitive diaphragm is designed to be part of the optical fiber with the same diameter [46–48]. In these miniaturized FPI pressure sensors, typically, a hollow-core fiber is first fusion spliced onto a cleaved endface of an SMF, and the other end of the hollow core fiber is cut off using a fiber cleaver under microscope where the length of the residual hollow core fiber can be precisely controlled. Subsequently, a thin diaphragm is bonded to the open end of the hollow core fiber to form a hermetic cavity, serving as the pressure sensing element, as schematically illustrated in Fig. 1. The diaphragm deflects under pressure, which can be accurately captured by the Fabry–Perot interference that occurs between the optical fiber endface and the diaphragm. Several materials were explored as the diaphragm for highly sensitive pressure measurements, such as a polymer–metal composite film [46], a graphene layer [47], and a nano-silver film [48]. However, the structural robustness and temperature stability of these pressure sensors are poor, which hinders their way forward for practical applications, especially in harsh environments. On the other hand, all-silica FPI pressure sensors were also developed as an alternative where harsh environments are involved. Several micromachining techniques were employed for fabricating all-silica pressure sensors. A series of all-silica FPI pressure sensors were successfully fabricated using the traditional splicing-and-cutting method, followed by polishing or HF etching to further reduce the thickness of the silica diaphragm, thereby improving the pressure sensitivity [49–53]. Alternatively, femtosecond laser micromachining and advanced fusion splicing are also employed to reduce the thickness of the diaphragm to avoid using hazardous chemical etching [54–57]. The method of femtosecond laser micromachining not only reduces the thickness of the silica diaphragm but also roughens one side to eliminate the additional reflections from the outer surface of the diaphragm (i.e., reduced parasitic interferences). Electric arc discharge techniques enabled by commercial fusion splicers are a more cost-effective way for thinning a diaphragm, where the thickness of the diaphragm can be reduced

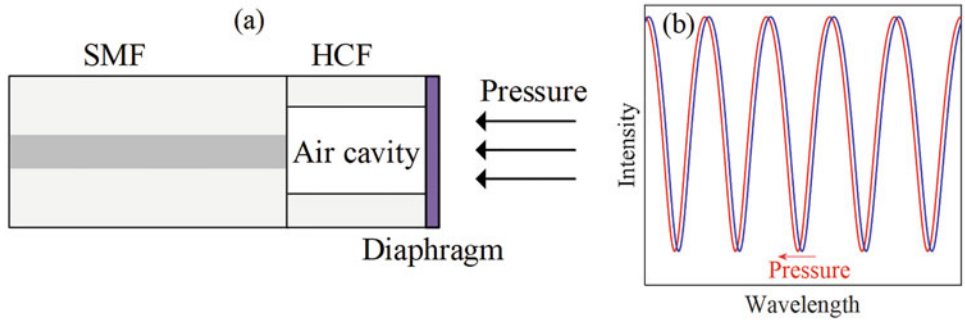


**Fig. 1** Schematic of a typical diaphragm-based optical fiber FPI pressure sensor. (**a**) Schematic illustration of the sensor structure. (**b**) Response of the sensor to an increase in pressure, i.e., a shift in the reflection spectrum. As the applied pressure increases, the diaphragm deflects, resulting in a decrease in the cavity length (i.e., the distance between the optical fiber endface and the diaphragm) and thus a blue-shift of the reflection spectrum

down to 170 nm [57]. The all-silica FPI pressure sensors fabricated with advanced micromachining techniques possess excellent mechanical and temperature stability and are more biocompatible and chemically resistive than metal-diaphragm-based pressure sensors. Most of these advanced sensors were only validated in the laboratory, while biomechanical and biomedical applications have not been demonstrated yet using these sensors.

The FBG is the most widely used OFSs for contact pressure measurements in the field of biomechanics and rehabilitation applications, where FBGs could be used for detecting stress in bones and intervertebral discs, pressure distribution in orthopedic joints and human–machine interfaces (HMIs), and forces induced by tendons and ligaments [58]. In minimally invasive surgery (MIS), haptic perception is of significant importance because it enables the surgeon to feel organic tissue hardness, measure tissue properties, and evaluate the anatomical structure and, therefore, allows the surgeon to commit appropriate force control actions for tissue manipulations [59]. The high sensitivity, flexibility, and capability of multiplexing make FBGs an outstanding candidate for single-point and multi-point tactile sensing [60]. Recently, an OFS-based technique was employed to address a common problem in medical procedures, recognized as a medical device-related pressure ulcer, where a polymer patch-embedded FBG was used to measure the contact pressure between a medical device and the tissue [61]. FBG-assisted bandaging was reported for in vivo observation of the sub-bandage pressure during compression therapy, where two arrays of FBGs were entwined in a double helix form with contact-force sensitivity and immunity to temperature variations, as shown in Fig. 2 [62]. In addition to FBGs, FPIs have also been demonstrated as a promising configuration for contact pressure measurements. A miniaturized optical fiber tactile sensor based on an FPI structure was reported

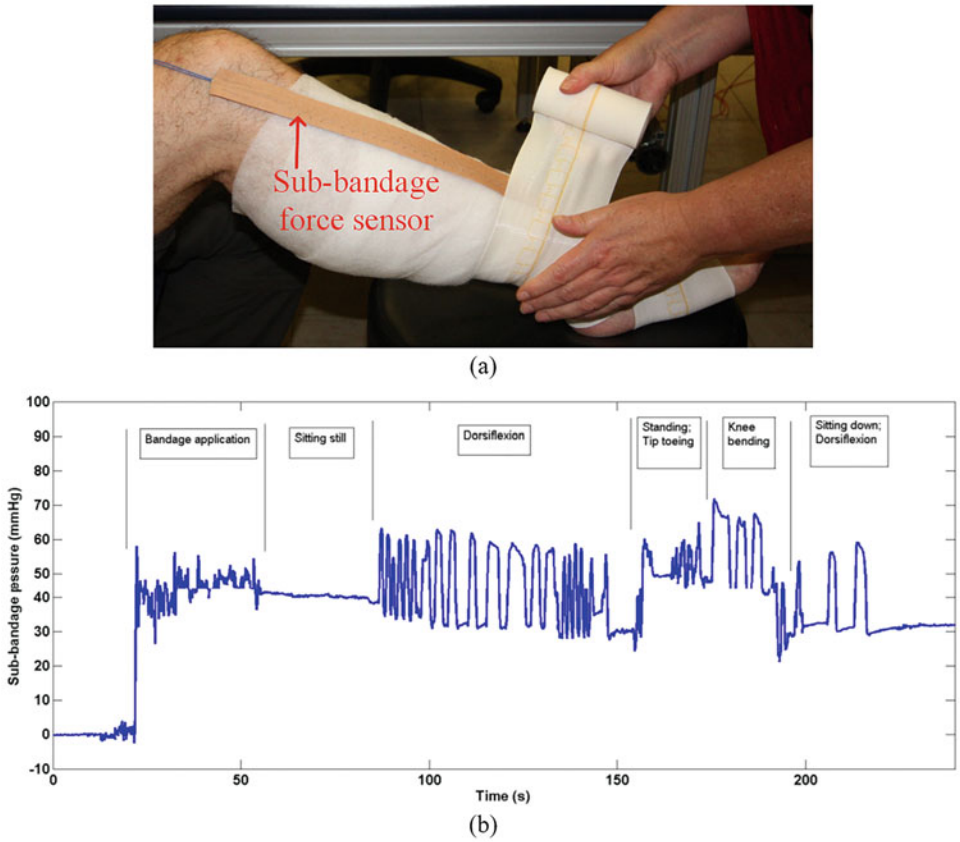


**Fig. 2** An FBG-based sub-bandage force sensor [62]. (**a**) In vivo sub-bandage pressure measurement sensor for monitoring a wounded leg. (**b**) Pressure measurements at the medical gaiter during simple movements

for high-resolution needle insertion force sensing in high-field MRI environments [63]. The miniaturized optical fiber force sensor was integrated into an MRI compatible piezoelectric actuated robot for prostate brachytherapy applications [64]. Another optical fiber force sensor was reported for vitreoretinal surgery applications, where a surgical tool was integrated with a miniaturized OFS [65]. The prototype device with an outer diameter smaller than 1 mm was demonstrated for simultaneously measuring axial and lateral forces. In these FPI-based tactile sensors, an extrinsic structure was employed. Further trends should include the advanced miniaturized fiber-line structure-based OFSs for force sensing in biomedical applications. On the other hand, a Rayleigh scattering-based OFDR system was also employed for tactile sensing where the sensing SMF is embedded in a soft prosthetic forefinger [66]. The strain distribution along the forefinger was precisely mapped with high spatial resolution (~3 mm), opening a new possibility for perceptive soft robots.

### 1.3 Respiratory, Heart Rate, and Blood Flow Sensors

Respiratory and heart rates are two vital signs of the human body that are monitored online during medical examinations and procedures. Typically, the respiratory and heart rate OFSs are configured as strain sensors, which are capable of measuring the periodic mechanical movement of the chest wall (i.e., contractions and expansions) induced by breathing or cardiac activities. Sensors that output modulations of light intensity, based on various microbending configuration, were originally used for this purpose due to their simplicity, ease of operation, and low cost [67]. Recently, due to their high sensitivity for strain measurements, FBGs and long-period fiber gratings (LPFGs) have been used for measurements of respiratory and heart rates, where the miniaturized OFSs were embedded into medical textiles to create wearable inconspicuous sensor devices [68, 69]. These OFSs have been particularly attractive for monitoring the vital signs of patients in MRI scanners due to their EMI and electrical insulation [70]. Besides strain-based monitoring, FBGs were also employed for measurements and analyses of arterial pulse waveforms, which make FBGs good diagnostic tools for clinical examinations and investigations of cardiovascular diseases [71, 72].

In addition to FBG sensors that sense body movements, another approach for monitoring respiration employs optical fiber-based humidity or temperature sensors placed in proximity to the patient's nose or mouth [28, 73–76]. The fundamental basis of this approach is that the exhaled air has higher humidity (~100%) and is warmer than the surrounding air. A miniature micromachined optical breathing sensor based on an agarose-infiltrated PCF was reported, where the humidity variations between inhaled and exhaled breath were measured in real-time for predicting the breathing rate and the breathing status of a patient during respiration [73]. Employing molecular-level self-assembly processing method, a fiber tip FPI interferometer was constructed by multilayered inorganic nanocluster and polymer thin films, showing high sensitivity to variations in humidity [74]. The performance of the prototype sensor was compared with a medical nasal thermistor and showed excellent potential for monitoring advanced breathing airflows. A simple PCF interferometer was demonstrated as a breathing sensor by monitoring humidity [75]. Two collapsed regions at the interfaces between an SMF and a PCF were intentionally fabricated as the cladding mode exciter and combiner by using a modified fusion splicing process. The PCF interferometer was extremely sensitive as the water molecules in exhaled air were adsorbed on or desorbed from the PCF surface.

Optical-fiber-coupled Doppler flowmetry is commonly used for non-invasive blood flow measurements, which relies on the Doppler frequency shift of the input light as a result of light scattering from moving blood cells [77]. The integrated optical fibers play a role in delivering and collecting light to and from the

measurement points. Several optical fiber micromachining processes were also employed in this application, including fusion splicing, high-accuracy cleaving, and laser micromachining. For example, fiber-in-line collimators including a quarter-pitch graded-index fiber and a micro-spherical lens at the tip of the delivery fiber were fabricated to enhance the performance of the Doppler flowmetry system [78].

### 1.4 Biochemical Sensors

In addition to physical sensors, in recent years, OFSs have been extensively explored for measuring a variety of chemical and biological parameters due to their unparalleled features, such as miniaturization, high sensitivity, and low limits of detection (LoD). Traditional OFSs (e.g., refractometers) are not yet suitable for biochemical applications due to their chemical non-specificity and non-selectivity, indicating that these types of sensors are not capable of detecting a particular measurand of interest in a complex matrix with other interfering measurands. Consequently, two approaches were developed to empower OFSs with selective responses, including fiber EW spectroscopy (FEWS) and functional-film-assisted OFS. FEWS relies on the fact that a wide range of biochemical molecules have vibrational modes in the fingerprint region localized in middle infrared (mid-IR) spectral range, allowing direct analysis of the spectrographs of analytes due to the interactions between the EW and the analytes [79, 80]. The optical fibers used in FEWS are typically made of IR-transparent materials, such as chalcogenide glasses, and fluoride or silver halide glasses, which support low-loss propagation of IR optical signals. FEWS has been used in a variety of applications, such as for the detection of pollutants in wastewater, online monitoring in chemical, industrial, and food processes, and biosensing [81–83]. A concern regarding the potential toxicity of the IR fibers (e.g., chalcogenide glasses) in biological systems was reported [84].

In a functional-film-assisted OFS, a chemically selective and sensitive functional coating is deposited onto the fiber surface of the OFS. The optical properties of the functional coating vary when it interacts with an analyte of interest, and the variations can be transformed into changes in the properties of the light propagating in the OFS. By analyzing the changes in the reflection/transmission spectrum derived from the OFS, quantitative and qualitative information of the chemical analyte can be obtained. The basic idea is the coupling of a highly sensitive OFS probe to a functional coating to form a biochemical sensor device. Separately, neither the OFS nor the functional coating functions as a practical sensor due to the chemical non-specificity of the former and the challenge in signal transduction of the later. However, combining the prominent advantages of the two (i.e., high sensitivity and chemical selectivity, respectively) offers a universal strategy, which applies to various functional coatings and consequently many analytes. Moreover,

the functional-film-assisted OFS motif offers the prospect for the development of compact, portable, and low-cost devices combined with cheap light source (e.g., LED) and photodetector. The operational wavelength of this type of OFS is defined by the coating properties instead of the absorption features of the analytes, which provides great design flexibility.

#### 1.4.1 Biosensors

In optical fiber biosensors, biological recognition molecules are bound to an OFS for the detection and quantification of specific biological analytes. The biological components can convert the recognition event into changes in the optical properties, which can be probed by the OFS. The changes in the optical properties may render in the form of fluorescence (e.g., emission or quenching), changes in absorbance, variations in the index of refraction, chemiluminescence, etc. Typical biological molecules can be enzymes, antibodies, nucleic acids, proteins, or whole cells, and are chosen for their specificity and affinity [85].

In general, optical fiber biosensors are configured for two modes: labeled and label-free detections. Fluorescence-labeled detection was widely employed in biosensors in earlier years, where the sensors utilize fluorescence labeling of the analytes of interest and monitor the variations in the fluorescence intensity induced by the interaction between the analyte and the biological recognition molecules [86, 87]. In recent years, label-free detection has been extensively proposed and demonstrated due to its low cost and ease of operation, where the complex labeling procedures and associated problems in fluorescence-labeled detection are avoided (e.g., short lifetime and photo-bleaching of the dye). Label-free detection typically relies on the measurement of changes in optical thickness, defined as the product of the index of refraction and physical length, induced by the binding of analytes of interest to the biological recognition molecules. In the construction of these sensors, typically, an OFS sensing platform with enhanced EW is preferred, such as a polished fiber and a tapered fiber, where the biological recognition molecules are deposited on the region where the fiber diameter is reduced [88–91], as shown in Fig. 3.

Besides these tapered or polished fiber-based OFS, long-period fiber grating (LPFG)-based optical fiber refractometers have also been demonstrated as a promising platform for label-free biosensing [92–97]. An LPFG is a core-cladding mode coupling device, where the high attenuation of the cladding modes results in a series of resonance bands centered at discrete wavelengths in the transmission spectrum, with each resonance band corresponding to the coupling of a different order of cladding mode [98]. The interaction between the cladding modes and the surroundings in an LPFG can provide precise analytical information about the optical thickness of the coating layer. Figure 4a illustrates the effect of the surrounding refractive index changes on the transmission spectrum

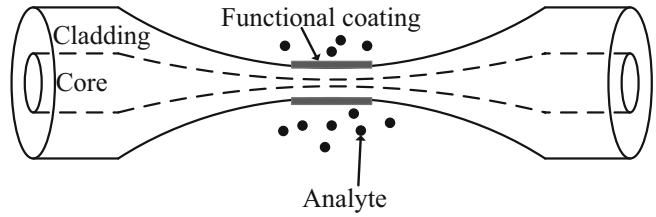


**Fig. 3** Schematic illustration of a functional-film-assisted tapered OFS for biochemical sensing

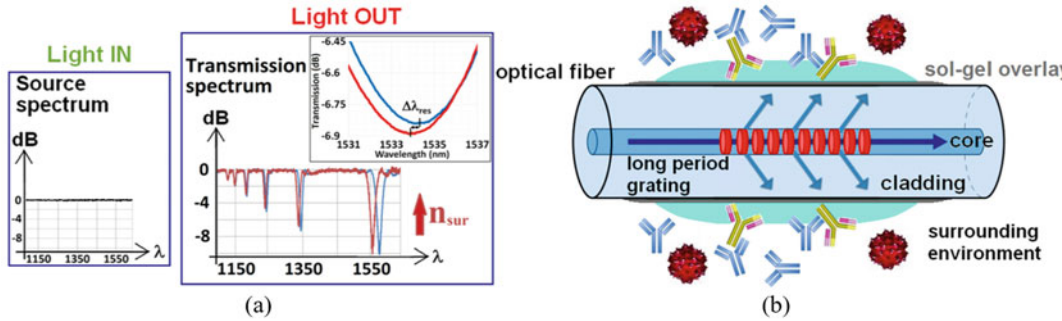


**Fig. 4** Schematic illustrations of the response of an LPFG to a change in the refractive index of the surrounding and an LPFG-based biosensor. (**a**) Schematic illustration of the effect of the surrounding refractive index changes on the transmission spectrum of an LPFG. (**b**) Schematic of a functional-film-assisted (sol-gel overlay) LPFG for biosensing [96]

of an LPFG. Typically, LPFGs are designed to operate at the phase matching turning point (PMTP) in biosensing, which provides the highest sensitivity to the surroundings. An LPFG coated with a thin film of biotin-modified silica core gold shell ($SiO_2$:Au) by a layer-by-layer method was reported for streptavidin detection with the LoD of 2.5 nM [92]. A traditional sol-gel dip-coating technique was also employed for coating functional film onto the surface of an LPFG, where the thickness of the film overlay could be flexibly controlled by adjusting the sol viscosity and the withdrawal speed during the dip-coating process, as shown in Fig. 4b. A sol-gel-based titania-silica-coated LPFG functionalized with a methacrylic acid/methacrylate copolymer integrated immunoglobulin G (IgG) was proposed as an effective and feasible label-free biosensor for the detection of anti-IgG with LoD of $10^{-11}$ M [96]. LPFG-based biosensors are also widely used for label-free DNA detection and quantification in complex DNA samples [93–95].

Another widely used configuration for label-free biosensing is a plasmonic OFS, which constitutes miniaturized counterparts to a traditional (localized) surface plasmon resonances (SPR) system where bulky prisms and microscopes are used [99]. In the construction of optical fiber SPR biosensors, a thin metal layer (e.g., gold, ~50 nm) or nanoparticles (NPs) are deposited on a

micromachined optical fiber for SPR/LSPR generation where the EW is enhanced and brought in direct contact with surroundings; bioreceptors or biological recognition molecules are then grafted and immobilized on the metal surface through covalent bonding [100]. The EW excited SPR/LSPR is highly sensitive to the binding of analytes to the bioreceptors. The plasmonic OFS is usually spectrally interrogated, where changes in the transmission or reflection spectra are measured. Most of the plasmonic OFSs operate at visible wavelengths (e.g., 500–800 nm). Compared to other optical fiber refractometer-based biosensors, the most advantageous feature of plasmonic OFSs is the high sensitivity and low LoD.

A variety of micromachined optical fibers have been investigated as building blocks for plasmonic OFSs. The most straightforward way of bringing the core-guided light in direct contact with the surroundings is to remove the silica cladding entirely or partially through chemical etching or side-polishing [101–104]. Except for the polished D-shaped fibers, another similar configuration fabricated by femtosecond laser micromachining was also proposed, where a narrow trench in the fiber cladding was ablated [105]. Self-assembled gold colloids were deposited onto the surface of the trench to produce LSPR for refractometry. The refractometric sensitivity of polished fiber-based plasmonic OFSs can reach 4000 nm/RIU (RIU, refractive index unit) [100]. Unclad fibers with cores directly exposed to the surrounding medium were also employed for plasmonic OFSs. An unclad fiber with a silver and silicon coating on the core followed by immobilization of an enzyme (glucose oxidase) using gel entrapment was demonstrated for low concentration glucose measurements [106]. Another building block for developing plasmonic OFSs is the tapered fiber, where the EW in the tapered region is greatly improved. Coating a thin noble metallic layer over the tapered region results in an SPR refractometer [107–111], where the sensitivity reaches up to 11,800 nm/RIU. A dielectric layer (e.g., indium nitride) was also explored as an SPR material [108]. Functionalizing these highly sensitive refractometers with specific bioreceptors makes it possible to develop selective biosensor with a low LoD. Hetero-core structures, realized by simply fusion splicing two types of fibers with different core diameters (e.g., SMF and thin-core fiber), have also been used in plasmonic OFSs [112]. The core mismatch couples core-guided light to cladding modes, which can excite plasmonic interactions at the outer surface of the sensing fiber when it is coated with a metal layer. The hybrid structure could be bent or tapered to further enhance the EW field in the sensing region, thus improving the measurement sensitivity [113, 114]. Bending a fiber is the most straightforward approach for bringing core-guided light to cladding modes due to the perturbations of the total internal reflection (TIR). Assisted by heating using a flame, U-shaped

structures with a bend radius as small as 0.5 mm were successfully obtained with satisfactory repeatability [115, 116]. Gold nanoparticles (GNPs) were bound to the U-bent region to excite LSPR, which was then functionalized with IgG as the bioreceptor for the detection of anti-IgG.

Instead of mechanically or chemically removing the cladding to access the core-guided light, grating-assisted fibers were also explored for the implementation of plasmonic OFSs without degrading the mechanical integrity of the silica optical fibers. LPFG has been demonstrated for this purpose due to the coupling core mode to cladding modes, which can excite a surface plasmon wave (SPW) [117, 118]. A traditional FBG is not suitable for plasmonic sensing since the light is confined in the fiber core, making it insensitive to changes in the surrounding medium. Tapering and chemical etching are effective approaches used to access the core-guided mode in an FBG [119, 120]. In recent years, a tilted FBG (TFBG) has been proposed with grating fringes that are not perpendicular to the axial direction of the fiber core. Cladding modes are consequently excited due to the tilted grating pattern, resulting in a dense comb-like transmitted amplitude spectrum with a series of narrowband cladding mode resonances on the short wavelength side of the Bragg resonance [121]. One attractive feature of a TFBG is that the Bragg resonance is immune to the surrounding medium, indicating that the Bragg resonance can be used to compensate for unwanted interference coming from temperature variations or light source power fluctuations. Assisted with a thin metal layer on the grating region, TFBGs have been demonstrated as plasmonic OFSs [122–125]. Compared with other plasmonic OFSs, the transmission spectrum of a TFBG-based sensor is a fine comb of narrowband resonances that overlap with the broader SPR resonance, providing a unique approach to accurately detect tiny shifts of the plasmonic resonance. A gold layer-coated TFBG, functionalized with a thrombin-binding aptamer was demonstrated to detect the protein human α-thrombin in its fibrinogen-binding exosite, as schematically shown in Fig. 5a [126]. The authors of the work also proposed a multiplexed TFBG-SPR device assisted with a fluidic channel, where multiple sensors could be embedded, as presented in Fig. 5b. Each of the SPR sensors can be functionalized with different bioreceptors to capture different targets, to provide a baseline reference data, or with the same bioreceptors to improve the LoD through statistical analysis of the response of the multiple sensors.

Microstructure optical fibers with air tunnels were also explored for plasmonic generation by coating the holes with NPs or filling some of the holes with metal [127, 128]. Another interesting plasmonic OFS is based on a single-ended optical fiber, where the cleaved end facet of the fiber is patterned or covered

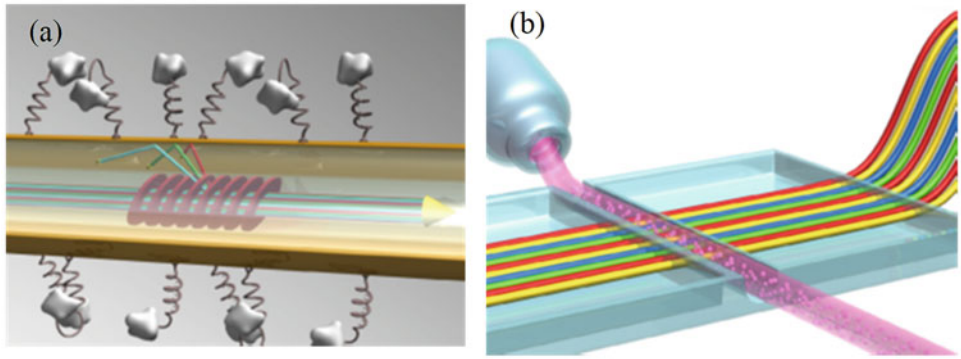


**Fig. 5** Schematic of a TFBG-based biosensor and the illustration of the potential multiplexing. (**a**) Schematic diagram of a gold-coated TFBG-SPR sensor covered with aptamer receptor molecules. (**b**) Conceptual illustration of multiplexed TFBG-SPR sensors embedded across a microfluidic channel [126]

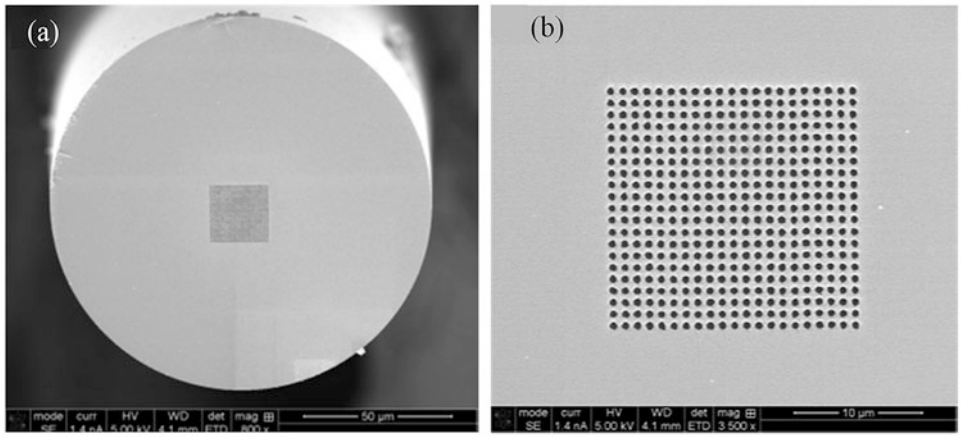


**Fig. 6** SEM images of the optical fiber SPR sensor fabricated by FIB micromachining [133]. (**a**) Overview of the fiber tip endface with the fabricated EOT structure. The diameter of the optical fiber is 125 μm. (**b**) An enlarged view of the EOT hole arrays on the fiber tip. The size of the holes varied from 522 to 625 nm, and the periods of the hole arrays ranged from 912 to 1056 nm

with an array of NPs [129–133], as illustrated in Fig. 6. In this case, the NPs are directly exposed to the core-guided mode in the fiber, yielding the generation of LSPR. Different approaches were exploited for patterning. For example, E-beam lithography nano-fabrication was used to pattern gold nano-dot arrays on the fiber end facet [132]; focused ion beam (FIB) milling machine was used to directly fabricate subwavelength hole arrays on the gold film coated on fiber endface [133]; microsphere photolithography was demonstrated for low-cost fabrication of nano-patterns on the fiber endface [134].

### 1.4.2 Chemical Sensors

The detection of chemical compounds found in the human body in clinical settings has been extensively explored because it offers the possibility for noninvasive diagnoses of diseases. The detection of compounds could be conducted in the gas phase, where the gas molecules of interest are exhaled in the breath or emitted from the skin; or, in the liquid phase, in liquid samples, such as blood, urine, saliva, and other liquids containing human metabolites.

pH is a significant parameter in biology; it is diagnostic of the functionality of many organs and parts of the human body. Accurate knowledge of pH provides useful and valuable information for the diagnosis of diseases. The pH of fluids in the human body varies over a wide range, depending on the functions of different cells [135]. The most widely used approach of optical fiber-based pH sensors relies on the use of dye indicators, which are immobilized in matrix materials and deposited on a cleaved end facet of an optical fiber [136, 137]. Various pH molecule indicators have been demonstrated for the construction of OFS-based pH devices, including acidochrome dye, fluorescein acrylamide, thymol blue, ethyl violet dye, neutral red, eosin, and other mixtures of organic molecules [138]. These sensors are typically interrogated by measuring changes in the optical properties of the indicator, such as absorbance, fluorescence, and fluorescence lifetime, to determine the variations of pH in the liquid sample. The optical fibers used in these sensors only play a role in delivering excitation light to the pH-sensitive dye and collecting the fluorescence emission. To further miniaturize the sensor head, tapered fibers are employed [139]. One concern for pH-indicator-based OFSs is the long-term deterioration induced by the bleaching of the indicator molecules. In recent years, functional film-assisted OFSs have been exploited for pH measurements, where the optical properties of the film change as a function of pH. Specifically, in OFS-based pH devices, nanostructured films are used, whose morphology, with emphasis on swelling, depends on pH. Since the refractive index (RI) of a swellable film (e.g., polyelectrolyte-deposited nanostructured material) is influenced by pH, one can design pH sensors through the measurement of the external RI. Various micromachined optical fiber refractometers were used as the building blocks for pH sensors, as discussed in the previous section, such as FPI, LPFG, TFBG, hetero-core structures [138, 140–143]. A thin-core fiber modal interferometer deposited with poly(allylamine hydrochloride) and poly(acrylic acid) nanocoating, employing electrostatic self-assembly techniques, was demonstrated as a wide-range pH sensor (2.5–10 pH unit) with a resolution of 0.013 pH unit [138]. The rise and fall times of the sensor were 120 s and 200 s, respectively. A Fabry–Perot nanocavity pH sensor, in which a nanostructured film was prepared on the surface of the fiber end-face, employed white-light interferometry for the measurements of

pH-induced swelling of the film, which in turn was used to determine the pH [140].

Oxygen ($O_2$) and carbon dioxide ($CO_2$) are two routinely measured parameters in biomedical applications as they are valuable for the analysis of circulatory and respiratory systems in the human body. Similar to OFS-based pH devices, the most popular approach used by OFS-based $O_2/CO_2$ sensors also relies on the use of fluorescence indicators attached to the tip of an optical fiber [144]. The optical properties of the indicator molecules change in the presence of $O_2$ or $CO_2$. A single OFS modified with two different indicators (i.e., $O_2$ and $CO_2$-sensitive materials) was demonstrated for the simultaneous measurement of both oxygen and carbon dioxide [145]. These two indicators have the same excitation wavelength but quite different emission maxima, offering the possibility to distinguish the separate responses of the two indicators. In very recent years, metal-organic frameworks (MOFs) were extensively used in the areas of gas separations and storage because their internal physical and chemical properties can be tailored for these applications using the judicious selection of inorganic and organic building blocks [146]. MOFs have also been explored for chemical sensing applications due to the great design flexibility and tailorable chemical selectivity [147]. Optical fiber $CO_2$ sensors based on an LPFG coated with a thin layer of MOF (HKUST-1) or an etched optical fiber coated with ZIF-8 were proposed for the detection of $CO_2$ with high sensitivity as shown in Fig. 7 [148, 149]. These MOF-integrated OFSs rely on the refractive index-based sensing mechanism, where the use of a MOF-based sensing layer results in an amplification of the increasing values of the effective refractive index associated with the adsorption of gases.

The identification and quantification of ammonia are also of interest in biomedical applications due to their correlation to specific diseases, such as dysfunction in the kidney and liver [150]. The detection of ammonia in exhaled air or urine provides a valuable clue for the early diagnosis of some diseases, where typically a sensor with an LoD of 50–2000 ppb and quick response time is desired [150]. Although OFSs have not been demonstrated for detecting ammonia in an individual's breath as of yet, due to the limited measurement sensitivity and LoD, the development of OFS-based ammonia sensors continues. Traditional optical fiber ammonia sensors rely on measuring the change in fluorescence intensity of a buffered pH indicator solution, where the presence of ammonia increases the pH of the solution [151]. More recently, functional film-assisted OFSs have been explored for ammonia gas detection [152–157]. Zinc oxide (with graphene oxide) and polyaniline are the most widely used coating materials for ammonia gas sensors, and various optical fiber structures are used as the sensing

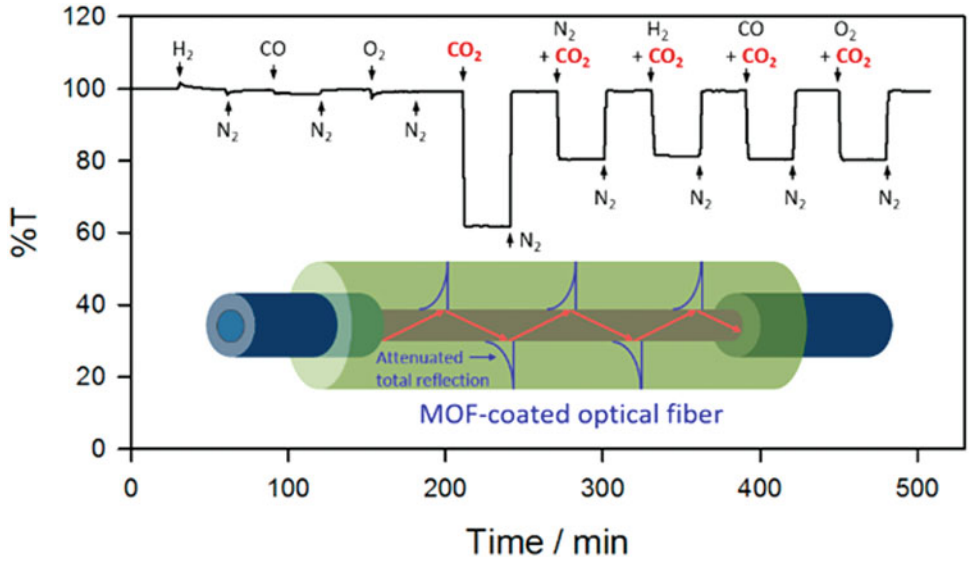


**Fig. 7** Etched optical fiber-based $CO_2$ sensor integrated with a thin film of MOF material. The light transmission of the sensor structure as a function of time is plotted above the sensor element [148]

platform, such as LPFG, tapered fibers (micro/nanofibers), heterocore structures, FPI.

In addition to sensing ammonia, the detection of volatile organic compounds (VOCs) has attracted great interest due to the high potential as a noninvasive early detection and diagnosis of microbial diseases. The relationship between the VOCs emitted from the human body and a disease or disorder was reported extensively [158]. A variety of "electronic noses" have been developed to detect and discriminate between the production profiles of VOCs from microbial infection in situ [159–162]. Combined with artificial intelligence and web-based knowledge systems, electronic noses were expected to have a valuable role in monitoring disease epidemiology [162]. The use of OFSs for this purpose has also been proposed. Compared to the electronic nose (e.g., an array of chemical sensors), OFS-based sniff systems provide significant advantages, such as small size, lightweight, ease of fabrication, low fabrication cost, and capability of multiplexing employing a single fiber. Preliminary studies have shown that a micromachined EW-based OFS modified with a functional layer (i.e., dye compound) was able to distinguish skin emissions from several different volunteers in the test [163]. Taking advantage of optical fiber micromachining techniques, several OFS-based VOC sensors have been demonstrated recently based on functional film-assisted configurations, i.e., micromachined optical fibers (e.g., LPG, tapered fiber, etc.) deposited with a sensitive layer [164–166]. These sensors do not yet play a meaningful role in medical applications due to insufficient sensitivity and chemical selectivity.

Humidity is another important quantity that is often measured and monitored in clinical settings. Humidity measurements not only can be used for respiratory monitoring (as discussed in the previous section) but also play a significant role in the monitoring of gas mixtures delivered to patients from ventilator care equipment [167]. In these applications, humidity sensors with fast response times and recovery times (e.g., <1 s) are required. One of the most popular configurations of OFS humidity devices is the FPI, where various humidity-sensitive films are employed to construct a micro Fabry–Perot cavity on the tip of an optical fiber [168]. The operational principle of these sensors relies on the detection of the RI change or swelling induced by the absorption of water molecules into the film. In addition to FPI configurations, other humidity-sensitive film-assisted structures, such as TFBG, tapered fibers, U-bend structures, LPFG, etc., have also been demonstrated for humidity sensing [169–171]. Very recently, graphene (oxide) has attracted a great deal of interest as the sensitive film for humidity sensing due to its two-dimensional structure of one-atom thickness, high specific surface area, chemical stability, and optical properties [172, 173], which can potentially provide an ultra-fast response to variations in humidity. A fiber-tip Fabry–Perot humidity sensor modified with a ~300-nm-thick graphene oxide (GO) film was fabricated (*see* Fig. 8) and exhibited a wide sensing range, spanning from ~10% to ~90% RH, and more significantly, an ultrafast response time of 60 ms and a recovery time of 120 ms [174]. A GO-coated TFBG was also shown to exhibit an ultrafast response time of ~42 ms. The rapid response time was due to the unimpeded permeation of water molecules through the GO interlayer [175]. Another important application of humidity measurements involves the monitoring of the microenvironments within chronic wounds [176], where accurate humidity detection enables

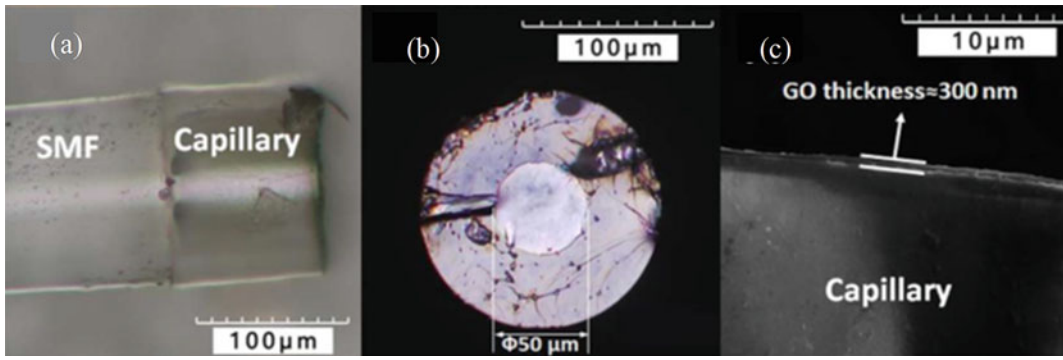


**Fig. 8** A fiber-tip FPI-based humidity sensor with a GO diaphragm. (**a**) Fiber-capillary tip with GO diaphragm. (**b**) The GO membrane-covered fiber-capillary tip. (**c**) SEM image of the thickness of the suspended diaphragm [174]

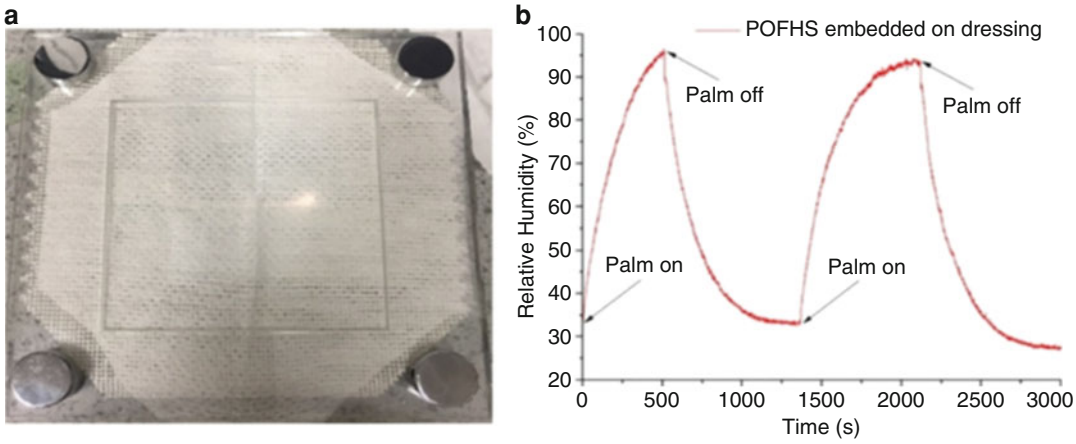


**Fig. 9** Proof-of-concept in vivo RH measurement using an OFS humidity sensor. (**a**) OFS humidity device embedded in a wound care dressing and covered by a clinical gauze as a secondary dressing for humidity measurements. The unclad visible part of the sensor is 30 mm long. (**b**) In vivo humidity measurements on the palm of a hand recorded with a humidity sensor embedded in a wound care dressing and covered with a clinical gauze as a secondary dressing [176]. Palm on: placing the hand on the device; palm off: moving the hand away from the device. The settling and recovery times were ~7.7 and ~9.7 min, respectively. The reason for the long response time was that the sensor was embedded in the dressing and covered by a clinical gauze

appropriate clinical interventions at proper healing stages, thus improving wound care (*see* Fig. 9).

*1.4.3 Intracellular Sensors*

The capability to monitor microenvironments at the single-cell level has been facilitated by the use of the MNF-based sensing platform, which takes advantage of optical fiber micromachining techniques, especially tapering in this case. The realization of intracellular chemical sensing was first reported in 1992, where a submicrometer optical fiber was employed for pH measurements at the single-cell level [177]. The sensor was fabricated by tapering a commercial optical fiber down to a submicrometer size, as small as 0.1 μm, followed by coating the thin fiber with a layer of aluminum; the endface was left as a transmissive aperture. A copolymer imbued with a pH-sensitive dye was attached covalently to the silanized fiber tip surface using a photopolymerization reaction, as shown in Fig. 10. This micro/nano-machined optical fiber tip sensor simultaneously achieved a thousandfold miniaturization of the probe head, a millionfold reduction of the sample size, and a hundredfold reduction of the response time (<20 ms) [177]. Since then, optical fiber nanoprobes have been extensively explored for sensing at the molecular and cellular levels in a variety of medical applications [178, 179]. Generally, antibodies, selective for target analyte molecules, are covalently bound to the tip of an MNF. The target molecules bound to the antibody molecules are excited by the strong EW field at the fiber tip when excitation light at a specific wavelength is launched into the fiber. The variations in the

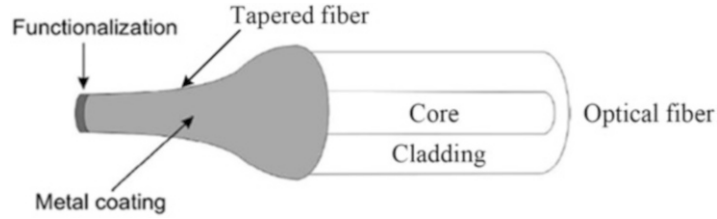


**Fig. 10** Schematic illustration of an intracellular sensor based on a functionalized MNF tip [5]

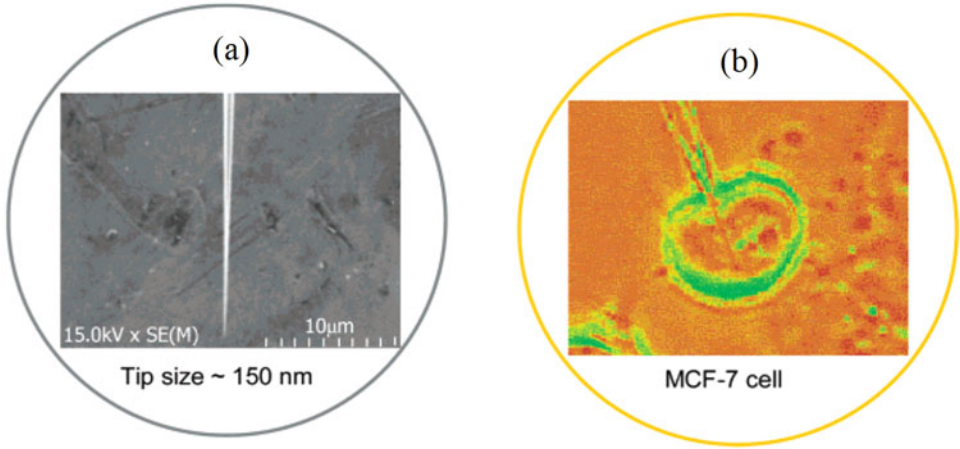


**Fig. 11** Nano-machined optical fiber for single-cell applications. (**a**) SEM image of a nano-tip after coating with 100 nm of silver metal, achieving a final tip diameter of 150 nm. (**b**) Image of optical nanoprobe inserted into a single live MCF-7 cell [182]

fluorescence emissions from analyte molecules are collected and analyzed to determine the concentrations of the analyte molecules. Antibody-based MNF sensors have been demonstrated for measurements of toxic chemicals contained within single cells (*see* Fig. 11), such as benzo[α]pyrene tetrol, benzo[α]pyrene [180–182]. Many efforts have also been put in improving the excitation and collection of the fluorescence signals by optimizing the geometry of the fiber tip [183, 184]. A hexagonal 1-in-6 fiber configuration enabled by advanced tapering procedures was proposed for intracellular single-cell pH measurements, which enabled the optimal signal collection and minimal interference [183]. In addition to fluorescence-based MNF biosensors, whispering-gallery-mode biosensors excited by tapered fibers were also employed for label-free biosensing down to the level of single molecules [185].

### *1.5 Lab-in-Fiber*

Compact and functional lab-on-chip (LOC) devices on planar or multilayered platforms have kept advancing the biological and chemical laboratory processes [186]. Optofluidic devices, enabled by LOC developments that include combining microfluidic

channels with optical sensing elements, have been exploited to harness the novel opportunities of integrated micro/nanostructure photonics [187]. A migration of integrated LOC devices into optical fiber platforms would open the revolutionary prospect of creating novel lab-on-fiber (LOF) or lab-in-fiber (LIF) devices for multifunctional sensing [188]. Recently, LOF has been extensively investigated for a variety of applications, including label-free chemical and biological sensing, as discussed in the previous sections. One of the main challenges for LOF sensing is bringing the core-guided light to the fiber cladding surface where sensing structures or functional chemicals can be introduced. Several mechanical or chemical strategies have been developed for addressing the challenges of transferring light from the core to the cladding, such as tapering, polishing, chemical etching, femtosecond laser micromachining. These methods are efficient in bringing a strong probing evanescent field to the cladding surface but with the disadvantage of degrading the mechanical integrity and strength of the fibers. On the other hand, the LIF concept provides the revolutionary prospects of optimizing the packaging and densification of multiple sensing elements, which are not possible for LOF. Three-dimensional patterning inside optical fibers by femtosecond laser direct writing, together with selective chemical etching, has been demonstrated as a powerful tool to inscribe all-in-fiber optical waveguides and gratings as well as microchannels and optical resonators [188–191].

An all-in-fiber assembly-free optofluidic device fabricated employing the FLICE technique was reported, consisting of horizontal and vertical microchannels [190]. The horizontal microchannel was conceived as an FP cavity while the vertical one was used as the inlet/outlet to the cavity. The novel device was demonstrated for measurements of the refractive index of the liquids that filled the microchannel. Also, the device afforded unique features, such as great design flexibility, ease of fabrication, mechanical robustness, and miniaturization. A more complicated LIF inside an SMF fabricated by an advanced FLICE technique was demonstrated recently, where optically smooth surfaces (~12 nm rms) were realized with ultra-low insertion loss [188]. Cladding waveguides, X-couplers, fiber Bragg gratings, microholes, mirrors, optofluidic resonators, and microfluidic reservoirs were fabricated in an SMF and a spliced piece of coreless fiber. These components were combined and integrated into multicomponent 3D optofluidic fiber sensors with enhanced functionality, improved intelligence, and capability for sensing enriched information (*see* Fig. 12). The LIF system for sensing applications was demonstrated as (1) fluorescence excitation and detection in the microhole through the SMF core waveguide, (2) in-line refractometry through the FPI in a coreless fiber, (3) the combination of a cladding FPI with an FBG for simultaneous measurements of refractive index,

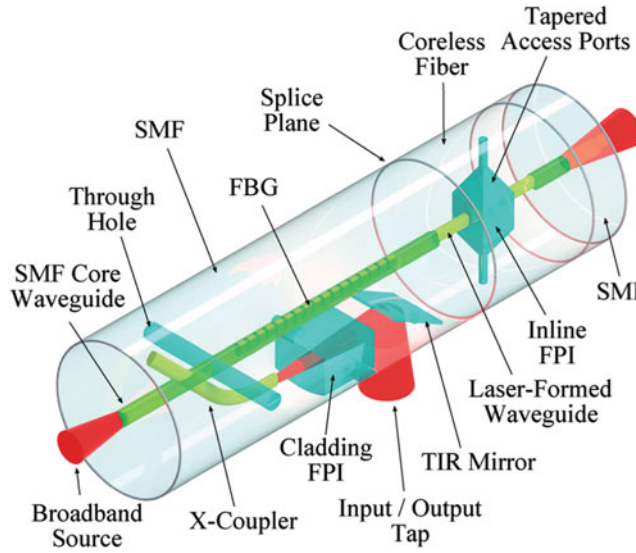


**Fig. 12** Schematic illustration of LIF sensing architecture: (1) a through-hole traversing across the SMF core waveguide for fluorescence detection or absorption spectroscopy, (2) an FBG concentric with the SMF core waveguide for temperature or strain detection, (3) an in-line FPI in a coreless optical fiber probed by laser-formed waveguides concentric with the spliced SMF's core for optofluidic applications or pressure sensing, and (4) an X-coupler tap and laser-formed waveguide for probing a cladding FPI for refractive index, pressure, or bend sensing. TIR mirrors are used to tap light either into or out of the fiber cladding for an alternative probing method or for scrubbing undesired cladding modes [188]

temperature, pressure, and bend. The flexible 3D writing techniques and multiplexed sensors were expected to open powerful prospects to migrate the advantages of LOCs into a more flexible and compact platform, optical fibers, via the LIF concept for highly functional and distributed sensing capabilities. Combined with the traditional optical fiber biosensing techniques, a new generation of multiplexed, extremely compact, highly functional, distributed smart biosensors can be developed, e.g., smarter catheter.

## 2 Materials

A typical OFS system consists of four basic components:

1. Light source, e.g., a tunable laser or broadband laser.
2. Light delivery component, e.g., optical fiber cable, optical fiber coupler, optical fiber circulator.
3. Photodetector or optical spectrum analyzer.
4. Micromachined sensor head.

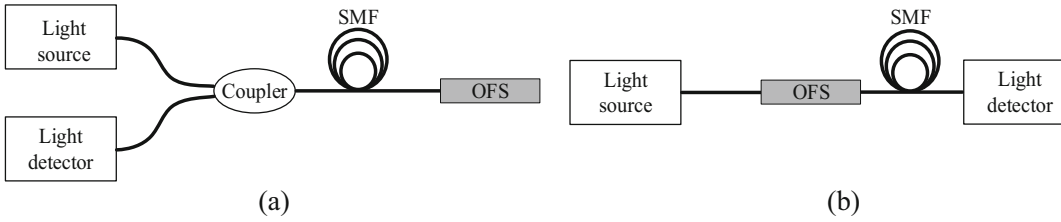


**Fig. 13** Typical OFS systems. (**a**) Reflection OFS system. (**b**) Transmission OFS system

The light source provides the EM wave for optical interrogation, which is typically a laser, a white light source, or an LED. The light characteristics offer a wide range of properties for different means of interrogation, including intensity, phase, wavelength/frequency, and state of polarization. The light delivery component delivers the light from the source to the OFS and also collects and directs the light from the OFS to the light detector via the same or different optical paths. The delivery component usually includes the optical fiber for light transmission and fiber coupler/circulator for light coupling. The sensor head, i.e., OFS, is essentially the light modulator, which can alter the properties of the input light through the influence of external perturbations (i.e., variations of physical and chemical parameters of interest). In other words, the external perturbations are correlated to the probing light signal via the OFS by modulating the properties of light. The light detector is employed to read and monitor the variations in the properties of the light that is guided back from the sensor head to the interrogator. Different renderings of the changes in the light properties (e.g., intensity variation, wavelength shift, etc.) are used for different OFSs and applications. Figure 13 shows two typical OFS characterization systems: (a) reflection mode and (b) transmission mode. The materials used in four different types of micromachining techniques for fabricating optical fiber sensors are listed below.

### *2.1 Fusion Splicing*

1. Two sections of optical fiber cables that need to be connected.
2. Optical fiber stripper and cleaver.
3. Lint-free Kimwipes.
4. Isopropyl alcohol or acetone.
5. Optical fiber fusion splicer.
6. Optical fiber protection sleeve heat shrinkable tube.

### *2.2 Tapering*

1. A section of optical fiber cable that needs to be tapered.
2. Two motorized linear translation stages.
3. A heat source, e.g., oxy-hydrogen torch.
4. Two optical fiber clamps.
5. Optical fiber stripper.

6. Lint-free Kimwipes.
7. Isopropyl alcohol or acetone.
8. A laser source and a photodetector or an optical spectrum analyzer.
9. Optical microscope.

### 2.3 Polishing

1. A section of optical fiber cable that needs to be polished.
2. Quartz block with a V-groove.
3. Epoxy.
4. Optical fiber stripper.
5. Optical fiber polishing machine.
6. Polishing powders and polishing pads.
7. Optical microscope.

### 2.4 Femtosecond Laser Micromachining

1. Femtosecond laser amplifier.
2. A micromachining workstation that includes an imaging system (a camera and a lens assembly), a high-precision three-dimensional translation stage assembly, and lens assembly that directs the laser beam from the laser amplifier to the sample holder on the stage assembly.
3. Two optical fiber magnetic clamps.
4. A section of optical fiber cable that needs to be micromachined.
5. Two sections of spacer fiber.
6. Microscope slide and cover-slip.
7. Index-matching gel.

## 3 Methods

### 3.1 Traditional Micromachining

#### 3.1.1 Fusion Splicing

Fusion splicing is the process of joining two optical fibers together by applying high temperature to the interface between the two fibers. The local high-temperature field is usually generated by an electric arc or laser irradiation. Fusion splicing is the most widely used method for connecting two optical fibers either of the same type or different types [192]. Compared to conventional connecting methods such as mechanical connecting, fusion splicing provides the lowest transmission loss and reflectance at the connecting point, as well as offering a reliable and somewhat robust mechanical joint. The instrument used for fusion splicing two fibers is called a fusion splicer. A schematic of a typical optical fiber fusion splicer is shown in Fig. 14b.

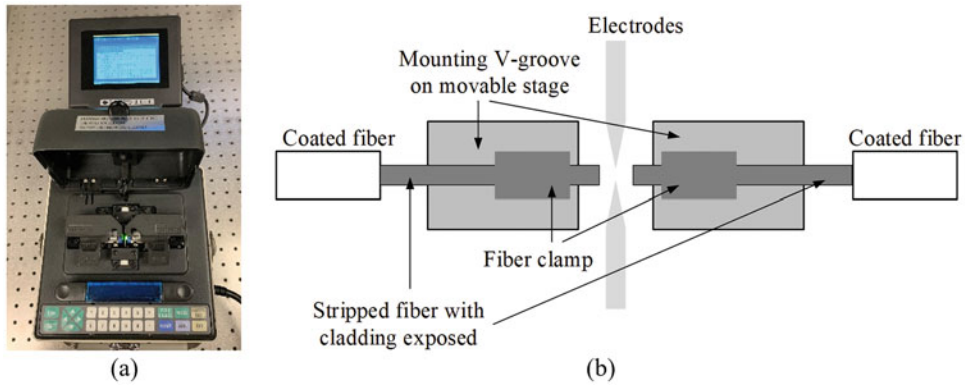


**Fig. 14** An overview image and schematic of a typical commercial optical fiber fusion splicer. (**a**) Photograph of a fusion splicer. (**b**) Schematic of a fusion splicer

The process involved in fusion splicing two optical fibers includes stripping, cleaning, cleaving, and splicing. Specifically, the details of the procedures are described as follows:

1. Strip the out jacket, the buffer layer, and the plastic coating to expose a certain length of bare fiber (e.g., 2–3 cm).
2. Clean the fiber to remove residual material and dust using lint-free Kimwipes. Ethanol/acetone is used to moisten the Kim-wipe for cleaning fibers.
3. Cleave the exposed bare fiber using a fiber cleaver to get a flat end face.
4. Place the fiber into the fusion splicer and clamp it.
5. Repeat **steps 1–4** above for the second fiber to be spliced.
6. Align the two fibers in the fusion splicer and set the gap between the fiber endfaces to approximately 1 mm.
7. Choose the appropriate fusion splicer program (including the arc power and arc time duration, etc.) and execute the program (*see* **Note 1**).
8. Remove the fusion-spliced contiguous fiber, and if appropriate, protect the spliced fiber section with a rigid heat shrink tube (*see* **Note 2**).

For advanced fusion splicers, **steps 6** and **7** can be done automatically. Examples of fusion splicing single-mode fibers (SMF) with several different types of optical fibers are shown in Fig. 15. Figure 15a shows a microscope image of the fusion joint of two SMFs; Fig. 15b shows an optical microscope image of a section of hollow-core fiber (HCF) spliced to two SMFs; Fig. 15c shows a microscope image of the fusion joint of an SMF and a photonic crystal fiber (PCF). It should be noted that when fusion-splicing holey core fibers (e.g., HCF and PCF), the splicing parameters

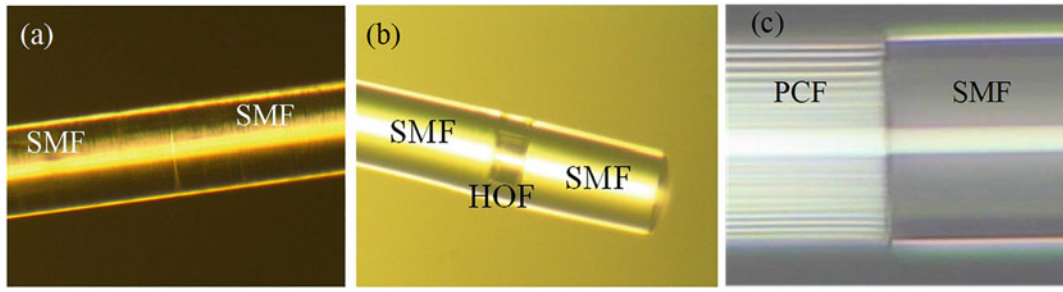


**Fig. 15** Examples of fusion splicing single-mode fiber (SMF) with different types of optical fibers. Microscope images of SMF fusion splicing with (**a**) SMF, (**b**) hollow-core fiber (HCF), and (**c**) photonic crystal fiber (PCF) [193]

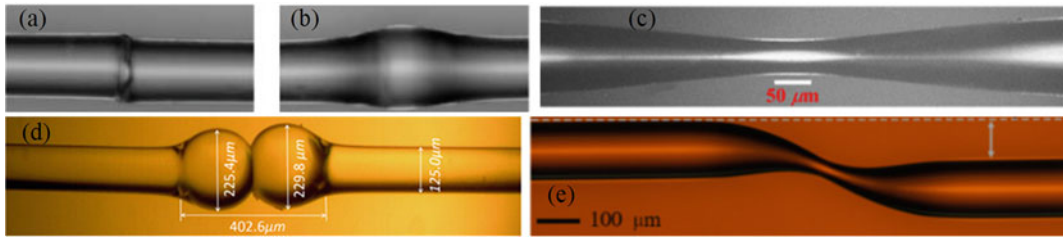


**Fig. 16** Examples of advanced fiber in-line structures fabricated by various advanced fusion splicing techniques [194–197]: (**a**) lateral offset, (**b**) up-taper, (**c**) down-taper, (**d**) peanut-shaped structure, and (**e**) S-taper. These advanced structures could be used as cladding mode exciters in constructing fiber in-line interferometers for sensing applications with improved compactness and enhanced measurement sensitivity and resolution

should be properly chosen to mitigate the micro-hole collapse effect which could induce extra insertion loss.

In addition to connecting two optical fibers, fiber-in-line special structures have also been fabricated using advanced fusion splicing techniques. Figure 16 shows examples of (a) lateral offset, (b) up-taper, (c) down-taper, (d) peanut-shaped structure, and more complicated structures, such as an (e) S-taper. These structures are widely employed as building blocks (e.g., mode exciter and combiner) for constructing micromachined OFSs with improved performance (e.g., compactness, measurement sensitivity, and resolution).

### *3.1.2 Tapering*

Tapering is a process of stretching an optical fiber at an elevated temperature generated by a heat source such as flame, microheater, or $CO_2$ laser irradiation. A schematic of a typical home-built optical fiber tapering setup is shown in Fig. 17a. The tapering setup includes two motorized linear translation stages separated by a specified distance (e.g., ~15 cm). Each stage has an optical fiber clamp mounted on the top of the stage, which is used to secure the

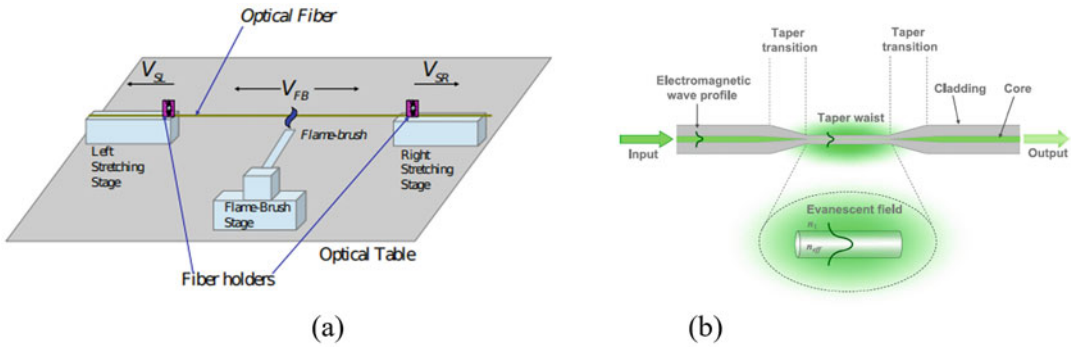


**Fig. 17** Schematics of a typical optical fiber tapering setup and a tapered optical fiber. (**a**) Schematic of a typical home-built setup for tapering optical fibers [198]. (**b**) Schematic illustration of a tapered optical fiber [43]. A typical tapered optical fiber consists of two regions: the taper waist and the taper transition

optical fiber to be processed. The process involved in tapering an optical fiber is described as follows:

1. Strip the plastic coating in the middle of a section of an optical fiber to expose a certain length of bare fiber (a few centimeters) using the optical fiber stripper.
2. Clean the fiber to remove residual material and dust using lint-free Kimwipes. Ethanol/acetone is typically used to moisten the Kimwipe for cleaning the fiber.
3. Secure the two ends of the optical fiber onto the left and right stretching stages in the tapering setup shown in Fig. 17a with the stripped optical fiber section in the middle between the two stages.
4. Approach the heat source toward the stripped optical fiber section to heat the optical fiber; turn on the motors of the two stages and set them to a constant moving speed.
5. A loss detection system and an imaging system are typically integrated into the tapering setup for monitoring the tapering process in real-time (*see* **Notes 3** and **4**).
6. After reaching the desired parameters of the taper, stop the movements of translation stages and remove the heat source.
7. Remove the tapered optical fiber from the setup and characterize the dimensional parameters of the taper using a microscope.

A tapered optical fiber consists of two regions: the taper waist and the taper transition, as illustrated in Fig. 17b. The tapered waist is a region of fiber with reduced but uniform diameter, while the taper transition is a conical section of fiber where the diameter changes to merge the taper waist with the original lead-in/out fiber. The geometrical parameters of a tapered optical fiber, including the diameter of the taper waist and the transition length, can be precisely controlled by the length of the heating region, heating

time, and the pulling speed of the stages. The processes of tapering optical fibers were initially developed for fabricating directional couplers, where two or more tapers were fused for light coupling. In fact, tapered optical fibers provided several unique features for sensor development, such as compactness, user-configurability, and strong evanescent wave (EW). Generally, the diameter of the taper waist can be reduced down to a few micrometers or even nanometers, making it attractive for biomedical applications where a minimally invasive intrusion is required. More importantly, tapering not only exposes the evanescent field to the surroundings but also increases the evanescent field and penetration depth due to the reduced diameter of the optical fiber, which degrades the confinement of the propagating electromagnetic (EM) wave. The smaller the diameter of the taper waist, the stronger the EW. The enhanced EW will interact with the surrounding medium, making a tapered optical fiber an excellent candidate for chemical/biological sensing. Figure 18 shows several scanning electron microscopy (SEM) images of microfibers/nanofibers (MNFs) fabricated by the tapering technique.

Another application of tapered optical fibers for sensor development is as cladding mode exciter (*see* Fig. 16c), where part of the transmitted light in the optical fiber core is coupled to the cladding when it passes through the tapered region. By employing a pair of in-line tapered optical fibers, a fiber-in-line Mach–Zehnder interferometer can be constructed for sensing applications, such as for measurements of strain and refractive index [202, 203].

### 3.1.3 Polishing

Fiber polishing is a micromachining technique developed to treat the side cylindrical surface or endface of an optical fiber for proper light guidance. Side-polished fibers are one of the most successful

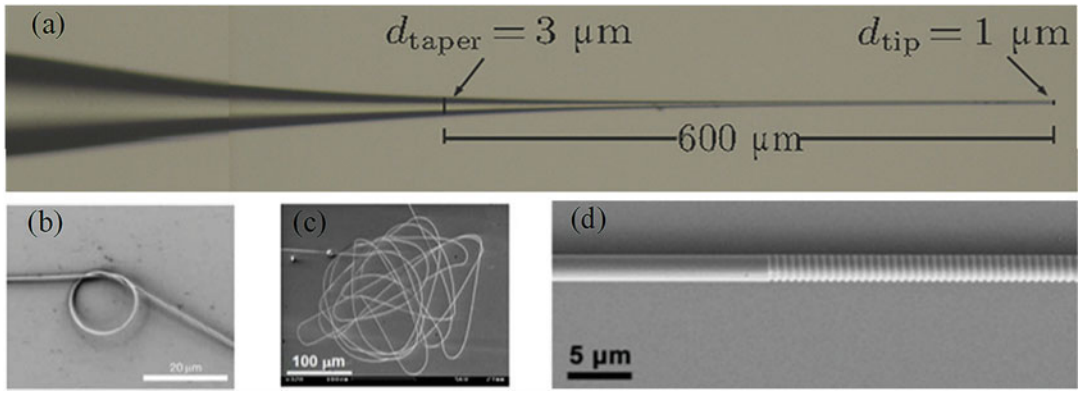


**Fig. 18** SEM images of tapered optical fibers with various structural features. (**a**) A simple tapered fiber tip [199]. (**b**) A micro-ring made with a 520 nm diameter silica microfiber [200]. (**c**) A coiled silica microfiber (with a diameter of 260 nm) with a total length of 4 mm [200]. (**d**) A fiber Bragg grating inscribed on a silica microfiber where the diameter of the fiber was tapered to 1.8 μm [201]

outcomes of the fiber polishing technique. In side-polished fibers, portions of the fiber cladding on one side of the optical fiber are normally removed by the polishing process, as illustrated in Fig. 19a (front view) and b (cross-sectional view), resulting in the exposure of the EW to the surroundings. Side-polished fibers have been extensively studied for evanescent field coupling applications, as well as for sensing due to the enhanced EW in the polished region. Side-polished fibers are also used as a platform for inscribing grating structures for sensing applications [204, 205]. The most significant parameter determining the strength of the EW in side-polished fibers is the thickness of the residual cladding, the thinner the residual cladding, the stronger the EW, thus the stronger the interaction with the external surroundings. Bending the polished region can also greatly enhance the EW, thus improving the sensitivity of the device for sensing applications.

Since optical fibers are generally too small (e.g., with a diameter of 125 μm) to be directly polished alone, blocks used to support fibers during the polishing process are typically required. Quartz or fused silica has been widely used for this purpose because it is essentially the same material as silica fibers. A typical step-by-step side polishing process is schematically illustrated in Fig. 19c and is described below:

1. Strip the plastic coating in the middle of a section of an optical fiber to expose a section of bare fiber with a length that is similar to the length of the V-groove used in the polishing setup (*see* **Note 5**).
2. Clean the fiber to remove residual material and dust using lint-free Kimwipes. Ethanol/acetone is typically used to moisten the Kimwipe for cleaning the fiber.
3. Place the stripped optical fiber section onto the curved V-groove with the application of a pre-strain.
4. Immobilize the optical fiber in the groove by gluing the fiber (*see* **Note 6**).
5. Examine the secured optical fiber under an optical microscope to ensure that the central region of the optical fiber sits properly in the groove.
6. Place the block with the embedded optical fiber on the mounting plate that is secured to the polishing jig of a polishing machine.
7. Polish the central region of the optical fiber using polishing powders and polishing pads with appropriate parameters (e.g., grit size ~0.05 μm, *see* **Note 7**).
8. Repeatedly clean and wipe the polished surface of the optical fiber during the polishing process.

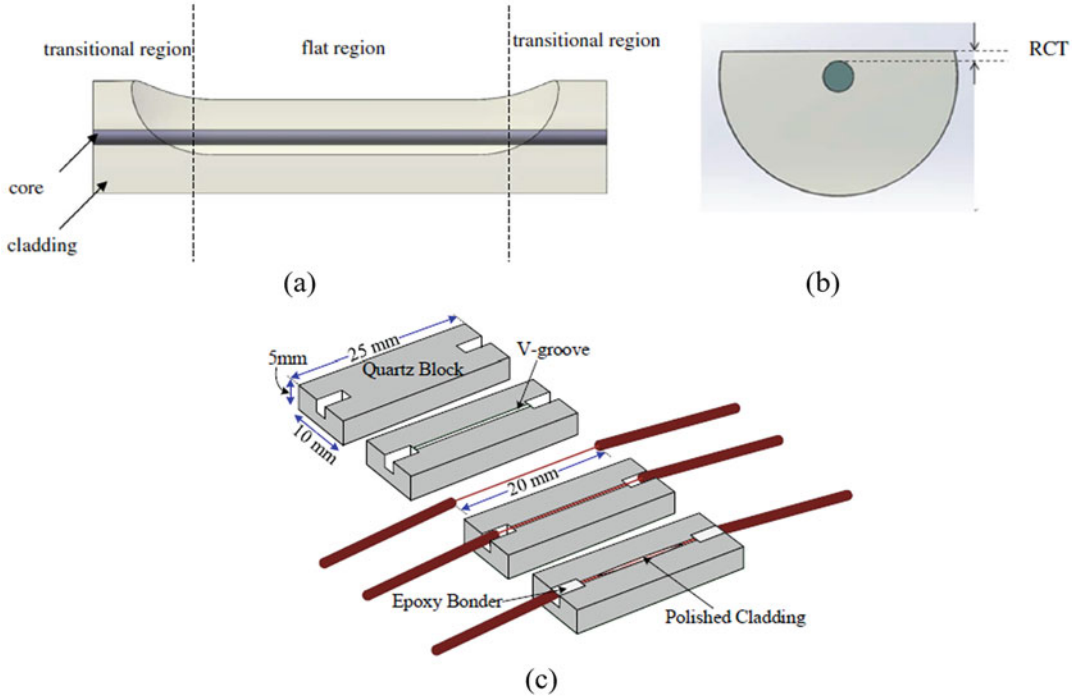


**Fig. 19** Overview of a polished optical fiber and the associated fabrication process. Schematic of a side-polished fiber (**a**) front view and (**b**) cross-sectional view in the polished region of the fiber. *RCT* residual cladding thickness [206]. (**c**) Schematic illustration of a typical step-by-step fabrication process for a side-polished fiber [207]

The thickness of the residual cladding after polishing can be estimated by the liquid-drop method [10] or checked under a microscope.

Another application of the fiber polishing technique is endface polishing, where the endface of an optical fiber can be polished to various angles. Optical fibers with angled endface are especially attractive for developing endoscopic probe or imaging device because the direction of propagation of the light output from the optical fibers can be guided to the internal organs and tissues of interest by the angled fiber endface [208]. Figure 20 shows a miniaturized surface-mountable optical fiber pressure sensor with a cross-axial configuration [209]. The cross-axial configuration was enabled by an optical fiber with a 45° angled endface, through which the incident probing light is directed to the sensing diaphragm engineered on the sidewall of the fiber. The cross-axial configuration is especially desirable for pressure measurements in fluids such as in blood vessels because the cross-axial configuration is easy to install and can distinguish the static pressure from the surface flow. The effect of dynamic pressure, i.e., the pressure

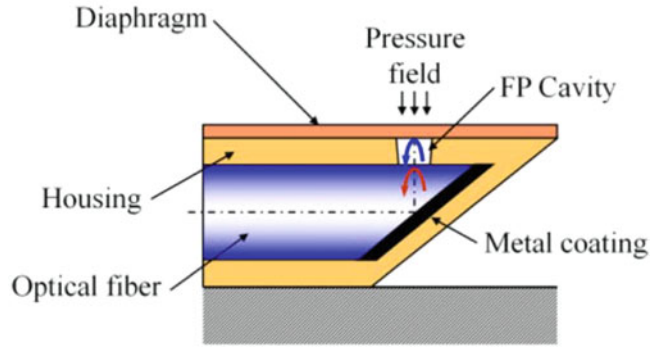


**Fig. 20** Schematic of a miniaturized surface-mountable Fabry–Perot (FP) pressure sensor constructed with a 45° angled fiber [209]. The 45° angled fiber was used to direct the incident probing light to the diaphragm engineered on the sidewall of the optical fiber to form the cross-axial configuration

variations induced by the flow hitting at the diaphragm if the diaphragm is perpendicular to the flow, is eliminated.

### 3.2 Femtosecond Laser Micromachining

Lasers with high intensities have been rapidly developed and used for precise material processing (e.g., welding or cutting) since the first demonstration in the 1960s [210]. With the advancement of laser technologies, especially mode-locking and chirped pulse amplification techniques, the intensities of commercial femtosecond laser (with ultrashort pulse width, in fs scale) have reached up to $10^{13}$ W/cm$^2$. Under the irradiation of lasers with such high intensities, most materials, especially transparent materials, will be ionized and exhibit nonlinear behavior, and consequently undergo a phase or structural modification, leaving behind a localized permanent change in the material (e.g., a change in refractive index or a void space) [11]. In recent years, femtosecond laser three-dimensional (3D) micromachining has found niche applications in material processing and one-step fabrication of photonic micro/nanostructures [211]. Due to the ultra-high intensities, femtosecond lasers can be employed to eliminate materials from the surface of solid structures (ablation) or to transform the local properties within hard or soft solid material structures (irradiation). Compared with traditional long-pulse lasers, femtosecond lasers offer unparalleled features when utilized in fabrication processes, such as high precision, negligible cracks, reduced or eliminated heat-affected zones, and the ability for subsurface 3D fabrication. Femtosecond laser micromachining involves methodologies centered around the interactions and 3D manipulations of femtosecond lasers with materials. OFSs involves methodologies centered around probing-light-measurand encoding and interrogation of the modulated light waves. Combining femtosecond laser

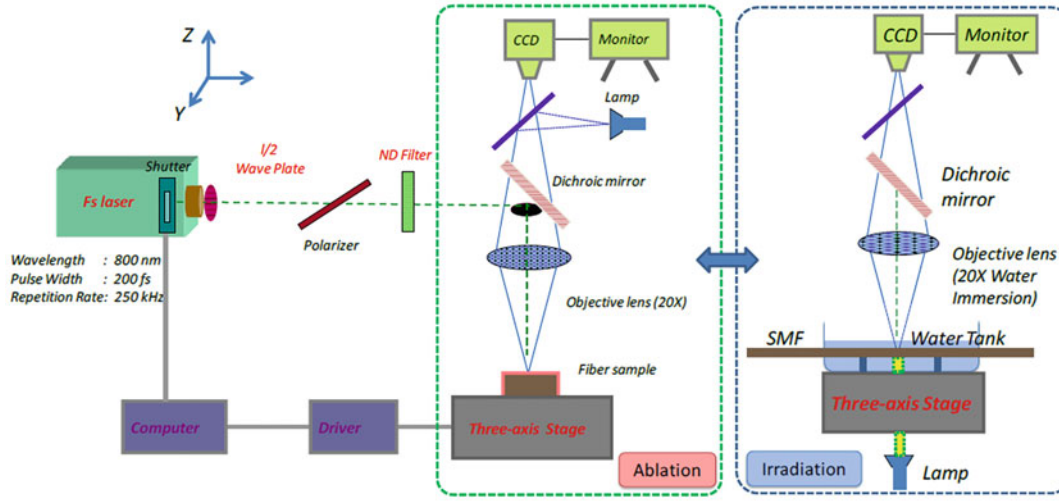


**Fig. 21** Schematic of a home-built femtosecond laser micromachining system [189]

micromachining methodologies with optical fiber sensing technologies prompts a new research topic, the lab-in/on-fiber (3D structuring of multiplexed components in/on fiber), which enables the opportunity to fabricate a novel generation of assembly-free smart sensors with combined advantages from the two different arenas.

A home-built femtosecond laser micromachining system is schematically illustrated in Fig. 21. A typical process involved in femtosecond laser micromachining an optical fiber is described below:

1. Load an optical fiber to be processed (with/without polymer coating) in the sample holder on top of a microscope slide. The sample holder is fixed on top of a high-precision translation stage assembly.
2. Secure the optical fiber using two magnetic clamps that are integrated into the stage assembly. A pre-strain is applied to the optical fiber between the two clamps to ensure the fiber section is straight (*see* **Note 8**).
3. Add two spacers (a small section of an optical fiber) on each side of the secured optical fiber on the microscope slide. Position the two spacers parallel and close to the optical fiber to be processed.
4. Add a drop of index-matching gel on top of the optical fiber to be processed and make sure that the index-matching gel is contained between the two spacers.
5. Place a microscope cover-slip on top of the optical fiber to be processed and make sure that the optical fiber is covered with a

uniform layer of the index-matching gel with no air bubble mixed in the gel.

6. Adjust the focus point of the femtosecond laser beam on the surface of the optical fiber for ablation or within the optical fiber for irradiation, according to the desired purpose, by moving the stage assembly. An online monitoring system composed of a camera and lens assembly is used to assist the alignment and visualize the fabrication process.
7. Open the shutter of the femtosecond laser amplifier for a short period of time (e.g., 20 ms) to cause minute visible damage in the optical fiber to precisely locate the focus point of the laser. Corresponding adjustments of the fiber position can then be made.
8. After fabrication, remove the processed optical fiber from the sample holder for characterization or follow-up chemical treatment.

   It should be noted that for the irradiation process, the fiber sample is typically immersed in water, oil, or index-matching gel to eliminate spherical aberrations due to the cylindrically shaped fiber. The properties of the micromachined features on/in an optical fiber are determined by the scanning speed of the translation stage, and the parameters of the femtosecond laser, which include pulse energy, repetition rate, polarization state, and beam profile (*see* **Note 9**).

#### *3.2.1 Direct Femtosecond Laser Writing in Optical Fibers*

Since the discovery by Davis et al. that tightly focused femtosecond laser beams can induce permanent modification to the local refractive index parameter inside a glass, numerous photonic micro/nanostructures have been developed for functional 3D optical circuits in a glass substrate [212]. The unique advantages of 3D femtosecond laser direct writing have also made it attractive to the fiber optic field. Successful examples that have been achieved using femtosecond laser direct writing in optical fibers include grating structures (i.e., fiber Bragg gratings and long-period gratings), ultra-weak in-line reflectors, micro-cavities, waveguides, 3D circuits, and other complex structures (e.g., a micro-cantilever), as shown in Fig. 22. All these microstructures have been demonstrated as building blocks for a new generation of assembly free smart OFS, which are desirable in biomedical applications over traditional OFSs due to the extreme compactness, robustness, improved flexibility, and enhanced functionality and intelligence.

In femtosecond laser direct writing of optical fibers, the accuracy of fabricating design elements of 3D microstructures strongly relies on the size of the focused laser spot. The relationship between the radius of the laser spot ($r$) and the numerical aperture (NA) of the objective lens used in the femtosecond laser system is approximated by [215]:

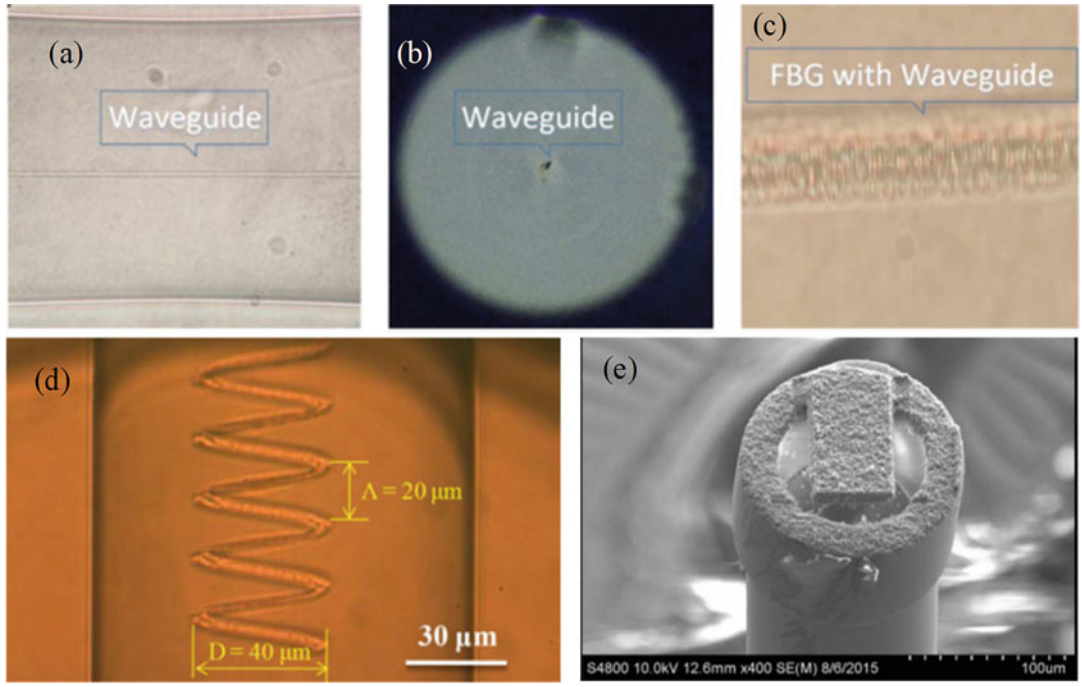


**Fig. 22** Examples of microstructures created on/in optical fibers by direct femtosecond laser writing. Microscope images of a waveguide-integrated fiber Bragg grating (FBG) device: (**a**) waveguide written in coreless fiber, (**b**) cross-sectional view of the device, and (**c**) FBG written in the waveguide [213]. (**d**) Microscope image of a helical structure in an optical fiber [189]. (**e**) SEM image of a micro-cantilever on the tip of an optical fiber fabricated by femtosecond laser ablation [214]

$$r = \frac{0.61}{\mathrm{NA}} \frac{\lambda}{n} \tag{1}$$

where $\lambda$ is the wavelength of the femtosecond laser beam, and $n$ is the refractive index of the fiber sample. For a given femtosecond laser micromachining system (fixed $\lambda$) and a given fiber sample, the larger NA will contribute to a smaller laser spot, resulting in greater accuracy of fabrication. However, there is always a tradeoff between fabrication time and accuracy. A general guide to choosing a proper objective in a femtosecond laser direct writing system is given by the following three guide points [189]:

1. Choose a microscope objective with a low NA (<0.1) for the rough fabrication of large-area surface elements.
2. Choose a microscope objective with an NA ranging from 0.1 to 0.5 for subsurface modification and high-precision surface ablation.
3. Choose a microscope objective with a large NA (e.g., liquid immersive lens) for high-accuracy modifications and ablation of a fiber.

### 3.2.2 Chemical-Assisted Femtosecond Laser Writing in Optical Fibers

In recent years, optofluidic systems have attracted extensive research interest due to their unparalleled features for chemical, biological, and biomedical sensing applications [187]. In an optofluidic-based system, microfluidic architectures are synergistically integrated into an optical waveguide, where the liquid of interest with an extremely small volume (e.g., microliter, nanoliter, or picoliter) can travel through the microfluidic architectures (e.g., microchannels) and then be analyzed using optical methods. Femtosecond laser irradiation followed by chemical etching (FLICE) has recently emerged as a promising method for fabricating microfluidic systems in waveguides [216]. The combination of the FLICE technique with femtosecond laser 3D direct writing in optical fibers has afforded a novel means of integrating optical circuits and microfluidic systems, which enables the emergence of ultra-compact, alignment-free all-in-fiber optofluidic devices [190]. Specifically, the FLICE technique relies on the high susceptibility of the femtosecond laser-irradiated region to chemical etching, such as hydrofluoric acid (HF) and potassium hydroxide (KOH). Employing the femtosecond laser direct writing technique, arbitrary 3D optical circuits can be fabricated inside an optical fiber. After laser irradiation, the etching process can be conducted. The etching rate of the laser-irradiated region is up to two orders of magnitude faster by than that of the un-irradiated region in the fiber cladding. Given sufficient etching time, satisfactory quality of microfluidic architectures with good surface roughness can be obtained. Compared to holey fiber (e.g., PCF)-based optofluidic devices, a FLICE-enabled lab-in-fiber offers much higher flexibility, where multi-microfluidic components can be integrated in 3D to achieve highly functional and multiplexed optofluidic sensing. Figure 23 shows several examples of microchannels fabricated in optical fibers using the FLICE technique.

In addition to FLICE-enabled fabrication of 3D microfluidic systems, an arbitrary microchannel can also be directly fabricated in an optical fiber using the femtosecond laser-induced water breakdown (FLIWD) method, where no hazardous chemicals are required [218]. The FLIWD technique relies on the interaction between the femtosecond laser and the water breakdown phenomenon. Compared to the FLICE technique, the FLIWD approach provides a more uniform diameter of the microchannel. However, in FLIWD micromachining, the surface roughness degrades and thus introducing significant insertion loss [189].

## 4 Notes

1. The model of the fusion splicer used in the fabrication was TYPE-36, Sumitomo Electric Industries, Ltd. The parameters for splicing two single-mode fibers were as follows: an arc

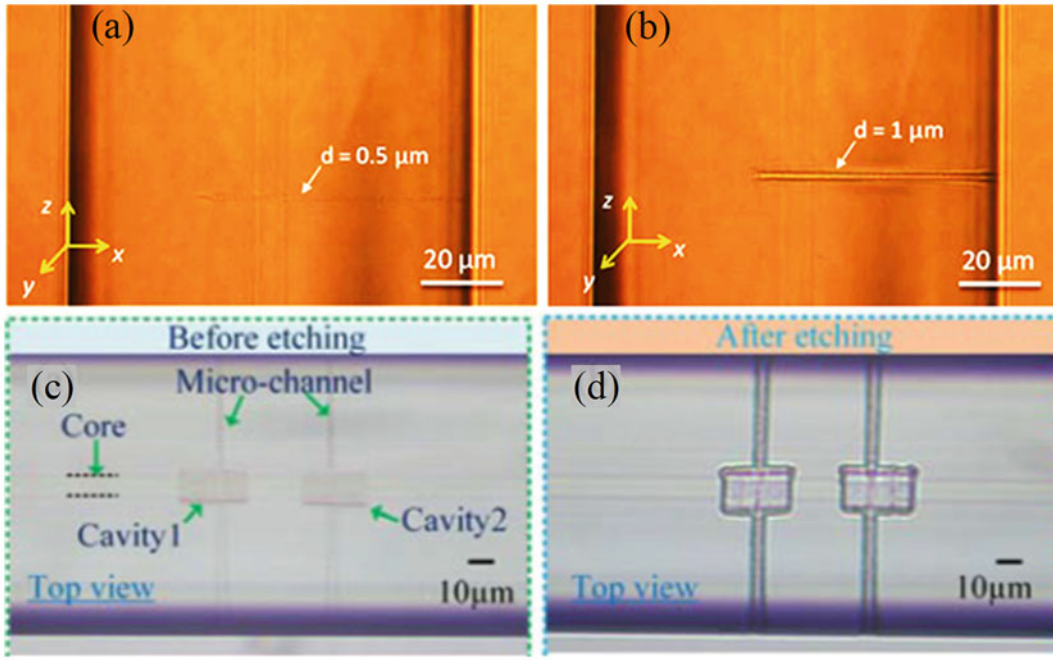


**Fig. 23** Examples of microfluidic architectures in optical fibers fabricated by the FLICE method. Microscope images of a blind microhole inside an SMF (**a**) before HF etching and (**b**) after HF etching [189]. Microscope images of an all-in-fiber optofluidic device (**c**) before HF etching and (**d**) after HF etching [217]

duration of 1.5 s, a prefusion of 0.1 s, an arc gap of 10 μm, an overlap of 15 μm, and an arc power of 64 steps. Note that for splicing a single-mode fiber with a hollow-core fiber, the arc duration and arc power should be correspondingly decreased to avoid the collapse of the hollow-core fiber at the joint point.

2. The fusion-spliced joint is not as strong as the original optical fiber, so a protective sleeve (e.g., a heat-shrinkable tube) is usually used to cover the joint and to protect it.
3. A loss detection system is always integrated with an optical fiber tapering setup for in situ monitoring of the transmission loss of the fiber under tapering. Two free ends of the optical fiber to be processed are connected to a laser source and a photodetector (or an optical spectrum analyzer).
4. A complete optical fiber tapering setup is also integrated with an imaging system (e.g., a microscope or simply an objective combined with a camera) for visualizing the tapering process such that the process can be immediately ceased once the desired dimensional parameters of the optical fiber taper are reached.
5. The parameters of the side-polished fiber, i.e., the length of the polished region and the thickness of the residual cladding, are

determined by the geometric parameters of the V-groove in the supporting block (the length, width, and depth of the groove).

6. In the immobilization of the optical fiber in the polishing process, epoxy should be applied to the central region of the optical fiber in the groove, and the fiber sections in the outer region should be glued after the applied epoxy in the central region cures. The process is necessary to minimize the possible motion of the optical fibers in the central region that will be polished.
7. Cautions should be taken in selecting an appropriate particle size of the powder and the proper polishing pad. If the particle size is too large ($>1$ μm), a large number of scratches could be created on the polished fiber surface, which randomly scatter transmission light.
8. It is necessary to apply a pre-strain to make the fiber straight when the optical fiber to be processed is secured using the two clamps. This process will greatly facilitate the subsequent alignment process especially when a relatively large structure (in length) needs to be fabricated, e.g., a fiber Bragg grating with a length of 5 mm.
9. The properties of the fabricated structure by femtosecond laser irradiation depend not only on the parameters of the femtosecond laser (including pulse energy, repetition rate, polarization state, and beam profile) but also on the movement of the translation stage during fabrication, coupled with the alignment accuracy. An example includes using the femtosecond laser to write a fiber Bragg grating structure by the point-by-point technique. During the fabrication, the translation stage moves at a constant velocity ($v$) along the longitudinal axis of the fiber; femtosecond laser pulses with a constant repetition rate are focused into the fiber core to cause a localized change in the refractive index. Each laser pulse produces a single grating line in the fiber core. The Bragg wavelength of the fabricated fiber Bragg grating is proportional to the ratio of the velocity of the translation stage to the repetition rate of the laser pulses. Therefore, the point-by-point femtosecond laser inscription of a fiber Bragg grating offers unparalleled design flexibility, where the Bragg wavelength and the index modulation profile can be easily adjusted.

## References

1. Bass M, Van Stryland EW (2002) Fiber optics handbook: fiber, devices, and systems for optical communications. McGraw-Hill, New York. vol Sirsi. i9780071386234. Optical Society of America
2. Yeh C (2013) Handbook of fiber optics: theory and applications. Academic
3. Krohn DA, MacDougall T, Mendez A (2014) Fiber optic sensors: fundamentals and applications. Spie Press, Bellingham, WA

4. Edmonson JM (1991) History of the instruments for gastrointestinal endoscopy. Gastrointest Endosc 37:S27–S56
5. Meglinski I (2015) Biophotonics for medical applications. Elsevier
6. Taffoni F, Formica D, Saccomandi P, Pino G, Schena E (2013) Optical fiber-based MR-compatible sensors for medical applications: an overview. Sensors 13 (10):14105–14120
7. Engin M, Demirel A, Engin EZ, Fedakar M (2005) Recent developments and trends in biomedical sensors. Measurement 37 (2):173–188
8. Yablon AD (2005) Optical fiber fusion splicing, vol 103. Springer Science & Business Media
9. Lou J, Wang Y, Tong L (2014) Microfiber optical sensors: a review. Sensors 14 (4):5823–5844
10. Tseng S-M, Chen C-L (1992) Side-polished fibers. Appl Opt 31(18):3438–3447
11. Gattass RR, Mazur E (2008) Femtosecond laser micromachining in transparent materials. Nat Photonics 2(4):219
12. Schena E, Tosi D, Saccomandi P, Lewis E, Kim T (2016) Fiber optic sensors for temperature monitoring during thermal treatments: an overview. Sensors 16(7):1144
13. Lee BH, Kim YH, Park KS, Eom JB, Kim MJ, Rho BS, Choi HY (2012) Interferometric fiber optic sensors. Sensors 12(3):2467–2486
14. Choi HY, Park KS, Park SJ, Paek U-C, Lee BH, Choi ES (2008) Miniature fiber-optic high temperature sensor based on a hybrid structured Fabry–Perot interferometer. Opt Lett 33(21):2455–2457
15. Tripathi SM, Kumar A, Varshney RK, Kumar YBP, Marin E, Meunier J-P (2009) Strain and temperature sensing characteristics of single-mode–multimode–single-mode structures. J Lightwave Technol 27(13):2348–2356
16. Chen P, Shu X (2018) Refractive-index-modified-dot Fabry-Perot fiber probe fabricated by femtosecond laser for high-temperature sensing. Opt Express 26(5):5292–5299
17. Zhu C, Zhuang Y, Zhang B, Muhammad R, Wang PP, Huang J (2018) A miniaturized optical fiber tip high-temperature sensor based on concave-shaped Fabry–Perot cavity. IEEE Photon Technol Lett 31(1):35–38
18. Jiang L, Yang J, Wang S, Li B, Wang M (2011) Fiber Mach–Zehnder interferometer based on microcavities for high-temperature sensing with high sensitivity. Opt Lett 36 (19):3753–3755
19. Hu T, Wang Y, Liao C, Wang D (2012) Miniaturized fiber in-line Mach–Zehnder interferometer based on inner air cavity for high-temperature sensing. Opt Lett 37 (24):5082–5084
20. Lu P, Chen Q (2011) Femtosecond laser microfabricated fiber Mach–Zehnder interferometer for sensing applications. Opt Lett 36 (2):268–270
21. Zhao Y, Zhao H, R-q L, Zhao J (2019) Review of optical fiber Mach–Zehnder interferometers with micro-cavity fabricated by femtosecond laser and sensing applications. Opt Lasers Eng 117:7–20
22. Mihailov SJ (2012) Fiber Bragg grating sensors for harsh environments. Sensors 12 (2):1898–1918
23. Chen J, Liu B, Zhang H (2011) Review of fiber Bragg grating sensor technology. Frontiers of Optoelectronics in China 4 (2):204–212
24. Mao Y, Zhang Y, Xue R, Liu Y, Cao K, Qu S (2018) Compact optical fiber temperature sensor with high sensitivity based on liquid-filled silica capillary tube. Appl Opt 57 (5):1061–1066
25. Yu Y, Li X, Hong X, Deng Y, Song K, Geng Y, Wei H, Tong W (2010) Some features of the photonic crystal fiber temperature sensor with liquid ethanol filling. Opt Express 18 (15):15383–15388
26. Geng Y, Li X, Tan X, Deng Y, Hong X (2013) Compact and ultrasensitive temperature sensor with a fully liquid-filled photonic crystal fiber Mach–Zehnder interferometer. IEEE Sensors J 14(1):167–170
27. Kuhlmey BT, Eggleton BJ, Wu DK (2009) Fluid-filled solid-core photonic bandgap fibers. J Lightwave Technol 27 (11):1617–1630
28. Yoo W-J, Jang K-W, Seo J-K, Heo J-Y, Moon J-S, Park J-Y, Lee B-S (2010) Development of respiration sensors using plastic optical fiber for respiratory monitoring inside MRI system. J Opt Soc Korea 14(3):235–239
29. Jasim AA, Harun SW, Arof H, Ahmad H (2012) Inline microfiber Mach–Zehnder interferometer for high temperature sensing. IEEE Sensors J 13(2):626–628
30. J-l K, Feng J, Ye L, Xu F, Lu Y-q (2010) Miniaturized fiber taper reflective interferometer for high temperature measurement. Opt Express 18(13):14245–14250
31. Kou J-L, Ding M, Feng J, Lu Y-Q, Xu F, Brambilla G (2012) Microfiber-based Bragg

gratings for sensing applications: a review. Sensors 12(7):8861–8876

32. Xue Y, Yu Y-S, Yang R, Wang C, Chen C, Guo J-C, Zhang X-Y, Zhu C-C, Sun H-B (2013) Ultrasensitive temperature sensor based on an isopropanol-sealed optical microfiber taper. Opt Lett 38(8):1209–1211
33. Hernández-Romano I, Monzón-Hernández D, Moreno-Hernández C, Moreno-Hernandez D, Villatoro J (2015) Highly sensitive temperature sensor based on a polymer-coated microfiber interferometer. IEEE Photon Technol Lett 27 (24):2591–2594
34. Talaverano L, Abad S, Jarabo S, Lopez-Amo M (2001) Multiwavelength fiber laser sources with Bragg-grating sensor multiplexing capability. J Lightwave Technol 19(4):553–558
35. Gifford DK, Soller BJ, Wolfe MS, Froggatt ME (2005) Distributed fiber-optic temperature sensing using Rayleigh backscatter. In: 2005 31st European conference on optical communication, ECOC 2005. IET, pp 511–512
36. Kurashima T, Horiguchi T, Tateda M (1990) Distributed-temperature sensing using stimulated Brillouin scattering in optical silica fibers. Opt Lett 15(18):1038–1040
37. Dakin J, Pratt D, Bibby G, Ross J (1985) Distributed optical fibre Raman temperature sensor using a semiconductor light source and detector. Electron Lett 21(13):569–570
38. Chen Z, Yuan L, Hefferman G, Wei T (2015) Ultraweak intrinsic Fabry–Perot cavity array for distributed sensing. Opt Lett 40 (3):320–323
39. Huang J, Lan X, Luo M, Xiao H (2014) Spatially continuous distributed fiber optic sensing using optical carrier based microwave interferometry. Opt Express 22 (15):18757–18769
40. Macchi EG, Tosi D, Braschi G, Gallati M, Cigada A, Lewis E (2014) Optical fiber sensors-based temperature distribution measurement in ex vivo radiofrequency ablation with submillimeter resolution. J Biomed Opt 19(11):117004
41. Poeggel S, Duraibabu D, Kalli K, Leen G, Dooly G, Lewis E, Kelly J, Munroe M (2015) Recent improvement of medical optical fibre pressure and temperature sensors. Biosensors 5(3):432–449
42. Ukil A, Braendle H, Krippner P (2011) Distributed temperature sensing: review of technology and applications. IEEE Sensors J 12(5):885–892
43. Correia R, James S, Lee S, Morgan S, Korposh S (2018) Biomedical application of optical fibre sensors. J Opt 20(7):073003
44. Roriz P, Ramos A, Santos JL, Simões JA (2012) Fiber optic intensity-modulated sensors: a review in biomechanics. Photonic Sensors 2(4):315–330
45. Cottler PS, Karpen WR, Morrow DA, Kaufman KR (2009) Performance characteristics of a new generation pressure microsensor for physiologic applications. Ann Biomed Eng 37 (8):1638–1645
46. Bae H, Yu M (2012) Miniature Fabry-Perot pressure sensor created by using UV-molding process with an optical fiber based mold. Opt Express 20(13):14573–14583
47. Ma J, Jin W, Ho HL, Dai JY (2012) High-sensitivity fiber-tip pressure sensor with graphene diaphragm. Opt Lett 37 (13):2493–2495
48. Xu F, Ren D, Shi X, Li C, Lu W, Lu L, Lu L, Yu B (2012) High-sensitivity Fabry–Perot interferometric pressure sensor based on a nanothick silver diaphragm. Opt Lett 37 (2):133–135
49. Zhu Y, Wang A (2005) Miniature fiber-optic pressure sensor. IEEE Photon Technol Lett 17(2):447–449
50. Zhu Y, Cooper KL, Pickrell GR, Wang A (2006) High-temperature fiber-tip pressure sensor. J Lightwave Technol 24(2):861–869
51. Guo X, Zhou J, Du C, Wang X (2019) Highly sensitive miniature all-silica fiber tip Fabry-Perot pressure sensor. IEEE Photon Technol Lett 31(9):689–692
52. Donlagic D, Cibula E (2005) All-fiber high-sensitivity pressure sensor with SiO 2 diaphragm. Opt Lett 30(16):2071–2073
53. Cibula E, Pevec S, Lenardič B, Pinet E, Đonlagić D (2009) Miniature all-glass robust pressure sensor. Opt Express 17 (7):5098–5106
54. Zhang Y, Yuan L, Lan X, Kaur A, Huang J, Xiao H (2013) High-temperature fiber-optic Fabry–Perot interferometric pressure sensor fabricated by femtosecond laser. Opt Lett 38 (22):4609–4612
55. Ma J, Ju J, Jin L, Jin W (2011) A compact fiber-tip micro-cavity sensor for high-pressure measurement. IEEE Photon Technol Lett 23 (21):1561–1563
56. Liao C, Liu S, Xu L, Wang C, Wang Y, Li Z, Wang Q, Wang D (2014) Sub-micron silica diaphragm-based fiber-tip Fabry–Perot interferometer for pressure measurement. Opt Lett 39(10):2827–2830

57. Liu S, Wang Y, Liao C, Wang Y, He J, Fu C, Yang K, Bai Z, Zhang F (2017) Nano silica diaphragm in-fiber cavity for gas pressure measurement. Sci Rep 7(1):787
58. Al-Fakih E, Osman A, Azuan N, Mahamd Adikan FR (2012) The use of fiber Bragg grating sensors in biomechanics and rehabilitation applications: the state-of-the-art and ongoing research topics. Sensors 12 (10):12890–12926
59. Puangmali P, Althoefer K, Seneviratne LD, Murphy D, Dasgupta P (2008) State-of-the-art in force and tactile sensing for minimally invasive surgery. IEEE Sensors J 8 (4):371–381
60. Abushagur A, Arsad N, Reaz M, Bakar A (2014) Advances in bio-tactile sensors for minimally invasive surgery using the fibre Bragg grating force sensor technique: a survey. Sensors 14(4):6633–6665
61. Correia R, Sinha R, Norris A, Korposh S, Talbot S, Hernandez F, Hayes-Gill B, Morgan S (2017) Optical fibre sensing at the interface between tissue and medical device. In: International Conference on Biophotonics V. International Society for Optics and Photonics, p 103400X
62. Wang DH-C, Blenman N, Maunder S, Patton V, Arkwright J (2013) An optical fiber Bragg grating force sensor for monitoring sub-bandage pressure during compression therapy. Opt Express 21(17):19799–19807
63. Su H, Zervas M, Furlong C, Fischer GS (2011) A miniature MRI-compatible fiber-optic force sensor utilizing fabry-perot interferometer. In: MEMS and Nanotechnology, vol 4. Springer, pp 131–136
64. Su H, Zervas M, Cole GA, Furlong C, Fischer GS (2011) Real-time MRI-guided needle placement robot with integrated fiber optic force sensing. In: 2011 IEEE international conference on robotics and automation. IEEE, pp 1583–1588
65. Liu X, Iordachita II, He X, Taylor RH, Kang JU (2012) Miniature fiber-optic force sensor based on low-coherence Fabry-Pérot interferometry for vitreoretinal microsurgery. Biomed Opt Express 3(5):1062–1076
66. Du Y, Yang Q, Huang J (2017) Soft prosthetic forefinger tactile sensing via a string of intact single mode optical fiber. IEEE Sensors J 17(22):7455–7459
67. Anwar Zawawi M, O'Keffe S, Lewis E (2013) Intensity-modulated fiber optic sensor for health monitoring applications: a comparative review. Sens Rev 33(1):57–67
68. Dziuda L, Skibniewski FW, Krej M, Lewandowski J (2012) Monitoring respiration and cardiac activity using fiber Bragg grating-based sensor. IEEE Trans Biomed Eng 59 (7):1934–1942
69. Allsop TD, Carroll K, Lloyd G, Webb DJ, Miller M, Bennion I (2007) Application of long-period-grating sensors to respiratory plethysmography. J Biomed Opt 12 (6):064003
70. Dziuda Ł (2015) Fiber-optic sensors for monitoring patient physiological parameters: a review of applicable technologies and relevance to use during magnetic resonance imaging procedures. J Biomed Opt 20(1):010901
71. Jia D, Chao J, Li S, Zhang H, Yan Y, Liu T, Sun Y (2017) A fiber Bragg grating sensor for radial artery pulse waveform measurement. IEEE Trans Biomed Eng 65(4):839–846
72. Sharath U, Sukreet R, Apoorva G, Asokan S (2013) Blood pressure evaluation using sphygmomanometry assisted by arterial pulse waveform detection by fiber Bragg grating pulse device. J Biomed Opt 18(6):067010
73. Mathew J, Semenova Y, Farrell G (2012) A miniature optical breathing sensor. Biomed Opt Express 3(12):3325–3331
74. Kang Y, Ruan H, Wang Y, Arregui F, Matias I, Claus R (2006) Nanostructured optical fibre sensors for breathing airflow monitoring. Meas Sci Technol 17(5):1207
75. Favero FC, Pruneri V, Villatoro J (2012) Microstructured optical fiber interferometric breathing sensor. J Biomed Opt 17 (3):037006
76. Yoo WJ, Jang KW, Seo JK, Heo JY, Moon JS, Jun JH, Park J-Y, Lee B (2011) Development of optical fiber-based respiration sensor for noninvasive respiratory monitoring. Opt Rev 18(1):132–138
77. Charrett TO, James SW, Tatam RP (2012) Optical fibre laser velocimetry: a review. Meas Sci Technol 23(3):032001
78. Khotiaintsev SN, Svirid V, Glebova L (1996) Laser Doppler velocimeter miniature differential probe for biomedical applications. In: Biomedical systems and technologies. International Society for Optics and Photonics, pp 158–165
79. Chahal R, Starecki F, Boussard-Plédel C, Doualan J-L, Michel K, Brilland L, Braud A, Camy P, Bureau B, Nazabal V (2016) Fiber evanescent wave spectroscopy based on IR fluorescent chalcogenide fibers. Sensors Actuators B Chem 229:209–216

80. Anne M-L, Keirsse J, Nazabal V, Hyodo K, Inoue S, Boussard-Pledel C, Lhermite H, Charrier J, Yanakata K, Loreal O (2009) Chalcogenide glass optical waveguides for infrared biosensing. Sensors 9(9):7398–7411
81. Michel K, Bureau B, Boussard-Plédel C, Jouan T, Adam J, Staubmann K, Baumann T (2004) Monitoring of pollutant in waste water by infrared spectroscopy using chalcogenide glass optical fibers. Sensors Actuators B Chem 101(1–2):252–259
82. Le Coq D, Michel K, Keirsse J, Boussard-Plédel C, Fonteneau G, Bureau B, Le Quéré J-M, Sire O, Lucas J (2002) Infrared glass fibers for in-situ sensing, chemical and biochemical reactions. C R Chim 5(12):907–913
83. Anne M-L, Le Lan C, Monbet V, Boussard-Plédel C, Ropert M, Sire O, Pouchard M, Jard C, Lucas J, Adam J-L (2009) Fiber evanescent wave spectroscopy using the mid-infrared provides useful fingerprints for metabolic profiling in humans. J Biomed Opt 14(5):054033
84. Wilhelm AA, Lucas P, DeRosa DL, Riley MR (2007) Biocompatibility of Te–As–Se glass fibers for cell-based bio-optic infrared sensors. J Mater Res 22(4):1098–1104
85. Leung A, Shankar PM, Mutharasan R (2007) A review of fiber-optic biosensors. Sensors Actuators B Chem 125(2):688–703
86. Siegmund H-U, Heiliger L, Van Lent B, Becker A (1998) Optical solid-phase biosensor based on polyionic layers labelled with fluorescent dyes. Google Patents
87. Flora K, Brennan JD (1999) Comparison of formats for the development of fiber-optic biosensors utilizing sol–gel derived materials entrapping fluorescently-labelled protein. Analyst 124(10):1455–1462
88. Tian Y, Wang W, Wu N, Zou X, Wang X (2011) Tapered optical fiber sensor for label-free detection of biomolecules. Sensors 11 (4):3780–3790
89. Latifi H, Zibaii MI, Hosseini SM, Jorge P (2012) Nonadiabatic tapered optical fiber for biosensor applications. Photonic Sensors 2 (4):340–356
90. Gupta RK, Periyakaruppan A, Meyyappan M, Koehne JE (2014) Label-free detection of C-reactive protein using a carbon nanofiber based biosensor. Biosens Bioelectron 59:112–119
91. Fan X, White IM, Shopova SI, Zhu H, Suter JD, Sun Y (2008) Sensitive optical biosensors for unlabeled targets: a review. Anal Chim Acta 620(1–2):8–26
92. Marques L, Hernandez F, James SW, Morgan S, Clark M, Tatam RP, Korposh S (2016) Highly sensitive optical fibre long period grating biosensor anchored with silica core gold shell nanoparticles. Biosens Bioelectron 75:222–231
93. Moreira L, Goncalves HM, Pereira L, Castro C, Jorge P, Gouveia C, Fernandes JR, Martins-Lopes P (2016) Label-free optical biosensor for direct complex DNA detection using Vitis vinifera L. Sensors Actuators B Chem 234:92–97
94. Chen X, Zhang L, Zhou K, Davies E, Sugden K, Bennion I, Hughes M, Hine A (2007) Real-time detection of DNA interactions with long-period fiber-grating-based biosensor. Opt Lett 32(17):2541–2543
95. Sozzi M, Coscelli E, Poli F, Cucinotta A, Selleri S, Corradini R, Marchelli R, Konstantaki M, Pissadakis S (2011) Long period grating-based fiber optic sensor for label-free DNA detection. In: 2011 International workshop on biophotonics. IEEE, pp 1–3
96. Chiavaioli F, Biswas P, Trono C, Jana S, Bandyopadhyay S, Basumallick N, Giannetti A, Tombelli S, Bera S, Mallick A (2015) Sol–gel-based titania–silica thin film overlay for long period fiber grating-based biosensors. Anal Chem 87(24):12024–12031
97. Biswas P, Chiavaioli F, Jana S, Basumallick N, Trono C, Giannetti A, Tombelli S, Mallick A, Baldini F, Bandyopadhyay S (2017) Design, fabrication and characterisation of silica-titania thin film coated over coupled long period fibre gratings: towards bio-sensing applications. Sensors Actuators B Chem 253:418–427
98. Bhatia V, Vengsarkar AM (1996) Optical fiber long-period grating sensors. Opt Lett 21 (9):692–694
99. Homola J, Yee SS, Gauglitz G (1999) Surface plasmon resonance sensors. Sensors Actuators B Chem 54(1–2):3–15
100. Caucheteur C, Guo T, Albert J (2015) Review of plasmonic fiber optic biochemical sensors: improving the limit of detection. Anal Bioanal Chem 407(14):3883–3897
101. Lin H-Y, Tsao Y-C, Tsai W-H, Yang Y-W, Yan T-R, Sheu B-C (2007) Development and application of side-polished fiber immunosensor based on surface plasmon resonance for the detection of Legionella pneumophila with halogens light and 850 nm-LED. Sens Actuators A Phys 138(2):299–305

102. Slavık R, Homola J, Brynda E (2002) A miniature fiber optic surface plasmon resonance sensor for fast detection of staphylococcal enterotoxin B. Biosens Bioelectron 17 (6–7):591–595
103. Kanso M, Cuenot S, Louarn G (2008) Sensitivity of optical fiber sensor based on surface plasmon resonance: modeling and experiments. Plasmonics 3(2–3):49–57
104. Huang C-T, Jen C-P, Chao T-C, Wu W-T, Li W-Y, Chau L-K (2009) A novel design of grooved fibers for fiber-optic localized plasmon resonance biosensors. Sensors 9 (8):6456–6470
105. Wu W-T, Jen C-P, Tsao T-C, Shen W-C, Cheng C-W, Chen C-H, Tang J-L, Li W-Y, Chau L-K (2009) U-shaped fiber optics fabricated with a femtosecond laser and integrated into a localized plasmon resonance biosensor. In: 2009 symposium on design, test, integration & packaging of MEMS/MOEMS. IEEE, pp 127–131
106. Singh S, Gupta BD (2013) Fabrication and characterization of a surface plasmon resonance based fiber optic sensor using gel entrapment technique for the detection of low glucose concentration. Sensors Actuators B Chem 177:589–595
107. Ahn JH, Seong TY, Kim WM, Lee TS, Kim I, Lee K-S (2012) Fiber-optic waveguide coupled surface plasmon resonance sensor. Opt Express 20(19):21729–21738
108. Esteban Ó, Naranjo FB, Díaz-Herrera N, Valdueza-Felip S, Navarrete M-C, González-Cano A (2011) High-sensitive SPR sensing with Indium Nitride as a dielectric overlay of optical fibers. Sensors Actuators B Chem 158 (1):372–376
109. Navarrete M-C, Díaz-Herrera N, González-Cano A, Esteban Ó (2014) Surface plasmon resonance in the visible region in sensors based on tapered optical fibers. Sensors Actuators B Chem 190:881–885
110. Chang Y-J, Chen Y-C, Kuo H-L, Wei P-K (2006) Nanofiber optic sensor based on the excitation of surface plasmon wave near fiber tip. J Biomed Opt 11(1):014032
111. Wieduwilt T, Kirsch K, Dellith J, Willsch R, Bartelt H (2013) Optical fiber micro-taper with circular symmetric gold coating for sensor applications based on surface plasmon resonance. Plasmonics 8(2):545–554
112. Iga M, Seki A, Watanabe K (2004) Heterocore structured fiber optic surface plasmon resonance sensor with silver film. Sensors Actuators B Chem 101(3):368–372
113. Takagi K, Sasaki H, Seki A, Watanabe K (2010) Surface plasmon resonances of a curved hetero-core optical fiber sensor. Sens Actuators A Phys 161(1–2):1–5
114. Wang P, Brambilla G, Ding M, Semenova Y, Wu Q, Farrell G (2011) High-sensitivity, evanescent field refractometric sensor based on a tapered, multimode fiber interference. Opt Lett 36(12):2233–2235
115. Sai V, Kundu T, Mukherji S (2009) Novel U-bent fiber optic probe for localized surface plasmon resonance based biosensor. Biosens Bioelectron 24(9):2804–2809
116. Gowri A, Sai V (2016) Development of LSPR based U-bent plastic optical fiber sensors. Sensors Actuators B Chem 230:536–543
117. He Y-J, Lo Y-L, Huang J-F (2006) Optical-fiber surface-plasmon-resonance sensor employing long-period fiber gratings in multiplexing. JOSA B 23(5):801–811
118. Schuster T, Herschel R, Neumann N, Schaffer CG (2011) Miniaturized long-period fiber grating assisted surface plasmon resonance sensor. J Lightwave Technol 30 (8):1003–1008
119. Nemova G, Kashyap R (2006) Fiber-Bragg-grating-assisted surface plasmon-polariton sensor. Opt Lett 31(14):2118–2120
120. Iadicicco A, Cusano A, Campopiano S, Cutolo A, Giordano M (2005) Thinned fiber Bragg gratings as refractive index sensors. IEEE Sensors J 5(6):1288–1295
121. Albert J, Shao LY, Caucheteur C (2013) Tilted fiber Bragg grating sensors. Laser Photonics Rev 7(1):83–108
122. Shevchenko YY, Albert J (2007) Plasmon resonances in gold-coated tilted fiber Bragg gratings. Opt Lett 32(3):211–213
123. Caucheteur C, Voisin V, Albert J (2013) Polarized spectral combs probe optical fiber surface plasmons. Opt Express 21 (3):3055–3066
124. Bialiayeu A, Bottomley A, Prezgot D, Ianoul A, Albert J (2012) Plasmon-enhanced refractometry using silver nanowire coatings on tilted fibre Bragg gratings. Nanotechnology 23(44):444012
125. Guo T, González-Vila Á, Loyez M, Caucheteur C (2017) Plasmonic optical fiber-grating immunosensing: a review. Sensors 17 (12):2732
126. Albert J, Lepinay S, Caucheteur C, DeRosa MC (2013) High resolution grating-assisted surface plasmon resonance fiber optic aptasensor. Methods 63(3):239–254

127. Hassani A, Skorobogatiy M (2007) Design criteria for microstructured-optical-fiber-based surface-plasmon-resonance sensors. JOSA B 24(6):1423–1429
128. Hautakorpi M, Mattinen M, Ludvigsen H (2008) Surface-plasmon-resonance sensor based on three-hole microstructured optical fiber. Opt Express 16(12):8427–8432
129. Nguyen H, Sidiroglou F, Collins S, Davis T, Roberts A, Baxter G (2013) A localized surface plasmon resonance-based optical fiber sensor with sub-wavelength apertures. Appl Phys Lett 103(19):193116
130. Consales M, Ricciardi A, Crescitelli A, Esposito E, Cutolo A, Cusano A (2012) Lab-on-fiber technology: toward multifunctional optical nanoprobes. ACS Nano 6 (4):3163–3170
131. Jeong H-H, Lee S-K, Park J-H, Erdene N, Jeong D-H (2011) Fabrication of fiber-optic localized surface plasmon resonance sensor and its application to detect antibody-antigen reaction of interferon-gamma. Opt Eng 50 (12):124405
132. Lin Y, Zou Y, Mo Y, Guo J, Lindquist RG (2010) E-beam patterned gold nanodot arrays on optical fiber tips for localized surface plasmon resonance biochemical sensing. Sensors 10(10):9397–9406
133. Lan X, Cheng B, Yang Q, Huang J, Wang H, Ma Y, Shi H, Xiao H (2014) Reflection based extraordinary optical transmission fiber optic probe for refractive index sensing. Sensors Actuators B Chem 193:95–99
134. Jasim I, Liu J, Yang Y, Qu C, Zhu C, Roman M, Huang J, Kinzel E, Almasri M (2019) Low-cost fabrication of functional plasmonic fiber-optic-based sensors using microsphere photolithography. In: Fiber optic sensors and applications XVI. International Society for Optics and Photonics, p 110000D
135. Schwalfenberg GK (2012) The alkaline diet: is there evidence that an alkaline pH diet benefits health? J Environ Public Health 2012:727630
136. Wolthuis R, McCrae D, Saaski E, Hartl J, Mitchell G (1992) Development of a medical fiber-optic pH sensor based on optical absorption. IEEE Trans Biomed Eng 39 (5):531–537
137. Lin J (2000) Recent development and applications of optical and fiber-optic pH sensors. TrAC Trends Anal Chem 19(9):541–552
138. Gu B, Yin M-J, Zhang AP, Qian J-W, He S (2009) Low-cost high-performance fiber-optic pH sensor based on thin-core fiber modal interferometer. Opt Express 17 (25):22296–22302
139. McCulloch S, Uttamchandani D (1997) Development of a fibre optic micro-optrode for intracellular pH measurements. IEE Proceedings-Optoelectronics 144 (3):162–167
140. Goicoechea J, Zamarreño C, Matias I, Arregui F (2009) Utilization of white light interferometry in pH sensing applications by mean of the fabrication of nanostructured cavities. Sensors Actuators B Chem 138(2):613–618
141. Corres JM, Del Villar I, Matias IR, Arregui FJ (2007) Fiber-optic pH-sensors in long-period fiber gratings using electrostatic self-assembly. Opt Lett 32(1):29–31
142. Shao L-Y, Yin M-J, Tam H-Y, Albert J (2013) Fiber optic pH sensor with self-assembled polymer multilayer nanocoatings. Sensors 13 (2):1425–1434
143. Corres JM, Matias IR, del Villar I, Arregui FJ (2007) Design of pH sensors in long-period fiber gratings using polymeric nanocoatings. IEEE Sensors J 7(3):455–463
144. Chu C-S, Lo Y-L, Sung T-W (2011) Review on recent developments of fluorescent oxygen and carbon dioxide optical fiber sensors. Photonic Sensors 1(3):234–250
145. Wolfbeis OS, Weis LJ, Leiner MJ, Ziegler WE (1988) Fiber-optic fluorosensor for oxygen and carbon dioxide. Anal Chem 60 (19):2028–2030
146. Zhou H-C, Long JR, Yaghi OM (2012) Introduction to metal–organic frameworks. ACS Publications
147. Kreno LE, Leong K, Farha OK, Allendorf M, Van Duyne RP, Hupp JT (2011) Metal–organic framework materials as chemical sensors. Chem Rev 112(2):1105–1125
148. Kim K-J, Lu P, Culp JT, Ohodnicki PR (2018) Metal–organic framework thin film coated optical fiber sensors: a novel waveguide-based chemical sensing platform. ACS sensors 3(2):386–394
149. Hromadka J, Tokay B, Correia R, Morgan SP, Korposh S (2018) Carbon dioxide measurements using long period grating optical fibre sensor coated with metal organic framework HKUST-1. Sensors Actuators B Chem 255:2483–2494
150. Timmer B, Olthuis W, Van Den Berg A (2005) Ammonia sensors and their applications—a review. Sensors Actuators B Chem 107(2):666–677
151. Wolfbeis OS, Posch HE (1986) Fibre-optic fluorescing sensor for ammonia. Anal Chim Acta 185:321–327

152. Ibrahim S, Rahman N, Bakar MA, Girei S, Yaacob M, Ahmad H, Mahdi M (2015) Room temperature ammonia sensing using tapered multimode fiber coated with polyaniline nanofibers. Opt Express 23 (3):2837–2845
153. Fu H, Jiang Y, Ding J, Zhang J, Zhang M, Zhu Y, Li H (2018) Zinc oxide nanoparticle incorporated graphene oxide as sensing coating for interferometric optical microfiber for ammonia gas detection. Sensors Actuators B Chem 254:239–247
154. Tanguy NR, Thompson M, Yan N (2018) A review on advances in application of polyaniline for ammonia detection. Sensors Actuators B Chem 257:1044–1064
155. Wang T, Yasukochi W, Korposh S, James SW, Tatam RP, Lee S-W (2016) A long period grating optical fiber sensor with nano-assembled porphyrin layers for detecting ammonia gas. Sensors Actuators B Chem 228:573–580
156. Liu D, Han W, Mallik AK, Yuan J, Yu C, Farrell G, Semenova Y, Wu Q (2016) High sensitivity sol-gel silica coated optical fiber sensor for detection of ammonia in water. Opt Express 24(21):24179–24187
157. Kanawade R, Kumar A, Pawar D, Late D, Mondal S, Sinha RK (2019) Fiber optic Fabry–Perot interferometer sensor: an efficient and fast approach for ammonia gas sensing. JOSA B 36(3):684–689
158. Shirasu M, Touhara K (2011) The scent of disease: volatile organic compounds of the human body related to disease and disorder. The Journal of Biochemistry 150 (3):257–266
159. Pavlou AK, Magan N, Jones JM, Brown J, Klatser P, Turner AP (2004) Detection of Mycobacterium tuberculosis (TB) in vitro and in situ using an electronic nose in combination with a neural network system. Biosens Bioelectron 20(3):538–544
160. Voss A, Baier V, Reisch R, von Roda K, Elsner P, Ahlers H, Stein G (2005) Smelling renal dysfunction via electronic nose. Ann Biomed Eng 33(5):656–660
161. Dalton P, Gelperin A, Preti G (2004) Volatile metabolic monitoring of glycemic status in diabetes using electronic olfaction. Diabetes Technol Ther 6(4):534–544
162. Turner AP, Magan N (2004) Electronic noses and disease diagnostics. Nat Rev Microbiol 2 (2):161
163. Selyanchyn R, Korposh S, Yasukochi W, Lee S-W (2011) A preliminary test for skin gas assessment using a porphyrin based evanescent wave optical fiber sensor1. Sensors & Transducers 125(2):54
164. Elosúa C, Matías I, Bariain C, Arregui F (2008) Detection of volatile organic compounds based on optical fibre using nanostructured films. Int J Smart Sens Intell Syst 1:123–136
165. Renganathan B, Sastikumar D, Srinivasan R, Ganesan A (2014) Nanocrystalline samarium oxide coated fiber optic gas sensor. Mater Sci Eng B 186:122–127
166. Hromadka J, James S, Davis F, Tatam RP, Crump D, Korposh S (2015) Detection of the volatile organic compounds emitted from paints using optical fibre long period grating modified with the mesoporous nanoscale coating. In: 24th international conference on optical fibre sensors. International Society for Optics and Photonics, p 96344K
167. Hernandez FU, Morgan SP, Hayes-Gill BR, Harvey D, Kinnear W, Norris A, Evans D, Hardman JG, Korposh S (2016) Characterization and use of a fiber optic sensor based on PAH/SiO 2 film for humidity sensing in ventilator care equipment. IEEE Trans Biomed Eng 63(9):1985–1992
168. Islam M, Ali M, Lai M-H, Lim K-S, Ahmad H (2014) Chronology of Fabry-Perot interferometer fiber-optic sensors and their applications: a review. Sensors 14(4):7451–7488
169. Ascorbe J, Corres J, Arregui F, Matias I (2017) Recent developments in fiber optics humidity sensors. Sensors 17(4):893
170. Konstantaki M, Pissadakis S, Pispas S, Madamopoulos N, Vainos NA (2006) Optical fiber long-period grating humidity sensor with poly (ethylene oxide)/cobalt chloride coating. Appl Opt 45(19):4567–4571
171. Alwis L, Sun T, Grattan K (2013) Optical fibre-based sensor technology for humidity and moisture measurement: review of recent progress. Measurement 46(10):4052–4074
172. Hernaez M, Zamarreño C, Melendi-Espina S, Bird L, Mayes A, Arregui F (2017) Optical fibre sensors using graphene-based materials: a review. Sensors 17(1):155
173. Zhao Y, X-G L, Zhou X, Y-N Z (2016) Review on the graphene based optical fiber chemical and biological sensors. Sensors Actuators B Chem 231:324–340
174. Li C, Yu X, Zhou W, Cui Y, Liu J, Fan S (2018) Ultrafast miniature fiber-tip Fabry–-Perot humidity sensor with thin graphene oxide diaphragm. Opt Lett 43 (19):4719–4722
175. Jiang B, Bi Z, Hao Z, Yuan Q, Feng D, Zhou K, Zhang L, Gan X, Zhao J (2019)

Graphene oxide-deposited tilted fiber grating for ultrafast humidity sensing and human breath monitoring. Sensors Actuators B Chem 293:336–341

176. Gomez D, Morgan SP, Hayes-Gill BR, Correia RG, Korposh S (2018) Polymeric optical fibre sensor coated by SiO2 nanoparticles for humidity sensing in the skin microenvironment. Sensors Actuators B Chem 254:887–895
177. Tan W, Shi Z-Y, Smith S, Birnbaum D, Kopelman R (1992) Submicrometer intracellular chemical optical fiber sensors. Science 258 (5083):778–781
178. Vo-Dinh T (2002) Nanobiosensors: probing the sanctuary of individual living cells. J Cell Biochem 87(S39):154–161
179. Velasco-Garcia M (2009) Optical biosensors for probing at the cellular level: a review of recent progress and future prospects. In: Seminars in cell & developmental biology, vol 1. Elsevier, pp 27–33
180. Cullum BM, Griffin GD, Miller GH, Vo-Dinh T (2000) Intracellular measurements in mammary carcinoma cells using fiber-optic nanosensors. Anal Biochem 277 (1):25–32
181. Kasili P, Cullum B, Griffin G, Vo-Dinh T (2002) Nanosensor for in vivo measurement of the carcinogen benzo [a] pyrene in a single cell. J Nanosci Nanotechnol 2(6):653–658
182. Kasili PM, Song JM, Vo-Dinh T (2004) Optical sensor for the detection of caspase-9 activity in a single cell. J Am Chem Soc 126 (9):2799–2806
183. Yang Q, Wang H, Chen S, Lan X, Xiao H, Shi H, Ma Y (2015) Fiber-optic-based microprobe using hexagonal 1-in-6 fiber configuration for intracellular single-cell pH measurement. Anal Chem 87(14):7171–7179
184. Yang Q, Wang H, Lan X, Cheng B, Chen S, Shi H, Xiao H, Ma Y (2015) Reflection-mode micro-spherical fiber-optic probes for in vitro real-time and single-cell level pH sensing. Sensors Actuators B Chem 207:571–580
185. Vollmer F, Arnold S (2008) Whispering-gallery-mode biosensing: label-free detection down to single molecules. Nat Methods 5 (7):591
186. Whitesides GM (2006) The origins and the future of microfluidics. Nature 442 (7101):368
187. Psaltis D, Quake SR, Yang C (2006) Developing optofluidic technology through the fusion of microfluidics and optics. Nature 442(7101):381
188. Haque M, Lee KK, Ho S, Fernandes LA, Herman PR (2014) Chemical-assisted femtosecond laser writing of lab-in-fibers. Lab Chip 14(19):3817–3829
189. Yuan L (2017) Femtosecond laser micromachining of advanced fiber optic sensors and devices. All Dissertations. 1954. https://tigerprints.clemson.edu/all_dissertations/1954
190. Yuan L, Huang J, Lan X, Wang H, Jiang L, Xiao H (2014) All-in-fiber optofluidic sensor fabricated by femtosecond laser assisted chemical etching. Opt Lett 39(8):2358–2361
191. Haque M (2014) Chemical-assisted femtosecond laser writing of lab-in-fiber sensors. University of Toronto (Canada)
192. Wang B, Mies E (2007) Advanced topics on fusion splicing of specialty fibers and devices. In: Passive components and fiber-based devices IV. International Society for Optics and Photonics, p 678130
193. Xiao L, Demokan M, Jin W, Wang Y, Zhao C-L (2007) Fusion splicing photonic crystal fibers and conventional single-mode fibers: microhole collapse effect. J Lightwave Technol 25(11):3563–3574
194. Zhang S, Zhang W, Gao S, Geng P, Xue X (2012) Fiber-optic bending vector sensor based on Mach–Zehnder interferometer exploiting lateral-offset and up-taper. Opt Lett 37(21):4480–4482
195. Yin G, Lou S, Zou H (2013) Refractive index sensor with asymmetrical fiber Mach–Zehnder interferometer based on concatenating single-mode abrupt taper and core-offset section. Opt Laser Technol 45:294–300
196. Huang R, Ni K, Ma Q, Wu X (2016) Refractometer based on a tapered Mach–Zehnder interferometer with Peanut-Shape structure. Opt Lasers Eng 83:80–82
197. Tian K, Zhang M, Farrell G, Wang R, Lewis E, Wang P (2018) Highly sensitive strain sensor based on composite interference established within S-tapered multimode fiber structure. Opt Express 26(26):33982–33992
198. Felipe A, Espíndola G, Kalinowski HJ, Lima JA, Paterno AS (2012) Stepwise fabrication of arbitrary fiber optic tapers. Opt Express 20 (18):19893–19904
199. Liu Z-H, Lei J-J, Zhang Y, Zhang Y-X, Yang X-H, Zhang J-Z, Yang Y, Yuan L-B (2018) Microparticle collection for water purification based on laser-induced convection. Chinese Physics B 27(5):054209
200. Tong L, Gattass RR, Ashcom JB, He S, Lou J, Shen M, Maxwell I, Mazur E (2003)

Subwavelength-diameter silica wires for low-loss optical wave guiding. Nature 426 (6968):816

201. Liu Y, Meng C, Zhang AP, Xiao Y, Yu H, Tong L (2011) Compact microfiber Bragg gratings with high-index contrast. Opt Lett 36(16):3115–3117
202. Lu P, Men L, Sooley K, Chen Q (2009) Tapered fiber Mach–Zehnder interferometer for simultaneous measurement of refractive index and temperature. Appl Phys Lett 94 (13):131110
203. Tian Z, Yam SS-H, Barnes J, Bock W, Greig P, Fraser JM, Loock H-P, Oleschuk RD (2008) Refractive index sensing with Mach–Zehnder interferometer based on concatenating two single-mode fiber tapers. IEEE Photon Technol Lett 20(8):626–628
204. Tien C-L, Chen H-W, Liu W-F, Jyu S-S, Lin S-W, Lin Y-S (2008) Hydrogen sensor based on side-polished fiber Bragg gratings coated with thin palladium film. Thin Solid Films 516(16):5360–5363
205. Jang HS, Park KN, Kim JP, Sim SJ, Kwon OJ, Han Y-G, Lee KS (2009) Sensitive DNA biosensor based on a long-period grating formed on the side-polished fiber surface. Opt Express 17(5):3855–3860
206. Luo Y, Wei Q, Ma Y, Lu H, Yu J, Tang J, Yu J, Fang J, Zhang J, Chen Z (2015) Side-polished-fiber based optical coupler assisted with a fused nano silica film. Appl Opt 54 (7):1598–1605
207. Khan M, Kang S-W (2014) A high sensitivity and wide dynamic range fiber-optic sensor for low-concentration VOC gas detection. Sensors 14(12):23321–23336
208. Chin LC, Whelan WM, Vitkin IA (2010) Optical fiber sensors for biomedical applications. In: Optical-thermal response of laser-irradiated tissue. Springer, pp 661–712
209. Bae H, Zhang X, Liu H, Yu M (2010) Miniature surface-mountable Fabry–Perot pressure sensor constructed with a 45 angled fiber. Opt Lett 35(10):1701–1703
210. Maiman TH (1960) Stimulated optical radiation in ruby. A Century of Nature, edited by Laura Garwin and Tim Lincoln, Chicago: University of Chicago Press, 2010, pp 113–114. https://doi.org/10.7208/9780226284163-019
211. Osellame R, Cerullo G, Ramponi R (2012) Femtosecond laser micromachining: photonic and microfluidic devices in transparent materials, vol 123. Springer Science & Business Media
212. Davis KM, Miura K, Sugimoto N, Hirao K (1996) Writing waveguides in glass with a femtosecond laser. Opt Lett 21 (21):1729–1731
213. Wang Q, Wang D, Zhang H (2019) Fiber Bragg grating with a waveguide fabricated in no-core fiber and multimode fiber. Opt Lett 44(11):2693–2696
214. Liu J, Yuan L, Lei J, Zhu W, Cheng B, Zhang Q, Song Y, Chen C, Xiao H (2017) Micro-cantilever-based fiber optic hydrophone fabricated by a femtosecond laser. Opt Lett 42(13):2459–2462
215. Gamaly EG, Juodkazis S, Nishimura K, Misawa H, Luther-Davies B, Hallo L, Nicolai P, Tikhonchuk VT (2006) Laser-matter interaction in the bulk of a transparent solid: confined microexplosion and void formation. Phys Rev B 73(21):214101
216. Taylor RS, Hnatovsky C, Simova E, Rayner DM, Bhardwaj V, Corkum PB (2003) Femtosecond laser fabrication of nanostructures in silica glass. Opt Lett 28(12):1043–1045
217. Zhou P, Liao C, Li Z, Liu S, Wang Y (2019) In-fiber cascaded FPI fabricated by chemical-assisted femtosecond laser micromachining for micro-fluidic sensing applications. J Lightwave Technol 37(13):3214–3221
218. Liu Y, Qu S, Li Y (2013) Single microchannel high-temperature fiber sensor by femtosecond laser-induced water breakdown. Opt Lett 38(3):335–337

# Part II

## Electrochemical and Piezoelectric

# Chapter 21

# Optical and Electrochemical Aptasensors for Sensitive Detection of Aflatoxin $B_1$ and Aflatoxin $M_1$ in Blood Serum, Grape Juice, and Milk Samples

**Mohammad Ramezani, Seyed Hamid Jalalian, Seyed Mohammad Taghdisi, Khalil Abnous, and Mona Alibolandi**

## Abstract

Aflatoxin food contamination with toxic and carcinogenic impacts on human health is a global concern. We have developed aptasensors for the detection of Aflatoxin $M_1$ ($AFM_1$) and $B_1$ ($AFB_1$) using electrochemical and optical methods. In the first method, an electrochemical aptasensor was designed for the detection of $AFM_1$ based on complementary strand of $AFM_1$ aptamer that was attached onto the gold nanoparticles and a hairpin-shaped $AFM_1$ aptamer. The designed electrochemical aptasensor showed high selectivity toward $AFM_1$ with a limit of detection (LOD) as low as 0.9 nM. Moreover, the developed aptasensor was successfully used to detect $AFM_1$ in milk and serum with LODs of 1.8 and 1.2 nM, respectively. In the second method, a novel electrochemical aptasensor was developed based on the π-shape structure of $AFB_1$ aptamer. The detection limit was found to be 2 pg/mL in buffer. Also, the developed aptasensor was used to analyze $AFB_1$ spiked human serum and grape juice samples, and the recoveries were 95.4–108.1%. In another method, a fluorescent sensing scheme was developed for $AFB_1$ detection based on a hairpin structure of G-quadruplex oligonucleotide-aptamer chimera, streptavidin-coated silica nanoparticles (SNP-streptavidin) and N-methyl mesoporphyrin IX (NMM). The LOD was reported as 8 pg/mL with a linear range of 30–900 pg/mL. Moreover, the developed sensor could detect $AFB_1$ in serum and grape juice with the LOD of 9.8 and 11.2 pg/mL, respectively.

**Key words** Aptasensor, Aptamer, Aflatoxin $M_1$, Aflatoxin $B_1$, Exonuclease I, π-shape structure, Fluorescence

## 1 Introduction

Aflatoxins, as members of mycotoxins, are toxic compounds produced by fungal species such as *Aspergillus flavus*, *A. parasiticus*, and *A. nomius* [1, 2]. The improper storage condition of various food materials and agriculture commodities, such as grains, peanuts, and fruits may lead to their contamination with mycotoxins [3]. Aflatoxin $B_1$ ($AFB_1$) is a potent toxin and carcinogen

Miguel R. Ossandon et al. (eds.), *Biomedical Engineering Technologies: Volume 1*, Methods in Molecular Biology, vol. 2393, https://doi.org/10.1007/978-1-0716-1803-5_21, 

compound which has been classified as group 1 human carcinogens by International Agency for Research on Cancer (IARC) [4]. It can be found in different food sources, including wine, milk, cereals, and fruits [5]. Studies show that $AFB_1$ has been implicated in human hepatocellular carcinoma (HCC) [5, 6]. The main carcinogenic metabolite of $AFB_1$ is Aflatoxin $M_1$ ($AFM_1$) which is produced by CYP1A2. $AFM_1$ can be secreted in milk within 12 h after consumption of the contaminated feeds [7]. It has been shown that the consumption of $AFM_1$-contaminated food products can lead to some health problems such as impaired liver function and increase of susceptibility to infectious diseases [8].

In most countries, regulations have been introduced to control the levels of aflatoxins in foodstuffs. Since pasteurization does not have efficient impact on the degradation of $AFM_1$, setting a standard is important to maintain the quality and safety of the food products [9]. According to the European Commission Regulation, the maximum residue levels (MRL) for $AFM_1$ in milk and infant formula are 50 ng/kg and 25 ng/kg, respectively [1]. Moreover, the MRL for $AFB_1$ in cereal grains and rice has been set as 5μg/kg for human consumption [10]. Thus, development of sensitive methods for the detection of aflatoxins in serum and foodstuffs are in great demand.

A variety of conventional analytical approaches including liquid chromatography with mass spectrometry (LC–MS), high-performance liquid chromatography (HPLC), and thin-layer chromatography (TLC) have been employed for the detection of aflatoxins [11–13]. However, sample pretreatment requirements, expensive laboratory facilities and the need for training skilled operators are the shortcomings of these techniques. Moreover, although the enzyme-linked immunosorbent assay (ELISA) has become popular for mycotoxins analysis, this technique has also some disadvantages such as false-positive results, lack of good recoverability and expensive procedures in antibody production and storage [14]. Therefore, development of new, rapid, and sensitive analytical techniques to improve the mentioned defects while efficiently detecting aflatoxins levels in foodstuffs is crucial.

Today, approaches like aptamer-based sensing methods have been widely used in analytical techniques [15, 16]. Aptamers are short single-stranded DNA (ssDNA) or RNA molecules with high specific recognition capabilities toward a wide range of targets, such as antibiotics, toxins, peptides, and cells [17]. Cheap synthesis, good thermal stability, ease of labeling, and lack of toxicity are the favorite aspects of aptamers leading to their application as sensing probes in a broad range of sensors [18, 19].

Among nanoparticles, gold nanoparticles (AuNPs) are widely applied for colorimetric, fluorescent, and electrochemical aptasensors due to their large surface area, ease of synthesis and

modification with other biomolecules, fine biocompatibility, and unique electronic and optical properties [20, 21].

Electrochemical biosensors are powerful analytical tools. The combination of aptamers with these sensors leads to sensitive, simple, fast, and low-cost biosensors. In order to detect a target, two main approaches are employed by electrochemical aptasensors including covalently labeled aptamers (with enzymes, metal nanoparticles, redox compound, etc.) and label-free techniques [22].

Fluorescent aptasensors have obtained great attention because of their rapid response, good sensitivity, ease of measurement, and low reaction volumes [23, 24].

In the first study presented in this chapter, a new electrochemical aptasensor is introduced for the detection of $AFM_1$. The method employs a combination of AuNPs, complementary strand of the aptamer (CS), and $AFM_1$ aptamer with a hairpin-shaped structure. In the presence of $AFM_1$, the hairpin structure of the aptamer is disassembled, and the CS which has been modified with AuNPs could bind to the aptamer leading to approaching of CS-modified AuNPs to close proximity of the electrode surface. Therefore, upon the addition of methylene blue as redox agent, a strong current signal can be recorded.

In the second study, an electrochemical aptasensor is presented based on the π-shape structure of $AFB_1$ aptamer and its complementary strand on the surface of electrode as well as exonuclease I (Exo I)-assisted signal amplification. In the absence of $AFB_1$, only a weak peak current is recorded because the π-shape structure could block the surface of gold electrode and efficiently inhibit the access of redox probe, $[Fe(CN)_6]^{3-/4-}$, to the surface of electrode. However, in the presence of $AFB_1$, the aptamer binds to its target, leading to disassembly of the π-shape structure. Therefore, upon addition of Exo I which degrades free ssDNA from its 3′-end, a strong current is recorded.

The mentioned electrochemical schemes are both simple and sensitive platforms, which can be translated into portable devices through treating with screen-printed gold electrodes (SPGEs).

In our third study, a fluorescent aptasensor based on hairpin structure of G-quadruplex oligonucleotide-aptamer chimera, silica nanoparticles (SNPs), and N-methyl mesoporphyrin IX (NMM) as the fluorophore is introduced for the detection of $AFB_1$ in grape juice and human serum samples. In the presence of $AFB_1$, the hairpin structure of chimera is disassembled, and large amounts of NMM could bind to G-quadruplex structure on the surface of SNPs, resulting in a strong fluorescence signal. Meanwhile, this method is a simple scheme with high sensitivity that can detect the target in a short time period. Moreover, the method can become portable because of functioning with a specific wavelength.

## 2 Materials

### 2.1 $AFM_1$ Electrochemical Aptasensor

#### 2.1.1 Materials

1. $AFM_1$ aptamer, 5′-TAA CAC GAG ACA CTG CTA GAG ATT TTC CAC ATT TCT CTT GTT CC-thiol-3′, and its complementary strand (CS), 5′-GTC TCG TGT TAC AAC CAT CAA-thiol-3′ (complementary regions have been indicated with the same color) (Bioneer, South Korea).
2. Vomitoxin (DON) (Sigma-Aldrich, USA).
3. Zearalenone (ZEN) (Sigma-Aldrich, USA).
4. $AFM_1$, aptamer (Sigma-Aldrich, USA).
5. $AFB_1$, aptamer (Sigma-Aldrich, USA).
6. Ochratoxin A (OTA) (Sigma-Aldrich, USA).
7. Gold (III) chloride trihydrate ($HAuCl_4$) (Sigma-Aldrich, USA).
8. Sodium citrate (Sigma-Aldrich, USA).
9. Methylene blue (Sigma-Aldrich, USA).
10. Tris (2-carboxyethyl) phosphine hydrochloride (TCEP) (Sigma-Aldrich, USA).
11. 6-Mercaptohexanol (MCH) (Sigma-Aldrich, USA).
12. Immobilization buffer (100 mM NaCl, 10 mM Tris–HCl, 1 mM EDTA, pH 7.4).

#### 2.1.2 Apparatus

1. Differential pulse voltammetry (DPV) and cyclic voltammetry (CV) (μstat 400 portable Biopotentiostat/Galvanostat) (DropSens, Spain).
2. SPGEs with silver reference electrode and gold counter electrode (DRP-C220BT) (DropSens, Spain).
3. Dimensions of the strips are 34 mm × 10 mm × 0.5 mm (length × width × height).
4. Data were analyzed using DropView8400 software.

### 2.2 $AFB_1$ Electrochemical Aptasensor

#### 2.2.1 Materials

1. The $AFB_1$ aptamer, 5′-thiol-GTT GGG CAC GTG TTG TCT CTC TGT GTC TCG TGC CCT TCG CTA GGC CCA CA-3′, its first complementary strand (CS1), 5′-thiol-AAC TGT GGG CCT AGC-3′, and its second complementary strand (CS2), 5′-AAC ACA CCA AGA CCT GGG CAC GAG ACA CAG AGA GAA CCA CAC A-3′ (complementary regions have been indicated with the same color) (Bioneer, South Korea).
2. MCH (Sigma-Aldrich, USA).
3. ZEN (Sigma-Aldrich, USA).
4. TCEP (Sigma-Aldrich, USA).

5. $AFB_1$ (Sigma-Aldrich, USA).
6. Microcystin-leucine-arginine (MC-LR) (Sigma-Aldrich, USA).
7. Potassium hexacyanoferrate(III) ($K_3[Fe(CN)_6]$) (Sigma-Aldrich, USA).
8. $AFM_1$ (Sigma-Aldrich, USA).
9. OTA (Sigma-Aldrich, USA).
10. Human serum (Sigma-Aldrich, USA).
11. DON (Sigma-Aldrich, USA).
12. OTA (Sigma-Aldrich, USA).
13. Potassium hexacyanoferrate(II) trihydrate ($K_4[Fe(CN)_6]\cdot 3H_2O$) (Sigma-Aldrich, USA).

#### 2.2.2 Apparatus

1. SPGE (DRP-C220BT) (DropSens, Spain).
2. μstat 400 portable Biopotentiostat/Galvanostat (DropSens, Spain).
3. Data were analyzed using DropView8400 software.
4. Particle size analyzer (Malvern, UK).
5. Transmission electron microscopy (TEM) (CM120) (Philips, The Netherlands).

#### 2.2.3 Optical Aptasensors

##### Materials

1. G-quadruplex oligonucleotide-Aptamer chimera, 5′-biotin **GTGGGTAGGGCGGGTTGGG** TTTTGTTGGGCACGTGTTGTCTCTCTGTGTCTCGTGCCCTTCGCTAGGCCCACA TTTACCCAACCCGCCC TACCCAC -3′ and FAM-labeled chimera, 5′-biotin **GTGGGTAGGGCGGGTTGGG** TTTTGTTGGGCACGTGTTGTCTCTCTGTGTCTCGTGCCCTTCGCTAGGCCCACA TTTACCCAACCCGCCC TACCCAC -FAM-3′ (the underlined sequence is AFB1 aptamer and the bolded sequence is G-quadruplex oligonucleotide) (Bioneer, South Korea).
2. N-Methyl mesoporphyrin IX (NMM) (Santa Cruz, USA).
3. $AFB_1$ (Sigma-Aldrich, USA).
4. $AFM_1$ (Sigma-Aldrich, USA).
5. MC-LR (Sigma-Aldrich, USA).
6. DON (Sigma-Aldrich, USA).
7. Human serum (Sigma-Aldrich, USA).
8. OTA (Sigma-Aldrich, USA).
9. Streptavidin-coated silica nanoparticles (SNP-streptavidin) (100 nm) (Micromod, Germany).
10. Grape juice (Takdaneh, Iran).

## 3 Methods

### 3.1 $AFM_1$ Electrochemical Aptasensor

In this study, the design of the electrochemical aptasensor was based on conformational change of hairpin structure of the $AFM_1$ aptamer in the presence and absence of the target. The principal of this electrochemical aptasensor has been shown in Scheme 1. In the absence of $AFM_1$, no CS-modified AuNPs could bind to the aptamer on the surface of gold electrode because of the hairpin structure of the $AFM_1$ aptamer. Addition of $AFM_1$ changed the conformation of the aptamer in a way that CS-modified AuNPs could bind to the aptamer and come to close proximity of the surface of the electrode. Therefore, upon the addition of the redox agent, methylene blue, a strong current signal could be recorded.

1. Synthesis of AuNPs

   AuNPs were prepared through the classical reduction of $HAuCl_4$ by sodium citrate [25] as described below.

   (a) Centrifuge the sample at 14,000 × *g* for 20 min at 4 °C.

   (b) Remove the supernatant of synthesized nanoparticles.

   (c) Determine the concentration of AuNPs through the extinction coefficient of $2.7 \times 108\ M^{-1}\ cm^{-1}$ at $\lambda = 520$ nm for 14 nm AuNPs.

   (d) Using a particle size analyzer and a TEM, investigate the size and morphology of AuNPs.

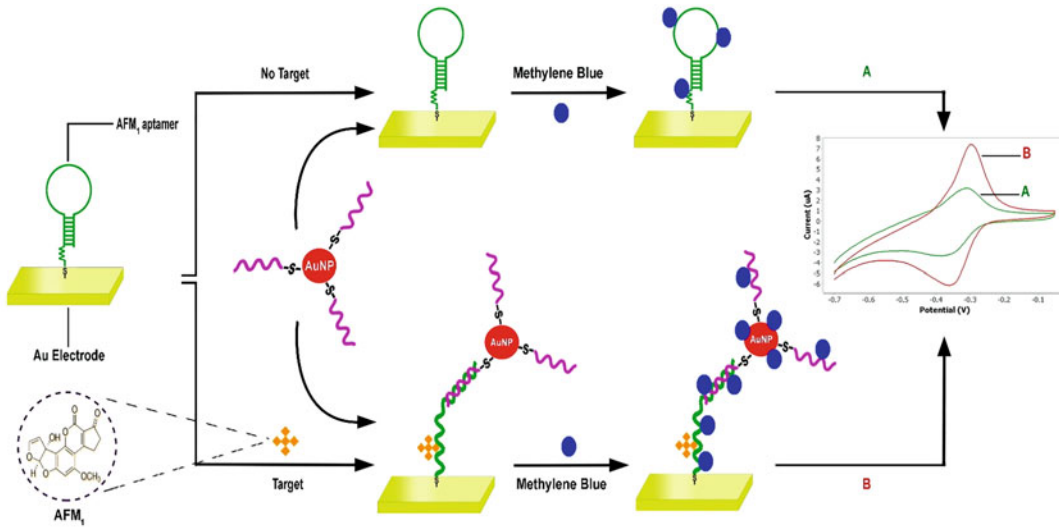


**Scheme 1** Schematic illustration of the electrochemical aptasensor for the detection of $AFM_1$ based on the hairpin structure of $AFM_1$ aptamer. Copied with permission from ref. 1

2. Preparation of Apt-Modified SPGE
   (a) Add 5 mM TCEP in immobilization buffer to the 1μM Apt (final concentration).
   (b) Incubate the mixture for 1 h at room temperature.
   (c) Take 10μL of the above solution and add it onto the surface of SPGEs.
   (d) Incubate the electrodes overnight at room temperature with 100% humidity.
   (e) In order to block non-aptamer bound sites of SPGEs, add 10μL MCH (1 mM) to the surface of the electrodes and incubate the electrodes for 1 h.
3. Preparation of CS-Modified AuNPs
   (a) Pretreat the CS with 5 mM TCEP.
   (b) Add 30μL of the TCEP-treated CS (16μM) to 970μL AuNPs (8 nM).
   (c) Incubate the mixture at room temperature for a night.
   (d) In order to confirm the formation and size of CS-modified AuNPs, use agarose gel (3%) and TEM, respectively (Fig. 1a, b). The size of the AuNPs should be $13.8 \pm 0.6$ nm.
4. Optimization of the incubation time of CS-modified AuNPs
   (a) Incubate the Apt-modified electrodes with 10μL $AFM_1$ (600 ng/L) for 50 min.
   (b) Add 10μL CS-modified AuNPs to the surfaces of Apt-modified electrodes for 0–60 min.
   (c) Add 10μL methylene blue (120μM).
   (d) Record the electrochemical signals after 10 min using differential pulse voltammetry (DPV) technique.
   (e) In order to conduct the previous step, set the scanning potential from −0.38 V to −0.26 V with the pulse time of 50 ms and the pulse potential of 50 mV.
   (f) Preform all measurements at room temperature (Fig. 1c) (*see* **Note 1**).
5. Function assessment of the developed electrochemical aptasensor

   Interaction of $AFM_1$ with the aptasensor was evaluated using CV. In the absence of $AFM_1$, the addition of the CS-modified AuNPs did not significantly change the electrochemical signal of Apt-modified SPGEs (Fig. 2a green curve, b curve). However, the current signal of the $AFM_1$-treated Apt-modified SPGE significantly increased following the addition of CS-modified AuNPs (red curve, c curve). The immobilization of the AuNPs on the surface of electrode via

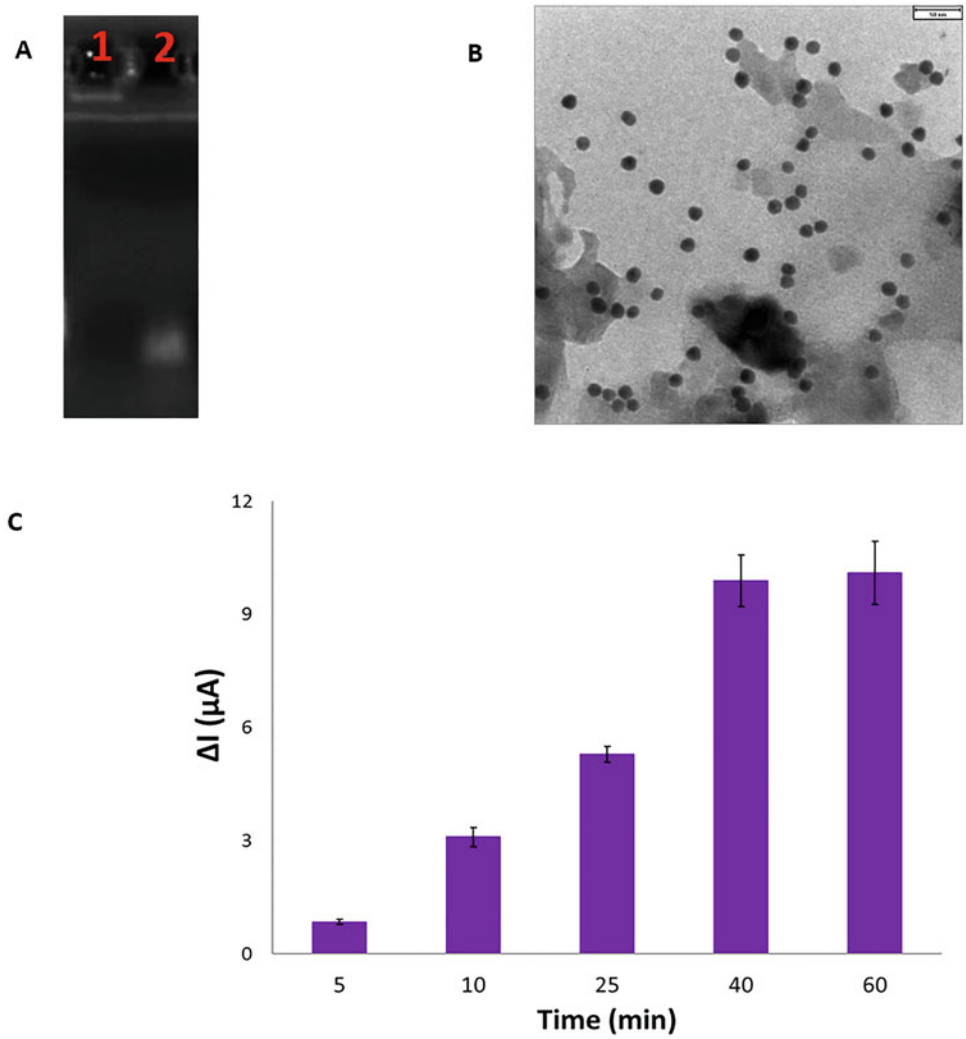


**Fig. 1** (**a**) Analysis of the CS-modified AuNP formation using agarose gel electrophoresis. Lane 1: CS-modified AuNPs, Lane 2: CS. (**b**) TEM image of AuNPs. (**c**) Optimum incubation time of CS-modified AuNPs. Copied with permission from ref. 1

hybridization between Apt and CS results in more accumulation of the methylene blue on the surface of electrode. Furthermore, the transfer of CS-modified AuNPs to the surfaces of Apt-modified SPGEs incubated with DON (orange curve, d curve) and $AFB_1$ (pink curve, e curve) could not enhance the electrochemical signal as much as $AFM_1$, confirming high specificity of the aptasensor (Fig. 2a).

6. Evaluation of the specificity of the aptasensor
   (a) Assess the selectivity of the aptasensor in the presence of 600 ng/L of AFB1, AFM1, DON, ZEN, and OTA (Fig. 2b).

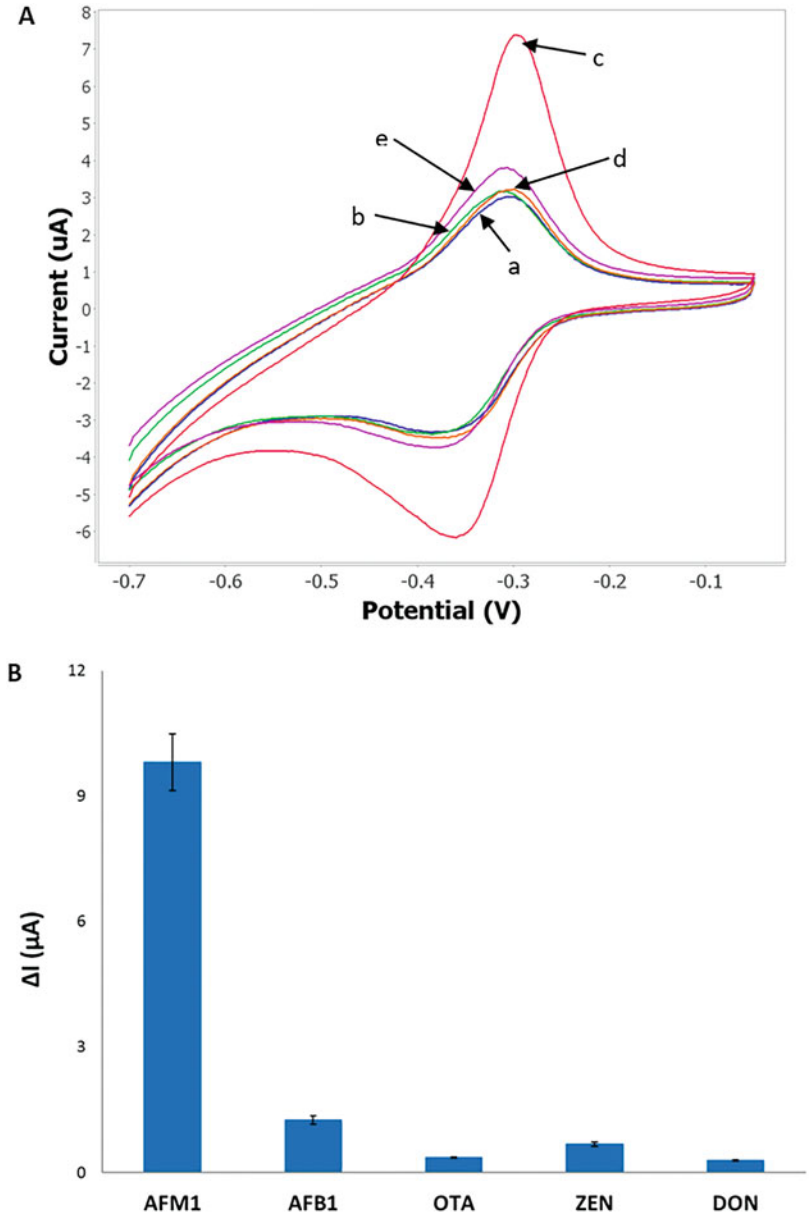


**Fig. 2** (**a**) Confirmation of the characterization and the function of the developed sensing method. CV profiles of: Apt-modified SPGE (blue curve, curve a), Apt-modified SPGE + CS-modified AuNPs (green curve, b curve), Apt-modified SPGE + AFM1 + CS-modified AuNPs (red curve, c curve), Apt-modified SPGE + DON + CS-modified AuNPs (orange curve, d curve), Apt-modified SPGE + AFB1 + CS-modified AuNPs (pink curve, e curve). The electrochemical signals were measured using CV, by scanning the potential from −0.7 V to 0 V at a scan rate of 100 mV/s. (**b**) The relative responses of the aptasensor towards AFM1 and other toxins (the concentration of each toxin was 600 ng/L). Copied with permission from ref. 1

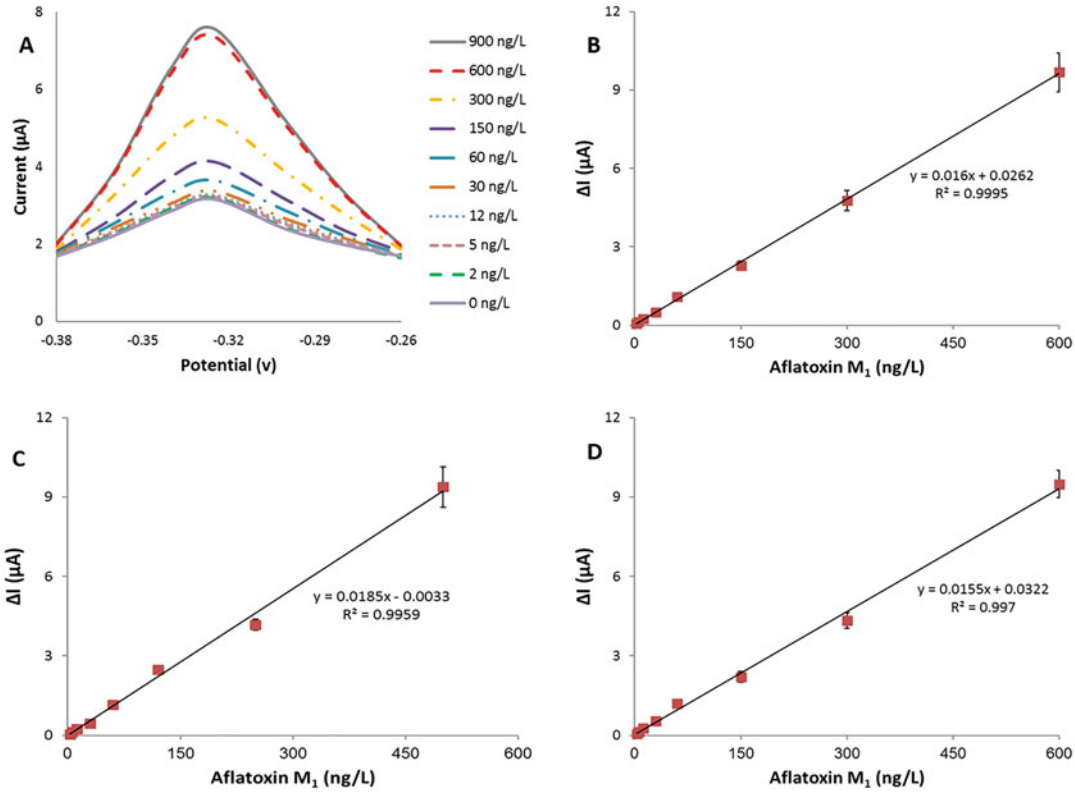


**Fig. 3** (**a**) Relative electrochemical signal of the aptasensor in the presence of different concentrations of $AFM_1$ (0–900 ng/L). (**b**) Calibration curve of the $AFM_1$ aptasensor. (**c**) Calibration curve of the $AFM_1$ aptasensor in serum. (**d**) Calibration curve of the $AFM_1$ aptasensor in milk. Copied with permission from ref. 1

7. Electrochemical Assay of AFM1
   (a) Prepare various concentrations of $AFM_1$ (0–900 ng/L).
   (b) Incubate the Apt-modified SPGEs with 10μL $AFM_1$ for 50 min at room temperature.
   (c) Wash the electrodes with 10 mM phosphate buffer saline (PBS) (NaCl 0.138 M, KCl 0.0027 M, pH 7.4).
   (d) Incubate 10μL CS-modified AuNPs with the electrodes for 40 min at room temperature.
   (e) Add with 10μL methylene blue (120μM) and incubate the electrodes for 10 min.
   (f) Record the electrochemical signals using DPV (Fig. 3a, b) (*see* **Note 2**).
8. Detection of AFM1 in real samples
   (a) Spike different concentrations of $AFM_1$ in milk and serum samples (treated with 30μg/mL salmon sperm DNA).
   (b) Measure the concentration of $AFM_1$ using the developed electrochemical aptasensor (Fig. 3c, d).

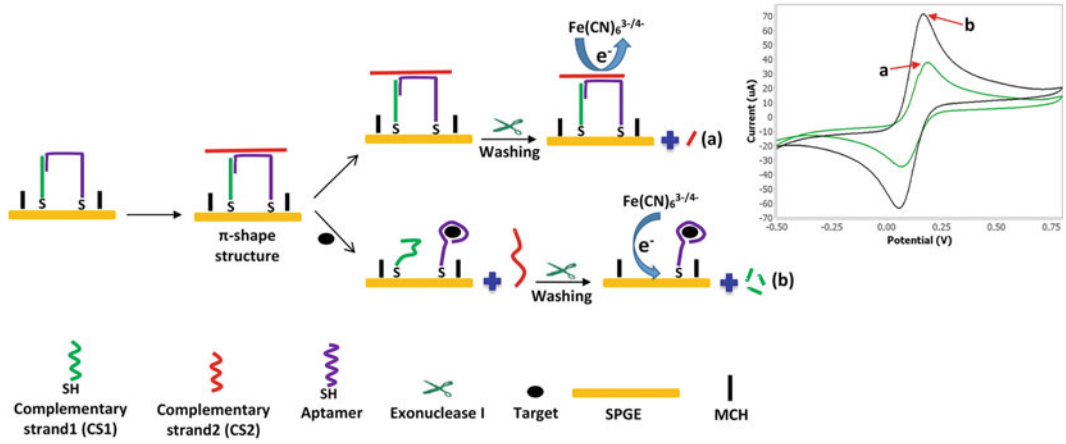


**Scheme 2** π-Shape electrochemical aptasensor for AFB1. (**a**) In the absence of AFB1, the π-shape structure remains intact generating a weak signal. (**b**) In the presence of AFB1, aptamer binds to its target and leaves the CSs. Then, Exo I digests CS1, resulting in more access of redox agent to the surface of electrode and thus, a strong current signal was recorded. Copied with permission from ref. 26

### *3.2 $AFB_1$ Electrochemical Aptasensor*

The design of the electrochemical aptasensor was based on the π-shape structure of $AFB_1$ aptamer and its CSs (CS1 and CS2) as well as target-induced release of aptamer from CSs and digestion of CS1 by Exo I. Exo I is a sequence-independent enzyme which specifically digests the ssDNA from its 3′-terminus. Low cost, buffer compatibility, and good selectivity are the advantages of this enzyme. As shown in Scheme 2, the π-shape structure on the surface of gold electrode except 3′-end of CS2 was preserved from digestion by Exo I in the absence of $AFB_1$. Therefore, because of limited access of the redox agent, $[Fe(CN)_6]^{3-/4-}$, to the surface of electrode, a weak electrochemical signal was measured. In the presence of $AFB_1$, the π-shape structure was disassembled and CS1 and CS2 were released. Furthermore, the CS1 was digested following the addition of Exo I, leading to more access of $[Fe(CN)_6]^{3-/4-}$ to the surface of electrode. Therefore, a strong current signal was observed.

1. Preparation of Apt-CS-modified electrode (π-shape structure)
   (a) Pretreat each oligonucleotide (400 nM final concentration) with 2 mM TCEP for 1 h (this step is required in order to cleave the disulfide bonds between CS1 and the aptamer).
   (b) Incubate the surface of gold electrode with 9μL of the above solution for 16 h.
   (c) Soak the electrode in 1 mM MCH solution for 1 h to block the unreacted gold surface.

(d) Add 9μL of hybridization buffer (50 mM NaCl, 10 mM Tris–HCl, 1 mM EDTA, pH 7.5) containing 400 nM CS2 to the surface of electrode and incubate for 1.5 h.

(e) Preform all of the above steps at room temperature.

2. Optimization of the Exo I concentration
   (a) Treat Apt-CSs-modified electrodes with 500 pg/mL $AFB_1$ for 30 min at room temperature.
   (b) Incubate the treated electrodes with different concentrations of Exo I (0–18 U) for 1.5 h at 37 °C.
   (c) Do the washing steps with plenty of water, and obtain the electrochemical signal using DPV technique with 3 mM electrolyte solution, $K_3[Fe(CN)_6]/K_4[Fe(CN)_6]$ (1:1), containing 0.1 M KCl.
   (d) Set the potential from 0 V to +0.4 V for DPV measurements.
   (e) Set the pulse potential and pulse time as 10 mV and 25 ms, respectively (Fig. 4a) (*see* **Note 3**).
3. Optimization of the incubation time of Exo I
   (a) Treat the Apt-CS-modified electrodes with 500 pg/mL $AFB_1$ for 30 min at room temperature.

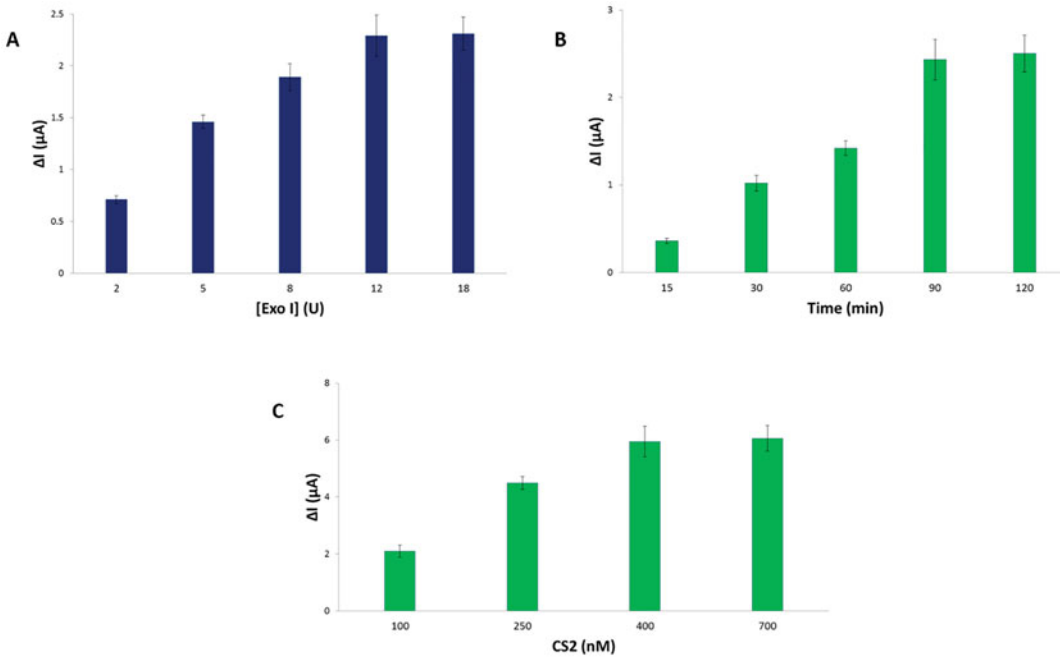


**Fig. 4** Optimization of the fabricated aptasensor parameters. (**a**) Optimization of the Exo I concentration. (**b**) Effect of the incubation time of Exo I on the relative electrochemical signal. (**c**) Optimization of the concentration of CS2. Copied with permission from ref. 26

(b) Add 12 U Exo I to the surfaces of theses electrodes and incubate them for different time periods (0–120 min) at 37 °C.

(c) Do the washing steps with water to preform DPV (Fig. 4b) (*see* **Note 4**).

4. Optimization of the CS2 concentration

CS2 concentration was optimized based on the concentrations of immobilized CS1 and Apt on the surface of electrode because CS2 was the last part for the formation of π-shape structure (Fig. 4c) (*see* **Note 5**).

5. Electrochemical assay of AFB1
   (a) Prepare various concentrations of $AFB_1$ in ethanol (0–800 pg/mL).
   (b) Incubate the Apt-CS-modified electrodes with these solutions for 45 min.
   (c) Wash the electrodes with water.
   (d) Add 12 U of Exo I to the surface of electrodes and incubate them for 1.5 h at 37 °C.
   (e) Record the signals using DPV technique (Fig. 5a, b) (*see* **Note 6**).
6. Evaluation of the specificity of the sensing method

The selectivity of the aptasensor was assessed in the presence of 500 pg/mL of $AFB_1$, $AFM_1$, OTA, ZEN, $AFB_2$, DON, and MC-LR (Fig. 5c).

7. Feasibility of the aptasensor in real samples
   (a) Spike $AFB_1$ in grape juice and serum samples (treated with 0.03 mg/mL salmon sperm DNA).
   (b) Record the amount of $AFB_1$ by the designed electrochemical aptasensor (Fig. 6).

### 3.3 Optical Aptasensors

Fluorescence method has been broadly applied as an analytical technique in biosensors design. Simplicity, sensitivity, and real-time detection are the advantages of this technique [27]. Here, a fluorescent aptasensor was developed for $AFB_1$ detection based on hairpin structure of chimera as a platform for attachment of N-methyl mesoporphyrin IX (NMM) (the fluorophore) to the surface of streptavidin-coated silica nanoparticles (SNP-streptavidin) (Scheme 3). In the presence of $AFB_1$, the hairpin structure of chimera is disassembled and G-quadruplex structure is formed. Therefore, NMM, which has a structural specificity for G-quadruplex structures rather than ssDNA or dsDNA, binds to the structure on the surface of SNP-streptavidin. This interaction results in a strong fluorescence signal. However, in the absence of the target, the G-quadruplex forming sequence is trapped in the

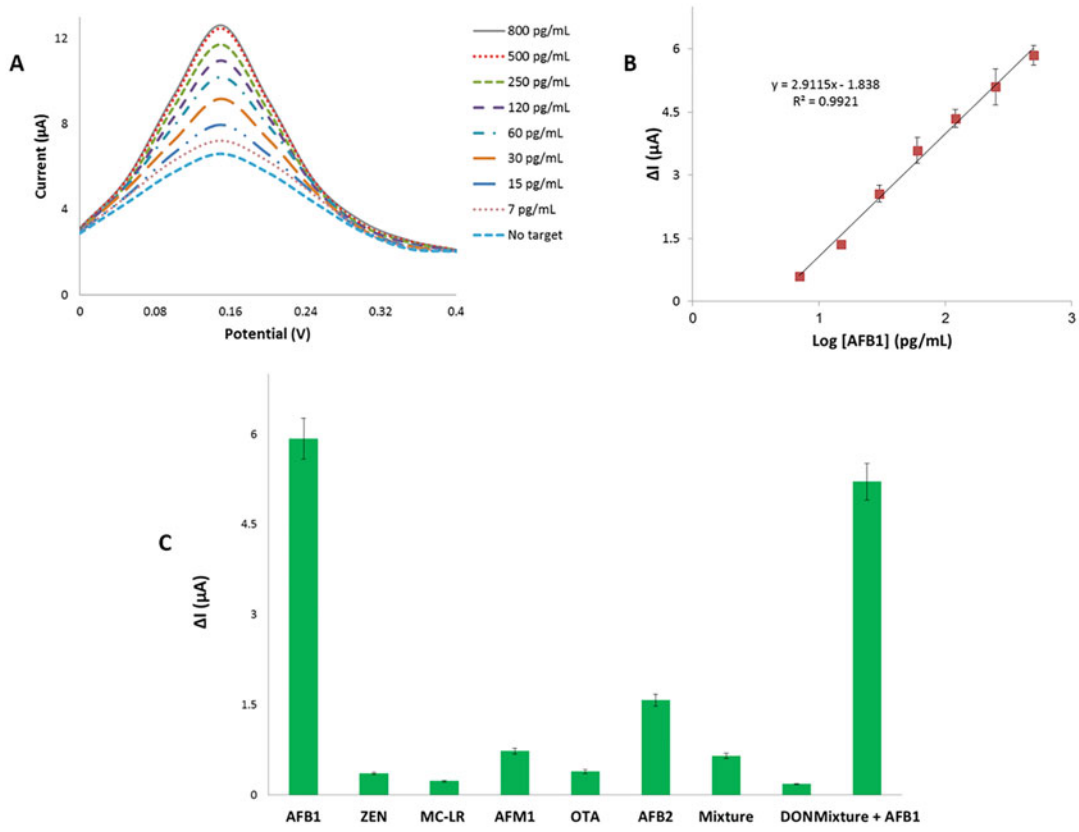


**Fig. 5** (**a**) Interaction of the π-shape electrochemical aptasensor with various concentrations of $AFB_1$ (0–800 pg/mL) using DPV technique. (**b**) The calibration plot in the presence of different concentrations of $AFB_1$. (**c**) Evaluation the specificity of the aptasensor in the presence of various toxins (the concentration of each toxin was 500 pg/mL). Copied with permission from ref. 26

hairpin structure of chimera. Thus, a weak fluorescence signal is recorded upon addition of NMM.

1. Optimization of the chimera-modified SNP-streptavidin concentration
   (a) Add SNP-streptavidin with different concentrations (0–70μg/mL) to 20μL FAM and biotin-labeled chimera (125 nM) in phosphate-buffered saline (10 mM PBS, pH 7.4) and incubate it for 1 h.
   (b) Evaluate the formation of chimera-modified SNP-streptavidin complex using a Synergy H4 microplate reader (Bio-TeK, USA) ($\lambda_{Ex} = 490$ nm).
   (c) Confirm the formation of chimera-modified SNP-streptavidin complex with 2.5% agarose gel electrophoresis (Fig. 7) (*see* **Note 7**).

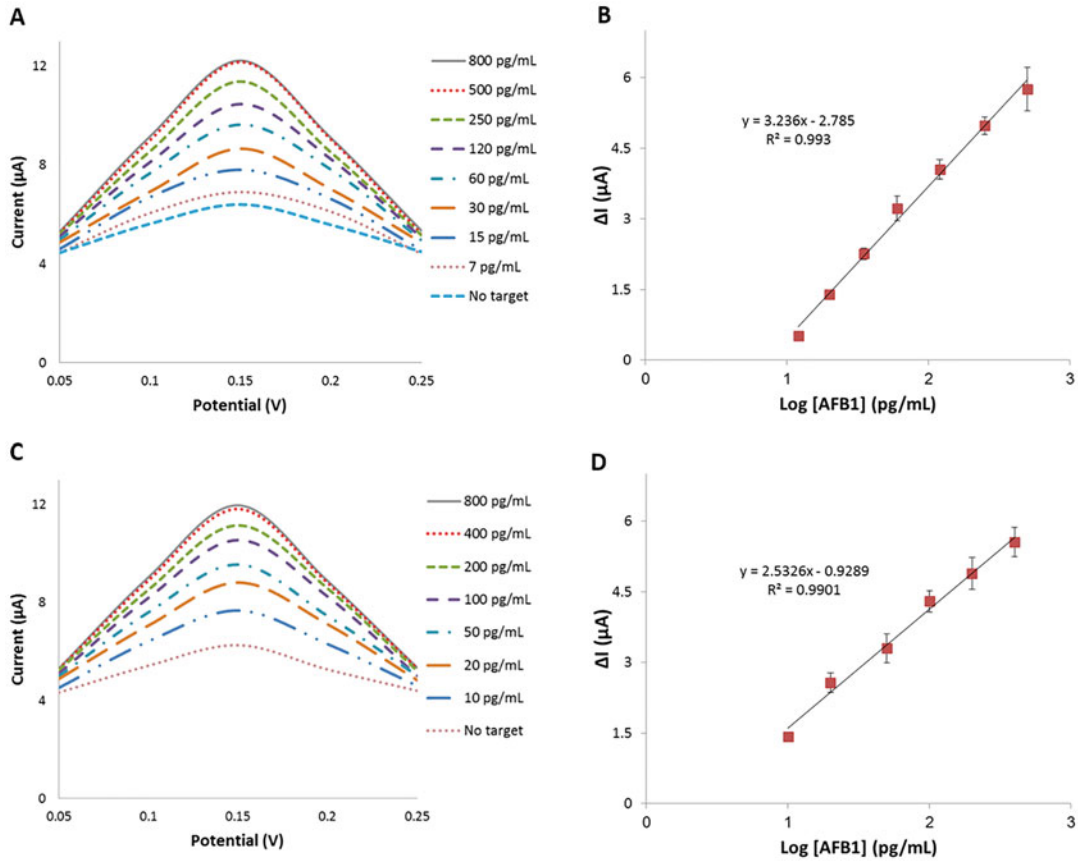


**Fig. 6** (**a**) Interaction of the electrochemical aptasensor with different concentrations of $AFB_1$ in grape juice recorded by DPV. (**b**) The standard curve of $AFB_1$ in grape juice. (**c**) Interaction of the electrochemical aptasensor with various concentrations of $AFB_1$ in serum. (**d**) The standard curve of $AFB_1$ in serum. Copied with permission from ref. 26

2. Fluorescent assay of $AFB_1$
   (a) Prepare various concentrations of AFB1 (0–1500 pg/mL) in PBS (10 mM PBS, pH 7.4).
   (b) Treat chimera-modified SNP-streptavidin complex (50μL, 50 nM chimera) with these concentrations of AFB1 and NMM (4μL, 2μM) for 30 min at 37 °C (final sample volume 154μL).
   (c) Record fluorescence intensities at emission and excitation wavelengths of 610 nm and 399 nm, respectively (Fig. 8a, b) (*see* **Note 8**).
3. Evaluation of the aptasensor selectivity
   (a) Assess the selectivity of the aptasensor in the presence of 900 pg/mL and 3000 pg/mL OTA, MC-LR, AFM1, DON, while the amount of AFB1 was 900 pg/mL (Fig. 8c).

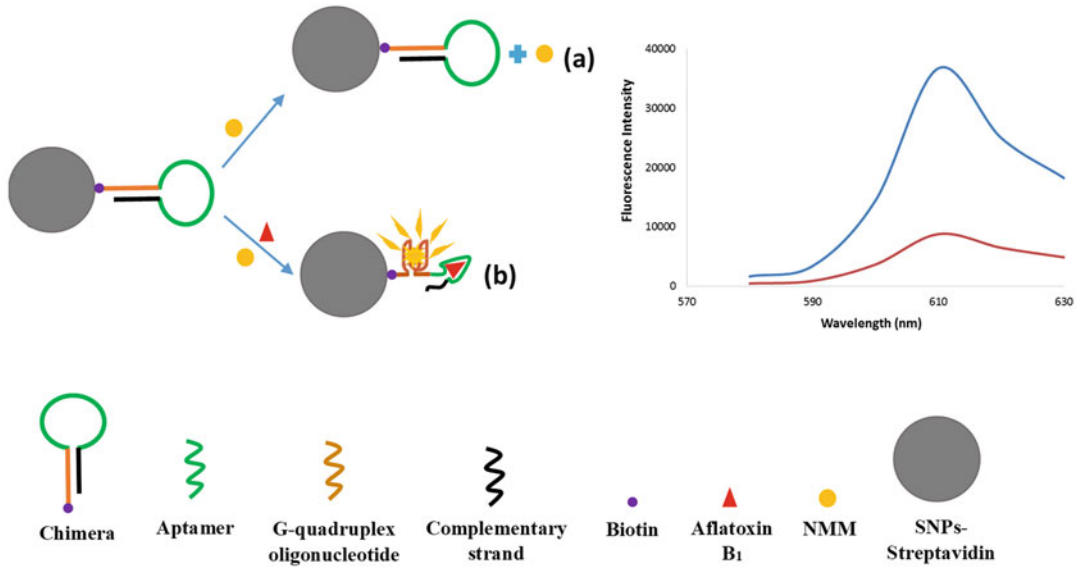


**Scheme 3** $AFB_1$ determination using fluorescent aptasensor. (**a**) In the absence of $AFB_1$, NMM could not bind to the G-quadruplex structure leading to a weak fluorescence signal. (**b**) In the presence of $AFB_1$, the hairpin structure of chimera is disassembled. Therefore, NMM could bind to the G-quadruplex structure on the surface of SNP-streptavidin, leading to the generation of a strong fluorescence signal. Copied with permission from ref. 28

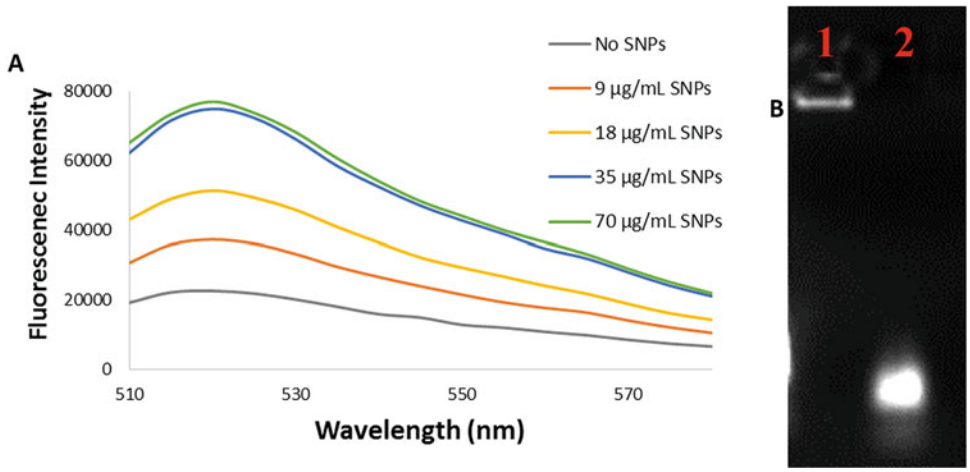


**Fig. 7** (**a**) The formation of chimera-modified SNP-streptavidin complex. Fluorescence spectra of FAM and biotin-labeled chimera in the presence of different amounts of SNP-streptavidin (0–70µg/mL). (**b**) Agarose gel electrophoresis of chimera-modified SNP-streptavidin complex. Lane 1: Chimera-modified SNP-streptavidin complex, Lane 2: Chimera. Copied with permission from ref. 28

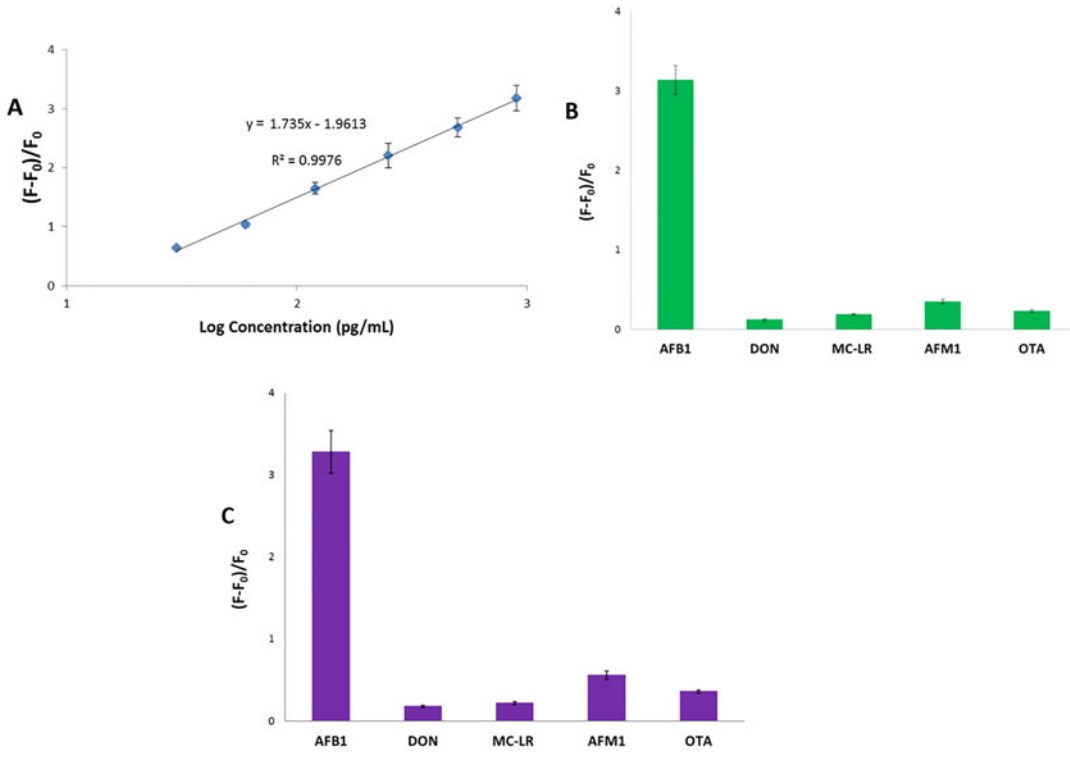


**Fig. 8** (**a**) Calibration curve in the presence of various concentrations of $AFB_1$. (**b**) Relative fluorescence signal of the aptasensor in the presence of 900 pg/mL concentration of different toxins. (**c**) Relative fluorescence signal of the aptasensor in the presence of 3000 pg/mL concentration of different toxins. Copied with permission from ref. 28

4. Application of the aptasensor in real samples
   (a) Prepare serum and grape juice samples containing different concentrations of $AFB_1$ (0–1500 pg/mL) (treated with 0.03 mg/mL salmon sperm DNA) in order to evaluate the analytical performance of the developed aptasensor.
   (b) Incubate chimera-modified SNP-streptavidin complex (50μL, 50 nM chimera) in 10 mM PBS (pH 7.4) with either 100μL serum or grape juice treated with salmon sperm DNA containing various concentrations of $AFB_1$ (0–1500 pg/mL) and NMM (4μL, 2μM) for 30 min at 37 °C (final volume 154μL).
   (c) Record fluorescence intensities with emission wavelength and excitation at 610 nm and 399 nm, respectively (Fig. 9).

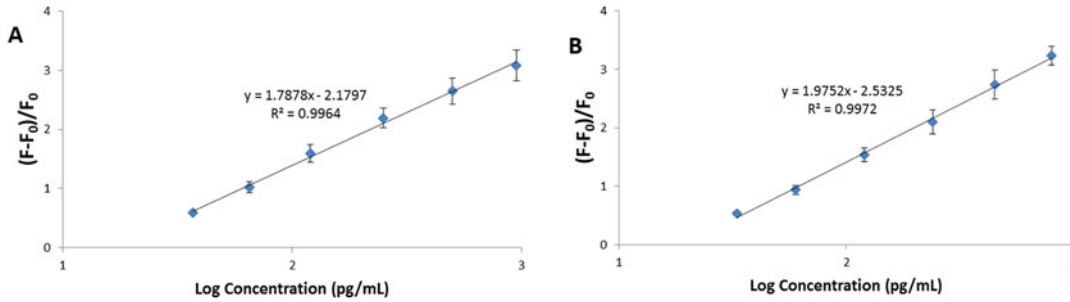


**Fig. 9** (**a**) Calibration curve in the presence of various concentrations of $AFB_1$ in grape juice. (**b**) Calibration curve in the presence of various concentrations of $AFB_1$ in serum. Copied with permission from ref. 28

## 4 Notes

1. The optimum required time for effective attachment of Apt-modified SPGE with CS-modified AuNPs is 40 min.
2. Based on the changes of the relative electrochemical response proportional to $AFM_1$ concentrations, a broad linear relationship is detected in the range of 2–600 ng/L with a limit of detection (LOD) of 0.9 ng/L using three signals-to-noise ratio (3S/N).
3. When the concentration of Exo I is 12 U, the maximum relative current signal is observed.
4. The optimum incubation time of Exo I for complete reaction with CS1 is 90 min.
5. When the concentration of CS2 is 400 nM, the maximum relative current response is observed for $AFB_1$ (500 pg/mL)-treated aptasensor.
6. A good linear relationship between the relative electrochemical response and the $AFB_1$ concentrations is detected in the range of 7–500 pg/mL. The LOD is estimated to be 2 pg/mL (LOD = 3 × standard deviation of blank/slope, based on International Union of Pure and Applied Chemistry, IUPAC).
7. The maximum fluorescence signal is obtained when the concentration of SNP-streptavidin is 35μg/mL.
8. A broad linear relationship is measured between the relative fluorescence intensity and the $AFB_1$ concentrations ranging from 30 to 900 pg/mL. The LOD of $AFB_1$ by using the presented aptasensor is calculated to be 8 pg/mL (3S/N).

## References


1. Jalalian SH, Ramezani M, Danesh NM, Alibolandi M, Abnous K, Taghdisi SM (2018) A novel electrochemical aptasensor for detection of aflatoxin M1 based on target-induced immobilization of gold nanoparticles on the surface of electrode. Biosens Bioelectron 117:487–492. https://doi.org/10.1016/j.bios.2018.06.055
2. Zheng N (2017) A survey of aflatoxin M1 of raw cow milk in China during the four seasons from 2013 to 2015. Food Control 78:176–182. https://doi.org/10.1016/j.foodcont.2017.02.055
3. Chauhan R, Singh J, Solanki PR, Manaka T, Iwamoto M, Basu T, Malhotra BD (2016) Label-free piezoelectric immunosensor decorated with gold nanoparticles: kinetic analysis and biosensing application. Sensors Actuators B Chem 222:804–814. https://doi.org/10.1016/j.snb.2015.08.117
4. Ostry V, Malir F, Toman J, Grosse Y (2017) Mycotoxins as human carcinogens—the IARC monographs classification. Mycotoxin Res 33 (1):65–73. https://doi.org/10.1007/s12550-016-0265-7
5. Juan C, Zinedine A, Moltó JC, Idrissi L, Mañes J (2008) Aflatoxins levels in dried fruits and nuts from Rabat-Salé area, Morocco. Food Control 19(9):849–853. https://doi.org/10.1016/j.foodcont.2007.08.010
6. Kew MC (2003) Synergistic interaction between aflatoxin B1 and hepatitis B virus in hepatocarcinogenesis. Liver Int 23 (6):405–409
7. Battacone G, Nudda A, Cannas A, Cappio Borlino A, Bomboi G, Pulina G (2003) Excretion of aflatoxin M1 in milk of dairy ewes treated with different doses of aflatoxin B1. J Dairy Sci 86(8):2667–2675
8. Afum C, Cudjoe L, Hills J, Hunt R, Padilla LA, Elmore S, Afriyie A, Opare-Sem O, Phillips T, Jolly PE (2016) Association between aflatoxin M(1) and liver disease in HBV/HCV infected persons in Ghana. Int J Environ Res Public Health 13(4):377. https://doi.org/10.3390/ijerph13040377
9. Sefidgar S, Mirzae M, Assmar M, Naddaf S (2011) Aflatoxin M1 in pasteurized milk in Babol city, Mazandaran Province, Iran. Iran J Public Health 40(1):115–118
10. Lee S, Kim G, Moon J (2013) Performance improvement of the one-dot lateral flow immunoassay for aflatoxin B1 by using a smartphone-based reading system. Sensors 13 (4):5109–5116
11. Khalil MMH, Gomaa AM, Sebaei AS (2013) Reliable HPLC determination of aflatoxin m1 in eggs. J Anal Methods Chem 2013:817091. https://doi.org/10.1155/2013/817091
12. Solfrizzo M, Gambacorta L, Lattanzio VMT, Powers S, Visconti A (2011) Simultaneous LC–MS/MS determination of aflatoxin M1, ochratoxin A, deoxynivalenol, de-epoxydeoxynivalenol, α and β-zearalenols and fumonisin B1 in urine as a multi-biomarker method to assess exposure to mycotoxins. Anal Bioanal Chem 401(9):2831. https://doi.org/10.1007/s00216-011-5354-z
13. Var I, Kabak B, Gök F (2007) Survey of aflatoxin B1 in helva, a traditional Turkish food, by TLC. Food Control 18(1):59–62. https://doi.org/10.1016/j.foodcont.2005.08.008
14. Istamboulie G, Paniel N, Zara L, Reguillo Granados L, Barthelmebs L, Noguer T (2016) Development of an impedimetric aptasensor for the determination of aflatoxin M1 in milk. Talanta 146:464–469. https://doi.org/10.1016/j.talanta.2015.09.012
15. Song S-H, Gao Z-F, Guo X, Chen G-H (2019) Aptamer-based detection methodology studies in food safety. Food Anal Methods 12 (4):966–990. https://doi.org/10.1007/s12161-019-01437-3
16. Willner I, Zayats M (2007) Electronic aptamer-based sensors. Angew Chem Int Ed 46 (34):6408–6418. https://doi.org/10.1002/anie.200604524
17. Liu X, Ren J, Su L, Gao X, Tang Y, Ma T, Zhu L, Li J (2017) Novel hybrid probe based on double recognition of aptamer-molecularly imprinted polymer grafted on upconversion nanoparticles for enrofloxacin sensing. Biosens Bioelectron 87:203–208. https://doi.org/10.1016/j.bios.2016.08.051
18. Jo EJ, Mun H, Kim SJ, Shim WB, Kim MG (2016) Detection of ochratoxin A (OTA) in coffee using chemiluminescence resonance energy transfer (CRET) aptasensor. Food Chem 194:1102–1107. https://doi.org/10.1016/j.foodchem.2015.07.152
19. Nguyen V-T, Kwon YS, Gu MB (2017) Aptamer-based environmental biosensors for small molecule contaminants. Curr Opin Biotechnol 45:15–23
20. Kim YS, Kim JH, Kim IA, Lee SJ, Jurng J, Gu MB (2010) A novel colorimetric aptasensor using gold nanoparticle for a highly sensitive and specific detection of oxytetracycline. Biosens Bioelectron 26(4):1644–1649. https://doi.org/10.1016/j.bios.2010.08.046

21. Zheng J, Feng W, Lin L, Zhang F, Cheng G, He P, Fang Y (2007) A new amplification strategy for ultrasensitive electrochemical aptasensor with network-like thiocyanuric acid/gold nanoparticles. Biosens Bioelectron 23 (3):341–347. https://doi.org/10.1016/j.bios.2007.04.015
22. Du P, Liu S, Wu P, Cai C (2007) Single-walled carbon nanotubes functionalized with poly (nile blue A) and their application to dehydrogenase-based biosensors. Electrochim Acta 53(4):1811–1823. https://doi.org/10.1016/j.electacta.2007.08.027
23. Zhang P, Liu H, Li X, Ma S, Men S, Wei H, Cui J, Wang H (2017) A label-free fluorescent direct detection of live Salmonella typhimurium using cascade triple trigger sequences-regenerated strand displacement amplification and hairpin template-generated-scaffolded silver nanoclusters. Biosens Bioelectron 87:1044–1049. https://doi.org/10.1016/j.bios.2016.09.037
24. Nameghi MA, Danesh NM, Ramezani M, Hassani FV, Abnous K, Taghdisi SM (2016) A fluorescent aptasensor based on a DNA pyramid nanostructure for ultrasensitive detection of ochratoxin A. Anal Bioanal Chem 408 (21):5811–5818. https://doi.org/10.1007/s00216-016-9693-7
25. Zhang Y, Liu W, Zhang W, Yu S, Yue X, Zhu W, Zhang D, Wang Y, Wang J (2015) DNA-mediated gold nanoparticle signal transducers for combinatorial logic operations and heavy metal ions sensing. Biosens Bioelectron 72:218–224. https://doi.org/10.1016/j.bios.2015.05.019
26. Abnous K, Danesh NM, Alibolandi M, Ramezani M, Sarreshtehdar Emrani A, Zolfaghari R, Taghdisi SM (2017) A new amplified π-shape electrochemical aptasensor for ultrasensitive detection of aflatoxin B1. Biosens Bioelectron 94:374–379. https://doi.org/10.1016/j.bios.2017.03.028
27. Taghdisi SM, Danesh NM, Nameghi MA, Ramezani M, Abnous K (2016) A label-free fluorescent aptasensor for selective and sensitive detection of streptomycin in milk and blood serum. Food Chem 203:145–149. https://doi.org/10.1016/j.foodchem.2016.02.017
28. Taghdisi SM, Danesh NM, Ramezani M, Abnous K (2018) A new amplified fluorescent aptasensor based on hairpin structure of G-quadruplex oligonucleotide—aptamer chimera and silica nanoparticles for sensitive detection of aflatoxin B1 in the grape juice. Food Chem 268:342–346. https://doi.org/10.1016/j.foodchem.2018.06.101

# Chapter 22

# DNA-Generated Electric Current Biosensor for Epidermal Growth Factor Receptor 2 (HER2) Analysis

**Xiaoqing Li, Congcong Shen, Minghui Yang, and Avraham Rasooly**

## Abstract

Electrochemical biosensors have been applied in the detection of human serum biomarkers for clinical applications. A kind of signal amplifying method using deoxyribonucleic acid (DNA) as signal probe was developed to construct electrochemical biosensor for biomarker detection. In addition to its primary function as genetic material, DNA is also a potential source of molecular electronics that generate redox currents. As an example of this new function, DNA-generated redox currents were used for electrochemical detection of human epidermal growth factor receptor 2 (HER2), a clinically important biomarker for breast cancer. In order to induce the redox current, the phosphate backbone of the single-stranded DNA was reacted with molybdate to form redox molybdophosphate precipitate and generate electrochemical current. Within a certain range, the peak current is linearly proportional to the concentration of HER2, thus realizing the quantitative analysis of HER2 in human serum.

**Key words** Electrochemical biosensor, DNA, Human epidermal growth factor receptor 2, Tumor marker, Square wave voltammetry (SWV)

## 1 Introduction

Electrochemical biosensors have been used for qualitative and quantitative analyses of biomarkers in vivo [1]. The equipment and principle of electrochemical biosensors are shown in Fig. 1. It is a signal analysis and testing device that converts biochemical recognition into electrical signal output with immobilized biological components as sensitive elements [2]. First, biochemical reaction occurs on the surface of specific electrode, and the electrochemical signal generated is converted into electrical signal through signal conversion elements. Then, the electrochemical detector will amplify, filter, and convert the received electrical signal to analog and digital, and finally send the processed signal to the computer to display. Electrochemical biosensors can be divided into potential sensors, current sensors, and conductance sensors according to their different output signals. Current-type sensors are increasingly

Miguel R. Ossandon et al. (eds.), *Biomedical Engineering Technologies: Volume 1*, Methods in Molecular Biology, vol. 2393, https://doi.org/10.1007/978-1-0716-1803-5_22, 

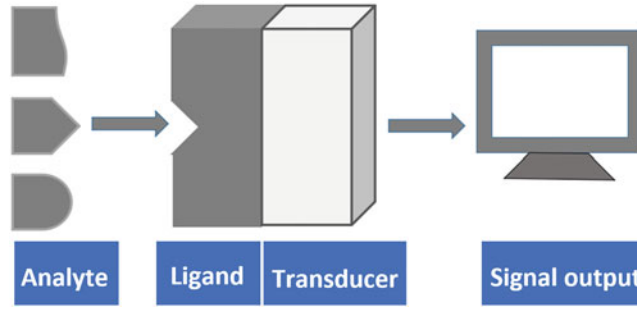


**Fig. 1** Elements of electrochemical sensors including the target analyte, specific ligand which specifically bind to the analyte and generate electrochemical signal, the transducer which converts the signal to electric signal which analyzed and displayed by the signal output component (reproduced from ref. 1)

used among them because the relationship between current signals and the concentration of the analytes are more intuitively. The current-type sensor oxidizes and reduces the compounds directly when the interface between electrode and electrolyte solution is kept at a constant potential. The current flowing through the external circuit is taken as the output signal of the sensor so the detection of the analyte can be realized. According to different analytical techniques, the current analysis method includes cyclic voltammetry (CV), current–time curve method (I-t), square-wave voltammetry (SWV), and so on. The electrochemical analysis instrument used for such sensors is usually a three-electrode system: a working electrode (WE), a reference electrode (RE), and an auxiliary electrode (CE) [3].

### *1.1 DNA-Based Electrochemical Sensors*

DNA has attracted attention in molecular electronics due to its unique physical and biological properties [4]. Molecular-scale electronics has the potential to overcome the limitations of traditional silicon-based integrated circuits and extend Moore's law beyond the limits of traditional electronics [5, 6]. Recently, many electrochemical biosensors based on DNA have been developed to detect biomarkers. DNA biosensor mainly consists of two parts, which are molecular recognition components and energy transducers. The identification element is mainly composed of the known sequence of DNA strands, which has a strong specific identification of the analyte to be determined. Energy transducers convert the signal perceived by the identifying element into the signal that can be observed and recorded (such as current magnitude, potential variation, conductivity variation). The main principle of electrochemical biosensor based on DNA is shown in Fig. 2. It works by using the specific recognition (molecular hybridization) of a specific sequence of single-stranded DNA (ssDNA) fixed on the surface of the electrode and the complementary sequence (cDNA) in the solution to form double-stranded DNA (dsDNA). For detection, the change

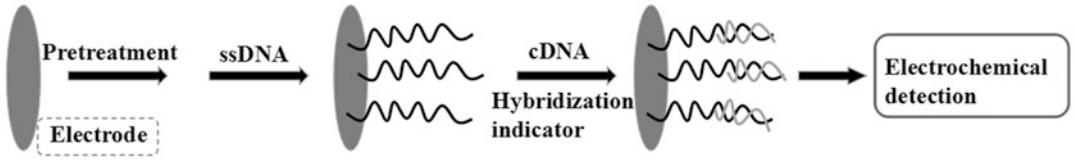


**Fig. 2** Composition of traditional DNA-based electrochemical sensors based on forming dsDNA which generate electrochemical signal by displacing an indicator or changes the conformation of indicator (reproduced from ref. 2)

of the electrochemical response signal of an indicator (e.g., displacement of nanoparticles) was used to achieve the purpose of qualitative analysis [7].

Similarly, when the concentration of complementary sequence DNA changes, the conformation of an embedded indicator supports electron transfer from the indicator to the electrode. The response signal of the indicator is linearly related to the concentration of DNA substance to be measured within limits. Thus, the quantitative purpose can be achieved. DNA has been used for conducting charge and logic gating in molecular electronics, as well as for unlabeled detection [7]. While in molecular electronics, DNA is often used only to guide changes in electrical signals or amplify them through DNA hybridization, rather than producing the electrical signals themselves. As a substance rich in a large number of biological groups, we should not ignore that it is also a potential source of bio-energy in molecular electronics.

Here, a new biosensor that directly generates electrochemical signals using the phosphate of the DNA in a chemical reaction as biological energy source is realized. Sandwich structures that composed of specific peptides, tumor markers, and specific adaptor DNA strands are constructed on the surface of solid electrode to realize the sensitive detection of tumor markers.

## 2 Materials

### *2.1 Electrochemical System for DNA Biosensors*

1. Selector switch of USB/serial communication port (Shanghai CH Instruments Co., China).
2. Serial communication port (Shanghai CH Instruments Co., China).
3. Electrolytic cell controller (Shanghai CH Instruments Co., China).
4. Electrode wire (Shanghai CH Instruments Co., China).
5. Electrolytic cell (Shanghai CH Instruments Co., China).
6. Electrode wire connector (Shanghai CH Instruments Co., China).

7. Signal output interface (output of voltage, current, and other signals) (Shanghai CH Instruments Co., China).
8. Auxiliary electrode (Pt electrode, Tianjin Ida Co., China) (*see* **Note 1**).
9. Reference electrode (Ag/AgCl electrode, Tianjin Gaossunion Co., China).
10. Working electrode (gold electrode, Tianjin Ida Co., China).

### 2.2 Components of DNA-Generated Electric Current Biosensor

1. A CHI-650D electrochemical workstation (Shanghai CH Instruments Co., China).
2. Conventional three-electrode system was used with a gold electrode (2 mm in diameter) as the working electrode, a platinum wire as the auxiliary electrode (Tianjin Ida Co., China), and an Ag/AgCl electrode as the reference electrode (Tianjin Gaossunion Co., China)(*see* **Note 2**).
3. Thiol-group-modified peptide specific to HER2 (CKLRLEW NR) (Shanghai GL Biochem Co., Ltd. China) stock solution: The stock solution was stored at −20 °C. Working solutions were prepared by diluting the stock solution with ultrapure water immediately before use (*see* **Note 3**).
4. Human epidermal growth factor receptor-2 (HER2) [Abcam Co., Ltd. (Cambridge, MA)] stock solution: The stock solution was stored at −80 °C. Working solutions were prepared by diluting the stock solution with ultrapure water immediately before use (*see* **Note 3**).
5. Anti-HER2 Ab [Abcam Co., Ltd. (Cambridge, MA)] stock solution. The stock solution was stored at −20 °C. Working solutions were prepared by diluting the stock solution with ultrapure water immediately before use (*see* **Note 3**).
6. Human serum [Zhenglong Biochem. Lab (Chengdu, China)] stock solution. The stock solution was stored at −20 °C. Working solutions were prepared by diluting the stock solution with ultrapure water immediately before use (*see* **Note 3**).
7. Aptamer with a sequence of 5′-GCA GCG GTG TGG GG-3′ (Shanghai Sangon Biotech Co., Ltd. China) stock solution. The stock solution was stored at −20 °C. Working solutions were prepared by diluting the stock solution with ultrapure water immediately before use (*see* **Note 3**).
8. Thiol-group-modified poly-cytosine (dC20) (Sangon Biotech Co., Ltd. Shanghai, China) stock solution. The stock solution was stored at −20 °C. Working solutions were prepared by diluting the stock solution with ultrapure water immediately before use (*see* **Note 3**).
9. Piranha solution is a mixture of concentrated sulfuric acid and 30% hydrogen peroxide (7:3, v/v) (*see* **Note 4**).

## 3 Methods

The electrochemical detection approach described here is based on the reaction of the DNA phosphate backbone with molybdate, forming redox molybdophosphate precipitate that generates an electrochemical current on the surface of the electrode. Square-wave voltammetry (SWV) is utilized to detect electrochemical signals (Fig. 3). The peak current is proportional to the concentration of analyte, which can be used for quantitative analysis.

### 3.1 Aptamer DNA-Generated Electric Current-Based Immunosensor

#### 3.1.1 Setup of Aptamer DNA-Generated Electric Current Biosensor

The electrochemical biosensor seating is based on CHI series electrochemical workstation equipped with three-electrode sensor.

As shown in Fig. 4, the corresponding electrode line and data line are connected according to different interfaces. The data line is connected with COM port of the control computer and serial communication port of the instrument using serial data line. USB cable can also be used to connect computers and instruments to transfer data. Four different color electrode wires correspond to different electrodes respectively. The working electrode (gold electrode) is connected to the electrode wire with green interface. The auxiliary electrode (platinum electrode) is connected to the electrode line with red interface. The reference electrode (Ag/AgCl electrode) is connected to the electrode line of the white interface, thus the complete three-electrode system is formed. SWV was used to detect the electrical signal of the modified electrode, and then the content of markers to be measured in human serum was quantitatively analyzed.

#### 3.1.2 Preparing for Aptamer DNA-Generated Electric Current Biosensor

1. Gold electrodes for electrochemical sensors were purchased from Tianjin Ida Co., China. The diameter of the gold electrode is 2 mm.
2. The gold electrodes are immersed in piranha solution to remove surface impurities, and the electrodes are polished and cleaned (*see* **Notes 5** and **6**).
3. The pretreated gold electrode was immersed overnight in a specific polypeptide solution to complete the self-assembly on the gold electrode surface and sealed with mercapto-1-hexanol for 1 h.

#### 3.1.3 Detection of HER-2 Concentration Using DNA-Generated Electric Current Biosensor Sandwich Assay

1. The tumor marker is captured by specific peptides, which takes about 1 h.
2. The sandwich structure is completed on the surface of the gold electrode after the specific aptamer DNA strand was linked to HER2, which took 1 h.
3. Reaction of polycytosine with molybdate to form molybdophosphate: the gold electrode assembled with sandwich structure is connected to the green interface and forms a

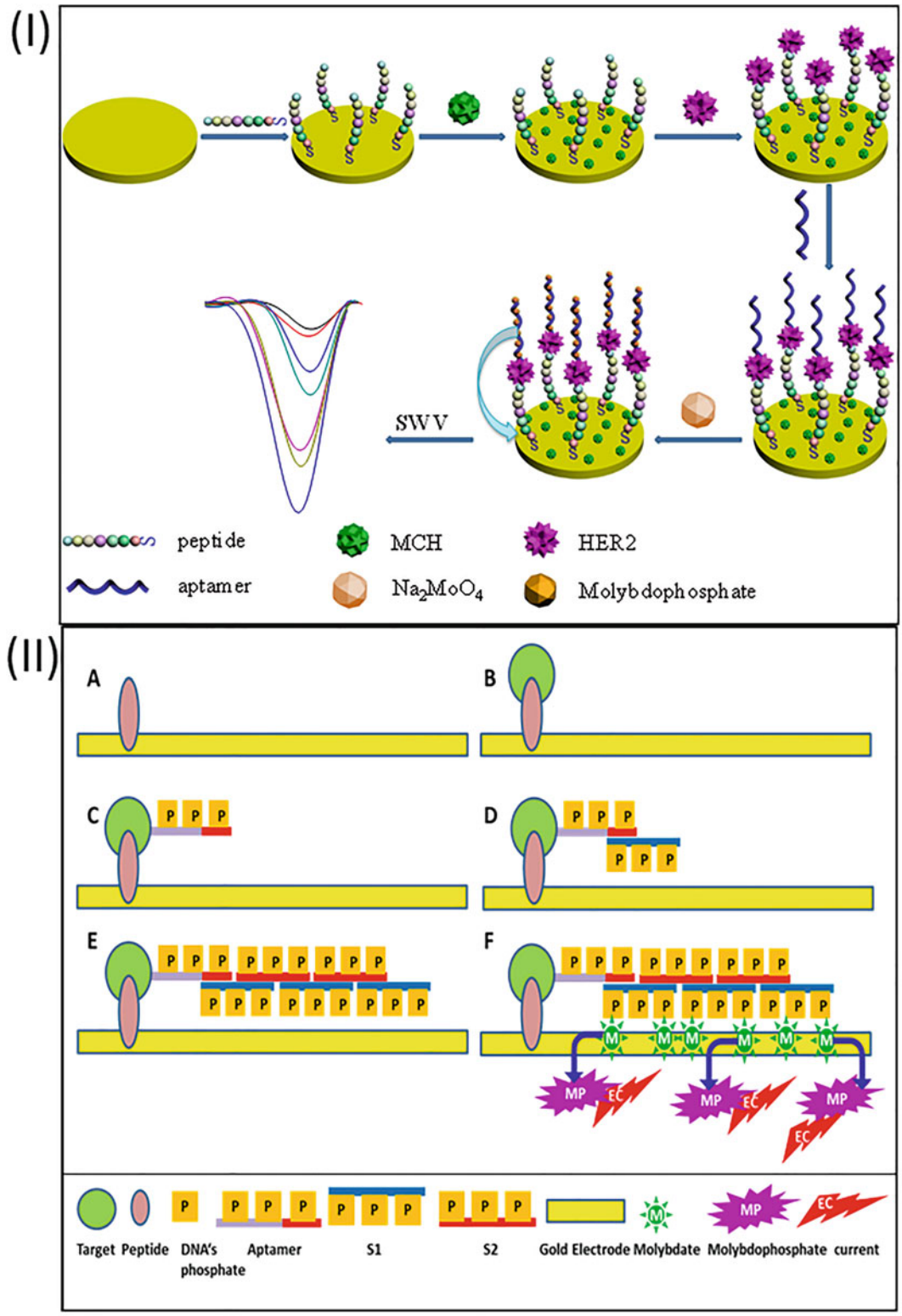


**Fig. 3** Electric current biosensor. (1) A sandwich assay with aptamer DNA binding to the target molecule to generated signal (reproduced from ref. 5). (2) Amplified aptamer DNA-generated electric current biosensor (reproduced from ref. 6). A sandwich assay similar to (1) utilizing DNA hybridization to generate longer double-strand DNA and increase the amount of DNA phosphate backbone which react with molybdate to generate higher electrochemical signal

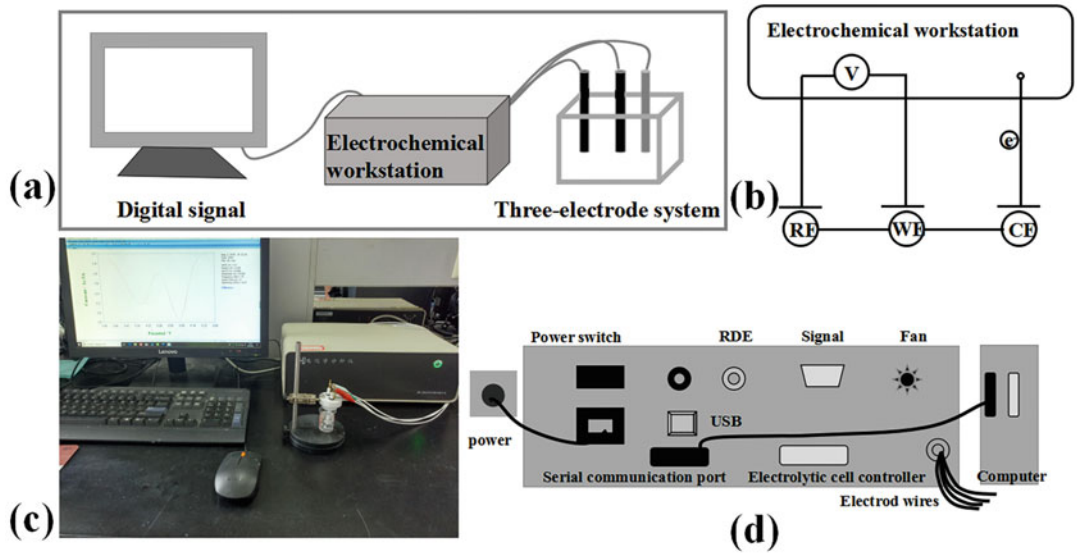


**Fig. 4** Diagram of electrochemical sensor equipment. (**a**) Schematics of electrochemical DNA biosensor. (**b**) Diagram of three-electrode system. (**c**) Photo of electrochemical sensor. (**d**) Assembly diagram of electrochemical sensor

three-electrode system with auxiliary electrode and reference electrode.

4. In 0.5 M $H_2SO_4$ solution, square-wave voltammetry (SWV) is used to record changes in current. The initial potential was 0.1 V, the terminal point was 0.5 V, the step height was 0.004, the amplitude was 0.025, the frequency was 15, and the sensitivity was $1.0 \times 10^{-6}$. Once HER2 with different concentrations is captured, the reaction between phosphate of aptamer and molybdate is triggered, and the obtained phosphomolybdate can produce electric current (*see* **Notes** 7 and **8**).

### *3.2 Polycytosine DNA Electric-Current-Generated Immunosensor*

The equipment and composition were identical except that the aptamer DNA was replaced by antibody/DNA immune complexes (Fig. 5).

#### *3.2.1 Setup of Polycytosine DNA Electric-Current-Generated Immunosensor*

The electrochemical setup is similar to the configuration described in Subheading 3.1.1. The green interface is connected to the working electrode, the red interface is connected to the auxiliary electrode (Tianjin Ida Co., China), and the white interface is connected to the reference electrode (Tianjin Ida Co., China). The three electrodes were immersed in 0.5 M $H_2SO_4$, the parameters of cyclic voltammetry and square-wave voltammetry were set respectively, and the scanning current was conducted within the voltage range of 0.1–0.5 V.

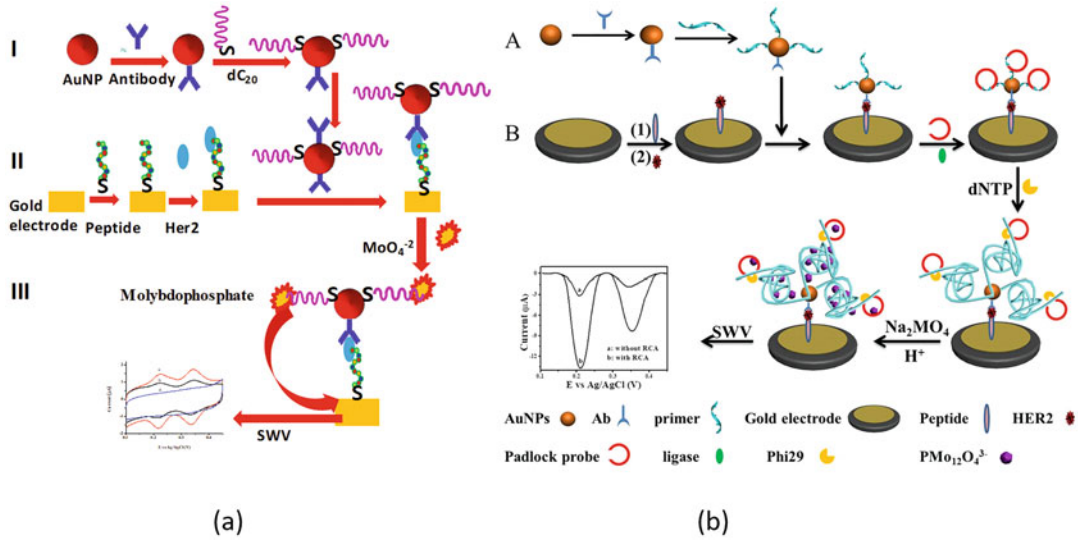


**Fig. 5** Polycytosine DNA electric-current-generated immunosensor. (**a**) Schematics of polycytosine DNA electric-current-generated immunosensor (reproduced from ref. 8): Gold nanoparticles (AuNPs) were used as a supporting matrix to capture HER2 by anti-HER2 antibody and to immobilize the polycytosine-DNA sequence (dC20) for electrochemical current generation. In the presence of target HER2, a sandwiched immunocomplex forms between the immobilized peptide specific to HER2 on the gold electrode and the anti-HER2 antibodies on the AuNPs, the phosphate of the immunocomplex reacted with $Na_2MoO_4$ and the current generated was measured (**b**) similar to (**a**) with the addition of rolling circle amplified polycytosine DNA to amplify the DNA generating electric current when reacted with $Na_2MoO_4$ (reproduced from ref. 9)

*3.2.2 Preparing for Polycytosine DNA Electric-Current-Generated Immunosensor*

1. Gold electrodes for electrochemical sensors were purchased from Tianjin Ida Co., China. The diameter of the gold electrode is 2 mm.
2. The gold electrode was soaked in fresh Piranha solution [$H_2O_2$ (30%): concentrated sulfuric acid = 3:7 (v/v)] for 15 min and washed extensively with ethanol and deionized water (*see* **Notes 4** and **5**).
3. Preparation of polycytosine and Ab modified AuNPs. Specifically, 50μL of Ab solution (50 ng/mL) was added to 2 mL of gold colloids and incubated for 1 h at room temperature. Then the mixture was centrifuged, and AuNPs were resuspended into 2 mL of deionized water. Afterward, 200μL of 10 mM polycytosine ($dC_{20}$)solution was added to the mixture described above and incubated for 16 h. Sodium chloride (1 M) was then added to the mixture every 8 h until the final concentration of sodium chloride was 0.2 M. After incubation overnight at room temperature with gentle shaking, the mixture was centrifuged again to remove free DNA molecules. The obtained AuNPs were resuspended in 2 mL of deionized water and stored at 4 °C until use.

4. The pretreated gold electrode was immersed overnight in a specific polypeptide solution to complete the self-assembly of the gold electrode surface and sealed with mercapto-1-hexanol for 1 h.
5. The tumor marker (HER2) was captured by specific peptides, which takes about 2 h.
6. The polycytosine and Ab-modified AuNPs were connected to HER2 on the gold electrode, and the immunologic process was completed, which took 1 h. The sandwich structure is completed on the surface of the gold electrode after the above process.
7. Reaction of polycytosine with molybdate to form molybdophosphate, 5μL of 5 mM $Na_2MoO_4$ solution was dropped on the electrode surface and incubated for 20 min before electrochemical analysis in 0.5 M $H_2SO_4$ with the electrochemical detector (*see* **Notes 7** and **8**).

*3.2.3 Detection of HER2 Concentration using Polycytosine DNA Electric-Current-Generated Immunosensor*

1. The gold electrode assembled with sandwich structure is connected to the green interface and forms a three-electrode system with auxiliary electrode and reference electrode.
2. In 0.5 M $H_2SO_4$ solution, square-wave voltammetry (SWV) is used to record changes in current. The initial potential was 0.1 eV, the terminal point was 0.5 eV, the step height was 0.004, the amplitude was 0.025, the frequency was 15, and the sensitivity was $1.0 \times 10^{-6}$. When HER2 in breast cancer patient is captured, the reaction between phosphate of DNA and molybdate is triggered, and the obtained phosphomolybdate can produce electric current (*see* **Notes 7** and **8**).

*3.2.4 Rolling Circle Amplified DNA Electric-Current-Generated Immunosensor*

For the preparation of the rolling circle amplified DNA electric-current-generated immunosensor, the procedures are similar to that given in Subheading 3.2.2, except, after the formation of the sandwich structure, the DNA on AuNPs serves as a primer to trigger rolling circle amplification. This results in the formation of a long DNA containing hundreds of copies of circular DNA sequence on the electrode surface, which generated higher current signal.

The rolling circle amplification procedures are as follows [9]: 0.2μM padlock probes were added onto the electrode for 2 h to hybridize with the primer on the AuNP surface. Next the solution of 2 U *E. coli* DNA ligase, 10× *E. coli* DNA ligase buffer, and 10× BSA (0.05%) was added onto the electrode at room temperature for 1 h to make the padlock probe form a circular template. Finally, the solution of 1 U *E. coli* DNA polymerase, 10× *E. coli* DNA polymerase buffer, and 1 mM dNTPs was dropped onto the electrode for 2 h. After washing again, 5 mM $Na_2MoO_4$ solution was dropped onto the electrode and incubated for 25 min before electrochemical detection.

## 4 Notes

1. The auxiliary electrode must be electrically conductive while inert within the range of potential studied.
2. The shape of the auxiliary electrode is consistent with the working electrode, its area is larger than the working electrode, and it should be placed in a position symmetric with the working electrode.
3. Biological drugs must be stored at low temperature, and their properties are easily affected by temperature. The solution must be prepared quickly during the experiment.
4. Piranha solution is a highly corrosive liquid that requires extreme care.
5. The working electrode is a noble metal electrode, which has good conductivity and easily decorated. The surface must be flat and smooth to prevent corrosion and passivation.
6. The polishing and cleaning of the working electrode have a great influence on the experimental results. The cleaning process must be carefully treated.
7. Special care should be taken in cleaning the modified electrode surface, washing out all nonspecific adsorbents.
8. The electrolyte must be kept at a constant temperature during the test, and the reaction conditions must be strictly controlled.

### References

1. Ronkainen NJ, Halsall HB, Heineman WR (2010) Electrochemical biosensors. Chem Soc Rev 39:1747–1763
2. Drummond TG, Hill MG, Barton JK (2003) Electrochemical DNA sensors. Nat Biotechnol 21:1192–1199
3. Wang G, Zhang L, Zhang J (2012) A review of electrode materials for electrochemical supercapacitors. Chem Soc Rev 41:797–828
4. Hsieh K, Patterson AS, Ferguson BS, Plaxco KW, Soh HT (2012) Rapid, sensitive, and quantitative detection of pathogenic DNA at the point of care through microfluidic electrochemical quantitative loop-mediated isothermal amplification. Angew Chem Int Ed 51:4896–4900
5. Hu L, Hu S, Guo L, Shen C, Yang M, Rasooly A (2017) DNA generated electric current biosensor. Anal Chem 89(4):2547–2552
6. Shen C, Zeng K, Luo J, Li X, Yang M, Rasooly A (2017) Self-assembled DNA generated electric current biosensor for HER2 analysis. Anal Chem 89(19):10264–10269
7. Xiao Y, Qu X, Plaxco KW, Heeger AJ (2007) Label-free electrochemical detection of DNA in blood serum via target-induced resolution of an electrode-bound DNA Pseudoknot. J Am Chem Soc 129:11896–11897
8. Li X, Shen C, Yang M, Rasooly A (2018) Polycytosine DNA electric-current-generated immunosensor for electrochemical detection of human epidermal growth factor receptor 2 (HER2). Anal Chem 90(7):4764–4769
9. Shen C, Liu S, Li X, Zhao D, Yang M (2018) Immunoelectrochemical detection of the human epidermal growth factor receptor 2 (HER2) via gold nanoparticle-based rolling circle amplification. Microchim Acta 185:547

# Chapter 23

# Agar-Integrated Three-Dimensional Microelectrodes for On-Chip Impedimetric Monitoring of Bacterial Viability

**Derrick Butler and Aida Ebrahimi**

## Abstract

Monitoring bacterial viability is critical in food safety, clinical microbiology, therapeutics, and microbial fuel cell applications. Traditional techniques for detecting and counting viable cells are slow, require expensive and bulky analytical tools and labeling agents, or are destructive to cells. Development of low-cost, portable diagnostics to enable label-free detection and in situ probing of bacterial viability can significantly advance the biomedical field (both applied and basic research). We developed a highly sensitive method for the detection of bacterial viability based on their metabolic activity using non-Faradaic impedimetric sensors comprised of three-dimensional (3D) interdigitated microelectrodes (3D-IDME). Specifically, the 3D-IDME is modified with electrolessly deposited gold (Au) nanoparticles which amplify the sensitivity by increasing the sensing area. A nutrient-rich agarose gel as the seeding layer is integrated with the sensor to enable direct culturing of bacteria and probing of their metabolic activity in situ. The proposed platform enables monitoring of bacterial viability, even in lag-phase, as they metabolize and release ionic species into the surrounding environment (nutrient agar layer). The sensor can detect down to $10^4$ CFU/mL (~2.5 CFU/mm$^2$) of *Escherichia coli* K12 (a model strain) in under 1 h without the need for any labeling. By integrating these sensors with agar layers containing different types/concentrations of antibacterial agents, this work can be expanded to enable rapid, high-throughput antibacterial susceptibility testing which can in turn assist caregivers in early prescription of the right treatment to patients with clinical conditions.

**Key words** Impedance, Biosensor, Bacteria, Viability, 3D-IDME, Microelectrode, Interdigitated

## 1 Introduction

Bacteria (e.g., *Escherichia coli*, *Salmonella*, and *Helicobacter pylori*) are responsible for an array of diseases and infections, such as urinary tract infections (UTIs) [1], typhoid fever [2], pneumonia [3], and gastroenteritis [4]. UTIs alone cost the United States an estimated $2.3 billion in 2010 [1], indicative of the financial burden these diseases create. Many pathogenic diseases are foodborne, and an estimated 360 million cases of global foodborne illness cases in 2010 were bacterial, resulting in more than 270,000 deaths [5]. According to the World Health Organization, low-income countries are disproportionally affected by common pathogenic

Miguel R. Ossandon et al. (eds.), *Biomedical Engineering Technologies: Volume 1*, Methods in Molecular Biology, vol. 2393, https://doi.org/10.1007/978-1-0716-1803-5_23, 

diseases, such as lower respiratory infections (e.g., pneumonia) and diarrheal diseases, which is attributed to a "lack of access to essential health services" [6]. Combined with the increasing prevalence of antibiotic-resistant bacteria, which are responsible for roughly 700,000 deaths each year and estimated to reach ten million by 2050 [7], there exists a technological, medical, and humanitarian need for rapid, cost-effective, label-free, and sensitive means of monitoring bacteria and their viability in food, water, and clinical samples at the point-of-care (PoC).

Gold standard techniques for detecting viable bacteria include broth dilution and disk diffusion, which require at least 1 day from isolated colonies to results [8]. Slow diagnosis leads to a delayed and/or miscalculated treatment which can increase fatality rate and indirectly speed up the spread of antibiotic resistant strains through natural selection [9]. Compared to conventional culture-based methods, molecular biology techniques such as polymerase chain reaction (PCR) and enzyme-linked immunosorbent assay (ELISA) have shortened detection times but can be expensive, require advanced skillsets, and lack the desired portability and simplicity necessary for PoC analysis [10]. To this end, researchers are actively developing methods that allow for rapid (even real-time) monitoring of bacterial viability [11] and how environmental stressors, namely antibiotics, heat, and osmotic irregularities, affect it.

Impedance-based detection and monitoring of pathogenic bacteria has been previously demonstrated as a practical alternative to more traditional techniques [10–15]. The electrical impedance is defined as $Z = \frac{V(t)}{I(t)}$, where $V(t)$ and $I(t)$ are the time-varying voltage and current measured between two electrodes, respectively. $Z$ is a generalized form of the direct current (DC) resistance, as it applies more broadly to systems with alternating current (AC) signals. The impedance can be separated into real ($Z'$) and imaginary ($Z''$) components, written as $\boldsymbol{Z}(\omega) = Z' - jZ''$, where $j \equiv \sqrt{-1}$. In its polar form, the impedance is written as $\boldsymbol{Z}(\omega) = |Z|e^{j\varphi}$, where $|Z| = \sqrt{(Z')^2 + (Z'')^2}$ is the impedance magnitude and $\varphi$ is the phase angle between the AC voltage and current. In electrochemical systems, the impedance is most often made up of resistive and capacitive components. Resistive components ideally show no dependence of the impedance on the frequency of the AC signal, such that $Z = R$ and $\varphi = 0$. Capacitive components, however, are frequency-dependent, with the impedance written as $Z = 1/j\omega C$ and $\varphi = \pi/2$, where $\omega$ is the angular frequency and $C$ is the capacitance.

In the context of electrochemical systems, impedance is commonly split into two categories: Faradaic and non-Faradaic. Faradaic processes involve charge transfer across the electrode–solution interface due to oxidation or reduction of a species in the solution. Non-Faradaic processes do not involve charge transfer across the electrode–solution interface but are instead due to the

dynamic accumulation and removal of charge at the interface when the applied potential is not sufficient for oxidation/reduction to occur. Both processes have been utilized for impedimetric analysis of pathogens [11], each with its own advantages and drawbacks. Compared to non-Faradaic methods, Faradaic impedance techniques are generally more suitable for characterizing highly ionic solutions (which is the case in biological samples). On the other hand, the requirement of a reference electrode for Faradaic sensors makes miniaturization more challenging compared to non-Faradaic techniques. Moreover, non-Faradaic techniques eliminate the use of redox indicators (usually required in Faradaic sensors) [16, 17] which make them more cost-effective. Besides, redox indicators may interfere with biological samples and affect the signal interpretation. For both methods, selectivity can be achieved by immobilization of biorecognition molecules (e.g., antibodies, aptamers, or nucleic acids) and measuring the change of impedance upon conjugation with the target analyte or change of Faradaic current through the electrode.

One of the most common techniques for probing bacterial viability is "impedance microbiology" which monitors temporal changes in the non-Faradaic impedance (i.e., conductivity) of the culture medium as bacteria grow and metabolize glucose and other nutrients for energy. In doing so, ions and electrolytes are released into the surrounding environment [11, 12]. Due to high background conductivity and limited sensitivity of the existing methods, cells can be detected after they reach a certain population, i.e., in log-phase when bacteria are multiplying exponentially before reaching a plateau, known as the stationary phase [11]. However, even in the lag-phase (the growth phase when cells are gathering enough nutrients from the surrounding environment without dividing), bacterial cells are still metabolizing. On the other hand, dead cells cannot actively metabolize and therefore do not contribute to changes in the solution impedance. This enables impedance microbiology to distinguish between viable and dead cells, which is necessary as dead bacteria are typically non-pathogenic [10, 11].

Previous reports have shown that the impedance of bacterial growth can be divided into two distinct contributions, the culture medium ($R_s$, the solution resistance) and the electrode/solution interface ($C_{dl}$, the double-layer capacitance) [11]. At high frequencies ($\geq$10 kHz), the impedance of the medium dominates, whereas at lower frequencies ($\leq$10 kHz), the electrode/electrolyte double-layer capacitance dominates. Splitting the impedance into two components allows users to isolate and monitor specific portions of the system with minimal interference. For example, in a previous report by Ebrahimi et al. [14], the working frequency was set to 15 kHz in order to (1) ensure limitations due to mass transport (typically dominant at low frequency) are negligible, (2) prevent the electric field from penetrating the bacterial cytoplasm of both live

and dead cells [18], and (3) ensure the solution resistance was the dominant contribution to the overall impedance. The authors studied the effect of heat stress on wild-type and heat-resistant *Salmonella typhimurium* using an impedimetric sensor made of microfabricated electrode arrays. Heat is a common and economical means of inactivating bacterial pathogens, especially in food preparation and safety. By monitoring the differential conductance (inverse of impedance) of a small droplet of culture medium as it evaporates, the authors found that in wild-type *Salmonella*, the conductance significantly increases at a critical temperature of 48 °C, whereas the heat-resistant strains do not show a noteworthy difference in conductance until 60 °C. Using the colony-counting method in parallel with conductance monitoring, the cell viability of the wild-type strain was reduced by more than 99% at a temperature of 53 °C. These experiments, along with the analytical model developed for cell permeability under heat stress, provide valuable insight into the mechanism of *Salmonella typhimurium* subject to mild heat stress.

In another report from Ebrahimi and Alam [15], the effect of osmotic stress on bacteria was studied by confining the cells in a droplet placed/pinned on the impedimetric sensor. Bacteria use osmoregulation to control the balance of charged ions between the inside of the cell and the surrounding environment, known as the turgor pressure. The uptake or release of charged species is controlled by activating "emergency valves" that enable the rapid transfer of charged ions to reestablish equilibrium. As the droplet evaporates, the ion concentration in the medium increases, which results in an increase of cells' turgor pressure, leading to an uptake of ions by *live* cells. By choosing the working frequency properly (resistive component of the total impedance dominating), the absorbed ions are shielded from contributing to the solution conductance. However, dead cells cannot contribute to osmoregulation, and therefore, the proposed sensor can be used to monitor cellular viability. Using the same method, the authors showed that the differential osmoregulatory response of various *Salmonella* mutants (with different potassium uptake transporters) can be captured on-chip and in real-time. In another report, non-Faradaic impedance measurements were used to monitor the susceptibility of *E. coli* cells to ampicillin [13]. Antibiotic susceptibility tests (AST) are crucial for determining bacterial response to antibiotics, allowing for more effective administration of antibiotics and mitigation of resistant strains. The impedimetric sensor detects an antibiotic dose-dependent increase in the conductance (taking into account any changes caused by the antibiotics themselves), which indicates the cells are responding to the antibiotics. Considering the high conductivity of the culture medium, a frequency of 15 kHz was chosen to ensure the resistive/conductive component is dominant. These reports clearly demonstrate the capability of

impedimetric sensors as a rapid, low-cost, portable, and label-free alternative to more traditional techniques, such as colony counting, disk diffusion, or fluorescent imaging, for probing bacterial viability and understanding their phenotypic changes to various environmental stressors.

The rise in impedimetric sensors has coincided with advancements in micro- and nano-fabrication tools and techniques. These fabrication methods have enabled significant device miniaturization, thereby increasing sensor portability, sensitivity, and compatibility with integrated circuit (IC) technology [19]. Many electrical and electrochemical biosensors are developed using microfabrication techniques, such as photolithography, metal deposition, and electrodeposition. Photolithography is based on the selective exposure of a polymer layer (termed as "photoresist") to light (typically ultraviolet (UV) with wavelength of $\lambda \sim 190$–$400$ nm) in order to create a desired pattern. The pattern is most commonly printed on a quartz or soda lime glass-based photomask, which allows light to selectively pass through specific transparent regions while the rest is reflected away (by patterned chromium or similar metallic layer). Once the photoresist is exposed, the sample is immersed in a specific chemical "developer" to remove the exposed (for a positive resist) or unexposed (for a negative resist) regions. With the pattern created, the user can then modify the exposed regions, for example, by depositing a metal (e.g., for contacts or interconnects). The resist is then stripped off leaving the processed region while the remainder of the sample is unmodified. Further device processing, such as electrodeposition (as in our work detailed in this chapter), may be performed afterward. Electrodeposition is an attractive, well-developed technique with applications in batteries [20], solar cells [21], and protective coatings [22]. For electrodeposition, a metal seed layer is deposited onto the substrate before the photolithography step. After the lithography and developing steps, the electrodeposition is performed by applying an electric bias to the electrode immersed in a specific solution containing the desired metal ions. Diffusion and migration, caused by the electric field generated through biasing the substrate, direct the metal ions to the substrate where they are deposited (through reduction or oxidation process depending on the polarity and magnitude of the potential) on the patterned regions. Detailed discussion about different microfabrication steps can be found elsewhere [23, 24].

Herein, we demonstrate a microfabricated impedimetric sensor for the direct growth and monitoring of bacteria as they metabolize in the lag phase. Early detection of viable cells, as early as lag phase, is critical for medical diagnosis. The sensor is comprised of a 3D-IDME-based sensing chip integrated with a thin nutrient-rich seeding layer. The 3D-IDME is fabricated using a combination of photolithography, metal deposition, wet chemistry, and electrodeposition. The sensitivity in measuring changes of medium

impedance upon cellular metabolism is enhanced by coating the 3D-IDMEs with gold nanoparticles through an electroless deposition process. To ensure biocompatibility of the electrodes, protect them against Faradaic oxidative reactions (hence minimizing corrosion), and enable reusability, the electrodes are passivated by drop casting an isolating agar gel layer. The seeding layer is made up of a nutrient-rich agarose layer that enables direct culturing of bacteria on-chip. As the bacteria metabolize, charged species diffuse into the gel layer and alter the impedance of the medium. Monitoring of the impedance over time allows for distinguishing between live and dead cells. The proposed sensor can be further expanded for use in AST or in situ monitoring of bacterial response to other environmental stressors. For example, in the case of AST, creating an array of sensors would allow for high-throughput testing of multiple types and doses of antibiotics simultaneously while the scale of the device would minimize spatial discrepancies in the environmental conditions. Integration of the sensor array with the necessary electronic readout circuitry would enable a system capable of sensing, analysis, processing, and data transmission. Furthermore, such a system would allow for real-time, in situ monitoring of bacterial response to various environmental stressors beyond antibiotics (such as heat, radiation, pH shock, etc.), a clear advantage over time-consuming culture-based techniques, bulky microscopy-based methods, or label-based ELISA.

## 2 Materials

### 2.1 Interdigitated 3D Microelectrode (Sensing Chip) Fabrication

1. Glass microscope slides cut into ~1″ × 1″ pieces using a diamond scriber.
2. Piranha solution: a 4:1 (by vol.) mixture of sulfuric acid ($H_2SO_4$) and 30% hydrogen peroxide ($H_2O_2$). Add the sulfuric acid to a pyrex beaker first, then slowly mix in the $H_2O_2$. *See* **Note 1** for additional safety information.
3. Hexamethyldisilazane (HMDS).
4. SPR 220.7 photoresist (Shipley Co., Marlborough, MA).
5. Nickel Etchant TFG (Transene Co., Danvers, MA).
6. Titanium Etchant TFTN (Transene Co., Danvers, MA).
7. 2-Propanol (IPA, J.T. Baker, Phillipsburg, NJ).
8. Deionized (DI) water.
9. CD-26 developer (tetramethylammonium hydroxide, Rohm and Haas Electronic Materials, Marlborough, MA). Development will require two pyrex pans to hold the CD-26 and the DI water for rinsing.

10. High-Speed Nickel Sulfamate Plating Solution (Technic Co., Cranston, RI).
11. Bright Electroless Gold Plating Solution (Transene Co., Danvers, MA).
12. Remover PG (N-methyl-2-pyrrolidinone, MicroChem, Newton, MA).
13. A 1 L pyrex beaker.
14. A spin-coater (Model WS-650, Laurell Technologies, North Wales, PA).
15. A hot plate with a thermocouple (VWR, Radnor, PA).
16. A potentiostat (PalmSens4, PalmSens Co., Houten, The Netherlands) with computer. Commercial instruments generally include software to control the potentiostat. Here, the PSTrace software is used.
17. A steel stand (~ 12″ × 2″ × 0.25″) for the counter/reference electrode (Fisher Scientific Co., Hampton, NH).
18. A photomask for patterning of the 3D-IDME (soda lime, NanoFilm, Westlake Village, CA, patterned at the Penn State Nanofabrication facility).
19. Metal deposition system (Model Lab 18, Kurt J. Lesker Co., Jefferson Hills, PA).

### 2.2 Bacteria Growth and Seeding Chip

Cell culture work requires specific equipment, such as an incubator, autoclave, and ideally a biosafety hood. The reader should ensure access to all of this equipment before undertaking the cell culture process.

1. *Escherichia coli* K12 are used as a model bacterium here.
2. Liquid culture medium: 18.5 g of brain heart infusion (BHI) powder (Millipore-Sigma, St. Louis, MO) is mixed with 500 mL of DI water and shaken to ensure complete mixing. Once mixed, the medium is sterilized in an autoclave at 121 °C for 15 min. BHI solution can be stored under refrigeration (4 °C). *See* **Note 2**.
3. Solid culture medium: For the agar-DI medium, 0.5% (by wt.) agarose powder (VWR Life Sciences) is mixed with DI water and sterilized in an autoclave at 121 °C for 15 min. For the BHI-agar nutrient layer, 1.8% (by weight) agarose powder is mixed with the previously prepared liquid BHI medium. The solution should be mixed at 150 °C to help dissolve the components uniformly. The resulting mixture is autoclaved at 121 °C for 15 min.
4. 70% (by vol.) IPA in DI water for disinfection.

5. 1:10 (by vol.) bleach in DI water for decontamination of disposables.
6. Phosphate-buffered saline (PBS, Corning Inc. Corning, NY): 1×, no added calcium or magnesium.
7. Sterile petri dishes.
8. Sterile cover slips.
9. Sterile bacteria culture tubes.
10. Sterile inoculation loops.
11. A 1-L glass bottle with lid.
12. A shaking incubator.
13. An autoclave.

### 2.3 Impedance Characterization

1. A HP Agilent 4192A LF or similar impedance analyzer with an auto-balancing bridge.
2. 1 m coaxial cables with T junctions.
3. An enclosed electrical probestation with two micromanipulator probes (Cascade Microtech, Beaverton, OR).
4. A computer.
5. National Instruments LabVIEW software [25] (optional).

## 3 Methods

### 3.1 Fabrication of the 3D Interdigitated Microelectrode Sensing Chip

Fabrication of the sensing chip is carried out in a cleanroom to minimize contamination. It is assumed the reader has some familiarity with and has access to nano- and micro-fabrication processes and equipment, such as photolithography and electron-beam (e-beam) evaporation. An interdigitated 3D-IDME structure is used as the sensing chip, which allows for the agar gel seed layer to adhere well. A schematic overview of the interdigitated 3D-IDME fabrication is shown in Fig. 1a. The digits are 2 mm long, 15μm wide, and 10μm thick with an interdigit spacing of 35μm (*see* Fig. 1b). The fabrication process for the sensing chip is outlined below.

1. The glass microscope slides are cut into ~1 × 1 $in^2$ pieces using a diamond scriber. The substrates are then cleaned in piranha solution for 30 min, followed by rinsing with DI water then IPA. The substrates are dried with clean $N_2$. *See* **Note 1**.
2. A metal seed layer [necessary for electrodeposition (Fig. 1c)] is deposited on the glass slides using e-beam evaporation in a Kurt J. Lesker Lab 18 deposition system. E-beam deposition systems focus a high energy beam of electrons onto the material to be deposited (held in a crucible), thereby evaporating or

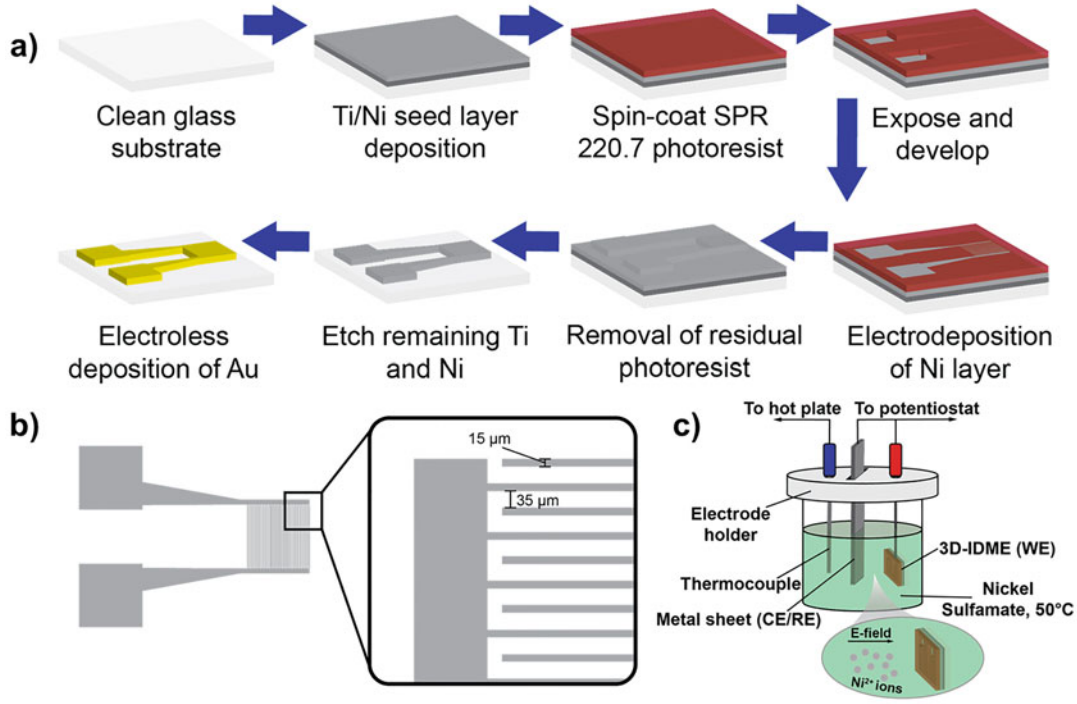


**Fig. 1** (**a**) An overview of the microelectrode fabrication process. *Note*—the schematic is not to scale. (**b**) The interdigitated microelectrode used for the sensing chip. The inset highlights the interdigitated structure of the microelectrode with relevant dimensions. (**c**) The electrodeposition set up used during the 3D-IDME fabrication. The Nickel Sulfamate solution is heated to 50 °C (monitored using a thermocouple connected to the hot plate) and the electrodeposition is controlled using a potentiostat. A metal sheet serves as the counter and reference electrode while the post-pattern development 3D-IDME serves as the working electrode

sublimating the material. The material then coats the inside of the process chamber [held at high vacuum (~$10^{-6}$ to $10^{-7}$ Torr)], which houses the substrates. Here, the substrates should be transferred to the evaporator as quickly as possible after cleaning to minimize ambient contamination. Ti/Ni (10/100 nm) layers are deposited sequentially at rates of 0.5 and 1 Å/s, respectively. The Ti layer serves as an adhesion layer between the Ni and the glass substrate. During evaporation, the substrate platen is rotated at a rate of 20 rpm to ensure even coating of the metal during deposition.

3. SPR 220.7 photoresist deposition (*see* **Note 3**).
   (a) Bake the substrate on a hot plate at 110 °C for 1 min to remove any moisture from the surface.
   (b) Spin-coat the HMDS onto the substrate at 2500 rpm for 45 s, followed by an additional bake at 97 °C for 1 min. The HMDS is used to promote adhesion between the resist and the substrate.

(c) SPR 220.7 is chosen due to its ability to withstand electroplating. Spin-coat the SPR 220.7 statically at 1500 rpm for 45 s. This should yield a resist layer that is ~10-μm thick according to the manufacturer's specifications. In static spin-coating, the resist is completely deposited onto the substrate before the spin process begins. In contrast, during a dynamic process, the resist is deposited onto the substrate during the spin process. During the spin process, cover the small hole over top of the substrate in order to minimize any debris from being drawn in toward the substrate during spinning. Use a razor blade to carefully remove a ~1-mm wide edge around the perimeter of the substrate. Typically, in spin-coating processes, and especially with a resist like SPR 220.7, there is an edge bead that is thicker than the remainder of the resist. Failure to remove the edge bead can further complicate the lithography process as there will be a small gap between the mask and the resist. This could lead to irregular exposure and poor pattern quality.

(d) A soft-bake is done on a hot plate at 97 °C for 90 s, followed by 115 °C for 90 s, then again at 97 °C for 90 s. This helps remove residual solvent from the resist and promotes solidification and adhesion to the substrate.

4. A Karl Suss MABA6 contact lithography instrument ($\lambda$ = 365 nm, Hg i-line) is employed here. Contact lithography is an efficient technique for devices with larger feature size, such as the 3D-IDME. In contrast, other lithography techniques, such as electron beam lithography, enable nano-scale feature size but are more expensive and lower throughput. The photomask was fabricated on soda lime glass at the Penn State Nanofabrication facility (*see* Fig. 2). Soda lime is a cheaper mask material than quartz, at the expense of a higher thermal expansion coefficient and lower optical transmittance at wavelengths below 350 nm, which may prove to be an issue for smaller feature sizes but is not an issue here. From the image, it is clear that light will pass through the open regions, thereby exposing the underlying photoresist, while the remaining light will be blocked. An exposure dose of 480 mJ/cm$^2$ is used for patterning of the resist. The light intensity of the specific tool being used must be known in order to calculate the correct exposure time. For example, in our process, a tool with an intensity of 6 mW/cm$^2$ was used in intervals of 10 s ON/15 s OFF repeated eight times, yielding a total dose of 480 mJ/cm$^2$. The user must know the intensity of their tool in order to calculate the number of process steps and achieve the desired dose. Allow the sample to sit for ~30 min after exposure before proceeding with the development step.

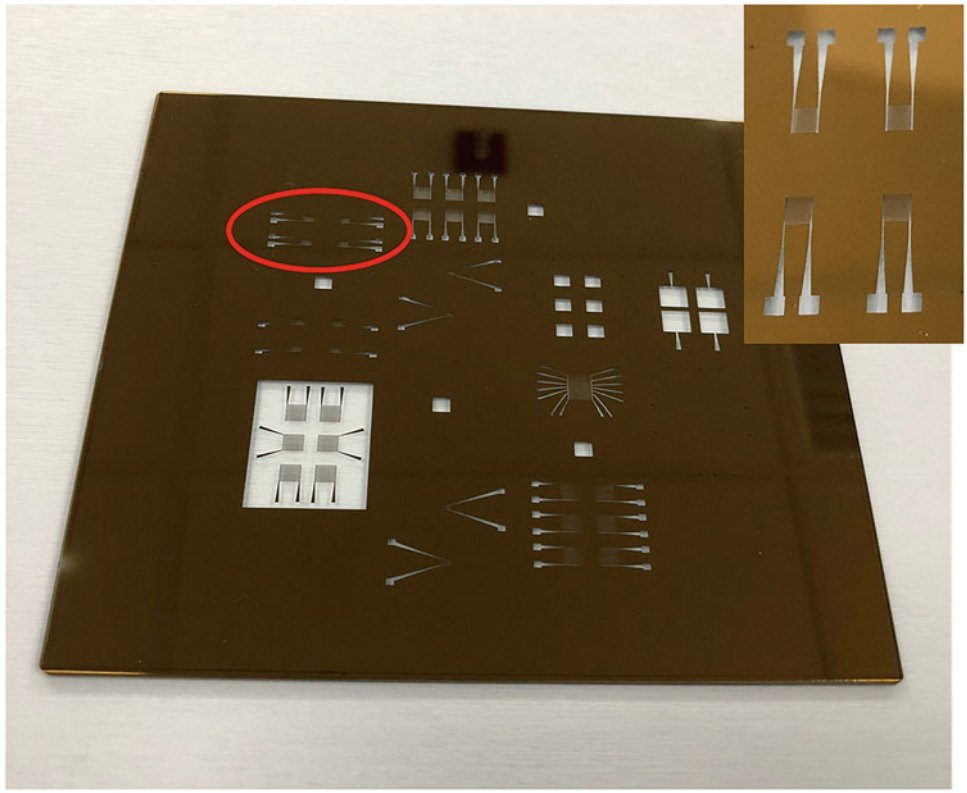

**Fig. 2** The photomask used for the lithography process. The mask is made of soda lime glass. The specific electrodes used for the 3D-IDME are circled and a closeup image is shown in the inset. The mask allows for exposure of four distinct 3D-IDMEs simultaneously

5. The development step removes the exposed photoresist, yielding the 3D-IDME pattern. The resist is developed in CD-26 developer for 1.25 min under mild agitation (i.e., lightly shaking container by hand to speed up diffusion of developer) followed by thorough rinsing in DI water and dry with $N_2$. The develop time may vary slightly for each user and it is advised that the reader ensures complete development of the resist by checking under an optical microscope with an appropriate filter (*see* **Note 4**).
6. The nickel layer is deposited electrochemically using Nickel Sulfamate solution (*see* Fig. 1c). Approximately 600 mL of solution is poured into a 1-L beaker with a 4″ magnetic stirrer at the bottom. The solution is heated on a hot plate to 50 °C with the magnetic stirrer set to 50 rpm. A thermocouple connected to the hot plate is used to ensure the solution temperature remains 50 °C by providing direct and continuous temperature feedback to the hot plate. Typically, the thermocouple plugs into a port at the rear of the hot plate, but this may vary with each model of hot plate. An in-house fabricated

Teflon electrode holder is used to mount the working electrode (which is to have Ni deposited on it), counter/reference electrode (a steel sheet), and thermocouple. The electrode holder sits on top of the beaker and holes drilled into the holder allow for the thermocouple and the working and counter/reference electrodes to reach the Nickel Sulfamate solution (*see* Fig. 1 for more details). The working and counter/reference electrodes are immersed in the solution facing one another and spaced ~5 cm apart. Polyimide tape is used to ensure only the patterned areas of the working electrode have nickel deposited on them (i.e., the resist around the edge that was removed with the razor blade will leave bare metal exposed, which must be covered up). The potentiostat is connected to the appropriate electrodes (if the potentiostat has leads for counter and reference electrodes, both can be connected to the metal sheet in this case). Acetone can be used to remove the resist and expose a small area to contact with the potentiostat (ensure only the patterned area of the working electrode is exposed to the solution). The potentiostat is used in the "chronopotentiometry" (constant current, varying potential) mode with a set current density of 6 $mA/cm^2$ (2 mA for the pattern we use which contains four individual 3D-IDMEs). The duration of the deposition is 125 min, which yields an electrode ~10μm thick. *See* **Note 5** for more detail.

7. After deposition, the remaining resist is stripped by immersing the samples in Remover PG at 70 °C for 30 min. The samples are then rinsed sequentially in acetone, IPA, and DI water before drying with $N_2$. Ensure full removal of the resist by checking with the optical microscope.
8. The remaining Ni and Ti are etched in Transene Nickel Etchant TFG and Titanium Etchant TFTN, respectively. First, the Ni is etched at 40 °C for 20 s (etch rate ~5 nm/s), followed by rinsing in DI water and drying with $N_2$. This will etch a small amount of the 3D-IDME but given the Ni seed layer is only 100 nm thick, there will be little impact on the 3D-IDME. However, it is important to make sure not to leave the sample in Ni etchant any more than is necessary in order to limit any unwanted etching of the 3D-IDME. It will become apparent once the Ni is removed as the underlying Ti layer will be semi-transparent. The Ti is then etched at 70 °C for 10 s (etch rate ~ 1 nm/s). This etch occurs quickly and the reader should remain attentive to ensure the sample is removed immediately after complete etching of the Ti layer. The sample is then rinsed in DI water and dried with $N_2$. Check under the optical microscope to verify the integrity of the 3D-IDME and ensure all residual metal has been removed in order to prevent any electrical shorting. *See* **Note 6**.

9. The final Au layer is electrolessly deposited using Bright Electroless Gold Plating Solution (contains cyanide, *see* **Note 7**) from Transene Co. The Au deposition creates small metallic microstructures on the electrode surface, thereby increasing the surface roughness and, effectively, the active surface area. The 3D-IDME is immersed in the solution at 70 °C for 5 min, followed by rinsing in DI water and dry with $N_2$. The effect of Au deposition time on surface roughness and contact angle was studied (*see* **Note 8**).

The 3D-IDME sensing chip is now complete and ready for integration with the bacteria seeding layer. The integrity of the sensing chip can be verified with an optical microscope. Ensure there are no significant defects in the electrode structure, such as holes, gaps, particles, or broken/delaminated digits. Furthermore, a multimeter can be used to verify that the digits are electrically isolated by measuring the resistance between them. If there is no short, the resistance should ideally be infinite. If a short is found, the 3D-IDME must be redone as it will now be impossible to monitor the impedance of the bacteria growth medium.

### 3.2 Bacterial Culture and Integration of the Seeding Layer with the 3D-IDME

For bacterial culture, it is important to maintain an aseptic work environment. That means using 70% IPA to frequently wash gloves and benchtop, a 10:1 water/bleach solution to dispose of any pipette tips, inoculation loops, etc., and using sterile Petri dishes, culture tubes, and other equipment. For this work, *E. coli* K12 (biosafety level 1) was used as the bacterium of choice, and the culture process reflects this. However, the reader may want to test other bacteria at their own discretion. If so, the protocol outlined here may require some tailoring to the specific strain of bacteria the reader chooses to use. The cell culture process for the *E. coli* K12 strain used in this experiment is outlined below.

1. To prepare the plates for the initial culture, liquid BHI-agar mixture is poured into a sterile petri dish to a depth of ~1 mm. The plates should be poured shortly after preparing the medium. Multiple plates can be prepared and stored under refrigeration for an extended period. Store the plates upside down (i.e., agar layer on top) to minimize any contamination due to condensation falling onto the agar. Parafilm or tape can be used to secure the lids of the petri dish and minimize potential contamination. Allow the plates to cool and solidify before using.
2. The initial culture starts from a frozen stock solution of *E. coli*. Allow the stock solution to reach room temperature. Using an inoculation loop, place a loop full of the stock solution into ~5 mL of BHI growth medium in a separate culture tube. Shake the loop to ensure all bacteria are removed. Once

finished, place the loop in a beaker containing a 10:1 dilution of bleach in DI water.

3. This culture is aerobically incubated overnight (~16 h) at 37 °C in an incubator shaking at 210 rpm. Secure the tube in a tube rack and place in the incubator. Loosen the cap of the tube slightly to allow oxygen to reach the solution but not too loose as it could fall off during incubation.
4. After incubation, the culture is plated. Gently vortex the culture to ensure it is well mixed. Allow the plates to reach room temperature if they were stored in the refrigerator. Then, pipette ~50μL of the culture onto the edge of the BHI-agar plate (from **step 1**). Using an inoculation loop, gently streak the culture solution back and forth across the plate. Once spread, the plates are incubated (no shaking) at 37 °C for 24 h. Cell streaking ensures the isolation of only one strain of bacteria.
5. Remove a single colony using an inoculation loop and resuspend in a culture tube containing ~5 mL of BHI medium. Shake the loop to ensure complete removal of the bacteria and vortex the resulting solution. Incubate overnight with shaking at 37 °C.
6. 100μL of the resulting culture is removed and resuspended in 10 mL of the BHI medium. The resulting solution is aerobically incubated overnight at 37 °C to establish the initial culture. This ensures the cells are in stationary phase during the following steps.
7. The cell density after incubation is ~$10^9$ CFU/mL. In order to better establish the cell concentration, prepare serial dilutions of the initial culture in PBS ($10^{-2}$, $10^{-4}$, $10^{-6}$) in culture tubes, making sure to thoroughly mix the solution before each dilution. From the $10^{-6}$ dilution, pipette 100μL onto the center of a BHI-agar plate and use a cell spreader to uniformly coat the plate will the cell suspension. Incubate the plate upside down overnight at 37 °C. Preparing multiple plates from the same dilution can result in a more accurate cell density value.
8. Count the number of colonies on the plate. A value of ~30–300 colonies is expected. Based on the dilution, the cell concentration of the original culture can be calculated. Once the cell concentration is known, dilutions can be prepared for testing the sensor.
9. If the reader would like to prepare additional solutions of dead cells, the culture can be heated in a water bath at 80 °C for 30 min. The resulting solution can be diluted to the desired concentrations for testing.

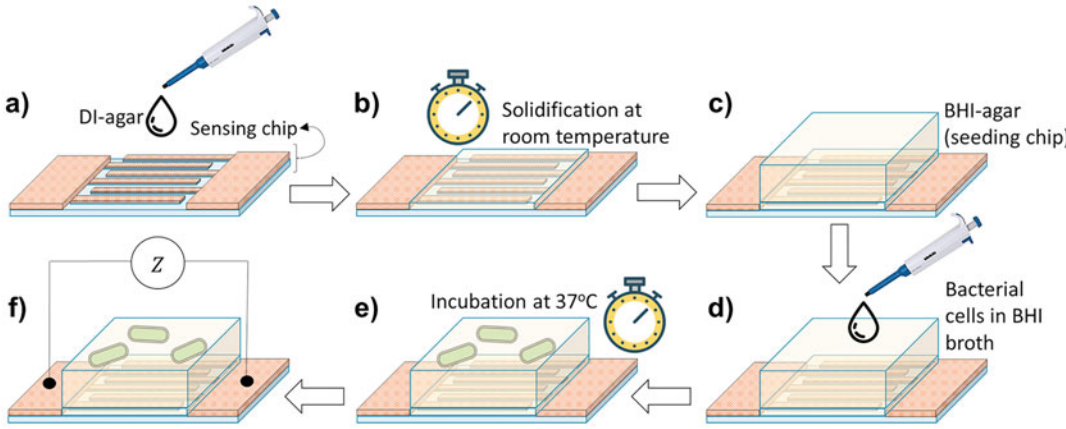


**Fig. 3** An overview of the fabrication process of the seeding layer and impedance testing. (**a**) Starting with the sensing chip fabricated in Subheading 3.1, pipette 20 μL of molten DI-agar solution over the sensing chip. (**b**) Allow the gel to solidify and (**c**) carefully place the $2\times2$ mm$^2$ BHI-agar pad on top of the DI-agar layer. (**d**) Add 1μL of cell suspension to the chip, and (**e**) incubate for a set amount of time, followed by (**f**) recording of the impedance. Reproduced from Butler et al. [12] with permission from Elsevier

In parallel with the cell culture process, the seeding layer is integrated with the sensing chip from Subheading 3.1 (*see* Fig. 3).

1. Start by heating the DI-agar solution (0.5% wt.) in a water bath set to 75 °C. Ensure the solution is completely molten before proceeding.
2. Pipette 20μL of the molten solution over the 3D-IDME and allow to solidify at room temperature.
3. A BHI-agar pad is used as the nutrient-rich growth layer. Using a sterile cover slip, cut a ~$2\times2$ mm$^2$ piece of the BHI-agar from one of the plates. Carefully place the piece on top of the DI-agar layer once it has solidified.

The sensor is now complete and ready for testing. Figure 4a shows an optical image of the 3D-IDME before and after bonding of the nutritious agar layer. The sensors can be stored in the refrigerator at 4 °C for later use. The effects of Au electroless deposition and % wt. of the DI-agar layer on the electrochemical characteristics of the sensor were evaluated using the $[Fe(CN)_6]^{3-/4-}$ redox-probe (*see* **Note 9**).

### *3.3 Impedance Testing of the Sensor with Bacteria*

The integrated sensor with the nutrient-rich seeding layer allows for direct growth of bacteria on the sensor. Rather than culturing bacteria off-chip and testing the supernatant, this chip allows the reader to directly monitor impedance shifts due to bacterial metabolic activity in real time. Because the non-Faradaic impedance of the medium will be monitored (as opposed to measuring Faradic reactions), there is no need for an external reference electrode.

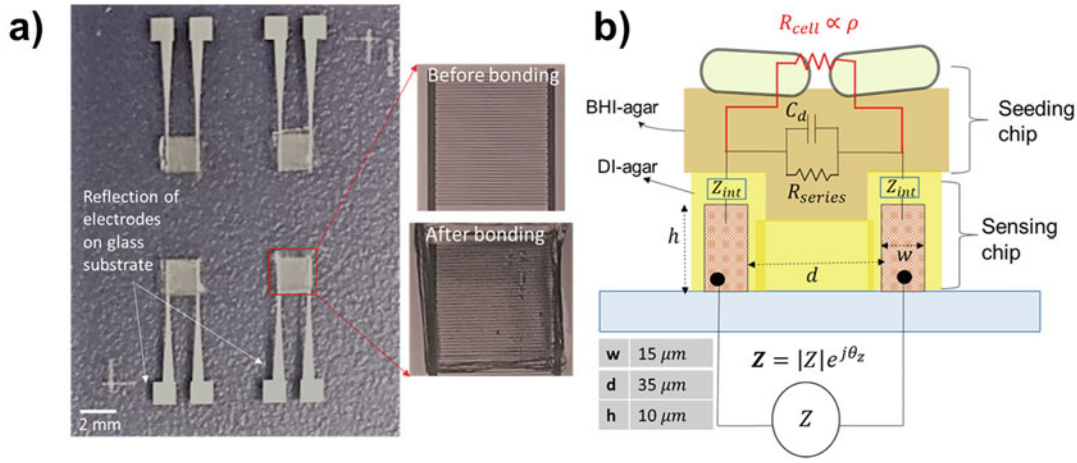


**Fig. 4** (**a**) An optical image of the completed 3D-IDMEs. The inset shows the electrode before and after bonding with the agar layer. (**b**) A schematic overview of the impedance components of the whole system under test. $R_{series}$ and $C_d$ correspond to the medium resistance and dielectric capacitance, respectively. $R_{cell}$ correlates to the impedance of the bacteria cells and is proportional to the concentration. $Z_{int}$, which contains the charge-transfer resistance ($R_{ct}$) and double-layer capacitance ($C_{dl}$), represents the impedance between the electrode and the medium. Reproduced from Butler et al. [12] with permission from Elsevier

Instead, the impedance will be measured between the two interdigitated electrodes of the 3D-IDME. A schematic overview of different impedance components is shown in Fig. 4b. The impedance testing procedure is outlined below.

1. Set up the impedance analyzer (e.g., HP Agilent 4192A LF) with an auto-balancing bridge. Connect the sensor to the impedance analyzer using the BNC connections of the micromanipulator probe and the coaxial cable from the impedance analyzer. Figure 5a–c shows close up images of the probestation and impedance analyzer.
2. An in-house designed LabVIEW [25] program is used to communicate with the impedance analyzer. The user interface of the LabVIEW program is shown in Fig. 6. The impedance analyzer is connected to the computer through a general-purpose interface bus (GPIB) connection. The program allows the user to manually change measurement parameters, such as frequency, AC bias, and DC bias while monitoring outputs, such as impedance, capacitance, phase angle, and admittance.
3. A sinusoidal AC signal of 50 mV at a frequency of 38 kHz will suffice. This frequency ensures the solution resistance dominates the impedance (*see* Fig. 7a, b). Pipette 1μL of the cell suspension onto one sensor and 1μL of BHI medium onto another. Incubate the sensors at 37 °C for 15 min, then record the impedance ($Z(t_0)$ and $Z_{BHI}(t_0)$).

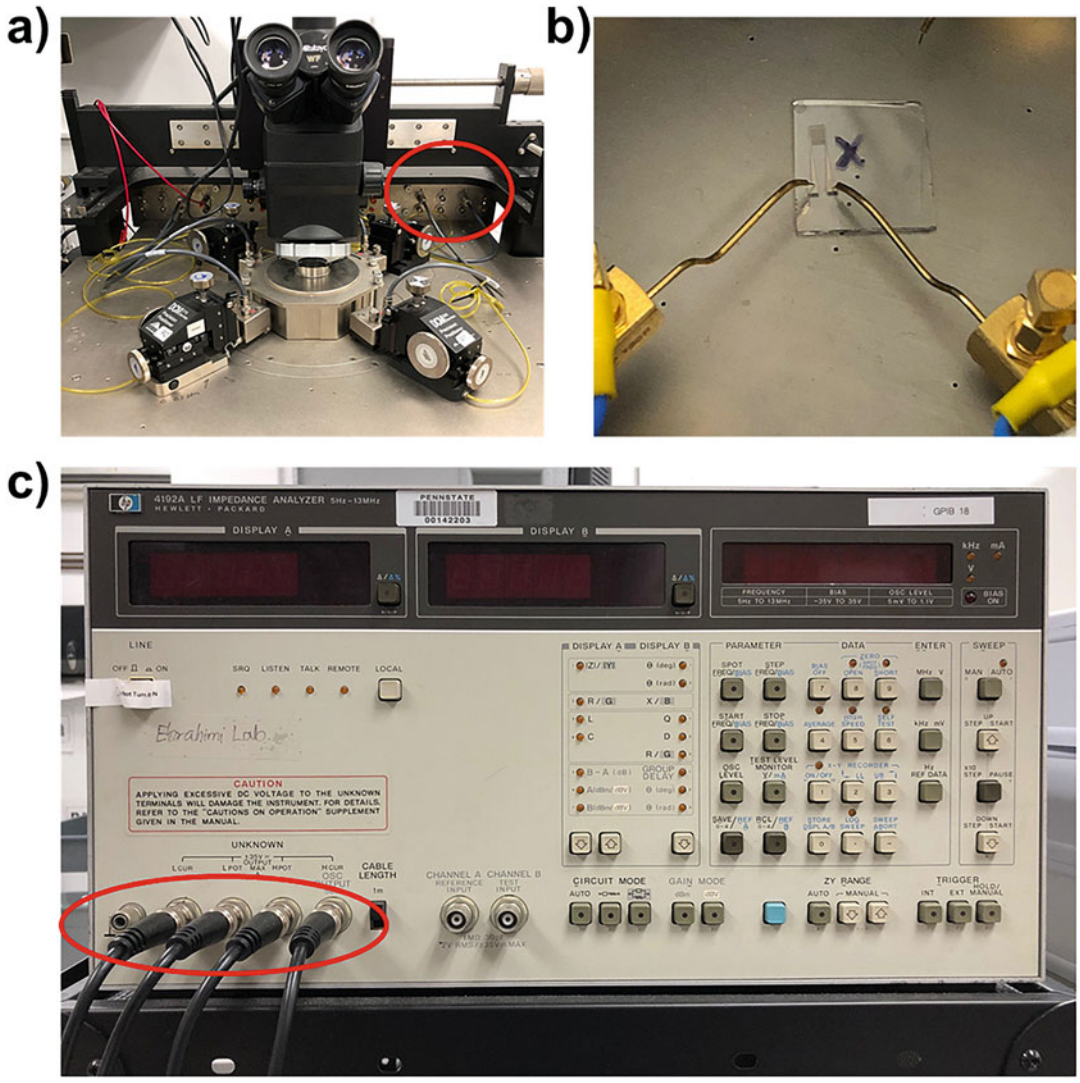


**Fig. 5** An overview of the testing setup. (**a**) The electrical probestation (connected to the building clean ground) with micromanipulator probes used to contact the 3D-IDME sensor. The enclosure helps to isolate the device from stray electromagnetic radiation. (**b**) A close up of two probes contacting the 3D-IDME. (**c**) The user interface of the HP Agilent 4192a impedance analyzer used to record the non-Faradaic impedance of the 3D-IDME as bacteria metabolize. The red circles in (**c**) show the coaxial cables connected to the impedance analyzer. The high current and potential cables are joined using a T junction before connecting to the back of the probestation (red circle in **a**). Likewise, the low current and potential cables are also joined and connected to the probestation. Each lead is connected to its respective micromanipulator and the device is tested

The differential impedance is defined as,

$$\frac{\beta}{\beta_0} \equiv \frac{1 - \frac{|Z(t)|}{|Z_{\mathrm{BHI}}(t)|}}{1 - \frac{|Z(t_0)|}{|Z_{\mathrm{BHI}}(t_0)|}}$$

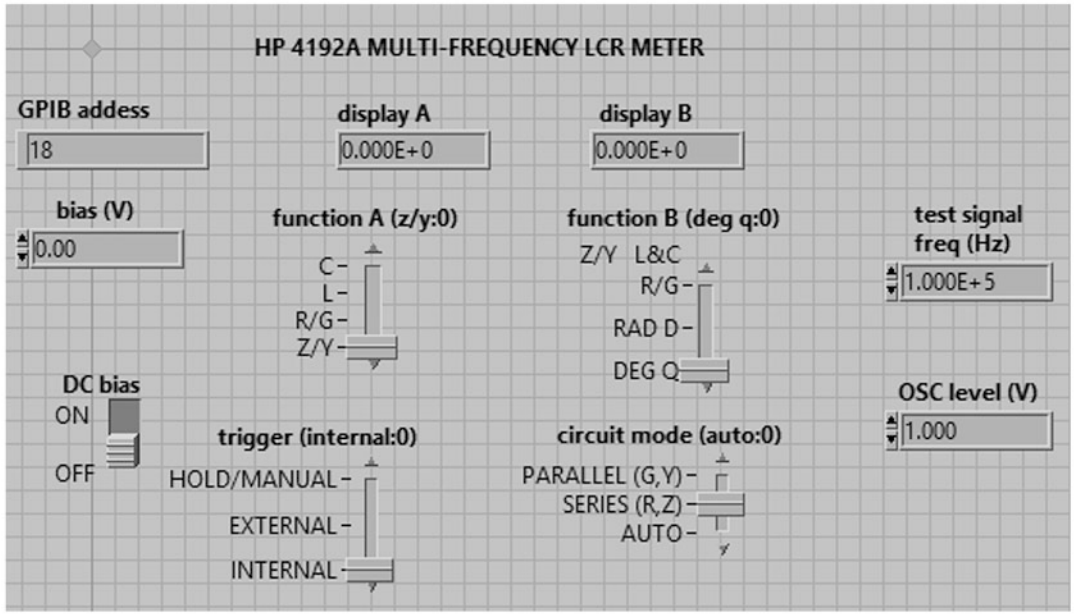


**Fig. 6** The LabVIEW program user interface

4. Place the sensors back in the incubator and record the impedance at sequential intervals. A large increase in the differential impedance should be seen around 30 min after $t_0$ (45 min total). The differential impedance will plateau after ~1 h (*see* Fig. 7c). The slope ($S$) is defined between the $t_0$ and $t_1$ (50 min) measurements. A comparison of the slope for viable and dead cells is shown in Fig. 7d for three different initial concentrations (*see* **Note 10**).

## 4 Notes

As a universal safety rule, before using any chemical, the user should first check with the manufacturer's safety data sheet (SDS) to ensure that proper personal protective equipment (PPE) is worn, waste is disposed of correctly, and any special instructions are followed.

1. Piranha solution is very dangerous and even explosive at $H_2O_2$ levels over 50%. Always use appropriate PPE when handling and prepare a fresh solution every time. All work with piranha solution should be done in a fume hood and the solution should NEVER be stored for later use (i.e., only prepare as much as needed for each round of substrate cleaning). Commercially available solutions may also be used as a safer

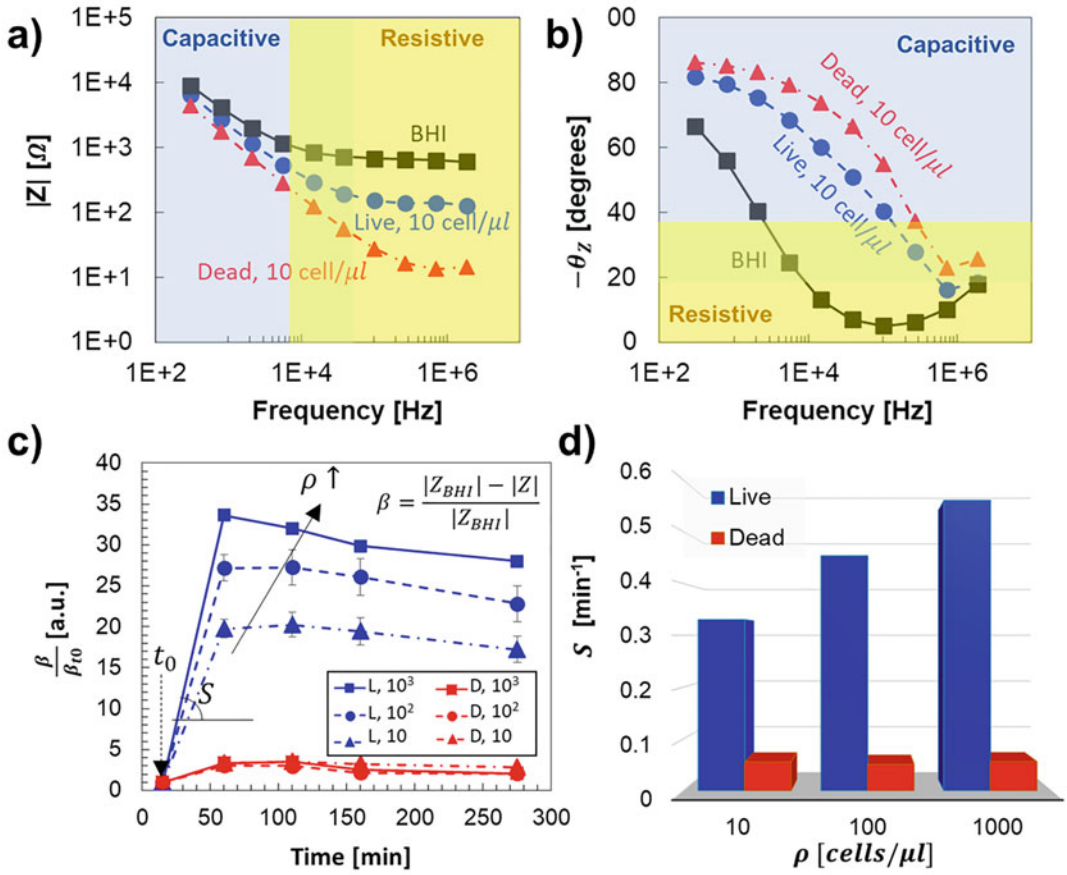


**Fig. 7** The impedance as a function of (**a**) frequency and (**b**) phase angle. The capacitive components are more dominant at low frequencies, which explains the dependence of the impedance on frequency. At higher frequencies, the impedance plateaus (i.e. does not change with frequency), which signifies the solution resistance is the dominant contribution to the overall impedance. (**c**) The time-dependent response of the differential impedance as the bacteria metabolize with the subsequent slope (*S*) shown in (**d**) for each concentration of live and dead cells. Reproduced from Butler et al. [12] with permission from Elsevier

alternative. Always use Teflon tweezers when removing substrates from piranha as the sulfuric acid can etch stainless steel.

2. When sterilizing a solution in an autoclave, be sure to leave the cap of the container slightly loosened because of the high pressure and temperature.
3. Because the SPR 220.7 resist is very thick, air bubbles can easily get trapped. Ensure that when pipetting the resist onto the substrate, there is excess resist in the pipette. Do not fully pipette out the entirety of the resist, as this will form air bubbles which can make lithography very difficult. When using a razor blade to remove the edge bead, be sure not to touch the resist that is to be exposed. In other words, grab the substrate with

tweezers very close to the edge to avoid touching the resist as it is still wet and can be easily damaged.

4. During the development process, it is important to periodically check the sample under an optical microscope so one can be sure the pattern is fully developed. For example, the reader is advised to try 1 min of development, followed by checking under the microscope. If the pattern is not fully developed, try an additional 10 s and repeat until fully developed. This also ensures the pattern is not overdeveloped. An underdeveloped pattern will have spots of resist that can be seen with the microscope. Also, be sure to use a filter with the optical microscope, as accidental exposure to white light will ruin the pattern. When developing, it is important to immediately remove the sample and place in DI water to stop the development reaction.
5. During electrodeposition of Ni, it is important to ensure the counter and working electrodes are facing one another. Using a planar metal counter electrode will provide a uniform electric field between the electrodes and facilitate a more uniform deposition. The reader is also advised to use caution when positioning the thermocouple in the solution. In particular, a metallic thermocouple placed in close proximity to the working and counter electrodes may result in nickel being deposited on the thermocouple. It is advised to position the thermocouple in such a way to isolate it from the electric field between the counter and working electrode. Use polyimide or other inert tape to block off any exposed metal areas of the working electrode that should not have Ni deposited on them. Failure to do so will lead to a miscalculation of the current density and could impact the deposition. Also, be aware that the sign of the specified current density is important. Incorrect sign could result in the Ni being deposited on the counter electrode.
6. The etch rate will depend on the temperature. The user is advised to check the etchant manufacturer's literature for a better understanding. Therefore, it is critical that the solution temperature is well-known and maintained at a consistent value. Because Ni is used as the seed layer, as well as the electrodeposited layer, the reader should remain vigilant during etching to prevent any unnecessary over-etching.
7. The Bright Electroless Gold Plating Solution contains cyanide. Therefore, any work should be done in a fume hood to minimize potential risks associated with handling and use extra caution.
8. The effect of Au electroless deposition time on the surface roughness was investigated using atomic force microscopy (AFM) and contact angle measurements (*see* Fig. 8a, b,

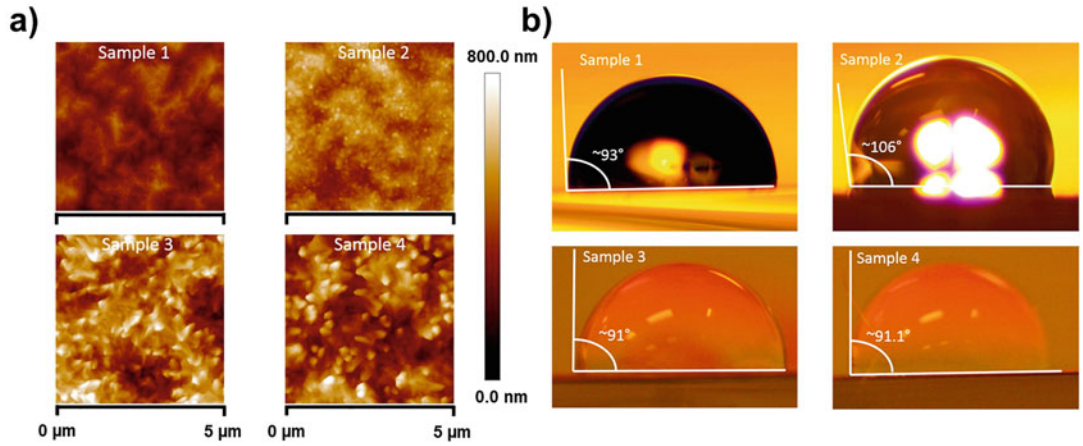


**Fig. 8** (**a**) Atomic force microscopy images for each Au deposition time, 0, 5, 30, 60 min, corresponding to Samples 1–4, respectively. The scale bar of each image corresponds to 5µm. (**b**) The corresponding contact angle measurements for Samples 1–4. Contact angle is indicative of the hydrophilicity of the sample, with higher contact angle correlating to lower hydrophilicity. Reproduced from Butler et al. [12] with permission from Elsevier

respectively). The most hydrophobic sample corresponds to 5-min electroless Au deposition, with a contact angle of 106° compared to 93° for 0 min. Increased hydrophobicity is important for ensuring a more consistent DI-agar droplet geometry from sample to sample. The contact angle for 30 and 60 min decreases down to ~91° despite a nearly twofold increase in average roughness between the 0- and 60-min samples (58 nm vs. 109 nm, respectively). This is likely due to the increased scaling of the Au nanoparticles in the case of 5-min deposition compared to the formation of Au microparticles for 30- and 60-min deposition, as seen in the AFM images. Due to the enhanced hydrophobicity of the 5-min sample, that duration was chosen as the optimized deposition condition.

9. The effects of Au electroless deposition and % wt. of the DI-agar layer on the electrochemical characteristics of the sensor were evaluated (*see* Fig. 9). Figure 9a shows the cyclic voltammetry (CV) curves of the 3D-IDME before and after Au deposition using the $[Fe(CN)_6]^{3-/4-}$ redox probe. The peak current ($I_p$) can be described by the Randles–Sevcik equation at room temperature,

$$I_p = (2.69 \times 10^5) A n^{3/2} \vartheta^{1/2} D^{1/2} C$$

where $A$ is the surface area, $n$ is the number of electrons transferred per each reaction ($n = 1$ here), $\vartheta$ is the CV scan rate (50 mV/s), $D$ is the diffusion coefficient of the $[Fe(CN)_6]^{3-/4-}$, and $C$ is the analyte concentration. Keeping testing conditions the same before and

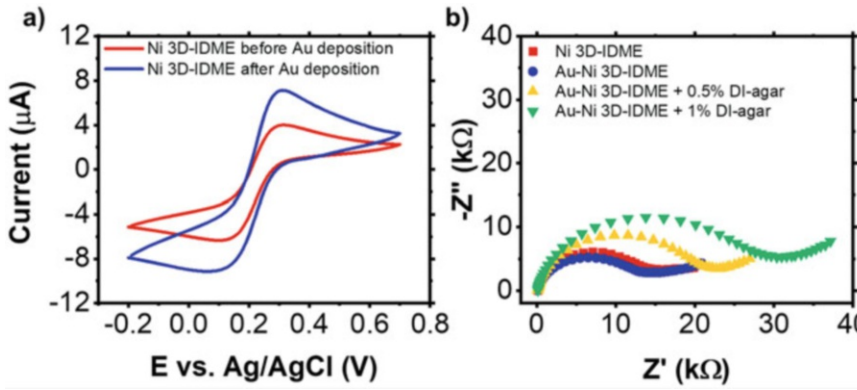


**Fig. 9** (**a**) Cyclic voltammetry (CV) of the 3D-IDME before and after Au deposition using the $[Fe(CN)_6]^{3-/4-}$ redox-probe. The increase in the peak current after deposition can be attributed to the increase in the electrochemically-active surface area due to the Au nanoparticles. (**b**) Electrochemical impedance spectroscopy (EIS) was used to understand the effects of the Au deposition and wt.% of the DI-agar on the charge-transfer resistance ($R_{ct}$), which is the diameter of the semicircle in the EIS spectra. Reproduced from Butler et al. [12] with permission from Elsevier

after Au deposition, the only explanation for the increase in $I_p$ is an increase in $A$. Under this assumption, Au deposition is estimated to increase the surface area by 51%. Because the redox peak separation, a common indicator of catalytic reversibility [26], does not change significantly after introduction of gold, it is likely that the increase in redox peak current is due to surface area enhancement and not due to catalytic properties of gold. Figure 9b shows the electrochemical impedance spectroscopy (EIS) data for each condition: Ni 3D-IDME, Au-Ni 3D-IDME, Au-Ni 3D-IDME +0.5% DI-agar layer, and Au-Ni 3D-IDME +1% DI-agar layer. EIS measurements utilize the $[Fe(CN)_6]^{3-/4-}$ redox probe and apply a small AC signal (10 mV here) on top of a DC potential chosen by the user (250 mV here). The frequency is then scanned from 1 MHz to 10 mHz (going from left to right in the figure). The semicircle formed corresponds to the Faradaic charge-transfer resistance ($R_{ct}$), an indicator of the electrode kinetics (i.e., smaller charge-transfer resistance generally corresponds to better reaction kinetics). The bare Ni 3D-IDME shows an $R_{ct} = 11.3\ k\Omega$ which decreases slightly after Au deposition ($R_{ct} = 10.7\ k\Omega$). The charge transfer resistance increases dramatically upon addition of a 0.5% DI-agar layer ($R_{ct} = 17.9\ k\Omega$), while 1% DI-agar shows the largest charge transfer resistance of 25.2 kΩ. Intuitively, this makes sense as the $[Fe(CN)_6]^{3-/4-}$ diffusion will be more sluggish with increasing gel density, and therefore, the reaction at the electrode will occur more slowly. Although the charge-transfer is largest for 1% (desirable for *non-Faradaic* measurements), the DI-agar can be difficult to deposit consistently and, additionally, the diffusion of conductive metabolites from bacteria will be hindered which could prolong the

detection time of the sensor. Therefore, we chose 0.5% for the DI-agar layer.

10. The user is encouraged to use the integrated sensor system for testing other environmental stressors, such as antibiotics and osmotic stress.

## 5 Parameters Affecting the Electrode Sensitivity

The sensitivity of interdigitated electrode sensors can be enhanced by optimization of the device structure and dimensions [19, 27, 28].

1. The geometry of the electrode is important as it can dictate the electric field distribution and diffusion layer around adjacent electrodes (digits). Digits spaced sufficiently far apart behave as isolated electrodes and do not affect one another. With the decrease of the interdigit spacing, the diffusion layers around electrodes can overlap, and the separate microelectrodes begin to behave as one continuous electrode. This leads to signal amplification (as the effective total electrode surface area increases), while minimizing the noise, and hence increasing the signal-to-noise ratio (SNR) [28]. Both the spacing of adjacent digits and digit width were found to impact the SNR as well when tested with $[Fe(CN)_6]^{3-/4-}$ [27]. The smallest width tested (2.7μm) and smallest spacing (1μm) showed the largest SNR of all the tested conditions, although the spacing showed a much more significant role in the SNR than the electrode width.
2. Increasing the number of digits was shown to have little to no impact on the SNR, since the background noise increases in parallel with the signal.
3. The electrode height was shown to play an important role in the sensitivity. Of the four electrode thicknesses tested, the SNR peaked at the second highest thickness (140 nm), while smaller thicknesses showed lower SNR values. This can be attributed, at least in part, to the increased surface area within the interdigit gaps of thicker electrodes [27].

   Clearly, the electrode geometry impacts the sensitivity significantly, due to changes in active surface area and diffusion layer geometry. As we have shown, modification of the 3D-IDME with Au particles can increase the nano-scale roughness and enhance the total effective surface area. In addition to the geometry, the electrode material can impact the sensitivity as well.
4. In the same previously discussed report [27], a comparison between Pt and Au electrode materials showed a significantly

enhanced SNR for Au compared to Pt (SNR = 1000 vs. 11.6). The relatively poor performance of Pt was attributed to its oxidation during the fabrication process, whereas Au remained unchanged. This difference points to broader implications in material choice when fabricating electrochemical sensors and devices. In particular, the catalytic and electronic properties of a material cannot be overlooked when considering device applications.

## Acknowledgments

The authors would also like to acknowledge the support of the Penn State College of Engineering and the Materials Research Institute (MRI), as well as a seed grant from MRI and Covestro Co.

### References

1. Foxman B (2010) The epidemiology of urinary tract infection. Nat Rev Urol 7:653–660
2. Kidgell C, Reichard U, Wain J et al (2002) *Salmonella typhi*, the causative agent of typhoid fever, is approximately 50,000 years old. Infect Genet Evol 2:39–45
3. Solh AAE, Pietrantoni C, Bhat A et al (2004) Indicators of potentially drug-resistant bacteria in severe nursing home—acquired pneumonia. Clin Infect Dis 39:474–480
4. Majowicz SE, Musto J, Scallan E et al (2010) The global burden of nontyphoidal *Salmonella* gastroenteritis. Clin Infect Dis 50:882–889
5. World Health Organization (2015) WHO estimates of the global burden of foodborne diseases. WHO, Geneva
6. World Health Organization (2019) World Health Statistics 2019: monitoring health for the SDGs, sustainable development goals. WHO, Geneva
7. Willyard C (2017) The drug-resistant bacteria that pose the greatest health threats. Nature 543:15
8. Jorgensen JH, Ferraro MJ (2009) Antimicrobial susceptibility testing: a review of general principles and contemporary practices. Clin Infect Dis 49:1749–1755
9. CDC (2019) Antibiotic resistance threats in the United States. CDC, Atlanta
10. Wang Y, Ye Z, Ying Y (2012) New trends in impedimetric biosensors for the detection of foodborne pathogenic bacteria. Sensors 12:3449–3471
11. Yang L, Bashir R (2008) Electrical/electrochemical impedance for rapid detection of foodborne pathogenic bacteria. Biotechnol Adv 26:135–150
12. Butler D, Goel N, Goodnight L et al (2019) Detection of bacterial metabolism in lag-phase using impedance spectroscopy of agar-integrated 3D microelectrodes. Biosens Bioelectron 129:269–276
13. Ebrahimi A, Alam MA (2017) Droplet-based non-faradaic impedance sensors for assessment of susceptibility of *Escherichia coli* to ampicillin in 60 min. Biomed Microdevices 19:27
14. Ebrahimi A, Csonka LN, Alam MA (2018) Analyzing thermal stability of cell membrane of *Salmonella* using time-multiplexed impedance sensing. Biophys J 114:609–618
15. Ebrahimi A, Alam MA (2016) Evaporation-induced stimulation of bacterial osmoregulation for electrical assessment of cell viability. Proc Natl Acad Sci U S A 113:7059–7064
16. Ebrahimi A, Dak P, Salm E et al (2013) Nanotextured superhydrophobic electrodes enable detection of attomolar-scale DNA concentration within a droplet by non-faradaic impedance spectroscopy. Lab Chip 13:4248–4256
17. Daniels JS, Pourmand N (2007) Label-free impedance biosensors: opportunities and challenges. Electroanalysis 19:1239–1257
18. Li H, Bashir R (2002) Dielectrophoretic separation and manipulation of live and heat-treated cells of *Listeria* on microfabricated devices with interdigitated electrodes. Sensors Actuators B Chem 86:215–221
19. Varshney M, Li Y (2009) Interdigitated array microelectrodes based impedance biosensors

for detection of bacterial cells. Biosens Bioelectron 24:2951–2960

20. Zhang H, Ning H, Busbee J et al (2017) Electroplating lithium transition metal oxides. Sci Adv 3:e1602427
21. Kim SS, Na SI, Jo J et al (2008) Plasmon enhanced performance of organic solar cells using electrodeposited Ag nanoparticles. Appl Phys Lett 93:073307
22. Tan Y, Xu Y, Zhang H et al (2019) Pulse electroplating of ultra-fine grained zinc coating on 316L stainless steel and its corrosion behaviour. Int J Electrochem Sci 14:5913–5922
23. Campbell SA (2013) Fabrication engineering at the micro- and nanoscale, 4th edn. Oxford University Press, New York
24. Chen JY (1990) CMOS devices and technology for VLSI. Prentice Hall, Englewood Cliffs, NJ
25. Elliott C, Vijayakumar V, Zink W et al (2007) National Instruments LabVIEW: a programming environment for laboratory automation and measurement. J Lab Autom 12:17–24
26. McCreery RL (2008) Advanced carbon electrode materials for molecular electrochemistry. Chem Rev 108:2646–2687
27. Min J, Baeumner AJ (2004) Characterization and optimization of interdigitated ultramicroelectrode arrays as electrochemical biosensor transducers. Electroanalysis 16:724–729
28. Štulík K, Amatore C, Holub K et al (2000) Microelectrodes. Definitions, characterization, and applications (technical report). Pure Appl Chem 72:1483–1492

# Chapter 24

# Quantitative and Selective DNA Detection with Portable Personal Glucose Meter Using Loop-Based DNA Competitive Hybridization Strategy

**Fei Liu, Bin Wang, Yanke Shan, Wenjie Kang, Jiahao Li, Xin Wang, and Jing Liu**

## Abstract

A portable, quantitative, and selective DNA detection biosensor, based on a loop-based DNA competitive hybridization assay and a personal glucose meter (PGM), is an advanced strategy for one-step target DNA recognition and signal reporter generation. In the presence of target DNA, the invertase–DNA conjugates are released due to the competitive binding of target DNA and collected with the help of a magnet subsequently. The released invertase-DNA could catalyze the hydrolysis of sucrose into glucose with millions of turnovers which is target concentration dependent. In addition, the sensor exhibits excellent anti-interference ability, having almost no effect on the detection performance in serum. The biosensor shown here is easier to operate owning its great potential in point of care testing in environments with limited resources and skilled personnel for rapid and sensitive detection of specific DNA sequence in real biological samples.

**Key words** DNA detection biosensor, Personal glucose meter, Competitive hybridization, Invertase, Rapid and selective detection

## 1 Introduction

The loop-based DNA structure has been utilized in hairpin-type molecular beacons for mRNA biomarkers detection [1, 2]. And personal glucose meter (PGM), due to its low cost, simple operation, and portability, have attracted worldwide attention for point-of-care testing (PoCT) [3–6]. Therefore, we developed a quantitative and selective DNA detection biosensor requiring only one step for DNA recognition and signal reporter generation using a loop-based DNA competitive hybridization assay and a PGM.

As shown in Fig. 1a [7], the biotinylated capture DNA is first immobilized on the streptavidin-coated magnetic beads (MBs) forming a loop structure after its hybridization with invertase–

Miguel R. Ossandon et al. (eds.), *Biomedical Engineering Technologies: Volume 1*, Methods in Molecular Biology, vol. 2393, https://doi.org/10.1007/978-1-0716-1803-5_24, 

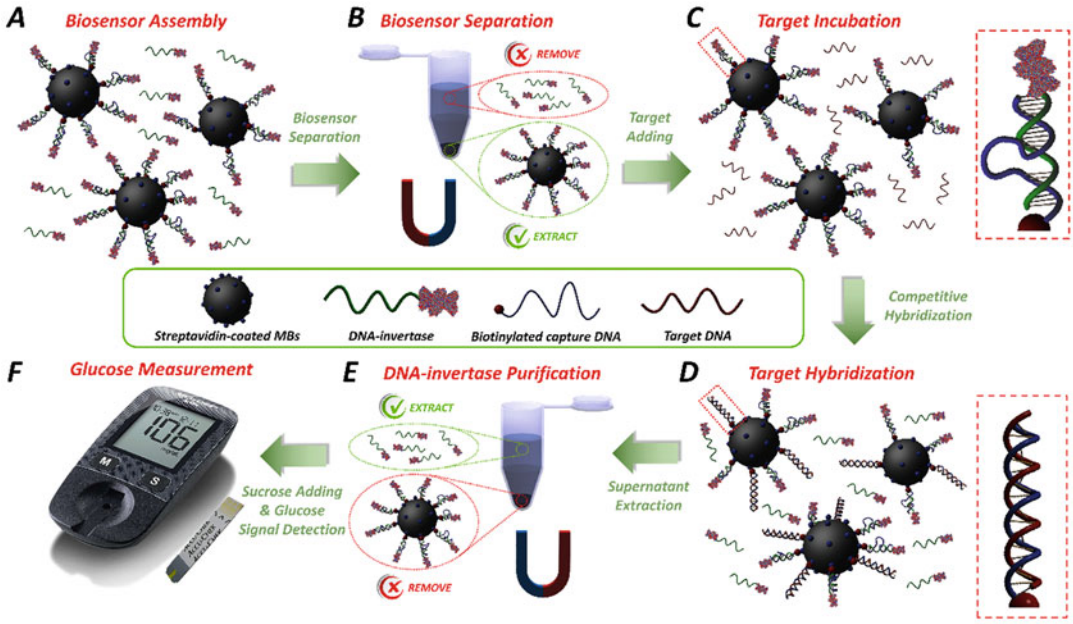


**Fig. 1** Schematic illustration of DNA detection using the PGM. (**a**) Biosensor assembly with biotinylated capture DNA, streptavidin-coated MBs, and invertase–DNA. (**b**) Biosensor separation using the magnetic separation device (presented as the magnet in **b**) to obtain the MB–capture DNA–invertase–DNA conjugates. (**c**) and (**d**) Target incubation and hybridization result in the release of the invertase–DNA from the biotinylated capture DNA to form a more stable DNA duplex. (**e**) Invertase–DNA purification by extracting the supernatant containing the released invertase–DNA using the magnetic separation device (presented as the magnet in **e**) for MBs removal. (**f**) Glucose measurements by adding the sucrose into the supernatant which is converted to glucose by the invertase for PGM detection to determine the target concentration

DNA conjugates as the biosensor assembly. Then as shown in Fig. 1b, the MB–capture DNA–invertase–DNA conjugates as the proposed DNA biosensor are precipitated with a magnetic separation device (presented as the magnet in Fig. 1b) and washed to remove the unimmobilized invertase–DNA. Next, after introducing the sample for incubation in Fig. 1c, the loop in the capture DNA can be completely hybridized with the target DNA forming a more stable DNA duplex, resulting in the release of the invertase–DNA from the biotinylated capture DNA as shown in Fig. 1d. Subsequently, as shown in Fig. 1e, the released invertase–DNA conjugates are separated and collected as the supernatant using a magnetic separation device (presented as the magnet in Fig. 1e). Then the sucrose is added into the supernatant and the released invertase which could catalyze the hydrolysis of sucrose into glucose that is detected by the PGM subsequently as shown in Fig. 1f. Therefore, the concentration of the target DNA is transformed into the level of glucose.

It is shown that the designed biosensor can specifically recognize and detect DNA sequences in one step. In absence of the

target DNA, the biosensor produced minimal background due to the high specificity of the capture DNA. The biosensor enabled sensitive detection of the target with a detection limit of 100 pM with a wide detectable linear concentration range from 100 pM to 100 nM using one-step procedure. Moreover, the biosensor exhibited excellent anti-interference ability in serum.

To the best of our knowledge, this is the first report on the use of a loop-based DNA competitive hybridization assay for sensitive DNA analysis in one-step by the PGM. The portable biosensor reported here is easier to operate owning its great potential in PoCT in environments with limited resources or access to laboratory facilities for rapid and sensitive detection of specific DNA sequence in molecular diagnosis, forensic analysis, environmental monitoring, and so on.

## 2 Materials

1. Sulfosuccinimidyl-4-(N-maleimidomethyl)-cyclohexane-1-carboxylate (Sulfo-SMCC) and Grade VII invertase from baker's yeast (*S. cerevisiae*) are purchased from Sigma-Aldrich (USA).
2. Sodium chloride (NaCl), sodium phosphate ($Na_3PO_4$), Sodium dihydrogen phosphate ($NaH_2PO_4$), disodium hydrogen phosphate ($Na_2HPO_4$), tris(hydroxymethyl)-aminomethane (Tris-HCl), ethylenediaminetetraacetic acid (EDTA), and Tween 20 are purchased from Sinophorm Chemical Reagent Co., Ltd. (China).
3. 50 mM Tris (2-carboxyethyl) phosphine (TCEP, 646547, Sigma, USA) solution is prepared by dissolving 0.143 g of TCEP in 10 mL of water.
4. Buffer I solution of pH 7.3 is prepared by dissolving 5.844 g of NaCl and 8.197 g of $Na_3PO_4$ in 500 mL of water.
5. Buffer II solution of pH 7.5 is prepared by dissolving 0.788 g of Tris-HCl, 0.146 g of EDTA, 29.22 g of NaCl, and 0.5 mL Tween 20 in 500 mL of water.
6. 0.2 M sodium phosphate buffer of pH 5.5 is prepared by dissolving 2.4 g of $NaH_2PO_4$ and 2.839 g of $Na_2HPO_4$ in 100 mL of water.
7. Streptavidin-coated MBs (2 μm in diameter) are purchased from Beaver (China).
8. The DNA oligonucleotides is synthesized by Nanjing GenScript Biotech Corporation (China).
9. Amicon-3 kDa centrifugal filters (Z740199, Millipore, Germany) and Amicon-100 kDa centrifugal filters (Z648043,

Millipore, Germany) are applied to purify thiol-DNA and invertase.

10. Personal glucose meter (PGM) is purchased from Roche (Switzerland).

## 3 Methods

### 3.1 DNA-Invertase Conjugation

1. 30 μL thiol-DNA (100 μM) is activated by 2 μL TCEP (50 mM) in 10 μL 0.2 M sodium phosphate buffer (pH = 5.5) at room temperature for 1 h.
2. 400 μL invertase (2 mg/mL) is activated by 1 mg sulfo-SMCC in Buffer I with gently shaking for 1 h at room temperature.
3. The activated thiol-DNA and invertase are then purified by Amicon-3 kDa centrifugal filters and Amicon-100 kDa centrifugal filters using Buffer I.
4. The purified sulfo-SMCC activated invertase and TCEP activated thiol-DNA are mixed together and kept at room temperature for 48 h (*see* **Note 1**).
5. The reaction mixtures are purified by Amicon-100 kDa centrifugal filters to remove unreacted thiol-DNA using Buffer I.

### 3.2 Preparation of DNA Biosensor

1. 400 μL biotinylated capture DNA (1 μM) and 400 μL invertase-DNA conjugates mixtures (1 μM) are first heated at 60 °C for 3 min and then naturally cooled down to room temperature (*see* **Note 2**).
2. The annealed DNA products are then immobilized with 50 μL 10 mg/mL streptavidin–coated MBs in Buffer II by shaking for 1 h at room temperature (*see* **Note 3**).
3. The MBs are precipitated by a magnetic separation device and washed three times with Buffer II to remove unimmobilized annealed DNA products (*see* **Note 4**).
4. The final MB–capture DNA–invertase–DNA conjugates (proposed *DNA biosensor*) are dispersed in 200 μL Buffer II.
5. The connection between the MBs, the capture DNA, and the invertase–DNA is required to be confirmed by dynamic light scattering (DLS, Zetasizer, Malvern, UK) at 25 °C.

### 3.3 DNA Detection Using DNA Biosensor and PGM

1. In DNA detection, 20 μL biosensor is incubated with 80 μL target DNA which is either in Buffer II or in serum at 37 °C for 45 min.
2. Subsequently, the MBs are precipitated from the reaction mixtures by a magnetic separation device in order to collect the supernatant with the released invertase-DNA.

**A**

| [DNA] (nM) | | 0 | 0.01 | 0.1 | 1 | 10 | 20 | 50 | 100 |
|---|---|---|---|---|---|---|---|---|---|
| PGM Signals (mg/dL) | Buffer | 65.30 ±1.33 | 67.55 ±1.64 | 73.28 ±2.26 | 77.04 ±2.38 | 92.93 ±3.33 | 114.46 ±2.98 | 170.80 ±3.58 | 238.68 ±4.59 |
| | Serum | 31.02 ±1.08 | 31.51 ±1.86 | 35.49 ±1.31 | 40.34 ±1.66 | 54.53 ±1.96 | 81.67 ±2.54 | 121.35 ±3.66 | 164.11 ±4.09 |

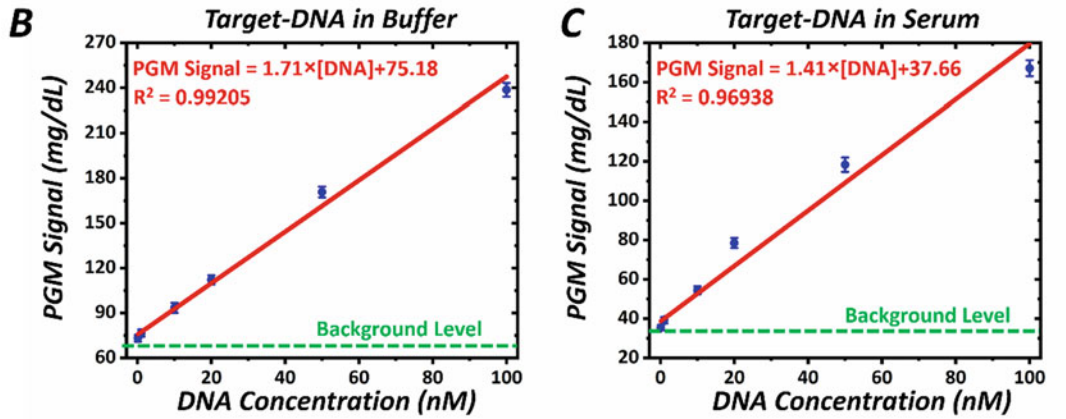


**Fig. 2** Performance certification of the PGM based DNA biosensor. (**a**) PGM signals with different concentrations of DNA in buffer and serum at the optimized experimental conditions determined in this figure, respectively. (**b**) Detection limit and fitted linear relation between the target DNA concentrations and the PGM signals in buffer detection mode. (**c**) Detection limit and fitted linear relation between the target DNA concentrations and the PGM signals in serum detection mode. The mean values and standard deviations in (**a**) and error bars in (**b**) and (**c**) were computed from 20 measurements ($p < 0.05$ by *t*-test)

3. 100 μL sucrose is added into the supernatant in the concentration of 0.5 M at 37 °C for 3 h.
4. After the reactions are finished, 5 μL sample is analyzed by the PGM and the PGM signals are influenced by the concentration of sucrose. Figure 2 shows the typical performance certification of the PGM based DNA biosensor at the optimized experimental conditions [7] (*see* **Note 5**).

## 4 Notes

1. The connection efficiency between the sulfo-SMCC activated invertase and the TCEP activated thiol-DNA may be slightly reduced if the pH of reaction solutions deviates from the neutral range (pH 7.2–7.5).
2. The annealing efficiency may be very low if the temperature suddenly drops, so we need to strictly control the temperature to naturally cool down to room temperature.

3. The streptavidin-coated MBs should be washed to remove the storage buffer of the streptavidin-coated MBs which may interfere with the activity of the invertase.
4. The constructed DNA biosensor should be fully washed to remove nonspecific interactions, otherwise it will cause low signal-to-noise ratio.
5. The length of the invertase–DNA in the designed DNA biosensor, the incubation temperature and time of target DNA with the biosensor, reaction time, and sucrose concentration should be optimized according to the actual application environment.

## References

1. Stobiecka M, Chalupa A (2016) DNA strand replacement mechanism in molecular beacons encoded for the detection of cancer biomarkers. J Phys Chem B 120:4782–4790
2. Ratajczak K, Krazinski BE, Kowalczyk AE et al (2018) Hairpin-hairpin molecular beacon interactions for detection of survivin mRNA in malignant SW480 cells. ACS Appl Mater Interfaces 10:17028–17039
3. Montagnana M, Caputo M, Lippi DG (2009) Overview on self-monitoring of blood glucose. Clin Chim Acta 402:7–13
4. Xiang Y, Lu Y (2012) Portable and quantitative detection of protein biomarkers and small molecular toxins using antibodies and ubiquitous personal glucose meters. Anal Chem 84:4174–4178
5. Xiang Y, Lu Y (2012) An invasive DNA approach toward a general method for portable quantification of metal ions using a personal glucose meter. Chem Commun 49:585–587
6. Yu X, Yi L (2011) Using personal glucose meters and functional DNA sensors to quantify a variety of analytical targets. Nat Chem 3:697–703
7. Shan YK, Zhang Y, Kang WJ et al (2019) Quantitative and selective DNA detection with portable personal glucose meter using loop-based DNA competitive hybridization strategy. Sens Actuators B Chem 282:197–203

# Chapter 25

# Electrochemical Aptamer-Based Sensors: A Platform Approach to High-Frequency Molecular Monitoring In Situ in the Living Body

**Philippe Dauphin-Ducharme, Kyle L. Ploense, Netzahualcóyotl Arroyo-Currás, Tod E. Kippin, and Kevin W. Plaxco**

## Abstract

The monitoring of specific molecules in the living body has historically required sample removal (e.g., blood draws, microdialysis) followed by analysis via cumbersome, laboratory-bound processes. Those few exceptions to this rule (e.g., glucose, pyruvate, the monoamines) are monitored using "one-off" technologies reliant on the specific enzymatic or redox reactivity of their targets, and thus not generalizable to the measurement of other targets. In response we have developed in vivo electrochemical aptamer-based (E-AB) sensors, a modular, receptor-based measurement technology that is independent of the chemical reactivity of its targets, and thus has the potential to be generalizable to a wide range of analytes. To further the adoption of this in vivo molecular measurement approach by other researchers and to accelerate its ultimate translation to the clinic, we present here our standard protocols for the fabrication and use of intravenous E-AB sensors.

**Key words** Aptamer, Electrochemical DNA biosensor, Square-wave voltammetry, In vivo sensing

## 1 Introduction

Electrochemical aptamer-based (E-AB) biosensors [1, 2] are emerging as a uniquely versatile platform for the real-time, high frequency measurement of a wide range of molecular analytes in situ in the living body. The ability of E-AB sensors to achieve this stems from the reagentless, reversible, highly selective signal transduction mechanism they employ, which is based on the electrochemical detection of binding-induced conformational changes in an electrode-bound, redox reporter-modified aptamer (Fig. 1). This conformational change alters the reporter's electron transfer rate in a manner monotonically related to the target concentration, an effect that can easily be monitored using square-wave

Miguel R. Ossandon et al. (eds.), *Biomedical Engineering Technologies: Volume 1*, Methods in Molecular Biology, vol. 2393, https://doi.org/10.1007/978-1-0716-1803-5_25, 

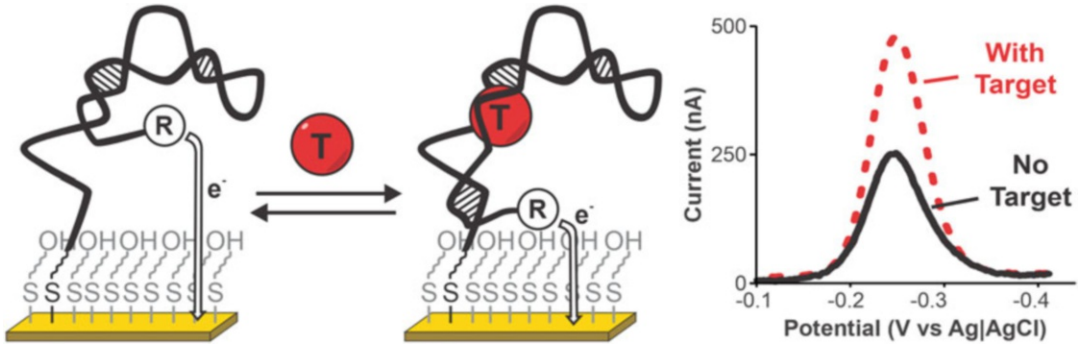


**Fig. 1** E-AB sensors are comprised of a target-recognizing aptamer that has been modified with a redox reporter (usually methylene blue), reengineered such that it undergoes a binding-induced conformational change [10, 19], and attached to a hydroxyl-terminated self-assembled thiol monolayer on a gold electrode. The binding-induced conformational change causes a target-dependent change in the reporter's electron transfer rate, an effect that is easily monitored using, for example, square-wave voltammetry

voltammetry [3], alternating-current voltammetry [4], or chronoamperometry [5].

Since we described the first [1], a dozen groups have described E-AB sensors targeting several dozen molecular analytes, including a range of both small molecules and proteins [6, 7], a half dozen of which have been adapted to high frequency, real-time measurements in the living body. Sensors adapted to in vivo use, which include those supporting the measurement of antibiotics (the aminoglycosides [5, 8, 9] and vancomycin [10]), chemotherapeutics (doxorubicin [9, 11, 12] and irinotecan [13]), the metabolite ATP [14], and the drug of abuse cocaine [15], have been used to perform unprecedentedly high precision pharmacokinetic measurements [10] and even closed-loop, feedback-controlled drug delivery [8, 10, 12]. Because of the wide range of molecules that can be detected by the approach (via the simple expedient of replacing the recognition aptamer), we are optimistic that E-AB sensors will prove an important platform for monitoring both endogenous and exogenous molecules, including drugs, metabolites, and molecular biomarkers, thus greatly advancing both biomedical research and clinical practice.

In the hopes that others might join us in expanding the E-AB platform's capabilities we present here the procedures we use in their creation and intravenous deployment. This chapter is divided in the following sections: (1) the fabrication of intravenous E-AB sensors, (2) their in vitro optimization, and (3) their deployment in situ in the veins of live rats.

## 2 Materials and Instruments

### 2.1 Electrode Fabrication

1. Polytetrafluoroethylene-coated gold (PTFE), silver and platinum wires (75 μm diameter, 64 μm insulation thickness) from A-M Systems (Sequim, WA).
2. Heat-shrink PTFE (HS Sub-Lite-Wall, 0.02 in, black-opaque) from ZEUS (Branchburg Township, CA).
3. Rubber stopper of BD 1 mL Tuberculin Slip Tip syringe (Fisher Scientific, CA).
4. 22-G BD Insyte Autoguard Shielded I.V. catheter (VWR International, CA).
5. External Ag|AgCl reference and platinum counter electrodes obtained from CH Instruments (Austin, TX).
6. Concentrated sodium hypochlorite solution (Fisher Scientific, CA).

### 2.2 Electrode Cleaning

1. Sodium hydroxide pellets (Fisher Scientific, CA).
2. Sulfuric acid (Fisher Scientific, CA).

### 2.3 Electrode Modification

1. Methylene blue-modified (https://www.biosearchtech.com/support/resources/oligo-modifications/methylene-blue44-on-c7-3-modification) and thiol-modified (https://www.biosearchtech.com/support/resources/oligo-modifications/thio-c6-linker-thiohexyl-5-modification) oligonucleotides (e.g., Biosearch Technologies, Petaluma, CA; Integrated DNA Technologies, Coralville, IA; IBA GmbH, Göttingen, Germany; or Biosynthesis, Lewisville, TX).
2. Tris(2-carboxyethyl)phosphine (TCEP) (Sigma-Aldrich).
3. 6-mercapto-1-hexanol (Sigma-Aldrich).
4. 0.22 μm-filtered 20× phosphate buffered saline (ChemCruz, Dallas, TX).
5. Potassium chloride.
6. Sodium chloride.

### 2.4 In Vitro Characterization

1. Heparinized bovine blood from Hemostat Laboratories (Dixon, CA) or BioIVT (Westbury, NY).
2. CHI1000C multipotentiostat (Austin, TX).

### 2.5 Implantation and In-Situ Measurements

1. Sprague-Dawley rats (3–5 months old, 250–600 g) from Charles River Laboratories (Santa Cruz, CA).
2. A catheter constructed using a bent steel cannula with a screw-type connector (Plastics One, Roanoke, VA) and silastic tubing (11 cm, i.d. 0.64 mm, o.d. 1.19 mm, Dow Corning, Midland, MI).

3. Sterile 6-0 silk suture (Fine Science Tools, Foster City, CA).
4. Exogenous molecules to be detected are infused using a KD Scientific pump, KDS 200 Legacy Series.
5. 3 mL BD syringe (Fisher Scientific, CA).
6. Portable potentiostat (CHI1240C—CH Instruments, Austin, TX).
7. Isoflurane (Midwest Veterinary Supply, MN).
8. Oxygen gas (Airgas, CA).
9. Square-wave voltammograms analyzed using an open-source software [16] (https://doi.org/10.1021/acs.analchem.9b02553).

## 3 Methods

### 3.1 Fabrication of Intravenous E-AB Sensors

#### 3.1.1 Electrode Fabrication

1. We cut 7.75 cm segments of polytetrafluoroethylene-coated, 75 μm-diameter gold, silver, and platinum wires before removing ~5 mm of insulation from each end using a surgical blade.
2. To strengthen the wires, we encase each in heat-shrinkable polytetrafluoroethylene (leaving the ends exposed).
3. Bundling the three in an additional heat-shrinkable polytetrafluoroethylene layer.
4. We then clip 2 mm from the exposed gold (*see* Fig. 2 for a full description of this step) leaving a 3 mm length that serves as the sensor (the electroactive surface area of the working electrode must be smaller than that of the counter electrode so as not to limit current).
5. We then insert the bundle into the lumen of an 18-G needle that has been passed through the rubber stopper of BD 1 mL Tuberculin Slip Tip syringe. Upon removal of the needle the sensor bundle is left tightly sealed in the stopper (Fig. 2iii, iv).

#### 3.1.2 Electrochemical Cleaning

1. We electrochemically clean and roughen E-AB sensors by first immersing the 3-electrode bundle in an aqueous solution of 0.5 M sodium hydroxide.
2. The gold working electrode potential is then cycled between −1.0 and −1.6 V (all potentials in this paper are reported relative to Ag|AgCl) at 1 V/s for 300 cycles to remove any potential organics contamination (Fig. 3a).
3. We next transfer the 3-electrode bundle to aqueous 0.5 M sulfuric acid and use chronoamperometry to pulse the potential 16,000 times between 0 and 2 V using a 20 ms pulse length (CHI1000C multipotentiostat). The resulting roughening produces a two- to threefold increase in the sensor's

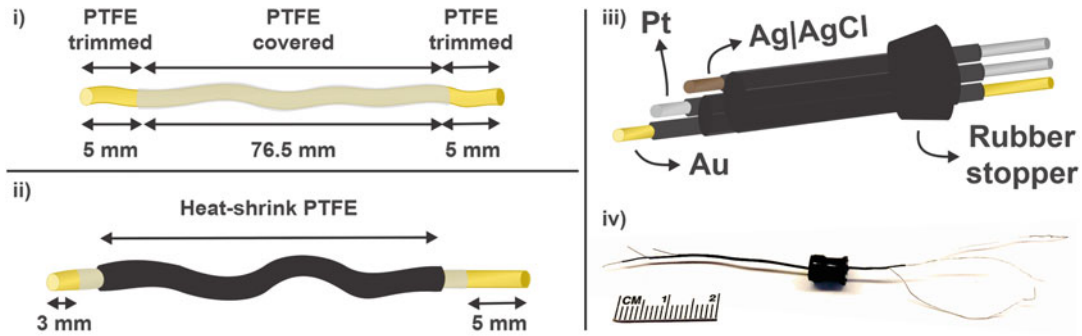


**Fig. 2** We manufacture intravenous E-AB sensors by bundling polytetrafluoroethylene-coated gold, silver and platinum wires trimmed at their extremities to allow sensor fabrication and electrical connectivity

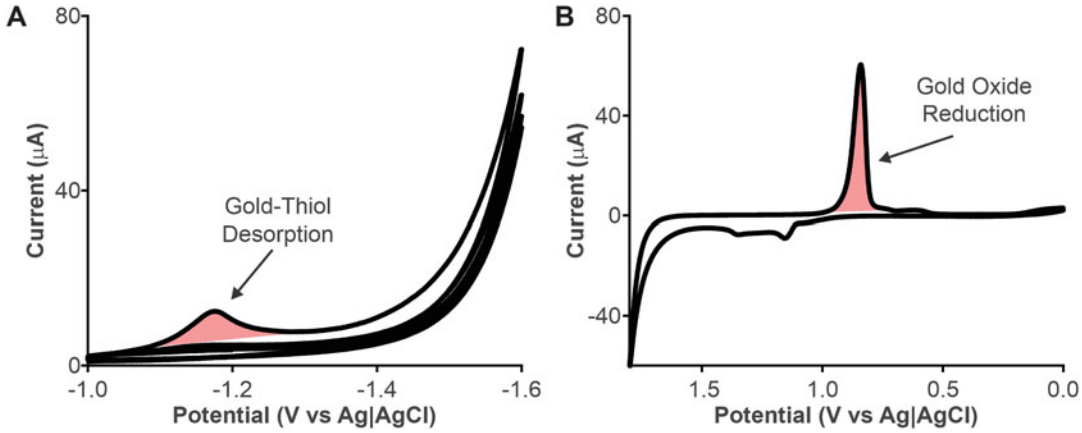


**Fig. 3** (**a**) To remove organic contaminants (particularly important when we reuse electrodes), we first electrochemically reduce the gold surface in alkaline environments by cycling the potential between −1 and 1.6 V. (**b**) To increase the microscopic surface area of the electrode we perform electrochemical roughening (*see* Subheading 3.1.2), after which we determine their electroactive area by recording a cyclic voltammogram between 0 and 1.8 V at 0.1 V/s and integrating the area under the peak associated with gold reduction and dividing it 400 μC/cm$^2$ [18], a constant associated with the charge density of a monolayer of chemisorbed oxygen on gold

microscopic surface area, measured via the integration of the gold oxide reduction peak, increasing its signaling current and thus its signal-to-noise ratio [17].

4. To determine the electroactive surface area of the gold working electrode (the first step in checking the aptamer packing density) we immerse the 3-electrode bundle in 0.05 M sulfuric acid and acquire a cyclic voltammogram between 0 and 1.8 V at 0.1 V/s (Fig. 3b).
5. Integrating the area under the peak associated with gold oxide reduction from the voltammogram's baseline and dividing by 400 μC/cm$^2$ (a constant associated with the charge density corresponding to the formation of a complete monolayer of

chemisorbed oxygen on gold [18]). We typically obtain electroactive surface areas of 0.02–0.04 $cm^2$.

### 3.1.3 Electrode Modification

1. To fabricate our E-AB sensor we rely on aptamers that have previously been selected using systematic evolution of ligands by exponential enrichment (SELEX).
2. The minimum sequence necessary to support target binding is often shorter than the length of the sequences employed in the random SELEX starting library; we typically employ aptamers that have been truncated to their minimum binding length.
3. Many minimum-binding-length aptamers undergo a sufficient conformational change upon target binding to support high-gain (>100% signal change) E-AB signaling. For those that do not we typically employ further deletions, which will destabilize the aptamer's native state, causing it to undergo binding-induced folding. Alternative strategies include the insertion of an unstructured loop or the introduction of a complementary sequence. We refer the readers to reports describing these approaches to aptamer redesign [10, 19].
4. We deposit the aptamer on the gold working electrode using solutions containing 200–500 nM of the reduced aptamer. This is prepared by first aliquoting 2 μL of a 100 μM stock aptamer (use as received from our supplier and resuspended in deionized water) in a microcentrifuge tube (Fig. 4).
5. We then reduce the thiol modification on the aptamer by adding 2 μL of 10 mM TCEP stock in deionized water (*TCEP is light-sensitive and is stored sealed at 4 °C).
6. Following reduction (~1 h at 25 °C) we determine the concentration of the reduced aptamer by measuring its absorbance at 260 nm using the molar extinction coefficient provided by the supplier. Using this value we adjust the volume using 1-×-phosphate buffered saline to achieve the desired concentration of aptamer.
7. We rinse the freshly electrochemically cleaned gold electrode bundle with deionized water, separate it from the bundle (Fig. 4), and immerse it in the aptamer solution for 1 h.
8. Upon removal we rinse the electrode with deionized water and, then, immerse it in 5 mM 6-mercapto-1-hexanol in 1-×-phosphate buffer overnight at room temperature.
9. In parallel, the silver wire is immersed overnight in a different microcentrifuge tube containing concentrated hypochlorite solution to form an AgCl film that acts as a reference electrode (right panel in Fig. 4).
10. Following these incubations we rinse the electrode bundle thoroughly in deionized water and then insert it into a 22-G

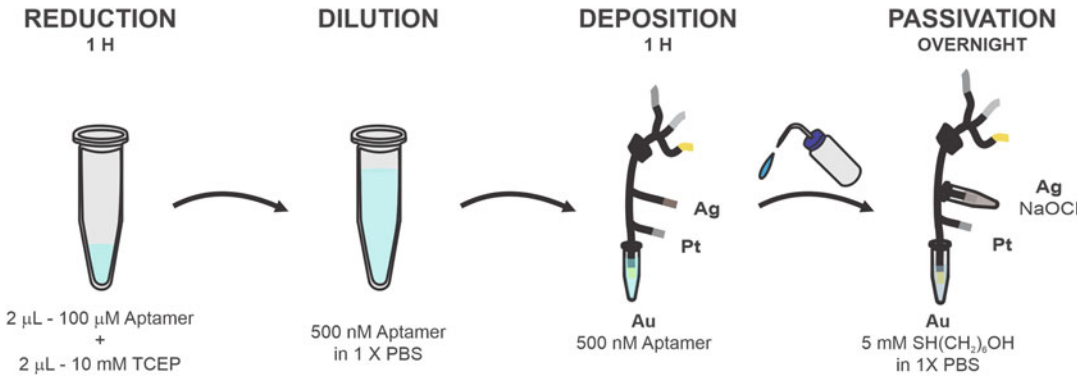


**Fig. 4** To prepare intravenous E-AB sensors, we (1) reduce the thiol on the aptamer using TCEP, (2) adjust the aptamer concentration by adding 1×-phosphate buffered saline, (3) immerse a freshly electrochemically cleaned gold electrode into the solution for 1 h, and then, finally, (4) rinse the electrode and immerse in 5 mM 6-mercapto-1-hexanol overnight. The silver wire is simultaneously immersed in a second tube containing concentrated sodium hypochlorite to form the AgCl film used as a reference electrode

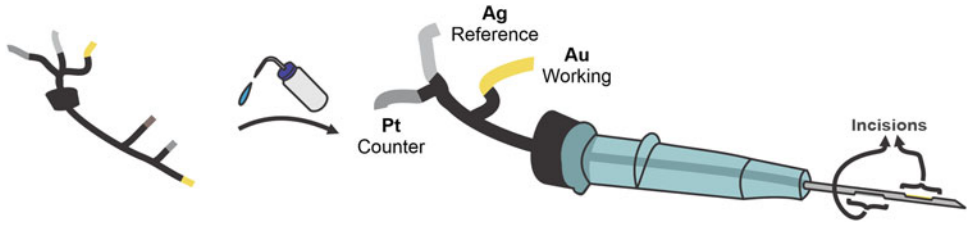


**Fig. 5** Intravenous E-AB sensors are encased in a 22G catheter modified with two small incisions at its extremity that permit blood to reach the sensor. Immediately prior to use we fill this with 1×-phosphate buffered saline to insure electrical connectivity between the working, counter and reference electrodes seal this using the previously installed rubber stopper

BD Insyte Autoguard Shielded I.V. catheter modified by cutting small incisions that allow blood to access the sensor when it is implanted in the animal (Fig. 5).

11. We then seal the distal end of the catheter using the previously installed rubber syringe stopper. To insure conductivity between all electrodes for the entire length of our experiments we backfill (i.e., through the septum) the catheter with 1-×-phosphate buffer using a 24-G needle syringe.

### *3.2 Optimization of the Sensor's Analytical Performance*

#### *3.2.1 Determination of Aptamer Packing Density*

E-AB sensor gain is strongly dependent on aptamer packing density (number of aptamer molecules per unit area) [4], which we regularly measure in order to ensure reproducible sensor performance. To do so we immerse a freshly fabricated sensor in an electrochemical cell filled with 10 mL of 1×-phosphate buffered saline and record a cyclic voltammogram between 0 and −0.5 V at 0.1 V/s, which oxidize and reduce the methylene blue redox reporter ($E_0 \approx -0.3$ V). Integrating the area under the peak associated

with the reduction of methylene blue (Fig. 6), we can calculate the number of redox reporters per surface area (i.e., surface packing density, $\Gamma$, in molecules/cm$^2$) using the following equation

$$\Gamma = \frac{Q\ N_A}{v\ n\ F\ A} \tag{1}$$

Here $Q$ represents the charge transferred (in coulombs) determined from the area under the peak of the reduction of the redox reporter, $N_A$ is Avogadro's number (molecules/mol), $v$ is the scan rate used to acquire the voltammogram, $n$ is the number of electrons transferred in the reaction (for methylene blue this is 2), $F$ is Faraday's constant (in C/mol), and $A$ is the electroactive surface area of the sensor (in cm$^2$) as determined above in Subheading 3.1.2. This protocol yields packing densities 4–6 pmol/cm$^2$ [17], and can be further increased/lowered by adjusting the deposition time and aptamer solution concentration.

*3.2.2 Determination of Optimal Electrochemical Parameters*

1. E-AB signal gain (relative signal change at saturating target) is a strong function of square-wave frequency. Enough so that, at some (typically lower) frequencies, target binding decreases the peak current (i.e., the sensor is "signal-off"), and at others (typically higher frequencies) the sensor's response to target is "signal-on" (Fig. 7a) [3, 20]. Paired signal-on and signal-off frequencies are required to perform drift correction (*see* below).
2. To identify the frequencies with the highest signal-on (positive) and signal-off (negative) gain we first adjust the square-wave frequency [3] by recording voltammograms (using increments of 1 mV over the range 0 and −0.5 V) at 10 square-wave frequencies per decade in both the absence of target and in the presence of a high (typically saturating) concentration of the target. We recommend frequencies in the range 2–1000 Hz, as lower frequencies exhibit baseline issues attributable to oxygen reduction and at higher frequencies the signal becomes overwhelmed by capacitive effects [20].
3. We next optimize the square-wave amplitude, another electrochemical parameter that impacts sensor performance. For this we interrogate the sensor in the absence and presence of target at the selected signal-on and signal-off square-wave frequencies while varying the square-wave amplitude in 5–10 mV increments from 1 to 100 mV. We recommend square-wave amplitudes of between 10 and 25 mV [3]; smaller amplitudes do not yield sufficiently large pulses to subtract the current produced from the formation of an electrical double layer, and larger pulses produce asymmetric square-wave voltammograms [3].

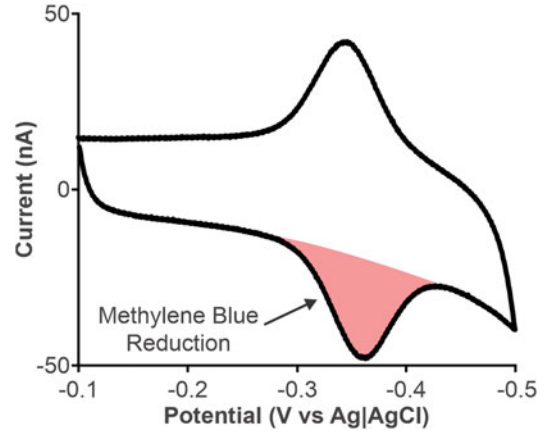


**Fig. 6** Aptamer packing density is an important variable to control. To ensure that we have done so we determine the number of redox-reporter-modified aptamers on the electrode by recording a cyclic voltammogram between 0 and −0.5 V and integrating the area under the peak associated with the reduction of methylene blue. Using this number and the microscopic surface area of the electrode (determined above; Fig. 3) we calculate the number of aptamers per unit area on the electrode

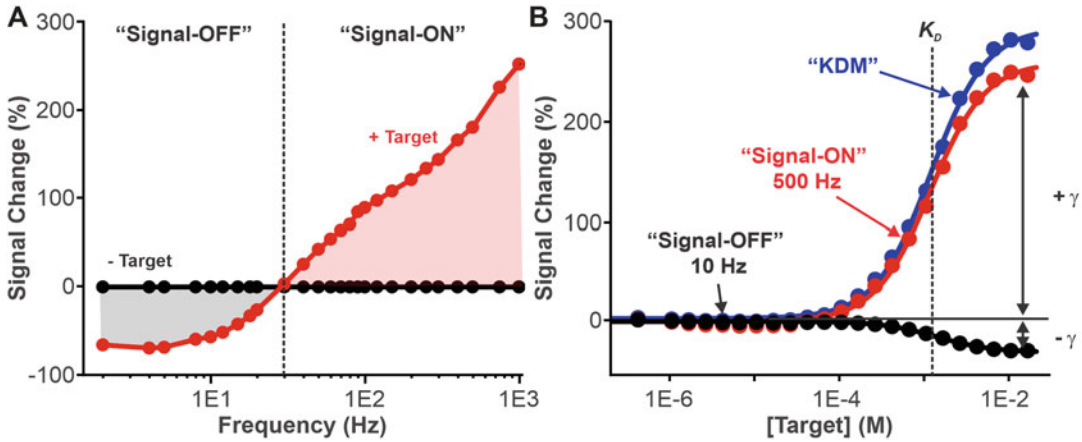


**Fig. 7** We determine the optimal electrochemical parameters to interrogate the E-AB sensor first by acquiring square-wave voltammograms at varying square-wave frequencies over the range 2–1000 Hz in the presence and absence of target. (**a**) This allows us to (1) determine if binding-induced change in electron transfer occurs, (2) determine the square-wave frequencies that generate the highest signal gain (relative signal change at saturating target; $\gamma$), and (3) determine the sign of response (i.e., "signal-on" or "signal-off"). (**b**) Using the selected signal-on and signal-off square-wave frequency we then calibrate the sensor in undiluted whole blood containing increasing amounts of target. The difference between the normalized signals obtained at these two frequencies returns the "Kinetic differential measurement" (labeled "KDM"), which improves gain and removes the drift seen when sensors are deployed in vivo [11]. We fit the resulting KDM signal versus concentration relationship to a binding isotherm to determine the parameters needed to calibrate the sensor (i.e., $K_D$ and $\gamma$)

#### 3.2.3 Kinetic Differential Measurement

To remove the drift seen in vivo and to increase signal gain we employ kinetic differential measurements (labelled "KDM" in Fig. 7b). This consists of subtracting the normalized response of the sensor collected at its signal-on and signal-off frequencies:

$$\mathrm{KDM} = \frac{i_{\mathrm{ON}}}{i_{\mathrm{min,ON}}} - \frac{i_{\mathrm{OFF}}}{i_{\mathrm{min,OFF}}} \tag{2}$$

where $i_{\mathrm{min,ON}}$ and $i_{\mathrm{ON}}$ represent the peak currents measured at the signal-on frequency in the absence and presence of target, respectively, and $i_{\mathrm{min,OFF}}$ and $i_{\mathrm{OFF}}$ represent the equivalent measurements performed at the signal-off frequency. KDM likewise provides means with which drift can be subtracted due to sensor degrading when deployed in the living body (*see* Subheading 3.3.2 for additional details).

#### 3.2.4 In Vitro Calibration

1. We calibrate each sensor in vitro in undiluted, heparinized bovine blood. This is done by measuring square wave peak heights (at both signal-on and signal-off frequencies) as the sensor responds to increasing concentrations of target (Fig. 7b).
2. We fit the resulting plot of KDM signal versus concentration relationship to a binding isotherm (Eq. 3), which returns the sensor's dissociation constant ($\mathrm{K_D}$) and "gain" ($\gamma$), the latter being the relative change in square-wave peak current in absence and presence of target.
3. From knowledge of these parameters and of $i_{\mathrm{min}}$, the current seen in the absence of target, we can derive target concentration from measurements of the sensor's KDM signal, $i_{\mathrm{KDM}}$, using

$$[T] = \mathrm{K_D}\frac{i_{\mathrm{KDM}} - i_{\mathrm{min}}}{\gamma i_{\mathrm{min}} - i_{\mathrm{KDM}}} \tag{3}$$

We have previously determined that in doing so we obtain values that approach those obtained using the standard, benchtop approaches [21].

### 3.3 In Vivo Sensor Deployment

The protocol discussed below has been approved by the University of California, Santa Barbara Institutional Animal Care and Use Committee (IACUC) and adheres to the guidelines given by the NIH Guide for Care and Use of Laboratory Animals (eighth edition, National Academy Press, 2011) [22].

#### 3.3.1 Sensor Implantation

1. We place a rat under anesthesia using a flow of 5% isoflurane–oxygen mixture in a Plexiglas anesthesia chamber and maintain it under anesthesia during the entire length of the experiment using a 2–3% isofluorane–oxygen mixture.

2. We then shave the chest above the arms to the neck to expose the skin above the jugular veins and clean the area with 10% betadine in water followed by 70% ethanol (3×).
3. We first insert a drug-delivery catheter in the left jugular vein. To do so we expose the vein using tissue spreading scissors and then expand the tissue further using the tips of sharp surgical scissors.
4. We isolate the vein using two sets of number 7 Dumont forceps by passing it and the associated connective tissue between the two forceps until no connective tissue remains.
5. We then raise the isolated vein by inserting a spatula beneath it, tie it off to prevent bleeding, and make an incision using spring-loaded microscissors.
6. We insert the silastic catheter into the incision using number 7 Dumont forceps and tie it using 6.0 silk sutures placed above (to prevent bleeding) and below (to seal the needle of the catheter into the vein) the insertion site (Fig. 8).
7. We then insert the sensor in the right jugular using the same procedure we use to insert the drug delivery catheter in the left. We infuse 30 units of heparin in the rat prior to any recording.

#### 3.3.2 *In Vivo Sensing*

1. We connect the respective working, counter, and reference electrodes of the sensor bundle to the potentiostat using "mini-grabber" clips.
2. We repeatedly record square-wave voltammograms between 0 and −0.5 V at the two square-wave frequencies (and amplitudes) identified above during the in vitro calibration (*see* Subheading 3.2.2).
3. Following stabilization of the sensor's output (~30 min), we infuse the target molecule using the infusion line. Doing so generates a sensor response that we measure from the peak height of the square-wave voltammograms using analysis software developed in Python and now available as open source software [16].
4. This algorithm plots the resulting square-wave voltammograms and their peak heights in real time, while simultaneously deriving the KDM corrected signal. The resulting KDM response can then easily be converted into measured target concentration using the calibration curve obtained in vitro (Fig. 9).

## 4 Notes

We have identified a series of debugging steps that can be followed to troubleshoot sensor fabrication and in vivo deployment.

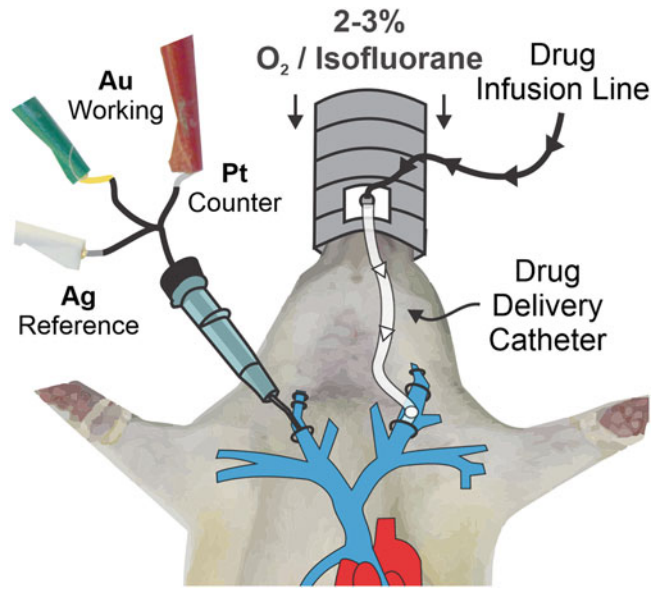


**Fig. 8** We install the intravenous E-AB sensor in the right jugular vein and, if needed, a target infusion catheter in the left

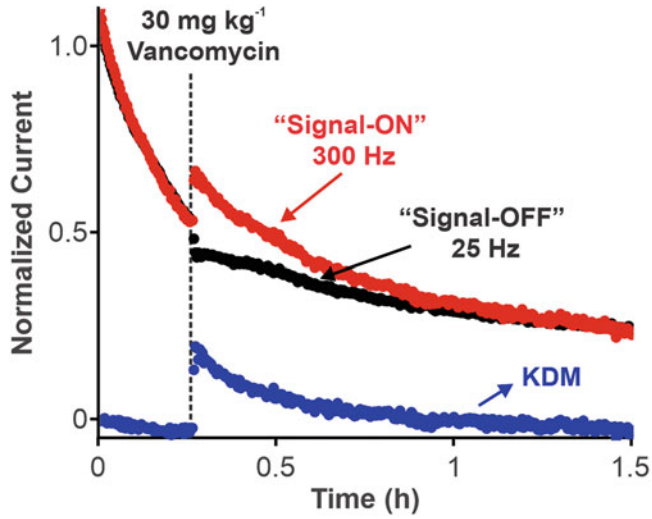


**Fig. 9** We repeatedly measure the peak height of square-wave voltammograms recorded between 0 and −0.5 V, alternating between square-wave frequencies at which the sensor responds to target in a signal-on and a signal-off fashion. Using these two measurements we perform "kinetic-differential measurements" (KDM), which removes drift, and then calculate the concentration of the target from the KDM calibration curve obtained in vitro (Fig. 7b)

1. *The E-AB sensors do not produce any voltammogram in vitro.* This may indicate faulty fabrication of the sensor. The heat-shrink polymer, if heated for too long at high temperatures, can

melt through and short the three electrodes. This can be tested using a multimeter to determine if any pair of wires is shorted.

2. *The square-wave voltammograms appear deformed or their baselines jump from side to side of the voltage scale.* This indicates a faulty electrical connection, most likely originating from bad connections to the mini-grabber clips or air bubbles trapped inside the E-AB encasing (the plastic catheter). These can be solved by checking the mini-grabber connections and/or removing the rubber septum and reflushing the catheter with 1×-phosphate buffer.
3. *The square-wave voltammograms are noisy.* Noise often originates from poor mini-grabber connections. Although convenient, commercial mini-grabber clips are not electrically shielded and can pick up significant environmental noise from fields generated by other equipment. You may try to connect the sensors directly to the potentiostat, turn off any unnecessary electrical equipment, or place the entire setup under a faraday cage. You can also use commercially available electrically grounded mats to minimize noise derived from, for example, static charging of the animal's fur.
4. *Sensors that perform well in vitro produced no signal in vivo.* This likely originates from missing blood/buffer in the catheter. We fix this by flushing the catheter with 1×-phosphate buffered saline as described above.
5. *The square-wave frequencies selected in vitro do not drift in concert in vivo or do not respond to target injections.* The chemical composition of blood in vivo differs from that seen in vitro. Always be ready to adjust the frequency pair you use when E-AB sensors are deployed in vivo.

## References


1. Xiao Y, Lubin AA, Heeger AJ, Plaxco KW (2005) Angew Chem Int Ed 44:5456–5459
2. Xiao Y, Piorek BD, Plaxco KW, Heeger AJJ (2005) Am Chem Soc 127:17990–17991
3. Dauphin-Ducharme P, Plaxco KW (2016) Anal Chem 88:11654–11662
4. White RJ, Phares N, Lubin AA, Xiao Y, Plaxco KW (2008) Langmuir 24:10513–10518
5. Arroyo-Currás N, Dauphin-Ducharme P, Ortega G, Ploense KL, Kippin TE, Plaxco KW (2018) ACS Sensors 3:360–366
6. Schoukroun-Barnes LR, Macazo FC, Gutierrez B, Lottermoser J, Liu J, White RJ (2016) Annu Rev Anal Chem 9:163–181
7. Lubin AA, Plaxco KW (2010) Acc Chem Res 43:496–505
8. Arroyo-Currás N, Ortega G, Copp DA, Ploense KL, Plaxco ZA, Kippin TE, Hespanha JP, Plaxco KW (2018) ACS Pharmacol Transl Sci 1:110–118
9. Arroyo-Currás N, Somerson J, Vieira PA, Ploense KL, Kippin TE, Plaxco KW (2017) Proc Natl Acad Sci U S A 114:645–650
10. Dauphin-Ducharme P, Yang K, Arroyo-Currás N, Ploense KL, Zhang Y, Gerson J, Kurnik M, Kippin TE, Stojanovic MN, Plaxco KW (2019) ACS Sensors 4:2832–2837
11. Ferguson BS, Hoggarth DA, Maliniak D, Ploense K, White RJ, Woodward N, Hsieh K, Bonham AJ, Eisenstein M, Kippin TE, Plaxco KW, Soh HT (2013) Sci Transl Med 5:213ra165

12. Mage PL, Ferguson BS, Maliniak D, Ploense KL, Kippin TE, Soh HT (2017) Nat Biomed Eng 1:0070
13. Idili A, Arroyo-Currás N, Ploense KL, Csordas AT, Kuwahara M, Kippin TE, Plaxco KW (2019) Chem Sci 10:8164–8170
14. Li H, Li S, Dai J, Li C, Zhu M, Li H, Lou X, Xia F, Plaxco KW (2019) Chem Sci 10:10843–10848
15. Taylor IM, Du Z, Bigelow ET, Eles JR, Horner AR, Catt KA, Weber SG, Jamieson BG, Cui XT (2017) J Mater Chem B 5:8417–8417
16. Curtis SD, Ploense KL, Kurnik M, Ortega G, Parolo C, Kippin TE, Plaxco KW, Arroyo-Currás N (2019) Anal Chem 91:12321–12328
17. Arroyo-Currás N, Scida K, Ploense KL, Kippin TE, Plaxco KW (2017) Anal Chem 89:12185–12191
18. Trasatti S, Petrii OA (1991) Pure Appl Chem 63:711–734
19. White RJ, Rowe AA, Plaxco KW (2010) Analyst 135:589–594
20. White RJ, Plaxco KW (2010) Anal Chem 82:73–76
21. Vieira PA, Shin CB, Arroyo-Currás N, Ortega G, Li W, Keller AA, Plaxco KW, Kippin TE (2019) Front Mol Biosci 6:69
22. National Research Council (US) Committee for the Update of the Guide for the Care and Use of Laboratory Animals (2010) Guide for the care and use of laboratory animals. National Academies Press

# Chapter 26

# Smartphone-Based Electrochemical System for Biosensors and Biodetection

**Daizong Ji, Sze Shin Low, Diming Zhang, Lei Liu, Yanli Lu, and Qingjun Liu**

## Abstract

With the advantages of high popularity, convenient operation, open-source operation systems, high resolution imaging, and excellent computing capabilities, smartphones have been widely used as the core of detection system for calculation, control, and real-time display. Hence, smartphones play an important role in electrochemical detection and optical detection. Smartphone-based electrochemical systems were combined with screen-printed electrode and interdigital electrodes for in situ detection. The electrodes were modified with biomaterials, chemical materials, and nanomaterials for biosensors and biodetection, such as 3-amino phenylboronic acid nanocomposites, graphene, gold nanoparticles, zinc oxide nanoparticles, carbon nanotubes, proteins, peptides, and antibodies. With the modified electrodes, the smartphone-based impedance system was used to detect acetone, bovine serum albumin, human serum albumin, and trinitrotoluene, while smartphone-based amperometric system was employed to monitor glucose, ascorbic acid, dopamine, uric acid, and levodopa. The smartphone-based electrochemical system for biosensors and biodetection has provided miniaturized and portable alternative for diagnosis, which is promising to find application in point-of-care testing (POCT).

**Key word** Smartphone, Electrochemistry, Nanomaterials, Screen-printed electrodes and interdigital electrodes, Biochemical detection

## 1 Introduction

Biosensors are defined as analytical devices incorporating biological or biological-derived sensing elements either integrated within or intimately associated with physicochemical transducers for analyte detections [1, 2]. In the past few decades, there has been rapid development in biosensors due to their high sensitivity and selectivity [3–6]. Various biological materials are used as transducers such as cells, enzymes, antigen–antibody complexes, peptides, and nucleic acids [7–11]. Furthermore, chemical materials and nanomaterials were also modified on the sensors for biochemical molecules detection to enhance the sensitivity and selectivity. These chemical, nano-, and biomaterials modified sensors were combined with electrochemical detectors to perform biodetection. Coupled

Miguel R. Ossandon et al. (eds.), *Biomedical Engineering Technologies: Volume 1*, Methods in Molecular Biology, vol. 2393, https://doi.org/10.1007/978-1-0716-1803-5_26, 

with readout processing system, these biosensors and biodetectors have been successfully applied in clinical diagnosis, drug screening, and environmental monitoring [12–14]. With the development of micro/nano processing technology, biosensors can be integrated into "lab-on-a-chip" for biochemical detection [15]. Although there has been great progress in sensitivity and automation of these micro/nano biosensors, they usually need bulky readout devices to implement sensing processes, detect response signals, analyze data, and display results [16]. In the past few years, the miniaturization of biosensor and biodetection system has become research hotspot to perform the convenient and real-time detection [17, 18]. Therefore, large volume and high cost of readout devices became one of the main obstacles for miniaturization of biosensors to be used for portable and efficient detection.

Since the advent of the first smartphone in 1983, smartphones have brought tremendous reformation to the market, with the number of worldwide users bound to reach 3.5 billion by 2019 [19]. Due to the high popularity, convenient operation, open-source operation systems, high resolution imaging, and excellent computing capabilities, smartphones play a pivotal role in human life. With these advantages, the combination of smartphones and biosensing technologies provides a solution to this issue [16, 20]. With the advantages of high reliability, easy operation, low detection limit and cost, electrochemical detection has been used as an excellent quantitative detection technology [21–23]. These features made it conducive to the miniaturization and integration of the electrochemical detection system. Hence, smartphones have been combined with portable electrochemical devices as an integrated platform to control, record, and display. According to different sensing technologies, the electrochemical sensing on a smartphone can be divided into amperometric [17, 24–27], potentiometric [25, 28, 29], and impedance techniques [18, 30, 31]. Moreover, smartphones have wireless communication, smaller volume, and user-friendly interface to enable easy operation for all ages [32, 33]. Mobile Health (mHealth) is defined as "medical and public health practice supported by mobile devices, such as mobile phones . . . and other wireless devices." In recent years, researchers are beginning to focus on the development of mHealth devices to support health services [34]. Users can use the related mHealth applications on smartphone to self-monitor their condition, such as hypertension and diabetes [26, 35]. They can also receive remote health services since their physiological data can be transferred by online mHealth application to doctors in clinical houses or hospitals [36, 37].

In our work, a smartphone-based electrochemical system is combined with screen-printed electrode and interdigital electrode for in-situ detection. The electrodes ae modified with chemical materials, nanomaterials, and biological materials. The

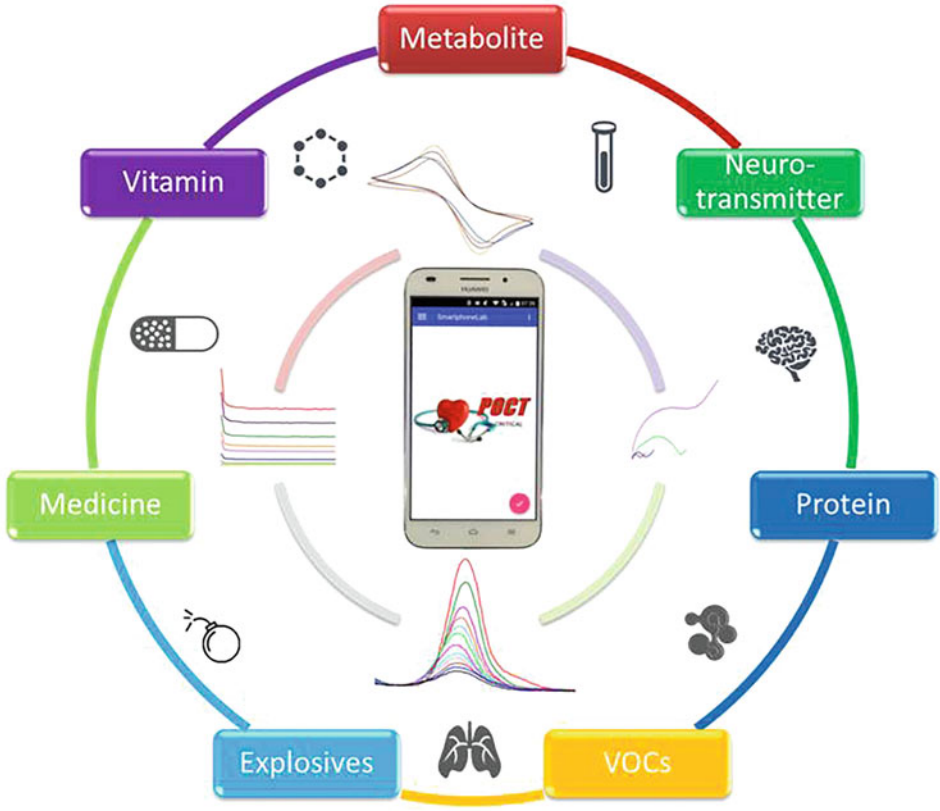


**Fig. 1** Overview diagram of the smartphone-based electrochemical system for biosensors and biodetection

smartphone-based system reported consists mainly two kinds of electrochemical detection, namely, impedance and amperometry. As shown in Fig. 1, the smartphone-based system would be a potential candidate for point-of-care testing (POCT) device for various substance detections, such as proteins, vitamins, neurotransmitters, drugs, explosives, and volatile organic compounds (VOCs).

## 2 Materials

### *2.1 Electrochemical Measurement System*

1. Screen-printed electrode (GSI Technologies, Illinois, USA).
2. Electrochemical workstation (CHI 660E, CH Instruments, Texas, USA).
3. Interdigital electrode.
4. Interdigital gold electrode (ACEA Biosciences, California, USA).

### 2.2 Acquisition and Immobilization of Sensitive Materials

1. Liquid volatile organic compounds (VOCs).
2. Ethanol (Sigma-Aldrich, Missouri, USA).
3. Acetone (Sigma-Aldrich, Missouri, USA).
4. Formaldehyde (Sigma-Aldrich, Missouri, USA).
5. Acetic acid (Sigma-Aldrich, Missouri, USA).
6. TNT-specific peptides (WHWQRPLMPVS) (GenScript, Nanjing, China).
7. Phosphate buffer saline (PBS) (*see* **Note 1**).
8. Beta-ionone (Sigma-Aldrich, Missouri, USA).
9. Isoamyl acetate (Sigma-Aldrich, Missouri, USA).
10. Butanedione (Sigma-Aldrich, Missouri, USA).
11. $K_4[Fe(CN)_6]/K_3[Fe(CN)_6]$ (Sigma-Aldrich, Missouri, USA).
12. 2,4,6-Trinitrotoluene (TNT) (Sigma-Aldrich, Missouri, USA).
13. Octapeptides (Cys-Leu-Val-Pro-Arg-Gly-Ser-Cys, CLVPRGSC) (GenScript, Nanjing, China) (*see* **Note 2**).
14. Eleven-peptides (Trp-His-Trp-Gln-Arg-Pro-Leu-Met-Pro-Val-Ser, THTGAPLMPVS) (GenScript, Nanjing, China) (*see* **Note 2**).
15. Chloroauric acid ($HAuCl_4$, 0.01%, Sigma-Aldrich, Missouri, USA).
16. 3-amino phenylboronic acid nanocomposites (APBA, 2 mL, 5 mM, in absolute ethanol).
17. Sodium sulfate (0.1 M).
18. N-hydroxysulfosuccinimide (NHS) and 1-ethyl-3-(3-dimethylamino-propyl)carbodiimide hydrochloride (EDC).
19. Chitosan (0.5%).
20. Polyvinyl butyral (PVB).

### 2.3 Synthesis of Nanomaterials

1. Graphene and graphene oxide (XFNANO Materials Tech Co., Ltd., Nanjing, China).
2. ZnO nanoparticles (Aladdin, Shanghai, China).
3. Nitrocellulose membrane (Beyotime, Shanghai, China).
4. Scanning electron microscope (SEM, XL30-ESEM, Philips, Netherland).
5. Single-walled carbon nano tube (SWCNT) (XFNANO Materials Tech Co., Ltd., Nanjing, China).
6. Gold nanoparticles (AuNPs).

### 2.4 Fabrication of Device

1. Impedance converter network analyzer (AD5933, ADF4001, ADG884, LM358).
2. Microcontroller (Arduino board, C8051f005).

3. Bluetooth module (HC-06).
4. Smartphone.
5. Battery (3.3 V, 6 V, 9 V).
6. Peristaltic pump.
7. Potentiostat (AD8608, OPA2349).
8. Digital–analog converter (DAC8552).

## 3 Methods

### *3.1 General Structure of Smartphone-Based Biosensing System*

As shown in Fig. 2, the system is composed of detection circuit as the detector, modified electrodes as sensors and smartphone equipped with App.

1. After connecting to the App via Bluetooth, the detector began to work. Based on the sent parameters of smartphone, the circuit would generate electrical signal to the sensor.
2. Then, sensor converted the chemical reaction signals into measurable electrical signals. The circuit can convert the analog signals into digital signals and then transmit the data to the smartphone. The data can be converted to current value through the App.

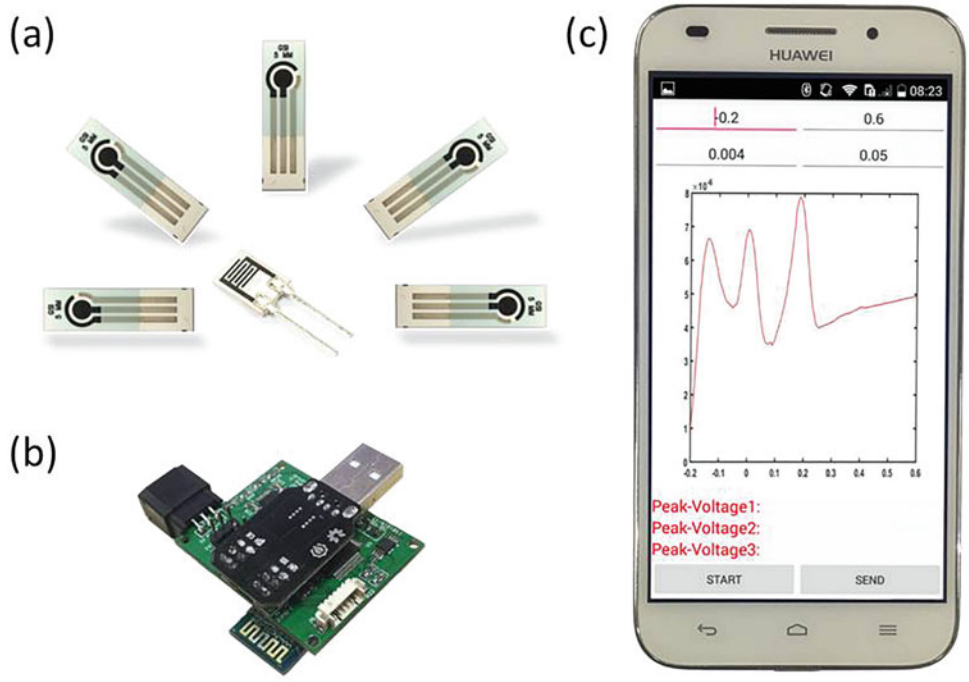


**Fig. 2** Components of the smartphone-based electrochemical system. (**a**) Screen-printed electrode and interdigital electrode. (**b**) Detector used in the system. (**c**) Smartphone equipped with app

3. Ultimately, the data curve can be displayed on the smartphone in real time.
4. After the detection, smartphone can be used to calculate the concentration of sample and display them on the screen.

### 3.2 Fabrication of Smartphone-Based Amperometry Detector

The handheld detector plays a key role in the smartphone-based biosensing system, linking smartphone with biosensors for application in point-of-care (POC) diagnostics. The handheld amperometry detector generally comprises a microcontroller unit, a potentiostat module, a power management module, a Bluetooth module, a digital–analog converter (DAC), and an analog–digital converter (ADC) unit, as shown in Fig. 3a. As an example, we describe smartphone-based differential pulse amperometry in detail.

1. The Bluetooth component accomplishes communication between the detector and smartphone. The microcontroller unit is used to control DAC to generate analog signals of differential pulse amperometry, which are applied to the electrodes. The ADC on the MCU converts the measured voltage signals to digital signals.
2. In differential pulse amperometry, two kinds of potential pulses are applied and the current at the end of each pulse is recorded.

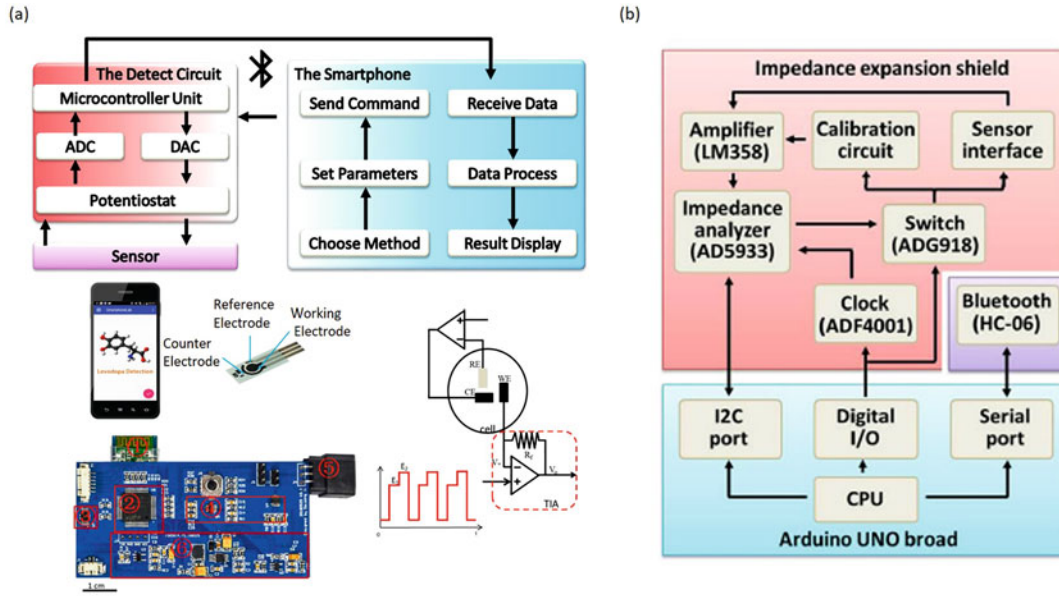


**Fig. 3** Schematic diagram of the smartphone-based electrochemical system. (**a**) Smartphone-based amperometry system. ① Bluetooth module ② microcontroller unit ③ digital–analog converter ④ potentiostat module ⑤ electrode socket ⑥ power management module. The schematic diagram of transimpedance amplifier and the wave form of differential pulse amperometry. (**b**) Schematic diagram of the smartphone-based impedance system

The difference between the two current samples is calculated as a function of time and displayed on the screen of smartphone.

3. The potentiostat applies an excitation voltage signal between the working electrode and the reference electrode of the sensor. The subsequent current is measured with a transimpedance amplifier (TIA). Thus, the current in the electrochemical cell is described by the following eq.

$$I = \frac{V_o - V_W}{R_f} \quad (1)$$

where $V_w$ and $V_o$ are the input potentials and output potentials of the amplifier, respectively, while $R_f$ is the value of feedback resistor.

4. The App on smartphones serves as the interface between smartphone and circuit, giving commands to the circuit and receiving digital signal from the circuit.
5. In addition, it processes the received data and plots the result. A five-point moving average filter is programmed in the App to reduce the influence of electrochemical and electronic noise for acquisition of accurate current.
6. At the same time, a power management module is also designed on the circuit to provide steady reference voltage for each module. The power units offer 5 V and 3.3 V voltages for the handheld amperometry detector.

The handheld impedance device, connected with the interdigital electrode, includes an impedance converter network analyzer, a microcontroller, and a Bluetooth module, as shown in Fig. 3b.

### 3.3 Fabrication of Smartphone-Based Impedance Detector

1. The impedance monitoring system is designed to record time-impedance scanning. The impedance analyzer sends out sinusoidal signals into the sensors as AC stimuli, and monitored feedback signals from the reference and counterelectrodes.
2. In presence of target substance, impedance signals can be changed and sent back to the smartphone through Bluetooth module, and displayed on the screen of smartphone.
3. The microcontroller, Arduino board, can receive commands from smartphone through Bluetooth module and control impedance parameters of AD5933 circuit, such as starting, finishing point and AC frequency of the stimuli signals. AD5933 circuit and Bluetooth module is integrated into an expansion printed circuit board, which can snap on the top of Arduino board.
4. An App is developed on smartphone to control impedance measurement, receive real-time data and plot impedance changes on screen. There are four buttons on welcome screen

of the App. The "Connect" button is used to search and link the portable impedance monitoring device with the smartphone through Bluetooth. The "Calibrate" button is setup to calibrate the measurement device with reference sample resistance. The "Start" and "Exit" buttons have functions to enter real-time monitoring user interface and terminate the program respectively.

5. In the measurement, impedance monitoring curve can be plotted in real time and impedance values are given synchronously.
6. Finally, the concentration of target substance can be reported on the screen of the smartphone.

### 3.4 Electrodes Preparation

Graphene and ZnO nanoparticles can be prepared for use in smartphone-based electrochemical biosensing system for the specific detection of VOCs. Interdigital electrode fabricated with fine pitch is modified with nitrocellulose, graphene, and ZnO nanoparticles.

#### 3.4.1 Modification of Electrode with Nanomaterials

1. The interdigital electrode contains six horizontal carbon electrodes with 4 mm in length and 300μm in width, with the six carbon electrodes spaced 400μm from each other.
2. Graphene (4 mg), ZnO nanoparticles (10 mg) and nitrocellulose membrane (1 cm × 1 cm) are mixed with methanol (2 mL) and stirred for 1 min at room temperature. The mixed solution (3μL) is dropped on the electrode uniformly for two times.
3. The electrodes are dried for 1 min to ensure complete evaporation of methanol.
4. The modified electrodes are then stored at room temperature for further usage in VOC detection

#### 3.4.2 rGO–APBA Modified Screen-Printed Electrode

rGO–APBA modified screen-printed electrode is prepared for use in smartphone-based cyclic voltammetry biosensing system for glucose detection.

1. GO is made by Hummers's method and dispersed in deionized water (5 mL) for the dispersion of GO nanosheets.
2. APBA is immobilized to GO via NHS (5 mg) and EDC (2 mg). These two solutions are added into the GO supernatant (5 mL) and sonically oscillated in ice–water bath (0 °C) for 1 h and then mixed with APBA.
3. The solution is oscillated for 1 min and then incubated at 0 °C for 4 h. Then the mixed solution is centrifuged at 5600 × *g* (4 °C) for 2 h to obtain the clear and well-precipitated GO–APBA sediment.
4. After the preparation, the GO–APBA solution (50μL) and sodium sulfate (50μL, 0.1 M) are dropped onto SPE. In

order to reduce the GO-APBA for electrode modification through CV, initial voltage (−1 V), final voltage (1 V), cycles (20), and scan rate (0.05 V/s) are configured with the App of the smartphone. The modified electrode can be stored at indoor temperature (25 °C) for glucose detection.

*3.4.3 rGO–AuNP Modified Screen-Printed Electrode Voltammetry Biosensing*

rGO–AuNP modified screen-printed electrode is prepared for use in smartphone-based differential pulse voltammetry biosensing system for ascorbic acid, dopamine, and uric acid detection.

1. Graphene oxide prepared by Hummers's method is dispersed in phosphate buffer solution (0.1 M) via sonically oscillation in ice–water bath for 3 h. The solution of modification is the mixture of the graphene oxide (1 mg/mL) and chloroauric acid solution ($HAuCl_4$, 0.1 mM) at a volume ratio of 10:1.
2. To modify the electrodes, graphene oxide–$HAuCl_4$ solution (100μL) is spotted onto the electrodes. Then the reduced graphene oxide–gold nanoparticles are modified on the electrode through cyclic voltammetry. The initial voltage (0.2 V), final voltage (−1.4 V), cycles (5), and scan rate (0.05 V/s) are configured with the App of the smartphone. After modification, the screen-printed electrodes are washed by water and used for detection after drying.

   SWCNT–AuNP modified screen-printed electrode is prepared to be use in smartphone-based differential pulse amperometry biosensing system for levodopa detection.
3. Gold nanoparticles are prepared as follows. First, 10 mL of chloroauric acid ($HAuCl_4$, 0.01%) is heated to 80 °C with continuous stirring. Second, 185μL trisodium citrate ($Na_3C_6H_5O_7$, 1%) is added quickly for the reduction of chloroauric acid at 80 °C. The solution is kept at 80 °C for 60 min with continuous stirring and then cooled down to room temperature through stirring for 15 min. Third, the obtained gold nanoparticles solution is stored at 4 °C in an opaque glass container.
4. The chitosan solution (0.5%) is obtained via dissolving 50 mg chitosan in 10 mL acetic acid (1%).
5. After the above preparations, the gold nanoparticles /single-wall carbon nanotubes /chitosan solution is obtained by dissolving the centrifugate of 1 mL gold nanoparticles solution and 2 mg single-wall carbon nanotubes in 1 mL chitosan solution with ultrasonication for 2 h.
6. After these steps, 6.0μL gold nanoparticles /single-wall carbon nanotubes /chitosan solution is dropped evenly onto the working electrode and the electrode is air-dried for 30 min.

### 3.5 Immobilization of Ligands

#### 3.5.1 Immobilization of Antibodies

Immunoreaction between antigen and antibody is a common bio-inspired strategy in the fabrication of biosensors. The interaction between antigen and antibody is highly specific, thereby ensuring highly accurate detection of analyte.

1. Nitrocellulose (20μL, 5%) dissolved in methanol is dropcasted onto the working electrode. The electrode is air-dried for 10 min at room temperature for the evaporation of methanol.
2. Anti-BSA (20μL, 100μg/mL) is evenly injected onto the nitrocellulose membrane-modified electrode. The anti-BSA is incubated at 25 °C for 2 h to guarantee the anti-BSA are totally embedded on the nitrocellulose membrane.
3. The electrodes are washed with PBS, dried using nitrogen gas and ready to be used for immunodetections of BSA.

#### 3.5.2 Immobilization of Peptide

Enzymatic reaction is a typically used protein recognition method in bio-detections. Peptides are usually immobilized on electrodes via two methods, namely direct physical absorption and self-assembly.

Direct Physical Absorption

1. Peptide solution (30μL, 250μg/mL) are spotted on the surface of working electrodes and incubated for 12 h at 4 °C.
2. The peptide is immobilized on the electrode surface via physical absorption and the electrodes are stored at 4 °C.

Self-Assembly

1. The gold interdigital electrodes are rinsed thoroughly with ethanol and ultrapure water, respectively to remove any organic residues, and dried in nitrogen.
2. Polyethylene glycol (HS-PEG-COOH, 200μL, 1.5 mg/mL) is added to the electrodes and incubated for approximately 24 h to generate stable Au-S bonds.
3. Unbound HS-PEG-COOH is removed by washing with ultrapure water for the establishment of self-assembly monolayer of PEG on the electrodes.
4. Equal volume (60μL) of EDC (8 mg/mL) and NHS (16 mg/mL) solutions are added successively to the electrodes to activate the carboxyl group of COOH-PEG-SH for 15 min.
5. After adjusting the pH to 7.2–7.5 with sodium bicarbonate, octapeptide solution (50μL, 100μg/mL) is added and incubated for 2 h to form amide linkages between octapeptide and HS-PEG-COOH on the electrodes.
6. The electrodes are washed with ultrapure water to remove unbound octapeptides.
7. Repeat **steps 4** and **5** but replacing the octapeptide solution with BSA solution. Finally, layers containing PEG, octapeptide,

BSA are formed respectively on the electrodes from bottom to top for detection of protein.

8. The bio-modified electrodes are kept at 4 °C and remained active for about 2 months.

## 3.6 Smartphone-Based Biosensor Detection

### 3.6.1 ZnO and Graphene Modified Electrodes for VOC Detection

Volatile organic compounds (VOCs) are groups of saturated, unsaturated, and oxygenated derivatives. and the VOCs in exhaled breath can reflect the physiological and pathological conditions of humans to some degree. Gas sensor based on metal oxide nanoparticles can only operate at high temperature, resulting in high power consumption and obstruction to miniaturization. Graphene-based gas sensors have poor selectivity and reversibility due to indistinctive gas adsorption via weak van der Waals forces. Thus, a combination of ZnO and graphene is anticipated to achieve sensitive and specific detection of VOCs at room temperature [31].

1. The smartphone-based VOC sensing system is set up as shown in Fig. 4a. Pure air bottle, peristaltic pump and gas bottles are connected to a sealed glass container (sensing container). The graphene, ZnO and nitrocellulose modified interdigital electrode in the sensing container is connected to the constructed impedance device.
2. Pure air is purged into the sensing container for 90 s to establish baseline. Acetone is then purged for 60 s and the impedance ($R_S$) change is recorded by the impedance device.
3. The $R_S$ increased rapidly to a plateau phase and is stable afterwards. At 150 s, pure air is purged to remove acetone. The $R_S$ decrease quickly and returned to the initial base line, indicating the rapid response and good reversibility of the modified electrode.
4. Different concentrations of acetone (2 ppm, 4 ppm, 6 ppm, 8 ppm, 10 ppm) are purged into the sensing container and their respective $R_S$ are shown in Fig. 4b. Good linear relationship is observed for $R_S$ against acetone concentrations.
5. Test of human exhaled breath collected at rest and while exercise are illustrated in Fig. 4c. The main composition of the exhaled breath of subjected after exercising for 30 min is acetone, which is in agreement with the fact that acetone concentration increased during exercise.

### 3.6.2 Enzymatic Cleavage-Assisted Explosive Detection

Explosive detections are significant due to their threats to public security and human health as pollutants in natural water, soil and air. TNT-specific peptides are employed as bio-sensitive components for the detection of 2,4,6-trinitrotoluene (TNT) (Fig. 5a). When exposed to TNT, the biosensor showed significant increase in impedance at low frequency range. Based on this, the TNT can be detected using the smartphone-based biosensing system [30].

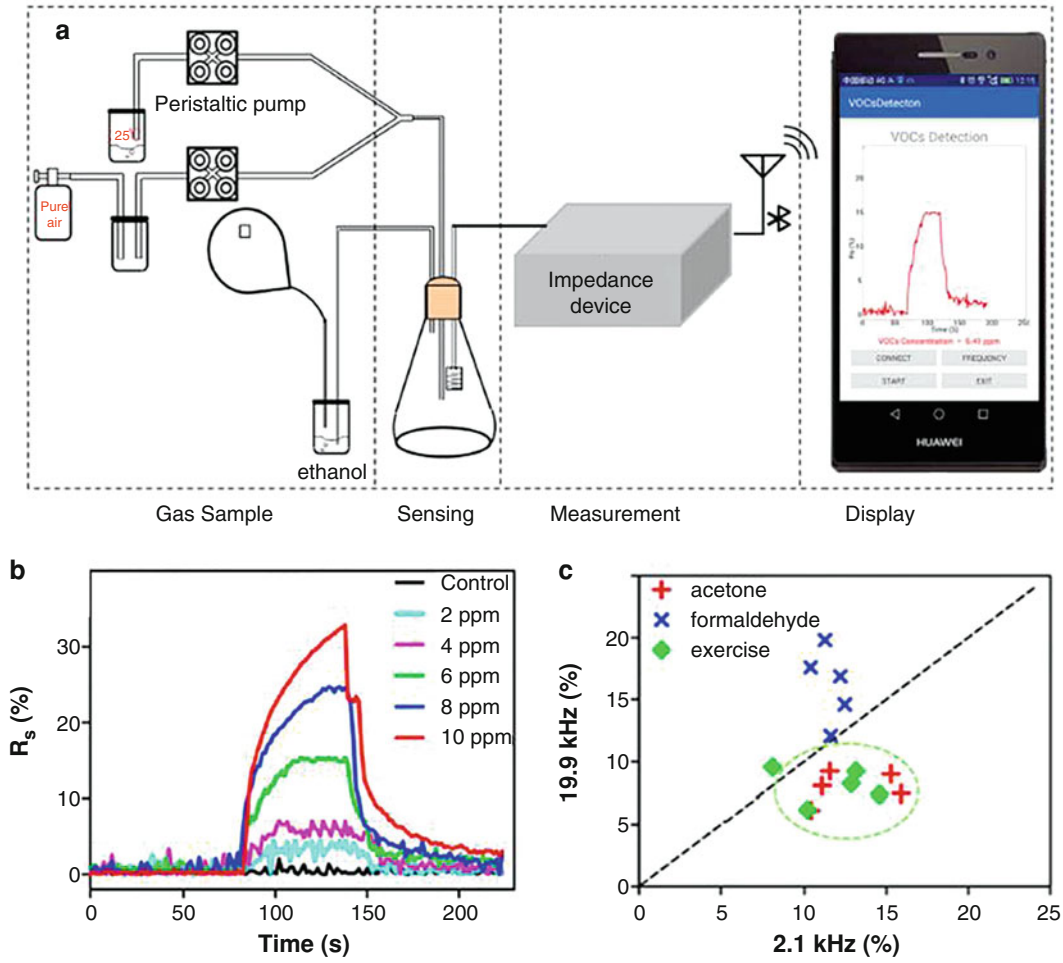


**Fig. 4** Smartphone-based system for VOC detection. (**a**) The setup of the smartphone-based gas sensing system with peristaltic pump purging VOCs to the sensing container. The impedance device detect the impedance change of the electrode and communicate with smartphone via Bluetooth. (**b**) Real-time $R_S$ to acetone of different concentrations. (**c**) $R_S$ of exhaled breath after 30 min exercise with AC impedance change larger at 2.1 kHz, indicating the presence of more acetone

1. 10μL TNT and 10μL $K_4[Fe(CN)_6]/K_3[Fe(CN)_6]$ are added to the TNT-specific peptide functionalized electrode. EIS is performed with frequency range of 10 kHz to 1000 kHz alternating voltage of 200 mV for 120 s. The impedance change is largest at 20 kHz, which is set at the optimal frequency for further impedance measurement as shown in Fig. 5b.
2. Different concentrations ($1 \times 10^{-3}$, $1 \times 10^{-4}$, $1 \times 10^{-5}$ M) of TNT are prepared with anhydrous methanol. 10μL TNT is added to the electrode at 50 s and the real-time impedance change is normalized and displayed on smartphone (Fig. 5c).

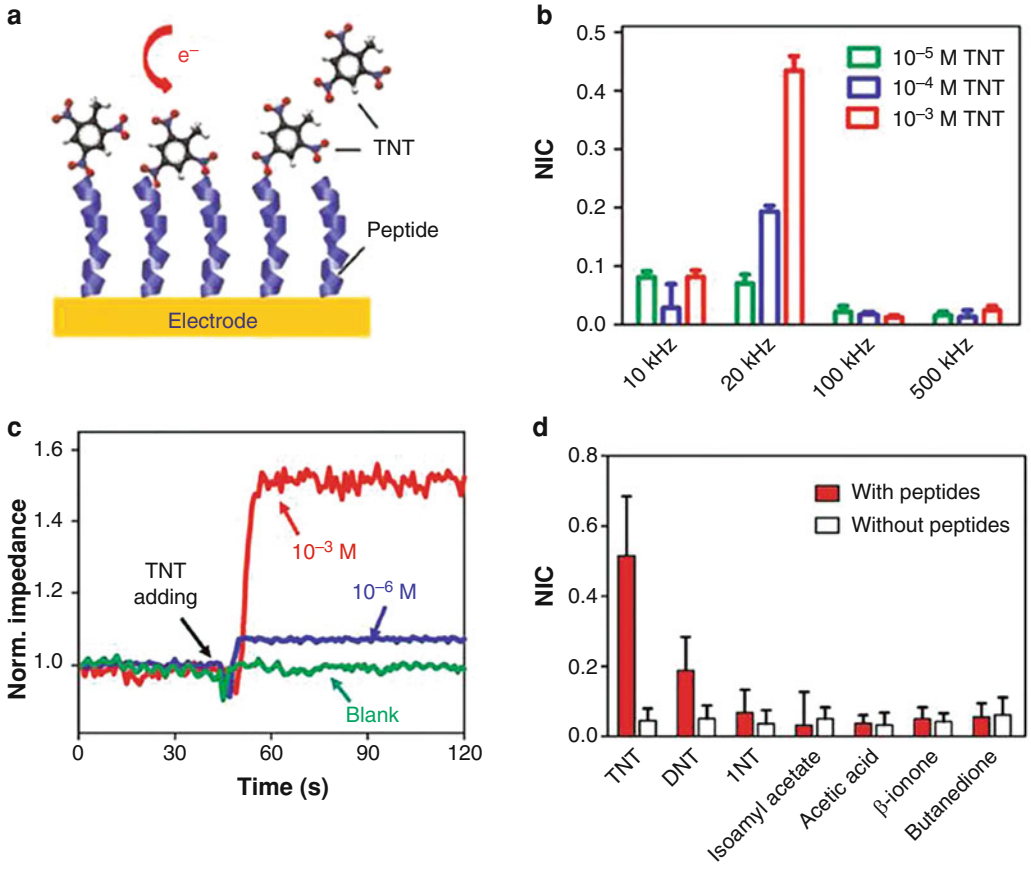


**Fig. 5** Smartphone-based system for TNT detection. (**a**) Binding of TNT to peptide immobilized electrode can block electron transfer, thereby increasing interface impedance. (**b**) Statistics for NIC with TNT at different frequency points where 20 kHz was chosen as the optimum value. (**c**) Real-time monitoring of TNT with different concentrations. (**d**) Specificity test of the system with DNT, 1NT, isoamyl acetate, acetic acid, beta-ionone, and butanedione at a concentration of 1 mM, respectively (mean ± SD, $n = 10$)

3. To confirm the function of TNT-specific peptides, electrodes without functionalization are employed for TNT and other interfering substances (DNT, 1NT, isoamyl acetate, acetic acid, beta-ionone, butanedione) detection. Figure 5d shows that only electrodes functionalized with TNT-specific peptides displayed response specifically in the presence of TNT.

### *3.6.3 Impedance Spectroscopy for Protein Detection*

Proteins play crucial roles in biological activities and show close relationship with human diseases as biomarkers. Therefore, rapid, sensitive, selective and portable sensing system for protein detection is in high demand for point-of-care (POC) testing. Smartphone-based biosensor system developed with electrochemical impedance spectroscopy (EIS) is promising in delivering POCT of protein [18].

(A) Immunodetection of BSA

1. For immunodetection of BSA, anti-BSA is immobilized on the nitrocellulose membrane modified working electrode as shown in Fig. 6a. With the addition of BSA, conjunctions of BSA and anti-BSA block the electron transfer and increased the interface impedance.
2. The EIS is scanned from 10 Hz to 10 kHz with AC stimuli fixed at 200 mV and bias voltage of 1 V. 5 mM $K_4[Fe(CN)_6]$/$K_3[Fe(CN)_6]$ is added to the electrode as the supporting electrolyte.
3. Different concentrations of BSA from 5μg/mL to 100μg/mL are incubated with the anti-BSA immobilized electrode. Figure 6b showed that the impedance increased with increasing

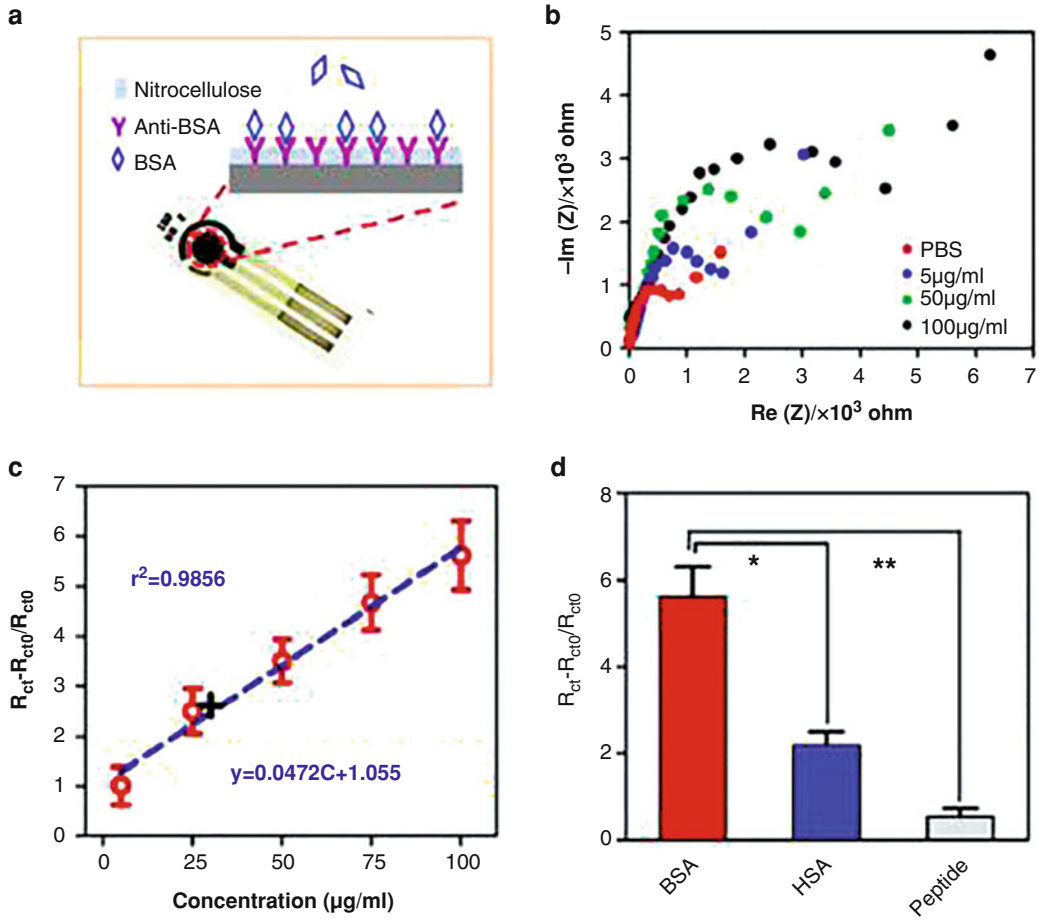


**Fig. 6** Immunodetection of BSA using smartphone-based system. (**a**) Screen-printed electrode was modified nitrocellulose membrane for the immobilization of anti-BSA to perform BSA detection. (**b**) Nyquist plot of EIS measurement with increasing concentration of BSA. (**c**) Linear-dose dependent responses of normalized impedance versus concentration of BSA. (**d**) Selectivity test with BSA, HSA, and eleven-peptide (mean ± SD, $n = 5$)

BSA concentration and linear relationship between impedance changes against BSA concentration is plotted in Fig. 6c.

4. To test the specificity of the anti-BSA immobilized electrode, BSA, HSA and eleven-peptide are added and the impedance changes are illustrated in Fig. 6d. Normalized indexes of impedance responses to BSA are significantly larger than HSA and peptide, indicating the good specificity of the biosensor.

(B) Immunodetection of BSA Thrombin

Smartphone-based biosensing system combined with enzymatic cleavages of proteases is applied for the detection of thrombin. As shown in Fig. 7a, PEG, octapeptide and BSA are immobilized on the surface of interdigital gold electrode.

1. Thrombin (1μg/mL) is added to the BSA-conjugated octapeptide immobilized electrode and incubated for 20 min, 40 min and 60 min before EIS measurement as displayed in Fig. 7b. In

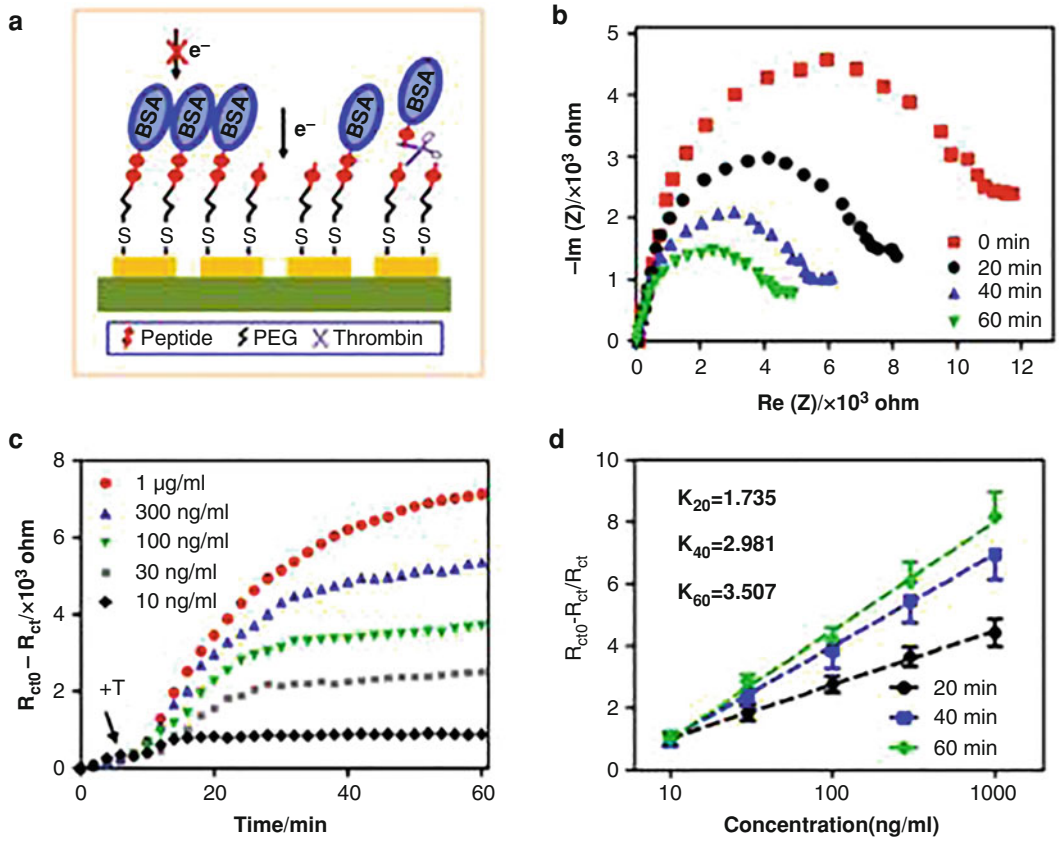


**Fig. 7** Smartphone-based system for thrombin detection. (**a**) Interdigital gold electrode was modified with PEG, octapeptide and BSA via self-assembly for thrombin detection. (**b**) Nyquist plots of EIS with 1μg/mL of thrombin for 60 min. (**c**) Impedance changes of time-dependent responses for different concentrations of thrombin. (**d**) Linear dose-dependent responses of normalized impedance versus thrombin concentration at different incubation times (mean ± SD, $n = 5$)

the presence of thrombin, it cleaved the Arg-Gly bonds of the octapeptides, removing BSA from the electrodes, thereby improving charge transfer capacities of the electrode.

2. Different concentrations of thrombin (1μg/mL, 300 ng/mL, 100 ng/mL, 30 ng/mL and 10 ng/mL) are prepared, and incubated for 60 min. It can be observed in Fig. 7c that the impedance increased with time and reached plateau around 60 min, with high thrombin concentration having more rapid and larger impedance changes.
3. Linear relationship is obtained with normalized impedance change against log concentrations of thrombin shown in Fig. 7d. The detection limit of the system for thrombin detection is 2.97 ng/mL.

*3.6.4 rGO–APBA Modified Electrodes for Glucose Detection*

Glucose plays an important role in the field of biology as it is the energy source of living cells and the intermediate product of metabolism. Hence, rapid, sensitive, selective and portable sensing system for glucose detection is in high demand for point-of-care (POC) testing. As shown in Fig. 8, smartphone-based electrochemical system developed with cyclic voltammetry (CV) is promising in delivering POCT of glucose [26].

1. For glucose detection, SPE is linked with the sensor electrical sockets of the handheld CV detector to execute electrochemical measurement. The voltage range is set on the App from −0.8 V to 0.8 V and scan rate is 0.01 V/s.
2. Glucose is diluted into five different concentrations with human blood serum. 50μL glucose and 50μL redox couple is added to the electrode, while blood serum without glucose is used as blank control.
3. Uric acid (UA), ascorbic acid (AA), sodium chloride (NaCl), and bovine serum albumin (BSA) are used for selective tests. The latter three substances are prepared at 5 mM in deionized water and blood serum, while uric acid (5 mM) is diluted with sodium hydroxide (NaOH, 1 M).
4. A dose-dependent curve of the smartphone-based CV system is adjusted with normalized peak-to-peak current change based on responses of glucose at different concentrations from 0.1 mM to 10 mM. The limit of detection (LoD) for glucose is 0.026 mM with 3δ/slope calculation.

*3.6.5 rGO–AuNP Modified Electrodes for Simultaneous Detection of Ascorbic Acid, Dopamine, and Uric Acid*

It is important to simultaneously determine multi-analytes in mixed solution for disease diagnosis. Ascorbic acid (AA), dopamine (DA), and uric acid (UA) are essential and coexisting biomolecules in human metabolism process and biological fluids, such as blood and urine. Since it is necessary to monitor biomolecules in real time and their oxidation potentials are similar, developing a highly

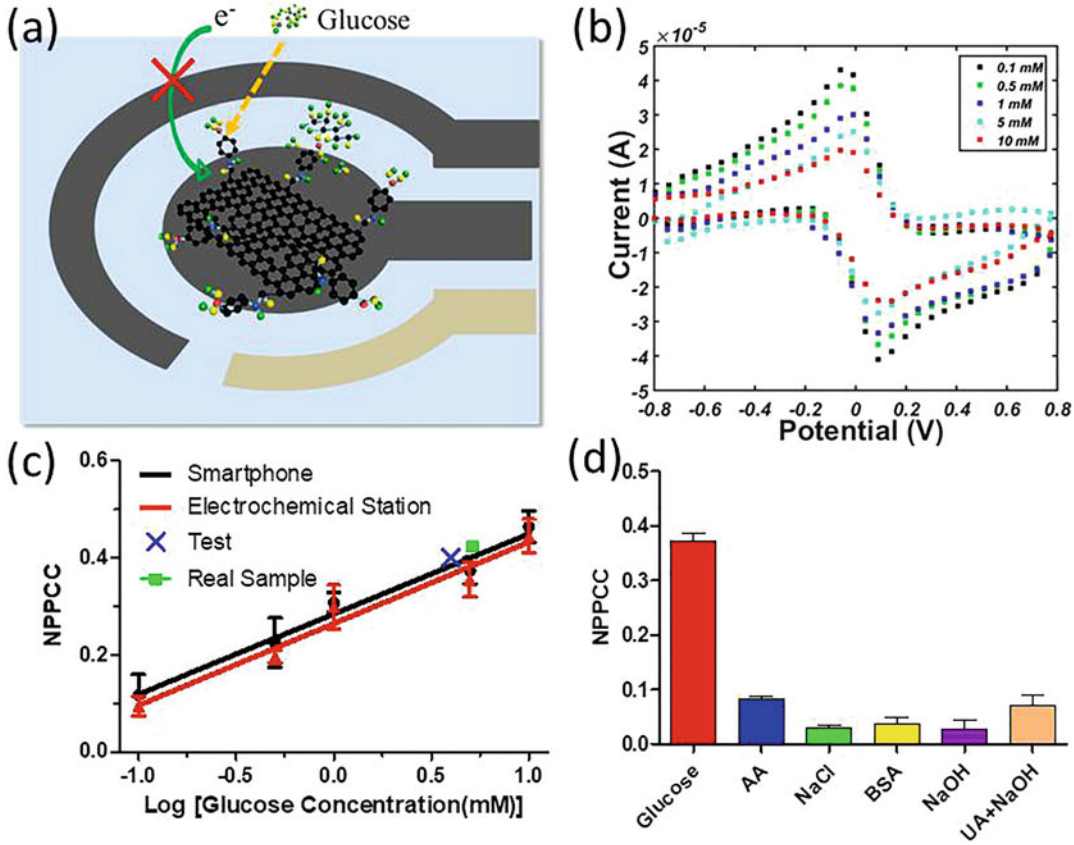


**Fig. 8** Smartphone-based system for glucose detection. (**a**) The detection principle of rGO–APBA modified screen-printed electrode for glucose detection. (**b**) CV measurement using the system for detection of glucose of different concentrations. (**c**) The dose-dependent curve of the system (black circle) and the commercial electrochemical workstation (red triangle). The NPPCC response to prepared glucose solution at $4 \times 10^{-3}$ M is shown as blue cross. The real sample of blood glucose is shown as green square. (**d**) Statistic for selective testing for glucose

sensitive and selective method with portable device to monitor them is very useful in biomedical research, diagnosis, and pathology (Fig. 9) [27].

1. Phosphate buffer solution (0.1 M), artificial urine and real urine are prepared as solvents. Ascorbic acid, dopamine, and uric acid are dissolved in phosphate buffer solution and artificial urine respectively to gain a series of ascorbic acid, dopamine, and uric acid solutions with different concentrations.
2. For simultaneous detection of ascorbic acid, ascorbic acid solutions with different concentrations (0.06, 0.08, 0.11, 0.15, 0.225, 0.30, 0.375 mM) are mixed with dopamine (0.075 mM) and uric acid (0.09 mM). For simultaneous detection of dopamine, dopamine solutions with different concentrations (0.02, 0.03, 0.05, 0.075, 0.10, 0.125, 0.16 mM) are

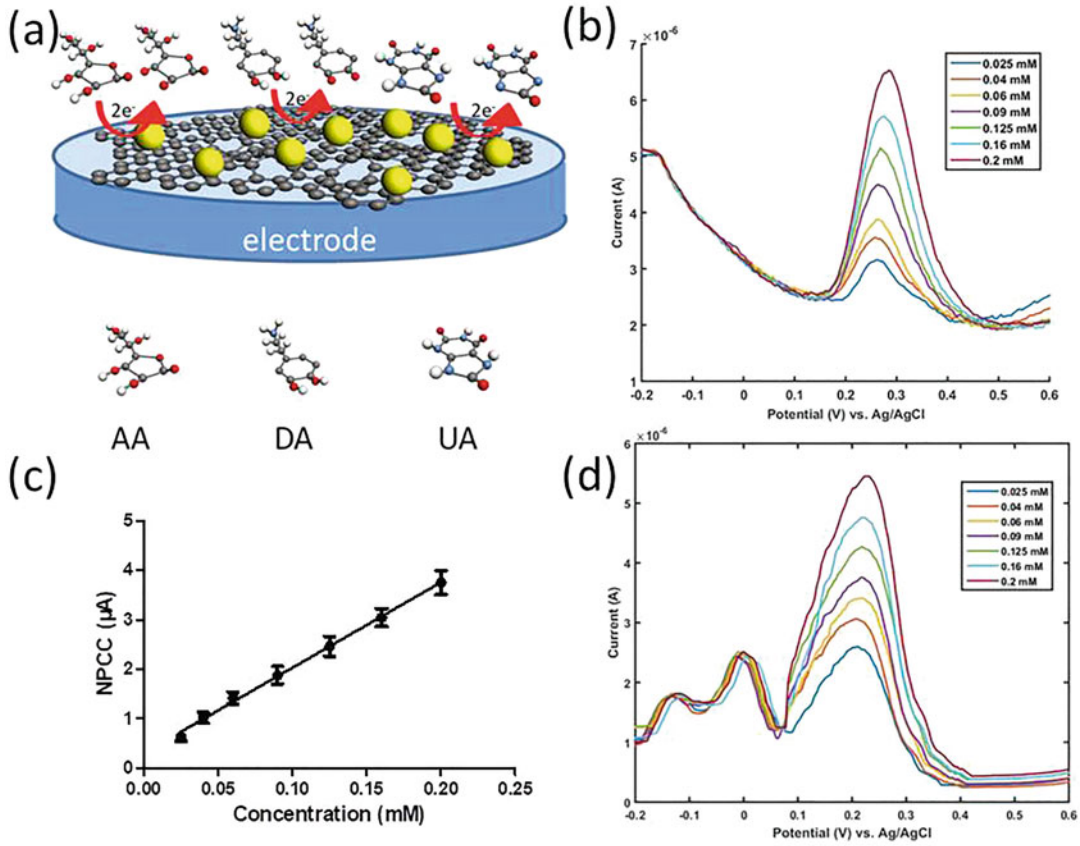


**Fig. 9** Smartphone-based systems for ascorbic acid, dopamine, and uric acid detection. (**a**) The detection principle of rGO–APBA modified screen-printed electrode for ascorbic acid, dopamine, and uric acid detection. (**b**) Differential pulse voltammetry measurement using the system for detection of uric acid at different concentrations. (**c**) The dose-dependent curve of uric acid. (**d**) The simultaneous detection for ascorbic acid, dopamine, and uric acid using smartphone-based voltammetry system

mixed with ascorbic acid (0.15 mM) and uric acid (0.09 mM). For simultaneous detection of uric acid, uric acid solutions with different concentrations (0.025, 0.04, 0.06, 0.09, 0.125, 0.16, 0.20 mM) are mixed with ascorbic acid (0.15 mM) and dopamine (0.075 mM).

3. The mixed solution are detected by the smartphone-based integrated voltammetry system through differential pulse voltammetry (initial voltage −0.2 V, final voltage 0.6 V, pulse voltage 50 mV, step voltage 4 mV).
4. Different concentrations of uric acid in phosphate buffer solution are detected at different potentials, respectively. The peak currents of differential pulse voltammetry curves increase with higher concentrations of uric acid.

5. Three peak currents are observed at −120 mV, 10 mV, and 220 mV, which correspond to ascorbic acid, dopamine, and uric acid, respectively. The peak currents of these three molecules increase linearly with their concentrations.

### 3.6.6 SWCNT–AuNP Modified Electrodes for Levodopa Detection

Parkinson's disease (PD) is a neurodegenerative disease of the central nervous system, and commonly occurs in the elderly. Traditional therapies replenish excessive dopamine or levodopa in patients, resulting in the activation of wrong neurons. Therefore, the rapid, convenient, and real-time levodopa concentration detection in vivo not only reduces side effects caused by overreplenishment of levodopa but also provides a reference for doctor's diagnosis, improving the quality of life of Parkinson's disease patients [17].

1. As shown in Fig. 10, levodopa solutions of 0.5, 1, 2.5, 5, 10, 25, 50, 75, 100, 150, and 200μM are obtained by dissolving levodopa into artificial serum. With gold nanoparticles and

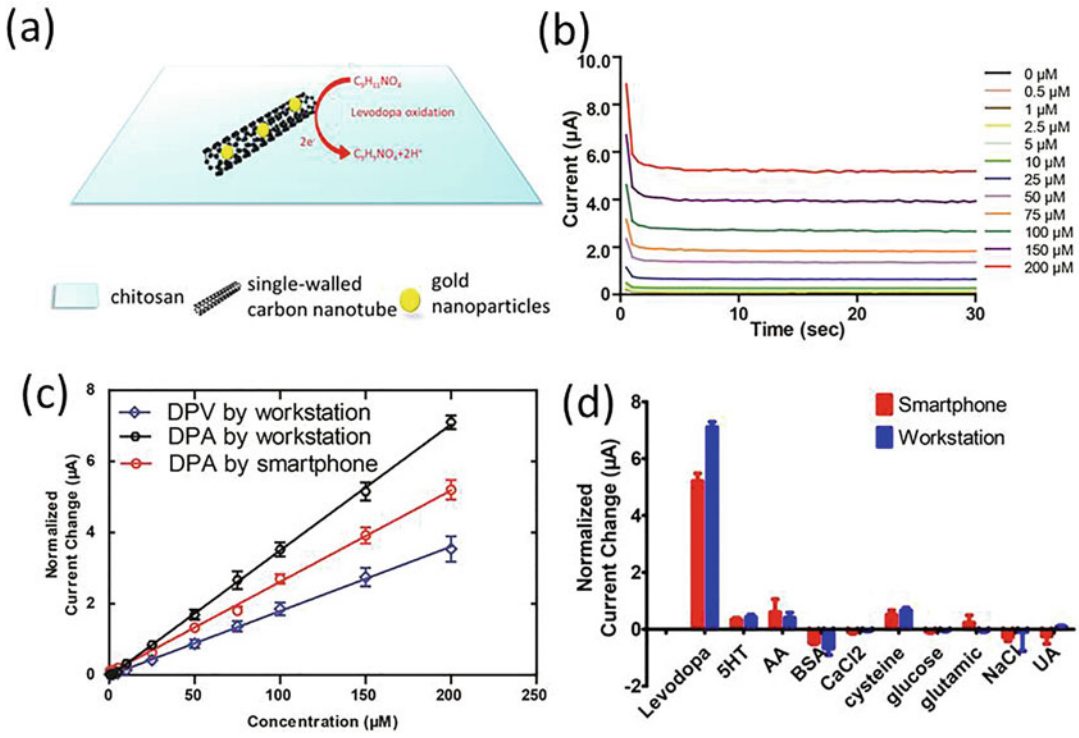


**Fig. 10** Smartphone-based system for levodopa detection. (**a**) Oxidation of levodopa on the surface of the modified working electrode. (**b**) Differential pulse amperometry measurement using the system for detection of levodopa at different concentrations. (**c**) The dose-dependent curve of levodopa using the system and electrochemical workstation with differential pulse amperometry (DPA) and differential pulse voltammetry (DPV), $n = 3$. (**d**) The diagram of specific test of levodopa using smartphone-based system and electrochemical workstation through differential pulse amperometry

single-wall carbon nanotubes modified screen-printed electrodes, differential pulse amperometry are performed by smartphone-based electrochemical system.

2. When the levodopa reacted on the surface of the electrode, the current values changed obviously compared to the serum without levodopa. The currents of levodopa at stability climbed from 0.1μA to 9μA linearly as the concentrations of levodopa increased from 0.5μM to 200μM.
3. The limit of detection (LOD) of levodopa with the system is estimated at 0.1μM with 3δ/slope calculation for the dose-dependent fitting curve in serum.

## 4 Notes

1. Phosphate buffer saline (PBS) is used as the solvent for proteins. The solution is prepared by dissolving 137 mM NaCl, 2.68 mM KCl, 1.47 mM $KH_2PO_4$, and 8.10 mM $Na_2HPO_4$ in pure water and pH is fixed at 7.4.
2. Peptides used in our study are synthesized by the standard solid phase method. Synthesized peptides are tested by high performance liquid chromatography (HPLC) and mass spectrometry (MS) to verify amino acid sequence and purity. The peptides are stored in the form of freeze-dried powders before experiments and dissolved in PBS at 500μg/mL.

## Acknowledgments

This work was supported by National Key Research and Development Program (Grant No. 2018YFC1707701), the National Natural Science Foundation of China (Grant No. 81801793, 31671007), the China Postdoctoral Science Foundation (Grant No. 2018 M630677, 2019 T120518).

### References

1. Turner APF (2013) Biosensors: sense and sensibility. Chem Soc Rev 42(8):3184–3196. https://doi.org/10.1039/c3cs35528d
2. Turner APF (2000) Biochemistry—biosensors sense and sensitivity. Science 290 (5495):1315–1317. https://doi.org/10.1126/science.290.5495.1315
3. Healy DA, Hayes CJ, Leonard P, McKenna L, O'Kennedy R (2007) Biosensor developments: application to prostate-specific antigen detection. Trends Biotechnol 25(3):125–131
4. Goode J, Rushworth J, Millner P (2014) Biosensor regeneration: a review of common techniques and outcomes. Langmuir 31 (23):6267–6276
5. Velasco-Garcia MN, Mottram T (2003) Biosensor technology addressing agricultural problems. Biosyst Eng 84(1):1–12
6. Fan X, White IM, Shopova SI, Zhu H, Suter JD, Sun Y (2008) Sensitive optical biosensors for unlabeled targets: a review. Anal Chim Acta 620(1–2):8–26

7. Védrine C, Leclerc J-C, Durrieu C, Tran-Minh C (2003) Optical whole-cell biosensor using Chlorella vulgaris designed for monitoring herbicides. Biosens Bioelectron 18(4):457–463
8. Gorton L, Lindgren A, Larsson T, Munteanu F, Ruzgas T, Gazaryan I (1999) Direct electron transfer between heme-containing enzymes and electrodes as basis for third generation biosensors. Anal Chim Acta 400(1–3):91–108
9. Conroy PJ, Hearty S, Leonard P, O'Kennedy RJ (2009) Antibody production, design and use for biosensor-based applications. In: Seminars in cell & developmental biology, vol vol 1. Elsevier, pp 10–26
10. Wang J (2002) Electrochemical nucleic acid biosensors. Anal Chim Acta 469(1):63–71
11. Brandt O, Hoheisel JD (2004) Peptide nucleic acids on microarrays and other biosensors. Trends Biotechnol 22(12):617–622
12. Singh R, Mukherjee MD, Sumana G, Gupta RK, Sood S, Malhotra B (2014) Biosensors for pathogen detection: a smart approach towards clinical diagnosis. Sensors Actuators B Chem 197:385–404
13. Joseph S, Rusling JF, Lvov YM, Friedberg T, Fuhr U (2003) An amperometric biosensor with human CYP3A4 as a novel drug screening tool. Biochem Pharmacol 65(11):1817–1826
14. Wang J, Rivas G, Cai X, Palecek E, Nielsen P, Shiraishi H, Dontha N, Luo D, Parrado C, Chicharro M (1997) DNA electrochemical biosensors for environmental monitoring. A review. Anal Chim Acta 347(1–2):1–8
15. Balakrishnan SR, Hashim U, Letchumanan G, Kashif M, Ruslinda A, Liu W, Veeradasan P, Prasad RH, Foo K, Poopalan P (2014) Development of highly sensitive polysilicon nanogap with APTES/GOx based lab-on-chip biosensor to determine low levels of salivary glucose. Sensors Actuators A Phys 220:101–111
16. Zhang D, Liu Q (2016) Biosensors and bioelectronics on smartphone for portable biochemical detection. Biosens Bioelectron 75:273–284
17. Ji D, Xu N, Liu Z, Shi Z, Low SS, Liu J, Cheng C, Zhu J, Zhang T, Xu H (2019) Smartphone-based differential pulse amperometry system for real-time monitoring of levodopa with carbon nanotubes and gold nanoparticles modified screen-printing electrodes. Biosens Bioelectron 129:216–223
18. Zhang D, Lu Y, Zhang Q, Liu L, Li S, Yao Y, Jiang J, Liu GL, Liu Q (2016) Protein detecting with smartphone-controlled electrochemical impedance spectroscopy for point-of-care applications. Sensors Actuators B Chem 222:994–1002
19. Sood VR, Gururajan R, Hafeez-Baig A, Wickramasinghe N (2018) Adoption of mobile devices in the Australian healthcare: a conceptual framework approach. In: Technology adoption and social issues: concepts, methodologies, tools, and applications. IGI Global, pp 954–977
20. Bisetty K (2018) Smartphone based bioanalytical and diagnosis applications: a review. Biosens Bioelectron 102:136–149
21. Lisdat F, Schäfer D (2008) The use of electrochemical impedance spectroscopy for biosensing. Anal Bioanal Chem 391(5):1555
22. Biran I, Babai R, Levcov K, Rishpon J, Ron EZ (2000) Online and in situ monitoring of environmental pollutants: electrochemical biosensing of cadmium. Environ Microbiol 2 (3):285–290
23. Kerman K, Kobayashi M, Tamiya E (2003) Recent trends in electrochemical DNA biosensor technology. Meas Sci Technol 15(2):R1
24. Guo J (2016) Uric acid monitoring with a smartphone as the electrochemical analyzer. Anal Chem 88(24):11986–11989
25. Nemiroski A, Christodouleas DC, Hennek JW, Kumar AA, Maxwell EJ, Fernández-Abedul MT, Whitesides GM (2014) Universal mobile electrochemical detector designed for use in resource-limited applications. Proc Natl Acad Sci 111(33):11984–11989
26. Ji D, Liu L, Li S, Chen C, Lu Y, Wu J, Liu Q (2017) Smartphone-based cyclic voltammetry system with graphene modified screen printed electrodes for glucose detection. Biosens Bioelectron 98:449–456
27. Ji D, Liu Z, Liu L, Low SS, Lu Y, Yu X, Zhu L, Li C, Liu Q (2018) Smartphone-based integrated voltammetry system for simultaneous detection of ascorbic acid, dopamine, and uric acid with graphene and gold nanoparticles modified screen-printed electrodes. Biosens Bioelectron 119:55–62
28. Sun A, Wambach T, Venkatesh A, Hall DA (2014) A low-cost smartphone-based electrochemical biosensor for point-of-care diagnostics. In: Biomedical circuits and systems conference (BioCAS), 2014 IEEE. IEEE, pp 312–315
29. Zhang L, Yang W, Yang Y, Liu H, Gu Z (2015) Smartphone-based point-of-care testing of salivary α-amylase for personal psychological measurement. Analyst 140(21):7399–7406
30. Zhang D, Jiang J, Chen J, Zhang Q, Lu Y, Yao Y, Li S, Liu GL, Liu Q (2015) Smartphone-based portable biosensing system

using impedance measurement with printed electrodes for 2, 4, 6-trinitrotoluene (TNT) detection. Biosens Bioelectron 70:81–88

31. Liu L, Zhang D, Zhang Q, Chen X, Xu G, Lu Y, Liu Q (2017) Smartphone-based sensing system using ZnO and graphene modified electrodes for VOCs detection. Biosens Bioelectron 93:94–101
32. Guo J (2017) Smartphone-powered electrochemical dongle for point-of-care monitoring of blood β-ketone. Anal Chem 89 (17):8609–8613
33. Wang X, Gartia MR, Jiang J, Chang T-W, Qian J, Liu Y, Liu X, Liu GL (2015) Audio jack based miniaturized mobile phone electrochemical sensing platform. Sensors Actuators B Chem 209:677–685
34. Martínez-Pérez B, De La Torre-Díez I, López-Coronado M (2013) Mobile health applications for the most prevalent conditions by the World Health Organization: review and analysis. J Med Internet Res 15(6):e120
35. Guo J, Ma X (2017) Simultaneous monitoring of glucose and uric acid on a single test strip with dual channels. Biosens Bioelectron 94:415–419
36. Aronoff-Spencer E, Venkatesh A, Sun A, Brickner H, Looney D, Hall DA (2016) Detection of hepatitis C core antibody by dual-affinity yeast chimera and smartphone-based electrochemical sensing. Biosens Bioelectron 86:690–696
37. Xu D, Huang X, Guo J, Ma X (2018) Automatic smartphone-based microfluidic biosensor system at the point of care. Biosens Bioelectron 110:78–88

# Chapter 27

# Preparation of Notch-4 Receptor Containing Quartz Crystal Microbalance Biosensor for MDA MB 231 Cancer Cell Detection

**Monireh Bakhshpour, Ayse Kevser Piskin, Handan Yavuz, and Adil Denizli**

## Abstract

Quartz crystal microbalance (QCM) is a highly sensitive system that is used as a biosensor for biomolecules and cells. Detection and characterization of cancer cells in circulation or biopsy samples is of crucial importance for cancer diagnosis. Here, we introduce approaches for breast cancer cell detection via their surface molecules. The sensor system is based on preliminary coating of QCM chip with polymeric nanoparticles to increase the surface area and allow for the attachment of proteins to the chip surface. This is followed by the attachment of a specific protein in order to functionalize the chip. Breast cancer cells and fibroblast cells as control are cultured and applied to this chip. The functionalized QCM system can detect breast cancer cells with high affinity and selectivity. Here, we present the preparation methods of QCM-based sensors for selective detection of MDA MB 231 cancer cells. Selectivity of QCM-based sensor is carried out in the presence of L929 mouse fibroblast cells.

**Key words** Quartz crystal microbalance, Nanoparticles, Breast cancer, Cell detection, Sensor

## 1 Introduction

It is expected that cancer will rank worldwide as the leading cause of mortality in this century. According to estimations of the World Health Organization (WHO), cancer is the first or second leading cause of death in ages before 70 years in 91 of 172 countries. In males and females together, lung cancer is the most common cancer and the leading cause of cancer death followed by female breast cancer. Breast cancer is the most common cancer in women [1]. Recent estimates show that there will be approximately 62,930 new cases of female breast carcinoma in situ in the USA alone in 2019 [2].

Early diagnosis of primary and recurrent tumors is of prime importance in the prevention of mortality. Current diagnostic procedures are based on radiological imaging, histological, and molecular analyses which are either time-consuming or costly. Therefore,

Miguel R. Ossandon et al. (eds.), *Biomedical Engineering Technologies: Volume 1*, Methods in Molecular Biology, vol. 2393, https://doi.org/10.1007/978-1-0716-1803-5_27, 

there is an urgent need for sensitive, selective, rapid, and cost-effective cancer cell detection systems. Such a system may detect and discriminate malignant cells in circulation or in biopsy samples efficiently. Breast cancer cells display aberrant or overexpressed proteins in their plasma membranes. Some of these that are not in common use like transferrin, E-cadherin, and notch receptor have been shown to correlate well with breast cancer degree of malignancy [3–6].

Notch receptors play important roles in mammary tissue development as well as tumorigenesis. They function as recognition elements using a specific interaction between the target cell and the binding region of the receptor to initiate a great number of cellular events. As shown in Fig. 1, Notch receptor intracellular domain is detached upon ligand binding and is released in the cytosol where it can affect its target genes like HES [7, 8].

The high affinity of an antibody for the notch receptor is in the picomolar range [9]. Using this antibody in a sensor system, in turn, provides a high affinity toward breast cancer cells. Many types of sensor systems can be used for the detection of target molecules. One of these systems is optical sensors whereby detection can occur by measuring a change in the optical characteristics of the transducer surface. In the literature, there are multiple optical sensors, including the resonant mirror optical sensor, optrode-based fiber-optic sensors, time-resolved fluorescence, evanescent wave fiber optical sensors, interferometric sensors, and surface plasmon resonance sensors [10–14]. Sensors are used as an original application

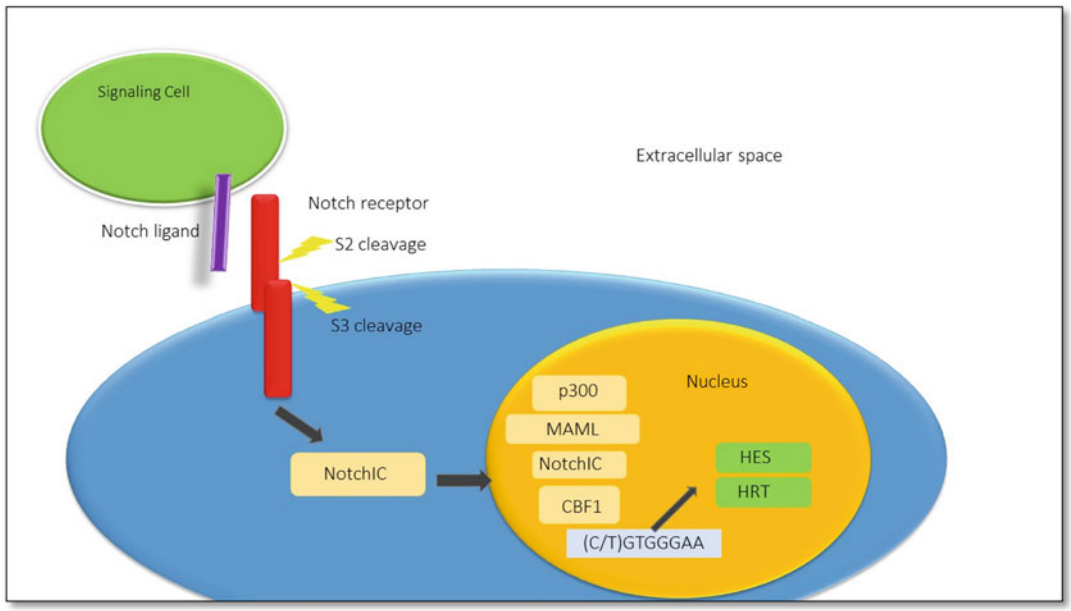


**Fig. 1** Mechanism of notch receptor antibody

in many fields including food safety, diagnosis, laboratory medicine, and especially clinical examinations. Piezoelectric sensors are another type of sensor system. Here, piezoelectric crystals sensitive to any mass change or pressure on their surfaces are used, thus finding use in trace quantitative analysis and microbalances for thin-film technology. The binding of the target on the surface of piezoelectric crystals decreases the oscillating frequency. A combination of a simple converter receptor can be used for the detection of a target in the sensors system. Among current sensor systems, QCM as a highly sensitive piezoelectric sensor plays an important role in the detection of biomolecules and cells [15, 16]. A QCM sensor is a simple and convenient sensor platform. This approach is well suited as transducer elements for chemical sensors. A QCM sensor is an extremely sensitive mass-measuring device in the range of nanograms. Dynamic monitoring of biochemical interactions is possible in QCM sensor systems. The advantages of these systems are quick response time, cost-effectiveness, mass sensitivity, and high resolution. The mass of the QCM sensor increases with the binding of the template but the oscillating frequency decreases. QCM sensors have been used in a variety of areas such as food, clinical, and environmental analyses [17, 18].

QCM sensors have the ability to show the detection of biomolecules in real time. The Sauerbrey equation [19] demonstrates the relation between mass changes and frequency changes.

$$\Delta \mathrm{f} = \left( -\frac{2f^2}{\rho_q \upsilon_q} \right) \times \Delta m / A \tag{1}$$

Here, $\Delta m$ is mass changes (g or cells) due to binding/rebinding biomolecules or cells, $\Delta \mathrm{f}$ is the frequency changes (Hz), $A$ is the sensing surface area, and $\mathrm{f}$ is the initial frequency (Hz). $\rho_{\mathrm{q}}$ and $\upsilon_{\mathrm{q}}$ are the shear wave velocity and density of the quartz crystal. The resonator oscillation frequency of the QCM changes with addition of any mass on the QCM resonator. Therefore, the detection of biomolecules occurs by measuring the shift in the frequency of the resonator [20, 21]. The QCM is a simple, high-resolution mass sensing, sensitive, and inexpensive technique using mechanical acoustic waves [22, 23].

Nanomaterials such as nanoparticles have been used in several analytical methods. Proper nanoparticles that are used on the surface of chips show a bright prospect. Many types, different sizes, and different kinds of nanoparticles have been reported in the literature for their use in sensors systems. The unique chemical and physical properties of nanoparticles make them effective for applying on the surface of the QCM chips to detect nanoscale mass changes.

The sensor system is based on the preliminary coating of the QCM chip with polymeric nanoparticles to increase the surface

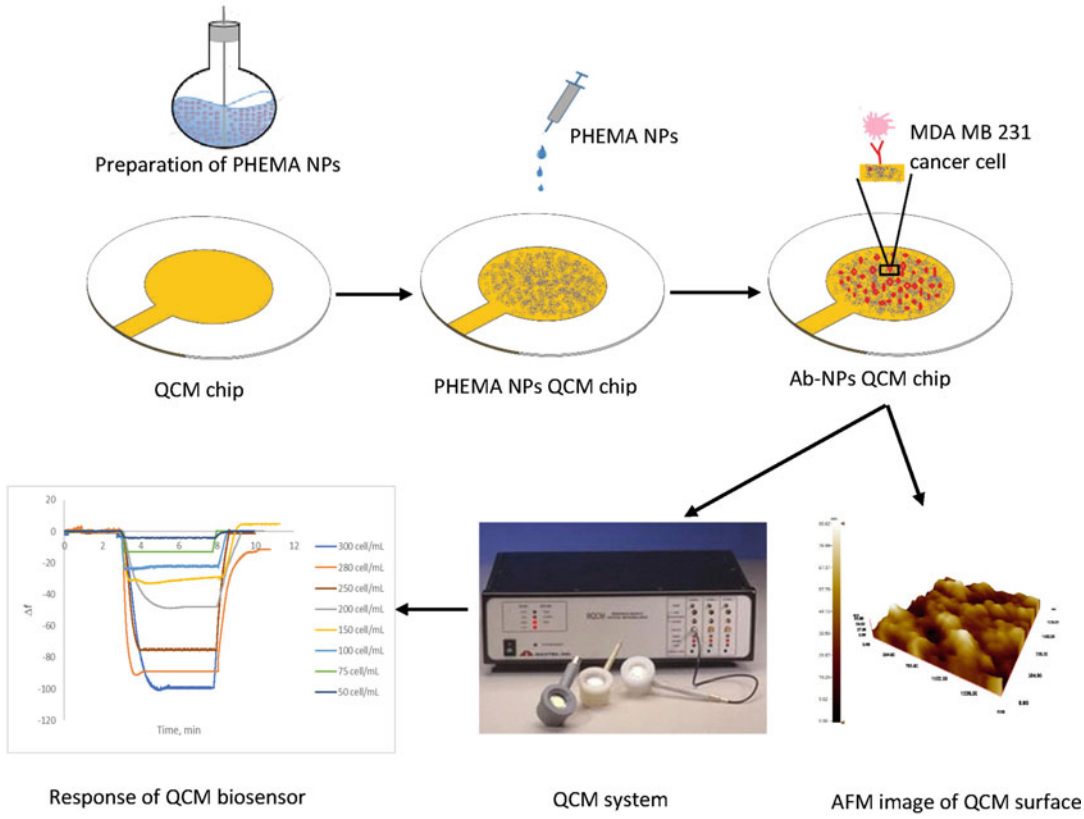


**Fig. 2** Schematic view of QCM chip [23]

area and allow the attachment of proteins to the chip surface. The lower limit of detection with using nanoparticles and the signal of mass change increase [24–26]. QCM sensors with nanoparticles on their chip surfaces are found by further functionalizing with a notch-4 receptor antibody. Therefore, this QCM sensor detects MDA MB 231 breast cancer cells with high sensitivity and selectivity. Here, selectivity of the QCM sensor is shown with L929 mouse fibroblast cells. This method can be used for detection of other templates by using the affinity molecules. Figure 2 shows the schematic view of preparation QCM chip for detection of MDA MB 231 cancer cell.

## 2 Materials

Sterile conditions are provided by proper autoclaving of all glassware, solutions, and other labware. Cells are handled under sterile conditions in a laminar flow cabin. All the water used for experiments in this study is purified using a reverse osmosis unit with a high flow cellulose acetate membrane followed by organic/colloid

removal and ion exchange packed-bed system ($R = 18.2$ MΩ/cm). All buffer and sample solutions are prepared and stored at 25 °C. Poly(vinyl alcohol) (PVAL MW:140,000, 98% hydrolyzed), sodium dodecyl sulfate (SDS), 2-hydroxyethyl methacrylate (HEMA), ethylene glycol dimethacrylate (EGDMA) are purchased from Sigma-Aldrich, St. Louis, USA. The QCM chips are obtained from Maxtek Inc. New York, USA. Dulbecco's Modified Eagle Medium, (DMEM, D6429/500 mL), penicillin–streptomycin (A5955/100 mL), L-glutamine (G7513/100 mL), fetal calf serum (FBS, F2442/100 mL), sodium bicarbonate, and potassium persulfate are purchased from Sigma-Aldrich, St. Louis, USA. Notch-4 receptor antibody is obtained from Novus Biologicals, CO, USA.

### 2.1 Nanoparticle Components

*First aqueous phase*:

1. 93.7 mg PVAL.
2. 14.4 mg SDS.
3. 11.7 mg sodium bicarbonate.
4. 50 mL deionized water.

*Second aqueous phase*:

5. 50 mg PVAL.
6. 50 mg SDS.
7. 100 mL deionized water.

*Organic phase*:

8. 0.45 mL HEMA.
9. 1.05 mL EGDMA.
10. 0.44 mg/mL potassium persulfate.

The polymerization system apparatus that is used in the section is shown in Fig. 3a. Also, the nanoparticles are washed with water and water/ethyl alcohol mixtures, in order to remove unreacted monomers, surfactant, and initiator. Allegra-64R Beckman Coulter, USA centrifuge apparatus is used (Fig. 3b).

### 2.2 Cell Culture Media

1. Dulbecco's Modified Eagle Medium (DMEM).
2. Fetal calf serum.
3. Glutamine.
4. Trypsin–ethylenediaminetetraacetic acid (trypsin–EDTA).
5. 3-(4,5-dimethylthiazol-2-yl)-2,5-diphenyltetrazolium bromide (MTT).
6. Dimethyl sulfoxide (DMSO), $(CH_3)_2SO$.
7. Phosphate buffer solution (PBS), pH 7.4.

Binding events are followed using a QCM with a phase-lock oscillator, Kynar crystal holder, 100 μL cell volume flow cell, and

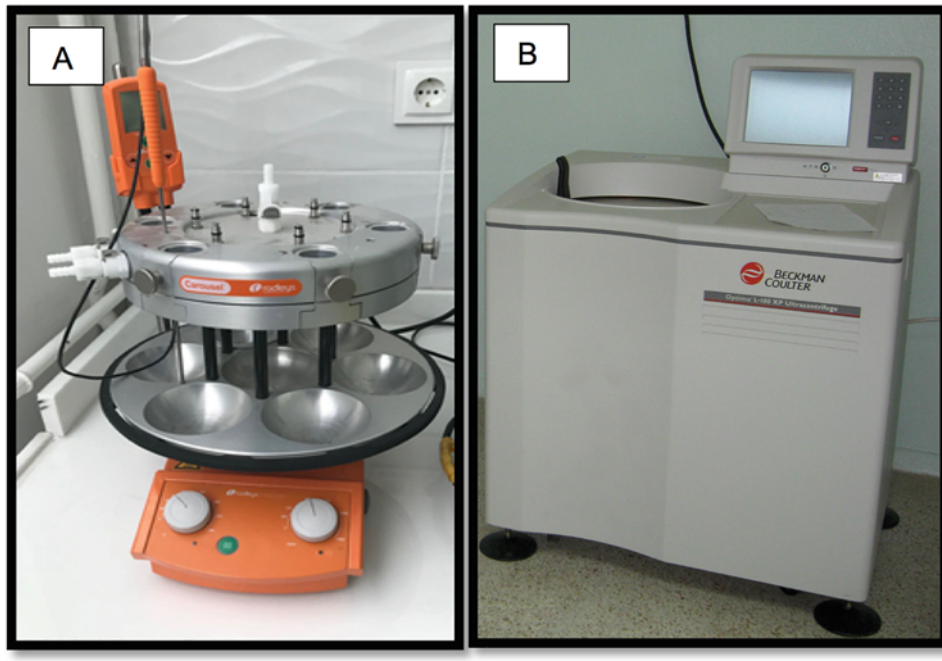


**Fig. 3** (**a**) Polymerization system and (**b**) Centrifuge apparatus

1 in., Ti/Au, AT-cut, 5 MHz quartz crystals. The holder is mounted with the crystal face positioned 90° to the ground to minimize gravity precipitation onto the surface. A variable-flow peristaltic pump with 0.51 mm PVC tubing is used. Fresh tubing is cut before each run in order to keep contamination at a minimum level and to limit flow-rate deviations. All measurements are recorded at room temperature. Sensitivity is known to be 56.6 Hz $cm^2/\mu g$ for a 5 MHz crystal.

A schematic of the QCM system (RQCM, INFICON Acquires Maxtek Inc., New York, USA) is shown in Fig. 4a. For providing the fluidics for cell solution, a peristaltic pump is used (Fig. 4b). Also, Fig. 4c shows the step-by-step placement of the QCM chip in the apparatus of the sensor system.

## 3 Methods

Carry out all procedures at room temperature, unless otherwise specified.

### *3.1 QCM Chip Modification*

1. Wash the gold surface of the QCM chips (Fig. 5) with ethanol and deionized water.
2. Wash the clean bare chips with piranha solution (*see* **Note 1**).


**Fig. 4** (**a**) Quartz crystal microbalance (QCM) apparatus, (**b**) Peristaltic pump, and (**c**) Schematic of QCM sensor system preparation

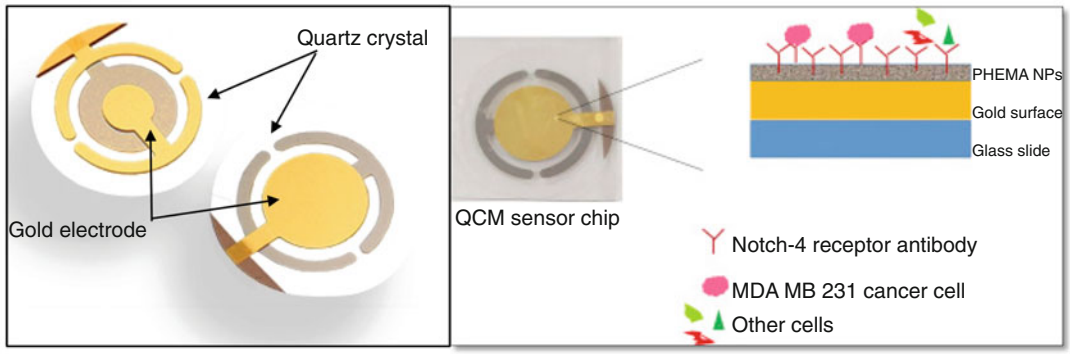


**Fig. 5** Quartz crystal microbalance chips without modification [23]

### *3.2 Synthesis of Nanoparticles*

1. Weigh 93.7 mg of poly(vinyl alcohol) for the first phase, put into a glass beaker, and dissolve in 50 mL of deionized water (*see* **Note 2**).
2. Weigh 14.4 mg sodium dodecyl sulfate, add it to the solution and stir for 1 h (*see* **Note 3**).

3. Weigh 11.7 mg sodium bicarbonate, add it to the solution and stir for 1 h.
4. Weigh 93.7 mg of poly(vinyl alcohol) for the second phase, put into a glass beaker, and dissolve in 100 mL of deionized water.
5. Weigh and add 50 mg sodium dodecyl sulfate to this solution.
6. Put 0.45 mL 2-hydroxyethyl methacrylate and 1.05 mL ethylene glycol dimethacrylate into a glass beaker for preparing the monomer phase.
7. Add the first phase into the second phase and stir at room temperature for 30 min.
8. Add monomer phase into this mixture and homogenize at 50,000 rpm for 30 min.
9. Dissolve 0.44 mg of potassium persulfate as an initiator in 1 mL deionized water and add into the mixture (*see* **Note 4**).
10. Complete the polymerization in 24 h at 600 rpm at 40 °C.
11. Wash the obtained poly(2-hydroxyethyl methacrylate) nanoparticles (PHEMA-NPs) with deionized water and 50% ethanol several times (*see* **Note 5**).
12. Put 0.02% sodium azide ($NaN_3$) buffer into PHEMA-NPs and store at 4 °C until use (*see* **Note 5**).
13. Characterize the PHEMA-NPs by using a zeta-sizer (nanoS, Malvern Instruments, London, UK).

### 3.3 Nanoparticle Adsorption on the Chip Surface

1. Wash the gold surface of the QCM chip with deionized water and then with ethanol.
2. Wash the QCM chip with piranha solution and dry in the vacuum incubator under 200 mmHg, 37 °C.
3. Drop 10 μL of PHEMA-NPs on the gold surface of the QCM chip, spread PHEMA-NPs on the gold surface of the QCM chip (*see* **Note 6**).
4. Dry the PHEMA-NP QCM chip in the oven for 30 min at 37 °C.
5. Wash the PHEMA-NP QCM chip with ethanol and deionized water 3 times, and dry in a vacuum incubator under 200 mmHg pressure at 40 °C.
6. Dip PHEMA-NP QCM chip into the 1/10,000 diluted solution of notch-4 receptor antibody with 5 mg carbodiimide solution (*see* **Note 7**).
7. Wash the PHEMA-NP QCM chip functionalized with notch-4 receptor antibody (Ab-NPs QCM chip) with phosphate buffer solution pH 7.4.

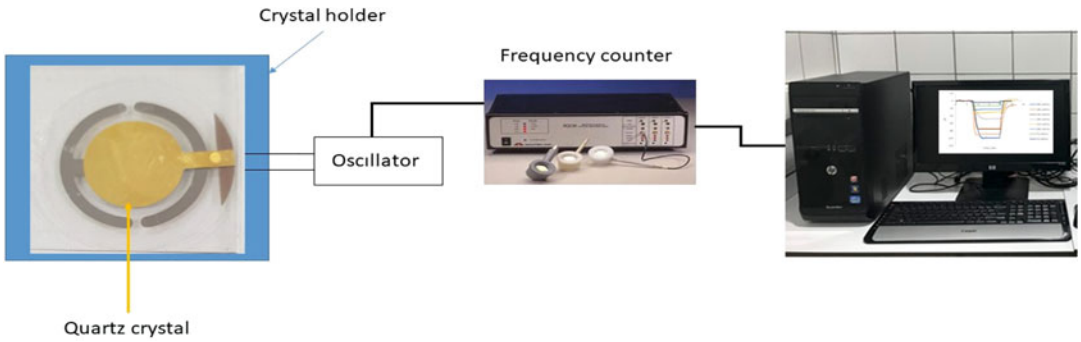


**Fig. 6** Schematic representation of experimental setup

8. Dry the Ab-NP QCM chip and place the QCM chip in the apparatus of the sensor system for detection studies as shown in Fig. 6.

### 3.4 Culturing and Preparation of Cell Sample

1. MDA MB 231 (ATTC-HTB-26) human breast cancer cells and L929 mouse fibroblast cells (Fig. 7) are cultured and prepared for sensor application (*see* **Note 8**).
2. Culture cells in Dulbecco's Modified Eagle's Medium (DMEM) supplemented with 10% (v/v) fetal bovine serum (FBS), 100 U/mL penicillin + 100 mg/mL streptomycin, and 2 mM L-glutamine.
3. Place cell in 25 cm culture flasks and incubate at 37 °C' under 95% $O_2$ and 5% $CO_2$'li in an incubator (Heraeus Instruments, BBD 6220, Germany).
4. Monitor cell by an inverted microscope (Meiji Techno Co. Ltd., TC5300, Japan) and passage every 2 days at 75% confluence (*see* **Notes 9** and **10**).
5. Wash the cells with PBS and apply trypan blue test using a hemocytometer as follows,

Cell number is determined as described below:
Staining with a trypan blue dye exclusion assay is used to evaluate cell numbers.

1. Mix 10 μL of cell sample with the same amount of 4% (w/v) trypan blue solution. The cell suspension is mixed with trypan blue dye, followed by visualization and counting to determine the number of stained and unstained cells.
2. Take 10 μL of solution and dilute the cells to 50%.
3. 10 μL of this mixture is placed in a hemocytometer counting chamber using a light microscope with a 40× magnification, and cells are counted. The number of vital cells is determined according to the equation below:

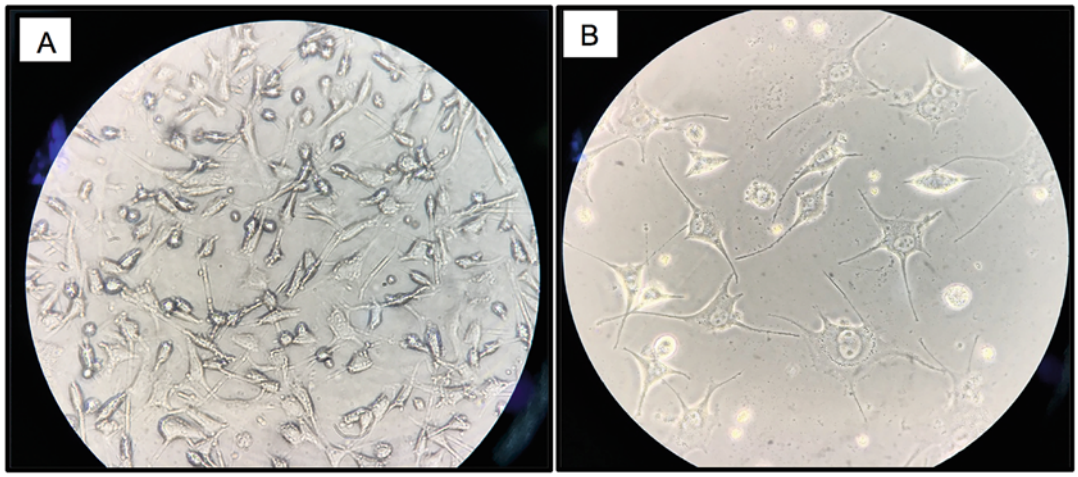


**Fig. 7** (**a**) MDA-MB 231 cells, and (**b**) L929 mouse fibroblast cells

$$\text{Number of cells}/\mu\text{L} = \text{number of cells in medium square} \times 250.00$$

About 20–30 square fields with a determined volume are counted in each observation and the average number is reported.

### *3.5 Characterization of PHEMA-NPs and the QCM Chip*

The PHEMA NPs are characterized by zeta sizer that the average size of PHEMA NPs is found to be 62.18 nm with polydispersity of 0.185. The sensitivity of QCM sensor may increase by the low size of nanoparticles. The best performance is provided using nanoparticles with large surface area on surface of QCM sensor. This advantage allows more targets to be bound to the QCM sensor surface. The specific surface area of the PHEMA NPs is found to be 1899 $m^2/g$.

QCM chip surfaces are characterized with ellipsometer (Nanofilm EP3, Germany), atomic force microscopy (AFM) and water contact angle measurements. Contact angle measurements are determined with KRUSS DSA100 (Hamburg, Germany) instrument as seen in Fig. 8a. The size characterization of the PHEMA-NPs is obtained by using a zeta-sizer (nanoS, Malvern Instruments, London, UK Fig. 8b). Ellipsometer measurements are carried out by an autonulling imaging ellipsometer (Fig. 8c). In the layer thickness analysis, a four-zone autonulling procedure integrating over a sample area of approximately 100 μm × 100 μm followed by a fitting algorithm has been performed. A four-phase model, air/-polymeric nanoparticles/gold/chromium and quartz is assumed for QCM chips. Refractive index data imported from the library of the ellipsometry system. Measurements are carried out as three different points of QCM sensor surface and the results are reported as mean value of the measurements with standard deviations. All

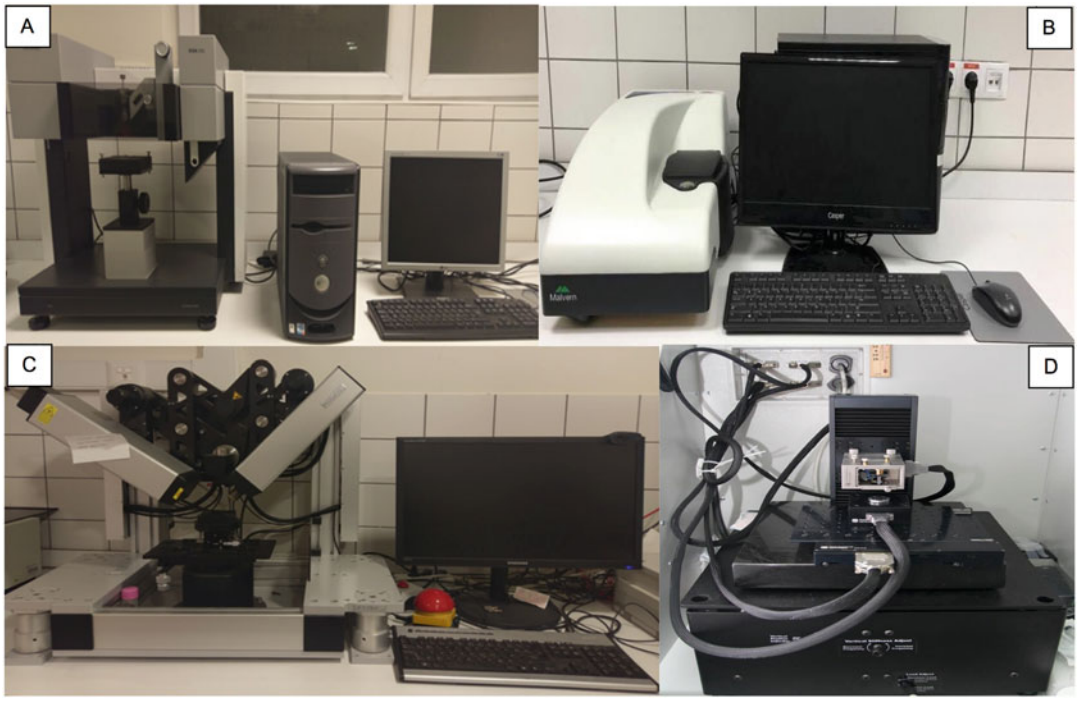


**Fig. 8** (**a**) Contact angle, (**b**) zeta sizer, (**c**) ellipsometer, and (**d**) atomic force microscopy apparatuses

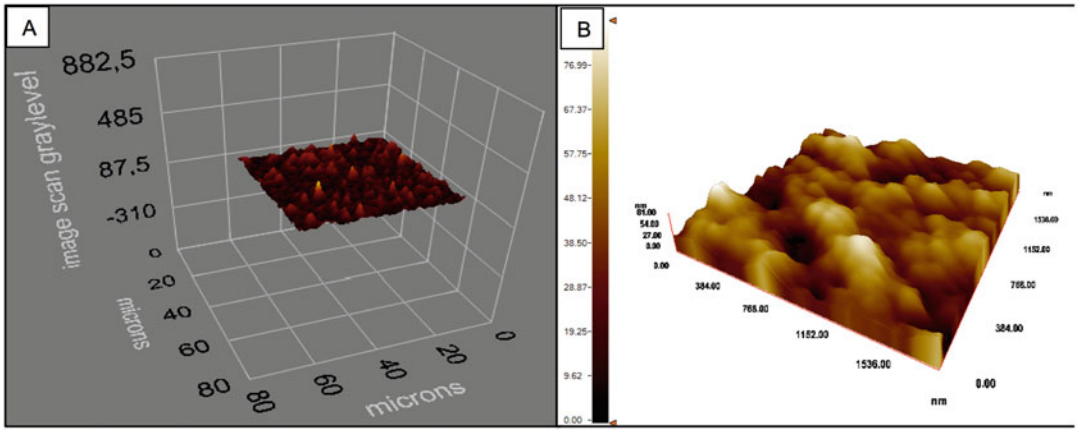


**Fig. 9** Characterization studies of the QCM chip by (**a**) Ellipsometer and (**b**) AFM [23]

thickness measurements have been performed at a wavelength of 532 nm with incidence angles of 62°. As seen in Fig. 8d, AFM observations are carried out by an ambient AFM (Nanomagnetics Instruments, Oxford, UK, Fig. 8d) in tapping mode. Samples are scanned with 2 μm/s scanning rate at 256 × 256 pixel resolution.

The thickness of the QCM chips is shown in Fig. 9 (a. Ellipsometer photographer and b. AFM photographer). Based on these measurements, it is possible to say that nanoparticles are

applied to the surface homogeneously. The depth of the QCM chip is found to be 89.6 ± 2.9 nm and 81.01 nm, respectively, by ellipsometer and AFM. A liquid in contact with the solid surface forms a certain amount of an angle. This angle varies depending on the contacted solid and the contact fluid and good data for recognizing the surface. If the contact angle is greater than 90°, it can be said that surface is hydrophobic. The contact angles 66.9 ± 0.32 for QCM chip, that the –OH groups of PHEMA NPs increase the hydrophilic properties of the chip.

### 3.6 Real Time Monitoring of Cell Binding

The QCM sensor is used for real-time detection of cell from aqueous solution. For this purpose, a QCM system (RQCM, INFICON Acquires Maxtek Inc., New York, USA) is used (Fig. 4a). The applied experimental procedure can be briefly summarized as: the QCM sensor is sequentially washed with deionized water, and equilibration buffer (pH:7.4 phosphate buffer). Then, the QCM sensor response is monitored until it reached stable frequency. After that, cell solutions with 1.0 mL/min flow-rate are applied to the QCM sensor and frequency shifts are monitored. Here, we use a peristaltic pump to provide the fluidics for cell solution (Fig. 4b). Therefore, we observe the detection of different concentration of MDA MB 231 cells in this part.

1. Dry QCM chip with a $N_2$ gas stream and place in the QCM instrument.
2. Use for baseline stabilization in the QCM device circulated with a peristaltic pump at 1.0 mL/min for 3 min before measurement.
3. Apply 50–300 MDA MB 231 cells into the QCM sensor system for 3 min (*see* **Note 11**).
4. Save the resonance frequency ($f_0$) until 8 min.
5. Use 1.0 M NaCl solution to detach the cells from the chip surface (*see* **Note 12**).
6. Apply 150 cells/mL of MDA MB 231 cell samples and L929 mouse fibroblast cells to show the selectivity of Ab-NP QCM chip (*see* **Note 13**).
7. Apply 150 cells/mL of MDA MB 231 cell samples to the Ab-NP QCM chip and nonfunctional PHEMA-NP QCM chip (*see* **Note 14**).
8. Apply 150 cells/mL of MDA MB 231 cell samples for 5 times to show the reusability of QCM sensor.

### 3.7 QCM Sensorgram

The increase in density of MDA MB 231 cells (50–300 cells/mL) can be caused by an increase in the QCM sensor response. The plateau can be reached after 5–8 min (Fig. 10). For removing of MDA MB 231 cells, 1.0 M NaCl is used as removing solution by

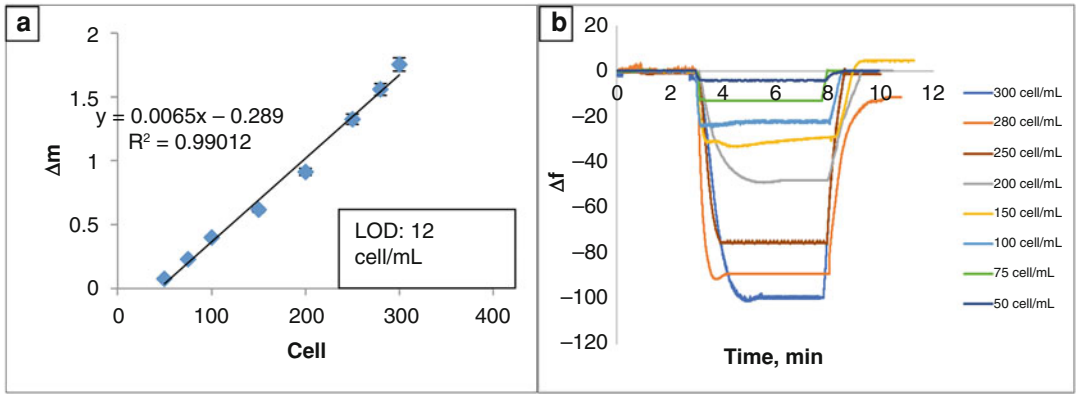


**Fig. 10** Kinetics of QCM sensor (**a**, **b**) [23]

adding it onto the QCM sensor. The binding, removing, and regeneration cycle for each experiment is completed in about 12 min. As seen in Fig. 10a, the equation of the linear graph for the concentration range of 50–300 cells/mL is calculated as $y = 0.0065x - 0.289$. The linearity of this equation is calculated as $R^2 = 0.9901$. The limit of detection (LOD) and limit of quantification (LOQ) values are confirmed according to Eqs. 2 and 3.

$$\mathrm{LOD} = 3\,S/m \tag{2}$$

$$\mathrm{LOQ} = 10\,S/m \tag{3}$$

where $S$ is the standard deviation of the intercept and $m$ is the slope of the regression line. LOD and LOQ values are found to be 12 and 42 cell/mL, respectively. This indicates that the QCM biosensor detects MDA MB 231 cells quantitatively. The detection limit values of other sensors are also given in Table 1. Here, different methods are used for detection of cancer cells.

### 3.8 Isotherm Analysis

The Freundlich model is an isotherm model for adsorption on heterogeneous surfaces. By adapting the standard parameters for QCM sensor, the following formula is obtained.

$$\Delta m = \frac{\Delta m C}{K_{\mathrm{D}}} + [C] \tag{4}$$

Langmuir isotherm is obtained by assuming that the molecules on the surface are adsorbed uniformly. The formulation of Langmuir isotherm equations adapted to the QCM sensor $\Delta m$ value is as follows.

$$\Delta m = \Delta m_{\max}[C]^{1/n} \tag{5}$$

A combination of Langmuir–Freundlich isotherm model is also used by the formulation given below.

**Table 1**
**Comparison of various cell detection methods**

| Detection systems | Cells | LOD (cells/mL) | References |
|---|---|---|---|
| QCM biosensor | Human lung carcinoma | 100 | [27] |
| Chitosan-based QCM biosensor | Breast cancer | 430 | [28] |
| Aptamer based QCM biosensor | Leukemia | 1160 | [29] |
| Leaky surface acoustic wave aptasensor array | MCF-7 | 32 | [30] |
| QCM biosensor | MDAMB 231 | 500 | [22] |
| Electrochemical impedance cytosensor | MDAMB 231 | 10 | [31] |
| Electrochemical impedance spectroscope | MCF-7 | 10 | [32] |
| Electrochemical impedance spectroscope | SW 620 | 79 | [33] |
| Differential pulse voltammograms | HepG2 | 30 | [34] |
| QCM biosensor | MDAMB 231 | 12 | [23] |
| Electrochemical immunosensor | SK-BR-3 | 26 | [35] |
| Gold nanoparticle–based colorimetric | SK-BR-3 | 100 | [36] |
| Acoustic aptasensor | SK-BR-3 | 550 | [37] |
| Chitosan-based QCM biosensor | MCF-7 | 430 | [28] |
| Aptamer-based leaky surface acoustic wave biosensor array | MCF-7 | 10 | [30] |
| Mannosyl electrochemical impedance cytosensor | MDAMB 231 | 10 | [31] |

$$\Delta m = \left\{ \Delta m_{\max} [C]^{1/n} / K_{\mathrm{D}} + [C]^{1/n} \right\} \tag{6}$$

Freundlich, Langmuir and Freundlich–Langmuir isotherms are taken in order to examine the interaction between cells and notch-4 receptor antibody based QCM sensor and given in Table 2, where $\Delta m$ defines the amount of increased mass on the unit area of a QCM sensor (cells/cm$^2$); $C$ is the cell number (cells/mL); $1/n$ is the Freundlich exponent; $k_a$ (cells/mL) and $k_d$ (s$^{-1}$) are forward and reverse kinetic rate constants; $K_A$ (cells/mL) and $K_D$ (mL/cells) are forward and reverse equilibrium constants; and subscripts ex, max, and eq indicate experimental, maximum, and equilibrium, respectively. After carrying out the equilibrium kinetic analysis, we have calculated slopes of curves and plotted concentration vs. slope curve to determine $k_a$ and $k_d$, respectively. As seen in the results, a successful binding is observed in the Langmuir model. This model shows that the QCM chip surface is a homogeneously distributed monolayer with coenergy and minimal lateral interaction between cells and notch-4 receptor antibody.

**Table 2**
**Calculated Freundlich, Langmuir, and Langmuir–Freundlich isotherm parameters [23]**

| Langmuir | Freundlich | Langmuir–Freundlich |
|---|---|---|
| $\Delta m_{max}$: 1.4 | $\Delta m_{max}$: 1.6 | $\Delta m_{max}$: 0.68 |
| $K_A$, cells/mL: 0.002 | $1/n$: 1.24 | $1/n$: 0.69 |
| $K_D$, mL/cells: 407.1 | $R^2$: 0.90 | $K_A$, cells/mL: 0.021 |
| $R^2$: 0.99 | | $K_D$, mL/cells: 47.31 |
| | | $R^2$: 0.91 |

### 3.9 Selectivity and Reusability Studies

Measurements are made with L929 mouse fibroblast cells (150 cells/mL) to determine the selectivity of the notch-4 receptor antibody on the QCM sensor. Measurements are made to see whether the high affinity based on the receptor interaction of MDA MB 231 cell shows equally high affinity for the L929 mouse fibroblast cells. According to the results, there is negligible interaction between notch-4 receptor antibody and L929 mouse fibroblast cells. Selectivity coefficient ($k$) and relative selectivity coefficient ($k'$) of the prepared QCM sensor are determined by subtracting from the Eqs. 7 and 8.

$$k = \Delta m_{\text{MDA MB 231}} / \Delta m_{\text{L929 Mouse fibroblast}} \tag{7}$$

$$k' = k_{\text{Ab-NPs}} / k_{\text{PHEMA}}\text{NPs} \tag{8}$$

For MDA MB 231 cells, the QCM sensor showed 17.5 times more selectivity than L929 mouse fibroblast cells.

In the reusability study, 150 cells/ml of MDA MB 231 cell samples in pH 7.4 PBS is given to the QCM sensor. The reusability procedure are shown in Fig. 11. As seen in the figure, almost the same $\Delta m$ value is obtained for each repeated sample. Furthermore, the stability of QCM sensor is tested at 1, 2, and 3 months (Fig. 11c) and the results have showed the stability of QCM sensor is acceptable.

## 4 Notes

1. Use $H_2O_2$ and $H_2SO_4$ as a mixture at a ratio of 1:3 (v/v) for preparing piranha solutions.
2. This solution is stirred magnetically at room temperature.
3. Sodium bicarbonate is added slowly into this solution and stirred magnetically at room temperature for 30 min.
4. Use nitrogen gas to remove dissolved oxygen for about 2 min.

(A)

| Cells | Ab-NPs QCM | | PHEMA NPs QCM | | |
|---|---|---|---|---|---|
| | Δm | k | Δm | k | k' |
| MDA MB 231 | 1.75 | - | 0.1 | - | - |
| L929 Mouse fibroblast | 0.1 | 17.50 | 0.1 | 1.0 | 17.5 |

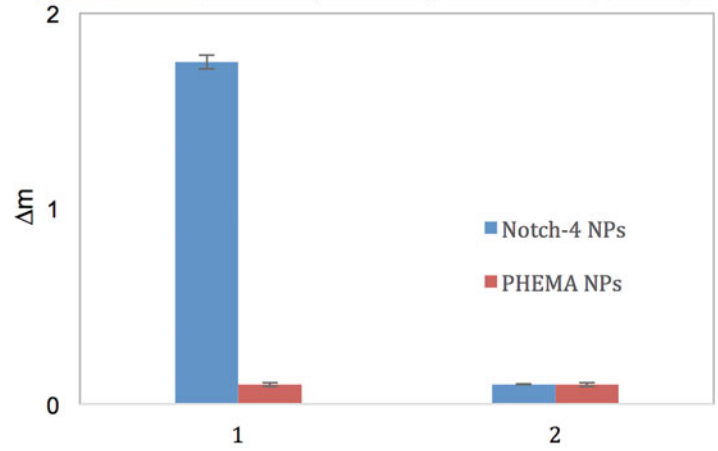


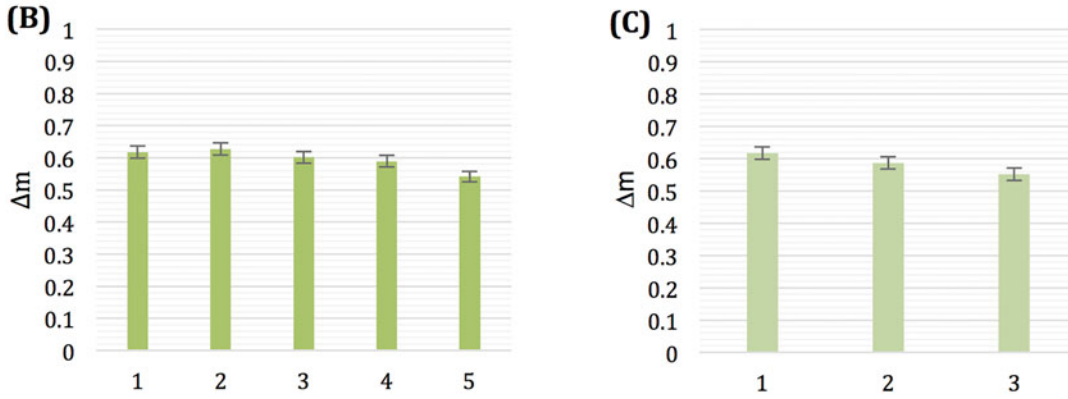


**Fig. 11** Selectivity (**a**), reusability (**b**), and stability (**c**) of Ab-NP QCM sensor [23]

5. Nanoparticles are washed with water and water–ethyl alcohol mixtures, in order to remove unreacted monomers, surfactants and initiators. For each washing step, the solution is centrifuged at 64,400 × *g* (30,000 rpm) for 30 min (Allegra-64R Beckman Coulter, USA); then, the nanoparticles are dispersed in a fresh washing solution. After the last washing step, the nanoparticles are dispersed in deionized water containing 0.02% sodium azide and stored at 4 °C.
6. Spread PHEMA-NPs on the gold surface of the QCM chip to prepare the monolayer and homogeneous surface.

7. Mix slowly the PHEMA-NP QCM chip with this solution at 100 rpm for 24 h.
8. Supplement the DMEM with 10% FBS, 2 mM L-glutamine, and 1% antibiotic–antimycotic solution under the atmosphere containing 5% carbon dioxide and 95% oxygen at 37 °C.
9. Equilibrate Ab-NP QCM chip with 0.1 M PBS buffer for 3 min, apply 50–300 cells/mL MDA MB 231 cell samples on the QCM system for 8 min. Remove the cells with 1.0 M NaCl solution for 2–3 min.
10. For passaging the cells culture media is aspirated and 1 mL of trypsin-EDTA solution is added and incubated for 2 min. The detached cells are collected by 10 mL of PBS in a conical 15 mL tube and centrifuged at 1200 × *g* for 3 min.
11. PBS is quickly aspirated and 5 mL of supplemented DMEM is added to the cell pellet.
12. Data is evaluated with an RQCM (Maxtek) software system.
13. 150 cells/mL in PBS (pH 7.4) of MDA MB 231 cells are applied to the QCM chip surface and then for showing the selectivity of QCM sensor 150 cells/mL in PBS (pH 7.4) mouse of fibroblast cells are applied to the QCM chip surface.
14. 150 cells/mL in PBS (pH 7.4) of MDA MB 231 cells applied to PHEMA NP QCM sensor that is prepared similarly without attaching notch-4 antibody.

## References


1. Bray F, Ferlay J, Soerjomataram I, Siegel RL, Torre LA, Jemal A (2018) Global cancer statistics 2018: GLOBOCAN estimates of incidence and mortality worldwide for 36 cancers in 185 countries. CA Cancer J Clin 68:394–424
2. Siegel RL, Miller KD, Jamal AJ (2019) Cancer statistics. CA Cancer J Clin 69:7–34
3. Siegel RL, Jemal A, Wender RC, Gansler T, Ma J, Brawley OW (2018) An assessment of progress in cancer control. CA Cancer J Clin 68:329–339
4. Siegel R, Ma J, Zou Z, Jemal A (2014) Cancer statistics. CA Cancer J Clin 64:9–29
5. Patel N, Weekes D, Drosopoulos K, Gazinska P, Noel E, Rashid M, Mirza H, Quist J, Brasó-Maristany F, Mathew SF, Pereira RAMP, Noor C, Francesch-Domenech F, Marlow E, de Rinaldis R, Grigoriadis E, Linardopoulos A, Marra S, Tutt P, A.N.J. (2018) Integrated genomics and functional validation identifies malignant cell specific dependencies in triple negative breast cancer. Nat Commun 9:1044
6. Knott SRV, Wagenblast E, Khan S, Kim SY, Soto M, Wagner M, Turgeon M-O, Fish L, Erard N, Gable AL, Maceli AR, Dickopf S, Papachristou EK, D'Santos CS, Carey LA, Wilkinson JE, Harrell JC, Perou CM, Goodarzi H, Poulogiannis G, Hannon GJ (2018) Asparagine bioavailability governs metastasis in a model of breast cancer. Nature 554:378–381.5
7. Kontomanolis EN, Kalagasidou S, Pouliliou S, Anthoulaki X, Georgiou N, Papamanolis V, Zacharias Fasoulakis N (2018) The Notch pathway in breast cancer progression. Sci World J 2018:2415489
8. Blanco R, Gerhardt H (2013) VEGF and Notch in tip and stalk cell selection. Cold Spring Harb Perspect Med 3:a006569
9. Koch U, Radtke F (2007) Notch and cancer: a double edged sword. Cell Mol Life Sci 64:2746–2762
10. Perçin I, Idil N, Bakhshpour M, Yılmaz E, Mattiasson B, Denizli A (2017) Microcontact imprinted plasmonic nanosensors: powerful

tools in the detection of *Salmonella paratyphi*. Sensors 6:1375

11. Wolfbeis OS (2016) Fiber-optic chemical sensors and biosensors. Anal Chem 78:3859–3874
12. Gür SD, Bakhshpour M, Denizli A (2019) Selective detection of *Escherichia coli* caused UTIs with surface imprinted plasmonic nanoscale sensor. Mater Sci Eng C 104:109869–109876
13. Battal D, Akgönüllü S, Yalcin MS, Yavuz H, Denizli A (2018) Molecularly imprinted polymer based quartz crystal microbalance sensor system for sensitive and label-free detection of synthetic cannabinoids in urine. Biosens Bioelectron 111:10–17
14. Saylan Y, Erdem O, Ünal S, Denizli A (2019) An alternative medical diagnosis method: biosensors for virus detection. Biosensors 9:65–87
15. Liss M, Petersen B, Wolf H, Prohaska E (2002) An aptamer-based quartz crystal protein biosensor. Anal Chem 74:4488–4495
16. Hao R, Wang D, Zhang XE, Zuo G, Wei H, Yang R, Zhang Z, Cheng Z, Guo Y, Cui Z (2009) Rapid detection of Bacillus anthracis using monoclonal antibody functionalized QCM sensor. Biosens Bioelectron 24:1330–1335
17. Bunde RL, Jarvi EJ, Rosentreter JJ (1998) Piezoelectric quartz crystal biosensors. Talanta 46:1223–1236
18. Büyüktiryaki S, Say R, Denizli A, Ersöz A (2017) Phosphoserine imprinted nanosensor for detection of Cancer Antigen 125. Talanta 167:172–180
19. Sauerbrey G (1959) Verwendung von Schwingquarzen zur Wägung dünner Schichten und zur Mikrowägung. Phys Z 155:206–222
20. Karczmarczyk K, Haupt KHF (2017) Development of a QCM-D biosensor for Ochratoxin A detection in red wine. Talanta 166:193–197
21. Bakhshpour M, Özgür E, Bereli N, Denizli A (2017) Microcontact imprinted quartz crystal microbalance nanosensor for protein C recognition. Colloids Surf B 151:264–270
22. Atay A, Pişkin K, Yılmaz F, Çakır C, Yavuz H, Denizli A (2016) Quartz crystal microbalance based biosensors for detecting highly metastatic breast cancer cells via their transferrin receptors. Anal Methods 8:153–161
23. Bakhshpour M, Piskin AK, Yavuz H, Denizli A (2019) Quartz crystal microbalance biosensor for label-free MDA MB 231 cancer cell detection via notch-4 receptor. Talanta 204:840–845
24. Reimhult K, Yoshimatsu K, Risveden K, Chen S, Ye L, Krozer A (2008) Characterization of QCM sensor surfaces coated with molecularly imprinted nanoparticles. Biosens Bioelectron 23:1908–1914
25. Shen Z-Q, Wang J-F, Qiu Z-G, Jin M, Wang X-W, Chen Z-L, Li J-W, Cao, F.- H. (2011) QCM immunosensor detection of Escherichia coli O157:H7 based on beacon immunomagnetic nanoparticles and catalytic growth of colloidal gold. Biosens Bioelectron 26:3376–3381
26. Sener G, Ozgur E, Yılmaz E, Uzun L, Say R, Denizli A (2010) Quartz crystal microbalance based nanosensor for lysozyme detection with lysozyme imprinted nanoparticles. Biosens Bioelectron 26:815–821
27. Ma Z, Wu J, Zhou T, Chen Z, Dong Y, Tang J, Sui SF (2002) Detection of human lung carcinoma cell using quartz crystal microbalance amplified by enlarging Au nanoparticles in vitro. New J Chem 26:1795–1798
28. Zhang S, Bai H, Luo J, Yang P, Cai J (2014) A recyclable chitosan-based QCM biosensor for sensitive and selective detection of breast cancer cells in real time. Analyst 139:6259–6265
29. Shan W, Pan Y, Fang H, Guo M, Nie Z, Huang Y, Yao S (2014) An aptamer-based quartz crystal microbalance biosensor for sensitive and selective detection of leukemia cells using silver-enhanced gold nanoparticle label. Talanta 126:130–135
30. Chang K, Pi Y, Lu W, Wang F, Pan F, Li F, Jia S, Shi J, Deng S, Chen M (2014) Label-free and high-sensitive detection of human breast cancer cells by aptamer-based leaky surface acoustic wave biosensor array. Biosens Bioelectron 60:318–324
31. Tang Y-H, Lin H-C, Lai C-L, Chen P-Y, Lai C-H (2018) Mannosyl electrochemical impedance cytosensor for label-free MDA-MB-231 cancer cell detection. Biosens Bioelectron 116:100–107
32. Shen H, Yang J, Chen Z, Chen X, Wang L, Hu J, Ji F, Xie G, Feng W (2016) A novel label-free and reusable electrochemical cytosensor for highly sensitive detection and specific collection of CTCs. Biosens Bioelectron 81:495–502
33. Han L, Liu P, Petrenko VA, Liu A (2016) A label-free electrochemical impedance cytosensor based on specific peptide-fused phage selected from landscape phage library. Sci Rep 6:22199–22200
34. Sun D, Lu J, Chen Z, Yu Y, Mo M (2015) A repeatable assembling and disassembling electrochemical aptamer cytosensor for

ultrasensitive and highly selective detection of human liver cancer cells. Anal Chim Acta 885:166–173

35. Zhu Y, Chandra P, Shim Y-B (2013) Ultrasensitive and selective electrochemical diagnosis of breast cancer based on a hydrazine–Au nanoparticle–aptamer bioconjugate. Anal Chem 85:1058–1064
36. Lu W, Arumugam SR, Senapati D, Singh AK, Arbneshi T, Khan SF, Yu H, Ray PC (2010) Multifunctional oval-shaped gold-nanoparticle-based selective detection of breast cancer cells using simple colorimetric and highly sensitive two-photon scattering assay. ACS Nano 4:1739–1749
37. Poturnayová A, Dzubinová Ľ, Buríková M, Bízik J, Hianik T (2019) Detection of breast cancer cells using acoustics aptasensor specific to HER2 receptors. Biosensors 9:72–85

# Chapter 28

# Studying Viscoelastic Changes of Skin Cells Using QCM-D Measurements

**Anna Sobiepanek and Tomasz Kobiela**

## Abstract

The viscoelastic properties of cells are responsible for the adhesion process to different surfaces and for cell motility. Therefore, it is very important to develop specific, label-free biosensors with the use of whole cells to study the effect of various factors on the survival and properties of selected type of normal and pathological cells. The quartz crystal microbalance with dissipation energy monitoring (QCM-D) is a technique which enables to track these changes in cells during real-time experiments. One of the applied procedures of the evaluation of the cells' viscoelastic changes is based on the investigations of interactions between specific, different glycans, present on the surface of the primary tumor and its metastases with specific lectins. Two procedures have been developed to detect the differences in the cellular glycosylation profile using cell-based sensors (adherent cells cultured on sensors) and suspension cell-based sensors (adherent cells mechanically detached and inserted into the QCM-D chamber with a sensor). Furthermore, in this work some cell-based sensor regeneration protocols have been described and a lectin-ELISA assay with a fluorescently labeled lectin, thus enabling a qualitative and quantitative tracking of each step of the lectin–glycan binding and unbinding process performed on whole cells.

**Key words** QCM-D biosensor, Viscoelastic properties of cells, Melanoma, Skin cancer, Glycosylation profile, Lectins

## 1 Introduction

Despite the efforts to prevent, diagnose, and treat cancer, it is the leading cause of morbidity and mortality worldwide [1]. The World Health Organization has reported over 14 million newly diagnosed cases and over eight million deaths in 2012. Over the next two decades, an increase in the number of new cancer cases by 70% and cancer-related deaths by 50% is expected [2, 3].

Particularly, the last decades brought the increasing risk of melanoma, skin cancer with the highest mortality in the worldwide

**Supplementary Information** The online version of this chapter (https://doi.org/10.1007/978-1-0716-1803-5_28) contains supplementary material, which is available to authorized users.

Miguel R. Ossandon et al. (eds.), *Biomedical Engineering Technologies: Volume 1*, Methods in Molecular Biology, vol. 2393, https://doi.org/10.1007/978-1-0716-1803-5_28, 

human population. The highest risk of melanoma is due to the fact that there is no available treatment for that cancer after it approaches the metastatic phase [4]. The exceptionally high metastatic potential of melanoma may result from the origin of the melanocytes that derive from the embryonic neural crest as compared to the epithelial cells that develop from the ectoderm. Melanoma prognosis depends on the degree of the penetration of the primary melanoma cells through the skin layers which determines its invasiveness and clinical symptoms.

The shape, adhesion, motility, and viscoelastic properties are differentiated characteristics which determine cell behavior during morphogenesis and after neoplastic transformation [5]. A large variety of molecules is involved in establishing and maintaining these characteristics. Common phenomena are increased cell proliferation rate and change of cell phenotype. Such transformations are responsible for not only development of embryo and organ remodeling, and wound repair and regeneration mechanisms but also for organ fibrosis, promotion of carcinoma progression, and metastasis, through a variety of mechanisms. The normal cells, characterized as epithelial phenotype, undergo transformation into mesenchyme-like type cells due to the changes of the intracellular homeostasis under the influence of the microenvironment [6]. The molecules and mechanisms involved in the epithelial–mesenchymal transformation (EMT) are becoming increasingly recognized and understood [7].

Of particular interest are the cell surface molecules involved in these interactions. In the development and maintenance of normal skin structure one of the major cell to cell adhesion molecules belonging to the family of cadherins, a calcium-dependent glycoproteins, are of great importance [8]. Melanocytes, localized in the basal layer of epidermal keratinocytes, can undergo transition into primary and malignant melanoma after UV radiation. It has been shown that normally cultured human melanocytes express four types of cadherin (E, N, P, and T) of different functions [9]. E-cadherin is primarily responsible for the adhesion of normal melanocytes to keratinocytes [10]. N-cadherin is expressed in highly invasive tumor cell lines that usually lack E-cadherin expression [11, 12]. Thus, the expression of either type of cadherin becomes a marker of melanoma malignancy. The alterations in the glycophenotype of cell surface glycans are also promising markers of malignancy [13].

Their structural alterations were found to accompany the neoplastic transformation of many tumor cells including melanoma [14]. The expression of the branched and sialylated or fucosylated complex type N-linked oligosaccharides in malignant tumor cells appears to be directly associated with their metastatic potential [9]. A recent analysis of N-glycosylation profile of proteins from various melanoma cells indicated N-cadherins as one of the proteins

undergoing changes in oligosaccharide composition in different melanoma cell lines [11, 15].

In the pharmaceutical industry, a plethora of tests are carried out over a period of several months to determine the specificity of various substances reacting with the target protein tested as pathogenic. Factors that directly affect the time and cost of introducing a new drug on the market are multistaged and time-consuming processes with a high reagent consumption. Currently, there are many techniques that allow for a direct detection of analytes without prior labeling. They are used to measure certain physical properties of biological compounds as DNA, peptide, protein, virus molecules, or entire cells [16]. All these structures have specific physicochemical and mechanical properties including mass, volume and are characterized by viscosity and elasticity. These parameters can be used to detect the presence of analyte using a suitable detector. One of the elements of the construction of a "label-free" sensor is a transducer, which is responsible for converting one of the physical values (e.g., mass of substance deposited on the active surface of the sensor) into a measurable signal which can be assessed by a proper method [17].

One of the applied procedures of the evaluation of these parameters is based on the investigations of interactions between various specific glycans present on the surface of the cells (normal cells, cells from the primary tumor, or cells after metastasis) with specific lectins, using the quartz crystal microbalance with dissipation energy monitoring (QCM-D). The quartz crystal microbalance is an extremely sensitive mass balance which measures mass per unit area changes at the nanogram level. The device consists of a thin AT-cut crystal quartz disc sandwiched between two electrodes deposited on each side of the disc. The crystal can be made to oscillate at its resonant frequency when an appropriate voltage through the metal electrodes is applied. In 1959, a German physicist Günter Hans Sauerbrey was the first to demonstrate that the frequency change ($\Delta f$) of the oscillating quartz is linearly related to its mass change ($\Delta m$) [18]. Conventionally, the QCM was used in vacuum or in a gaseous atmosphere. In 1984, Kanazawa and Gordon [19] derived a simple relationship expressing the change in oscillation frequency of a quartz crystal in contact with a fluid in terms of material parameters of the fluid and the quartz [20]:

$$\frac{\Delta f_L}{f_0} = -\sqrt{\frac{f_0 \rho_L \eta_L}{\pi \rho_q \mu_q}}$$

where $\rho_L$ and $\eta_L$ are the absolute viscosity and density of the liquid, respectively, and $\mu_q$ and $\rho_q$ are the elastic modulus and density of the quartz. This equation expresses an increase in the measurement sensitivity as a function of ($f_0$), that is inversely proportional to the crystal's thickness and its quality factor (Q factor) [21]. The Q

factor is a dimensionless parameter that describes the damping of the oscillation at resonance by relating the amount of energy stored in the oscillation to the amount of energy lost. The energy loss, or the dissipation ($D$), is the inverse of the Q factor [22]. The development of the QCM measurement system capable of simultaneously measuring frequency, dissipation, and amplitude of the quartz crystal oscillation significantly expanded the number of potential QCM applications, especially in all kinds of biological studies [23]. If the properties of the viscoelastic films have to be quantified, information about $f$ and $D$ at multiple harmonics is needed. From a theoretical perspective, this information is only possible to achieve by means of impedance and decay time methods [22].

QCM-D method enables not only kinetic analysis of the ligand–analyte interaction in real-time [24] but also glycosylation profile analysis on the whole cells with use of label-free lectins [25, 26]. In order to obtain some additional data concerning the viscoelastic properties of the forming layer, the analysis of the dissipation energy is applied. The decrease in dissipation indicates the formation of an ordered layer on the surface of the sensor. Therefore, the use of the quartz crystal microbalance with the energy dissipation monitoring allows for the simultaneous measurement of two separate parameters characterizing the ligand–analyte interactions. The frequency shift ($\Delta f$) provides information about the mass adsorbed on the sensor while changes in the energy dissipation ($\Delta D$) show the viscoelastic properties of the layer. The QCM-D device can be also integrated with a nanoplasmonic sensor, which allows to obtain at the same time the complementary refractive index change.

Specific types of biosensors utilize whole cells as ligands. Living or fixed adherent cells may be used for designing cell-based sensors. A construction of such a system always requires optimization of detailed conditions allowing for cell culture on the modified surface of the biosensor with their normal adhesion, viability, and proliferation. Since these properties depend on cell type, it is necessary to establish experimentally specific conditions providing an appropriate function of the biosensor and reproducibility of the measurements. Elaboration of the optimal procedure of measurement includes choosing the right buffer system, washing procedure, and temperature. It is also necessary to establish appropriate negative and positive controls. A separate issue concerns analyte sample preparation. Further steps comprise evaluation of proper activity of the immobilized ligand and finding the relevant procedure for biosensor regeneration which ought to allow a complete dissociation of the analyte from the ligand, preventing changes in its integrity and function. The last part is dedicated to shortening of the procedure. That is why cell-based sensors are being replaced with suspension cell-based sensors.

## 2 Materials

### 2.1 QCM-D Materials and Reagents

Quartz Crystal Microbalance with Dissipation Energy Monitoring with a flow module, Q-Sense Explorer (Biolin Scientific).

Sensors: AT-cut quartz crystals with gold film (QSX 301) and gold film with polystyrene-coating (QSX 305) (Biolin Scientific).

2% aquatic Deconex® solution (Borer Chemie AG).

2% aquatic Hellmanex® II solution (Borer Chemie AG).

70% aquatic ethanol solution.

2% aquatic sodium dodecyl sulfate (SDS) solution.

Piranha-like solution (Milli-Q, $H_2O_2$, $NH_3$ aq.; 5:1:1).

Milli-Q water.

Phosphate buffered saline (PBS) pH 7.4.

QCM-D buffer solution (e.g., PBS with 0.025% Tween 20 [PBST]).

QCM-D examined analyte solution (e.g., lectin Concanavalin A [Con A] dissolved in PBST).

3.7% paraformaldehyde (PFA) solution in PBS.

10 mM glycine solution in PBST (pH 2.0).

10 mM NaOH solution in PBST.

Poly-L-lysine (PLL).

### 2.2 Cell Culture Reagents and Materials

Full growth medium (e.g., RPMI with 10% fetal bovine serum and 1% mixture of antibiotics penicillin–streptomycin) appropriate for the selected cell type.

Trypsin–EDTA solution appropriate for the selected cell type (e.g., 0.05%).

PBS buffer.

24-well and 6-well plates suitable for adherent cells.

Plastic scraper.

### 2.3 Additional Materials and Reagents for QCM Complementary Methods

Fluorescent microscope.

Microplate reader with fluorescence.

1 μg/ml Hoechst 33342 dye solution in PBS.

Con A-FITC reagent dissolved in PBST.

### 2.4 Software

ImageJ free software (National Institutes of Health, https://imagej.nih.gov/ij/).

Microsoft excel (Microsoft).

QSoft (Biolin Scientific).
QTools (Biolin Scientific).

## 3 Methods

With the developed procedures both adherent cells (the 3-day procedure) and those in suspension (the 1-day procedure) can be used for the specific ligand–analyte interaction measurements and the study of viscoelastic changes in real-time. Those experiments could bring much more beneficial information about the surface receptors present on cells (like changes in glycans during the cancer progression) or the interaction of different compounds with the cells which change their glycosylation. Also, in the case of the 1-day procedure, it provided knowledge about the cell adhesion process. In order to generate high-quality data before the measurements, the following parameters should be taken into consideration: the unspecific binding check, determination of the amount of cells and their condition (e.g., living/fixed cells) as well as the flow rate selection and length of the measurement. If measurements are to be performed on living cells, they have to be kept in 37 °C in the flow module, which should be equipped with the temperature stabilization loop to ensure full control over the temperature. However, due to the limitations of the oxygen diffusion in the flow system, the cell culture cannot stay continuously living/active on the sensor. Usually, the measurements described in literature with living cells last up to 24 h [27], but if adequate gas exchange and temperature conditions are ensured, the measurements could be performed longer [28]. Moreover, in case of long measurements the cells need to be supplied with the essential products for the cell culture. Thus, the measurements should be performed in adequate cell medium. In general, it is recommended to optimize these parameters for each type of experiment separately.

The quartz crystal microbalance (QCM) is a quite popular laboratory equipment available from companies like Attana AB, Bio-Logic Science Instruments, and Stanford Research Systems. The QCM with the dissipation energy monitoring (QCM-D) can be purchased from openQCM, GAMRY Instruments, KSV Instruments or the Q-Sense from Biolin Scientific. The standard QCM-D system consists of (1) the chamber, where inside of the flow module a sensor is placed; (2) the electronic unit with an oscillator connected to a computer; and (3) the peristaltic pump which forces the buffer/analyte solution flow through the tubes (Fig. 1). Vessels with the buffer and the lectin solutions should be warmed up to the selected temperature used during the measurement with a water bath. The vessel with waste should be emptied at least at the end of each day.

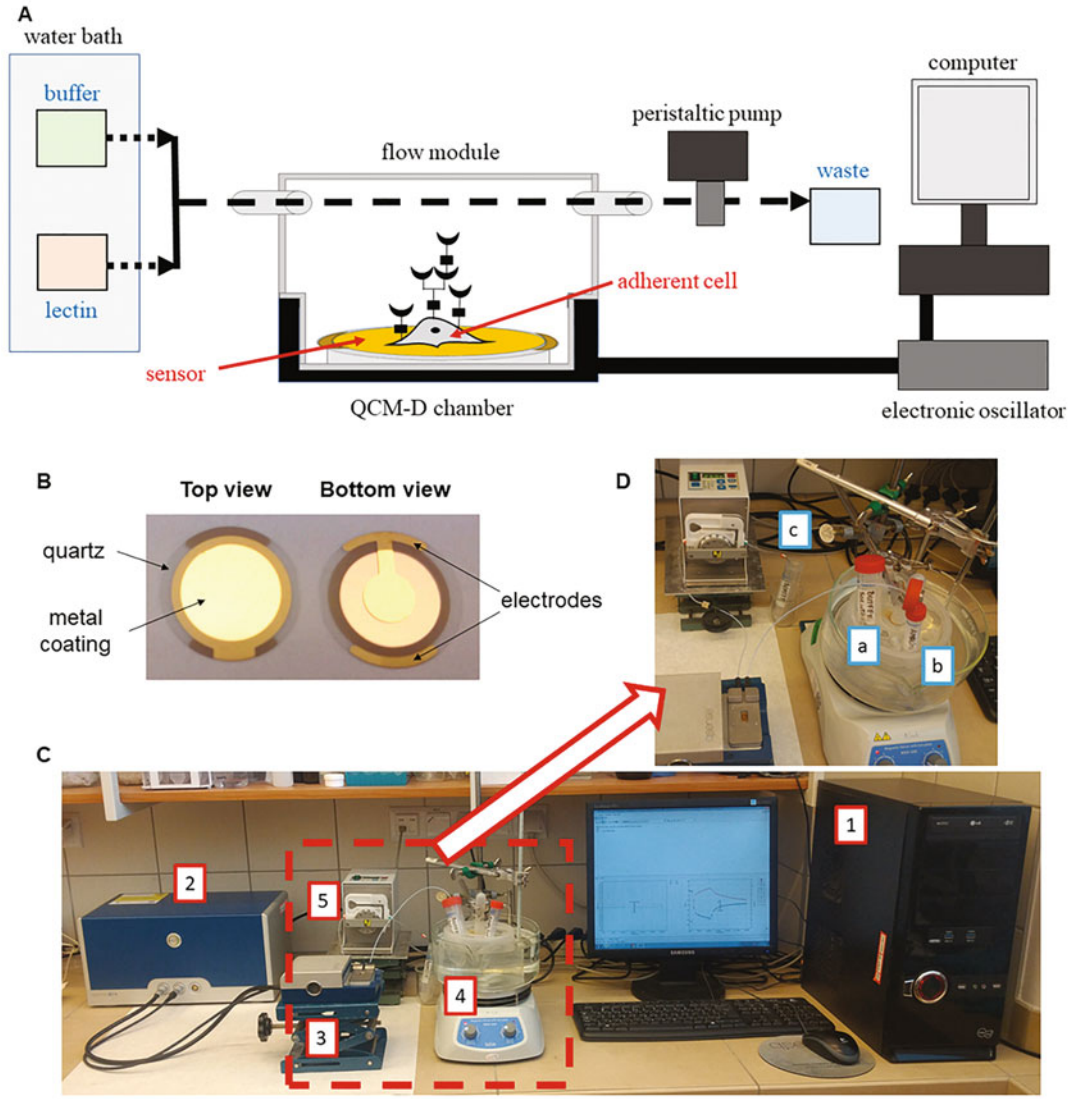


**Fig. 1** (**a**)—A schematic diagram representing the standard QCM-D system which is used for the study of lectin interaction with glycans present on the cells in the 3-day procedure. (**b**)—The top and bottom view of the quartz crystal sensor. (**c**)—A photo of the used QCM-D system (1—computer, 2—electronic oscillator, 3—QCM-D chamber with the flow chamber, 4—water bath with buffer or analyte container, 5—peristaltic pump and a waste container). (**d**)—Containers with the used solution during the QCM-D measurements (a—buffer, b—analyte like lectin, c—waste)

### *3.1 Preparation of Sensors*

The selection of sensor type for each measurement seems one of the crucial parameters for the cell study and in case of the possibility of unspecific binding during the measurement. Gold surfaces are well-known for their high unspecific affinity for proteins. This is why, in the experiments performed with cells and lectins, the gold surface of the sensor has to be secured by blocking the surface with other

types of proteins without carbohydrates (e.g., BSA) [29] or by coating with chemicals like polymers: polystyrene (PS) or poly-L-lysine (PLL) [30]. The adherent cell culture is typically carried out on glass or a properly prepared polystyrene surface with charged groups (like carboxyl or sulfonate) [31]. On the other hand, PLL due to its positively charged groups facilitates cell adhesion through the attraction of the negatively charged cell membrane [32]. That is why, for the lectin–glycan interaction measurements (cell-based sensors) we recommend the usage of gold sensors with polystyrene-coating and for the adhesion measurements (suspension cell-based sensors) gold sensors with poly-L-lysine-coating.

Before the first use, new sensors should be washed. This step can be done by using the solutions recommended by the manufacturer.

Gold sensors with polystyrene coating (Au-PS sensor)

1. Place the sensors in 2% SDS solution for at least 30 min.
2. Rinse the sensors well with Milli-Q water.
3. Place the sensors in 2% Deconex® solution for 30 min in the water bath with ultrasounds heated up to 60 °C.
4. Rinse the sensors well with Milli-Q water for at least 2 h before drying with nitrogen gas.

Gold sensors with poly-L-lysine-coating (Au-PLL sensor)

1. Place the sensors in 2% SDS solution for at least 30 min.
2. Prepare the piranha-like solution and heat it up to 70 °C in the water bath.
3. Place the sensors in the heated solution for 15 min for active washing (beware of the rising foam).
4. Rinse the sensors well with Milli-Q water for at least 1 h before drying with nitrogen gas.
5. Place the sensor on a flat surface and apply 100 μl of PLL solution for at least 5 min.
6. Again, rinse the sensors well with Milli-Q water and dry with nitrogen gas.

### 3.2 Three-Day Procedure of the Ligand–Analyte Interaction Study

For the adherent cells, the 3-day procedure is typically used and it consists of three main stages (Fig. 2): cell seeding, the incubation of cells on the Au-PS sensor (*possible addition of a compound in the meantime) and the ligand–analyte interaction study performed on the whole cells. (*If there are doubts whether the nonspecific interactions may occur for a given surface, a measurement should be made without cells grown on the sensor—**steps 13–17** of this procedure).

The proper preparation of the cell-based sensor is of great importance. The number of cells seeded onto the Au-PS sensor is

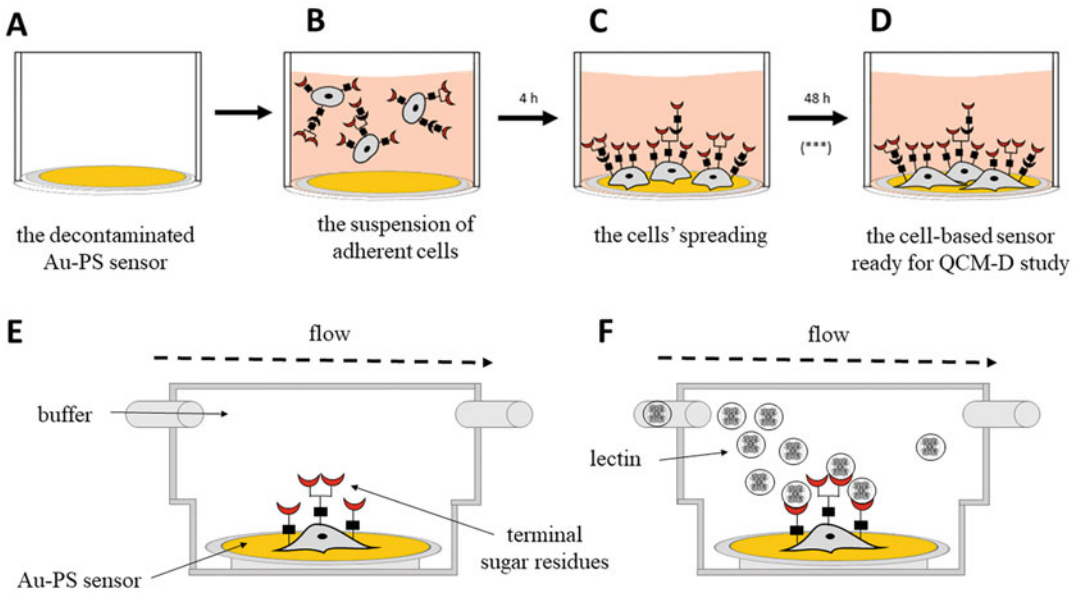


**Fig. 2** The following stages of the 3-day procedure. (**a**)—After the decontamination, the Au-PS sensor is placed in one of the wells of the 24-well plate; (**b**)—the suspension of the adherent cells is added to the well with the sensor; (**c**)—the cells are allowed to spread after seeding (***—time for adding compounds which may change the glycosylation profile of the cells, optional); (**d**)—the living cell-based sensor is ready for the QCM-D measurement (the fixation of cells is optional); (**e**)—rinsing of the cell-based sensor with the buffer solution to remove any unbound or weakly bound cells; (**f**)—the insertion of the lectin solution into the module and the measurement of its interaction with glycans present on the cells

essential. A large number may cause problems to detect the sensor by the oscillator. On the other hand, a small number of cells may give an undetectable change in frequency during the measurement. We recommend the cell density in the range of $5 \times 10^4$ to $1 \times 10^5$ per sensor (if doubling time of the cell line is approximately 24 h), which could be calculated to the cell coverage of the sensor after 48 h ranging from 50% up to 85%. The cell coverage on the sensor should not be less than 50% due to bigger surface area vulnerable to the non-specific binding of lectin to the proteins of the extracellular matrix (ECM) which are naturally produced by adherent cells after they spread well on the surface. At the same time, sufficient time should elapse between the cell seeding and measurements. We recommend 48 h during which it is possible to add compounds changing the cell properties.

1. Remove the medium from the cultivation flask.
2. Gently wash the cells with PBS (5 ml).
3. Add trypsin–EDTA solution (1 ml) and incubate the flask in 37 °C until the cells detach from the surface.
4. Add the equivalent amount of full growth medium to trypsin and resuspend the cells.

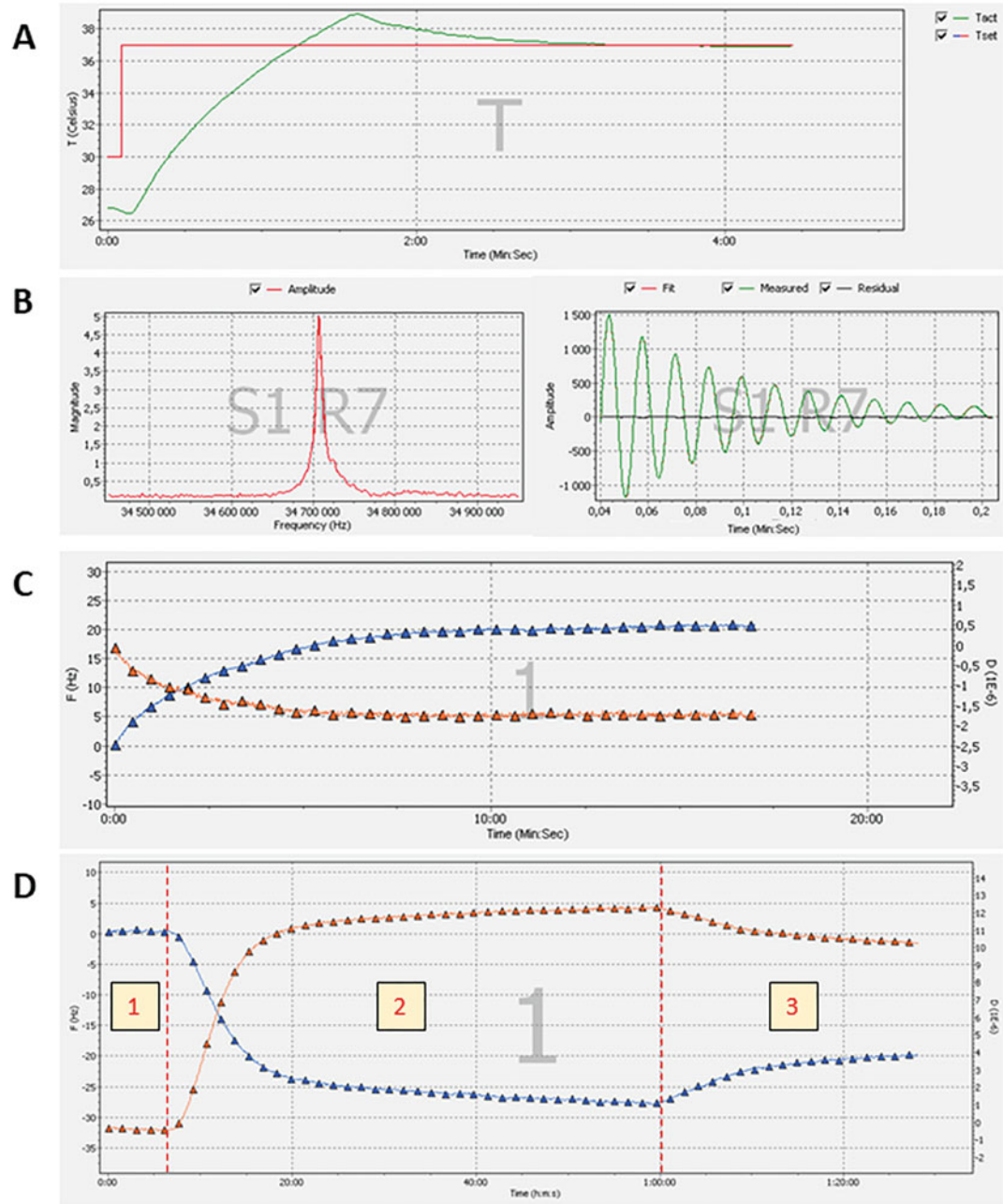


**Fig. 3** Subsequent charts received during the ligand–analyte measurement set up on QCM-D. (**a**)—The stabilization process of the selected temperature; (**b**)—Finding of the resonant frequencies and determining the amplification of the drive amplifier; (**c**)—$f(t)$ and $D(t)$ recordings of the cell-based sensor rinsing process; (**d**)—$f(t)$ and $D(t)$ measurements of lectin interaction with glycans present on cells

5. Centrifuge the cells (5 min, 209 × *g*) and once more resuspend the cells in fresh medium (2 ml).
6. Count the cells with a manual or automatic hemocytometer.

7. Depending on the expected result the concentration should be in the range of $5 \times 10^4$ to $1 \times 10^5$ cells per sensor.
8. Before placing the Au-PS sensor in the 24-well plate, a decontamination step is required. Each sensor should be rinsed with a 70% ethanol solution. Next, the sensor should be rinsed with a PBS buffer and placed in the well (Fig. 2a).
9. 400 μl of cell solution in full growth medium should be gently seeded onto the middle part of the sensor and incubated for typically 48 h in 37 °C in a 5% $CO_2$ atmosphere (*the addition of some compounds influencing the cells is optional and can be performed 24 h after the cell seeding) (Fig. 2b, c).
10. Before the QCM measurement, the cell-based Au-PS sensor should be gently rinsed with PBS (500 μl/well) (Fig. 2d). Optionally, the fixation of cells with 3.7% PFA in PBS (500 μl/well) for 15 min in room temperature can be now performed followed by a second rinse with PBS in the amount of 500 μl per well (*living cell measurements are also possible, but they are more difficult and may require a more detailed optimization of the parameters of measurement).
11. Next, sensors should be gently removed from the well and the bottom part of the sensor (without the cells) must be dried before inserting the sensor to the QCM chamber. Connect the tubes to the chamber and turn on the peristaltic pump to deliver the buffer solution (e.g., PBST) to the QCM chamber with the sensor (Fig. 2e).
12. After the buffer reaches the chamber turn on the Q-Sense software, set the temperature to 37 °C and follow the temperature stabilization process (Fig. 3a). Next, find the resonant frequencies and determine the amplification of the drive amplifier (Fig. 3b). To remove the poorly spread cells the initial flow rate of 100 μl/min of the buffer should be applied for 15–30 min with the temperature set to 37 °C until a flat baseline is reached for both measured parameters (frequency—*f* and dissipation energy—*D*). The detachment of cells is observed as the increase of the *f* value and ordering of the layer as the decrease of the *D* value (Fig. 3c).

    From this point of the procedure, the main part of *the ligand–analyte interaction study* begins (Fig. 2f). The examined analyte solutions (e.g., lectin) should be prepared just before the measurement.
13. A new record of the experiment should be started. For 2 min allow the buffer solution to flow through the tubes (flow rate = 25 μl/min) and the flow module to show a flat baseline (Fig. 3d-1).
14. In the second minute pause the float, move the tube from the vessel with the buffer to the vessel with the measured analyte solution and restart the float.

15. Allow the analyte to flow through the tubes and the flow module for an appropriate amount of time (e.g., 30–60 min). The occurrence of the ligand–analyte interaction will be observed as a decrease in the *f* value and by the increase of dissipation energy value due to creating an unstructured layer (Fig. 3d-2).
16. After the appropriate amount of time the float should be paused, the tube from the vessel with the measured analyte solution should be moved to the vessel with the buffer and the float should be restarted. Rinsing off the excess of the unbound or weakly bound analyte is observed as an increase of the *f* value and the ordering of the layer as the decrease of the *D* value (Fig. 3d-3).
17. End the record, allow the tube system to be aerated and remove the sensor from the module. (*If the regeneration of the cell-based sensor is required move to Subheading 3.3) Prior to the sensor washing (Subheading 3.1) the sensor with cells should be placed in the trypsin–EDTA solution to remove the cells from the surface of the sensor. The new cell-based Au-PS sensor can be placed in the module and the subsequent measurement can start.

### 3.3 Reuse of the Cell-Based Sensor

In case of rarely dividing cells, it is hard to obtain the appropriate amount of cells for just a few sensors. In these cases, it is possible to regenerate the cell-based sensor (remove the bound lectin from the glycans) by the following procedure, although we recommend to use one sensor for a single measurement. To apply this procedure skip **step 17** of the procedure 3.2. (Do not aerate the tube system, nor remove the sensor from the module and especially avoid placing the sensor in a trypsin–EDTA solution!). The cell-based sensor after the ligand–analyte interaction measurement stays in the QCM-D module and the following washing steps should begin:

1. A new record of the experiment should be started. Allow the buffer solution (PBST) to flow through the tubes and the flow module for 15 min (set the flow rate to 50 μl/min).
2. Pause the float, move the tube from the vessel with the buffer to the vessel with the 10 mM glycine solution and restart the float. Allow the solution to flow through the tubes and the flow module for 10 min.
3. Pause the float, move the tube from the vessel with the glycine solution directly to the vessel with the 10 mM NaOH solution, and restart the float. Allow the solution to flow through the tubes and the flow module for the next 10 min.
4. Pause the float, move the tube from the vessel with the NaOH solution to the vessel with the buffer solution and restart the float. Allow the buffer to flow through the tubes and the flow

module for the next 15 min. At this point, the record of the experiment can be terminated.

The procedure of the cell-based sensor regeneration is finished and a new *ligand–analyte interaction study* can be started (**steps 13–16** of the Subheading 3.2).

In literature, there are descriptions of other procedures of the sensor regeneration (e.g., instead of the NaOH solution: a 10 mM HCl solution can be used) [33–35]. However, in our case the described protocol with the use of the glycine buffer prerinsing and next the NaOH solution rinsing worked best. The effectiveness of the regeneration process can be visually followed step-by-step under a fluorescent microscope, if the lectin-ELISA method is applied (Fig. 4a–d).

### *3.4 The Quantitative Lectin-ELISA or Qualitative Immunofluorescent Staining*

One of the methods for a complementary ligand–analyte interaction study is the pseudo enzyme-linked immunosorbent assay. Standard ELISA requires the usage of antibodies; however, in this protocol we suggest the usage of a labeled lectin (e.g., Con A-FITC). What is more, the utilization of different concentrations of the Con A-FITC solutions ensures that the measurement can be

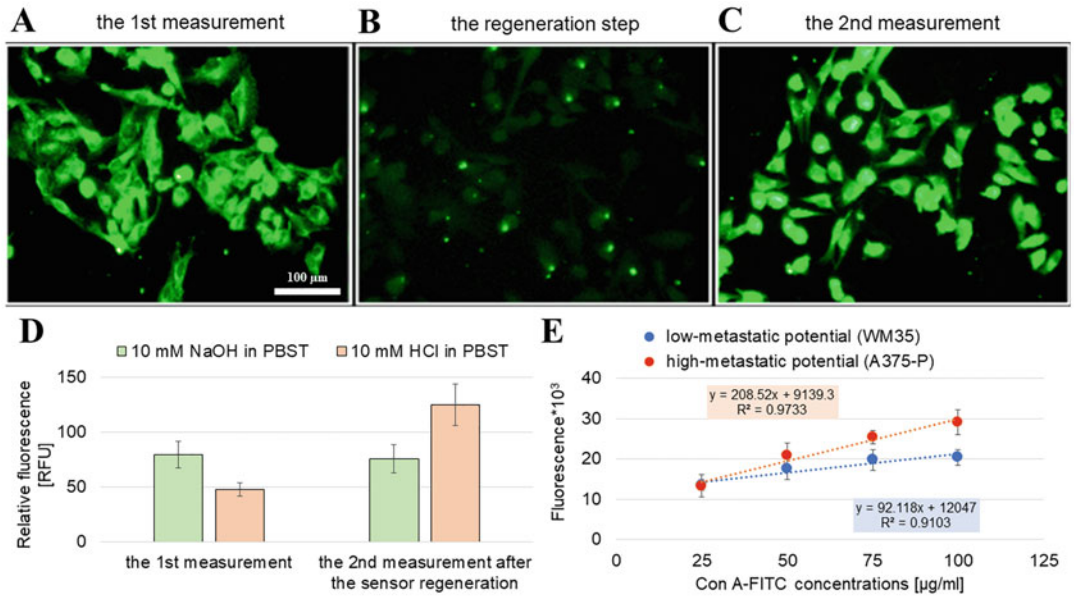


**Fig. 4** The sample results of the sensor regeneration process obtained with the lectin-ELISA cell staining of the metastatic A375-P cell line (methological details in Subheading 3.4). The qualitative results of the cell-based sensor regeneration process with the NaOH solution (**a**–**c**) with the calculation of the fluorescence performed with the ImageJ software for the NaOH and HCl solutions comparison (**d**). The quantitative analysis of the amount of the Con A-FITC lectin bound to the surface glycans of melanoma cells with different metastatic potential as a function of lectin concentration performed on a microplate reader (**e**). WM35—melanoma cell line from the radial growth phase; A375-P—melanoma metastasis to the lungs

also used for a quantitative analysis. We recommend the usage of at least four different concentrations of the Con A-FITC solutions in a PBST buffer for a quantitative analysis. For this protocol adherent cells are used, but it may be easily adapted for suspension cell culture by plate centrifugation after each step of staining.

1. Seed the cells in the 96-well plate at the density of $1 \times 10^4$ cells per well in the volume of 100 μl.
2. Incubate the plate with the cells for typically 48 h in 37 °C in 5% $CO_2$ atmosphere (*the addition of some compounds influencing the cells is optional and can be performed 24 h after the cell seeding).
3. Remove the medium and rinse the cells with PBS (100 μl/well).
4. In this procedure, the fixation step is recommended (otherwise for living cells shorten the length of the staining with Con A-FITC and Hoechst 33342). Add 50 μl per well of 3.7% PFA in the PBS solution and incubate for 15 min at room temperature. Next, rinse the cells with PBS (100 μl/well).
5. Add the prepared concentrations of the Con A-FITC solution (50 μl/well) and incubate the plate in darkness and room temperature for 30–60 min.
6. Rinse the cells with PBS (100 μl/well) avoiding the excessive exposure to daylight.
7. Add the prepared 1 μg/ml Hoechst 33342 dye solution in PBS (50 μl/well) and incubate the plate in darkness and room temperature for 15 min.
8. Once again rinse the cells with PBS (100 μl/well) avoiding the excessive exposure to daylight.
9. Remove completely PBS buffer and measure the fluorescence with a microplate reader or visualize the samples with a fluorescent microscope. Use the following wavelengths for excitation/emission: for the Con A-FITC sample staining 492 ± 9 nm/518 ± 9 nm and for the Hoechst 33342 sample staining 350 ± 20 nm/461 ± 20 nm.

On the microscopic images the fluorescence can be used for a qualitative comparison (Fig. 4a–c) or a quantitative one if special software like ImageJ is available (Fig. 4d). Moreover, a quantitative analysis of the amount of lectin bound to the surface glycans on the whole cell is obtained with the microplate reader. While plotting the fluorescence versus the lectin concentration a linear relationship is obtained. The slope can bring information about the types of the measured cells (normal/cancerous). Highly-glycosylated cells are those with a high-metastatic potential and they present a greater

slope than the normal ones or the primary tumor cells (with non- or low-metastatic potential) (Fig. 4e).

### 3.5 One-Day Procedure of Cell Adhesion Study Followed by Ligand–Analyte Interaction Study

This procedure allows to shorten the time of the analysis from 3 days to 1, which is a very practical approach, especially if applied in diagnostics. Cells that grow in suspension can be used directly for this procedure. However, adherent cells may also be used after obtaining a solution of the suspended cells. It is recommended to use the mechanical dissociation of cells from the substrate not the enzymatic one, because trypsin catalyzes the hydrolysis of the surface peptides which are mainly responsible for the recognition of microorganisms and the attachment of cells to other cells, as well as to various substrates including the extracellular matrix [36]. The partition of those proteins may significantly reduce the ligand–analyte interaction.

The 1-day procedure consists of four stages (Fig. 5): preparation of the sensor, obtaining the cell suspension, measurement of cell adhesion (suspension cell–based sensors), and ligand–analyte interaction study performed on the whole cells. The addition of a compound to the cells is also possible, but the incubation should be carried out before the cells are suspended. In this procedure, the most important thing is the knowledge or experimental check of

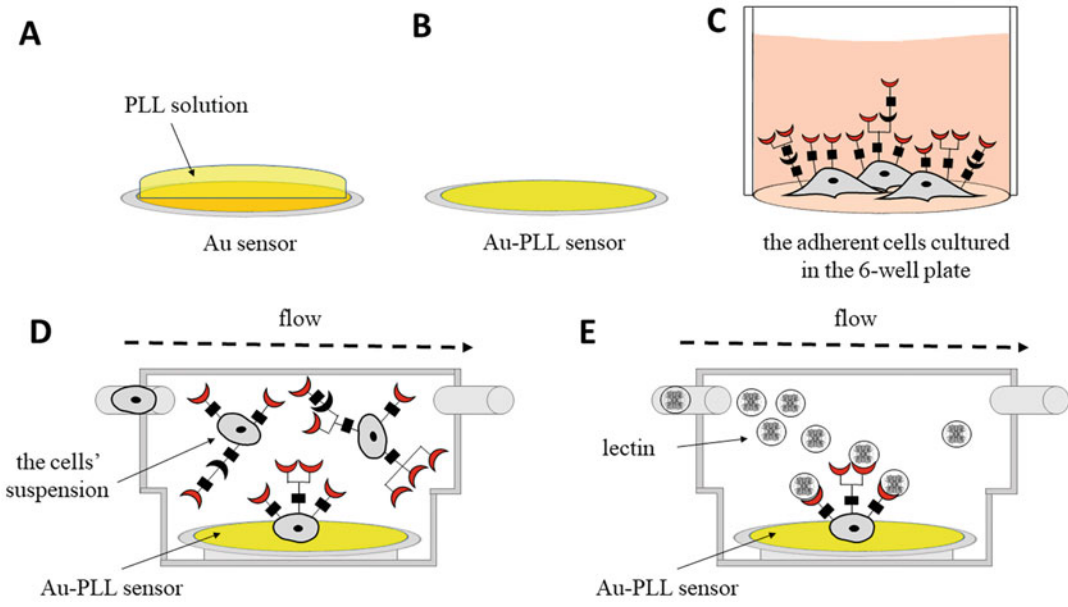


**Fig. 5** The following stages of the 1-day procedure. (**a**)—The functionalization of the Au sensor with poly-L-lysine solution; (**b**)—the prepared Au-PLL sensor is ready for use after rinsing with Milli-Q water and drying; (**c**)—adherent cells ready for the mechanical detachment from the surface of the 6-well plate; (**d**)—the injection of the cell suspension into the module and the measurement of the cell adhesion process; (**e**)—the insertion of the lectin solution into the module and the measurement of its interaction with glycans present on the cells

the concentration of the studied analyte which could possibly be used to avoid its nonspecific binding to the surface. For example, the application of lectins in the experiments on poly-L-lysine coated gold sensor is possible in much lower concentrations than in the measurements with polystyrene coated gold sensors [37]. Furthermore, the first injection of highly concentrated cells in suspension assures that only small areas on the sensor would be available for the lectin to bind and give changes in the frequency signal on the QCM-D. However, lowering the concentration of lectin in the second injection causes that the non-specific signal would be very small in comparison with the signal obtained from lectin bound specifically to the cells.

1. Prepare the Au-PLL sensor as described in Subheading 3.1 (Fig. 5a, b).
2. Remove the medium from the selected number of wells of the 6-well plate (depending on the required amount of cells for the experiment) (Fig. 5c).
3. Gently wash the cells with PBS (1–2 ml/well).
4. Add fresh PBS (2 ml) to the well and detach mechanically the cells from the surface with a plastic scraper.
5. Resuspend the cells and transfer them to a centrifuge tube.
6. Centrifuge the cells (5 min, 581 $\times g$) and once more resuspend the cells in fresh PBS.
7. Count the cells with a manual or automatic hemocytometer.
8. Depending on the expected result the concentration should range from $5 \times 10^5$ to $1 \times 10^6$cells per sensor.
9. Prepare the required concentration of cells in 1 ml of PBST.
10. Insert the Au-PLL sensor to the QCM chamber. Connect the tubes to the chamber and turn on the peristaltic pump to deliver the buffer to the QCM chamber with a sensor.
11. After the buffer reaches the chamber turn on the Q-Sense software, set the temperature to 37 °C and follow the temperature stabilization process. To remove the unbound poly-L-lysine from the surface of the sensor the initial flow rate of 100 μl/min of the buffer should be applied for 15–30 min with the temperature set to 37 °C until a flat baseline is reached for both $f$ and $D$ parameters. The detachment of PLL is observed as the increase of the $f$ value and the ordering of the layer as the decrease of the $D$ value.

From this point of the procedure, the main part of *the cell adhesion study* begins (Fig. 5d). The cell suspension should be prepared just before measurement.

12. A new record of the experiment should be started. For 2 min allow the buffer solution to flow through the tubes (flow rate = 25 μl/min) and the flow module to show a flat baseline.
13. In the second minute pause the float, move the tube from the vessel with the buffer to the vessel with the cell suspension and restart the float.
14. Allow the cells to flow through the tubes and the flow module for an appropriate amount of time (e.g., 30 min). The binding of the cells to the surface of the Au-PLL sensor will be observed as a decrease in the *f* value and the increase of dissipation energy value is due to the creation of an unstructured layer. In time, the *D* parameter may begin to decrease while the *f* parameter will be constant (no or little change in mass will be notable) which suggests not only the adhesion of the cells on the surface of the sensor but also the beginning of the cell spreading process (more details in Subheading 3.7, Fig. 7).
15. After an appropriate time, the float should be paused, the tube from the vessel with the cells should be moved to the vessel with the buffer, and the float should be restarted. Rinsing off the excess of the unbound or weakly bound cells is observed as an increase of the *f* value and the ordering of the layer as the decrease of the *D* value.
16. End the recording of the cell adhesion study.

From this point of the procedure, the main part of the *ligand–analyte interaction study* begins (Fig. 5e). The examined analyte solutions (e.g., lectin) should be prepared just before measurement.

17. Begin a new record of the experiment and wait until a flat baseline is reached. Pause the float, move the tube from the vessel with the buffer to the vessel with the measured analyte solution and restart the float.
18. Allow the solution to flow through the tubes and the flow module for an appropriate amount of time (e.g., 30–60 min). The occurrence of the ligand–analyte interaction will be observed as a decrease in the *f* value and the increase of the *D* value.
19. After the appropriate amount of time the float should be paused, the tube from the vessel with the measured analyte solution should be moved to the vessel with the buffer and the float should be restarted. Rinse off the excess of the unbound or weakly bound analyte.
20. End the record, allow the tube system to be aerated and remove the sensor from the module. Prior to the sensor washing, sensor with cells should be placed in the trypsin–EDTA solution to remove the cells from the surface of the

sensor. The new Au-PLL sensor can be placed in the module and the subsequent measurement can start.

### 3.6 QCM-D Chamber Cleaning

After the measurements the QCM chamber has to be cleaned. This procedure is performed with the appropriate solutions recommended by the manufacturer.

1. Insert a new sensor without the cells into the chamber, connect the tubes and turn on the peristaltic pump (set the flow to 200 μl/min).
2. Rinse the chamber with a 2% Hemanex® II solution for 5 min.
3. Rinse the chamber with Milli-Q water for 5 min.
4. Rinse the chamber with a 70% Ethanol solution for 2 min.
5. Rinse the chamber with Milli-Q water for 5 min.
6. Disconnect the tubes, take out the sensor and dry the chamber with nitrogen.

### 3.7 Analysis of Viscoelastic Properties of Cells with QCM-D

The quartz crystal microbalance is predominately used for kinetic and thermodynamic analysis of the ligand–analyte interactions. It allows to determine the association ($k_{on}$) and the dissociation ($k_{off}$) rates constant, as well as the association constant ($K_A$) and the dissociation constant ($K_D$). A complementary method enabling the kinetic analysis with the determination of $k_{off}$ and also the energy landscape is the atomic force microscopy (AFM)-based force spectroscopy. However, it requires not only a detailed preparation of the sample, the AFM tip functionalization with the analyte, laborious measurements performed by a specially trained employee and last but not least tedious data analysis. What is more, for this calculation it is required to first determine the effective spring constant ($k_{eff}$) which reflects not only the spring constant of the cantilever and the occurred molecular interaction but also the elasticity of the cell [25]. To elaborate the cell elasticity the AFM with force spectroscopy with a bare tip can also be applied [38]. On the other hand, the surface plasmon resonance (SPR) enables the kinetic analysis and is a method similar to QCM-D in actions concerning the preparation of the experiment. But in this method in order to observe the direct ligand–analyte binding interaction, it should take place near the metal surface which is about 200 nm high [39]. This is a serious problem due to the height of the cell that could reach even 5–10 μm depending on the cell type. That is why, for these studies, QCM-D is the most effective method.

Besides the standard kinetic analysis, with QCM-D the observation of changes in the cells' viscoelastic properties can be detected. It is due to the correlation of both measured parameters during the QCM-D experiments—changes in the dissipation energy ($\Delta D$) versus changes in frequency ($\Delta f$). What is more, the

$D(f)$ plot is a very useful tool for presenting the obtained results. The plotting can be done in different programs like R-software, Matlab, and Excel after the raw data export.

1. Open the *QTools software* and download the measurement file (*.qsd*). Open as many measurement files as are required for the *Df* plot analysis.
2. Select *Plot→New* (Fig. S1a).
3. As soon as the *New plot* window appears, select the first measurement to be plotted from the *Data window*. Select the data to be plotted on the *X*-axis and $\Upsilon$-axis (e.g., *X*-axis frequency 7 overtone, $\Upsilon$-axis dissipation 7 overtone). The *Df* plot should appear on the figure (Fig. S1b).
4. For the next measurements to be plotted on the same *Df* graph, add each measurement by the (+) button present on the left side of the *New Plot* window and follow the guidelines from **step 3** for each measurement (Fig. S1b).
5. As soon as all the measurements are placed on the *Df* plot select the *Show Plot Editor* window (Fig. S1c). The names of the *X* and $\Upsilon$ axises can be changed here as well as the names in the legend. To keep the order of the added measurements the *Autosort series order* box should be unchecked (Fig. S1d).
6. In the *Show Plot Editor* window, one can also change the colors of the data, the width of the points and the symbol appearing on the graph (Fig. S1d).
7. For more advanced changes in text editing (font, size, etc.) as well as chart axis editing (minimum, maximum, increment, etc.) or legend editing (position, check boxes, etc.) select *Advanced Plot Editor* available from the *Plot editor window* or *Copy plot→Plot exporting dialog* (Fig. S1d–g).
8. To export *Df* plot in a form of a graph, select *Advanced Plot Editor* (available from the *Plot editor window* or *Copy plot→Plot exporting dialog*), select the *Export* tab and pick the format in which the graph should be saved (e.g., bitmap, GIF, JPEG, PNG). Click the *Save...* button and select the place to save the data (Fig. S1h).
9. The *Df* plot can also be saved (*File→Save as...*) as a (*.qtp*) file. However, it should be kept in mind that after saving, no more data can be added to the graph. To remove data from the saved plot (*.qtp* file), the data on the legend can be unchecked.

In the measurements of lectin–glycan interaction the largest difference in the $D(f)$ are observed for cells with highly-glycosylated surface receptors (e.g., cells with high metastatic potential) in comparison to low-glycosylated receptors of the cells (e.g., cells with low- or nonmetastatic potential, like: normal cells

or primary tumor cells) (Fig. 6). MALDI-MS analysis of glycoproteins isolated from cells showed the presence of macromolecular glycoproteins in primary tumor cells, whereas in metastatic cells it confirmed the presence of smaller glycoproteins [15]. The data from both independent analyzes performed by different techniques are consistent and confirm the occurrence of short low-branched glycoproteins terminated with α-D-mannose or α-D-glucose on the surface of cells from the primary tumor and long branched sugar structures at surface of metastatic cells. This shows the possibility of discriminating cells in different progression stages what can be a useful method in cancer diagnostics (Fig. 6b). Introduction of this method requires further, extensive research of cells isolated from a suitably large group of patients with detected melanoma in order to confirm the diagnosis of the stage of the cancer. This methodology may also allow the study of the effects of new substances on the inhibition of EMT to develop a procedure that allows the

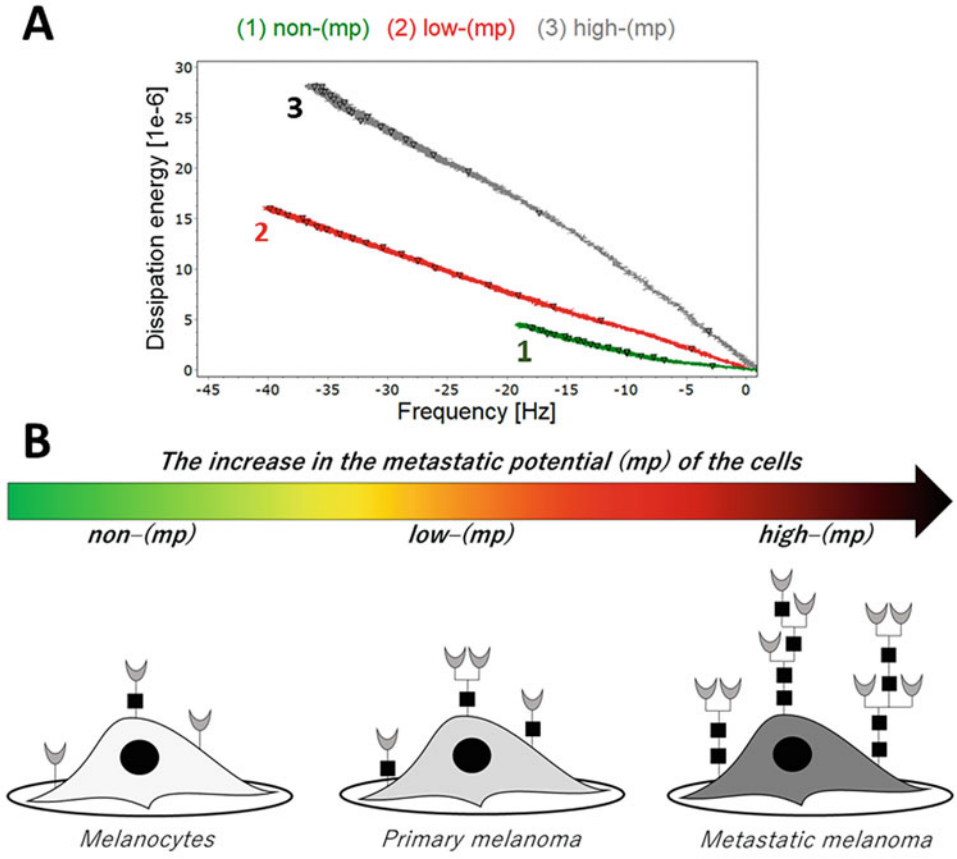


**Fig. 6** The viscoelastic properties of cells during the lectin–glycan interaction. (**a**)—Differences in the $D(f)$ plots obtained during the lectin–cell surface glycan interaction; (**b**)—The interpretation of the $D(f)$ results with the glycosylation profile of melanoma cells from different progression stages

characterization of new therapeutic agents for primary and advanced melanoma.

To investigate the value of the angle of the data on *Df* plots, it is recommended to export the data to Excel (*File→Export...*) (Fig. S1i) and then to determine the linear regression and slope of the data curve (Fig. S1j). If the curve cannot be approximated with a linear regression due to the low value of $R^2$, we recommend to reduce the amount of data to the beginning of the curve.

1. Open Microsoft Excel file with the data from the measurements.
2. Insert the data for Time, Frequency (e.g., 7th overtone) and Dissipation energy (e.g., 7th overtone) to another sheet for all measurements intended for analysis.
3. Draw a scatter plot where *F* values are on *X*-axis and *D* values on *Y*-axis for all of the measurements. In the value of *X*/*Y* series, insert the formula [=Sheet1!$F$...:$F$...], where in places of the dots (...) insert the first and the last number of rows with the data.
4. Approximate the data with the linear regression ($Y = aX^*b$). The tgα can be obtained from the slope value ($a$). The bigger the angle of the curve is observed, the higher viscoelastic properties of the created lectin–glycan complex is obtained (Fig. S1j).

By monitoring the cells' behavior with the QCM-D the observed $D(f)$ dependencies bring many beneficial information [40] concerning the time needed for binding to the surface and spreading (Fig. 7a), the occurrence of intracellular transformations (Fig. 7b) or even the negative impact (dehydration, cell lysis, rounding or detachment from the growth surface) which some compounds can have on the cells (Fig. 7c). The adsorption of cells to the surface is a cell-dependent process which takes about 1–3 h (Fig. 7a-1). The more invasive the cell is (highly metastatic), the quicker the adsorption takes place. When determining the time needed for the cells to attach to the surface, one can facilitate performing other tests (like cell staining with crystal violet) dedicated to monitoring cell adhesion after treatment with different compounds. In case of the growth surface modification study it should be recommended to track changes occurring in the cells' cytoskeleton or the extracellular matrix remodeling (Fig. 7b-3, more information in [27]). On the other hand, if a monolayer of the cells is already growing on the sensor and the detection of a real-time influence of a compound [40] (or microorganisms [41]) is to be studied, the $D(f)$ plot can show some common cytotoxic effects on cells like membrane permeabilization (Fig. 7c-5), rounding of cells (Fig. 7c-6), and their detachment from the surface of the sensor (more information in [42]).

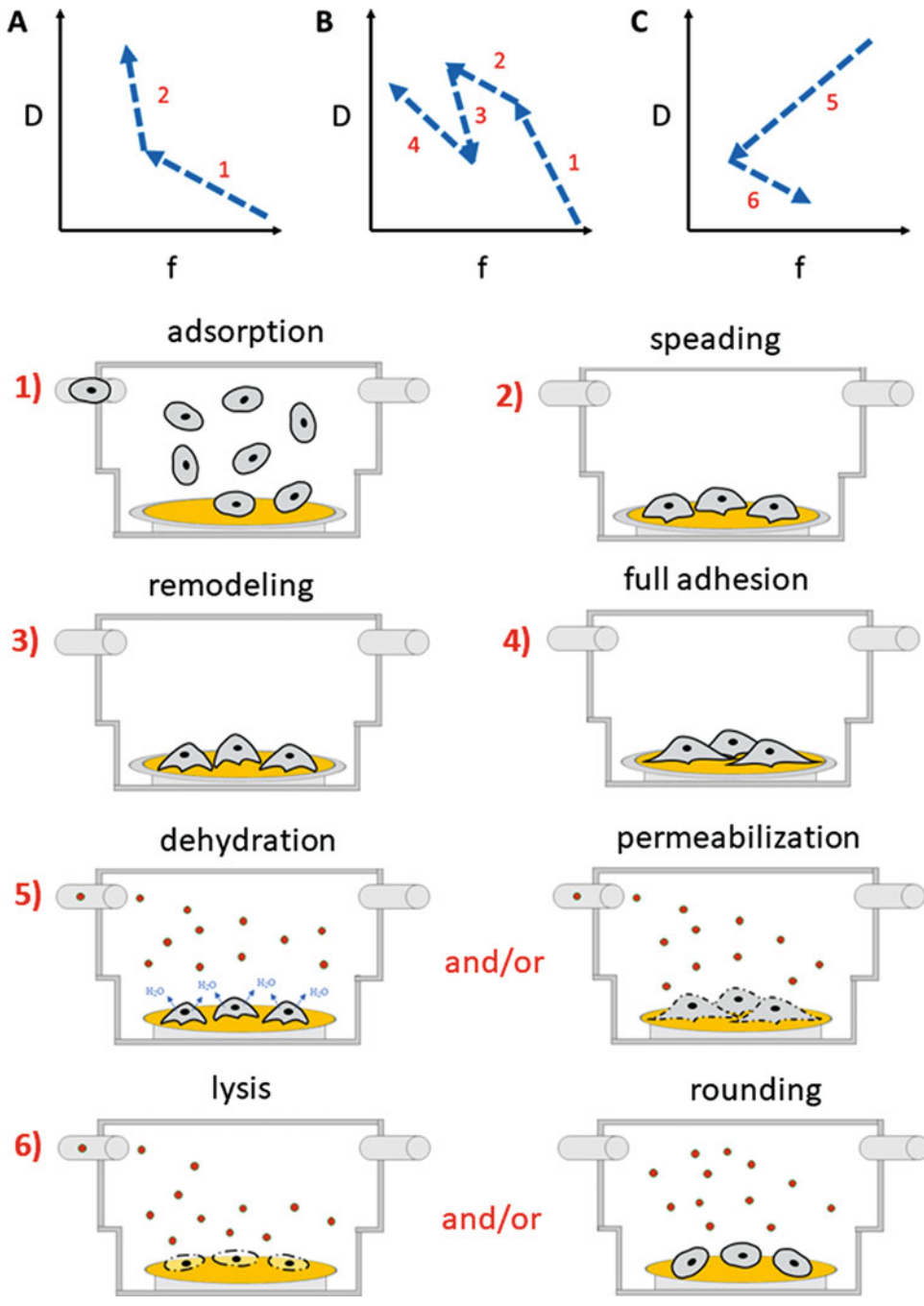


**Fig. 7** Schematic representation of the viscoelastic properties of cells during their adhesion to the surface (**a**)—the adsorption of cells to the surface (1) and cell spreading (2); (**b**)—the remodeling of the ECM and changes in the cells' cytoskeleton (3) followed by further cell adhesion to the surface (4); and also changes in the cells' viscoelastic properties due to some cytotoxic compounds (**c**)—dehydration (5) and as a consequence the cell lysis (6)

## Acknowledgments

This work was supported by the National Science Centre (Poland) grant no. 2017/27/N/ST4/01389 and by the Warsaw University of Technology. Additionaly, AS would like to acknowledge the National Science Centre (Poland) for the scholarship ETIUDA 6 (no. 2018/28/N/ST4/00511). We thank our students Nina Knapik (MSc. Eng.), Natalia Kulczakiewicz (MSc. Eng.), Patrycja Kowalska (MSc. Eng.), and Paulina Kośka (MSc. Eng.) for their assistance in the development of the protocols.

**Conflict of Interests**: *The authors declare that there are no conflicts of interest.*

### References

1. Peitzsch C, Tyutyunnykova A et al (2017) Cancer stem cells: the root of tumor recurrence and metastases. Semin Cancer Biol 44:10–24
2. McGuire S (2016) World cancer report 2014. Geneva, Switzerland: World Health Organization, International Agency for Research on Cancer, WHO Press, 2015. Adv Nutr 7 (2):418–419
3. Pearlman PC, Divi R et al (2016) The National Institutes of Health Affordable Cancer Technologies Program: improving access to resource-appropriate technologies for cancer detection, diagnosis, monitoring, and treatment in low- and middle-income countries. IEEE J Transl Eng Health Med 4:1–8
4. Alexander M, Bendas G (2011) The role of adhesion receptors in melanoma metastasis and therapeutic intervention thereof. In: Murph M (ed) Research on melanoma—a glimpse into current directions and future trends. InTech
5. Kato M, Saunders S et al (1995) Loss of cell surface syndecan-1 causes epithelia to transform into anchorage-independent mesenchyme-like cells. Mol Biol Cell 6(5):559–576
6. Thiery JPL, Acloque H et al (2009) Epithelial-mesenchymal transitions in development and disease. Cell 139(5):871–890
7. Valastyan S, Weinberg RA (2011) Tumor metastasis: molecular insights and evolving paradigms. Cell 147(2):275–292
8. Aberle H, Schwartz H, Kemler R (1996) Cadherin-catenin complex: protein interactions and their implications for cadherin function. J Cell Biochem 61(4):514–523
9. Janik ME, Hoja-Lukowicz D, Przybylo M (2016) Cadherins and their role in malignant transformation: implications for skin cancer progression. In: Blumenberg M (ed) Human skin cancer, potential biomarkers and therapeutic targets. InTech
10. Keswell D, Kidson SH, Davids LM (2015) Melanocyte migration is influenced by E-cadherin-dependent adhesion of keratinocytes in both two- and three-dimensional in vitro wound models: melanocyte migration and keratinocyte adhesion. Cell Biol Int 39 (2):169–176
11. Qi J, Wang J et al (2006) Involvement of Src family kinases in N-cadherin phosphorylation and β-catenin dissociation during transendothelial migration of melanoma cells. Mol Biol Cell 17(3):1261–1272
12. Wheelock MJ, Johnson KR (2003) Cadherins as modulators of cellular phenotype. Annu Rev Cell Dev Biol 19(1):207–235
13. Glavey SV, Huynh D et al (2015) The cancer glycome: carbohydrates as mediators of metastasis. Blood Rev 29(4):269–279
14. Dennis J (1999) Glycoprotein glycosylation and cancer progression. Biochim Biophys Acta 1473(1):21–34
15. Ciołczyk-Wierzbicka D, Amoresano A et al (2004) The structure of the oligosaccharides of n-cadherin from human melanoma cell lines. Glycoconj J 20(7–8):483–492
16. Cooper MA (2009) Label-free biosensors: techniques and applications. Cambridge University Press, New York
17. Sobiepanek A, Kobiela T (2018) Application of biosensors in cancer research. Rev Res Cancer Treat 4(1):4–12
18. Sauerbrey G (1959) Verwendung von Schwingquarzen zur Wäigung diinner

Schichten und zur Mikrowäigung*. Z Phys 155:206–222
19. Kanazawa KK, Ii JGG (1985) The oscillation frequency of a quartz resonator in contact with a liquid. Anal Chm Acta 175:99–105
20. Alassi A, Benammar M, Brett D (2017) Quartz crystal microbalance electronic interfacing systems: a review. Sensors 17(12):2799
21. Casteleiro-Roca JL, Calvo-Rolle JL et al (2014) New approach for the QCM sensors characterization. Sensors Actuators A Phys 207:1–9
22. Edvardsson M (2019) QCM-D in relation to other QCMs, what are the differences, and does it matter which one is used? Biolin Sci White Paper
23. Rodahl M, Höök F et al (1995) Quartz crystal microbalance setup for frequency and Q-factor measurements in gaseous and liquid environments. Rev Sci Instrum 66(7):3924–3930
24. Saint-Guirons J, Ingemarsson B (2012) Using a quartz crystal microbalance biosensor for the study of metastasis markers on intact cells. In: Metastasis research protocols, vol 878. Humana Press, Totowa, NJ, pp 175–183
25. Sobiepanek A, Milner-Krawczyk M et al (2017) AFM and QCM-D as tools for the distinction of melanoma cells with a different metastatic potential. Biosens Bioelectron 93:274–281
26. Sobiepanek A (2017) Rola glikokoniugatów powierzchniowych w diagnostyce nowotworów złośliwych skóry [The role of surface glycoconjugates in the diagnosis of skin malignancies]. In: Zagadnienia aktualnie poruszane przez młodych naukowców, vol 11. CREATIVETIME, pp 24–28
27. Kılıç A, Kok FN (2018) Quartz crystal microbalance with dissipation as a biosensing platform to evaluate cell–surface interactions of osteoblast cells. Biointerphases 13(1):11001
28. Yan T-R, Lee C-F, Chou H-C (2012) QCM as cell-based biosensor. In: Ekinci D (ed) W chemical biology. InTech
29. Pei Z, Anderson H et al (2005) Study of real-time lectin–carbohydrate interactions on the surface of a quartz crystal microbalance. Biosens Bioelectron 21(1):60–66
30. Sobiepanek A, Baran J et al (2020) Different types of surface modification used for improving the adhesion and interactions of skin cells. Open Access J Biomed Sci 2(1):275–278
31. Curtis AS, Forrester JV et al (1983) Adhesion of cells to polystyrene surfaces. J Cell Biol 97 (5):1500–1506
32. Blau A (2013) Cell adhesion promotion strategies for signal transduction enhancement in microelectrode array in vitro electrophysiology: an introductory overview and critical discussion. Curr Opin Colloid Interface Sci 18 (5):481–492
33. Yakovleva ME, Safina GR, Danielsson B (2010) A study of glycoprotein–lectin interactions using quartz crystal microbalance. Anal Chim Acta 668(1):80–85
34. Safina G, Vanlier M, Danielsson B (2008) Flow-injection assay of the pathogenic bacteria using lectin-based quartz crystal microbalance biosensor. Talanta 77(2):468–472
35. Peiris D, Spector AF et al (2017) Cellular glycosylation affects herceptin binding and sensitivity of breast cancer cells to doxorubicin and growth factors. Sci Rep 7:srep43006
36. Huang H-L, Hsing H-W et al (2010) Trypsin-induced proteome alteration during cell subculture in mammalian cells. J Biomed Sci 17 (1):36
37. Wang W, Yang Y et al (2012) Label-free measuring and mapping of binding kinetics of membrane proteins in single living cells. Nat Chem 4(10):846–853
38. Sobiepanek A, Milner-Krawczyk M et al (2016) The effect of delphinidin on the mechanical properties of keratinocytes exposed to UVB radiation. J Photochem Photobiol B Biol 164:264–270
39. Lakayan D, Tuppurainen J et al (2018) Angular scanning and variable wavelength surface plasmon resonance allowing free sensor surface selection for optimum material- and bio-sensing. Sensors Actuators B Chem 259:972–979
40. Tonda-Turo C, Carmagnola I, Ciardelli G (2018) Quartz crystal microbalance with dissipation monitoring: a powerful method to predict the in vivo behavior of bioengineered surfaces. Front Bioeng Biotechnol 6:158
41. Staniszewska M, Sobiepanek A et al (2020) Sulfone derivatives enter the cytoplasm of Candida albicans sessile cells. Eur J Med Chem 191:112139
42. Fatisson J, Azari F, Tufenkji N (2011) Real-Time QCM-D monitoring of cellular responses to different cytomorphic agents. Biosens Bioelectron 26(7):3207–3212

# Part III

## Monitoring and Imaging

# Chapter 29

# Hyperpolarized Micro-NMR Platform for Sensitive Analysis of In Vitro Metabolic Flux in Living Cells

**Sangmoo Jeong and Kayvan R. Keshari**

## Abstract

Metabolism represents an ensemble of cellular biochemical reactions, and thus metabolic analyses can shed light on the state of cells. Metabolic changes in response to external cues, such as drug treatment, for example, can be rapid and potentially an early indicator of therapeutic response. Unfortunately, conventional techniques to study metabolism, such as optical microscopy or mass spectrometry, have functional limitations in specificity and sensitivity. To address this technical need, we developed a sensitive analytical tool based on nuclear magnetic resonance (NMR) technology, termed hyperpolarized micro-NMR, that enables rapid quantification of multiple metabolic fluxes in a small number of cells, down to 10,000 cells, nondestructively. This analytical capability was achieved by miniaturization of an NMR detection coil along with hyperpolarization of endogenous metabolites. Using this tool, we were able to quantify pyruvate-to-lactate flux in cancer stem cells nondestructively within 2 min, which has not been possible with other techniques. With further optimization, we envision that this novel device could be a powerful analytical platform for sensitive analysis of metabolism in mass-limited samples.

**Key words** Hyperpolarization, Microfluidics, Micro-coil, NMR, Metabolic flux

## 1 Introduction

Metabolism fundamentally regulates our daily lives, as it not only generates energy and building blocks but also plays a major role in redox balance [1] and epigenetic regulation [2]. Due to its relevance in biochemical homeostasis, altered metabolism has been implicated in a wide range of diseases, including cancer [3]. For example, a common metabolic feature of cancer cells is significantly upregulated glucose consumption and lactate generation, regardless of oxygen availability, commonly referred to as the "Warburg effect." This feature allows cancer cells to meet the metabolic needs for deregulated proliferation [4] and evade immune surveillance in the tumor microenvironment [5]. Targeting metabolic vulnerabilities of cancer cells has emerged as a promising therapeutic approach, with numerous clinical trials inhibiting metabolic

Miguel R. Ossandon et al. (eds.), *Biomedical Engineering Technologies: Volume 1*, Methods in Molecular Biology, vol. 2393, https://doi.org/10.1007/978-1-0716-1803-5_29, 

enzymes or metabolite transporters underway (e.g., NCT02632708, NCT03875313, NCT01791595).

The recent surge of interest in metabolic dysfunction has led to the advancement of technologies aimed at interrogating metabolism. Particularly, nuclear magnetic resonance (NMR) spectroscopy and magnetic resonance imaging (MRI) techniques in conjunction with hyperpolarization of nuclear spins have emerged as a novel approach, as they allow nondestructive analysis of metabolic "flux" [6]. Metabolic flux, the rate of a metabolic reaction, indicates the activity of a metabolic pathway of interest at a given moment and sensitively changes in response to various factors, including drug treatment. Flux analysis can be beneficial for evaluating treatment response before clinicopathological changes occur and for investigating how cells rewire their metabolism under varying environmental conditions. Hyperpolarization, which increases the polarization level of target nuclei beyond the level at thermodynamic equilibrium, has been reported to enhance the sensitivity of NMR/MRI detection methods by a factor of more than 10,000 [7]. Multiple approaches have been developed to achieve hyperpolarization, including parahydrogen-induced polarization and dissolution dynamic nuclear polarization (dDNP) [8]. dDNP, in particular, achieves the highest polarization level among hyperpolarization methods—up to 70% [9]—and utilizes endogenous metabolites, including pyruvate [10–13] and glutamine [14]. Due to these advantages, several ongoing clinical trials with dDNP technology seek to evaluate its capacity to diagnose disease and monitor treatment (e.g., NCT03830151, NCT03502967, NCT02526368, NCT02647983). However, even with dDNP technology, numerous cells (order of $10^7$ cells) are required to analyze metabolic fluxes, and it has thus been challenging to apply dDNP to studying metabolism in mass-limited samples, including stem cells or tumor organoids.

To address this limitation, we have developed the hyperpolarized micro-NMR platform, which allows for metabolic flux analysis in a small number of cells (down to $10^4$ cells) [15]. This sensitive tool is based on the development of a miniaturized NMR detection coil (micro-coil) optimized for hyperpolarized experiments. As shown in Fig. 1a, the micro-coil is fabricated inside a block made of elastomer, which is mounted on top of our custom-designed printed circuit board. Because the micro-coil, with a detection volume of ~2 μL, is integrated with a microfluidic channel, it is easy to load and unload liquid samples, such as a mixture of cell suspension and hyperpolarized substrates (Fig. 1b). The metabolic flux of pyruvate-to-lactate conversion can be calculated based on the changes in NMR signals. The NMR signal of hyperpolarized molecules decays exponentially with a spin-lattice relaxation constant $T_1$; signal decays faster than $T_1$ indicate that a hyperpolarized substrate is being consumed. Figure 2 shows an example of

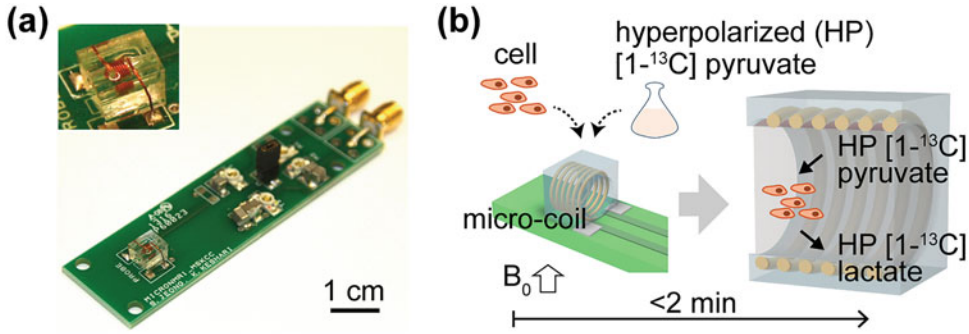


**Fig. 1** Hyperpolarized micro-NMR platform, (**a**) Optical picture of the micro-NMR circuit. Inset shows the micro-coil embedded in a PDMS block, (**b**) Assay schematic with the hyperpolarized micro-NMR platform. Total assay can be finished within 2 min. $B_0$, magnetic field. Adapted from reference [15]

$^{13}$C-NMR spectra acquired from the hyperpolarized micro-NMR system, as described in Fig. 1b: [1-$^{13}$C] pyruvate signal decreases faster than its exponential decay (Fig. 2b), which indicates that pyruvate was being consumed by these cells, and [1-$^{13}$C] lactate signal decreases slower than its exponential decay (Fig. 2c), which indicates that lactate was being generated by cells (from pyruvate).

## 2 Materials

### *2.1 Micro-coil*

1. SYLGARD-184 Silicone Elastomer Clear (Dow).
2. 32-AWG magnetic wire (Belden 8056).
3. Metal rod with a diameter of 1.4 mm.
4. Disposable plastic petri dish with a diameter of 60 mm.
5. Vacuum desiccator.
6. All-purpose glue (e.g., Krazy glue).
7. Razor blade.

### *2.2 Micro-NMR Circuit*

1. Custom-designed printed circuit board.
2. Non-magnetic passive circuit components (e.g., resistor, capacitor, and SMA connector).
3. Soldering equipment.

### *2.3 Hyperpolarization of Metabolites*

1. [1-$^{13}$C] pyruvic acid (Sigma-Aldrich).
2. AH-111501 radical (GE).
3. SPINlab polarizer (GE).
4. 10N sodium hydroxide solution.
5. Trizma hydrochloride (Sigma-Aldrich).

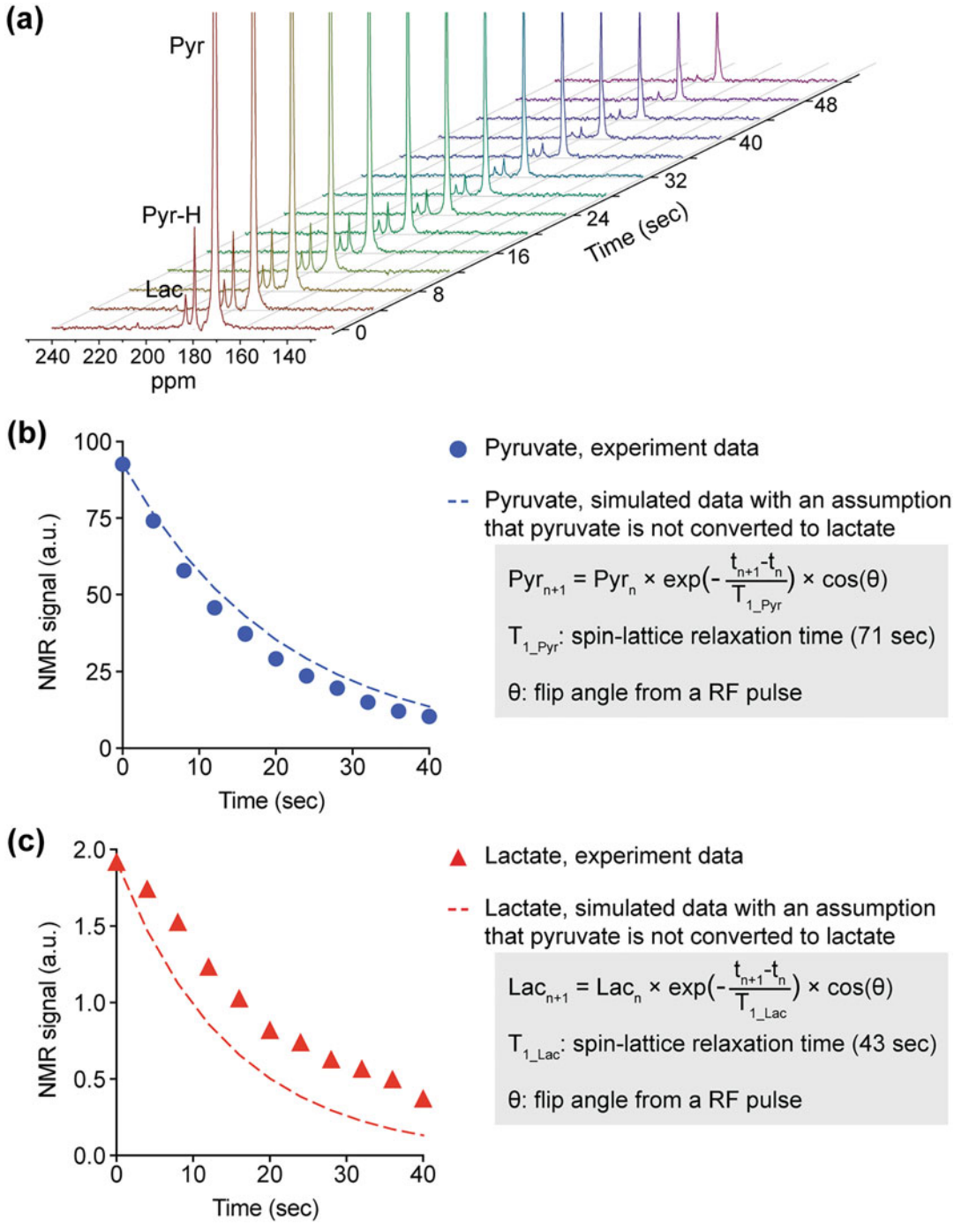


**Fig. 2** Analysis of pyruvate-to-lactate metabolic flux in UOK262 cells with the hyperpolarized micro-NMR system, (**a**) $^{13}$C-NMR spectra acquired from the hyperpolarized micro-NMR system with [1-$^{13}$C] pyruvate and UOK262 cells (renal cancer cell line). The cell number in the micro-coil was approximately 50,000. *Pyr* pyruvate, *Pyr-H* pyruvate hydrate, *Lac* lactate. (**b**, **c**) Comparison of experimental and simulated data of NMR signal from hyperpolarized molecules, [1-$^{13}$C] pyruvate (**b**) and [1-$^{13}$C] lactate (**c**). The simulated data models a spin-lattice relaxation decay with a relaxation constant $T_1$. Adapted from reference [15]

### 2.4 Hyperpolarization Experiments

1. Centrifuge.
2. MRI scanner (preclinical or clinical version).

## 3 Methods

### 3.1 Fabrication of Micro-coil

1. Magnetic wire is tightly wound around a metal rod, and its length determines the sample volume of a micro-coil (Fig. 3a). To maintain the shape of the wire around the rod, a tiny amount of super-glue can be applied to the wire, not between the wire and rod.
2. A SYLGARD-184 Silicone Elastomer Clear kit has two components: elastomer base and curing agent. They are mixed with a ratio of 10:1 (elastomer base:curing agent) in a disposable petri dish (or any disposable container). As the mixing step generates bubbles inside the mixture, the petri dish is put in a vacuum desiccator to remove all the bubbles, which takes approximately 30 min.
3. The elastomer mixture is slowly poured over the wire-wound rod and put inside a vacuum desiccator again, as this pouring step also generates bubbles.
4. Once all the bubbles are removed, the wire-wound rod embedded inside the elastomer mixture is put into an oven at 90 °C overnight, which makes the mixture hardened. *See* **Note 1**.
5. The hardened mixture is cut with a razor blade to a certain size and the metal rod needs to be slowly pulled out, which makes a microfluidic channel passing through the micro-solenoid coil (Fig. 3b).

### 3.2 Fabrication of Micro-NMR Circuit

1. The micro-NMR circuit is a resonance circuit with the micro-coil embedded in the elastomer block and two capacitors (one for resonance tuning and another for resonance matching) (Fig. 4a).
2. To make a resonance circuit with the micro-coil, the $C_M$ and $C_T$ values need to be calculated (Fig. 4b). As the fabrication step of the micro-coil determines its inductance and resistor values and the magnetic field for NMR analysis determines the resonance frequency $\omega$, the $C_M$ and $C_T$ values can be calculated with the pre-defined values. *See* **Note 2**.
3. The fabricated micro-coil and tuning/matching capacitors are soldered into a printed circuit board designed to make a resonance circuit (Fig. 1a).

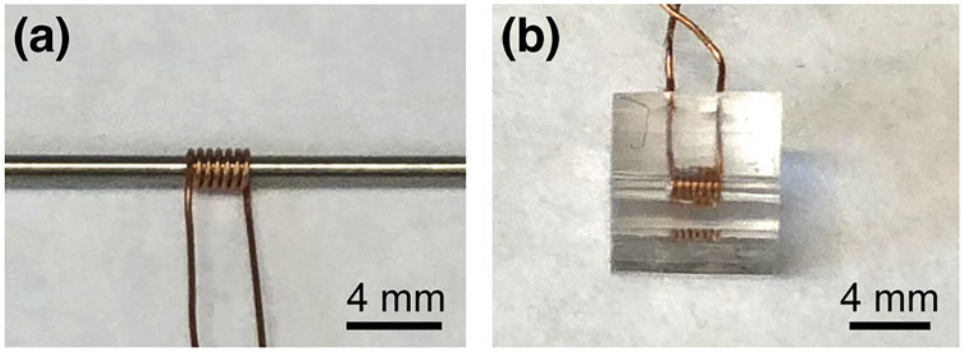


**Fig. 3** Fabrication steps of micro-coil, (**a**) 32-AWG magnetic wire is wound around a 1.4-mm-diameter metal rod. (**b**) Once the wire-wound rod is embedded in an elastomer block, the rod is pulled out so that a micro-coil is formed with a microfluidic channel inside

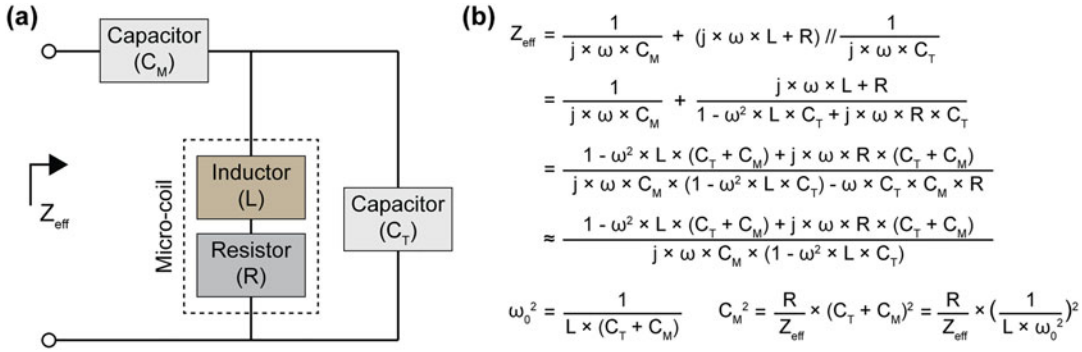


**Fig. 4** Design of the micro-NMR circuit, (**a**) Schematic of the circuit. $Z_{eff}$ effective impedance of the circuit, $C_M$ capacitance of a matching capacitor, $C_T$ capacitance of a tuning capacitor, $L$ inductance of micro-coil, $R$ resistance of micro-coil, (**b**) Mathematical analysis of $C_M$ and $C_T$ values. The resonance frequency, $\omega$, and the characteristics of the micro-coil, L and R, are pre-defined based on the system hardware

### *3.3 Hyperpolarized NMR Experiment with Cells*

1. The hyperpolarization technology used in our study is dDNP; we use a SPINlab machine (Fig. 5a) to hyperpolarize [1-$^{13}$C] pyruvic acid.
2. 15 mM of AH-111501 (radical agent) is mixed with [1-$^{13}$C] pyruvic acid thoroughly, and 100 μL of the mixture is loaded into a sample cup. The cup is glued to the fluid path designed for dissolution (Fig. 5b).
3. 40 mM of Trizma hydrochloride solution with 0.4 mM EDTA (a chelating agent) is prepared as a buffer solution for dissolution, 20 mL of which is loaded into a syringe connected to the fluid path (Fig. 5b).
4. The fluid path is air-tightly sealed with Luer fittings and loaded into the SPINlab hyperpolarizer. It takes approximately 2 h to achieve >30% of polarization.

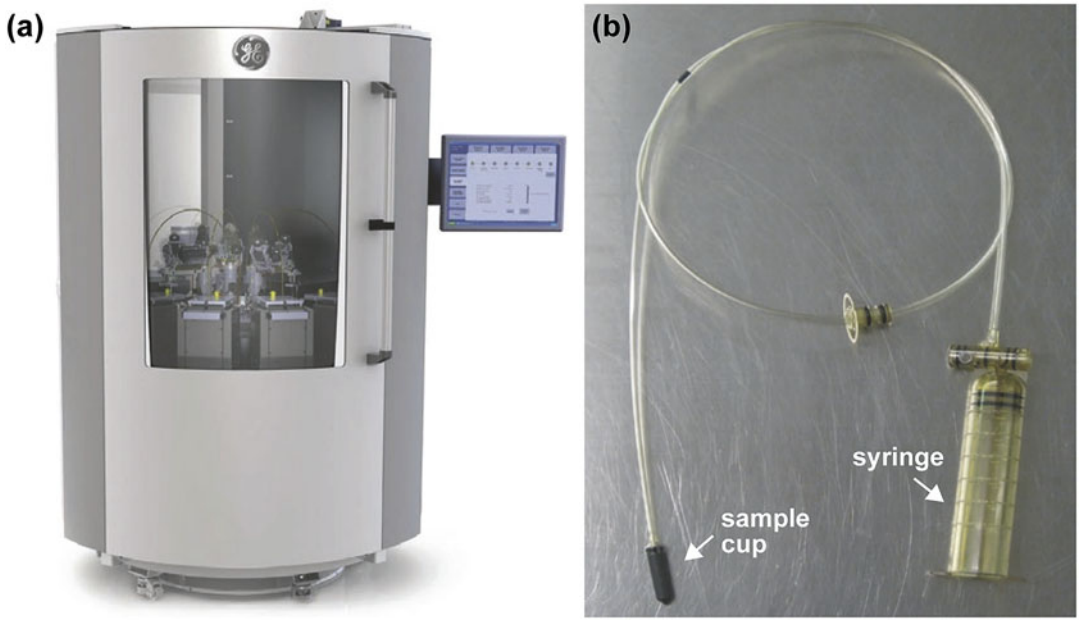


**Fig. 5** Pictures of SPINlab hyperpolarizer and a fluid path for sample loading, (**a**) A SPINlab machine has four separate channels so that different molecules can be hyperpolarized simultaneously, (**b**) A fluid path designed for sample loading into a SPINlab has a sample cup, where molecules to be hyperpolarized are loaded, and a syringe, where dissolution buffer solution is loaded. After 1–2 h of hyperpolarization in the SPINlab, the dissolution buffer is warmed and pushed through the sample cup, dissolving all the hyperpolarized molecules out of the SPINlab machine. Adapted from reference [8]

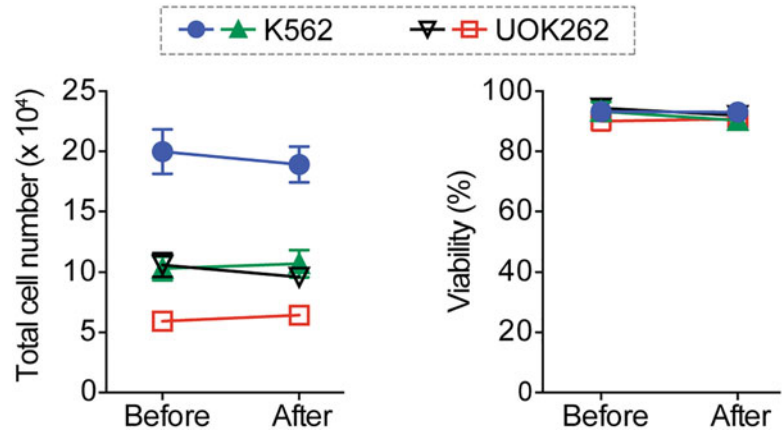


**Fig. 6** Comparison of total cell number and viability before and after hyperpolarized micro-NMR experiments. Two cancer cell lines (K562, chronic myeloid leukemia; UOK262, renal cancer cell) were tested for the experiments, and the cell number and viability were examined before and after. All measurement were conducted in duplicate. Error bars show the standard deviation. Adapted from reference [15]

5. After 2 h of hyperpolarization, target cells need to be prepared for metabolic flux analysis; 200–500k cells are collected from the flask, centrifuged, and resuspended in 45 μL of fresh media without fetal bovine serum.
6. When the cells are ready, the dissolution of the hyperpolarized pyruvic acid is initiated; the buffer solution is rapidly pushed through the fluid path, dissolving all the pyruvate-radical mixture from the sample cup to the outside of the hyperpolarizer. The dissolved [1-$^{13}$C] pyruvic acid sample is neutralized with 120 μL of 10 N sodium hydroxide solution. *See* **Note 3**.
7. The hyperpolarized and neutralized [1-$^{13}$C] pyruvate is mixed with the cell suspension with a ratio of 1:10, 8 μL of which is loaded into the micro-coil.
8. The micro-NMR circuit system is inserted into the center of the magnetic field in a conventional MRI system, followed by $^{13}$C-NMR signal acquisition. The NMR signal is acquired every 4 s with a flip angle of 30° radiofrequency pulse.
9. After 2 min of signal acquisition, the micro-NMR circuit system is removed from the MRI system and the cells are collected from the micro-coil for downstream molecular analyses, such as Western blot or PCR. Hyperpolarized NMR analysis is nondestructive and rapid, such that the cell viability after an experiment is unchanged (Fig. 6).

## 4 Notes

1. The elastomer block that houses the micro-coil should not have any bubbles, as the air trapped inside bubbles can disrupt magnetic field homogeneity. Also, the bubbles between the wires can distort the overall shape of the micro-coil when the metal rod is removed.
2. The inductance of the micro-coil can be an order of $10^{-9}$ H, which requires relatively higher capacitors (an order of $10^{-9}$ C) for tuning and matching.
3. A hyperpolarized spin state decays with a spin-lattice relaxation time constant $T_1$, which can be very short—less than 20 s—for certain molecules. The $T_1$'s of [1-$^{13}$C] pyruvate and [1-$^{13}$C] dehydroascorbate (DHA) are relatively long, >70 s at 1 Tesla magnetic field [16], which motivates the wide use of these molecules in the field of hyperpolarized NMR/MRI. For molecules with a short $T_1$, such as [6-$^{13}$C] arginine (~7 s), various approaches, including $^{15}$N-enrichment or dissolution with $D_2O$, have been demonstrated [17, 18].

## Acknowledgments

This technology development was supported by the research grants from the U.S. National Institutes of Health (NIH); K99CA226357 (S.J.), R00EB014328 (K.R.K.), and R21CA212958-01 (K.R.K.); Cancer Center Support Grant P30CA008748 (K.R.K.); as well as the Center for Molecular Imaging and Nanotechnology at Memorial Sloan Kettering Cancer Center.

### References

1. DeBerardinis RJ, Chandel NS (2016) Fundamentals of cancer metabolism. Sci Adv 2: e1600200
2. Reid MA, Dai Z, Locasale JW (2017) The impact of cellular metabolism on chromatin dynamics and epigenetics. Nat Cell Biol 19:1298–1306
3. Pavlova NN, Thompson CB (2016) The emerging hallmarks of cancer metabolism. Cell Metab 23:27–47
4. Heiden MGV, Cantley LC, Thompson CB (2009) Understanding the Warburg effect: the metabolic requirements of cell proliferation. Science 324:1029–1033
5. Chang CH, Qiu J, O'Sullivan D et al (2015) Metabolic competition in the tumor microenvironment is a driver of cancer progression. Cell 162:1229–1241
6. Keshari KR, Wilson DM (2014) Chemistry and biochemistry of 13C hyperpolarized magnetic resonance using dynamic nuclear polarization. Chem Soc Rev 43:1627–1659
7. Ardenkjaer-Larsen JH, Fridlund B, Gram A et al (2003) Increase in signal-to-noise ratio of >10,000 times in liquid-state NMR. Proc Natl Acad Sci U S A 100:10158–10163
8. Schroeter A, Rudin M, Gianolio E et al (2017) MRI. In: Small animal imaging. Springer, Cham, pp 227–324
9. Ardenkjaer-Larsen JH, Bowen S, Petersen JR et al (2019) Cryogen-free dissolution dynamic nuclear polarization polarizer operating at 3.35 T, 6.70 T, and 10.1 T. Magn Reson Med 81:2184–2194
10. Di Gialleonardo V, Aldeborgh HN, Miloushev V et al (2017) Multinuclear NMR and MRI reveal an early metabolic response to mTOR inhibition in sarcoma. Cancer Res 77:3113–3120
11. Dong Y, Eskandari R, Ray C et al (2018) Hyperpolarized MRI visualizes Warburg effects and predicts treatment response to mTOR inhibitors in patient-derived ccRCC xenograft models. Cancer Res 79:242–250
12. Miloushev VZ, Granlund KL, Boltyanskiy R et al (2018) Metabolic imaging of the human brain with hyperpolarized 13C Pyruvate demonstrates 13C lactate production in brain tumor patients. Cancer Res 78:3755–3760
13. Granlund KL, Vargas H, Lyashchenko S et al (2020) Hyperpolarized MRI of human prostate cancer reveals increased lactate with tumor grade driven by monocarboxylate transporter 1. Cell Metab 31(1):105.e3–114.e3
14. Salamanca-Cardona L, Shah H, Poot AJ et al (2017) In vivo imaging of glutamine metabolism to the oncometabolite 2-hydroxyglutarate in IDH1/2 mutant tumors. Cell Metab 26:830.e3–841.e3
15. Jeong S, Eskandari R, Park SM et al (2017) Real-time quantitative analysis of metabolic flux in live cells using a hyperpolarized micromagnetic resonance spectrometer. Sci Adv 3: e1700341
16. Tee SS, DiGialleonardo V, Eskandari R et al (2016) Sampling hyperpolarized molecules utilizing a 1 Tesla permanent magnetic field. Sci Rep 6:1–6
17. Cho A, Eskandari R, Granlund KL et al (2019) Hyperpolarized [6-13C, 15-N3]-arginine as a probe for in vivo arginase activity. ACS Chem Biol 14:665–673
18. Cho A, Eskandari R, Miloushev VZ et al (2018) A non-synthetic approach to extending the lifetime of hyperpolarized molecules using D2O solvation. J Magn Reson 295:57–62

# Chapter 30

# Mixed Modeling Frameworks for Analyzing Whole-Brain Network Data

**Sean L. Simpson**

## Abstract

Brain network analyses have exploded in recent years and hold great potential in helping us understand normal and abnormal brain function. Network science approaches have facilitated these analyses and our understanding of how the brain is structurally and functionally organized. However, the development of statistical methods that allow relating this organization to health outcomes has lagged behind. We have attempted to address this need by developing mixed modeling frameworks that allow relating system-level properties of brain networks to outcomes of interest. These frameworks serve as a synergistic fusion of multivariate statistical approaches with network science, providing a needed analytic (modeling and inferential) foundation for whole-brain network data. In this chapter we delineate these approaches that have been developed for single-task and multitask (longitudinal) brain network data, illustrate their utility with data applications, detail their implementation with a user-friendly Matlab toolbox, and discuss ongoing work to adapt the methods to (within-task) dynamic network analysis.

**Key words** Brain networks, Matlab toolbox, Mixed model, Graph theory, Connectivity, fMRI

## 1 Introduction

Brain network analysis remains at the forefront of neuroimaging research, serving as a distinct subfield of connectivity analysis in which functional or structural associations are quantified for all $n$ parcellated brain subdivisions yielding an $n \times n$ connection matrix and creating an interconnected representation of the brain (a brain network) [1–4]. The application of network science (an interdisciplinary offshoot of graph theory) has facilitated these analyses and enabled examining the brain as an integrated system that produces complex behaviors [5–7]. The appeal of the network approach lies in its ability to provide profound insight into the organization of the brain in health and disease [8]. We focus here on functional brain networks derived from functional magnetic resonance imaging (fMRI), but the delineated approaches are equally applicable to structural and functional networks generated

Miguel R. Ossandon et al. (eds.), *Biomedical Engineering Technologies: Volume 1*, Methods in Molecular Biology, vol. 2393, https://doi.org/10.1007/978-1-0716-1803-5_30, 

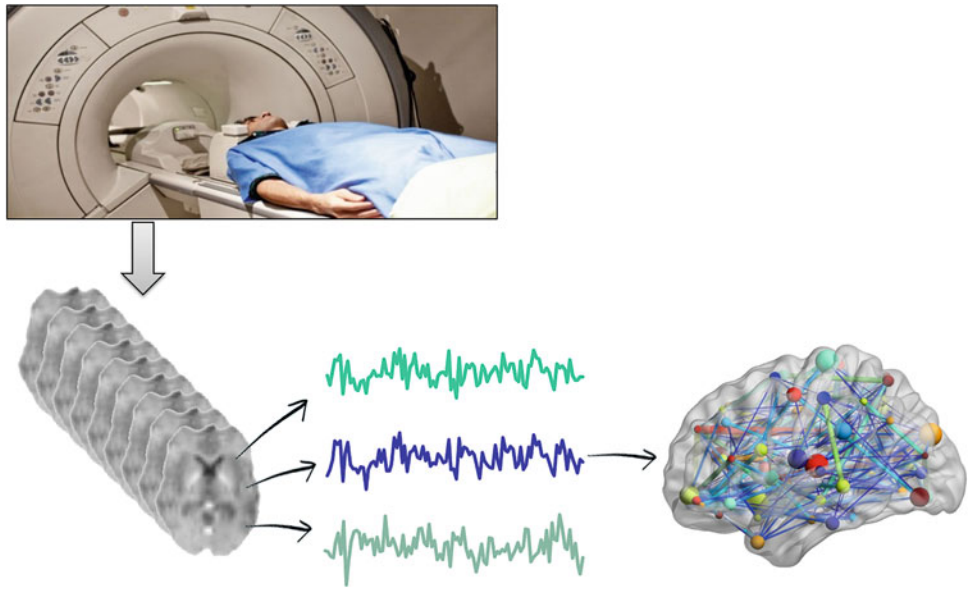

**Fig. 1** Schematic for generating brain networks from fMRI time series data. Here the nodes (vertices) represent brain regions and the edges represent the strength of functional connections between them (often quantified by the correlation coefficient)

from other neuroimaging modalities (e.g., diffusion MRI, EEG, MEG, functional NIRS). A schematic exhibiting the fMRI network generation process is presented in Fig. 1. Here the nodes (vertices) represent brain regions and the edges represent the strength of functional connections between them (often quantified by the correlation coefficient). The networks (connection matrices) are generally thresholded to remove negative connections (for reasons noted in [7, 9] and others) resulting in sparse weighted networks.

Despite the recent explosion of brain network studies, the current statistical tools and toolboxes used to analyze these network data have lagged behind, failing to fully harness the wealth of information present and provide the flexibility of the modeling and inferential tools developed for fMRI activation data [1, 10]. The systemic organization present in brain networks confers much of our brains' functional abilities as functional connections may be lost due to an adverse health condition, but compensatory connections may develop to maintain organizational consistency and functional performance. Consequently, brain network analysis necessitates a suite of tools including a multivariate modeling framework to assess the effects of multiple variables of interest and topological network features on the overall network structure. That is, if we have

$$\text{Data}\begin{cases} \boldsymbol{\Upsilon}_i : \text{network of participant } i \\ \boldsymbol{X}_i : \text{covariate information (metrics, demographics, etc.)} \end{cases},$$

we want the ability to model the probability density function of the network given the covariates $P(\boldsymbol{\Upsilon}_i|\boldsymbol{X}_i,\boldsymbol{\theta}_i)$, where $\boldsymbol{\theta}_i$ are the parameters that relate the covariates to the network structure. Previous attempts to develop such a framework employed exponential random graph models (ERGMs) [11–13]. While useful in some contexts, ERGMs can be labor intensive with large samples, and problems can arise when conducting multi-subject comparisons or incorporating novel metrics [14–16]. The multivariate distance matrix regression (MDMR) framework [17] and permutation network framework (PNF) [18] also provide relatively recent, important additions to this suite of analysis tools. The MDMR framework allows controlling for confounding covariates when comparing groups of brain networks; however, it lacks the ability to simulate brain networks or make predictions as it does not directly model $P(\boldsymbol{\Upsilon}_i|\boldsymbol{X}_i,\boldsymbol{\theta}_i)$. It also fails to account for the dependence in connectivity patterns across regional pairs. The PNF provides a group comparison approach by assessing the topological consistency of key node sets within and between groups. However, it lacks the ability to quantify, predict, and simulate relationships between continuous disease outcomes and network structure.

To address these needs and further add to the suite of tools for brain network analysis, we first developed a two-part mixed modeling framework for single-task brain network data that directly models $P(\boldsymbol{\Upsilon}_i|\boldsymbol{X}_i,\boldsymbol{\theta}_i)$ and enables quantifying the relationship between phenotype and connectivity patterns in the brain after controlling for confounders, predicting connectivity structure based on phenotype, simulating networks to gain a better understanding of normal ranges of topological variability, and thresholding individual networks leveraging group information for a given task [10]. Conceptually, this approach allows multivariately relating entire brain networks (all connections simultaneously) to endogenous variables (that summarize network topology) and exogenous variables (those of biological relevance that may be associated with changes in network topology) (Fig. 2) [10, 19]. A corresponding user-friendly toolbox provides a Matlab graphical user interface (GUI) for easy implementation [20]. We secondly extended this framework to multitask (longitudinal) brain network data [21] and

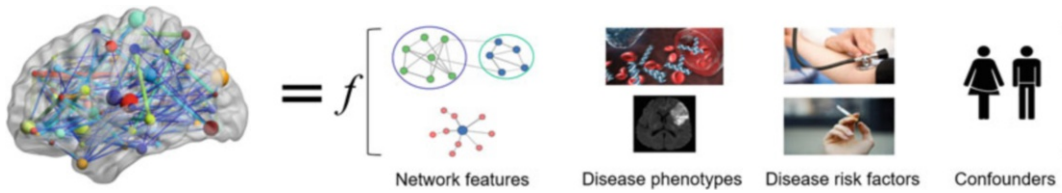


**Fig. 2** Modeling a brain network as a function of endogenous variables (that summarize network topology) and exogenous variables (those of biological relevance that may be associated with changes in network topology)

plan to update the functionality of the toolbox to allow its implementation.

Here we delineate the single-task and multitask approaches along with illustrative applications and discussion of their implementation with a user-friendly Matlab toolbox. We also introduce ongoing work to adapt the methods to (within-task) dynamic network analysis.

## 2 Materials

### 2.1 Single-Task Mixed Modeling Framework for Brain Network Analysis

1. Functional MRI images from 74 participants (*see* **Note 1**).
2. Matlab.
3. WFU_MMNet Matlab Toolbox (*see* **Note 2**).

### 2.2 Multitask Mixed Modeling Framework for Brain Network Analysis

1. Functional MRI images from 39 participants (*see* **Note 3**).
2. SAS [Future work will update the WFU_MMNet toolbox to incorporate this multitask extension].

### 2.3 Future Work: Mixed Modeling Framework for Dynamic Brain Network Analysis

1. Dynamic brain network data.
2. SAS [Future work will also update the WFU_MMNet toolbox to incorporate this dynamic network extension].

## 3 Methods

### 3.1 Data Preprocessing Steps

**(Steps 1–4 were used for the data discussed here but are independent of the mixed modeling methods, thus other preprocessing approaches can be used)**

1. Normalize the data from functional magnetic resonance imaging (fMRI) scans to the Montreal Neurological Institute (MNI) standard space with a $4 \times 4 \times 4$ mm$^3$ voxel size (other normalization approaches can also be used as the mixed modeling method is independent of this preprocessing step).
2. Filter the data using a band pass filter (0.009–0.08 Hz). Regress out motion parameters, global signal, and mean white matter (WM) and cerebral spinal fluid (CSF) from the imaging time series data.
3. Obtain the node time courses by averaging the voxel time courses in the 116 distinct anatomical regions (116 ROIs-Regions of Interest) defined by the Automated Anatomical Labeling atlas (AAL; [22]).

4. Construct the brain networks for each participant's dataset by calculating Pearson correlation coefficients between these denoised motion-corrected time courses for all node pairs (*see* Fig. 1).
5. Threshold the resulting 116 × 116 connection matrices to remove negative connections (*see* **Note 4**). This will result in a sparse weighted network.

### 3.2 Single-Task Mixed Modeling Framework for Brain Network Analysis

1. Download and install the WFU_MMNet Matlab Toolbox (*see* **Note 2**).
2. Implement the single-task mixed modeling framework (*see* **Note 5**) following the prompts in the toolbox.

### 3.3 Multitask Mixed Modeling Framework for Brain Network Analysis

1. Acquire the SAS macro for model fitting in Supplementary Appendix S1 in [21].
2. Implement the multitask mixed modeling framework (*see* **Note 6**).

### 3.4 Future Work: Mixed Modeling Framework for Dynamic Brain Network Analysis

1. Acquire the SAS macro for model fitting (to be made available in future work).
2. Implement the mixed modeling framework for dynamic brain networks (*see* **Note 7**).

## 4 Notes

1. To illustrate the appeal of our single-task mixed modeling framework we focus on the data analyzed in [19]. The data come from a larger project "Pesticide Exposures & Neurological Outcomes for Latinos: PACE4," which is an ongoing community-based study focused on migrant farmworker health. The parent study participant population comprises 447 Latino males including farmworkers recruited from east central North Carolina, and non-farmworkers from Forsyth County in west central North Carolina. Further details about this population and the parent study can be found in [23]. The subpopulation analyzed here comprises 74 (of the 81) PACE4 (48 farmworkers and 26 non-farmworkers) participants who were recruited to have a brain MRI scan and had complete data: brain image, at least one blood sample for cholinesterase measurements, and one urine sample for cotinine measurements. Further details about this subpopulation can be found in [24].

   Each fMRI scan for these data employed a Siemens 3T Skyra scanner equipped with a 32-channel head coil along with a whole-brain gradient echo-planar imaging (EPI) sequence to acquire the blood-oxygenation level-dependent

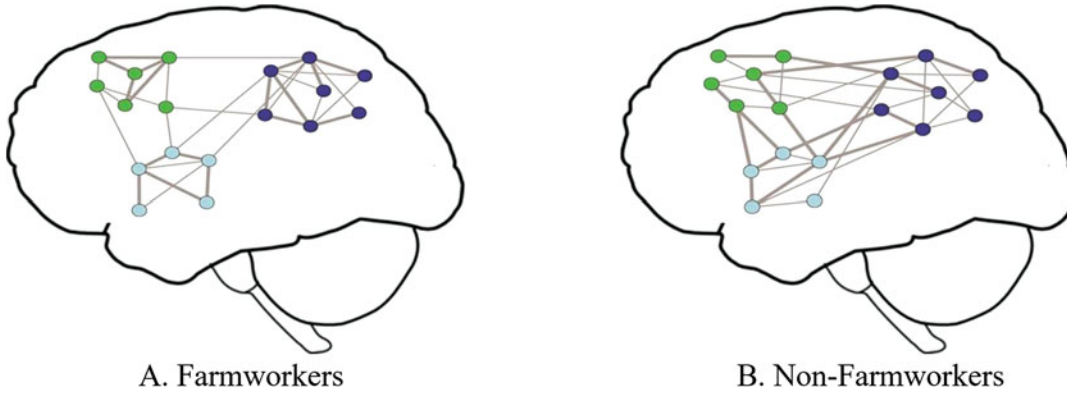


**Fig. 3** Cartoon model of brain networks for farmworkers (**A**) and non-farmworkers (**B**). The nodes represent brain regions, the edge thickness represents the strength of functional connections between them, and the node color indicates the module membership

(BOLD) contrast images with the following parameters: slice thickness = 4.0 mm, in-plane resolution = 4 mm × 4 mm, TR = 1700 ms, and 157 volumes with 35 contiguous slices per volume. The first 8 image volumes were discarded to allow tissue magnetization to achieve steady-state. High-resolution (0.98 mm × 0.98 mm × 1.0 mm) T1-weighted scans were acquired in the sagittal plane using a single-shot 3D MPRAGE GRAPPA2 sequence with the following parameters: acquisition time = 5.0 min and 30 s, TR = 2.3 s, TE = 2.99 ms, 192 slices. High-resolution images were used in preprocessing the functional images.

The covariate of interest (*COI*) for this analysis was Farmworker Status (FWS), a binary variable distinguishing farmworkers from non-farmworkers, and the unique confounders (*Con*) included blood acetylcholinesterase (AChE), butyrylcholinesterase (BChE), urinary cotinine level, age, education level, pack years of smoking, and smoking status. The main results from the mixed model fit are visually depicted in Fig. 3 (reproduced from [19]) which shows a set of cartoon brain networks that typify the differences found between farmworkers and non-farmworkers. In summary, farmworkers have brain networks that are more modularly organized with higher functional specificity and lower inter-modular integrity, an architecture at rest that has been linked to various detrimental outcomes [25–28].

2. To make the single-task mixed modeling framework (*see* **Note 5**) widely accessible to neuroimaging researchers, we developed a corresponding user-friendly software package, WFU_MMNet [20]. WFU_MMNet employs a Matlab GUI (Figs. 4, 5, and 6; reproduced from [20]) that interfaces with SAS, R, and Python for model fitting. It also provides a clustering-based

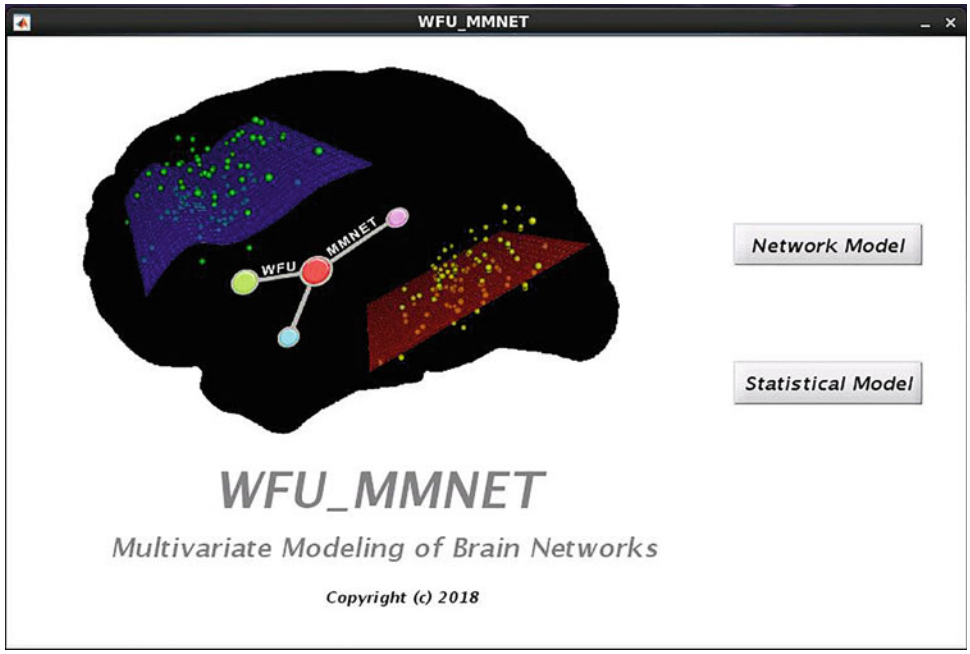


**Fig. 4** WFU_MMNET main (starting) graphical user interface. Modeling is done in two main steps. In the first step, using imaging data files (and atlas files), initial modeling files, such as an initial data frame, are constructed through the "Network_Model" GUI. This step is independent of the second step and can be repeated for different imaging data or different options on the same dataset. In the second step, using generated files from the first step, final modeling files, including modeling datasets, equations, and options are generated, and the statistical models are fitted. The second step is done through the "Statistical_Model" GUI. This step can also be done repeatedly for different options as long as an initial modeling file is available

data reduction method to facilitate model convergence and reduce modeling time for large datasets when needed. While our focus has been on fMRI data, the toolbox is equally applicable to a variety of neuroimaging data such as EEG, MEG, DTI, and DWI, making it useful for a wide range of structural and functional brain network studies. See [20] and the accompanying toolbox, software manual, and a case study at https://www.nitrc.org/projects/wfu_mmnet for further details about the software package and its implementation.

3. To illustrate the appeal of the multitask mixed modeling framework we focus on the data analyzed in [10], and reanalyzed in [21], in order to contrast and clearly distinguish the utilities of the single-task and multitask frameworks, as well as to illuminate the differences in conclusions that can occur by fitting this more appropriate multitask model to multitask data.

The data come from a prior study that aimed to assess the neurological underpinnings of age-related cognitive decline by examining the effects of aging on the integration of sensory information [29]. The study has two age groups, healthy young adults

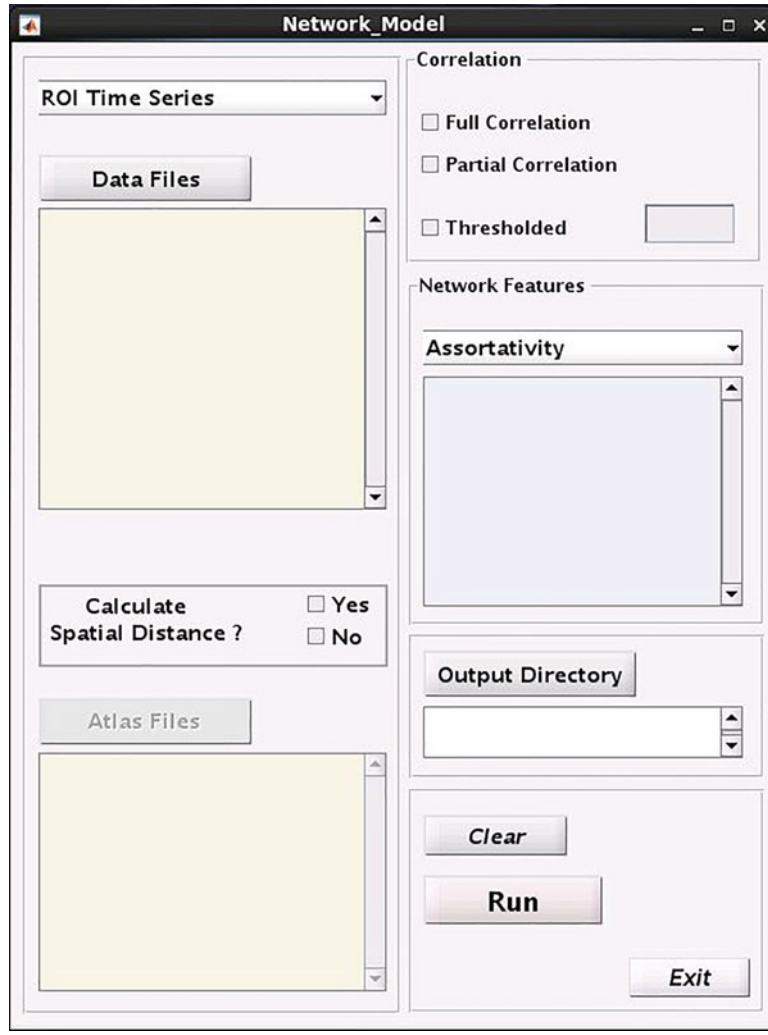


**Fig. 5** The "Network Model" GUI. After loading required files and selecting desired options, initial modeling files are constructed and saved in the output directory. These saved files are used in the "Statistical Model" GUI to generate final modeling files and fit statistical models

aged $27 \pm 5.8$ years old ($n = 20$) and healthy older adults aged $73 \pm 6.6$ years old ($n = 19$). Three separate conditions of fMRI scans were used, resting, visual (viewing of a silent movie), and multisensory (MS) (visual and auditory - movie with sound), each lasting 5.6 min. Further details about these conditions along with additional network analyses can be found in [30]. For each fMRI scan, blood-oxygen-level dependence (BOLD) contrast was measured using a 1.5T MRI scanner and a whole-brain gradient echo- planar imaging (EPI) sequence with the following parameters: 200 volumes with 24 contiguous slices per volume; slice

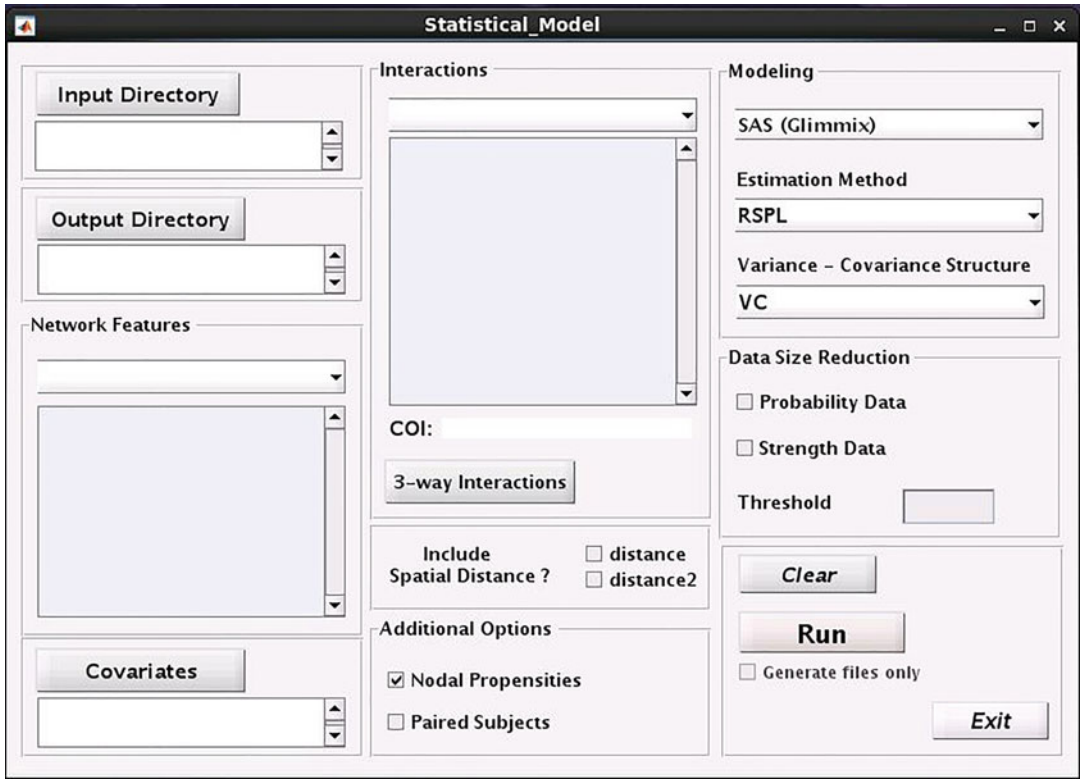


**Fig. 6** The "Statistical Model" GUI. Generated modeling files from the "Network Model" GUI are used here to make the final modeling datasets, equations, and options, and fit statistical models. Modeling is conducted automatically via a system call of SAS, R, or Python executable files

thickness = 5.0 mm; in-plane resolution of 3.75 mm × 3.75 mm; TR = 3000 ms.

The COI for this analysis was age group (*age*), a binary variable distinguishing the young from the older adults, and the unique confounders (*Con*) included sex and years of education. We fitted three single-task mixed models, one to each condition (rest, visual, multisensory), and two multitask mixed models, one to the rest and visual data combined and one to the rest and multisensory data combined. We took this approach with the multitask framework given our interest here in rest-to-task network changes and given convergence issues that arose when attempting to fit the data from all three tasks combined. Below we highlight a few of the notable differences in within-task results produced by the single and multitask fits and illustrate the unique ability of the multitask framework to enable investigating how age is related to between-task organizational changes.

As evidenced by the simulation results in Table 1 (reproduced from [21]), the multitask model provides a better fit to the data than the single-task model (i.e., enables simulating more realistic

**Table 1**
**Weighted network metrics of observed and simulated networks from the aging study data produced from the single-task and multitask mixed model fits**

| | | **Observed ($N = 39$)** | **Simulated ($N = 100$) [Mean (SE)]** | | |
|---|---|---|---|---|---|
| Condition | Metric | Mean (SE) | Single-task | Rest/visual | Rest/MS |
| Rest | Clustering coefficient ($C$) | 0.149 (0.001) | 0.155 (0.000) | 0.124 (0.000) | 0.132 (0.000) |
| | Global efficiency (*Eglob*) | 0.231 (0.001) | 0.214 (0.000) | 0.237 (0.000) | 0.250 (0.000) |
| | Characteristic path length ($L$) | 4.677 (0.109) | 4.720 (0.004) | 4.274 (0.006) | 4.080 (0.005) |
| | Mean nodal degree ($K$) | 10.649 (0.055) | 12.747 (0.016) | 9.723 (0.029) | 10.321 (0.026) |
| | Leverage centrality ($l$) | 2.678 (0.015) | 1.945 (0.003) | 2.103 (0.005) | 2.025 (0.004) |
| | Modularity ($Q$) | 0.342 (0.001) | 0.136 (0.000) | 0.218 (0.000) | 0.188 (0.000) |
| Visual | Clustering coefficient ($C$) | 0.150 (0.001) | 0.150 (0.000) | 0.131 (0.000) | NA |
| | Global efficiency (*Eglob*) | 0.232 (0.001) | 0.205 (0.000) | 0.245 (0.000) | NA |
| | Characteristic path length ($L$) | 4.553 (0.073) | 4.992 (0.008) | 4.161 (0.005) | NA |
| | Mean nodal degree ($K$) | 10.656 (0.056) | 12.379 (0.025) | 9.884 (0.025) | NA |
| | Leverage centrality ($l$) | 2.671 (0.015) | 2.155 (0.010) | 2.021 (0.004) | NA |
| | Modularity ($Q$) | 0.348 (0.001) | 0.136 (0.000) | 0.194 (0.000) | NA |
| Multisensory | Clustering coefficient ($C$) | 0.140 (0.001) | 0.165 (0.000) | NA | 0.132 (0.000) |
| | Global efficiency (*Eglob*) | 0.230 (0.001) | 0.218 (0.000) | NA | 0.250 (0.000) |
| | Characteristic path length ($L$) | 4.431 (0.011) | 4.700 (0.008) | NA | 4.080 (0.005) |
| | Mean nodal degree ($K$) | 10.547 (0.052) | 13.830 (0.027) | NA | 10.321 (0.026) |
| | Leverage centrality ($l$) | 2.862 (0.014) | 2.054 (0.006) | NA | 2.025 (0.004) |
| | Modularity ($Q$) | 0.327 (0.001) | 0.123 (0.000) | NA | 0.188 (0.000) |

**Table 2**
**Aging data: estimates, standard errors (se), and *P*-values for the single-task mixed model fit to Rest data and multitask fit to Rest (and Multisensory) data**

| | Rest (single-task) | | | Rest (with MS) | | |
|---|---|---|---|---|---|---|
| **Parameter** | **Estimate** | **SE** | ***P*-value** | **Estimate** | **SE** | ***P*-value** |
| $\beta_{r,C}$ | 0.7807 | 0.3424 | 0.0355 | ***7.2829*** | 1.7689 | ***0.0001*** |
| $\beta_{r,age}$ | -0.0438 | 0.0773 | 0.5709 | -0.0906 | 0.0779 | 0.2568 |
| $\beta_{r,age\times C}$ | 1.1249 | 0.7986 | 0.1943 | ***-1.8954*** | 2.3517 | 0.4203 |
| $\beta_{s,Q}$ | -0.0373 | 0.1723 | 0.8285 | ***-0.2990*** | 0.1611 | ***0.1613*** |
| $\beta_{s,age}$ | -0.0106 | 0.0124 | 0.4262 | -0.0121 | 0.0127 | 0.5306 |
| $\beta_{s,age\times Q}$ | -0.6957 | 0.2464 | 0.0071 | -0.2458 | 0.1976 | ***0.4454*** |

brain networks [31]). This table displays the results of simulating 100 networks based on separate single-task model fits and joint multitask rest/visual and rest/multisensory data fits, and then calculating several (weighted) descriptive metrics commonly used in the network neuroscience literature for the observed and simulated networks: clustering coefficient ($C$), global efficiency ($Eglob$), characteristic path length ($L$), mean nodal degree ($K$), leverage centrality ($l$), and modularity ($Q$). The multitask approach better captures the topological properties of the observed networks, with the average Euclidean distance between these properties for the simulated networks and the observed networks being 0.5901 for the single-task models and 0.3087 for the multitask models, a 48% improvement.

The utility of providing a better fit to the data engenders more confidence in the results yielded by the multitask framework. Here, for the sake of brevity, we highlight just two of the several notable differences resulting from the multitask fit to the rest/multisensory data as compared to the single-task fit. Table 2 displays a subset of the parameter estimates, standard errors, and *P*-values for the single and multitask fits to the rest and rest/multisensory data, respectively. Bolded and italicized values indicate substantial differences in the estimated relationships between covariates and network connectivity at rest between the two model fits. Clustering coefficient ($C$) plays an even greater role in explaining the connectivity between two regions at rest for both young and older adults as indicated by the change in the order of magnitude of $\beta_{r,C}$, the increase in $\left(\beta_{r,C}+\beta_{r,age\times C}\right)$, and the change in two orders of magnitude of the *P*-value for $\beta_{r,C}$ for the multitask fit. Additionally, the change in sign of $\beta_{r,age\times C}$ provides (weak) evidence that older adults actually have a weaker relationship between clustering and connectivity than young adults, whereas the opposite conclusion

**Table 3**
**Aging data (multitask rest/visual fit): estimates for visual and rest, and estimates, standard errors (SE), and *P*-values for the between-task differences**

| | **Visual** | **Rest** | **Difference (Visual - rest)** | | |
|---|---|---|---|---|---|
| Parameter | Estimate | Estimate | Estimate | SE | *P*-value |
| $\beta_{r,0}$ | -0.2897 | -0.2488 | -0.0409 | 0.0659 | 0.5351 |
| $\beta_{r,k}$ | -1.9930 | -1.5229 | -0.4701 | 0.2029 | **0.0591** |
| $\beta_{r,age}$ | 0.1655 | -0.0806 | 0.2461 | 0.1005 | **0.0467** |
| $\beta_{r,age\times k}$ | 0.5917 | 0.2682 | 0.3235 | 0.2605 | 0.3430 |
| $\beta_{s,0}$ | 0.2157 | 0.2253 | -0.0096 | 0.0120 | 0.4231 |
| $\beta_{s,Eglob}$ | 1.4452 | 1.0693 | 0.3759 | 0.1996 | **0.0676** |
| $\beta_{s,k}$ | -0.2828 | -0.2438 | -0.0390 | 0.0196 | **0.0607** |
| $\beta_{s,Q}$ | -0.5634 | 0.0364 | -0.5998 | 0.3306 | 0.0740 |
| $\beta_{s,age}$ | -0.0008 | -0.0080 | 0.0072 | 0.0143 | 0.6136 |
| $\beta_{s,dist}$ | -0.1830 | -0.1717 | -0.0113 | 0.0042 | **0.0124** |
| $\beta_{s,age\times Eglob}$ | -0.0395 | 0.6452 | -0.6847 | 0.2648 | **0.0150** |
| $\beta_{s,age\times k}$ | 0.0037 | -0.0054 | 0.0091 | 0.0277 | 0.7430 |
| $\beta_{s,age\times Q}$ | 0.1467 | -0.6588 | 0.8055 | 0.4180 | **0.0655** |

results from the single-task model fit. As evidenced by the change in the order of magnitude of $\beta_{s,Q}$ and the 81% reduction in its associated *P*-value for the multitask fit, modularity has an even stronger negative relationship with connection strength for young adults . Additionally, as indicated by the two orders of magnitude increase in the *P*-value associated with $\beta_{s,age\times Q}$, older adults are no longer estimated to have a stronger negative relationship between modularity and connection strength than young adults.

The greatest appeal of the multitask framework is its ability to enable investigating how phenotypic characteristics are related to between-task organizational differences. Here, again for the sake of brevity, we highlight a few of the notable findings from the multitask fit to the rest/visual data. The last three columns of Table 3 display a subset of the parameter estimates, standard errors, and *P*-values for the differences in the relationships between the covariates and the probability and strength of connections between brain areas for the resting-state and visual-state networks for both age groups. Bolded values indicate important age-related inferential results used to draw the conclusions detailed below (also detailed in [21]). Variance estimates for the random effects parameters (excluding for the propensities and distance random effects), presented in Table 4, also inform the conclusions below. These estimates quantify the extent to which the within-task brain networks

**Table 4**
**Aging data: variance estimates for random effects (excluding propensities and distance) for the multitask rest and visual data fit**

| | Variance estimate | | | |
|---|---|---|---|---|
| | Rest | | Task | |
| Parameter | Young | Older | Young | Older |
| $b_{ri,0}$ | 0.01388 | 0.03261 | 0.02263 | 0.03586 |
| $b_{ri,C}$ | 47.30740 | 29.17890 | 69.86910 | 5.86460 |
| $b_{ri,Eglob}$ | 29.53790 | 77.37150 | 117.9700 | 143.9900 |
| $b_{ri,k}$ | 0.58320 | 0.35250 | 0.75910 | 0.44390 |
| $b_{ri,l}$ | 0.11070 | 0.21230 | 0.22110 | 0.17890 |
| $b_{si,0}$ | 0.00097 | 0.00031 | 0.00095 | 0.00038 |
| $b_{si,C}$ | 0.38000 | 0.54220 | 0.94000 | 0.08553 |
| $b_{si,Eglob}$ | 0.49290 | 0.13280 | 0.38670 | 0.19420 |
| $b_{si,k}$ | 0.00336 | 0.00419 | 0.00663 | 0.00618 |
| $b_{si,l}$ | 0.00250 | 0.00044 | 0.00239 | 0.00013 |

and between-task differences in the brain networks of individuals within each age group deviate from their respective populations.

i. Young adults become more degree assortative (presence and strength) when comparing their visual-state to resting-state networks, whereas older adults do not [Variability: Greater increase in variability (presence and strength) in assortativity for young adults than older adults when comparing their visual-state to resting-state networks].

ii. Older adults gain connections (presence) (i.e., have more dense networks) when comparing their visual-state to resting-state networks, whereas younger adults do not [Variability: Older adults have more variability in their density than young adults during both rest and the visual task. However, the variability of young adults increases more than older adults when comparing their visual-state to resting-state networks].

iii. Global efficiency plays an even greater role in explaining the connection strength between two regions for younger adults when comparing their visual-state to resting-state networks, whereas it plays less of a role for older adults [Variability: Young adults have more variability in the global efficiency/strength relationship than older adults during both rest and the visual task. The variability in this relationship goes up for older adults when comparing their visual-state to resting-state networks, but goes down for young adults].

iv. Brain regions farther apart in distance tend to have relatively weaker connections when comparing visual-state to resting-state networks for both age groups.

v. Young adults have relatively weaker overall connectivity as their brains become more modular when comparing their visual-state to resting-state networks, whereas the converse is true for older adults.

vi. There is an overall larger increase in variability for young adults than older adults when comparing their visual-state to resting-state networks.

Overall Conclusion: The brain networks of young adults shift to a functional architecture comprising a resilient core of interconnected high-degree/high-strength/globally efficient hubs (i.e., a "rich-club" organization as detailed in [32]) without increasing wiring cost, by minimizing inter-module connectivity, when comparing their visual-state to resting-state networks. This shift does not occur for older adults, and further, their wiring cost increases (i.e., their networks become more densely connected with random connections). These additional connections may serve to partially compensate for this lack of shifting into tight communities for efficient task performance. The relative lack of a shift toward a resilient core of interconnected high-degree/high-strength/globally efficient hubs suggests that a rest to visual task transition does not strengthen connections within the task-relevant networks as much for older adults. These results are visually depicted in Fig. 7 (reproduced from [21]) which shows two sets of cartoon brain networks that typify the differences found between the brain networks in young and older adults when comparing their visual-state to resting-state networks.

We focused here on rest-to-task network changes, but the multitask framework is equally applicable to the assessment of network changes for any repeated task paradigm. Future work will update the WFU_MMNet toolbox to incorporate this multitask extension.

4. Negative correlations have ambiguous biological explanations and are undefined for certain network metrics [7, 9].

5. Given our focus on sparse weighted networks, we developed a two-part mixed modeling framework for single-task brain network data that allows modeling both the probability of a connection (presence/absence) and the strength of a connection if it exists while accounting for among-edge dependencies [10], thus increasing the power to detect network-phenotype relationships and decreasing false positive rates when compared to the univariate approaches that have dominated the field [33, 34]. Two-part models provide a valid statistical approach

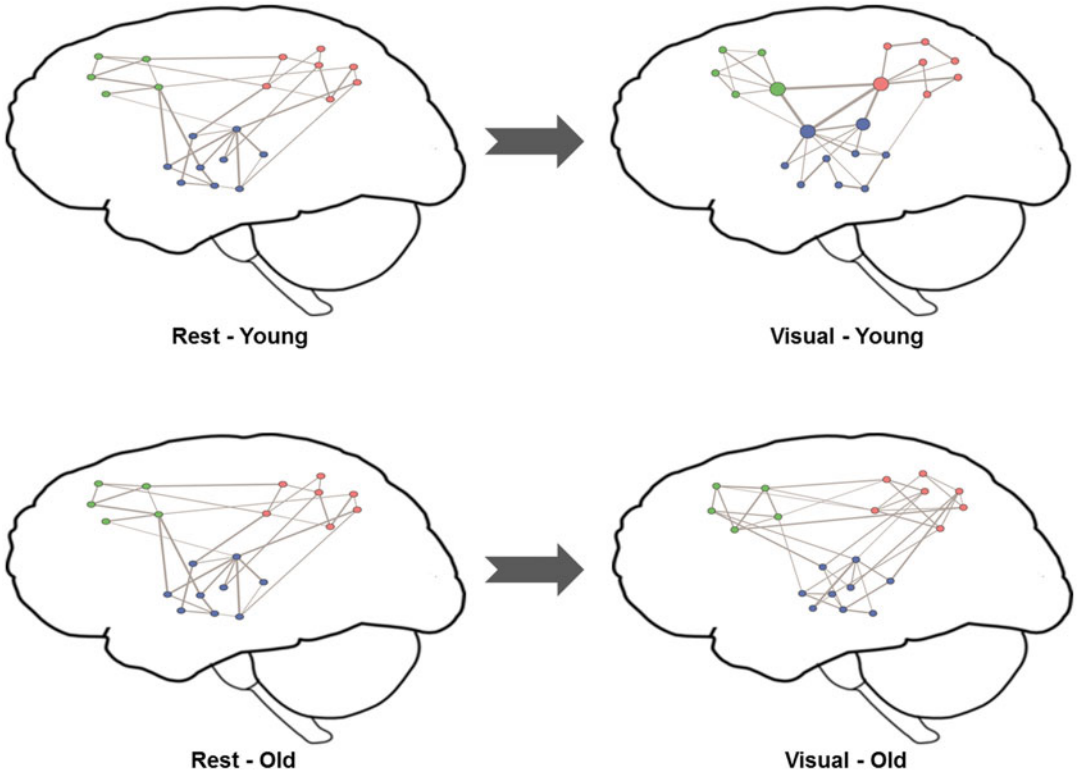


**Fig. 7** Cartoon depiction of important differences found between the brain networks in young and older adults when comparing their visual-state to resting-state networks. The nodes represent brain regions, the edge thickness represents the strength of functional connections between them, and the node color indicates the module membership. Young adults' brains shift to a functional architecture comprising a resilient core of interconnected high-degree/high-strength/globally efficient hubs without increasing wiring cost, by minimizing inter-module connectivity, when comparing their visual-state to resting-state networks. This shift does not occur for older adults, and further, their wiring cost increases (i.e., their networks become more densely connected with random connections)

to modeling semicontinuous outcomes in which a large portion of responses equal 0 (non-connections in our case) and the remaining responses come from a continuous distribution (strength values in our case) [35, 36]. The outcome variable in our framework comprises the entire brain connectivity matrix (all connections simultaneously) of each participant, while the explanatory variables comprise endogenous (summaries of network topology) and exogenous (relevant phenotypic characteristics) covariates (*see* Fig. 2 and formal definition below).

Let $Y_{ijk}$ represent the *strength* of the connection (quantified as the correlation in our case) and $R_{ijk}$ indicate whether a connection is present (*presence* variable) between node $j$ and node $k$ for the $i^{\text{th}}$

subject. Thus, $R_{ijk}=0$ if $\Upsilon_{ijk}=0$, and $R_{ijk}=1$ if $\Upsilon_{ijk}>0$ with conditional probabilities

$$P\left(R_{ijk}=r_{ijk}|\boldsymbol{\beta}_r;\ \boldsymbol{b}_{ri}\right)=\begin{cases}1-p_{ijk}(\boldsymbol{\beta}_r;\ \boldsymbol{b}_{ri}) & \text{if } r_{ijk}=0\\ p_{ijk}(\boldsymbol{\beta}_r;\ \boldsymbol{b}_{ri}) & \text{if } r_{ijk}=1\end{cases}, \quad (1)$$

where $\boldsymbol{\beta}_r$ is a vector of population parameters (fixed effects) that relate the probability of a connection to a set of covariates $\left(\boldsymbol{X}_{ijk}\right)$ for each subject and nodal pair (dyad), and $\boldsymbol{b}_{ri}$ is a vector of subject- and node-specific parameters (random effects) that capture how this relationship varies about the population average $(\boldsymbol{\beta}_r)$ by subject and node $\left(\boldsymbol{Z}_{ijk}\right)$. Here $\boldsymbol{Z}_{ijk}$ is the design matrix for subject $i$ that contains the covariate values corresponding to the respective random effects $\boldsymbol{b}_{ri}$ (i.e., it is analogous to $\boldsymbol{X}_{ijk}$ for the fixed effects $\boldsymbol{\beta}_r$). Hence, $p_{ijk}(\boldsymbol{\beta}_r;\ \boldsymbol{b}_{ri})$ is the probability of a connection between nodes $j$ and $k$ for subject $i$. We then have the following logistic mixed model (part I model) for the probability of this connection:

$$logit\left(p_{ijk}(\boldsymbol{\beta}_r;\ \boldsymbol{b}_{ri})\right)=\boldsymbol{X}'_{ijk}\boldsymbol{\beta}_r+\mathrm{Z}'_{ijk}\boldsymbol{b}_{ri}. \quad (2)$$

For the part II model, which aims to model the strength of a connection given that there is one, we let $S_{ijk}=\left[\Upsilon_{ijk}|R_{ijk}=1\right]$. In our case, the $S_{ijk}$ are the values of the correlation coefficients between nodes $j$ and $k$ for subject $i$. We can then use Fisher's Z-transform, denoted as *FZT*, and assume normality for the following mixed model (part II model)

$$FZT\left(S_{ijk}(\boldsymbol{\beta}_s;\ \boldsymbol{b}_{si})\right)=\boldsymbol{X}'_{ijk}\boldsymbol{\beta}_s+\mathrm{Z}'_{ijk}\boldsymbol{b}_{si}+e_{ijk}, \quad (3)$$

where $\boldsymbol{\beta}_s$ is a vector of population parameters that relate the strength of a connection to the same set of covariates $\left(\boldsymbol{X}_{ijk}\right)$ for each subject and dyad, $\boldsymbol{b}_{si}$ is a vector of subject- and node-specific parameters that capture how this relationship varies about the population average $(\boldsymbol{\beta}_s)$ by subject and node $\left(\boldsymbol{Z}_{ijk}\right)$, and $e_{ijk}$ accounts for the random noise in the connection strength of nodes $j$ and $k$ for subject $i$. Again $\boldsymbol{Z}_{ijk}$ is the design matrix for subject $i$ that contains the covariate values corresponding to the respective random effects $\boldsymbol{b}_{si}$.

The covariates $\left(\boldsymbol{X}_{ijk}\right)$ used to explain and predict both the presence and strength of connection are (1) *Net*: the average of the following network measures (categorized in Table 5 and further detailed in [1, 37]) in each dyad: Clustering ($C$), Global Efficiency (*Eglob*), Degree ($k$) (difference instead of average to capture "assortativity"), Modularity ($Q$), and Leverage Centrality ($l$); (2) *COI*s: Covariates of Interest; (3) *Int*: Interactions of the Covariates of Interest with the metrics in (1) and with other variables if desired; and (4) *Con*: Confounders (including Spatial Distance (between nodes) [importance of geometric distance noted by [38]], and the square of Spatial Distance). Thus, we can decompose $\boldsymbol{\beta}_r$ and $\boldsymbol{\beta}_s$ into

**Table 5**
**Explanatory network metrics by category**

| Category | Metric(s) |
|---|---|
| (1) Functional segregation | Clustering coefficient |
| (2) Functional integration | Global efficiency |
| (3) Resilience | Degree difference |
| (4) Centrality and information flow | Leverage centrality |
| (5) Community structure | Modularity |

$\boldsymbol{\beta}_r = \left[\beta_{r,0}\ \boldsymbol{\beta}_{r,net}\ \boldsymbol{\beta}_{r,coi}\ \boldsymbol{\beta}_{r,int}\ \boldsymbol{\beta}_{r,con}\right]'$ and $\boldsymbol{\beta}_s = \left[\beta_{s,0}\ \boldsymbol{\beta}_{s,net}\ \boldsymbol{\beta}_{s,coi}\ \boldsymbol{\beta}_{s,int}\ \boldsymbol{\beta}_{s,con}\right]'$ to correspond with the population intercepts and these covariates. For the random effects vectors we have that $\boldsymbol{b}_{ri} = \left[b_{ri,0}\ \boldsymbol{b}_{ri,net}\ \boldsymbol{b}_{ri,dist}\ \boldsymbol{\delta}_{ri,j}\ \boldsymbol{\delta}_{ri,k}\right]'$ and $\boldsymbol{b}_{si} = \left[b_{si,0}\ \boldsymbol{b}_{si,net}\ \boldsymbol{b}_{si,dist}\ \boldsymbol{\delta}_{si,j}\ \boldsymbol{\delta}_{si,k}\right]'$, where $b_{ri,0}$ and $b_{si,0}$ quantify the deviation of subject-specific intercepts from the population intercepts $\left(\beta_{r,0}\text{ and }\beta_{s,0}\right)$, $\boldsymbol{b}_{ri,net}$ and $\boldsymbol{b}_{si,net}$ contain the subject-specific parameters that capture how much the relationships between the network measures in (1) and the *presence* and *strength* of a connection vary about the population relationships $\left(\boldsymbol{\beta}_{r,net}\text{ and }\boldsymbol{\beta}_{s,net}\right)$ respectively, $\boldsymbol{b}_{ri,dist}$ and $\boldsymbol{b}_{si,dist}$ contain the subject-specific parameters that capture how much the relationship between spatial distance and the *presence* and *strength* of a connection vary about the population relationships, respectively, $\boldsymbol{\delta}_{ri,j}$ and $\boldsymbol{\delta}_{si,j}$ contain nodal-specific parameters that represent the propensity for node $j$ (of the given dyad) to be connected and the magnitude of its connections, respectively, and $\boldsymbol{\delta}_{ri,k}$ and $\boldsymbol{\delta}_{si,k}$ contain nodal-specific parameters that represent the propensity for node $k$ (of the given dyad) to be connected and the magnitude of its connections, respectively. Figure 8 diagrams this modeling approach (reproduced from [20]).

We assume that $\boldsymbol{b}_{ri}$, $\boldsymbol{b}_{si}$, and $\boldsymbol{e}_i = \left\{e_{ijk}\right\}$ are normally distributed and mutually independent, with variance component covariance structures for $\boldsymbol{b}_{ri}$ and $\boldsymbol{b}_{si}$, and the standard conditional independence structure for $\boldsymbol{e}_i$. That is, $\boldsymbol{b}_{ri} \sim N(\mathbf{0}, \boldsymbol{\Sigma}_{ri}(\boldsymbol{\tau}_r) = \text{diag}(\boldsymbol{\tau}_r))$ where $\boldsymbol{\tau}_r = (\sigma^2_{r,0}, \boldsymbol{\sigma}^2_{r,net}, \boldsymbol{\sigma}^2_{r,dist}, \sigma^2_{r,node1}, \sigma^2_{r,node2}, \ldots, \sigma^2_{r,nodeN})'$ and $\boldsymbol{b}_{si} \sim N(\mathbf{0}, \boldsymbol{\Sigma}_{si}(\boldsymbol{\tau}_s) = \text{diag}(\boldsymbol{\tau}_s))$ where $\boldsymbol{\tau}_s = (\sigma^2_{s,0}, \boldsymbol{\sigma}^2_{s,net}, \boldsymbol{\sigma}^2_{s,dist}, \sigma^2_{s,node1}, \sigma^2_{s,node2}, \ldots, \sigma^2_{s,nodeN})'$ are the $q(= N + 8) \times 1$ vectors of variances for each element of the random effects vectors, and $\boldsymbol{e}_i \sim N\left(\mathbf{0}, \boldsymbol{\Sigma}_{ei} = \sigma^2 \boldsymbol{I}\right)$. Thus, each nodal variance component serves as the average (latent) propensity of a node to be connected (and the magnitude of its connections) above and beyond other factors in the model that contribute to its connectivity. Here parameter estimation is conducted via restricted pseudo-likelihood [39] with the

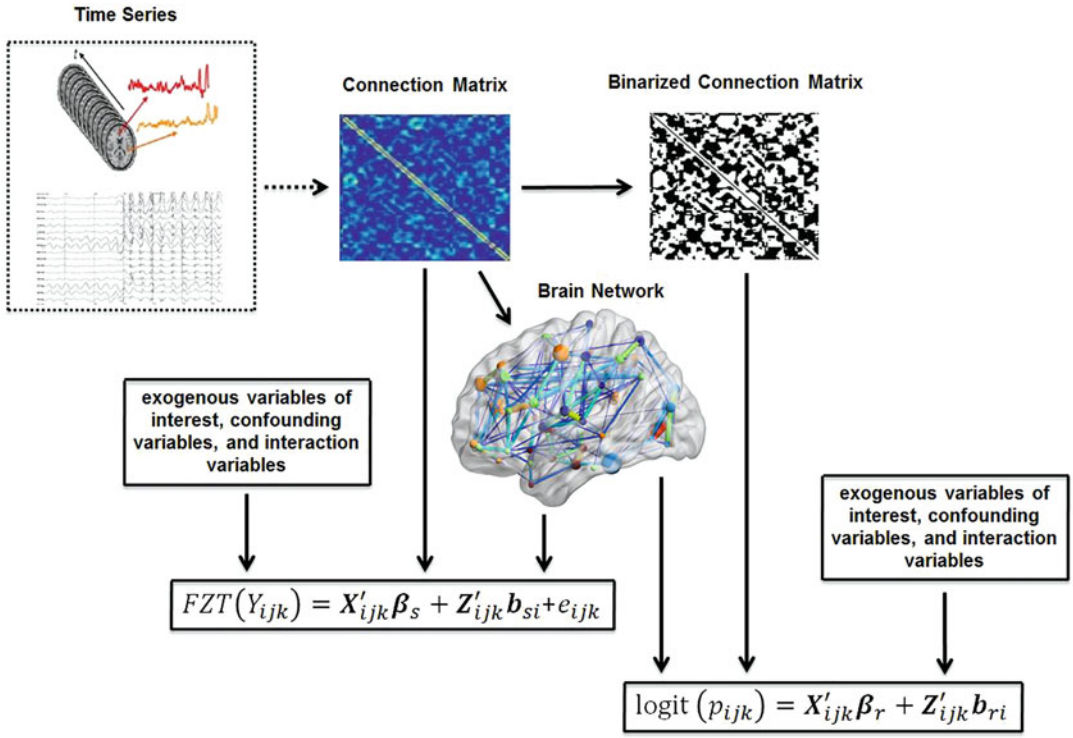


**Fig. 8** Diagram of the mixed modeling approach. The time series are used to compute the connection matrix with negative values set to zero. The binarized connection matrix is obtained by setting all nonzero values of the connection matrix to one. The network measures extracted from the connection matrix along with exogenous variables of interest, the interaction variables, and confounding variables are then used as covariates in the modeling framework

residual approximation of the *F*-test for a Wald statistic employed for inference. However, the model can also be imbedded within other appropriate estimation and inferential approaches.

Additional covariates can also be incorporated into the modeling framework as guided by the scientific question of interest or biological context. For example, regional and subnetwork analyses have become prominent in the literature recently, with most studies extracting these subnetworks from whole-brain networks and analyzing them independently. This approach neglects the interactions (dependencies) of these subnetworks with each other and with the rest of the brain. Thus it precludes identifying potential compensatory mechanisms outside the analyzed subnetworks and can yield misleading and erroneous results regarding the subnetworks under investigation [40]. To address this, Bahrami et al. [40] extended the single-task mixed modeling framework to allow for the modeling and analysis of both global (i.e., system-level or whole-brain) and local (i.e., regional or subnetwork) brain networks through the incorporation of subnetwork indicator variables. We showed that the analysis of brain subnetworks within the context of their whole-

brain networks can yield meaningfully different results when compared to analyzing them as independent networks, and can better disentangle whether an observed population effect is present globally or is restricted to local subnetworks. The approach has great appeal for researchers interested in understanding the coordination of brain activity and how it facilitates complex behavioral and cognitive tasks [4, 41], and how abnormalities in local and global brain circuits relate to complex psychiatric and neurological disorders [42].

Specific utilities of the framework include the following:

i. *Explain*: The framework allows explaining (quantifying) the relationship between endogenous network features and the probability and strength of a connection between brain areas via estimation of $\boldsymbol{\beta}_{r,net}$ and $\boldsymbol{\beta}_{s,net}$, the relationship between exogenous covariate(s) of interest and confounders and the probability and strength of connections via estimation of $\boldsymbol{\beta}_{r,coi}$, $\boldsymbol{\beta}_{r,con}$, $\boldsymbol{\beta}_{s,coi}$, and $\boldsymbol{\beta}_{s,con}$, and if (and how) the relationships between network features and the probability and strength of connections vary for different values of the covariate(s) of interest via estimation of $\boldsymbol{\beta}_{r,int}$ and $\boldsymbol{\beta}_{s,int}$. Specific interpretations of fixed effect parameters can be found in the Appendix of [10].

ii. *Compare*: This framework also allows making formal statistical assessments about relationships between phenotype (e.g., health status, age) and connectivity and network structure.

iii. *Predict*: The approach enables making predictions about connectivity and topology based on individual characteristics, and network structure and its variability via simulations from fitted models.

iv. *Simulate*: As alluded to above, the framework can also be used to simulate random realizations of networks (that retain constitutive characteristics of the original networks) from the fitted models. Consequently, group- and individual-level networks can be simulated that prove useful for model goodness-of-fit assessments, group-based representative network creation, and network variability assessment.

v. *Threshold*: The approach allows leveraging group-level data to better distinguish between "true" weak connections and noise in individual-level networks.

Further elucidation of these benefits can be found in [10].

6. As with single-task analyses, multitask analyses have also been dominated by univariate comparisons [34], in this case across tasks, precluding the assessment of the relationship between phenotype and between-task changes. This assessment is important for many areas given that the underlying mechanisms causing many health and behavioral outcomes are likely

related to how the brain changes from one task to another, and not just to the network structure during a given task. Here we detail the extension of our single-task model from the previous Note to the multitask context.

We extend the single-task model detailed in Eqs. 1–3 (and the accompanying text) to the multitask context by adding an additional dimension to the model for *task* indexed by $l$. That is, we now let $\Upsilon_{ijkl}$ represent the *strength* of the connection and $R_{ijkl}$ indicate whether a connection is present (*presence* variable) between node $j$ and node $k$ for the $i^{\text{th}}$ subject during the $l^{\text{th}}$ task. Thus, $R_{ijkl} = 0$ if $\Upsilon_{ijkl} = 0$, and $R_{ijkl} = 1$ if $\Upsilon_{ijkl} > 0$ with conditional probabilities

$$P\left(R_{ijkl} = r_{ijkl} | \boldsymbol{\beta}_{rl};\ \boldsymbol{b}_{rli}\right) = \begin{cases} 1 - p_{ijkl}(\boldsymbol{\beta}_{rl};\ \boldsymbol{b}_{rli}) & \text{if } r_{ijkl} = 0 \\ p_{ijkl}(\boldsymbol{\beta}_{rl};\ \boldsymbol{b}_{rli}) & \text{if } r_{ijkl} = 1 \end{cases}, \tag{4}$$

where $\boldsymbol{\beta}_{rl}$ is a vector of population parameters (fixed effects) that relate the probability of a connection to a set of covariates $\left(\boldsymbol{X}_{ijkl}\right)$ for each subject and nodal pair (dyad) for the $l^{\text{th}}$ task, and $\boldsymbol{b}_{rli}$ is a vector of subject- and node-specific parameters (random effects) that capture how this relationship varies about the population average $(\boldsymbol{\beta}_{rl})$ by subject and node $\left(\boldsymbol{Z}_{ijkl}\right)$ for the $l^{\text{th}}$ task. Hence, $p_{ijkl}(\boldsymbol{\beta}_{rl};\ \boldsymbol{b}_{rli})$ is the probability of a connection between nodes $j$ and $k$ for subject $i$ during the $l^{\text{th}}$ task. We then have the following logistic mixed model (part I model) for the probability of this connection:

$$logit\left(p_{ijkl}(\boldsymbol{\beta}_{rl};\ \boldsymbol{b}_{rli})\right) = \boldsymbol{X}'_{ijkl}\boldsymbol{\beta}_{rl} + \mathrm{Z}'_{ijkl}\boldsymbol{b}_{rli}. \tag{5}$$

For the part II model, we now let $S_{ijkl} = \left[\Upsilon_{ijkl} | R_{ijkl} = 1\right]$, where $S_{ijkl}$ are the values of the correlation coefficients (strength of connections) between nodes $j$ and $k$ for subject $i$ during the $l^{\text{th}}$ task. We again use *FZT*, and assume normality for the following part II model

$$FZT\left(S_{ijkl}(\boldsymbol{\beta}_{sl};\ \boldsymbol{b}_{sli})\right) = \boldsymbol{X}'_{ijkl}\boldsymbol{\beta}_{sl} + \mathrm{Z}'_{ijkl}\boldsymbol{b}_{sli} + e_{ijkl}, \tag{6}$$

where $\boldsymbol{\beta}_{sl}$ is a vector of population parameters that relate the strength of a connection to the same set of covariates $\left(\boldsymbol{X}_{ijkl}\right)$ for each subject and nodal pair (dyad) for the $l^{\text{th}}$ task, $\boldsymbol{b}_{sli}$ is a vector of subject- and node-specific parameters that capture how this relationship varies about the population average $(\boldsymbol{\beta}_{sl})$ by subject and node $\left(\boldsymbol{Z}_{ijkl}\right)$ for the $l^{\text{th}}$ task, and $e_{ijkl}$ accounts for the random noise in the connection strength of nodes $j$ and $k$ for subject $i$ during the $l^{\text{th}}$ task.

The covariates $\left(\boldsymbol{X}_{ijkl}\right)$ are the same as detailed in the previous section but now include a set of them for each task. Thus, we can decompose $\boldsymbol{\beta}_{rl}$ and $\boldsymbol{\beta}_{sl}$ into $\boldsymbol{\beta}_{rl} = \left[\boldsymbol{\beta}_{rl,0}\ \ \boldsymbol{\beta}_{rl,net}\ \boldsymbol{\beta}_{rl,coi}\ \boldsymbol{\beta}_{rl,int}\ \boldsymbol{\beta}_{rl,con}\right]'$

and $\boldsymbol{\beta}_{sl} = \left[\, \boldsymbol{\beta}_{sl,0} \;\; \boldsymbol{\beta}_{sl,net} \, \boldsymbol{\beta}_{sl,coi} \, \boldsymbol{\beta}_{sl,int} \, \boldsymbol{\beta}_{sl,con} \right]'$, and $\boldsymbol{b}_{rli}$ and $\boldsymbol{b}_{sli}$ into $\boldsymbol{b}_{rli} = \left[\, \boldsymbol{b}_{rli,0} \;\; \boldsymbol{b}_{rli,net} \, \boldsymbol{b}_{rli,dist} \, \boldsymbol{\delta}_{rli,j} \, \boldsymbol{\delta}_{rli,k} \right]'$ and $\boldsymbol{b}_{sli} = \left[\, \boldsymbol{b}_{sli,0} \;\; \boldsymbol{b}_{sli,net} \, \boldsymbol{b}_{sli,dist} \, \boldsymbol{\delta}_{sli,j} \, \boldsymbol{\delta}_{sli,k} \right]'$. Parameters for all $t$ tasks $(l = 1, 2, \ldots, t)$ are estimated or predicted simultaneously from the model.

We assume that $\boldsymbol{b}_{ri} = [\, \boldsymbol{b}_{r1i} \, \boldsymbol{b}_{r2i} \ldots \boldsymbol{b}_{rti}]'$, $\boldsymbol{b}_{si} = [\, \boldsymbol{b}_{s1i} \, \boldsymbol{b}_{s2i} \ldots \boldsymbol{b}_{sti}]'$, and $\boldsymbol{e}_i = \left\{ \boldsymbol{e}_{ijk} = \left[\, e_{ijk1} \; e_{ijk2} \ldots e_{ijkt} \right]' \right\}$ are normally distributed and mutually independent, with variance component covariance structures for $\boldsymbol{b}_{rli}$ and $\boldsymbol{b}_{sli}$, and the standard conditional independence structure for $\boldsymbol{e}_i$. That is, $\boldsymbol{b}_{rli} \sim N(\mathbf{0}, \boldsymbol{\Sigma}_{rli}(\boldsymbol{\tau}_{rl}) = \mathrm{diag}(\boldsymbol{\tau}_{rl}))$ where

$$\boldsymbol{\tau}_{rl} = \left( \sigma^2_{rl,0}, \, \boldsymbol{\sigma}^2_{rl,net}, \, \boldsymbol{\sigma}^2_{rl,dist}, \, \boldsymbol{\sigma}^2_{rl,node1}, \, \boldsymbol{\sigma}^2_{rl,node2}, \, \ldots, \, \sigma^2_{rl,nodeN} \right)'$$

and $\boldsymbol{b}_{sli} \sim N(\mathbf{0}, \boldsymbol{\Sigma}_{sli}(\boldsymbol{\tau}_{sl}) = \mathrm{diag}(\boldsymbol{\tau}_{sl}))$ where

$$\boldsymbol{\tau}_{sl} = \left( \sigma^2_{sl,0}, \, \boldsymbol{\sigma}^2_{sl,net}, \, \boldsymbol{\sigma}^2_{sl,dist}, \, \boldsymbol{\sigma}^2_{sl,node1}, \, \boldsymbol{\sigma}^2_{sl,node2}, \, \ldots, \, \sigma^2_{sl,nodeN} \right)'$$

are the $(N + 8) \times 1$ vectors of variances for each element of the random effects vectors, and $\boldsymbol{e}_i \sim N\left(\mathbf{0}, \boldsymbol{\Sigma}_{ei} = \sigma^2 \boldsymbol{I}\right)$. Additionally, the model contains covariance parameters for each random effect and its counterparts across tasks yielding $(N + 8) \times \binom{t}{2}$ covariance parameters for both the *presence* and *strength* models. That is, the overall random effects covariance is modeled with unstructured covariance matrices (parameterized through their Cholesky roots) for each random effect and its counterparts across tasks. For example, in the 2-task case we have that

$$Cov(\boldsymbol{b}_{rl_1 i}, \boldsymbol{b}_{rl_2 i}) = \begin{pmatrix} \boldsymbol{\Sigma}_{rl_1 i} & \boldsymbol{D}_{rl_1 l_2 i} \\ \cdots & \boldsymbol{\Sigma}_{rl_2 i} \end{pmatrix}, \text{ where } \boldsymbol{D}_{rl_1 l_2 i} = \mathrm{diag}(\boldsymbol{\lambda}_r),$$

and $Cov(\boldsymbol{b}_{sl_1 i}, \boldsymbol{b}_{sl_2 i}) = \begin{pmatrix} \boldsymbol{\Sigma}_{sl_1 i} & \boldsymbol{D}_{sl_1 l_2 i} \\ \cdots & \boldsymbol{\Sigma}_{sl_2 i} \end{pmatrix}$, where $\boldsymbol{D}_{sl_1 l_2 i} = \mathrm{diag}(\boldsymbol{\lambda}_s)$.

These covariance parameters, contained in the $\boldsymbol{\lambda}_r$ and $\boldsymbol{\lambda}_s$ vectors for the example, provide insight into whether individual (and group) differences in between-task variability relate to health and behavioral outcomes. Parameter estimation and inference are conducted as discussed in the previous note.

Additional utilities of this framework include the following:

i. *More accurate and precise within-task results*: The multitask framework yields more accurate and precise estimation of the relationship between systemic brain properties and health outcomes within a given task since it is able to leverage information from other tasks, particularly through the covariance parameters that capture correlations across tasks.

ii. *Ability to assess population network differences and individual variability in network differences within and between tasks*: The multitask formulation enables investigating how phenotypic traits are related to within-task brain network organization and between-task organizational changes at the group and individual level.

7. Until recently, most brain network studies have focused on putatively stationary patterns of functional connectivity in which static networks are defined as an average of the associations between brain regions during an entire within-task scanning period. However, scientific interest toward within-task dynamic changes during these scans has exploded over the last few years [43–45], with these fluctuations of connectivity patterns over shorter periods likely underlying a variety of phenomena such as cognitive and behavior responses [3, 46, 47], learning [48], brain disorders [49, 50] and consciousness [51, 52]. Despite these insights, as has been the case with static network analyses, appropriate statistical tools have lagged behind, leaving the link between this within-task network variability (dynamics) and health and behavioral outcomes vastly underexplored [53]. Current approaches rudimentarily compare the variability of connection strengths or network metrics across groups [54–58], failing to fully harness the wealth of information present. Here we briefly outline planned future work aimed at extending our mixed modeling framework to provide a parsimonious, comprehensive, and systemic analytical approach for dynamic brain network analysis.

Following the notation of Eqs. 2 and 3, we propose the following modified part I and II models for dynamic network analysis (additional components in parentheses):

$$\begin{aligned} logit\left(p_{ijk}(\boldsymbol{\beta}_r;\ \boldsymbol{b}_{ri})\right) &= \boldsymbol{X}'_{ijk}\boldsymbol{\beta}_r + \left(\sum_{k=1}^{n}\gamma_{rk}s_{(k)}(X_t)\right) \\ &\quad + \mathbf{Z}'_{ijk}\boldsymbol{b}_{ri} + \left(\sum_{k=1}^{n}\boldsymbol{d}_{rk}s_{(k)}(Z_t)\right) \end{aligned} \tag{7}$$

$$\begin{aligned} FZT\left(S_{ijk}(\boldsymbol{\beta}_s;\ \boldsymbol{b}_{si})\right) &= \boldsymbol{X}'_{ijk}\boldsymbol{\beta}_s + \left(\sum_{k=1}^{n}\gamma_{sk}s_{(k)}(X_t)\right) \\ &\quad + \mathbf{Z}'_{ijk}\boldsymbol{b}_{si} + \left(\sum_{k=1}^{n}\boldsymbol{d}_{sk}s_{(k)}(Z_t)\right) + e_{ijk}. \end{aligned} \tag{8}$$

The additional components $\sum_{k=1}^{n}\gamma_{rk}s_{(k)}(X_t)$ and $\sum_{k=1}^{n}\gamma_{sk}s_{(k)}(X_t)$ correspond to population-level $n^{\text{th}}$ order orthonormal polynomial models capturing the dynamic trends in the *presence* and *strength* of connections across time ($t$ = number of time points/networks per individual). The additional components $\sum_{k=1}^{n}\boldsymbol{d}_{rk}s_{(k)}(Z_t)$ and $\sum_{k=1}^{n}\boldsymbol{d}_{sk}s_{(k)}(Z_t)$ correspond to individual-level $n^{\text{th}}$ order orthonormal polynomial models capturing how much the subject-specific trends deviate from the population trends. Employing an orthonormal polynomial model in this manner has been shown to accurately represent the trend in time series data while avoiding the computational issues resulting from the use of natural polynomials [59, 60]. Augmenting the covariance assumptions for the random effects and random errors, we now assume that $\boldsymbol{b}_{ri}$, $\boldsymbol{d}_r = [\ \boldsymbol{d}_{r1}\ \boldsymbol{d}_{r2}\ldots\boldsymbol{d}_{rn}]'$, $\boldsymbol{b}_{si}$, $\boldsymbol{d}_s = [\boldsymbol{d}_{s1}\ \boldsymbol{d}_{s2}\ldots\boldsymbol{d}_{sn}]'$,

and $\boldsymbol{e}_i = \{e_{ijk}\}$ are normally distributed and mutually independent, with variance component covariance structures for $\boldsymbol{b}_{ri}$, $\boldsymbol{d}_r$, $\boldsymbol{b}_{si}$, and $\boldsymbol{d}_s$, and the standard conditional independence structure for $\boldsymbol{e}_i$. These variance parameters will provide insight into whether individual (and group) differences in variability in dynamics relate to health and behavioral outcomes.

This extension will enable: (1) assessing the relationship between within-task network dynamics and health outcomes; (2) assessing the relationship between individual and group variability in dynamics and health outcomes; and (3) accounting for the connectivity/network dynamics when assessing group differences and phenotype-health outcome relationships, to avoid confounding and drawing erroneous conclusions.

We anticipate the field moving next toward multitask dynamic brain network analyses, and plan to subsequently develop an analog of the multitask model for this context to ensure appropriate methods are available, and combat the lag in principled statistical methods that has plagued the field. This analog will likely entail a fusion of the frameworks discussed in this and the previous section.

## Acknowledgements

This work was supported by National Institute of Biomedical Imaging and Bioengineering R01EB024559, and Wake Forest Clinical and Translational Science Institute (WF CTSI) NCATS UL1TR001420.

### References

1. Simpson SL, Bowman FD, Laurienti PJ (2013) Analyzing complex functional brain networks: fusing statistics and network science to understand the brain. Stat Surv 7:1–36
2. Simpson SL, Laurienti PJ (2016) Disentangling brain graphs: a note on the conflation of network and connectivity analyses. Brain Connect 6(2):95–98
3. Sporns O (2010) Networks of the brain. The MIT Press, Cambridge
4. Sporns O (2018) Graph theory methods: applications in brain networks. Dialog Clin Neurosci **20**(2):111
5. Bullmore E, Sporns O (2009) Complex brain networks: graph theoretical analysis of structural and functional systems. Nat Rev Neurosci 10(3):186
6. Simpson SL, Burdette JH, Laurienti PJ (2015) The brain science interface. Significance 12 (4):34–39
7. Telesford QK, Simpson SL, Burdette JH, Hayasaka S, Laurienti PJ (2011) The brain as a complex system: using network science as a tool for understanding the brain. Brain Connect 1(4):295–308
8. Bassett DS, Bullmore ET (2009) Human brain networks in health and disease. Curr Opin Neurol 22(4):340
9. Cao M, Wang JH, Dai ZJ, Cao XY, Jiang LL, Fan FM, et al (2014) Topological organization of the human brain functional connectome across the lifespan. Develop Cognit Neurosci 7:76–93
10. Simpson SL, Laurienti PJ (2015) A two-part mixed-effects modeling framework for analyzing whole-brain network data. NeuroImage 113:310–319
11. Simpson SL, Hayasaka S, Laurienti PJ (2011) Exponential random graph modeling for complex brain networks. PLoS One 6(5):e20039

12. Simpson SL, Moussa MN, Laurienti PJ (2012) An exponential random graph modeling approach to creating group-based representative whole-brain connectivity networks. Neuroimage 60(2):1117–1126
13. Solo V, Poline JB, Lindquist MA, Simpson SL, Bowman FD, Chung MK, Cassidy B (2018). Connectivity in fMRI: blind spots and breakthroughs. IEEE Trans Med Imag 37(7), 1537–1550
14. Handcock MS (2003) Statistical models for social networks: inference and degeneracy. In: Breiger R, Carley K, Pattison PE (eds) Dynamic social network modelling and analysis: workshop summary and papers. National Academy Press, Washington, DC, pp 229–240
15. Rinaldo, A., Fienberg SE, Zhou Y (2009) On the geometry of discrete exponential families with application to exponential random graph models Electron J Stat 3:446–484
16. O'Malley AJ (2013) The analysis of social network data: an exciting frontier for statisticians. Stat Med 32(4):539–555
17. Shehzad Z, Kelly C, Reiss PT, Cameron Craddock R, Emerson JW, McMahon K, et al (2014) A multivariate distance-based analytic framework for connectome-wide association studies. NeuroImage **93**:74–94
18. Simpson SL, Lyday RG, Hayasaka S, Marsh AP, Laurienti PJ (2013) A permutation testing framework to compare groups of brain networks. Front Comput Neurosci 7:171
19. Bahrami M, Laurienti PJ, Quandt SA, Talton J, Pope CN, Summers P, Burdette JH, Chen H, Liu J, Howard TD, Arcury TA, Simpson SL (2017) The impacts of pesticide and nicotine exposures on functional brain networks in Latino immigrant workers. NeuroToxicology 62:138–150
20. Bahrami M, Laurienti PJ, Simpson SL (2019) A Matlab toolbox for multivariate analysis of brain networks. Hum Brain Mapp 40 (1):175–186
21. Simpson, S. L., Bahrami M, Laurienti PJ (2019) A mixed-modeling framework for analyzing multitask whole-brain network data. Network Neurosci 3(2):307–324
22. Tzourio-Mazoyer N, Landeau B, Papathanassiou D, Crivello F, Etard O, Delcroix N, Mazoyer B, Joliot M (2002) Automated anatomical labeling of activations in SPM using a macroscopic anatomical parcellation of the MNI MRI single-subject brain. NeuroImage 15:273–289
23. Arcury, T. A., Nguyen HT, Summers P, Talton JW, Holbrook LC, Walker FO, . . ., Quandt SA (2014) Lifetime and current pesticide exposure among Latino farmworkers in comparison to other Latino immigrants. Am J Ind Med 57 (7):776–787
24. Laurienti PJ, Burdette JH, Talton J, Pope CN, Summers P, Walker FO, . . .Arcury TA (2016) Brain anatomy in Latino farmworkers exposed to pesticides and nicotine. J Occup Environ Med 58(5):436
25. Schultz DH, Cole MW (2016) Integrated brain network architecture supports cognitive task performance. Neuron 92(2):278–279
26. Lebedev AV, Westman E., Simmons A, Lebedeva A, Siepel FJ, Pereira JB, Aarsland D (2014) Large-scale resting state network correlates of cognitive impairment in Parkinson's disease and related dopaminergic deficits. Front Syst Neurosci 8:45
27. Baggio HC, Sala-Llonch R, Segura B, Marti MJ, Valldeoriola F, Compta Y, . . .Junqué C (2014) Functional brain networks and cognitive deficits in Parkinson's disease. Hum Brain Mapp 35(9):4620–4634
28. Gamboa OL, Tagliazucchi E, von Wegner F, Jurcoane A, Wahl M, Laufs H, Ziemann U (2014). Working memory performance of early MS patients correlates inversely with modularity increases in resting state functional connectivity networks. Neuroimage 94:385–395
29. Hugenschmidt CE, Mozolic JL, Tan H, Kraft RA, Laurienti PJ (2009) Age-related increase in cross-sensory noise in resting and steady-state cerebral perfusion. Brain Topogr 21 (3–4):241–251
30. Moussa MN, Vechlekar CD, Burdette JH, Steen MR, Hugenschmidt CE, Laurienti PJ (2011) Changes in cognitive state alter human functional brain networks. Front Hum Neurosci 5:103–113
31. Hunter DR, Goodreau SM, Handcock MS (2008) Goodness of fit of social network models. J Am Stat Assoc 103(481):248–258
32. Van Den Heuvel, MP, Sporns O (2011) Rich-club organization of the human connectome. J Neurosci 31(44):15775–15786
33. Edwards LJ (2000). Modern statistical techniques for the analysis of longitudinal data in biomedical research. Pediatr Pulmonol 30 (4):330–344
34. Ginestet CE, Fournel AP, Simmons A (2014) Statistical network analysis for functional MRI: mean networks and group comparisons. Front Comput Neurosci 8:51
35. Albert PS, Shen J (2005) Modelling longitudinal semicontinuous emesis volume data with serial correlation in an acupuncture clinical

trial. J R Stat Soc Ser C (Appl Stat) 54 (4):707–720

36. Liu L, Ma JZ, Johnson BA (2008) A multilevel two-part random effects model, with application to an alcohol-dependence study. Stat Med 27(18):3528–3539
37. Rubinov M, Sporns O (2010) Complex network measures of brain connectivity: uses and interpretations. Neuroimage 52:1059–1069
38. Friedman EJ, Landsberg AS, Owen JP, Li YO, Mukherjee P (2014) Stochastic geometric network models for groups of functional and structural connectomes. NeuroImage 101:473–484
39. Wolfinger R, O'connell M (1993). Generalized linear mixed models a pseudo-likelihood approach. J Stat Comput Simul 48 (3–4):233–243
40. Bahrami M, Laurienti PJ, Simpson SL (2019) Analysis of brain subnetworks within the context of their whole-brain networks. Hum Brain Mapp 40(17):5123–5141
41. McIntosh AR (2000) Towards a network theory of cognition. Neural Netw 13 (8–9):861–870
42. Menon V (2011) Large-scale brain networks and psychopathology: a unifying triple network model. Trends Cognit Sci 15(10):483–506
43. Mokhtari F, Akhlaghi MI, Simpson SL, Wu G, Laurienti PJ (2019). Sliding window correlation analysis: modulating window shape for dynamic brain connectivity in resting state. NeuroImage 189:655–666
44. Laurienti PJ, Bahrami M, Lyday RG, Casanova R, Burdette JH, Simpson, SL (2019) Using low-dimensional manifolds to map relationships between dynamic brain networks. Front Hum Neurosci 13:430
45. Chang, C., Keilholz S, Miller R, Woolrich M (2018) Mapping and interpreting the dynamic connectivity of the brain. NeuroImage 180 (PB):335–336
46. Petersen SE, Sporns O (2015) Brain networks and cognitive architectures. Neuron 88 (1):207–219
47. Park HJ, Friston K (2013) Structural and functional brain networks: from connections to cognition. Science 342(6158):1238411
48. Bassett DS, Wymbs NF, Porter MA, Mucha PJ, Carlson JM, Grafton ST (2011) Dynamic reconfiguration of human brain networks during learning. Proc Natl Acad Sci 108 (18):7641–7646
49. Rashid B, Arbabshirani MR, Damaraju E, Cetin MS, Miller R, Pearlson GD, Calhoun VD (2016) Classification of schizophrenia and bipolar patients using static and dynamic resting-state fMRI brain connectivity. Neuroimage 134:645–657
50. Zhang J, Cheng W, Liu Z, Zhang K, Lei X, Yao Y, . . ., Feng J (2016) Neural, electrophysiological and anatomical basis of brain-network variability and its characteristic changes in mental disorders. Brain 139(8):2307–2321
51. Barttfeld P, Uhrig L, Sitt JD, Sigman M, Jarraya B, Dehaene S (2015) Signature of consciousness in the dynamics of resting-state brain activity. Proc Natl Acad Sci 112 (3):887–892
52. Godwin, D., Barry RL, Marois R (2015) Breakdown of the brain's functional network modularity with awareness. Proc Natl Acad Sci 112(12):3799–3804
53. Medaglia JD, Lynall ME, Bassett DS (2015). Cognitive network neuroscience. J Cognit Neurosci 27(8):1471–1491
54. Hutchison RM, Womelsdorf T, Allen EA, Bandettini PA, Calhoun VD, Corbetta M, . . ., Handwerker DA (2013) Dynamic functional connectivity: promise, issues, and interpretations. Neuroimage 80:360–378
55. Shine JM, Bissett PG, Bell PT, Koyejo O, Balsters JH, Gorgolewski KJ, . . ., Poldrack RA (2016) The dynamics of functional brain networks: integrated network states during cognitive task performance. Neuron 92(2):544–554
56. Fukushima M, Betzel RF, He Y, de Reus MA, van den Heuvel MP, Zuo XN, Sporns O (2018) Fluctuations between high-and low--modularity topology in time-resolved functional connectivity. NeuroImage 180:406–416
57. Sizemore AE, Bassett DS (2018) Dynamic graph metrics: tutorial, toolbox, and tale. NeuroImage 180:417–427
58. Elton A, Gao W (2015). Task-related modulation of functional connectivity variability and its behavioral correlations. Hum Brain Mapp 36(8):3260–3272
59. Edwards LJ, Simpson SL (2014) An analysis of 24-hour ambulatory blood pressure monitoring data using orthonormal polynomials in the linear mixed model. Blood Pressure Monit 19 (3):153
60. Simpson SL, Edwards LJ (2013) A circular LEAR correlation structure for cyclical longitudinal data. Stat Methods Med Res 22 (3):296–306

# Chapter 31

# Rapid In Vivo Quantification of Creatine Kinase Activity by Phosphorous-31 Magnetic Resonance Spectroscopic Fingerprinting ($^{31}$P-MRSF)

**Charlie Wang, Kihwan Kim, and Xin Yu**

## Abstract

Creatine kinase (CK) plays an important role in tissue metabolism by providing a buffering mechanism for maintaining a constant supply of adenosine triphosphate (ATP) during metabolic perturbations. Phosphorous-31 magnetic resonance spectroscopy ($^{31}$P-MRS) employing magnetization transfer techniques is the only noninvasive method for measuring the rate of ATP synthesis via creatine kinase. However, due to the low concentrations of phosphate metabolites, current $^{31}$P-MRS methods require long acquisition time to achieve adequate measurement accuracy. In this chapter, we present a new framework of data acquisition and parameter estimation, the $^{31}$P magnetic resonance spectroscopic fingerprinting ($^{31}$P-MRSF) method, for rapid quantification of CK reaction rate constant in the hindlimb of small laboratory animals.

**Key words** Magnetic resonance fingerprinting, Phosphorous-31 magnetic resonance spectroscopy, Creatine kinase, Muscle metabolism

## 1 Introduction

Phosphorous-31 magnetic resonance spectroscopy ($^{31}$P-MRS) has been used in evaluating cellular metabolism since the 1970s [1, 2]. The first in vivo $^{31}$P-MRS experiment was performed on rat skeletal muscle using a surface coil [3]. Since then, $^{31}$P-MRS has emerged as a powerful tool for studying tissue metabolism in vivo. The technique allows the quantification of the concentrations of major phosphate metabolites such as adenosine triphosphate (ATP) and phosphocreatine (PCr) in living tissues [4–9]. The noninvasive nature of the technique also enables repeated measurements from the same tissue, thus the response to an acute event (e.g., exercise, electrical stimulation, ischemia/reperfusion), or long-term treatment (e.g., dietary manipulation, pharmacological therapy) can be evaluated.

Miguel R. Ossandon et al. (eds.), *Biomedical Engineering Technologies: Volume 1*, Methods in Molecular Biology, vol. 2393, https://doi.org/10.1007/978-1-0716-1803-5_31, 

Creatine kinase (CK) catalyzes the exchange of a high-energy phosphate group between PCr and ATP [10–12]. It plays an important role in metabolic homeostasis by maintaining constant ATP supply during transient periods of metabolic perturbations such as exercise and ischemia [13–15]. $^{31}$P-MRS in combination with magnetization transfer (MT) provides the only methodology for in vivo quantification of CK activity [16–21]. The technique entails measurements of changes in PCr signal after the saturation or inversion of the γATP signal. The forward rate constant of ATP synthesis via CK is determined by fitting the Bloch-McConnell model to measured PCr signal as a function of saturation or inversion time [22–24]. Typically, a range of saturation or inversion time covering the entire dynamics of PCr signal changes is sampled to ensure robust parameter estimation. Further, because the concentrations of phosphate metabolites are four to five orders of magnitude lower than that of water protons, a large number of signal averages is necessary for achieving adequate signal-to-noise ratio (SNR). As such, these MT-MRS techniques require long data acquisition time and have found limited clinical and preclinical applications.

Magnetic resonance fingerprinting (MRF) is a new framework of data acquisition and parameter estimation that allows for more flexible pulse sequence design with dramatically improved acquisition efficiency [25]. By using an unconventional data acquisition framework, MRF creates a signal evolution pattern, or fingerprint, that is uniquely associated with tissue properties such as relaxation times. Knowledge of the spin physics is used to create a dictionary that encompasses all possible fingerprints. By using pattern matching algorithms to select the dictionary entry that best matches the acquired signal, efficient and simultaneous quantification of multiple tissue properties has been demonstrated, with drastically reduced sensitivity to measurement errors and significantly improved data acquisition efficiency. Since its invention, various MRF methods have been developed and successfully used for fast and robust measurement of proton relaxation times in brain [26–28], abdomen [29], heart [30], prostate [27], cartilage and bone [31], and cerebral vasculature [32]. High-resolution MRF methods for preclinical applications in small animals are also emerging [33–35].

With the incorporation of magnetization modulation processes that are sensitive to magnetization transfer via chemical exchange, MRF also has the potential of estimating metabolic fluxes with significantly improved efficiency. We recently explored the potential of using MRF for rapid quantification of CK rate constant in vivo [36]. The approach is still at its early stage of development, and the pulse sequence is far from being optimized. This chapter describes our initial experience in developing a $^{31}$P spectroscopic MRF method ($^{31}$P-MRSF) for measuring CK rate constant in the skeletal

muscle of small laboratory animals. The $^{31}$P-MRSF method can be combined with other protocols, e.g., ischemia-reperfusion or muscle contraction induced by electrical stimulation, to study the effect of physiological/metabolic perturbations on CK activity. These protocols are also described in this chapter.

## 2 Materials

### 2.1 Preclinical MRI Scanner and Peripherals

1. Bruker 9.4T horizontal bore scanner (Bruker Biospin Inc., Billerica, MA, USA).
2. $^{1}$H volume coil (Bruker Biospin Inc., Billerica, MA, USA).
3. $^{31}$P volume coil.

### 2.2 Animal Setup

1. Vaporizer (E-Z Systems Inc., Palmer, PA, USA).
2. Isoflurane USP (Patterson Veterinary, Denvens, MA, USA).
3. Oxygen gas (Airgas, Radnor Township, PA, USA).
4. Respiratory sensing pad (SA Instruments, Inc., Stony Brook, NY, USA).
5. Rectal temperature probe (SA Instruments, Inc., Stony Brook, NY, USA).
6. Physiological monitoring system (SA Instruments, Inc., Stony Brook, NY, USA).
7. Feedback heating system (SA Instruments, Inc., Stony Brook, NY, USA).
8. Anesthesia chamber.
9. Nose cone.
10. Animal cradle.
11. Tapes.

### 2.3 Stimulation-Induced Muscle Contraction

1. Platinum subdermal needle electrodes (iWorx Systems, Inc., Dover, NH, USA).
2. S48 Grass stimulator and isolation unit (AstroNova, Inc., West Warwick, RI, USA).

### 2.4 Ischemia-Recovery

1. E20 cuff inflator and AG101 cuff inflator air source (D.E. Hakanson, Inc., Bellevue, WA, USA).
2. Inflatable cuff.

## 3 Methods

The methods presented here are specifically designed for small animal studies on a Bruker 9.4T preclinical MR system. The protocols can be adapted for use in other animal models with necessary adjustments.

### 3.1 Animal Preparation

1. Place the animal in the anesthesia chamber and anesthetize the animal with 3% isoflurane in oxygen initially.
2. Place the anesthetized animal in lateral position in the animal cradle and maintain the anesthesia with 1–1.5% isoflurane in oxygen delivered via the nose cone.
3. Secure the respiratory sensing pad to the abdomen of the animal and connect it to the physiological monitoring system. Adjusting the anesthesia level during the imaging protocol to maintain a respiratory rate of >40 breaths per min for rats and >80 breathes per min for mice.
4. Insert the rectal temperature probe into the animal. Connect the temperature probe to the physiological monitoring and feedback heating system. Set the targeted body temperature for the heating system to 37 °C.
5. Place the leg to be measured within the $^{31}$P volume coil and secure the leg in a position such that the gastrocnemius muscle is in the middle of the $^{31}$P coil's sensitive volume.
6. Transfer the entire cradle with the animal and the $^{31}$P coil into the MRI scanner. Place the $^{31}$P coil at the center of the $^{1}$H volume coil, which is placed in the isocenter of the MRI scanner.

### 3.2 The $^{31}$P-MRSF Method

1. Implement the $^{31}$P-MRSF pulse sequence.

   Schematics of the $^{31}$P-MRSF pulse sequence are shown in Fig. 1. Following a nonselective adiabatic inversion pulse, the sequence is comprised of interleaved acquisition of PCr and γATP signals in 32 acquisition blocks using spectrally selective excitation pulses (Fig. 1a). Each block consists of a train of 10 excitation pulses with alternating phase and a constant repetition time (TR) of 12.8 ms. A 4-ms frequency selective Gaussian pulse is used for spectrally selective excitation. The flip angle (FA) in each block is linearly ramped-up and ramped-down. The entire acquisition is organized into two 16-block segments with the maximal flip angle in each block varied sinusoidally (Fig. 1b). Following each excitation, 7.7 ms of the free induction decay (FID) signal is collected with 256 data points, yielding a spectral resolution of 130 Hz. A 490-ms spectrally selective saturation block is applied between two acquisition blocks. The saturation frequency is set at the resonance frequency of γATP in the second acquisition segment and at the frequency contralateral to γATP in the first segment (*see* **Note 1**). A total of 320 FID signals are collected in one fingerprint. The acquisition time of one fingerprint is 20 s. The current sequence parameters are selected as reasonably optimal for studies of rodent hindlimb on a 9.4T preclinical system. Adjustment of parameters may be necessary for optimal acquisition efficiency at other field strengths.

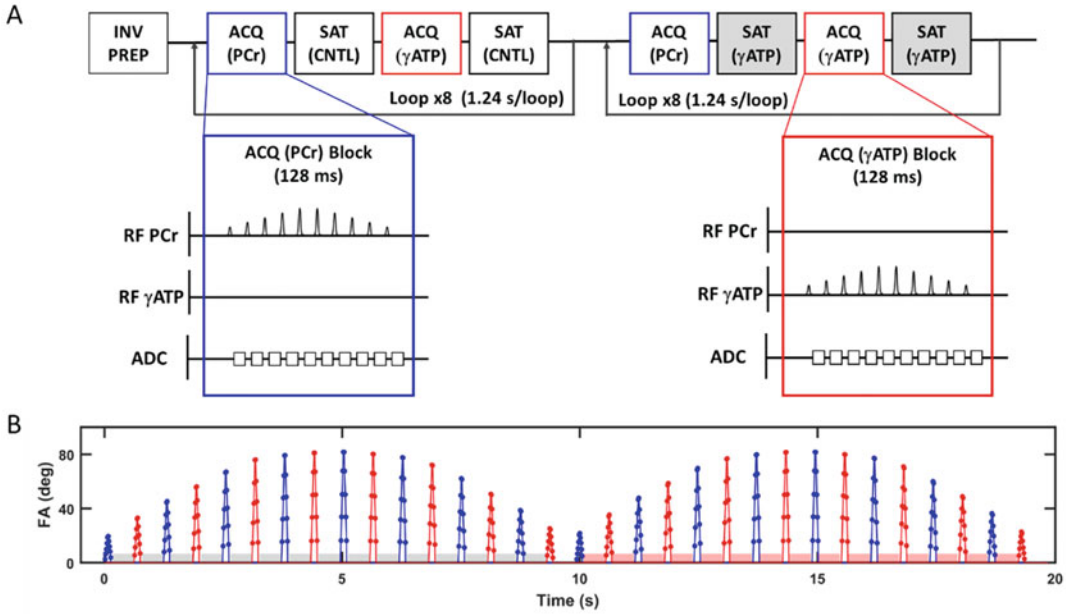


**Fig. 1** $^{31}$P-MRSF sequence. (**a**) Schematic diagram of the pulse sequence. INV-PREP: inversion preparation; ACQ(PCr) and ACQ(γATP): acquisition blocks for PCr and γATP, respectively; SAT(CNTL) and SAT(γATP): contralateral and γATP saturation blocks, respectively. (**b**) Timing and nominal flip angles of all excitation pulses. Blue and red colors indicate PCr and γATP excitation, respectively. Red- and gray-shaded boxes indicate γATP and contralateral saturation blocks, respectively

2. Choose the parameters for the $^{31}$P-MRSF dictionary.

   The dictionary in the MRF framework is a library of fingerprints for selected values of tissue parameters that may influence the fingerprint. The nine parameters used in $^{31}$P-MRSF simulations are listed in Table 1. Matching for all these parameters will be computationally challenging. The $^{31}$P-MRSF sequence was designed to be relatively insensitive to the $T_1$ relaxation time of γATP ($T_1^{\gamma ATP}$), the $T_2$ relaxation time of both PCr and γATP ($T_2^{PCr}$ and $T_2^{\gamma ATP}$), and the linewidth (LW) (*see* **Note 2**). Further, the resonance frequency of γATP ($\omega^{\gamma ATP}$) can be constrained by the chemical shift difference between PCr and γATP (2.4 ppm). Hence, only four parameters, i.e., the forward CK rate constant ($k_f^{CK}$), the $T_1$ relaxation time of PCr ($T_1^{PCr}$), the resonance frequency of PCr ($\omega^{PCr}$), and the PCr-to-ATP ratio ($M_R^{PCr}$), are estimated from fingerprint matching. The dictionary for fingerprint matching should encompass the physiologically expected ranges of variations for these parameters. Table 1 also lists the parameter ranges we have used in our study on normal rats and mice, as well as the values of the fixed parameters, which were obtained from pilot studies.

**Table 1**
**Parameters in Fingerprint Simulation**

| Symbols | Units | Parameter description | Range |
|---|---|---|---|
| $k_f^{CK}$ | $s^{-1}$ | Forward CK rate constant | 0.2–0.6 |
| $T_1^{PCr}$ | Ms | $T_1$ relaxation time of PCr | 2000–5000 |
| $T_1^{\gamma ATP}$ | Ms | $T_1$ relaxation time of γATP | 800[a] |
| $T_2^{PCr}$ | Ms | $T_2$ relaxation time of PCr | 120[a] |
| $T_2^{\gamma ATP}$ | Ms | $T_2$ relaxation time of γATP | 16[a] |
| $\omega^{PCr}$ | Hz | Chemical shift of PCr | −15 to 15 |
| $\omega^{\gamma ATP}$ | Hz | Chemical shift of γATP | 2.4 ppm from PCr |
| $M_R^{PCr}$ | n.a. | PCr-to-ATP ratio | 2.0–6.0 |
| LW | Hz | Linewidth | 15[a] |

[a]Fixed parameter values obtained from pilot studies (*see* **Note 3**)

3. Generate the dictionary by simulating the fingerprints for each set of parameters.

   Fingerprint simulation uses the two-pool Bloch-McConnell model that can be expressed in matrix form as

$$\frac{d\boldsymbol{M}}{dt} = A\boldsymbol{M} + \boldsymbol{C} \tag{1}$$

   where $\boldsymbol{M}$ is a vector that describes the evolution of the transverse and longitudinal magnetization of PCr and γATP, i.e.,

$$\boldsymbol{M} = \left[M_x^{PCr} \;\; M_y^{PCr} \;\; M_z^{PCr} \;\; M_x^{\gamma ATP} \;\; M_y^{\gamma ATP} \;\; M_z^{\gamma ATP}\right]^T \tag{2}$$

   $\boldsymbol{C}$ is a vector that describes the steady-state magnetization weighted by the longitudinal relaxation time of the corresponding nuclei, i.e.,

$$\boldsymbol{C} = \left[0 \quad 0 \quad \frac{M_0^{PCr}}{T_1^{PCr}} \quad 0 \quad 0 \quad \frac{M_0^{\gamma ATP}}{T_1^{\gamma ATP}}\right]^T \tag{3}$$

   where $M_0^{PCr}$ and $M_0^{\gamma ATP}$ are the steady-state magnetization and $T_1^{PCr}$ and $T_1^{\gamma ATP}$ are the longitudinal relaxation time of PCr and γATP, respectively. $A$ is a matrix that describes the precession, relaxation, and magnetization transfer between PCr and ATP. In a rotating frame of frequency $\omega$, assuming the observed resonance frequencies for PCr and γATP are $\omega^{PCr}$ and $\omega^{\gamma ATP}$, respectively, $A$ can be expressed as:

$$A = \begin{bmatrix} -\frac{1}{T_2^{\mathrm{PCr}}} - k_f^{\mathrm{CK}} & \Delta\omega^{\mathrm{PCr}} + \Delta\omega_0 & & k_r^{\mathrm{CK}} & & \\ -\Delta\omega^{\mathrm{PCr}} - \Delta\omega_0 & -\frac{1}{T_2^{\mathrm{PCr}}} - k_f^{\mathrm{CK}} & \omega_s & & k_r^{\mathrm{CK}} & \\ & -\omega_s & -\frac{1}{T_1^{\mathrm{PCr}}} - k_f^{\mathrm{CK}} & & & k_r^{\mathrm{CK}} \\ k_f^{\mathrm{CK}} & & & -\frac{1}{T_2^{\gamma ATP}} - k_r^{CK} & \Delta\omega^{\gamma\mathrm{ATP}} + \Delta\omega_0 & \\ & k_f^{\mathrm{CK}} & & -\Delta\omega^{\gamma\mathrm{ATP}} - \Delta\omega_0 & -\frac{1}{T_2^{\gamma\mathrm{ATP}}} - k_r^{\mathrm{CK}} & \omega_s \\ & & k_f^{\mathrm{CK}} & & -\omega_s & -\frac{1}{T_1^{\gamma\mathrm{ATP}}} - k_r^{\mathrm{CK}} \end{bmatrix} \tag{4}$$

where $T_2^{\mathrm{PCr}}$ and $T_2^{\gamma\mathrm{ATP}}$ are the transverse relaxation time of PCr and γATP, respectively. $\Delta\omega^{\mathrm{PCr}}$ and $\Delta\omega^{\gamma\mathrm{ATP}}$ are the difference between the resonance frequency of PCr ($\omega^{\mathrm{PCr}}$) and γATP ($\omega^{\gamma\mathrm{ATP}}$) from the frequency of the rotating frame ($\omega$), i.e., $\Delta\omega^{\mathrm{PCr}} = \omega^{\mathrm{PCr}} - \omega$ and $\Delta\omega^{\gamma\mathrm{ATP}} = \omega^{\gamma\mathrm{ATP}} - \omega$. $\Delta\omega_0$ is the off-resonance frequency used to account for $B_0$ field inhomogeneity. $\omega_s$ is the power of the excitation or saturation pulse applied on resonance. $k_f^{\mathrm{CK}}$ and $k_r^{\mathrm{CK}}$ are the forward and reverse exchange rate from PCr to γATP, respectively. Chemical equilibrium is assumed for all simulations such that

$$k_r^{\mathrm{CK}} = k_f^{\mathrm{CK}} \frac{M_0^{\mathrm{PCr}}}{M_0^{\gamma\mathrm{ATP}}} \tag{5}$$

Starting from a fully relaxed spin system, a fingerprint is simulated by iteratively solving for $\boldsymbol{M}$ in discrete time steps ($\Delta t$) using the discrete time solution to Eq. (1):

$$\boldsymbol{M}^{N+1} = e^{A\Delta t}\boldsymbol{M}^{N} + \left(\mathrm{e}^{A\Delta t} - I\right)A^{-1}\boldsymbol{C} \tag{6}$$

where $\boldsymbol{M}^{N}$ and $\boldsymbol{M}^{N+1}$ are the magnetization vectors before and after an iteration.

Excitation pulses are modeled as discretized instantaneous rotations about the $x$- and $y$-axes of the rotating frame:

$$\boldsymbol{M}^{+} = R_x(\alpha_x)R_y\left(\alpha_y\right)\boldsymbol{M}^{-} \tag{7}$$

where $\boldsymbol{M}^{-}$ and $\boldsymbol{M}^{+}$ are the magnetization vectors before and after the excitation pulse, $R_x(\alpha_x)$ and $R_y(\alpha_y)$ are the rotation matrix about the $x$- and $y$-axes with the flip angles $\alpha_x$ and $\alpha_y$, respectively, i.e.,

$$R_x(\alpha_x) = \begin{bmatrix} 1 & & & & & \\ & \cos\alpha_x & -\sin\alpha_x & & & \\ & \sin\alpha_x & \cos\alpha_x & & & \\ & & & 1 & & \\ & & & & \cos\alpha_x & -\sin\alpha_x \\ & & & & \sin\alpha_x & \cos\alpha_x \end{bmatrix} \tag{8}$$

and

$$R_y(\alpha_y) = \begin{bmatrix} \cos\alpha_y & & -\sin\alpha_y & & & \\ & 1 & & & & \\ \sin\alpha_y & & \cos\alpha_y & & & \\ & & & \cos\alpha_y & & -\sin\alpha_y \\ & & & & 1 & \\ & & & \sin\alpha_y & & \cos\alpha_y \end{bmatrix} \quad (9)$$

The effects of $B_0$ inhomogeneity can be simulated with varied off-resonance frequency ($\Delta\omega_0$). The total signal, $S(t)$, can then be calculated as the weighted sum of all simulations:

$$S(t) = \sum\nolimits_{\Delta\omega_0} W(\Delta\omega_0) M_\perp(t, \Delta\omega_0) \quad (10)$$

where $W(\Delta\omega_0)$ is the corresponding weight for a frequency component derived from a Lorentzian lineshape with a linewidth LW:

$$W(\Delta\omega_0) = \frac{\mathrm{LW}^2}{(\Delta\omega_0)^2 + \mathrm{LW}^2} \quad (11)$$

$M_\perp$ is the transverse magnetization defined as

$$M_\perp = \begin{bmatrix} M_\perp^{\mathrm{PCr}} \\ M_\perp^{\gamma\mathrm{ATP}} \end{bmatrix} = \begin{bmatrix} M_x^{\mathrm{PCr}} + iM_y^{\mathrm{PCr}} \\ M_x^{\gamma\mathrm{ATP}} + iM_y^{\gamma\mathrm{ATP}} \end{bmatrix} \quad (12)$$

The range of off-resonance frequency to be simulated should be chosen according to the shimming of the scanner. With a linewidth of 15 Hz, we typically simulate 51 values of off-resonance frequency ranging from −75 to 75 Hz, with a step-size of 3 Hz.

### 3.3 Data Acquisition and Parameter Estimation by $^{31}$P-MRSF

1. Perform initial spectrometer setup including tuning/matching of the coils, calibrating the frequency and power, and magnet shimming.

   We recommend performing localized shimming within the sensitive volume of the $^{31}$P coil for maximized SNR.

2. Acquire $^{31}$P-MRSF data continuously.

   For acquisition with multiple repetitions, no delays are necessary. A single dummy acquisition is acquired at the beginning of each series of acquisitions. If $^{31}$P-MRSF data are acquired before and after metabolic perturbation, acquire post-perturbation data when metabolic steady-state has been reestablished.

3. Fourier transform each of the 320 FIDs of a fingerprint.

4. Apply phase correction to each of the 320 spectra.

5. Extract the complex-valued data points corresponding to PCr or γATP peaks in each of the 320 spectra (*see* **Note 4**).

   This step will give rise to a time course signal that represents the evolution of the PCr and γATP signals.

6. Calculate the inner products between the fingerprint and all entries in the dictionary.
7. Find the dictionary entry that produces the largest magnitude of the inner product as the best match (*see* **Note 5**).
8. Obtain the parameter values associated with the best match as the estimated parameters.

### 3.4 Expected Results

Figure 2 shows representative in vivo spectra acquired using the $^{31}$P-MRSF sequence, and the corresponding fingerprint and its matched dictionary entry. The PCr and ATP signals show 16 lobes each acquired in an alternating manner. The negative amplitude of the first lobe in PCr signal is due to the inversion pulse applied at the beginning of the pulse sequence. The reduced amplitude of the last 8 lobes in PCr signal is due to the saturation of

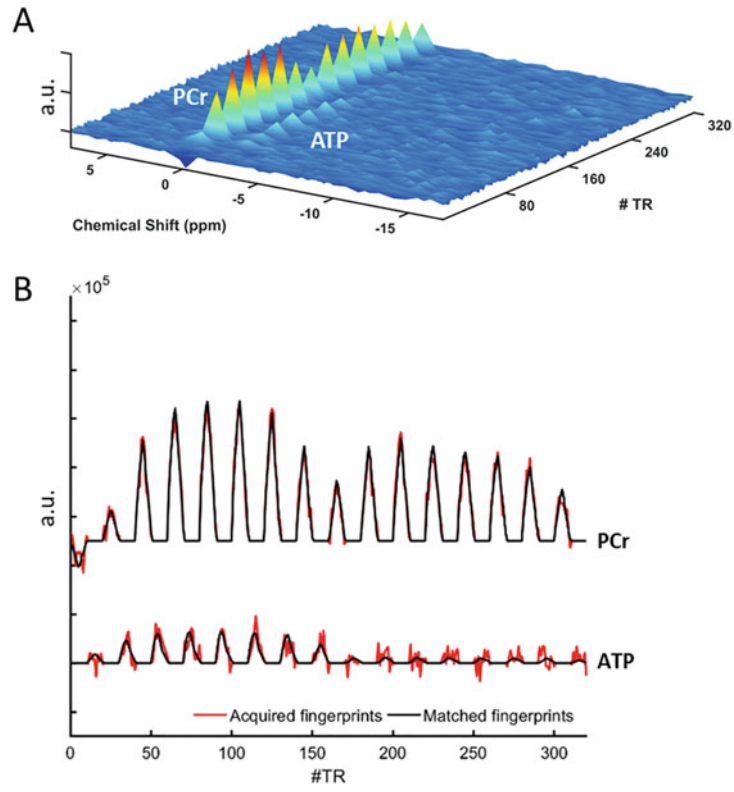


**Fig. 2** $^{31}$P-MRSF spectra and fingerprints. (**a**) Single-repetition $^{31}$P spectra from rat hindlimb. (**b**) The extracted fingerprint (red) with its corresponding dictionary match (black)

**Table 2**
**Parameters for Electrical Stimulation**

| | Voltage (V) | Frequency (Hz) | Pulse duration (ms) |
|---|---|---|---|
| Rat | 5–15 | 1–5 | 2 |
| Mouse | 2–5 | 1–5 | 1 |

[a]These are recommended parameters. They can be adjusted according to the needs of a specific study

γATP. The last 8 lobes of ATP signal is below the detection level because of the saturation pulse applied before data acquisition, although simulated fingerprint shows a slight signal recovery during data acquisition.

For rat experiments, a single-repetition acquisition (20 s acquisition time) will typically give rise to rate constant measurement with <4% variations. For mouse studies, variations in measured rate constant is about 20% for a single-repetition acquisition. Hence, 16 to 20 signal averages are needed to achieve a measurement variation of <5%, corresponding to 5–7 min of acquisition time (*see* **Note 6**).

### *3.5 Electrical Stimulation*

1. To include an electrical stimulation protocol in the study, insert two transcutaneous surface electrodes over the third lumbar vertebrae and over the greater trochanter, respectively. Secure the electrodes with tapes.
2. Secure the foot of the animal to the coil with tapes to reduce motion during electrical stimulation.
3. Set the electrical stimulator to parameters shown in Table 2.
4. During the imaging protocol, turn on the electrical stimulator for 3–5 min to induce muscle contraction, then turn off the stimulator.

### *3.6 Ischemia-Reperfusion*

1. To include an ischemia-reperfusion protocol in the study, place the inflatable cuff around the thigh of the animal.
2. During the imaging protocol, inflate the cuff using the air pump such that the femoral artery will be occluded.
3. Maintain the occlusion for 20–30 min, then turn off the air pump to deflate the cuff.

## 4 Notes

1. We choose to use the continuous wave pulse for γATP saturation due to its simplicity. The spillover effect on PCr is partially corrected by applying contralateral saturation. Our simulations show that the errors introduced by such an approach are power

dependent and are comparable to those observed in conventional $^{31}$P MT-MRS methods. These errors may be correctable by performing $B_1$ mapping of the saturation pulse and incorporating the saturation power into dictionary simulation. Alternatively, the continuous wave pulse may be replaced by other saturation pulses such as BISTRO with reduced spillover effects [37].

2. For the purposes of reducing matching time and memory requirements, only four parameters are matched. The values of $T_1$ of γATP, $T_2$ of both PCr and γATP, and linewidth are fixed in dictionary generation. We have performed simulation studies to evaluate the sensitivity of matched parameters to these fixed parameters. Our results suggest that quantification of CK rate constant is insensitive to the linewidth and the $T_2$ of both PCr and γATP such that varying these parameters by 50% will only lead to <5% deviation from its true value. While insensitivity to $T_1$ of γATP is less ideal, a 25% variation will still give rise to only 5% matching error in CK rate constant. On the other hand, the $T_1$ of γATP is affected by multiple physical and chemical processes such as the cross-relaxation between γATP and βATP, and the chemical exchanges among ATP, PCr, and inorganic phosphate [24]. As such, there may be physiological significance in measuring the $T_1$ of γATP. In this case, expanding parameter matching to include the matching of $T_1$ of γATP may be considered. This will require adding another dimension to the dictionary.
3. A constant linewidth of 15 Hz was used in generating the dictionary used in our studies. This linewidth is based on the shimming we typically achieve on our scanner. While linewidth may vary considerably from experiment to experiment, our simulations suggest that all the matched parameters are insensitive to fluctuations in linewidth such that the same dictionary can be used despite deviations from the true linewidth.
4. Unlike conventional MRS methods that acquire spectra with high spectral resolution (<5 Hz), $^{31}$P-MRSF uses short TR to gain acquisition efficiency. Hence, only 7.7 ms of the FID signal is acquired, which gives rise to a spectral resolution of 130 Hz. As a result, the resonance peaks are largely compressed into a single spectral bin, which has the benefit of significantly simplified spectral quantification. However, for data acquired with poor $B_0$ homogeneity (>50 Hz linewidth for PCr), signal leakage to the neighboring spectral bins may occur. Under these circumstances, spectral quantification may need to include 3–7 spectral bins depending on the severity of $B_0$ inhomogeneity.

5. The volume coils we use in our experiments are of relatively high $B_1$ homogeneity. Many $^{31}$P-MRS studies use surface coils to gain SNR. These coils typically have poor $B_1$ homogeneity. While our simulation results suggest that the measurement of CK rate constant is tolerant to $B_1$ variations, we have not compared measurements using surface coils. Under the circumstances that $B_1$ variation exceeds 50%, the large inhomogeneity needs to be accounted for in fingerprint simulation to achieve accurate parameter matching.
6. Similar to conventional MRS, the precision of parameter estimation for $^{31}$P-MRSF also increases by the square root of the number of signal averages. If signal averaging is necessary, a dummy scan needs to be acquired and discarded in dictionary matching. Accordingly, the pulse sequence also needs to be simulated twice with the first simulation discarded when generating the dictionary.

## References


1. Hoult DI, Busby SJW, Gadian DG, Radda GK, Richards RE, Seeley PJ (1974) Observation of tissue metabolites using 31P nuclear magnetic resonance. Nature 252(5481):285–287
2. Seeley PJ, Busby SJ, Gadian DG, Radda GK, Richards RE (1976) A new approach to metabolite compartmentation in muscle. Biochem Soc Trans 4(1):62–64
3. Ackerman JJ, Grove TH, Wong GG, Gadian DG, Radda GK (1980) Mapping of metabolites in whole animals by $^{31}$P NMR using surface coils. Nature 283(5743):167–170
4. Ingwall JS (1982) Phosphorus nuclear magnetic resonance spectroscopy of cardiac and skeletal muscles. Am J Phys 242(5): H729–H744
5. Bak MI, Wei JY, Ingwall JS (1998) Interaction of hypoxia and aging in the heart: analysis of high energy phosphate content. J Mol Cell Cardiol 30(3):661–672
6. Ingwall JS (2004) Transgenesis and cardiac energetics: new insights into cardiac metabolism. J Mol Cell Cardiol 37(3):613–623
7. Kolwicz SC, Tian R (2010) Assessment of cardiac function and energetics in isolated mouse hearts using $^{31}$P NMR spectroscopy. J Vis Exp 42:2069
8. Lei H, Zhu X, Zhang X, Ugurbil K, Chen W (2003) In vivo 31P magnetic resonance spectroscopy of human brain at 7 T: an initial experience. Magn Reson Med 49(2):199–205
9. Balaban RS, Kantor HL, Ferretti JA (1983) In vivo flux between phosphocreatine and adenosine triphosphate determined by two-dimensional phosphorous NMR. J Biol Chem 258(21):12787–12789
10. Jacobus WE, Lehninger AL (1973) Creatine kinase of rat heart mitochondria. Coupling of creatine phosphorylation to electron transport. J Biol Chem 248(13):4803–4810
11. Wallimann T, Wyss M, Brdiczka D, Nicolay K, Eppenberger HM (1992) Intracellular compartmentation, structure and function of creatine kinase isoenzymes in tissues with high and fluctuating energy demands: the "phosphocreatine circuit" for cellular energy homeostasis. Biochem J 281(1):21–40
12. Schlattner U, Klaus A, Ramirez Rios S, Guzun R, Kay L, Tokarska-Schlattner M (2016) Cellular compartmentation of energy metabolism: creatine kinase microcompartments and recruitment of B-type creatine kinase to specific subcellular sites. Amino Acids 48(8):1751–1774
13. Chen W, Zhu XH, Adriany G, Ugurbil K (1997) Increase of creatine kinase activity in the visual cortex of human brain during visual stimulation: a 31P magnetization transfer study. Magn Reson Med 38(4):551–557
14. Gupta A, Akki A, Wang Y, Leppo MK, Chacko VP, Foster DB et al (2012) Creatine kinase-mediated improvement of function in failing mouse hearts provides causal evidence the failing heart is energy starved. J Clin Invest 122 (1):291–302
15. Akki A, Su J, Yano T, Gupta A, Wang Y, Leppo MK et al (2012) Creatine kinase overexpression improves ATP kinetics and contractile

function in postischemic myocardium. Am J Physiol Heart Circ Physiol 303(7): H844–H852

16. Brown TR, Gadian DG, Garlick PB, Radda GK, Seeley PJ, Styles P (1978) Creatine kinase activities in skeletal and cardiac muscle measured by saturation transfer NMR. In: Dutton PL, Leigh JS, Scarpa A (eds) Frontiers of Biological Energetics. Academic Press, Cambridge, Massachusetts, p 1341
17. Bottomley PA, Hardy CJ (1992) Mapping creatine kinase reaction rates in human brain and heart with 4 tesla saturation transfer 31P NMR. J Magn Reson 99(2):443–448
18. Nicolay K, van Dorsten FA, Reese T, Kruiskamp MJ, Gellerich JF, van Echteld CJ (1998) In situ measurements of creatine kinase flux by NMR. The lessons from bioengineered mice. Mol Cell Biochem 184(1–2):195–208
19. Ren J, Sherry AD, Malloy CR (2015) A simple approach to evaluate the kinetic rate constant for ATP synthesis in resting human skeletal muscle at 7 T. NMR Biomed 2015:1240–1248
20. Clarke WT, Robson MD, Neubauer S, Rodgers CT (2017) Creatine kinase rate constant in the human heart measured with 3D-localization at 7 tesla. Magn Reson Med 78(1):20–32
21. Parasoglou P, Xia D, Chang G, Convit A, Regatte RR (2013) Three-dimensional mapping of the creatine kinase enzyme reaction rate in muscles of the lower leg. NMR Biomed 26(9):1142–1151
22. Leibfritz D, Dreher W (2001) Magnetization transfer MRS. NMR Biomed 14(2):65–76
23. Befroy DE, Rothman DL, Petersen KF, Shulman GI (2012) $^{31}$P-magnetization transfer magnetic resonance spectroscopy measurements of in vivo metabolism. Diabetes 61 (11):2669–2678
24. Ren J, Yang B, Sherry AD, CR M (2015) Exchange kinetics by inversion transfer: integrated analysis of the phosphorus metabolite kinetic exchanges in resting human skeletal muscle at 7 T. Magn Reson Med 73 (4):1359–1369
25. Ma D, Gulani V, Seiberlich N, Liu K, Sunshine JL, Duerk JL et al (2013) Magnetic resonance fingerprinting. Nature 495(7440):187–192
26. Jiang Y, Ma D, Seiberlich N, Gulani V, Griswold MA (2015) MR fingerprinting using fast imaging with steady state precession (FISP) with spiral readout. Magn Reson Med 74 (6):1621–1631
27. Yu AC, Badve C, Ponsky LE, Pahwa S, Dastmalchian S, Rogers M et al (2017) Development of a combined MR fingerprinting and diffusion examination for prostate cancer. Radiology 283(3):729–738
28. Ma D, Jiang Y, Chen Y, McGivney D, Mehta B, Gulani V et al (2018) Fast 3D magnetic resonance fingerprinting for a whole-brain coverage. Magn Reson Med 79(4):2190–2197
29. Chen Y, Jiang Y, Pahwa S, Ma D, Lu L, Twieg MD et al (2016) MR fingerprinting for rapid quantitative abdominal imaging. Radiology 279(1):278–286
30. Hamilton JI, Jiang Y, Chen Y, Ma D, Lo WC, Griswold M et al (2017) MR fingerprinting for rapid quantification of myocardial T1, T2, and proton spin density. Magn Reson Med 77 (4):1446–1458
31. Cloos MA, Assländer J, Abbas B, Fishbaugh J, Babb JS, Gerig G et al (2019) Rapid radial T1 and T2 mapping of the hip articular cartilage with magnetic resonance fingerprinting. J Magn Reson Imaging 50(3):810–815
32. Lemasson B, Pannetier N, Coquery N, Boisserand LSB, Collomb N, Schuff N et al (2016) MR vascular fingerprinting in stroke and brain tumors models. Sci Rep 6:1–11
33. Gao Y, Chen Y, Ma D, Jiang Y, Herrmann KA, Vincent JA et al (2015) Preclinical MR fingerprinting (MRF) at 7 T: effective quantitative imaging for rodent disease models. NMR Biomed 28(3):384–394
34. Gu Y, Wang CY, Anderson CE, Liu Y, Hu H, Johansen ML et al (2018) Fast magnetic resonance fingerprinting for dynamic contrast-enhanced studies in mice. Magn Reson Med 80(6):2681–2690
35. Anderson CE, Wang CY, Gu Y, Darrah R, Griswold MA, Yu X et al (2018) Regularly incremented phase encoding - MR fingerprinting (RIPE-MRF) for enhanced motion artifact suppression in preclinical cartesian MR fingerprinting. Magn Reson Med 79(4):2176–2182
36. Wang CY, Liu Y, Huang S, Griswold MA, Seiberlich N, Yu X (2017) 31P magnetic resonance fingerprinting for rapid quantification of creatine kinase reaction rate in vivo. NMR Biomed 30(12):e3786
37. Luo Y, de Graaf RA, Delabarre L, Tannús A, Garwood M (2001) BISTRO: An outer-volume suppression method that tolerates RF field inhomogeneity. Magn Reson Med 45 (6):1095–1102

# Chapter 32

# Nanoparticle-Assisted Nuclear Relaxation-Based Detection of Oligonucleotides

**Rebecca N. Silva and Peng Zhang**

## Abstract

Nuclear relaxation-based techniques rely on the capability of paramagnetic center to affect the transverse relaxation time ($T_2$) of the water protons. These changes are sensitive to the microenvironment of the paramagnetic center, which can be used to detect a variety of targets. In this work, we present an "on-off" oligonucleotide detection scheme in aqueous solutions, which uses gadolinium phthalocyanine (GdTcPc)-grafted silica nanoparticles as the paramagnetic centers. A probe oligonucleotide strand was conjugated to the GdTcPc to act as a recognition element. In the presence of the target oligonucleotide, which was complementary to the probe, an increase in the $\Delta T_2$ value, which was measured by subtracting the characteristic $T_2$ value of the background solution from that of the sample using a benchtop relaxometer, was observed. The magnitude of this increase was proportional to the target oligonucleotide concentration. A linear range was obtained from 30 to 140 nM, with a detection limit of 15 nM. The developed nuclear relaxation-based detection scheme is shown to be a simple, fast, and selective method to detect oligonucleotide and could be useful in point-of-care diagnostic applications.

**Key words** Nuclear relaxation, Paramagnetic nanoparticle, Oligonucleotide sensing, Phthalocyanine, Gadolinium ion

## 1 Introduction

In a nuclear magnetic relaxation process, the proton spins under an external magnetic field ($B_o$) are flipped to the *xy* plane after an RF pulse is applied, creating a magnetization component ($M_{xy}$). Nuclear relaxation is the process where the spins return to the equilibrium position, causing a decrease in the magnetization on the *xy* plane. This process follows an exponential decay with a time constant $T_2$, the transverse relaxation time, which is the time required for the magnetization falling to ~37% ($1/e$) of its initial value (Fig. 1) [1]. The relaxation process is affected by the local magnetic field fluctuations around the proton. The presence of paramagnetic ions or magnetic nanoparticles can enhance these

Miguel R. Ossandon et al. (eds.), *Biomedical Engineering Technologies: Volume 1*, Methods in Molecular Biology, vol. 2393, https://doi.org/10.1007/978-1-0716-1803-5_32, 

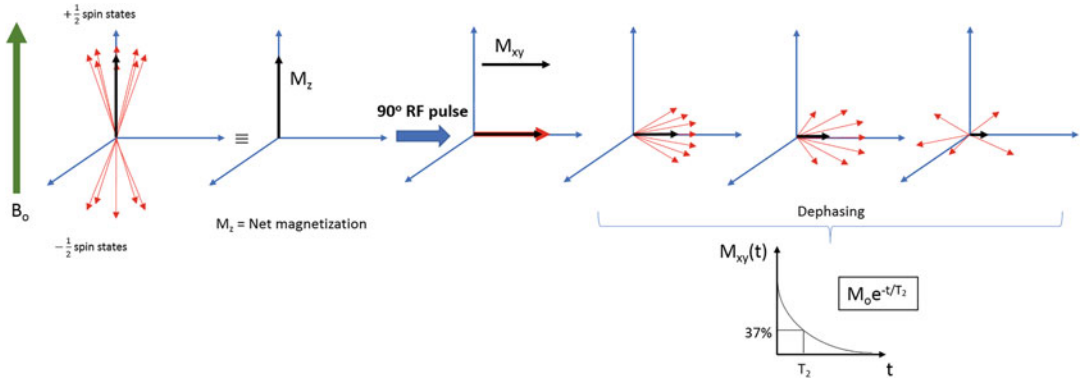


**Fig. 1** Transverse relaxation process

fluctuations and accelerate the relaxation process, reducing the $T_2$ value.

The interaction between the water protons and the magnetic centers is critical to the $T_2$ magnitude, where small changes in the microenvironment of the magnetic center can cause significant changes in the $T_2$ value [2–4]. Based on this principle, a sensitive and selective scheme of dopamine detection was reported using the paramagnetic $Fe^{3+}$ and its dopamine-recognition capability [5]. In the absence of dopamine, the water protons can easily interact with the iron center, resulting in a low $T_2$ value of the water protons (Fig. 2). When dopamine is present, the strong interaction between $Fe^{3+}$ and dopamine reduces the interaction between the water molecules and the iron center, causing an increase in the relaxation time $T_2$ of water protons, the magnitude of which is proportional to the dopamine concentration. Among the paramagnetic ions, gadolinium ($Gd^{3+}$) ion is one of the most explored species in the nuclear relaxation studies, typically used in clinical applications as contrast agents [6, 7]. Its ability to affect the $T_2$ of water protons was exploited in a nanoparticle-based magnetic relaxation sensing scheme to selectively detect phosphate ions in commercial fertilizer samples without purification [8].

Nuclear magnetic relaxation measurement is an established quantitative technique to investigate the relaxation time of nuclei of interest, particularly hydrogen, fluorine, phosphorus, and others. The relaxometer is commercially available typically as a benchtop equipment, where the liquid sample is placed inside an NMR tube for measurement. Inside the sample holder compartment, which is held at a constant temperature, the analyte is submitted to a permanent magnetic field and radio-frequency (RF) pulses. The magnetic field magnitude and RF energy can vary from 0.2 mT to 1.6 T and 0.01 to 70 MHz, respectively [6]. Portable relaxometers have also been developed, which allow analysis of samples in situ [3, 9]. Nuclear magnetic relaxation measurement has found

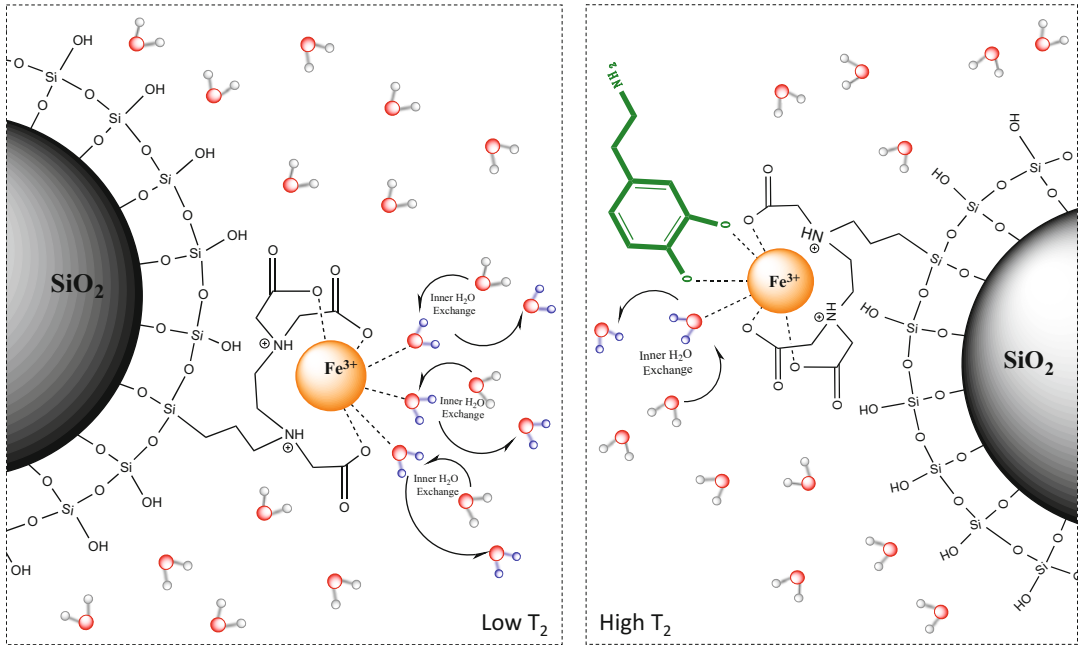


**Fig. 2** Transverse nuclear magnetic sensor to detect dopamine

applications in the food industry, agriculture, and petrochemical industry, such as determining solid fat content in fat composition (ISO 8292 & IUPAC 2.150 methods), oil and moisture in seed and oilseed residues (ISO 10565 & 10632 methods), and hydrogen content in hydrocarbons (ASTM D 7171 method).

In this chapter we describe a method to detect oligonucleotides using a nuclear magnetic relaxation-based technique. The detection principle is shown in Fig. 3. $Gd^{3+}$ is bound to a tetracarboxyphthalocyanine ring, forming a metal complex, Gd-tetracarboxyphthalocyanine (GdTcPc). This complex is then grafted onto silica nanoparticles to act as the magnetic centers. Subsequently, a probe DNA with sequence complementary to the target DNA is conjugated to GdTcPc on the silica nanoparticle surface. Interaction between water molecules and GdTcPc on the silica nanoparticle surface would reduce the $T_2$ value of the water proton. The presence of a target DNA would form a double-stranded DNA with the probe DNA attached to GdTcPc, acting as a blocking unit to hinder the access of water molecules to GdTcPc and causing the increase of the $T_2$ value of water proton, with magnitude proportional to the target DNA concentration. Upon further development, this scheme would be suitable for point-of-care applications, due to its simplicity and short measurement time. Additionally, the method could be adapted to investigate other biological interactions, such as protein–protein and aptamer–small molecule interactions.

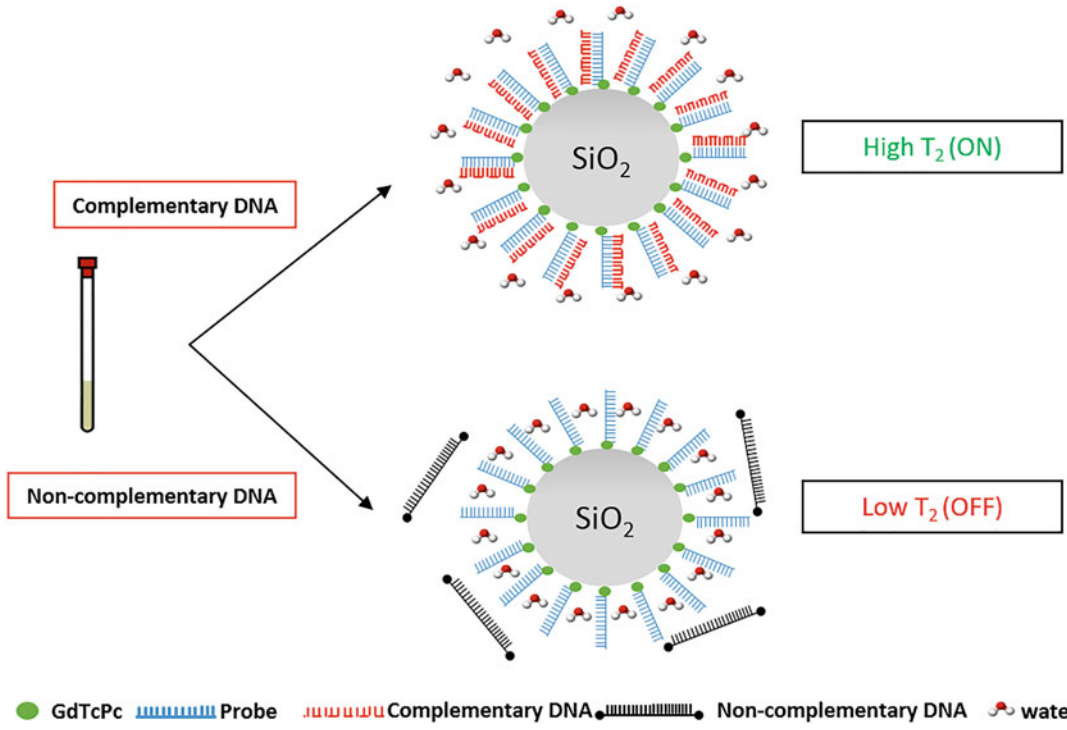


**Fig. 3** Detection scheme of the oligonucleotide based on the nuclear relaxation time of the water protons. When the complementary DNA is present, the conjugation between the DNA hinders the water access to the gadolinium center, which causes an increase in $T_2$. When a noncomplementary DNA is present, the water can easily access the $Gd^{3+}$, decreasing the $T_2$ value

## 2 Materials

### 2.1 Equipment

1. Stir plate (Fisher Scientific, Isotemp, Model 11-600-49S).
2. Eppendorf bench-top centrifuge (Model 5424).
3. Nanotrac analyzer (Microtrac).
4. Transmission electron microscope (FEI CM-20).
5. Ocean Optics USB 4000 UV-Vis spectrometer.
6. Spectrofluorometer (QM-40).
7. Nuclear relaxometer (Bruker Minispec mq60).
8. Millipore Milli-DI System.
9. Quantitative filter paper (Whatman™, grade 41).
10. Microcentrifuge (Thermo Scientific™ Sorvall™ Legend™ Micro 21).
11. NMR tube (Bruker™).
12. Vortex mixer (Fisher Scientific).

### 2.2 Chemicals

1. Tetraethylorthosilicate (TEOS).
2. Triton X-100.
3. *n*-Hexanol.
4. Cyclohexane.
5. Ammonium hydroxide (30 wt%).
6. (3-Aminopropyl) triethoxysilane (APTES).
7. *N*-(3-dimethylaminopropyl)-*N*′-ethylcarbodiimide (EDC).
8. Gadolinium(III) chloride hydrate (1–8 obtained from Sigma-Aldrich, St. Louis, MO).
9. Urea.
10. Ammonium molybdate tetrahydrate.
11. Sodium hydroxide (NaOH).
12. Sodium chloride (NaCl).
13. Hydrochloric acid (HF).
14. SYBR Green I (SG I).
15. *N*-Hydroxysuccinimide (NHS) (9–15 obtained from Thermo Fisher Scientifics, Rockford, IL).
16. Trimellitic anhydride was obtained from TCI America (Montgomeryville, PA).
17. All oligonucleotides were from IDT DNA (Coralville, IA) and the Taq Mg-free reaction buffer 1× (10 mM Tris–HCl, 50 mM KCl pH 8.3@25 °C) (Catalogue No. B9015S) was from New England BioLabs.
18. In the synthesis of GdTcPc, 1 M HCl was prepared in deionized (DI) water and the solution was saturated with NaCl. NaOH (0.1 mM) was prepared in DI water.

## 3 Methods

### 3.1 Synthesis of GdTcPc

1. 502.6 mg of trimellitic anhydride (2.6 mmol), 852.7 mg of $GdCl_3$ hydrate (2.3 mmol), 1.3191 g of urea (22 mmol), 85.3 mg of ammonium molybdate (0.7 mmol) were mixed (*see* **Note 1**) and refluxed in 15 mL of nitrobenzene for 4 h [10].
2. To purify the product, the resulting solid was washed with methanol until all nitrobenzene was removed, followed by the dissolution of the solid in 1 M HCl saturated with NaCl [11]. The mixture was boiled and cooled down to room temperature.
3. The green precipitate was filtered, dissolved in 0.1 M NaOH, heated to 80 °C, and a hot filtration was performed to remove the insoluble impurities.

4. Ethanol was added to the resultant filtrate to double the initial volume. The purified product was recovered by filtration after 24 h.

### 3.2 Synthesis of $SiO_2$@$NH_2$-GdTcPc-DNA1

#### 3.2.1 $SiO_2$ Nanoparticle (NP) Synthesis

1. 1.77 g of Triton X-100, 7.50 mL of cyclohexane, 1.60 mL of *n*-hexanol, and 0.48 mL of water were put in a container and stirred for 5 min, followed by the addition of 60μL of $NH_4OH$. After mixing for 20 min, 100μL of TEOS was added and the mixture was stirred for 48 h.
2. 20 mL of acetone and 10 mL of ethanol were added to the mixture and a pellet was obtained after centrifugation (32,869 × *g*, 20 min). The resulting $SiO_2$ NPs were washed thrice with 20 mL of acetone, ethanol, and DI water, respectively. Due to their high colloidal stability, the $SiO_2$ NPs can be stored for several weeks at 4 °C or used immediately for the subsequent surface modifications.

#### 3.2.2 $SiO_2$@$NH_2$ Synthesis

100μg of $SiO_2$ NPs was dispersed in ethanol followed by the addition of 100μL of APTES. After 2 h, the resulting NPs were collected by centrifugation (20,570 × *g*, 15 min), washed thrice with ethanol and re-dispersed in DI water.

#### 3.2.3 $SiO_2$@$NH_2$-GdTcPc Synthesis

3μg of EDC and 5μg of NHS (molar ratio EDC/NHS = 1/4) were added to 2 mL of cold GdTcPc solution (1 mg $L^{-1}$), and 2 mL of $SiO_2$@$NH_2$ NP dispersion (4 g $L^{-1}$) was added in sequence. After 4 h of reaction at room temperature, the resultant particles were collected by centrifugation (20,570 × *g*, 15 min) and washed thrice with DI water.

#### 3.2.4 $SiO_2$@$NH_2$-GdTcPc-DNA Synthesis

3μg of EDC and 5μg of NHS was dissolved in 2 mL of cold $SiO_2$@$NH_2$-GdTcPc dispersion (4 g $L^{-1}$). 250μL of 100μM DNA1 solution was added to the mixture and stirred overnight. The DNA1 sequence is presented in Table 1. The final $SiO_2$@$NH_2$-GdTcPc-DNA1 NPs were recovered by centrifugation (20,570 × *g*, 15 min) and the pellet washed thrice with DI water.

### 3.3 Nanoparticle Zeta Potential and Size Analysis

1. The zeta potential of the NPs after each surface modification was recorded in a Nanotrac analyzer (Microtrac) with a built-in liquid sample holder. Three measurements were averaged for the particle zeta potential determination, with results shown in Table 2.
2. The size of $SiO_2$@$NH_2$-GdTcPc-DNA1 NPs was measured using a transmission electron microscopy (TEM). On a formvar-covered carbon-coated copper grid (Electron Microscopy Sciences), a drop of $SiO_2$@$NH_2$-GdTcPc-DNA1 solution was deposited and dried at room temperature in the fume hood. The TEM image and size distribution of the NPs are shown in Fig. 4a ($d = 67 \pm 5$ nm).

**Table 1**
**Sequences of DNA strands used in this study**

| Oligonucleotide | Sequence |
|---|---|
| DNA1 (as probe) | 5′-/Amine$C_6$/CA GTA ACG GCA GA-3′ |
| DNA2 (as complementary strand, target) | 5′-TC TGC CGT TAC TG-3′ |
| DNA3 (as noncomplementary strand, random sequence) | 5′-C TCC ACC GTG CAG CTC ATC ATG CAG CTC ATG CCC TTC G-3′ |

**Table 2**
**Zeta potential of nanoparticles dispersed in DI water after each surface modification step**

| Particle | $SiO_2$ | $SiO_2$@$NH_2$ | $SiO_2$@$NH_2$-GdTcPc | $SiO_2$@$NH_2$-GdTcPc-DNA1 |
|---|---|---|---|---|
| Zeta potential/mV | −27 | +25 | +13 | −26 |

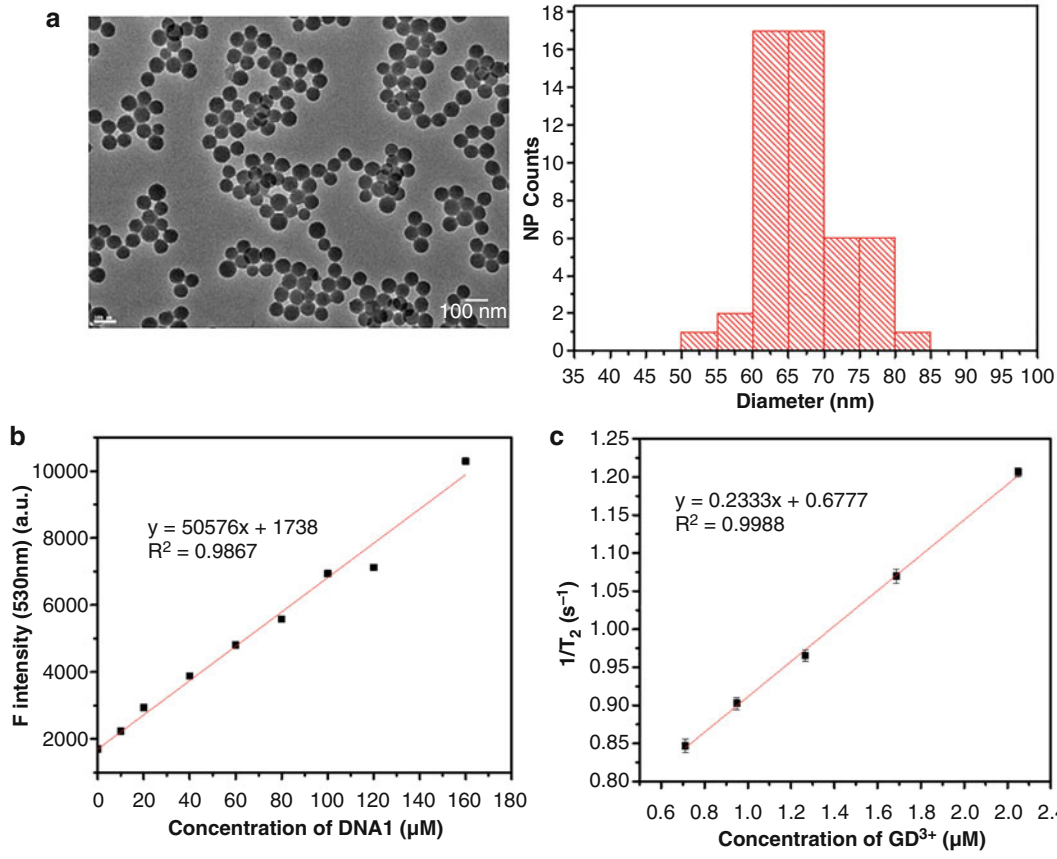


**Fig. 4** (**a**) TEM image (left) and size distribution (right) of $SiO_2$@$NH_2$-GdTcPc-DNA1. (**b**) Standardization curve to determine the amount of DNA1 conjugated to $SiO_2$@$NH_2$-GdTcPc. (**c**) Transverse relaxation rate, $R_2$, determination of $SiO_2$@$NH_2$-GdTcPc

### 3.4 Determination of DNA1 Content in $SiO_2$@$NH_2$-GdTcPc-DNA1

1. Solutions of DNA1 (10, 20, 40, 60, 80, 100, 120, and 160 nM) were mixed with SYBR Green I (SG I) (0.1× as final concentration). To obtain a standardization curve (Fig. 4b), the emission spectra at 510–580 nm with excitation at 480 nm were collected using a spectrofluorometer with 1-mm slit width.
2. The same amount of SG I was added to $SiO_2$@$NH_2$-GdTcPc-DNA1 solution (0.01 g $L^{-1}$) and its emission spectrum was recorded. The amount of the conjugated DNA1 was calculated to be 40μmol $L^{-1}$ based on the obtained standardization curve.

### 3.5 Determination of the $R_2$ Value of $SiO_2$@$NH_2$-GdTcPc

1. The ability of $SiO_2$@$NH_2$-GdTcPc to change the water protons' relaxation time is an important factor affecting the sensitivity of this detection scheme. The transverse relaxation rate ($R_2$) of $SiO_2$@$NH_2$-GdTcPc is used as an indicator to evaluate the nuclear relaxation capability of the NPs. To determine the $R_2$ value of $SiO_2$@$NH_2$-GdTcPc, the $T_2$ values of the solutions containing different concentrations of $SiO_2$@$NH_2$-GdTcPc were measured. The nanoparticle solution was added to an NMR tube and inserted in the nuclear relaxometer sample holder. The measurement was taken after the sample temperature was stabilized at 40 °C. The same instrumental parameters were used for all $T_2$ measurements (*see* **Notes 2** and **3**).
2. The amount of gadolinium present in a $SiO_2$@$NH_2$-GdTcPc stock solution was determined by mass spectrometry (ICP-MS). First, a standardization curve of gadolinium ions was obtained (10, 20, 50, and 100μg $L^{-1}$). Then, the $SiO_2$@$NH_2$-GdTcPc nanoparticles were digested using concentrated hydrofluoric acid and neutralized before the analysis.
3. The $R_2$ value is determined as the slope of the curve obtained when plotting the $1/T_2$ value as a function of the gadolinium concentration in the $SiO_2$@$NH_2$-GdTcPc solution (Fig. 4c). The $R_2$ value was determined to be 233 $mM^{-1}$ $s^{-1}$. Compared to the commercial contrast agent Gd-diethylenetriamine pentaacetic acid (Gd-DTPA) complex, which is commonly used in clinical applications ($R_2$ = 4.6 $mM^{-1}$ $s^{-1}$) [16], the observed $R_2$ value of $SiO_2$@$NH_2$-GdTcPc NPs is much higher, suggesting the feasibility of using it as a relaxation center.

### 3.6 Detection of Target DNA by T2 Measurement and Interference Study

All measurements of the nuclear relaxation time $T_2$ were performed under 1.41 T and 40 °C (*see* **Notes 2** and **3**). Experimental steps in a typical run are described below:

1. A $T_2$ measurement was first taken using 200μL of $SiO_2$@$NH_2$-GdTcPc-DNA1 solution in buffer, as a blank control. This measurement was repeated until the temperature was stabilized and the last recorded value was considered as $T_{2\ \mathrm{blank}}$.

2. Afterwards, 2.5μL of DNA2 (target DNA) was added, mixed for 10 s using a vortex, and placed back in the relaxometer.
3. After temperature stabilization, $T_2$ of the solution was recorded (*see* **Note 4**). A total of 8 aliquots of 2.5μL of DNA2 solution was added every 15 min to cover the concentration range (5, 15, 30, 47, 67, 90, 115, and 140 nM). Same procedure was followed for the interference study with DNA3, which has a random sequence not complementary to that of DNA1.

The change in the $SiO_2$@$NH_2$-GdTcPc solution's $T_2$ upon addition of the target DNA2 was calculated as:

$$\Delta T_2 = T_{2,\text{sample}} - T_{2,\text{blank}}$$

where $T_{2,\text{ sample}}$ is the $T_2$ reading after DNA2 addition and $T_{2,\text{ blank}}$ is the initial $T_2$ value of the $SiO_2$@$NH_2$-GdTcPc-DNA1 solution (*see* **Note 5**). The working principle was tested by adding different concentrations of DNA2 (5–140 nM) into $SiO_2$@$NH_2$-GdTcPc-DNA1 solution (Fig. 5). A significant $\Delta T_2$ increase was observed after each DNA2 addition with a linear relationship observed from 30 to 140 nM ($R^2 = 0.988$). The limit of detection (LoD) for DNA2 is calculated to be 15 nM (LoD = $3\sigma_{\text{blank}}$/slope).

The specificity of this detection is evaluated by measuring the difference between the presence of the complementary target DNA (DNA2) and that of noncomplementary DNA of random sequence

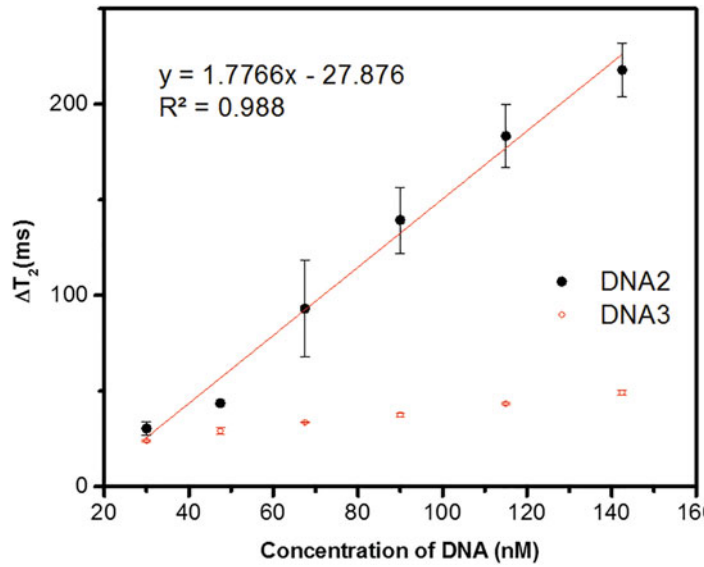


**Fig. 5** Sensitivity and selectivity of NR-based scheme. Different concentrations of DNA2 or DNA3 (30, 48, 68, 90, 115, and 127 nM) were tested. The error bars indicate the standard deviation ($n = 3$)

(DNA3). $T_2$ value of the $SiO_2$@$NH_2$-GdTcPc solution was measured when DNA3 was added in the same concentration range as of DNA2 (Fig. 5). It is observed that the change in $\Delta T_2$ was much more pronounced when DNA2 was added compared to that of DNA3 addition, indicating the specificity of this detection scheme toward the complementary target DNA2. To be considered as an "on/off" detection scheme, the threshold for an "on" reading can be determined as the lowest concentration at which the method is able to differentiate between DNA2 and DNA3. It was observed that 30 nM is the lowest DNA2 concentration tested with the $\Delta T_2$ being statistically different from the $\Delta T_2$ for DNA3 (Student's *t*-test at 95% confidence). Therefore, 30 nM is considered as the threshold of the "on/off" detection.

In conclusion, a simple, fast, and specific "on/off" detection scheme (Fig. 6) for oligonucleotides was developed based on the $T_2$ change of the water protons surrounding the $Gd^{3+}$ center of $SiO_2$@$NH_2$-GdTcPc-DNA1 NPs. A linear relationship was observed between $\Delta T_2$ and the target DNA concentration, with a LoD of 15 nM. The results demonstrated a proof-of-concept for this scheme to detect specific DNA sequences. Its short time measurement (*see* **Note 6**) and simplicity highlight the potential of this method to be used in point-of-care applications.

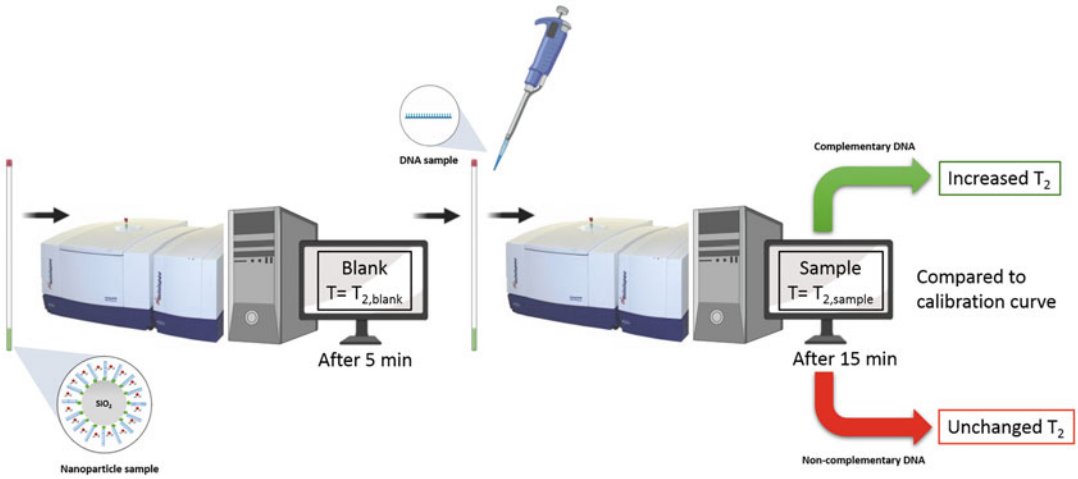


**Fig. 6** Schematic of the overall procedures for the detection of oligonucleotide (DNA) target in the nanoparticle-assisted nuclear relaxation-based approach. After the $T_2$ value of a blank (only nanoparticles) is measured, the DNA sample is added, vortexed, and inserted back into the relaxometer. If the sample contains the target DNA, an increase in $\Delta T_2$ value is observed, of which concentration is quantified by comparing to a calibration curve. If no target DNA is present in the sample, no significant change in $\Delta T_2$ value will be observed

## 4 Notes

1. In the synthesis of GdTcPc, it is important to avoid moisture. In order to do so, weight the solids quickly and add it to the nitrobenzene. Do no try to mix the solids before adding to the nitrobenzene since the gadolinium salt is highly hydroscopic.
2. Carr-Purcell-Meiboom-Gill (CPMG) spin-echo pulse sequence was applied to limit the effect of magnetic inhomogeneity of the instrument.
3. Specific instrumental parameters were listed in Table 3. The temperature stabilization was determined when the software indicated that the temperature inside the sample holder reached 40 °C.
4. Several $T_2$ measurements are taken until a stable reading is reached, which means that the difference between the last measurement and the previous one is within the instrument error.
5. The $\Delta T_2$ value is used instead of the $T_2$ value as it can overcome the small variation in the synthesized $SiO_2$@$NH_2$-GdTcPc-

**Table 3**
**Instrumental parameters for measurements done in this work**

| Parameter | Setting |
|---|---|
| 90° pulse length | 2.22μs |
| 180° pulse length | 4.36μs |
| Det. Angle (broad) | 297° |
| Det. Angle (narrow) | 297° |
| Gain | 56 dB |
| Recycle delay | 2 s |
| Magnetic field steps | −80 |
| NMR frequency | 59.95 mHz |
| Numbers of scans | 8 |
| Recycle delays | 2 s |
| Bandwidth | Narrow 20,000 kHz |
| 90–180° pulse separation (tau) | 6 ms |
| Number of data points for fitting | 250 |
| Number of not fitted echoes | 1 |
| Delay between two repetitive measurements | 10 s |
| Delay until repetitive measurement | 1 |

DNA1 NPs from batch to batch. The concentration effect is removed when the blank is subtracted.

6. Once the standardization curve is obtained, the measurement of each sample would take around 15 min to be completed.

## References


1. Ling Y (2010). Nuclear magnetic resonance readable sensors. Ph.D. Dissertation, Massachusetts Institute of Technology, Cambridge, MA
2. Shen J, Zhang Y, Yang H, Yang Y, Zhou Z, Yang S (2014) Detection of melamine by a magnetic relaxation switch assay with functionalized $Fe/Fe_3O_4$ nanoparticles. Sensors Actuators B Chem 203:477–482
3. Lee H, Sun E, Ham D, Weissleder R (2008) Chip-NMR biosensor for detection and molecular analysis of cells. Nat Med 14:869–874
4. Wang W, Ma P, Dong H, Krause HJ, Zhang Y, Willbold D, Offenhaeusser A, Gu Z (2016) A magnetic nanoparticles relaxation sensor for protein–protein interaction detection at ultralow magnetic field. Biosens Bioelectron 80:661–665
5. Ahmadov TO, Joshi P, Zhang J, Nahan K, Caruso JA, Zhang P (2015) Paramagnetic relaxation based biosensor for selective dopamine detection. Chem Commun 51:11425–11428
6. Rohrer M, Bauer H, Mintorovitch J (2005) Comparison of magnetic properties of MRI contrast media solutions at different magnetic field strengths. Investig Radiol 40:715–724
7. Caravan P, Ellison J, McMurry T, Lauffer R (1999) Gadolinium(III) chelates as MRI contrast agents: structure, dynamics, and applications. Chem Rev 99:2293–2352
8. Ozkaya-Ahmadov T, Wang P, Zhao H, Zhang P (2017) Magnetic relaxation-based sensing of phosphate ion. Talanta 162:256–260
9. Cai S, Liang G, Zhang P, Chen H, Zhang S, Liu B, Kong J (2011) A miniature chip for protein detection based on magnetic relaxation switches. Biosens Bioelectron 26:2258–2263
10. Mikhalenko EA, Solov'eva SA, Luk'yanets LI (2004) Phthalocyanines and related compounds: XXXVII. Synthesis of covalent conjugates of carboxy-substituted phthalocyanines with amino acids. Russ J Gen Chem 74:451–459
11. Weber JH, Busch DH (1965) Complexes derived from strong field ligands. XIX. Magnetic properties of transition metal derivatives of 4,4′,4″,4‴-tetrasulfophthalocyanine. Inorg Chem 4:469–471

# Chapter 33

# Imaging Biomarker Development for Lower Back Pain Using Machine Learning: How Image Analysis Can Help Back Pain

**Bilwaj Gaonkar, Kirstin Cook, Bryan Yoo, Banafsheh Salehi, and Luke Macyszyn**

## Abstract

State-of-the-art diagnosis of radiculopathy relies on "highly subjective" radiologist interpretation of magnetic resonance imaging of the lower back. Currently, the treatment of lumbar radiculopathy and associated lower back pain lacks coherence due to an absence of reliable, objective diagnostic biomarkers. Using emerging machine learning techniques, the subjectivity of interpretation may be replaced by the objectivity of automated analysis. However, training computer vision methods requires a curated database of imaging data containing anatomical delineations vetted by a team of human experts. In this chapter, we outline our efforts to develop such a database of curated imaging data alongside the required delineations. We detail the processes involved in data acquisition and subsequent annotation. Then we explain how the resulting database can be utilized to develop a machine learning-based objective imaging biomarker. Finally, we present an explanation of how we validate our machine learning-based anatomy delineation algorithms. Ultimately, we hope to allow validated machine learning models to be used to generate objective biomarkers from imaging data—for clinical use to diagnose lumbar radiculopathy and guide associated treatment plans.

**Key words** Machine learning, Deep learning, Spine MRI, Image segmentation, Degenerative disease

## 1 Introduction

Low back pain (LBP) is the leading cause of disability, productivity loss and activity limitation throughout the world [1]. LBP levies an enormous economic burden on individuals, communities, and governments. LBP accounts for one of the highest disability-adjusted life years. As the population ages, the prevalence of degenerative disorders will only increase. In the United States, LBP remains one of the costliest diseases with an estimated $100–200 billion spent annually in treatment [2].

The central challenge in changing the status quo of lower back pain diagnosis and treatment is the lack of an understanding of its causative factors [3]. LBP with no known etiology, also called

Miguel R. Ossandon et al. (eds.), *Biomedical Engineering Technologies: Volume 1*, Methods in Molecular Biology, vol. 2393, https://doi.org/10.1007/978-1-0716-1803-5_33, 

nonspecific LBP constitutes 80% of all back pain [4]. Its prevalence is estimated to be between 60% and 70% in industrialized nations. Though several risk factors have been identified (including occupational posture, depressive moods, obesity, body height, and age), the causes of the onset of nonspecific LBP remain obscure and diagnosis difficult to make [4]. Treatment is currently guided by the philosophy that nonspecific LBP is not a disease but a constellation of symptoms. Thus, the vast majority of patients who present with LBP are treated for symptoms as opposed to etiology. Billions of dollars are spent on unnecessary surgeries, opioids, and non-opioid pain killers, and spine adjustment by chiropractors and physical therapists, *without* objective knowledge of why the individual is experiencing back-pain [2]. As a consequence, treatment outcomes remain disappointing for a majority of cases.

To improve treatment outcomes for LBP, we must understand which treatments are effective for each type of LBP. Certain types of LBP are caused by nerve compression, disc degeneration, or skeletal pathology in the lumbar spine [5, 6]. These can be treated surgically [6]. Certain other types are purely muscular, and these should be treated with physiotherapy [7]. Certain other types may resolve without treatment and certain other types should be treated with injections and stimulators [8, 9].

In the developed world, a lumbar MRI is often acquired before triaging the patient as either a surgical or a nonsurgical candidate. MR scanners are becoming more ubiquitous and the cost of acquiring MRI is going down. This practice is increasingly permeating the developing world as well. When LBP patients are referred to surgery, prior MR imaging guides the surgeon in determining the optimal treatment option. While MRI is standard in the treatment of LBP, it is almost always evaluated by an attending radiologist or surgeon. This introduces human subjectivity to treatment planning and is problematic. Consider giving a patient a subjective diagnosis of HIV or Hepatitis! It would be intolerable from a patient's as well as a physician's perspective. There is very little subjectivity in the diagnosis of HIV because we possess highly specific and sensitive diagnostic tests for detecting the disease. Yet, for back pain, which is a larger and costlier problem, we lack comparable tests to guide treatment. Instead, we use subjective criteria to make diagnostic and treatment decisions.

To elucidate this subjectivity further we present a small study. We asked three different radiologists to rate the same set of 50 neuroforamina as mildly, moderately, or severely stenosed. Physician opinions differed on more than 40% of the cases surveyed (*see* Fig. 1). Patients rated as moderately stenosed by one physician were rated as normal by another. This and other studies have repeatedly confirmed radiological subjectivity in diagnosis. For patients, subjectivity in diagnosis and treatment of back pain leads to variable, inconsistent, and failed treatment [10]. In the absence

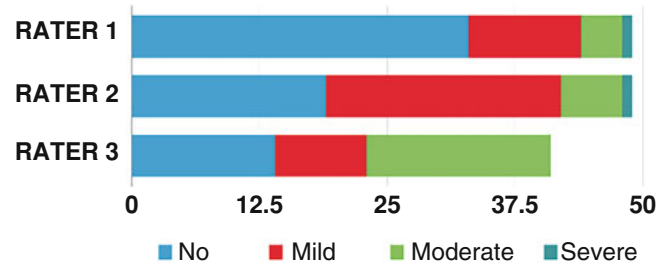


**Fig. 1** Data demonstrating high variability in rating degree of stenosis; from our survey of expert neuroradiologists

of a precise understanding of the etiology of pain, each physician treats the patient to the best of their ability, but based on his or her own incomplete and subjective understanding of the disease. This lack of standardization in diagnosis leads to downstream variation in treatment. Every physician consulted by the patient provides a different treatment recommendation. This confuses patients, who often "try out" several treatment options before eventually settling on one or developing an addiction to pain-killers which provide temporary symptomatic relief [10]. In either case, the patient suffers, and the cost of treatment continues to mount.

Thus, a central problem in diagnosing and treating back pain is knowing objectively which treatment is optimal for a given patient. To develop such an objective standard for classifying back pain patients into treatment categories we must first be able to quantify the underlying pathology. For example, if we can precisely measure the degree of nerve compression, disk degeneration, or the extent of skeletal malalignment, we could understand when surgical treatment of LBP becomes effective. The same would be true for pathologies associated with muscle degeneration. Currently we cannot reliably and reproducibly make measurements of anatomical extents. This chapter describes the tools and techniques required to combine computer vision and MR imaging to make automated precise measurements of anatomical ROIs in the lumbar spine a possibility. This technology has the potential to create an objective standard for diagnosing and treating back pain by exact quantification of lower back anatomy.

A key stumbling block in using computer vision algorithms to bring objectivity to anatomy measurement on spine MRI is data. Data collection and curation is an enormous challenge in health IT in general. The Health Insurance Portability and Accountability Act of 1996 is a United States legislation that pertains to the protection of sensitive patient information. Among other things, HIPAA levies stiff penalties on clinical organizations for noncompliance. This has permeated a culture where information security officers and investigators in the majority of healthcare organizations are paranoid. While it is possible to create software tools to scrub

personal health information (PHI) off imaging data, due to the foresightedness of the DICOM standard, few possess the expertise required to do this. Furthermore, there is also simply no technology available to reliably scrub PHI off physician notes and other "text" entries by hospital staff. This limits the data collection capacity for research and development. Yet, large databases of annotated images for algorithm training and validation are the bedrock of developing automated anatomy measurement algorithms. For example in light photography, the ImageNet [11] and COCO [12] teams focused on the development of well-annotated training datasets for object detection and image segmentation. In neuroimaging, ADNI [13] and ENIGMA [14] took a similar approach and archived neuroimaging data along with associated clinical and genomic data. The LIDC [15] executed the creation of a similar database for diagnostic and lung cancer screening. The TCIA [16] maintains and operates a public repository that archives cancer imaging data. ADNI, ENIGMA, LIDC, and TCIA all yielded novel science and facilitated the development of objective image-based diagnostics for their respective fields. Spineweb [17] is currently the only effort for collecting and annotating spine images. It is not annotated, much smaller, and more heterogeneous than ADNI or ENIGMA. In short, ground truth anatomical delineations necessary for developing and validating algorithms that can provide quantitative measurements of anatomical ROIs other than vertebral bodies and discs are simply unavailable in the public domain. Yet, most hospital systems collect thousands of clinical spine MRIs every month. This represents a vastly underutilized resource which could be leveraged to create objective imaging biomarkers for a host of diseases using deep machine learning techniques. To apply these algorithms, clinical images need to be properly processed, anonymized and the associated clinical informatics data need to be extracted, annotated, and archived alongside these images. There are many nuances to this process which we present in this chapter. We discuss the techniques and tools involved in our efforts to develop a database for training computer vision algorithms to measure lumbar anatomy using MR imaging by leveraging preexisting clinical and informatics databases at the University of California, Los Angeles (UCLA). With the right variations, we believe that the process can be replicated for other anatomical structures, other imaging modalities and at other institutions.

## 2 Materials

### 2.1 Data

We queried our institution's clinical data warehouse to determine what subset of patients obtained a lumbar MRI scan at any point during treatment at UCLA using *Current Procedural Terminology*

[18] (CPT) codes 72148/72158 during the last 3 years. This query returned:

1. 39,000+ patients (17,335 males and 21,959 females).
   (a) Age range: 18–80 years old.
   (b) More than 5000 cases occurring in each decade of life between ages 20 and 80.
2. Additional data on demographics, diagnoses by International Classification of Diseases (ICD-9 [19]) codes, laboratory tests, procedure history, medications, and physician/surgeon visit details were available as part of this dataset.

This Query and Result process was facilitated by the Clinical Translational Sciences Institute (CTSI) at UCLA.

Based on these data (*see* **Note 1**) we obtained images as described in Subheading 3.

### 2.2 Computing Facilities Necessary for Deep Learning

Computing facilities needed for machine learning research include GPUs, high memory workstations and high bandwidth, low latency data storage. Materials used for work outlined here include:

Lambda Quad (Specialized computer for Deep Learning)

1. Processor: IntelTM Core® i7-6850k (6 core).
2. GPUs: 4× NVIDIA GeForce GTX 1080Ti.
3. Memory: 128 GB DDR4 RAM.
4. Storage: 2 TB SSD (OS install) + 4 TB RAID 5 (3× 2 TB HDD).
5. Software: TensorFlow, PyTorch, Caffe, Caffe 2, Keras, CUDA, cuDNN, SimpleITK.
6. Operating system: Ubuntu 16.04.

Laboratory workstations.

1. Memory 4 GB or higher 1600 MHz DDR3.
2. Intel i5 –Dual Core, 1.5 GHz or higher CPU.
3. 128 GB or higher onboard storage.
4. 128-bit Encryption with a 256-bit key.
5. Apple macOS El Capitan OS.
6. Elastic Stack 6.4.
7. Simple ITK 1.0.
8. ITK-SNAP.

DICOM Download Server(s) configuration.

1. Apple macOS X El Capitan/ Windows 10 or higher.
2. NVIDIA P5000 16GB GPU for deep learning computations.

3. Memory configuration 32G or higher.
4. Storage 512GB solid-state drives or higher.
5. CPUs Intel i7 6-core or higher.
6. 128-bit Encryption with a 256-bit key.
7. Simple ITK 1.0.

Large Database storage configurations.

1. WD 16 TB my book duo with 128-bit encryption.
2. 2×WD 2 TB Passport Drives with 128-bit encryption.
3. Drobo 5D3 with. 5×12 TB IronWolf hard-drive.
4. SSL data transfer and automatic encryption of uploaded data.

## 3 Methods

### *3.1 Image and Clinical Metadata Acquisition and Archival in Laboratory from Lumbar MRI*

We automatically downloaded and archived MR images using a custom-built DICOM client based on the pyDicom software package. The workflow is shown in Fig. 2. Images are downloaded from clinical picture archiving and communications systems (PACS). Steps in this process are outlined next.

#### *3.1.1 Image Data Acquisition and Storage*

1. Download and Archive the MRI images: This process is automatically done using a custom-built DICOM client based on the pyDicom software package.
2. Anonymize the data: The data was anonymized automatically by replacing each DICOM field containing protected health information (PHI) by randomly generated numbers and characters.
3. Link the appropriate images studies with clinical data: De-identified clinical data from UCLA's clinical data warehouse was linked with the appropriate imaging studies (*see* **Note 1**) using custom encryption.
4. Store data in a research PACS for manual annotation.
5. Manually annotate relevant anatomy in research PACS.

#### *3.1.2 Clinical Metadata Archival and Storage*

1. Relevant clinical data is obtained by export from Epic using the FHIR protocol from CTSI.
2. Exported data is parsed using custom code into elastic indices.
3. Indices are stored in an Elastic Stack data store on an encrypted firewalled server (*see* **Note 2**).

The human spine is made up of muscles, nerves, discs, ligamentous tissue, and connective tissue. Deficits and aberrations in any of these regions may manifest as pathology linked to LBP. To

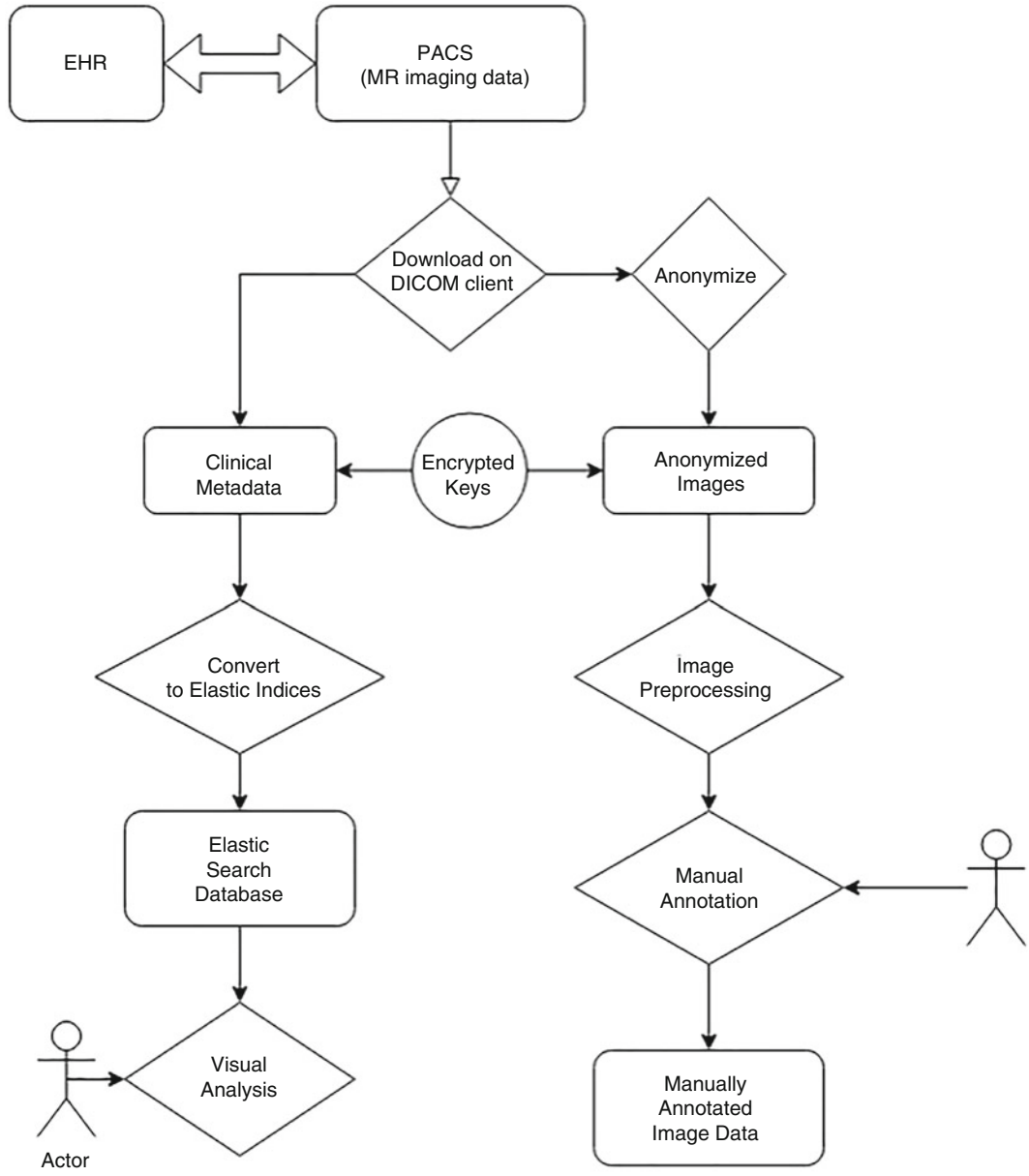


**Fig. 2** Image and clinical data acquisition and archival. DICOM data is downloaded from the PACS. Clinical metadata is separated from the raw imaging data. Clinical metadata extracted from the DICOM header is stored in an Elastic Search database after conversion to Elastic Indices. Encrypted Keycodes are generated linking raw imaging data to the clinical metadata. Raw images are preprocessed (resizing and histogram matching to a template), annotated (anatomy delineation by human experts), and stored in a separate database

quantitatively measure damage we must be able to precisely measure each anatomical region. We plan to train computer vision segmentation algorithms to this end, which first necessitates the

### 3.2 Creating Annotated Database for Machine Learning to Perform Image Segmentation

creation of an annotated database to train these models. Such a database may be created using manual or semi-manual data annotation. Each of these approaches are further elucidated below.

#### 3.2.1 Manual Data Annotation

Machines learn from humans. Machine learning algorithms get better if more human-generated data are available to "train" [20, 21] Thus, more manually annotated scans lead to a superior algorithm. Human effort is cheap in light photography annotation that was used to create databases like ImageNet [22]. However, manually annotating clinical images is expensive. Such annotation is more nuanced and can only be accurately completed by trained experts. We are using a multi-tiered approach to obtain manually labeled data at UCLA. We summarize this approach below:

1. The raw imaging data is downloaded from the PACS in the DICOM [23] format.
2. We anonymize this data and convert it to the Neuroimaging Informatics Technology Initiative (NifTI) [23] format with coded filenames.
3. The relevant DICOM metadata and the code key connecting the NifTI filenames to the original DICOMs are stored in a secure and encrypted relational database.
4. NifTI images are used for manual segmentation. The segmentations are performed using ITK-SNAP [24] (*see* **Note 3**).
5. These segmentations are then verified and, where needed, corrected by physicians. Resident physicians constitute Tier-1 raters, while faculty physicians are the Tier-2 raters (*see* Fig. 3 for workflow).

Our previous experience using manually derived training/segmentation data has proven that the manual segmentation process is extremely time-consuming [25, 26], and the time of Tier-2 raters is significantly constrained. This two-tiered approach improves efficiency, accuracy, and ultimately renders manual segmentation of large datasets feasible. On average, a trained manual rater requires 30–40 min to annotate even a relatively simple anatomical region such as a spinal canal in a single MR series. Thus, the enormity of the effort cannot be under-estimated. Hence, we have also begun a parallel project to utilize a semi-automatic workflow for generating manual segmentation. This is described next.

#### 3.2.2 Semi-Manual Data Annotation

While human-generated annotation is expensive to obtain, it is possible to train suboptimal deep-learning algorithms to perform some of the initial work. Figure 4 explains the pipeline for such training. We use the extreme augmentation [26] methodology for

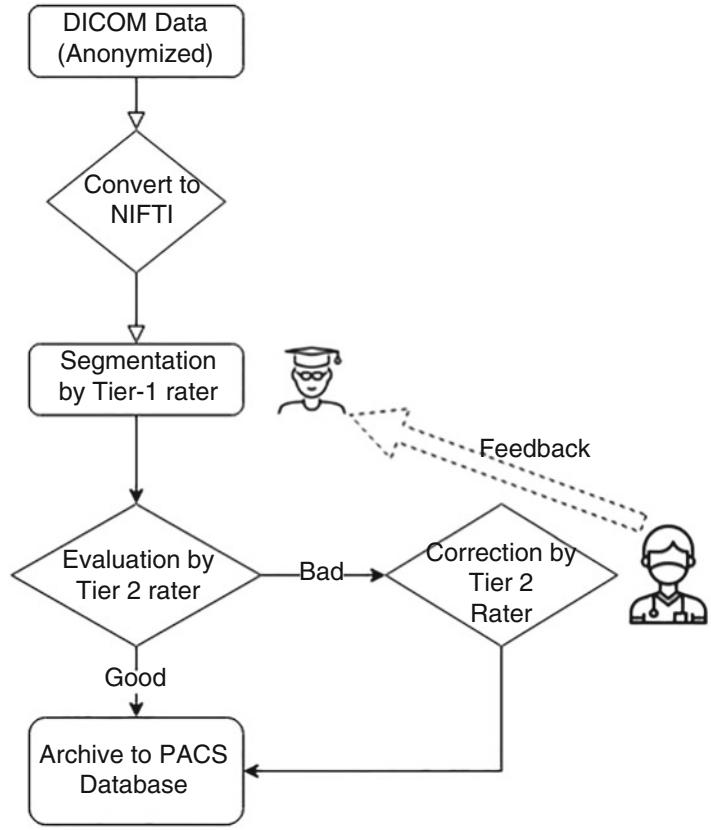


**Fig. 3** Manual segmentation workflow. We use a two-tiered workflow for manual segmentation. Raters of the first tier are physicians or associates who are in early training compared to raters in Tier 2. Tier-1 raters, whose time is less constrained perform a first pass segmentation—which is then checked by Tier-2 raters. Any corrections are performed by Tier-2 raters and corresponding feedback is provided to Tier-1 raters. Ultimately, annotated data is stored in a PACS database

training the suboptimal algorithms (*see* **Note 4**). The steps involved are as follows:

1. Split data to be manually annotated into a small and a large subset.
2. Manually annotate smaller subset.
3. Train a simple algorithm such as Extreme augmentation [26] on the smaller subset.
4. Use model trained on smaller subset to segment images in larger subset.
5. Refer the images segmented by algorithms to human experts who either approve the segmentation or correct the machine-generated segmentation.

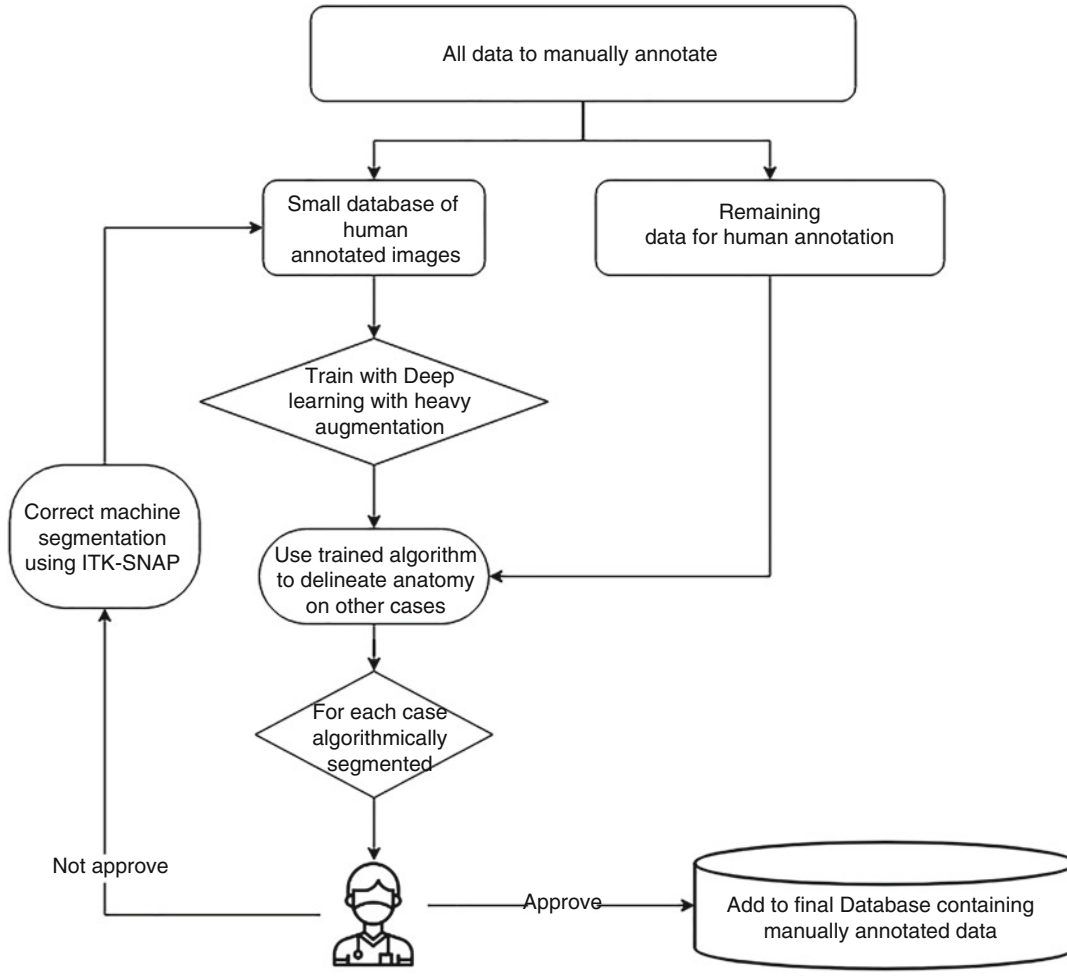


**Fig. 4** Protocol for semi-manual delineation for the generation of a manual database of segmented scans. A small database of scans is first segmented. This small set is used to train an algorithm which is then used to delineate anatomy on other cases. *For each case segmented algorithmically*, a manual expert checks the annotation. If approved, the delineation is added to the database of segmented cases. If not, it is corrected, and the corrected case is added to the training database and the algorithm is retrained

6. When machine-generated segmentation is corrected it is added to the annotated subset and extreme augmentation algorithm is retrained.

This process generates a curated dataset wherein each case has been reviewed and corrected by a human rater. More importantly, this approach allows speedier creation of such a dataset, as compared to purely manual delineation.

### 3.3 Machine Learning Using Annotated Data

#### 3.3.1 Training a U-Net

Convolutional Neural Networks (CNN) have effectively become the dominant class of algorithms for addressing computer vision problems in the last decade. A particular CNN called the U-Net [27] has been successfully applied in the biomedical image segmentation domain. The U-Net contains:

1. a down-sampling path responsible for extracting coarse semantic features; followed by
2. a symmetric up-sampling path trained to recover the input image resolution at the output of the model; and
3. feed-forward connections between the two to recover fine-grained information.

A typical U-Net algorithm has several tunable parameters including the number of layers used in the down-sampling and up-sampling pathways, the number of filters trained at each level, kernel size for convolution network depth, and the degree of dropout. We use a deep U-Net with five down-sampling and up-sampling layers, starting with 32 channels and an input image size of either $256 \times 256$ or $128 \times 128$ pixels. We want the reader to note (*see* **Note 5**) that these parameter choices are not universal and hyper-parameter optimization is nontrivial. Here we outline the concrete steps involved in training a U-Net model to perform automated image segmentation.

Collect MR images as well as associated segmentations at a specific location on hard drive.

1. Quality checks.
   (a) Check if Axial and Sagittal MRIs are both present.
   (b) Check if specific images are not spine at all despite DICOM tagging to that effect.
2. Preprocessing
   (a) Resample each MR image in the series to a fixed symmetric frame size of $256 \times 256$.
   (b) Linearly scale intensities of each MR series to lie between a maximum of one and a minimum of zero.
   (c) Resample manual segmentations to a frame size of $256 \times 256$.
3. Data augmentation step.
   (a) Rotate each resampled MR image by an angle between +20 and $-20^{\circ}$.
   (b) Scale each resampled MR image by 20% up or down.
   (c) Add augmented data to the training set to create "augmented training set" [26].

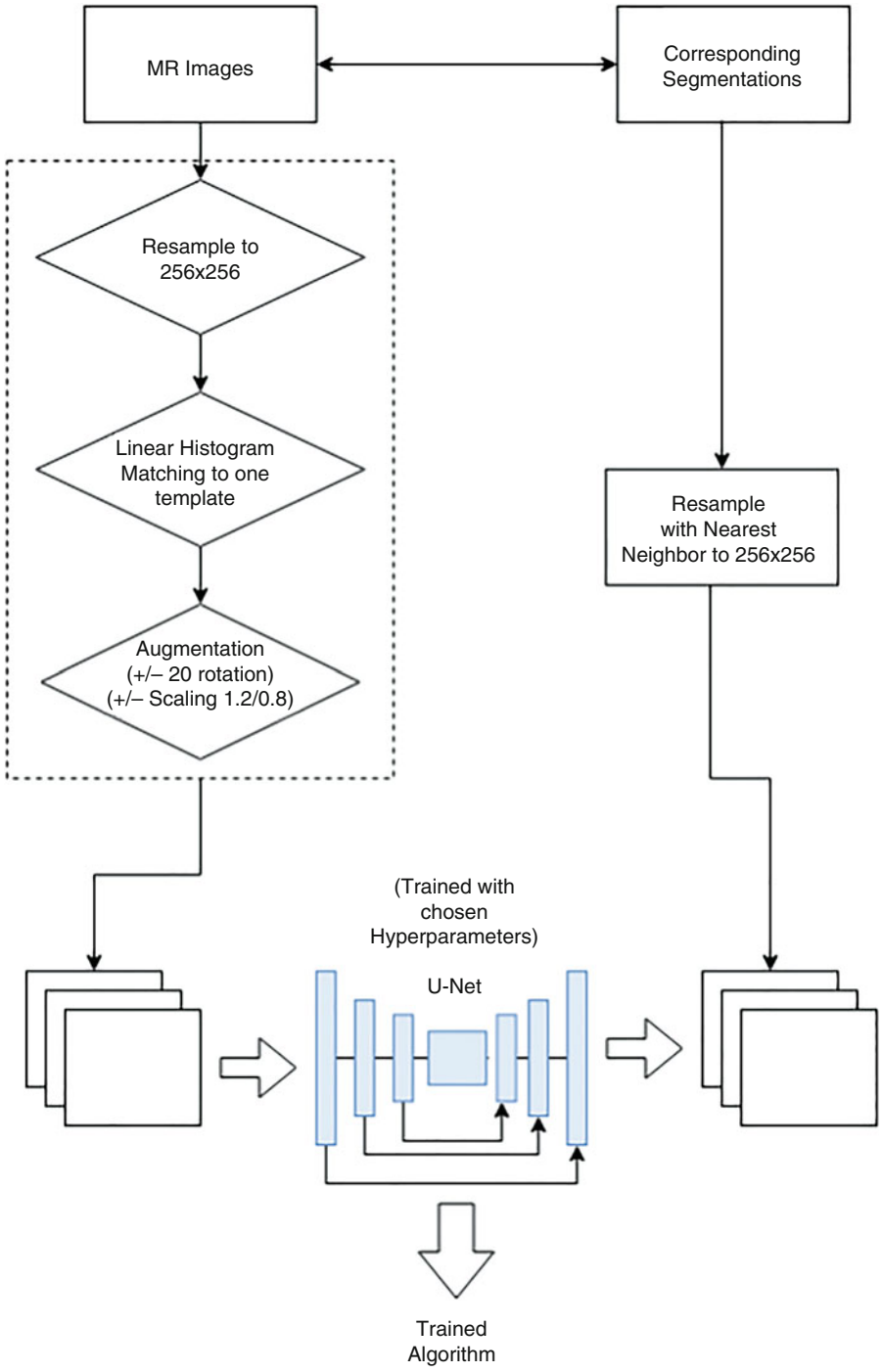


**Fig. 5** Machine learning framework preprocessing and training. MR images in the manually annotated database are resampled slice-wise to 256 $\times$ 256 pixels and preprocessed using linear histogram matching to a template image. Each 2D acquisition is rotated and scaled, along with the associated delineation using nearest neighbor interpolation. This augmented dataset is used to train U-Net models—which are used as the final algorithm

4. Training the U-Net.
   (a) Initialize the U-Net algorithm using Glorot [28] initialization.
   (b) Set hyper-parameters including the number of layers, activation, window size, filters, and kernel size.
      - We use 5 rectified linear unit (ReLU) activation layers, with filter sizes of 32, 64,128, 256, and 512 in the down-sampling arm and 5 layers of up-sampling with filter sizes 512, 256, 128, 64, and 32 followed by a sigmoid layer.
      - We also use a 25% dropout [29] for regularization at all intermediate layers.
      - Filter sizes on all layers are $3 \times 3$.
   (c) Set number of epochs, metric, and optimization method.
      - We use 1000 epochs, the Dice metric, and the Adagrad [30] optimization method.
5. Execute the algorithm on a GPU to obtain the trained model.

Figure 5 shows the aforementioned steps diagrammatically. The training process can consume between 8 and 40 GB of GPU memory and run for anywhere between a few hours to a week for each model trained. Often an ensemble of many deep learning models is required to obtain performance comparable to human radiologists.

#### 3.3.2 Validating the Trained U-Net

The traditional approach to validating medical image segmentation algorithms has been to compare algorithmically generated segmentations against a large database of comparable human-generated segmentations. However, this method hides the fact that there is substantial inter-rater variability amongst human experts about how to segment a scan [31]. The superior approach to validation is to obtain segmentations from two independent human raters at the same level of expertise, and document inter-rater variation prior to comparing with algorithms. Thus, the validation method we use consists of the following key steps.

1. Have two human experts segment the chosen anatomical ROI on a reserved set of validation images.
2. Compute measures of overlap between these experts.
   We use three measures of overlap:
   (a) The Sorenson-Dice [32] coefficient, also known as the Dice coefficient.
   (b) The Hausdorff distance metric [31].
   (c) The Average Surface Distance metric [31].

**Table 1**
**Comparing humans to machines—R1 and R2 are radiologists and DL is the machine**

| | R1 vs. DL | R2 vs. DL | R1 vs. R2 |
|---|---|---|---|
| Dice | 0.85 | 0.84 | 0.93 |
| ASD (mm) | 1.11 | 1.14 | 0.17 |
| HSD (mm) | 17.24 | 15.92 | 12.12 |

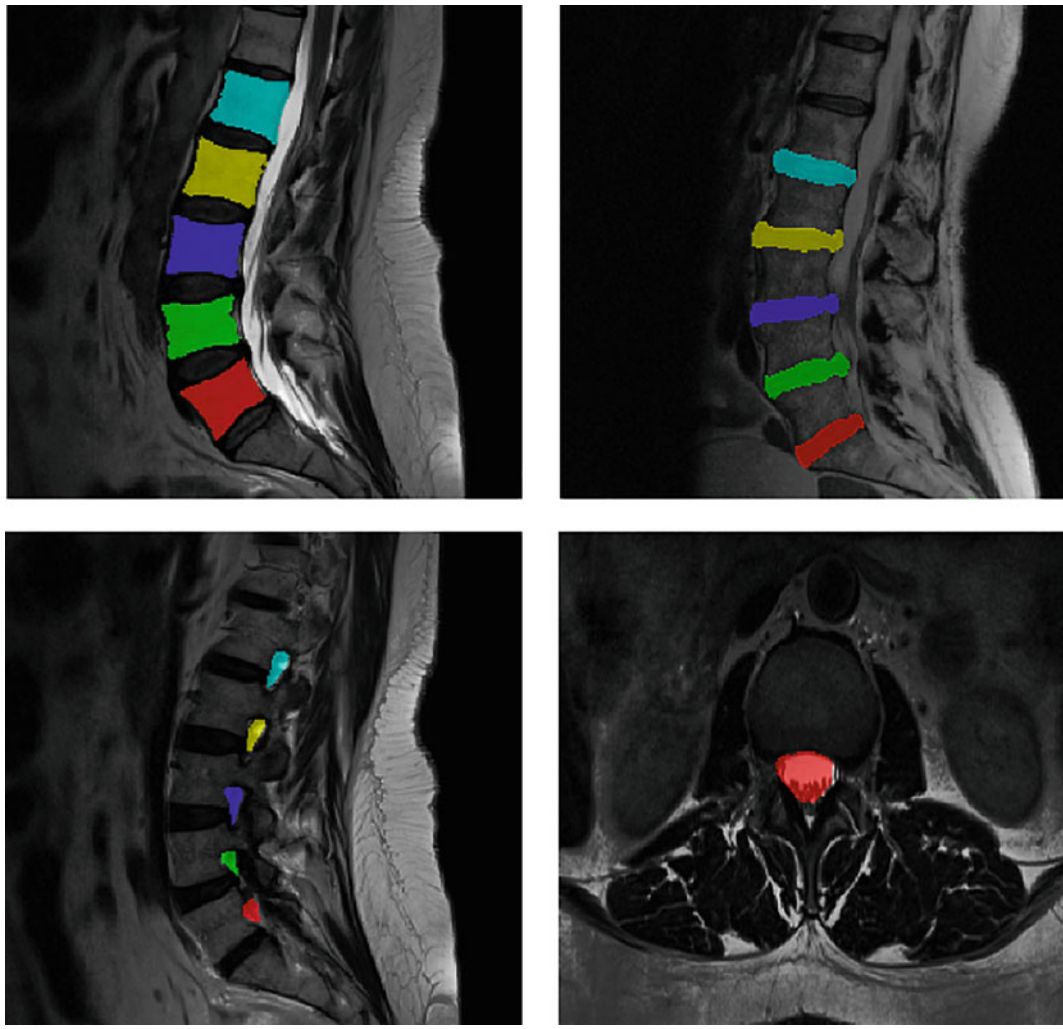

**Fig. 6** Automated delineation of various spinal regions of interest using machine learning. (Top-left) Vertebral bodies (Top-right) Intervertebral Discs (Bottom-left) Neural foramina and (Bottom-right) Spinal canals

3. We compute the measure(s) of overlap between each expert- and automated algorithm-generated segmentation.
4. Present and interpret the comparisons.

Table 1 presents validation of the U-Net algorithm trained to segment canals. Figure 6 shows examples of segmentations of vertebral bodies, intervertebral disks, neural foramina, and central canals. Notice that the algorithm achieves an average Dice coefficient of 0.85 across two expert radiologists. The experts agree with each other with a Dice coefficient of about 0.93. We can interpret this as the algorithm being $0.85/0.93 \times 100 = 91.3\%$ efficient compared to human raters. In future work, we aim to push this figure to approximately 95%.

### 3.4 Packaging Deep Learning Algorithms for Translational Usage

Trained deep learning algorithms constitute weights associated with each layer of the chosen neural network architecture stored alongside the architecture itself. These weights are typically stored as Hierarchical Data Format (HDF) files by Tensorflow. The architecture along with the weights is sufficient for a skilled machine learning practitioner to recreate the model for use in a translational setting in any clinic.

## 4 Notes

1. The linked data included imaging impressions, imaging narratives, ICD codes associated with any diagnoses as well as physician notes—but was provided in a free text format. Processing these raw data to extract pathologies within these images is an unaddressed text processing challenge.
2. The Elastic Stack is a versatile data management, visualization, and analysis system which is useful for sifting through unstructured text data in a computationally efficient manner. The ability to organize images based on both structured meta-data like ICD codes and unstructured meta-data in radiological impressions and physician notes makes Elastic a superior alternative to a traditional file system or database-driven storage.
3. The segmentation was done by residents and physicians in the departments of Neurosurgery and Neuroradiology.
4. The extreme augmentation methodology is a technique we have devised to enable deep learning methods to perform segmentation using small amounts of manually annotated data. The data is augmented by affine transformation several times (20 to 50 times) to produce a faux dataset which is 20 to 50 times larger than the original data. Neural networks trained on the faux data outperform those trained on raw data. Ideally, future algorithms will be able to "learn" to produce "reasonable segmentations" without artificial augmentation—but this is a workaround that can be used until such algorithms become available. We refer the reader to our work [26].

5. Hyper-parameters of a deep neural network include parameters associated with network architecture and structure that are pre-chosen and not explicitly optimized using training data. For a U-Net, the depth of the network, number of channels, and width and number of convolutional filters are all hyper-parameters. Explaining each of these parameters and their effects is beyond the scope of this chapter and the interested reader should refer to a standard textbook of deep learning. What is important to know is that changing these hyper-parameters tends to affect the training and segmentation capability of the model. Due to the black-box nature of deep learning, it is not always possible to predict how hyper-parameters will affect training in practice. Often, the only way to discover appropriate hyper-parameters is through trying out several different values and using a set of values that works reasonably well. Deep learning algorithms can be coaxed to work with appropriate hyper-parameter tuning for most medical image segmentation problems. It has been found that for specific anatomical regions, certain hyper-parameter choices seem to work more effectively. For instance, small regions such as neuroforamina are difficult to segment using U-Net models with a relatively large number of layers. However, relatively larger regions, like vertebral bodies, are segmented well by U-Net models with a relatively large number of layers. Another noteworthy consideration is that U-Nets are generally susceptible to over-segmentation when the number of training iterations (epochs) is small. Nuances of determining hyper-parameters make the use of deep learning algorithms as much an art as it is a science.

## References


1. Vos T, Flaxman AD, Naghavi M et al (2012) Years lived with disability (YLDs) for 1160 sequelae of 289 diseases and injuries 1990–2010: a systematic analysis for the global burden of disease study 2010. Lancet 380 (9859):2163–2196. https://doi.org/10.1016/S0140-6736(12)61729-2
2. Duthey B. Update on 2004 Background Paper, BP 6.24 Low back pain. Prior Med Eur World "A Public Heal Approach to Innov" Geneva: World Health Organization. 2013;24(1):79-89. doi:https://doi.org/10.1080/13561820020022891
3. Friedly JL, Comstock BA, Turner JA et al (2014) A randomized trial of epidural glucocorticoid injections for spinal stenosis. N Engl J Med 371(1):11–21
4. Wand BM, O'Connell NE (2008) Chronic non-specific low back pain—sub-groups or a single mechanism? BMC Musculoskelet Disord 9:11. https://doi.org/10.1186/1471-2474-9-11
5. Gregory DS, Seto CK, Wortley GC, Shugart CM (2008) Acute lumbar disk pain: navigating evaluation and treatment choices. Am Fam Physician 78(7):835–842
6. Chou R, Loeser JD, Owens DK et al (2009) Interventional therapies, surgery, and interdisciplinary rehabilitation for low back pain: an evidence-based clinical practice guideline from the American pain society. Spine (Phila Pa 1976) 34(10):1066–1077. https://doi.org/10.1097/BRS.0b013e3181a1390d
7. Gerwin RD (2010) Low back pain of muscular origin. In: Muscle pain: diagnosis and treatment. https://doi.org/10.1007/978-3-642-05468-6_6

8. Harris A, Moe TF, Eriksen HR et al (2017) Brief intervention, physical exercise and cognitive behavioural group therapy for patients with chronic low back pain (the CINS trial). Eur J Pain:1–11. https://doi.org/10.1002/ejp.1041
9. Jeon YH (2012) Spinal cord stimulation in pain management: a review. Korean J Pain 25 (3):143. https://doi.org/10.3344/kjp.2012.25.3.143
10. Liddle SD, Baxter GD, Gracey JH (2007) Chronic low back pain: patients' experiences, opinions and expectations for clinical management. Disabil Rehabil 29(24):1899–1909. https://doi.org/10.1080/09638280701189895
11. Deng J, Dong W, Socher R, Li L-J, Li K, Fei-Fei L (2009) ImageNet: A large-scale hierarchical image database. In: 2009 IEEE Conference on Computer Vision and Pattern Recognition, pp 248–255. https://doi.org/10.1109/CVPRW.2009.5206848
12. He K. Mask R-CNN 2017. https://arxiv.org/pdf/1703.06870.pdf
13. Jones-Davis DM, Buckholtz N (2015) The impact of the Alzheimer's Disease Neuroimaging Initiative 2: what role do public-private partnerships have in pushing the boundaries of clinical and basic science research on Alzheimer's disease? Alzheimers Dement 11 (7):860–864. https://doi.org/10.1016/j.jalz.2015.05.006
14. Thompson PM, Stein JL, Medland SE et al (2014) The ENIGMA consortium: large-scale collaborative analyses of neuroimaging and genetic data. Brain Imaging Behav 8 (2):153–182. https://doi.org/10.1007/s11682-013-9269-5
15. Armato SG, McLennan G, Bidaut L et al (2011) The lung image database consortium (LIDC) and image database resource initiative (IDRI): a completed reference database of lung nodules on CT scans. Med Phys 38 (2):915–931. https://doi.org/10.1118/1.3528204
16. Clark K, Vendt B, Smith K et al (2013) The cancer imaging archive (TCIA): maintaining and operating a public information repository. J Digit Imaging 26(6):1045–1057. https://doi.org/10.1007/s10278-013-9622-7
17. SpineWeb: Main/HomePage: browse. http://spineweb.digitalimaginggroup.ca/. Accessed August 17, 2017
18. Terminology CP (1970) Current procedural terminology (CPT). JAMA 212:873–874. https://doi.org/10.1001/jama.212.5.873b
19. Centers for Disease Control and Prevention, National Center for Health Statistics. ICD - ICD-9-CM - International Classification of Diseases, Ninth Revision, Clinical Modification. Classif Dis Funct Disabil. 2013;2008:1–2. http://www.cdc.gov/nchs/icd/icd9cm.htm#ftp
20. Halevy A, Norvig P, Pereira F (2009) The unreasonable effectiveness of data. IEEE Intell Syst. https://doi.org/10.1109/MIS.2009.36
21. Gaonkar B, Macyszyn L. EigenRank by Committee: a data subset selection and failure prediction paradigm for robust deep learning based medical image
22. Russakovsky O, Deng J, Su H et al (2015) ImageNet large scale visual recognition challenge. Int J Comput Vis 115(3):211–252. https://doi.org/10.1007/s11263-015-0816-y
23. Larobina M, Murino L (2014) Medical image file formats. J Digit Imaging 27(2):200–206. https://doi.org/10.1007/s10278-013-9657-9
24. Yushkevich PA, Piven J, Hazlett HC et al (2006) User-guided 3D active contour segmentation of anatomical structures: significantly improved efficiency and reliability. NeuroImage 31(3):1116–1128
25. Gaonkar B, Xia Y, Villaroman DS et al (2017) Multi-parameter ensemble learning for automated vertebral body segmentation in heterogeneously acquired clinical MR images. IEEE J Transl Eng Heal Med 5:1800412. https://doi.org/10.1109/JTEHM.2017.2717982
26. Gaonkar B, Edwards M, Bui A, Brown M, Macyszyn L. Extreme Augmentation: Can deep learning based medical image segmentation be trained using a single manually delineated scan ?
27. Ronneberger O, Fischer P (2015) Brox T. U-net: convolutional networks for biomedical image segmentation. In: Medical Image Computing and Computer-Assisted Intervention {\textendash} MICCAI. Springer, Cham, pp 234–241
28. Glorot X, Bengio Y (2010) Understanding the difficulty of training deep feedforward neural networks. J Mach Learn Res
29. Srivastava N, Hinton G, Krizhevsky A, Sutskever I, Salakhutdinov R (2014) Dropout: a simple way to prevent neural networks from overfitting. J Mach Learn Res 15:1929–1958. https://doi.org/10.1214/12-AOS1000
30. Dyer C (2011) Notes on AdaGrad. Cmu
31. Gaonkar B, Villaroman D, Beckett J et al (2019) Quantitative analysis of Spinal Canal areas in the lumbar spine: an imaging

informatics and machine learning study. Am J Neuroradiol 40(9):1586–1591. https://doi.org/10.3174/ajnr.a6174

32. Zou KH, Warfield SK, Bharatha A et al (2004) Statistical validation of image segmentation quality based on a spatial overlap index. Acad Radiol 11(2):178–189. https://doi.org/10.1016/S1076-6332(03)00671-8

# Chapter 34

# Acoustic Angiography: Superharmonic Contrast-Enhanced Ultrasound Imaging for Noninvasive Visualization of Microvasculature

**Isabel G. Newsome and Paul A. Dayton**

## Abstract

Acoustic angiography is a contrast-enhanced ultrasound technique that relies on superharmonic imaging to form high-resolution, three-dimensional maps of the microvasculature. In order to obtain signal separation between tissue and contrast, acoustic angiography has been performed with dual-frequency transducers with nonoverlapping bandwidths. This enables a high contrast-to-tissue ratio, and the choice of a high frequency receiving element provides high resolution. In this chapter, we describe the technology behind acoustic angiography as well as the step-by-step implementation of this contrast enhanced microvascular imaging technique.

**Key words** Ultrasound, Microbubbles, Contrast agent, Angiography, Angiogenesis, Microvasculature

## 1 Introduction

### *1.1 Significance of Microvascular Imaging*

In many diseases, the presence, structure, and development of microvasculature is important for disease progression, and these characteristics can be utilized for disease diagnosis and prognosis. This is true in the case of wound healing [1–3], atherosclerosis [4, 5], kidney function [6, 7], and cancer [8–10], among others. However, current imaging methods for assessing vasculature suffer some important limitations. For preclinical research, microscopy [11, 12] and micro-computed tomography [13] are often used to evaluate microvasculature in cell and small animal models. While these methods offer excellent resolution of microvascular features, they can suffer limited field of view and can be highly invasive and expensive. Conversely, magnetic resonance (MR) or computed tomography (CT) modalities are typically used for clinical angiography [14], limited by the use of ionizing radiation in CT, high cost and time necessary for MR, and relatively poor resolution for both

Miguel R. Ossandon et al. (eds.), *Biomedical Engineering Technologies: Volume 1*, Methods in Molecular Biology, vol. 2393, https://doi.org/10.1007/978-1-0716-1803-5_34, 

(~700 μm with the best current clinical systems) [15, 16]. In addition, none of these imaging techniques are portable or low cost. In this arena, ultrasound imaging is uniquely poised as a safe, noninvasive, portable, and affordable modality for both clinical and preclinical imaging. To image blood flow with ultrasound, Doppler processing techniques [17] and contrast-enhanced imaging schemes [18] have been developed. This chapter focuses on a unique contrast-enhanced approach, known as "acoustic angiography" [19].

### 1.2 Contrast-Enhanced Ultrasound Imaging

For ultrasound imaging of vascular perfusion, microbubble contrast agents are used to enhance the blood pool. These contrast agents are composed of suspensions of microbubbles, which typically consist of a high-molecular-weight gas core stabilized by a lipid or protein shell [20]. Microbubble contrast agents produce acoustic contrast in two ways: (1) the difference in acoustic impedance between the gaseous bubbles and physiological tissue enhances scattered signal and (2) the compressibility of the gas allows the microbubbles to oscillate under acoustic stimulation [20, 21]. This oscillation generates broadband echoes that extend over multiples of the frequency of excitation [21]. Different contrast-enhanced ultrasound schemes are based on receiving these echoes in different frequency bands. Fundamental contrast imaging, the most basic approach often used for standard tissue imaging, receives at the excitation frequency, also called the "fundamental" frequency [22]. The most commonly used contrast-enhanced ultrasound modes are variants of harmonic imaging, in which reception occurs at the second harmonic, or twice the fundamental frequency [22, 23]. These imaging schemes can be applied on clinical ultrasound transducers and scanners, but their optimal performance is fundamentally restricted by the limited bandwidth of commercial transducers and the fact that contrast signal is easily contaminated by the acoustic response of tissue at the fundamental and lower harmonic frequencies [24].

Another approach, known as superharmonic imaging, instead receives the higher order harmonic signals produced by microbubbles [25, 26], such as the third harmonic and higher. In the superharmonic frequency range, the tissue response is essentially negligible at typical acoustic imaging parameters, allowing superharmonic contrast imaging to achieve higher contrast-to-tissue-ratio (CTR) than other contrast-enhanced ultrasound techniques [25, 26]. In addition, because of the wideband response of oscillating microbubbles, the combination of a transmit pulse near contrast agents' resonant frequency can be used in combination with a much higher receive frequency bandwidth, resulting in high resolution, yet requiring only one-way attenuation of the high-frequency signal. Due to the very large nonoverlapping bandwidths required, this technique requires ultra-wideband transducers and

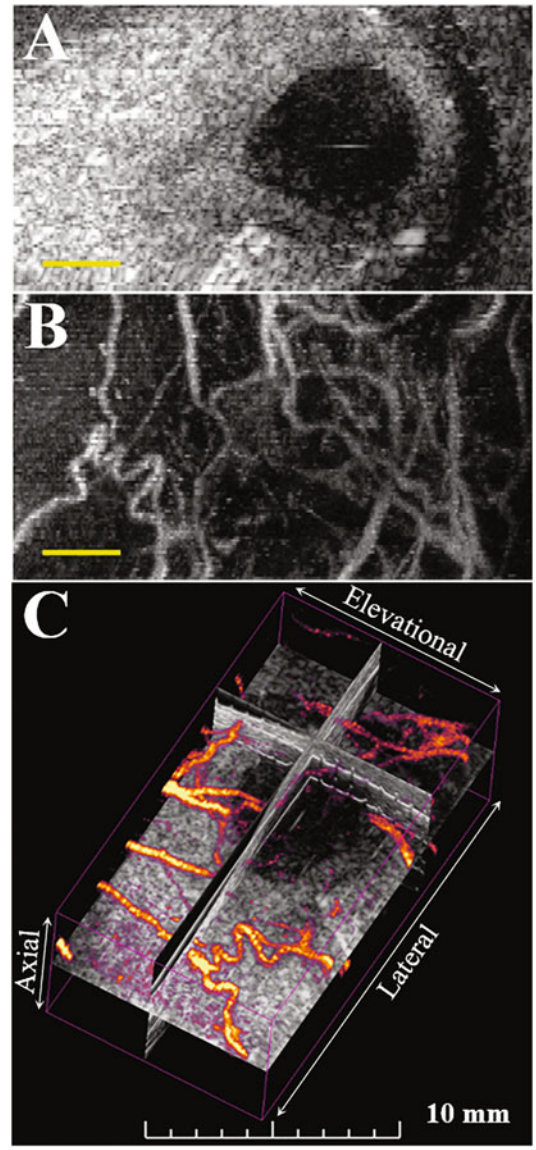


**Fig. 1** Example images of a subcutaneous rat fibrosarcoma tumor. (**a**) High-frequency B-mode ultrasound slice, (**b**) acoustic angiography maximum intensity projection of the same region, and (**c**) volumetric rendering of the acoustic angiography data displayed over orthogonal B-mode slices for tissue reference. Scale bar = 3 mm unless otherwise labeled

systems that can support transmission and reception at widely separated frequencies [25, 26], capabilities that are not currently available in most commercial systems.

### *1.3 Acoustic Angiography*

Acoustic angiography is a three-dimensional (3D) implementation of superharmonic imaging that utilizes dual-frequency (DF) transducers for volumetric imaging of microvasculature

[19]. Figure 1 provides an example of conventional B-mode ultrasound imaging (Fig. 1a) compared to acoustic angiography (Fig. 1b, c) in a rodent fibrosarcoma tumor. In this example, acoustic angiography reveals the tortuous microvasculature that is characteristic of tumor growth and cannot be seen with conventional grayscale ultrasound. In acoustic angiography, a DF dual-element transducer is used to perform superharmonic imaging with low-frequency transmit to excite microbubble contrast agents and high-frequency receive to isolate intravascular microbubble echoes [19, 27]. Using these transducers, acoustic angiography resolves vessels on the order of 100–200 μm in vivo, and this technique can be used to noninvasively differentiate tumors from healthy tissue [28, 29], monitor tumor response to therapy [30–33], and evaluate vascularization in other research models and techniques [34–36]. In this chapter, we focus on the dual-frequency wobbler technology which has enabled preclinical acoustic angiography. However, improvements in transducer technology are currently being explored by our group and collaborators, as well as others, in order to achieve deeper imaging and move towards clinical translation. Hybrid DF transducers that combine single-element prototypes with commercial arrays are being explored for plane wave acoustic angiography [37, 38], which allows faster acquisition speeds and advanced processing techniques, such as ultrasound localization microscopy [39]. Furthermore, integrated DF arrays are in development for clinical acoustic angiography [40].

### 1.4 Future Directions

Given the ability of acoustic angiography to visualize microvascular features with high resolution and CTR, we expect that this technology may find a role in clinical applications to enable improved differentiation of suspicious lesions. Early clinical studies using the aforementioned DF wobblers have demonstrated the ability to resolve microvessels on the order of 200 μm in human breast tissue, although performance was limited by sensitivity at clinical contrast doses and the >25 MHz frequency receive range, which resulted in high resolution but shallow and limited depth of field. Future iterations in acoustic angiography technology for clinical use will likely involve dual frequency arrays, which are now being tested [37, 38, 40] and will allow improved sensitivity at lower mechanical indices, faster acquisition speeds, and advanced processing techniques, such as superharmonic ultrasound localization microscopy [39].

## 2 Materials

1. Dual-frequency wobbler transducer for performing conventional ultrasound and acoustic angiography imaging, (modified RMV707 or RMV710, FUJIFILM VisualSonics, Inc., Toronto, ON, Canada).

2. High-frequency ultrasound scanner for controlling conventional ultrasound and high-frequency receive during acoustic angiography (Vevo 770, FUJIFILM VisualSonics, Inc., Toronto, ON, Canada).
3. Linear motion stage for acquiring 3D image stacks (FUJIFILM VisualSonics, Inc., Toronto, ON, Canada).
4. Arbitrary waveform generator (AWG 2021, Tektronix, Beaverton, OR, USA) and power amplifier (model 240L, Electronics & Innovation, Ltd., Rochester, NY, USA) for driving low frequency transmit during acoustic angiography.
5. Hydrophone and recording system for characterizing DF transducers (Onda Corporation, Sunnyvale, CA, USA).
6. Microbubble contrast agent. Our studies utilized an in-house-made contrast agent previously described [29, 41], although commercial agents are available, such as Definity (Lantheus Medical Imaging, N. Billerica, MA, USA) or MicroMarker (FUJIFILM VisualSonics, Inc., Toronto, ON, Canada).
7. Infusion pump for controlling contrast administration (Pump 11 Elite, Harvard Apparatus, Holliston, MA, USA).
8. Phosphate buffered or sterile saline for diluting microbubble contrast to desired concentration.
9. Ultrasound gel for coupling the transducer to the imaging target (Aquasonic Clear Ultrasound Gel, Parker Laboratories, Inc., Fairfield, NJ, USA).

## 3 Methods

### *3.1 Design of Experimental Equipment and Setup*

#### *3.1.1 Overall System Design*

The acoustic angiography system designed by our group utilized a modified Vevo 770 (FUJIFILM VisualSonics, Inc., Toronto, ON, Canada) micro-ultrasound system coupled with an external low-frequency pulser. VisualSonics RMV imaging probes, modified for dual-frequency use, were used as the transducers.

#### *3.1.2 Probe Design*

Separation of the transmit and receive frequency bandwidths is of utmost importance for acoustic angiography, as vascular microbubble signal cannot be isolated from the surrounding tissue if the bandwidths overlap. This is accomplished by using transducers fabricated with confocally aligned independent elements for transmission and reception [19, 27]. These devices can be created by modifying commercial high-frequency piston transducers, such as RMV707 or RMV710 scanheads (FUJIFILM VisualSonics, Inc., Toronto, ON, Canada), by placing a low-frequency annular element around the preexisting high-frequency element [27].

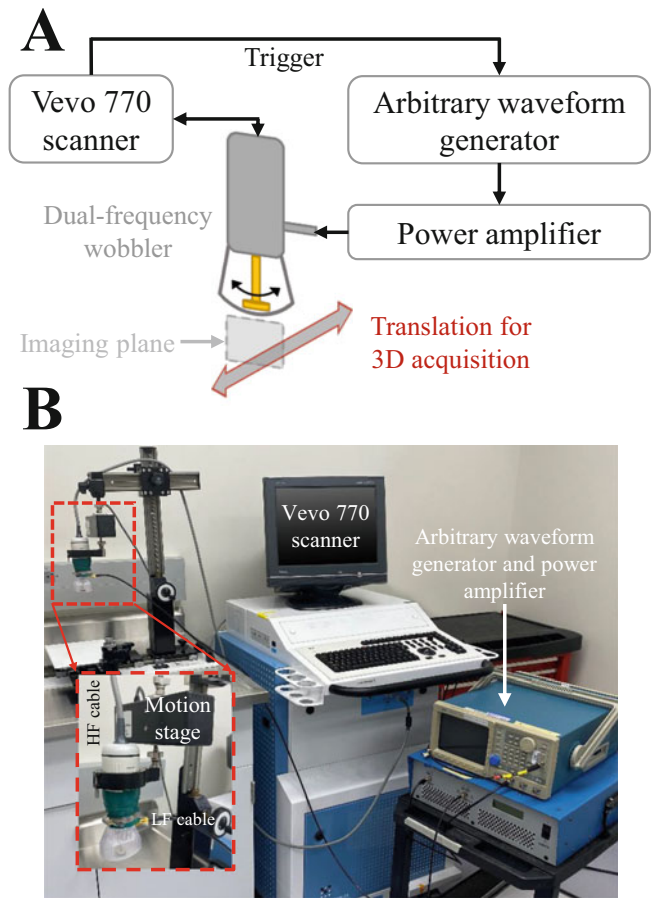


**Fig. 2** Description of the acoustic angiography system. (**a**) Schematic diagram and (**b**) photograph of the acoustic angiography imaging system

*3.1.3 Probe Characteristics*

The low-frequency element should be designed with the same radius of curvature as the high-frequency element (13 mm for 30 MHz elements or 16 mm for 25 MHz elements in the above-mentioned RMV scanheads) for confocal alignment of the acoustic beams. The elements need to be controlled by independent electrical circuitry for isolated transmit and receive paths. For the system described here, a 4 MHz element was used as the transmitter, and a 25 MHz element was used as the receiver.

*3.1.4 Driving System*

A Vevo 770 scanner is used to control high-frequency element data acquisition, timing of transmission for the low-frequency element, and mechanical steering of the beam. This system used for acquiring acoustic angiography images is shown in the schematic diagram and photograph in Fig. 2.

To control low-frequency transmission, an arbitrary waveform generator, such as the AWG 2021 (Tektronix, Beaverton, OR, USA), should be synchronized with the imaging system. In our

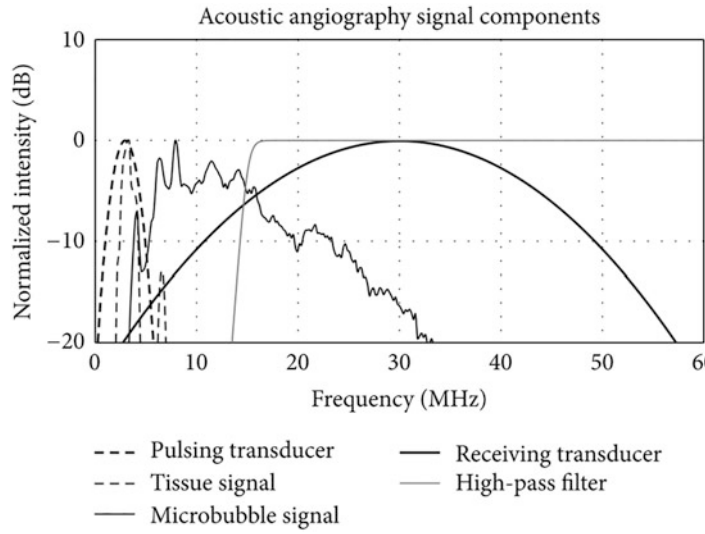


**Fig. 3** Frequency domain representation of the acoustic angiography technique. Example spectra for the low- and high-frequency element bandwidths from a dual-frequency wobbler, high-pass filter, and representative frequency responses from tissue and microbubbles. (Reprinted under Creative Commons Attribution License (CC BY 3.0) from Gessner *et al.*, "Acoustic angiography: a new imaging modality for assessing microvasculature architecture," *Int J Biomed Imag*, vol. 2013, article ID 936593, 9 pages, 2013)

example, we connected the "trigger out" from the Vevo 770 system with a BNC cable to the waveform generator, with the generator output being further amplified with a 55 dB radiofrequency amplifier (model 240L, Electronics & Innovation, Ltd., Rochester, NY, USA) in order to have sufficient voltage to excite the transmitter element.

Because of the large bandwidth of the high-frequency element, a high-pass filter can be added on the receive line of the Vevo 770 before analog-to-digital conversion to remove any low-frequency tissue signal that persists in the received data (Fig. 3). The system described herein included a seventh order Chebyshev type I filter with 15 MHz cutoff frequency (TTE Filters, Arcade, NY, USA).

### *3.1.5 Imaging Parameters*

Peak negative pressures and frame rates for acoustic angiography using the described system are in the range of 700–1300 kPa and 1–5 fps, respectively [28, 29, 42–44], although this method also performs well at lower pressures and higher frame rates with array devices [39]. As described in previous work, the waveform typically used for acoustic angiography is a single-cycle cosine-windowed sine wave [43] to provide high CTR.

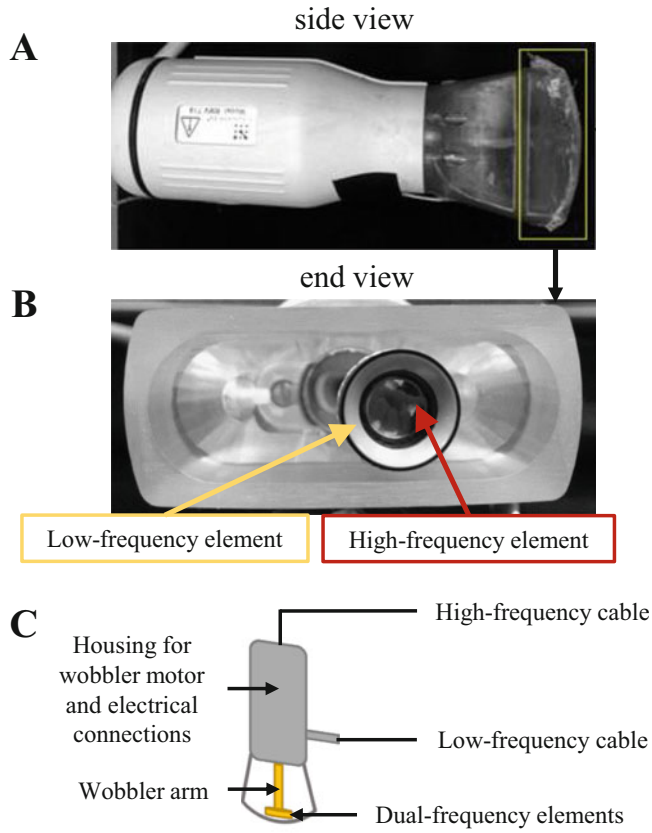


**Fig. 4** Description of dual-frequency transducers for acoustic angiography. (**a**) Side-view photograph of a dual-frequency transducer, (**b**) end-view photograph of the transducer, showing the confocally aligned low- and high-frequency elements, and (**c**) schematic of the dual-frequency transducer

#### *3.1.6 Mechanical Scanning*

In order to produce 2D image planes with a piston transducer, a mechanical arm, known as a "wobbler," scans the transducer elements back and forth, a method that has been widely used for high-frequency ultrasound imaging [45]. One such DF wobbler probe is depicted in the photograph and schematic in Fig. 4. For 3D acquisition, translation of the wobbler perpendicularly to its motion axis is required. We performed this with the VisualSonics linear motion stage, which is provided with the Vevo 770 and synchronized with the imaging system.

### *3.2 Characterization of the System*

#### *3.2.1 Pressure Field Characterization*

To characterize the acoustic pressure field of the DF transducer, a calibrated needle hydrophone, such as the HNA-0200 (Onda Corporation, Sunnyvale, CA, USA), should be used to measure the acoustic beam pattern and bandwidth of each element. Figure 5 shows the pressure map measured via hydrophone for an example high-frequency element of a DF wobbler with the −6 dB beamwidths of the low- and high-frequency elements denoted by the

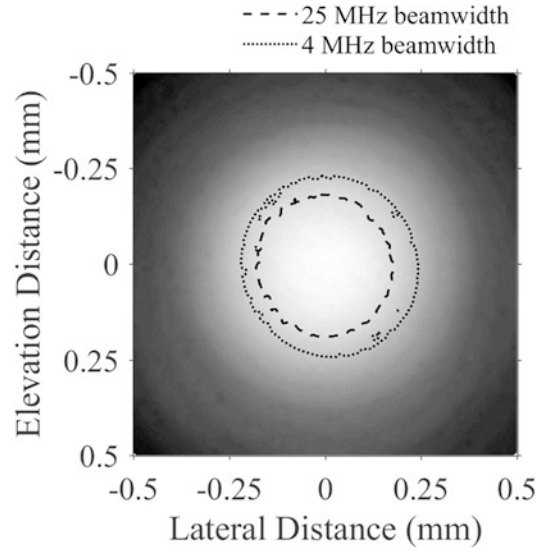


**Fig. 5** Beam patterns of dual-frequency transducer. Pressure map of the high-frequency element from a dual-frequency wobbler transducer overlaid with the −6 dB contours for the 4 and 25 MHz beamwidths

dotted and dashed contours, respectively. It is crucial that the high-frequency beam is completely aligned within the low-frequency beam for confocal imaging. In the example wobbler system described here, the probes have fixed focal depth in the range of 13–16 mm and field of view ranging from 8 to 12 mm based on their lensing, which is sufficient for imaging shallow vascular targets in preclinical research models. Example transducer bandwidths are provided in Fig. 3, along with representative tissue and microbubble responses and an example high-pass filter for preserving only higher harmonic signals. Further details on DF transducers for acoustic angiography can be found in previous works [19, 27, 46].

#### *3.2.2 Resolution Determination*

To characterize the point spread function (PSF) of the complete imaging system, a sub-resolution target must be imaged. One such system typically used for characterization is a microtube phantom, where a sub-resolution microtube is imaged in a water bath or a phantom during infusion of contrast through the tube. The system PSF can be estimated by measuring the full-width at half-maximum of flowing microbubbles in the lateral and axial dimensions. This measurement should be performed and averaged over several samples (e.g. $\geq$30 single bubbles). The PSF measured in this way represents the actual resolution achievable by the imaging system. The system described herein has axial and lateral PSFs in the range of 150–200 μm, dependent on small differences in DF wobbler probe construction.

### 3.3 Acoustic Angiography Imaging Protocol

#### 3.3.1 Target Preparation and Coupling

Before imaging begins, prepare the imaging target. For in vitro experiments (e.g. vascular phantoms), couple the transducer to the phantom with ultrasound gel or degassed water. For in vivo applications (e.g. rodent models), couple the transducer to the skin with ultrasound gel after shaving or depilating the skin over the target. As with any ultrasound imaging technique, coupling of the transducer to the imaging target is imperative to form high-quality images.

#### 3.3.2 Contrast Agent Preparation

Prepare microbubble contrast according to the manufacturer's instructions. Once contrast is activated, dilute microbubbles to a concentration of $10^6$ to $10^8$ bubbles/mL in either phosphate buffered saline or sterile saline for in vitro or in vivo experiments, respectively. Infuse the diluted bubble solution with a syringe pump at a rate of 10–50 μL/min, depending on the imaging target. For in vivo imaging in rodents, intravenous infusion via tail vein catheter is a common method of contrast administration.

#### 3.3.3 Alignment Process

With the low frequency element inactive, use the high-frequency element for transmit and receive. This enables fundamental grayscale ultrasound imaging, which is optimal to align the target region of interest in the imaging plane to the focal depth of the DF transducer. Once the region of interest has been identified, disable the high-frequency transmit on the system, and commence transmit with the low-frequency element, using the high-frequency receiver to acquire superharmonic echoes from the target.

#### 3.3.4 Volume Acquisition

To acquire an image volume, trigger the linear motion stage to translate the DF transducer by a given step size and range that has been set by the user. The user can choose to save any number of frames at each position of the stage for postprocessing.

### 3.4 Acoustic Angiography Image Analysis

#### 3.4.1 Image Display

Once acoustic angiography images have been acquired, they can be displayed and analyzed in many ways. Displaying 3D data in a 2D form can be difficult, but the maximum intensity projection (MIP, Fig. 1b) is a useful method of displaying volumetric images in a 2D projection. However, information on depth in the direction of the projection is lost in this method; a depth-encoded MIP, which can be formed with common software (e.g. temporal color code plugin, Image-J, National Institutes of Health, Bethesda, MD, USA), can provide a 2D representation while preserving 3D information. Figure 6 provides an example depth-encoded acoustic angiography MIP depicting microvasculature surrounding a human lung tissue implant in a mouse flank [35]. Alternatively, interactive or animated volumetric renderings can be created in 3D Slicer, an open-source software for 3D medical image analysis [47].

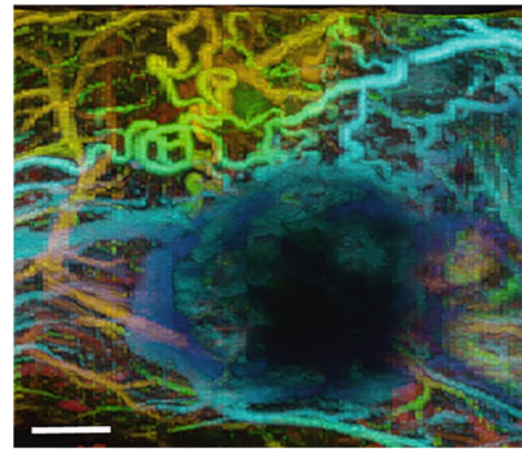

**Fig. 6** Depth-encoded maximum intensity projection of acoustic angiography data from a human lung tissue implant in a mouse flank. Vessel depth ranges from 8 mm (blue) to 20 mm (red) from the transducer surface. Scale bar = 3 mm

*3.4.2 Image Analysis*

Microvascular characteristics, such as tortuosity and vascular density, can be measured from acoustic angiography images to gain insight into disease state and progression. To perform morphological analysis of acoustic angiography images, our group has employed segmentation techniques [48] and tortuosity metrics [49, 50] previously described for MR angiography analysis. For analysis, vessels are extracted from the background tissue, and different calculations (e.g. distance metric, sum of angles metric, inflection count metric) can be performed to quantify the tortuosity of the microvasculature [49]. In addition to tortuosity analysis, vascular density can be quantified inside a region of interest (e.g. tumor) by examining the proportion of voxels that contain vascular signal. Previous work has shown that both tortuosity and vascular density as measured from acoustic angiography are significantly increased in cancerous tumors compared to healthy tissue [28, 29]. Overall, acoustic angiography can provide both qualitative and quantitative assessment of microvasculature.

## 4 Notes

***4.1 Preparation and Selection of Appropriate Microbubble Contrast Agents***

1. Contrast should be prepared according to the manufacturer's instructions and must be handled with care, as microbubbles can be destroyed by pressure changes within the vial or by infusion through a catheter which is too small [51].
2. The stock concentration is often higher than that desired during imaging, so microbubbles should be diluted in saline to a desired concentration. For acoustic angiography, concentrations between $10^6$ and $10^8$ bubbles/mL are commonly used.

To monitor microbubble size and concentration, a particle sizing device can be used, such as the Accusizer (Particle Sizing Systems, Santa Barbara, CA, USA) or Multisizer (Beckman Coulter Life Sciences, Indianapolis, IN, USA).

The broadband response generated by microbubble contrast depends on many factors, including bubble composition, diameter, and excitation frequency and pressure. We have previously studied differences in superharmonic production from different types of microbubble contrast, and data illustrate that microbubble formulation can play a significant role in superharmonic signal generation [41]. Using the DF wobbler transducers described here, our results indicated that phospholipid shell, perfluorocarbon core microbubbles less than approximately 2 μm in diameter generate greater superharmonic signal than larger bubbles with different shell or core compositions [41], which can lead to improved sensitivity in acoustic angiography. Those results were dependent on the pressure and frequency of the transmit waveform in that particular study—it is important to consider all these variables in the context of the imaging application at hand.

### 4.2 Selection of Transmit and Receive Frequencies

To choose excitation and reception frequencies for superharmonic imaging, one must consider several variables. The frequency used on receive is the main determinant of resolution and penetration depth, while the frequency of transmission affects the extent of broadband signal produced by microbubbles. A study of the role of frequency selection for acoustic angiography has been published previously [44]. For imaging of shallow preclinical targets, receiving at 25–30 MHz provides excellent resolution with sufficient penetration depth, while transmitting at 2–4 MHz excites microbubble contrast near its resonance frequency, generating sufficient superharmonic content.

## Acknowledgments

The described work would not have been possible without the efforts of many collaborators who appear as coauthors in works cited here, not only from the University of North Carolina at Chapel Hill but also from the University of Toronto at Sunnybrook, North Carolina State University, Visualsonics, Inc., and Kitware, Inc.

*Financial Acknowledgements*: The authors wish to thank the National Institutes of Health for financial support of this research program through R01 CA170665, R01 CA170665S1, R01 EB026897, R01 CA189479, R44 CA165621, and R01 EB015508. I.G.N. has been partially supported in her training through National Institutes of Health Grants T32 HL069768 and F31 CA243177. Additional funding has been supplied by the

Department of Defense through project W81XWH-12-1-0303, as well as from UNC Lineberger Comprehensive Cancer Center pilot grants.

*Conflict of Interest*: P.A.D. declares that he is an inventor on a patent describing dual-frequency imaging and is a cofounder of SonoVol, Inc., which has licensed this patent and manufactures commercial devices that use acoustic angiography.

## References


1. Rege A, Thakor NV, Rhie K, Pathak AP (2012) In vivo laser speckle imaging reveals microvascular remodeling and hemodynamic changes during wound healing angiogenesis. Angiogenesis 15:87–98. https://doi.org/10.1007/s10456-011-9245-x
2. Tonnesen MG, Feng X, Clark RAF (2000) Angiogenesis in wound healing. J Investig Dermatol Symp Proc 5:40–46. https://doi.org/10.1046/j.1087-0024.2000.00014.x
3. Chong DC, Yu Z, Brighton HE et al (2017) Tortuous microvessels contribute to wound healing via sprouting angiogenesis. Arterioscler Thromb Vasc Biol 37:1903–1912. https://doi.org/10.1161/ATVBAHA.117.309993
4. Feinstein SB (2006) Contrast ultrasound imaging of the carotid artery vasa Vasorum and atherosclerotic plaque neovascularization. J Am Coll Cardiol 48:236–243. https://doi.org/10.1016/j.jacc.2006.02.068
5. Mantella LE, Colledanchise KN, Hétu M-F et al (2019) Carotid intraplaque neovascularization predicts coronary artery disease and cardiovascular events. Eur Heart J Cardiovasc Imaging 1:1–9. https://doi.org/10.1093/ehjci/jez070
6. Mayer G (2011) Capillary rarefaction, hypoxia, VEGF and angiogenesis in chronic renal disease. Nephrol Dial Transplant 26:1132–1137. https://doi.org/10.1093/ndt/gfq832
7. Maeshima Y, Makino H (2010) Angiogenesis and chronic kidney disease. Fibrogenesis Tissue Repair 3:25–30. https://doi.org/10.1186/1755-1536-3-13
8. Jain RK (2001) Normalizing tumor vasculature with anti-angiogenic therapy: a new paradigm for combination therapy. Nat Med 7:987–989. https://doi.org/10.1038/nm0901-987
9. Folkman J (1971) Tumor angiogenesis: therapeutic implications. N Engl J Med 285:1182–1186
10. Hanahan D, Weinberg RA (2011) Hallmarks of cancer: the next generation. Cell 144:646–674. https://doi.org/10.1016/j.cell.2011.02.013
11. Lagerweij T, Dusoswa SA, Negrean A et al (2017) Optical clearing and fluorescence deep-tissue imaging for 3D quantitative analysis of the brain tumor microenvironment. Angiogenesis 20:533–546. https://doi.org/10.1007/s10456-017-9565-6
12. Fukumura D, Duda DG, Munn LL, Jain RK (2010) Tumor microvasculature and microenvironment: novel insights through intravital imaging in pre-clinical models. Microcirculation 17:206–225. https://doi.org/10.1111/j.1549-8719.2010.00029.x
13. Ehling J, Theek B, Gremse F et al (2014) Micro-CT imaging of tumor angiogenesis quantitative measures describing micromorphology and vascularization. Am J Pathol 184:431–441. https://doi.org/10.1016/j.ajpath.2013.10.014
14. Wu G, Yang J, Zhang T et al (2016) The diagnostic value of non-contrast enhanced quiescent interval single shot (QISS) magnetic resonance angiography at 3T for lower extremity peripheral arterial disease, in comparison to CT angiography. J Cardiovasc Magn Reson 18:71. https://doi.org/10.1186/s12968-016-0294-6
15. Pinker K, Bogner W, Baltzer P et al (2014) Clinical application of bilateral high temporal and spatial resolution dynamic contrast-enhanced magnetic resonance imaging of the breast at 7 T. Eur Radiol 24:913–920. https://doi.org/10.1007/s00330-013-3075-8
16. Reiner CS, Roessle M, Thiesler T et al (2013) Computed tomography perfusion imaging of renal cell carcinoma. Investig Radiol 48:1. https://doi.org/10.1097/rli.0b013e31827c63a3
17. Bercoff J, Montaldo G, Loupas T et al (2011) Ultrafast compound doppler imaging: providing full blood flow characterization. IEEE Trans Ultrason Ferroelectr Freq Control 58:134–147. https://doi.org/10.1109/TUFFC.2011.1780

18. Klibanov AL, Hossack JA (2015) Ultrasound in radiology: from anatomic, functional, molecular imaging to drug delivery and image-guided therapy. Investig Radiol 50:657–670. https://doi.org/10.1097/RLI.0000000000000188
19. Gessner RC, Frederick CB, Foster FS, Dayton PA (2013) Acoustic angiography: a new imaging modality for assessing microvasculature architecture. Int J Biomed Imaging 2013:936593. https://doi.org/10.1155/2013/936593
20. Ferrara K, Pollard R, Borden M (2007) Ultrasound microbubble contrast agents: fundamentals and application to gene and drug delivery. Annu Rev Biomed Eng 9:415–447. https://doi.org/10.1146/annurev.bioeng.8.061505.095852
21. De Jong N, Bouakaz A, Frinking P (2002) Basic acoustic properties of microbubbles. Echocardiography 19:229–240. https://doi.org/10.1046/j.1540-8175.2002.00229.x
22. Kim AHY, Choi BIHN, Kim KWON et al (2001) Comparison of contrast-enhanced fundamental imaging, second-harmonic imaging, and pulse-inversion harmonic imaging. Invest Radiol 36:582–588
23. Eckersley RJ, Chin CT, Burns PN (2005) Optimising phase and amplitude modulation schemes for imaging microbubble contrast agents at low acoustic power. Ultrasound Med Biol 31:213–219. https://doi.org/10.1016/j.ultrasmedbio.2004.10.004
24. Tranquart F, Grenier N, Eder V, Pourcelot L (1999) Clinical use of ultrasound tissue harmonic imaging. Ultrasound Med Biol 25:889–894. https://doi.org/10.1016/S0301-5629(99)00060-5
25. Bouakaz A, Frigstad S, Ten Cate FJ, DE Jong N (2002) Super harmonic imaging: a new imaging technique for improved contrast detection. Ultrasound Med Biol 28:59–68
26. Kruse DE, Ferrara KW (2005) A new imaging strategy using wideband transient response of ultrasound contrast agents. IEEE Trans Ultrason Ferroelectr Freq Control 52:1320–1329. https://doi.org/10.1109/TUFFC.2005.1509790
27. Gessner R, Lukacs M, Lee M et al (2010) High-resolution, high-contrast ultrasound imaging using a prototype dual-frequency transducer : in vitro and in vivo studies. IEEE Trans Ultrason Ferroelectr Freq Control 57:1772–1781
28. Gessner RC, Aylward SR, Dayton PA (2012) Mapping microvasculature with acoustic angiography yields quantifiable differences between healthy and tumor-bearing tissue volumes in a rodent model. Radiology 264:733–740. https://doi.org/10.1148/radiol.12112000
29. Shelton SE, Lee YZ, Lee M et al (2015) Quantification of microvascular tortuosity during tumor evolution using acoustic angiography. Ultrasound Med Biol 41:1896–1904. https://doi.org/10.1016/j.ultrasmedbio.2015.02.012
30. Rojas JD, Papadopoulou V, Czernuszewicz T et al (2018) Ultrasound measurement of vascular density to evaluate response to antiangiogenic therapy in renal cell carcinoma. IEEE Trans Biomed Eng 66(3):873–880. https://doi.org/10.1109/TBME.2018.2860932
31. Marvin CM, Ding S, White RE et al (2019) On command drug delivery via cell-conveyed phototherapeutics. Small 15:1901442. https://doi.org/10.1002/smll.201901442
32. Kasoji SK, Rivera JN, Gessner RC et al (2018) Early assessment of tumor response to radiation therapy using high-resolution quantitative microvascular ultrasound imaging: erratum. Theranostics 8:4601–4603. https://doi.org/10.7150/thno.19703
33. Kasoji SK, Rivera JN, Gessner RC et al (2018) Early assessment of tumor response to radiation therapy using high-resolution quantitative microvascular ultrasound imaging. Theranostics 8:156–168. https://doi.org/10.7150/thno.19703
34. Mohanty K, Papadopoulou V, Newsome IG et al (2019) Ultrasound multiple scattering with microbubbles can differentiate between tumor and healthy tissue in vivo. Phys Med Biol 64:115022. https://doi.org/10.1088/1361-6560/ab1a44
35. Wahl A, De C, Abad Fernandez M et al (2019) Precision mouse models with expanded tropism for human pathogens. Nat Biotechnol 37:1163–1173. https://doi.org/10.1038/s41587-019-0225-9
36. Panfilova A, Shelton SE, Caresio C et al (2019) On the relationship between dynamic contrast-enhanced ultrasound parameters and the underlying vascular architecture extracted from acoustic angiography. Ultrasound Med Biol 45:539–548. https://doi.org/10.1016/j.ultrasmedbio.2018.08.018
37. Newsome IG, Lindsey BD, Shelton SE et al (2017) Characterization of a prototype transmit 2 MHz receive 21 MHz array for superharmonic imaging. In: Proc IEEE Int Ultrason Symp. IEEE, Washington, DC, pp 20–22. https://doi.org/10.1109/ULTSYM.2017.8092674

38. Cherin E, Yin J, Forbrich A et al (2019) In vitro Superharmonic contrast imaging using a hybrid dual-frequency probe. Ultrasound Med Biol 45:2525–2539. https://doi.org/10.1016/j.ultrasmedbio.2019.05.012
39. Kierski TM, Espíndola D, Newsome IG et al (2020) Super harmonic ultrasound for motion-independent localization microscopy: applications to microvascular imaging from low to high flow rates. IEEE Trans Ultrason Ferroelec, Freq Contr. 67(5):957–967. https://doi.org/10.1109/TUFFC.2020.2965767
40. Newsome IG, Kierski TM, Carnevale C et al (2019) Enhanced depth of field acoustic angiography with a prototype 288-element dual-frequency Array. In: Proc - IEEE Int Ultrason Symp. IEEE, Washington, DC, pp 1941–1943
41. Newsome IG, Kierski TM, Dayton PA (2019) Assessment of the Superharmonic response of microbubble contrast agents for acoustic angiography as a function of microbubble parameters. Ultrasound Med Biol 45:2515–2524. https://doi.org/10.1016/j.ultrasmedbio.2019.04.027
42. Shelton SE, Lindsey BD, Tsuruta JK et al (2016) Molecular acoustic angiography: a new technique for high-resolution SUPERHARMONIC ultrasound molecular imaging. Ultrasound Med Biol 42:769–781. https://doi.org/10.1016/j.ultrasmedbio.2015.10.015
43. Lindsey BD, Shelton SE, Dayton PA (2015) Optimization of contrast-to-tissue ratio through pulse windowing in dual-frequency "'acoustic angiography'" imaging. Ultrasound Med Biol 41:1884–1895. https://doi.org/10.1016/j.ultrasmedbio.2015.02.011
44. Lindsey BD, Rojas JD, Martin KH et al (2014) Acoustic characterization of contrast-to-tissue ratio and axial resolution dual-frequency contrast-specific acoustic angiography imaging. IEEE Trans Ultrason Ferroelec, Freq Contr 61:1668–1687. https://doi.org/10.1109/ULTSYM.2014.0440
45. Foster FS, Pavlin CJ, Harasiewicz KA et al (2000) Advances in ultrasound biomicroscopy. Ultrasound Med Biol 26:1–27
46. Heath Martin K, Lindsey BD, Ma J et al (2014) Dual-frequency piezoelectric transducers for contrast enhanced ultrasound imaging. Sensors 14:20825–20842. https://doi.org/10.3390/s141120825
47. Fedorov A, Beichel R, Kalpathy-Cramer J et al (2012) 3D slicer as an image computing platform for the quantitative imaging network. Magn Reson Imaging 30:1323–1341. https://doi.org/10.1016/j.mri.2012.05.001.3D
48. Aylward SR, Bullitt E (2002) Initialization, noise, singularities, and scale in height ridge traversal for tubular object centerline extraction. IEEE Trans Med Imaging 21:61–75. https://doi.org/10.1109/42.993126
49. Bullitt E, Gerig G, Pizer SM et al (2003) Measuring tortuosity of the intracerebral Vasculature from MRA images. IEEE Trans Med Imaging 22:1163–1171. https://doi.org/10.1109/TMI.2003.816964
50. Bullitt E, Muller KE, Jung I et al (2005) Analyzing attributes of vessel populations. Med Image Anal 9:39–49. https://doi.org/10.1016/j.media.2004.06.024
51. Talu E, Powell RL, Longo ML, Dayton PA (2008) Needle size and injection rate impact microbubble contrast agent population. Ultrasound Med Biol 34:1182–1185. https://doi.org/10.1016/j.ultrasmedbio.2007.12.018

# Chapter 35

# Patch Clamp Technology for Focused Ultrasonic (FUS) Neuromodulation

Eun Sok Kim and Su-youne Chang

## Abstract

Electrical stimulation of neural tissue, such as deep brain stimulation (DBS) and cortical stimulation, is widely applied therapeutic neuromodulation techniques for neurologic disorders. Penetrating electrodes (e.g., microwires and silicon probes) for DBS provide high spatial resolution, but are invasive, displacing neural tissue, producing acute insertion trauma, and potentially eliciting a foreign-body response. Surface electrodes, while less invasive, cannot generate a highly localized electrical field. Motivated by these limitations, the goal of this chapter is to provide a protocol to run patch clamp experiments on rat brain slices with a focused ultrasonic transducer that offers minimally invasive and highly localized neuronal stimulation (and that is thin enough to let light to pass through for optical observation of neuron cells for patching). Though focused acoustic beams with high energy are traditionally used for cellular ablation, the goal here is to use low acoustic energy to avoid any ablation or lesion, exploiting the unprecedented features of self-focusing acoustic transducers (SFATs) that can focus 2–20 MHz sound waves at a submillimeter-sized area. The experimental procedures described here will allow intracellular and extracellular experiments to determine the value and underlying mechanisms of neuromodulation effects induced by SFAT-based ultrasonic stimulation. The aims of this protocol are (1) to fabricate SFATs for the proposed intracellular and extracellular experiments and (2) to characterize the neuromodulatory function evoked by SFAT-based ultrasound stimulation in normal brain slices. Using patch clamp methods, one can monitor ionic flux and local field potentials, while varying the acoustic stimulation frequency, intensity, pulse width, pulse shape and pulse repetition frequency as well as the focal spot(s), focal size and force direction. The patch clamp experiments will provide insights into biologic mechanisms of ultrasonic neural stimulation, and could be a critical step toward the development of a minimally invasive alternative to neuromodulation by electrical stimulation in the treatment of neurologic disorders such as epilepsy. If the underlying mechanisms of ultrasonic neural stimulation are well understood, a transcranial focused ultrasound beam can possibly modulate pathological neural activities, without surgery, running wire, or any damaging effects from penetrating probe.

**Key words** Ultrasonic neural stimulation, Focused ultrasound, Patch clamp, Self-focusing acoustic transducer, Rat brain slice

## 1 Introduction

The key component of the experiment is a MEMS-based Self-Focusing Acoustic Transducer (SFAT) that allows relatively easy patch clamp experiments for investigating ultrasound's

Miguel R. Ossandon et al. (eds.), *Biomedical Engineering Technologies: Volume 1*, Methods in Molecular Biology, vol. 2393, https://doi.org/10.1007/978-1-0716-1803-5_35, 

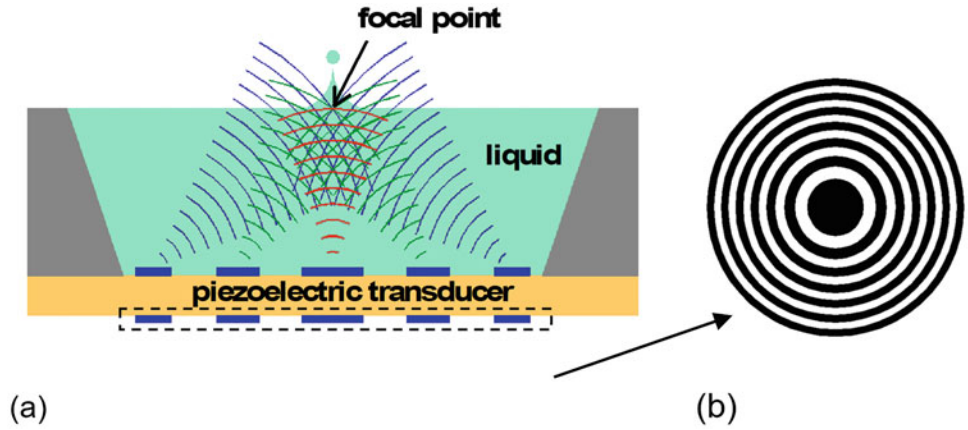


**Fig. 1** (**a**) Cross section of self-focusing acoustic transducer that produces acoustic waves such that the waves interfere constructively at the focal point. (**b**) Top view of the electrode pattern

neuromodulation properties for potential application in neurologic diseases such as epilepsy. The SFATs are thin, small, light, implantable, and capable of producing micron-sized focal stimulation. Although ultrasound stimulators have been reported [1], the SFAT is the first transducer that allows easy patch clamp experiments for studying highly localized neurostimulation.

The SFAT can focus 2–300 MHz sound waves onto an area 5–800 μm in diameter, without thermal injury or cavitation. Its ability to deliver a focused acoustic beam onto a micron-sized area has potential to enable an unprecedented delivery of stimuli to narrowly targeted regions/populations of neurons for various therapeutic applications. Since the transducer will be positioned between a tissue slice and a light source for the patch clamp experiments, the lensless SFAT (Fig. 1) with thin transducer thickness will be ideal, as the nonactive areas (i.e., the areas without electrodes) are translucent, unlike opaque electrode, and allow light to pass, if the transducer is built on a relatively thin 127 μm thick lead zirconate titanate (PZT) substrate.

The SFAT is capable of producing high frequency (2–100 MHz) focused acoustic beam on micron-sized focal spot, while allowing light to pass through the SFAT. Conventional focused ultrasound (FUS) transducers are optically opaque, and consequently, only blind patch clamp experiment (which is very challenging) is possible (due to the inability to see the neuronal cells on the tissue that is being sonicated with the transducer), unless a special and complicated scheme is arranged.

The first part of this chapter is to design and fabricate SFATs that can focus 20 MHz sound waves into 70 μm sized points within rat brain cortex and are capable of delivering sufficient acoustic power (without heat or cavitation) to evoke neural responses.

It will present detailed fabrication and packaging processes that are suitable for intracellular and extracellular experiments, which will be described in the second part.

## 2 Equipment and Materials

### 2.1 SFAT Microfabrication

1. Microfabrication Equipment:
   (a) Dicing Saw (e.g., Dicing Technology's Uni-Dice IV).
   (b) Spin Coater (e.g., KW-4E Spin Coater), Mask Aligner (e.g., Karl Suss MJB6 Mask Aligner).
   (c) Reactive Ion Etcher (e.g., Samco's RIE-1C).
   (d) Parylene Deposition System (e.g., Specialty Coating Systems PDS-2010 Parylene Deposition System).
   (e) Oven (e.g., Thermo Scientific PR305225G Gravity Convection Oven).
2. Lithography material
   (a) Iron Oxide Photomask (e.g., 4″ × 4″ × 060″ Iron Oxide plates with 0.5 microns of Rohm & Haas Microposit® S1818 Photoresist from Towne Technologies, Inc.).
   (b) Iron Oxide Mask Etch (e.g., Iron Oxide Mask Etch 9028 from Transene Company), 16″ × 8″ Film Photomask (e.g., 50,800 DPI Film from Fine Line Imaging).
   (c) Photoresist AZ 5214-E, Parylene D dimer.
   (d) Nickel Etchant Type TFG, Acetone, Methanol, Isopropyl Alcohol (IPA)
3. SFAT fabrication.
   (a) PZT sheet: 36.2 mm × 36.2 mm × 127 μm bulk PZT sheet (e.g., PZT-5A from Piezo.com).
   (b) Temperature Wire: 0.5 mm Thick Wires (e.g., 36-Gauge Low-Voltage High-Temperature Wire from McMaster-Carr).

### 2.2 SFAT Testing

1. Function Generator (e.g., Tektronix AFG 3252).
2. Power Amplifier (e.g., AR 75A250).
3. Oscilloscope (e.g., RIGOL DS4014).

### 2.3 Brain Slice Preparation

1. Isoflurane (Forane Isoflurane 100% Inhalation Anesthesia, Baxter Corporation) and a sliding top chamber (Kent Scientific Corporation) for anesthesia.
2. Guillotine (e.g., small animal decapitator guillotine [Harvard Apparatus]).

3. Tissue adhesive (Vetbond, 3 M) to attach the brain onto the cutting stage.
4. Live tissue slicer (e.g., Leica VT 1000S vibratome [Leica]).
5. Prechamber for brain slices to maintain them alive (e.g., BSC-PC (Warner Instruments).
6. Artificial cerebrospinal fluid (ACSF) (aerated with 95% $O_2$/5% $CO_2$), which contains (in mM): 124 NaCl, 2.5 KCl, 1.25 $KH_2PO_4$, 1 $MgSO_4$, 2 $CaCl_2$, 26 $NaHCO_3$, and 11 D-glucose. Chemicals are purchased form Sigma-Aldrich Corporation.

### 2.4 Patch Clamp Experiment with SFAT

1. Vibration isolation table with Faraday cage (e.g., CleanBench Table [TMC]).
2. Upright microscope with water immersion lens (e.g., Eclipse FN1 microscope (Nikon) with NIR Apo 40× lens).
3. Water bath to preheat bath perfusion solution (e.g., ISO-TEMP205 [Fisher Scientific]).
4. Temperature controller (e.g., TC-324B in-line temperature controller (Warner Instrument)).
5. Gravity driven perfusion system and vacuum chamber for bath solution circulation.
6. Recording chamber (e.g., RC-27 [Warner Instruments]).
7. Light-curing dental cement (Prime-Dent) to secure the SFAT on the cover glass of the bottom of the recording chamber.
8. Amplifier (e.g., Multiclamp 700B amplifier (Molecular Devices]).
9. Noise eliminator (e.g., Hum bug [Quest Scientific]).
10. Low-noise data acquisition system (e.g., Axon Digidata 1550A) with acquisition and data collection software (e.g., Clampex and Clampfit [Molecular Devices]).
11. Micromanipulator (e.g., MPC-200 manipulator (ROE-200) [Sutter Instrument]).
12. Borosilicate glass capillary (e.g., glass capillary with filament [Warner Instruments]).
13. Micropipette puller (e.g., P-97 [Sutter Instrument]).
14. Glass electrode polisher (e.g., MF-830 microforge [Narishige]).

## 3 Methods

### 3.1 SFAT Design

The Fresnel half-wave band sources can be made of two types: a *positive* type with open center (Fig. 2), and a *negative* type with closed or electroded center (Fig. 1). In order to allow enough light

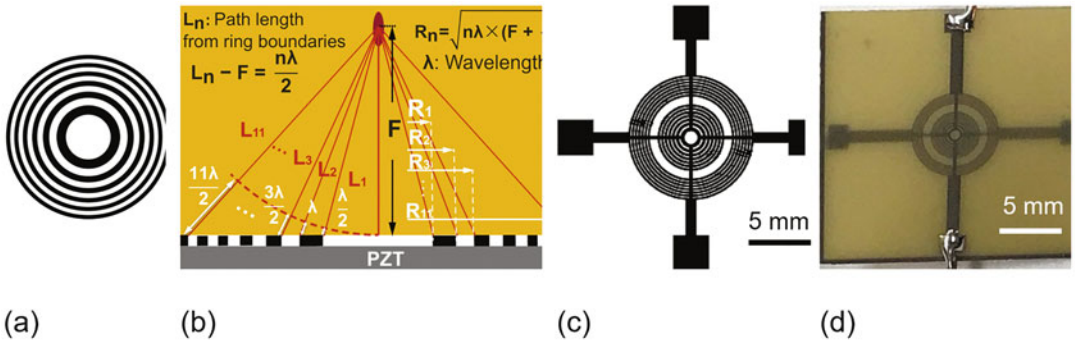


**Fig. 2** Conceptual top view (**a**) and cross-sectional view (**b**) of the electrode patterned into Fresnel half-wave band (FHWB) sources to focus the acoustic waves. (**c**) Top-view electrode patterns (both Mask 1 and Mask 2 overlapped, *see* Fig. 3 for details) with open center area and omitted middle rings. (**d**) Photo of a fabricated positive-type SFAT shown in (**c**), with the two solder pads (on the tope side) having wires soldered, while the two solder pads on the bottom side showing up on the photo due to translucency of the thin 127μm thick PZT

to past through the SFAT to the focal point of the ultrasound where cells are patched, we use the positive type such as the one shown in Fig. 2c, d.

The SFAT design is similar to optical Fresnel lens in that we make only certain areas of the piezoelectric substrate generate acoustic waves, which arrive at a focal point in phase for constructive wave interference. The other areas (that generate waves with phase difference of $\approx\pi$ at the focal point) are designed not to generate any acoustic wave. One way to achieve this kind of near-field wave interference is to use Half-Wave-Band source such as the one shown in Fig. 2a. The acoustic waves generated by the successive annular sources are designed to arrive at the focal point (with $F$ being the focal length) with finite delays (equal to multiples of the wavelength ($\lambda$) in tissue medium) by ensuring that the radii $R_n$ satisfy the following equation [2]:

$$\sqrt{R_n^2 + F^2} - F = \frac{n\lambda}{2}$$

where $n = 1,2,3,....$, as indicated in Fig. 2b.

Solving the above equation for $R_n$ results

$$R_n = \sqrt{n\lambda \times \left(F + \frac{n\lambda}{4}\right)}$$

The 14 rings with 3 omitted rings in the SFAT shown in Fig. 2c are designed according to the equation above for a focal length of 0.4 mm in water with a SFAT driving frequency of 18.7 MHz (corresponding to 81.9 μm of wavelength $\lambda$ in water).

### 3.2 Photomask Fabrication

1. Laydown photomask patterns on a computer with a layout software such as Autocad or L-Edit, and create a GDS file (or any other file format that a photomask pattern generator

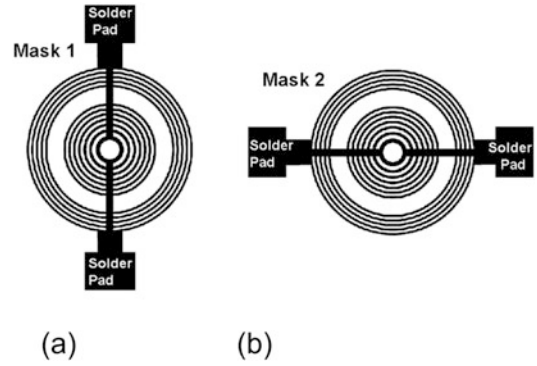


**Fig. 3** Top view patterns of (**a**) Mask 1 and (**b**) Mask 2

can accept) from the layout tool, and have it processed by a vendor who produces the opaque patterns on a transparent film with high-resolution ink jet printing. Add some straight lines called dicing lines for easiness in dicing.

2. There are typically two photomasks that are needed for the SFAT, one for the top electrode (say, Mask 1) and the other for the bottom electrode (Mask 2). The ultrasound-generating region has essentially the same pattern for both Mask 1 and Mask 2, as illustrated in Fig. 3. But the areas for the solder pads as well as any electrical wire out to those pads should be designed on the masks such that there is no overlap between the top solder pad and the bottom solder pad in order to avoid any unwanted ultrasound generation from the solder pad areas.
3. Transfer the patterns from the transparent film to an Iron Oxide Photomask with photoresist by blanket expose of the film over the photomask, followed by photoresist development and etching with Iron Oxide Mask Etch.

### *3.3 SFAT Fabrication*

#### *3.3.1 Photolithography*

1. Spin-coat AZ 5214 photoresist (1.2 krpm for 60 s) on one side of PZT sheet, with a spin coater.
2. Bake for 3 min in an oven set at 90 °C.
3. Spin-coat AZ 5214 (1.2 krpm for 60 s) on the other side of PZT sheet, with a spin coater.
4. Bake for 5 min in an oven set at 90 °C.
5. Align Mask #1 (with electrode patterns) to one side of PZT sheet, using one of its corners as reference, in a mask aligner.
6. Expose with 140 mJ/cm$^2$ energy level in a mask aligner.
7. Align Mask #2 (with same electrode patterns but different soldering-pad patterns to avoid overlapping so that the soldering pads on the top and bottom of the PZT may not generate acoustic waves) to the other side of PZT sheet, using the same corner as reference, in a mask aligner.

8. Expose with 140 mJ/cm$^2$ energy level, in a mask aligner.
9. Develop the photoresist for 60 s using 1:4 diluted 400K developer solution. Flip the PZT sheet every 15 s.
10. Rinse with DI water and dry with $N_2$ flow.
11. Bake for 15 min in an oven set at 90 °C.

*3.3.2 Nickel Electrode Etching*

1. Preheat the TFG nickel etchant at 35 °C on a hot plate [3].
2. Soak PZT sheet in TFG for enough time (~6.5 min) to make sure etching all nickel on both surfaces. Flip the PZT sheet every 30 s.
3. Rinse with DI water and dry with $N_2$ flow.

*3.3.3 Dicing*

1. Dice the PZT sheet along the dicing lines using a dicing saw.
2. Clean the diced PZT sheets with acetone in an ultrasonic bath for 5 min, then rinse with methanol, isopropyl alcohol (IPA) and DI water. Dry with $N_2$ flow.

*3.3.4 Wire Connections*

1. Each transducer has to have at least two wires soldered, one on the top and the other one on the bottom. Though SFAT operation needs only the two wires, two extra wires (or more) may be connected for backup and/or mechanical symmetry, as shown in Fig. 4. Choose wires that are as flexible (or thin) as possible, so that the wires near the solder points may not damage the solder points (or the PZT sheet) when any of the wires is bent or handled crudely.

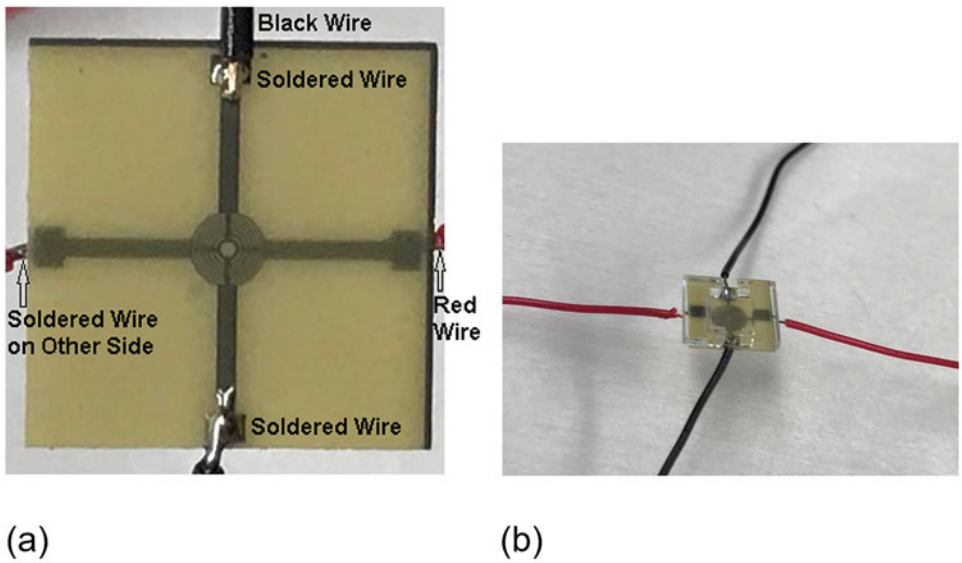


**Fig. 4** Top view photos of SFATs with wires soldered on four points; two on the top and two on the bottom side of SFAT; (**a**) a close-up photo of an SFAT and (**b**) a distant photo of another SFAT (with laser-machined acrylic sheet as a mechanical support)

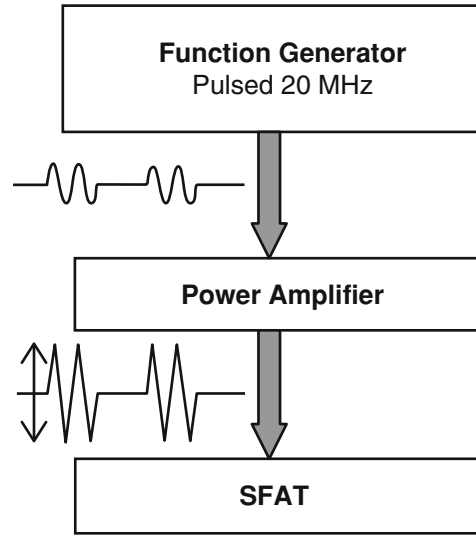


**Fig. 5** Schematic of the electronic drive setup

#### 3.3.5 Parylene Deposition

1. Dehydrate the sample in an oven for more than 5 min.
2. Deposit ≈10 μm thick Parylene film as an electrically insulating layer by using about 10 g of Parylene D dimer powder. As the Parylene deposition is conformal over any shape of surface, the whole device that is in the Parylene coating system gets coated with Parylene all over. Thus, it would be prudent to cover up the connection points of the wires with some tapes before Parylene deposition and then remove the tapes to have those points free of Parylene coating.

### 3.4 SFAT Testing and Operation

#### 3.4.1 Electronic Setup

The output of a function generator (Tektronix AFG 3252) goes to the input of a power amplifier (AR 75A250) and gets amplified. The amplified signal from the amplifier output then goes to SFAT (or being monitored by an oscilloscope), and would look like what is illustrated in Fig. 5 with the frequency of the sinusoidal wave being chosen to be the resonant frequency of the PZT's thickness-mode vibration, which is around 20 MHz. The oscilloscope can be used to monitor the input and/or the output signals of the power amplifier. If the output signal is too high, a voltage attenuator would be needed to avoid damaging the oscilloscope.

#### 3.4.2 Initial Test

Before driving the device, make sure you remove the cable connecting the output of the power amplifier to the oscilloscope. Initial test can be done with the SFAT immersed in water with the height of the water being close to the SFAT focal length. Drive the SFAT with 100 $V_{pp}$ voltage at the drive sinusoidal frequency (around 20 MHz), 300–1000 Cycles, 16.67 ms pulse repetition period (or 60 Hz pulse repetition frequency). As you vary the drive

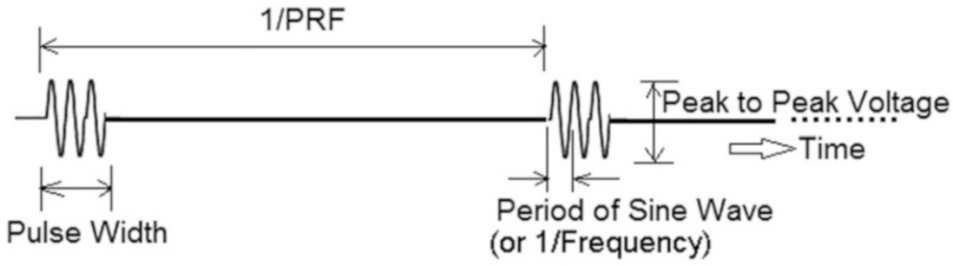


**Fig. 6** Pulse repetition frequency (PRF), pulse width and sine-wave period. The number of sinusoidal cycles per pulse is equal to pulse width divided by sine-wave period

sinusoidal frequency around 20 MHz, you will see vibration on the water surface, which suggests that the device is working. Determine the SFAT's resonant frequency by varying the drive sinusoidal frequency around 20 MHz and observing the vibration on the water surface. When the drive frequency matches the SFAT's resonant frequency, you will see a much larger vibration of the water surface. By adjusting the water level, you may even see ejections of very tiny water droplets (about 80 μm in diameter) at a certain water level.

#### *3.4.3 SFAT Operation*

1. Drive Sinusoidal Frequency.

   Vary the drive sinusoidal frequency around 20 MHz to determine the best frequency where the SFAT generates largest acoustic intensity.

2. Voltage.

   Voltage determines the acoustic intensity at focal point. The acoustic intensity at the focal point versus the drive voltage ($V_{pp}$) for a 20 MHz SFAT can be calculated with the following empirical formula [4]: Intensity [$W/cm^2$] $\approx$ ($V_{pp}{}^2/2 - V_{pp}$)/1000. A good starting point may be 180 $V_{pp}$.

3. Cycles and Pulse Repetition Frequency (PRF)

   The number of sinusoidal cycles per pulse (or the pulse width for a given sinusoidal frequency) and pulse repetition frequency (PRF) (Fig. 6) along with the acoustic intensity determine the total energy applied onto the tissue. A good starting point may be 1200 cycles (corresponding to 60 μs pulse width, since 1200 cycles = (60 μs pulse width) × (20 MHz)) and 60 Hz PRF (or 16.67 ms pulse repetition period). A longer pulse width or a higher PRF means a higher acoustic energy being applied but at more heat generation on the transducer due to the PZT's tangent loss.

### *3.5 Brain Slice Preparation*

1. *Anesthesia*: Rat needs to be fully anesthetized with isoflurane. Open technique can be used in the chemical fume hood. The

rat is placed in a clear container. Then, isoflurane is administered. To prevent direct contact with liquid isoflurane, isoflurane (0.3–0.5 ml) is applied on gauze within a tissue cassette and placed in the anesthesia container. Respiration rate needs to be carefully watched.

2. *Transcardiac Perfusion*: Once the animal is fully anesthetized, the animal is transferred to the ice-cold plate. Thoracic cavity is opened with surgical scissors to expose the heart. A small hole is made into the apex of the heart to allow a blunt ended cannula to be passed through the apex and into the aorta. Approximately 200 ml of cold ACSF is flushed through the rat's circulatory system with 50 ml syringe, draining out through an incision in the right ventricle. This process allows for the brain to become rapidly cooled down. During this procedure, isoflurane can be continuously applied with a nose cone. However, since this procedure takes fairly short amount of time (less than a few minutes), the continuous isoflurane administration is not necessary.
3. *Slice the Brain*: After transcardiac perfusion with cold ACSF, decapitation is performed with a guillotine. The skull is carefully removed with bone cutter and rongeur. The intact whole brain is isolated and transferred to the 95% $O_2$/5% $CO_2$ aerated cold ACSF. The brain can be trimmed with a razor blade to minimize the slicing volume. The trimmed brain tissue is glued down onto the bottom of slicer with a tissue adhesive (Vetbond 3M). Slices are made in 300–400 μm thickness in the vibratome.
4. *Maintenance of Live Slices*: After cutting, the slices are trimmed to 5–7 mm by 5–7 mm dimension so that the slice size is large enough to fully cover the active region of the SFAT and small enough not to touch the solder pad. Then, the slices are transferred to the prechamber, which is placed inside the temperature-controlled water bath at 35 °C, and incubated in the prechamber with ACSF for 15 min. After 15 min incubation, the prechamber is taken outside of the water bath and kept at room temperature for at least 1 h before patch clamp recording. After the recovery period, the slices are maintained in the prechamber filled with ACSF at room temperature up to 8 h before the recording. ACSF is continuously aerated with 95% $O_2$/5% $CO_2$.

### 3.6 Patch Clamp Experiment

1. *Slice Placement in a Recording Chamber*: The SFAT is thin and designed to pass the light (Figs. 7 and 8). Before the patch clamp experiment, the SFAT is attached onto the cover glass of the recording chamber with light-curing dental cement. Once the SFAT is fixed on the recording chamber bottom, the SFAT is connected to the power amplifier, of which the input comes

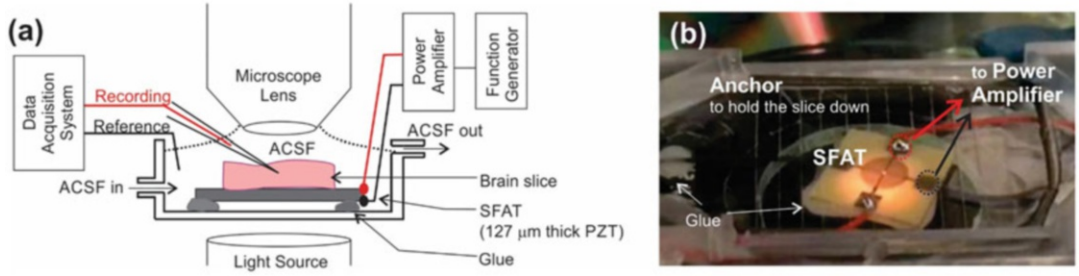


**Fig. 7** Schematic and photo of the set-up for brain-tissue patch clamp experiment with SFAT: (**a**) The SFAT is attached on the bottom of the recording chamber, to prevent the SFAT floating. Since the recording chamber bottom is a cover glass, a light-curing dental cement is used to glue the SFAT down on the cover glass. ACSF aerated with 95% $O_2$ and 5% $CO_2$ is continuously applied to the bath of the recording chamber. The hippocampal slice is placed over (and abuts) the SFAT, and an anchor (a metallic grill grate) is placed over the slice to prevent the slice from moving. Using a high-magnification water immersion lens, a cell is identified for patch clamp. A reference electrode is placed in the bath and a glass capillary is used as a recording electrode. The SFAT is connected to the power amplifier, which is in turn connected to the function generator that generates pulsed sinusoidal waves. (**b**) Photo of the recording chamber which shows SFAT attached on the cover glass with a dental cement (glue), the grill grate acting as an anchor weight for the slice, the solder pads, and the four connecting wires soldered to the solder pads

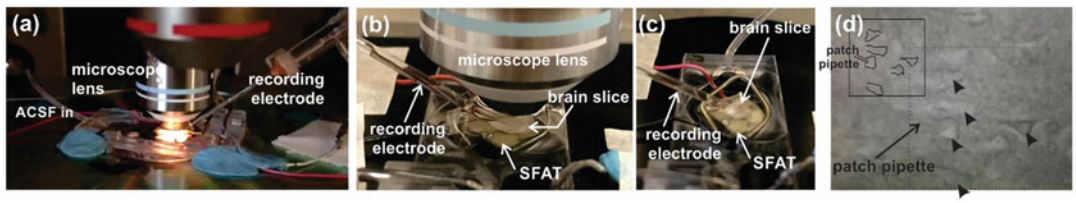


**Fig. 8** Photos of the set-up for brain-tissue patch clamp experiment with SFAT: (**a**) overview, (**b**) and (**c**) detailed views, and (**d**) infrared microscopic view that allows us to visualize the cells in the slice on top of the SFAT. The inlet is the trace view inside the dotted box. Arrow heads indicate cell bodies and traced cells

from a function generator that outputs pulsed sinusoidal signals. The brain slice is placed on top of the SFAT. ACSF is continuously perfused at a flow rate of 2–3 ml/min. Gravity feeding method is used to deliver ACSF to the bath chamber. Sixty-milliliter syringe with a small hole on the barrel close to the needle hub is placed inside the 120 ml syringe barrel. This double-syringe system is placed vertically to the needle hub orienting down. The solution release rate from the 60 ml syringe is limited due to the plunge of 60-ml syringe. When air bubble comes into the 60-ml syringe, the solution is released from the syringe and thus the solution level is maintained at the level of the hole of the 60-ml syringe. The height of the whole double syringe system is adjusted to keep the flow rate 2–3 ml/min. Using this double-syringe method, the flow rate is maintained constantly without the pump.

2. *Patch the Cell*: Light can pass through the nonelectroded areas of the thin SFAT, and cells in the slice are visualized under the microscope, as illustrated in Fig. 7a and shown in Fig. 8d. To make a whole-cell patch clamp under the microscope, a borosilicate glass capillary is pulled with a horizontal puller to 3–6 MΩ tip resistance when filled with patch pipette solution. The patch pipette solution consists of 125 K-gluconate; 10 KCl; 10 HEPES, 1 EGTA, 2 $MgCl_2$; 0.1 $CaCl_2$; and 4 ATP-$Na_2$, all in mM. When the glass capillary approaches to the identified cell, mild positive pressure is applied the capillary. When the glass capillary touches the cell membrane, the positive pressure is immediately removed and mild negative pressure is applied. Once Giga-ohm seal is made, the membrane is ruptured with a short burst negative pressure. This pressure needs to be empirically determined.
3. *Measurement of US-induced Membrane Potential Changes*: In a current clamp mode (Bridge mode), membrane potential can be read through an amplifier and acquisition system with data sampling rate of 10 kHz. If cells generate spontaneous action potentials, action potentials are counted and the action potential rates can be calculated (action potential rate (Hz) = number of action potentials per sec). Before US stimulation is applied, the membrane potential and the action potential rate can be measured. Then, while US stimulation is applied, membrane potentials and action potential generation are recorded to determine the US stimulation effect on the membrane potential and action potential generation. To evaluate effects of various parameters of US stimulation, baseline recording may be performed first without the US stimulation, and then one varied parameter (after another) of US stimulation may be applied one after another. Each time the applied acoustic stimulation parameters such as acoustic intensity, PRF, duty cycle, etc. can be varied. In addition, since the patch clamping targets a single cell, if the US-induced neuronal response is determined at the focal point of the SFAT, patch clamping another cell in a distance from the focal point and measuring cellular response to US stimulation can be used to determine the effective area of the US stimulation. Calcium and/or membrane potential imaging can be an alternative method to determine the SFAT effective areas.
4. *Measurement of US-modulated Ion Channel Activities*: In a voltage clamp mode of the whole-cell patch clamp recording, ionic channels can be isolated by controlling the membrane potential (through which channels can be activated or inactivated) and applying selective channel blockers. To determine the effect of US stimulation on ionic flux, US stimulation can be applied during the period when channels are opened by

holding the membrane potential at the voltage of channel activation [5]. Then, the current by ionic flux with US stimulation can be compared with that without US stimulation.

5. *Measurement of US-modulated Synaptic Currents*: US stimulation effect on synaptic response can be characterized by measuring local field potential (LFP) and spontaneous/miniature synaptic currents. LFP can be measured while an electrical stimulation is applied [6] before, during, and after US stimulation to observe its effect on LFP. With patch clamp, spontaneous and miniature post-synaptic currents can be monitored before, during and after US stimulation. If the current and/or voltage changes during US stimulation can be measured, this will be ideal. However, the electrical signal used for US stimulation tends to produce electromagnetic interference in the current/voltage recording. Comparison between before and immediately after US stimulation can be used to evaluate the US stimulation effect on the synaptic currents.

### 3.7 Recording with Whole-Cell Patch Clamp

1. For the quantitative detection of the US stimulation, the membrane potentials before and during the US stimulation are measured, and the membrane potential changes are determined. If the activation induced by US stimulation is strong enough, action potentials are generated. The number of action potentials can be counted to quantitate the US-induced stimulation.
2. PRF and pulse width as well as the applied peak-to-peak voltage level (Fig. 6) are varied. The frequency of the sine wave is set at the best frequency where the SFAT generates largest acoustic intensity. The pulse width cannot be too long to keep the temperature rise less than 1 °C. The temperature rise at the focal spot due to the focused ultrasound is expected to be negligible in the typical SFAT operating conditions that this chapter suggests. However, the PZT in the SFAT has tangent loss, which can raise the temperature in the PZT, if the applied pulse width is long. As can be seen in Fig. 6, the frequency of the sine wave and the pulse width determine the number of sine-wave cycles per pulse, which along with PRF needs to be low enough to avoid temperature rise due to the tangent loss of the PZT. The amplitude of the output voltage is gradually increased.

## 4 Notes

1. The SFAT is made on a thin rigid substrate (i.e., 127 μm thick PZT), and needs to be handled with care.

2. The output voltage of the power amplifier needs to be stable, since transient or intermittent high voltage can damage SFAT.
3. Viability of cells in the slice is important for a patch clamp experiment. To increase the number of live cells in the slice, transcardiac perfusion of cold ACSF can be performed. If juvenile rats younger than 3–4 weeks are used, the transcardiac perfusion may not be necessary.
4. For patch clamp experiment, it is important to keep the access resistance between the patch pipette and the cell membrane consistent. To do so, the access resistance needs to be measured repetitively during the whole cell recording. If the access resistance before and after the recording changes over 10%, the data cannot be trusted.

## References

1. Tufail Y et al (2010) Transcranial pulsed ultrasound stimulates intact brain circuits. Neuron 66(5):681–694
2. Huang D, Kim ES (2001) Micromachined acoustic-wave liquid ejector. IEEE/ASME J Microelectromech Syst 10:442–449
3. https://engineering.tufts.edu/microfab/documents/SOP_TFG_nickelEtch.pdf
4. Wang L, Li Y, Lin A, Choe Y, Gross M, Kim ES (2013) A self-focusing acoustic transducer that exploits cytoskeletal differences for selective cytolysis of cancer cells. IEEE/ASME J Microelectromech Syst 22(3):542–552
5. Kubanek J, Shi J, March J, Chen D, Deng C, Cui J (2016) Ultrasound modulates ion channel currents. Sci Rep 6:24170
6. Chang S, DeVera C, Yang Z, Yang T, Song I, McDowell A, Xiong Z, Simon R, Zhou A (2020) Hippocampal changes in mice lacking an active prohormone convertase 2. Hippocampus 30:1–9. https://doi.org/10.1002/hippo.23195

# Chapter 36

# Wireless Wearable Ultrasound Sensor to Characterize Respiratory Behavior

**Ang Chen, Rachel Diane Rhoades, Andrew Joshua Halton, Jayden Charles Booth, Xinhao Shi, Xiangli Bu, Ning Wu, and Junseok Chae**

## Abstract

A wireless wearable sensor on a paper substrate was used to continuously monitor respiratory behavior that can extract and deliver clinically relevant respiratory parameters to a smartphone. Intended to be placed horizontally at the midpoint of the costal margin and the xiphoid process as determined through anatomical analysis and experimental test, the wearable sensor is compact at only $40 \times 35 \times 6$ mm$^3$ in size and 6.5 g weight including a 2.7 g lithium battery. The wearable sensor, consisting of an ultrasound emitter, an ultrasound receiver, wireless transmission system, and associated data acquisition, measures the linear change in circumference at the attachment location by recording and analyzing the changes in ultrasound pressure as the distance between the emitter and the receiver changes. Changes in ultrasound pressure corresponding to linear strain are converted to temporal lung volume data and are wirelessly transmitted to an associated custom-designed smartphone app. Processing the received data, the mobile app is able to display the temporal volume trace and the flow rate vs. volume loop graphs, which are standard plots used to analyze respiration. From the plots, the app is able to extract and display clinically relevant respiration parameters, including forced expiratory volume delivered in the first second of expiration ($FEV_1$) and forced vital capacity (FVC). The sensor was evaluated with eight volunteers, showing a mean difference of the $FEV_1$/FVC ratio as bounded by 0.00–4.25% when compared to the industry-standard spirometer results. By enabling continuous tracking of respiratory behavioral parameters, the wireless wearable sensor helps monitor the progression of chronic respiratory illnesses, including providing warnings to asthma patients and caregivers to pursue necessary medical assistance.

**Key words** Wearable, Wireless, Respiration monitoring, Asthma control, $FEV_1$/FVC ratio, Paper substrate, Smartphone app

## 1 Introduction

Asthma is a severe disease impacting 1–18% of the population in various countries worldwide, with the global economic and health burden increasing significantly throughout the last 40 years [1, 2]. In particular, there has been an increase in diagnoses of 50% per decade, resulting in approximately 300 million people

Miguel R. Ossandon et al. (eds.), *Biomedical Engineering Technologies: Volume 1*, Methods in Molecular Biology, vol. 2393, https://doi.org/10.1007/978-1-0716-1803-5_36, 

currently plagued by asthma worldwide [3]. Within the United States, about 1 out of every 12 people suffers from asthma, making up 25 million people diagnosed across all age groups. Of those 25 million patients, approximately 7 million are children who will have to continue to deal with asthma throughout their lifetime [4].

The characteristics of asthma stress the importance and need for continuous respiratory behavior monitoring. Asthma is a chronic disease that causes variable airway inflammation, which presents as an array of time-varying respiratory symptoms such as wheezing, shortness of breath, chest tightness, and coughing [1]. Clinical diagnosis is based on patient history, recorded symptoms, and response to therapy [5]. However, symptom-dependent diagnosis is not clinically approved, as other health conditions can present the same respiratory symptoms as asthma. Young children and infants are more difficult to diagnose by symptoms alone as treatment response in this age range is often ambiguous, and the smaller airways can more easily be obstructed due to other causes [6]. Due to these challenges, it is beneficial to monitor daily respiratory behavior parameters, especially the $FEV_1/FVC$ ratio, to aid diagnosis and response to asthma [1].

Spirometry is currently the clinically approved method to characterize lung function, particularly in determining the $FEV_1/FVC$ ratio. This test uses a large piece of equipment to measure the characteristic inhalation or exhalation of volumes of air over time, producing a record of either volume or flow. However, due to the larger size and prohibitive cost, continuous respiration monitoring is limited using this method.

Other groups have also explored possible sensors to resolve the need for respiratory behavior monitoring. Some sensors utilize embedded coils surrounding the chest cavity to detect the change of circumference and thereby monitor respiratory inductance plethysmography [7, 8]. Similarly, Davis et al. reported employing fiber-optical plethysmography to monitor respiration by wrapping a fiber-optic strain gauge around the abdomen and chest [9]. Other methods that also measured chest wall circumference change were reported, such as the utilization of a resistive strain gauge rather than coils or fiber-optic strain gauges [10], exploit of the principle that the anterior-posterior motion of the chest wall can be captured by detecting the attenuated reflected ultrasound signal [11], and so on [12–14]. However, most reported sensors used respiratory rate as the metric of respiratory behavior, which has limited value in a clinical setting [15], and almost none produce parameters such as the $FEV_1/FVC$ ratio which have demonstrable clinical value in regard to asthma control.

This work presents a wireless wearable sensor that was designed on the principle of analyzing the changes in chest cavity circumference to characterize respiratory behavior. The overall lung volume change is emulated in the localized change of a section of the chest

wall. This lung volume change is characterized by two movements during inhalation and exhalation. During inhalation, the pump handle movement enlarges the rib cage due to the diaphragm contracting and the intercostal muscles pulling the ribs upwards. Additionally, the bucket handle movement occurs due to the increase in the anteroposterior diameter of the thorax which causes the lowermost ribs to swing outward. These two movements lifting the front and sides of the ribs combine to cause an increase in the circumference of the chest wall during inspiration. Alternatively, during exhalation, the aforementioned muscles relax, allowing the ribs to return to a neutral anatomical position and thereby decreasing the chest circumference [16, 17]. The wearable sensor was designed to measure the localized strain of the chest wall circumference and is composed of an ultrasound emitter used to emit ultrasound and an ultrasound receiver to receive the distance-elapsed attenuated ultrasound, as shown in Fig. 1a. During inspiration, the increase in chest wall circumference creates more distance between the ultrasound emitter and receiver, resulting in a more attenuated ultrasound signal received; on the other hand, during expiration the emitter and receiver become closer together, resulting in an increased power level of the received ultrasound signal. To generate the ultrasound, a non-polarized pulse stimulatory signal generated by onboard voltage-controlled oscillator was applied on a piezo-electric material, polyvinylidene difluoride (PVDF) film [18–21]. The electric field resulting from the stimulatory signal generated mechanical strain of the same frequency, 1 MHz, on the PVDF film. This carrier was modulated by the respiratory behavior, and the modulated signal was received by another PVDF film receiver. The PVDF film, a piezo-material, converted the modulated ultrasound generated by the emitter to electrical signal, which was amplified by a low noise FET-input operational amplifier and demodulated by an envelope detector. After demodulation and amplification, the respiratory signal was extracted, digitized by an onboard 12 bit Analog-to-Digital converter, and then wirelessly transmitted by the onboard Bluetooth to a mobile phone in the process shown in Fig. 1b.

## 2 Materials

### 2.1 Paper Substrate

1. 110-μm thick PVDF film having electrodes sputtered by 70 nm/10 nm of copper and nickel on both sides (3-1003702-7, TE Connectivity Inc.).
2. A general laser printer that can print patterns on thick glossy paper with a resolution of at least 600 dpi.
3. Glossy paper for laser printer (OL177WS, Online Labels, Inc.).
4. Atom A-DUCT-1 Silver epoxy (Atom Adhesive Inc.).

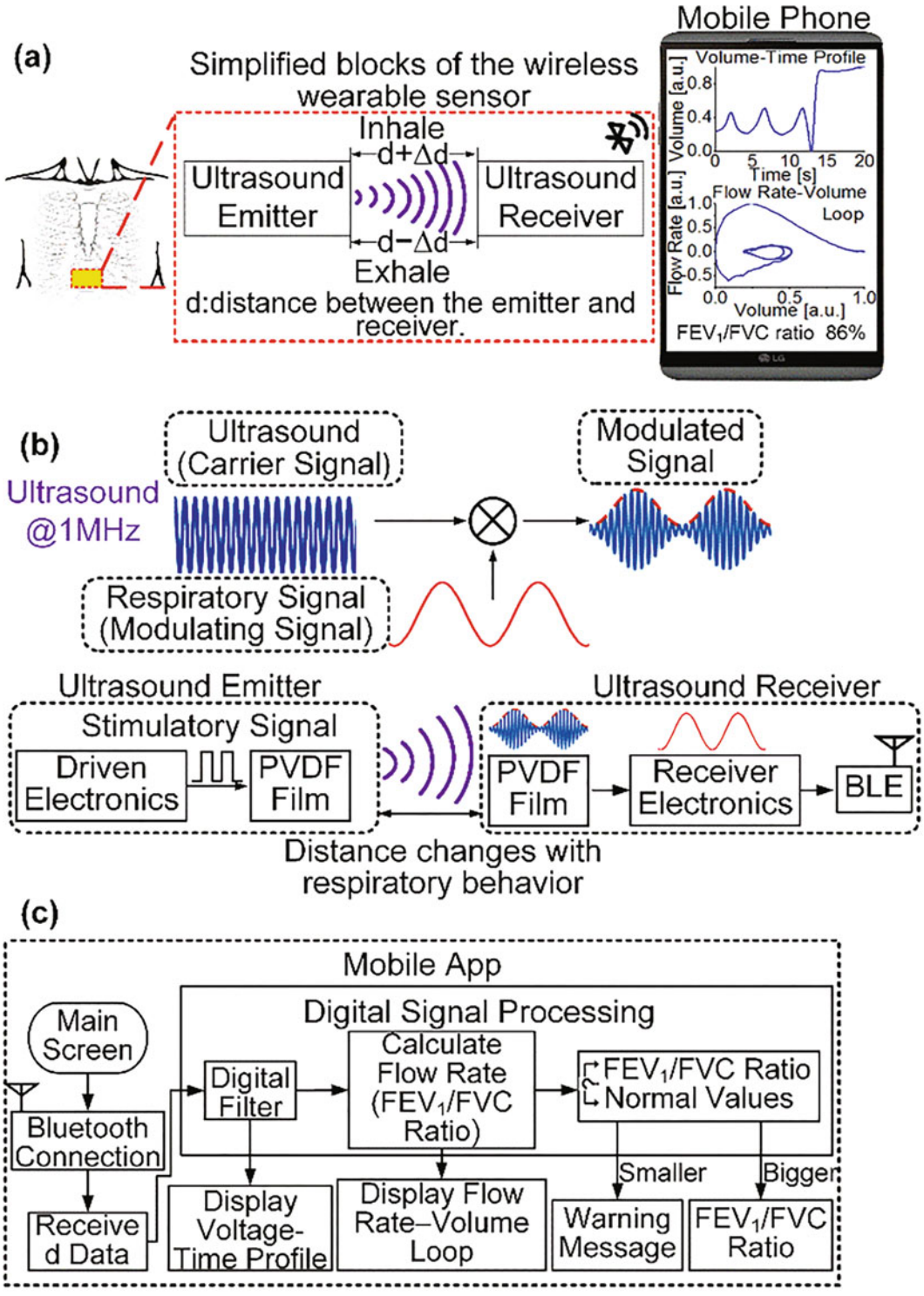


**Fig. 1** (**a**) The wearable wireless sensor, attached on the midline of the chest, measures a local strain of chest circumference as a function of time, to characterize respiratory behavior. The local strain is measured by modulated signal on an ultrasound carrier. The temporal data is processed on board and transmitted to a smartphone, where a custom-made app displays respiratory behavior plots and computes clinically relevant

5. Hot air blower that can blow hot air ~200 °C.
6. Jumbo cotton ball.

### 2.2 Circuits

1. Two-part conductive sliver epoxy (Electron Microscopy Sciences, 12642-14).
2. A micropower DC/DC converter LM2704 (Texas Instruments Inc.).
3. 3.7 V lithium battery.
4. A voltage-controlled oscillator LTC6990 (Analog Devices Inc.).
5. A low noise, FET-input operational amplifier OPA657 (Texas Instruments Inc.).
6. An envelope detector ADL5511 (ADI).
7. A Bluetooth Low Energy Nano V2 (RedBearLab).
8. Thin-film resistors with a tolerance of ±10% (surface mount) (Table 1).
9. Ceramic capacitors with a tolerance of ±10% (surface mount) (Table 2).
10. One 10μH inductor, one 2.2μH, two diodes.

### 2.3 Respiratory Behavior Collection

1. Pneumotrac Spirometer, Model6800 (Vitalograph Inc.).
2. Laptop that has Spirotrac software (Vitalograph Inc.) installed.
3. Nose clip.
4. Mouthpiece.

## 3 Methods

### 3.1 Study Design

We studied the accuracy and effectiveness of the wireless wearable sensor in recording respiration as expected based on anatomical and experimental analysis. Feasibility was exhibited through the gathering of respiratory parameters from volunteers who wore the wireless wearable sensor on their body. Investigators were not blinded, and randomization was not applicable for this study. All participants provided informed consent, and the studies were

**Fig. 1** (continued) quantitative parameters. (**b**) Operating principle of the sensor. The ultrasound carrier, generated by an on-chip ultrasound emitter, is mixed with the respiratory signal, from the local strain of the chest circumference. The mixed modulated signal is processed on board and transmitted to a smartphone via Bluetooth. (**c**) The custom-made mobile app receives the data and uses DSP (digital signal processing) filters and calculates clinically relevant respiratory behavior parameters, FEV1, FVC, and the FEV1/FVC ratio. Then, the app displays temporal tracing and differential plots that show the respiratory behavior of a wearer in pseudoreal time

**Table 1**
**Resistor values in sensor circuit Fig. 2b**

| Resistor | Resistance |
|---|---|
| $R_1$ | 1 MΩ |
| $R_2$ | 330 kΩ |
| $R_3$ | 240 kΩ |
| $R_4$ | 27 kΩ |
| $R_5$ | 50 kΩ |
| $R_6$ | 50 kΩ |
| $R_7$ | 50 kΩ |
| $R_8$ | 75 Ω |

**Table 2**
**Capacitor values in sensor circuit Fig. 2b**

| Capacitor | Capacitance |
|---|---|
| $C_1$ | 4.7μF |
| $C_2$ | 4.7 pF |
| $C_3$ | 4.7μF |
| $C_4$ | 4.7μF |
| $C_5$ | 1μF |
| $C_6$ | 0.1μF |
| $C_7$ | 1 pF |
| $C_8$ | 1 pF |
| $C_9$ | 0.1μF |
| $C_{10}$ | 0.1μF |
| $C_{11}$ | 0.1μF |
| $C_{12}$ | 100 pF |
| $C_{13}$ | 2.2μF |
| $C_{14}$ | 3.3μF |

approved by the Arizona State University Institutional Review Board (IRB).

### 3.2 Fabrication of the Wireless Wearable Sensor

The wireless wearable sensor was manufactured on a paper substrate (Fig. 2a). The footprint and weight of the sensor were $40 \times 35 \times 6$ mm$^3$ and 6.5 g, including a 2.7 g battery, respectively. Circuit traces were designed using EAGLE (a PCB design software from Autodesk company) and printed by a general laser printer

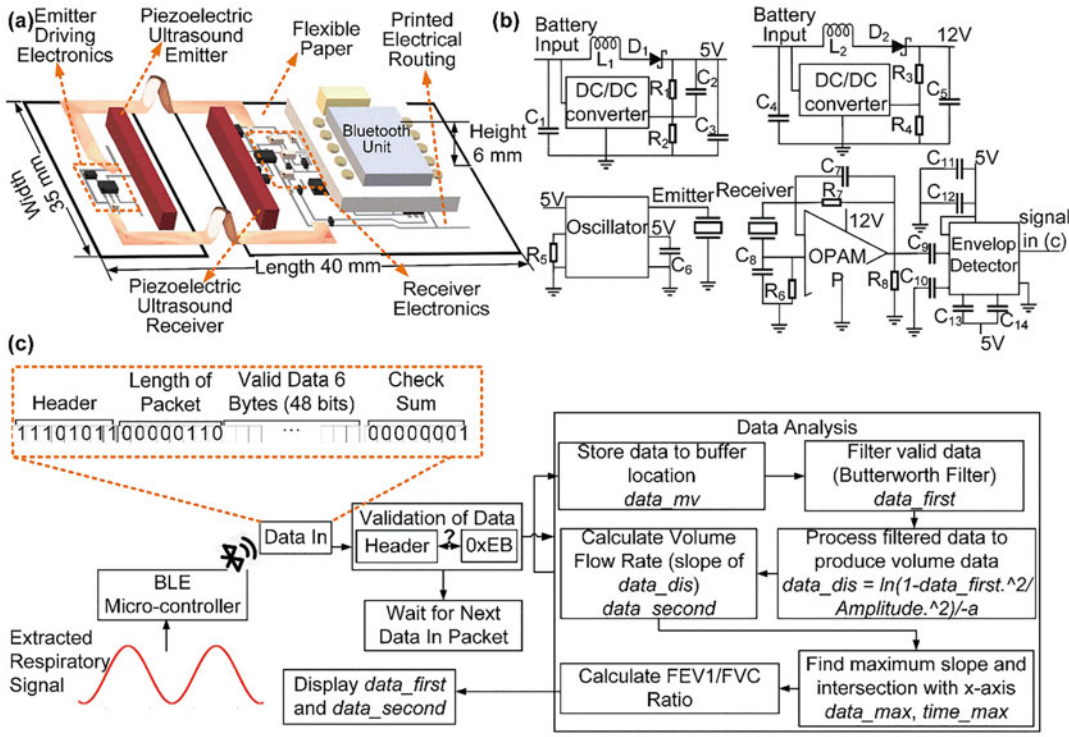


**Fig. 2** (**a**) Fully assembled wireless wearable sensor schematic. The low-profile sensor has a footprint of 40 mm × 35 mm × 6 mm on a paper substrate, including emitter driving electronics to excite a piezoelectric PVDF film to emit ultrasound wave, receiver electronics to convert the modulated ultrasound wave to electrical signal, and a Bluetooth module to digitize the electrical signal and wirelessly send it to the mobile app. (**b**) The circuit diagram of the sensor. The wireless sensor electronics consist of two DC-to-DC converters to provide adequate power to corresponding electronic modules, an op-amp to amplify the modulated signal, and an envelope detector to extract the respiratory behavior signal for wireless transmission. (**c**) The extracted respiratory behavior signal is digitized and coded by onboard microcontroller into four kinds of strings, header, length of the packet, valid data, and checksum. Then, the strings are sent to a custom-designed mobile app wirelessly by Bluetooth. The app analyzes the transmitted data, including checking the header for validity, filtering the valid data, and extracting the clinically relevant parameters

with a resolution of at least 600 dpi on a paper substrate and made conductive using silver epoxy (*see* **Note 1**). Small amounts of this silver epoxy were spread evenly across the printed circuit and dried out by blowing hot air (~200 °C) in a lateral motion for 1 min over the entire circuit (*see* **Note 2**). This process also melted the toner particles, which was primarily composed of granulated plastic that was able to form a bond between the silver epoxy and the glossy paper in the shape of the circuit as it melted.

The specific paper substrate had a top glossy layer of white clay called kaolin that filled between the paper fibers to produce a very smooth surface. Due to this layer, the organic epoxy was unable to adhere to the paper except where bonded by the melted toner, allowing the excess unbonded epoxy to be removed easily using a

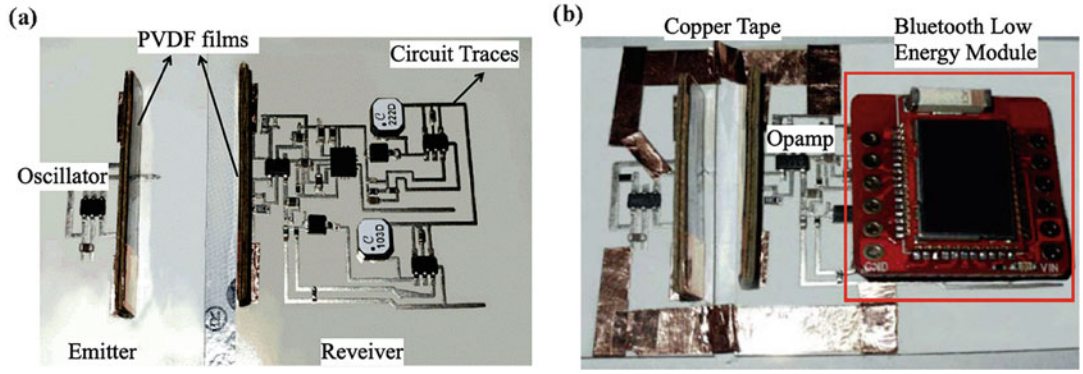


**Fig. 3** Photos of the fabricated wireless wearable sensor. (**a**) The wireless wearable sensor on a paper substrate with electronics mounted on. (**b**) The fully assembled wireless wearable sensor with the copper-tape bridges connecting and providing power supply to the emitter. BLE Nano2 was mounted on the receiver side to transmit the collected signal to external instrument, such as mobile phone via Bluetooth

cotton ball (*see* **Note 3**). These two steps were repeated until the silver epoxy on the circuit traces became fully conductive at conductivity 0.9 Ω/cm with a width of 0.3 mm (*see* **Notes 4** and **5**). The electrical components were then mounted to the printed circuit using a higher-adhesion silver epoxy through a microscope (*see* **Note 6**). A rigid paper sheet was used for standing support for the 110-μm thick PVDF film having electrodes sputtered by 70 nm/10 nm of copper and nickel on both sides. Copper tape served a dual purpose of connecting the PVDF films to the circuit due to its characteristic robust connection and bridging the two pieces of the sensor to provide power and ensure the halves of the sensor stay together. When using copper tape to connect the PVDF film to circuit, a minimum width of 5 mm was recommended. After attaching the copper tape on the PVDF film, the firm connection can be reinforced by clamping across the layers of the copper tape and the PVDF film for several minutes (*see* **Note 7**). The fabricated wearable sensor was shown in Fig. 3.

### *3.3 Electronics of the Wireless Wearable Sensor*

Shown in Fig. 2b, the 3.7 V power supply provided by the lithium battery was stepped up using a micropower DC/DC converter to provide 5 or 12 V with associated current limits of 120 or 40 mA, respectively. The PVDF film of the emitter was stimulated by a voltage-controlled oscillator to produce the desired 1 MHz ultrasound signal. The receiver PVDF film sent the received modulated signal to a low noise, FET-input operational amplifier which is characterized by a high gain-bandwidth product (1.6 GHz) and can provide 1600 V/V (64 dB) gain for a 1 MHz signal with a single stage as used in this work. From this amplified signal an envelope detector extracts the respiratory signal and sends it to a Bluetooth Low Energy (BLE) at a sampling frequency of 100 Hz to minimize power consumption. The BLE onboard system digitized

the respiratory signal using a 12-bit resolution analog to digital converter and transmitted the resulting digital signal to external Bluetooth devices for analysis.

### 3.4 Mobile App

Figure 2c shows the simplified schematic of the processing algorithm within the custom-designed mobile application. When the mobile application received the signal via Bluetooth, it was filtered using a Butterworth low-pass filter with a cutoff of 0.5 Hz. Two graphs of this signal were displayed: temporal voltage corresponding to volume vs. time and the flow rate vs. volume plots, the second of which is important for determining the $FEV_1/FVC$ ratio. The back-extrapolation method has been identified by the American Thoracic Society as the most reliable and recognized technique for extrapolating $FEV_1$, which once determined should not be greater than the larger of either 5% of the FVC or 150 mL. Instead of determining the extrapolated volume as in spirometry, the wireless wearable sensor determined the extrapolated voltage. The voltage was scaled such that one unit of voltage from the wireless wearable sensor signal correlated to an output of 1 mL from the spirometry test. Using the back-extrapolation method to determine the extrapolated voltage, the section of the forced exhalation curve with the greatest tangential slope was identified by analyzing the temporal output. From this, a trend line can be created using the most significant value and one data point on either side of this value. Where this trend line intersects with the $x$-axis is defined as the new start time of $t = 0$, and the corresponding $y$-axis value on the temporal plot is designated $y_0$ and is the desired extrapolated voltage. The corresponding $y$-axis value at $t = 1$ s based on the new start time is designated $y_1$, and the maximum voltage is considered to be correlated to FVC. From this, the desired parameter can be calculated as follows:

$$FEV_1/FVC = \frac{y_1 - y_0}{V_{max}} \times 100\%$$

The calculated $FEV_1/FVC$ ratio is compared to the nominal value of 75%, with a warning message informing of abnormal respiratory behavior appearing on the device if the ratio was lower than the threshold (Fig. 1c).

### 3.5 Respiratory Behavior Collecting Protocol

Each volunteer completed one practice procedure through the mouthpiece with a nose clip on by completing three routine respiration cycles and a fourth cycle of the FVC maneuver. For this maneuver, the volunteer inhaled as deeply as possible to reach maximum lung capacity and then exhaled thoroughly as quickly as possible to maximize airflow in the first second and continued to breach out for at least 6 s to ensure sufficient results. During this process, volunteers were asked to keep their backs straight to ensure the rib cage would not weigh on the abdominal wall which could

decrease the accuracy of the results [22]. After the first trial of the procedure and with the chest appropriately relaxed, the wireless sensors were placed at the designated location and volunteers were asked to repeat the procedure. Due to the design for comfort and convenience, the wireless sensor has minimal effect on the spirometer, allowing the two sensors to be used simultaneously to reduce error due to unexpected variables as much as possible.

## 4 Notes

1. Glossy paper for laser printer can be replaced by photo paper (S400034, EPSON), the alternative silver epoxy will be the part A of silver epoxy.
2. When spreading the silver epoxy over entire circuit, a piece of glossy paper can be used. The glossy side of the paper can smoothly spread the silver epoxy over the circuit without damaging the circuit traces.
3. When using a cotton ball to remove the excess silver epoxy gently, make sure all motions are in the same direction for removal. Moving cotton ball backward and forward will damage the conductive traces.
4. More conductive circuits traces can be made by stacking multiple silver epoxy layers on top of each other. As the number of layers of silver epoxy increases, the circuit traces need more time to be completely dry.
5. Distance between traces being smaller than 0.3 mm is not recommended in order to leave enough space for silver epoxy lateral expansion when spreading the silver epoxy over the entire circuit.
6. To mount the electronics with a package of LFCSP-16 more easily using silver epoxy through microscope, a shrinking standard footprint is very helpful.
7. One end of the copper tape to circuit was connected by silver epoxy, the other end of the copper tape connecting to PVDF film doesn't need additional bonding material to make it conductive if the copper tape was firmly attached to PVDF film. The clamping time is flexible. As long as the resistance measured by a digital multimeter is less than 10 Ω, the copper tape has been firmly attached to the PVDF film. If the resistance is greater than 10 Ω, the width of copper tape can slightly increase. It should not be wider than half of the length of the PVDF film since the copper tape covering more area of the PVDF film will result in worse performance and ultimately a smaller electrical signal.

## Acknowledgments

The authors thanks Boehringer Ingelheim for leasing the spirometer from Vitalograph.

### References

1. Ramanathan AK, Headings LM, Dapino MJ (2018) Near DC force measurement using PVDF sensors. In: SPIE smart structures and materials + nondestructive evaluation and health monitoring. SPIE, Bellingham, Washington, p 13
2. Chen A, Halton AJ, Rhoades RD, Booth JC, Shi X, Bu X, Wu N, Chae J (2019) Wireless wearable ultrasound sensor on a paper substrate to characterize respiratory behavior. ACS Sens 4(4):944–952. https://doi.org/10.1021/acssensors.9b00043
3. Braman SS (2006) The global burden of asthma. Chest 130(1 Suppl):4S–12S. https://doi.org/10.1378/chest.130.1_suppl.4S
4. Gibson GJ, Loddenkemper R, Lundback B, Sibille Y, (2013) Respiratory health and disease in Europe: the new European Lung White Book. Eur Respir J 42(3):559–63
5. Malka J, Spahn JD (2016) When cough wheeze and shortness of breath Don't equal asthma. J Allergy Clin Immunol Pract 4 (1):179–181.; ; quiz 182-173. https://doi.org/10.1016/j.jaip.2015.08.008
6. Milgrom H, Wood RP, Ingram D (1998) Respiratory conditions that mimic asthma. Immunol Allergy Clin 18(1):113. https://doi.org/10.1016/S0889-8561(05)70351-9
7. Cohen KP, Ladd WM, Beams DM, Sheers WS, Radwin RG, Tompkins WJ, Webster JG (1997) Comparison of impedance and inductance ventilation sensors on adults during breathing, motion, and simulated airway obstruction. IEEE Trans Biomed Eng 44(7):555–566. https://doi.org/10.1109/10.594896
8. Semmes BJ, Tobin MJ, Snyder JV, Grenvik A (1985) Subjective and objective measurement of tidal volume in critically III patients. Chest 87(5):577–579
9. Davis C, Mazzolini A, Murphy D (1997) A new fibre optic sensor for respiratory monitoring. Australas Phys Eng Sci Med 20 (4):214–219
10. Eriksson I, Berggren L, Hallgren S (1986) CO2 production and breathing pattern during invasive and non-invasive respiratory monitoring. Acta Anaesthesiol Scand 30(6):438–443
11. Min SD, Yoon DJ, Yoon SW, Yun YH, Lee M (2007) A study on a non-contacting respiration signal monitoring system using Doppler ultrasound. Med Biol Eng Comput 45 (11):1113–1119. https://doi.org/10.1007/s11517-007-0246-2
12. Cop W (1988) Methods devices used in ventilatory monitoring. Encyl Med Dev Instrum 4:2870–2877
13. Nakajima K, Tamura T, Miike H (1996) Monitoring of heart and respiratory rates by photoplethysmography using a digital filtering technique. Med Eng Phys 18(5):365–372. https://doi.org/10.1016/1350-4533(95)00066-6
14. Nilsson L, Johansson A, Kalman S (2000) Monitoring of respiratory rate in postoperative care using a new photoplethysmographic technique. J Clin Monit Comput 16(4):309–315. https://doi.org/10.1023/A:1011424732717
15. Folke M, Cernerud L, Ekstrom M, Hok B (2003) Critical review of non-invasive respiratory monitoring in medical care. Med Biol Eng Comput 41(4):377–383. https://doi.org/10.1007/bf02348078
16. Fenn WO (1951) Mechanics of respiration. Am J Med 10(1):77–90
17. Wade OL (1954) Movements of the thoracic cage and diaphragm in respiration. J Physiol 124(2):193–212. https://doi.org/10.1113/jphysiol.1954.sp005099
18. Guin P, Roy A (2016) Design of efficient loadcell for measurement of mechanical impact by piezoelectric PVDF film sensor. AIP Adv 6 (9):095122. https://doi.org/10.1063/1.4964148
19. Harris GR, Preston RC, Dereggi AS (2000) The impact of piezoelectric PVDF on medical ultrasound exposure measurements, standards, and regulations. IEEE Trans Ultrason Ferroelectr Freq Control 47(6):1321–1335. https://doi.org/10.1109/58.883521
20. O'Reilly MA, Hynynen K (2010) A PVDF receiver for ultrasound monitoring of transcranial focused ultrasound therapy. IEEE Trans Biomed Eng 57(9):2286–2294. https://doi.org/10.1109/TBME.2010.2050483

21. Magori V (1994) Ultrasonic sensors in air. In: 1994 Proceedings of IEEE Ultrasonics Symposium, 31 Oct.-3 Nov. 1994, vol 471, pp 471–481. https://doi.org/10.1109/ULTSYM.1994.401632

22. Agostoni E, Mognoni P, Torri G, Saracino F (1965) Relation between changes of rib cage circumference and lung volume. J Appl Physiol 20(6):1179. https://doi.org/10.1152/jappl.1965.20.6.1179

# Chapter 37

# Forming Large Effective Ultrasound Arrays Using the Swept Synthetic Aperture Technique

**Nick Bottenus**

## Abstract

Ultrasound image quality is intrinsically linked to the hardware used to collect image data. For deep abdominal imaging, diffraction-limited resolution prevents the detection of small targets such as cancerous lesions. Larger ultrasound arrays produce finer lateral image resolution and improved image quality. We introduced a method called "swept synthetic aperture" (SSA) imaging to synthetically create large effective arrays with reduced complexity of both transducer and scanner hardware. A commercial 2-D transducer array and ultrasound scanner were used to form a large effective aperture. Array position and orientation were carefully prescribed throughout a sweep of the transducer using mechanical fixtures to rigidly control the motion. Calibration of the mechanical fixture was measured using a point target phantom and applied in post-processing. Improvements in resolution and contrast as functions of aperture size were measured from point and lesion target phantoms, respectively. SSA imaging presents a technique to both evaluate the performance of large array designs in the presence of clutter-inducing body wall targets and achieve high-quality imaging from reduced-complexity ultrasound hardware.

**Key words** Ultrasound imaging, Large aperture, Synthetic aperture, High resolution, Image quality, Acoustic clutter, Abdominal, Liver

## 1 Introduction

The typical ultrasound array is composed of individual piezoelectric elements connected to transmit and receive circuitry, with the complexity of the required circuitry scaling with the number of elements. Typical element counts for a 1-D (planar) array range from 64 to 256 independently controlled elements. Alternatively, large effective arrays can be formed by coherently combining data from multiple spatial positions after accounting for differences in the propagation path between the positions. A single transducer element or an array of elements are moved across a field of view (mechanically [1] or electronically by multiplexing [2]), varying the spatial interrogation of the target. The "swept synthetic aperture" (SSA) technique [3, 4] is closely related to synthetic transmit

Miguel R. Ossandon et al. (eds.), *Biomedical Engineering Technologies: Volume 1*, Methods in Molecular Biology, vol. 2393, https://doi.org/10.1007/978-1-0716-1803-5_37, 

aperture techniques found in wide-ranging fields beyond ultrasound. The term "synthetic" refers to the combination of data from multiple transmit-receive events to mimic a larger physical array. A ship carrying a sonar transducer or array [5] or an aircraft carrying a radar transducer or array [6] transmits and receives backscattered energy as it moves past a target, forming an effective array much larger than the size of the vessel itself. Similarly, "Earth-rotation synthetic aperture" has been demonstrated using radio telescopes in a very long baseline interferometer to image the M87 black hole event horizon [7]. In ultrasound, swept apertures have been used to produce synthetic aperture volumetric images from linear arrays [8] or even single elements [9]. The SSA technique focuses instead on improving transverse resolution within the imaging plane (or volume) by extending the total coherent aperture size for a fixed bandwidth and imaging depth. Note that this is distinct from the goal of "extended field of view" techniques that use transducer motion to stitch together images in-plane to produce a panorama [10] or out-of-plane to form a volume [11]. SSA imaging can form large effective apertures to produce high-resolution images without the cost or complexity of a large aperture (high element count) imaging system.

In this work, we detail the assembly, calibration, use, and evaluation of the SSA system for ex vivo applications as demonstrated in [12]. Figure 1 shows the assembled sample SSA system.

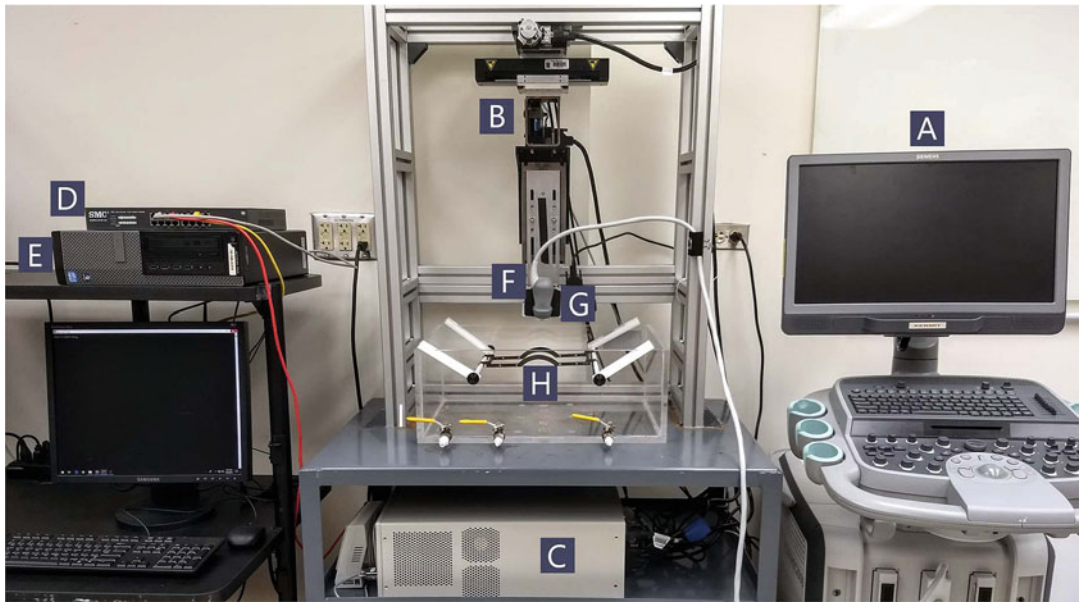


**Fig. 1** Automated swept synthetic aperture acquisition system components. The clinical ultrasound scanner (**a**) and the translation stage (**b**) (with its controller (**c**)), are networked through a switch (**d**) to a controlling PC (**e**) to properly sequence transducer motion and ultrasound acquisition throughout the scan. The matrix array (**f**) is held by a custom transducer holder (**g**) over the tissue frame (**h**) in a water tank (**i**)

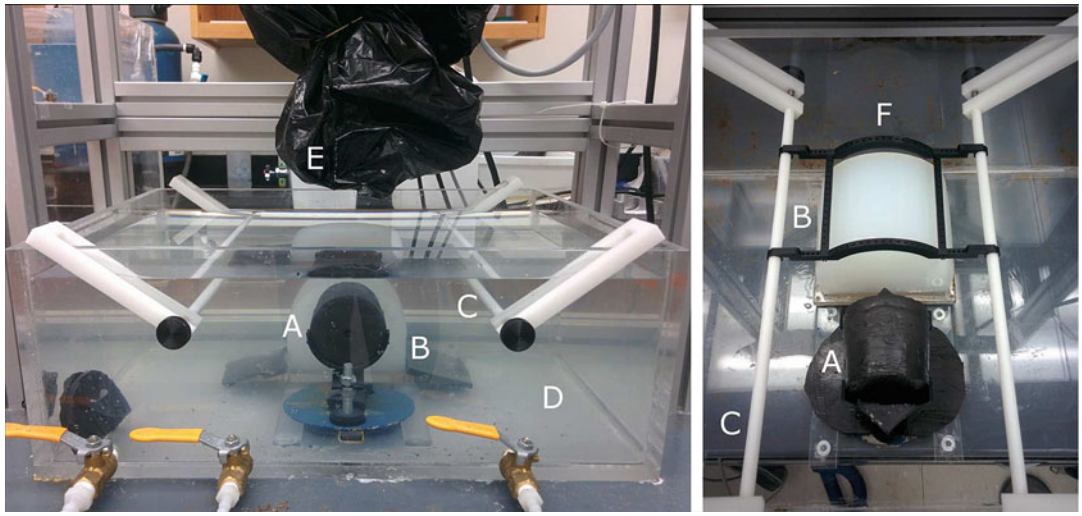


**Fig. 2** Translation stage experimental setup. (**a**) Anechoic lesion target phantom. (**b**) Point target phantom. (**c**) Tissue support rails. (**d**) Saline, sound speed $c \approx 1540$ m/s. (**e**) Volumetric transducer mounted to translation/rotation stage, covered with black plastic except for the face. (**f**) Tissue support structure, pictured positioned over the point target phantom. (Reprinted from [12] with permission from Elsevier)

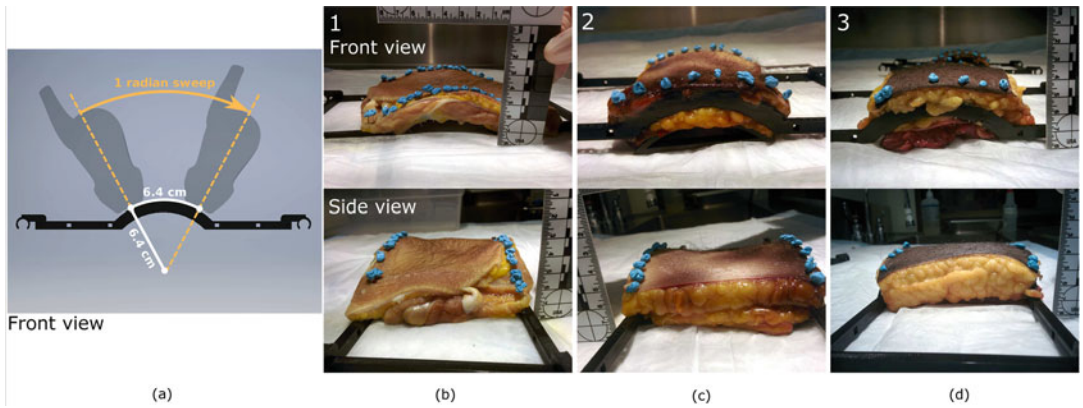


**Fig. 3** (**a**) Tissue holder model for mounting the tissue samples with setup geometry. A 1-radian sweep was performed, giving a 6.4-cm arc length at 6.4-cm radius. (**b–d**) Views of each tissue sample from the front and side after mounting. (Reprinted from [12] with permission from Elsevier)

The goal of this system was to automate and synchronize the motion and ultrasound acquisition process to enable repeatable and relatively rapid sampling of the target. Known imaging targets—points and cylindrical anechoic lesions—were placed in a water tank as in Fig. 2 under an abdominal wall tissue sample shown in Fig. 3 for image quality characterization. A central computer coordinated the other equipment given a preconfigured motion profile. As will be discussed below, the duration of the acquisition depends on the total number of spatial positions desired and the acquisition rate of the scanner. Individual received channel

data were stored for offline processing, so the beamforming procedure is not included in the system diagram. The system required a single spatial calibration procedure before the sample acquisitions were performed and maintained registration for the duration of the experiment. In its most general description, SSA imaging requires ultrasound channel data from overlapping transmissions with known spatial positions. It is important to note that the materials detailed below are only one example of equipment capable of SSA imaging and that similar components can be interchanged where available.

## 2 Materials

### 2.1 Ultrasound Equipment

1. Acuson SC2000 ultrasound system (Siemens Healthineers, Mountain View, CA).
2. Siemens 4Z1c matrix (volumetric) transducer (Siemens Healthineers, Mountain View, CA).
3. SMC EZ Network Switch SMCGS16 (SMC Networks, Irvine, CA) + 3 ethernet cables.
4. Windows PC with ethernet adapter.
5. PsExec software (Microsoft, Redmond, WA).
6. Python software (Python Software Foundation, Wilmington, DE).

### 2.2 Phantom Manufacturing

1. 265 mL deionized water.
2. 14 mL *n*-propanol.
3. 18 g 200 bloom porcine gelatin (Gelatin Innovations Inc., Franklin Park, IL).
4. 45 g 4239 vein graphite powder (Superior Graphite, Chicago, IL).
5. Formaldehyde dilution: 3 mL formaldehyde + 20 mL deionized water.
6. 750 mL beaker.
7. Water bath + thermometer.
8. Vaseline petroleum jelly.
9. Hot plate.
10. Acrylic phantom mold (tapered cylinder 6.3 cm—7.5 cm) + end caps.
11. Vacuum chamber.
12. Custom rotating mold holder (Fig. 4) with Dayton 90 V DC Speed Control and Dayton 4Z135D 1/8 HP DC motor.

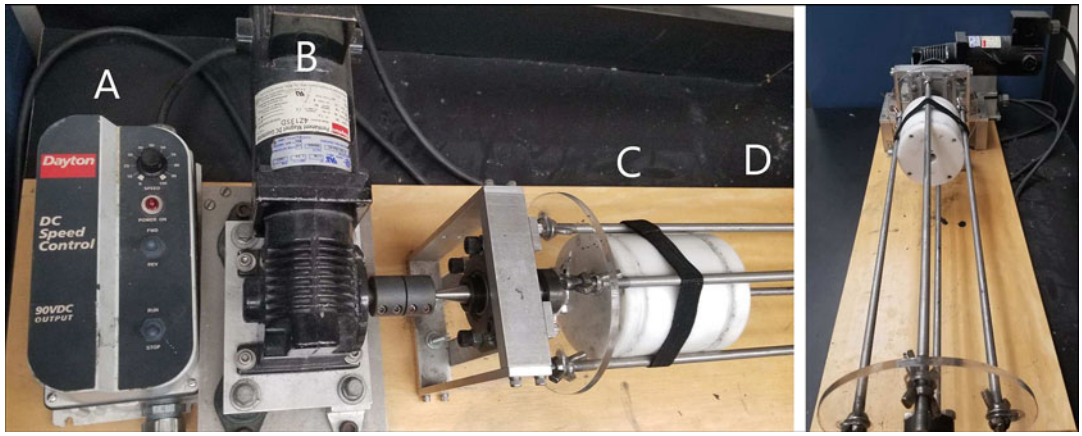


**Fig. 4** Custom rotation apparatus for producing speckle-generating phantoms. A motor controller (**a**) operates a continuous rotation motor (**b**) to turn the acrylic mold (**c**), held tightly by the metal bars (**d**), about its cylindrical axis at approximately 1 rotation per second

13. 9 mm cork borer.
14. 200μm glass beads.

***2.3 Positioning Fixtures***

1. Assorted 80/20 T-slot extruded aluminum and hardware (80/20 Inc., Columbia City, IN).
2. 3 UTM100/ILS100 motorized linear translations stages (Newport, Irvine, CA).
3. 1 URS50 motorized rotation stage (Newport, Irvine, CA).
4. XPS-Q8 motion controller (Newport, Irvine, CA).
5. Soft PLA filament (MatterHackers, Foothill Ranch, CA).
6. Lulzbot Taz 5 3D printer (Aleph Objects, Loveland, CO).

***2.4 Signal and Image Processing***

1. Matlab software (MathWorks, Natick, MA).

## 3 Methods

***3.1 Scanner Pulse Sequence Design***

1. With research support from Siemens, we used the SC2000 ultrasound scanner and a custom sequence to acquire the pulse echo ultrasound channel data from a matrix array. A standard live imaging mode was used to guide initial transducer positioning relative to the target and no data were stored during this phase of the procedure.
2. This scanner was modified to enable an acquisition mode where it would transmit independently from each 3 × 3 element group (1.2 mm × 1.2 mm) along the elevation dimension in the lateral center of the array and store individual

received channel data from 192 (16 × 12) effective elements (3 × 3 groups).

3. A second custom sequence was designed to collect the "complete data set," transmitting on all 3 × 3 element groups on the array in sequence and recording the received channel data.
4. PsExec software from Windows Sysinternals was used to remotely run the acquisition command over the local network from the controlling PC.
5. Data were stored with a temporal sampling rate of 2.5 MHz after baseband demodulation to produce in-phase and quadrature (I/Q) data. Data were transferred over the network to the controlling PC by mounting the scanner storage drive as a network-shared drive.

### 3.2 Phantom Manufacturing

1. Two phantoms were produced to be placed into the water tank and provide a controlled target for image quality assessment (*see* **Note 1**).
2. To make a speckle-generating phantom with a cylindrical anechoic lesion (directions adapted from [13]):
   (a) Coat the inside of the phantom mold with a thin coat of petroleum jelly to allow release of the phantom after cooling.
   (b) Mix the gelatin and n-propanol into the deionized water in a heat-safe beaker at room temperature until dissolved.
   (c) Hold at vacuum (−25 in. Hg) for 5 min to remove air bubbles. Slowly release vacuum to prevent reintroduction of air into the mixture.
   (d) Cover beaker with plastic wrap, create holes for ventilation, and place beaker in a 45 °C water bath for 1 h.
   (e) Remove beaker from water bath and gently stir in graphite to minimize the introduction of air bubbles.
   (f) Allow to cool to 33 °C at room temperature.
   (g) Add the formaldehyde dilution with gentle stirring.
   (h) Pour the mixture into the cylinder mold that had been prepared with petroleum jelly and cap.
   (i) Continuously rotate the mold during cooling at room temperature overnight (*see* **Note 2**).
   (j) Remove the phantom from the mold.
   (k) Use the cork borer to create a hole along the axis of the cylinder (*see* **Notes 3** and **4**).
   (l) The same procedure as above can be used to create a point target phantom, replacing the graphite scatterers with a small number of glass beads (*see* **Note 5**). The point target

phantom used in this experiment was produced by the University of Wisconsin-Madison using 200μm glass beads as scatterers.

### 3.3 Abdominal Sample Mounting

1. Cadaveric anterior abdominal wall samples were excised with IRB approval and frozen for transport without chemical tissue fixation. The samples included skin, subcutaneous fat, muscle, and connective tissue layers and ranged from 26 mm to 49 mm in thickness (*see* **Note 6**).
2. Samples were thawed in a refrigerator for 24 h before mounting.
3. Hair was removed from the skin with a razor.
4. Samples were trimmed with a scalpel to fit the 10 mm × 10 mm tissue frame.
5. In addition to prescreening for infectious disease, samples were handled while wearing protective gloves and all equipment that contacted the tissue were properly disinfected or disposed of.
6. A 3-D printed tissue frame was designed to hold the tissue using straight pins through all tissue layers (*see* **Note 7**). The frame was designed with an arced section with curvature matching the desired scan sweep to maintain firm contact between the transducer and skin (*see* **Note 8**). This frame is pictured in Figs. 1 and 2 without tissue, and Fig. 3 with the mounted abdominal wall.
7. Mounted tissue samples were placed in a bath of 45 g/L saline solution (*see* **Note 9**) at room temperature (23 °C) for at least 1 h and manually massaged to remove air bubbles trapped between the tissue layers.

### 3.4 Translation Stage Setup

1. Motion of the transducer relative to the targets was accomplished by affixing it to an assembled 4-axis translation/rotation stage:
   (a) A rigid frame to support the stages was created using 80/20 aluminum pieces.
   (b) Translational motion was performed in the $X$ (lateral), $Y$ (elevation), and $Z$ (axial) directions by the linear motorized stages (*see* **Note 10**). The three stages were mounted in orthogonal directions with an adjustable mounting plate attached to the $Z$-axis to allow coarse manual positioning of the transducer.
   (c) The rotation stage was connected to the $Z$-axis to provide $X$–$Z$ plane rotation.
   (d) The stages were connected to the motion controller, which was connected to a standard network switch and received motion commands for all axes from the

controlling PC over the ethernet port. The stage responded over ethernet with the actual positions achieved for each axis.

2. An aluminum box was mounted to the rotation stage to accept a transducer mold. The mold was designed by using a 3-D model of the transducer. The model was manually aligned to the *Z*-axis of the stage and rotated to align the long axis of the transducer face with the *X*-axis before subtracting it from the shape of the box (*see* **Note 11**). The complete transducer holder (box and mold) is shown in Fig. 1.
3. The experiment water tank was filled with deionized water at least 24 h in advance (*see* **Note 12**) and salt was added to bring the concentration to 45 g/L. The volume of water was chosen to rise just above the tissue sample height to provide acoustic coupling between the transducer and tissue with minimal contact force.
4. The phantoms were fixed to the bottom of the tank with magnetic fixtures and positioned so that they could both be scanned by moving the transducer in elevation (*see* **Note 13**).

### *3.5 Acquisition Procedure (See Note 14)*

1. Before experimental scanning, a speed of sound calibration scan was performed using the point target. Without the tissue present, 10 acquisitions were performed using the translation stage to move axially by 1 mm between each. By plotting the observed target distance $z_{\text{obs}}$ formed with an assumed speed of sound $c$ against the applied motion $\Delta z$, a linear regression was used to solve for the actual speed of sound $\widehat{c}$:

$$z_{\text{obs}} = \left(\frac{c}{\widehat{c}} - 1\right)\Delta z + \widehat{z}_0$$

2. During each scan, a complete data set acquisition was performed, followed by a sweep acquisition, and finished with another complete data set acquisition to check for consistency. The sweep acquisition consisted of 207 discrete steps of $\lambda/2$ length along a 6.4 cm arc of a 6.4 cm radius circle, with the transducer rotated to face the center (*see* **Note 15**). In total, this sequence could be performed in approximately 20 min with the equipment described (*see* **Note 16**).
3. The scan was performed fully automatically once launched from the controlling PC. For each position, the PC sent a command to the translation stage to move to the next specified location, then sent a command to the scanner to perform an acquisition. At the end of the sequence, the tissue was manually slid in elevation to the other target and the sequence was repeated at that position.

4. The data files were transferred only at the end of all acquisitions for a given tissue sample, while tissue samples were being changed in the water tank.

### 3.6 Individual Frame Beamforming

1. Individual frames of data from each sweep were processed by beamforming using the applied position recorded by the translation stage and the known array geometry. Diverging wave beamforming was used, requiring the time of flight $\tau$ between each transmitting element location $\overrightarrow{x_j}$, the points in the spatial field $\vec{r}$, and each receiving element location $\overrightarrow{x_{ij}}$. Each vector represents the 3-D spatial coordinate, and the receiving element locations vary during the sweep. The spatial field points were held constant between all frames to provide a common grid for beamforming.

$$\tau\left(\overrightarrow{x_j}, \vec{r}, \overrightarrow{x_{ij}}\right) = \frac{\left|\overrightarrow{x_j} - \vec{r}\right| + \left|\vec{r} - \overrightarrow{x_{ij}}\right|}{c}$$

The recorded channel data for $M$ receiving elements were recorded as $s(t, i)$, focused using the time of flight calculated above, and summed across receive channels:

$$s_{foc}\left(\vec{r}\right) = \sum_{i=1}^{M} s\left(t = \tau\left(\overrightarrow{x_j}, \vec{r}, \overrightarrow{x_{ij}}\right), i\right)$$

All data and images were processed using Matlab.

2. The array element locations required for beamforming were calculated by considering both the applied motion $B(i) = TR_y$ (a translation followed by rotation about the y-axis) and an unknown 6-degree-of-freedom transformation $X$. The matrix $X$ represents the calibration of the unknown relationship between the face of the array and the rotation point of the stage, created by positioning within the fabricated mold (*see* **Note 17**). Therefore, the element positions $r_{trans}(i)$ were found from the original array geometry $r$ by:

$$r_{trans}(i) = X^{-1}B(i)Xr$$

### 3.7 Spatial Calibration

1. Spatial calibration to find the matrix $X$ was performed by searching the 6 degrees of freedom space described by the matrix to minimize the reconstruction precision of a point target across beamformed frames within a sweep. Reconstruction precision (RP) was defined for $N$ observations of the point target at locations $p_i$ as:

$$\mathrm{RP} = \left(\frac{1}{N}\sum_{i=1}^{N}\left|\left|p_i - \overline{p}\right|\right|\right)^{\frac{1}{2}}$$

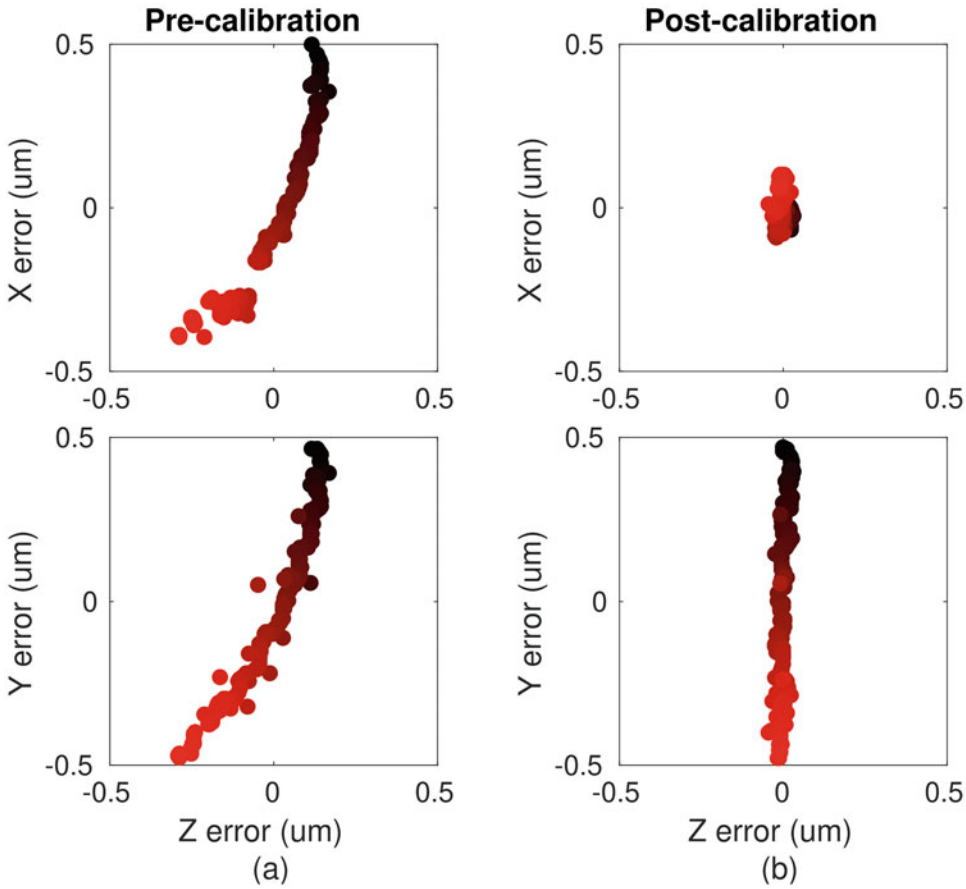


**Fig. 5** (**a**) Pre-calibration reconstruction precision based on caliper measurement of array position. (**b**) Post-calibration reconstruction precision designed to minimize *X*–*Z* plane error, where the resolution will be highest in the SSA image

2. Reconstruction precision was calculated independently for the axial, lateral, and elevation dimensions.
3. Data were acquired before each scanning session without sample tissue present to perform this spatial calibration.
4. To reduce the computational burden of the search, the calibration matrix was initialized using the distance between the point of rotation and the face of the array as measured with calipers. Empirical adjustment was then performed by applying small offsets in each degree of freedom and observing changes in the reconstructed point pattern (*see* **Note 18**).
5. An axial reconstruction precision of 13.9μm and lateral reconstruction precision of 41.4μm was achieved, both significantly less than the point spread function size. The reconstructed points before and after calibration are shown in Fig. 5 (*see* **Note 19**).

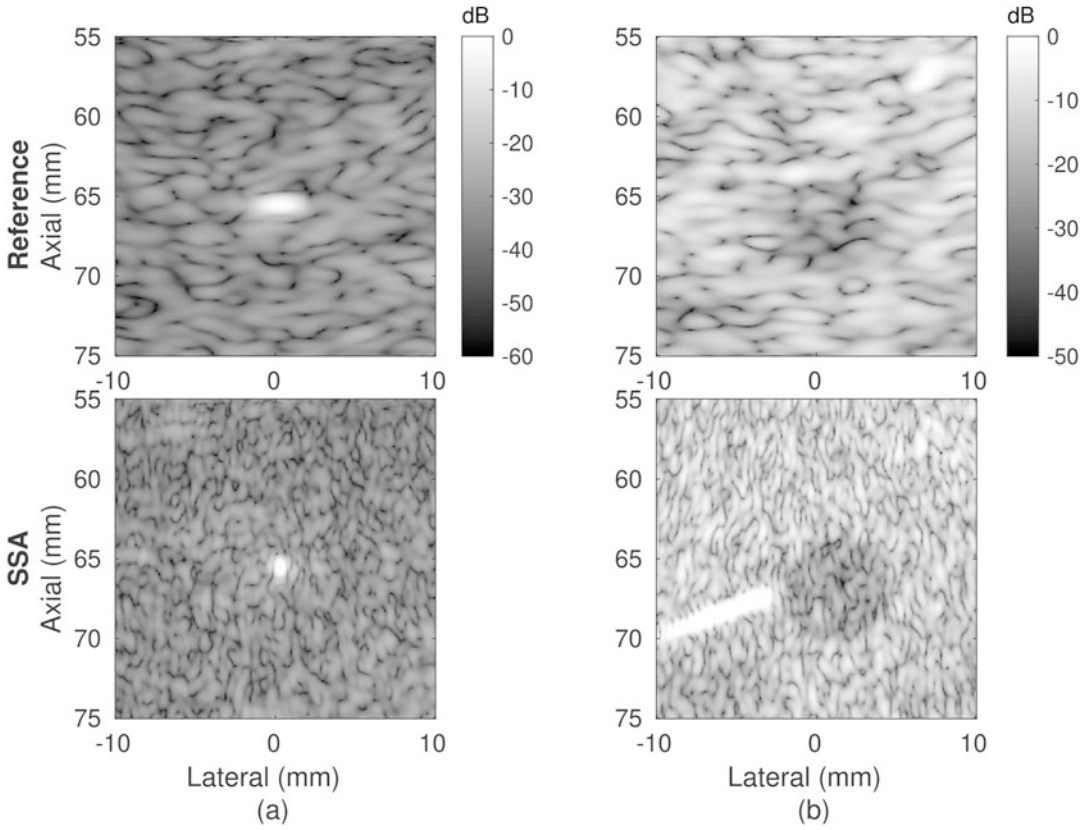


**Fig. 6** Sample reference and SSA images through abdominal wall tissue. (**a**) Point target. (**b**) Anechoic lesion target. A specular reflection from the water tank is visible in the SSA image and is not part of the target

### *3.8 Swept Synthetic Aperture Beamforming*

1. Swept synthetic aperture images were formed following the same procedure as described above but with the calibrated $X$ matrix.
2. All transmissions from a given sequence were beamformed to produce a set of focused RF data frames for a set of 2-D ($X$–$Z$ plane) grid points (*see* **Note 20**).
3. The resulting RF data were then summed coherently across transmissions, envelope detected and logarithmically compressed to produce an SSA image that appears as if it came from a physically larger array, approximately equal to the extent of the sweep (*see* **Note 21**).
4. Sample point and lesion images are shown in Fig. 6 from the reference acquisition and the SSA acquisition (*see* **Note 22**).
5. The SSA data set is useful for several other analyses as well. Apertures of varying effective extents can be produced by summing portions of the available data, as in Fig. 7.
6. Instead of coherent summation, alternative beamforming methods such as spatial compounding or coherence estimation can be performed using the focused RF frames [14] as shown in Fig. 8.

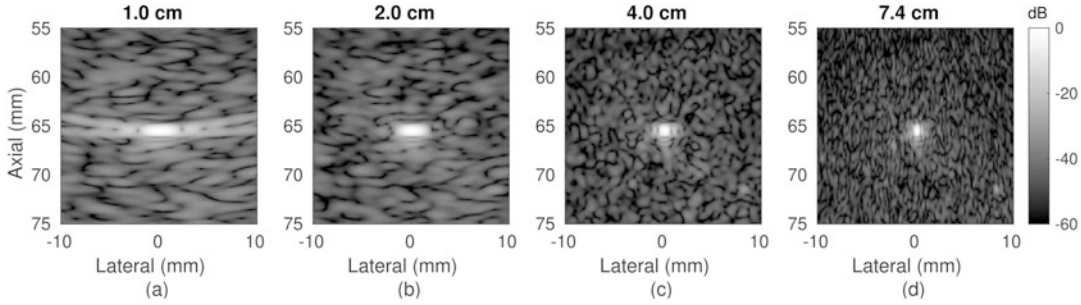


**Fig. 7** SSA images of a point target at various effective aperture sizes (**a**–**d**) in the control case (water path only)

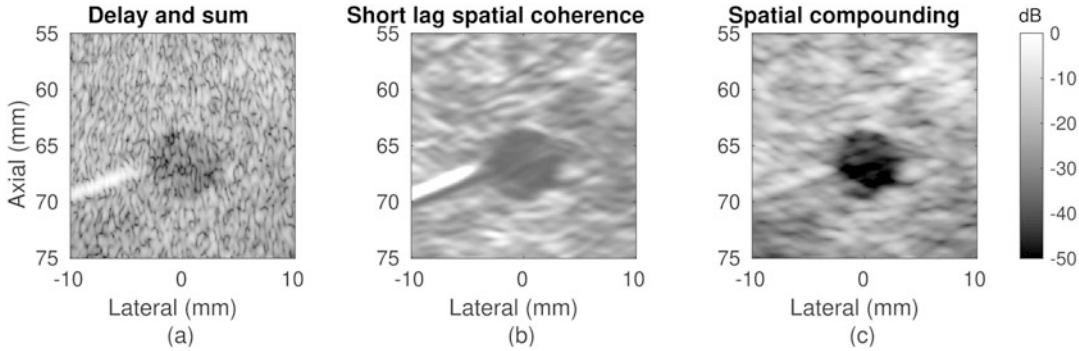


**Fig. 8** Application of several beamforming methods to lesion target SSA data through abdominal wall. Dynamic range of displayed images is matched for visual comparison. (**a**) Delay and sum. (**b**) Short lag spatial coherence. (**c**) Spatial compounding

7. Previous work has demonstrated that these data can also be used to extract arrival time estimates at each position for aberration correction [3].

## 4 Notes

1. The image quality targets selected for this study were chosen to characterize both the imaging system and the degradation of image quality with acoustic clutter. The axial and lateral extents of the point target provide the resolution, while the levels of the side lobes and any distortions to the target predict the effects of off-axis scattering and aberration. An anechoic lesion target provides a way to measure both edge resolution and additive clutter due to reverberation and off-axis scattering. The "contrast-to-noise ratio" provides a single metric based on these two measurements that captures observed contrast, image texture, and resolution [15]. These targets do not provide imaging contrast—the ability to resolve targets with

different scattering strengths—as we do not expect SSA to behave differently from conventional imaging in this regard.

2. Rotation prevents the graphite from settling during cooling, providing a uniform distribution of sub-wavelength particles to produce speckle. *See* Fig. 4 for a custom rotation apparatus that spins the cylindrical mold along its axis at roughly 1 rotation per second.
3. The cork borer creates a hole that is slightly smaller than its own diameter due to compression of the material during cutting.
4. The lesion phantom can be used with a hole in the middle but may trap air bubbles when placed in the water tank or deform under its own weight. The phantom procedure can be repeated omitting graphite scatterers and the mixture poured into the hole to produce a more stable low-scattering target.
5. The number of glass beads should be chosen to be sufficiently low as to isolate individual beads in the final phantom but high enough to make it likely that a bead ends up near the middle for scanning. Alternatively, a bead can be placed into the phantom during cooling and the rotating step omitted, but precise timing is required to avoid the bead either sinking to the bottom or leaving a track in the partially cooled material.
6. The effects of the different tissue layers on acoustic clutter generation is largely unknown and still under investigation.
7. Although sutures would hold the tissue more firmly than straight pins, we found it difficult to cut through all tissue layers with a suture needle and thread.
8. The tissue frame and rail system were designed with sufficient length to keep the acrylic rails away from the target structure, preventing bright off-axis scattering.
9. The salinity used in the sample water tank was higher than that of the body but was not expected to change the tissue properties significantly over the duration of the experiment. This concentration at 23 °C provides a speed of sound of 1540 m/s to mimic the body.
10. The linear translation stages maintain 5μm on-axis accuracy with a maximum travel range of 100 mm. The rotation stage provides 0.03° accuracy. The motorized stages used were selected for a combination of sub-wavelength accuracy and travel speed.
11. Any misalignment in the transducer orientation to the directions of motion caused by the mold-making or mounting process was compensated for during the calibration step.
12. Allowing the water tank to sit after filling ensures that bubbles and dissolved air are allowed to escape before phantoms and tissues are introduced.

13. The tissue needed to be slid manually from one phantom to the other along the rails, meaning that the two targets did not necessarily receive the same acoustic clutter realization.
14. The sample acquisition procedure was designed with several goals in mind:
    (a) Minimize the duration of the scan to reduce the chance of tissue sample degradation.
    (b) Scan both point and lesion targets repeatably between samples to test only the changing acoustic clutter realization.
    (c) Ensure that the tissue and target did not move during the sweep scan due to contact between them.
15. The spacing of the swept synthetic aperture scan was selected to prevent the appearance of grating lobes in the final beamformed image from the synthetic array. The sweep radius and extent were dictated by the finite extent of the translation stage used, after including the 39 mm offset from the rotation point to the face of the array.
16. The sweep acquisition was automated using Python to control the translation stage and ultrasound scanner in sequence. The scan time was mostly accounted for by the channel data acquisition tools and could be reduced by using a research-grade system designed for parallel channel data access. We demonstrated the use of such a parallel channel data system in [3] using different ultrasound and positioning equipment and, as a result, a different acquisition procedure. We used a Verasonics Vantage research system that was designed for rapid channel data acquisition, but only had access to a phased array (1-D) instead of a matrix array. We designed a manually operated rotating arm with encoder-based measurement to allow for a faster sweep than a motorized system would. Rather than use a central controlling PC, the Verasonics scanner triggered a recording from the encoder each time it made a transmission. This resulted in a data set equally spaced in time rather than space. The data were resampled to provide more equal spatial spacing before beamforming in order to produce a more evenly sampled $k$-space and in turn a better point spread function.
    Although the beamforming procedure was the same as described above, the calibration procedure required for a 1-D array is slightly different from the 2-D case. It is not possible to directly visualize the 3-D point target location from the $X$–$Z$ plane, making the calibration problem underdetermined. Several groups have proposed specific phantoms for this case [16]. In our application, the rotating arm restricted the motion to the $X$–$Z$ plane such that we could assume that only small deviations in the elevation

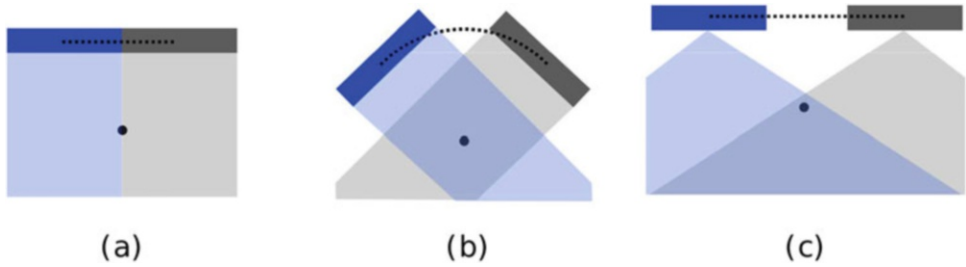


**Fig. 9** (**a**) Plane wave transmission limits the spatial extent of the sweep. (**b**) Rotation allows for extension of both the effective transmit and receive apertures. (**c**) Diverging transmit similarly enables effective aperture extension, with or without rotation

dimension would occur and would fall under the elevation slice thickness. Calibration was therefore performed as before to minimize reconstruction precision in the $X$–$Z$ plane, allowing only small changes to the calibration in the $\Upsilon$ axis and $X$–$\Upsilon$ and $\Upsilon$–$Z$ rotation dimensions.

17. For the reference complete data set acquisition, application of the calibration matrix is not necessary and only affects the positioning of the target in the frame, not the quality of the beamformed image. However, to match the complete data set and swept aperture images, the same calibration was used for both cases.
18. It was observed that translation in the elevation plane and rotations about the $\Upsilon$-axis had little effect on the reconstruction and that these could be omitted from the calibration optimization process.
19. Reconstruction precision in the $X$–$Z$ plane was prioritized in the optimization because the low resolution in the $\Upsilon$-axis of the synthesized permitted more uncertainty.
20. Although planar data were created during beamforming, these represent full 3-D focusing from the matrix array. Alternatively, a 3-D volume could be created.
21. The effective aperture size is dictated by both the transmit and sweep geometries, as shown in Fig. 9. In the most limited case, a plane wave transmission (zero delay, whole aperture) restricts the field of view from each transmission to directly in front of the array. For a linear scan, the transmit field is nearly constant with respect to the transducer position, so the effective transmit aperture size is the same as the physical array extent. The receive aperture extent is equal to two aperture lengths, corresponding to the array entirely to the left and right of the target. The effective aperture size is therefore $1.5\times$ the original array length, providing minimal benefit.

    The plane wave case can be improved by either adaptively steering the plane wave towards the target or rotating the array

during the sweep. The total effective array size is then only limited by element angular sensitivity and available sweep extent respectively. Transmitting a diverging wave also removes the effective size constraint, as the wave can reach beyond the footprint of the array even in a linear scan. For an opening angle of $\theta$ in front of the array, the achievable transmit $F$-number is $F = \frac{z}{D} = \frac{1}{2\tan(\theta/2)}$ in a linear scan. An opening angle of 53.1 degrees is sufficient to achieve $F/1$ imaging in this scan format. The effective receive aperture size is one array length longer than the transmit aperture size due to the half-array extent on either side of the sweep. In this work, a diverging wave was combined with a rotating scan to ensure the target remained in the field of view across all selected positions. The effective aperture size was therefore the extent of the sweep plus half the physical aperture extent.

22. SSA images are expected to differ from images formed by a fully sampled large array of the same extent. This is most clearly illustrated in $k$-space [17], where a fully sampled array produces a triangle weighting in the lateral dimension and most heavily emphasizes low spatial frequencies. A swept synthetic aperture forms an individual rectangle in k-space at each transducer location (due to the lack of transmit focusing), which then coherently sum to form a trapezoid. The trapezoid weights all included spatial frequencies roughly equally, resulting in an image with higher lateral spatial frequency content than usual. SSA images have higher apparent lateral resolution than expected and often have some lateral ringing artifacts due to the higher frequencies.

    A more conventional image can be formed by $k$-space filtering, correcting the trapezoid to the triangle shape in the summed RF data. Alternatively, the individual transducer position data can be weighted to the correct shape because each position approximately corresponds to a lateral location in $k$-space. In practice, we have found that using a Tukey window for the correction weights gives the best visual impression even though it does not truly restore the triangle shape (the low-frequency weights are too low).

    We also expect that the clutter realization will be different between a fully sampled array and an SSA acquisition. In the SSA acquisition, transmit and receive propagation only occurs within the physical extent of the array even though the synthesized array will extend further. A fully sampled array forms propagation paths from one end of the array to the other, possibly providing more spatially varied clutter realizations. We believe that this will lead to more severe acoustic clutter for SSA imaging than in the fully sampled array case.

## References


1. Ylitalo JT, Ermert H (1994) Ultrasound synthetic aperture imaging: monostatic approach. IEEE Trans Ultrason Ferroelectr Freq Control 41(3):333–339
2. Corl PD, Grant PM, Kino GS (1978) A Digital Synthetic Focus Acoustic Imaging System for NDE. In: 1978 Ultrason. Symp. IEEE, Cherry Hill, NJ, USA, pp 263–268
3. Bottenus N et al (2016) Feasibility of swept synthetic aperture ultrasound imaging. IEEE Trans Med Imaging 35(7):1676–1685
4. Zhang HK, Cheng A, Bottenus N, Guo X, Trahey GE, Boctor EM (2016) Synthetic tracked aperture ultrasound imaging: design, simulation, and experimental evaluation. J Med Imaging 3(2):027001
5. Hansen RE (2011) Introduction to Synthetic Aperture Sonar. In: Kolev PN (ed) Sonar systems. InTech, London, pp 3–29
6. Wiley CA (1985) Synthetic aperture radars–a paradigm for technology evolution. IEEE Trans Aerosp Electron Syst 21(3):440–443
7. Akiyama K et al (2019) First M87 event horizon telescope results. II. Array and instrumentation. Astrophys J 875(1):L2
8. Andresen H, Nikolov SIS, Pedersen MMM, Buckton D, Jensen JA (2010) Three-dimensional synthetic aperture focusing using a rocking convex array transducer. IEEE Trans Ultrason Ferroelectr Freq Control 57 (5):1051–1063
9. Andresen H, Nikolov SI, Jensen JA (2011) Synthetic aperture focusing for a single-element transducer undergoing helical motion. IEEE Trans Ultrason Ferroelectr Freq Control 58(5):935–943
10. Weng L, Tirumalai A, Lowery C (1997) US extended-field-of-view imaging technology. Radiology 203(3):877–880
11. Treece GM, Gee AH, Prager RW, Cash CJ, Berman LH (2003) High-definition freehand 3-D ultrasound. Ultrasound Med Biol 29 (4):529–546
12. Bottenus N, Long W, Morgan M, Trahey G (2018) Evaluation of large-aperture imaging through the ex vivo human Abdominal Wall. Ultrasound Med Biol 44(3):687–701
13. Anderson PG, Rouze NC, Palmeri ML (2011) Effect of graphite concentration on shear-wave speed in gelatin-based tissue-mimicking phantoms. Ultrason Imaging 33(2):134–142
14. Bottenus N, Üstüner KF (2015) Acoustic reciprocity of spatial coherence in ultrasound imaging. IEEE Trans Ultrason Ferroelectr Freq Control 62(5):852–861
15. Smith SW, Wagner RF, Sandrik JM, Lopez H (1983) Low contrast detectability and contrast/detail analysis in medical ultrasound. IEEE Trans Sonics Ultrasonund 3(3):164–173
16. Mercier L, Langø T, Lindseth F, Collins DL (2005) A review of calibration techniques for freehand 3-D ultrasound systems. Ultrasound Med Biol 31(4):449–471
17. Walker WF, Trahey GE (1998) The application of k-space in pulse echo ultrasound. IEEE Trans Ultrason Ferroelectr Freq Control 45 (3):541–558

# Chapter 38

# Quantitative Bioluminescence Tomography for In Vivo Volumetric-Guided Radiotherapy

**Zijian Deng, Xiangkun Xu, Hamid Dehghani, Daniel M. Sforza, Iulian Iordachita, Michael Lim, John W. Wong, and Ken Kang-Hsin Wang**

## Abstract

Several groups, including ours, have initiated efforts to develop small-animal irradiators that mimic radiation therapy (RT) for human treatment. The major image modality used to guide irradiation is cone-beam computed tomography (CBCT). While CBCT provides excellent guidance capability, it is less adept at localizing soft tissue targets growing in a low image contrast environment. In contrast, bioluminescence imaging (BLI) provides strong image contrast and thus is an attractive solution for soft tissue targeting. However, commonly used 2D BLI on an animal surface is inadequate to guide irradiation, because optical transport from an internal bioluminescent tumor is highly susceptible to the effects of optical path length and tissue absorption and scattering. Recognition of these limitations led us to integrate 3D bioluminescence tomography (BLT) with the small animal radiation research platform (SARRP). In this chapter, we introduce quantitative BLT (QBLT) with the advanced capabilities of quantifying tumor volume for irradiation guidance. The detail of system components, calibration protocol, and step-by-step procedure to conduct the QBLT-guided irradiation are described.

**Key words** Bioluminescence tomography, Small animal irradiation, Image-guided radiation therapy

## 1 Introduction

A major challenge facing investigators is to correctly deliver radiation to animal models, so that their preclinical investigations are closely aligned with clinical practice. Our group has developed the SARRP to resemble a clinical radiation machine [1–4]. SARRP employs a dual focal X-ray source for irradiation and CBCT imaging. For irradiation, the X-ray source combined with a 360° isocentric gantry and a 4D robotic couch can achieve noncoplanar radiation delivery. CBCT imaging is acquired by rotating animal between the stationary X-ray source and detector panel. While CBCT provides valuable irradiation guidance [5–7], it is unable to localize soft tissue targets growing in a low image contrast environment.

Miguel R. Ossandon et al. (eds.), *Biomedical Engineering Technologies: Volume 1*, Methods in Molecular Biology, vol. 2393, https://doi.org/10.1007/978-1-0716-1803-5_38, 

Because of strong soft tissue contrast and nonionizing features, bioluminescence imaging (BLI) offers an attractive solution to localize soft tissue targets. Although BLI has been extensively applied in preclinical oncology studies [8–10], the resulting 2D image on the animal surface is inadequate to guide radiation delivery. Because optical transport from an internal light source is highly susceptible to the irregular torso and tissue optical properties, BLI of the surface emission cannot be used reliably to infer the internal source location for radiation guidance [11]. This recognition led us to integrate 3D BLT with SARRP for target localization [12, 13]. In BLT, a forward model of light propagation through tissue to the skin surface is employed, in conjunction with an optimization algorithm, to reconstruct the underlying 3D source distribution, which minimizes the difference between calculated and measured surface BL signal.

We introduce our innovation QBLT, which incorporates several important developments to achieve quantitative optical imaging, beyond our previous development BLT-reconstructed center of mass (CoM)-guided RT [12, 13]. To address the ill-posedness of optical tomography inverse problem, a multi-projection and multispectral approach was developed to maximize the available data points for optical reconstruction. The bioluminescence commonly used in biology studies is in the wavelength range of 450–700 nm. The efficiency of the light penetration through an animal from its origin at this wavelength range largely depends on the overlying tissue scattering and absorption properties, and the penetration depth is expected to be less than 5 mm. Widely used single projection 2D BLI is inevitably subject to the penetration limitation, especially for deep-seated target. The multi-projection setting therefore provides the researcher the option to image target at the location with optimal efficiency of light penetration. Due to our noncontact imaging geometry, the accurate mapping of the measured signal on a 2D detector, charge coupled device (CCD), plane onto the 3D surface of animal CBCT image is necessary to ensure a precise target reconstruction. An optimization approach was developed to retrieve the system geometrical parameters and achieve an accurate mapping [14]. Multispectral BLT heavily relies on the accurate quantification of the emission spectrum of bioluminescent tumor cells and the temporal change of in vivo signal. The methodology and steps for quantifying the spectrum and in vivo signal used in the multispectral BLT is described. Because of the noncontact imaging geometry, the light propagation from tissue surface to CCD detector was accounted. A spectral derivative (SD) BLT algorithm was proposed recently [15] and adapted to our BLT system. This algorithm effectively eliminated the known issue of free space light propagation error. To ensure radiation coverage and QBLT uncertainties in target localization, we have

also determined a target margin in line with clinic practice for conformal RT.

Our BLT system is a standalone platform. Its integration with SARRP is carried out by a transportable mouse bed which allows imaged animal transferred between the systems. The fiducial markers attached on the bed can be imaged in both systems to register the coordinate of the optical system and SARRP. An orthotopic bioluminescent glioblastoma (GL261-*Luc2*) model growing in a low CBCT imaging contrast environment is chosen as an example to demonstrate the procedure of conducting QBLT-guided RT in vivo. In the following sections, we provide the details of our system components and calibration procedure, and surgical and study protocol. We expect that with the step-by-step details outlined in this chapter, one would be able to realize the requirements and understand the insight to perform optical tomography-guided irradiation.

## 2 Materials

### 2.1 BLT System Components

The BLT system is built as a standalone and mobile system. It consists of a transportable mouse bed with a support, an optical assembly, a thermostatic system, a 1D-linear stage, and a computer console. The optical assembly includes a light-tight enclosure, a CCD camera, a lens, a filter wheel, a 3-mirror system, a rotary stage, and four LEDs. The thermostatic system includes a resistor, a thermocouple, a thermocouple monitor, seven fans, and a heat gun.

1. Transportable mouse bed is in-house constructed and used for holding imaged object in the optical system and SARRP as well as for supporting the animal transfer between the two systems. The bed base consists of a frame, a central circular plate, and a nose cone connected with two anesthesia hoses (inner diameter: 3.2 mm, outer diameter: 6.4 mm; U.S. Plastic Corp., Lima, OH). Eight ball bearings (BBs, polytetrafluoroethylene, 3/32″ diameter; McMaster-Carr, Elmhurst, IL), glued on the bed, are used as the fiducials to register the coordinates of BLT system and SARRP.
2. Mouse bed support is used to hold the bed at imaging position. The support consists of a T-slotted aluminum extrusion, a spacer, and a clamp lock. The mouse bed can be fixed firmly by using the clamp lock to hold the mouse bed tightly.
3. Light-tight enclosure, black acrylic painted with nonreflective black paint, is home-built to shield ambient light from bioluminescent signal emitted from imaged objects. The front end of light-tight enclosure is imaging chamber.

4. Charge coupled device (CCD) camera (iKon-L 936, Andor Technology, Belfast, UK, 27.6 mm × 27.6 mm back-illuminated sensor at 13.5-μm pixel size, operating at −80 °C) is used for image acquisition.
5. Lens (50-mm, f/1.2; Nikkor, Nikon Inc., Melville, NY) is used to focus the optical signal from imaging plane to CCD camera.
6. Filter wheel (Edmund Optics Inc., Barrington, NJ) is used to mount band-pass filters ($\lambda = 590, 610, 630, 650$ nm, full width at half maximum (FWHM) = 20 nm, transmission >90%; Chroma Technology Corp., Bellows Falls, VT) to achieve multispectral image acquisition.
7. Three-mirror system (silver-coated glass mirrors with 98% reflectivity, H. L. Clausing, Inc., Skokie, IL) is used to direct the optical signal emitted from imaged object to the filter-lens-CCD.
8. Rotary stage, which consists of a microstep stepper motor with built-in controller (item # CRK523PMBKP; Oriental Motor, Torrance, CA), a timing belt (Catalog # A 6Z16-068037; SDP/SI, Hicksville, New York) and two timing pulleys (Catalog # A 6A16-020DF3706 (small), A 6M16-048DF2508 (big); SDP/SI, Hicksville, New York), is used to rotate the 3-mirror system to capture the optical signal at different projection angles around imaged object.
9. Four blue light emitting diode (LED) sources (peak at 468 nm; Digi-Key Part Number: 160-1827-1-ND; Lite-On Inc., Milpitas, CA) are used to illuminate imaged object and the BBs on the mouse bed to identify the positions of these objects.
10. Resistor, acquired from an egg incubator (Brower Equipment, Houghton, IA), is used to raise and maintain the temperature of the imaging chamber.
11. Thermocouple, acquired from the egg incubator, is used to measure the temperature of the imaging chamber.
12. Thermocouple monitor, acquired from the egg incubator, is used for displaying the temperature measured by the thermocouple.
13. Seven fans (Digi-Key Part Number: 102-4362-ND; CUI Inc., Tualatin, OR) are used to circulate hot air in the imaging chamber.
14. Heat gun (TR89200, 1500 W; TR Industrial, Pomona, CA) is used to boost the temperature to 37 °C before bioluminescence imaging session.
15. One-dimensional linear stage (Parker 406XR, B.W.Rogers Co, Morgantown, PA) is used to drive the optical assembly to dock into the transportable mouse bed.

16. Computer console is used to control the CCD camera for image acquisition, and the movement of filter wheel, rotary stage, and 1D linear stage. It consists of a mainframe, which is positioned in mobile cart cabinet, and accessories including a monitor, a keyboard, and a mouse, which are supported by a cantilever linked to mobile cart frame.
17. Mobile cart, which is made of T-slotted aluminum extrusions and acrylic boards, mechanically supports all components of the BLT system. It consists of a cabinet and a cart frame. The cabinet accommodates the computer mainframe and power connections to all BLT components. The cart frame is used to support the optical assembly, thermostatic system, computer accessories with cantilever, and transportable mouse bed with mouse bed support.

### 2.2 SARRP Components

SARRP (Xstrahl Inc., Suwanee, GA) is commercially available, and the detail of the system can be found in Refs. 1–4. In this section, we list the main SARRP components.

1. Radiation shielding protects operator from SARRP radiation exposure.
2. Sliding door equipped with a leaded glass window provides an access to the interior space of SARRP.
3. Dual focal X-ray source; 0.4-mm and 3-mm focal spot are used for CBCT imaging and irradiation, respectively.
4. Isocentric gantry is able to rotate the X-ray source at 360° for irradiation.
5. Four-dimensional robotic base is used to position the animal in $x$, $y$, $z$ translation and 360° rotation.
6. Mouse bed support is used to hold the transportable bed at position for imaging and irradiation. The bed is fixed firmly by a clamp lock.
7. Amorphous silicon flat panel detector (20.5 cm × 20.5 cm, 200 μm pixel pitch) is used to capture X-ray projection image for CBCT imaging.
8. Collimating cone assembly is used to collimate the X-ray beam into desired field size. The collimator is available in the size of 0.5 and 1 mm in diameter circular field, 3 × 3, 5 × 5, and 10 × 10 $mm^2$ square field, and 3 × 9 $mm^2$ rectangular field in our institute.
9. SARRP graphical user interface (GUI) is used to control SARRP CBCT imaging and irradiation.
10. MuriPlan (version 2.2.0), a SARRP treatment planning system, is used to design radiation plan, based on the coordinate

defined by SARRP CBCT image and QBLT-delineated target volume.

### 2.3 Software for System Design, Optical Data Acquisition, and Analysis

1. PTC Creo (version 3.0; Parametric, Needham, MA, US) is used for mechanical design.
2. Andor Solis (Version 4.24.30004.0, Andor Technology, Belfast, UK) is used to control the CCD camera for image acquisition.
3. Optec HSFW Control (Edmund Optics Inc., Barrington, NJ) is used to control the filter wheel and change filters for multispectral imaging.
4. Home-built motor control GUI, coded in C++ language, was designed to control the motor of the 1D linear stage and the rotary stage in the BLT system.
5. MATLAB (version R2019b; The MathWork Inc., Natick, MA) was chosen as the programming platform for data post-processing and optical reconstruction.
6. NIRFAST (version 8.0) [16–18] was chosen as the platform for the finite element 3D calculation for continuous wave optical tomography reconstruction. We adapted the NIRFAST in MATLAB environment for our QBLT reconstruction routine.
7. NIRView (version 1.12 Beta; Kitware, Inc., Clifton Park, New York) is used to segment mouse body from SARRP CBCT image for QBLT reconstruction.
8. 3D Slicer (version 4.10.2) [19–21] is used for contouring contrast-labeled GBM for QBLT validation, generating the contour from QBLT reconstructed target volume, and adding a margin to the reconstructed volume to form a planning target volume.

### 2.4 Materials for GBM Cell Culture

Although cell culture is a common protocol, we provide the detail of our materials as well as the process described in Subheading 3 to facilitate the reproducibility, if one would like to repeat the study.

1. GL261-*Luc2* cell line is cultivated to establish orthotopic BL GBM mouse model.
2. Water bath (Model 182; Precision Scientific Inc., Chicago, IL) is used for thawing the reagents used for cell cultivation.
3. Biological safety cabinet (SterilGARD III Advance; Baker, Sanford, ME) provides a sterile working environment for cell cultivation.
4. Micropipettes (2–20, 20–200, 100–1000 μL; Eppendorf, Hauppauge, NY) mounted with matched sterile tips (Eppendorf, Hauppauge, NY) are used to dispense small liquid volume.

5. Pipette controller (Accu-jet® pro; BrandTech Scientific, Essex, CT) mounted with a sterile serological pipette (1, 2, 5, 10, 25 mL; Falcon®, Corning Inc. Life Sciences, Durham, NC) is used to dispense large measured volume of liquid.
6. T25 tissue culture flask (25 $cm^2$ surface area for approximate $2.8 \times 10^6$ cells; Sarstedt, Newton, NC) is used as the plate for cell cultivation after cell thawing.
7. T75 tissue culture flask (75 $cm^2$ surface area for approximate $8.4 \times 10^6$ cells; Sarstedt, Newton, NC) is used as the plate for cell passaging when the cells reach 80–90% confluency in T25 flask.
8. Dulbecco's modified eagle medium (DMEM; Gibco™; Life Technologies Corp., Grand Island, NY) is used as the medium for cell culture.
9. Fetal bovine serum (FBS; BenchMark™; Gemini, West Sacramento, CA) is mixed with DMEM at 10% concentration for cell culture.
10. Phosphate buffer solution (PBS; pH 7.4, 1×) is used for washing the plate to remove the serum in the medium, so that trypsin will be able to detach the cells from the plate.
11. Trypsin-EDTA (0.05%, 1×; Gibco™; Life Technologies Corp., Grand Island NY) is used to dissociate the cells from the plate.
12. Conical centrifuge tube (50-mL, Sarstedt, Newton, NC) is used to contain the medium with dissociated cells for centrifuging.
13. Centrifuge (5810R, Eppendorf, Hauppauge, NY) is used to centrifuge the dissociated cells from the medium in the 50 mL conical centrifuge tube.
14. Trypan blue (0.4%; Gibco™; Life Technologies Corp., Grand Island NY) is used to stain the dead cells for cell counting.
15. Eppendorf tube (1 mL, Eppendorf, Hauppauge, NY) is used for cell counting and intracranial injection.
16. Automated cell counter (Cellometer Auto T4; Nexcelom Bioscience, Lawrence, MA) with cell counter slide (two 20-μL chambers, Nexcelom Bioscience, Lawrence, MA) is used for cell counting.

### 2.5 Common Materials for Animal Preparation for Surgery and Imaging

1. Heat pad (IPower, Irwindale, CA) is used to keep animal warm to reduce the risk of hypothermia.
2. Ultra-fine insulin syringe (0.5-mL; BD, Franklin Lakes, NJ) is used for intraperitoneal (IP) and subcutaneous injection.

3. Clipper (Model 9918C; WAHL Clipper Corp., Sterling, Illinois, IL) and hair remover lotion (Nair™; Church & Dwight Co., Inc., Ewing, NJ) are used to remove animal hair.
4. C57BL/6 mice (6–8 weeks old, female; The Jackson Laboratory, Bar Harbor, ME) are used for in vivo GBM implantation and BLT imaging. We use 25 g as the conservative animal weight to calculate the volume of the injected solution.
5. D-Luciferin (30 mg/mL, 150 mg/kg dosage, about 125 μL per 25 g mouse; PerkinElmer, Waltham, MA) is used as light-emitting compound for bioluminescence generation through the catalysis process by luciferase.
6. Lubricant eye ointment (LubriFreshTM P.M.; Major® Pharmaceuticals, Livonia, MI) can be used for preventing dryness of mouse cornea during long-term anesthesia.
7. Iodixanol agent 160 μL with iodine at 320 mg/mL (Visipaque, GE Health Care, Chicago, IL) was administrated through retro-orbital injection for contrast CBCT imaging.

### 2.6 Anesthesia

Two types of anesthetics can be used for the survival surgery of GBM model preparation: Ketamine-Xylazine mixture (IP-injected anesthetic) and isoflurane-oxygen airflow (inhalation anesthetic).

The materials for Ketamine-Xylazine mixture are listed below:

1. Ketamine (100 mg/mL, 90 mg/kg dosage, 22.5μL per mouse; KetaVed®; Vedco Inc., St. Joseph, MO) is mixed with Xylazine for IP-injected anesthetic.
2. Xylazine (100 mg/mL, 10 mg/kg dosage, 2.5 μL per mouse; XylaMed™; Bimeda, Inc., Le Sueur, MN) is mixed with Ketamine for IP-injected anesthetic.
3. PBS (pH 7.4, 1×) is used for resolving the Ketamine and Xylazine at 9:1 ratio.

The materials for isoflurane-oxygen airflow are listed below:

1. Isoflurane vaporizer (E-Z Anesthesia; Euthanex Corp., Palmer, PA) is used for vaporizing isoflurane (Fluriso™, VETOne®; MWI Animal Health, Boise, ID) mixed with oxygen to make inhalation anesthetic.
2. Anesthesia box is utilized for anesthesia induction for imaged animals.
3. Two hoses (inner diameter: 6.4 mm, outer diameter: 9.5 mm; U.S. Plastic Corp., Lima, OH) are linked to the isoflurane vaporizer to conduct the anesthesia gas to the BLT system and SARRP, respectively.

### 2.7 Survival Surgery for Intracranial Injection

1. Buprenorphine-SR LAB (1 mg/mL, 1 mg/kg dosage, 25 μL per mouse; Zoopharm, Windsor, CO) is used for preemptive analgesia.
2. Two-in-one LED lamp with magnifying lens (2.25× magnification; LightView™; Brightech Inc., Van Nuys, CA) is used to provide illumination and magnification during surgery.
3. Povidone-iodine solution (10%, 1% iodine; Dynarex, Orangeburg, NY) is used for sterilizing mice scalp before incision.
4. Cotton swab is used for soaking povidone-iodine solution for sterilization. We also use the cotton swab for cleaning the blood around incision site during surgery.
5. Stainless steel scalpel (Miltex Inc., York, PA) is used for incising mice scalp.
6. The materials from the vendor Stoelting (Wood Dale, IL) for animal surgery are included in this point; (1) stereotaxic instrument (Catalog No. 51730) is an integrated apparatus for the animal surgery, which includes a base, a 100-μm-ruling 3-axis manipulator arm with holder connector, an anesthesia gas adaptor with mouse snout clamp and incisor bar, and dual-sided ear bars, (2) drill holder (Catalog No. 51630), (3) micromotor high-speed drill with 0.5-mm diameter drill bit (Catalog No. 51449) for drilling a burr hole on mouse skull for intracranial injection, (4) Hamilton 10-μL gastight syringe with removable 32-gauge blunt-tip needle (1700 series; Catalog No. 53485-1) for cell injection into mouse brain, and (5) probe holder (Catalog No. 51633) to holding the 10-μL syringe onto the stereotaxic instrument.
7. Tissue adhesive (Vetbond™; 3 M, St.Paul, MN) is used for closing surgical opening.
8. Ethanol solution (70%) and PBS (pH 7.4, 1×) are used for cleaning the 10-μL syringe after the intracranial injection, sequentially.

## 3 Methods

In this section, we follow the order of introducing the configuration, assembling, and calibration process of our BLT system, the configuration of the SARRP, the integration of SARRP and the optical system, procedures for cell and animal preparation, quantification of system-specific source spectrum, and the procedures of image acquisition, QBLT reconstruction, and QBLT-guided irradiation.

### 3.1 Configuration of the BLT System

Figure 1a1 shows the actual BLT system, and Figure 1a2-3 illustrate the schematic drawing of our optical assembly and the interior layout of the imaging chamber, respectively. The details of the

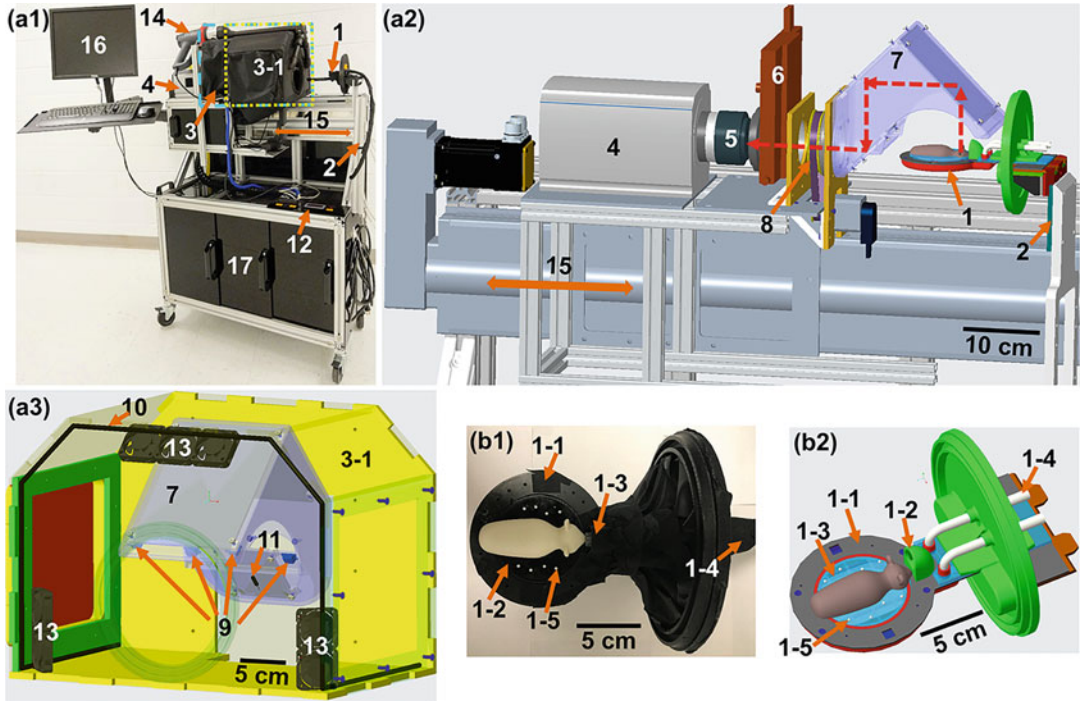


**Fig. 1** The numbering of the components shown in this figure follows the order described in Subheading 2.1. (**a1**) Photo of the BLT system; the blue dash box layouts the light-tight enclosure and the yellow dash box shows the imaging chamber as the front part of the light-tight enclosure. (**a2**) is a schematic of the optical assembly, mouse bed, and 1D linear stage; the optical assembly can be docked to the mouse bed by the 1D linear stage. The optical path from the imaging plane through the 3-mirror system and selected filter to the front surface of the lens (red dash line) is 45 cm. (**a3**) A schematic of the configuration inside imaging chamber (yellow dash box in **a1**), including the layout of thermostatic system, the position of 4 LEDs, and 7 fans; (**b1-2**) are the photo and the detailed drawing of the mouse bed. The bed is transportable and compatible for both BLT system and SARRP. Label: (1) transportable mouse bed, (1-1) frame, (1-2) central circular plate, (1-3) nose cone, (1-4) anesthesia hose, (1-5) BBs; (2) mouse bed support; (3) light-tight enclosure (blue dash box in **a1**), (3-1) imaging chamber (yellow dash box in **a1**); (4) CCD camera; (5) lens; (6) filter wheel; (7) 3-mirror system; (8) rotary stage; (9) LED; (10) resistor; (11) thermocouple; (12) thermocouple monitor; (13) fan; (14) heat gun; (15) 1D linear stage; (16) computer console; (17) mobile cart

transportable mouse bed are shown in Figure 1b1-2. The numbering of the components shown in Figure 1 follows the order described in Subheading 2.1. We describe the technical detail of the main components as follows.

1. Optical assembly and its configuration for imaging acquisition: The optical assembly includes the CCD camera (#4) and light-tight enclosure (#3) (Figure 1a1-2). The back end of enclosure includes the 50-mm f/1.2 lens (#5), filter wheel (#6), and rotary stage (#8), and the front end of enclosure is the imaging chamber (#3-1) (Figure 1a1-2). Inside the imaging chamber, there are the motorized 3-mirror system (#7), 4 LEDs (#9), thermostatic system (*see* **step 3**), and transportable mouse bed

(#1) (Figure 1b1-2). The entire light-tight enclosure was connected to the 1D linear stage by T-slotted aluminum extrusions. For BLI, the optical assembly can be driven to the mouse bed by the 1D linear stage (#15). The optical path from the imaging plane through the mirrors to the front surface of the lens is 45 cm (red dash line in Figure 1a2), and the depth of field (DOF) is 21 mm (Subheading 3.3, **step 1**). For BLI, the signal emitted from object surface is directed by the 3-mirror system, filtered by selected filter, and captured by the lens-camera setup (Figure 1a2). Band-pass filters are mounted in the filter wheel, enabling multispectral BLI acquisition to improve BLT reconstruction accuracy [22, 23]. The choice of the filter central wavelength is based on the interest of BL spectrum as well as in vivo tissue absorption spectrum. Light at shorter wavelength is absorbed stronger than that of longer wavelength in tissue within the wavelength range of BL signal. The use of multispectral data provides more input information for reconstruction algorithm in terms of target location compared to single wavelength approach. The 3-mirror system can also rotate 180° around imaged object and capture multi-projection images. Because the SARRP CBCT is used to generate tetrahedral mesh of imaged animal for optical reconstruction and define the coordinate for radiation, the 2D BLIs were mapped onto the animal surface of the CBCT image and used as the input data for the optical reconstruction. Eight BBs (Figure 1b1-2) were attached on the mouse bed to register the optical and CBCT coordinates. The BBs can be identified both in optical photo image with the LED on and in CBCT image (*see* **Note 1**). The LEDs are mounted on the four corners of the 3-mirror system to uniformly illuminate imaged objects and BBs to identify the positions of animal and BBs (Figure 1a3).

2. Pixel dimension of BLI: The pixel scale at 1 × 1 binning of BLI is 0.117 mm (*see* Subheading 3.3, **step 3**) at the image plane approximately 11 mm above the animal bed. To balance the image acquisition time and BLT reconstruction accuracy, we use 8 × 8 binning (0.96 mm/pixel) for BLI acquisition. The rule of thumb is to keep the pixel scale close to 1 mm which is about the order of photon scattering length in tissue. A pixel scale smaller than 1 mm is unlikely to make significant improvement in reconstruction accuracy.
3. Thermostatic system: The thermostatic system is used to keep the imaging chamber at 37 °C during BLI session (*see* **Note 2**). It consists of the resistor (#10, black line around the imaging chamber, Figure 1a3), thermocouple (#11) and the monitor (#12), fans (#13), and a heat gun (#14) (Figure 1a1, a3). The resistor was positioned at bottom edges of the side wall and all

the edges at front face except its bottom edge. Four fans were placed at the front corners, two at each corner, and three fans were placed on the front-top end of the chamber to circulate the hot air generated from the resistor to maintain uniform temperature throughout the chamber. The thermocouple was fixed at the location of the 3-mirror system, where it can closely measure the temperature around imaged animal (Figure 1a3). The heat gun outlet was linked to the top of imaging chamber. The heat gun to imaging chamber consists of a 3D printed heat gun adapter, a 1.5" PVC pipe, and a 3D printed imaging chamber adapter. The 3D printed parts were designed in PTC Creo, and printed by ABSplus P430 in an uPrint SE Plus 3D printer (Stratasys, Eden Prairie, MN, US). Before we start BLI acquisition, we used the heat gun to boost the chamber temperature to 37 °C and relied on the resistor to maintain the temperature.

4. Transportable mouse bed: To transfer the animal between the optical system and SARRP, we designed the transportable mouse bed (Figure 1b1-2) consisting of a bed frame (#1-1), central circular plate (#1-2), a nose cone (#1-3), two anesthesia hoses (#1-4), and eight BBs (#1-5). The bed frame and nose cone were designed in PTC Creo. The top of the bed frame is made by computer numerical control (CNC) machined carbon fiber plate (thickness 1/16″). The bottom part of the frame and the nose cone are made by 3D printed ABS. The central plate 1/16″ made by clear cast acrylic sheet was laser cut by a laser cutter (VLS6.60; Universal Laser Systems Inc., Scottsdale, AZ). The purpose of the central plate is to have flexibility that we can exchange with different plate such as a transparent kind to allow external light source irradiating animal for future fluorescence tomography development. Two anesthesia hoses are connected to the nose cone, allowing the animal to be anesthetized during imaging, irradiation, and the transportation between the systems. For BL imaging setting, the bed is connected to the mouse bed support (#2, Figure 1a1-2) in the BLT system, and the light-tight enclosure is docked to the bed. The center of the bed is designed close to the center of the image field of view.

### 3.2 Steps of the Optical System Assembling

The order of assembling the optical system is described as following.

1. Assemble the mobile cart, and mount the mouse bed with support and 1D linear stage to the cart frame.
2. Assemble the rotary stage to the 3-mirror system.
3. Set up the assembly of T-slotted aluminum extrusions on the 1D linear stage, and assemble the motorized 3-mirror system onto this assembly.

4. Attach the filter wheel to the 3-mirror system, such that the 3-mirror system optical axis (red arrow in Figure 1a2) is coaxial to the center of the selected filter set in the filter wheel.
5. Assemble CCD camera onto the aluminum frame such that the optical axis of the 3-mirror system and CCD camera axis are coaxial.
6. Assemble the front end of light-tight enclosure, i.e. imaging chamber including the thermostatic system,
7. Mount the LEDs on the four corners of the 3-mirror system.
8. Assemble the back end of light-tight enclosure.
9. Mount the lens to the CCD camera, use f/1.2 aperture, and adjust lens focusing and the distance between the lens front and filter wheel to ensure the imaging plane is approximately 10 mm above the mouse bed.
10. Seal the gaps around the light-tight enclosure with opaque black tape.

### 3.3 Calibration Procedures for the BLT System

To ensure clear BLIs acquired at different projection/image acquisition angles, we need to determine the DOF and focal plane position of our optical system. As described in Subheading 3.1, we also quantified the pixel scale at the focal plane for our optical images. The calibration procedure for image uniformity was bypassed since ratio image instead of conventional spectral image was used as the input data for the SD-method based BLT reconstruction. The process of assessing image distortion and background signal is also outlined in the following.

1. Depth of field (DOF): A 45° wedge with a series of line pairs attached on its hypotenuse is placed on the mouse bed. A photo of the wedge was taken at 1 × 1 image binning with the LED on (Fig. 2a). The contrast of a line pair is defined as $\frac{I_{\max}-I_{\min}}{I_{\max}+I_{\min}}$, where $I_{max}$ and $I_{min}$ are the maximum and minimum intensity of the white and black line of a pair from the photo, respectively. By using the wedge setup, we can map the line pair contrast to the physical height above the mouse bed (Fig. 2b). We defined the DOF as the physical range, corresponding to the height above the bed, of the contrast larger than 30% of the normalized maximum value, which was calculated from the 1 line pair (lp)/mm pattern. The DOF of our system is $21 \pm 0.4$ mm ($n = 3$). This value also serves as a quality control baseline to maintain constant imaging performance.
2. Focal plane: From our C57BL/6 mice cohort ($n = 10$), the height and width of mouse head are $19.2 \pm 0.6$ and $13.6 \pm 0.7$ mm, respectively, and for abdomen, the height and width are $19.2 \pm 1.2$ and $26.1 \pm 2.0$ mm, respectively. With the DOF as 21 mm, we aim to place the focal plane at

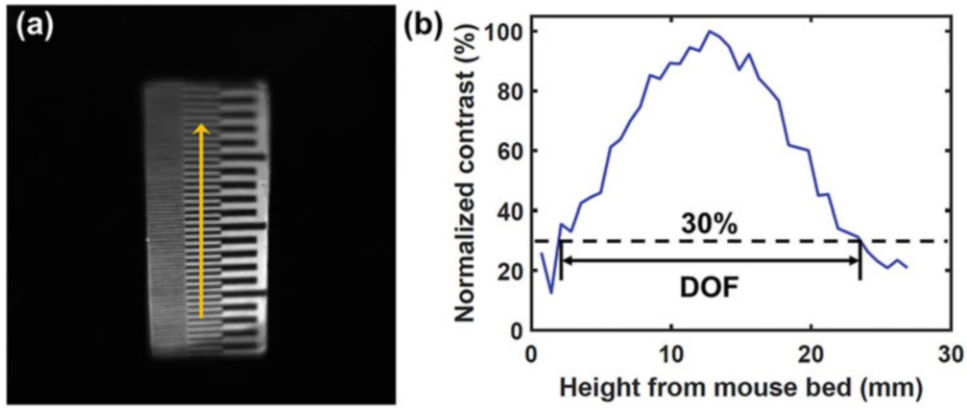


**Fig. 2** (**a**) Photo of a 45° wedge with line pairs of 0.5 lp/mm, 1 lp/mm, and 2 lp/mm; the wedge was placed on the mouse bed. (**b**) shows the normalized contrast variation of the 1 lp/mm along the yellow arrow in (**a**) following the height above the mouse bed

10–15 mm above the mouse bed to have clear BLIs acquired at all projections. Figure 2b shows a representative result of the image contrast of the 1 lp/mm, where the focal plane is estimated at 12 mm above mouse bed where the maximum contrast stands. From three independent experiments, the average focal plane location with standard deviation is at $11.1 \pm 1.8$ mm and image depth range is from $2.6 \pm 0.4$ to $23.6 \pm 0.4$ mm ($n = 3$) above the mouse bed.

3. Pixel scale: The pixel scale is the corresponding physical size of the CCD pixel at imaging plane. The pixel scale is measured with a ruler placed horizontally on the focal plane. We use the physical distance between the scales on the ruler to calculate the pixel scale which is 0.117 mm per CCD pixel on the focal plane.
4. Image distortion: A paper with dot grid is placed on the mouse bed ($10 \times 10$ cm$^2$ field of view around the image center at mirror 0°). Photo image at $1 \times 1$ binning is acquired. The measured distance of the dot center to the image center is compared to the actual distance to examine image distortion. No distortion is observed in our system.
5. Background signal: To check the background signal, we use 120 s exposure time to take open field (without filters) images at −90°, 0°, and 90° mirror angle with the same imaging parameters as common BLI acquisition, $8 \times 8$ binning, 4× preamplifier gain, and 1 MHz readout rate. A region of interest (90 pixel × 90 pixel, 10 cm × 10 cm) around the image center was selected for background signal analysis. The background signal level is at about 860 counts per pixel.

### 3.4 Configuration of the SARRP

Figure 3a and a1 illustrate the schematic of the SARRP. As described in Subheading 2.2, the main components of the SARRP includes shielding (#1), sliding door (#2), dual focal X-ray source (#3), isocentric gantry (#4), 4D robotic base (#5), mouse bed support (#6), flat panel detector (#7), and collimating cone assembly (#8). The dual focal X-ray source employs 0.4-mm and 3-mm focal spots for CBCT imaging at 65 kVp and 0.7 mA with 1-mm-thick aluminum filter and for irradiation at 220 kVp and 13 mA with 0.15-mm-thick copper filter, respectively. The gantry carries the X-ray source and allows 360° rotation around the isocenter, set at 35 cm away from the X-ray focal spot. The transportable mouse bed is mounted on the mouse bed support attached to the 4D robotic base. For CBCT imaging, the collimating cone assembly is removed. CBCT image is acquired by rotating the animal with the 4D robotic base between the stationary X-ray source at gantry 90° and the flat panel detector, placed at 29 cm away from the isocenter (Fig. 3b). For irradiation, the collimating cone is mounted onto the X-ray source. The distal end of the cone assembly is at 5 cm to the isocenter (Fig. 3c). MuriPlan is used to design BLT-guided radiation plan, based on the coordinate defined by SARRP CBCT image and the QBLT-delineated target volume. Noncoplanar conformal irradiation can be achieved by the combination of gantry and couch position.

### 3.5 Integration Between the Optical System and SARRP

The integration between the standalone optical system and SARRP is carried out by the transportable mouse bed (Figure 1b1-2). For BLT imaging workflow, the bed is attached to the mouse bed support in the BLT system and animal is imaged for surface BLIs acquisition (Figure 1a2). After the BLI session, the anesthetized animal along the bed is detached from the BLT system, transferred to SARRP, and attached to the mouse bed support on the 4D robotic base (Fig. 3) for CBCT imaging and BLT reconstruction, followed by BLT-guided irradiation. The BLT system was operated in close proximity (within 2 m) to the SARRP to minimize animal transport [24].

### 3.6 Procedures for Cell Culture and Preparation for Intracranial Injection

1. We first calculate the total cell amount required for the intracranial injection; we use $1.2 \times 10^5$ GL261-*Luc2* cells (*see* **Note 3**) in 2 μL of PBS for each injection per mouse. Due to the potential loss of cells during preparation, we suggest cultivating at least five times of the required cell amount for the surgery.
2. We start with a vial containing $10^6$ GL261-*Luc2* cells in 1 mL of cell cryopreservation medium (95% FBS, 5% dimethyl sulfoxide), preserved in liquid nitrogen.
3. We thaw the cells by gently shaking the vial in 37 °C water bath for 3 min and also keep the vial cap out of the water. We warm the DMEM (with 10% FBS) in the water bath for 10 min. We

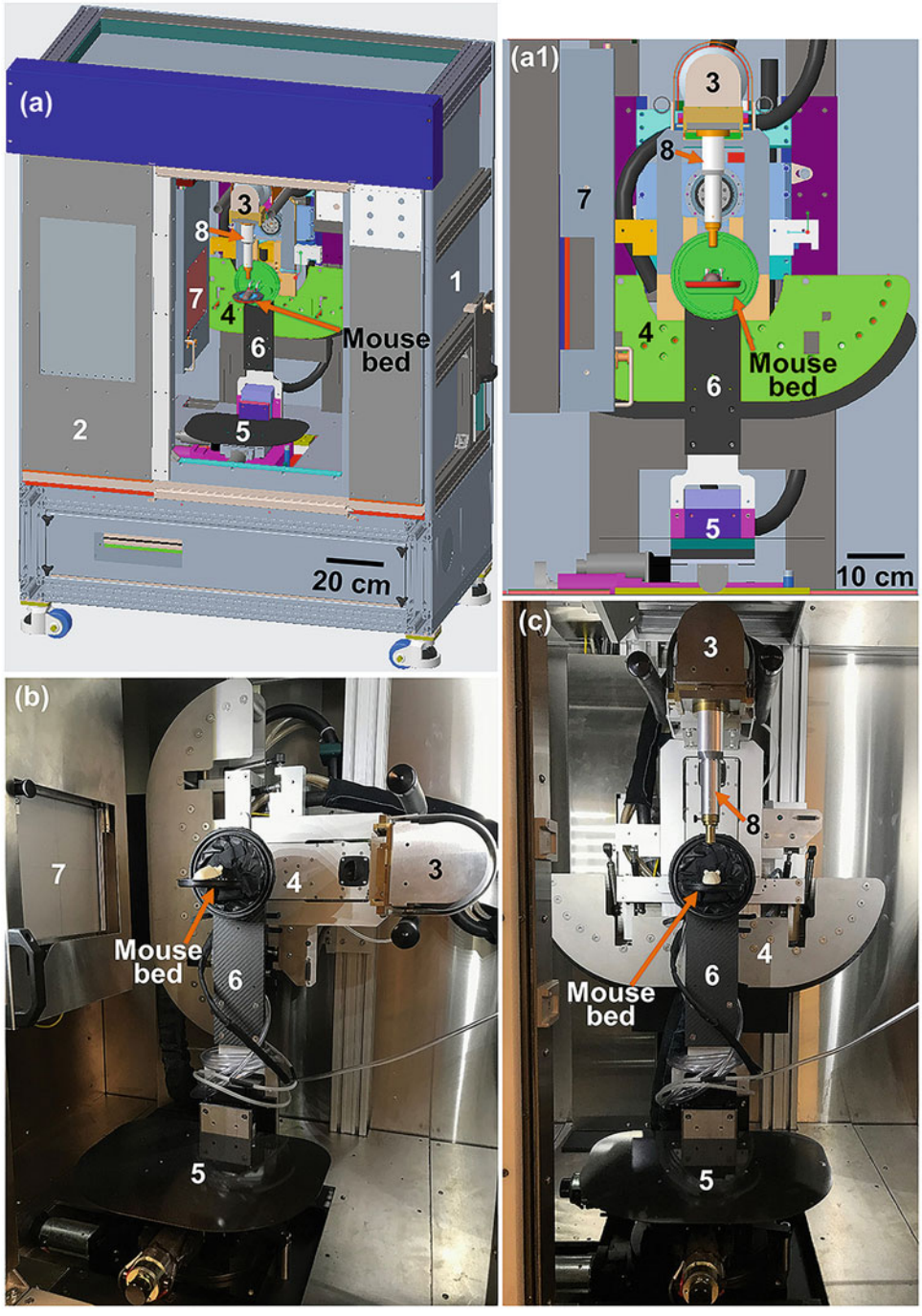


**Fig. 3** The numbering of the components shown in this figure follows the order described in Subheading 2.2. Schematics of SARRP in (**a**) full and (**a1**) detail view, (**b**) CBCT and (**c**) irradiation configurations; after BLI session, the animal along with mouse bed is transported to SARRP for CBCT imaging, followed by BLT-guided irradiation. Label: (1) radiation shielding; (2) sliding door; (3) dual focal X-ray source; (4) 360° isocentric gantry; (5) 4D robotic base; (6) mouse bed support; (7) flat panel detector; (8) collimating cone

wipe the vial and medium bottle dry after the thawing/warming.

4. Spray the vial, medium bottle, and gloved hands with 70% ethanol and wipe dry. Immediately after, transfer the vial and medium bottle into the biological safety cabinet.
5. Put 4 mL of sterile medium into a T25 flask, open the vial, transfer cells in 1 mL medium from the vial into the flask, and mix gently.
6. Incubate the T25 flask with cells at 37 °C, 5–6% $CO_2$, 100% humidity overnight.
7. Examine the cells under microscope next day. If the cells reach 80–90% confluency, start cell passaging. If not, change medium (5 mL), and return the T25 flask back to the incubator. Change medium every 3–4 days until the cells reach 80–90% confluency.
8. Start passaging cells when the cells are ready. Remove medium from the flask and add 5 mL of sterile, room temperature PBS. Gently swirl the PBS a few times over the cells, and remove the PBS immediately.
9. Add 1 mL of sterile, warm Trypsin into the flask, and gently swirl the Trypsin to allow it to coat the plate completely. Incubate the flask at 37 °C for 2–3 min to allow the cells to dissociate from the flask.
10. Confirm the cell dissociation by examining the flask under microscope. If the cell is not dissociated, return the flask back to incubator for further incubation until most of cells dissociated.
11. Neutralize the Trypsin with 2× medium, and suspend the cells by gently scouring the plate 3–5 times.
12. Transfer the cell suspension into a T75 flask, and add 15 mL of medium. Incubate the T75 flask and change the medium every 3–4 days until the cells reach 80–90% confluency. If more cells are needed, one can repeat **steps 7–10** using 15 mL PBS, 3 mL Trypsin for the T75 flask instead, and split the cell into 3–7 T75 flasks based on the required cell amount. T150 flask with 30 mL PBS and 4 mL Trypsin and T175 with 35 mL PBS and 5 mL Trypsin can also be utilized for cultivating cells.
13. When the cells are confluent, ready for surgery, we change the medium 1 day before the surgery.
14. On the day of the surgery, we repeat **steps 7–10**, and use pipette to pour the cell suspension into a 50-mL conical centrifuge tub for centrifuging (300 × *g* for 6 min at 4 °C).
15. Keep the tube inside ice after the first centrifuging. Remove the supernatant, add 10 mL of cold PBS (kept inside the ice as well), and resuspend the cells.

16. We add 63 μL of the cell suspension into a 1-mL Eppendorf tube, and mix 7 μL of Trypan blue into the cell suspension to stain dead cells. We then add 20 μL of the mixture into each chamber of cell counter slide, and prepare three chambers to obtain the averaged living cell concentration. We then calculate the total cell amount, and the desired cell suspension volume to reach the concentration of $6.0 \times 10^4$ cells/μL for injection.
17. We again centrifuge the cell suspension ($300 \times g$ for 6 min at 4 °C), remove the supernatant, and add PBS until the desired cell suspension volume is reached. We transfer the cell suspension to 1-mL Eppendorf tube for ease of drawing the cell suspension into a 10-μL syringe. We keep the tube inside ice until the surgical process is finished.

### 3.7 Procedures for In Vivo GBM Surgery

1. Place mice cage on the heat pad.
2. Set up the stereotaxic instrument; fixing the drill holder to the instrument, installing the 0.5-mm drill bit into the micromotor high-speed drill, and mount the drill onto the drill holder (Fig. 4a, a1).
3. Inject Buprenorphine-SR LAB subcutaneously by penetrating the skin of mouse back.
4. Anesthetize the mouse. To use the Ketamine-Xylazine mixture, one can inject the mixture intraperitoneally. To use the isoflurane-oxygen airflow as anesthesia, one can put the mouse into the anesthesia box, and turn on the isoflurane vaporizer at 3–5% of isoflurane airflow. When the mouse is under anesthesia, move the mouse to operation bench, and maintain the anesthesia with 1–3% of isoflurane flow using a hose linking the vaporizer to the mouse nose.
5. Shave mouse scalp, and sterilize the surface by applying povidone-iodine solution with cotton swabs.
6. Prior to immobilize the mouse onto the stereotaxic instrument, pinch the paw to test reflexes to determine if the mouse is under deep anesthesia.
7. Use the ear bars and incisor bar on the stereotaxic instrument to immobilize the mouse head at prone position (Fig. 4a), and apply eye ointment on the eyes. Connect the isoflurane vaporizer to anesthesia gas adaptor on the stereotaxic instrument if isoflurane-oxygen airflow will be used for anesthesia.
8. Make a 5–8 mm incision on the scalp.
9. Adjust the *x*, *y*, and *z* micromanipulators of stereotaxic instrument to guide the drill bit to the lambda location of mouse skull (Fig. 4a, a1, b, c). We first raise the drill bit 1 mm, shift the bit 2 mm left to the sagittal suture and 2 mm anterior to the lambdoid suture, and lower the bit to the surface of skull,

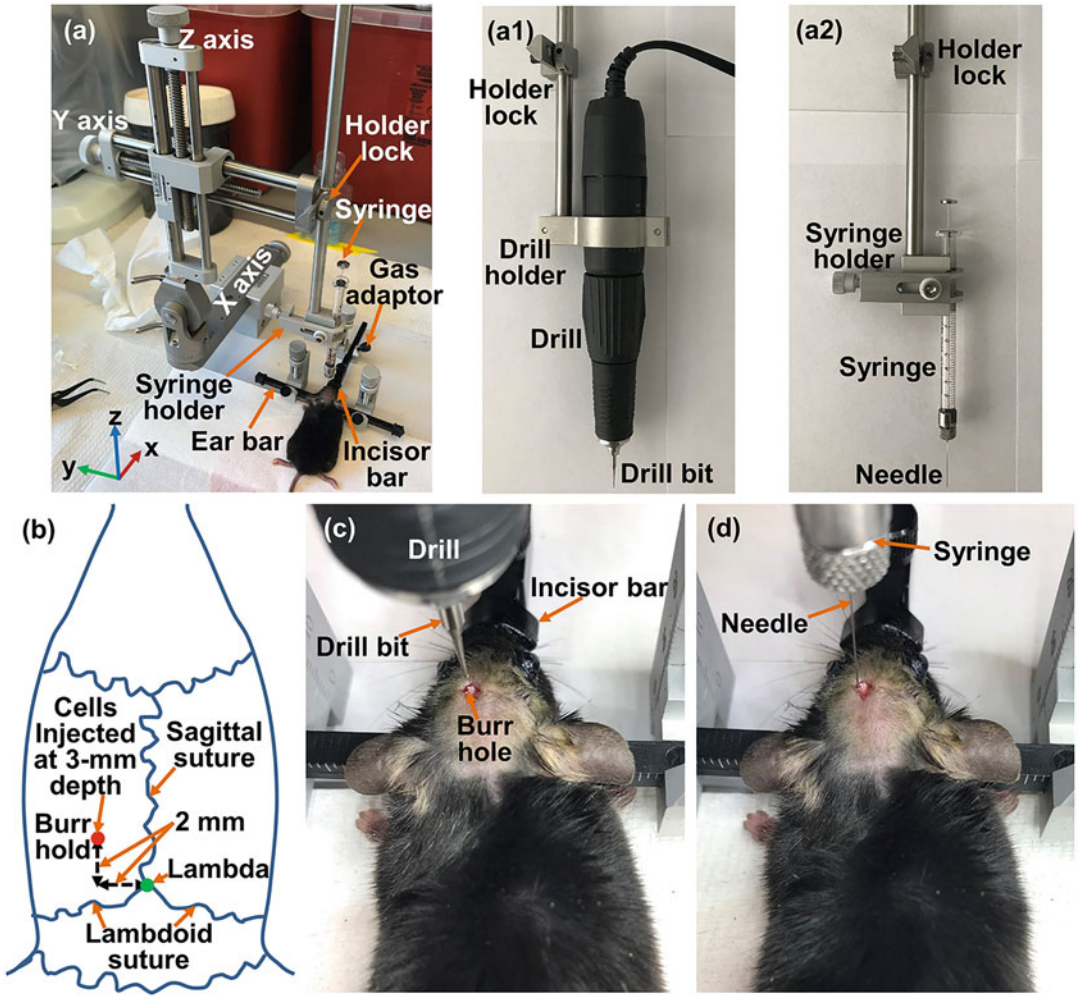


**Fig. 4** (**a**) Photo of stereotaxic instrument; the stereotaxic instrument can be equipped with (**a1**) a drill or (**a2**) a syringe for drilling burr hole or intracranial injection, respectively. (**b**) A schematic of lambda point, sagittal suture, lambdoid suture, and burr hole on a rodent skull; two zoom-in photos show (**c**) the use of drill for drilling a burr hole on skull and (**d**) the intracranial injection of the cells through the burr hole, respectively

activate the drill, and further lower the bit until breaking through the skull with a 0.5-mm-diameter burr hole. Once the skull is broken through, deactivate the drill, raise the drill bit away from the skull, and remove the drill along with the drill holder from the stereotaxic instrument. The magnifying lens with LED lamp is recommended for identifying parietal structures and positioning the bit on the skull. Different injection locations for in vivo GBM establishment are also published elsewhere [25, 26].

10. Clean the 10-μL syringe with 70% ethanol solution and PBS successively, swirl the cell suspension, and draw 2 μL of cell suspension into the syringe.

11. Fix the probe holder to the stereotaxic instrument, and mount the 10-μL syringe onto the probe holder (Fig. 4a2).
12. Adjust the micromanipulators to position the tip of syringe to the upper surface of burr hole, lower the syringe 3.5 mm, raise it back 0.5 mm to make a small cavity for injection (Fig. 4d).
13. Inject 1 μL of cell suspension, and wait 1 min. Repeat these two steps until all suspension is injected.
14. After **step 13** is completed, raise the syringe 1 mm, and wait for 1 min. Repeat these two steps until the tip is completely moved out of mouse head.
15. Use tissue adhesive to seal the burr hole and close the scalp incision. Once the incision is closed completely, move the mouse out of the stereotaxic instrument.
16. Make a label on the mouse ear for identification and return the mouse to the cage.
17. Take out the 10-μL syringe from the probe holder and clean it with 70% ethanol solution and PBS in sequence. Remove the probe holder from the stereotaxic instrument.
18. After mouse recovers from surgery and become consciousness, observe the animal to determine if there is any abnormal behavior or pain, such as holding head down, not eating, and not grooming, due to surgery. If so, treat it with further analgesics.
19. Move the mice back to animal facility when all the mice are awake from anesthesia and no pain is observed. The mice should be further evaluated for signs of pain or distress. One can give analgesics to the animal when needed.

### *3.8 Quantification of System-Specific Source Spectrum*

For the multispectral BLT, it is important to quantify the system spectral response and source spectrum. Instead of separating the system spectral response and the source spectrum, for simplicity, we used the BLT system to measure the so-called system-specific source spectrum combing the spectral response from the optical system and source of interest. Using the GBM case as an example for the spectrum measurement, we transferred *GL261-Luc2* cells to petri dish (> 80% cells confluency), and the cells were incubated at 37 °C, 5–6% $CO_2$, and 100% humidity overnight. The next day, the cell medium was changed to PBS, and concentration of 0.75 mg of D-Luciferin per 1 mL of PBS per dish was added. The BLIs from the dishes were acquired at 37 °C in sequence of "open field, 590 nm, open field, 610 nm, open field, 630 nm, open field, 650 nm, open field." We record the time point for each image and use the open field image to build an in vitro time-resolved signal curve to account for the change of the spectral signal of the cells during the luciferin incubation. The intensity of the spectral BLIs taken at

different time points is normalized to the time-resolved curve, and the normalized values at different wavelength are the system-specific source spectrum, used as input parameter for BLT reconstruction. The resulted system-specific *GL261-Luc2* spectrum at 590, 610, 630, and 650 nm are 1, $0.916 \pm 0.014$, $0.674 \pm 0.019$, $0.389 \pm 0.012$ ($n = 20$), respectively.

### 3.9 Procedure of Image Acquisition for Optical Reconstruction

The choice of wavelength for the multispectral BLT is based on the luciferase spectra. To minimize the absorption of BL signal by tissue medium, the luciferase spectrum is preferable closer to tissue near-infrared window. For the *Luc2* used in this work, the peak of luciferase spectra is at 609 nm [27], and the FWHM is about 100 nm. Therefore, 590, 610, 630, and 650 nm were selected for multispectral BLT. However, the detected in vivo signal at 590 nm is much lower than that at the other 3 wavelengths, and the large ratio of BL signals between 610 and 590 nm could introduce numerical error for our SD-based reconstruction. For the in vivo GBM study introduced in this chapter, despite 590 nm data was taken, we only used the BLIs at 610, 630, and 650 nm for BLT reconstruction. The following describes the step-by-step procedure for the imaging acquisition.

1. Place the mice cage on heat pad.
2. Move the BLT system within 2 m away from the SARRP, and power on the BLT system components including the CCD camera, filter wheel, rotary stage, 1D linear stage, thermostatic system, and computer. All the components of the thermostatic system except the heat gun are automatically turned on when we power on the BLT system.
3. Confirm the 3-mirror position at 0° projection with a digital level attached to the 3-mirror assembly front edge.
4. Initialize the positioning of the 1D linear stage using the home-built motor control GUI, set the CCD camera temperature at −80 °C using the Andor Solis software, and turn on the heat gun to boost the chamber temperature until the thermocouple monitor reaches 37 °C, and turn off the heat gun.
5. Set the CCD camera acquisition parameters for BLIs in the software Andor Solis: select 8 × 8 binning, 4× preamplifier gain, 1 MHz readout rate at 16 bit, and check both horizontal and vertical flips for image orientation.
6. Turn on the SARRP, warm up the X-ray source, and initialize the couch and gantry using the SARRP GUI.
7. Calibrate the SARRP flat panel detector using the SARRP GUI: select the 0.4-mm focal spot as the X-ray source setting, ensure no collimator attached to the X-ray source, use aluminum filter as the X-ray filtration, move the X-ray source to 90°

gantry position, and pull the detector to working position, open detector cover, calibrate the detector for dark and flood fields by turning off and on the 65 kVp X-ray beams, respectively.

8. Anesthetize the mouse: put the mouse into the anesthesia box, and turn on the isoflurane vaporizer at 3–5% of isoflurane airflow. When the mouse is under anesthesia, move the mouse to operation bench, and maintain the anesthesia with 1–3% of isoflurane flow using a hose linking the vaporizer to the mouse nose.
9. Shave mouse scalp, apply hair remover lotion to remove remaining hair, use cotton pad to wipe the lotion gently, and soak a bit water into another pad to completely remove all lotion on the scalp. Return the mouse to the cage.
10. Once the mouse awakens from anesthesia, intraperitoneally inject D-luciferin into the mouse, and return the animal to the cage for 3 min to facilitate the circulation of the luciferin.
11. Put the mouse back to anesthesia box (3–5% of isoflurane) for anesthesia. Meanwhile, connect the anesthesia hose of the BLT system to the isoflurane vaporizer and mouse bed.
12. Once the mouse is under anesthesia, place the mouse at the mouse bed, and place the nose into the nose cone to keep it under anesthesia (1–3% of isoflurane). Use black tape to immobilize its limbs and tail, and bend down its ears to avoid blocking the BL signal from both sides of the mouse head.
13. Ensure that the 3-mirror system is at 0°, dock the imaging chamber to mouse bed using the home-built motor control GUI. About 10–15 min after D-luciferin injection, we can start the BLI session.
14. Open field images without filters are taken before and after each spectral BLI to quantify the in vivo signal variation over time. For the spectral image, since 590-nm image acquisition typically requires the longest exposure time among all the spectral image acquisition, we choose the 590-nm filter to determine the exposure time for filtered images. Based on our experience for BLT reconstruction, we suggest that adjusting the exposure time until both open field and 590-nm images have at least 2000 counts at the pixel, within region of interest, with maximum counts after background signal subtraction. We acquire the BLIs by using the Andor Solis in the sequence of "open field, 590 nm, open field, 610 nm, open field, 630 nm, open field, 650 nm, open field" at 0° projection. The software Optec HSFW Control is used to change the filters. The optical images are saved as tif files with parameters: 16-bit gray format, 0-65535 date range, full area for area to export, currently displayed scan for scan range.

15. One can acquire BLIs at other projection angles depending on tumor model and location using the home-built motor control GUI. For example, if BLI acquisitions at 90° and −90° are demanded, we can rotate the 3-mirror system using the home-built motor control GUI to the desired angle and repeat the same imaging sequence described in **step 14**.
16. Image acquisition for data mapping from BLIs to 3D CBCT: Turn on the LED, rotate the filter wheel to empty slot using the Optec HSFW Control, change the CCD camera binning to 1 × 1 binning in the Andor Solis, rotate the 3-mirror system to five symmetrically distributed angles using the home-built motor control GUI, such as the order of −90°, −45°, 0°, 45°, 90°, and take the photo image at each angle using the Andor Solis. Make sure that the imaging exposure time is sufficient to distinguish all the BBs on the mouse bed clearly without saturation.
17. Move the 3-mirror system back to 0° position, drive the imaging chamber out of the bed using the home-built motor control GUI, and transfer the imaged mouse along the bed to SARRP for CBCT imaging using the SARRP GUI.

### *3.10 Procedure for QBLT Reconstruction and Target Volume Determination*

The data post-processing and QBLT reconstruction (**steps 1–6**) were conducted by an in-house built MATLAB-NIRFAST-NIRView package, and the 3D Slicer was chosen to generate contouring and planning target volume for irradiation guidance. The detail and steps for the reconstruction process and the target volume determination are presented in this section.

1. Postprocessing for surface BLIs: We removed background signal for each BLI by subtracting the BLIs by the minimum pixel value of the entire field of view. To remove singular noise, hot spot, randomly happened at some pixels, we calculated the coefficient of variation for a given pixel from all the spectral BLIs. If the coefficient of variation is larger than the threshold 1.0 determined empirically, the data on that pixel is considered as hot spot and removed. We then normalized the BLIs by imaging exposure time. Figure 5a shows a representative example of surface BLIs at 630 nm taken at 3 projections for a GBM-bearing mouse.
2. Quantify the temporal change of in vivo bioluminescence signal: Because the in vivo bioluminescence signal can change overtime and it is animal specific, it is important to quantify the time-resolved in vivo signal to have accurate input data for the reconstruction. To build the time-resolved curve for each projection during BLI course, the open field images taken before and after each spectral image (Subheading 3.9, **step 14**) along with the time points when the images were taken

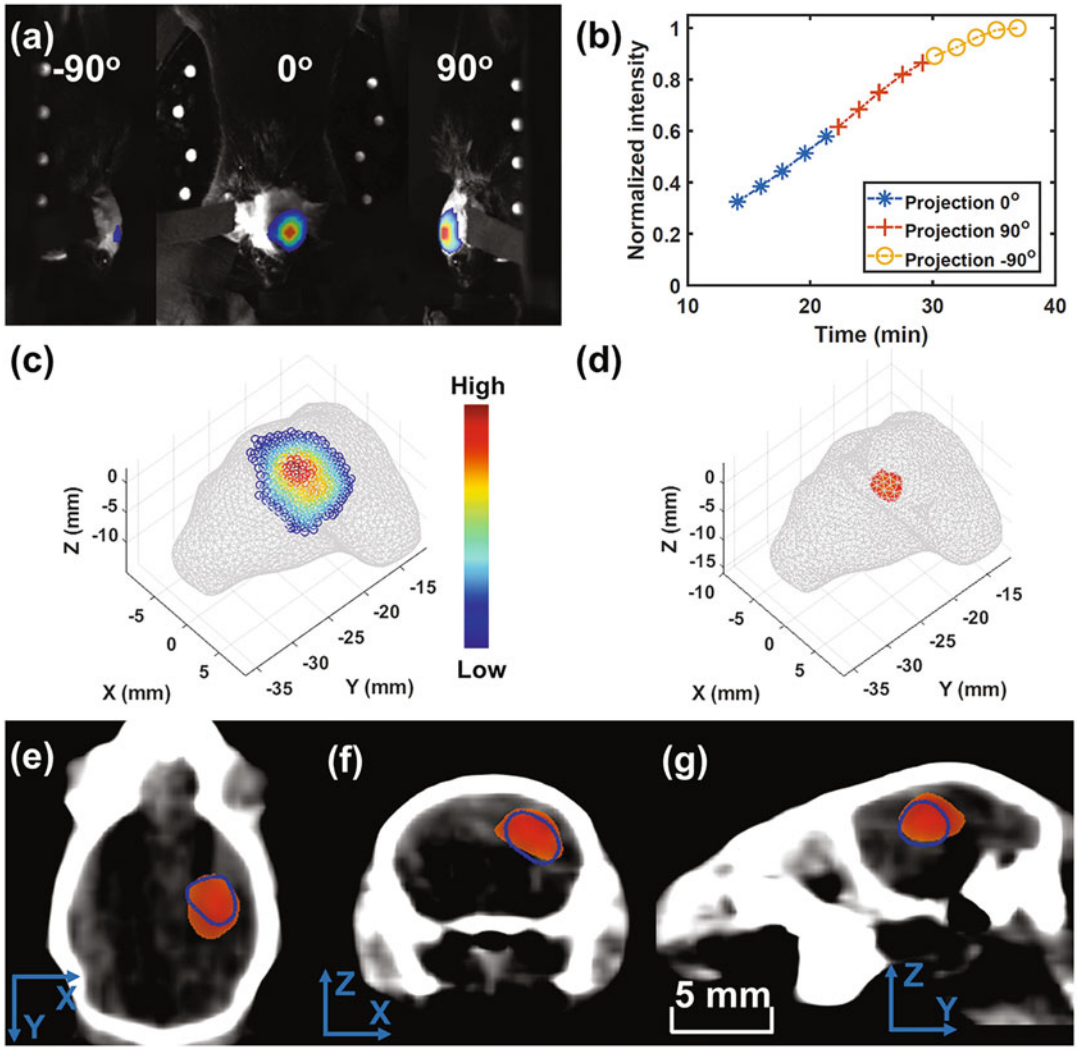


**Fig. 5** An example of QBLT reconstruction for a GBM-bearing mouse; (**a**) is the surface BLIs (colormap, 630 nm) of a GBM-bearing mouse second week after cell implantation taken at −90°, 0°, and 90° projection. (**b**) Shows the dynamic change of in vivo bioluminescence signal after luciferin injection, normalized to maximum intensity. The curve was generated with the open field images taken at 0°, 90°, and −90° projections. (**c**) Shows the image of the three-projection BLIs (**a**) mapped onto the surface of the numerical mesh generated from the mouse CBCT image. Data with value larger than 10% of the maximum among all the three projections is displayed in (**a**) and (**c**). (**d**) Shows the QBLT reconstruction result (heat map). A threshold of 0.5 of maximum QBLT reconstructed value was used to display the reconstruction result. The overlap of $GTV_{QBLT}$, heat map, and contrast-labeled GTV, blue contour, were shown in (**e**) coronal, (**f**) transverse, (**g**) sagittal views

were used to record the signal change overtime. A region of interest (ROI) 10 × 10 pixel around maximum pixel value in the open field image was chosen to quantify the dynamic of the in vivo signal. Because the ROIs chosen at different projection was not from the same physical location of animal surface, to

build the time-resolved curve describing the signal change over the image course, we need to link the time-resolved curves between two adjacent projections. We extrapolated the light intensity from the time-resolved curve of the first projection to the time point when the first open field image at the second projection was measured. We scaled the light intensity recorded from the second projection at the first time point to the extrapolated light intensity from the first projection. We can then combine the time-resolved curves among different projections to form a global curve (Fig. 5b), which we can use to correct the intensity of each spectral image taken at certain time point.

3. Numerical mesh generation for BLT reconstruction: We generated the numerical mesh from SARRP animal CBCT image, used for finite element method (FEM)-based reconstruction calculation. The CBCT image was imported to NIRView. A ROI of the CBCT volume was cropped. The K-means and Markov Random Field algorithm were used to segment the mouse body. Holes in the segmentation were automatically filled by iterative filling function in NIRView. Paintbrush function can be used to manually improve the imperfection of segmented volume. The segmentation is saved as a binary contour file (.mhd). The contour is further processed with median filtering, hole-filling and islands removing functions (medfilt2, imfill and bwareaopen; MATLAB). We use NIRFAST meshing toolbox to generate tetrahedral mesh from the contour.
4. Data mapping for multi-projection BLIs: Our published geometry calibration method [14] was used to map the BLIs at a given projection to the mesh surface generated from the CBCT image. Our approach includes (1) registering 3D CBCT coordinate to 3D optical coordinate, and (2) projecting the 3D optical coordinate to the 2D optical coordinate at the CCD plane. Once the CBCT and optical image plane is registered, the BLI acquired at a given projection can be mapped onto the CBCT image. There are 12 geometrical parameters of our system needed to be known for the data mapping process. A program automatically identifying the BBs location in both optical photo and CBCT images was developed by our group based on image contrast. An in-house program with the constrained multivariable optimization function (fmincon, MATLAB) was developed to retrieve the geometrical parameters by minimizing the difference between the calculated and measured BB positions in the 2D optical coordinate; the BB positions at −90°, −45°, 0°, 45°, and 90° projection were used as the measured positions, and the corresponding BB positions retrieved from the in-house routine based on the optimized geometrical parameters and the BB positions in

CBCT were used as the 2D calculated positions. The geometric calibration was performed for each animal imaging session to ensure accurate data mapping for reconstruction.

We use the centers of mesh surface triangles as the positions of the surface data point for reconstruction. If the angle between the normal vector of a surface triangle and camera viewing is larger than a set angle threshold (60°), the surface data is removed to minimize the discrepency between the actual and measured fluence rate. For the overlapped region between two projections, the maximum value at a given surface point among the projections is chosen as the data value. The mapped surface data with values larger than a threshold (10%) of the maximum value among all the surface points were used as the final input data for reconstruction (*see* Fig. 5c as an example).

5. Spectral-derivative (SD) algorithm for QBLT reconstruction: The mathematical framework has been published in Ref. 15. Briefly, we use the diffusion approximation (DA) of the light transport equation with Robin-type boundary condition to model light propagation in tissue, because light transport in biological tissue is dominated by scattering. In our noncontact imaging geometry, a major challenge is accounting for the light propagation from subject surface to the optical detector. Instead of directly using surface BLIs acquired at different wavelengths, we use the spectral derivative (SD) of the BLI data (the ratio of the BLIs at adjacent wavelength) [15]. Our assumption is the BLIs at adjacent wavelengths encountering a near-identical system response, i.e. light emitted from a surface point at the adjacent wavelength passing approximately same optical path toward the detector, CCD. By utilizing the ratio of the BLI data, we can eliminate the geometric dependence of the free spacing light propgation, and therefore, the need for complicated system modeling. We can write a systematic linear equations derived from DA as:

$$G_\lambda w_\lambda S = b_\lambda n \tag{1}$$

where $G_\lambda$ is the sensitivity matrix describing the changes of boundary/surface fluence rate related to source $S$ for a given wavelength $\lambda$, which can be constructed from prior knowledge of the optical property of imaged subject, $w_\lambda$ is the system-specific source spectrum, and $n$ is angular dependent factor, assumed to be spectrally invariant, to account for the difference between actual surface fluence rate and BLI measurement $b_\lambda$. By applying logarithm to Eq. (1) and considering the ratio of the data between two neighboring wavelengths $\lambda_i$ and $\lambda_{i+1}$, we can write the SD form of Eq. (1) as:

$$\left[\frac{\log b_{\lambda_i} n}{b_{\lambda_i} n} G_{\lambda_i} w_{\lambda_i} - \frac{\log b_{\lambda_{i+1}} n}{b_{\lambda_{i+1}} n} G_{\lambda_{i+1}} w_{\lambda_{i+1}}\right] S = \log \frac{b_{\lambda_i}}{b_{\lambda_{i+1}}} \quad (2)$$

The $G_\lambda$ matrix is generated by a modified version of our MATLAB-NIRFAST package. The source distribution $S$ in the SD form (Eq. 2) is iteratively solved by applying a compressive sensing conjugate gradient (CSCG) optimization algorithm [28]. The values of absorption coefficient 0.1610, 0.0820 and 0.0577 $mm^{-1}$ and reduced scattering coefficient 1.56, 1.51, and 1.46 $mm^{-1}$ of mouse brain for 610, 630, and 650 nm, respectively, were used for the GBM QBLT reconstruction [29].

6. QBLT-reconstructed volume: With the above preparation, one can reconstruct BL source distribution $S$ (Eq. (2)) using the QBLT approach. The source distribution also depends on the choice of threshold value, which determines the boundary of source distribution. We assessed the optimal threshold using the Dice coefficient between the gross target volume (GTV) delineated by contrast CBCT, taken as ground truth, and the GTV reconstructed by QBLT ($GTV_{QBLT}$). We found threshold 0.5 of maximum QBLT reconstructed value providing the maximum Dice coefficient or overlap between the GTV and $GTV_{QBLT}$ for our GBM-bearing mice cohort ($n = 10$, second week after the cell implantation surgery). Figure 5d shows an example of the QBLT reconstructed GBM, and Fig. 5e–g show the comparison between the GTV and $GTV_{QBLT}$.
7. Margin and planning target volume determination for irradiation guidance: Although the $GTV_{QBLT}$ qualitatively matches the GTV (Fig. 5e–g), there is still deviation between the two in terms of volume and positioning. A margin accounting for these uncertainties of QBLT target localization was added to $GTV_{QBLT}$ to form a planning target volume ($PTV_{QBLT}$) for radiation guidance (Fig. 6). The margin size is determined by achieving the optimal balance between GTV coverage and normal tissue coverage. The GTV coverage is defined by $(PTV_{QBLT} \cap GTV)/GTV$. The normal tissue coverage is defined by $(PTV_{QBLT} - PTV_{QBLT} \cap GTV)/V_{head}$, where $V_{head}$ is the volume of mouse head. From our animal cohort ($n = 10$), with 0.5 mm margin, the GTV coverage by $PTV_{QBLT}$ can be achieved at 98% in average. To add the margin onto the $GTV_{QBLT}$, we imported the $GTV_{QBLT}$ from the MATLAB to the 3D Slicer and used the function "Margin" in module "Segment Editor" of the 3D Slicer to expand the $GTV_{QBLT}$ to form the $PTV_{QBLT}$.

### 3.11 Procedure for QBLT-Guided Irradiation

In the section, we provide the steps for the SARRP irradiation based on the QBLT-reconstructed target volume $GTV_{QBLT}$ and $PTV_{QBLT}$. With the target volume in place, one can design

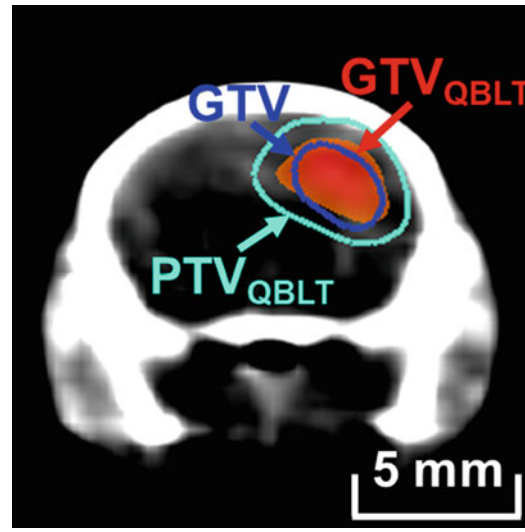


**Fig. 6** A uniform margin 0.5 mm added to a $GTV_{QBLT}$ (heat map) to form a $PTV_{QBLT}$ (cyan) for radiation guidance on a GBM-bearing mouse. The GTV is delineated (blue contour) from contrast CBCT

treatment plan in the MuriPlan with the desired dose coverage for the $GTV_{QBLT}$ and $PTV_{QBLT}$. The SARRP GUI is used to execute the beam delivery based on the treatment plan designed by the MuriPlan. The steps for treatment planning and irradiation are listed as follow:

1. Load animal SARRP CBCT image in the MuriPlan and segment the image into air, lung, fat, tissue, and bone by using thresholds of CBCT values.
2. Following the **step 7** in Subheading 3.10, we export the $GTV_{QBLT}$ and $PTV_{QBLT}$ in nrrd labelmap file format using the module "Segmentations" from the 3D Slicer and import the file/$GTV_{QBLT}$ and $PTV_{QBLT}$ into the MuriPlan.
3. Because the external volumes imported from the 3D Slicer is not compatible with MuriPlan, we duplicate the $GTV_{QBLT}$ and $PTV_{QBLT}$ by following the imported volume and contouring the volume slice by slice.
4. We set the CoM of the $GTV_{QBLT}$, retrieved from the optical reconstruction, as the isocenter for SARRP irradiation beam, and input an initial dose estimation at the isocenter.
5. In MuriPlan, the radiation beam can be designed by type (static/arc), weighting, collimator type, robotic base, and gantry angles.
6. After setting the beam geometry, we use MuriPlan to calculate dose distribution and to display isodose curves and dose-volume histogram (DVH). We review the DVH and dose

coverage for target volume i.e. $GTV_{QBLT}$ and $PTV_{QBLT}$. We can further adjust the dose setting at isocenter to ensure desired dose coverage for the target volumes.

7. Before irradiation, we set the SARRP in the irradiation configuration (Fig. 2c): shield the flat panel detector and set it at off-duty position, change the aluminum filter to the copper filter, mount collimating cone, and select the 3-mm focal spots as X-ray source.
8. After the planning, the beam geometry and parameters including delivery time are sent from the MuriPlan to the SARRP GUI. The GUI automatically deploys the gantry and robotic base to required positions, and execute the beam at instructed delivery time.

## 4 Notes

1. To effectively identify the BBs from both optical photo and CBCT image for data mapping (Subheading 3.10, **step 4**), the color and density of the BBs and bed base should be significantly different. In our design, white polytetrafluoroethylene BBs and black acrylic bed base were used. Other materials, such as white ceramic BBs and black-painted carbon fiber bed base could be another choice. In addition, the low-density bed base can also ease the work on mouse body segmentation (Subheading 3.10, **step 3**), which is partly in contact with the bed surface.
2. Because temperature could affect the spectrum and intensity of luciferase expressing cells [30], it is important to keep mouse body temperature during in vivo experiment, consistent with the system-specific source spectrum measurement (Subheading 3.8). Our optical imaging chamber was maintained at 37 °C for both spectrum measurement and in vivo experiment.
3. Other commercially available cell lines such as *GL261-Red-FLuc* [31] can produce brighter, red-shifted signal than the *GL261-Luc2* illustrated in this chapter. Despite there is potential immune response occurred in C57BL/6 mice, one can consider the *Red-Fluc*-expressed cell line for the study with immunodeficiency mice to shorten image acquisition time.

## Acknowledgements

The authors would like to thank the funding support from CPRIT RR200042, NIH-NCI (R21CA223403, R37CA230341, R01CA240811, and P30CA006973), and Xstrahl Inc.

## References


1. Wong J, Armour E, Kazanzides P et al (2008) High-resolution, small animal radiation research platform with X-ray tomographic guidance capabilities. Int J Radiat Oncol Biol Phys 71:1591–1599
2. Matinfar M, Ford E, Iordachita I et al (2009) Image-guided small animal radiation research platform: calibration of treatment beam alignment. Phys Med Biol 54:891–905
3. Dilworth JT, Krueger SA, Wilson GD et al (2014) Preclinical models for translational research should maintain pace with modern clinical practice. Int J Radiat Oncol Biol Phys 88:540–544
4. SARRP by Xstrahl Inc. https://xstrahl.com/us/life-science-systems/small-animal-radiation-research-platform/
5. Herter-Sprie GS, Korideck H, Christensen CL et al (2014) Image-guided radiotherapy platform using single nodule conditional lung cancer mouse models. Nat Commun 5:5870
6. Seifert L, Werba G, Tiwari S et al (2016) Radiation therapy induces macrophages to suppress T-cell responses against pancreatic tumors in mice. Gastroenterology 150:1659–1672
7. Chandra A, Lin T, Tribble MB et al (2014) PTH1-34 alleviates radiotherapy-induced local bone loss by improving osteoblast and osteocyte survival. Bone 67:33–40
8. Thorne SH, Contag CH (2005) Using in vivo bioluminescence imaging to shed light on cancer biology. Proc IEEE 93:750–762
9. O'Neill K, Lyons SK, Gallagher WM et al (2010) Bioluminescent imaging: a critical tool in pre-clinical oncology research. J Pathol 220:317–327
10. Close DM, Xu TT, Sayler GS et al (2011) In vivo bioluminescent imaging (BLI): noninvasive visualization and interrogation of biological processes in living animals. Sensors 11:180–206
11. Yu JJ, Zhang B, Iordachita II et al (2016) Systematic study of target localization for bioluminescence tomography guided radiation therapy. Med Phys 43:2619–2629
12. Zhang B, Wang KKH, Yu JJ et al (2016) Bioluminescence tomography-guided radiation therapy for preclinical research. Int J Radiat Oncol Biol Phys 94:1144–1153
13. Deng Z, Xu X, Garzon-Muvdi T et al (2020) In vivo bioluminescence tomography center of mass-guided conformal irradiation. Int J Radiat Oncol Biol Phys 106:612–620
14. Zhang B, Iordachita I, Wong JW et al (2016) Multi-projection bioluminescence tomography guided system for small animal radiation research platform (SARRP). SPIE BiOS 2016: multimodal biomedical imaging XI, San Francisco, CA, USA. Proc SPIE 9701:97010J. https://doi.org/10.1117/12.2211869
15. Dehghani H, Guggenheim JA, Taylor SL et al (2018) Quantitative bioluminescence tomography using spectral derivative data. Biomed Opt Express 9:4163–4174
16. Jermyn M, Ghadyani H, Mastanduno MA et al (2013) Fast segmentation and high-quality three-dimensional volume mesh creation from medical images for diffuse optical tomography. J Biomed Opt 18:10
17. Dehghani H, Eames ME, Yalavarthy PK et al (2009) Near infrared optical tomography using NIRFAST: algorithm for numerical model and image reconstruction. Commun Numer Methods Eng 25:711–732
18. NIRFAST. https://www.dartmouth.edu/~nir/nirfast/
19. Kikinis R, Pieper SD, Vosburgh KG (2014) 3D slicer: a platform for subject-specific image analysis, visualization, and clinical support. In: Jolesz FA (ed) Intraoperative imaging and image-guided therapy. Springer New York, New York, NY, pp 277–289. https://doi.org/10.1007/978-1-4614-7657-3_19
20. Fedorov A, Beichel R, Kalpathy-Cramer J et al (2012) 3D slicer as an image computing platform for the quantitative imaging network. Magn Reson Imaging 30:1323–1341
21. 3D Slicer. https://www.slicer.org/
22. Kuo C, Coquoz O, Troy TL et al (2007) Three-dimensional reconstruction of in vivo bioluminescent sources based on multispectral imaging. J Biomed Opt 12:024007
23. Dehghani H, Davis SC, Jiang SD et al (2006) Spectrally resolved bioluminescence optical tomography. Opt Lett 31:365–367
24. Zhang B, Wong JW, Iordachita II et al (2016) Evaluation of on- and off-line bioluminescence tomography system for focal irradiation guidance. Radiat Res 186:592–601
25. Zeng J, See AP, Phallen J et al (2013) Anti-PD-1 blockade and stereotactic radiation produce long-term survival in mice with intracranial gliomas. Int J Radiat Oncol Biol Phys 86:343–349
26. Kindy MS, Yu J, Zhu H et al (2016) A therapeutic cancer vaccine against GL261 murine glioma. J Transl Med 14:9
27. Ogoh K, Akiyoshi R, May MT et al (2014) Bioluminescence microscopy using a short

focal-length imaging lens. J Microsc 253:191–197

28. Basevi HRA, Tichauer KM, Leblond F et al (2012) Compressive sensing based reconstruction in bioluminescence tomography improves image resolution and robustness to noise. Biomed Opt Express 3:2131–2141
29. Lin AJ, Koike MA, Green KN et al (2011) Spatial frequency domain imaging of intrinsic optical property contrast in a mouse model of Alzheimer's disease. Ann Biomed Eng 39:1349–1357
30. Zhao H, Doyle TC, Coquoz O et al (2005) Emission spectra of bioluminescent reporters and interaction with mammalian tissue determine the sensitivity of detection in vivo. J Biomed Opt 10:41210
31. Branchini BR, Southworth TL, DeAngelis JP et al (2006) Luciferase from the Italian firefly Luciola italica: molecular cloning and expression. Comp Biochem Physiol B Biochem Mol Biol 145:159–167

# Chapter 39

# Evaluation of Pulmonary Structure and Function in Patients with Cystic Fibrosis from Electrical Impedance Tomography Data

**Jennifer L. Mueller**

## Abstract

Electrical impedance tomography (EIT) is a medical imaging technique in which low frequency, low amplitude electromagnetic fields applied through electrodes on the skin are used to compute the conductivity and/or permittivity inside the body and form functional images from the reconstructed values. This work describes methods of computing EIT-derived surrogate measures of pulmonary function and identifying regions of air trapping and consolidation from functional EIT images. These methods were developed for pediatric patients with cystic fibrosis, for whom a real-time non-ionizing imaging modality can be of great benefit for monitoring disease progression or a pulmonary exacerbation.

**Key words** Pulmonary imaging, Cystic fibrosis, Electrical impedance tomography

## 1 Introduction

Individuals with chronic lung disease often have conditions that are very difficult to diagnose without the aid of imaging technology. The gold standard, CT scanning, exposes the patient to ionizing radiation and may be harmful in children. Electrical impedance tomography (EIT) is a noninvasive, non-ionizing functional imaging technique that can be performed as needed with no harmful side effects. The data can be collected without sedation in any position and can be collected simultaneously with pulmonary function tests. It is acquired as fast as 50 frames/s, and with fast algorithms, images can be formed in real time.

Patients with cystic fibrosis often experience pulmonary exacerbations with complications including air trapping, atelectasis, and airway occlusion, requiring hospitalization. Treatment for pulmonary exacerbations generally consists of antibiotics and augmented airway clearance. Intravenous (IV) antibiotic therapy is generally used for patients with severe symptoms and those who

Miguel R. Ossandon et al. (eds.), *Biomedical Engineering Technologies: Volume 1*, Methods in Molecular Biology, vol. 2393, https://doi.org/10.1007/978-1-0716-1803-5_39, 

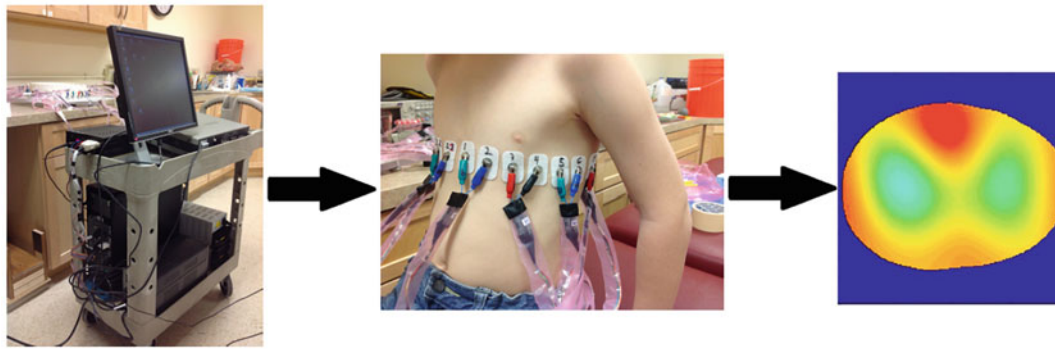

**Fig. 1** Left: The ACE 1 EIT system on a cart in the lab at Colorado State University. Center: Electrodes on a healthy 8-year-old subject. Right: Example of an EIT image of the chest during ventilation. Regions of high conductivity are shown in red, and low conductivity regions in blue. The heart is at the top of the image and appears red; the lungs are blue

unresponsive to oral and nebulized therapy. For such patients, a non-ionizing imaging technique to assess lung function and structure as a means of monitoring disease progression, or pre- and post pulmonary exacerbations or airway clearance therapy could be highly beneficial.

In EIT imaging, electrodes are placed on the surface of the body, and low amplitude, low frequency current is applied on the electrodes. This results in a voltage distribution on the electrodes which can then be measured. From these voltages, an image is formed depicting the conductivity and/or permittivity distribution within the region of interest. Often, difference images are formed to show conductivity changes relative to a point of reference, such as full exhalation. For pulmonary applications, EIT can be used to image ventilation, perfusion, or ventilation/perfusion ratio maps. Figure 1 shows the ACE 1 EIT system [15] on a cart as was used in the studies [17, 19], a healthy 8-year-old subject being imaged in the lab at Colorado State University, and an example of an EIT image of the chest during ventilation.

EIT is based on the fact that the conductivity (and permittivity) of the tissues in the body varies significantly, and reconstruction of these spatially and temporally dependent properties allows one to form an image. Typical values of conductivity and permittivity are listed in Table 1.

Since the measured voltages depend nonlinearly on the conductivity distribution in the interior, and since the data depends discontinuously on the conductivity, the reconstruction problem in EIT is a severely ill-posed nonlinear inverse problem, and as a result, the inversion method requires regularization and results in blurred, low-resolution images. This is in stark contrast to MRI and CT

**Table 1**
**Conductivity values [3] and permittivity values [7] for tissues and organs in the human chest at 100 kHz**

| Tissue | Conductivity (mS/cm) | Permittivity (μF/m) |
|---|---|---|
| Blood | 6.7 | 0.05 |
| Liver | 2.8 | 0.49 |
| Bone | 0.06 | 0.0027 |
| Cardiac muscle | 6.3 (longitudinal) | 0.88 |
| | 2.3 (transversal) | 0.36 |
| Lung | 1.0 (expiration) | 0.44 |
| | 0.4 (inspiration) | 0.22 |
| Fat | 0.36 | 0.18 |
| Skin | 0.0012 | 0.0144 |

scanning which are both linear and very mildly ill-posed, except in the case of sparse or limited-angle data. The advantages of EIT lie in its ability to provide real-time functional images using a non-ionizing modality that can be performed as needed. For patients with cystic fibrosis, this means that the extent and location of air trapping can be assessed regularly, providing an opportunity to monitor the effectiveness of air clearance therapies, monitor mucus plugging, and assess lung health pre- and post pulmonary exacerbations, which have been identified as a key pathway to long-term respiratory decline in these patients.

Through NIH support, our team has developed methods of identifying regions of air trapping and consolidation in CF patients from EIT measurements and EIT-derived surrogate measures of pulmonary function including FEV1, FVC, and FEV1/FVC. These methods are described here. Three groups of subjects were enrolled in the study: control subjects with healthy lungs, patients with cystic fibrosis clinically indicated for a CT scan, and CF patients being admitted for a pulmonary exacerbation. The study was conducted in accordance with the amended Declaration of Helsinki. Data were collected at Children's Hospital Colorado (CHCO), Aurora, CO under the approval of the COMIRB (approval number COMIRB 14-0652) with CHC and the University of Colorado Denver and the IRB of Colorado State University. Informed written parental consent and children's informed assent was obtained from subjects under age 18, and informed written consent from subjects age 18 and up were obtained prior to participation. Results of our study were published in [17, 19].

## 2 Materials

1. Electrical impedance tomography system (*see* Note 4.1 for sources and description)
2. Disposable adhesive pediatric EKG electrodes (Phillips 13951C)
3. Flexible rulers
4. Tape measure
5. Alcohol wipes
6. Electric razor if working with subjects who may have a hairy chest
7. Spirometer and nose clip, if data will be collected during spirometry
8. Fiducial markers if a CT scan is to be performed
9. EKG system, such as BIOPAC
10. Matlab software

## 3 Methods

### 3.1 Data Collection

1. Measure the circumference of the subject's chest with the tape measure at the level of the 5th intercostal space
2. The Phillips pediatric EKG electrodes are 7/8 inch wide, and the electrodes should be placed at least 1/8 inch apart to avoid contact between them, but if the subject will be laying down, 1/4 inch is recommended. Calculate the electrode spacing and number to ensure that the minimum gap is maintained with the maximum number of electrodes applied. A simple Matlab script is handy for this purpose.
3. Be sure the subject's chest is clean and free from sweat or lotion. If in doubt, wipe the region with alcohol wipes. If the chest is hairy, it should be shaved.
4. Peel off each electrode and apply to the surface of the chest circumferentially, as in Fig. 2 with the desired spacing. Place one electrode on the subject's shoulder to serve as ground.
5. Connect each electrode to the correct lead of the EIT system. Note that some systems have alligator clips for connections, some have snaps, and some have pre-prepared belts. If the system has snap connectors, it is recommended to connect the electrode to the snap before peeling off and adhering so that it does not become necessary to apply excessive pressure to the subject's chest when connecting the electrode to the EIT lead. Likewise, if the system uses a belt, it is likely that the

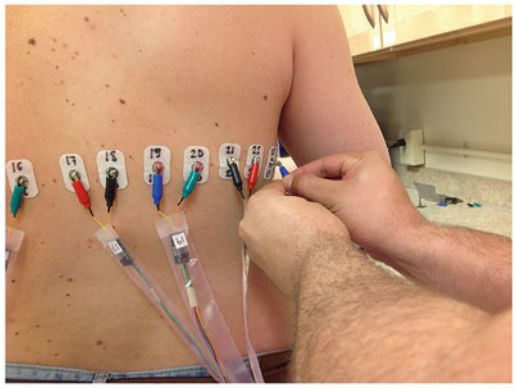
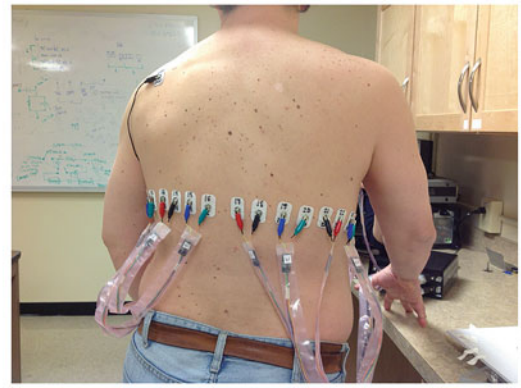

**Fig. 2** Application of electrodes from the ACE 1 EIT system. Note the ground electrode on the subject's shoulder

electrode number and spacing is prepared in advance on the belt.

6. Connect a 3-lead EKG to the subject, following the EKG system instructions.
7. Collect EIT and EKG data simultaneously during
   (a) 30 s of tidal breathing
   (b) 10 s of breath-holding, if possible
   (c) During spirometry maneuvers, if desired

   In our studies [17, 19], data collection during spirometry maneuvers were performed while the subject was standing, while the data collection during tidal breathing and breath-holding was performed with the subject seated. For the spirometry data collection, a clip was placed over the nose and the subject was asked to breathe into the spirometry tube. One to three normal breaths were taken prior to a deep inhalation followed by rapid forcible exhalation, all into the tube, with volume and flow rate measured by the spirometer. The EIT data collected during spirometry captured one or more breaths prior to the deep inhalation, the forced rapid exhalation, and one or more recovery breaths. Subjects should perform spirometry several times to obtain the best repeatable spirometry output, and EIT data should be collected during each of them.
8. Using the flexible rulers, measure the subject's chest shape. See notes for further details on an effective technique for accurate measurement.
9. Turn off the EIT system and remove the electrodes gently from the subject's skin, placing a fiducial marker at the center of each electrode if a CT scan is to be performed after the EIT data collection.

### 3.2 Image Reconstruction

In our work, reconstructions of the conductivity in the plane of electrodes were computed using the 2-D D-bar method [12, 16]. The D-bar method is a direct (non-iterative) reconstruction method based on equations of inverse scattering. A real-time implementation was presented in [6]. Other methods of reconstruction can be substituted for the D-bar method, but it is important to note that the results will be affected by the choice of reconstruction algorithm, choice of regularization method, and the chosen regularization parameter.

The general outline of the D-bar method consists of four steps:

1. Using the measured voltage data and the applied current patterns, compute a matrix formulation of the voltage-to-current density mapping.
2. Compute an approximation to the nonlinear Fourier transform, known as the scattering transform.
3. Solve the D-bar equation numerically on a finite grid determined by the cutoff frequency for the scattering transform.
4. Determine the conductivity by evaluating the solution of the D-bar equation at frequency $k = 0$.

Each of these steps is described in further detail in Subsection 4.2 of the Notes (Subsection 4).

### 3.3 Computation of EIT-Derived Measures of Spirometry

A schematic overview of the steps in the calculations of the EIT-derived measures of spirometry and spatial coefficients of variation is found in Fig. 3.

1. Once the sequence of EIT reconstructions of the conductivity has been computed, identify the frames corresponding to the key time points in the in the spirometry maneuver from plot of the first principal component in a principal component analysis (PCA) of the dynamic sequence of images. The first component in the PCA provides a means of visualizing the dominant temporal conductivity changes in the sequence in an easy-to-read plot with the frame number on the x-axis. In data sets collected during spirometry or tidal breathing, the dominant changes are due to ventilation. A plot of the PCA output from a CF patient performing spirometry is found in Fig. 4. The time points of interest are:

TLC(totallungcapacity) = theonsetoftheforcedexhalationmaneuver(maximuminspiration),
1s(onesecondafterTLC) = onesecondaftertheonsetoftheforcedexhalationmaneuver,
EFE(totallungcapacity) = theendoftheforcedexhalationmaneuver(maximumexhalation).

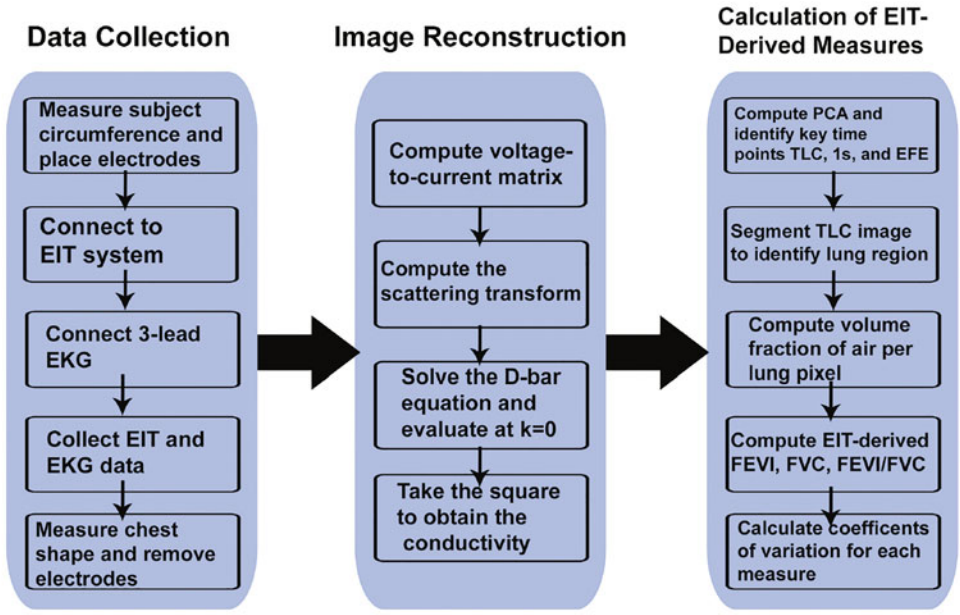


**Fig. 3** Schematic overview of the steps in the calculations of the EIT-derived measures of spirometry and spatial coefficients of variation

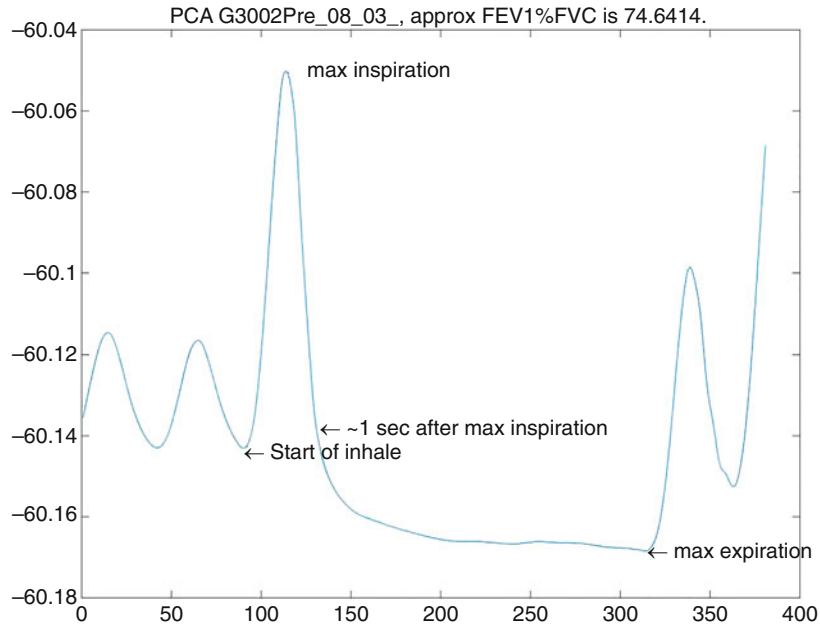


**Fig. 4** PCA output for EIT data collected during spirometry on a Group 3 subject used to identify the key time points TLC, 1s, and EFE in the EIT data collection

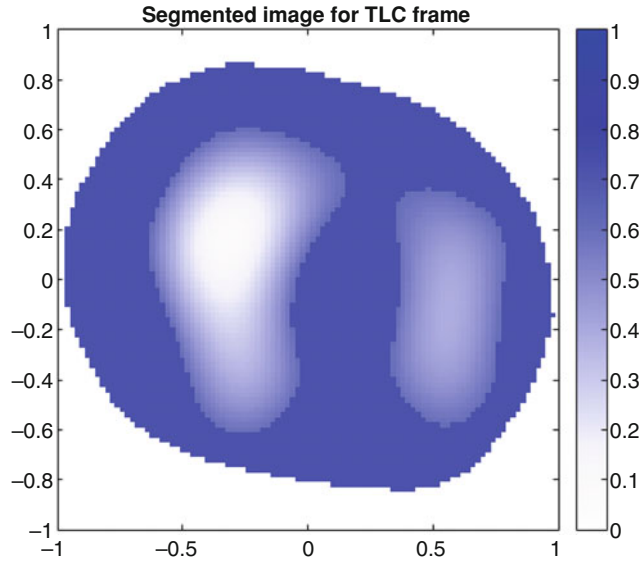


**Fig. 5** Segmented max inspiratory EIT image from a Group 2 subject (frame TLC)

TLC and EFE are readily identifiable on the PCA. The 1s frame is computed using the knowledge of the EIT system frame rate and TLC.

2. Segment the image corresponding to the TLC frame to identify the lung region during full inspiration. A level set method with an empirical choice of threshold to ensure inclusion of the full lung region without including other organs is an effective method of segmentation. *See* Fig. 5 for an example of a segmented image.
3. Compute the volume fraction of air per pixel for a given frame from the conductivity value in that pixel as follows. The three frames of interest are TLC, 1s, and EFE, and so denote the volume fraction of air in pixel $p$ for each of these frames by $f_{\mathrm{TLC}}(p)$, $f_{1\mathrm{s}}(p)$, and $f_{\mathrm{EFE}}(p)$, respectively. Let $\sigma_M$ and $\sigma_m$ be the maximum and minimum conductivities, respectively, over all pixels and all frames in the data set. Then the volume fractions of air per pixel can be calculated from the formulas

$$\begin{aligned} f_{\mathrm{TLC}}(p) &= \frac{\sigma_{\mathrm{TLC}}(p) - \sigma_M}{\sigma_m - \sigma_M}, \\ f_{1\mathrm{s}}(p) &= \frac{\sigma_{1\mathrm{s}}(p) - \sigma_M}{\sigma_m - \sigma_M}, \\ f_{\mathrm{EFE}}(p) &= \frac{\sigma_{\mathrm{EFE}}(p) - \sigma_M}{\sigma_m - \sigma_M}, \end{aligned}$$

where these quantities range from 0 to 1. The volume $vol(p)$ in liters associated with a pixel is estimated by 1000 times

the area of the pixel times the electrode height in meters. In our work, all pixels had equal area (and hence volume).

4. Calculate the EIT-derived pixel-wise measure of forced expiratory volume after one second, denoted by FEV1(p), by computing the volume fraction difference between $f_{1s}(p)$ and $f_{TLC}(p)$ multiplied by the volume of a pixel:

$$FEV1(p) = (f_{TLC}(p) - f_{1s}(p)) * vol(p).$$

The EIT-derived measure of forced vital capacity, FVC(p), is defined analogously:

$$FVC(p) = (f_{TLC}(p) - f_{EFE}(p)) * vol(p).$$

The EIT-derived measure FEV1/FVC(p) is a ratio of the difference in conductivity at TLC and the conductivity one second after peak inspiration to the difference in conductivity at TLC and the conductivity at the end of forced expiration. To calculate FEV1/ FVC(p) ratio for each pixel $p$ in the segmented lung region, use the formula:

$$FEV1/FVC(p) = \frac{FEV1(p)}{FVC(p)} = \frac{\sigma_{TLC}(p) - \sigma_{1s}(p)}{\sigma_{TLC}(p) - \sigma_{EFE}(p)}$$

. Note that by plotting FEV1/FVC(p), one has a single image representing the ratio of the conductivity change in each pixel at the 1s frame to that of the EFE frame, relative to the TLC frame. A global value, denoted by FEV1/FVC, is obtained by summing over all pixels in the lung region for TLC:

$$FEV1/FVC = \frac{\sum_{i=1}^{N} FEV1(p)}{\sum_{i=1}^{N} FVC(p)}.$$

One can also compute regional values of FEV1/FVC by summing pixels over the region of interest.

A comparison of the spirometry measurements FEV1 % predicted and the global EIT-derived FEV1 across groups in our study is given in Fig. 6. The distribution of the observed values for both outcomes is shown. The best FEV1 % predicted used in the statistical analysis is the FEV1 spirometry output that was the highest % predicted, where % predicted was computed using the Global Lung Initiative equations [22, 23], and was also repeatable.

5. Calculate coefficients of variation as in [28] for each measure. These coefficients provide a measure of the degree of heterogeneity in the lung region for a chosen frame. The formulas are

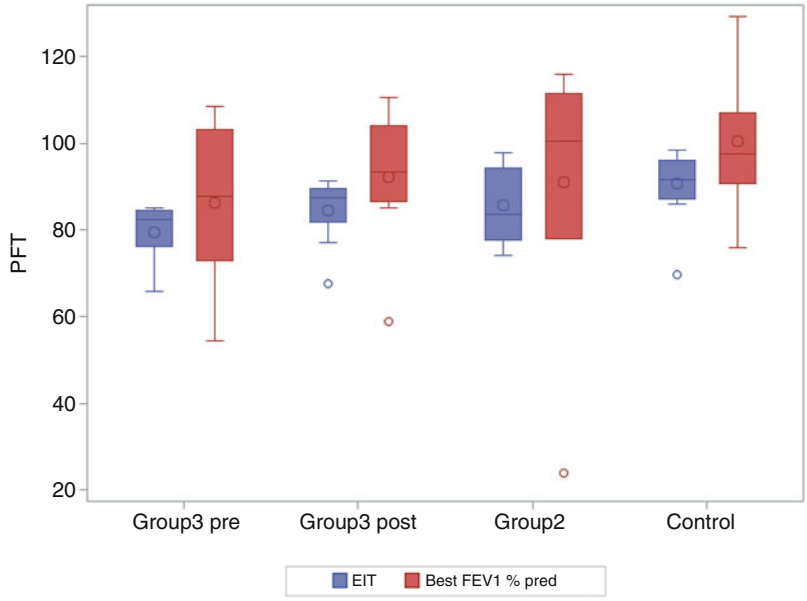


**Fig. 6** Comparison of the spirometry measurements FEV1 % predicted and global EIT-derived FEV1 across groups. Distribution of the observed values is provided for both outcomes

$$
\begin{aligned}
CV_{FEV1} &= \frac{\text{std(FEV1(p))}}{\text{mean(FEV1(p))}}, \\
CV_{FVC} &= \frac{\text{std(FVC(p))}}{\text{mean(FVC(p))}}, \\
CV_{FEV1/FVC} &= \frac{\text{std(FEV1/FVC(p))}}{\text{mean(FEV1/FVC(p))}}.
\end{aligned}
$$

Coefficients of variation can also be computed from data collected during tidal breathing. In this case the PCA from the tidal breathing reconstruction sequence is used to identify the breath with maximal conductivity difference between inhalation and exhalation. Denoting the frame corresponding to maximal inspiration for the chosen breath by MI, and the frame corresponding to the moment of maximal exhalation for the same breath by ME, we define the pixel-wise conductivity change between these two frames by TidalBreathing(p):

$$\text{TidalBreathing}(p) = \sigma_{MI}(p) - \sigma_{ME}(p).$$

Plotting TidalBreathing(p) results in a difference image between these two time points in the reconstructions. The corresponding coefficient of variation for TidalBreathing is

$$CV_{TidalBreathing} = \frac{\text{std(TidalBreathing(p))}}{\text{mean(TidalBreathing(p))}}.$$

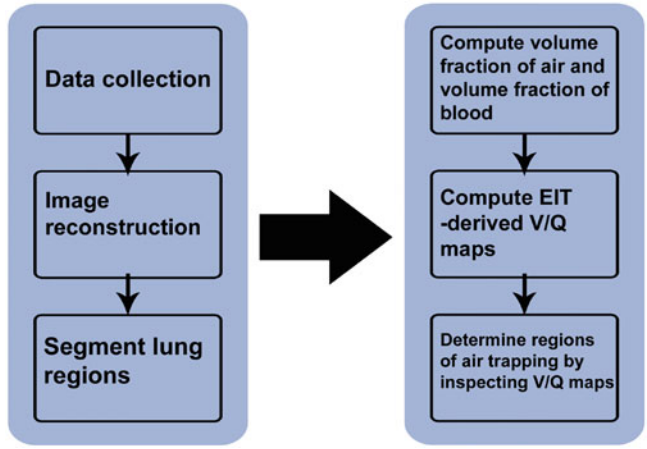


**Fig. 7** Schematic overview of the steps in the calculations of the estimation of regions and volumes of air trapping

### *3.4 Estimation of Regions and Volumes of Air Trapping*

A schematic overview of the steps in the calculations of the estimation of regions and volumes of air trapping is found in Fig. 7.

1. Compute the dynamic reconstructions of conductivity from the tidal breathing data sets and the data collected during breath-holding to obtain ventilation and pulsatile perfusion image sequences, respectively.
2. Segment the images to determine lung regions as follows. Determine the patient's heart rate from the EKG collected during the breath-holding data set. Use this to identify a small set of cardiac pixels in the perfusion images by selecting the pixels of highest conductivity in the heart region that change at the cardiac frequency. Since pulmonary perfusion will be out of phase with the cardiac pixels, perfused pulmonary pixels can be identified as those with low statistical correlation ($r < -0.5$) with the cardiac pixels. Next, select a lung pixel manually from the respiratory image sequence, noting that the respiratory rate can be determined from the PCA of the tidal breathing reconstruction sequence. Ventilated pixels can then be identified as pixels highly correlated in the time domain with the chosen lung pixel ($r > 0.7$). The segmented lung region is then formed by taking the union of the perfused pulmonary pixels and the ventilated pixels.
3. The EIT-derived ventilation/perfusion ratio, or $\dot{V}/\dot{Q}$ index, $i(p)$, for each pixel $p$ is an approximation to the ratio of air flow in liters per minute to blood flow in liters per minute through the voxel defined by pixel $p$. It can be calculated according to the method derived in [18], as follows.

   Let $\sigma_b(p, t)$ denote the relative conductivity in in pixel $p$ at time $t$ corresponding to the reconstruction of the breath-

holding image sequence, and let $\sigma_a(p, t)$ denote the relative conductivity in in pixel $p$ at time $t$ corresponding to the reconstruction of the ventilation image sequence. Let $\sigma_{bM}$ and $\sigma_{bm}$ be the maximum and minimum values, respectively, of the conductivity over the breath-holding data, and $\sigma_{aM}$ and $\sigma_{am}$ be the maximum and minimum values, respectively, of the conductivity over ventilation data.

Now the volume fraction of blood $f_b(p, t)$ and air $f_a(p, t)$ are computed from

$$f_b(p,t) = \frac{\sigma_b(p,t) - \sigma_{bm}}{\sigma_{bM} - \sigma_{bm}},$$

and

$$f_a(p,t) = \frac{\sigma_a(p,t) - \sigma_{aM}}{\sigma_{am} - \sigma_{aM}},$$

respectively. Denoting the volume of the voxel corresponding to pixel $p$ by $vol(p)$ and the average duration of one cardiac or ventilatory cycle, respectively, by $\Delta t_b$ and $\Delta t_a$, the ventilation rate, $\dot{V}(p)$, is approximated by

$$\dot{V}(p) \approx \frac{f_a(p,t_{aM}) - f_a(p,t_{am})}{\Delta t_a} \cdot vol(p), \tag{1}$$

and the perfusion rate, $\dot{Q}(p)$, is approximated by

$$\dot{Q}(p) \approx \frac{f_b(p,t_{bM}) - f_b(p,t_{bm})}{\Delta t_b} \cdot vol(p), \tag{2}$$

where $t_{aM}$ and $t_{am}$ denote the times at which $f_a(p, t)$ attains its maximum and minimum, respectively, over the period of ventilation data collection. Similarly, let $t_{bM}$ and $t_{bm}$ denote the times at which $f_b(p, t)$ attains its maximum and minimum, respectively, over the period of breath-holding data collection. The $\dot{V}/\dot{Q}$ index, $i(p)$, is then computed from the formula

$$\frac{\dot{V}}{\dot{Q}} \approx i(p) = \frac{f_a(p,t_{aM}) - f_a(p,t_{am})}{f_b(p,t_{bM}) - f_b(p,t_{bm})} \cdot \frac{\Delta t_b}{\Delta t_a}. \tag{3}$$

A regional ventilation-perfusion index, $I(R)$, may also be computed for the collection of pixels in a specified region, $R$. This is useful for comparing EIT-derived $\dot{V}/\dot{Q}$ indices with standard global lung values of the $\dot{V}/\dot{Q}$ ratio. For such a comparison, the region $R$ should be chosen to be all pixels identified to be in the lungs. The region may also be chosen to isolate each lung, individually, or lobes of lungs, to compare regional gas exchange performance. As in [18], define this regional ventilation-perfusion index as

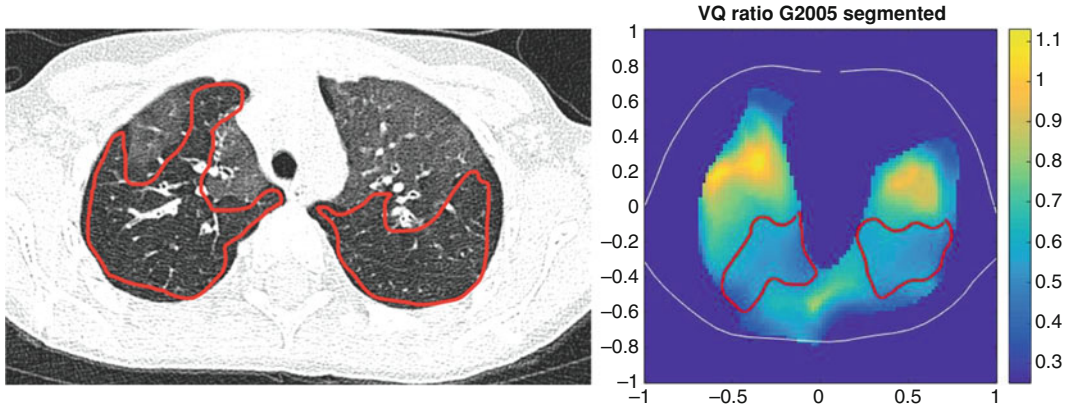


**Fig. 8** Left: One slice of an expiratory CT scan of a CF patient. Right: The EIT-derived $\dot{V}/\dot{Q}$ index map with the suspected air-trapped region outlined in red, identified by regions of low $\dot{V}/\dot{Q}$ index

$$I(R) = \frac{\sum_{p \in R} \dot{V}(p)}{\sum_{p \in R} \dot{Q}(p)}. \tag{4}$$

4. Regions of air trapping are determined by inspecting the $\dot{V}/\dot{Q}$ maps qualitatively for regions of low $\dot{V}/\dot{Q}$. This qualitative analysis is analogous to identifying regions of air trapping in CT scan images, in which regions of visual inspection of expiratory images is used to identify lung regions of low density as air trapped.

Figure 8 shows an example of an EIT-derived $\dot{V}/\dot{Q}$ index map and one slice of a CT scan of the same CF patient from our study. The radiologist's report stated that the patient was found to have "focal air trapping in the upper lobes", which we have outlined in red in Fig. 8. The EIT-derived $\dot{V}/\dot{Q}$ index map shows the suspected air-trapped region outlined in red.

## 4 Notes

### 4.1 The EIT System

There are only a handful of commercially available EIT systems. These include the ENLIGHT® by Timpel [8, 27], PulmoVista® 500 by Dräger [26], Swisstom $BB^2$ [25], the Sheffield MK 3.5 by Maltron [13, 29], and the Goe MF II previously produced by CareFusion [1, 9, 21]. The Genesis system is a prototype by General Electric [2] and is based on the ACT III EIT system [5] developed Rensselaer Polytechnic Institute. (Note, however, that ACT III is no longer in use.) Academic systems include: the Sheffield Mk 3a [1, 29], the Dartmouth High-speed Electrical Impedance Tomography System [10], and the active complex electrode (ACE1) EIT system [15].

The ACE1 (Active Complex Electrode) electrical impedance tomography system used in our studies is a custom system that applies alternating current at 125 kHz at up to 5.0 mA and measures the resulting voltage amplitude and phase on all electrodes. The reader is referred to [14, 15] for an analysis of the performance of the ACE 1 system. It has a modular design consisting of the tomograph box containing multiplexers, direct current (DC) supply regulators, a logic circuit for active electrode switch control, and the current source; cables with active electrodes that connect the tomograph to the subject or tank; 32-channel analog-to-digital (ADC) boards (two GE ICS 1640 boards each with 16 channel 24-bit 2.5 Msamples/second); a function generator (Stanford Research Systems Model DS360 Ultra Low Distortion); and a DC power supply (Mastech DC Power Supply HY3005F-3).

Pairwise, or bipolar current patterns means that two electrodes at a time actively inject current of equal magnitude and opposite sign pairs of electrodes sequentially. Such patterns are also referred to as "skip $n$" patterns in the literature where $n$ indicates the number of electrodes between the two injection electrodes. The skip 0 patterns is also referred to as the adjacent current injection pattern in EIT literature. A complete set of current patterns consists of sequentially activating each pair of electrodes in the skip $n$ sequence. In fact, the number $K$ of linearly independent patterns is given by $K = L - \gcd(L, \alpha + 1)$, where $L$ is the number of electrodes (excluding ground) applied to the subject, and it is sufficient to apply $K$ patterns for a complete data set. The resulting voltage from the $k$th pattern is measured on each of the $L$ electrodes. This set of $L$ measurements from $K$ current patterns ($L$ times $K$ voltages) comprises the data required to reconstruct a single frame in the sequence of conductivity images. The formulation of this data as a discrete matrix, known as the Dirichlet-to-Neumann, or DN, matrix needed for the reconstruction algorithm is described in Subsection 4.2.1. Note that the maximum number of linearly independent current patterns possible is $L-1$, due to Kirchhoff's Law, and that it is desirable to choose a skip pattern that results in the maximum number of linearly independent patterns in order to have the richest data set possible; the number of patterns will depend on the number of electrodes applied.

### 4.2 Reconstruction of the Conductivity by the D-Bar Method

While there are numerous choices of reconstruction algorithms in EIT, the results presented in [17, 19] from the clinical data were computed with the D-bar algorithm, which has the attributes of being a direct (non-iterative) method with a real-time implementation [6]. The most common approaches to EIT reconstruction are Gauss-Newton based iterative methods (see, for example, [11]), or one step of a Gauss-Newton method, resulting in a fast linearized reconstruction [4]. We present here an overview of the D-bar method based on [12, 20] and refer the reader to [16] for

background, further computational details, and other versions of the D-bar method.

#### 4.2.1 Approximating the Dirichlet-to-Neumann (DN) Map from Measured Data

The inverse conductivity problem has a unique solution mathematically if the data is the Dirichlet-to-Neumann map $\Lambda_\sigma$, where $\sigma(x, y)$ denotes the conductivity at a point $(x, y)$ in the region of interest, and knowledge of $\Lambda_\sigma$ corresponds to knowledge of the current that arises from any given voltage distribution on the boundary. In practice, we approximate this infinite-dimensional mapping by a discrete matrix of dimension $L$ by $K$.

Denote the basis of orthonormal current patterns by $\phi^n$, where $n = 1, \ldots, N$, $N < L$, and denote the vector of voltages on the electrodes arising from the $n$th current pattern by $U^n$. If the applied current patterns do not form an orthonormal set, the Gram-Schmidt algorithm can be applied to them to obtain an orthonormal basis, and in this case, the voltages must be synthesized through the change of basis formula to correspond to the voltages that would arise had the current patterns that arise from the Gram-Schmidt algorithm actually been applied. The DN matrix, which we will denote by $\mathbf{L}_\sigma$, is the inverse of the matrix approximation $\mathbf{R}_\sigma$ to the Neumann-to-Dirichlet, or current-to-voltage, map, provided that the voltage measurements sum to zero for each current pattern. Since the ACE 1 system, as well as most EIT systems, applies current and measures voltage, one first forms $\mathbf{R}_\sigma$ by computing a discrete inner product, and inverts $\mathbf{R}_\sigma$ to obtain $\mathbf{L}_\sigma$. As long as the matrix of current patterns is full rank, $\mathbf{R}_\sigma$ will be a well-conditioned matrix. Thus, first compute the $m$, $n$th entry of the matrix $\mathbf{R}_\sigma$:

$$\mathbf{R}_\sigma(m, n) = \sum_{\ell=1}^{L} s_\ell \phi^m \cdot U^n, \tag{5}$$

where $s_\ell$ is the arc length of the boundary segment connecting the centers of electrodes $\ell$ and $\ell + 1$, and $\cdot$ denotes the vector dot product. Then compute the DN matrix by taking the matrix inverse:

$$\mathbf{L}_\sigma = \mathbf{R}_\sigma{}^{-1}. \tag{6}$$

#### 4.2.2 Computation of the Scattering Transform

A simplification to reduce the computational cost of the D-bar method was introduced in [24] and has proven effective on human data sets. It is known as the $\mathbf{t}_{dif}^{\exp}$ approximation and was also employed in [17, 19]. It is a kind of nonlinear Fourier transform, and so its argument is the (artificial) complex frequency $k \in \mathbb{C}$. Due to the heavy use of complex arithmetic in this method, points $(x, y) \in \Omega$ are identified with complex numbers $z = x + iy$. The $\mathbf{t}_{dif}^{\exp}$ approximation to the scattering transform is defined as:

$$\mathbf{t}_{dif}^{\exp}(k) = \int_{\partial\Omega} e^{i\bar{k}\bar{z}} (\Lambda_\sigma - \Lambda_{ref}) e^{ikz} ds. \tag{7}$$

Here, $\Lambda_{ref}$ refers to the DN map corresponding to a reference data set. This reference set could be a single frame in the reconstructed sequence of images, or an average over all frames in the sequence. In [17, 19], $\Lambda_{ref}$ was an average. The discrete matrix $\mathbf{L_{ref}}$ was computed by averaging the voltages for a given electrode and a given current pattern over all frames to obtain one set of average voltages, and this was used in the computation of $\mathbf{R_{ref}}(m, n)$ in Eq. 5. The exponential function $e^{ikz}$ in 7 is expanded in the orthonormal basis of current patterns:

$$e^{ikz} = 1 + \sum_{n=1}^{N} b_n(k)\phi^n(z), \tag{8}$$

where the 0th order term in the expansion, 1, accounts for the fact that no basis function $\phi^n$ can be a constant function due to Kirchhoff's law. The coefficients $b_n(k)$ are defined by

$$b_n(k) = \sum_{\ell=1}^{L} e^{i\bar{k}\zeta_\ell}\phi^n(\zeta_\ell)),$$

where $\zeta_\ell$ is the point corresponding to the center of the $\ell$th electrode. Note that since $\Lambda_\sigma 1 = 0$ for any $\sigma$, we see that in the formula for computing $\mathbf{t}^{\exp}$ the 0th order term is annihilated. Let $\delta\Lambda = \Lambda_\sigma - \Lambda_{ref}$ and its discrete approximation $\delta\mathbf{L} = \mathbf{L_\sigma} - \mathbf{L_{ref}}$. Then

$$\delta\Lambda e^{ikz} = \sum_{n=1}^{N} b_n(k)\delta\Lambda\phi^n(z).$$

Define $\Phi$ to be the matrix of current patterns formed by setting the $n$th column of $\Phi$ to be $[\phi^n(\zeta_1), \ldots, \phi^n(\zeta_L)]^T$. Then $\delta\Lambda\phi^n(\zeta_\ell) \approx (\Phi\delta\Lambda)(\ell, n)$. The discrete approximation to the scattering transform is computed by discretizing the integral in 7 as follows.

$$\mathbf{t}^{\exp}_{dif}(k) \approx \sum_{\ell=1}^{L}\int_{e_\ell} e^{i\bar{k}\bar{z}}\delta\Lambda\sum_{n=1}^{N} b_n(k)\phi^n(z)ds \approx \sum_{\ell=1}^{L}\sum_{n=1}^{N} A_\ell e^{i\bar{k}\bar{z}_\ell} b_n(k)(\mathbf{\Phi}\delta L)(\ell, n),$$

where $A_\ell$ is the area of the $\ell$th electrode. Note that the approximate scattering transform must be set zero for $|k|$ outside of some radius $R$, typically equal to 4, due to blow-up caused by noise in the measured data. This radius can be determined empirically.

#### 4.2.3 The D-Bar Equation

The D-bar equation in integral form is

$$\mu_R(z, s) = 1 + \frac{1}{(2\pi)^2}\int_{|k|\le R} \frac{\mathbf{t}^{\exp}_{dif}(k)}{(s-k)\bar{k}} e_{-z}(k)\mu_R(\bar{z}, k)dk_1 dk_2. \tag{9}$$

An efficient method of solution is provided in detail in [16], and is omitted here for brevity. Matlab code also accompanies the text [16]. Equation 9 can be solved independently in parallel for each point $z = (x, y)$ in the region of interest, and then the conductivity is simply computed from

$$\sigma(z) = \mu^2(z, 0). \tag{10}$$

Tomographic images are then formed by plotting $\sigma(x, y)$ at each point in the region of interest, using, for example, Matlab's imagesc command.

## Acknowledgements

This manuscript was made possible by Grant Number R01EB026710 and 1R21EB016869-01 from the National Institutes of Health. Its contents are solely the responsibility of the authors and do not necessarily represent the official views of the NIH.

### References

1. Adler A, Amato MB, Arnold JH, Bayford R, Bodenstein M, Böhm SH, Brown BH, Frerichs I, Stenqvist O, Weiler N, Wolf GK (2012) Whither lung EIT: Where are we, where do we want to go and what do we need to get there? Physiol Measure 33:679–694
2. Ashe J, Shoudy D, Boverman G, Sabatini J, Kao T, Amm B (2014) A high precision parallel current drive experimental EIT system. In: 15th international conference on biomedical application of EIT, vol. 14. IEEE, New York, pp 24–26
3. Barber DC, Brown BH (1990) Progress in electrical impedance tomography. In: Inverse problems in partial differential equations. SIAM, Philadelphia, PA, pp 151–164
4. Cheney M, Isaacson D, Newell J, Simske S, Goble J (1990) Noser: an algorithm for solving the inverse conductivity problem. Int J Imag Syst Technol 2:66–75
5. Cook RD (1992) ACT3: a high-speed, high-precision electrical impedance tomograph, PhD thesis, Rensselaer Polytechnic Institute, Troy, New York, July 1992
6. Dodd M, Mueller JL (2014) A real-time d-bar algorithm for 2-d electrical impedance tomography data. Inverse Probl Imag 8:1013–1031
7. Fuks L, Cheney M, Isaacson D, Gisser D, Newell J (1991) Detection and imaging of electric conductivity and permittivity at low frequency. IEEE Trans Biomed Eng 38:1106–1110
8. Gaggero PO (2011) Miniaturization and distinguishability limits of electrical impedance tomography for biomedical application. PhD thesis, University of Neuchatel, Neuchatel, Switzerland, June 2011
9. Hahn G, Just A, Dittmar J, Fromm KH, Quitel M (2013) Synchronous absolute EIT in three thoracic planes at different gravity levels. J Phys Conf Ser **434**. XV international conference on electrical bio-impedance & XIV conference on electrical impedance tomography. Institute of Physics Publishing
10. High-speed electrical impedance tomography system. http://engineering.dartmouth.edu/bioimpedance/high-speed-EIT.html. Nov 2014. Thayer School of Engineering at Dartmouth Technology Research Projects
11. Holder D (ed) (2005) Electrical impedance tomography; methods, history, and applications. IOP publishing Ltd., Bristol
12. Knudsen K, Lassas M, Mueller J, Siltanen S (2009) Regularized D-bar method for the inverse conductivity problem. Inverse Probl Imag 3:599–624
13. Maltron sheffield mk 3.5 (2014) http://www.maltronint.com/eit/msmk35.php. Maltron Company Website
14. Mellenthin MM, Mueller JL, Camargo EDLB, de Moura FS, Hamilton SJ, Gonzalez Lima R (2015) The ACE1 thoracic electrical impedance tomography system for ventilation and perfusion. In: Proceedings of the 37th annual international conference of the IEEE engineering in medicine and biology society, 2015, pp. 4073–4076
15. Mellenthin MM, Mueller JL, de Camargo EDLB , de Moura FS, Santos TBR, Lima RG, Hamilton SJ, Muller PA, Alsaker M (2019) The ACE1 electrical impedance tomography system for thoracic imaging. IEEE Trans. Instrum Measure 68:3137–3150
16. Mueller J, Siltanen S (2012) Linear and nonlinear inverse problems with practical applications. SIAM, Philadelphia, PA (2012)
17. Mueller J, Muller P, Mellenthin M, DeBoer E, Murthy R, Capps M, Alsaker M, Deterding R, Sagel S (2018) A method of estimating regions of air trapping from electrical impedance

tomography data. Physiol Measure 39:05NT01

18. Muller P, Li T, Isaacson D, Newell J, Saulnier G, Kao T, Ashe J (2015) Estimating a regional ventilation-perfusion index. Physiol Measure 36:1283–1295
19. Muller P, Mueller J, Mellenthin M, Murthy R, Capps M, Wagner B, Alsaker M, Deterding R, Sagel S, Hoppe J (2018) Evaluation of surrogate measures of pulmonary function derived from electrical impedance tomography data in children with cystic fibrosis. Physiol Measure 39(4):045008
20. Nachman AI (1996). Global uniqueness for a two-dimensional inverse boundary value problem. Ann Math 143, 71–96 (1996)
21. Pulletz S, Elke G, Zick G, Schädler D, Scholz J, Weiler N, Frerichs I (2008) Performance of electrical impedance tomography in detecting regional tidal volumes during one-lung ventilation. Acta Anaesthesiol Scand 52:1131–1139
22. Quanjer PH, Stanojevic S, Cole T, et al (2012) Multi-ethnic reference values for spirometry for the 395 year age range: the global lung function 2012 equations: report of the global lung function initiative (GLI), ERS task force to establish improved lung function reference values. Eur Resp J 40:1324–1343
23. E. T. F. Report (2012) Multi-ethnic reference values for spirometry for the 395-yr age range: the global lung function 2012 equations. Eur Respir J 40:1324–1343
24. Siltanen S, Mueller J, Isaacson D (2000) An implementation of the reconstruction algorithm of A. Nachman for the 2-D inverse conductivity problem. Inverse Probl 16:681–699
25. Swisstom $BB^2$ product information 2st100–112, rev. 000. http://www.swisstom.com/wp-content/uploads/BB2_Brochure_2ST100-112_Rev.000_EIT_inside.pdf. Swisstom AG Manufacturer Brochure
26. Technical datasheet: Dräger pulmovista 500. http://www.draeger.com/sites/assets/PublishingImages/Products/rsp_pulmovista500/Attachments/rsp_pulmovista_500_pi_9066475_en.pdf, 2010. Dräger Manufacturer Brochure
27. Timpel enlight: technology (2010) http://www.timpel.com.br/technology. Timpel Company Website
28. Vogt B, Pulletz S, Elke G, Zhao Z, Zabel P, Weiler N, Frerichs I (2012) Spatial and temporal heterogeneity of regional lung ventilation determined by electrical impedance tomography during pulmonary function testing. J Appl Physiol 113:1154–1161
29. Wilson AJ, Milnes P, Waterworth AR, Smallwood RH, Brown BH (2001) Mk3.5l a modular, multi-frequency successor to the Mk3a EIS/EIT system. Physiol Measure 22:49–54

# Chapter 40

# In Vivo Quantitative Whole-Body Perfusion Imaging Using Radiolabeled Copper(II) Bis(Thiosemicarbazone) Complexes and Positron Emission Tomography (PET)

**Mark A. Green, Carla J. Mathias, Nathaniel J. Smith, Monica Cheng, and Gary D. Hutchins**

## Abstract

Traditional quantitative perfusion imaging methods require complex data acquisition and analysis strategies; typically require ancillary arterial blood sampling for measurement of input functions; are limited to single organ or tissue regions in an imaging session; and because of their complexity, are not well suited for routine clinical implementation in a standardized fashion that can be readily repeated across diverse clinical sites. The whole-body perfusion method described in this chapter has the advantages of on-demand radiotracer production; simple tissue pharmacokinetics enabling standardized estimation of perfusion; short-lived radionuclides, facilitating repeat or combination imaging procedures; and scalability to support widespread clinical implementation. This method leverages the unique physiological characteristics of radiolabeled copper(II) bis(thiosemicarbazone) complexes and the detection sensitivity of positron emission tomography (PET) to produce quantitatively accurate whole-body perfusion images. This chapter describes the synthesis of ethylglyoxal bis(thosemicarbazonato)copper(II) labeled with copper-62 ([$^{62}$Cu]Cu-ETS), its unique physiological characteristics, a simple tracer kinetic model for estimation of perfusion using image-derived input functions, and validation of the method against a reference standard perfusion tracer. A detailed description of the methods is provided to facilitate implementation of the perfusion imaging method in PET imaging facilities.

**Key words** Quantitative perfusion imaging, Positron emission tomography, [$^{62}$Cu]Cu-ETS, Tracer kinetic modeling, Whole-body imaging, Perfusion estimation

## 1 Introduction

### *1.1 Imaging Tissue Perfusion*

Characterization of the magnitude and variation of perfusion has long been a research and clinical objective of the biomedical imaging community, with perfusion imaging methods now available in each of the major imaging modalities (PET, SPECT, MRI, CT, and ultrasound). Perfusion imaging methods have played an important role in advancing our understanding of the manifestation of many diseases, their progression, and response to therapy. Nonetheless,

Miguel R. Ossandon et al. (eds.), *Biomedical Engineering Technologies: Volume 1*, Methods in Molecular Biology, vol. 2393, https://doi.org/10.1007/978-1-0716-1803-5_40, 

many quantitative tissue perfusion imaging methods require complex data acquisition and analysis strategies; typically require ancillary arterial blood sampling for measurement of input functions; are limited to single organ or tissue regions in an imaging session; and because of their complexity, are not well suited for routine clinical implementation in a standardized fashion that can be readily repeated across diverse clinical sites. The positron emission tomography (PET) whole-body perfusion imaging method described in this chapter is a novel approach that overcomes many of the logistical limitations of other imaging-based quantitative perfusion methods.

### 1.2 Positron Emission Tomography

Positron emission tomography (PET) is a nuclear medicine imaging technique that is used clinically to study neurological disorders and diseases, cardiovascular disease, and cancer. PET imaging measures physiological and biochemical characteristics of tissue using molecular probes labeled with short-lived radioisotopes. Unique characteristics of PET imaging methods include the availability of radioisotopes that can be easily incorporated into small biologically active molecules (for example $^{11}$C, $^{13}$N, $^{15}$O, $^{18}$F, $^{60,61,62,64}$Cu, or $^{68}$Ga) and extremely high detection sensitivities that enable measurement of picomolar to nanomolar concentrations of radioisotopes in vivo. The ability of PET to measure very small molecular concentrations enables biological processes to be traced without pharmacologic perturbation by the radiolabeled agent administered to the patient. These imaging agents are commonly referred to as radiotracers. Specifically designed PET radiotracers enable the generation of quantitative in vivo images of numerous tissue properties including metabolism, protein or enzyme expression, receptor expression, blood volume, and tissue perfusion.

Radioisotopes which undergo positron decay tend to have atomic masses that are less than the stable isotope(s) of that element, and thus contain an excess number of protons relative to neutrons in the nucleus. A positron is a subatomic particle with the mass of an electron, but a positive charge (i.e., an "anti-electron"). When a radioisotope decays by positron emission, a proton in the nucleus is converted into a neutron with concurrent emission of a positron and a neutrino. The positrons emitted by any given radionuclide will exhibit a characteristic energy spectrum, and an associated density-dependent mean positron path length through the surrounding tissue. As it travels through tissue, the positron will be progressively slowed by electrostatic interactions, following a circuitous (but radially short) path before eventually being captured by an electron. That positron-electron pair will annihilate, converting their mass into two 511 keV photons ($E = mc^2$) emitted at an angle of approximately 180° (momentum must be conserved).

PET imaging systems, generally organized in ring configurations, consist of radiation detectors that are optimized for the

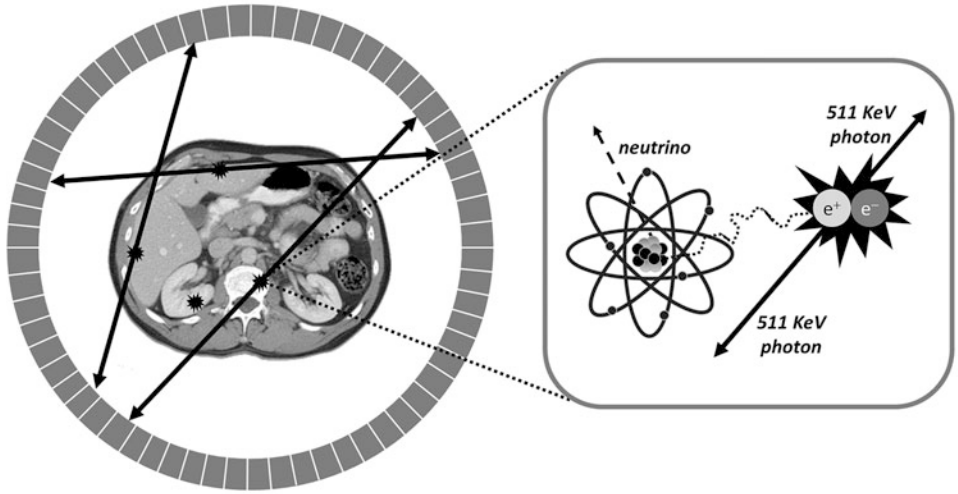


**Fig. 1** Physical Foundation of PET Imaging. Right: Positron emission occurs when a proton in the nucleus is converted into a neutron. The positron travels a short distance before it is captured by an electron and the pair of subatomic particles annihilate producing two 511-keV photons emitted at an angle of approximately 180-degrees. Left: For imaging, individual radioisotope decay events are detected in the PET scanner by rings of detectors for the 511-keV photons. The near simultaneous, or coincident, detection of 511-keV photons in two detectors defines a line along which the event occurred. PET images are then generated using mathematical algorithms that convert the detected events into an estimated radioisotope distribution. The detectors of current clinical PET cameras achieve timing resolutions as low as 210 ps. Note, there will be photons lost due to tissue attenuation of the 511-keV radiation. Correction for that photon loss by attenuation is required, if the PET image is to quantitatively map regional radionuclide concentrations. Fortunately, the net attenuation is a constant for any given line of coincidence, regardless of the annihilation location along the back-projection line between the detectors. Thus, quantitative correction for attenuation losses becomes straightforward in PET by directly measuring the net attenuation along each back-projection line. The required net attenuation factors can be estimated from a CT scan covering the PET field-of-view, or obtained directly using an independently acquired transmission scan collected by imaging a positron-emitting (511-keV photon) source positioned between the patient and the detectors

efficient detection of the 511-keV annihilation photons. The near simultaneous, or coincident, detection of both 511-keV annihilation photons defines a line along which the annihilation occurred, and the time difference between detection of each 511-keV photon provides information about the relative location of the event along the line of response. The time difference between the detection of each photon from an annihilation pair is determined by the time-of-flight for each photon. The process of positron decay, positron-electron annihilation, and 511-keV annihilation photon detection for PET is illustrated in Fig. 1. In a typical PET study millions of coincidence events are detected by the PET system, and images of the radioisotope distribution are generated using mathematical algorithms that relate the geometry of the PET system and characteristics of the photon detection process (lines of response and photon arrival time differences) to physical space within the PET

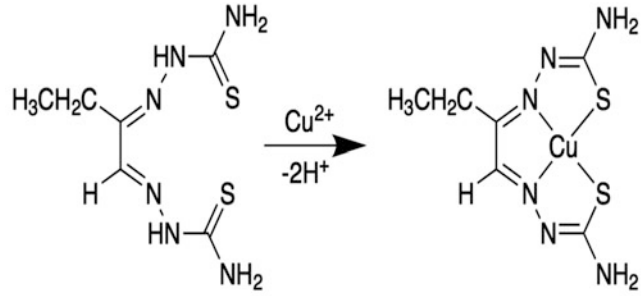


**Fig. 2** Synthesis and structural formula of the uncharged, lipophilic, [$^{62}$Cu]Cu-ETS radiotracer, in which the $^{62}Cu^{2+}$ ion is bound in a square-planar $N_2S_2$ coordination sphere by the tetradentate bis(thiosemicarbazone) ligand derived from ethylglyoxal

scanner field-of-view. PET images can be generated to represent the radioisotope distribution at a fixed point in time, or as a temporal sequence of images to measure the pharmacokinetic properties of the radiotracer.

### *1.3 Copper(II) Bis (Thiosemicarbazone) Complexes as Perfusion Tracers*

Copper(II) bis(thiosemicarbazone) complexes represent a promising class of radiotracers for quantitative whole-body imaging of perfusion [1–16]. Figure 2 shows the chemical structure for Cu-ETS (ethylglyoxal bis(thiosemicarbazonato)copper(II)). The copper bis(thiosemicarbazone) complexes can have a high first-pass extraction fraction, readily cross cell membranes, and rapidly undergo reductive decomposition (in the intracellular fluid and in mitochondria) releasing the Cu radioisotope and effectively trapping it in the cell. The delivery and "trapping" process for these compounds is illustrated in Fig. 3.

Cu radioisotopes that can be employed for whole-body PET imaging studies include $^{60}$Cu ($T_{1/2}$: 23.6 min; 93% $\beta^+$ emission); $^{61}$Cu ($T_{1/2}$: 3.3 h; 62% $\beta^+$ emission); $^{62}$Cu ($T_{1/2}$: 9.8 min; 98% $\beta^+$ emission); and $^{64}$Cu ($T_{1/2}$: 12.8 h; 19% $\beta^+$ emission). The methods described for [$^{62}$Cu]Cu-ETS synthesis can be similarly implemented with any of these other copper nuclides, simply recognizing that the required quantity of the $H_2$ETS chelating ligand may need to be increased to reflect total copper content of the radionuclide sample. (Molar radioactivity for the no-carrier-added copper radionuclide will predictably vary with nuclide half-life, as well as the elapsed time between radionuclide production and tracer synthesis.) In most imaging scenarios, a short half-life is preferred to enable the performance of repeat studies, or to couple perfusion imaging with other radiotracers that provide complementary information (e.g., $^{18}$F labeled 2-fluoro-2-deoxy-D-glucose for cellular metabolism). Consequently, $^{62}$Cu has been the most commonly employed radioisotope for Cu-ETS imaging studies to date. The

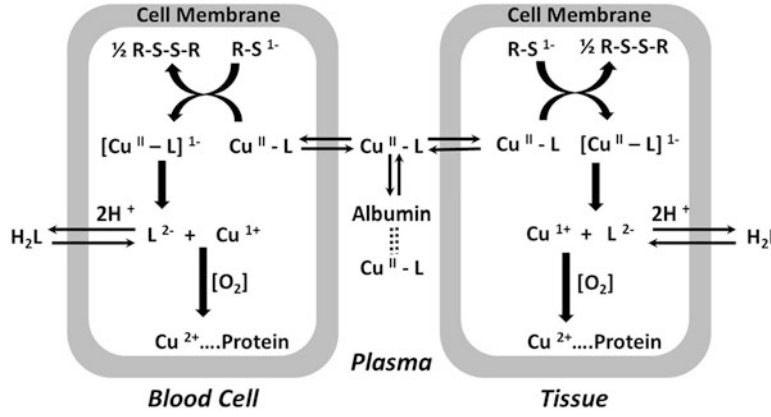


**Fig. 3** Copper (II) bis(thiosemicarbazone) complex cellular trapping mechanism. The copper(II) bis(thiosemicarbazone) complexes are lipophilic uncharged molecules that readily diffuse across capillary/tissue/cell membrane interfaces. In the intracellular environment the copper(II) complex is reductively decomposed by reaction with abundant thiols (e.g., glutathione), leading to dissociation of copper (I) from the bis(thiosemicarbazone) ligand. In the presence of oxygen, the liberated Cu(I) will be rapidly reoxidized to Cu(II), effectively trapping the radiocopper within the cell as it simply enters the endogenous cellular copper pool

perfusion imaging methods described in the subsequent sections of this chapter will focus on [$^{62}$Cu]Cu-ETS.

### 1.4 Quantitative Whole-Body Perfusion Tracer Kinetic Model

[$^{62}$Cu]Cu-ETS exhibits properties that are nearly ideal for quantitative perfusion imaging. These characteristics include: (1) a high first-pass extraction fraction over the dynamic range of perfusion levels of physiologic relevance; (2) rapid depletion of the pool of radiolabeled molecules (parent tracer or metabolites) in the vascular system that are free to exchange between tissue and blood; (3) long tissue radionuclide retention times, enabling whole body imaging protocols; and (4) a radiotracer that can be readily prepared and distributed for widespread use. These characteristics enable use of a simple tracer kinetic model for the quantitative estimation of tissue perfusion (Fig. 4). In this model, the average concentration of the Cu radioisotope within a tissue volume of interest (VOI) over the time interval $t_1$ to $t_2$ ($C_{VOI}(t_1,t_2)$) is described by eq. 1, where $f_{BV}$ is the fraction of the VOI volume occupied by blood, $C_T(t)$ is the tissue radionuclide concentration, and $C_A(t)$ is the radionuclide concentration in the arterial blood.

$$C_{VOI}(t_1,t_2) = \frac{(1-f_{BV})}{(t_2-t_1)}\int_{t_1}^{t_2} C_T(\tau)d\tau + \frac{f_{BV}}{(t_2-t_1)}\int_{t_1}^{t_2} C_A(\tau)d\tau \quad (1)$$

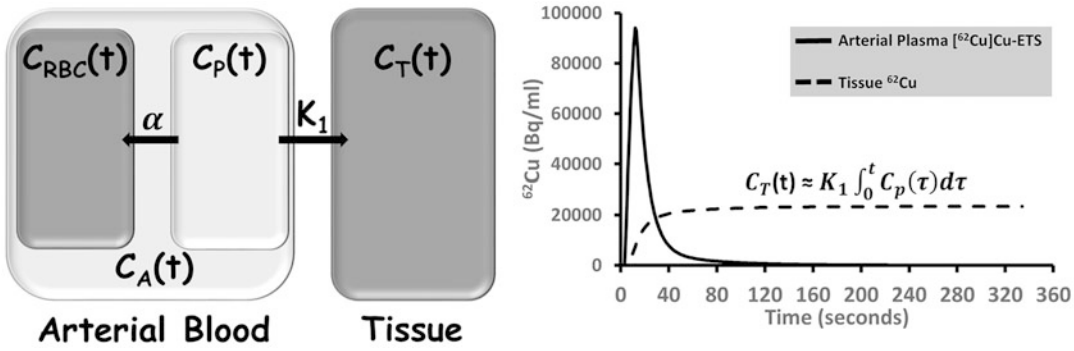


**Fig. 4** [$^{62}$Cu]Cu-ETS Tracer Kinetic Model. Parameters include tracer delivery ($K_1$), fractional blood volume ($F_{BV}$), and [$^{62}$Cu]Cu-ETS decomposition rate in blood ($\alpha$)

In eq. 1, VOI is used to describe a 3-dimensional region in space. This can be a single voxel element within an image volume or a larger region that is defined by a using standard medical image analysis software that is available through PET scanner manufacturers and third-party vendors. In the context of the imaging methods described in this chapter, whole-body perfusion calculations are being performed on every pixel or voxel of the three-dimensional PET image.

Equation 1 can be simplified to eq. 2 for image acquisition periods that occur after the radiotracer concentration in the blood becomes negligible relative to tissue radionuclide concentrations ($t_1 > 5$ min). In eq. 2 the tissue concentration ($C_T(t)$) has been replaced with the product of the rate of radiotracer delivery ($K_1$) and the integral of the parent radiotracer concentration in the arterial blood plasma ($C_p(t)$).

$$C_{VOI}(t_1, t_2) \approx \frac{(1 - f_{BV})}{(t_2 - t_1)} K_1 \int_{t_1}^{t_2} \int_0^{\infty} C_p(\tau) d\tau dt \tag{2}$$

The term $K_1$ in this model represents the product of perfusion, the first pass extraction of the radiotracer, and tissue density (eq. 3), where $F$ is tissue perfusion (mL/g/min), $E$ is the first pass extraction fraction, $\rho$ is tissue density (g/mL), and PS is the permeability surface area product (mL/g/min).

$$K_1 = FE\rho = F\rho\left(1 - e^{-PS/F}\right) \tag{3}$$

Equation 4 describes the relationship between tissue perfusion ($F$) and the imaging measurements.

$$F(1 - e^{-PS/F}) \approx \frac{C_{VOI}(t_1, t_2)(t_2 - t_1)}{(1 - f_{BV})\rho \int_{t_1}^{t_2} \int_0^{\infty} C_p(\tau) d\tau dt} \tag{4}$$

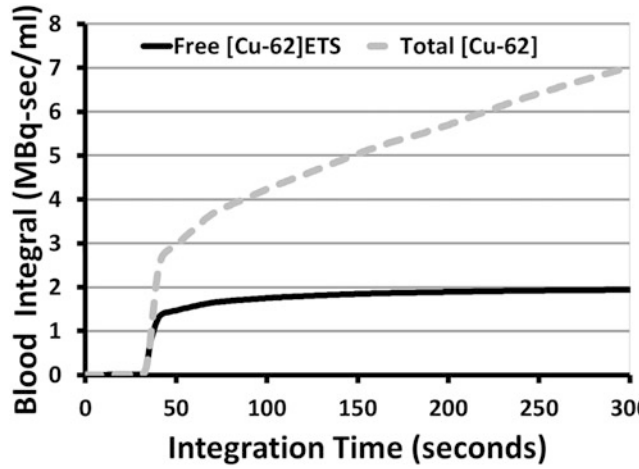


**Fig. 5** [$^{62}$Cu]Cu-ETS Arterial Blood Curve Integrals. The dashed curve is the total $^{62}$Cu in the blood (free [$^{62}$Cu]Cu-ETS plus trapped $^{62}$Cu). The solid curve is for [$^{62}$Cu]Cu-ETS available to exchange with tissue. When the solid curve plateaus, the perfusion model assumption has been achieved

A critical radiotracer property that enables simplification of the quantitative perfusion method is the rapid depletion of radiolabeled molecules (parent tracer or metabolites) in the vascular system that are free to exchange between tissue and blood. Figure 5 plots a representative arterial blood integral curve from a [$^{62}$Cu]Cu-ETS patient study. Venous blood samples were assayed for the free [$^{62}$Cu]Cu-ETS and trapped $^{62}$Cu fractions. The free fraction as a function of time was used to correct the image-based arterial blood curve to generate the [$^{62}$Cu]Cu-ETS model input function. As demonstrated in Fig. 5, the blood concentration of free [$^{62}$Cu]Cu-ETS is rapidly depleted over the first few minutes following intravenous administration. Consequently, the integral of the free [$^{62}$Cu]Cu-ETS in arterial blood plateaus quickly (within 300 s) providing a good approximation for the integral term in the denominator of eq. 4.

### 1.5 Generation of Whole-Body Perfusion Images

Figure 6 provides an example of whole-body PET perfusion images in a renal cell carcinoma (RCC) patient following the administration of ~600 MBq [$^{62}$Cu]Cu-ETS prior to and during Sunitinib therapy. The imaging protocol for this study consisted of a 360-s temporal imaging sequence of the heart followed by a 20-min whole-body scan. The initial temporal imaging sequence was used to generate arterial blood curves ($C_A(t)$ defined previously). Serial venous blood samples were collected and assayed to determine the parent [$^{62}$Cu]Cu-ETS in blood ($Cp(t)$) over the temporal imaging sequence. Relative organ/tissue $^{62}$Cu retention patterns are consistent with expected tissue perfusion levels. High retention is observed in the kidney, thyroid, heart, liver, spleen, and multiple

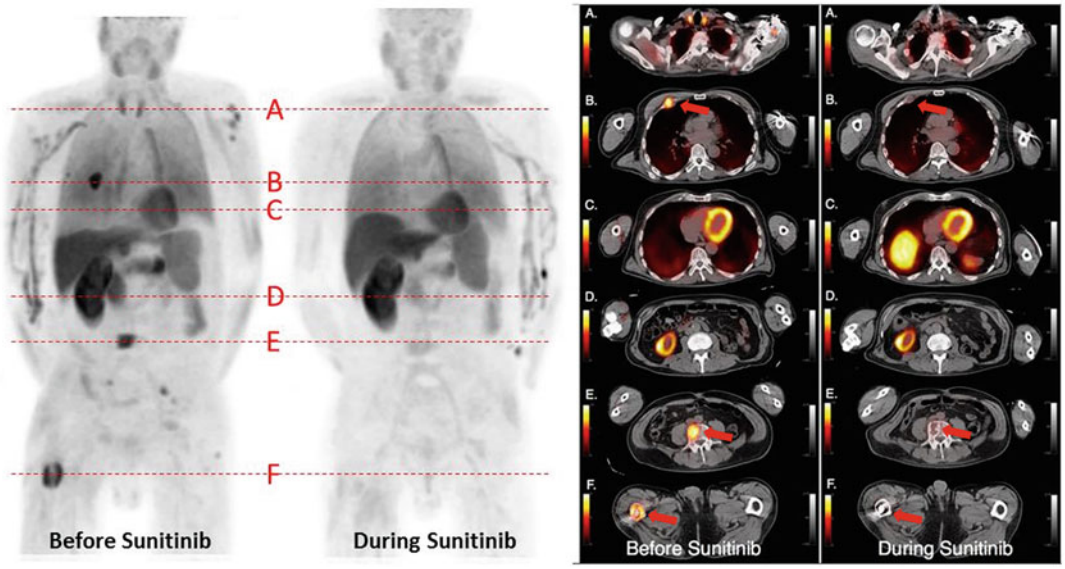


**Fig. 6** Whole body [$^{62}$Cu]Cu-ETS PET perfusion images from a patient with advanced renal cell carcinoma (RCC). PET/CT images were acquired on a Siemens Biograph-64 system and reconstructed using the vendor provided filtered backprojection reconstruction algorithm. Transaxial images on the right are from the slice locations A-F as indicated by the dashed lines on the whole-body projection images (log display scale to highlight distribution of uptake even in low flow tissues). These include a transaxial slice through: A—the thyroid; B—a metastatic tumor in a rib (red arrows); C—the myocardium; D—the kidney (the other kidney was surgically removed in the patient's prior treatment); E—a metastatic tumor in the lumbar spine (red arrows); and F—a metastatic tumor in the femur (red arrows). Note that perfusion declines significantly in the metastatic lesions, and the thyroid, with sunitinib treatment. (Thyroid dysfunction is a known sunitinib side effect, and clearly is associated with a decline in thyroid perfusion, while myocardial and renal perfusion appear unaffected by the drug treatment)

RCC lesions. With Sunitinib treatment, statistically significant reductions in perfusion are observed for the RCC patient group in metastatic lesions ($p < 0.0001$) and thyroid ($p = 0.008$), while perfusion is unchanged on average in myocardium.

On first obtaining PET whole-body perfusion images, we were surprised to see the thyroid consistently appearing as one of the most highly perfused tissues. However, this finding is fully consistent with the established literature on *Reference Man* [17, 18], which allows estimation of average perfusion rates for many organs based on average organ masses, average cardiac output, and the known distribution of cardiac output (Table 1).

As Fig. 6 illustrates, the ability to perform whole-body perfusion imaging can be particularly important in oncology applications, where metastatic lesions can potentially appear in diverse anatomic locations, and the true extent and location of disease may be unknown prior to imaging.

**Table 1**
**Estimated average tissue perfusion rates based on established data for *Reference Man* [17, 18]**

| Organ | Fraction of cardiac output (at rest)[a] | Organ mass(g)[b] | Corresponding average rate of perfusion at rest ($mL \cdot min^{-1} \cdot g^{-1}$)[c] |
|---|---|---|---|
| Brain | 0.12 | 1400 | 0.56 |
| Heart | 0.04 | 330 | 0.79 |
| Kidneys | 0.19 | 310 | 3.98 |
| Liver (arterial flow) | 0.065 | 1800 | 0.23 |
| Spleen | 0.03 | 180 | 1.08 |
| Thyroid | 0.015 | 20 | 4.88 |
| Pancreas | 0.01 | 100 | 0.65 |
| Skeletal muscle | 0.17 | 28,000 | 0.039 |

[a]From reference 18
[b]From reference 17
[c]Perfusion estimates assume total cardiac output = 6500 mL/min

### *1.6 Validation with Perfusion Reference Standard*

[$^{62}$Cu]Cu-ETS has been validated using [$^{15}$O]$H_2O$ as a perfusion reference standard in renal cell carcinoma patients [16]. In Fig. 7, [$^{62}$Cu]Cu-ETS $K_1$ values are plotted versus [$^{15}$O]$H_2O$ $K_1$ values. A statistically significant linear relationship is observed in this plot demonstrating the utility of [$^{62}$Cu]Cu-ETS as a quantitative perfusion tracer. The solid line on the plot is derived by simultaneously fitting eq. 3 for [$^{62}$Cu]Cu-ETS and [$^{15}$O]$H_2O$ to this data set, providing estimates of PS values for both [$^{62}$Cu]Cu-ETS and [$^{15}$O]$H_2O$ (Fig. 7).

## 2 Materials

1. 1.5–3-μg $H_2$ETS [19, 20].
2. 2.0-mL $^{62}$Cu Generator Eluate ($^{62}$Zn-zinc chloride for generator was purchased from Zevacor, Inc., Noblesville, IN)
3. 4–15-mL of Ultrapure 0.2 M HCl: 1.8 M NaCl generator eluent (EM Science: Sigma-Aldrich, St. Louis, MO)
4. 2-mL Ultrapure 30% (8.5 M) HCl (EM Science, Gibbstown, NJ)
5. 20-mL of 14.6% (2.5 mEq/mL) Sodium Chloride Injection, USP (Hospira, Inc. Lake Forest, IL)
6. 10-mL Ethanol, Absolute, USP (DeCon Labs, Inc., King of Prussia, PA)

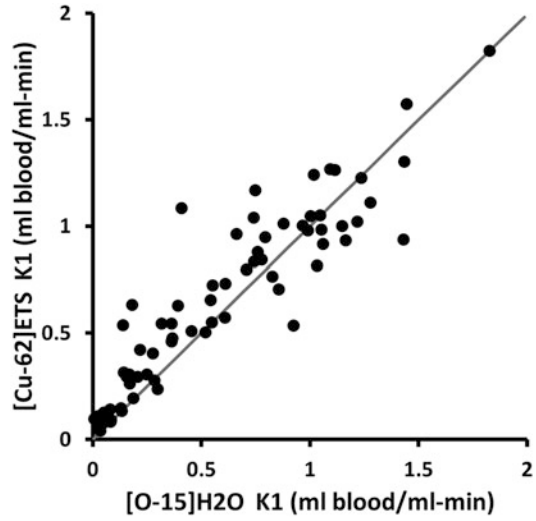


**Fig. 7** Observed relationship between [$^{62}$Cu]Cu-ETS and [$^{15}$O]$H_2O$ $K_1$ values in RCC patients. The data points represent both normal tissues (myocardium, muscle, thyroid, and lung) and primary and metastatic tumors

7. 20-mL Sodium Acetate Injection, USP, 2 mEq/mL (Hospira, Inc., Lake Forest, IL)
8. 1 itG iQS Fluidic Module (Radiomedix, Houston, TX)
9. 1 itG iQS Fluidic Module Disposable Sterile Plumbing Set (Radiomedix, Houston, TX)
10. 1 C18 SepPak Light solid phase extraction cartridge (Waters, Milford, MA)
11. 3 × 10-mL Sterile Water for Injection (Hospira, Inc., Lake Forest, IL)
12. 2 × 10-mL Sterile Saline for Injection (Hospira, Inc. Lake Forest, IL)
13. 3 3-way stopcocks, sterile (B Braun, Bethlehem, PA)
14. 6 5-cc sterile syringes with needles (B Braun, Bethlehem, PA)
15. 3 1-cc sterile syringes, all plastic (Henke Sass Wolf, Tuttlingen, Germany
16. 1 1-cc sterile syringe, Luer-Lock, Polycarbonate (BD, Franklin Lakes, NJ)
17. 4 12-cc sterile syringes, preferably Luer-Lock (Covidien, Mansfield, MA)
18. 1 10–20 cc sterile syringe, for final patient dose (Covidien, Mansfield, MA)
19. 1 18-Ga × 3.5-in. needle (BD, Franklin Lakes, NJ)
20. 2 syringe caps, sterile (B Braun, Bethlehem, PA)

21. 2 0.2-μm PDVF sterile filters, 13 mm or 25 mm diameter (Millipore, Co. Cork, Ireland)
22. 1 0.2-μm nylon, PVDF, or PTFE sterile filter, 13-mm or 25-mm, for venting vial (Saritorius, Goettingen, Germany)
23. 2 50-mL sterile centrifuge tubes (Corning, Corning, NY)
24. 5 counting vials (VWR, Radnor, PA)
25. 1–4 20-Ga 1-inch sterile syringe needles (BD, Franklin Lakes, NJ)
26. 1 18–21-Ga, 3-inch to 5-inch, sterile syringe needle (BD, Franklin Lakes, NJ)
27. 1 25-Ga 5/8-in. sterile needle (BD, Franklin Lakes, NJ)
28. 1 sterile septum-capped vial, 30-mL (Jubliant, Hollister-Stier, Spokane, WA)
29. 1 sterile pipette Tip—100-μL (Eppendorf N.A., Hauppage, NY)
30. 3 sterile pipette tips—1-10-μL (Eppendorf N.A., Hauppage, NY)
31. 1 Eppendorf pipette—10-100-μL (Eppendorf N.A., Hauppage, NY)
32. 1 Eppendorf pipette—0.5-10-μL (Eppendorf N.A., Hauppage, NY)
33. 4 sterile alcohol swabs (Covidien, Mansfield, MA)
34. 1 thioglycollate medium tube (Remel, Lenexa, KS)
35. 1 tryptic soy broth tube (Remel, Lenexa, KS)
36. 2 1 × 10-cm ITLC-SA (or ITLC-SG) strips (Agilent, Santa Clara, CA)
37. 1-2 mL 100% ethanol, for ITLC mobile phase
38. 1 TLC developing chamber (Corning, Corning, NY)
39. 1 Endosafe PTS cartridge w/30-mL water diluent vial (Charles River Laboratories, Charleston, SC)
40. 1 pH test strip (EMC Millipore, Billerica, MA)
41. 1 sterile alcohol spray (Texwipe, Kernersville, NC)
42. 2–3 sterile alcohol wipes
43. 2–3 Cavicide wipes (for hood cleaning) (Metrex Research, Romulus, MI)
44. 1 Cavicide spray (Metrex Research, Romulus, MI)
45. 1 low particulate lab coat (Valutek, Phoenix, AZ & VWR, Radnor, PA)
46. 2–4 low particulate sleeves (VWR, Radnor, PA)
47. 1–2 face mask (3 M, St. Paul, MN)

48. Nitrile gloves, powder-free (Halyard, Alpharetta, GA).
49. 1 monitoring plate; air sample (Remel, Lenexa, KS)
50. 2 monitoring plates; contact, touch (Remel, Lenexa, KS)
51. 5–8 1-mL disposable heparinized syringe for blood sampling (Line Draw Blood Sampling Kit with Dry Lithium Heparin, Smiths Medical ASD, Inc., Keene, NH).
52. Radionuclide dose calibrator with ion chamber and NaI (Tl) well counter (Capintec CRC 55tW, Capintec Instruments, Ramsey, NJ).
53. Centrifuge for 1.5-mL tubes (Eppendorf 5415, Brinkman, Westbury NJ).
54. Vortex mixer (*Vortex Genie—2*, Scientific Instruments, Inc., Bohemia, NY).
55. Radio-TLC scanner (Bioscan AR-2000, Eckert and Ziegler Radiopharma, Wilmington, MA).
56. 2 Sterile 22-ga catheters, one for radiopharmaceutical administration and one for blood sampling (BD Nexiva™ REF 383512, Becton Dickinson Infusion Therapy Systems, Sandy, UT).
57. PET camera (Studies presented were acquired on a Siemens Biograph-64 PET/CT, Siemens Healthineers AG, Erlangen, Germany. Any FDA-approved PET scanner that meets American College of Radiology accreditation standards can be used).
58. PET reconstruction software (Studies presented were reconstructed using Siemens Filtered Backprojection Reconstruction Algorithm, Siemens Healthineers AG, Erlangen, Germany. Any FDA-approved PET scanner that meets American College of Radiology accreditation standards when using vendor supplied reconstruction algorithms can be used.)
59. Kinetic modeling software (Interactive Data Language (IDL), L3HARRIS, Harris Geospatial Solutions, Broomfield, CO).

## 3 Methods

1. Synthesis of Ethylglyoxal Bis(thiosemicarbazone) ($H_2$ETS). The $H_2$ETS ligand is prepared by dropwise addition, over ~30-min, of an aqueous or ethanol solution of ethylglyoxal (2-oxobutanal; CAS 4417-81-6, Alfa Chemistry, Ronkonkoma, NY) to a hot (55–60 °C) stirred solution of thiosemicarbazide (T33405; Millipore-Sigma, St. Louis, MO) in

aqueous 5% acetic acid [19, 20]:

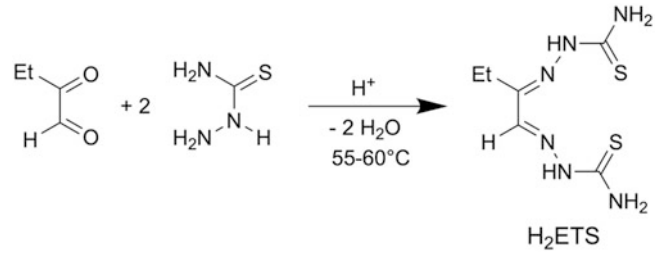


The reagent quantities should be controlled to provide a 1:2.2 mole ratio of ethylglyoxal to thiosemicarbazide in the final reaction mixture. Heating at 55–60 °C is continued for an additional 30-min, and the hot solution then allowed to slowly cool while standing overnight. The $H_2$ETS ligand precipitates upon cooling of the reaction mixture, and is isolated by filtration. The product is then recrystallized by slow cooling after dissolution in hot ethanol; again isolated by filtration; and dried under vacuum. The off-white to pale yellow solid $H_2$ETS has a long shelf-life, even at room temperature, but will typically be stored in a sealed container at <0 °C. Use of ultrapure acetic acid and ultrapure water is recommended in the synthesis, as the *bis*(thiosemicarbazone) ligand will avidly scavenge trace Cu(II) ions from the reaction solution to form the dark red Cu-ETS complex.

2. Radiotracer Synthesis.
   (a) The required $^{62}Zn^{2+}$ (~7.4 GBq/shipment) was obtained from Zevacor, Inc. (Noblesville, IN) in ~2 mL dilute HCl. This was adjusted to 2 M HCl with concentrated ultrapure HCl (*see* **Note 1**), and $^{62}Zn/^{62}Cu$ generators constructed by passing that $^{62}Zn^{2+}$ solution through a lead shielded 3 × 50-mm glass column of Dowex® 1 × 8 (200–400 mesh) ion exchange resin (Fig. 8). The generator is then switched to the desired eluent of 0.2 M HCl:1.8 M NaCl.).
   (b) At ~60 min after the flushing to transition to 0.2 M HCl:1.8 M NaCl eluent, the generator is eluted in 0.5-mL fractions to confirm its elution profile, assaying the fractions in a radionuclide dose calibrator (Fig. 9). The $^{62}Cu$-generator is then connected to the standard sterile plumbing pathway of an ITG *iQS® Fluidic Labeling Module* (Fig. 10), attaching the column outlet to the synthesis system in the same fashion as one would attach an ITG $^{68}Ga$ generator for $^{68}Ga$ radiopharmaceutical synthesis. Thus configured, the ITG Fluidic Module essentially recapitulates the configuration of a previously designed system

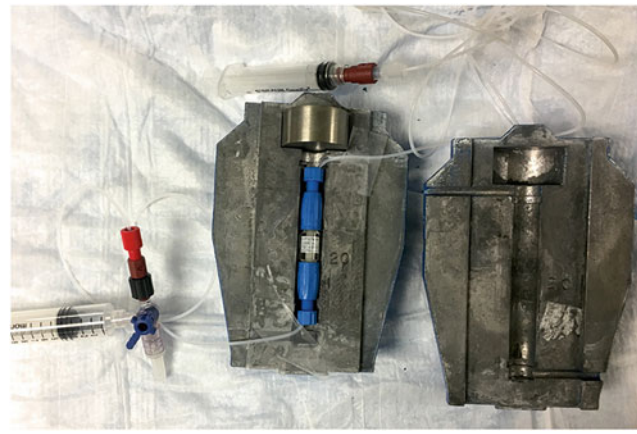

**Fig. 8** Glass column containing Dowex 1 × 8 anion exchange resin (200–400 mesh) positioned in lead shielding in preparation for loading with the aqueous HCl solution of $^{62}ZnCl_4^{2-}$

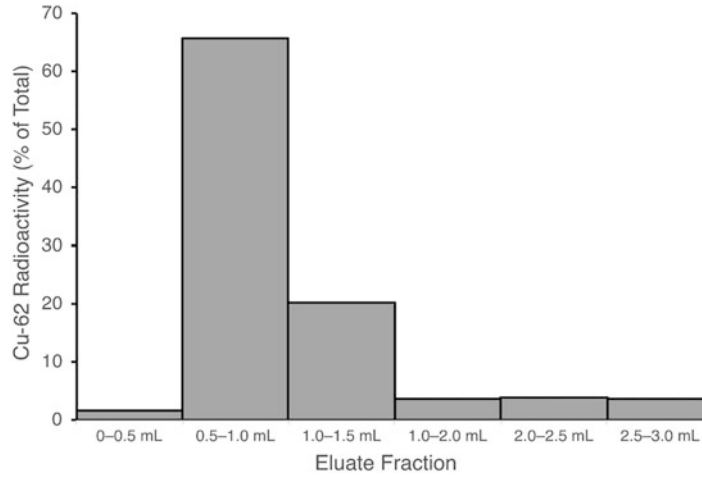


**Fig. 9** Typical elution profile for the $^{62}Zn/^{62}Cu$-generator constructed with a 3 × 50-mm column of Dowex® 1 × 8 (200–400 mesh) resin and eluted with 0.2 M HCl:1.8 M NaCl

for [$^{62}$Cu]Cu-PTSM synthesis [21]. Figure 11 schematically illustrates the layout of the associated fluid pathways.

(c) [$^{62}$Cu]Cu-ETS is prepared by loading the Fluidic Module plumbing system with 1.5–3.0μg $H_2$ETS in 0.2-mL ethanol, and 0.4 mL USP Sodium Acetate for Injection (2 M), followed by elution of the $^{62}$Cu-generator with 2-mL 0.2 M HCl:1.8 M NaCl. This is quickly followed by a sequential flush from the reagent addition port (labeled "Peptide Syringe" on the apparatus) with 5-mL air, 1-mL sterile water, and 2 × 5-mL air to effect complete reagent transfer to the room temperature reaction vial.

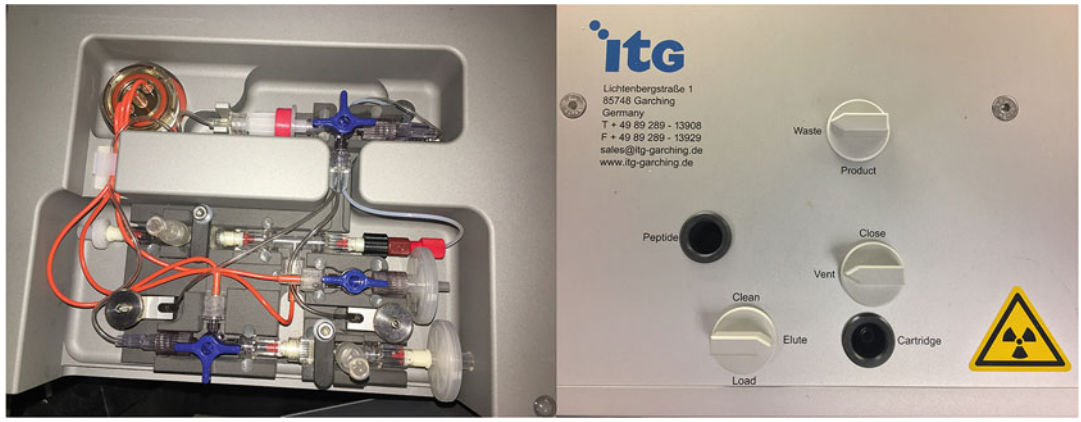


**Fig. 10** Left: Plumbing system of the ITG *iQS Fluidic Module*, attached to the $^{62}$Cu generator outlet and ready for $^{62}$Cu-radiotracer synthesis. Right: Upon closing the lid, the stopcock valves are firmly engaged by the knobs visible on the top of the lid, allowing user control of the fluid pathways required in various stages of synthesis. External Luer fittings are accessible via the "Peptide" and "Cartridge" ports for reagent additions, as well as for pressurization to effect required fluid transfers

(d) To mix the reactor contents, 2 × 5-mL air is then pushed through the dip tube of the reactor from the "Cartridge Syringe" position of the Fluidic Module, followed by 5-mL sterile water and 2 × 5-mL air. The valves are then repositioned to allow product transfer to a conditioned C18 SepPak Light® solid-phase extraction cartridge by syringe pressurization of the reactor headspace, collecting that SepPak® eluate as waste. The SepPak® is then washed with 5-mL sterile saline for injection, followed by air. The $^{62}$Cu-ETS product is then recovered by C18 SepPak® elution with 0.75-mL ethanol, followed by 1.0 mL sterile saline to rinse the lines, and diluted with 9-mL sterile saline before terminal sterilizing filtration through a 0.2-μm PVDF single-use unit (*see* **Notes 2** and **3**).

(e) Quality control for the first [$^{62}$Cu]Cu-ETS product batch of the day consists of TLC assessment of radiochemical purity (ITLC-SA strip eluted with ethanol—Fig. 12); confirmation of the bubble point of the filtration unit (50-psig for a Millipore Millex® 13-mm 0.2-μm PVDF filter unit, but the actual specification should always be re-confirmed by consulting the filter's Certificate of Analysis); measurement of final product pH; measurement of bacterial endotoxin levels in the final product; assessment of $^{62}$Zn-breakthrough; and a retrospective USP sterility test (*see* **Notes 4** and **5**). Consistent with the provisions of USP < 823>, subsequent preparations on the same day are regarded as sub-batches (*see* **Notes 6** and **7**).

3. PET Data Acquisition.

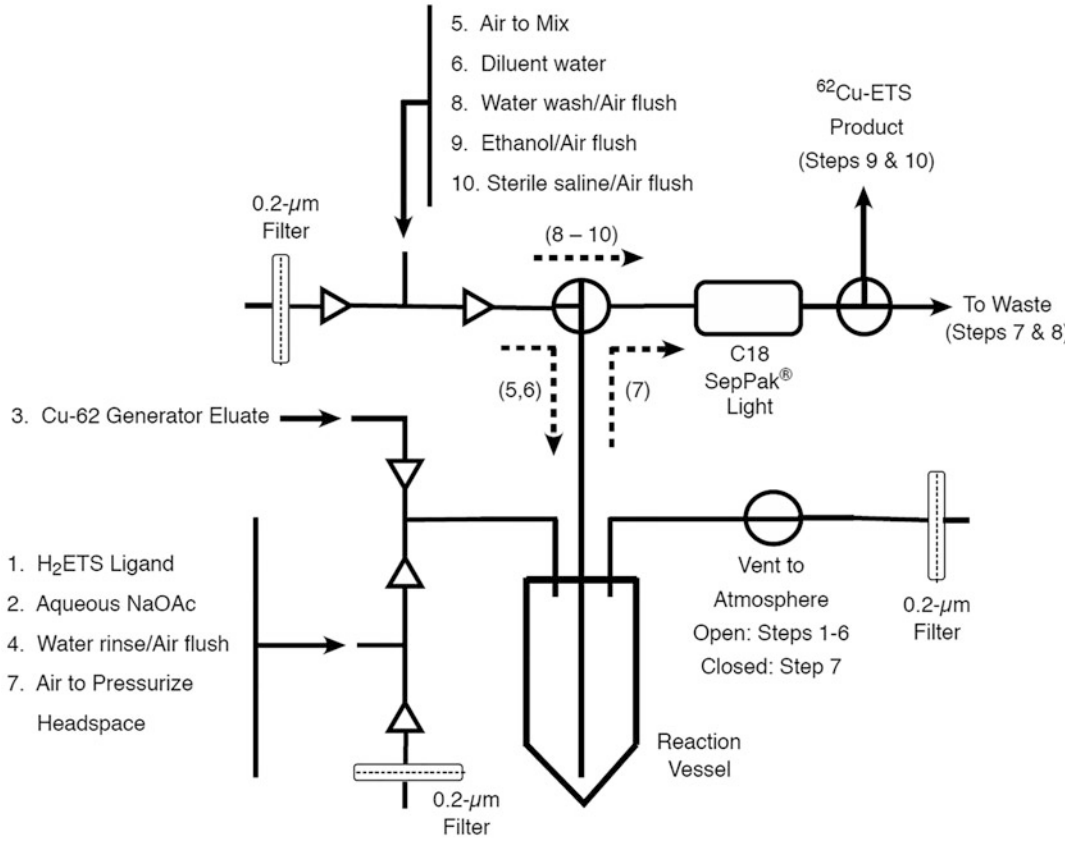


**Fig. 11** Schematic diagram of the disposable plumbing system for the ITG *iQS® Fluidic Module*, labeled to illustrate required fluid transfers in [$^{62}$Cu]Cu-ETS synthesis. The triangles (►) in the fluid pathway indicate the locations of one-way check-valves

(a) Patient is placed in supine position on the bed of the PET scanner and catheters are placed in the left and right antecubital veins for tracer administration and blood sampling used for [$^{62}$Cu]Cu-ETS blood decomposition rate measurements.

(b) The scanner is aligned over the thorax to include the left ventricular chamber of the heart.

(c) A low-dose X-ray CT is performed for attenuation correction of the PET data.

(d) A dynamic list-mode acquisition is performed for 6 min, starting immediately prior to the administration of approximately 0.65 GBq of [$^{62}$Cu]Cu-ETS. Radiotracer is administered as a slow bolus over approximately 30 s. (Administration rate is not critical, but requires consideration of the count rate tolerances of the camera; very rapid injection may risk flooding the detectors when the bolus

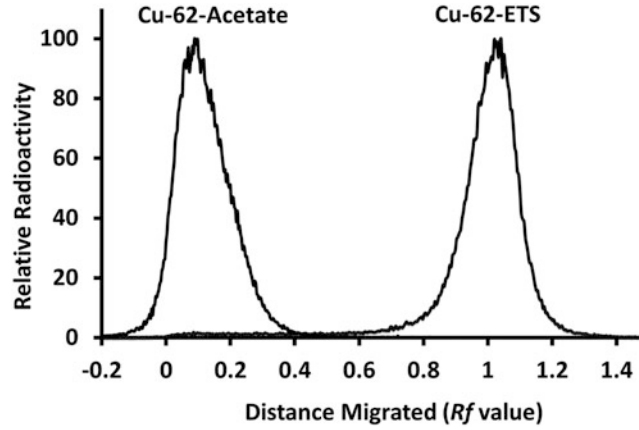


**Fig. 12** Overlaid sample radio-chromatograms for the [$^{62}$Cu]Cu-ETS product and its [$^{62}$Cu]Cu-acetate precursor, run on an ITLC-SA strip using ethanol as the mobile phase. The [$^{62}$Cu]Cu-acetate precursor remains at the origin, while the [$^{62}$Cu]Cu-ETS product migrates at or near the solvent front. (Use of a conventional silica gel TLC plate provides equivalent results and higher resolution, but the faster development time of the silica-gel impregnated fiberglass ITLC-SA strips makes them better suited to use in analyses with very short-lived nuclides)

passes through the ventricular chambers, interfering with characterization of the arterial input function.)

(e) A second X-ray CT scan of the whole body is performed for attenuation correction following the dynamic list-mode acquisition.

(f) Whole-body $^{62}$Cu images are acquired from 6 to 20 min post [$^{62}$Cu]Cu-ETS injection.

(g) Venous blood samples may be acquired at selected times post-injection (e.g., 1, 2, 3, 5 and 10-min) for assessment of [$^{62}$Cu]Cu-ETS decomposition rates in blood, allowing independent confirmation of the decomposition rate obtained by modeling of the image-derived blood curve data (*see* **Note 8**). The blood samples for radiochemical analysis and counting must be collected via a second venous catheter, not the catheter used in radiopharmaceutical administration.

(h) The fraction of $^{62}$Cu remaining in the blood as the intact [$^{62}$Cu]Cu-ETS radiotracer can be readily determined by prompt octanol extraction of collected blood samples [5, 6, 8, 16, 22]. Immediately after collection, a 10-μL to 100-μL sample of blood is added to a 1.5-mL polypropylene centrifuge tube containing 1-mL *n*-octanol. After vortex mixing, the *n*-octanol/blood suspension is centrifuged at 10,000 × *g* for 5 min. The octanol and cell debris

pellet are then separated for counting in a NaI(Tl) well counter (window centered at 511 keV), thereby allowing quantification of the fraction of total blood radioactivity present as the intact octanol-soluble [$^{62}$Cu]Cu-ETS radiotracer. After decay-correcting the measured sample count rates to a common time point, the fraction of $^{62}$Cu present as [$^{62}$Cu]Cu-ETS is calculated as the ratio of radioactivity in the octanol phase to the total sample radioactivity (octanol phase counts plus cell debris pellet counts) (*see* **Note 9**).

4. PET Image Reconstruction.
   (a) FDA-cleared software provided by the PET imaging system manufacturer is used to reconstruct the temporal and whole-body image data (*see* **Note 10**). The image reconstruction software must include corrections for tissue attenuation, random and scatter coincidences, count rate deadtime, and radioisotope decay. Filtered Backprojection reconstruction algorithms provided by Siemens Healthineers was used for the results presented in this chapter. The PET imaging system should be calibrated using phantoms with traceable radioisotope concentrations to ensure accurate quantification.
      - The temporal data sequence is binned into 12 × 5 s, 6 × 10 s, and 8 × 30 s duration scans.
5. Whole-Body Perfusion Estimation.
   (a) [$^{62}$Cu]Cu-ETS Input Function
      - A user-defined volume-of-interest (VOI) is placed within the left ventricular cavity of the heart on the temporal image sequence to extract an arterial $^{62}$Cu time-activity-curve. The VOI should be centered within the LV cavity in order to minimize distortion of the input function curve due to signal contamination (spillover) from adjacent myocardial tissue.
      - The arterial $^{62}$Cu time-activity-curve is multiplied by the fraction of $^{62}$Cu in the form of [$^{62}$Cu]Cu-ETS as determined by the blood decomposition analysis to generate the perfusion model input function.

   (b) Perfusion Calculation.
      - The perfusion model input function (parent [$^{62}$Cu]Cu-ETS in arterial blood) is integrated over the 6-min duration of the temporal imaging sequence.
      - Tissue perfusion is estimated by dividing the tissue $^{62}$Cu concentrations in the whole-body PET image by the integral of the input function calculated in the previous step.

## 4 Notes

1. When constructing the $^{62}Zn/^{62}Cu$ generator, use polyethylene frits rather than the default steel frits shipped with the column kit bundle—this avoids potential iron contamination. Fittings should be securely hand tightened.
2. When using PVDF filters at the generator column inlet, make they are pre-wetted with the HCl eluent solution to avoid pushing air bubbles into the columns.
3. The $^{62}$Cu-ETS synthesis is usually performed at room temperature, but if heating is desired, the ITG fluidic module should be pre-heated.
4. For TLC analysis, the radiochemical purity can be calculated as:

$$\text{Purity} = \frac{\text{Radioactivity on Top Half of ITLC Strip}}{\text{Sum of Radioactivity on Top and Bottom Halves of ITLC Strip}}.$$

5. If more than one batch of $^{62}$Cu-ETS is to be made, a freshly conditioned *C18 SepPak Light* should be employed for each sub-batch of $^{62}$Cu-ETS.
6. The $^{62}$Cu-ETS radiotracer is always produced for "immediate use." The labeled product expires no more than 60 min from the time of generator elution.
7. Quality control measures should verify the final $^{62}$Cu-ETS product for the following aspects:
   (a) Appearance—The product should be colorless in $\leq$7.5% ethanol.
   (b) pH—The product should have pH between 4.0 and 8.0.
   (c) Radionuclide identity—Repeated assays with a dose calibrator should show that the product has a half-life of $9.67 \pm 0.5$ min.
   (d) Radiochemical purity—The radioactivity in the product should be no less than 95% [$^{62}$Cu]Cu-ETS.
   (e) Radionuclidic purity—Assay a [$^{62}$Cu]Cu-ETS final product sample for $^{62}$Cu radioactivity, and retain this sample for re-assay after sufficient time for all the $^{62}$Cu to decay. At the later time, only $^{62}$Cu which is in transient equilibrium with any $^{62}$Zn breakthrough will be detectable. A NaI(Tl) well counter may be needed to measure the breakthrough $^{62}Zn/^{62}Cu$ content since the breakthrough level is likely too low to be detected by a radionuclide dose calibrator. This is, implicitly, a retrospective quality control test.
   (f) Membrane filter integrity—Prior to release for human administration, the 0.2μm PVDF sterilization filter should

pass a bubble point test to confirm that the used filter unit met the bubble point pressure standard specified by the filter manufacturer. A bubble point test should be performed for the primary and any subsequent sub-batches of [$^{62}$Cu]Cu-ETS product. A failure of the bubble point test requires solution processing through another sterile 0.2μm PVDF filter or rejection of the [$^{62}$Cu]Cu-ETS batch. The new filter should also be tested with a bubble point test accordingly.

(g) Only after all quality control measures are met should the radiotracer be released for human use.

8. Delay in adding the blood sample to the octanol will result in underestimation of the quantity of [$^{62}$Cu]Cu-ETS present at the time of blood sample collection.
9. Imaging system manufacturers normally provide analytical (filtered back-projection) and numerical (iterative) image reconstruction algorithms. When using iterative image reconstruction algorithms, the user should ensure that the number of interactions and subsets reach convergence in order to minimize errors in quantification of perfusion.
10. In blood sampling for $^{62}$Cu-ETS analysis, the residual volume of the sampling catheter should be pulled to a waste syringe immediately before collection of the blood sample to be analyzed. This is probably most conveniently effected by having the sterile sampling syringe and sterile waste syringe concurrently attached to the catheter by a sterile three-way stopcock.

## Acknowledgements

This work was supported by grants from the National Cancer Institute of the National Institutes of Health (CA202695 and CA140299), a National Institutes of Health Short-Term Training Program in Biomedical Sciences Grant (T35 HL110854), and a Radiological Society of North America (RSNA) Research & Education Foundation Research Medical Student Grant Award (Monica Cheng).

### References

1. Green MA, Mathias CJ, Welch MJ et al (1990) [$^{62}$Cu]-labeled pyruvaldehyde bis (N4-methylthiosemicarbazonato) copper(II): synthesis and evaluation as a positron emission tomography tracer for cerebral and myocardial perfusion. J Nucl Med 31:1989–1996
2. Shelton ME, Green MA, Mathias CJ et al (1989) Kinetics of copper-PTSM in isolated hearts: a novel tracer for measuring blood flow with positron emission tomography. J Nucl Med 30:1843–1847
3. Shelton ME, Green MA, Mathias CJ et al (1990) Assessment of regional myocardial and renal blood flow using copper-PTSM and positron emission tomography. Circulation 82:990–997

4. Mathias CJ, Green MA, Morrison WB, Knapp DW (1994) Evaluation of Cu-PTSM as a tracer of tumor perfusion: comparison with labeled microspheres in spontaneous canine neoplasms. Nucl Med Biol 21:83–87
5. Herrero P, Markham J, Weinheimer CJ et al (1993) Quantification of regional myocardial perfusion with generator-produced $^{62}$Cu-PTSM and positron emission tomography. Circulation 87:173–183
6. Herrero P, Hartman JJ, Green MA et al (1996) Assessment of regional myocardial perfusion with generator-produced $^{62}$Cu-PTSM and PET in human subjects. J Nucl Med 37:1294–1300
7. Mathias CJ, Welch MJ, Raichle ME et al (1990) Evaluation of a potential generator-produced PET tracer for cerebral perfusion imaging: single-pass cerebral extraction measurements and imaging with radiolabeled Cu-PTSM. J Nucl Med 31:351–359
8. Green MA, Mathias CJ, Willis LR et al (2007) Assessment of Cu-ETS as a PET radiopharmaceutical for evaluation of regional renal perfusion. Nucl Med Biol 34:247–255
9. Beanlands RS, Muzik O, Mintun MA et al (1992) The kinetics of copper-62-PTSM in the normal human heart. J Nucl Med 33:684–690
10. Beanlands RS, Muzik O, Hutchins GD et al (1994) Heterogeneity of regional nitrogen-13-labeled ammonia tracer distribution in the normal human heart: comparison with rubidium-82 and copper-62-labeled PTSM. J Nucl Cardiol 1:225–235
11. Okazawa H, Yonekura Y, Fujibayashi Y et al (1994) Clinical application and quantitative evaluation of generator-produced copper-62-PTSM as a brain perfusion tracer for PET. J Nucl Med 35:1910–1915
12. Tadamura E, Tamaki N, Okazawa H et al (1996) Generator-produced copper-62-PTSM as a myocardial PET perfusion tracer compared with nitrogen-13-ammonia. J Nucl Med 37:729–735
13. Lee KS, Mangner TJ, Petry NA (1991) Evaluation of Cu-62 PTSM in the detection of neural activation foci. J Nucl Med 32(suppl):1072
14. Okazawa H, Yonekura Y, Fujibayashi Y et al (1996) Measurement of regional cerebral blood flow with copper-62-PTSM and a three-compartment model. J Nucl Med 37:1089–1093
15. Fujibayashi Y, Wada K, Taniuchi H et al (1993) Mitochondria-selective reduction of $^{62}$Cu-pyruvaldehyde bis(N4-methylthiosemicarbazone) ($^{62}$Cu-PTSM) in the murine brain; a novel radiopharmaceutical for brain positron emission tomography (PET) imaging. Biol Pharm Bull 16:146–149
16. Fletcher JW, Logan TF, Eitel JA et al (2015) Whole-body PET/CT evaluation of tumor perfusion using generator-based [$^{62}$Cu]Cu-ETS: Validation by direct comparison to [$^{15}$O]water in metastatic renal cell carcinoma. J Nucl Med 56:56–62
17. ICRP Publication 23 (1975) Report of the task group on reference man (WS Snyder, chairman). Pergamon Press, Oxford
18. Leggett RW, Williams LR (1995) A proposed blood circulation model for reference man. Health Phys 69:187–201
19. John E, Green MA (1990) Structure-activity relationships for metal-labeled blood flow tracers: comparison of keto aldehyde bis (thiosemicarbazonato)copper(II) derivatives. J Med Chem 33:1764–1770
20. Petering HC, Buskirk HH, Underwood GE (1964) The anti-tumor activity of 2-keto-3-ethoxybutyraldehyde bis(thiosemicarbazone) and related compounds. Cancer Res 24:367–372
21. Mathias CJ, Margenau WH, Brodack JW et al (1991) A remote system for the synthesis of copper-62 labeled Cu(PTSM). Appl Radiat Isot 42:317–320
22. Mathias CJ, Bergmann SR, Green MA (1993) Development and validation of a solvent extraction technique for determination of Cu-PTSM in blood. Nucl Med Biol 20:343–349

# Chapter 41

# Biodegradable AuNP-Based Plasmonic Nanogels as Contrast Agents for Computed Tomography and Photoacoustics

**Mathilde Bouché and David P. Cormode**

## Abstract

Gold nanoparticles (AuNP) are well-established contrast agents in computed tomography (CT) and photoacoustic imaging (PAI). A wide variety of AuNP sizes, shapes, and coatings have been reported for these applications. However, for clinical translation, AuNP should be excretable to avoid long-term accumulation and possible side effects. Sub-5 nm AuNP have the benefit to be excretable through kidney filtration, therefore their loading in biodegradable nanogels holds promise to result in contrast agents that have long circulation times in the vasculature and subsequent biodegradation for excretion. Polyphosphazenes are intrinsically biodegradable polymers capable of forming nanogels with high payloads, and to release their payloads upon degradation. The significant development in polyphosphazenes that have tailored degradation kinetics, and their formulation with drugs or contrast agents, has shown potential as a biodegradable platform for imaging vasculature and endogenous molecules, by combination of CT and PA modalities. Therefore, we herein present methods for the formulation of AuNP assemblies loaded in nanogels composed of biodegradable polyphosphazenes, with a size range from 50 to 200 nm. We describe protocols for their characterization by UV-vis spectroscopy, Fourier-transform infrared spectroscopy, various microscopy techniques, elemental quantification by induced coupling plasma optical emission spectroscopy and contrast production in both CT and PAI. Finally, we detail the methods to investigate their effect on cells, distribution in cells and imaging properties for detection of endogenous molecules.

**Key words** Image segmentation, Degenerative disease, Gold nanoparticles, Polyphosphazene, Biodegradable, Photoacoustic, Computed tomography

## 1 Introduction

Gold nanoparticles (AuNP) are well-established contrast agents in computed tomography (CT) owing to their intrinsic attenuation of high-energy photons such as X-rays [1], and in photoacoustic imaging (PAI) thanks to their tunable surface plasmon resonance (LSPR) [2, 3]. Developments in AuNP-based biomaterials have led to a wide array of properties matching the requirements for use in living systems, especially high colloidal stability in aqueous media

Miguel R. Ossandon et al. (eds.), *Biomedical Engineering Technologies: Volume 1*, Methods in Molecular Biology, vol. 2393, https://doi.org/10.1007/978-1-0716-1803-5_41, 

and good safety profiles. Small AuNP (sub-5 nm) have been shown to be swiftly excreted from the body through the kidneys and urine, which is advantageous for clinical translation. Hence, their loading into biodegradable polymers appeared beneficial to increase their circulation time, shift their LSPR to the near infrared region (NIR), and enhance their local concentration.

Polyphosphazenes, and especially poly[di (carboxylatophenoxy)phosphazene] (PCPP), are biodegradable polymers that hydrolyze, leading to the cleavage of their polymeric backbone and production of phosphates and ammonia, which are pH neutral and harmless byproducts [4, 5]. Moreover, polyphosphazenes have shown remarkable biocompatibility in living systems [6, 7], and are valuable polymers for biomedical use and translation to patient care [8], as carriers for drugs [9–11], antigens [12, 13], or contrast agents [14, 15]. Cheheltani et al. highlighted the potential of PCPP for loading high payloads of contrast agents, thus achieving biodegradable hybrid nanogels that produced contrast in computed tomography (CT) and photoacoustic (PAI) and degrade over time to release their payloads [16]. Chhour et al. highlighted the possibility of functionalizing alternatively the core or the surface of the PCPP nanogels by modification of the organic coating on the nanocrystals payloads [17]. Surface loading of polyphosphazenes with AuNP can also be achieved by in situ reduction of a gold salt [18, 19], and allowed to proceed until full coverage of the PCPP nanogels in a gold shell [20].

Innovative polyphosphazenes were designed to display tunable degradation kinetics [21], and hydrolytic degradation was found faster for polyphosphazenes bearing glycine [22] or propylpyrrolidone side groups [23]. Moreover, polyphosphazenes can be designed to degrade specifically in response to stimuli [24, 25], such as light [26], or endogenous reducing agents such as glutathione (GSH) [27]. Functionalization of a hydrolytically unstable polyphosphazene core with phenylboronic ester grants the "on demand" degradation of the polymer by a self-immolation process triggered by hydrogen peroxide [28]. Their cross-linking into nanogels loaded with high amounts of AuNP provided contrast enhancement in CT and PA [29]. Moreover, their selective degradation in response to radical oxygen species (ROS), compared to PCPP-based nanogels, could be used to trigger a signal change in PA for detecting endogenous ROS in inflammation-stimulated macrophages.

In this chapter, we detail examples of hybrid nanogels based on biodegradable polyphosphazenes loaded with high payload of sub-5 nm AuNP, to provide high contrast enhancement both in CT and PA (Fig. 1). We also describe a route to activatable probes using a stimulus-responsive aryl boronate polyphosphazene (PPB) that grants molecular imaging by a biomolecule-triggered degradation. Their characterization is described here, using UV-visible

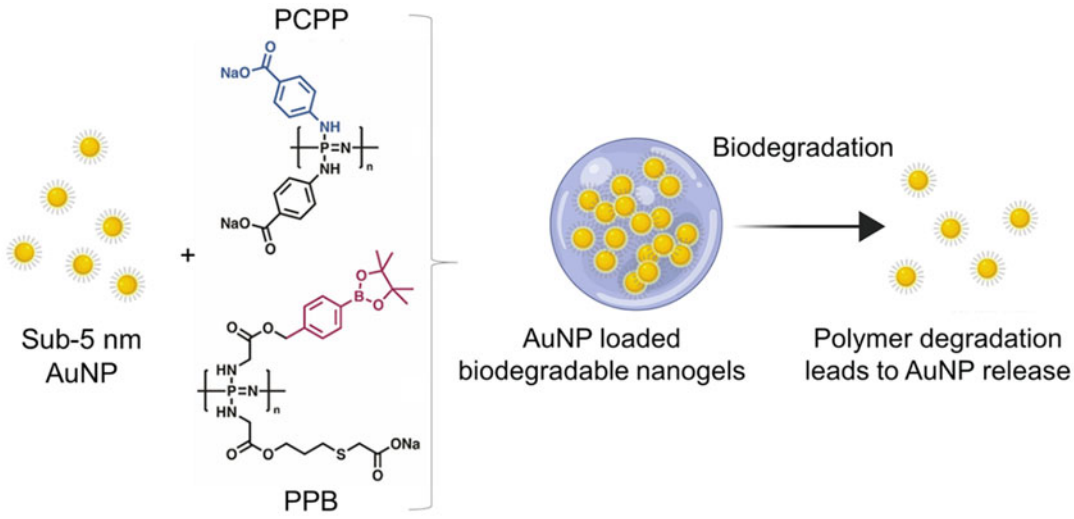


**Fig. 1** Formulation of sub-5 nm AuNP in nanogels composed of PCPP and PPB polyphosphazenes. Biodegradation of such nanogels leads to the release of their payload

spectroscopy, Fourier-transform infrared spectroscopy (FT-IR), transmission electron microscopy (TEM), scanning electron microscopy (SEM) coupled with energy dispersive X-ray spectroscopy (EDS), and inductively coupled plasma optical emission spectroscopy (ICP-OES). The contrast generation properties of those hybrid nanogels are also described in computed tomography (CT) and photoacoustic imaging (PAI). Further in vitro evaluation of those hybrid nanogels is highlighted, especially their effect on cell viability, their endogenous biomolecule triggered degradation, and their contrast generation properties in CT and PAI for molecular imaging.

## 2 Materials

### *2.1 Synthesis and Purification of Gold Nanoparticles and Nanogels*

1. 250 mL Erlenmeyer flasks.
2. Stock solution of gold chloride trihydrate: 39 mg of $HAuCl_4.3H_2O$ in 1 mL of DI $H_2O$.
3. Sodium borohydride stock solution (5 $mg.mL^{-1}$): 10 mg $NaBH_4$ in 2 mL of deionized (DI) $H_2O$, freshly prepared.
4. Glutathione stock solution: 104.5 mg of glutathione in 20 mL of DI $H_2O$.
5. Stock solutions of metal nanoparticles or other payload, GSH-AuNP for example, were obtained at a gold concentration over 25 $mg.mL^{-1}$ in DI $H_2O$ or DPBS (*see* **Note 1**).
6. Calcium chloride stock solution (8.8% w/v): 88 g of $CaCl_2$ in 912 mL of DI $H_2O$.

7. Stock solution of polyphosphazene derivative (5 $mg.mL^{-1}$): 5 mg of polyphosphazene powder in 1 mL of DPBS.
8. Stock solution of spermine (70 $mg.mL^{-1}$): 35 mg of spermine in 500 μL of DPBS.
9. Stock solution of PEG-PLL (34.5 $mg.mL^{-1}$): 10 mg of PEG-PLL in 290 μL of DPBS.
10. Herringbone mixer microfluidic chip (600 μm channel diameter).
11. Polyethylene tubing from VWR (Philadelphia, PA).
12. Male luers that were purchased from Microfluidic ChipShop (Jena, Germany).

### 2.2 Phantoms Preparation for CT and PAI

1. Agarose solution: 500 mg of agarose added to 50 mL of DI $H_2O$ (stirring at 40 °C is needed to achieve full agarose dissolution). Use while warm.
2. Dish.
3. Pipet tips.

### 2.3 Cell Culture

1. Dubecco's Modified Eagle Medium supplemented with 1% penicillin and 10% fetal bovine serum.
2. HepG2, RAW264.7, Renca, and SVEC4-10 cell lines, kept frozen at −80 °C, when not in use.
3. T25 flasks.
4. Cell scraper.
5. Trypsin.

### 2.4 Cell Viability Evaluation by LIVE/DEAD Assay

1. LIVE/DEAD kit assay.
2. Cocktail for cell staining: 1.5 μL of ethidium homodimer-1 solution and 0.5 μL of calcein AM in 2 mL of warm DPBS (prepare freshly prior to each experiment).
3. 35 mm dishes with 20 mm bottom wells.

### 2.5 Cell Stimulation by LPS/IFN-γ

1. LPS dissolved in DPBS (1 $mg.mL^{-1}$) and stored at 4 °C.
2. Stimulation cocktail: 10 μL of LPS stock solution and 0.5 μL of interferon-γ (IFN-γ) stock solution into FBS-free DMEM to a total volume of 5 mL (prepare freshly prior to each experiment).

### 2.6 Endogenous ROS Production by Carboxy-H2DCFDA Assay

1. Stock solution of carboxy-$H_2$DCFDA in DPBS (1 $mg.mL^{-1}$), stored frozen.
2. 96 wells plate.

### 2.7 Endogenous TNF-α Expression by ELISA Assay

1. 96 wells plate.
2. TNF-α ELISA assay kit.
2. Washing buffer: 50 mL of the stock solution from the kit in 950 mL of DI $H_2O$.
3. Assay buffer: 5 mL of the stock solution in 95 mL DI $H_2O$.
4. Biotin-conjugate stock solution: 30 μL of the stock solution diluted with assay buffer to a final volume of 3 mL (prepared 10 min before starting the assay).
5. Stock solution of TNF-α: mouse TNF-α diluted to 2 $ng.mL^{-1}$ in assay buffer (prepared 10 min before starting the assay).
6. Stock solution of streptavidin-HRP: 60 μL of the stock solution diluted in assay buffer to a final volume of 3 mL.

## 3 Methods

Figure 2 outlines the process followed from the formulation of hybrid nanogels and their characterization, to their evaluation in vitro and in vivo as a contrast agent for molecular imaging.

### 3.1 Synthesis and Purification of Gold Nanoparticles

AuNP with a core diameter lower than 5.5 nm have been suggested to be excretable through kidney filtration, which is desirable to limit gold retention in the body. Therefore, we detail here a procedure already reported by us [14].

1. Wash Erlenmeyers first with aqua regia (2/3 HCl and 1/3 $HNO_3$) and then with soap immediately prior to the synthesis to avoid interference during the nucleation growth of AuNP.
2. Add 200 μL of a stock solution of $HAuCl_4.3H_2O$ to 100 mL of DI $H_2O$ and stir vigorously in the Erlenmeyer flask.
3. Add 10 mg $NaBH_4$ by slowly dropping the freshly prepared stock solution to the Erlenmeyer.
4. Cover the top of the Erlenmeyer with aluminum foil and allow AuNP to grow for 10 min under vigorous stirring.
5. Add 2 mL of glutathione stock solution to coat the AuNP and stop the crystal growth.
6. Incubate at 4 °C for 12 h to ensure complete surface coating and colloidal stability.
7. Transfer the solution to MWCO filtration tubes (10 kDa cut-off) and concentrate the sample down to 1 mL by 5 min centrifugation at 7000 rpm.
8. Wash the AuNP solution with 19 mL of DI $H_2O$ and concentrate thrice.
9. Filtrate with a Millipore filter (200 μm).
10. Store at 4 °C in an Eppendorf tube until further use.

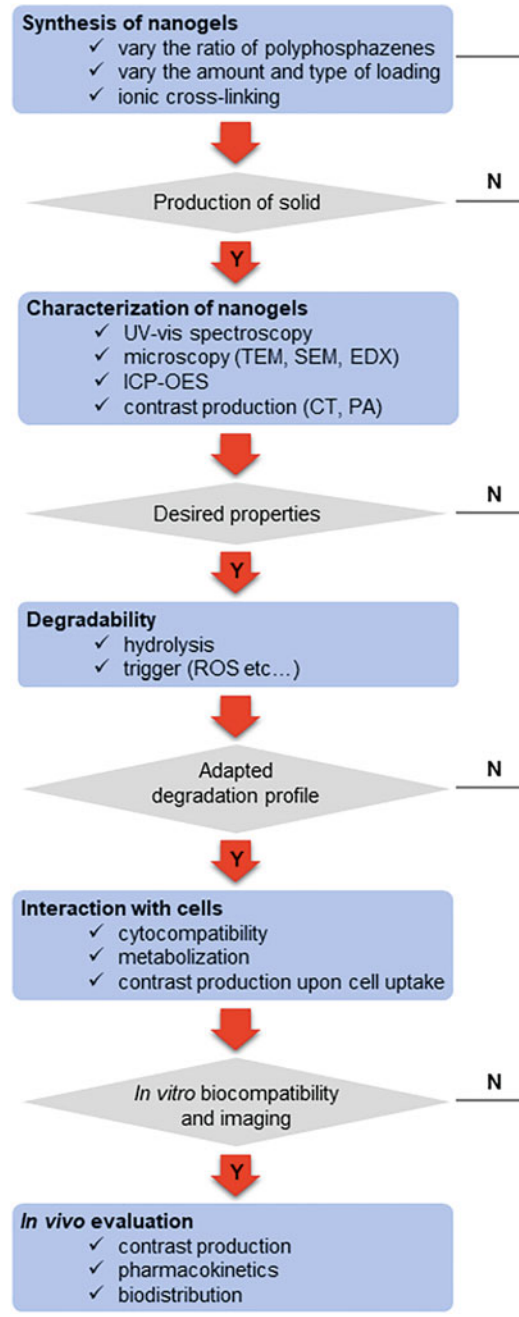


**Fig. 2** Flowchart for the formulation of nanogels and their evaluation *in vitro* and *in vivo*

11. Determine the gold concentration by UV-visible spectroscopy (*see* Subheading 3.3.1) or ICP-OES (*see* Subheading 3.3.5).

## 3.2 Synthesis and Purification of Plasmonic Nanogels

### 3.2.1 Formulation of Sub-5 nm AuNP in Nanogels Composed of Polyphosphazenes

Nanogels are nanometric-sized assemblies that have a high-water content [30, 31], and are formed by cross-linked polymers either by forming covalent chemical bonds [32], or by electrostatic interactions between polyelectrolyte and molecules of opposite charges, as we describe herein. We used a microfluidic approach to increase the control over size and homogeneity during the formulation process thanks to rates of mass-transfer that are typically not achievable using bulk systems (Fig. 3a) [33, 34]. The size of particles contributes in directing their fate in living systems, namely their biodistribution, cellular uptake and excretion profile [35]. Polyethylene glycol (PEG) additives contribute to controlling the size of the polymersomes in a range of 20–100 nm to adapt the particles' size to match the desired pharmacological properties [36]. Herein, we report on the use of the block copolymer PEG-b-poly-l-lysine (PEG-PLL) as an additive to 1 MDa polyphosphazene [15] to access a range of sizes of the nanogels showing variation of the plasmonic absorbance in UV-visible spectroscopy (Fig. 3b) by controlling the size of the nanogels (Fig. 3c, d). A typical procedure for formulation of polyphosphazene-based nanogels loaded with sub-5 nm AuNP is described here, yielding hybrid nanogels of about 100 nm core diameter.

1. Add 100 mL of $CaCl_2$ stock solution to an Erlenmeyer flask, and stir at 350 rpm. The nanogels' structure detailed herein relies on double cross-linking by ionic interactions to prevent early payload delivery by burst release, $Ca^{2+}$ being the primary cross-linker.
2. In a plastic tube, dilute 400 μL of the polyphosphazene stock solution with up to 5 mg AuNP, and complete the solution up to 2 mL with DPBS. Incubate for 15 min at room temperature.
3. In a second plastic tube, dilute 28 μL of the spermine stock solution with 1.4 μL of PEG-PLL stock solution (*see* **Note 2**), and complete the solution up to 2 mL with DPBS. Adjust the pH to 7.4 by addition of hydrochloric acid (*see* **Note 3**).
4. Wash the chip with 2 mL of DPBS. Chips with staggered herringbone pattern were preferred to enable a laminar flow regime that is found more consistent than bulk mixing conditions to lower size polydispersity.
5. Load one 10 mL syringe with the polyphosphazene solution prepared in **step 3**, and the other 10 mL syringe with the spermine and PEG-PLL mixed solution prepared in **step 4**. Place the two syringes into syringe pumps and use a speed of 6 $mL.min^{-1}$.

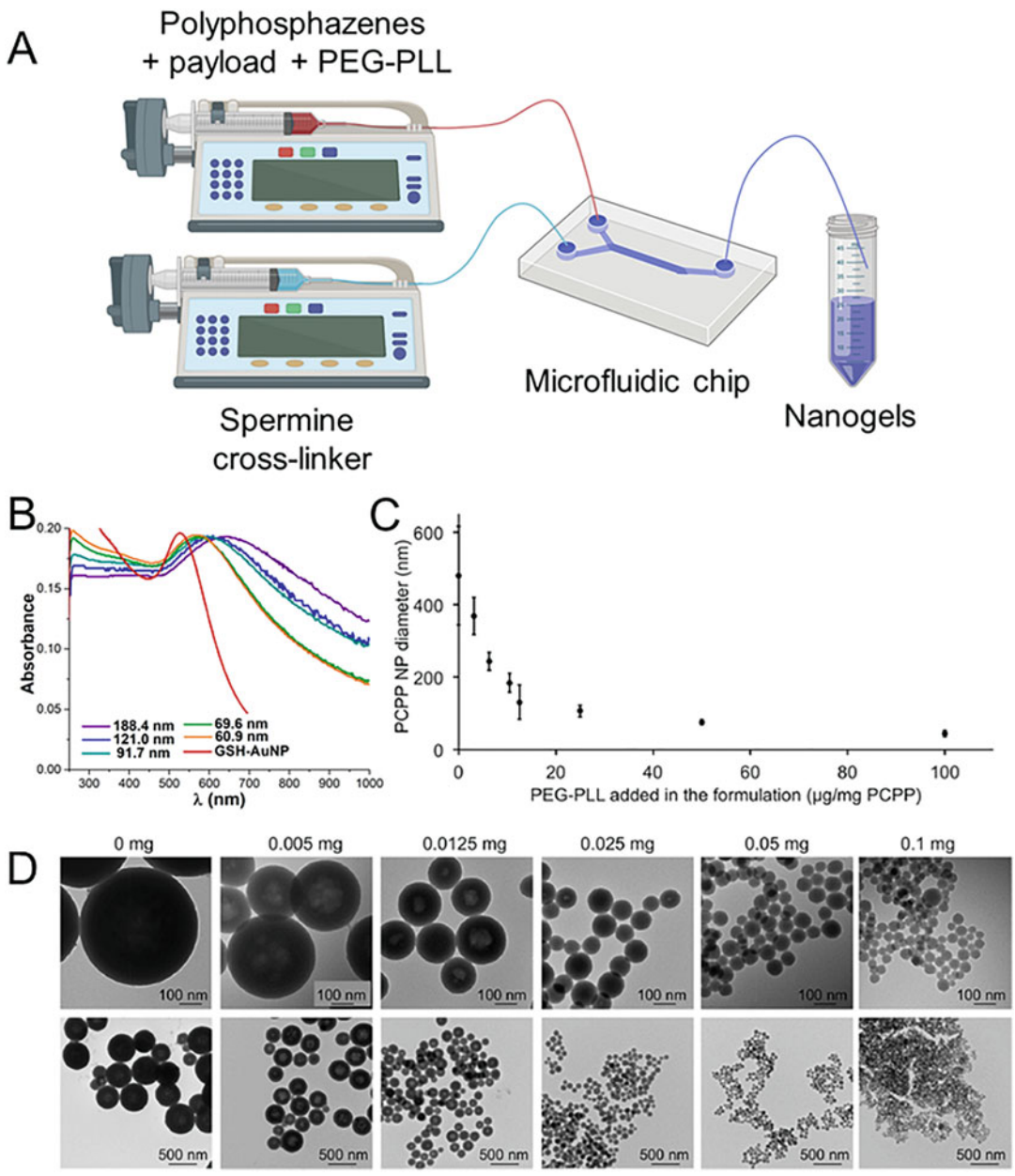


**Fig. 3** (**a**) Cartoon representing the microfluidic setup used for the formulation of polyphosphazenes based nanogels. (**b**) Shift of the plasmonic absorbance of AuNP loaded PCPP nanogels depending on their size diameter. (**c**) Evolution of the size diameter of the nanogels depending on the ratio of PEG-PLL per PCPP. (**d**) Representative TEM of PCPP based nanogels using increasing amounts of PEG-PLL to decrease the size diameter. (Figures **c** and **d** reused with permission from ref. 16)

6. Use polyethylene tubing to connect the syringes to the microfluidic chip and from the chip into a 15 mL collection tube.
7. Run the two syringe pumps in parallel, collect the eluted solution, and drop rapidly into the Erlenmeyer containing the $CaCl_2$ solution, prepared in **step 2**. Stir for 20 min at 25 °C.
8. Collect the solution in 50 mL plastic tubes, centrifuge (4 k rpm, 8 min), remove the supernatant, resuspend in 50 mL of DI $H_2O$, and repeat the purification process three times.
9. Resuspend the nanogels in 1 mL of DI $H_2O$ and store at 4 °C until use.

## 3.3 Characterization of Plasmonic Nanogels

AuNP are characterized by an intense LSPR peak in UV-visible spectroscopy that can be shifted to higher wavelengths proportionally to AuNP dense packing thanks to interparticle plasmon coupling [37].

### 3.3.1 UV-Visible Spectroscopy

1. Suspend the sample in deionized (DI) $H_2O$ at moderate concentration.
2. Add 1 mL of DI $H_2O$ for blank in a cuvette and wipe its surfaces.
3. Acquire background on the UV-vis spectrometer.
4. Add 1 mL of the sample into a clean, dry cuvette and wipe its surfaces.
5. Place the cuvette in the spectrometer and measure its spectrum.
6. The intensity of the LSPR peak should be around 1. If this is not the case, concentrate or dilute the sample and acquire another spectrum.
7. Analyze the collected data with software such as GraphPad.

### 3.3.2 Transmission Electron Microscopy

TEM is a microscopy technique commonly used for determining the size and shape of the core of particles, which relies on sample irradiation by an electron beam and transmission through the sample.

1. Drop the nanogels/nanoparticles suspended in DI $H_2O$ at a low concentration onto carbon-coated copper grids.
2. Allow to dry overnight.
3. Gently place the grid onto the holder to avoid carbon film disruption.
4. Insert the holder slowly into the vacuum chamber.
5. Focus the electron beam at the selected magnification.
6. Acquire micrographs using moderate electron beam illumination to avoid possible damage to the organic core of the nanogels.

7. Analyze the micrographs using software such as Image J (NIH, USA) and performing core measurement on a large number of particles (e.g. >100) to ensure the reliability of the measurement.

### 3.3.3 Scanning Electron Microscopy and Energy-Dispersive X-Ray Spectroscopy

SEM can be used to characterize the morphology of the nanogels by scanning the sample's surface with an electron beam and collecting the secondary electrons emitted by the excited sample.

1. TEM grids prepared as mentioned in Subheading 3.3.2. can be used for SEM analysis and mounted onto an SEM holder.
2. Insert the holder slowly into the vacuum chamber.
3. Focus the electron beam at the selected magnification.
4. Scan the sample's surface with a moderate electron beam to gain insights into the nanogels' morphology and acquire micrographs.
5. Should the SEM be equipped with an EDS analyzer, it is possible to perform semi-quantitative elemental analysis of the nanogels by EDS based on the X-ray excitation of the atomic electron shells in the sample as well as atomic mapping on the sample, which provides information on the spatial distribution of AuNP in the core of the nanogels.
6. Analyze the micrographs using software such as Image J (NIH, USA).

### 3.3.4 Fourier Transform Infrared Spectroscopy

Infrared (IR) spectroscopy is a fast, highly sensitive, and inexpensive technique to investigate the chemical structure of both organic and inorganic materials. While attenuated total reflectance (ATR) mode is generally preferred due to its ease of use, sample preparation with potassium bromide (KBr) pellets and spectrum acquisition by FT-IR should be preferred for analysis with a high peak definition of suspensions.

1. Prepare excess KBr in an open glass vial and have it dried in oven at 75 °C for at least 24 h along with the collar and anvils used for sample preparation, to avoid sample contamination by water absorption and the appearance of a broad band at 3657 $cm^{-1}$ characteristic of the symmetric stretching of the O-H bond in water.
2. Grind 25 mg of KBr using an agate mortar and pestle until a fine and homogeneous powder is obtained.
3. Add 1 mg of the sample to the dry KBr powder. The sample should either be dry or suspended in DI $H_2O$ at a high concentration to minimize the water content. Grind until the powder is dry and no longer aggregating.

4. Transfer the powder to a 7 mm collar, spread evenly to cover the bottom of the collar in a thin layer, and press the sample between the two anvils to yield a transparent pellet.
5. Rapidly, acquire the FT-IR spectrum on a JASCO FT/IR-480 PLUS, for example. If the intense and broad band at 3657 $cm^{-1}$ corresponding to water is observed, allow the pellet to dry in oven and repeat the experiment until full disappearance of the peak.
6. Perform baseline correction and plot showing the transmission as a function of the wavenumber.

#### *3.3.5 Inductively Coupled Plasma Optical Emission Spectroscopy*

To quantify the loading efficiency of the sub-5 nm AuNP in the nanogels, and to ensure the reliability of the in vitro measurements, the gold concentration can be determined using inductively coupled plasma optical emission spectroscopy (ICP-OES). Samples should be fully digested to ensure the accurate measurement of the elemental concentrations, and to avoid obstruction of the injection cables.

1. Prepare gold standards at concentrations ranging from 0 to 50 ppm for calibrating the ICP-OES machine. Dilute the commercially available stock solution at 1000 ppm (Ricca Chemicals, USA) to the desired gold concentrations using DI $H_2O$.
2. Vortex the sample to ensure the homogeneity of the sample, and transfer 5 μL of the sample to a 15 mL tube (*see* **Note 4**).
3. Prepare fresh aqua regia by cautiously diluting 2/3 of hydrochloric acid with 1/3 of nitric acid. Add 1 mL of aqua regia to the sample and allow 10 min incubation under a hood for full sample digestion. Allow longer incubation time in case of partial digestion of the sample to avoid obstruction of the injection cables of the ICP-OES machine.
4. Dilute the sample to a total volume of 6 mL by adding DI $H_2O$.
5. Calibrate the analyzer using the standards to allow linear regression of the gold concentration.
6. Perform ICP-OES measurements in triplicate for each sample.

#### *3.3.6 Contrast Enhancement in Computed Tomography*

In computed tomography, the attenuation rate of a defined element, for example gold in AuNP, is linearly correlated to its concentration, but depends on the energy and filtering of the X-ray beam used, as well as the size of the subject. Therefore, phantoms containing a range of concentrations of the contrast agent can be scanned as a preliminary step to establish the optimal dose of contrast agent to be injected to a patient so that imaging of the

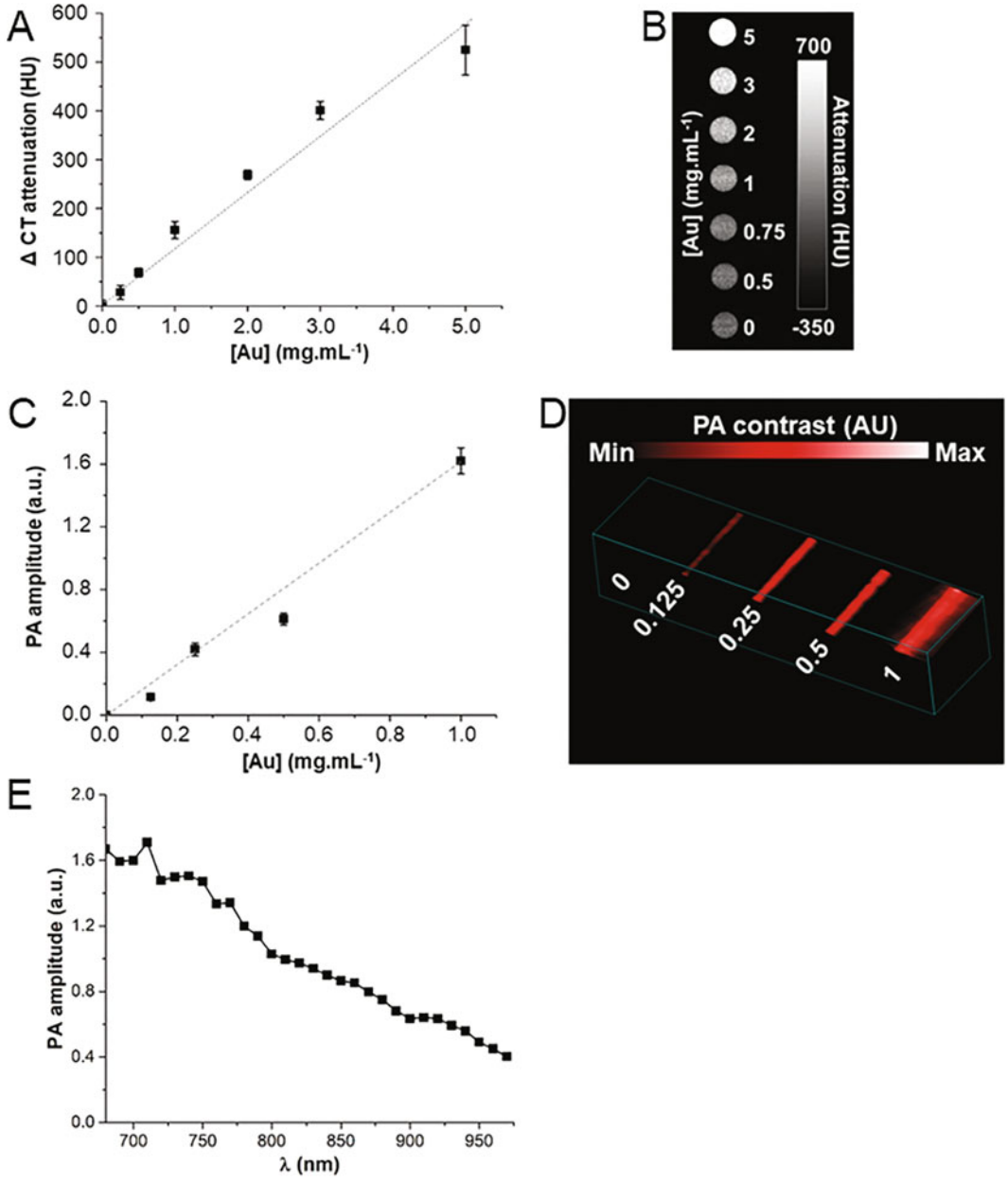


**Fig. 4** (**a**, **b**) Linear correlation of the contrast enhancement in CT depending on the gold concentration. (**c**, **d**) Linear correlation of the signal increase in PAI with increasing concentrations of gold. (**e**) Evolution of the PA amplitude from the AuNP loaded nanogels depending on the laser wavelength used. (Figures reused with permission from ref. 29)

blood or desired tissue is enabled. For quantification of the contrast enhancement produced in computed tomography (Fig. 4a, b):

1. Prepare 150 μL of solution of the nanoparticles at the desired gold concentration in DI $H_2O$ by adding in a 1.5 mL Eppendorf and mix with 150 μL of warm agarose (1%). Rapidly, transfer to a 250 μL Eppendorf tube while avoiding bubbles and cool on ice for 30 min.
2. Place the tubes in a rack (asymmetric placing can be valuable to be sure of sample location within the resulting CT images), wrap with parafilm to keep the tubes in place and immerse into a plastic tube filled with DI $H_2O$.
3. Tape the phantom in the CT tray, and scan with a microCT scanner such as MILabs operated with both a tube voltage of 55 kV, tube current of 190 μA and an exposure time of 75 ms.
4. Reconstruct the images with a 0.1 mm increment and upload them in a software program dedicated to image analysis such as Osirix. Draw a circular area for ROI measurement on the coronal view of each tube and repeat on five different slices for each sample. Normalize the ROI values to the blank sample that contains no nanoparticle.
5. Plot a standard curve based on the ROI values of the nanoparticle's standards and perform a linear regression as suggested on Fig. 4a. This can be used for the indirect measurement of gold nanoparticle concentration by CT.

### 3.3.7 Signal in Photoacoustic Imaging

Photoacoustic imaging (PAI) is a technique that relies on the effect that occurs upon pulsed light irradiation of the sample, thermoelastic expansion of the sample, and the production of ultrasound waves. PAI is a semi-quantitative technique, and evaluation of the signal provided as a function of increasing concentrations of the contrast agent can help for further quantification in living systems (Fig. 4c–e).

1. Prepare 500 μL aliquots of nanoparticles suspended in DI $H_2O$ at a gold concentration ranging from 0 to 1 $mg.mL^{-1}$.
2. Cut polyethylene tubes of 0.5 mm diameter and fix on the plastic holder, ensure proper alignment and that all tubes are fixed at the same height.
3. Load the tubes with nanoparticles suspensions and wipe off any spilled sample to avoid contaminating the immersion water.
4. Immerse the holder into degassed DI $H_2O$, add lubricant on the transducer while avoiding bubble formation, and fix the transducer at a distance of 10 mm from the samples, ensuring the transducer is fully immersed in the water for proper

ultrasound wave propagation. Confirm the distance separating the transducer from the sample with the ultrasound modality.

5. Acquire the photoacoustic signal arising from the sample having the highest concentration using adjusted laser settings, for example, 40 dB and 95% priority, and scan the samples at wavelengths from 680 to 970 nm to determine the wavelength providing the maximum PA amplitude. Ensure that no signal saturation is observed, or adjust the parameters by decreasing the PA gain until the signal is no longer saturated.
6. Once the optimal wavelength and settings for laser irradiation are confirmed, acquire PA images on the phantom.
7. Upload the images into a software program suitable for image analysis, such as ImageJ. Draw a circular area for ROI measurement on the coronal view of the phantom and repeat on five different slices along the tube. Normalize the ROI values to the $H_2O$ control that contains no nanoparticle. Those normalized ROI values can be used for comparison of the PA amplitudes produced by the nanoparticles at various gold concentrations, *see* Fig. 4c for example.

### 3.4 Degradability of Plasmonic Nanogels

Cellular stress production in living systems includes a large range of radicals and other reactive species derived from oxygen and/or nitrogen containing moieties ensuring the probes' selectivity toward an array of reactive species endogenously secreted is of importance.

#### 3.4.1 Preparation of Stock Solutions of Radical Oxygen Species

1. Reactive species, such as hydrogen peroxide ($H_2O_2$), perchlorate ($ClO^-$), or superoxide ($O_2^{-}\cdot$), can be generated in situ from inorganic salts that are commercially available.
2. OH is produced in situ by reaction of $H_2O_2$ with $Fe(ClO_4)_2$ in a 10:1 ratio [38].

#### 3.4.2 Investigation of the Degradability of the Nanogels

The biodegradability of biomaterials is an important consideration in view of their further translation; hence we report below a procedure for investigating the degradability of the nanogels that are either based on hydrolytically degradable or stimuli-responsive polyphosphazenes (Fig. 5a).

3. Use 1.5 mL Eppendorf tubes to suspend 1 mL of the nanogels at a fixed concentration of 0.5 $mg.mL^{-1}$ in the freshly prepared incubation medium. Other concentrations can be used, yet keep in mind that the degradation rate can depend on the concentration of the nanogels and is limited by the diffusion rate of the payload released in the incubation medium. Therefore, it is important for ensuring a reliable comparison to work at a constant concentration through the entire study.

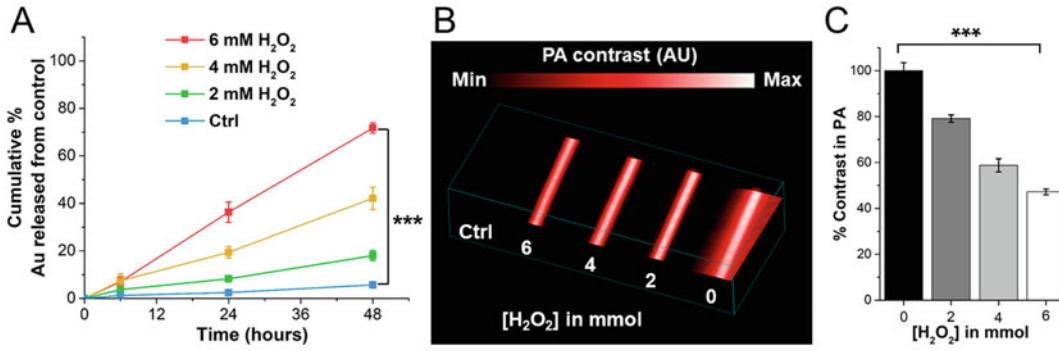


**Fig. 5** (**a**) Enhanced rate of gold release from ROS sensitive nanogels with increasing concentrations of $H_2O_2$. (**b**, **c**) Incubation of ROS sensitive nanogels with increasing concentrations of $H_2O_2$ leads to decreased PA signal

4. Incubate in a water bath at 37 °C until the desired time point for sampling.
5. Vortex the sample to avoid unreliable sampling due to the diffusion gradient from the degraded nanogels. Centrifuge the sample to precipitate the intact nanogels as a pellet and leave the payload released from degraded nanogels in the supernatant.
6. Sample out 200 μL of the supernatant while ensuring not to collect any pellet.
7. Discard the remaining supernatant. Resuspend the pellet into freshly prepared medium and incubate at 37 °C until the next time point.
8. Digest all the samples by incubation for 15 min in aqua regia, dilute to a total volume of 6 mL using DI $H_2O$, and quantify the elemental concentration of gold via ICP-OES, as described above.
9. Calculate the sample concentration by applying the dilution factor and plot as shown on Fig. 5a by summing the amounts of gold released from the nanogels at the different time points to determine the cumulative percentage of gold released (*see* **Note 5**).

### *3.5 Behavior of Plasmonic Nanogels with Cells*

#### *3.5.1 In Vitro Biocompatibility*

We report herein on the use of the LIVE/DEAD assay to determine the nanoparticles' effect on eukaryotic cell lines based on calcein AM staining of plasma membrane in live cells and Ethidium homodimer-1 (EthD-1) staining of DNA released from the nucleus of dead cells.

1. Plate cells in dishes of 35 mm diameter and 20 mm bottom, at a cell density of $10^5$ cells per well, and incubate for 24 h at 37 °C in a 5% $CO_2$ sterile atmosphere.

2. Wash the cells once with 400 µL of DPBS and treat the cells with nanoparticles suspended in cell medium at selected gold concentrations e.g. 0.125, 0.25, and 0.5 mg.mL$^{-1}$. For the control, treat the cells with 400 µL of nanoparticle-free cell medium. Incubate the cells for the selected duration, e.g. 8 h, at 37 °C in a 5% $CO_2$ sterile atmosphere.
3. Briefly, wash the cells with 400 µL of DPBS and, in the dark, add the freshly prepared dye cocktail containing calcein (1 µM) and EthD-1 (1.5 µM) in DPBS (*see* **Note 6**). Incubate in the dark for 20 min at 37 °C in a 5% $CO_2$ sterile atmosphere.
4. Using an epifluorescence microscope, acquire images in four different areas of the dishes using alternatively white light for bright field image, the excitation filters 495–515 nm or 528–617 nm for imaging live cells or dead cells respectively.
5. Cell counting can be performed with software like MATLAB using a custom-programmed code. Hence, it is possible to determine the number of live and dead cells per sample and calculate the cell viability as a percentage of the control untreated cells.

#### *3.5.2 Endogenous ROS Quantification*

The stress balance in living systems is very sensitive to changes in body condition, and span a large range of concentrations from low levels of ROS in physiological condition or elevated levels of ROS occurring as a consequence of diseases such as inflammation or cancer [39].

1. Plate RAW264.7 cells in a 96 wells plate at a cell density of $10^4$ cells per well and incubate for 18 h at 37 °C in a 5% $CO_2$ sterile atmosphere.
2. Wash with 100 µL of DPBS, and treat with either 100 µL of DPBS for nonstimulated cells or 100 µL of a freshly prepared stimulation cocktail containing LPS at a concentration of 1 µg.mL$^{-1}$ and IFN-γ at 50 ng.mL$^{-1}$ in DPBS. Incubate for 4 h at 37 °C in a 5% $CO_2$ sterile atmosphere. The mixture of lipopolysaccharide (LPS) and interferon gamma (IFN-γ) is known to induce the enhanced production of endogenous stress in the cells to model stress levels occurring in inflammation and stimulate the release of ROS from macrophages.
3. After 3.5 h of incubation, treat each well with 100 µL of carboxy-$H_2$DCFDA at 15 µM in DPBS, and incubate in the dark for 30 min at 37 °C in a 5% $CO_2$ sterile atmosphere. For a cell free control, add 100 µL of DPBS and 100 µL of the dye (15 µM). For a ROS control, add 100 µL of $H_2O_2$ diluted in DPBS (100 µM) and 100 µL of the dye (15 µM).
4. On a plate reader, read the fluorescence intensities collected at an excitation wavelength of 485 nm and emission wavelength

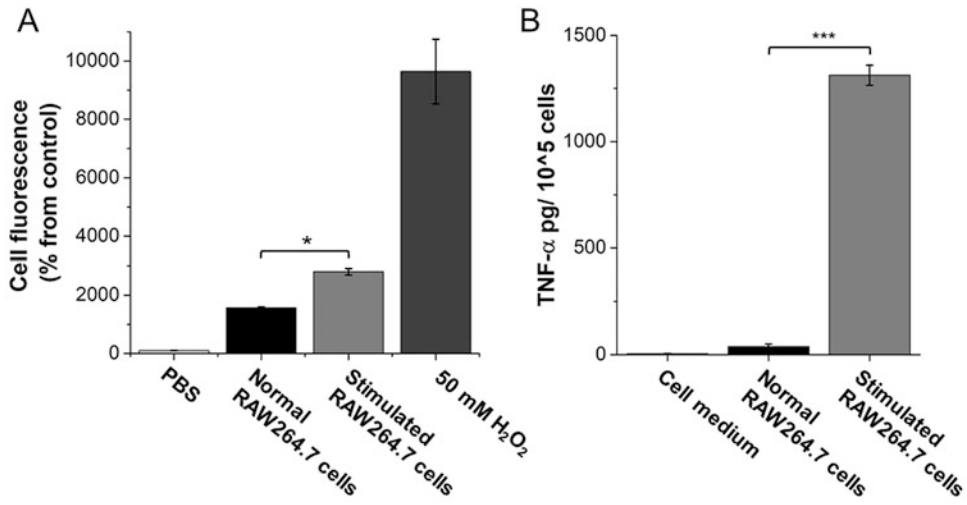


**Fig. 6** (**a**) Comparison of the levels of endogenous ROS production in LPS/IFN-γ stimulated and normal macrophages. (**b**) Evaluation of the TNF-α production in macrophages consequently to LPS/IFN-γ compared to the non-stimulated macrophages. (Figures reused with permission from ref. 29)

of 528 nm. Normalize the fluorescence intensity to the cell free control and determine the endogenous ROS production in the samples as suggested on Fig. 6a.

*3.5.3 Endogenous TNF-α Expression*

Tumor necrosis factor-alpha (TNF-α) is an inflammatory cytokine endogenously produced by macrophages to regulate immune cells and can be used as an indirect sign of stress in macrophages.

1. Plate RAW264.7 cells in a 96 wells plate at a cell density of $10^4$ cells per well and incubate for 18 h at 37 °C in a 5% $CO_2$ sterile atmosphere.
2. Wash each well with 100 μL of DPBS and treat the wells with 100 μL of either the freshly prepared stimulation cocktail or FBS-free DMEM for nonstimulated control. Incubate for 4 h at 37 °C in a 5% $CO_2$ sterile atmosphere (*see* **Note 7**). The assay is performed in triplicate.
3. Use six strips of microwells included in the TNF-α kit and wash it twice with 200 μL of wash buffer. Flip the microwells upside down for 30 s to remove excess of buffer.
4. Add 50 μL of assay buffer to the microwells.
5. Then, collect the cell supernatant from the 96 wells plate and dilute 50 μL of the sample to the microwell strips containing the assay buffer. For control wells, assay buffer is used instead of the sample. For mouse TNF-α standards, 130 μL of reconstituted TNF-α mouse standard is used for the highest standard and perform 1:2 serial dilution using assay buffer 5 times.

6. Add 50 μL of the biotin-conjugate solution to all microwells, wrap the plate in parafilm, and incubate for 2 h at 25 °C on a microplate shaker.
7. Remove the supernatant from all the microwells and wash them 6 times with 200 μL of wash buffer. Flip the microwells upside down for 30 s to remove excess buffer.
8. Pipette 100 μL of the streptavidin-HRP solution into each well, wrap the plate in parafilm and incubate for 1 h at 25 °C on a microplate shaker.
9. Remove the supernatant from all microwells, wash them 6 times with 200 μL of wash buffer. Flip the microwells upside down for 30 s to remove excess of buffer.
10. Pipette 100 μL of TMB substrate solution without prior dilution into all wells, wrap the plate in aluminum foil and incubate at 25 °C on a microplate shaker. After 20 min incubation, monitor every 2 min the absorbance value at 620 nm until it reaches a value of 0.9.
11. Rapidly, add 100 μL of stop solution to all wells to prevent further dye reaction.
12. Subsequently, blank the plate reader and measure the absorbance intensity at 450 nm.
13. Plot a standard curve based on the absorbances of the TNF-α mouse standards, perform a linear regression, and determine the TNF-α concentration from the standard curve as suggested on Fig. 6b.

#### 3.5.4 Preparation of Cells for Photoacoustic Imaging

The phantom preparation for PA imaging of fixed cells upon incubation with ROS sensitive nanogels can be pursued as follows (Fig. 7a):

1. Prepare the phantom by adding 25 mL of DI $H_2O$ to 500 mg of agarose in a 250 mL flask, cover with aluminum foil, and allow to stir vigorously in a water bath at 40 °C until full agarose dissolution. Agarose was preferred as it allows propagation of the photoacoustic waves from the sample to the transducer.
2. To a petri dish, rapidly pour a 0.5 cm layer of warm agarose (2%), cap, and allow to cool down at room temperature on a flat area. After 1 h, place 200 μL pipet tips upside down of the top of the first layer of agarose (2%) and pour a second 0.5 cm layer of warm agarose (2%). After another hour of cooling, once the second layer is fully gelled, remove gently the pipette tips to leave vacant the holes for the samples.

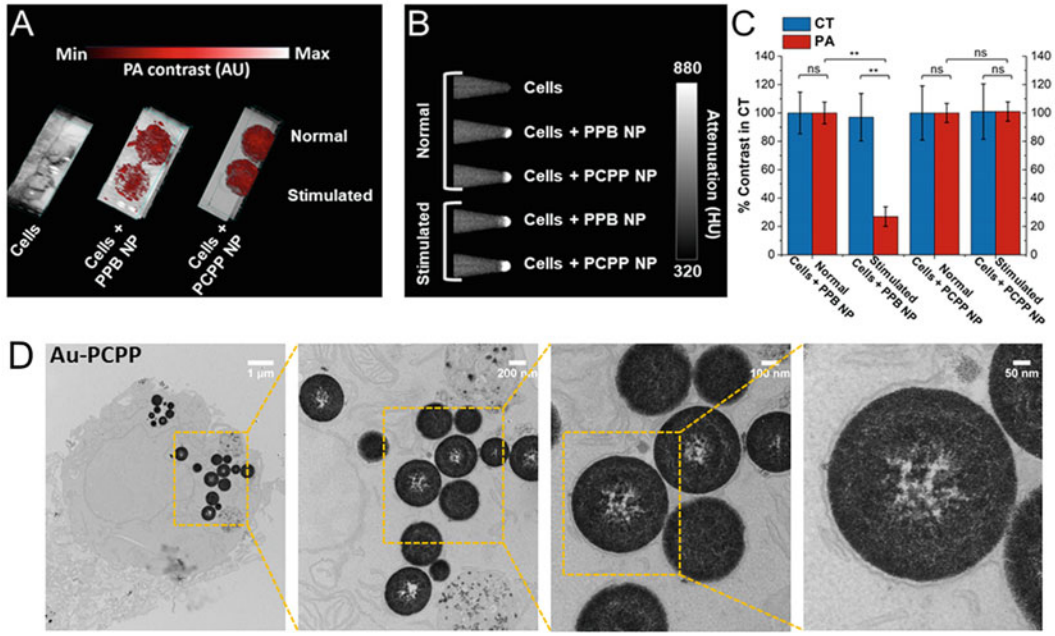


**Fig. 7** ROS imaging in stimulated macrophages using ROS sensitive nanogels by comparing the signals intensities in (**a**) PA to (**b**) CT, (**c**) to detect stimulated macrophages that produce elevated levels of endogenous ROS. (**d**) TEM at different magnifications of cells incubated with AuNP loaded nanogels and fixed showing the swelling and initiation of the intracellular biodegradation process. (Figures **a**–**c** reused with permission from ref. 29)

3. In parallel, plate RAW264.7 cells in 6-well plates at a cell density of $2 \times 10^6$ cells per well and incubate for 18 h at 37 °C in a 5% $CO_2$ sterile atmosphere.
4. Wash each well with 1 mL of DPBS and treat the wells with 1 mL of either the freshly prepared stimulation cocktail or FBS-free DMEM for nonstimulated control. Incubate for 4 h at 37 °C in a 5% $CO_2$ sterile atmosphere.
5. Treat the corresponding wells with the nanogels suspended in FBS-free DMEM at a total gold concentration of 0.1 mg.mL$^{-1}$ and incubate at 37 °C for 4 h in a 5% $CO_2$ sterile atmosphere.
6. Wash the cells twice with 1 mL of DPBS, gently add 1 mL of FBS-free DMEM, scrape the cells and collect them in a 15 mL tube prior to centrifugation (1 k rpm, 5 min).
7. Resuspend the cells in 150 µL of DI $H_2O$ and rapidly add 50 µL of warm agarose (2%) and pipette the resulting mixture into the phantom (*see* **Note 8**). Cool down for 10 min on ice.
8. Pour a third layer of 0.5 cm of warm agarose (2%) on the phantom, and cool for 20 min on ice.
9. Place the phantom in a bath of degassed DI $H_2O$, add lubricant on the transducer, for example LZ550, while avoiding bubble

formation. Fix the transducer at a distance of 10 mm from the samples, confirm the distance to sample by ultrasound imaging. Acquire the photoacoustic signal using laser settings adapted to the sample (desired wavelength and PA gain).

10. Upload the images on a software dedicated to image analysis, such as ImageJ. Draw a circular area for ROI measurement on the horizontal view of the phantom and repeat on three different slices among the sample. Normalize the ROI values to the cell sample that contains no nanoparticle. Those normalized ROI values can be used for comparison of the PA signal produced by the nanoparticles in the cell pellets, *see* Fig. 7a–c for example.

#### *3.5.5 Cell Fixation for CT or TEM Investigation*

Cell fixation allows for retaining the subcellular architecture and structure, and was used herein to further analyze by observation with microscopy techniques the localization of the nanogels and their degree of degradation by endogenous biomolecules (Fig. 7d).

1. Plate RAW264.7 cells in a 6 wells plate at a cell density of $10^5$ cells per well and incubate for 18 h at 37 °C in a 5% $CO_2$ sterile atmosphere.
2. Wash each well with 1 mL of DPBS and treat the wells with 1 mL of either the freshly prepared stimulation cocktail or FBS-free DMEM for nonstimulated control. Incubate for 4 h at 37 °C in a 5% $CO_2$ sterile atmosphere.
3. Remove the cell supernatant, briefly wash the cells twice with 1 mL of DPBS and add 1 mL of FBS-free DMEM to each well.
4. Gently scrape the cells, collect the suspended cells, transfer to a 15 mL tube, and centrifuge (1 k rpm, 5 min).
5. Remove the supernatant, gently resuspend the pellets in a fixative solution containing 2.5% of glutaraldehyde and 2% of formaldehyde in 0.1 M sodium cacodylate buffer (pH 7.4). Allow the cells to loosely settle into pellets in 250 μL centrifuge tubes. These pellets can either be further processed for further TEM imaging, or analyzed with CT.
6. For quantification of contrast enhancement in computed tomography:
   (a) Place the tubes in a rack and wrap in up with parafilm.
   (b) Tape the samples in the CT tray, and scan with a microCT scanner such as MILabs operated with both a tube voltage of 55 kV, tube current of 190 μA, and an exposure time of 75 ms.
   (c) Reconstruct the images with a 0.1 mm increment and upload them in a software program dedicated to image analysis such as Osirix. Draw a circular area for ROI measurement on the coronal view of each tube and repeat on

five different slices for each sample. Normalize the ROI values to the blank sample that contains no nanoparticles. Those normalized ROI values can be used for quantification of the indirect measure of the gold nanoparticle concentration in the cell pellets, *see* Fig. 7b, c for example.

7. For TEM:
   (a) After subsequent buffer washes, the samples were post-fixed in 2.0% osmium tetroxide for 1 h at 25 °C, and rinsed in DI $H_2O$ prior to *en bloc* staining with 2% uranyl acetate.
   (b) Perform serial dehydration through a graded ethanol series from 30% to 100% ethanol, infiltrate and embed the sample in Embed-812.
   (c) Cut the sample into thick sections of 60 nm and stain them with uranyl acetate and lead citrate.
   (d) Deposit each section of the sample on a TEM grid and examine with a system such as a JEOL 1010 electron microscope fitted with a Hamamatsu digital camera and AMT Advantage NanoSprint500 software (Fig. 7d).

## 4 Notes

1. For tuning the degradability of the nanogels, a combination of different polyphosphazenes can be used. For example, to achieve ROS-sensitive nanogels, screening the ideal ratio between the templating PCPP and the ROS degradable PPB, based on calculations of the ratio of cross-linking moieties in each, allows the balance between well-defined nanogels and high ROS sensitivity.
2. The procedure detailed as an example is for nanogels of size diameter of about 100 nm and thus require 1.4 μL of the PEG-PLL stock solution. However, a range of formulations with various sizes is accessible by tuning the amount of PEG-PLL reacted, from 0.5 μL of PEG-PLL for 200 nm nanogels to 5.2 μL of PEG-PLL for 50 nm nanogels.
3. As highlighted above, pH directs the cross-linking of the nanogels and therefore, pH adjustment must be adjusted freshly and precisely. Acidic conditions induce the partial protonation of the polyelectrolyte and hence its precipitation which will disrupt the microfluidic flow. Basic conditions induce the partial deprotonation of the ammonium of spermine to amine, which is neutral, and therefore cross-linking through ionic interactions will not occur.
4. The volume of sample to be used for ICP-OES should be adapted to the anticipated concentration, sampling greater

volumes for diluted samples and smaller volumes for concentrated samples.

5. To ensure the degradation profile measured for the nanogels indeed corresponds to degradation rather than payload release through diffusion out of the nanogel, joint measurement by ICP-OES of phosphorous along with gold for quantification of both the payload and the degraded polymer in the supernatant can be done.
6. The compact AuNP assembly occurring in plasmonic nanogels partially quenches the fluorescence from the Hoescht dye and prevents nucleus visualization by epifluorescence. Therefore, cell viabilities were calculated as a percentage of live cells to total number of cells (live plus dead), correlated with white light images to ensure correct quantification, and normalized to the untreated control group.
7. The time point for sampling the cell supernatant is a key parameter for its use in the ELISA assay, and might vary depending on the cell culturing conditions. Herein, we report on a 4 h incubation time point of the macrophages with the stimulation cocktail that was found to produce elevated levels of TNF-α.
8. It is important to differentiate between cell fixation in fixative solutions, such as formalin, and the cell fixation detailed below, which involves physical fixation of the cells in an agarose gel. Indeed, the cellular functions are not stopped as with formalin, so we recommend imaging this phantom immediately after preparation to prevent further nanogels metabolization by the cells.

## Acknowledgements

The Franco-American Commission Fulbright is kindly acknowledged for support to M.B. This work was also supported by NIH (R01 HL131557 and R01 CA227142).

### References

1. Cormode DP, Skajaa T, Fayad ZA, Mulder WJM (2009) Nanotechnology in medical imaging probe design and applications. Arterioscler Thromb Vasc Biol 29(7):992–1000
2. Mieszawska AJ, Mulder WJM, Fayad ZA, Cormode DP (2013) Multifunctional gold nanoparticles for diagnosis and therapy of disease. Mol Pharm 10(3):831–847
3. Cormode D, Zeglis B, Melancon M (2019) Novel agents for imaging and theranostics. Med Phys 46(6):E484–E485
4. DeCollibus DP, Marin A, Andrianov AK (2010) Effect of environmental factors on hydrolytic degradation of water-soluble polyphosphazene polyelectrolyte in aqueous solutions. Biomacromolecules 11(8):2033–2038
5. Iturmendi A, Teasdale I (2018) Water soluble (bio)degradable poly(organo)phosphazenes. ACS Symp Ser 129(9):183–209. https://doi.org/10.1021/bk-2018-1298.ch009
6. Teasdale I, Brüggemann O (2013) Polyphosphazenes: multifunctional, biodegradable

vehicles for drug and gene delivery. Polymers 5 (1):161–187

7. Andrianov AK, Marin A, Chen J (2005) Synthesis, properties, and biological activity of poly[di(sodium carboxylatoethylphenoxy) phosphazene]. Biomacromolecules 7 (1):394–399
8. Allcock H, Morozowich N (2012) Bioerodible polyphosphazenes and their medical potential. Polym Chem 3:578–590
9. Teasdale I, Wiflert S, Nischang I, Brüggemann O (2010) Multifunctional and biodegradable polyphosphazenes for use as macromolecular anti-cancer drug carriers. Polym Chem 2:828–834
10. Hou S, Chen S, Dong Y, Gao S, Zhu B, Lu Q (2018) Biodegradable cyclomatrix polyphosphazene nanoparticles: a novel pH-responsive drug self-framed delivery system. ACS Appl Mater Interfaces 10(31):25983–25993
11. Xu J, Zhu X, Qiu L (2016) Polyphosphazene vesicles for co-delivery of doxorubicin and chloroquine with enhanced anticancer efficacy by drug resistance reversal. Int J Pharm 498 (1–2):70–81
12. Eng NF, Garlapati S, Gerdts V, Potter A, Babiuk LA, Mutwiri GK (2010) The potential of polyphosphazenes for delivery of vaccine antigens and immunotherapeutic agents. Curr Drug Deliv 7(1):13–20
13. Cayatte C, Marin A, Rajani GM, Schneider-Ohrum K, Benett AS, Marshall JD, Andrianov AK (2017) PCPP-adjuvanted respiratory syncytial virus (RSV) sF subunit vaccine: self-assembled supramolecular complexes enable enhanced immunogenicity and protection. Mol Pharm 14(7):2285–2293
14. Hajfathalian M, Bouche M, Cormode DP (2018) Polyphosphazene-based nanoparticles as contrast agents for medical imaging. In: Polyphosphazenes in biomedicine, engineering, and pioneering synthesis. Oxford University Press 1298(4):77–100. https://doi.org/10.1021/bk-2018-1298.ch004
15. Hindlang MD, Soudakov AA, Imler GH, Laurencin CT, Nair LS, Allcock HR (2010) Iodine-containing radio-opaque polyphosphazenes. Polym Chem 1:1467–1474
16. Cheheltani R, Ezzibdeh RM, Chhour P, Pulaparthi K, Kim J, Jurcova M, Hsu JC, Blundell C, Litt HI, Ferrari VA, Allcock HR, Sehgal CM, Cormode DP (2016) Tunable, biodegradable gold nanoparticles as contrast agents for computed tomography and photoacoustic imaging. Biomaterials 102:87–97
17. Chhour P, Gallo N, Cheheltani R, Williams D, Al-Zaki A, Paik T, Nichol JL, Tian Z, Naha PC, Witschey WR, Allcock HR, Murray CB, Tsourkas A, Cormode DP (2014) Nanodisco balls: control over surface versus core loading of diagnostically active nanocrystals into polymer nanoparticles. ACS Nano 8:9143–9153
18. Wei X, Chen H, Tham HP, Zhang N, Xing P, Zhang G, Zhao Y (2018) Combined photodynamic and photothermal therapy using cross linked polyphosphazene nanospheres decorated with gold nanoparticles. ACS Appl Nano Mater 1:3663–3672
19. Yan Y, Fu J, Wang M, Liu S, Xin Q, Chen Z, Xu Q (2016) Fabrication of poly(cyclotriphosphazene-co-4,4′-sulfonyldiphenol) nanotubes decorated with Ag–Au bimetallic nanoparticles with enhanced catalytic activity for the reduction of 4-nitrophenol. RSC Adv 6:24921–24928
20. Hu Y, Meng L, Niu L, Lu Q (2013) Facile synthesis of superparamagnetic Fe3O4@polyphosphazene@Au shells for magnetic resonance imaging and photothermal therapy. ACS Appl Mater Interfaces 5:4586–4591
21. Rothemund S, Teasdale I (2016) Preparation of polyphosphazenes: a tutorial review. Chem Soc Rev 45:5200–5215
22. Andrianov A (2006) Water-soluble polyphosphazenes for biomedical applications. J Inorg Organomet Polym Mater 16(4):397–406
23. Martinez AP, Qamar B, Fuerst TR, Muro S, Andrianov AK (2017) Biodegradable "smart" polyphosphazenes with intrinsic multifunctionality as intracellular protein delivery vehicles. Biomacromolecules 18(6):2000–2011
24. Wilfert S, Iturmendi A, Schoefberger W, Kryeziu K, Heffeter P, Berger W, Brüggemann O, Teasdale I (2013) Water-soluble, biocompatible polyphosphazenes with controllable and pH-promoted degradation behavior. Polym Chem 52(2):287–294
25. Teasdale I (2018) Stimuli-responsive phosphorus-based polymers. Eur J Inorg Chem 11-12:1445–1456
26. Iturmendi A, Theis S, Maderegger D, Monkowius U, Teasdale I (2018) Coumarin-caged polyphosphazenes with a visible-light driven on-demand degradation. Macromol Rapid Commun 39(18):e1800377
27. Jing X, Zhi Z, Jin L, Wang F, Wu Y, Wang D, Yan K, Shao Y, Meng L (2019) pH/redox dual-stimuli-responsive cross-linked polyphosphazene nanoparticles for multimodal imaging-guided chemo-photodynamic therapy. Nanoscale 11:9457–9467
28. Iturmendi A, Monkowius U, Teasdale I (2017) Oxidation responsive polymers with a triggered degradation via arylboronate self-immolative

motifs on a polyphosphazene backbone. ACS Macro Lett 6(2):150–154

29. Bouché M, Pühringer M, Iturmendi A, Amirshaghaghi A, Tsourkas A, Teasdale I, Cormode DP (2019) Activatable hybrid polyphosphazene-AuNP nanoprobe for ROS detection by bimodal PA/CT imaging. ACS Appl Mater Interfaces 11(32):28648–28656
30. Karimi M, Ghasemi A, Zangbad PS, Rahighi R, Basri SMM, Mirshekari H, Amiri M, Pishabad ZS, Aslania A, Bozorgomid M, Ghosh D, Beyzavi A, Vaseghi A, Aref AR, Haghani L, Bahrami S, Hamblin MR (2016) Smart micro/nanoparticles in stimulus-responsive drug/gene delivery systems. Chem Soc Rev 45(5):1457–1501
31. Molina M, Asadian-Birjand M, Balach J, Bergueiro J, Miceli E, Calderon M (2015) Stimuli-responsive nanogel composites and their application in nanomedicine. Chem Soc Rev 44(17):6161–6186
32. Highley CB, Prestwich GD, Burdick JA (2016) Recent advances in hyaluronic acid hydrogels for biomedical applications. Curr Opin Biotechnol 40:35–40
33. Xu Z, Lu C, Riordon J, Sinton D, Moffitt MG (2016) Microfluidic manufacturing of polymeric nanoparticles: comparing flow control of multiscale structure in single-phase staggered herringbone and two-phase reactors. Langmuir 32(48):12781–12798
34. Van Ballegooie C, Man A, Andreu I, Gates BD, Yapp D (2019) Using a microfluidics system to reproducibly synthesize protein nanoparticles: factors contributing to size, homogeneity, and stability. PRO 7(5):290
35. Danaei M, Dehghankhold M, Ataei S, Hasanzadeh Davarani F, Javanmard R, Dokhani A, Khorasani S, Mozafari MR (2018) Impact of particle size and polydispersity index on the clinical applications of lipidic nanocarrier systems. Pharmaceutics 10(2):E57
36. Andrianov AK, Marin A, Martinez AP, Weidman JL, Fuerst TR (2018) Hydrolytically degradable PEGylated polyelectrolyte nanocomplexes for protein delivery. Biomacromolecules 19(8):3467–3478
37. Saha K, Agasti SS, Kim C, Li X, Rotello VM (2012) Gold nanoparticles in chemical and biological sensing. Chem Rev 112:2739–2779
38. Wang H, Yu D, Li B, Liu Z, Ren J, Qu X (2019) Ultrasensitive magnetic resonance imaging of systemic reactive oxygen species in vivo for early diagnosis of sepsis using activatable nanoprobes. Chem Sci 10:3770–3778
39. Herman J, Zhang Y, Castranova V, Neal SL (2018) Emerging technologies for optical spectral detection of reactive oxygen species anal. Bioanal Chem 410(24):6079–6095

# Chapter 42

# Cationic Contrast Agents for Computed Tomography of Cartilage for Early Diagnosis of Osteoarthritis

**Chenzhen Zhang and Ambika G. Bajpayee**

## Abstract

Here we describe methods for synthesizing cationic contrast agents for computed tomography (CT) of cartilage for early diagnosis of tissue degeneration. CT imaging of soft tissues like cartilage is possible only if radio-opaque contrast agents (e.g., ioxaglate) can penetrate through the full thickness of tissue in sufficient concentrations. Ioxaglate (IOX), however, is anionic and is repelled by the negatively charged cartilage matrix resulting in poor CT attenuation. Here we demonstrate cartilage penetrating cationic contrast agents using multi-arm Avidin (mAv) conjugated to ioxaglate (mAv-IOX). mAv-IOX rapidly penetrates through the full thickness of cartilage in high concentrations owing to weak-reversible nature of electrostatic interactions resulting in high CT attenuation even with low doses unlike IOX. The technology has the potential for enabling clinical CT of cartilage and other negatively charged soft tissues.

**Key words** Bio-electrostatics, Computed tomography (CT), Cartilage, Negatively charged tissues, Cationic contrast agents, Ioxaglate, Avidin

## 1 Introduction

Early diagnosis of degenerative joint diseases like osteoarthritis (OA) is critical as there is only a narrow time-window during which therapeutic intervention can reverse disease progression. While computed tomography (CT) can diagnose changes in subchondral bone, it is not clinically viable for imaging joint soft tissues like cartilage, which exhibit early degenerative changes associated with OA onset. CT may be developed for soft tissue imaging by using radio-opaque contrast agents injected into the joint, as long as they are safe and the time to produce sufficient CT attenuation is short enough to be clinically viable. Contrast agents like ioxaglate (IOX) are anionic and thus repelled by negatively charged cartilage matrix containing high density of glycosaminoglycans (GAGs) that

Miguel R. Ossandon et al. (eds.), *Biomedical Engineering Technologies: Volume 1*, Methods in Molecular Biology, vol. 2393, https://doi.org/10.1007/978-1-0716-1803-5_42, 

hinders their intra-tissue penetration and partitioning resulting in poor CT attenuation [1]. This is further complicated by their short intra-tissue residence time owing to rapid clearance from the joint space. Higher doses are, therefore, required to enhance flux and achieve intra-cartilage concentrations sufficient for CT imaging which result in both local and systemic toxicity. The high negative fixed charge density of cartilage, however, offers a unique opportunity to utilize electrostatic interactions to enhance intra-tissue transport, uptake, and retention of positively charged contrast agents [2–4]. A cationic glycoprotein, Avidin, has been shown to penetrate through the full thickness of rabbit cartilage following intra-articular (IA) injection resulting in a high intra-cartilage uptake ratio of 180 (implying 180× higher concentration of Avidin inside cartilage than surrounding fluid at equilibration) and was still found to be present through the full-thickness of cartilage 2 weeks following its IA administration in a rabbit anterior cruciate ligament transection model of posttraumatic OA [5–7]. Avidin, thus, has been proven to be an effective carrier for local targeted delivery to cartilage inside the joint enabled via weak-reversible electrostatic interactions.

Here we present a protocol for synthesizing cationic contrast agents using Avidin with multiple branched arms [8] to deliver ioxaglate (mAv-IOX) in high concentrations through the full thickness of cartilage. Electrostatic interactions enable high partitioning up of mAv-IOX at the cartilage interface increasing its concentration from C to KC, where K is the Donnan partitioning factor (Fig. 1a, b). This enhances its rate of penetration into cartilage. Whereas, anionic IOX is repelled by the negatively charged cartilage matrix resulting in partitioning down by K'C reducing IOX's rate of transport and uptake into the tissue. As a result, mAv-IOX can enable high CT attenuation even at low doses for safe diagnosis of early stage OA (Fig. 1c). The technology also has the potential for clinical CT of other negatively charged joint soft tissues.

## 2 Materials

### 2.1 Synthesis of (Multi-Arm Avidin) mAv Nano-Construct System

1. 8-arm PEG-amine (Cat# 8AP0802, Advanced Biochemicals, Lawrenceville, GA)
2. NHS-biotin (Cat# 20217, Thermo Fisher Sc., Waltham, MA).
3. 3.5 kDa MWCO Snakeskin dialysis tubing
4. Dimethyl Sulfoxide (DMSO).
5. Sinapic acid.

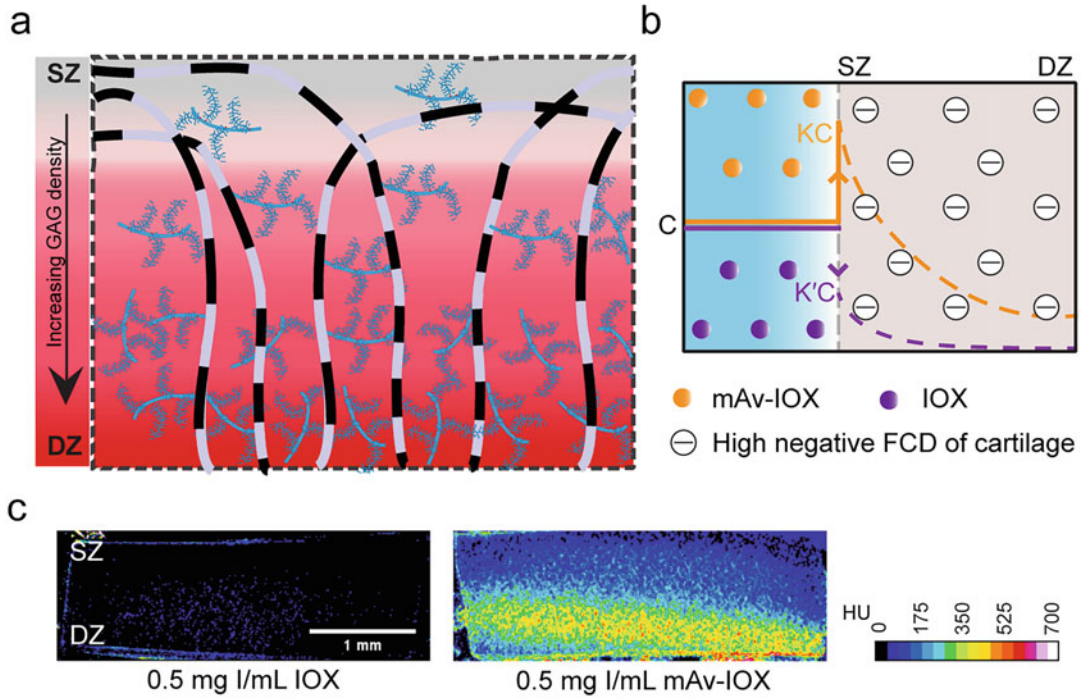


**Fig. 1** (**a**) Structure of cartilage tissue showing increasing concentration of negatively charged GAGs from superficial zone (SZ) to deep zone (DZ) of tissue giving it a high negative fixed charge density (FCD). (**b**) Cationic contrast agent, mAv-IOX, due to its optimal net charge can rapidly penetrate through the full thickness of cartilage in high concentrations owing to high Donnan partitioning factor (K) that increases its concentration at tissue interface by KC. On the contrary, transport of anionic IOX is hindered by negatively charged cartilage whose concentration at cartilage interface partitions down by K'C. (**c**) mAv-IOX results in high CT signal inside cartilage at a low concentration of 0.5 mg I/mL while anionic IOX cannot

6. Avidin (Cat# A887, Thermo Fisher Sc., Waltham, MA).
7. 20 mM ammonium bicarbonate buffer
8. 4′-hydroxybenzene-2-carboxylic acid (HABA) dye (Cat #28010, Thermo Fisher Sc., Waltham, MA)
9. Synergy H1 Microplate Reader (BioTek, Winooski, VT).
10. Hulamixer Sample Mixer (Cat#15920D, Thermo Fisher Sc., Waltham, MA).
11. MALDI-TOF (Bruker Microflex II, Bruker, Billerica, MA).
12. Freeze Dryer (Cat# 710201000, Labconco, Kansas City, MO).
13. Ultra-performance liquid chromatography (UPLC) (Acquity H-Class UPLC, Waters Corp, Milford, MA).
14. Acquity UPLC BEH200 Size Exclusion Column (200 Å, 1.7 μm column, 4.6 × 300 mm) (Cat# 186005226, Waters Corp, Milford, MA).

### 2.2 Conjugation of Ioxaglate (IOX) to 8-Arm Biotin-PEG

1. Ioxaglate (IOX) (Cat# Y0000141, Sigma-Aldrich St. Louis, MO).
2. Thionyl chloride (density: 1.64 g/cm$^3$) (Cat# AA4186818, Fisher scientific, Waltham, MA).
3. Anhydrous dimethylformamide (DMF).
4. Parafilm.
5. 1 N Sodium hydroxide solution (NaOH)
6. Dimethyl-d6 sulfoxide (DMSO-d6) (Cat# M3671, Thermofisher Acros Organics, Geel, Belgium).
7. 8-arm biotin-PEG (acquired from Subheading 3.1)
8. Triethylamine (TEA) (Cat# O4884-100, Fisher scientific, Waltham, MA).
9. 1× phosphate-buffered saline (PBS): 118.07 mM NaCl, 2.68 mM KCl, 4.60 mM $NaH_2PO_4$, 5.90 mM $Na_2HPO_4$. Adjust pH to 7.4 using 1 N NaOH.
10. Thermal shaker (Cat# H5000-HC*, Benchmark Scientific, Sayreville, NJ).
11. Proton Nuclear Magnetic Resonance ($^1$H-NMR) (Varian Inova. Agilent Technologies, Santa Clara, CA).
12. Eppendorf Centrifuge 5424/5424R (Cat# EP022620444, Sigma-Aldrich, St. Louis, MO).
13. High-performance liquid chromatography (HPLC) (Agilent Technologies 1260 infinity II, Agilent Technologies, Santa Clara, CA).

### 2.3 Application in Computed Tomography of Cartilage

1. 1 M sodium chloride solution
2. Bovine calf knee cartilage explant disks (3 mm diameter × 1 mm thick).
3. Protease Inhibitor (PI) Mini Tablets (Cat# PIA32953, Fisher scientific, Waltham, MA).
4. Low X-ray-absorption foam.
5. Zetasizer (Nano-ZS90, Malvern Panalytical, Westborough, MA).
6. Micro Osmometer (Model 3300, Advanced Instruments, Norwood, MA).
7. Incubator for tissue culture (Cat# 13-998-086, Thermo Fisher Sc., Waltham, MA).
8. Microcomputed tomographic imaging system (μCT35, Scanco Medical AG, Wangen-Brüttisellen, Switzerland).

### 2.4 Estimating Correlation Between Contrast-Enhanced CT Attenuation and GAG Density in Cartilage

1. Chondroitinase-ABC (Cat# C2905-5UN, Sigma-Aldrich St. Louis, MO).
2. Protease K (Cat# 3115879001, Sigma-Aldrich St. Louis, MO).

## 3 Methods

A flow chart of the main synthesis steps of cationic contrast agents for computed tomography is shown in Schematics 1.

### 3.1 Synthesis of (Multi-Arm Avidin) mAv Nano-Construct System

1. Dissolve 10.6 mg (0.001 mmol, 1.0 equiv.) of 8-arm PEG-amine in 500 μL of nanopure water (Table 1).
2. Dissolve 1.7 mg (0.005 mmol, 5.0 equiv.) of NHS-biotin in 500 μL of DMSO.
3. Add the NHS-biotin solution from **step 2** dropwise to the PEG solution from **step 1** (5:1 molar ratio, Table 1). React for 2 h under gentle rotation (at 10 rpm, HulaMixer Sample Mixer) at room temperature (Fig. 2a).
4. To remove excess unreacted NHS-biotin from the 8-arm biotin-PEG conjugate solution, dialyze against 1× PBS for 24 h at room temperature using 3.5 kDa dialysis membrane. The purified product is then lyophilized for future application.
5. A 5:1 molar ratio of NHS-biotin and 8-arm PEG-amine will enable conjugation of one biotin per PEG. Use MALDI-TOF spectrometry to confirm the increase in molecular weight of 8-arm PEG-amine after biotinylation. Add 10 μL of 8-arm PEG-amine or 10 μL of 8-arm biotin-PEG (1 mg/mL) to 10 μL sinapic acid. Add 2 μL of the mixture to the sample plate then insert into the MALDI-TOF machine. The molecule weight of 8-arm PEG will increase from 10,620 Da (Fig. 2b) to 10,902 Da following biotinylation (Fig. 2c) showing that an average 1.15 biotin per PEG are present.
6. To synthesize multi-arm Avidin nano-construct (mAv), dissolve 4 moles of 8-arm biotin-PEG (10.9 mg) acquired in **step 4** with one mole of Avidin (16.5 mg) in nanopure water for 30 min under gentle rotation using the Hulamixer at 10 rpm at room temperature.
7. The formation of mAv nano-construct system can be confirmed by using HABA colorimetric dye assay. Make 2.4 mg/mL HABA dye solution in 10 mL nanopure water and remove any undissolved dye by using a 0.2 μm filter. Add excess HABA dye to the Avidin solution to a final concentration of 0.82 mg/mL (initial absorbance of 1.2 detected by Microplate Reader at 500 nm). Add 20 μL of graded concentrations of 8-arm biotin-PEG to 180 μL of HABA-Avidin complex (1:1 through 8:1

**Table 1**
**Materials and molar equivalents for synthesis of mAv nanoconstruct**

| Composition | MW (g/mol) | Weight (mg) | Mole (mmol) | Molar equiv. |
|---|---|---|---|---|
| 8-arm PEG | 10,620 | 10.6 | 0.001 | 1.0 |
| NHS-biotin | 341.3 | 1.7 | 0.005 | 5.0 |
| 8-arm biotin-PEG | 10,902 | 10.9 | 0.001 | 1.0 |
| Avidin | 66,000 | 16.5 | 0.00025 | 0.25 |

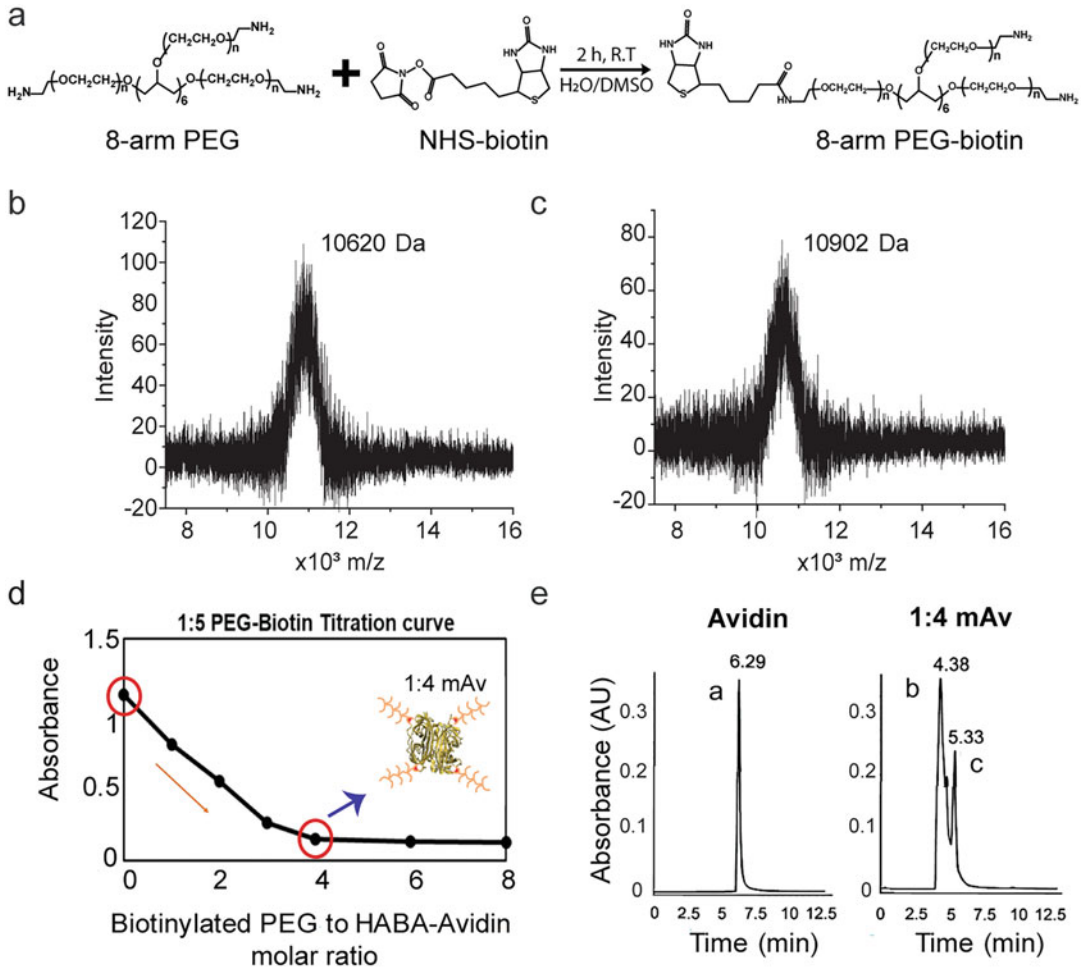


**Fig. 2** (**a**) Schematic of chemical synthesis of 8-arm biotin-PEG. (**b**–**c**) Confirmation of increase in molecular weight after biotinylation of 8-arm PEG. (**d**) Confirmation of the degree of Avidin PEGylation using HABA colorimetric dye assay. (**e**) UPLC analysis of Avidin and mAv nano-construct

molar ratio of biotin-PEG to HABA-Avidin) in order to competitively displace HABA from the biotin binding sites of Avidin (Fig. 6a), which will reduce the absorbance value [8, 9].

8. 100% PEGylation of Avidin will be achieved when the change in absorbance reaches a plateau. As shown in Fig. 2d, there is a reduction in absorbance value with increasing molar ratio of biotinylated PEG to HABA-Avidin from 1:1 to 4:1, following which a plateau is achieved indicating that a majority of biotin sites on Avidin have been occupied by biotin-PEG. This indicates the formation of 1:4 mAv, which has four 8-arm PEGs conjugated to Avidin (*see* **Note 1**).
9. To further confirm the structure, use H-Class Acquity UPLC (Waters Corp, Milford, MA) equipped with an Acquity UPLC BEH200 Size Exclusion Column (200 Å, 1.7 μm column, 4.6 × 300 mm) with 20 mM ammonium bicarbonate buffer as the mobile phase at 0.2 mL/min. Sample is detected at 280 nm.
10. UPLC analysis (Fig. 2e) of standard Avidin shows peak 'a' at 6.29 min. mAv formulation has a majority of Avidin with 4 PEGs (peak 'b' at 4.38 min) and a secondary population of Avidin with 2 PEGs (peak 'c' at 5.33 min).
11. It is recommended to first follow this Subheading 3.1 (with no IOX) to learn how to synthesize and characterize mAv nanoconstruct. Thereafter, replace 8-arm biotin-PEG with 8-arm biotin-PEG-IOX following below Subheading 3.2.

### *3.2 Conjugation of Ioxaglate (IOX) with Biotinylated PEG*

#### *3.2.1 Synthesis of Intermediate Product, Ioxaglate Chloride (IOX-cl)*

1. Weigh 12.7 mg of IOX (0.01 mmol, 20.0 equiv.) in 1.5 mL Eppendorf tube and suspend IOX with 110 μL thionyl chloride (1.5 mmol, 3000.0 equiv.) to form a gray insoluble mixture (Table 2).
2. Add 5 μL DMF to mixture as a catalyst.
3. Purge nitrogen gas to remove any moisture inside the tube and use parafilm to seal tube cap (*see* **Note 2**).
4. Keep mixture reacting for 6 h at 70 °C using Thermal Shaker, with 600 rpm shaking speed (Fig. 3a). IOX will dissolve at high temperature producing a brown solution.
5. After the reaction, cool down the synthesized intermediate product (IOX-Cl). To remove excessive unreacted thionyl chloride, keep the product under vacuum at 20 °C. Intermittent slight heating of thionyl chloride to 40 °C will also facilitate its evaporation. To protect the vacuum pump, thionyl chloride vapor should pass through a gas washing bottle containing 1 N NaOH solution (*see* **Note 3**).

**Table 2**
**Materials and molar equivalents for conjugating IOX to biotin-PEG**

| Composition | MW (g/mol) | Weight (mg) | Mole (mmol) | Molar equiv. |
|---|---|---|---|---|
| IOX | 1268.9 | 12.7 | 0.01 | 20.0 |
| $SOCl_2$ | 119.0 | 180.4 | 1.5 | 3000.0 |
| IOX-Cl | 1305.8 | 13.1 | 0.01 | 20.0 |
| 8-arm biotin-PEG | 10,902 | 5.5 | 0.0005 | 1.0 |

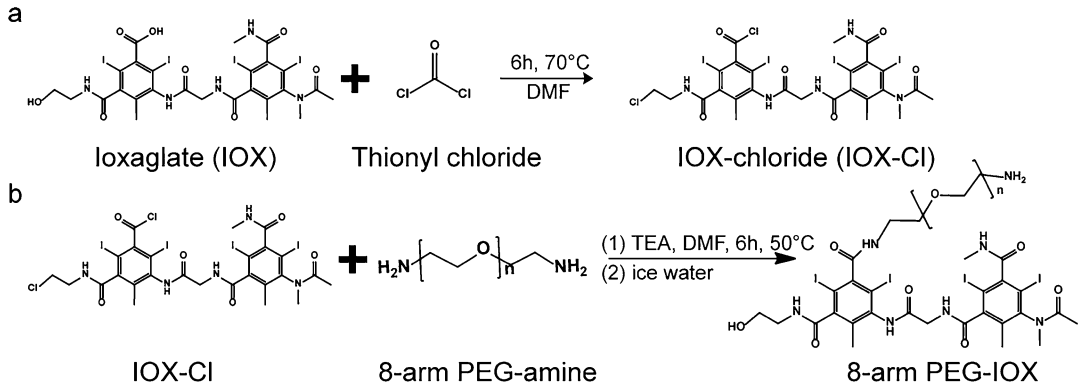


**Fig. 3** Schematic of synthesis of (**a**) intermediate product, IOX-Cl and (**b**) 8-arm PEG-IOX

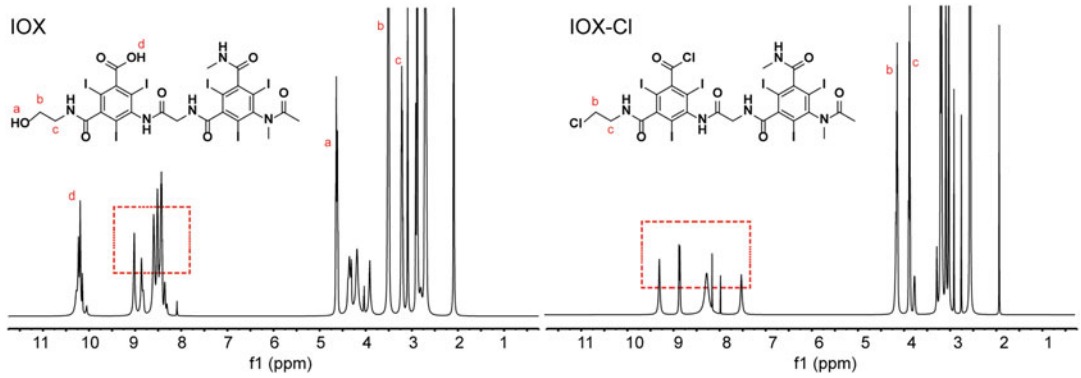


**Fig. 4** $^{1}$H-NMR spectra of IOX and IOX-Cl. The dashed box is hydrogen of amide bonds

6. Add 200 μL DMSO to dissolve the remaining solid and transfer the solution to a new 1.5 mL Eppendorf tube for lyophilization.
7. Dissolve 5 mg of standard IOX and IOX-Cl in 700 μL DMSO-d6 for 1H-NMR, respectively. The structure of IOX-Cl can be verified using 500 MHz $^{1}$H-NMR (Fig. 4). The disappearance of hydroxyl peak (peak 'a') and carboxyl peak (peak 'd') in IOX-Cl, compared to the IOX standard, confirms that hydroxyl and carboxyl groups of IOX have been chloritized.

*3.2.2 Conjugation of Ioxaglate Chloride (IOX-Cl) to 8-Arm Biotin-PEG to Synthesize Biotin-PEG-IOX*

1. Synthesize biotinylated 8-arm PEGs using Subheading 3.1.
2. To conjugate IOX-Cl to 8-arm biotin-PEG (Fig. 3b), first dissolve 13.1 mg of the lyophilized product, IOX-Cl (0.01 mmol, 20 equiv.) in 300 μL of anhydrous DMF using 1.5 mL Eppendorf tube.
3. Add 7.5 μL TEA dropwise to the solution from **step 2**. Keep this solution at 4 °C using a Thermal Shaker.
4. Dissolve 5.5 mg of 8-arm biotin-PEG in 100 μL DMF (0.0005 mmol, 1 equiv.) to make 8-arm biotin-PEG solution. Then, add it dropwise to the IOX-Cl solution from **step 3**.
5. Conduct this reaction in Thermal shaker at 4 °C, 600 rpm for 30 min and then at 50 °C, 600 rpm for 16 h.
6. After the reaction, transfer the reacted product (8-arm biotin-PEG-IOX) to 4 mL ice-water in order to precipitate unreacted IOX-Cl (*see* **Note 3**). Centrifuge the mixture at 10,000 × *g* for 5 min and collect the supernatant.
7. To further purify the product, add collected supernatant to 3.5 kDa dialysis membrane and then dialyze against PBS for 24 h and DI water for another 24 h at room temperature.
8. Then lyophilize the purified product, 8-arm biotin-PEG-IOX, and freeze at −80 °C for future applications.
9. To estimate the amount of IOX loaded on 8-arm biotin-PEG, use HPLC equipped with a Variable Wavelength Detector and an Advance Bio RP-mAb C4 4.6 × 150 mm column. Prepare a gradient of solvent A (0.1% TFA in water) and solvent B (0.1% TFA in acetonitrile). Linearly increase the concentration of solvent B from 5% to 65% over 26 min. Set column temperature at 45 °C and a flow rate of 1.0 mL/min. Standard IOX will elute at 3.710 min, and 8-arm biotin-PEG-IOX will be eluted between 18 and 24 min (254 nm) as PEG polymer does not have constant repeating units and the amount of IOX is not conjugated evenly to PEG (Fig. 5a). Estimate the total UV absorbance (mAU * s) of PEG-IOX by integrating the area under the curve and then estimate IOX concentration according to IOX standard curve. About an average of 3.82 ± 0.50 moles of IOX conjugated to one mole of 8-arm biotin-PEG is expected.
10. Following Subheading 3.1, **step 5**, prepare 10 μL of 8-arm biotin-PEG-IOX (10 mg/mL) and use MALDI-TOF to confirm the increase in its molecular weight compared to 8-arm biotin-PEG. Data in Fig. 5b shows that each mole of 8-arm biotin-PEG is conjugated to 2.33 moles of IOX on an average (*see* **Note 4**).

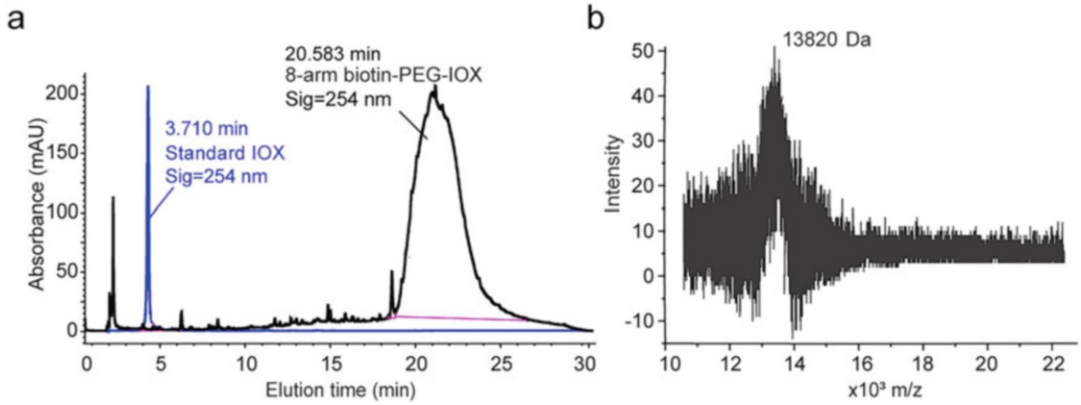


**Fig. 5** (**a**) HPLC and (**b**) MALDI-TOF of 8-arm biotin-PEG-IOX

### *3.3 Application in Computed Tomography of Cartilage*

1. Use Subheading 3.1 to conjugate 4 moles of biotin-PEG-IOX with Avidin at its biotin binding sites to synthesize mAv-IOX.
2. Use Zetasizer Nano-ZS90 to detect the zeta potential of unmodified Avidin and mAv-IOX in DI water; the zeta potential (ζ, mV) of Avidin and mAv-IOX should be around 18.3 ± 0.5 mV and 8.69 ± 0.7 mV, respectively.
3. Obtain 3 mm diameter × 1 mm height cylindrical cartilage discs with intact superficial zone (SZ) from femoropatellar grooves of 1–2-week-old bovine knee joints and freeze them in PBS containing protease inhibitors (PI) until further use.
4. Prepare (a) 0.5 mg I/mL IOX solution; (b) 16 mg I/mL IOX solution (*see* **Note 5**); (c) 0.5 mg I/mL mAv-IOX solution using PBS/PI (dissolve 1 tablet PI in 50 mL PBS buffer) as solvent. Use a freezing point osmometer to balance the osmolality of these contrast agent solutions to 400 ± 20 mOsm/kg by adding 1 M sodium chloride solution dropwise (*see* **Note 6**) [10].
5. Incubate 3 mm diameter cartilage explants in 96-well plate with 300 μL of different iodinated contrast agent solutions (0.5 mg I/mL IOX; 16 mg I/mL IOX and 0.5 mg I/mL mAv-IOX) for 24 h at 37 °C using an incubator.
6. Use the setup shown in Fig. 6a to secure cartilage explants using low X-ray-absorption foam inside a 20.5 mm CT scan tube (*see* **Note 7**). Ensure that the cartilage explant stays secured in the foam during CT imaging.
7. Take one of the equilibrated cartilage explants from contrast agent solution and gently using Kimwipes to remove solution from the tissue surface. Follow **step 6** to fix cartilage inside CT tube.

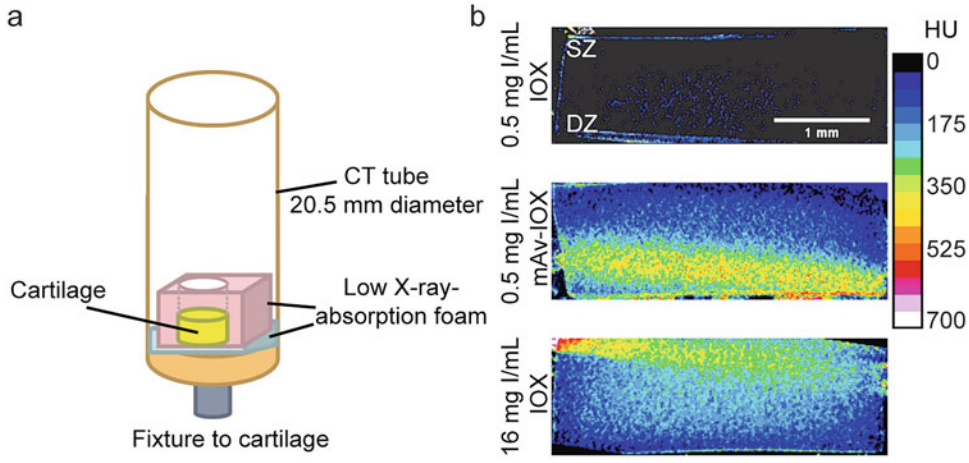


**Fig. 6** (**a**) Setup to secure cartilage explants using low X-ray absorption foam in 20.5 mm diameter CT tube. (**b**) 2D color map of cartilage treated with 0.5 mg I/mL IOX, 16 mg I/mL IOX and 0.5 mg I/mL mAv-IOX. 0.5 mg I/mL mAv-IOX produces high CECT attenuation than 0.5 I/mL IOX and shows similar CECT attenuation to 16 mg I/mL IOX

8. Set μCT35 with an isotropic voxel resolution of 10 μm, 70 kVp tube voltage, 113 μA current, and 200 ms integration time method (*see* **Note 7**). The CT data will be saved as DICOM format. ImageJ software will automatically display Hounsfield Unit (HU) by importing DICOM images.
9. Process the CT imaging data acquired from μCT35 using ImageJ software: (a) Go to Image →Stacks →Images to Stack to convert CT imaging data to a cartilage stack. (b) Go to Image →Stacks →Reslice and select "starting at top" to acquire a new stack showing vertical section of cartilage from superficial zone (SZ) to deep zone (DZ). The output spacing (mm) is 0.010 and select "Avoid interpolation." (c) Go to Image→Adjust→Threshold and apply range as −300 to +∞. Any intensities below −300, which are mostly background, will be set to "NaN" (*see* **Note 8**). (d) Use an ImageJ plugin (use the link in **Note 8**) to acquire Z-projection of average intensity of the cartilage stack. The cartilage stack will be converted to one image with average intensity. (e) Go to LUT→16 colors to create a color map of cartilage. (f) Go to Image →Adjust →Brightness/Contrast and set 0 minimum and 700 Maximum to show higher contrast among different intensities in cartilage color map. (g) Go to Analyze →Tools →Calibration Bar to add a calibration color bar.
10. The color maps of contrast agent spatial distributions in cartilage explants from SZ to DZ are shown in Fig. 6b. 0.5 mg I/mL mAv-IOX produced significantly high CECT attenuation with intensity increasing with GAG density from SZ to DZ

of cartilage. Similar IOX concentration did not show any signal, and 32× high concentration of IOX (16 mg I/mL) was needed to produce similar CT attenuation (*see* **Notes 9** and **10**).

### 3.4 Estimating Correlation Between Contrast-Enhanced CT Attenuation (CECT) and GAG Density in Cartilage

1. Incubate 3 mm diameter cartilage explants in 96-well plates with saline as blank control, 0.1 U/mL chondroitinase-ABC for 8 h and 16 h, 0.25 U/mL chondroitinase-ABC for 16 h and 24 h in order to induce varying degrees of GAG depleted cartilage to simulate different OA stages (early, mid, and late stage). After digestion of chondroitinase-ABC, wash each cartilage with PBS/PI for 3 times.
2. Incubate these explants in 0.5 mg I/mL mAv-IOX and 16 mg I/mL IOX to enhance CT imaging of these cartilages using the same CT imaging procedure as in Subheading 3.3.
3. Calculate mean attenuation of every slice in cartilage stack using ImageJ software: (a) Draw a region of interest (ROI) of cartilage and keep ROI same between different cartilage slices. (b) Go to Image →Adjust →Threshold and set range as −300 to +∞. Any intensity below −300 will be set to "NaN." (c) Go to Image →Stacks →Measure Stack to acquire the mean attenuation of each slice. (d) The average of the mean attenuation of all the cartilage slices is used as mean CECT attenuation of cartilage.
4. After CT imaging, digest each cartilage using 1 mL of 1 mg/mL protease K for 48 h at 57 °C. Vortex each vial properly and measure the total residual glycosaminoglycans (GAGs) in digested explants using the DMMB assay (*see* **Note 11**). The GAG content (mg/mg wet weight) is calculated as:

$$\text{GAG content} = \frac{\text{Total residual GAGs (mg)}}{\text{Wet weight of cartilage (mg)}}$$

5. Build up the correlation graph between CECT mean attenuation and GAG content in cartilage (total GAG concentration per unit wet weight of cartilage) as shown in Fig. 7. A strong positive correlation between mAv-IOX CECT attenuation and residual GAG content in cartilage explant should be observed indicating the high potential of cationic contrast agent, mAv-IOX, in diagnosing different stages of OA.

## 4 Notes

1. Another method to confirm the structure of mAv nanoconstruct system is native PAGE gel electrophoresis (Fig. 8) [8]. Figure 8a shows that Avidin had denatured, (d-Av, treated by β-mercaptoethanol and boiling) resulting in an Avidin

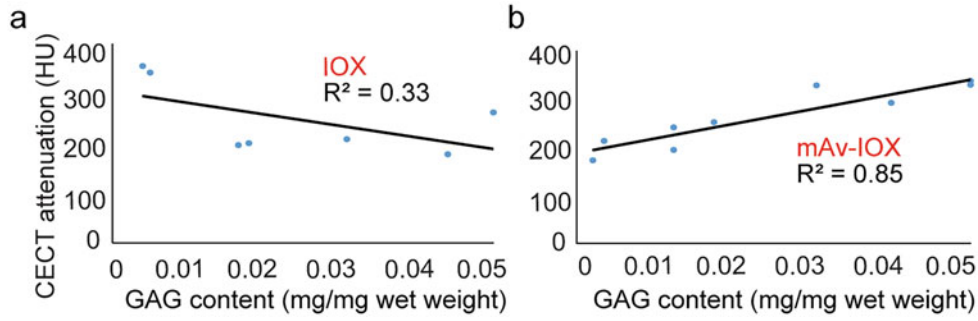


**Fig. 7** Correlation between CECT attenuation and GAG content of cartilage using (**a**) 16 mg I/mL IOX and (**b**) 0.5 mg I/mL mAv-IOX

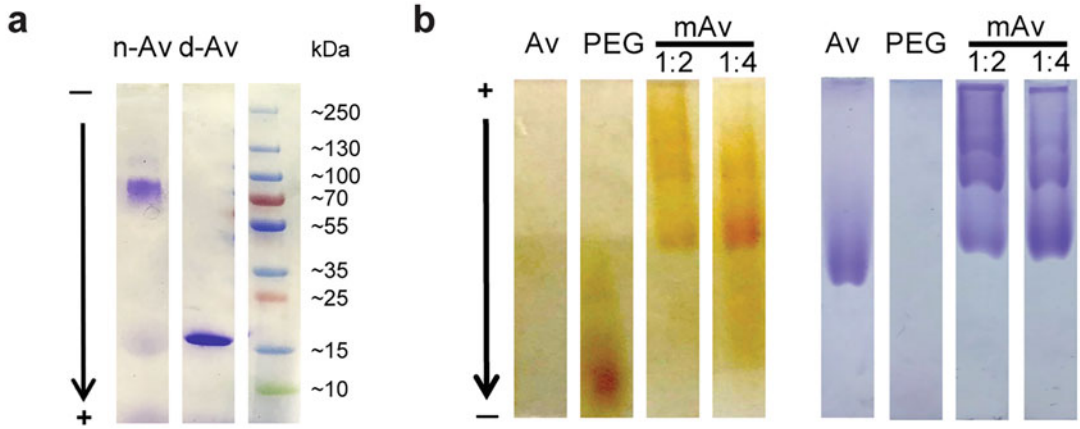


**Fig. 8** (**a**) SDS-PAGE gel (4–20%) of nondenatured Avidin (n-Av) and denatured Avidin (d-Av) stained with Coomassie Brilliant Blue R-250. (**b**) Native PAGE gel (7.5%) of Avidin (Av), PEG, 1:2 mAv and 1:4 mAv under reverse polarity stained with (left) iodine for PEGs and with (right) Coomassie Brilliant Blue R-250 for protein

monomer band (~17 kDa) in SDS-PAGE gel. The Avidin tetramer still dissociated despite efforts to prevent denaturing by mixing it with only 2× Laemmli Sample Buffer (n-Av). Therefore, native PAGE was used instead to confirm PEGylation of mAv. Figure 8b shows native PAGE gel in reverse polarity used to confirm PEGylation in 1:4 mAv containing four 8-arm PEGs. PEG was stained yellow with iodine and protein was stained blue with Coomassie Brilliant Blue R-250. In PEG-staining (left), bands only appear in the PEG and mAv channels. However, in protein-staining (right), bands only appear in the Avidin and mAv channels. Therefore, bands at the same position in the mAv channels with both PEG-staining and protein-staining verified the formation of mAv.

2. Try to maintain anhydrous organic environment. Even a small amount of water in organic solvent can convert the formed acyl

chloride back to carboxyl group, thereby decreasing the efficiency of forming amide bond, which is even worse than acyl chloride in aqueous environment.

3. The alkyl halide converted form hydroxyl group will be converted back to hydroxyl group in this step. Besides, when adding acquired 8-arm biotin-PEG-IOX to ice-water, there may appear fogs above the liquid surface because $SO_2$ gas released from remaining $H_2SO_3$ in product will absorb water vapor from the air. To remove the remaining $H_2SO_3$ of IOX-Cl, there is an alternative method to purify IOX-Cl after Subheading 3.1, **step 5**: Transfer the yellow solid into a 1.5 mL Eppendorf tube and dissolve in 600 μL of ethyl acetate. To this, add saturated $NaHCO_3$ solution (200 μL), and mix for 20–25 min. Discard the aqueous layer and wash the organic layer with saturated $NaHCO_3$ solution (200 μL) and brine (200 μL) [10].
4. Both HPLC and MALDI-TOF analyses confirm the conjugation of 8-arm biotin-PEG-IOX, but the amounts of IOX loaded on PEG detected are different between HPLC data and MALDI-TOF data. Due to the limitation of MALDI-TOF in analyzing polymers with wide polydispersity [11], we have used the results of HPLC for calculating IOX loading (an average 3.82 IOX per 8-arm biotin-PEG).
5. It can be difficult to dissolve large amounts of IOX in PBS or water. Use 1 N NaOH to increase the pH of the solution and enhance IOX's solubility and then decrease the pH to normal.
6. The osmolality of 1× PBS is 286 ± 2 mOsm/kg detected using a freezing point osmometer. The osmolality of synovial fluid in normal joint is 404 ± 57 mmol/kg [12]. To avoid the influence of osmolality, it is important to balance osmolality to 400 ± 20 mOsm/kg.
7. Decreasing available field of view and tube voltage to 15 mm and 55 kVp may increase the resolution of CT imaging.
8. When a value is assigned "NAN" (Not-A-Number), it is excluded from average intensity calculations. This way, any background signal can be excluded from data processing. The function "Z-project" in ImageJ, however, calculates average intensity by including "NaN" values. Therefore, a new plugin script that can ignore "NaN" values should be used and is available online (https://imagej.nih.narkive.com/tKH91mp1/images-with-nans). The procedure of adding a new plugin to ImageJ is: (a) Copy the plugin script on website; (b) Go to ImageJ →Plugins →New →Plugin Tool →Paste plugin script in the tool and save it in Plugin file of ImageJ; (c) Go to ImageJ →Plugins →Install Plugin →choose saved new plugin; (d) Reopen ImageJ and new plugin is available to use.

9. When making high concentration of mAv-IOX for CECT imaging (e.g. 2 mg I/mL), aggregation can occur, which will limit its use and its penetration into cartilage. Use of 50 mM arginine and 50 mM glutamic acid buffer can reduce aggregation and promote protein solubility. However, note that the aggregation problem may not be completely resolved. This solubility issue can limit its application when high concentrations of mAv-IOX are required.
10. Increase the volume of contrast agent solution (300 μL) in Subheading 3.3, **step 5** and conjugate more IOX to per 8-arm biotin-PEG in Subheading 3.1, **step 2** to optimize the resolution and contrast of mAv-IOX in CECT imaging.
11. Cartilage explant digestion and manual of DMMB assay are indicated in previously published papers [13].

## Acknowledgements

This work was supported by the United States Department of Defense through the Congressionally Directed Medical Research Programs (CDMRP) and National Institutes of Health (R03 EB025903; Trailblazer R21 EB028385). We are grateful to Prof. Julia Charles from Brigham and Women's Hospital for access to the μCT 35 machine.

### References

1. Pouran B, Arbabi V, Bajpayee AG, van Tiel J, Toyras J, Jurvelin JS, Malda J, Zadpoor AA, Weinans H (2018) Multi-scale imaging techniques to investigate solute transport across articular cartilage. J Biomech 78:10–20. https://doi.org/10.1016/j.jbiomech.2018.06.012
2. Bajpayee AG, Wong CR, Bawendi MG, Frank EH, Grodzinsky AJ (2014) Avidin as a model for charge driven transport into cartilage and drug delivery for treating early stage post-traumatic osteoarthritis. Biomaterials 35:538–549. https://doi.org/10.1016/j.biomaterials.2013.09.091
3. Vedadghavami A, Wagner EK, Mehta S, He T, Zhang C, Bajpayee AG (2019) Cartilage penetrating cationic peptide carriers for applications in drug delivery to avascular negatively charged tissues. Acta Biomater 93:258–269. https://doi.org/10.1016/j.actbio.2018.12.004
4. Bajpayee AG, Grodzinsky AJ (2017) Cartilage-targeting drug delivery: can electrostatic interactions help? Nat Rev Rheumatol 13:183–193. https://doi.org/10.1038/nrrheum.2016.210
5. Bajpayee AG, De la Vega RE, Scheu M, Varady NH, Yannatos IA, Brown LA, Krishnan Y, Fitzsimons TJ, Bhattacharya P, Frank EH, Grodzinsky AJ, Porter RM (2017) Sustained intra-cartilage delivery of low dose dexamethasone using a cationic carrier for treatment of post traumatic osteoarthritis. Eur Cell Mater 34:341–364. https://doi.org/10.22203/eCM.v034a21
6. Bajpayee AG, Scheu M, Grodzinsky AJ, Porter RM (2014) Electrostatic interactions enable rapid penetration, enhanced uptake and retention of intra-articular injected avidin in rat knee joints. J Orthop Res 32:1044–1051. https://doi.org/10.1002/jor.22630
7. Bajpayee AG, Scheu M, Grodzinsky AJ, Porter RM (2015) A rabbit model demonstrates the influence of cartilage thickness on intra-articular drug delivery and retention within cartilage. J Orthop Res 33:660–667. https://doi.org/10.1002/jor.22841
8. He T, Zhang C, Vedadghavami A, Mehta S, Clark HA, Porter RM, Bajpayee AG (2019) Multi-arm Avidin nano-construct for intra-

cartilage delivery of small molecule drugs. JCR. https://doi.org/10.1016/j.jconrel.2019.12.020

9. Bajpayee AG, Quadir MA, Hammond PT, Grodzinsky AJ (2016) Charge based intra-cartilage delivery of single dose dexamethasone using Avidin nano-carriers suppresses cytokine-induced catabolism long term. Osteoarthritis Cartilage 24:71–81. https://doi.org/10.1016/j.joca.2015.07.010
10. Stewart RC, Patwa AN, Lusic H, Freedman JD, Wathier M, Snyder BD, Guermazi A, Grinstaff MW (2017) Synthesis and preclinical characterization of a cationic iodinated imaging contrast agent (CA4+) and its use for quantitative computed tomography of ex vivo human hip cartilage. J Med Chem 60:5543–5555. https://doi.org/10.1021/acs.jmedchem.7b00234
11. Byrd HCM, McEwen CN (2000) The limitations of MALDI-TOF mass spectrometry in the analysis of wide polydisperse polymers. Anal Chem 72:4568–4576. https://doi.org/10.1021/ac0002745
12. Shanreld S, Campbell P, Baumgarten M, Bloebaum R, Sarmiento A (1988) Synovial fluid osmolality in osteoarthritis and rheumatoid arthritis. Clin Orthop Relat Res 235:289–295
13. Mehta S, Akhtar S, Porter RM, Onnerfjord P, Bajpayee AG (2019) Interleukin-1 receptor antagonist (IL-1Ra) is more effective in suppressing cytokine-induced catabolism in cartilage-synovium co-culture than in cartilage monoculture. Arthritis Res Ther 21:238. https://doi.org/10.1186/s13075-019-2003-y

# Chapter 43

# Economical Production of Radiopharmaceuticals for Preclinical Imaging Using Microdroplet Radiochemistry

**Jia Wang and R. Michael van Dam**

## Abstract

The short-lived radiolabeled "tracers" needed for performing whole body imaging in animals or patients with positron-emission tomography (PET) are generally produced via automated "radiosynthesizers". Most current radiosynthesizers are designed for routine production of relatively large clinical batches and are very wasteful when only a small batch of a tracer is needed, such as is the case for preclinical *in vivo* PET imaging studies. To overcome the prohibitively high cost of producing small batches of PET tracers, we developed a droplet microreactor system that performs radiochemistry at the 1–10μL scale instead of the milliliter scale of conventional technologies. The overall yield for the droplet-based production of many PET tracers is comparable to conventional approaches, but 10–100× less reagents are consumed, the synthesis can be completed in much less time (<30 min), and only a small laboratory footprint and minimal radiation shielding are needed. By combining these advantages, droplet microreactors enable the economical production of small batches PET tracers on demand. Here, we describe the fabrication method of the droplet microreactor and the droplet-based synthesis of an example radiotracer ([$^{18}$F]fallypride).

**Key words** Radiochemistry, Radiosynthesis, Microfluidics, Droplet chemistry, Radiopharmaceutical, Positron-emission tomography (PET), Green chemistry, Molecular imaging, *In vivo* imaging

## 1 Introduction

Positron-emission tomography (PET) is a dynamic *in vivo* imaging technique that can be used to observe the rate of specific biomolecular processes or metabolism throughout the whole body, the distribution and density of specific molecular targets, or the dynamic distribution of a drug compound to determine its pharmacokinetics. PET is extensively used as a research tool in basic science [1, 2] and drug development [3–5] as well as a clinical diagnostic tool [6, 7]. To perform a PET scan, the animal or patient is injected with a tiny amount of a tracer (or "probe") that is labeled with a short-lived positron-emitting radionuclide. When the radionuclide decays, the emitted positron annihilates with a nearby electron creating a pair of anti-parallel gamma rays that are detected

Miguel R. Ossandon et al. (eds.), *Biomedical Engineering Technologies: Volume 1*, Methods in Molecular Biology, vol. 2393, https://doi.org/10.1007/978-1-0716-1803-5_43, 

by the PET scanner. Image reconstruction methods are then used to infer the three-dimensional distribution of the radiotracer in the body.

PET tracers are generally produced using automated radiosynthesizers operated within radiation shielded fume hoods ("hot cells") that protect the operator from radiation exposure. These complex instruments contain reaction vessels, temperature control systems, and electronically controlled pumps and valves to automatically perform the multi-step synthesis of PET tracers [8, 9]. Due to the short half-life of radioisotopes such as fluorine-18 (110 min), the shelf life of PET tracers is very short (e.g., several hours for fluorine-18), and their production must be carried out just before use.

Generally, existing radiosynthesizers are optimized for relatively large batches of clinical-grade PET tracers, i.e., amounts sufficient for imaging multiple patients (e.g., >10s–100s of mCi [>100s–1000s of MBq]). Each batch consumes 10s of milligrams of the expensive precursor material and reactions are performed in milliliter volumes. While the high cost of PET tracer production can be tolerated for clinical diagnostic use or clinical trials, the cost is prohibitive—making tracers inaccessible—for many investigators focused on preclinical or *in vitro* research where only much smaller quantities of tracers are needed (e.g., ~0.1 mCi [3.7 MBq] for one mouse). While there are a couple of tracers that are commercially available at reasonable price (e.g., 2-[$^{18}$F]fluoro-2-deoxy-D-glucose ([$^{18}$F]FDG)), this is only possible by leveraging significant economies of scale due to the widespread use of this tracer, a situation that does not apply to the vast majority of the thousands of other known PET tracers. Thus, new approaches are needed that can actually reduce the cost of producing each batch of PET tracers.

In recent years, there has been growing interest in applying microfluidic techniques to radiochemistry [10, 11]. Microfluidic techniques can reduce the infrastructure and equipment needs by reducing the footprint of the automated radiosynthesizer, enabling it to be operated in a smaller hot cell or to be self-shielded, especially if lower amounts of radioactivity are needed (and thus thinner shielding is acceptable). Furthermore, by performing radiopharmaceutical syntheses in microliter volumes, significant (up to orders of magnitude) reduction in reagents is possible while still producing quantities of PET tracers sufficient for preclinical or even clinical use. The synthesis time can often be appreciably shortened due to improved heat transfer of microfluidic reactor designs (e.g., coiled capillary continuous-flow microreactor [12]) or the reduced time needed for heating or evaporating small reaction volumes (e.g., microliter-scale batch microreactors [13]). Another important advantage of microreactors is the ability to produce tracers with high molar activity (e.g., >~740 GBq/μmol [>~20 Ci/μmol]), even when only a small amount of starting radioactivity is used

(~37 MBq [~1 mCi]) [14]. High molar activity production in conventional radiosynthesizers requires >10s of GBq (>1 Ci) of starting activity, most of which would be wasted if the batch is being produced only for preclinical imaging.

Our research group has been striving to develop droplet-based platforms for producing PET tracers, including electrowetting-on-dielectric (EWOD) devices in which droplets are manipulated by electric fields only [15], patterned wettability devices that rely on tapered pathways to spontaneously transport droplets [16] and, most recently, devices based on hydrophilic liquid traps to contain the reaction droplet [17]. Our latest system relies micro-solenoid valves to deliver precise amounts of reagents to the reaction site and the chip is mounted to a heater to control temperature, which is in turn mounted on a rotary actuator to position the reaction site under different dispensers depending on the reagent needed. Though the reagent loading and transfer mechanisms and temperature control strategies differ among these platforms, the common feature is that radiochemical reactions are all carried out in a 1–10 μL sized droplet.

At this volume scale, reagents needed for a radiosynthesis are often reduced by 10–100× or more [16, 18], the resulting molar activity is high [14], and purification is faster and simpler [16, 19]. Due to the open geometry and high thermal conductivity of chip materials, the synthesis time on the microreactor is less than half of typical macroscale protocols [17]. The simplicity of droplet radiochemistry also enables a tiny overall synthesizer footprint (i.e., 10 × 6 × 12 cm; W × D × H, comparable to the size of a 350 mL [12 oz] coffee cup) and minimal shielding for safe operation.

By reducing waste of precursor and radioisotope by orders of magnitude, and by drastically shrinking the size of the radiosynthesizer and its shielding, droplet-based microfluidic systems provide an economical approach for the preparation of small batches of PET tracers on demand for preclinical *in vivo* imaging or *in vitro* studies. Affordable cost could increase the availability of PET tracers, thereby facilitating the use of diverse tracers to study the biology of disease in animal models, the development of useful new imaging tracers, and the discovery and optimization of new therapies to treat disease. In this chapter, we describe the fabrication of the simple droplet microreactor chips, and, as an example, the droplet-based synthesis of the PET tracer [$^{18}$F]fallypride on the chip for preclinical use. While [$^{18}$F]fallypride is shown as an example, this technique can easily be adapted to the synthesis of many other PET tracers, including [$^{18}$F]FDG [16], [$^{18}$F]FET, [$^{18}$F]Florbetaben and [$^{18}$F]FDOPA [20], and can also be extended to other isotopes, including gallium-68. Furthermore, with the addition of a simple radionuclide concentrator [21], droplet microreactors can be scaled up to produce clinically relevant amounts of PET tracers

[22], with potential to reduce costs of clinical trials or diagnostic imaging, and/or to increase access to PET around the world.

## 2 Materials and Equipment

### 2.1 Fabrication of Droplet Microreactor Chips (See Note 1)

- Silicon wafers (4″ diameter; 525 μm thickness; p type; Silicon Valley Microelectronics Inc., Santa Clara, CA, USA) (*see* **Note 2**).
- Teflon® AF 2400 (1% solution in FC-40; Chemours, Wilmington, DE, USA).
- Positive photoresist (MEGAPOSIT SPR 220-7.0; MicroChem, Westborough, MA, USA) (*see* **Note 3**).
- Photoresist developer (MEGAPOSIT MF-26A; MicroChem) (*see* **Note 3**).
- Transparency photomask (printed by CAD/Art Services Inc., Bandon, OR, USA) (*see* **Note 4**).
- Methanol (MeOH; cleanroom grade).
- Acetone (cleanroom grade).
- Isopropanol (IPA; cleanroom grade).
- Spin coater (PWM32; Headway Research Inc., Garland, TX, USA) (*see* **Note 5**).
- Hotplate (Super Nuova; Thermo Fisher Scientific, Waltham, MA, USA) (*see* **Note 5**).
- High-temperature oven (HT 6/28; Carbolite Gero Ltd., UK) (*see* **Note 5**).
- Mask aligner (MA6; Karl Suss, Garching, Germany) (*see* **Note 5**).
- Reactive ion etching (RIE) system (PlasmaLab 80 Plus; Oxford Instruments, UK) (*see* **Note 5**).
- Silicon wafer cutter (Either an automated dicing saw (DAD321; Disco Corporation, Japan; **Note 5**) or manual diamond scribe (Structure Probe Inc., West Chester, PA, USA; **Note 6**)).

### 2.2 Droplet Synthesis of [$^{18}$F] Fallypride

- Droplet microreactor chip (see above).
- Thermal conducting paste (OMEGATHERM™ 201Silicone Paste; OMEGA® Engineering, Norwalk, CT, USA) (*see* **Note 6**).
- [$^{18}$F]fluoride in [$^{18}$O]$H_2O$ was produced in a cyclotron (*see* **Note 7**).
- A [$^{18}$F]fluoride stock solution was prepared by mixing 30 μL [$^{18}$F]fluoride/[$^{18}$O]$H_2O$ (~ 220 MBq [~ 6 mCi]) with 20 μL of 75 mM $TBAHCO_3$ solution (pharmaceutical grade; ABX

Advanced Biochemical Compounds; **Note 8**) using a micropipette. The final $TBAHCO_3$ concentration in the stock solution was 30 mM.

- A precursor stock solution was made by dissolving 1.0 mg tosylfallypride (fallypride precursor, >90%, ABX Advanced Biochemical Compounds; **Note 8**) in a 50 μL mixture of 2,3-dimethyl-2-butanol (thexyl alcohol; analytical grade) and acetonitrile (MeCN; analytical grade) (1:1, v/v). The final concentration of precursor stock solution was 39 mM (*see* **Note 9**).
- A stock solution of collection solvent (for recovering the crude product after reactions) was prepared by mixing 450 μL MeOH (analytical grade) and 50 μL deionized (DI) water.
- Fallypride (reference standard for [$^{18}$F]fallypride, >95%; ABX Advanced Biochemical Compounds; **Note 8**).
- Ceramic heater (Ultramic CER-1-01-00093, Watlow, St. Louis, MO, USA) (*see* **Note 5**).
- Cooling fan (4-202004UA76153; Cool Innovations, Concord, Canada) (*see* **Note 5**).
- Lead bricks for radiation shielding (Capintec, Inc., Florham Park, NJ, USA) (*see* **Note 6**).

### 2.3 Purification and Formulation of [$^{18}$F]Fallypride

- Reversed-phase analytical-scale high-performance liquid chromatography (HPLC) column (Kinetix C18; 250 × 4.6 mm; 5 μm particle size; Phenomenex, Torrance, CA, USA) (*see* **Note 5**).
- Radio-HPLC system, including a Smartline HPLC system (Knauer, Berlin, Germany), a degasser (Model 5050, Eckert & Ziegler, Berlin, Germany), a pump (Model 1000, Eckert & Ziegler), a UV detector (Eckert & Ziegler), a gamma-radiation detector and counter (B-FC-4100 and BFC-1000, Bioscan, Inc., Poway, CA, USA), and an analog-to-digital converter (GinaStar, raytest USA, Inc., Wilmington, NC, USA) (*see* **Note 5**).
- HPLC mobile phase was prepared by dissolving 1580 mg of ammonium formate ($NH_4HCO_2$; analytical grade) and 10 mL of triethylamine (TEA; analytical grade) in 1.0 L of a 3:2 (v/v) mixture of acetonitrile (analytical grade) and deionized (DI) water. The concentration of $NH_4HCO_2$ in the final solution was 25 mM.
- Sterile saline (0.9% w/v) was purchased from Hospira (Lake Forest, IL, USA) (*see* **Note 8**).
- Sterile syringe filter (13 mm diameter, 0.22 μm pore size, PVDF; Fisherbrand™, ThermoFisher Scientific, Waltham, MA,USA) (*see* **Note 6**).

- Glass syringe (725 N; Hamilton company, Reno, NV, USA) (*see* **Note 6**).
- Sterile 2 mL glass vial (SEV213; ALK, Denmark) (*see* **Note 6**).

### 2.4 Analysis of [$^{18}$F] Fallypride

- Radio-HPLC system (same system as used in the previous section).
- Mobile phase for radio-HPLC was prepared as described above for purification of [$^{18}$F]fallypride.

### 2.5 Analysis of Synthesis Performance

- Calibrated dose calibrator (CRC-25R; Capintec, Florham Park, NJ, USA) (*see* **Note 5**).
- Radio-TLC scanner (MiniGITA star, Raytest, Straubenhardt, Germany) (*see* **Note 5**).
- Mobile phase for radio-TLC was the same as for radio-HPLC.
- A TLC plate (50 mm × 60 mm) was cut using scissors from a larger TLC plate (silica gel 60 $F_{254}$; aluminum backing; 50 mm × 200 mm; Merck KGaA, Darmstadt, Germany) (*see* **Note 6**).

### 2.6 Preclinical Imaging

- Isoflurane (USP; VetOne, Boise, ID, USA) (*see* **Note 8**).
- Subject to be imaged (e.g., mouse, female C57Bl/6 J 10-week old; Jackson Laboratory, Bar Harbor, ME, USA).
- Preclinical PET/CT scanner (G8 PET/CT, Sofie Biosciences, Culver City, CA, USA) (*see* **Note 5**).

## 3 Methods

### 3.1 Fabrication of Droplet Microreactor Chips

Microreactor chips are fabricated from 4″ silicon wafers using standard photolithographic processes as outlined in Fig. 1. Photoresist processing parameters below were determined from the manufacturer's datasheet and should be modified if a different photoresist and developer are used.

1. A photomask with the desired pattern for the droplet microreactor chip is prepared (Fig. 2a). The 4″ photomask contains patterns for 7 chips along with multiple odd-shaped chips that can also be used if desired (Fig. 2c) (*see* **Note 10**).
2. A silicon wafer is installed on the vacuum chuck of a spin coater.
3. 1 mL of Teflon®AF solution is slowly loaded at the center of the silicon water with a micropipette and allowed to sit for 2 min (to let any small bubbles rise to the surface and pop) before spin-coating at 1000 rpm for 30 s.

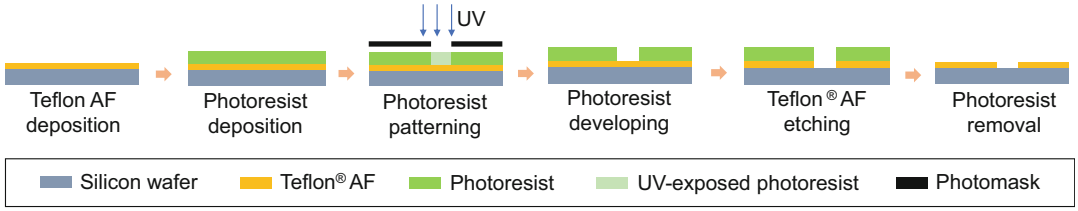


**Fig. 1** Photolithography process for fabrication of the droplet microreactor chip. (Adapted from Wang et al. [17] with permission of the Royal Society of Chemistry)

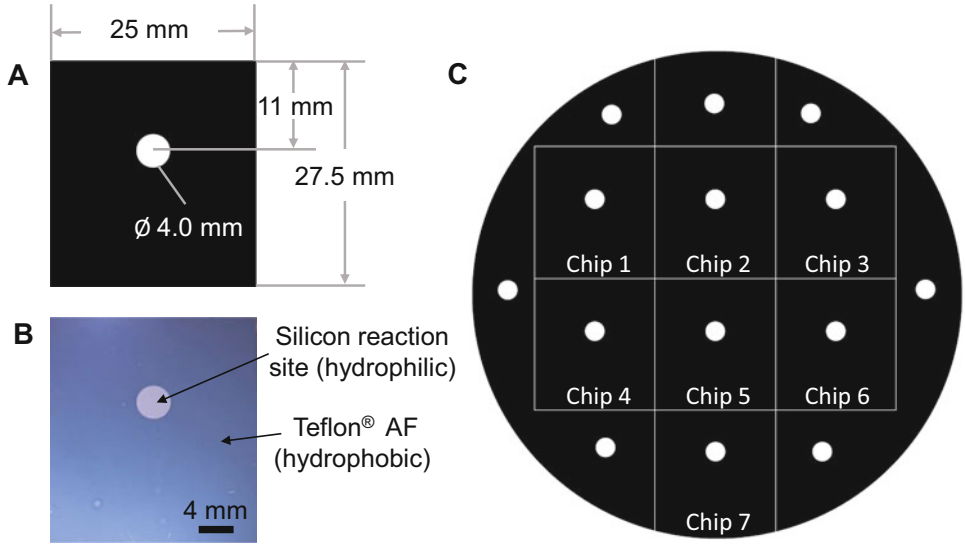


**Fig. 2** (**a**) Photomask pattern used to fabricate the droplet microreactor chip. (**b**) Photograph of the droplet microreactor chip. (Adapted from Wang et al. [17] with permission of the Royal Society of Chemistry). (**c**) Photomask pattern used to fabricate the 4″ silicon water (7 chips on one wafer)

4. The coated water is then removed from the spin coater and heated on a hotplate at 160 °C for 10 min and 245 °C for 10 min to remove the solvent, and then baked in a high-temperature oven (with nitrogen atmosphere) at 340 °C for 3.5 h. The resulting Teflon® AF layer should have a thickness of ~120 nm.
5. To form an etch mask, the coated wafer is re-installed on the spin coater.
6. Photoresist is carefully poured on the top of Teflon layer and then spin-coated at 3000 rpm for 30 s.
7. The coated wafer is removed from the spin coater and baked on the hotplate at 115 °C for 3 min.
8. The wafer and photomask are installed in a mask aligner.

9. Using the mask aligner, the photoresist is exposed through the mask to UV light for 14 s at 12 mW/cm$^2$ lamp intensity and 365 nm wavelength.
10. After removing the wafer from the mask aligner, the photoresist is developed by rinsing in the developer for 2 min and then rinsing with DI water for 1 min, leaving regions of exposed Teflon® AF (4 mm diameter circles).
11. The uncovered regions are then removed via reactive ion etching using 30 s exposure to oxygen plasma at 100 mTorr pressure, 200 W power, and 50 sccm oxygen flow.
12. The wafer is then diced into individual 25.0 × 27.5 mm chips manually using a dicing saw or a manual silicon wafer cutter. A total of 7 full-sized chips are produced from one water.
13. The diced chips are rinsed in acetone for 1 min, IPA for 1 min, and then dried with nitrogen, to remove photoresist.
14. The fabricated chips (Fig. 2b) are designed for one-time use.

### 3.2 Droplet Synthesis of [$^{18}$F] Fallypride

To control the reaction temperature, droplet reactions are performed atop a custom, computer-operated heating platform comprised of a 25 mm × 25 mm ceramic heater, and a cooling fan (Fig. 3) (*see* **Note 11**). Liquid handling operations (addition of reagents to the chip, or collection of crude product from the chip) can be performed automatically using an apparatus as described in [17] or can be performed manually via a micropipette.

Approval of the local radiation safety committee must be obtained prior to any work with radioactive materials. Appropriate radiation shielding and ALARA principles (as low as reasonably achievable) must be used.

1. A new droplet microreactor chip is mounted on top of the heating platform with a thin, uniform, intervening layer of thermal conducting paste applied to improve heat transfer.
2. Lead shielding (e.g., stacks of lead bricks) is placed around the apparatus to shield the operator from radiation exposure.
3. An overview of the droplet synthesis process is shown in Fig. 4.
4. First, an 8 μL droplet of [$^{18}$F]fluoride stock solution (~37 MBq [~1 mCi]) is loaded on the reaction site of the droplet microreactor chip.
5. The chip is heated on the ceramic heater at 100 °C for 15 s to shrink the droplet size (to avoid splattering), and then heated to 105 °C for 45 s to evaporate the remaining solvent. A dried residue of [$^{18}$F]TBAF complex remains at the reaction site after the chip is cooled to room temperature (~60 s).

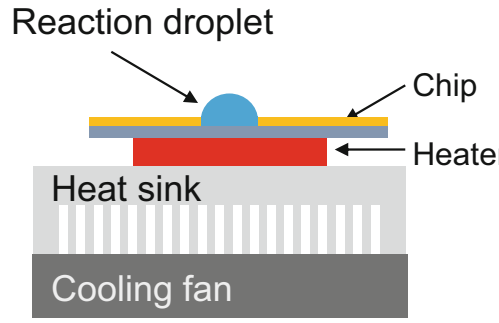


**Fig. 3** Side view schematic of the experimental setup for the microdroplet radiochemistry. (Adapted from Rios et al. [19] with permission of the Royal Society of Chemistry)

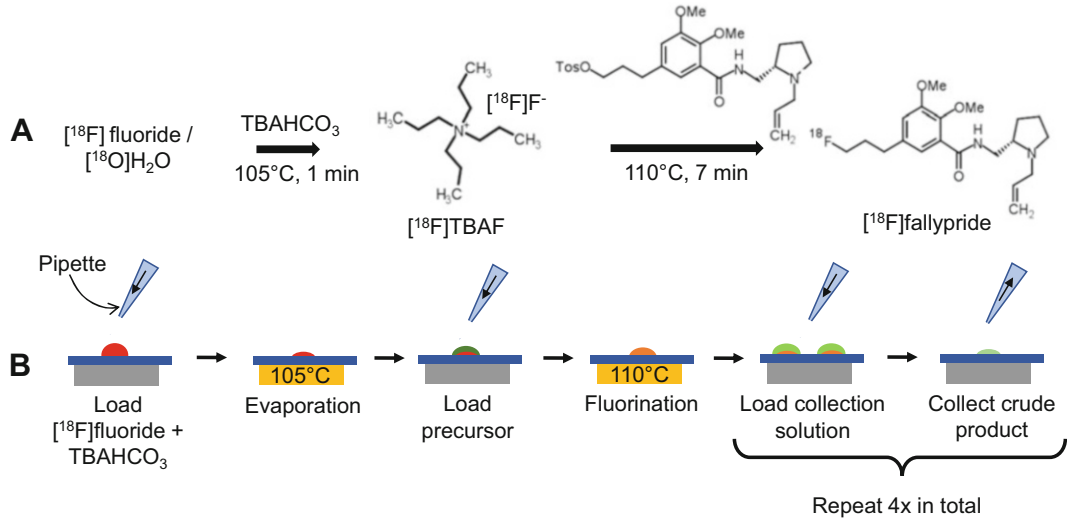


**Fig. 4** (**a**) [$^{18}$F]fallypride synthesis scheme. (**b**) Schematic of droplet-based [$^{18}$F]fallypride synthesis process on the droplet microreactor chip. (Adapted from Rios et al. [19] with permission of the Royal Society of Chemistry)

6. If higher activity level is needed, additional [$^{18}$F]fluoride/[$^{18}$O]$H_2O$ can be loaded on the reaction site and dried in the same manner.
7. Then, a 6 μL droplet of precursor stock solution is loaded on the reaction site to dissolve the dried residue. Care is taken not to touch the surface with the pipette tip.
8. The chip is heated to 110 °C and held for 7 min to perform the radiofluorination reaction and then cooled to room temperature.
9. A 20 μL droplet of collection solution is then loaded on the reaction site to dilute the crude product. After pipetting up and down 10× (to effect mixing), the diluted solution is transferred into a collection vial. The collection process (collection

solution loading, mixing, and transferring) should be repeated a total of four times to minimize the residual product left behind on the chip.

### 3.3 Purification and Formulation

1. Prior to beginning the synthesis, the radio-HPLC system is set up and the column is cleaned and then equilibrated with the HPLC mobile phase for 10 min at 1.5 mL/min flow rate.
2. The collected crude [$^{18}$F]fallypride product is mixed with 80 μL of HPLC mobile phase to minimize the radioactivity loss in the following step.
3. Using a 250 μL glass syringe (with a blunt needle), the diluted solution is injected into the radio-HPLC system and separated at 1.5 mL/min.
4. By observing the UV and gamma detector signals, and controlling the fraction collection valve, the [$^{18}$F]fallypride fraction (~2 mL) is collected (retention time ~ 4.5 min) into a glass vial. Chromatograms are recorded using the radio-HPLC software (Fig. 5a).
5. The product is then heated in an oil bath at 110 °C for 8 min with nitrogen flow to remove the solvent.
6. Finally, sterile saline is added into the glass vial to redissolve the dried product. The volume is adjusted to ensure the concentration of [$^{18}$F]fallypride is at least ~2.6 MBq (~70 μCi) per 200 μL for mouse injections. A dose calibrator is used for radioactivity measurement.
7. The formulated product is then passed through a sterile filter and collected into a sterile glass vial.

### 3.4 Analysis of [$^{18}$F] Fallypride

1. The radiochemical purity (RCP) of the filtered [$^{18}$F]fallypride is verified with the same radio-HPLC system. After cleaning and re-equilibrating the HPLC column, a small sample (10 μL) of the filtered tracer is injected. The resulting radiation detector chromatogram exhibited a [$^{18}$F]fluoride peak at 1.4 min retention time (not always present) and a [$^{18}$F]fallypride peak at 4.4 min. The RCP is calculated from the radiation detector chromatogram as the area under the [$^{18}$F]fallypride peak divided by the sum of the areas of all peaks (Fig. 5b). The purity must be >95%.
2. The identity of the product is confirmed by co-injecting a sample of the filtered [$^{18}$F]fallypride mixed with ~150 nmol of the non-radioactive fallypride reference standard (Fig. 5c). The retention time of the [$^{18}$F]fallypride (peak in radiation detector chromatogram) must match that of the fallypride reference standard (peak in UV detector chromatogram).

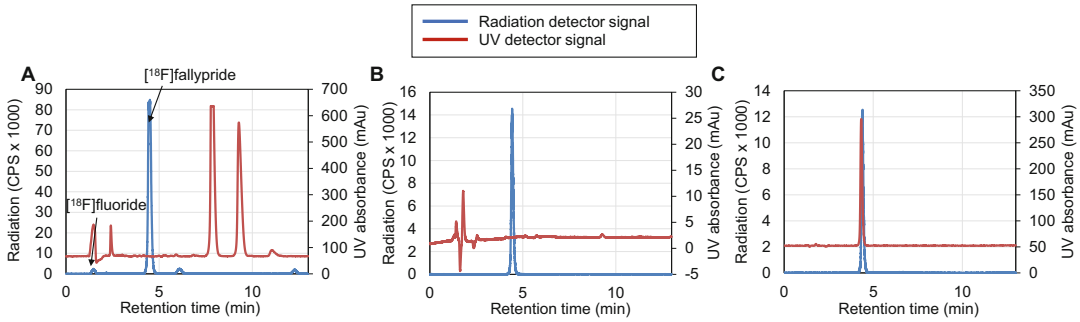


**Fig. 5** Example radio-HPLC chromatograms of (**a**) crude [$^{18}$F]fallypride collected from the chip, (**b**) purified [$^{18}$F]fallypride (radiochemical purity was ~100%), and (**c**) purified [$^{18}$F]fallypride co-injected with fallypride reference standard. (Reproduced from Wang et al. [17] with permission of the Royal Society of Chemistry)

### 3.5 Analysis of Synthesis Performance

Optionally, the synthesis performance can be assessed through radio-TLC analysis of the crude product composition combined with measurements of radioactivity (using the calibrated dose calibrator) at several times throughout the synthesis, purification, and formulation processes. Radioactivity measurements are all decay-corrected to a common timepoint.

1. Radioactivity recovery is calculated as the ratio of radioactivity of collected crude product to starting radioactivity on the chip.
2. Fluorination efficiency is determined using radio-TLC analysis. A 1 μL droplet of the crude product collected from the chip is spotted on a pre-cut radio-TLC plate using a micropipette. The TLC plate is dried in air for 5 min to remove the solvent, and then is separated in the TLC mobile phase. After the solvent front moves by the desired separation distance (35 mm), the plate is dried for 5 min. The resulting TLC plate is then scanned with a radio-TLC scanner (*see* **Note 12**). The chromatograms (Fig. 6) obtained with the scanner showed two peaks: unreacted [$^{18}$F]fluoride ($R_f$ = 0.0) and [$^{18}$F]fallypride ($R_f$ = 0.9). Fluorination efficiency was calculated by dividing the peak area of the [$^{18}$F]fallypride peak by the area of both peaks (*see* **Note 13**).
3. Radioactivity should remain localized to the reaction site during all steps, and negligible radioactivity should be present on the chip surface after collection of the crude product (*see* **Note 14**).

### 3.6 Preclinical Imaging

Provided the filtered [$^{18}$F]fallypride meets the radiochemical identity and purity requirements stated above, it can be used for preclinical microPET imaging. The imaging experiment should be designed with appropriate controls and appropriate number of replicates to achieve the desired statistical power. All preclinical work requires prior approval by the local oversight committee.

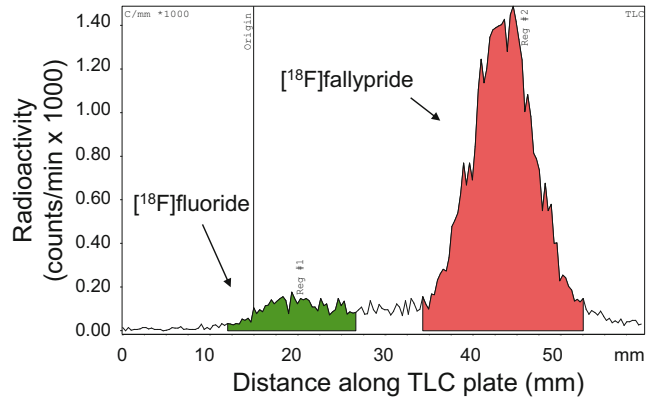


**Fig. 6** Example chromatogram of crude [$^{18}$F]fallypride product analyzed using a radio-TLC scanner

1. The mouse is pre-warmed and anesthetized with 2% isoflurane in oxygen.
2. An aliquot of the filtered [$^{18}$F]fallypride (e.g., ~2.6 MBq [~70 μCi]) in 50–200 μL sterile saline is injected into the mouse via the tail vein.
3. After a 60 min uptake period under anesthesia, a 10 min static PET scan is obtained with a preclinical PET/CT scanner, using an energy window of 150–650 keV.
4. Right after the PET scan, a 50 s CT scan is carried out on the same scanner for anatomical co-registration and attenuation correction using an X-ray source (50 kVp, 200 μA).
5. The PET image is reconstructed based on maximum-likelihood expectation maximization, and processed with corrections, including CT-based photon attenuation, detector normalization, and radioisotope decay (without applying scatter correction), and then converted to units of percent injected dose per cubic centimeter (%ID/cc).
6. The CT image is reconstructed using an analytical Feldkamp algorithm, a mathematical process that generates tomographic images from X-ray projection data acquired at many different angles around the subject and results in 3D images with low possible noise without sacrificing image accuracy and spatial resolution.
7. The resulting PET/CT images (Fig. 7) are then qualitatively or quantitatively analyzed using appropriate commercial or open source analysis software (*see* **Note 15**).

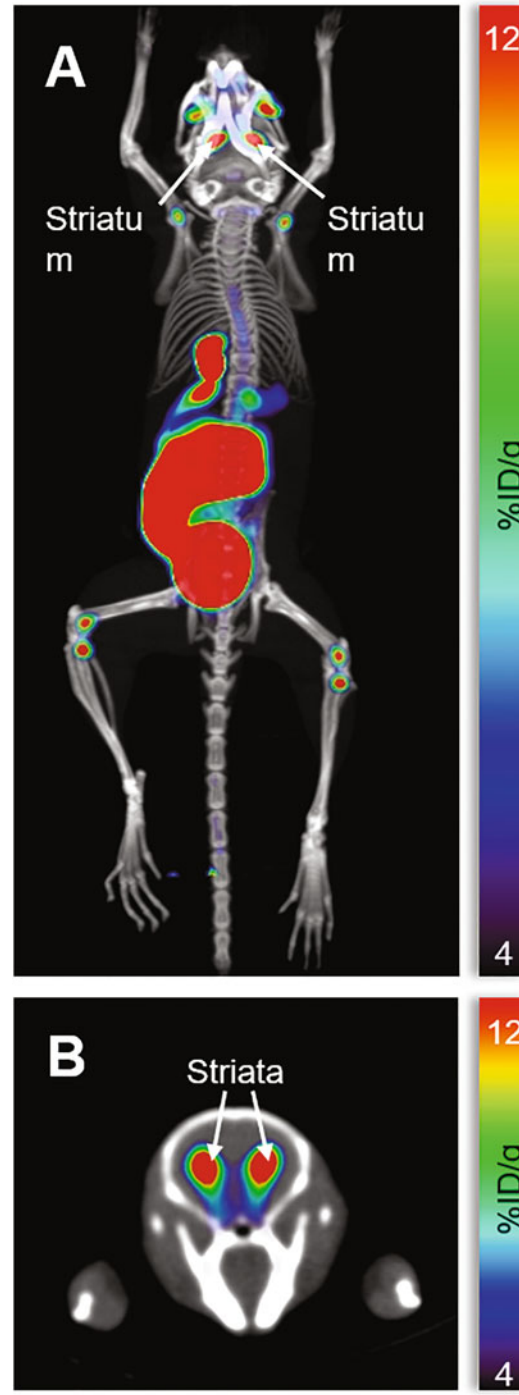


**Fig. 7** Example *in vivo* mouse image with filtered [$^{18}$F]fallypride. (**a**) Maximum intensity projection (MIP) image of whole mouse. (**b**) Transverse view of the brain. (Reproduced from Wang et al. [16] with permission of the Royal Society of Chemistry)

## 4 Notes

1. The equipment listed in this section is often available in shared cleanroom facilities (e.g., at academic institutions) on a usage fee basis. Furthermore, some cleanroom facilities offer foundry services and may be able to carry out the entire fabrication process for a fee.
2. Suitable silicon wafers are available from numerous vendors.
3. Many other types of photoresist (and corresponding developer) can be used, provided there is a method of stripping the resist after the Teflon® AF etching step.
4. Numerous vendors can supply custom-designed photomasks.
5. Similar equipment with similar capabilities is available from numerous vendors.
6. Suitable substitutes are readily available from other vendors.
7. Several vendors can supply batches of [$^{18}$F]fluoride in [$^{18}$O]$H_2O$.
8. This material is also available from other vendors.
9. Even though only 6 μL of the precursor stock solution is needed, 50 μL was prepared to ensure the mass of the precursor could be accurately measured.
10. Photomasks can also be fabricated such that each chip contains multiple reaction sites. This enables multiple reactions to be performed simultaneously, which can be useful for optimization of reaction conditions (Fig. 8) [19].
11. A small hotplate can also be used as a temperature control system, but the heating and cooling time are longer.
12. Radio-TLC plates can alternatively be analyzed via Cerenkov luminescence imaging (CLI), with the advantage that multiple samples can be spotted side by side, and then can be separated and analyzed simultaneously. For quantitative analysis, regions of interest (ROIs) are drawn to enclose the radioactive regions in the image (Fig. 9). The fluorination efficiency corresponding to a particular sample is calculated as the integrated intensity of the product ROI divided by the sum of the integrated intensities of all ROIs for that particular sample [23].
13. If needed, the molar activity can be computed during the radio-HPLC purification step using the procedures outlined in Sergeev et al. [14].
14. Radioactivity distribution on the chip at any stage of the synthesis can be observed via Cerenkov luminescence imaging (CLI) of the chip [16, 24].
15. For example, region-of-interest analysis to determine biodistribution can be performed using AMIDE [25].

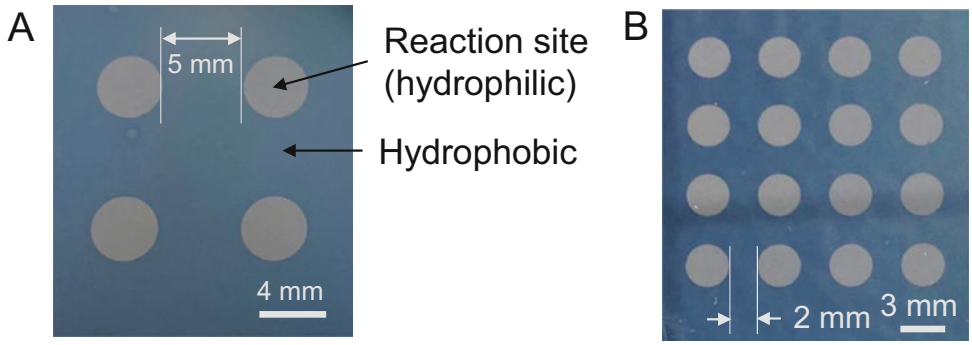


**Fig. 8** Photographs of multi-site droplet microreactor chips for performing high-throughput studies such as reaction optimization. (**a**) 4-spot array of 4 mm reaction sites at 9 mm pitch. (**b**) 16-spot array of 3 mm reaction sites at 5 mm pitch. (Adapted from Rios et al. [19] with permission of the Royal Society of Chemistry)

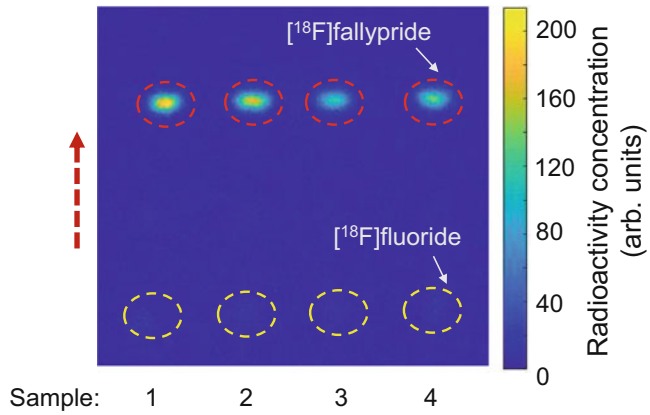


**Fig. 9** Example of high-throughput radio-TLC analysis using Cerenkov luminescence imaging (CLI). The TLC plate was spotted with four 1μL droplets of crude product from the same [$^{18}$F]fallypride synthesis. The red arrow indicates the direction of mobile phase movement during separation. Yellow dashed circles mark the ROIs corresponding to unreacted [$^{18}$F]fluoride, and the red dashed circles mark the ROIs corresponding to [$^{18}$F]fallypride

## References

1. Phelps ME (2000) Positron emission tomography provides molecular imaging of biological processes. Proc Natl Acad Sci 97:9226–9233. https://doi.org/10.1073/pnas.97.16.9226
2. Yao R, Lecomte R, Crawford ES (2012) Small-animal PET: what is it, and why do we need it? J Nucl Med Technol 40:157–165. https://doi.org/10.2967/jnmt.111.098632
3. Aboagye EO, Price PM, Jones T (2001) In vivo pharmacokinetics and pharmacodynamics in drug development using positron-emission tomography. Drug Discov Today 6:293–302. https://doi.org/10.1016/S1359-6446(01)01684-1
4. Hargreaves R (2008) The role of molecular imaging in drug discovery and development. Clin Pharmacol Ther 83:349–353. https://doi.org/10.1038/sj.clpt.6100467
5. Hargreaves R, Hoppin J, Sevigny J et al (2015) Optimizing central nervous system drug development using molecular imaging. Clin Pharmacol Ther 98:47–60. https://doi.org/10.1002/cpt.132
6. Weber J, Haberkorn U, Mier W (2015) Cancer stratification by molecular imaging. Int J Mol

Sci 16:4918–4946. https://doi.org/10.3390/ijms16034918

7. Challapalli A, Aboagye EO (2016) Positron emission tomography imaging of tumor cell metabolism and application to therapy response monitoring. Front Oncol 6:44. https://doi.org/10.3389/fonc.2016.00044
8. Keng PY, Esterby M, van Dam RM (2012) Emerging Technologies for Decentralized Production of PET tracers. In: Hsieh C-H (ed) Positron emission tomography - current clinical and research aspects. InTech, Rijeka, pp 153–182
9. Thompson S, Scott PJH (2019) Equipment and instrumentation for radiopharmaceutical chemistry. In: Lewis JS, Windhorst AD, Zeglis BM (eds) Radiopharmaceutical chemistry. Springer International Publishing, Cham, pp 481–499
10. Audrain H (2007) Positron emission tomography (PET) and microfluidic devices: a breakthrough on the microscale? Angew Chem Int Ed 46:1772–1775. https://doi.org/10.1002/anie.200603509
11. Keng PY, Sergeev M, van Dam RM (2016) Advantages of radiochemistry in microliter volumes. In: Kuge Y, Shiga T, Tamaki N (eds) Perspectives on nuclear medicine for molecular diagnosis and integrated therapy. Springer Japan, Tokyo, pp 93–111
12. Lu S, Giamis AM, Pike VW (2009) Synthesis of [18F]fallypride in a micro-reactor: rapid optimization and multiple-production in small doses for micro-PET studies. Curr Radiopharm 2:1–13
13. Elizarov AM, van Dam RM, Shin YS et al (2010) Design and optimization of coin-shaped microreactor chips for PET radiopharmaceutical synthesis. J Nucl Med 51:282–287. https://doi.org/10.2967/jnumed.109.065946
14. Sergeev M, Lazari M, Morgia F et al (2018) Performing radiosynthesis in microvolumes to maximize molar activity of tracers for positron emission tomography. Commun Chem 1:10. https://doi.org/10.1038/s42004-018-0009-z
15. Chen S, Javed MR, Kim H-K et al (2014) Radiolabelling diverse positron emission tomography (PET) tracers using a single digital microfluidic reactor chip. Lab Chip 14:902–910. https://doi.org/10.1039/C3LC51195B
16. Wang J, Chao PH, Hanet S, van Dam RM (2017) Performing multi-step chemical reactions in microliter-sized droplets by leveraging a simple passive transport mechanism. Lab Chip 17:4342–4355. https://doi.org/10.1039/C7LC01009E
17. Wang J, Chao PH, van Dam RM (2019) Ultra-compact, automated microdroplet radiosynthesizer. Lab Chip 19:2415–2424. https://doi.org/10.1039/C9LC00438F
18. Lisova K, Sergeev M, Evans-Axelsson S et al (2018) Microscale radiosynthesis, preclinical imaging and dosimetry study of [18F] AMBF3-TATE: a potential PET tracer for clinical imaging of somatostatin receptors. Nucl Med Biol 61:36–44. https://doi.org/10.1016/j.nucmedbio.2018.04.001
19. Rios A, Wang J, Chao PH, van Dam RM (2019) A novel multi-reaction microdroplet platform for rapid radiochemistry optimization. RSC Adv 9:20370–20374. https://doi.org/10.1039/C9RA03639C
20. Wang J, Holloway T, Lisova K, van Dam RM (2019) Green and efficient synthesis of the radiopharmaceutical [18F]FDOPA using a microdroplet reactor. React Chem Eng. https://doi.org/10.1039/C9RE00354A
21. Chao PH, Lazari M, Hanet S et al (2018) Automated concentration of [18F]fluoride into microliter volumes. Appl Radiat Isot 141:138–148. https://doi.org/10.1016/j.apradiso.2018.06.017
22. Wang J, Chao PH, Slavik R, van Dam RM (2020) Multi-GBq production of the radiotracer [18F]fallypride in a droplet microreactor. RSC Adv 10:7828–7838. https://doi.org/10.1039/D0RA01212B
23. Wang J, Rios A, Lisova K et al (2020) High-throughput radio-TLC analysis. Nucl Med Biol 82–83:41–48. https://doi.org/10.1016/j.nucmedbio.2019.12.003
24. Dooraghi AA, Keng PY, Chen S et al (2013) Optimization of microfluidic PET tracer synthesis with Cerenkov imaging. Analyst 138:5654–5664. https://doi.org/10.1039/C3AN01113E
25. Loening AM, Gambhir SS (2003) AMIDE: a free software tool for multimodality medical image analysis. Mol Imaging 2:131–137

# Chapter 44

# Preparation of Radiolabeled Antibodies for Nuclear Medicine Applications in Immuno-Oncology

**Junnian Wei, David Y. Oh, and Michael J. Evans**

## Abstract

The mixed patient responses to antibodies targeting immune checkpoint proteins (e.g., CTLA-4, PD-1, PD-L1) have generated tremendous interest in discovering biomarkers that predict which patients will best respond to these treatments. To complement molecular biomarkers obtained from biopsies, the nuclear medicine community has begun developing radiopharmaceuticals that may provide a more holistic assessment of the biological character of all disease sites in patients. On the leading edge of clinical translation are a spectrum of radiolabeled antibodies targeting immune checkpoint proteins or T cell-specific antigens. The adoption of these reagents requires development of efficient and versatile methods for antibody bioconjugation and radiochemistry. We report herein protocols for the preparation of an anti-PD-L1 IgG1 (termed C4) labeled with zirconium-89. The approach is time and cost economical, high yielding, and adaptable to numerous antibody clones and platforms of interest to the immune-oncology community. Included also are representative methods for characterizing the pharmacology of the antibody post bioconjugation, and conducting an in vivo assessment of radiotracer biodistribution in tumor bearing mouse models.

**Key words** Positron emission tomography, Molecular imaging, Biomarker, Cancer immunotherapy, Radiochemistry

## 1 Introduction

The recent clinical success of inhibitors of immune checkpoint proteins (e.g., CTLA-4, PD-1, PD-L1), which are thought in large part to stimulate T cell responses against tumors, has revolutionized cancer therapy [1, 2]. However, since the majority of patients across tumor types do not respond to these agents, there is an urgent need to develop translational biomarkers to identify patients most likely to respond to immunotherapy, as well as to quickly distinguish treatment-responsive and resistant tumors early after the start of therapy [2].

Biomarkers assayed from fresh or archival tissue biopsies (e.g., expression levels of immune checkpoint proteins such as PD-L1, tumor mutational burden, mutations in DNA damage repair

Miguel R. Ossandon et al. (eds.), *Biomedical Engineering Technologies: Volume 1*, Methods in Molecular Biology, vol. 2393, https://doi.org/10.1007/978-1-0716-1803-5_44, 

machinery) may have a high degree of false positive and negative prediction for treatment response [3–5]. Moreover, sampling tissue from only one metastatic lesion may not capture the overall character of the patient's disease, as tumors are often heterogeneous even within the same patient. These considerations have motivated the hypothesis that a functional imaging platform could provide a more holistic assessment of tumor biology, as well as enable longitudinal measurements of tumor biology pre- and post-therapy, to better distinguish responders from non-responders [6].

Unfortunately, standard of care imaging with $^{18}$F-fluorodeoxyglucose positron emission tomography (PET) and/or quantitative computed tomography (CT) are not useful for predicting early response to immunotherapy. On PET, a "flare" effect is commonly observed in tumors that are responding to treatment due to the influx of activated T cells, and the flare of course mimics the imaging findings characteristic of tumor progression [7]. Early tumor regression post treatment is not always seen using standard CT quantitative guidelines like RECIST, and a pseudoprogression effect with early enlargement of tumors is often observed prior to much later radiographic regressions [8].

With these shortcomings in mind, the molecular imaging community has aggressively developed numerous imaging technologies to more rigorously distinguish responders from non-responders. On the leading edge of clinical translation are a panel of antibodies targeting T cell markers (e.g., CD4, CD8) and immune checkpoint proteins (e.g., PD-1, PD-L1). Early human data have established that antigen concentration in metastases from several solid tumor types is generally measurable on PET and highly variable, even among metastases within the same patient [9, 10]. This is likely to be biologically relevant, as the degree of heterogeneity in expression of neoantigens (tumor antigens generated by somatic alterations) within a given patient can be related to the likelihood of clinical benefit with anti-PD-1 [11]. Moreover, preliminary associations between pre-treatment imaging findings and patient outcome have begun to reveal provocative trends, for instance, that higher cumulative tumor $SUV_{max}$ for radiotracers targeting PD-L1 is predictive of a favorable patient response to anti-PD-1/PD-L1 therapies [9].

These encouraging findings suggest that antibody-based imaging may soon become routine for patients receiving immunotherapies, which underscores the importance of disseminating rigorous protocols for antibody bioconjugation and radiolabeling for immunoPET. Herein, we describe a protocol we have utilized to synthesize $^{89}$Zr-labeled C4, an anti-PD-L1 IgG we are actively studying in clinically relevant mouse models of cancer [12, 13]. This template protocol has been verified by our lab using other IgG clones, smaller antibody platforms (e.g., Fabs), and biomolecules [14–20] (Fig. 1). We also include some additional methods for assessing

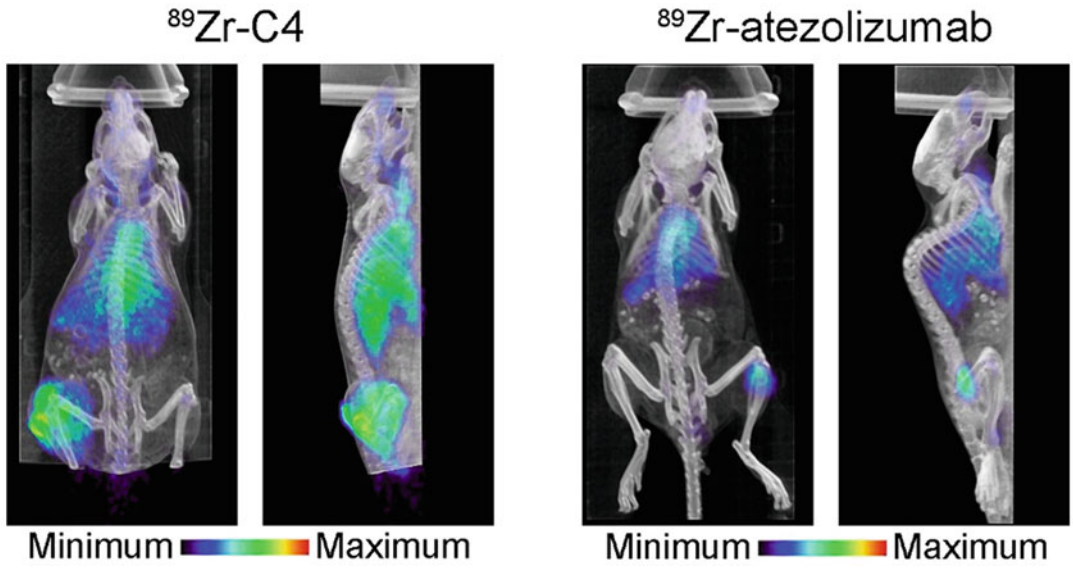


**Fig. 1** Maximum intensity projections showing the typical imaging findings for $^{89}$Zr-labeled IgGs targeting PD-L1. A coronal and sagittal view is shown for each antibody at 48 h post injection. Note the intense radiotracer uptake in the subcutaneous flank tumor and radiotracer accumulation in the liver due to clearance, as expected. Radiochemical yield for the zirconium-89 coupling to the antibody-chelate conjugate is typically >90%, and radiochemical purity after reaction workup is typically >99%

essential properties of the antibody post functionalization, and performing biodistribution studies in animal models of cancer.

## 2 Materials

### *2.1 Reagents for Bioconjugation and Radiolabeling of Antibodies*

1. Phosphate-Buffered Saline (PBS) of pH 7.4, Thermo Fisher, cat. no. 10010023.
2. Deionized water, Milli-Q; greater than 18 MΩ cm resistance.
3. Sodium carbonate; 0.1 M and 2.0 M solutions in water.
4. Sodium bicarbonate; 0.1 M solutions in water.
5. Dimethyl sulfoxide (DMSO).
6. PD-L1 antibody (typically 3–10 mg/mL in PBS).
7. *p*-Isothiocyanatobenzyldesferrioxamine (Df-Bz-NCS), molecular weight = 752.9 g/mol; Macrocyclics, cat. no. B-705; 20 mM in DMSO.
8. PD-10 Desalting Columns, GE Healthcare, cat. no. GE17-0851-01.
9. Normal 0.9% saline.
10. HEPES buffer solution, Invitrogen, cat. no. 15630-049; 0.5 M water solutions.

11. Citric acid monohydrate, Fluka, cat. no. 27491.
12. ITLC strips, Biodex, cat. no. 150-771.
13. [$^{89}$Zr]Zr-oxalate in 1.0 M oxalic acid ($\geq$0.15 GBq/nmol).
14. Ammonium acetate, Sigma-Aldrich, cat. no. A1542; 0.2 M solutions in water.

### 2.2 Unique Reagents for B16 F10 Cell Culture and the Establishing Subcutaneous Xenografts in Mice

1. Dulbecco's Modified Eagle's Medium (DMEM), ATCC, cat. no. 30-2002.
2. L-glutamine, Corning, cat. no. 01618003.
3. Penicillin/streptomycin, Gibco, cat. no. 15140-122.
4. Fetal Bovine Serum (FBS), Thermo Fisher, cat. no. 16000044.
5. Trypsin-EDTA (0.25%), Thermo Fisher, cat. no. 25200056.
6. Matrigel Matrix, Corning, cat. no. 354230.

### 2.3 Other Reagents Involved

1. Instant thin layer chromatography (ITLC) eluent (pH 4.9–5.1): Dissolve 420 mg citric acid monohydrate in 100 ml deionized water, add 1 mL 2.0 M sodium carbonate. Mix well and check the pH. Acceptance range: pH 4.9–5.1.
2. Diethylenetriaminepentaacetic acid (DTPA), ACROS, cat. no. AC114322500.
3. Zirconium(IV) chloride ($ZrCl_4$), ACROS, cat. no. AC206410050.
4. Bovine Serum Albumins (BSA), Sigma-Aldrich, A9418.

### 2.4 Equipment

1. NanoDrop™ 2000 Spectrophotometer or equivalent.
2. Calibrated pH meter, with Biotrode, Hamilton, cat. no. 238140.
3. Octet RED384 instrument.
4. ITLC reader.
5. Dose calibrator.
6. γ-counter.

## 3 Methods

### 3.1 Bioconjugation of Desferrioxamine (Df) to C4 IgG1

1. Dilute an aliquot of 200 μL C4 IgG1 (9.6 mg/mL) with 0.1 M sodium bicarbonate to a final volume of 500 μL. Adjust the pH to 9.0 using up to 50 μL 0.1 M sodium carbonate.
2. Add 2–4 μL of 20 mM solution of Df-Bz-NCS in DMSO to the antibody solution and vortex gently (*see* **Note 1**).
3. Incubate the reaction for 30–45 min in a water bath heated to 37°C. Vortex the reaction gently every 10 min.

4. During the reaction, prepare a PD-10 column (14.5 mm × 50 mm) adding 1 volume of 0.2 M ammonium acetate, and allowing it to pass through the column via gravity.
5. After 30–45 min, and after the ammonium acetate has passed through the PD-10 column, transfer the reaction mixture onto the PD-10 column. Discard the flow-through from the column (*see* **Note 2**).
6. Pipette 2 mL of 0.2 M ammonium acetate onto the PD-10 column and allow it to pass through the column. Discard the flow-through.
7. Pipette 0.6 mL of 0.2 M ammonium acetate onto the PD-10 column. Collect this flow-through as it will contain the Df-C4 conjugate. Repeat this step four times, and combine the flow-through fractions.
8. Measure the concentration using the protein setting on a NanoDrop 2000, or an equivalent spectrophotometer.

### 3.2 Radiolabeling Df-C4 with Zr-89

1. Neutralize a solution of $^{89}$Zr-oxalic acid (3 mCi; 6 μL) with 2 M $Na_2CO_3$ (3 μL).
2. After 1 min, add 0.30 mL of 0.5 M HEPES (pH 7.1–7.3) and 0.4 mg of Df-C4 (in 0.2 M ammonium acetate) into a reaction vial.
3. Check the pH. Up to an additional 0.3 mL of 0.5 M HEPES could be added as needed to adjust the pH to 6.8–7.2.
4. Incubate the reaction for 120 min at room temperature. Monitor the reaction progress at 120 min using ITLC. Blot 1 μL of the reaction on an ITLC strip and resolve the labeled constituents using a 20 mM citric acid (pH 4.9–5.1) mobile phase. $^{89}$Zr-C4 will remain on the baseline of the ITLC plate. Any radioactivity with $R_f > 0.2$ represents radioactivity not bound to C4 (*see* **Note 3**).
5. During the radiolabeling reaction, rinse a PD-10 column (14.5 mm × 50 mm) with 1 volume of 0.2 M ammonium acetate.
6. Pipette the reaction mixture onto the PD-10 column and discard the flow-through.
7. Pipette 2.0 mL of 0.2 M ammonium acetate onto the PD-10 column and discard the flow-through.
8. Pipette 2 mL of 0.2 M ammonium acetate onto the PD-10 column and collect $^{89}$Zr-C4.
9. While waiting to collect fractions from the first PD-10 column, begin rinsing a PD-10 column with 1 volume of 0.5 M HEPES.

10. Pipette the fraction from the first PD-10 column containing $^{89}$Zr-C4 onto the PD-10 column and discard the flow-through.
11. Pipette 1.0 mL of 0.5 M HEPES onto the PD-10 column and discard the flow-through.
12. Pipette 2 mL of 0.5 M HEPES onto the PD-10 column and collect $^{89}$Zr-C4.
13. Measure the radioactivity by the dose calibrator. And analyze the purified radiolabeled mAb by ITLC again. Blot 1 μL of the reaction on an ITLC strip and resolve the labeled constituents using a 20 mM citric acid (pH 4.9–5.1) mobile phase. $^{89}$Zr-C4 will remain on the baseline of the ITLC strip. Any radioactivity with $R_f > 0.2$ represents radioactivity not bound to C4 (*see* **Note 4**).

### 3.3 Determination of the Binding Constant of Df-C4 Compared to Unmodified C4 Using Biolayer Interferometry (see Note 5)

1. Prepare a 300 nM solution of Df-C4 or C4 in PBS with 0.5% (*w/v*) BSA. Aliquot into a 384-well plate.
2. Prepare six concentrations of antigen in PBS with 0.5% (*w/v*) BSA and aliquot into the same 384-well plate. Position the plate on the Octet Red384.
3. Flow the antibody onto the anti-human IgG Capture biosensors for 180 s.
4. Allow 60 s for equilibration to establish a baseline signal.
5. Individually flow each concentration of antigen to allow for 600 s of association, followed by 1200 s for disassociation. Between each sample, regenerate the biosensor surface by exposing them to 10 mM glycine, pH 1.5, for 5 s followed by PBS for 5 s. Repeat this washing step three times.
6. Perform data analysis using a 1:1 interaction model on the ForteBio data analysis software version 8.2.

### 3.4 Determination of Antibody Chelate Number with a Radiometric Isotopic Dilution Assay

1. Prepare a series of 12 × 100 μL solutions containing $^{89}$Zr oxalate (10 μL, 20 μCi, pH 7.7–7.9) in a descending range of nonradioactive $ZrCl_4$ concentrations from 1000–0.5 pmol. Adjust the pH if needed to maintain 7.7–7.9.
2. Vortex the solutions for 30 s before adding 5 μL of Df-C4 IgG1 to each solution (stock concentration of Df-C4 is 5 mg/mL in sterile PBS).
3. Incubate the solutions at room temperature for at least 2 h before quenching with DTPA (20 μL, 50 mM, pH 7.0).
4. Measure the extent of $^{89}$Zr complexation to Df-C4, resolve the solution components on ITLC (ITLC eluent, 20 mM citric acid). $^{89}$Zr-C4 will remain on the baseline, while $^{89}$Zr-oxalate will migrate on the ITLC strip.

5. Plot the fraction of $^{89}$Zr-C4 versus the amount of nonradioactive $ZrCl_4$ added in the solution.
6. Calculate the number of antibody chelates by determining the concentration of $ZrCl_4$ at which only 50% of the protein was labeled by $^{89}$Zr, multiplying by a factor of 2, and then dividing by the moles of protein present in the reaction.

### 3.5 Establishing Subcutaneous Flank Tumors for Radiotracer Biodistribution Studies

1. Maintain B16 F10 cells in a 15 cm sterile tissue cultures plates, and store in a sterile 37° C incubator with 5% $CO_2$(g). The media formulation should be DMEM. Grow the cells to ~80% confluence prior to harvesting.
2. Remove the plates from the incubator and transfer to a biosafety cabinet. Aspirate the cell media with a sterile pipette, preferably under vacuum.
3. Wash the adherent cells gently by pipetting ~5 mL of PBS onto the cells. Aspirate the PBS to remove all traces of serum that contains trypsin inhibitor. Repeat this step up to three times if desired.
4. Add 2 mL of Trypsin-EDTA solution directly to the cells and wait ~3–5 min for the cells to detach from the tissue culture plate (*see* **Note 6**).
5. Add 6.0–8.0 mL of complete growth medium to inactivate the trypsin and dilute the cells.
6. Gently and repeatedly pipette and dispense the cells into the tissue culture plate to encourage disruption of large clusters of cells.
7. Transfer the cells to a sterile 50 mL Falcon tube, and place the tube in a benchtop centrifuge. Spin to pellet the cells for 4 min at 400 × *g* (~1400 rpm).
8. Return the Falcon tube to the biosafety cabinet and aspirate the culture medium. Add 6 mL PBS to rinse the cells to remove the traces of medium, trypsin, and dead cells.
9. Cap the Falcon tube, return the tube to the centrifuge, and pellet the cells at 400 x g for 4 min.
10. Aspirate the PBS.
11. Disperse the cells in 10 mL PBS, counting the cell numbers. Then spin the cells down at 400 × *g* for 4 min.
12. Discard the PBS. And disperse the cells with the appropriate amount of PBS to get a ten million cells/mL suspension. Then keep it on ice.
13. Add Matrigel 1:1 ratio into the cell suspension and mix cells by gently pipetting. Keep it on ice, do not go above room temperature before the next step!

14. Three- to five-week-old male C57BL/6 mice were inoculated with $1 \times 10^6$ B16F10 cells (0.2 mL) subcutaneously into one flank. Tumors were palpable within 3–5 days after injection.

### 3.6 Radiopharmaceutical Biodistribution Studies to Determine Relative Uptake in Tumor Versus Normal Tissues over Time

1. Measure the radioactivity of the $^{89}$Zr-C4 by the dose calibrator just before the injection. Dilute the $^{89}$Zr-C4 with PBS to get a final concentration about 1 mCi/mL. And typically dose of 50–100 μCi/mouse was used for the biodistribution study. For the PET/CT imaging, up to 200 μCi was acceptable; however, normally 50 μCi was enough to obtain a satisfied image.
2. Prior to the tail vein injection, warm the mice for 5–10 min to dilate the veins. Animal may by warmed by placing the animal in a commercially available warming box or by using a warm water circulating pad placed under the mice. And it is recommended to lightly anesthetize the animal before the tail vein injection. Record the radioactivity in each syringe and the time you measured the activity.
3. The 30 ga catheter and the 1/2 cc insulin syringe 28 ga needle were used for injection. Preload the catheter with saline. Position the anesthetized mouse on its side so the lateral tail vein is uppermost. Clean the tail with a 70% alcohol prep pad. Blood will enter the catheter if the needle is in the vein. If the needle is in the vein, the plunger moves easily and the dark colored vein clears as the saline is injected. Inject the mice with $^{89}$Zr-C4 via the catheter, then rinse the catheter with 50 μL of the saline. Measure and record the radioactivity remaining in the syringe.
4. Weigh vials for the storage of the organs. The weight need to be accurate to 0.1 mg.
5. At the dedicated time after radiotracer injection, collect blood via cardiac puncture using a syringe with a 23–25 gauge needle. Typically 0.5 mL to 1 mL blood was collected per mouse (*see* **Note** 7).
6. Humanely euthanize mice to begin biodistribution studies.
7. Puncture the skin, open the chest, and collect the organs. The blood on the organs can be cleaned by gently rinsed in water.
8. Dry the organs and store them in the pre-weighed vials.
9. Reweigh the vials to calculate the mass of the tissues.
10. 50 μCi of activity was dissolved in 100 mL water, and 1 mL was taken out into the vials as the reference to be measured on the gamma counter (with five replicates).
11. Collect the amount of gamma emissions from each vial using a gamma counter. For $^{89}$Zr, 1 min was used to measure one vial.
12. The gamma counter will give the total counts for each vial. And the radioactivity of each reference vial contained 0.5 μCi. Use

these data to calculate the μCi/count per minute. Then the $^{89}$Zr-mAb in each vial containing the organs could be calculated by the counts by comparison to the reference vials. The data should be background- and decay-corrected, and the tissue uptake was expressed in units of percentage injected dose per gram of dry tissue (% ID/g)

## 4 Notes

1. For the bioconjugation chemistry, the final concentration of DMSO in the reaction mixture should be kept below 2% *v/v* to avoid any antibody precipitation.
2. If very high antibody concentrations are desired, the flow-through fractions can be kept separate to identify the fraction with highest concentration. Alternatively, the fractions can be combined.
3. Reaction progress on ITLC can be determined using area under the curve analysis. By 120 min, conversion is typically >90%.
4. We found empirically that one PD10 purification step often results in trace $^{89}Zr^{4+}$ salts that, while not a significant impurity on ITLC, produce high signal in mouse bone tissue in vivo. Typically after the double purification procedure by the PD-10 columns, the purity is >98% on ITLC, and no appreciable bone signal is observed on PET after injection of the formulation. After the double purification, the radiolabeled antibody is stable for 48 h at 4 °C.
5. As an alternative to biolayer interferometry, relative binding affinities for Df-conjugated antibodies can be determined on cells using a displacement assay. We typically use a fixed concentration of $^{125}$I-Ab, and co-incubate with a range of concentrations of Df-Ab or unlabeled Ab. The data can be fit using standard graphing software packages (e.g., GraphPad PRISM) to determine the inflection point.
6. Cells that are difficult to detach may be placed at 37 °C to facilitate dispersal.
7. The timing post injection at which biodistribution studies are performed will vary depending on unique experimental details. In general, large antibody platforms (IgG, minibody) require days to fully equilibrate in complex biological systems, while small platforms (scFv) require hours. We advise conducting pilot studies, perhaps also involving serial imaging with small animal PET/CT, to identify the optimal window post injection to study the antibody.

## Acknowledgments

We gratefully acknowledge members of the Evans laboratory for feedback on this contribution. M.J.E was supported by the American Cancer Society, the National Institute of Biomedical Imaging and Bioengineering (R01EB025207, R01EB029429), the National Cancer Institute (R01CA258297), the National Institute of Allergy and Infectious Diseases (R01AI161027) and the National Institute for Mental Health (R01MH115043). D.Y. Oh is supported by NIH 4T32 CA177555, 1K08 AI139375, the Harry F. Bisel, MD Endowed Young Investigator Award from the Conquer Cancer Foundation of the American Society of Clinical Oncology, the Bladder Cancer Advocacy Network Palm Beach New Discoveries Young Investigator Award, and the Prostate Cancer Foundation Young Investigator Award.

### References

1. Leach DR, Krummel MF, Allison JP (1996) Enhancement of antitumor immunity by CTLA-4 blockade. Science 271:1734–1736
2. Schumacher TN, Kesmir C, van Buuren MM (2015) Biomarkers in cancer immunotherapy. Cancer Cell 27:12–14
3. Rizvi NA, Hellmann MD, Snyder A, Kvistborg P, Makarov V, Havel JJ, Lee W, Yuan J, Wong P, Ho TS et al (2015) Cancer immunology. Mutational landscape determines sensitivity to PD-1 blockade in non-small cell lung cancer. Science 348:124–128
4. Le DT, Uram JN, Wang H, Bartlett BR, Kemberling H, Eyring AD, Skora AD, Luber BS, Azad NS, Laheru D et al (2015) PD-1 blockade in tumors with mismatch-repair deficiency. N Engl J Med 372:2509–2520
5. Patel SP, Kurzrock R (2015) PD-L1 expression as a predictive biomarker in cancer immunotherapy. Mol Cancer Ther 14:847–856
6. Ehlerding EB, England CG, McNeel DG, Cai W (2016) Molecular imaging of immunotherapy targets in cancer. J Nucl Med 57:1487–1492
7. Aide N, Hicks RJ, Le Tourneau C, Lheureux S, Fanti S, Lopci E (2019) FDG PET/CT for assessing tumour response to immunotherapy: report on the EANM symposium on immune modulation and recent review of the literature. Eur J Nucl Med Mol Imaging 46:238–250
8. Nishino M, Ramaiya NH, Hatabu H, Hodi FS (2017) Monitoring immune-checkpoint blockade: response evaluation and biomarker development. Nat Rev Clin Oncol 14:655–668
9. Bensch F, van der Veen EL, Lub-de Hooge MN, Jorritsma-Smit A, Boellaard R, Kok IC, Oosting SF, Schroder CP, Hiltermann TJN, van der Wekken AJ et al (2018) (89)Zr-atezolizumab imaging as a non-invasive approach to assess clinical response to PD-L1 blockade in cancer. Nat Med 24:1852–1858
10. Niemeijer AN, Leung D, Huisman MC, Bahce I, Hoekstra OS, van Dongen G, Boellaard R, Du S, Hayes W, Smith R et al (2018) Whole body PD-1 and PD-L1 positron emission tomography in patients with non-small-cell lung cancer. Nat Commun 9:4664
11. McGranahan N, Furness AJ, Rosenthal R, Ramskov S, Lyngaa R, Saini SK, Jamal-Hanjani M, Wilson GA, Birkbak NJ, Hiley CT et al (2016) Clonal neoantigens elicit T cell immunoreactivity and sensitivity to immune checkpoint blockade. Science 351:1463–1469
12. Moroz A, Lee CY, Wang YH, Hsiao JC, Sevillano N, Truillet C, Craik CS, Fong L, Wang CI, Evans MJ (2018) A preclinical assessment of (89)Zr-atezolizumab identifies a requirement for carrier added formulations not observed with (89)Zr-C4. Bioconjug Chem 29:3476–3482
13. Truillet C, Oh HLJ, Yeo SP, Lee CY, Huynh LT, Wei J, Parker MFL, Blakely C, Sevillano N, Wang YH et al (2018) Imaging PD-L1 expression with ImmunoPET. Bioconjug Chem 29:96–103
14. Truillet C, Cunningham JT, Parker MFL, Huynh LT, Conn CS, Ruggero D, Lewis JS, Evans MJ (2017) Noninvasive measurement of mTORC1 signaling with (89)Zr-transferrin. Clin Cancer Res 23:3045–3052

15. Aggarwal R, Behr SC, Paris PL, Truillet C, Parker MFL, Huynh LT, Wei J, Hann B, Youngren J, Huang J et al (2017) Real-time transferrin-based PET detects MYC-positive prostate cancer. Mol Cancer Res 15:1221–1229
16. Doran MG, Carnazza KE, Steckler JM, Spratt DE, Truillet C, Wongvipat J, Sawyers CL, Lewis JS, Evans MJ (2016) Applying (8)(9) Zr-transferrin to study the pharmacology of inhibitors to BET Bromodomain containing proteins. Mol Pharm 13:683–688
17. Martinko AJ, Truillet C, Julien O, Diaz JE, Horlbeck MA, Whiteley G, Blonder J, Weissman JS, Bandyopadhyay S, Evans MJ et al (2018) Targeting RAS-driven human cancer cells with antibodies to upregulated and essential cell-surface proteins. Elife 7:e31098
18. Pai CS, Simons DM, Lu X, Evans M, Wei J, Wang YH, Chen M, Huang J, Park C, Chang A et al (2019) Tumor-conditional anti-CTLA4 uncouples antitumor efficacy from immunotherapy-related toxicity. J Clin Invest 129:349–363
19. Doran MG, Watson PA, Cheal SM, Spratt DE, Wongvipat J, Steckler JM, Carrasquillo JA, Evans MJ, Lewis JS (2014) Annotating STEAP1 regulation in prostate cancer with 89Zr immuno-PET. J Nucl Med 55:2045–2049
20. Evans MJ (2012) Measuring oncogenic signaling pathways in cancer with PET: an emerging paradigm from studies in castration-resistant prostate cancer. Cancer Discov 2:985–994

# Chapter 45

# A Wireless Fully-Passive Acquisition of Biopotentials

**Shiyi Liu, Xueling Meng, Jianwei Zhang, and Junseok Chae**

## Abstract

Biopotential signals contain essential information for assessing the functionality of organs and diagnosing diseases. We present a flexible sensor, capable of measuring biopotentials, in real time, in a wireless and fully-passive manner. The flexible sensor collects and transmits biopotentials to an external reader without wire, battery, or harvesting/regulating element. The sensor is fabricated on a 90 μm-thick polyimide substrate with a footprint of $18 \times 15 \times 0.5$ mm$^3$. The wireless fully-passive acquisition of biopotentials is enabled by the RF (Radio Frequency) microwave backscattering effect where the biopotentials are modulated by an array of varactors with incoming RF carrier that is backscattered to the external reader. The flexile sensor is verified and validated by emulated signal and electrocardiogram (ECG), electromyogram (EMG), and electrooculogram (EOG), respectively. A deep learning algorithm analyzes the signal quality of wirelessly acquired data, along with the data from commercially available wired sensor counterparts. Wired and wireless data shows <3% discrepancy in deep learning testing accuracy for ECG and EMG up to the wireless distance of 240 mm. Wireless acquisition of EOG further demonstrates accurate tracking of horizontal eye movement with deep learning training and testing accuracy reaching up to 93.6% and 92.2%, respectively, indicating successful detection of biopotentials signal as low as 250 $\mu V_{PP}$. These findings support that the real-time wireless fully-passive acquisition of on-body biopotentials is indeed feasible and may find various uses for future clinical research.

**Key words** Fully-passive, Backscattering, ECG, EMG, EOG, Deep learning

## 1 Introduction

Biopotentials provide doctors with vital information to check organ function and diagnose abnormalities for subsequent treatment. For example, electrocardiogram (ECG) and electromyogram (EMG) help to diagnose heart arrhythmias [1] and identify neuromuscular disorders [2], respectively; electrooculogram (EOG) is helpful to study disorders of eye movement [3]. Traditional biopotentials measurement requires using cables and wires to connect electrodes with external bulky instrument [4]. These cumbersome cables and wires cause severe movement restriction to individuals, prohibiting long-term ambulatory biopotential recording. Commercialized wireless sensors exist, yet the vast majority of current

Miguel R. Ossandon et al. (eds.), *Biomedical Engineering Technologies: Volume 1*, Methods in Molecular Biology, vol. 2393, https://doi.org/10.1007/978-1-0716-1803-5_45, 

commercialized wireless sensors rely on batteries to operate. As wireless communication protocols consume high power, these battery-powered devices generally have a limited continuous recording time. The state of art wireless sensors offer an average of 1 or 2 days continuous operating time [5]. The data from 1 or 2 days continuous biopotential recording, such as the ECG data from Holter monitors, has been accepted by clinicians as an effective diagnosing tool; still, there are diseases or abnormalities requiring extended long period recordings for months or even years to produce high diagnose yields, such as syncope and atrial fibrillation (AF) [6, 7]. The lack of long-term continuous wireless biopotentials monitoring greatly limits the diagnosis and study of those diseases or abnormalities.

In order to overcome the limitation associated with batteries, researchers have developed wireless battery-free sensors, such as RFID (Radio Frequency Identification) technology-enabled devices [4, 5, 8]. These sensors can harvest power wirelessly, from either inductive or RF coupling. Recent research of such wireless battery-free sensors focus on flexible and light-weight, small-sized epidermal electronics that have wireless communication capability [9]. Studies have demonstrated epidermal electronics for measuring temperature [10], pulse [9], and electrophysiology [11]. To achieve biopotential acquisition in a completely wireless, battery-free manner, Chung et al. [12] presented flexible epidermal electronics which harness power via inductive coupling. Unfortunately, wireless telemetry presented in those works suffers from either the limited communication protocol, i.e., near field communication (NFC), or the stringent requirement of precise alignment between primary and secondary coils. This work introduces a small-size, light-weight, flexible sensor, capable of acquiring biopotentials in real time in a wireless and fully-passive manner. RF backscattering wireless communication is used to allow bi-directional communication by reflecting the incident RF (Radio Frequency) wave. The term "fully-passive" denotes that the sensor is comprised entirely by passive components, i.e., batteries and power-consuming active circuitry are completely excluded. We present wireless acquisition of various body biopotential, including ECG, EMG, and EOG of as low as 250 $\mu V_{pp}$, up to a maximum distance of 240 mm in a fully-passive manner. The presented sensor may find applications in real-time, long-term biopotential monitoring for various clinical diagnosis and research purposes, in the form of small-size, flexible, epidermal or even implanted electronic systems.

## 2 Material

### 2.1 Wireless Fully-Passive Sensor

1. Manufactured polyimide flexible printed circuit board (Rush PCB, Inc).
2. Discrete electronic components

| Components | Model/values |
|---|---|
| Varactors | MA46H120 (MACOM) |
| Inductors | 27 nH (TDK Corporation) |
| Capacitors | 33 pF (Murata Electronics) |

3. 120 μm-thick stainless steel sheet foil (McMaster-Carr).
4. Parylene C dimer (Specialty Coating System).
5. Conductive sliver epoxy (12642-14, Electron Microscopy Science).

### 2.2 External Interrogator

1. RF signal generator (E4432B; Agilent).
2. Low-noise preamplifier (SR560; Stanford Research System).
3. Arbitrary waveform generator (33250A; Agilent).
4. Spectrum analyzer (HP 8563E; Agilent).
5. DC power supply (PS280; Tektronix).
6. 2350–2800 MHz band-pass filter (VBFZ-2575-S+; Mini-Circuits).
7. 4200–4700 MHz band-pass filter (VBF-4440+; Mini-Circuits).
8. 3500–9500 MHz high-pass filter (VHF-3100+; Mini-Circuits).
9. 2300–7600 MHz frequency mixer (ZX05-762H-S+; Mini-Circuits).
10. 4.5–6.0 GHz low-noise amplifier (LNA-4560; RF bay, Inc).
11. 2.0–4.2 GHz power splitter (ZAPD-4-S+; Mini-Circuits).
12. 2.4–2.5 GHz RF power amplifier (MPA-24-20; RF bay, Inc).
13. Phase shifter (JSPHS-2484+; Mini-Circuits).
14. RF circulator (CS-144; Microwave Communication Laboratories, Inc).
15. 3400–7200 MHz multiplier (ZX90-2-36-S+; Mini-Circuits).
16. Dual-band ceramic chip antenna (A10194; Antenova).
17. Data acquisition system (DAQ) (NI USB-6361; National Instrument) and software interface (NI SignalExpress; National Instrument).

18. A PC (Dell) with data processing software, including MATLAB (Mathworks) and Python keras package with Tensorflow backend.

### 2.3 Other Material

1. Disposable silver/silver chloride electrode (H124SG, Covidien).
2. MyoWare muscle sensor (SparkFun Electronics).
3. ECG sensor (AD8232, Sparkfun).
4. Robotic arm (Elenco Teach Tech).
5. SMA to N-Type RF cable (Fairview Microwave) × 2.
6. SMA to SMA RF cable (Fairview Microwave) × 10.
7. BNC to SMA RF cable (Fairview Microwave) × 2.
8. BNC to alligator clips testing cable (Elenco) × 2.
9. Alligator clips testing cable (Eiechip) × 10.
10. Banana plug cords (Pomona Electronics) × 10.
11. Double-sided tape (Scotch).
12. Soldering station (5040-XR3; X-Tronic).
13. Hook-up strand 14 AWG (Alpha Wire).

## 3 Methods

### 3.1 Wireless Fully-Passive Sensor

Figure 1 shows the simplified operating principle of the wireless system, comprising two sub-systems: (1) the wireless fully-passive sensor (Fig. 1a) for acquiring biopotentials and (2) the external interrogator (Fig. 1b) for wireless data readout and display. Wireless communication between the two sub-systems is accomplished by utilizing the RF backscattering effect.

#### 3.1.1 Fabrication of the Sensor

1. Construct the geometry of the sensor (Fig. 2a) in High Frequency Structure Simulator (HFSS, Ansoft). Note that annotated dimensions are critical for the wireless backscattering operations. The highlighted part is the varactor mixing circuitry where all the discrete components are mounted. For simulation purposes, neglect the detailed circuit structure and represent it as an excitation port (blue square, Fig. 2c). Set the conductive material (orange part in Fig. 2c) as copper and the substrate (transparent part in Fig. 2c) as polyimide. Add two LRC boundary conditions on the outer rectangular of the antenna to represent the two 33 pF capacitors (small blue square in Fig. 2c). Add external radiation boundary and run the simulation. The antenna should achieve 0 dB gain at two frequencies (2.33 GHz and 4.66GHz, Fig. 2d, e).

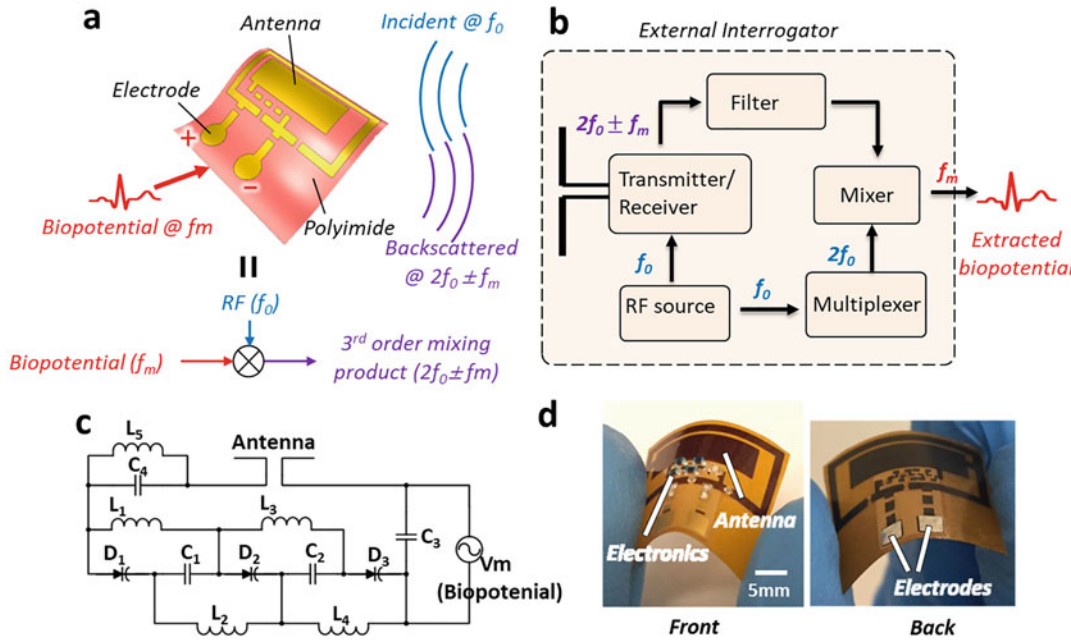


**Fig. 1** (**a**) Schematic of the operating principle of the wireless fully-passive sensor. The external interrogator shines RF carrier ( $f_0$) to the sensor, where an array of varactor diodes receives and mixes the carrier with biopotentials ( $f_m$) collected at the electrodes. The third-order ($2f_0 \pm f_m$) mixing product is reflected back to the interrogator where the biopotential signals are extracted. (**b**) The simplified structure of external Interrogator. (**c**) Equivalent electronic circuit model diagram of the sensor. Voltage source $V_m$ represents low-frequency biopotentials ( $f_m$) collected at the electrodes. (**d**) Photos of a fabricated and assembled sensor on a polyimide substrate, having a footprint of 18 × 15 × 0.5 $mm^3$. The 65μm-thick polyimide substrate contains antenna, discrete surface mount electronic components, and contact electrodes located at the backside to collect biopotentials

2. Construct the circuit (Fig. 1c) in Advanced Design System (ADS, Keysight, Fig. 3a). The varactor diodes are represented by nonlinear capacitors whose capacitance are controlled by voltages. Its parameter is obtained from Tyler expansion using MATLAB (Mathworks). The wireless links are simulated using a two port S-parameter component, whose parameter is imported from the previous HFSS simulation result. Run the harmonic balance simulation to obtain the power of third-order mixing products at the external antenna. Verify that the backscattered power of third-order mixing products achieves at least −80 dBm when RF power is at 25 dbm and input biopotential is at 1 mV (Fig. 3b, c). If the power does not achieve the desired level, it means the antenna design is not optimized. Go back to **step 1** and change the critical dimensions of the antenna and run the simulation again. Repeat this step until the simulation result in ADS achieved the desired level (*see* **Note 1**).

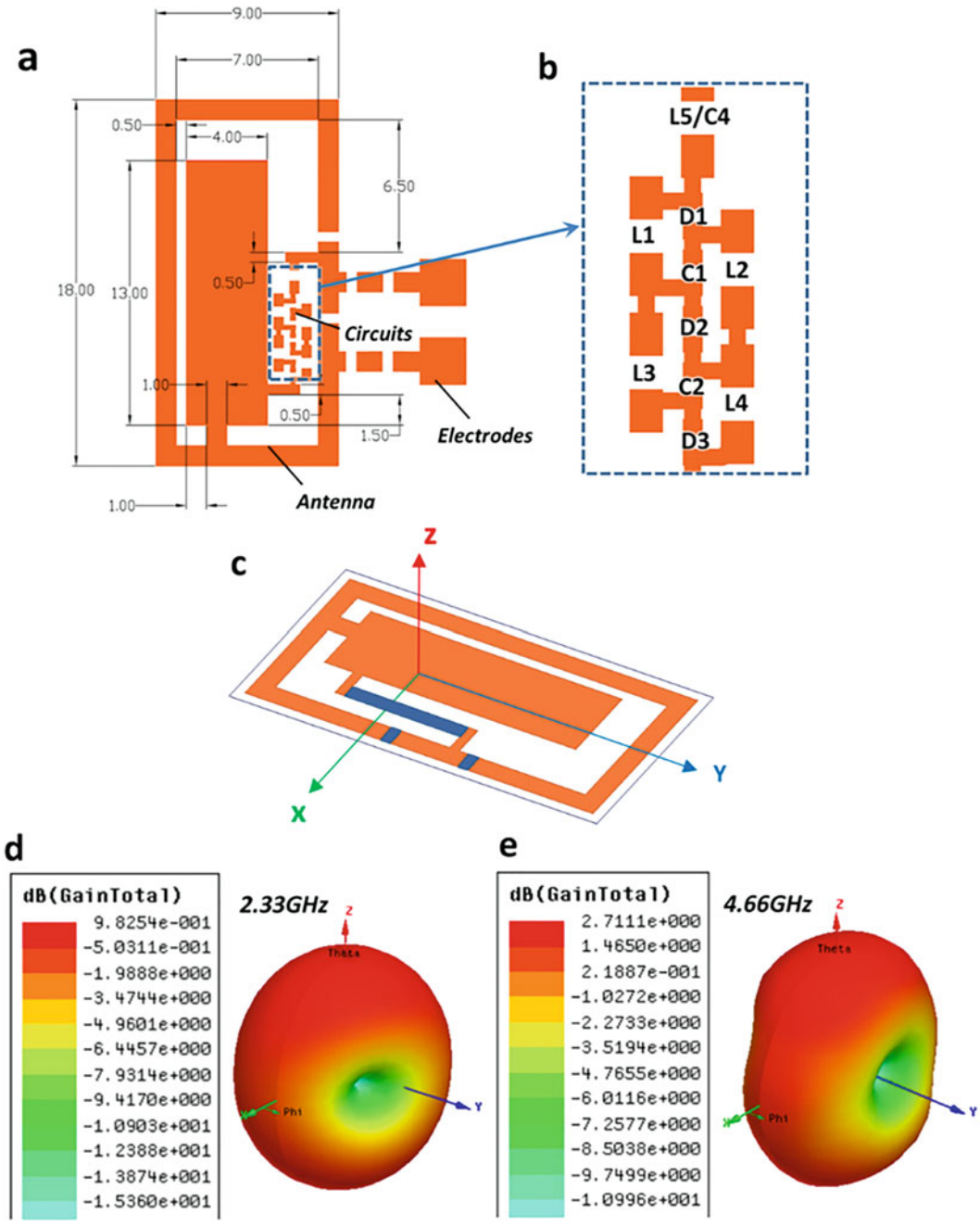


**Fig. 2** (**a**) Layout of the wireless fully-passive sensor. The sensor contains subcomponents: antenna, electrodes, and passive electronics. Critical dimensions are annotated. (**b**) Highlighted area represents the structure of electronics, consisted entirely by passive electronic components. The integrated antenna on the sensor is designed and simulated in ANSYS HFSS. (**c**) Constructed 3D model in HFSS, the long blue rectangle represents output port of the antenna which connects to the circuits shown in (**b**). The two short blue rectangles are bypass capacitors to isolate input biopotential signals. (**d**, **e**) Simulation result of antenna gain at 2.33 GHz (**d**) and 4.66 GHz (**e**). The maximum gain of the designed antenna at z direction is 0.98 dB for 2.33 GHz and 2.71 dB for 4.66 GHz, respectively

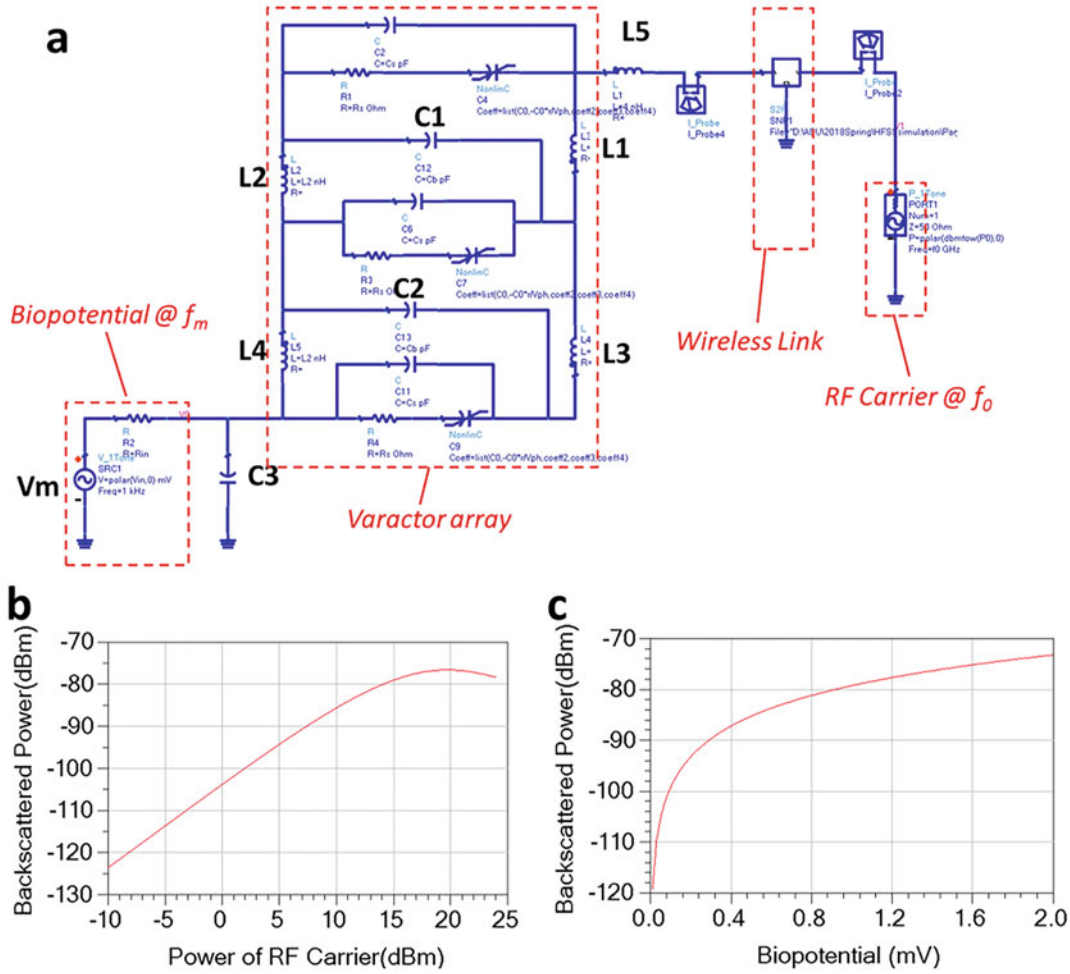


**Fig. 3** (**a**) Equivalent circuit model constructed in ADS (Advanced Design System, Keysight) simulation. The two ports S-parameter network models the wireless link between the external antenna and integrated antenna of the sensor. S-parameter data at the $f_m$, $f_0$, and $2f_0$ are imported from HFSS simulation results. The varactors are modeled as nonlinear capacitors whose capacitance is controlled by the voltage applied on terminals. The parasitic parallel capacitance, serial resistance, and inductance are also included. Biopotential signals are represented by a voltage source with a large (>1 MOhm) input impedance. The ADS simulation model uses harmonic balance simulation to calculate third-order harmonic mixing products picked up at the external antenna. (**b**, **c**) Simulation results of backscattered power of third-order harmonic mixing products ($2f_0 \pm f_m$) as a function of RF carrier power (**b**) and input biopotential amplitude (**c**). In (**b**) the input biopotential is 2 $mV_{pp}$ and in (**c**) the RF power is 25 dBm. Distance between the sensor and the external antenna is fixed at 50 mm

3. Once the desired simulation result is obtained, the geometry of the sensor is fixed and imported to Altium Designer (Altium). The circuitry and soldering pad for discrete components are added to finalize the PCB design file. The PCB design file is then sent to a manufacturer (Rush PCB, Inc).

4. The sensor is fabricated with standard PCB etching process. Fabricated sensor PCB consists of 1 mil polyimide substrate, 0.7mils copper, and 2mils polyimide coverlay. The exposed metal pads use ENIG (electroless nickel immersion gold) surface finish.
5. After receiving the fabricated polyimide-based sensor, discrete electronic components including varactor diodes, inductors, and capacitors are soldered onto the sensor using conductive epoxy (12642-14, Electron Microscopy Science). Mix the two parts of the conductive epoxy with a 1:1 ratio and use a tweezer to apply a small amount of the mixed epoxy onto the soldering pads. Place the electronic component onto the pad and apply 100 °C for 5 min to enable the conductive to cure. Repeat the steps until all electronics components are soldered onto the sensor.
6. After all the electronic components are soldered, the electrode pads are soldered with electrical leads to enable connection to external reference electrodes. The sensor is then coated with 10 μm-thick parylene C film. After the coating completes, the parylene film on the electrical leads is removed using a razor blade to expose the metal contact. The sensor has a total footprint of $18 \times 15 \times 0.5$ mm$^3$. Figure 1d shows photos of an assembled wireless fully-passive sensor, demonstrating its small size and high flexibility.

### 3.2 The External Interrogator

1. Figure 4a shows the structure of the external interrogator. Assemble the external interrogator by first connecting the RF source (RF function generator E4432B, Agilent) with the input port of a power splitter (ZAPD-4-S+; Mini-Circuits). Use the correct type RF cable to enable the connection. The RF function generator has an N-type connector while the splitter has an SMA connector. Thus, an N-type to SMA RF cable is required.
2. Assemble the first path (transmitting signal path) of the external interrogator. The first output port of the splitter is connected in series with a power amplifier (MPA-24-20; RF bay) and a band-pass filter (VBFZ-2575-S+; Mini-Circuits). All connections can be placed with SMA to SMA cables.
3. The output of the band-pass filter (VBFZ-2575-S+; Mini-Circuits) is connected to the port 1 of the circulator (CS-144; Microwave Communication Laboratories, Inc) with an SMA cable. The port 2 of the circulator is then connected to the dual-band antenna (A10194; Antenova). For this connection, use a long SMA cable (at least 1 m) as the antenna needs to be placed far from the other components of the external interrogator.

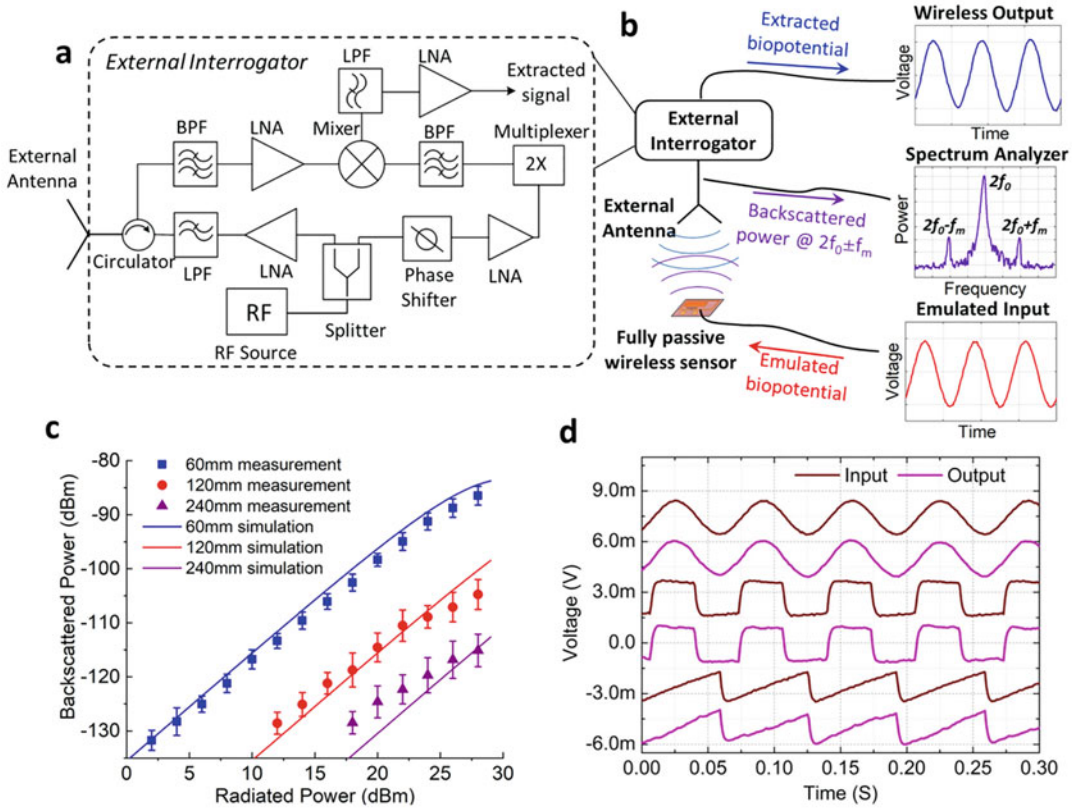


**Fig. 4** (**a**) Detailed structure of the external interrogator. (**b**) Experiment setup of benchtop characterization of the wireless fully-passive sensor. Arbitrary function generator inputs emulated biopotentials to the sensor through electrodes. The RF backscattering wireless telemetry is verified by both in time and frequency domain. (**c**) Measured and simulated spectrum power of backscattered third-order harmonic mixing products, $2f_0 \pm f_m$, as a function of external antenna radiation power at 60, 120, and 240 mm wireless distances, using the emulated biopotentials of 2 $mV_{pp}$ at 1 KHz. Error bar represents standard deviation. (**d**) Temporal profiles of the emulated inputs and extracted wireless outputs show almost all types of inputs can be extracted by the wireless fully-passive telemetry (emulated inputs (brown) are 2 $mV_{pp}$ and 15 Hz periodic sine, square, and triangle wave, respectively, whereas wireless outputs (pink) are normalized and offset to facilitate the comparison)

4. Start assembling the second path (LO path). Connect the second output port of the power splitter to the input port of the phase shifter (JSPHS-2484+; Mini-Circuits) with an SMA cable.
5. The control port of the phase shifter is connected to a tunable DC power supply (PS280; Tektronix) using an SMA to banana cable. Use one of the DC power supply output ports to provide 0–10 V adjustable DC voltage.
6. The output port of the phase shifter is connected in series with a frequency multiplexer (ZX90-2-36-S+; Mini-Circuits), a low-noise amplifier (LNA-4560; RF bay, Inc), and a band-

pass filter (VBF-4440+; Mini-Circuits). All connections can be done using SMA cables.

7. Connect the output port of the band-pass filter (VBF-4440+; Mini-Circuits) to the LO port of the frequency mixer (ZX05-762H-S+; Mini-Circuits) using an SMA cable.
8. Start assembling the third path (backscattered signal path). Connect the port 3 of the circulator (CS-144; Microwave Communication Laboratories, Inc) in series with a band-pass filter (VBF-4440+; Mini-Circuits) and a low-noise amplifier (LNA-4560; RF bay, Inc) using SMA cable.
9. The output port of the amplifier (LNA-4560; RF bay, Inc) is connected to the RF port of the frequency mixer (ZX05-762H-S+; Mini-Circuits) with an SMA cable.
10. Assemble the final amplifying and filtering stage of the external interrogator. This is done by simply connecting the IM port of the frequency mixer to the preamp (SR560, Stanford Research System). Use a long SMA to BNC cable (about 1 M) for this connection as the preamp maybe placed far from other components.
11. Connect all the power supplies. The amplifiers in the external interrogator require two kinds of DC supply: 5 V and 12 V. These voltages can be provided with the DC power supply (PS280; Tektronix). The RF power amplifier (MPA-24-20; RF bay, Inc) uses 12 V; the low-noise amplifier (LNA-4560; RF bay, Inc) uses 5 V. Connect the output ports of the power supply to the amplifiers using banana cables with alligator clips.
12. The output of the preamp (SR560, Stanford Research System) is connected to the DAQ (NI-6361; National Instrument) analog input (AI0) using a BNC cable. The DAQ is then connected to a PC (Dell) with a USB cable.
13. Turn on all power supplies. Set the output of the RF source (RF function generator E4432B, Agilent) to be 2.33 GHz, 10 dBm. To change the frequency, press "frequency," then input 2.33 GHz. To change amplitude, press "amplitude," then input 10 dBm.
14. In the PC, start the Signal Express software and create a new project. In the project, chose "Add Step"—"Acquire Signals"—"Daqmx Acquire"—"Analog Input"—"Voltage." Chose the channel AI0. Set the sampling frequency to 10 KHz and the samples to read to 1 K. Run the program.
15. The setting up for the external interrogator is finished (*see* **Note 2**). For testing of the external interrogator, see the next section.

### 3.3 Benchtop Characterization

1. Use the arbitrary waveform generator (33250A; Agilent) to create a 1 Khz sine wave with 2 mVpp amplitude. This is done by press the "sine"—"Amplitude"—input 2 mVpp. Frequency can be changed by press "Frequency"—input 1 KHz.
2. Connect the output of the arbitrary waveform generator to the sensor leads using a BNC to alligator clips cable. One lead is connected to the ground, while the other is connected to the signal.
3. Place the sensor on the bench and fix its position with double-sided tape.
4. Use a robotic arm (Elenco Teach Tech) to hold the antenna (A10194; Antenova) above the sensor with 60–240 mm distance (Fig. 4b).
5. Set the filtering and amplifying parameters of the preamp (SR560). Select 300–3000 Hz band-pass filter with an amplifying gain of 50×.
6. In Signal Express, run the program and observe the waveform in the Data View window. A sine wave should display on the screen. The signal should have the same waveform as the input signal of the arbitrary waveform generator. If the waveform is noisy, adjust the distance and angle between the external antenna and the sensor until a clear waveform can be observed. This step verifies that the sensor and the system are working properly.
7. If the overload indicator on the preamp (SR560) lights up, it means the gain of the amplifier is set too high. Try lowering the gain until the overload indicator goes off.
8. Record the waveform data by click "record" in the Signal Express program. Recorded data can be used for future data analysis.
9. Disconnect the port 3 of the circulator (CS-144; Microwave Communication Laboratories, Inc) from the rest of the external interrogator components, then connect it to a spectrum analyzer (HP 8563E; Agilent) using an SMA to N-Type RF cable.
10. Turn on the spectrum analyzer (HP 8563E; Agilent). Set the center frequency to be 4.66 GHz by pressing the "frequency" button and inputting 4.66 GHz. A peak should be seen at the center of the spectrum waveform.
11. Adjust the frequency span by pressing "span" button and rotating the knob of the spectrum analyzer to zoom up on the center peak at 4.66 GHz until it becomes multiple peaks that are symmetrically distributed along the 4.66 GHz center frequency. The side bands which are closest to the center

frequency are the third-order mixing products that we are interested in.

12. Press the "cursor" button on the spectrum analyzer and a cursor will appear on the screen. The cursor reads the spectrum power at the corresponding frequency point. Move the cursor by rotating the knob until the cursor is aligned with the peak of the third-order mixing product ($2f_0 \pm f_m$). Read and record the amplitude of the spectrum power. This corresponds to the backscattered power of the third-order mixing product.
13. Change the input power of the RF generator (E4432B, Agilent) by pressing "amplitude" button and input a new amplitude value. Record the change of backscattered power at third-order mixing product ($2f_0 \pm f_m$) as the RF power changes from 0 dBm to 30 dBm (after amplifying).
14. Use the robotic arm to change the distance between the antenna and sensor and repeat the measurement of backscattered power (**step 13**). Plot the data points (Fig. 4c). For a 2 $mV_{pp}$ sine wave input signal, the sensor achieves a 240 mm working distance.
15. Disconnect the spectrum analyzer from the port 3 of the circulator (CS-144; Microwave Communication Laboratories, Inc) and reconnect the port 3 with the filter (VBF-4440+; Mini-Circuits). Run the Signal Express program to record the temporal waveform (Fig. 4d).
16. Change the output of the arbitrary waveform generator to square and triangle waves. Observe that the wireless recovered signals exhibit the minimum discrepancy with inputs (Fig. 3d). This demonstrates the sensor's capability to reliably extract both simple (sine) and complicated (square and triangle) waveforms.

### 3.4 Biopotential Recording

#### 3.4.1 ECG Recording

1. Two electrodes (H124SG, Covidien) are placed on the subject's right shoulder and lower edge of the left ribcage (RA and LL), respectively (Fig. 5a). This electrodes arrangement measures the lead II of the standard ECG [13].
2. Attach the fully-passive sensor to the subject's left chest using a double-sided tape.
3. Connect the electrodes with the leads of the wireless sensor using cables with alligator clips.
4. Place a third electrode on the subject's left shoulder (LA).
5. A wired ECG sensor (AD8232, Sparkfun) is used as reference. To connect the wired ECG sensor to the system, connect the "+" signal (red wire) with the electrode RA, "-" signal (blue wire) with electrode LL, and the ground (black wire) with

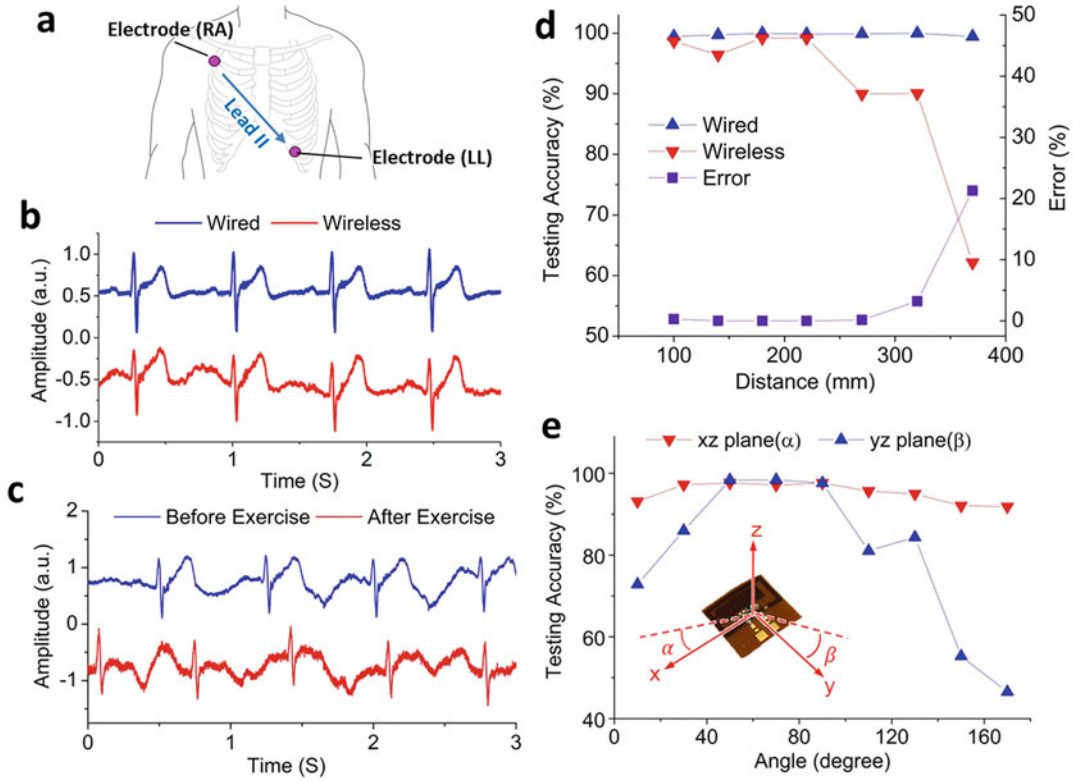


**Fig. 5** Wireless fully-passive acquisition of electrocardiogram (ECG). (**a**) Electrodes placement position for measuring lead II ECG. The two measurement electrodes RA (right arm) and LL (left leg) are connected to the wireless fully-passive sensor as well as a commercial wired sensor through electrical leads. A third electrode placed at the left shoulder (not shown in the plot) provides reference potential for the commercial sensor. (**b**) ECG recorded from the wireless fully-passive sensor in comparison with the output of the commercial wired ECG sensor that is recorded simultaneously. Both signals are normalized. (**c**) Wireless fully-passive recording of ECG before/after the participant performs a 5-min running exercise. (**d**) Signal quality of wireless and wired ECG data as a function of wireless distances. Higher deep learning testing accuracy represents better signal quality, i.e., less noise and distortion. Error represents the percentage of miscounted heartbeat in wireless data, comparing to the wired counterpart. (**e**) Signal quality of wireless ECG data varies as a function of angle between the external antenna and the sensor. Inlet shows the coordinate used in this measurement. The labeled angle represents the direction where the external antenna locates

electrode LA. This sensor records wired ECG signal concurrently for real-time data comparison.

6. Connect the DC power supply (PS280; Tektronix) to the wired ECG sensor. The sensor uses a single 3.3 V DC voltage.
7. Connect the output and the GND port of the AD8232 sensor to the analog input channel 1 (AI1) of the DAQ (NI-6361; National Instrument). This can be done using a BNC to alligator clips testing cable.

8. Let the testing subject sit down on a chair. Use the robotic arm to hold the antenna and place the external antenna around 60 mm distance away from the sensor on the subject's chest.
9. Set the filtering and amplifying parameters of the preamp (SR560). Select 3–100 Hz band-pass filter with an amplifying gain of 50x.
10. In the Signal Express (National Instrument) program, select "Step Setup" – "+" – "voltage" – "AI1." Set the "sampling frequency" to 1 KHz and "samples to read" to 500.
11. Run the program by click "recording." Both the wireless and wired ECG signals are recorded using the data acquisition system (NI USB-6361) (*see* **Note 3**).
12. An example of recorded ECG signal is shown in Fig. 5b. Both wired and wireless ECG signals clearly show the QRS complex and the T wave. However, the P wave is barely distinguishable in wireless recorded waveform.
13. The testing subject performs a jogging practice at 6 ~ 7 km/h for 5 min to induce a change in the heartbeat rhythm.
14. Repeat the wired/wireless ECG recording to verify the change of subject's heartbeat rate. Figure 5c demonstrates an example of heartbeat rate changing from 80/min to 94/min after the short-term running practice.
15. Place the sensor on the bench, increase the distance between the sensor and the external antenna to 100–370 mm, and repeat the ECG recording. At each distance, the subject's ECG signal is recorded continuously for 10 min.
16. The number of heartbeat in wired/wireless recording in each distance is compared to calculate error (Fig. 5d).
17. Within 270 mm distance, wireless heartbeat measurement shows very small errors (<0.5%). At distances larger than 270 mm, the heartbeat measurement error of wireless sensor exhibits exponential increase, which is primarily due to the SNR loss.
18. Fix the distance between the sensor and the antenna, repeat the ECG recording as a function of antenna radiation angle. Figure 5e shows the variation of deep learning testing accuracy as the radiation angle changes in two vertical planes (XZ plane and YZ plane), at a given distance of 140 mm (*see* **Note 4**).

#### 3.4.2 EMG Recording

1. Two electrodes (H124SG, Covidien) are placed on the testing subject's biceps brachii. Arrange the electrodes along the muscle with an inter-electrode distance (IED) of 40 mm (Fig. 6a).
2. Connect the electrodes with the leads of the wireless sensor using cables with alligator clips.

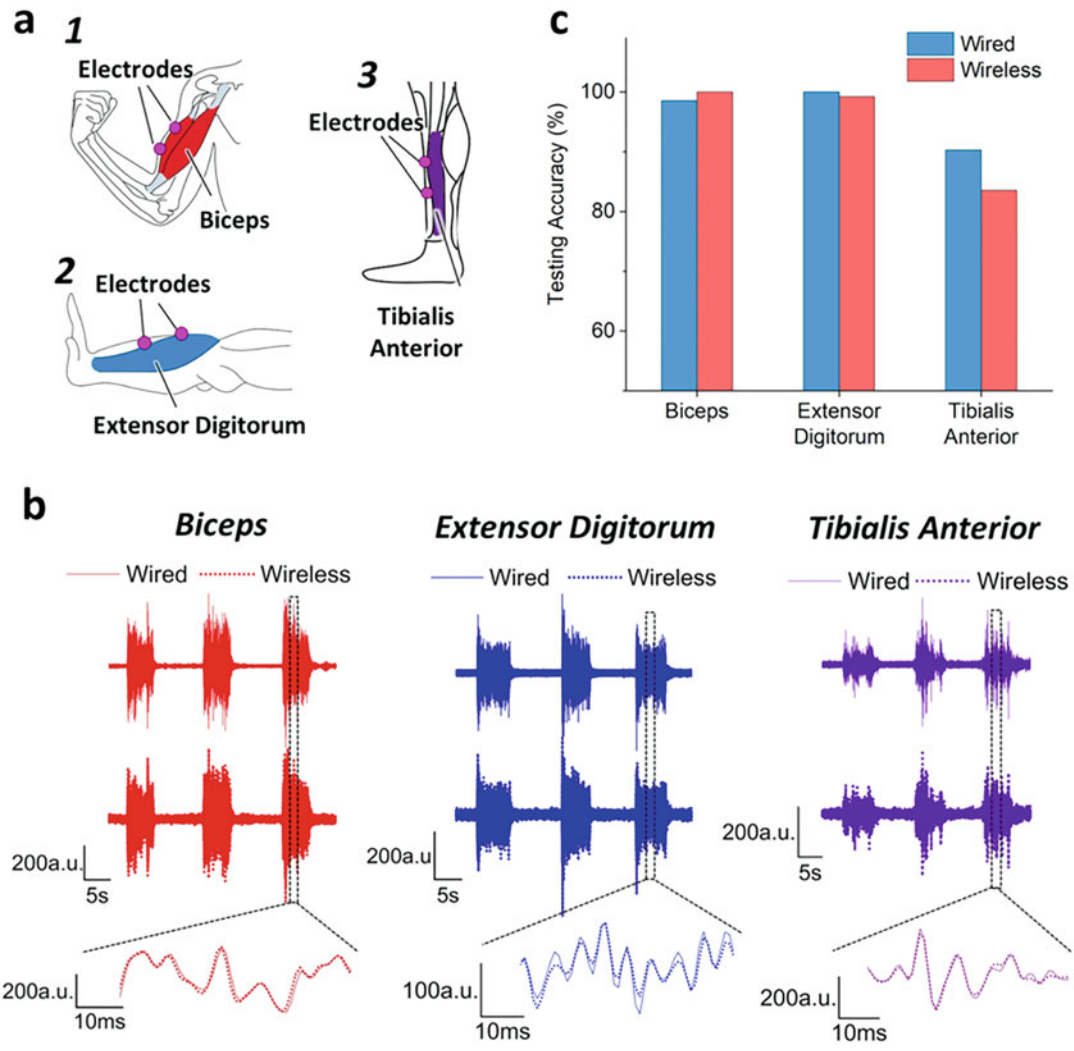


**Fig. 6** Wireless fully-passive acquisition of electromyography (EMG). (**a**) Schematic of electrodes placement for the EMG recording. Colored regions highlight the targeting muscles, including biceps (red), extensor digitorum (blue), and tibialis anterior (violet). Electrodes are connected to the wireless sensor via electrical leads, together with a commercial wired sensor for simultaneous recording. (**b**) EMG signal of biceps (red), extensor digitorum (blue), and tibialis anterior (violet) from wired/wireless sensors during 45 s. Straight lines (top) represent EMG recorded from the commercial wired sensor, while dotted lines (middle) depict their wireless counterparts. Bottom plots show zoom-in of EMG signals in the marked regions. Data from wireless/wired sensors are normalized and aligned to demonstrate their closeness to each other. (**c**) EMG signal quality analysis by deep learning algorithm, which trains the computer to distinguish EMG signal from noise. For each muscle, the training data set comes from 270 s of EMG recording

3. Place a third electrode on the subject's elbow. This electrode will be used as the reference electrode for the commercial wired sensor.

4. Solder two wires on the "E" and "M" pin of the MyoWare muscle sensor (SparkFun Electronics). Then connect the wires on "E" and "M" to the two electrical leads of the sensor using cables with alligator clips. This connection ensures the EMG signal goes to the wired and wireless sensor simultaneously.
5. Solder two wires on the "+" and "-" pins of the MyoWare muscle sensor, respectively. Connect the wires to 3.3 V DC voltage provided by DC power supply (PS280; Tektronix).
6. Solder two wires on "Raw" and "GnD" pins of the MyoWare muscle sensor, respectively. Connect these wires to the analog input channel 1 (AI1) of the DAQ (NI-6361; National Instrument) using a BNC to alligator clips testing cable.
7. Set the filtering and amplifying parameters of the preamp (SR560). Select 30–300 Hz band-pass filter with an amplifying gain of 50×.
8. In the Signal Express (National Instrument) program, select "Step Setup"—"+"—"voltage"—"AI1". Set the "sampling frequency" to 1 KHz and "samples to read" to 500.
9. Run the program by click "recording." Both the wireless and wired ECG signals are recorded using the data acquisition system (NI USB-6361).
10. Let the testing subject slowly bend his elbow to 90° to generate EMG signal.
11. Observe the waveform in the Data View window in the Signal Express software. Watch the difference of waveform when the subject generates EMG signals.
12. Let the subject perform muscle contraction for 5 s, relax the muscles for 10 s, and then repeat for 3 times to complete one cycle.
13. Repeat the cycle for 6 times with 1-min resting between each cycle.
14. Stop the recording. Change the target muscle to extensor digitorum and tibialis anterior. Place the electrodes as shown in Fig. 5a. To generate EMG at the extensor digitorum, let the testing subject bend his wrist upward; to generate EMG at the tibialis anterior, let the testing subject pull his foot upward.
15. Figure 5b shows an example of wired and wirelessly recorded EMG waveforms. For all of the three muscles, wireless EMG signals show excellent correspondence with the wired counterparts. Zooming in on the waveforms reveals wireless data almost overlap with wired data.
16. Compare data quality of recorded EMG signal using deep learning analysis. Figure 5c shows the deep learning testing accuracy for biceps, extensor digitorum, and tibialis anterior.

### 3.4.3 EOG Recording

1. EOG measures the inherent electrical potential between the cornea and retina [14]. This potential changes as eyes move, producing the EOG signal which can be used to track eye movement.
2. Two electrodes (H124SG, Covidien) are used. The recording electrode (+) is placed beside the external canthus of the testing subject's left eye; reference electrode (−) is placed at the center of the forehead. Both electrodes are connected to the leads of the sensor cables with alligator clips.
3. To minimize the impact of artifacts associated with motion and other sources, fix the sensor on top of the bench using a double-sided tape.
4. Use a robotic arm (Elenco Teach Tech) to hold the antenna. Adjust the robotic arm so the antenna is located 30 mm above the sensor.
5. Let the testing subject sit down on a chair and reduce movement as much as possible.
6. Set the filtering and amplifying parameters of the preamp (SR560). Select 3–30 Hz band-pass filter with an amplifying gain of 50×.
7. In the Signal Express (National Instrument) program, set the "sampling frequency" to 1 KHz and "samples to read" to 500.
8. Run the program by clicking "recording." The wireless EOG signals are recorded using the data acquisition system (NI USB-6361) (*see* **Note 5**).
9. Give commands to the testing subject to let him perform tasks of horizontal eye movement.
10. Observe the waveform in the Data View window in the Signal Express software. Watch the difference of waveform when the subject moves eye left or right.
11. Figure 6b shows the normalized EOG signal when the participant rotates his eyeballs left and right. The angle of this rotation, according to previous studies, is approximately 60 degrees [15]. The amplitude of the EOG signal is in the range of 0.12–1.2 $mV_{pp}$, generated by 60 degrees of eyes movement [14].
12. Stop the recording. On a separate computer monitor, open the prepared eye tracking MATLAB program.
13. Run the MATLAB program. In this program, a black dot is created and programmed to move horizontally across the computer monitor.
14. Let the testing subject focus his gaze upon the moving dot. Adjust the distance between the subject eyes and the computer

monitor so that the location change of the dot will result in approximately 18° of eye rotation.

15. Run the Signal Express and MATLAB program together. The location of the dot and the wireless EOG signal are both recorded simultaneously.
16. Figure 6d shows the wireless EOG signal closely follows the path of the moving target. The position change of target dot from 0 to 1 corresponds to approximately 18° of eye rotation, showing the wireless sensor successfully records EOG signals as low as ~250 $\mu V_{pp}$.
17. Use deep learning algorithm to analyze the data quality of wireless EOG.

### 3.5 Signal Analysis by Deep Learning

A supervised deep learning algorithm is adopted as a tool for signal quality comparison between data from the wired sensor and that from the wireless fully-passive sensor. We develop the deep learning algorithm on a PC using Python keras package with Tensorflow backend.

#### 3.5.1 Dataset Preparation

1. Slice the ECG data into segments with a length of 555.6 ms (200 points, 360 Hz sampling rate) using a shifting window. In order to ensure the continuity of the analysis, window is shifted with a length of 138.9 ms (50 points, 360 Hz sampling rate). This produces 150 overlapped data points between two adjacent segments.
2. Normalize the sliced ECG data segments and use 70% of the segments as training data set, the other 30% as testing data set.
3. Manually label the QRS complex and noise from the ECG data.
4. Slice the EMG data into segments of 1 s (1000 points, 1000 Hz sampling rate). The shifting of the slicing window is 0.25 s (250 points).
5. Normalize the sliced EMG data. Use 70% of the segments as training data set, the other 30% as testing data set.
6. Manually label the EMG signals and the noise from the EMG data. EMG signals are continuous and have rather random temporal shapes.
7. For EOG data, the signal is precisely sliced at the points when the change of eye potential occurs. The duration of the potential change spans approximately 1 s, which aligns with the length of one sliced segment (1000 points, 1000 Hz). The noise segments are sliced where the eye potential stabilizes and the length of the noise segments is chosen as 1 s (1000 points).
8. Normalize the sliced EOG data. 280 EOG slices are used as training data set and 77 slices are used as testing data set.
9. Manually label the EOG signal as “left,” “right,” or “noise” (Fig. 7b).

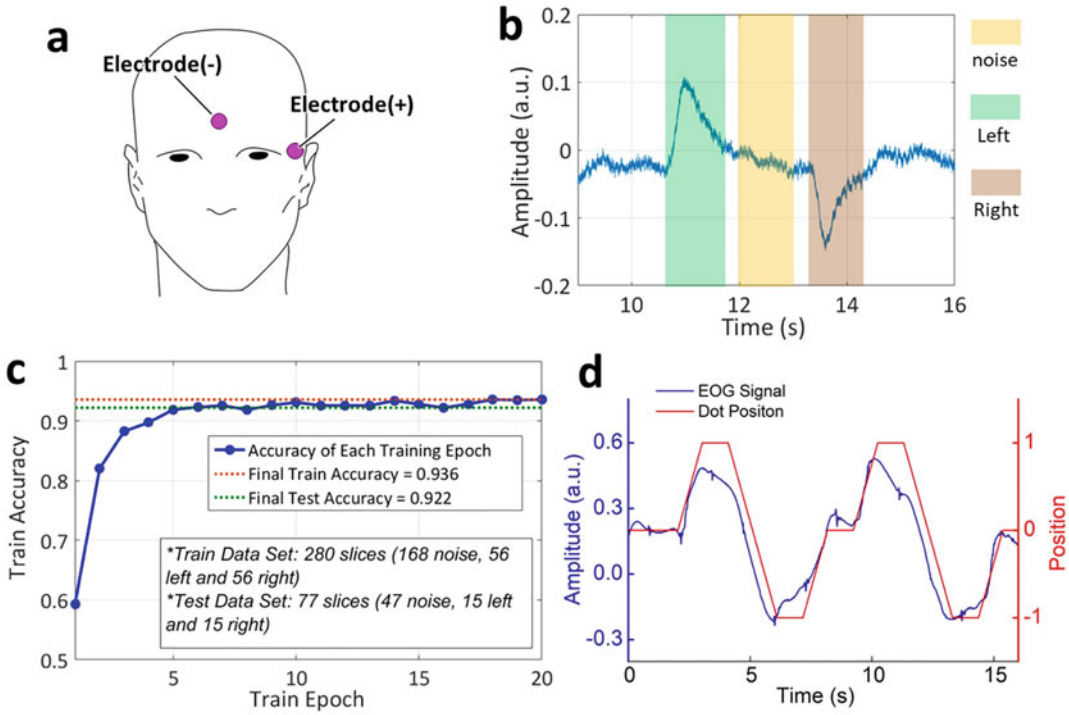


**Fig. 7** Wireless fully-passive acquisition of electrooculography (EOG). (**a**) Electrode location for measuring horizontal EOG. (**b**) The wireless recorded EOG signal when the participant moves his eyes left and right. Colored regions represent the segment of data used to train the deep learning model. (**c**) EOG signal analysis using the deep learning algorithm. EOG training data set is labeled as shown in (**b**). One training epoch represents one pass of complete data set into the deep learning training model. The inlet details the composition of training and testing data set. (**d**) Wireless recorded EOG signal of participant's eyes tracking a moving dot on a computer screen. The target dot is programmed to perform horizontal movement within an 18.5 in. width computer monitor. The participant focuses his gazes upon the moving dot while EOG signal and the location of the dot are recorded simultaneously. The red line represents the movement trail of the dot, where the location "0", "1", and "-1" represent center, left, and right end of the monitor, respectively

*3.5.2 Structure of the Deep Learning Model*

Various deep learning models are used to analyze the biopotentials. ECG and EMG, whose signal shapes are rather complex, require two 1D CNN layers with three full-connection dense layers. A simply shaped EOG only demands three full-connection dense layers (Fig. 8). Each model is trained by 30 epochs of training data set, followed by being tested with the testing data set to obtain testing accuracy.

## 4 Notes

1. The antenna and electronics of the sensor play the most critical role in determining its performance and signal quality. The antenna needs to achieve the optimized gain at two frequency bands ( $f_0$, 2.33 GHz, and $2f_0$, 4.66 GHz) and its port impedance needs to match with the capacitance of varactor diodes.

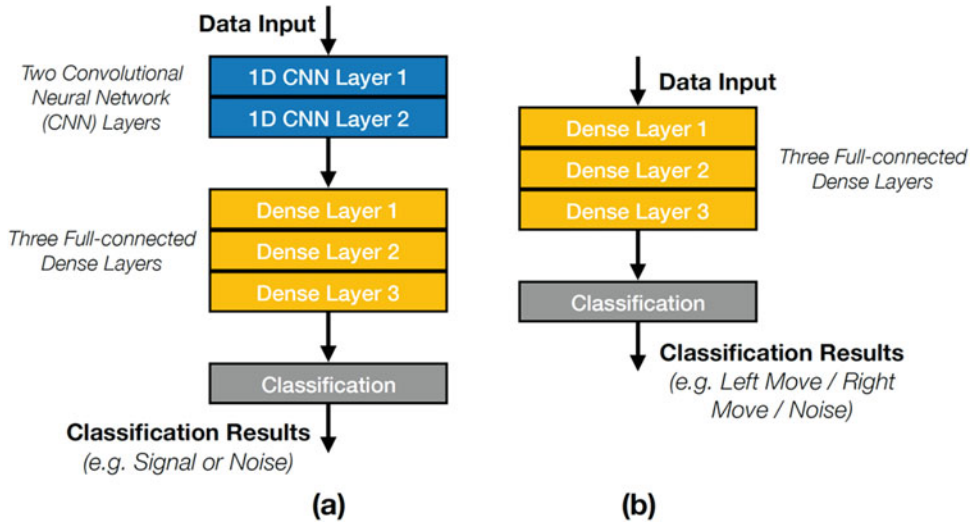


**Fig. 8** Structure diagram of the deep learning model applied for biopotential analysis. (**a**) is used for analyzing the ECG and EMG which are composed of rather complex shapes. The 1D CNN is able to recognize the signal changes in a short time period, making it ideal for ECG and EMG signal analysis. For ECG signal analysis, the first CNN layer has 36 $1 \times 5$ convolutional kernels, and the second CNN layer has 72 $1 \times 5$ convolutional kernels. For EMG signal analysis, the first CNN layer has 256 $1 \times 7$ convolutional kernels, and the second CNN layer has 512 $1 \times 7$ convolutional kernels. The dense layer is the most basic method in deep learning, allowing simple classification of the input data. The results from CNN layers are fed to three dense layers and then the model gives out the final classification results. (**b**) is used for analyzing the EOG signal. For simple-shaped signals, the deep learning model is preferred to be simple, otherwise, the model may run into the overfitting challenge. The model for EOG analysis adopts three dense layers for the classification

2. The cost of the current system is primarily dominated by the equipment used in external interrogator. However, the cost can be substantially reduced by replacing the equipment with a custom-designed monolithic microwave integrated circuit (MMIC).
3. Motion artifacts can greatly affect the wireless sensor, harming its signal integrity. To reduce motion artifact, unnecessary movement should be reduced as much as possible. In addition, low-frequency motion artifact can be reduced by applying polynomial fitting to remove baseline signal.
4. The position of the external antenna can greatly affect the wireless signal quality (Fig. 5d, e). To achieve the best result, place the external antenna perpendicular to the wireless sensor (90°) and keep the distance within 240 mm.
5. EOG signal is much harder to obtain due to its small amplitude. To generate better EOG signals, wash and clean the skin before placing the electrode. Place the external antenna 30 mm above the sensor.

## References


1. Romhilt DW, Estes EH (1968) A point-score system for the ECG diagnosis of left ventricular hypertrophy. Am Heart J 75(6):752–758. https://doi.org/10.1016/0002-8703(68)90035-5
2. Inbar GF, Noujaim AE (1984) On surface EMG spectral characterization and its application to diagnostic classification. IEEE Trans Biomed Eng BME-31(9):597–604. https://doi.org/10.1109/TBME.1984.325303
3. Dey N, Biswas D, Roy AB, Das A, Chaudhuri SS (2012) DWT-DCT-SVD based blind watermarking technique of gray image in electrooculogram signal. In: 2012 12th international conference on intelligent systems design and applications (ISDA). pp 680–685
4. Besnoff JS, Deyle T, Harrison RR, Reynolds MS (2013) Battery-free multichannel digital ECG biotelemetry using UHF RFID techniques. In: 2013 IEEE international conference on RFID (RFID). pp 16–22. https://doi.org/10.1109/RFID.2013.6548130
5. Dementyev A, Smith JR (2013) A wearable UHF RFID-based EEG system. In: 2013 IEEE international conference on RFID (RFID). pp 1–7. https://doi.org/10.1109/RFID.2013.6548128
6. Thomsen PEB et al (2010) Long-term recording of cardiac arrhythmias with an implantable cardiac monitor in patients with reduced ejection fraction after acute myocardial Infarction-Clinical perspective: the cardiac arrhythmias and risk stratification after acute myocardial infarction (CARISMA) study. Circulation 122(13):1258–1264. https://doi.org/10.1161/CIRCULATIONAHA.109.902148
7. Israel CW, Grönefeld G, Ehrlich JR, Li Y-G, Hohnloser SH (2004) Long-term risk of recurrent atrial fibrillation as documented by an implantable monitoring device: implications for optimal patient care. J Am Coll Cardiol 43(1):47–52. https://doi.org/10.1016/j.jacc.2003.08.027
8. Philipose M, Smith JR, Jiang B, Mamishev A, Roy S, Sundara-Rajan K (2005) Battery-free wireless identification and sensing. IEEE Pervasive Comput 4(1):37–45. https://doi.org/10.1109/MPRV.2005.7
9. Kim J et al (2016) Battery-free, stretchable optoelectronic systems for wireless optical characterization of the skin. Sci Adv 2(8):e1600418. https://doi.org/10.1126/sciadv.1600418
10. Kim J et al (2015) Miniaturized flexible electronic systems with wireless power and near-field communication capabilities. Adv Funct Mater 25(30):4761–4767. https://doi.org/10.1002/adfm.201501590
11. Xu S et al (Apr. 2014) Soft microfluidic assemblies of sensors, circuits, and radios for the skin. Science 344(6179):70–74. https://doi.org/10.1126/science.1250169
12. Chung HU et al (2019) Binodal, wireless epidermal electronic systems with in-sensor analytics for neonatal intensive care. Science 363(6430):eaau0780
13. Hockman CH, Mauck HP Jr, Hoff EC (1966) ECG changes resulting from cerebral stimulation: II. A spectrum of ventricular arrhythmias of sympathetic origin. Am Heart J 71(5):695–700
14. Bulling A, Ward JA, Gellersen H, Troster G (2011) Eye movement analysis for activity recognition using electrooculography. IEEE Trans Pattern Anal Mach Intell 33(4):741–753. https://doi.org/10.1109/TPAMI.2010.86
15. Darrell T, Pentland A (1993) Recognition of space-time gestures using a distributed representation. Vision and Modeling Group, Media Laboratory, Massachusetts Institute of Technology

# Chapter 46

# Fabrication of Skin-Mountable Flexible Sensor Patch for Monitoring of Swallowing Function

**Heun Park, Min Ku Kim, Georgia A. Malandraki, and Chi Hwan Lee**

## Abstract

Swallowing is a critical function that enables humans to sustain life. When swallowing is compromised, the consequences can be devastating and include malnutrition, dehydration, respiratory compromise, and even death. Swallowing disorders (i.e., dysphagia) are very common in many disorders and diseases, such as stroke, ALS, Parkinson disease, and more, and in fact millions of people across the world are diagnosed with oropharyngeal swallowing disorders every year. Current rehabilitative interventions for dysphagia can be effective, but require daily performance of swallowing exercises that primarily rely on expensive biofeedback devices (e.g., oral manometers, electromyographic (EMG) devices, and endoscopic devices). These types of devices are often only available in medical facilities. However, it is not feasible or economically viable for patients to make multiple visits per day or week to a clinic to receive intensive treatment, especially given mobility limitations that many affected patients often experience. This can reduce treatment adherence and result in decreased rehabilitation potential, re-hospitalizations, and increased healthcare costs. To address this gap, we designed a novel specialized portable skin-mounted flexible sensor system that allows remote signal acquisition of swallowing-related signals. Herein, we report technical details for the fabrication of the skin-mounted flexible sensor patch that is tailored for the human submental (under the chin) area, enabling the continuous, reliable monitoring of both muscles' activity (i.e., EMG signals) and laryngeal movements during swallowing events. The sensor patch is wired to a portable reusable wireless (Bluetooth) unit compatible with smart watches, phones, and tablets for post-data analysis and reporting through a cloud server, which would potentially enable telemonitoring of patients with dysphagia.

**Key words** Submental sensor patches, Oropharyngeal swallowing disorders, Dysphagia, Remote monitoring, Electromyography, Strain sensor

## 1 Introduction

Swallowing requires the precise coordination of more than 30 pairs of muscles of the head and neck, six pairs of cranial nerves, the brainstem, and many brain areas [1, 2]. Any disruption in one of these structures or pathways can cause oropharyngeal swallowing disorders (a.k.a. oropharyngeal dysphagia). Dysphagia is commonly caused by stroke, cerebral palsy, Parkinson disease, dementia, head and neck cancer, and its treatment, trauma, and genetic

Miguel R. Ossandon et al. (eds.), *Biomedical Engineering Technologies: Volume 1*, Methods in Molecular Biology, vol. 2393, https://doi.org/10.1007/978-1-0716-1803-5_46, 

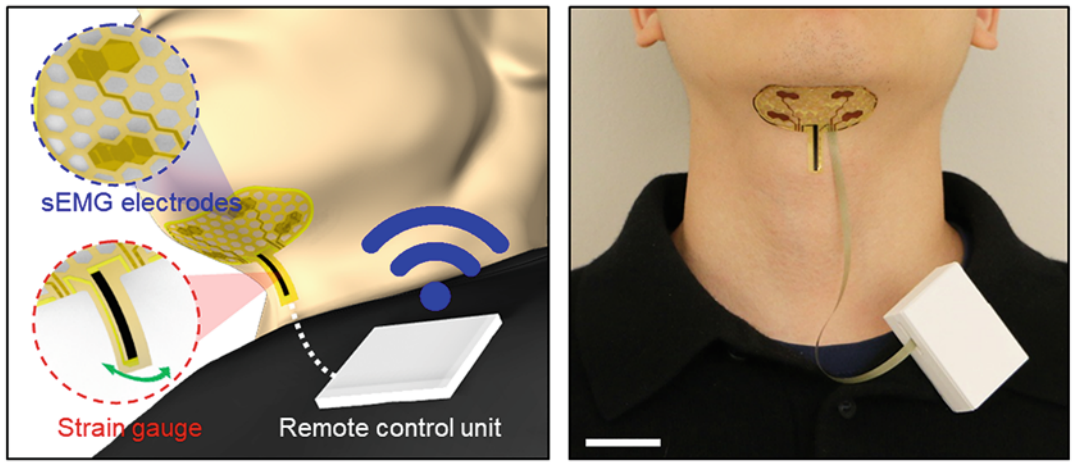


**Fig. 1** Schematic illustration (left) and photo (right) of the sensor patch connected to the portable wireless unit for remote data transmission and powering. Scale bar is 2.5 cm. (From *Science Advances* **2019**, 5, eaay3210. © The Authors, some rights reserved; exclusive licensee American Association for the Advancement of Science. Distributed under a Creative Commons Attribution NonCommercial License 4.0 (CC BY-NC) http:/creativecommons.org/licenses/by-nc/4.0/")

syndromes [3, 4]. Critically, without proper treatment, dysphagia can interfere with daily life and cause respiratory infections or result in death due to malnutrition, dehydration, and aspiration of food or liquid into the lungs [5, 6]. Current rehabilitation treatment of dysphagia can be effective, but it typically requires the use of expensive biofeedback devices such as oral manometers, electromyographic devices, and endoscopy [7–9]. Most current electromyography devices are unsuitable for the curved surface of the submental area due to rigid or semi-flexible platforms. As a result, data collection with current EMG devices results in suboptimal data and causes discomfort to patients. Recent advances of flexible and stretchable electronics could alleviate these issues by exploiting ultra-thin form factors to promote intimate, conformable contact of devices to the skin of the submental area [10, 11]. However, significant additional advances are required for translating this technology into clinical practice, where factors such as continuous remote data transmission, signal accuracy and reliability, mechanical durability for cost-effective multiple uses on a daily or weekly basis, ease-of-use, and the ability to accommodate patients are necessary.

Herein, we report technical details of the fabrication of a mechanically compliant and non-invasive skin sensor patch platform (Fig. 1) that can be attached and detached multiple times without irritating the wearer and damaging the device. The sensor patch is specifically designed for integrating with the submental area and assessing both muscle activity (i.e., EMG signals) and laryngeal movement during swallowing and swallowing maneuvers [12]. The sensor patch is wired to a custom-built, portable collar

unit clipped on the wearer's clothing via a flexible cable, allowing for remote data transmission. The materials, design layouts, and fabrication methods developed in this study form a foundation that can be adjusted and upscaled for future applications in the monitoring of speech and voice disorders.

## 2 Materials

### 2.1 Sensor Patch Fabrication

1. Double-sided Cu clad (Pyralux AP7413R, Dupont USA) composed of 9 μm-thick copper layers and 13 μm-thick polyimide (PI).
2. A laser cutter (PLS6MW, universal Laser Systems, $CO_2$, $\lambda = 10.6$ μm).
3. Photoresist (negative type, Riston MM540, Dupont).
4. Cu etchant (CE-100, Transene).
5. Hot roller laminator (AL13P, Apache).
6. Sodium carbonate ($Na_2CO_3$, 791768, Sigma-Aldrich).
7. Ferric chloride ($FeCl_3$, 415, MG Chemicals).
8. Sodium hydroxide (NaOH, S318-1, Fisher Chemicals).
9. UV exposure (Model 18, Jetlight Company).
10. 24 k Pure Gold plating solution (Gold Plating Services).
11. A piezoresistive strip (Velostat, 3 M, sheet resistivity: $<30$ kΩ/$cm^2$).
12. A conductive epoxy adhesive (#8331, MG Chemicals).
13. A Silbione (HC2 2022, Bluestar Chemicals).
14. Ecoflex™ (00-30, Smooth-On).

### 2.2 Portable Wireless Unit

1. Flexible anisotropic conductive film (ACF, HST-9805-210, Elform Inc.).
2. Analog-to-digital converter (ADS1294, Texas Instrument, USA, 12 mm × 12 mm × 1 mm).
3. Bluetooth module (HC-06, Guangzhou HC Information Technologies Co., Ltd., China, 38 mm × 17 mm × 4 mm).
4. Rechargeable battery (PRT-13813, Sparkfun Electronics, USA, 1000 mAh, 50 mm × 34 mm × 6 mm).
5. 3D-printed plastic case made of acrylonitrile butadiene styrene (ABS).
6. A custom-built MATLAB code (MATLAB Inc., Natick, MA).

### 2.3 Clinical Evaluation

1. Varibar thin liquid barium (Cat. no. 105, E-Z-EM Canada Inc.).

2. Varibar barium pudding (Cat. no. 125, E-Z-EM Canada Inc.).
3. Videofluoroscopy C-arm system (OEC 9800 Plus Digital Mobile 12″ GE).
4. BioRadio™ system (GLNeuro Tech Inc.).
5. MATLAB (MATLAB Inc., Natick, MA).
6. MDR digital video recorder (Pacsgear).

## 3 Method

### 3.1 Sensor Patch Fabrication

The overall procedure for the fabrication of the sensor patch is schematically illustrated in Fig. 2. The fabrication process was performed using laser cutting method for cost-effective and rapid prototyping followed by photolithographic patterning. Figure 3 shows the optical image of EMG electrodes. The sensor patch was gently attached to the submental skin of individuals of four age groups who have different physical properties of the skin such as the ages of 26, 35, 45, and 64 years as shown in Fig. 4 [13]. Figure 5 shows the adhesion test of the patch sensor to examine for skin irritation and signal qualities with a young and an older subject (26 and 79 years old, respectively) (*see* **Notes 1** and **2**).

To make sensor patch, the detailed fabrication steps are explained below.

1. The device design, outline, and honeycomb network (hexagon edge *l*: 4.5 mm, line width *w*: 1 mm) were predefined using a CAD software as shown in Fig. 6.

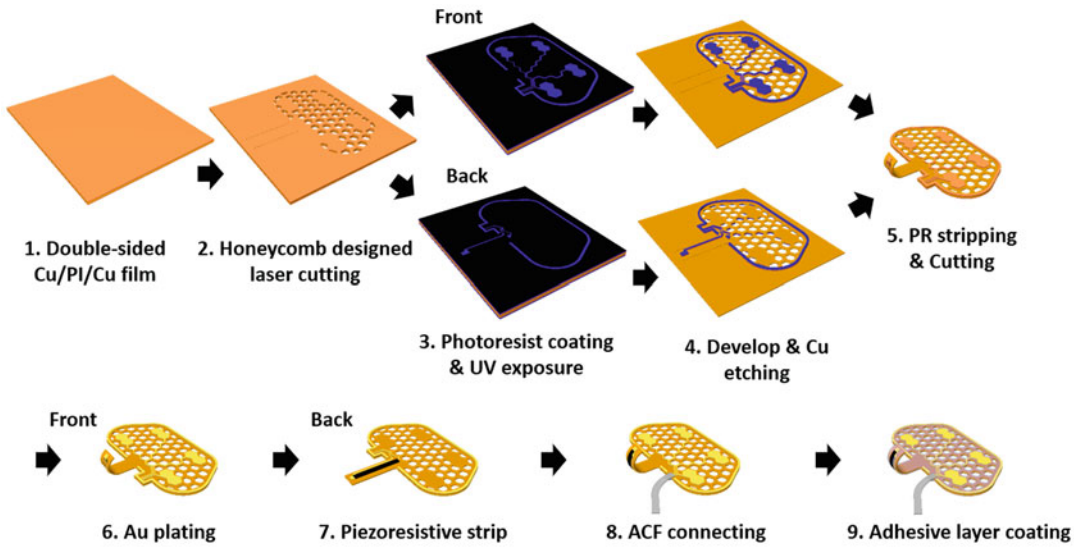


**Fig. 2** Schematic of the fabrication processes of the submental sensor patch

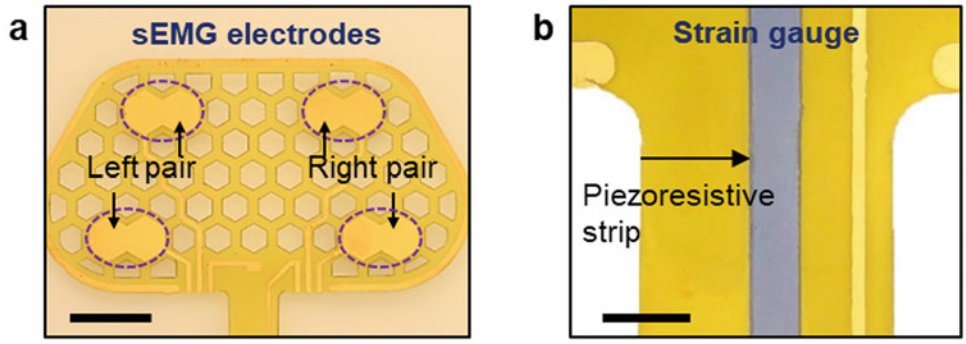


**Fig. 3** Optical images of (**a**) the surface electromyogram (sEMG) recording electrodes and (**b**) the piezoresistive strip in the strain gauge. Scale bars are 1 cm and 3 mm, respectively. (From *Science Advances* **2019**, 5, eaay3210. © The Authors, some rights reserved; exclusive licensee American Association for the Advancement of Science. Distributed under a Creative Commons Attribution NonCommercial License 4.0 (CC BY-NC) http:/creativecommons.org/licenses/by-nc/4.0/")


**Fig. 4** Photograph of the sensor patch attached on the subjects of different ages from 26 to 64 years. The scale bar is 3.5 cm. (From *Science Advances* **2019**, 5, eaay3210. © The Authors, some rights reserved; exclusive licensee American Association for the Advancement of Science. Distributed under a Creative Commons Attribution NonCommercial License 4.0 (CC BY-NC) http:/creativecommons.org/licenses/by-nc/4.0/")

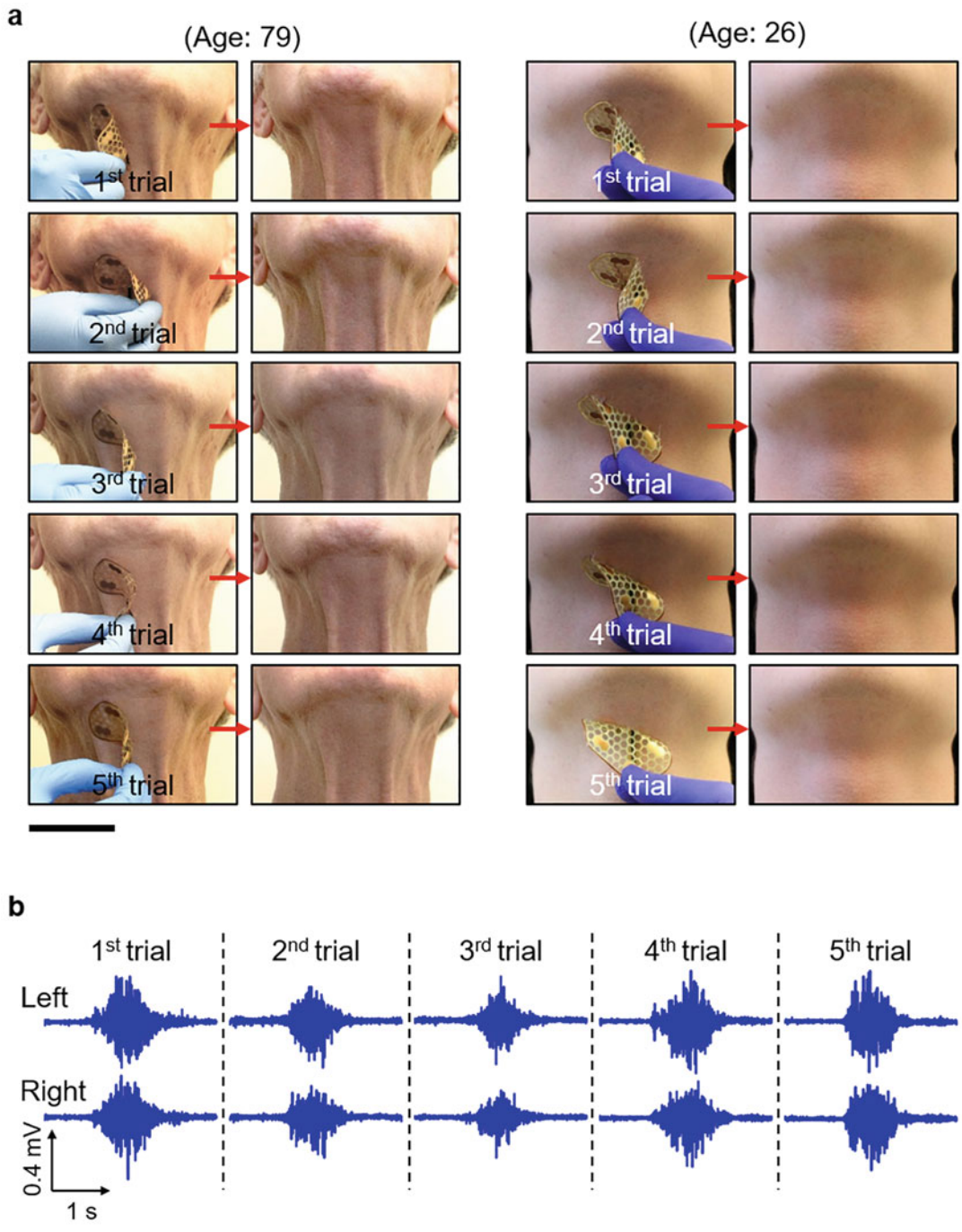


**Fig. 5** (**a**) Photograph of the sensor patch repeatedly attached and detached from the submental skin of subjects (79 and 26 years). The scale bar is 5 cm. (**b**) The corresponding sEMG data obtained from a 26-year-old subject with multiple trials. From *Science Advances* **2019**, 5, eaay3210. © The Authors, some rights reserved; exclusive licensee American Association for the Advancement of Science. Distributed under a Creative Commons Attribution NonCommercial License 4.0 (CC BY-NC) http:/creativecommons.org/licenses/by-nc/4.0/")

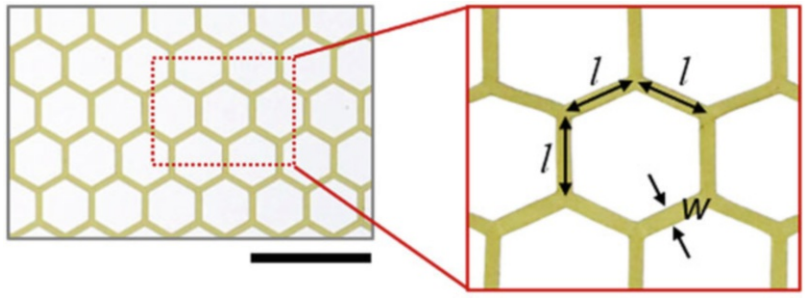


**Fig. 6** Photograph images of the honeycomb network. (hexagon edge *l*: 4.5 mm, line width *w*: 1 mm) The scale bar is 16 mm

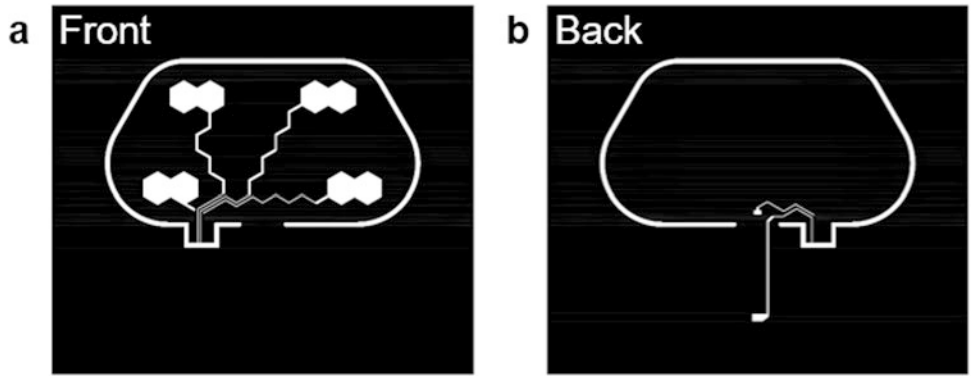


**Fig. 7** (**a**) Front and (**b**) back side of photomask (negative type) design for EMG electrodes, interconnecting trace lines and strain sensor connections

2. The overall outline of the device was patterned using a laser cutter to create a honeycomb network layout on a commercially available double-sided Cu clad of 9 μm-thick copper and 13 μm-thick PI mounted on the glass substrate (*see* **Note 3**). During the cutting process, the laser cutter was set at 15 W power, 50 kHz frequency, and at 90% speed.
3. Negative type dry film photoresist (Riston MM540, Dupont) was laminated with a hot roller laminator on both sides of the double-sided Cu clad of PI on the glass substrate at a temperature of 120 °C. The dry film photoresist was processed through the laminator at 2.5 cm/s twice to ensure good adhesion between the photoresist fill and the copper substrate.
4. The photomask (negative type) was designed using a CAD program which defined the EMG electrodes, interconnecting trace lines and strain sensor connections as shown in Fig. 7.
5. The laminated photoresist film layer was processed under a standard photolithographic patterning that involved an UV exposure for 120 s (exposure energy, 50 mJ/cm$^2$, Model 18, Jetlight Company) and then developed with a solution of

0.85 wt% sodium carbonate ($Na_2CO_3$) for 2 min (*see* **Note 4**). A foam brush was used to agitate and accelerate the removal of photoresist residue during the development process.

6. The UV-exposed photoresist/Cu film was chemically etched in a solution of ferric chloride ($FeCl_3$, Cu etchant), for 180 s at 70 °C to form the 2-channels of differential EMG electrodes, interconnecting trace lines and strain sensor connections. The remaining photoresist was removed by immersing the entire structure in a solution of 1% sodium hydroxide (NaOH) for 2 min, and fully dried with nitrogen gas.
7. A thin layer (~500 nm thick) of Au was electroplated (Gold Plating Services, Universal Plater Kit) via brushing method on the Cu film with applied voltage of 3.0 V to prevent Cu oxidation and ensure biocompatibility.
8. Large sheet of piezoresistive materials (Velostat, 3 M, sheet resistivity: $<30\ k\Omega/cm^2$) was cut down to size with a blade, 25 mm × 2 mm. On the other side (opposite to EMG electrodes), a piezoresistive strip was bonded at the strain sensor location using a conductive epoxy adhesive (#8331, MG Chemicals) to serve as a strain sensing element for the laryngeal movement.
9. Conductive epoxy adhesive was cured in a convection oven at 70 °C for 30 min (*see* **Note 5**).
10. The piezoresistive strip was passivated with a thin layer of PDMS. PDMS layer was prepared by spin coating (Laurell Technologies WS-650Mz-23NPPB) process with 1000 rpm, 30 s.
11. Bilayers of silicone elastomers that contain Silbione (HC2 2022, Bluestar Chemicals, ~100 μm thick) and Ecoflex (00-30, Smooth-On, ~100 μm thick) were subsequently spin-coated (Laurell Technologies WS-650Mz-23NPPB) with two-step process, 500 rpm for 10 s and 800 rpm for 30 s, while the surface of the EMG recording electrodes was temporarily masked with hexagonal shaped PDMS pad.
12. The silicone elastomer layers (silbione and Ecoflex) were cured in a convection oven at 70 °C for 1 h (*see* **Note 6**).
13. The PDMS masking pad was removed after completing the entire process.
14. An anisotropic conductive film (ACF, HST-9805-210, Elform Inc.) cable was bonded to the sensor patch using a heated press (Model# VS129, Vidal Sassoon Appliances) at 120 °C for 30 s to connect to a custom-built, portable wireless unit (*see* Subheading 3.2).

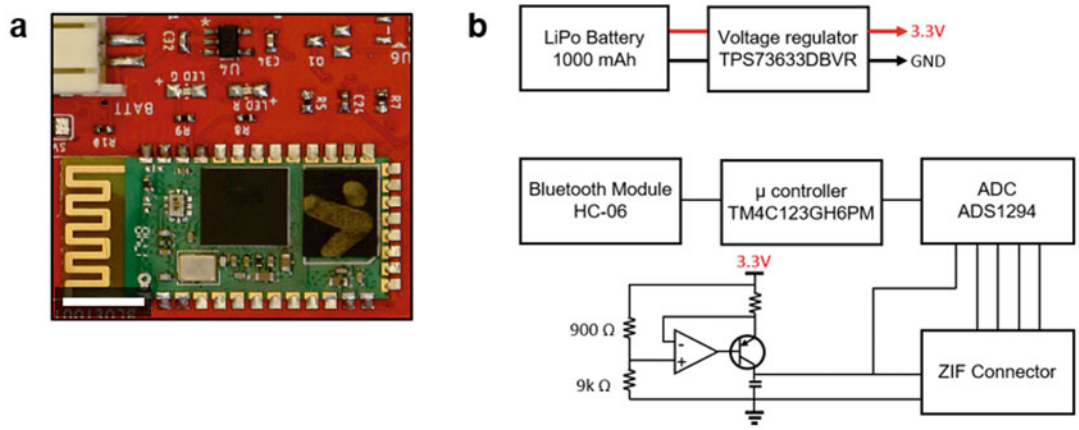


**Fig. 8** (**a**) Optical image and (**b**) circuit diagram of the unpackaged printed circuit board with integrated components of the portable wireless unit. Scale bar is 5 mm

### *3.2 Portable Wireless Unit*

Figure 8 shows photograph and circuit diagram of the custom-built, portable wireless unit, which consists of 2 stacked layers of printed circuit boards (PCBs) with commercial circuit components configured with features for remote data transmission and powering.

1. The first layer of the PCB contains a front-end 24-bit analog-to-digital converter (ADS1294, Texas Instruments) and a microcontroller (TM4C123GH6PM, Texas Instruments) on each side.
2. The second layer of the PCB contains a Bluetooth module with integrated antenna (HC-06, Guangzhou HC Information Technologies). The battery life was approximately 16 h while transmitting data over the Bluetooth module, which was approximately twice the transmission time enabled by a commercial wireless unit (BioRadio™) (*see* **Note 7**).
3. The data acquisition front-end differential input 24-bit analog-to-digital converter (ADS1294, Texas Instruments) was programmed in terms of sampling rate (500 Hz ~ 20 kHz) and sample resolution (10 bits ~24 bits) to optimize the measurement condition to extend battery life while maintaining comparable signal acquisition performance to the commercial unit.
4. The assembled PCB unit along with a lithium polymer battery was packaged in a 3D printed plastic case for housing.
5. The remote data collection was performed by exploiting a zero-insertion force (ZIF) connector (FH19C-6S-0.5SH(10), Hirose Electric) placed on the board to connect with the ACF cable from the sensor patch. The ACF was connected by sliding the cable into the connector housing and closing the latch to secure the connector. The conductor pitch (0.5 mm) of the

ACF cable and the ZIF connector were specifically matched for direct connection without adapters.

6. Both EMG signals and strain waveforms were captured during swallowing events by a differential input, 24-bit resolution analog-to-digital converter at the sampling rate of 1 kHz and 100 Hz for the EMG and strain data, respectively (*see* **Note 8**).
7. The collected data was remotely transmitted through the Bluetooth module to an external data acquisition system.
8. The received data was digitally processed with finite impulse response filter on MATLAB with a fourth-order Butterworth bandpass filter with the cutoff frequency of 20–500 Hz and 0.1–20 Hz for the recordings of EMG signals and strain waveforms, respectively.

### 3.3 Data Acquisition

#### 3.3.1 Remote Monitoring of both Muscle Activity and Laryngeal Movement

Demonstration of the sensor patch was performed on a healthy young subject (23-years old female). The skin of the submental area was prepared in advance by cleaning the area with a rubbing alcohol wipe and air drying it for minimum 30 s, which removes any oil residue and contaminants to improve the sensor patch adherence to the skin. A conducting gel was applied to each of the EMG electrodes of the sensor patch, then the clinician carefully aligned the sensor patch and attached to the submental skin of the subject. The ACF cable was connected to the portable wireless unit which was fixed to the shirt collar and we ensured no strain was applied on to the ACF cable. Then the subject was asked to move their head to confirm head movement was not restricted. The subject was comfortably seated in a chair while the data collection occurred.

Muscle Activity (EMG Signals)

The EMG signals were collected from the left and right submental muscles during swallows of 5 mL Varibar thin liquid barium at the sampling rate of 1 kHz with 24-bit resolution with reference to the ground electrode placed on the mastoid process (behind the ear). The remotely collected EMG data from the portable wireless unit was comparable to that obtained using a commercial wireless unit (BioRadio™). Figure 9 shows the simultaneously recorded submental EMG signals (top plots) and strain waveforms (bottom plot) during two swallows, clearly indicating the amplitude (force generation), duration, and relative onset times of submental muscle activity.

Laryngeal Movement (Strain Waveforms)

Figure 9 (*top plots*) shows that the EMG signals collected through the sensor patch were comparable to those obtained with commercial EMG recording electrodes (Red Dot, 3 M). Figure 9a (*bottom plot*) shows the "W"-shaped waveforms occurred during the swallows, representing a rapid upward shift of the thyroid notch and the hyoid bone at the onset of swallowing (T1), followed by an anterior and superior movement to reach the most superior-anterior

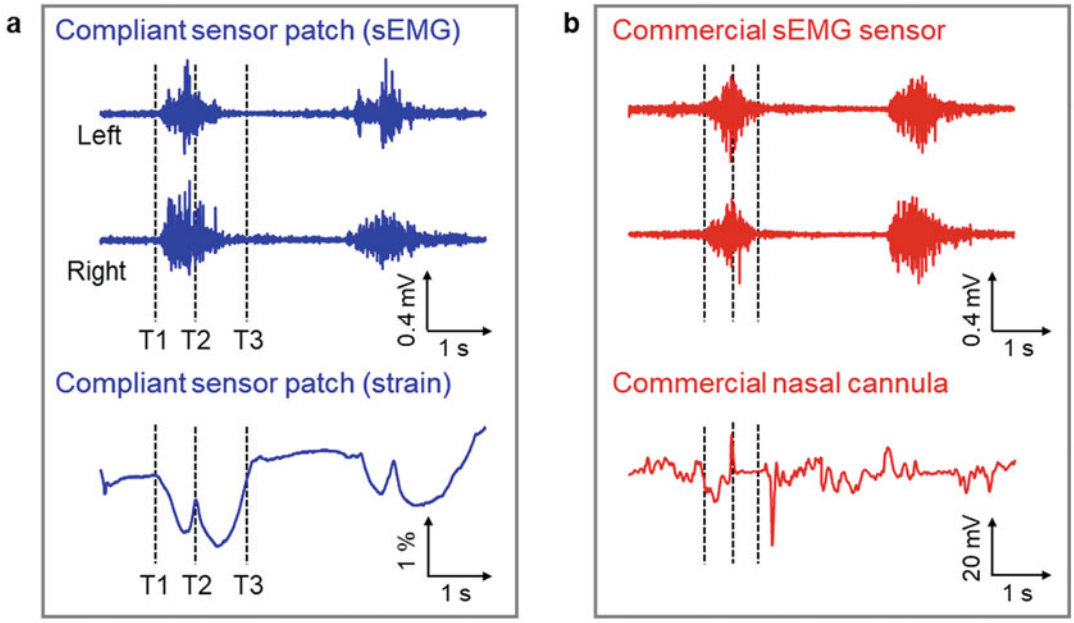


**Fig. 9** (**a**) Simultaneously recorded submental sEMG and strain waveforms during swallows of 5 mL barium liquid using (**a**) the compliant sensor patch, and (**b**) the conventional commercial recording electrode with a commercial nasal cannula. (From *Science Advances* **2019**, 5, eaay3210. © The Authors, some rights reserved; exclusive licensee American Association for the Advancement of Science. Distributed under a Creative Commons Attribution NonCommercial License 4.0 (CC BY-NC) http:/creativecommons.org/licenses/by-nc/4.0/")

position (T2), and finally return to the original position upon completion of a swallow (T3). These strain waveforms were effectively distinguishable at lower noise levels than those obtained using a standard nasal airflow cannula to detect swallow apnea as a control measurement (Fig. 9b, *bottom plot*).

### 3.3.2 *Clinical Evaluation*

Analysis of EMG Signals and Strain Waveforms

The participated patient produced 3 trials of the maximum lingual press using the Iowa Oral Performance Instrument (IOPI). The tongue bulb was inserted into the mouth of the subject. Submental EMG signal was recorded while the subject pressed on the tongue bulb with their tongue as hard as possible for a period of approximately 5 s. The corresponding pressure reading from IOPI was also recorded. The mean amplitude of the 3 EMG signals acquired during the maximum tongue presses was used as a reference signal to allow for normalization of the data. After a series of swallowing maneuver exercises, the recorded EMG signals were post-processed using a custom-built MATLAB code. The EMG signals obtained from the left and right channels in each trial were smoothed and analyzed in terms of normalized amplitude and burst duration. The onset and offset of each trial were selected to calculate the amplitude of the EMG signals and the burst duration. Identification of

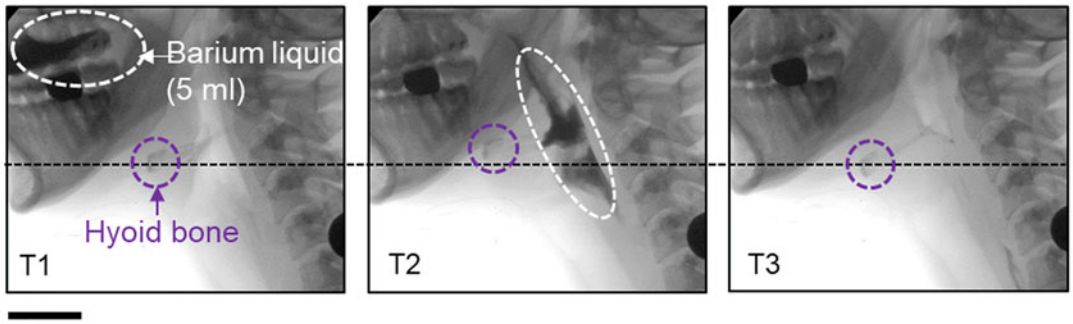


**Fig. 10** A series of screen-captured images from the simultaneous videofluoroscopic swallowing study (VFSS) recording. Scale bar is 5.5 cm. (From *Science Advances* **2019**, 5, eaay3210. © The Authors, some rights reserved; exclusive licensee American Association for the Advancement of Science. Distributed under a Creative Commons Attribution NonCommercial License 4.0 (CC BY-NC) http:/creativecommons.org/licenses/by-nc/4.0/")

swallow events was semi-automatic and sorted by analyzing the recorded strain waveforms corresponding to the EMG signals.

Recording of VFSS (Videofluoroscopic Swallowing Study)

The VFSS images were obtained using a videofluoroscopic C-arm system at full resolution (30 pulses/s) and recorded at 30 frames/s on a medical digital recorder (MDR) as shown in Fig. 10. The patient was seated in an upright position and visualized on the lateral view, to allow visualization of the lips, oral and nasal cavities, cervical vertebrae, and the upper esophagus. The patient then completed the following swallows (2 times each): Regular swallows of 5 mL Varibar thin liquid barium, 10 mL Varibar thin liquid, and 5 cc Varibar barium pudding [14, 15]. In addition, the patient was asked to perform effortful swallow (hard swallow) and Mendelsohn maneuver (long swallow) of 5 mL Varibar thin liquid barium and 5 cc Varibar barium pudding. Barium liquid and pudding were used as the contrast agent because they are visible in videofluoroscopy. The measured data provide clinically useful information to the patient and clinician in terms of identifying anomalies in swallowing muscle activity [16].

### *3.3.3 Cost Estimation*

The estimated fabrication cost of the sensor patch including the constituent electronic components, encapsulation and substrate materials at a lab scale, is about $13.92, and $52 for the portable wireless unit (Fig. 11). The sensor patch was reused multiple times through sterilization with 70% ethanol for additional cost-savings, while the portable wireless unit can be used across different patients until the end of its lifetime.

| | Name | Cost per device |
|---|---|---|
| Electronic components | Pyralux (PI/Copper clad) | $0.50 |
| | Piezoresistive (Velostat) | $0.01 |
| | ACF cable | $0.71 |
| Packaging materials | PDMS | $0.05 |
| | Silbione | $0.05 |
| Processing materials | Photoresist Film | $0.10 |
| | Process chemicals | $2 |
| | Conductive adhesive | $1 |
| Labor | $60/hr | $10 |
| **Sensor patch unit** | | $13.92 |
| Wireless modules | PCB | $10 |
| | Bluetooth module | $10 |
| | ADC | $22 |
| | Additional components | $10 |
| **Remote control unit** | | $52 |

**Fig. 11** Cost estimation of the submental sensor patch and the remote control unit. (From *Science Advances* **2019**, 5, eaay3210. © The Authors, some rights reserved; exclusive licensee American Association for the Advancement of Science. Distributed under a Creative Commons Attribution NonCommercial License 4.0 (CC BY-NC) http:/creativecommons.org/licenses/by-nc/4.0/")

## 4 Notes

1. The quality of the physical and electrical contact undergoes negligible changes even with various head and neck motions and repetitive attachments and detachments of the sensor. In addition, multiple attachments and detachments of the sensor patch did not cause any irritation of the skin.
2. The recorded EMG signals from five separate swallowing trials (subject age: 26) show the consistent device performance after the repeated attachments and detachments.
3. The outline was designed with CAD software (AutoCAD, Autodesk). The double-sided Cu clad PI film size is 75 mm (L) × 75 mm (W). The film was laser cut with speed of 20 mm/s.
4. The UV was exposed for 120 s with the power of 0.3 $mW/cm^2$.
5. The piezoresistive strip (25 mm × 2 mm × 0.1 mm) was bonded to the sensor patch with conductive epoxy adhesive that was cured in a convection oven at 70 °C for 30 min.
6. The encapsulation layer was cured in a convection oven at 70 °C for 1 h.

7. The size of the portable wireless unit is 5.6 cm × 3.8 cm × 1.8 cm, which is almost 3 times smaller than that of the commercial wireless unit (BioRadio™, 10 cm × 6 cm × 2 cm).
8. The sampling rate for the EMG and strain sensors was 1 kHz and 100 Hz, respectively.

## References


1. Perlman AL, Palmer PM, McCulloch TM, Vandaele DJ (1999) Electromyographic activity from human laryngeal, pharyngeal, and submental muscles during swallowing. J Appl Physiol 86:1663–1669
2. Sörös P, Inamoto Y, Martin RE (2009) Functional brain imaging of swallowing: an activation likelihood estimation meta-analysis. Hum Brain Mapp 30:2426–2439
3. Hutcheson KA, Lewin JS, Barringer DA, Lisec A, Gunn GB, Moore MWS, Holsinger FC (2012) Late dysphagia after radiotherapy-based treatment of head and neck cancer. Cancer 118:5793–5799
4. Rofes L, Vilardell N, Clavé P (2013) Post-stroke dysphagia: progress at last. Neurogastroenterol Motil 25:278–282
5. Langmore SE, Skarupski KA, Park PS, Fries BE (2002) Predictors of aspiration pneumonia in nursing home residents. Dysphagia 17:298–307
6. Baijens LW, Clavé P, Cras P, Ekberg O, Forster A, Kolb GF, Leners J-C, Masiero S, Mateos-Nozal J, Ortega O, Smithard DG, Speyer R, Walshe M (2016) European Society for Swallowing Disorders - European Union Geriatric Medicine Society white paper: oropharyngeal dysphagia as a geriatric syndrome. Clin Interv Aging 11:1403–1428
7. Robbins J, Kays SA, Gangnon RE, Hind JA, Hewitt AL, Gentry LR, Taylor AJ (2007) The effects of lingual exercise in stroke patients with dysphagia. Arch Phys Med Rehabil 88:150–158
8. Martin-Harris B, McFarland D, Hill EG, Strange CB, Focht KL, Wan Z, Blair J, McGrattan K (2015) Respiratory-swallow training in patients with head and neck cancer. Arch Phys Med Rehabil 96:885–893
9. Malandraki GA, Rajappa A, Kantarcigil C, Wagner E, Ivey C, Youse K (2016) The intensive dysphagia rehabilitation approach applied to patients with neurogenic dysphagia: a case series design study. Arch Phys Med Rehabil 97:567–574
10. Lee Y, Nicholls B, Sup LD, Chen Y, Chun Y, Siang AC, Yeo W-H (2017) Soft electronics enabled ergonomic human-computer interaction for swallowing training. Sci Rep 7:46697
11. Constantinescu G, Jeong J-W, Li X, Scott DK, Jang K-I, Chung H-J, Rogers JA, Rieger J (2016) Epidermal electronics for electromyography: an application to swallowing therapy. Med Eng Phys 38:807–812
12. Li Q, Hori K, Minagi Y, Ono T, Chen Y-J, Kondo J, Fujiwara S, Tamine K, Hayashi H, Inoue M, Maeda Y (2013) Development of a system to monitor laryngeal movement during swallowing using a bend sensor. PLoS One 8: e70850
13. Jang K-I, Chung HU, Xu S, Lee CH, Luan H, Jeong J, Cheng H, Kim G-T, Han SY, Lee JW, Kim J, Cho M, Miao F, Yang Y, Jung HN, Flavin M, Liu H, Kong GW, Yu KJ, Rhee SI, Chung J, Kim B, Kwak JW, Yun MH, Kim JY, Song YM, Paik U, Zhang Y, Huang Y, Rogers JA (2015) Soft network composite materials with deterministic and bio-inspired designs. Nat Commun 6:6566
14. Doeltgen SH, Ong E, Scholten I, Cock C, Omari T (2017) Biomechanical quantification of Mendelsohn maneuver and effortful swallowing on pharyngoesophageal function. Otolaryngol Head Neck Surg 157:816–823
15. McCullough GH, Kamarunas E, Mann GC, Schmidley JW, Robbins JA, Crary MA (2012) Effects of Mendelsohn maneuver on measures of swallowing duration post stroke. Top Stroke Rehabil 19:234–243
16. Kantarcigil C, Sheppard JJ, Gordon AM, Friel KM, Malandraki GA (2016) A telehealth approach to conducting clinical swallowing evaluations in children with cerebral palsy. Res Dev Disabil 55:207–217

# Chapter 47

# The Intelligent Phenotypic Plasticity Platform ($IP^3$) for Precision Medicine-Based Injury Prevention in Sport

**Adam W. Kiefer, Cortney N. Armitano-Lago, Anoop Sathyan, Ryan MacPherson, Kelly Cohen, and Paula L. Silva**

## Abstract

The best predictor of future injury is previous injury and this has not changed in a quarter century despite the introduction of evidence-based medicine and associated revisions to post-injury treatment and care. Nearly nine million sports-related injuries occur annually, and the majority of these require medical intervention prior to clearance for the athlete to return to play (RTP). Regardless of formal care, these athletes remain two to four times more likely to suffer a second injury for several years after RTP. In the case of children and young adults, this sets them up for a lifetime of negative health outcomes. Thus, the initial injury is the tipping point for a post-injury cascade of negative sequelae exposing athletes to more physical and psychological pain, higher medical costs, and greater risk of severe long-term negative health throughout their life. This chapter details the technologies and method that make up the automated *Intelligent Phenotypic Plasticity Platform* ($IP^3$)—a revolutionary new approach to the current standard of post-injury care that identifies and targets deficits that underly second injury risk in sport. $IP^3$ capitalizes on the biological concept of phenotypic plasticity (PP) to quantify an athlete's functional adaptability across different performance environments, and it is implemented in two distinct steps: (1) phenomic profiling and (2) precision treatment. Phenomic profiling indexes the fitness and subsequent phenotypic plasticity of an individual athlete, which drives the personalization of the precision treatment step. $IP^3$ leverages mixed-reality technologies to present true-to-life environments that test the athlete's ability to adapt to dynamic stressors. The athlete's phenotypic plasticity profile is then used to drive a precision treatment that systematically stresses the athlete, via a combination of behavioral-based and genetic fuzzy system models, to optimally enhance the athlete's functional adaptability. $IP^3$ is computationally light-weight and, through the integration with mixed-reality technologies, promotes real-time prediction, responsiveness, and adaptation. It is also the first ever phenotypic plasticity-based precision medicine platform, and the first precision sports medicine platform of any kind.

**Key words** Precision medicine, Phenomics, Phenotypic plasticity, Fitness, Musculoskeletal injury, Injury prevention, Genetic fuzzy systems, Mixed-reality

## 1 Introduction

The most accurate predictor of future athletic injury is previous injury [1–19] and this has not changed in a quarter century, despite

Miguel R. Ossandon et al. (eds.), *Biomedical Engineering Technologies: Volume 1*, Methods in Molecular Biology, vol. 2393, https://doi.org/10.1007/978-1-0716-1803-5_47, © Springer Science+Business Media, LLC, part of Springer Nature 2022

the introduction of evidence-based sports medicine [20]. One of the expectations of the evidence-based approach was that it would accelerate discoveries to reduce the significant negative health impact of these injuries [21]. Unfortunately, athletes of today remain at two to over 100 times increased risk of second injury—this includes both re-injury and new injury—for up to 2 years after they return to competition [13–17]. Thus, despite consistent evidence-based revisions to surgical and therapeutic interventions and treatment strategies, there remains a critical need to transform injury treatment to meaningfully improve outcomes for athletes returning to competition following injury.

### 1.1 Current Methods for Second Injury Prevention

Empirical evidence strongly indicates that after any type of injury, athletes develop deficits in their ability to utilize perceptual information (i.e., visual and proprioceptive) to dynamically control movement strategies [22, 23]. These perceptual-motor deficits are reflected in biomechanically inefficient strategies (e.g., excessive knee valgus or ankle inversion during unanticipated cutting) related to injury risk (e.g., knee and ankle sprains, respectively) and/or an over-reliance on certain types of perceptual information at the decrement of others [24]. Not surprisingly, altered perceptual-motor function is highly associated with second injury in sport [13, 25–36]. In response, neuromuscular-based rehabilitation (NMR), a class of interventions specifically designed to teach safer and biomechanically efficient movement patterns, has been promoted as the standard of care for the last 15 years [21]. Despite the dynamic exercises and targeted training of NMR to alleviate these deficits, second injury remains a significant health burden for athletes [13].

There are several reasons for the limited effectiveness of NMR to prevent second injury. First, while NMR is more advanced than a one-size-fits-all injury-specific approach to treatment, there remains a large amount of variability and subjectivity among providers and programs in terms of the degree of personalization offered to athletes. In addition, NMR interventions focus on correcting joint-specific movement patterns in sterile clinical environments, but fail to facilitate integration of learned patterns into more global motor strategies employed by the athlete in the field of play [37]. Exercise progression of an NMR program is also based on a linear loading strategy: as the athlete successfully performs a given exercise, load is increased incrementally (e.g., weight is added prior to the next exercise repetition) [38]. This strategy is adequate to facilitate stress-based adaptations in local body function (e.g., increased muscle strength), but is insufficient to challenge the more global perceptual-motor processes that support complex, sports performance in highly variable environments [39]. Furthermore, current NMR only promotes robustness to experienced loads and is not optimally equipped to encourage positive

adaptability to future loads that are outside of the trained range [40, 41]. To compound the problem, the training strategies used to teach safe biomechanics require injured athletes to think explicitly about how they are controlling their body movement, and analytically about how to use feedback to improve their biomechanics. The resulting internal focus of attention can hamper motor learning, and may even impair global movement performance in complex sports contexts [42, 43]. Additionally, it can magnify kinesiophobia by directing the attention of athletes to the injured location [44, 45]. As a result of promoting internal focus of attention, current NMR often inadvertently impairs the automaticity of perceptual-motor processes that it is supposed to promote.

### 1.2 Precision Phenomics in Sports Medicine: An Alternative Approach

To stem the tide of second injury, radical changes to existing methods of assessment and intervention are required. Specifically, the field of sports medicine needs an approach that allows for the objective and precise profiling and personalized targeting of the complex system of components and processes that underlie injury-related dysfunction—including the perceptual-motor processes that underlie adaptable performance. Importantly, these must be considered in the context of the athlete embedded in the environment rather than with the athlete in isolation [13, 37, 46]. This requires technologies (i.e., mixed-reality environments presented via wireless head mounted displays) that allow for the presentation of true-to-life environments while tightly controlling for systematic variations to objectively quantify the athletes' responses in meaningful ways. This allows for the development of interventions that take into account the dynamics of athletes' responses to changes in environmental parameters (i.e., the *dose-response* dynamics). Importantly, these responses must be indexed via changes to athlete-specific performance variables relative to the environmental parameters within which the athlete performs. Ultimately, such an approach must deliver the right intervention with the correct dose at the right time, with minimal negative consequences and maximum efficiency, the explicit goal of the *Precision Medicine Initiative* [47].

Precision medicine approaches that profile and target complex disease states have shown great promise in the medical specialties of oncology, immunology, and pharmacology [48, 49]. These approaches utilize panomic technologies via molecular genotyping to inform precision treatments. As a result, this model provides a starting point to transform second injury care but, unfortunately, a direct translation of the classic genomics model of precision medicine to sports medicine is not generally practical. For example, genomic and epigenetic markers are often expensive in terms of financial, time, and physical resources (e.g., blood draws require trained experts, medical-grade materials and hygienic processes, and freezers capable of extreme low temperatures for longer-term

storage). While technological and analytic advances are being made to obtain these types of data in more efficient ways (e.g., sensor clothing, salivary markers), such markers have demonstrated high sensitivity to physiological adaptation due to exercise and physical activity, and can be easily conflated with a variety of additional factors that are not necessarily meaningful to injury recovery [50, 51].

To address these limitations in the context of sports medicine, the current chapter presents a parallel approach and methodology that leverages behavioral phenomics in place of genomics to support a biomedical software platform we call the Intelligent Phenotypic Plasticity Platform ($IP^3$). This platform supports the intelligent assessment and computation of individualized behavioral (i.e., phenomic) profiles that capture an athlete's readiness to adapt to variable environmental conditions (i.e., individualized adaptability profiles). It then delivers personalized interventions based on these profiles to optimally load the perceptual-motor system of the athlete and simultaneously (and implicitly) facilitates the athlete's adaptive responses to contextual adversities.

### 1.3 Athlete Profiles of Phenotypic Plasticity

The construction of a phenomic profile to index an athlete's risk for second injury requires the assessment of interacting factors that support an athlete's ability to modify behavior in response to dynamic sport environments. In short, it requires assessment of the athlete's phenotypic plasticity [46, 52]. *Phenotypic plasticity* is a modifiable, global characteristic of an athlete that captures their capability to positively adapt to environmental challenges, or stressors [53]. Importantly, phenotypic plasticity is ubiquitous across myriad systems and behavioral scales. It is assessed through the computation of stress-response profiles [53], which are constructed with successive measurements of athletes' behavioral responses obtained as they perform a task under various levels of environmental stress [46]. Mixed-reality (XR) uniquely allows for the control and presentation of environmental stress to the athlete, and the athlete's behavioral responses can be captured in real time at multiple scales, using one or more associated *fitness* variables. Fitness is contingent on a number of phenotypic characteristics including, for example, neural, epigenetic and perceptual-motor plasticity [52], and fitness variables represent the emergent behavior of the underlying system processes as a function of specific types of stress (Fig. 1). Each fitness stress-response curve is thus a profile of phenotypic plasticity, which indexes to what extent a target function would thrive under various amounts of stress.

Profiles of athletes' phenotypic plasticity, built from their fitness response(s) to variations in contextual conditions, inform the development of precise guidelines to promote local responses and global adaptation to stress. The first step is the identification of specific behavioral (i.e., fitness) variables that are relevant to

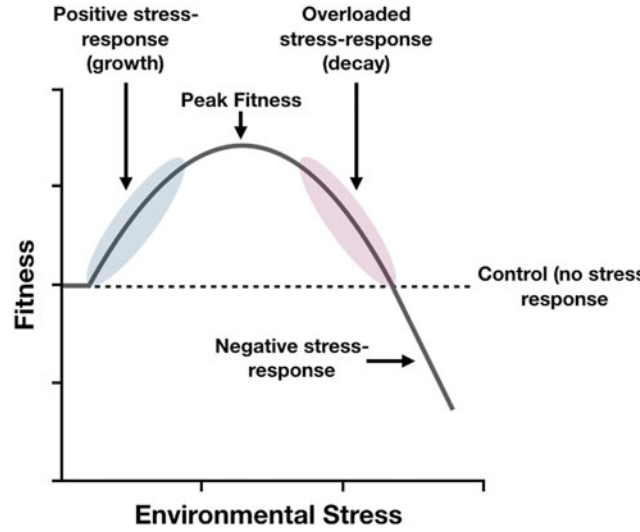


**Fig. 1** An example of a stress-response curve. Note the areas of growth and decay on opposite sides of the peak response region of the curve. The dotted line indicates the fitness response relative to a "no-stress" condition

adaptive performance within a given performance context (*see* Methods Subheading 3.1, **steps 3** and **4**). The change of the fitness variable(s) is then measured relative to a continuum of low stress-high stress performance contexts. The result is an ordinal fitness-based stress-response curve based on the value of the fitness variable relative to each increase in stress, or adversity (Fig. 2). The area under the curve is the phenotypic plasticity relative to the specific fitness measure(s) across the specific continuum of environmental performance contexts through which it was assessed.

Phenotypic plasticity provides a comprehensive approach to objectively index athletic adaptability to heterogeneous sport environments and performance contexts. Its computation recognizes the dynamic nature of adaptive processes underlying functional performance, which emerge from the interaction of the athlete with the task environment. Specifically, phenotypic plasticity is highly sensitive to the behavioral transitions the athlete makes to achieve more efficient performance states. This is because it is an index of change due to embeddedness of the athlete and the environment—i.e., behavioral change as a function of environmental change. What follows is a description of IP$^3$, the automated platform our team has developed to profile the phenotypic plasticity of athletes, and the method for leveraging the identified profiles to precisely target injury-induced performance deficits. This platform is thus optimally adapted to support precision phenomics in sports medicine.

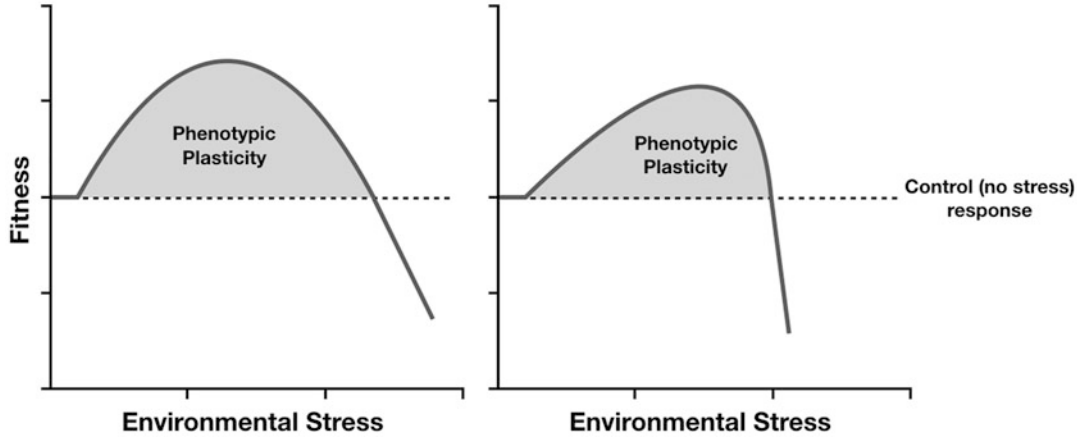


**Fig. 2** Two examples of ordinal fitness curves. The *left* curve is an example of a gradual increase to a peak fitness response, followed by an equally gradual decay. The *right* curve is an example of a more gradual increase to a lower overall peak fitness response (compared to the left example). Following the peak response there is a rapid decay of fitness. In comparison, the system on the right did not achieve as high of a peak fitness response and was overwhelmed by stress sooner, with a more rapid decline in fitness, compared to the system on the left

## 2 Materials

IP$^3$ leverages behavioral measures at multiple scales of measurement (e.g., neurophysiological, biomechanical, perceptual) that are assessed in the context of task performance within dynamic mixed-reality environments. The materials used to assess fitness, and thus phenotypic plasticity, will be described in turn.

### 2.1 Neuro-physiological Measurement System

1. Eight *Trigno*™ *Avanti* wireless electromyographic (EMG) sensors (27 × 37 × 13 mm, mass: 14 g; Delsys, Inc., Natick, MA) capture surface muscle activation at a sampling rate of 2000 Hz.

### 2.2 Physiological Measurement System

1. An *E4* wristband (Empatica, Inc., Boston, MA) records physiological data (case: 44 × 40 × 16 mm, max wristband length: 190 mm, mass: 25 g). Onboard sensors include:
   (a) Triaxial accelerometer (sampling rate: 32 Hz).
   (b) Photoplethysmogram (PPG) sensor (sampling rate: 64 Hz).
   (c) Galvanic Skin Response (GSR) sensor (sampling rate: 64 Hz).
   (d) Infrared (IR) thermopile (sampling rate: 64 Hz).

### 2.3 Performance Self-Report

1. A customized 10-point Likert scale indexes the rate of perceived exertion from a verbal self-report of perceived exertion and is sampled at the conclusion of each performance trial.

### 2.4 Kinematic Measurement System

1. Twelve digital video cameras (90 × 25 × 25 mm, maximum range: 10 m; Intel® RealSense™ Depth Camera D435, Intel Corp., Santa Clara, CA), each equipped with a Red-Green-Blue (RGB) sensor resolution of 1920 × 1080 (frame rate: 30 frames per second; field of view of 69.4° × 42.5° × 77°), a monochromatic stereo depth field of view of 87° ± 3° × 58° ± 1° × 95° ± 3° (max output resolution: 1280 × 720, frame rate: 90 frames per second), two infrared (IR) time of flight sensors, and a global shutter allowing for capture at up to 240 Hz.
2. Proprietary pose-estimation software (wrnchAI, Inc. Montreal, QC, CA) digitizes kinematic movements and behaviors via pose-estimation algorithms and computer-vision based extrinsic calibration techniques to calculate positions from the RGB and/or IR video streams listed in Subheading 2.4, **item 1**. This software enables real-time capture with a solver frequency exceeding 100 Hz.

### 2.5 Perceptual-Motor and Positional Measurement (and Display) System

1. An Oculus Quest (wireless head mounted display (HMD; weight: 571 g; Facebook Technologies, LLC, Irvine, CA) with a display resolution of 1440 × 1600 per eye (sampled at 72 Hz) presents immersive simulation environments with a field of view approximately equal to 100°. The athlete's position and orientation are tracked in both the real and simulated environment via onboard real-time inside-out tracking as indexed via Inertial Measurement Unit and IR depth sensors.
2. Custom binocular eye-gaze tracking technology (Tobii, Inc., Stockholm, SE) is integrated into the HMD eye-gaze tracking technology to capture binocular eye gaze (i.e., oculomotor) variables at 100 Hz.

## 3 Methods

IP$^3$ is implemented in two distinct steps: (1) phenomic profiling (*see* Subheading 3.1) and (2) precision treatment (*see* Subheading 3.2). A flow diagram schematic of IP$^3$ can be seen in Fig. 3, and a software schematic of IP$^3$ can be seen in Fig. 4.

### 3.1 Phenomic Profiling

The computation of phenomic profiles requires the design of task environments that vary in their characteristics depending on the particular type of function to be optimized. The following describes the initial task environment that our team has implemented and tested. This particular task environment assesses an athlete's ability to safely and efficiently navigate a general sports environment (e.g., appropriately responding to task constraints while avoiding high-risk injury maneuvers).

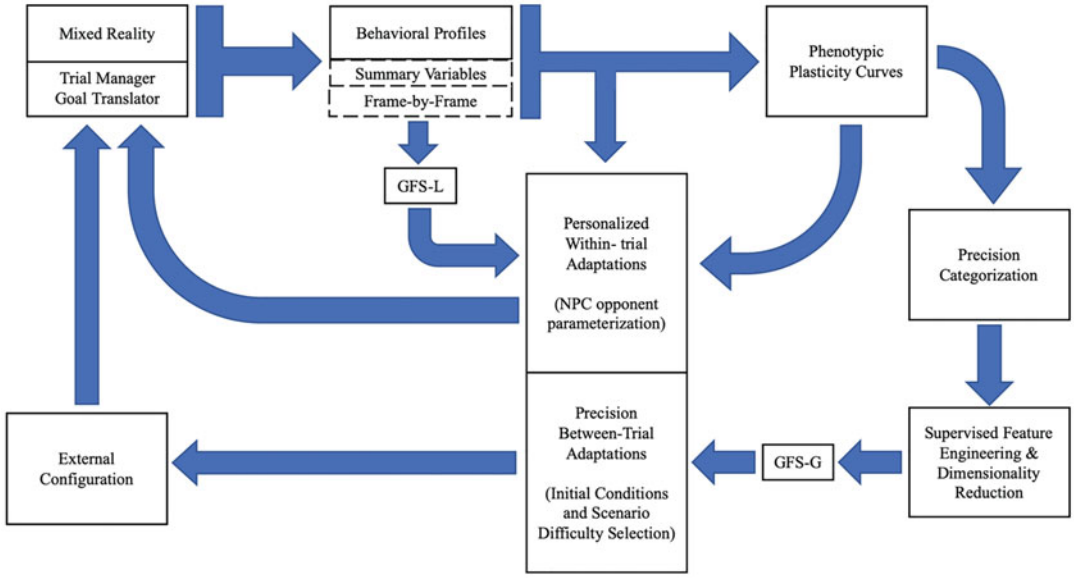


**Fig. 3** A schematic of the IP$^3$ system. External configuration files form the foundational *component* of the logic system that drives progression through IP$^3$. This component is responsible for deploying Unity 3D modules that, in turn, are the building blocks for each mixed-reality scenario, including both the performance task context and the initial positions and subsequent behaviors of all non-player characters (NPCs) present in a given scenario—*see* Subheading 3.1, **step 1**. Behavioral profiles and summary variables are computed and processed (*see* Subheading 3.1). Phenotypic plasticity curves (*see* Subheading 3.1, **step 3**) are computed and submitted to the genetic fuzzy system global (GFS-G) model (*see* Subheading 3.3, **step 2**) to determine the between-trial loading adaptations. Likewise, summary variables and frame-by-frame data are fed into the genetic fuzzy system local (GFS-L) model (*see* Subheading 3.3, **step 1**) to personalize the within-trial behaviors of NPCs

The first step, phenomic profiling, indexes the fitness and phenotypic plasticity of an individual athlete for personalizing the Precision Treatment of **step 2** (*see* Subheading 3.2).

1. Athletes are presented with sport-like scenarios in XR via a wireless HMD. These scenarios consist of virtual non-player characters (i.e., NPCs) with behaviors that are parameterized to challenge the athlete. These NPCs perform one of two roles in the scenario: (1) as competitors that will interfere with the athlete's task performance or (2) teammates that will cooperate with the athlete to achieve task goals. Each scenario requires the athlete to intercept a moving NPC *target* either by itself, or in the presence of three NPC *opponents*, with the functional simulation space equal to 16 × 10 m (*see* Figs. 5 and 6). The scenarios were built using the Unity 3D game engine before being compiled into an application and deployed to the XR HMD. The application is responsible for accepting real-time streaming data inputs from the various peripheral systems described in Subheading 3.5. Each scenario presents the athlete

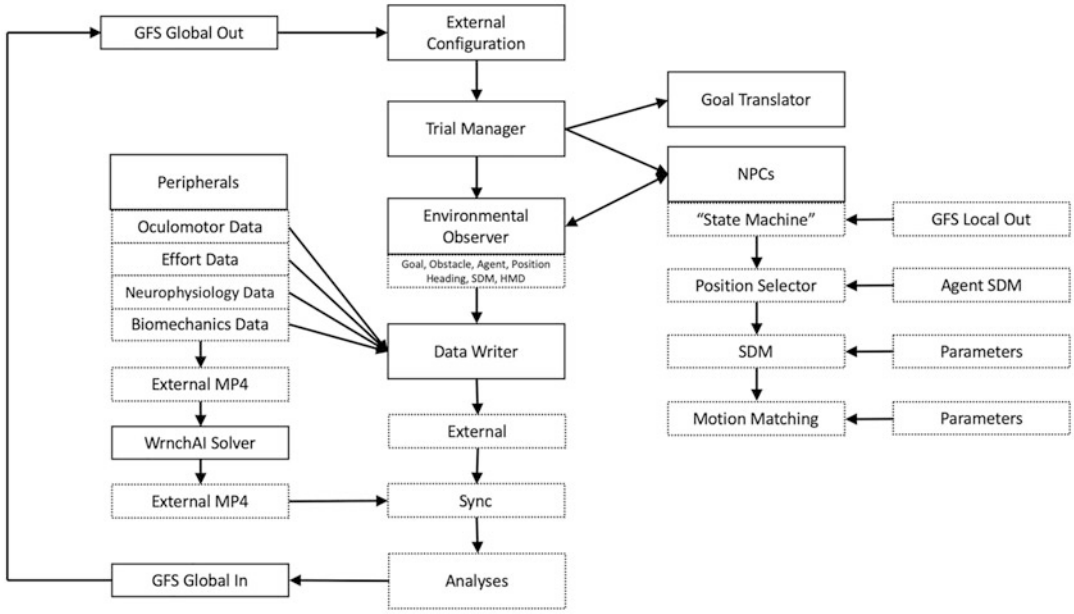


**Fig. 4** Schematic showing interactions between the various scripting components, data streams, and GFS models. External configuration data are passed to the Trial Manager component which implements a given configuration by dictating the initial conditions of the Goal Translator and the opponent NPCs. An Environmental Observer component has complete knowledge of the scene and generates a representation of the state of the virtual environment at each time step, including the positions, orientations, and velocities of the athlete, the goal NPC and all opponent NPCs. In order for the NPCs to respond appropriately in the environment, the NPCs State Machine component polls the environmental state data structure from the Observer. The Observer is polled at a variable rate to control the responsiveness of the athlete, and individual subsystems drive the NPC behavior for a given trial (*see* Subheading 3.4). At each time step, the environment state and all data from peripheral devices (i.e., devices utilized to capture neurophysiological data, physiological effort data, and pose estimations for kinematic data (*see* Subheadings 3.1 and 3.5) are passed to the Data Writer component, where they are collated, time stamped, and exported to an external file. Once a given session is completed, these data are synced with the WrnchAI pose estimation solver for analysis. The resultant information from the analysis is used as the input for GFS-G. The product of the GFS-G model is then used to modify the external configuration for subsequent trials

with a level of difficulty based on NPC behavioral characteristics that are driven by changes made to parameter values in Eq. 1 (*see* Subheading 3.4)—i.e., the $k$ and $b$ parameters, which determine the sensitivity of the NPC opponent responsiveness to the athlete. Therefore, each scenario presents a different level of difficulty that the athlete must perform three times: that is, the athlete performs three trials of equal difficulty but each trial begins with a unique set of initial conditions (i.e., the starting position of all NPCs are pseudo-random). Seven scenarios are presented in a block randomized order so that the athlete experiences a scenario with the same level of difficulty on three consecutive trials (block), with the order of each scenario (block) randomized (*see* **Note 1** for specific session

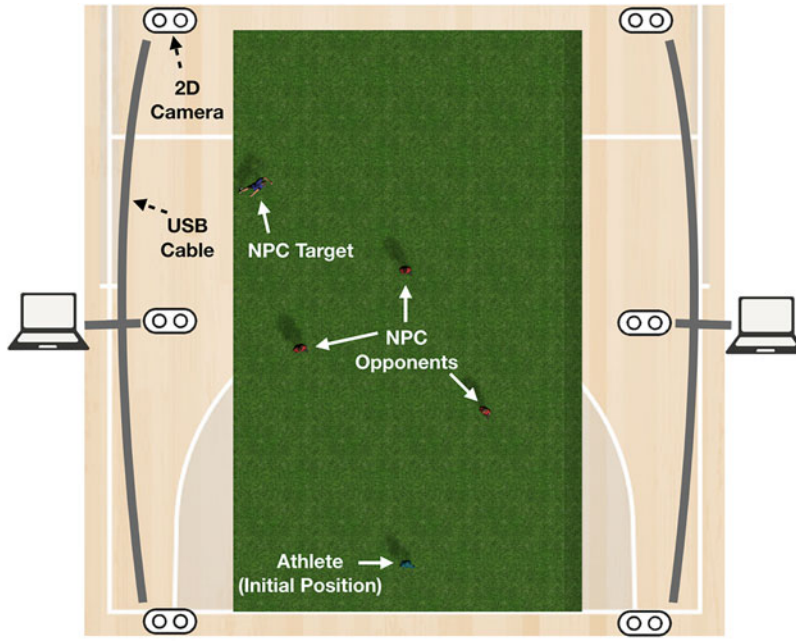


**Fig. 5** Schematic of portable camera configuration. Each camera emplacement consists of 2 cameras on a single tripod, connected via 10 m USB-C cables to a controlling laptop. Laptops calibrate to the same origin, creating a single 16 × 10 m capture volume in which the virtual scenario is placed. *See* **Note 3** for a description of each piece of equipment represented in this figure

details). This is the number of levels needed to build a reliable fitness curve (*see* Subheading 3.1, **step 3** and **Note 1**). The athletes are also presented with six *control* trials in which they must intercept a moving NPC target in the absence of any NPC opponents. These are used for the normalized computation of fitness, and the resulting phenotypic plasticity, as described in Subheading 3.1, **step 3**.

2. During each trial, data describing the state of the scenario environment is collected on a frame-by-frame basis. Data is also summarized at the end of each trial, at which time all data is exported to serialized JSON files. *See* Fig. 7 for a schematic of the data output pipeline. Per-trial data includes measures of difficulty and athlete summary performance outcomes (i.e., time-to-target interception and number of collisions with NPCs). Frame-by-frame data includes time series of global position and velocities for the target, athlete, and NPCs. Additionally, NPC and athlete behavioral data is collected, including current behavioral state, and local positions of body segments (*see* Subheading 3.4 for NPC and Subheading 3.5 for athlete for more details).
3. These data are compiled and summary measures are computed for each trial and each scenario block. *See* Subheading 3.5 for a

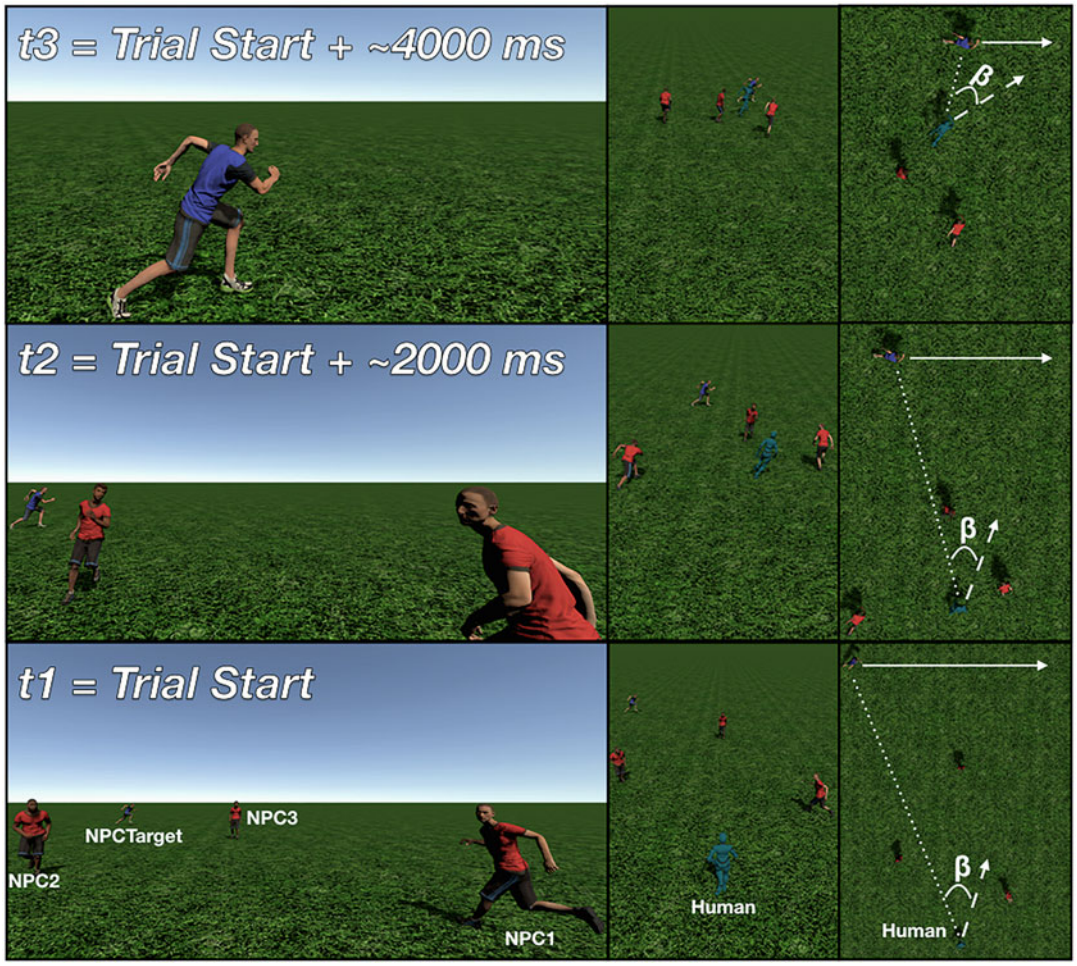


**Fig. 6** Bottom row—Initial conditions for an example three NPC trial from three perspectives: (1) First person view of the participant at the start of the trial (left), (2) third person view from behind the participant (middle), and (3) top down view (right). Middle row—Trial conditions at approximately 2000 ms into the trial, with left, middle, and right panels providing the same views as described above. Top row—Trial conditions at approximately 4000 ms into the trial, with left, middle, and right panels providing the same views as described above. The variable, β, indicates the bearing angle at each time, with a greater difference in β from *t*1 through *t*3 indicating less efficient interception performance of the NPC target by the human participant

list and description of individual measures. The summary data are then further divided into five fitness dimensions: (1) neurophysiological, (2) oculomotor, (3) biomechanical, (4) effort, and (5) locomotor behavior. The values of fitness variables that characterize each of these dimensions are normalized relative to values obtained on the control trials (discussed in Subheading 3.1, **step 1**) and plotted against scenario difficulty (*see* Fig. 2). The area under the curve is then computed and indexes the athlete's phenotypic plasticity for each fitness dimension. *See*

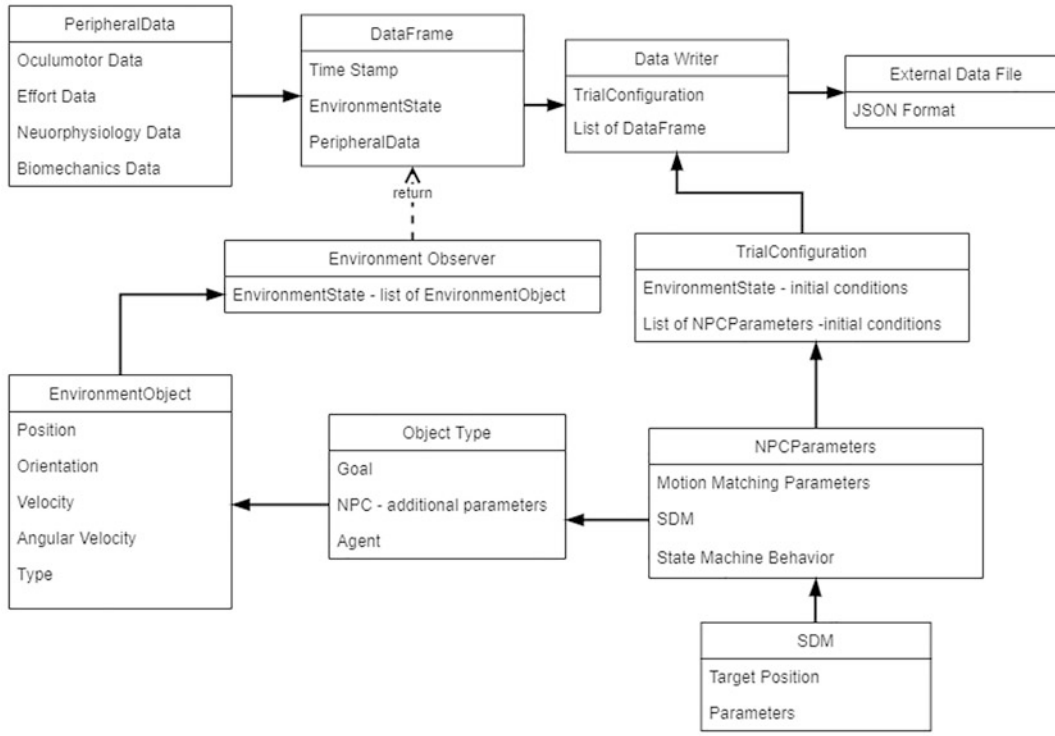


**Fig. 7** Schematic diagram illustrating interrelated classes and data structures that are saved for each trial. The DataWriter class collates per-trial initial condition data (a TrialConfiguration) and a list of per-timestep DataFrames. A DataFrame is a timestamped container for EnvironmentState data and PeripheralData from connected devices. The EnvironmentState for a given frame is a collection of EnvironmentObjects, which possess descriptors of position, heading, and object type—Goal, NPC, or Agent (the participant). NPC EnvironmentObjects possess additional descriptors, including Steering Dynamics Model data, Motion Matching animation parameters, and current state machine behaviors. All of this data is exported as a JSON, which is a hierarchical data format that maintains the relationships between these data structures

**Note 2** for an explanation of how our approach differs relative to the classic biological computation of fitness.

4. These data are also divided into within-trial epochs to extract time series of data (taken from each time step) from the time at which an athlete was within 2 m of a given NPC until the athlete's forward position in coordinate space indicates their passing of, or collision with, the NPC.

### *3.2 Precision Treatment*

The second step, Precision Treatment, utilizes all data collected during Phenomic Profiling (*see* Subheading 3.1). These data are used to train machine learning models that inform the presentation order and scenario characteristics of treatment (personalization of stresses). Each athlete returns for this treatment step on a different day from their participation in step one (*see* **Note 4** for specific session details).

1. Two types of genetic fuzzy system (GFS) machine learning models are trained based on data collected during the

Phenomic Profiling step (*see* Subheading 3.1): GFS local (GFS-L) and GFS global (GFS-G). GFS-L is trained via data inputs described in Subheading 3.1, **step 4** and is used to further parameterize NPC behaviors beyond the NPC steering control models described in Subheading 3.4 to personalize the within-trial difficulty of the opponent NPCs. For example, a GFS-L prediction of the direction an athlete will move to navigate the environment at a given time point may guide a given NPC to move towards the athlete's expected future position before the athlete reaches that position, thus forcing the athlete to adapt their navigation trajectory. GFS-G is trained based on two sets of inputs: (1) summary scores for a given fitness scenario difficulty for each of the five fitness dimensions and (2) the overall phenotypic plasticity score for each fitness dimension. The output of this model is used to specify the initial conditions of each trial, which determine the presentation order of trial to trial difficulty. GFS-L and GFS-G combine to make up the artificial intelligence (AI) system for $IP^3$, and each is trained and validated via a proprietary Fuzzy Bolt method (*see* Subheading 3.3 for details).

2. As in step one (*see* Subheading 3.1, **step 1**), each athlete is again presented with sport-like scenarios in XR via a wireless HMD. Each scenario again requires the athlete to intercept a moving NPC *target* in the presence of three NPC *opponents*, with the functional simulation space the same as in step one. The treatment step first presents seven scenarios to the athlete that match the seven scenario difficulties that the athlete was presented with in step one. The athlete performs two trials each of these scenarios, with each scenario presented in random order. The athlete's performance on these scenarios are used to build a fitness curve that is then compared to the athlete's fitness and phenotypic plasticity computed during step one. If major deviations exist (i.e., a standard deviation of a given fitness value that is greater than 2.5 times the step one fitness value), then the GFS-G model will be updated with the new fitness values and phenotypic plasticity score.
3. Following completion of the seven scenarios, the athlete is then presented with up to 35 scenarios (two trials per scenario) in which the presentation order of scenario difficulty is determined by the GFS-G model. The data from the athlete's current performance, identical to those described in Subheading 3.1, **step 3**, are used as inputs into the GFS-G model to generate a performance prediction (*see* Subheading 3.3, **step 2**). The output of the model is then submitted to a scenario difficulty selection heuristic. Specifically, each scenario difficulty is identified via a cutoff threshold such that only scenario difficulties that would result in an athlete fitness score of

75–100% of their previously demonstrated maximum fitness score are utilized. *See* **Note 4** for specific treatment details. In addition, within-trial NPC characteristics are driven by real-time prediction analytics of GFS-L—based on data from the athlete's moment-to-moment performance as per Subheading 3.1, **step 4** and combined with predicted navigation behaviors from the steering dynamics model equations presented in Subheading 3.4, **step 2**. In other words, the GFS-L model prediction is integrated with predictions of the athlete's overall locomotor trajectory for a given trial—the median trajectory based on 100 simulations run at each time point (i.e., frame). *See* Subheading 3.3, **step 1** for full GFS-L model details.

### 3.3 Artificial Intelligence System

The GFS portion of the AI system is trained using a proprietary Fuzzy Bolt method. Fuzzy Bolt is a GA-based algorithm that can be used for training fuzzy inference systems (FIS) with several inputs. Unlike previous approaches of training fuzzy systems, Fuzzy Bolt scales well to large input spaces. Fuzzy Bolt intelligently reduces the search space via a standard single $n$-input-$p$-output system and is also able to reduce the number of parameters that need to be tuned. This also reduces the chances of overfitting. Fuzzy Bolt is computationally efficient as it is able to train even large systems with tens or hundreds of inputs within minutes on a basic 8GB RAM CPU. The number of parameters does not increase substantially even when the number of membership functions for the inputs and outputs are increased. This provides more flexibility for the designer as they can make changes to design parameters with minimal effect on the overall training time.

Irrespective of model type (i.e., GFS-L or GFS-G), relevant input-output data pairs are split into training and hold-out validation sets (80% and 20% of the total data, respectively). The GFS parameters are changed based on the model performance relative to the training data only. During each generation, the best GFS in that generation is evaluated on the validation set to ensure that the model generalizes well on data that has not been used for tuning the parameters. Minimum and maximum normalization are applied to the training data such that all attribute values are in the range $[-1, 1]$. The same minimums and maximums are used to normalize the validation set as well. Genetic algorithms (GA) tune the parameters of the GFS to minimize the defined cost function.

Two GF model systems were trained, that combine to form our GF-based AI system for personalized and precision treatment.

1. The GFS-L model is a hybrid model that classifies for whether an athlete will pass to the right or left of a given NPC during a

local athlete-NPC interaction (*see* **Note 5**) and integrates these predictions with the results of a real-time implementation of the steering dynamics model (SDM; *see* **Note 5**) for trajectory prediction. The classifier utilizes 11 inputs that are computed in real time and fed into the model at each time step: (1) absolute NPC angle relative to a static reference axis, (2) rate of change of the absolute NPC angle, (3) rate of approach of the athlete with respect to the NPC, (4) rate of change of the heading angle, (5) athlete heading relative to the NPC angle, (6) relative distance of the athlete to the NPC, (7) the NPC's current heading, (8) the NPC's current speed, (9) the athlete's current heading, (10) the athlete's current speed, and (11) the solution to the SDM model equation for that specific time step. The model then takes into account the median location prescribed by 100 SDM (eqs. 1 and 2 in **Note 6**) simulations to output a predicted location for each time point *(t)* through $t + 2000$ ms. The purpose of the GFS-L model is thus to make the most accurate prediction of the probabilistic navigation trajectory the athlete will take up to 2000 ms prior to the actualization of the behavior. Since the objective is to ensure the GFSs are able to make accurate predictions, a suitable performance function can act as a fitness function. In this case, since the objective is to improve accuracy, we define *prediction accuracy* as the fitness function for evolving each GFS model.

2. The GFS-G model specifies the initial conditions of each trial, as well as the difficulty level of the next scenario to be presented. As per Subheading 3.2, **step 1**, this model is trained on summary scores for a given fitness scenario difficulty for each of the five dimensions, as well as the overall phenotypic plasticity score for each fitness dimension. Specifically, the model will train to predict the outcome of how efficiently the athlete intercepted the moving NPC target, irrespective of scenario difficulty. Efficiency is indexed via a control strategy in which the athlete minimizes the change in the target-athlete bearing angle, $\dot{\beta}$ (*see* Fig. 6). Via Fuzzy Bolt, the GFS-G model will be trained to minimize the root mean squared error between predicted and actual $\dot{\beta}$ (*see* **Note 5**).

### 3.4 NPC Behaviors

1. *NPC Target Behavior*

   The NPC target follows a pre-determined linear trajectory that is orthogonal to the length of the capture space, with the target's initial position always originating in the athlete's field of view (*see* Fig. 6).

2. *NPC Opponent Behavior*

   Each opponent NPC is programmed to intelligently impede the progress of the human athlete via four interrelated

systems that, together, drive NPC navigation and locomotor behavior. The first is a finite state machine that defines several high-level behaviors, including interception, pursuit, and containment and the heuristics for transitioning among them. In addition, the output from our customized GFS-L model (*see* Subheading 3.3, **step 1**) provides the state machine with specific inputs, personalized to the individual athlete, which constantly redefines NPC movement behaviors. Second, a goal identification heuristic system determines where the NPC needs to move in order to fulfill the NPC's movement goal (i.e., to impede the athlete's progress at a given time step). This system considers the most recent state received from the observer (*see* Subheading 3.1) in combination with the predicted trajectory space for the athlete at a given time step. The input from this system is then provided to the third (NPC steering) system to inform each NPC's direction of travel. *See* **Note 6** for model details.

The rate of change in speed, or acceleration, of each NPC is controlled independently from the NPC steering system via an animation system grounded in real human biomechanics (*see* **Note 7** for details and an alternative strategy). This system enables NPCs to smoothly decelerate to realistically avoid collisions with obstacles (or the athlete) in its path. In cases when the NPC cannot realistically modify its heading direction (as specified by the steering system) relative to the proximity of the human athlete or another NPC and their respective movement speeds, then the NPC will come to a complete stop. The top end speed of each NPC is dependent on the human from which the NPCs biomechanics are motion matched. The outputs of this process (i.e., NPC position, orientation, and speed) feed back to the observer (Fig. 4) in real time, and are distributed to all NPCs in the scene.

### 3.5 Data Collection Peripherals and Associated Variables of Interest

Each data type is filtered and smoothed using previously published parameters specific to each modality prior to the computation of specific variables of interest. *See* **Note 8** for data reduction details.

1. *Neurophysiological*

   Wireless EMG sensors are used to capture surface EMG data from sites on both the right and left side of the body: (1) quadriceps femoris, (2) biceps femoris, (3) soleus, and (4) latissimus dorsi. This data indexes muscle pre-activation and activation during acceleration, deceleration, and cutting maneuvers as the athletes interact with each mixed-reality scenario. Prior to placement of each EMG sensor onto the skin, the target surface area is cleaned using an alcohol pad and abraded. Each sensor is attached on top of the skin at each belly of the designated muscle using double-sided tape. The

sensors are aligned with muscle fiber orientation to optimally capture motor unit firing. Indices of muscle activation are mapped to biomechanical data and both proportional muscle activation levels—based on the maximal activation of each muscle during the athlete's entire profiling session—and ratios of muscle activation asymmetries are computed, for a total of 12 summary variables (eight variables of proportional activation that correspond to the right and left muscle sites, and four variables of asymmetry based on the four right-left muscle site pairs).

2. *Oculomotor*

   Binocular eye-gaze tracking technology is embedded within the HMD. Two-dimensional gaze position data (x- and y-coordinate positions) are collected for each eye. Several eye movement variables are computed from a given scenario trial: (1) the total number of saccades, (2) average saccade velocity, (3) variability of saccade velocity, (4) total number of fixations, (5) average fixation time, (6) variability of fixation time, and (7) total gaze area—a composite measure based on both head and eye position that quantifies the amount of the visual environment that was scanned for a given trial.

3. *Biomechanical*

   Pose-estimation data are streamed over a network connection and saved locally to JSON format. Twenty-one kinematic measures are computed from the pose-estimation data to index the angular excursions around the sagittal, frontal, and transverse planes for each of the ankles, knees, hips, and trunk.

4. *Effort*

   At the end of each scenario block, athletes self-report their level of perceived exertion, perceived performance and frustration level on separate 10-point visual Likert scales displayed in the HMD. Real-time physiological data are also recorded via a wearable wristband sensor. These data are used to objectively quantify physical exertion levels at three time points: (1) baseline, prior to participation in any XR scenarios, (2) after completion of half of the presented XR scenarios, and (3) at the conclusion of the session. For each of the three time points, heart rate variability and galvanic skin response data will be computed, based on 60 s of data at each time point.

5. *Locomotor Behavior*

   The HMD provides frame-by-frame positional data related to locomotor heading trajectories, locomotor speed, and simulated collision forces between the athlete and virtual characters during a scenario trial. From these data, eight summary performance measures of the athlete are computed: (1) time it took to reach the target, (2) number of collisions with NPCs,

(3) average movement speed in direction of travel, (4) maximum impulse—the maximum change in velocity standardized to the athlete's body mass, (5) maximum turning rate, (6) minimum distance to an NPC, (7) variability of acceleration along the straight-ahead axis, and (8) number of turns standardized to the number of NPCs present.

### 3.6 Data Synchronization

The EMG, eye-gaze, and physiological data peripherals provide Software Development Kits (SDKs) enabling the programming of custom software. The Unity engine is able to natively run the SDKs from these systems to deliver the digital data over remote network connections to enable processing and timestamping of all data at each frame. For those data captured at different frequencies than the Unity platform, the data was saved in separate files within the Unity platform and back-processed post-hoc with the timestamp from the environment capture.

## 4 Notes

1. *Phenomic Profiling*

   In step one, the athlete performs up to 111 trials of an athletic navigation task in the AR environment in which he or she runs to intercept a moving NPC target while avoiding NPC opponents. There are two evaluation sessions that consist of 35 sub-blocks, with 1 to 2 trials per sub-block to equal 3 total trials for a given condition across the entire session. In addition, each block contains 3 control trials where there are no NPCs in the virtual scene. Thus, each assessment block contains either 55 or 56 total trials, counterbalanced for each athlete, resulting in up to 111 total trials across the evaluation session. Athletes are also given a ~5–10 min break between the two assessment blocks.

2. *Fitness and Phenotypic Plasticity Profiles*

   Traditionally, biological fitness and, thus, phenotypic plasticity, has been indexed via a single fitness variable and the change of that variable across stress, respectively [53]. We innovate on this approach by constructing several fitness factors via a confirmatory factor analysis that linearly combines a group of related (fitness) variables into a single fitness dimension (Fig. 8). We have targeted, *a priori*, five dimensions of fitness, including: (1) neurophysiological, (2) oculomotor, (3) biomechanical, (4) effort, and (5) locomotor behavior. Each of these dimensions served as a singular input for the genetic fuzzy system AI, described in Subheading 3.3.

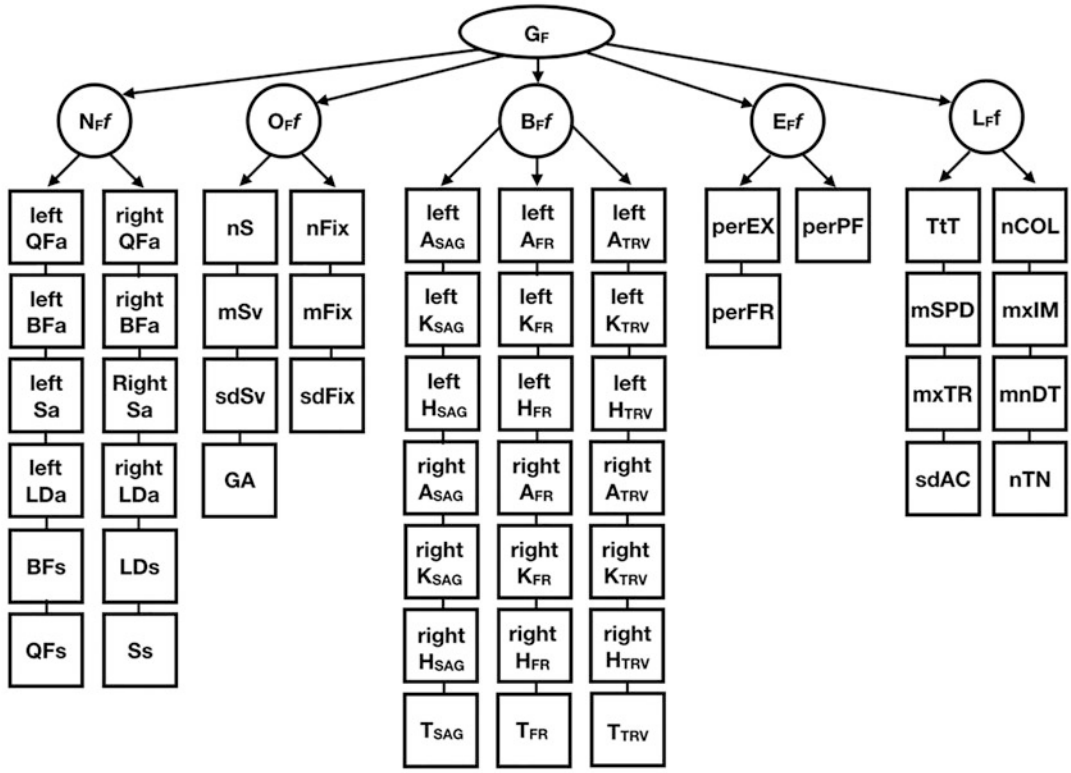


**Fig. 8** An illustration of our factor analysis design. $G_F$ (Global Fitness) is a second-order latent variable, with $N_F$f (Neurophysiological Fitness factor), $O_F$f (Oculomotor Fitness factor), $B_F$f (Biomechanical Fitness factor), $E_F$f (Effort Fitness factor), and $L_F$f (Locomotor Fitness function) as latent variables (i.e., dimensions). Each square below the latent variables symbolizes a specific measured variable within each dimension. *Abbreviations*—Under $N_F$f: QF = quadriceps femoris, BF = biceps femoris, S = soleus, LD = latissimus dorsi, a = activation, s = synchronization; Under $O_F$f: S = saccades, Fix = fixations, v = velocity, n = number, m = mean, sd = standard deviation, GA = gaze area; Under $B_F$f: A = ankle, K = knee, H = hip, T = Trunk, SAG = sagittal plane, FR = frontal plane, TRV = transverse plane; Under $E_F$f: EX = exertion, PF = performance, FR = frustration, per = perceived; Under $L_F$f: TtT = time to target, COL = collisions, SPD = speed, IM = impulse, TR = turning rate, DT = distance to NPC, AC = acceleration, TN = turns, m = mean, mx = maximum, mn = minimum, sd = standard deviation, n = number

3. *Equipment Specifications*

(a) *Laptop*

The laptops in Fig. 5 are outfitted with Intel ninth generation i7-9850H processors, Nvidia Quadro RTX4000 Graphics cards with 16 GB of system RAM.

(b) *Cameras*

Intel® Realsense cameras were used for all kinematic movement capture. The cameras were extrinsically calibrated using a proprietary *wrnchAI* computer-vision system, which tracks the position and orientation of a ChArUco board in the scene (*see* Fig. 9). The origin of

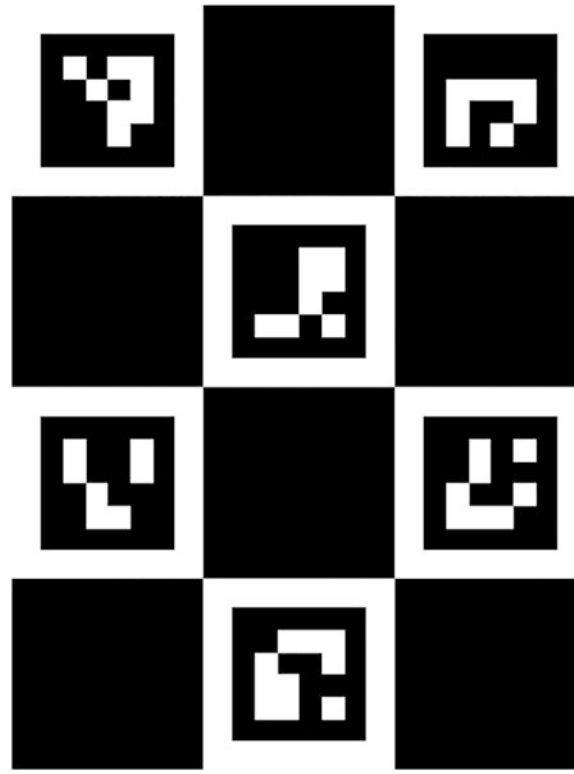

**Fig. 9** A sample 3′ × 4′ ChArUco board (each square equates to 1 ft.$^2$)

the capture volume is set by placing the board on the floor in full view of the master camera. Individual cameras are calibrated in a chain. The ChArUco board is held, and positioned such that is viewable by the master camera and a second camera. Once the second camera is calibrated, the board is positioned in view of the second and camera and third. This process is repeated until the position and orientation of all cameras are transitively calibrated relative to the origin.

A software platform designed to digitize movements and behaviors is integrated with motions captured from the cameras via the *wrnchAI* proprietary software. The software uses a pose-estimation algorithm to calculate positions from RGB or IR video streams. Additionally, the software platform uses a computer-vision based extrinsic calibration technique which accounts for multiple camera angles and collates the data from each camera into 3D joint positions. The collaboration between the portable camera setup and the software platform results in real-time performance capture with a solver frequency exceeding 100 Hz. Recorded camera data is utilized for post-hoc

pose estimations allowing for more solver iterations and a sampling rate equal to that of the cameras.

(c) *Miscellaneous*

Additional equipment represented in Fig. 5 consists of: (a) twelve 10 m powered male-female USB-C 3.0 cables with active repeaters, (b) two seven slot powered USB 3.0 hubs (one per laptop), and (c) six standard 6.5′ adjustable tripods with custom 2-camera mounts on each tripod.

4. *Treatment Strategy*

Step two occurs no later than 3 weeks after step one and consists of three blocks of up to 96 total trials. The first block consists of 12 trials (six sub-blocks of two trials each) in order to mimic the NPC difficulty levels from the originally constructed fitness curve from step one. The second block consists of 14 trials (seven sub-blocks of two trials each) that mimics the condition-based loading difficulty levels of the originally constructed fitness curve from step one. The third block consists of up to 35 sub-blocks of two trials each, equaling 70 total trials. The difficulty order of these sub-blocks (as related to overall difficulty and NPC parameters) is determined by the athlete's personal fitness curve. The environments prescribed for treatment are identified via a cutoff threshold, in that only environments that result in an athlete fitness score at 75% or higher of their maximum fitness score are utilized. Performance is expected to reach a maximal value at a particular range of trial difficulty and then performance will begin to decrease until failure. Based on biology-based hormetic (i.e., bi-phasic dose-response) models [54], it is likely that athletes will adapt most efficiently during the (positive) growth phase of the dose-response curve, with dose targeting of that area of the curve, via the GFS-G model. This selection heuristic is driven by the hormetic framework (cf. Calabrese & Mattson [55]) in which small stressors are presented to induce positive adaptations and, as a result, higher fitness.

5. *Fuzzy Bolt Implementation*

GFS-L specifically integrates the results of our previously developed athlete-NPC interaction classifier for right vs. left passing [56] with the steering dynamics model (*see* **Note 6**). The control strategy to minimize the change in the target-athlete bearing angle, $\dot{\beta}$, is a well-defined and previously operationalized strategy for efficient and successful target interception during over-ground locomotion [57].

6. *Steering Dynamics Model*

The Steering Dynamics Model (SDM [57])—specifically, the moving goal (Eq. 1) and moving obstacle components of

the model (Eq. 2)—is used to update each NPC's direction of travel, or heading, by an angular acceleration value at each time step:

$$\ddot{\phi} = -b\dot{\phi} - k_t\left(-\dot{\psi}_t\right)\left(d_t + 1\right), \tag{1}$$

$$\ddot{\phi} = -b\dot{\phi} + k_m\left(-\dot{\psi}_t\right)e^{-c_5\left|\dot{\psi}\right|}\ e^{-c_6 d_m}. \tag{2}$$

Equations 1 and 2 describe how turning rate of the NPCs in a given task environment is influenced by their ongoing relationship to the athlete (the goal) and other NPCs (obstacles to be avoided on the way to the goal). Equation 1 relates the acceleration of a given NPC ($\ddot{\phi}$) to the rate of change of its orientation with respect to ($\dot{\psi}_t$). Acceleration for a given $\dot{\psi}_t$ depends on $k_t$—a stiffness term that captures how promptly the NPC responds to the athlete. The effect of $k_t$ on NPC acceleration is, in turn, modulated by the distance $d_t$. As the NPC turns towards the athlete (i.e., towards when $\dot{\psi}_t = 0$), acceleration goes to zero. Equation 1 has, therefore, a nullcline (or pseudoattractor) at $(\phi, \dot{\phi}) = (\dot{\psi}_t, 0)$. The damping term (b) simply avoids oscillations around the pseudoattractor.

Equation 2 generates turning accelerations of a given NPC as a function of the rate of change of its orientation with respect to other NPCs ($-\dot{\psi}$). Formally, this component adds a saddle point that creates repulsion away from $(\phi, \dot{\phi}) = (\dot{\psi}, 0)$. At any point, the current heading direction of a given NPC is determined by the resultant of attractive (Eq. 1) and repelling forces (Eq. 2), acting on an NPC. "Path selection" is, thus, a product of the unfolding of the NPCs interactions with the environment (here represented by the athlete performing the task, and the behavior of the other NPCs). The SDM always maintains perfect knowledge of the state of the environment, including the position of every other NPC and the athlete included in the model at each time step. The moving goal model is parameterized as $b = 3.25$, $k = 7.5$ and both $c1$ and $c2 = 0.4$. The moving obstacle model is parameterized as $b = -7.75$, $k = 6.00$, with both $c5$ and $c6 = 0.25$.

7. *Motion Matching System for Speed Control*

Motion Matching [58] was used to drive the speed control in the current version of the platform. Motion Matching selects an animation action from a library of motion-capture animations that adhere to biomechanical constraints of the human—in this case a separate data collection of the kinematics of volunteer athletes performing athletic maneuvers—from which they were collected. A given NPC is thus empowered to smoothly decelerate to realistically avoid collisions with obstacles (or the athlete) in its path. In cases when the NPC cannot realistically (i.e., via inherent biomechanical capabilities

of the NPC as specified via motion matching) modify its heading direction (as specified by the SDM) relative to the proximity of the human athlete or another NPC and their respective movement speeds, then the NPC will come to a complete stop. The outputs of the process, as feed through the observer and distributed to all in-scene NPCs (in real time) therefore provide a true-to-life presentation of the perception-action behaviors that emerge from each NPC-environment interaction.

An alternative approach to the motion matching method described in Subheading 3.4, **step 2** is to utilize a hybrid model. In this approach, the rate of speed, or acceleration, of each NPC is controlled independently from the SDM via a hybrid motion matching-soft-collision model (Eq. 3) system:

$$\dot{a} = \psi(\alpha) = -b_{\mathrm{d}}\left(x + d_{\mathrm{p}}\right) - b_{\mathrm{v}}\left(v - v_{\mathrm{p}}\right) - b_{\mathrm{a}}\left(\frac{a - a_{\mathrm{ideal}}}{a_{\mathrm{ideal}} - a_{\mathrm{min}}}\right). \quad (3)$$

The model is parameterized the same as the original instantiation [59], based on distance to the athlete. NPCs always attempt to accelerate to a speed that matches a preferred speed (4 m/s$^2$), with an affordance-based deceleration factor applied via Eq. 3 and also based on the distance to the NPC's defined target position, or to the nearest obstacle in the forward arc. The Motion Matching portion [58] selects an animation action from a library of motion-capture animations that adhere to biomechanical constraints of a given NPC. In combination with the soft collision model, a given NPC is empowered to smoothly decelerate to realistically avoid collisions with obstacles (or the athlete) in its path. In cases when the NPC cannot realistically (i.e., via inherent biomechanical capabilities of the NPC as specified via motion matching) modify its heading direction relative to the proximity of the human athlete or another NPC and their respective movement speeds, then the NPC will come to a complete stop via Eq. 3. The outputs of this process (i.e., NPC position, orientation and speed) feed back to the observer in real time just as they do in the primary method discussed in Subheading 3.4.

8. *Data Reduction*
   (a) *Neurophysiological Data*

   Raw EMG data are full-wave rectified and filtered using a band-pass Butterworth filter at 15–500 Hz and using a common mode rejection ratio of 130 db [60, 61]. The degree of muscle activity is determined by calculating the RMS for the amplitude of each EMG signal using a bin width of 30 ms [62].

(b) *Oculomotor Data*

For any missing data, linear interpolation is used to fill gaps of missing data ≤67 ms (four samples) [63]. The raw data are smoothed using a non-weighted, symmetrical moving average filter with an averaging window 83 ms (five samples) in length allowing for samples before and after the current sample to produce an average at that position [64]. If interpolation is needed, the filter is adjusted to account for samples less than 83 ms (see DiCesare et al. [63] for adjustment). After filtering, data are converted to absolute measures of displacement (cm) relative to the center of the target.

(c) *Biomechanical Data*

Prior to computation of joint-specific angles via custom algorithms, the raw kinematic data are output as three-dimensional position time series and each position time series is smoothed using a fourth-order, zero lag Butterworth filter with a cutoff frequency of 6.5 Hz [65, 66].

(d) *Locomotor Data*

The raw position time series data are submitted to a forward and backward fourth-order low-pass Butterworth filter with a cutoff frequency of 1 Hz, to remove any positional noise and attenuate high-frequency anterior-posterior fluctuations due to the athlete's step cycle.

## References


1. Steffen K, Myklebust G, Andersen TE, Holme I, Bahr R (2008) Self-reported injury history and lower limb function as risk factors for injuries in female youth soccer. Am J Sports Med 36(4):700–708. https://doi.org/10.1177/0363546507311598
2. Hägglund M, Walden M, Ekstrand J (2013) Risk factors for lower extremity muscle injury in professional soccer: The UEFA injury study. Am J Sports Med 41(2):327–335. https://doi.org/10.1177/0363546512470634
3. Freckleton G, Pizzari T (2013) Risk factors for hamstring muscle strain injury in sport: a systematic review and meta-analysis. Br J Sports Med 47(6):351–358. https://doi.org/10.1136/bjsports-2011-090664
4. Malliaropoulos N, Bikos G, Meke M et al (2018) Higher frequency of hamstring injuries in elite track and field athletes who had a previous injury to the ankle - a 17 years observational cohort study. J Foot Ankle Res 11(1):1–8. https://doi.org/10.1186/s13047-018-0247-4
5. Malliaropoulos N, Ntessalen M, Papacostas E, Longo UG, Maffulli N (2009) Reinjury after acute lateral ankle sprains in elite track and field athletes. Am J Sports Med 37(9):1755–1761. https://doi.org/10.1177/0363546509338107
6. Bahr R, Bahr I (1997) a. Incidence of acute volleyball injuries: a prospective cohort study of injury mechanisms and risk factors. Scand J Med Sci Sports 7(3):166–171. https://doi.org/10.1136/bjsports-2014-093593
7. Paterno MV, Rauh MJ, Schmitt LC, Ford K, Hewett T (2012) Incidence of contralateral and ipsilateral anterior cruciate ligament (ACL) injury after primary ACL reconstruction and return to sport. Clin J Sport Med 22(2):116–121. https://doi.org/10.1097/JSM.0b013e318246ef9e
8. Arøen A, Helgø D, Granlund OG, Bahr R (2004) Contralateral tendon rupture risk is increased in individuals with a previous Achilles tendon rupture. Scand J Med Sci Sports 14:30–33

9. Zemper ED (2003) Two-year prospective study of relative risk of a second cerebral concussion. Am J Phys Med Rehabil 82 (9):653–659. https://doi.org/10.1097/01.PHM.0000083666.74494.BA
10. Guskiewicz KM, Weaver NL, Padua DA, Garrett WE (2000) Epidemiology of concussion in collegiate and high school football players. Am J Sports Med 28(5):643–650. https://doi.org/10.1177/03635465000280050401
11. Nordström A, Nordström P, Ekstrand J (2014) Sports-related concussion increases the risk of subsequent injury by about 50% in elite male football players. Br J Sports Med 48 (19):1447–1450. https://doi.org/10.1136/bjsports-2013-093406
12. Hägglund M, Waldén M, Ekstrand J (2006) Previous injury as a risk factor for injury in elite football: a prospective study over two consecutive seasons. Br J Sports Med 40 (9):767–772. https://doi.org/10.1136/bjsm.2006.026609
13. Fulton J, Wright K, Kelly M et al (2014) Injury risk is altered by previous injury: a systematic review of the literature and presentation of causative neuromuscular factors. Int J Sports Phys Ther 9(5):583–595. http://www.pubmedcentral.nih.gov/articlerender.fcgi?artid=4196323&tool=pmcentrez&rendertype=abstract
14. Salmon L, Russell V, Musgrove T, Pinczewski L, Refshauge K (2005) Incidence and risk factors for graft rupture and contralateral rupture after anterior cruciate ligament reconstruction. Arthroscopy 21(8):948–957. https://doi.org/10.1016/j.arthro.2005.04.110
15. Paterno MV, Rauh M, Schmitt LC, Ford K, Hewett T (2013) Incidence of second anterior cruciate ligament (ACL) injury 2 years after primary ACL reconstruction and return to sport. Orthop J Sport Med 1 (4 Suppl):2013–2015. https://doi.org/10.1177/2325967113S00002
16. Herman DC, Jones D, Harrison A et al (2017) Concussion may increase the risk of subsequent lower extremity musculoskeletal injury in collegiate athletes. Sport Med 47(5):1003–1010. https://doi.org/10.1007/s40279-016-0607-9
17. Herman D, Zaremski J, Vincent H, Vincent K (2015) Effect of neurocognition and concussion on musculoskeletal injury risk. Curr Sports Med Rep 14(3):194–199. https://doi.org/10.1249/JSR.0000000000000157
18. Gabbe BJ, Bennell KL, Finch CF, Wajswelner H, Orchard JW (2006) Predictors of hamstring injury at the elite level of Australian football. Scand J Med Sci Sports 16 (1):7–13. https://doi.org/10.1111/j.1600-0838.2005.00441.x
19. Arnason A, Sigurdsson SB, Gudmundsson A, Holme I, Engebretsen L, Bahr R (2004) Risk factors for injuries in football. Am J Sports Med 32(1 Suppl):5S–16S. https://doi.org/10.1177/0363546503258912
20. Guyatt G, Cairns J, Churchill D et al (1992) Evidence-based medicine: a new approach to teaching the practice of medicine. JAMA 268 (17):2420–2425. https://doi.org/10.1001/jama.1992.03490170092032
21. MacAuley D, Best T (eds) (2003) Evidence-based sports medicine, 2nd edn. Blackwell Publishing, Malden, MA. https://doi.org/10.1080/00016470310014030
22. Kiefer AW, Ford KR, Paterno MV et al (2013) Inter-segmental postural coordination measures differentiate athletes with ACL reconstruction from uninjured athletes. Gait Posture 37(2):149–153. https://doi.org/10.1016/j.gaitpost.2012.05.005
23. Paterno MV, Kiefer AW, Bonnette SH et al (2014) Deficits in hip-ankle coordination in female athletes who suffer a second anterior cruciate ligament (ACL) injury after ACL reconstruction and return to sport. Orthop J Sport Med 2(2 Suppl):1–3. https://doi.org/10.1177/2325967114S00039
24. Song K, Burcal CJ, Hertel J, Wikstrom EA (2016) Increased visual use in chronic ankle instability: a meta-analysis. Med Sci Sports Exerc 48(10):2046–2056. https://doi.org/10.1249/MSS.0000000000000992
25. Waldén M, Hägglund M, Ekstrand J (2006) High risk of new knee injury in elite footballers with previous anterior cruciate ligament injury. Br J Sports Med 40(2):158–162; discussion 158-62. https://doi.org/10.1136/bjsm.2005.021055
26. Bressel E, McNair PJ (2001) Biomechanical behavior of the plantar flexor muscle-tendon unit after an Achilles tendon rupture. Am J Sports Med 29(3):321–326. https://doi.org/10.1177/03635465010290031201
27. Mahieu N (2007) Detection and approach of intrinsic risk factors for Achilles tendinopathy. https://lib.ugent.be/fulltxt/RUG01/001/050/069/RUG01-001050069_2010_0001_AC.pdf. Accessed 20 April 2018
28. Edouard P, Chatard J-C, Fourchet F et al (2011) Invertor and evertor strength in track and field athletes with functional ankle instability. Isokinet Exerc Sci 19:91–96. https://doi.org/10.3233/IES-2011-0402

29. Hertel J, Buckley WE, Denegar CR (2001) Serial testing of postural control after acute lateral ankle sprain. J Athl Train 36 (4):363–368. http://www.ncbi.nlm.nih.gov/pubmed/12937477. Accessed 20 April 2018
30. Brockett CL, Morgan DL, Proske U (2004) Predicting hamstring strain injury in elite athletes. Med Sci Sport Exerc 36(3):379–387. https://doi.org/10.1249/01.MSS.0000117165.75832.05
31. Fousekis K, Tsepis E, Poulmedis P, Athanasopoulos S, Vagenas G (2011) Intrinsic risk factors of non-contact quadriceps and hamstring strains in soccer: a prospective study of 100 professional players. Br J Sports Med 45(9):709–714. https://doi.org/10.1136/bjsm.2010.077560
32. Willems T (2004) Intrinsic risk factors for sports injuries to the lower leg and ankle (Doctoral dissertation, Ghent University)
33. O'Sullivan K, O'Ceallaigh B, O'Connell K, Shafat A (2008) The relationship between previous hamstring injury and the concentric isokinetic knee muscle strength of irish gaelic footballers. BMC Musculoskelet Disord 9 (1):30. https://doi.org/10.1186/1471-2474-9-30
34. Ageberg E, Fridén T (2008) Normalized motor function but impaired sensory function after unilateral non-reconstructed ACL injury: patients compared with uninjured controls. Knee Surg Sports Traumatol Arthrosc 16 (5):449–456. https://doi.org/10.1007/s00167-008-0499-9
35. Button K, van Deursen R, Price P (2008) Recovery in functional non-copers following anterior cruciate ligament rupture as detected by gait kinematics. Phys Ther Sport 9 (2):97–104. https://doi.org/10.1016/J.PTSP.2008.03.001
36. St A, Gibson C, Lambert MMI (2000) Quadriceps and hamstrings peak torque ratio changes in persons with chronic anterior cruciate ligament deficiency. J Orthop Sports Phys Ther 30(7):418–427. https://doi.org/10.2519/jospt.2000.30.7.418. Accessed 20 April 2018
37. Meeuwisse WH, Tyreman H, Hagel B, Emery C (2007) A dynamic model of etiology in sport injury: The recursive nature of risk and causation. Clin J Sport Med 17(3):215–219. https://doi.org/10.1097/JSM.0b013e3180592a48
38. Mathews D, Fox E (1976) The physiological basis of physical education and athletics. Saunders, Philadelphia
39. Fajen BR, Riley MA, Turvey MT (2009) Information, affordances, and the control of action in sport. Int J Sport Psychol 40(1):79–107
40. Kiefer AW, Myer GD (2015) Training the antifragile athlete: a preliminary analysis of neuromuscular training effects on muscle activation dynamics. Nonlinear Dynamics Psychol Life Sci 19(4):489–510
41. Taleb N (2012) Antifragile: things that gain from disorder (Incerto). Random House, New York
42. Benjaminse A, Gokeler A, Dowling AV et al (2015) Optimization of the anterior cruciate ligament injury prevention paradigm: novel feedback techniques to enhance motor learning and reduce injury risk. J Orthop Sports Phys Ther 45(3):170–182. https://doi.org/10.2519/jospt.2015.4986
43. Eckenrode BJ, Carey JL, Sennett BJ, Zgonis MH (2017) Prevention and management of post-operative complications following ACL reconstruction. Curr Rev Musculoskelet Med 10(3):315–321. https://doi.org/10.1007/s12178-017-9427-2
44. Gokeler A, Benjaminse A, Welling W, Alferink M, Eppinga P, Otten B (2015) The effects of attentional focus on jump performance and knee joint kinematics in patients after ACL reconstruction. Phys Ther Sport 16 (2):114–120. https://doi.org/10.1016/J.PTSP.2014.06.002
45. Gokeler A, Benjaminse A, Hewett TE et al (2013) Feedback techniques to target functional deficits following anterior cruciate ligament reconstruction: implications for motor control and reduction of second injury risk. Sports Med 43(11):1065–1074. https://doi.org/10.1007/s40279-013-0095-0
46. Kiefer A, Silva P, Harrison H, Araujo D (2018) Antifragility in sport: leveraging adversity to enhance performance. Sport Exerc Perform Psychol 7(4):342–350. https://doi.org/10.1037/spy0000130
47. Obama BH. State of the union address. 2015
48. Ashley EA (2016) Towards precision medicine. Nat Rev Genet 17(9):507–522. https://doi.org/10.1038/nrg.2016.86
49. Collins F, Varmus H (2015) A new initiative on precision medicine. N Engl J Med 372 (9):793–795. https://doi.org/10.1056/NEJMp1002530
50. Bray MS, Hagberg JM, Pérusse L et al (2009) The human gene map for performance and health-related fitness phenotypes: the 2006–2007 update. Med Sci Sports Exerc 41 (1):35–73. https://doi.org/10.1249/MSS.0b013e3181844179

51. Collins M, Raleigh SM (2009) Genetic risk factors for musculoskeletal soft tissue injuries. Med Sport Sci 54(February):136–149. https://doi.org/10.1159/000235701
52. Agrawal AA (2001) Phenotypic plasticity in the interactions and evolution of species. Science 294(5541):321–326. https://doi.org/10.1126/science.1060701
53. Calabrese EJ, Mattson MP (2011) Hormesis provides a generalized quantitative estimate of biological plasticity. J Cell Commun Signal 5 (1):25–38. https://doi.org/10.1007/s12079-011-0119-1
54. Calabrese EJ (2005) Hormetic dose-response relationships in immunology: occurrence, quantitative features of the dose response, mechanistic foundations, and clinical implications. Crit Rev Toxicol 35(2–3):89–295. https://doi.org/10.1080/10408440590917044
55. Mattson MP, Calabrese EJ (2010) In: Mattson MP, Calabrese EJ (eds) Hormesis: a revolution in biology, toxicology and medicine. Springer, New York, NY. https://doi.org/10.1007/978-1-60761-495-1
56. Sathyan A, Harrison H, Kiefer A, Silva P, MacPherson R, Cohen K (2019) Genetic fuzzy system for anticipating athlete decision making in virtual reality. In: Govdeli Y, Tran AT, Kayacan E (eds) Fuzzy techniques: theory and applications - Proceedings of the 2019 joint world congress of the international fuzzy systems association and the annual conference of the North American Fuzzy Information Processing Society IFSA/NAFIPS'2019, vol 1000. Springer International Publishing, Lafayette, LA, pp 270–284. https://doi.org/10.1007/978-3-030-21920-8
57. Fajen BR, Warren WH (2007) Behavioral dynamics of intercepting a moving target. Exp Brain Res 180(2):303–319. https://doi.org/10.1007/s00221-007-0859-6
58. Clavet S (2016) Motion matching and the road to next-gen animation. In: Proceedings of the game developers conference. https://www.gdcvault.com/play/1023280/Motion-Matching-and-The-Road
59. Harrison HS, Turvey MT, Frank TD (2016) Affordance-based perception-action dynamics: a model of visually guided braking. Psychol Rev 123(3):305–323. https://doi.org/10.1037/rev0000029
60. De Luca C, Gilmore L, Kuznetsov M, Roy S. Filtering the surface EMG signal: movement artifact and baseline noise contamination. J Biomech 2010;43(8):1573–1579. https://www.sciencedirect.com/science/article/pii/S0021929010000631?casa_token=Qt7TLtY5bI4AAAAA:UJH79Tl6k1bMgEJFd8XlaKszjeEC0QGoYDmy8zn97h3NSTE9PlmK289yBBZYopkHoZD_t7oR
61. Smoliga JM, Myers JB, Redfern MS, Lephart SM (2010) Reliability and precision of EMG in leg, torso, and arm muscles during running. J Electromyogr Kinesiol 20(1):e1–e9. https://doi.org/10.1016/j.jelekin.2009.09.002
62. Solnik S, Rider P, Steinweg K, Devita P, Hortobágyi T (2010) Teager-Kaiser energy operator signal conditioning improves EMG onset detection. Eur J Appl Physiol 110(3):489–498. https://doi.org/10.1007/s00421-010-1521-8
63. DiCesare CACA, Kiefer AWAW, Nalepka P, Myer GDGD (2015) Quantification and analysis of saccadic and smooth pursuit eye movements and fixations to detect oculomotor deficits. Behav Res Methods 49(1):258–266. https://doi.org/10.3758/s13428-015-0693-x
64. Olsen A (2012) The Tobii I-VT Fixation filter: algorithm description. https://www.tobiipro.com/siteassets/tobii-pro/learn-and-support/analyze/how-do-we-classify-eye-movements/tobii-pro-i-vt-fixation-filter.pdf
65. Winter DA, Sidwall HG, Hobson DA (1974) Measurement and reduction of noise in kinematics of locomotion. J Biomech 7 (2):157–159. https://doi.org/10.1016/0021-9290(74)90056-6
66. Winter D (2009) Biomechanics and motor control of human movement. Wiley, Hoboken, NJ. https://doi.org/10.29057/xikua.v1i1.1175

# INDEX

## A




Miguel R. Ossandon et al. (eds.), *Biomedical Engineering Technologies: Volume 1*, Methods in Molecular Biology, vol. 2393, https://doi.org/10.1007/978-1-0716-1803-5, © Springer Science+Business Media, LLC, part of Springer Nature 2022

## B

## C

## D

## E

## F

## G



## H

## I



## J



## K



## L

## M

## N



## O

## P

## Q

## R



## S

## T

## U



## V



## W

## Y



## Z